FIRST SEARCH FOR THE EMC EFFECT AND NUCLEAR SHADOWING IN NEUTRINO NUCLEUS DEEP INELASTIC SCATTERING AT MINERVA

By

JOEL A. MOUSSEAU

DISSERTATION PRESENTED TO THE GRADUATE SCHOOL
OF THE UNIVERSITY OF FLORIDA IN PARTIAL FULFILLMENT
OF THE REQUIREMENTS FOR THE DEGREE OF
DOCTOR OF PHILOSOPHY

UNIVERSITY OF FLORIDA

2015

© 2015 Joel A. Mousseau

To all my teachers

ACKNOWLEDGEMENTS

If it takes a village to raise a child, it takes a city to graduate a PhD student. As a result it would be impossible for me to thank everyone who made this all possible.

First off, I need to thank all of the mentors I have had throughout my years as a graduate student. This includes foremost my advisor Heather Ray who always provided patient guidance throughout the years. I must extend special thanks to all of the folks at and around Fermilab: Jorge Morfin, Kevin McFarland, Debbie Harris and Laura Fields. It was always comforting to know all of you were never more than a few steps away from any question I may have had, no matter how big or how small. While not at Fermilab most of the time, I need to thank Jeff Nelson for providing a significant amount of advice and insight as the analysis developed.

Secondly, I need to extend my thanks to all of my family who supported me through all my PhD years. This extends foremost to my wife Rebecca, who stood by me day after day no matter what challenge was baffling me at the time. I would also like to thank my parents, Rick and Rebecca for all of their support during (and before) graduate school. I need to extend extra special thanks to my mother and father in-law Arthur and Suzanne, who have both tolerated a very erratic son-in-law for the past five years. All of my siblings deserve a huge amount of gratitude. Alex, Sam, Liz, Tom thank you for filling my life with laughter whenever we found time to meet up.

Finally, I must acknowledge and thank all of the graduate students and post-docs that make Fermilab a great place to work and Chicago a great place to live. Jesse, Cheryl, Maya, and Rob have been the best officemates I could ask for. Thank you for the thoughtful and oftentimes productive discussions. It was an honor to carpool with Ritoban, Walter, Sam and Marcelle day in and day out, thank you for making the long morning drives on I-290 much more tolerable. Joe and Mohammed, thank you for being crazy enough to move with me from sunny Florida to less-than sunny Illinois.

TABLE OF CONTENTS

page

ACKNOWLEDGEMENTS 4

LIST OF TABLES 10

LIST OF FIGURES 11

ABSTRACT 57

CHAPTER

1 INTRODUCTION 58

1.1 Neutrinos and the Standard Model 58
1.2 Neutrino Oscillations 61
1.3 Neutrino Masses and the Hierarchy Problem 67
1.4 Majorana Neutrinos 68
1.5 Sources of Neutrinos 71

2 THEORY 74

2.1 Neutral Current Interactions 74
2.2 Charged Current Interactions 75
2.2.1 Charged Current Quasi Elastic (CCQE) 76
2.2.2 Charged Current Resonance (CCRES) 76
2.2.3 Inelastic Transition Region 77
2.3 Charged Current Deep Inelastic Scattering (DIS) 77
2.3.1 Definition of DIS 77
2.3.2 Scaling and Bjorken-x 81
2.4 Nuclear Effects in DIS 84
2.4.1 Non-Isoscalarity 84
2.4.2 Nuclear Structure Functions 85
2.4.3 Nuclear Shadowing 86
2.4.4 Anti-Shadowing 88
2.4.5 The EMC Effect 88
2.4.6 Fermi Motion 89

3 EVENT SIMULATION 91

3.1 The GENIE Event Generator 91
3.2 GENIE's Model for DIS 92
3.3 Final State Interactions 94

4 NEUTRINO BEAMLINE 96

4.1 Overview 96
4.2 The Fermilab Accelerator Complex and Main Injector 96
4.3 Neutrinos at the Main Injector 98
4.4 Neutrino Flux Modeling 101
4.4.1 Primary Hadron Production 102
4.4.2 Secondary and Tertiary Hadron Production 104
4.4.3 Magnetic Field and Target Modeling 104
4.5 Summary 106

5 THE MINERνA DETECTOR AND SIMULATION 107

5.1 Detector Hardware 107
5.1.1 Construction and Description 107
5.1.2 The MINERνA Coordinate System 110
5.1.3 Veto Wall and Helium Target 110
5.1.4 Nuclear Targets 111
5.1.5 Tracker and Calorimeters 113
5.2 Readout Electronics 113
5.3 MINERνA Detector Simulation 115
5.4 Detector Calibration 116
5.4.1 Module Mapper 116
5.4.2 PMT Gains 117
5.4.3 Detector Alignment 118
5.4.4 Strip to Strip Normalization 119
5.4.5 Absolute Energy Calibration 120

6 EVENT RECONSTRUCTION 123

6.1 Goals of Event Reconstruction 123
6.2 Time Slicing 124
6.3 Hit Clustering 124
6.4 Tracking 125
6.5 Vertex Reconstruction 126
6.6 Muon Reconstruction 127
6.6.1 Muon Energy 127
6.6.2 Muon Angle 129
6.7 Hadron Energy Reconstruction 130
6.7.1 Definition of Recoil Energy 130
6.7.2 Material Correction 131
6.7.3 Energy Fits 132

7 OVERVIEW OF THE MEASUREMENT 138

7.1 A Note on Units . . . 138
7.2 Cross Section Formula . . . 138

8 EVENT SELECTION AND EFFICIENCY . . . 140

8.1 Data and MC Samples Used . . . 140
8.2 Pre-Cuts . . . 140
8.3 Event Efficiencies and Purities . . . 144
8.4 Event Sample (Data and MC) . . . 145

9 BACKGROUNDS . . . 149

9.1 Non-DIS Backgrounds . . . 149
9.1.1 Construction of Sidebands . . . 152
9.1.2 Fitting Prescription . . . 156
9.1.3 Fit Results . . . 160
9.2 Plastic Background Subtraction . . . 160
9.3 Upstream Energy Cuts . . . 165
9.3.1 z-Vertex Biases in the Nuclear Targets . . . 165
9.3.2 Updated Upstream Energy Cuts . . . 166
9.3.3 Event Scans . . . 167
9.3.4 Upstream Energy Ratio . . . 172
9.3.5 Results of Updated Upstream Energy Cuts . . . 176

10 SYSTEMATIC UNCERTAINTIES . . . 180

10.1 Calculating Systematic Uncertainties . . . 180
10.2 GENIE Uncertainties . . . 180
10.2.1 Rewightable GENIE Uncertainties . . . 180
10.2.2 GENIE FSI Uncertainties . . . 181
10.2.3 Non-Rewightable GENIE Uncertainties . . . 181
10.3 Flux . . . 182
10.4 Absolute Normalization . . . 182
10.5 Non-DIS Background Subtraction . . . 183
10.6 Plastic Background Subtraction . . . 184
10.7 Detector Resolution . . . 184

11 RECONSTRUCTED AND UNFOLDED EVENT YIELDS . . . 187

11.1 Unfolding . . . 187
11.1.1 Unfolding Procedure . . . 188
11.1.2 Unfolding Tunning . . . 188
11.1.2.1 Unfolding With Predicted Backgrounds . . . 190
11.1.2.2 Unfolding True DIS Events . . . 193
11.1.2.3 Summary . . . 194

11.2 Event Yields per Nuclei . . . 198
11.2.1 Reconstructed Kinematics . . . 198
11.2.2 Unfolded Kinematics . . . 206

12 EFFICIENCY CORRECTION AND FLUX DIVISION . . . 215

12.1 Efficiency Correction . . . 215
12.1.1 Overall Efficiency . . . 215
12.1.2 FSI Uncertainties . . . 217
12.2 Flux Division . . . 217
12.3 Target Counting . . . 217

13 CROSS SECTION RESULTS . . . 219

13.1 Closure Tests . . . 219
13.2 Absolute Cross Sections . . . 220
13.3 Cross Section Ratios . . . 224

14 CONCLUSIONS . . . 229

APPENDIX

A SIDEBAND PLOTS . . . 230

A.1 Low W Sideband: $Q^2 \geq 1.0$ (GeV/c)^2 $1.3 \leq W < 1.8$ GeV/c^2 (Before Fitting) 230
A.2 Scale Factors derived per Target / Nucleus for the Low W Sideband: $Q^2 \geq 1.0$ (GeV/c)^2 $1.3 \leq W < 1.8$ GeV/c^2 . . . 280
A.3 Low W Sideband: $Q^2 \geq 1.0$ (GeV/c)^2 $1.3 \leq W < 1.8$ GeV/c^2 (After Fitting) . 281
A.4 Low Q^2 Sideband: $Q^2 < 0.8$ (GeV/c)^2 $W \geq 2.0$ GeV/c^2 (Before Fitting) . . . 331
A.5 Scale Factors derived per Target / Nucleus for the Low Q^2 Sideband: $Q^2 < 0.8$ (GeV/c)^2 $W \geq 2.0$ GeV/c^2 . . . 381
A.6 Low Q^2 Sideband: $Q^2 < 0.8$ (GeV/c)^2 $W \geq 2.0$ GeV/c^2 (After Fitting) . . . 382

B NON-DIS EVENT UNCERTAINTIES (AFTER TUNING) . . . 432

C PLASTIC BACKGROUND SUBTRACTION . . . 527

C.1 Predicted vs. True CH Background . . . 527
C.2 CH Background Data / MC . . . 551
C.3 CH Background Uncertainty Breakdown . . . 563

D MIGRATION MATRICES . . . 575

D.1 Migration Plots . . . 575
D.2 Migration Plots Bin by Bin . . . 595

E EVENT YIELDS (RECONSTRUCTED) 615

E.1 DIS Event Yields Before CH Subtraction 615
E.2 Uncertainties on DIS Event Yield Before CH Subtraction 675
E.3 DIS Event Yields After CH Subtraction 789
E.4 Uncertainties on DIS Event Yield After CH Subtraction 801

F DIS EVENT YIELDS (UNFOLDED KINEMATICS) 821

F.1 DIS Event Yields (Unfolded) 821
F.2 Unfolding Uncertainties 841

G EFFICIENCY PLOTS 879

G.1 Overall Efficiency 879
G.2 Efficiency Uncertainty 917

LIST OF REFERENCES 955

BIOGRAPHICAL SKETCH 961

LIST OF TABLES

Table		page
3-1	Possible intranuclear interactions in GENIE	95
4-1	NuMI focusing uncertainties	106
5-1	Fiducial masses in MINERνA	111
6-1	Minimum ionizing energy of MINERνA materials	132
6-2	Calorimetric scale factors per target	133
8-1	Breakdown of pre-cuts for iron of target 3	144
8-2	Efficiency and purity by target	146
8-3	Inelastic efficiency by target	147
8-4	Non-DIS contamination by target	148
9-1	Breakdown of non-DIS backgrounds	150
9-2	Scale factors from data to MC fit	155
9-3	Final scale factors from data to MC fit	160
9-4	Results of data hand scan	172
9-5	Results of MC hand scan	172
9-6	Comparison of data and MC hand scan	172
9-7	True origin of events upstream of target 3 (unoptimized cuts)	176
9-8	True origin of events upstream of target 3 (optimized cuts)	176

LIST OF FIGURES

Figure		page
1-1	Particles in the Standard Model	59
1-2	Beta Decay spectrum of tritium	60
1-3	SNO results	64
1-4	Neutrino mass hierarchy	67
1-5	Diagram of the KATRIN experiment	69
1-6	Neutrinoless double beta decay	71
1-7	NOvA Sensitivity	73
2-1	Neutral current scattering off an electron	75
2-2	ν_μ nucleon deep inelastic scattering	78
2-3	x_{bj} depdenent effects from e^- DIS	87
2-4	EMC effect of various nuclei	89
4-1	Fermilab booster parameters	97
4-2	Main injector time profile	99
4-3	NuMI target assembly	99
4-4	Neutrino fluxes at MINERνA	100
4-5	NuMI beamline	101
4-6	NA49 data vs. Bertini	103
4-7	MINERνA flux uncertainties	105
5-1	MINERνA detector schematic	108
5-2	MINERνA module	109
5-3	MINERνA detector views	110
5-4	MINERνA nuclear targets	112
5-5	The MINERνA mapper	117
5-6	Gain of MINERνA PMTs	119
5-7	Final MEU fit	122

5-8 Michel energy spectrum in MINERνA 122
6-1 Time profile of a MINERνA readout gate 124
6-2 Track residuals of rock muons 127
6-3 Hadronic energy resolutions 135
6-4 Hadronic energy resolutions 135
6-5 Hadronic energy resolutions 136
6-6 Hadronic energy resolutions 136
6-7 Hadronic energy resolutions 137
8-1 Candidate DIS events in iron of target 2 and tracker modules 45-50 147
9-1 DIS events and backgrounds vs. Q^2 and W 151
9-2 MC contribution to sidebands in fine bins of Q^2 and W 153
9-3 Sideband tuning in Q^2 and W 153
9-4 Data and MC of low W sideband before fitting 154
9-5 Data and MC of low Q^2 sideband before fitting 154
9-6 Scale factors per faux target (low Q^2 template) 158
9-7 Scale factors per faux target (low Q^2 template) compared to the average . . 158
9-8 Scale factors per target for targets containing lead (low Q^2 template) 159
9-9 DIS signal and background before and after background tuning 161
9-10 CH background for carbon of target 3 per faux target set 163
9-11 CH background using 9 faux sets vs. 7 faux sets 164
9-12 True origin of CC inclusive events vs. W (unoptimized cuts) 168
9-13 True origin of DIS events in z 169
9-14 Event display of a mis-identified DIS event 170
9-15 Upstream energy ratio for carbon of target 3 173
9-16 Upstream energy ratio for iron of target 3 174
9-17 Upstream energy ratio for lead of target 3 174
9-18 Data / MC of upstream energy ratio for carbon and iron of target 3 175

9-19 Data / MC of upstream energy ratio for lead of target 3 175
9-20 True origin of CC inclusive events(optimized cuts) 177
9-21 CH backgrounds before and afer upstream energy cut optimization 179
10-1 Systematic uncertainties on mis-identified DIS events 183
10-2 Systematic uncertainty on CH background extrapolation 185
11-1 E_ν migration 189
11-2 x_{bj} migration 189
11-3 Reweight function for unfolding stuides 190
11-4 Fake data univerese for unfolding tuning 191
11-5 Unfolding backgrounds subtracted fake data: E_ν(CH) 192
11-6 Unfolding backgrounds subtracted fake data: x_{bj}(CH) 193
11-7 Unfolding backgrounds subtracted fake data: E_ν(C) 194
11-8 Unfolding backgrounds subtracted fake data: x_{bj}(C) 195
11-9 Unfolding true DIS fake data: E_ν(CH) 195
11-10 Unfolding true DIS fake data: x_{bj}(CH) 196
11-11 Unfolding true DIS fake data: E_ν(C) 196
11-12 Unfolding true DIS fake data: x_{bj}(C) 197
11-13 C and CH DIS events as a function of E_ν 199
11-14 Fe and CH DIS events as a function of E_ν 199
11-15 Pb and CH DIS events as a function of E_ν 200
11-16 CH DIS events as a function of E_ν 200
11-17 C and CH DIS events as a function of x_{bj} 201
11-18 Fe and CH DIS events as a function of x_{bj} 201
11-19 Pb and CH DIS events as a function of x_{bj} 202
11-20 CH DIS events as a function of x_{bj} 202
11-21 C only DIS events as a function of E_ν 203
11-22 Fe only DIS events as a function of E_ν 203

11-23 Pb only DIS events as a function of E_ν 204
11-24 C only DIS events as a function of x_{bj} 204
11-25 Fe only DIS events as a function of x_{bj} 205
11-26 Pb only DIS events as a function of x_{bj} 205
11-27 C only DIS events as a function of unfolded E_ν 207
11-28 Fe only DIS events as a function of unfolded E_ν 207
11-29 Pb only DIS events as a function of unfolded E_ν 208
11-30 CH only DIS events as a function of unfolded E_ν 208
11-31 C only DIS events as a function of unfolded x_{bj} 209
11-32 Fe only DIS events as a function of unfolded x_{bj} 209
11-33 Pb only DIS events as a function of unfolded x_{bj} 210
11-34 CH only DIS events as a function of unfolded x_{bj} 210
11-35 Reconstructed vs. unfolded comparison of E_ν (C) 211
11-36 Reconstructed vs. unfolded comparison of E_ν (Fe) 211
11-37 Reconstructed vs. unfolded comparison of E_ν (Pb) 212
11-38 Reconstructed vs. unfolded comparison of E_ν (CH) 212
11-39 Reconstructed vs. unfolded comparison of x_{bj} (C) 213
11-40 Reconstructed vs. unfolded comparison of x_{bj} (Fe) 213
11-41 Reconstructed vs. unfolded comparison of x_{bj} (Pb) 214
11-42 Reconstructed vs. unfolded comparison of x_{bj} (CH) 214
12-1 Overall efficiency for lead of target 4 as a function of E_ν 216
12-2 Overall efficiency for lead of target 4 as a function of W 216
12-3 Leading uncertainties on overall efficiency 218
13-1 Reconstructed vs. unfolded comparison of x_{bj} (lead) 219
13-2 DIS $\sigma(E_\nu)$ for C 221
13-3 DIS $\sigma(E_\nu)$ for Fe 221
13-4 DIS $\sigma(E_\nu)$ for Pb 222

13-5 DIS $\sigma(E_\nu)$ for CH 222
13-6 DIS $\frac{d\sigma}{dx_{bj}}$ for C 223
13-7 DIS $\frac{d\sigma}{dx_{bj}}$ for Fe 223
13-8 DIS $\frac{d\sigma}{dx_{bj}}$ for Pb 224
13-9 DIS $\frac{d\sigma}{dx_{bj}}$ for CH 224
13-10 DIS σ^C/σ^{CH} 226
13-11 DIS σ^{Fe}/σ^{CH} 226
13-12 DIS σ^{Pb}/σ^{CH} 227
13-13 DIS $\frac{d\sigma^C}{dx_{bj}}/\frac{d\sigma^{CH}}{dx_{bj}}$ 227
13-14 DIS $\frac{d\sigma^{Fe}}{dx_{bj}}/\frac{d\sigma^{CH}}{dx_{bj}}$ 228
13-15 DIS $\frac{d\sigma^{Pb}}{dx_{bj}}/\frac{d\sigma^{CH}}{dx_{bj}}$ 228
A-1 Data / MC low W sideband before fitting: target 01 Fe (E_ν) 230
A-2 Data / MC low W sideband before fitting: target 01 Pb (E_ν) 231
A-3 Data / MC low W sideband before fitting: target 02 Fe (E_ν) 231
A-4 Data / MC low W sideband before fitting: target 02 Pb (E_ν) 232
A-5 Data / MC low W sideband before fitting: target 03 C (E_ν) 232
A-6 Data / MC low W sideband before fitting: target 03 Fe (E_ν) 233
A-7 Data / MC low W sideband before fitting: target 03 Pb (E_ν) 233
A-8 Data / MC low W sideband before fitting: target 04 Pb (E_ν) 234
A-9 Data / MC low W sideband before fitting: target 05 Fe (E_ν) 234
A-10 Data / MC low W sideband before fitting: target 05 Pb (E_ν) 235
A-11 Data / MC low W sideband before fitting: tracker mods. 27-32 (E_ν) 235
A-12 Data / MC low W sideband before fitting: tracker mods. 33-38 (E_ν) 236
A-13 Data / MC low W sideband before fitting: tracker mods. 39-44 (E_ν) 236
A-14 Data / MC low W sideband before fitting: tracker mods. 45-50 (E_ν) 237
A-15 Data / MC low W sideband before fitting: tracker mods. 51-56 (E_ν) 237
A-16 Data / MC low W sideband before fitting: tracker mods. 57-62 (E_ν) 238

A-17 Data / MC low W sideband before fitting: tracker mods. 63-68 (E_ν) 238
A-18 Data / MC low W sideband before fitting: tracker mods. 69-74 (E_ν) 239
A-19 Data / MC low W sideband before fitting: tracker mods. 75-80 (E_ν) 239
A-20 Data / MC low W sideband before fitting: target 01 Fe (Q^2) 240
A-21 Data / MC low W sideband before fitting: target 01 Pb (Q^2) 241
A-22 Data / MC low W sideband before fitting: target 02 Fe (Q^2) 241
A-23 Data / MC low W sideband before fitting: target 02 Pb (Q^2) 242
A-24 Data / MC low W sideband before fitting: target 03 C (Q^2) 242
A-25 Data / MC low W sideband before fitting: target 03 Fe (Q^2) 243
A-26 Data / MC low W sideband before fitting: target 03 Pb (Q^2) 243
A-27 Data / MC low W sideband before fitting: target 04 Pb (Q^2) 244
A-28 Data / MC low W sideband before fitting: target 05 Fe (Q^2) 244
A-29 Data / MC low W sideband before fitting: target 05 Pb (Q^2) 245
A-30 Data / MC low W sideband before fitting: tracker mods. 27-32 (Q^2) 245
A-31 Data / MC low W sideband before fitting: tracker mods. 33-38 (Q^2) 246
A-32 Data / MC low W sideband before fitting: tracker mods. 39-44 (Q^2) 246
A-33 Data / MC low W sideband before fitting: tracker mods. 45-50 (Q^2) 247
A-34 Data / MC low W sideband before fitting: tracker mods. 51-56 (Q^2) 247
A-35 Data / MC low W sideband before fitting: tracker mods. 57-62 (Q^2) 248
A-36 Data / MC low W sideband before fitting: tracker mods. 63-68 (Q^2) 248
A-37 Data / MC low W sideband before fitting: tracker mods. 69-74 (Q^2) 249
A-38 Data / MC low W sideband before fitting: tracker mods. 75-80 (Q^2) 249
A-39 Data / MC low W sideband before fitting: target 01 Fe (x_{bj}) 250
A-40 Data / MC low W sideband before fitting: target 01 Pb (x_{bj}) 251
A-41 Data / MC low W sideband before fitting: target 02 Fe (x_{bj}) 251
A-42 Data / MC low W sideband before fitting: target 02 Pb (x_{bj}) 252
A-43 Data / MC low W sideband before fitting: target 03 C (x_{bj}) 252

A-44 Data / MC low W sideband before fitting: target 03 Fe (x_{bj}) 253
A-45 Data / MC low W sideband before fitting: target 03 Pb (x_{bj}) 253
A-46 Data / MC low W sideband before fitting: target 04 Pb (x_{bj}) 254
A-47 Data / MC low W sideband before fitting: target 05 Fe (x_{bj}) 254
A-48 Data / MC low W sideband before fitting: target 05 Pb (x_{bj}) 255
A-49 Data / MC low W sideband before fitting: tracker mods. 27-32 (x_{bj}) 255
A-50 Data / MC low W sideband before fitting: tracker mods. 33-38 (x_{bj}) 256
A-51 Data / MC low W sideband before fitting: tracker mods. 39-44 (x_{bj}) 256
A-52 Data / MC low W sideband before fitting: tracker mods. 45-50 (x_{bj}) 257
A-53 Data / MC low W sideband before fitting: tracker mods. 51-56 (x_{bj}) 257
A-54 Data / MC low W sideband before fitting: tracker mods. 57-62 (x_{bj}) 258
A-55 Data / MC low W sideband before fitting: tracker mods. 63-68 (x_{bj}) 258
A-56 Data / MC low W sideband before fitting: tracker mods. 69-74 (x_{bj}) 259
A-57 Data / MC low W sideband before fitting: tracker mods. 75-80 (x_{bj}) 259
A-58 Data / MC low W sideband before fitting: target 01 Fe (E_μ) 260
A-59 Data / MC low W sideband before fitting: target 01 Pb (E_μ) 261
A-60 Data / MC low W sideband before fitting: target 02 Fe (E_μ) 261
A-61 Data / MC low W sideband before fitting: target 02 Pb (E_μ) 262
A-62 Data / MC low W sideband before fitting: target 03 C (E_μ) 262
A-63 Data / MC low W sideband before fitting: target 03 Fe (E_μ) 263
A-64 Data / MC low W sideband before fitting: target 03 Pb (E_μ) 263
A-65 Data / MC low W sideband before fitting: target 04 Pb (E_μ) 264
A-66 Data / MC low W sideband before fitting: target 05 Fe (E_μ) 264
A-67 Data / MC low W sideband before fitting: target 05 Pb (E_μ) 265
A-68 Data / MC low W sideband before fitting: tracker mods. 27-32 (E_μ) 265
A-69 Data / MC low W sideband before fitting: tracker mods. 33-38 (E_μ) 266
A-70 Data / MC low W sideband before fitting: tracker mods. 39-44 (E_μ) 266

A-71 Data / MC low W sideband before fitting: tracker mods. 45-50 (E_μ) 267
A-72 Data / MC low W sideband before fitting: tracker mods. 51-56 (E_μ) 267
A-73 Data / MC low W sideband before fitting: tracker mods. 57-62 (E_μ) 268
A-74 Data / MC low W sideband before fitting: tracker mods. 63-68 (E_μ) 268
A-75 Data / MC low W sideband before fitting: tracker mods. 69-74 (E_μ) 269
A-76 Data / MC low W sideband before fitting: tracker mods. 75-80 (E_μ) 269
A-77 Data / MC low W sideband before fitting: target 01 Fe (θ_μ) 270
A-78 Data / MC low W sideband before fitting: target 01 Pb (θ_μ) 271
A-79 Data / MC low W sideband before fitting: target 02 Fe (θ_μ) 271
A-80 Data / MC low W sideband before fitting: target 02 Pb (θ_μ) 272
A-81 Data / MC low W sideband before fitting: target 03 C (θ_μ) 272
A-82 Data / MC low W sideband before fitting: target 03 Fe (θ_μ) 273
A-83 Data / MC low W sideband before fitting: target 03 Pb (θ_μ) 273
A-84 Data / MC low W sideband before fitting: target 04 Pb (θ_μ) 274
A-85 Data / MC low W sideband before fitting: target 05 Fe (θ_μ) 274
A-86 Data / MC low W sideband before fitting: target 05 Pb (θ_μ) 275
A-87 Data / MC low W sideband before fitting: tracker mods. 27-32 (θ_μ) 275
A-88 Data / MC low W sideband before fitting: tracker mods. 33-38 (θ_μ) 276
A-89 Data / MC low W sideband before fitting: tracker mods. 39-44 (θ_μ) 276
A-90 Data / MC low W sideband before fitting: tracker mods. 45-50 (θ_μ) 277
A-91 Data / MC low W sideband before fitting: tracker mods. 51-56 (θ_μ) 277
A-92 Data / MC low W sideband before fitting: tracker mods. 57-62 (θ_μ) 278
A-93 Data / MC low W sideband before fitting: tracker mods. 63-68 (θ_μ) 278
A-94 Data / MC low W sideband before fitting: tracker mods. 69-74 (θ_μ) 279
A-95 Data / MC low W sideband before fitting: tracker mods. 75-80 (θ_μ) 279
A-96 Low W scale factors per target 280
A-97 Data / MC low W sideband after fitting: target 01 Fe (E_ν) 281

A-98 Data / MC low W sideband after fitting: target 01 Pb (E_ν) 282
A-99 Data / MC low W sideband after fitting: target 02 Fe (E_ν) 282
A-100 Data / MC low W sideband after fitting: target 02 Pb (E_ν) 283
A-101 Data / MC low W sideband after fitting: target 03 C (E_ν) 283
A-102 Data / MC low W sideband after fitting: target 03 Fe (E_ν) 284
A-103 Data / MC low W sideband after fitting: target 03 Pb (E_ν) 284
A-104 Data / MC low W sideband after fitting: target 04 Pb (E_ν) 285
A-105 Data / MC low W sideband after fitting: target 05 Fe (E_ν) 285
A-106 Data / MC low W sideband after fitting: target 05 Pb (E_ν) 286
A-107 Data / MC low W sideband after fitting: tracker mods. 27-32 (E_ν) 286
A-108 Data / MC low W sideband after fitting: tracker mods. 33-38 (E_ν) 287
A-109 Data / MC low W sideband after fitting: tracker mods. 39-44 (E_ν) 287
A-110 Data / MC low W sideband after fitting: tracker mods. 45-50 (E_ν) 288
A-111 Data / MC low W sideband after fitting: tracker mods. 51-56 (E_ν) 288
A-112 Data / MC low W sideband after fitting: tracker mods. 57-62 (E_ν) 289
A-113 Data / MC low W sideband after fitting: tracker mods. 63-68 (E_ν) 289
A-114 Data / MC low W sideband after fitting: tracker mods. 69-74 (E_ν) 290
A-115 Data / MC low W sideband after fitting: tracker mods. 75-80 (E_ν) 290
A-116 Data / MC low W sideband after fitting: target 01 Fe (Q^2) 291
A-117 Data / MC low W sideband after fitting: target 01 Pb (Q^2) 292
A-118 Data / MC low W sideband after fitting: target 02 Fe (Q^2) 292
A-119 Data / MC low W sideband after fitting: target 02 Pb (Q^2) 293
A-120 Data / MC low W sideband after fitting: target 03 C (Q^2) 293
A-121 Data / MC low W sideband after fitting: target 03 Fe (Q^2) 294
A-122 Data / MC low W sideband after fitting: target 03 Pb (Q^2) 294
A-123 Data / MC low W sideband after fitting: target 04 Pb (Q^2) 295
A-124 Data / MC low W sideband after fitting: target 05 Fe (Q^2) 295

A-125 Data / MC low W sideband after fitting: target 05 Pb (Q^2) 296
A-126 Data / MC low W sideband after fitting: tracker mods. 27-32 (Q^2) 296
A-127 Data / MC low W sideband after fitting: tracker mods. 33-38 (Q^2) 297
A-128 Data / MC low W sideband after fitting: tracker mods. 39-44 (Q^2) 297
A-129 Data / MC low W sideband after fitting: tracker mods. 45-50 (Q^2) 298
A-130 Data / MC low W sideband after fitting: tracker mods. 51-56 (Q^2) 298
A-131 Data / MC low W sideband after fitting: tracker mods. 57-62 (Q^2) 299
A-132 Data / MC low W sideband after fitting: tracker mods. 63-68 (Q^2) 299
A-133 Data / MC low W sideband after fitting: tracker mods. 69-74 (Q^2) 300
A-134 Data / MC low W sideband after fitting: tracker mods. 75-80 (Q^2) 300
A-135 Data / MC low W sideband after fitting: target 01 Fe (x_{bj}) 301
A-136 Data / MC low W sideband after fitting: target 01 Pb (x_{bj}) 302
A-137 Data / MC low W sideband after fitting: target 02 Fe (x_{bj}) 302
A-138 Data / MC low W sideband after fitting: target 02 Pb (x_{bj}) 303
A-139 Data / MC low W sideband after fitting: target 03 C (x_{bj}) 303
A-140 Data / MC low W sideband after fitting: target 03 Fe (x_{bj}) 304
A-141 Data / MC low W sideband after fitting: target 03 Pb (x_{bj}) 304
A-142 Data / MC low W sideband after fitting: target 04 Pb (x_{bj}) 305
A-143 Data / MC low W sideband after fitting: target 05 Fe (x_{bj}) 305
A-144 Data / MC low W sideband after fitting: target 05 Pb (x_{bj}) 306
A-145 Data / MC low W sideband after fitting: tracker mods. 27-32 (x_{bj}) 306
A-146 Data / MC low W sideband after fitting: tracker mods. 33-38 (x_{bj}) 307
A-147 Data / MC low W sideband after fitting: tracker mods. 39-44 (x_{bj}) 307
A-148 Data / MC low W sideband after fitting: tracker mods. 45-50 (x_{bj}) 308
A-149 Data / MC low W sideband after fitting: tracker mods. 51-56 (x_{bj}) 308
A-150 Data / MC low W sideband after fitting: tracker mods. 57-62 (x_{bj}) 309
A-151 Data / MC low W sideband after fitting: tracker mods. 63-68 (x_{bj}) 309

A-152 Data / MC low W sideband after fitting: tracker mods. 69-74 (x_{bj}) 310
A-153 Data / MC low W sideband after fitting: tracker mods. 75-80 (x_{bj}) 310
A-154 Data / MC low W sideband after fitting: target 01 Fe (E_μ) 311
A-155 Data / MC low W sideband after fitting: target 01 Pb (E_μ) 312
A-156 Data / MC low W sideband after fitting: target 02 Fe (E_μ) 312
A-157 Data / MC low W sideband after fitting: target 02 Pb (E_μ) 313
A-158 Data / MC low W sideband after fitting: target 03 C (E_μ) 313
A-159 Data / MC low W sideband after fitting: target 03 Fe (E_μ) 314
A-160 Data / MC low W sideband after fitting: target 03 Pb (E_μ) 314
A-161 Data / MC low W sideband after fitting: target 04 Pb (E_μ) 315
A-162 Data / MC low W sideband after fitting: target 05 Fe (E_μ) 315
A-163 Data / MC low W sideband after fitting: target 05 Pb (E_μ) 316
A-164 Data / MC low W sideband after fitting: tracker mods. 27-32 (E_μ) 316
A-165 Data / MC low W sideband after fitting: tracker mods. 33-38 (E_μ) 317
A-166 Data / MC low W sideband after fitting: tracker mods. 39-44 (E_μ) 317
A-167 Data / MC low W sideband after fitting: tracker mods. 45-50 (E_μ) 318
A-168 Data / MC low W sideband after fitting: tracker mods. 51-56 (E_μ) 318
A-169 Data / MC low W sideband after fitting: tracker mods. 57-62 (E_μ) 319
A-170 Data / MC low W sideband after fitting: tracker mods. 63-68 (E_μ) 319
A-171 Data / MC low W sideband after fitting: tracker mods. 69-74 (E_μ) 320
A-172 Data / MC low W sideband after fitting: tracker mods. 75-80 (E_μ) 320
A-173 Data / MC low W sideband after fitting: target 01 Fe (θ_μ) 321
A-174 Data / MC low W sideband after fitting: target 01 Pb (θ_μ) 322
A-175 Data / MC low W sideband after fitting: target 02 Fe (θ_μ) 322
A-176 Data / MC low W sideband after fitting: target 02 Pb (θ_μ) 323
A-177 Data / MC low W sideband after fitting: target 03 C (θ_μ) 323
A-178 Data / MC low W sideband after fitting: target 03 Fe (θ_μ) 324

A-179 Data / MC low W sideband after fitting: target 03 Pb (θ_μ) 324
A-180 Data / MC low W sideband after fitting: target 04 Pb (θ_μ) 325
A-181 Data / MC low W sideband after fitting: target 05 Fe (θ_μ) 325
A-182 Data / MC low W sideband after fitting: target 05 Pb (θ_μ) 326
A-183 Data / MC low W sideband after fitting: tracker mods. 27-32 (θ_μ) 326
A-184 Data / MC low W sideband after fitting: tracker mods. 33-38 (θ_μ) 327
A-185 Data / MC low W sideband after fitting: tracker mods. 39-44 (θ_μ) 327
A-186 Data / MC low W sideband after fitting: tracker mods. 45-50 (θ_μ) 328
A-187 Data / MC low W sideband after fitting: tracker mods. 51-56 (θ_μ) 328
A-188 Data / MC low W sideband after fitting: tracker mods. 57-62 (θ_μ) 329
A-189 Data / MC low W sideband after fitting: tracker mods. 63-68 (θ_μ) 329
A-190 Data / MC low W sideband after fitting: tracker mods. 69-74 (θ_μ) 330
A-191 Data / MC low W sideband after fitting: tracker mods. 75-80 (θ_μ) 330
A-192 Data / MC low Q^2 sideband before fitting: target 01 Fe (E_ν) 331
A-193 Data / MC low Q^2 sideband before fitting: target 01 Pb (E_ν) 332
A-194 Data / MC low Q^2 sideband before fitting: target 02 Fe (E_ν) 332
A-195 Data / MC low Q^2 sideband before fitting: target 02 Pb (E_ν) 333
A-196 Data / MC low Q^2 sideband before fitting: target 03 C (E_ν) 333
A-197 Data / MC low Q^2 sideband before fitting: target 03 Fe (E_ν) 334
A-198 Data / MC low Q^2 sideband before fitting: target 03 Pb (E_ν) 334
A-199 Data / MC low Q^2 sideband before fitting: target 04 Pb (E_ν) 335
A-200 Data / MC low Q^2 sideband before fitting: target 05 Fe (E_ν) 335
A-201 Data / MC low Q^2 sideband before fitting: target 05 Pb (E_ν) 336
A-202 Data / MC low Q^2 sideband before fitting: tracker mods. 27-32 (E_ν) 336
A-203 Data / MC low Q^2 sideband before fitting: tracker mods. 33-38 (E_ν) 337
A-204 Data / MC low Q^2 sideband before fitting: tracker mods. 39-44 (E_ν) 337
A-205 Data / MC low Q^2 sideband before fitting: tracker mods. 45-50 (E_ν) 338

A-206 Data / MC low Q^2 sideband before fitting: tracker mods. 51-56 (E_ν) 338
A-207 Data / MC low Q^2 sideband before fitting: tracker mods. 57-62 (E_ν) 339
A-208 Data / MC low Q^2 sideband before fitting: tracker mods. 63-68 (E_ν) 339
A-209 Data / MC low Q^2 sideband before fitting: tracker mods. 69-74 (E_ν) 340
A-210 Data / MC low Q^2 sideband before fitting: tracker mods. 75-80 (E_ν) 340
A-211 Data / MC low Q^2 sideband before fitting: target 01 Fe (W) 341
A-212 Data / MC low Q^2 sideband before fitting: target 01 Pb (W) 342
A-213 Data / MC low Q^2 sideband before fitting: target 02 Fe (W) 342
A-214 Data / MC low Q^2 sideband before fitting: target 02 Pb (W) 343
A-215 Data / MC low Q^2 sideband before fitting: target 03 C (W) 343
A-216 Data / MC low Q^2 sideband before fitting: target 03 Fe (W) 344
A-217 Data / MC low Q^2 sideband before fitting: target 03 Pb (W) 344
A-218 Data / MC low Q^2 sideband before fitting: target 04 Pb (W) 345
A-219 Data / MC low Q^2 sideband before fitting: target 05 Fe (W) 345
A-220 Data / MC low Q^2 sideband before fitting: target 05 Pb (W) 346
A-221 Data / MC low Q^2 sideband before fitting: tracker mods. 27-32 (W) 346
A-222 Data / MC low Q^2 sideband before fitting: tracker mods. 33-38 (W) 347
A-223 Data / MC low Q^2 sideband before fitting: tracker mods. 39-44 (W) 347
A-224 Data / MC low Q^2 sideband before fitting: tracker mods. 45-50 (W) 348
A-225 Data / MC low Q^2 sideband before fitting: tracker mods. 51-56 (W) 348
A-226 Data / MC low Q^2 sideband before fitting: tracker mods. 57-62 (W) 349
A-227 Data / MC low Q^2 sideband before fitting: tracker mods. 63-68 (W) 349
A-228 Data / MC low Q^2 sideband before fitting: tracker mods. 69-74 (W) 350
A-229 Data / MC low Q^2 sideband before fitting: tracker mods. 75-80 (W) 350
A-230 Data / MC low Q^2 sideband before fitting: target 01 Fe (x_{bj}) 351
A-231 Data / MC low Q^2 sideband before fitting: target 01 Pb (x_{bj}) 352
A-232 Data / MC low Q^2 sideband before fitting: target 02 Fe (x_{bj}) 352

A-233 Data / MC low Q^2 sideband before fitting: target 02 Pb (x_{bj}) 353
A-234 Data / MC low Q^2 sideband before fitting: target 03 C (x_{bj}) 353
A-235 Data / MC low Q^2 sideband before fitting: target 03 Fe (x_{bj}) 354
A-236 Data / MC low Q^2 sideband before fitting: target 03 Pb (x_{bj}) 354
A-237 Data / MC low Q^2 sideband before fitting: target 04 Pb (x_{bj}) 355
A-238 Data / MC low Q^2 sideband before fitting: target 05 Fe (x_{bj}) 355
A-239 Data / MC low Q^2 sideband before fitting: target 05 Pb (x_{bj}) 356
A-240 Data / MC low Q^2 sideband before fitting: tracker mods. 27-32 (x_{bj}) 356
A-241 Data / MC low Q^2 sideband before fitting: tracker mods. 33-38 (x_{bj}) 357
A-242 Data / MC low Q^2 sideband before fitting: tracker mods. 39-44 (x_{bj}) 357
A-243 Data / MC low Q^2 sideband before fitting: tracker mods. 45-50 (x_{bj}) 358
A-244 Data / MC low Q^2 sideband before fitting: tracker mods. 51-56 (x_{bj}) 358
A-245 Data / MC low Q^2 sideband before fitting: tracker mods. 57-62 (x_{bj}) 359
A-246 Data / MC low Q^2 sideband before fitting: tracker mods. 63-68 (x_{bj}) 359
A-247 Data / MC low Q^2 sideband before fitting: tracker mods. 69-74 (x_{bj}) 360
A-248 Data / MC low Q^2 sideband before fitting: tracker mods. 75-80 (x_{bj}) 360
A-249 Data / MC low Q^2 sideband before fitting: target 01 Fe (E_μ) 361
A-250 Data / MC low Q^2 sideband before fitting: target 01 Pb (E_μ) 362
A-251 Data / MC low Q^2 sideband before fitting: target 02 Fe (E_μ) 362
A-252 Data / MC low Q^2 sideband before fitting: target 02 Pb (E_μ) 363
A-253 Data / MC low Q^2 sideband before fitting: target 03 C (E_μ) 363
A-254 Data / MC low Q^2 sideband before fitting: target 03 Fe (E_μ) 364
A-255 Data / MC low Q^2 sideband before fitting: target 03 Pb (E_μ) 364
A-256 Data / MC low Q^2 sideband before fitting: target 04 Pb (E_μ) 365
A-257 Data / MC low Q^2 sideband before fitting: target 05 Fe (E_μ) 365
A-258 Data / MC low Q^2 sideband before fitting: target 05 Pb (E_μ) 366
A-259 Data / MC low Q^2 sideband before fitting: tracker mods. 27-32 (E_μ) 366

A-260 Data / MC low Q^2 sideband before fitting: tracker mods. 33-38 (E_μ) 367
A-261 Data / MC low Q^2 sideband before fitting: tracker mods. 39-44 (E_μ) 367
A-262 Data / MC low Q^2 sideband before fitting: tracker mods. 45-50 (E_μ) 368
A-263 Data / MC low Q^2 sideband before fitting: tracker mods. 51-56 (E_μ) 368
A-264 Data / MC low Q^2 sideband before fitting: tracker mods. 57-62 (E_μ) 369
A-265 Data / MC low Q^2 sideband before fitting: tracker mods. 63-68 (E_μ) 369
A-266 Data / MC low Q^2 sideband before fitting: tracker mods. 69-74 (E_μ) 370
A-267 Data / MC low Q^2 sideband before fitting: tracker mods. 75-80 (E_μ) 370
A-268 Data / MC low Q^2 sideband before fitting: target 01 Fe (θ_μ) 371
A-269 Data / MC low Q^2 sideband before fitting: target 01 Pb (θ_μ) 372
A-270 Data / MC low Q^2 sideband before fitting: target 02 Fe (θ_μ) 372
A-271 Data / MC low Q^2 sideband before fitting: target 02 Pb (θ_μ) 373
A-272 Data / MC low Q^2 sideband before fitting: target 03 C (θ_μ) 373
A-273 Data / MC low Q^2 sideband before fitting: target 03 Fe (θ_μ) 374
A-274 Data / MC low Q^2 sideband before fitting: target 03 Pb (θ_μ) 374
A-275 Data / MC low Q^2 sideband before fitting: target 04 Pb (θ_μ) 375
A-276 Data / MC low Q^2 sideband before fitting: target 05 Fe (θ_μ) 375
A-277 Data / MC low Q^2 sideband before fitting: target 05 Pb (θ_μ) 376
A-278 Data / MC low Q^2 sideband before fitting: tracker mods. 27-32 (θ_μ) 376
A-279 Data / MC low Q^2 sideband before fitting: tracker mods. 33-38 (θ_μ) 377
A-280 Data / MC low Q^2 sideband before fitting: tracker mods. 39-44 (θ_μ) 377
A-281 Data / MC low Q^2 sideband before fitting: tracker mods. 45-50 (θ_μ) 378
A-282 Data / MC low Q^2 sideband before fitting: tracker mods. 51-56 (θ_μ) 378
A-283 Data / MC low Q^2 sideband before fitting: tracker mods. 57-62 (θ_μ) 379
A-284 Data / MC low Q^2 sideband before fitting: tracker mods. 63-68 (θ_μ) 379
A-285 Data / MC low Q^2 sideband before fitting: tracker mods. 69-74 (θ_μ) 380
A-286 Data / MC low Q^2 sideband before fitting: tracker mods. 75-80 (θ_μ) 380

A-287 Low Q^2 scale factors per target 381
A-288 Data / MC low Q^2 sideband after fitting: target 01 Fe (E_ν) 382
A-289 Data / MC low Q^2 sideband after fitting: target 01 Pb (E_ν) 383
A-290 Data / MC low Q^2 sideband after fitting: target 02 Fe (E_ν) 383
A-291 Data / MC low Q^2 sideband after fitting: target 02 Pb (E_ν) 384
A-292 Data / MC low Q^2 sideband after fitting: target 03 C (E_ν) 384
A-293 Data / MC low Q^2 sideband after fitting: target 03 Fe (E_ν) 385
A-294 Data / MC low Q^2 sideband after fitting: target 03 Pb (E_ν) 385
A-295 Data / MC low Q^2 sideband after fitting: target 04 Pb (E_ν) 386
A-296 Data / MC low Q^2 sideband after fitting: target 05 Fe (E_ν) 386
A-297 Data / MC low Q^2 sideband after fitting: target 05 Pb (E_ν) 387
A-298 Data / MC low Q^2 sideband after fitting: tracker mods. 27-32 (E_ν) 387
A-299 Data / MC low Q^2 sideband after fitting: tracker mods. 33-38 (E_ν) 388
A-300 Data / MC low Q^2 sideband after fitting: tracker mods. 39-44 (E_ν) 388
A-301 Data / MC low Q^2 sideband after fitting: tracker mods. 45-50 (E_ν) 389
A-302 Data / MC low Q^2 sideband after fitting: tracker mods. 51-56 (E_ν) 389
A-303 Data / MC low Q^2 sideband after fitting: tracker mods. 57-62 (E_ν) 390
A-304 Data / MC low Q^2 sideband after fitting: tracker mods. 63-68 (E_ν) 390
A-305 Data / MC low Q^2 sideband after fitting: tracker mods. 69-74 (E_ν) 391
A-306 Data / MC low Q^2 sideband after fitting: tracker mods. 75-80 (E_ν) 391
A-307 Data / MC low Q^2 sideband after fitting: target 01 Fe (W) 392
A-308 Data / MC low Q^2 sideband after fitting: target 01 Pb (W) 393
A-309 Data / MC low Q^2 sideband after fitting: target 02 Fe (W) 393
A-310 Data / MC low Q^2 sideband after fitting: target 02 Pb (W) 394
A-311 Data / MC low Q^2 sideband after fitting: target 03 C (W) 394
A-312 Data / MC low Q^2 sideband after fitting: target 03 Fe (W) 395
A-313 Data / MC low Q^2 sideband after fitting: target 03 Pb (W) 395

A-314 Data / MC low Q^2 sideband after fitting: target 04 Pb (W) 396
A-315 Data / MC low Q^2 sideband after fitting: target 05 Fe (W) 396
A-316 Data / MC low Q^2 sideband after fitting: target 05 Pb (W) 397
A-317 Data / MC low Q^2 sideband after fitting: tracker mods. 27-32 (W) 397
A-318 Data / MC low Q^2 sideband after fitting: tracker mods. 33-38 (W) 398
A-319 Data / MC low Q^2 sideband after fitting: tracker mods. 39-44 (W) 398
A-320 Data / MC low Q^2 sideband after fitting: tracker mods. 45-50 (W) 399
A-321 Data / MC low Q^2 sideband after fitting: tracker mods. 51-56 (W) 399
A-322 Data / MC low Q^2 sideband after fitting: tracker mods. 57-62 (W) 400
A-323 Data / MC low Q^2 sideband after fitting: tracker mods. 63-68 (W) 400
A-324 Data / MC low Q^2 sideband after fitting: tracker mods. 69-74 (W) 401
A-325 Data / MC low Q^2 sideband after fitting: tracker mods. 75-80 (W) 401
A-326 Data / MC low Q^2 sideband after fitting: target 01 Fe (x_{bj}) 402
A-327 Data / MC low Q^2 sideband after fitting: target 01 Pb (x_{bj}) 403
A-328 Data / MC low Q^2 sideband after fitting: target 02 Fe (x_{bj}) 403
A-329 Data / MC low Q^2 sideband after fitting: target 02 Pb (x_{bj}) 404
A-330 Data / MC low Q^2 sideband after fitting: target 03 C (x_{bj}) 404
A-331 Data / MC low Q^2 sideband after fitting: target 03 Fe (x_{bj}) 405
A-332 Data / MC low Q^2 sideband after fitting: target 03 Pb (x_{bj}) 405
A-333 Data / MC low Q^2 sideband after fitting: target 04 Pb (x_{bj}) 406
A-334 Data / MC low Q^2 sideband after fitting: target 05 Fe (x_{bj}) 406
A-335 Data / MC low Q^2 sideband after fitting: target 05 Pb (x_{bj}) 407
A-336 Data / MC low Q^2 sideband after fitting: tracker mods. 27-32 (x_{bj}) 407
A-337 Data / MC low Q^2 sideband after fitting: tracker mods. 33-38 (x_{bj}) 408
A-338 Data / MC low Q^2 sideband after fitting: tracker mods. 39-44 (x_{bj}) 408
A-339 Data / MC low Q^2 sideband after fitting: tracker mods. 45-50 (x_{bj}) 409
A-340 Data / MC low Q^2 sideband after fitting: tracker mods. 51-56 (x_{bj}) 409

A-341 Data / MC low Q^2 sideband after fitting: tracker mods. 57-62 (x_{bj}) 410
A-342 Data / MC low Q^2 sideband after fitting: tracker mods. 63-68 (x_{bj}) 410
A-343 Data / MC low Q^2 sideband after fitting: tracker mods. 69-74 (x_{bj}) 411
A-344 Data / MC low Q^2 sideband after fitting: tracker mods. 75-80 (x_{bj}) 411
A-345 Data / MC low Q^2 sideband after fitting: target 01 Fe (E_μ) 412
A-346 Data / MC low Q^2 sideband after fitting: target 01 Pb (E_μ) 413
A-347 Data / MC low Q^2 sideband after fitting: target 02 Fe (E_μ) 413
A-348 Data / MC low Q^2 sideband after fitting: target 02 Pb (E_μ) 414
A-349 Data / MC low Q^2 sideband after fitting: target 03 C (E_μ) 414
A-350 Data / MC low Q^2 sideband after fitting: target 03 Fe (E_μ) 415
A-351 Data / MC low Q^2 sideband after fitting: target 03 Pb (E_μ) 415
A-352 Data / MC low Q^2 sideband after fitting: target 04 Pb (E_μ) 416
A-353 Data / MC low Q^2 sideband after fitting: target 05 Fe (E_μ) 416
A-354 Data / MC low Q^2 sideband after fitting: target 05 Pb (E_μ) 417
A-355 Data / MC low Q^2 sideband after fitting: tracker mods. 27-32 (E_μ) 417
A-356 Data / MC low Q^2 sideband after fitting: tracker mods. 33-38 (E_μ) 418
A-357 Data / MC low Q^2 sideband after fitting: tracker mods. 39-44 (E_μ) 418
A-358 Data / MC low Q^2 sideband after fitting: tracker mods. 45-50 (E_μ) 419
A-359 Data / MC low Q^2 sideband after fitting: tracker mods. 51-56 (E_μ) 419
A-360 Data / MC low Q^2 sideband after fitting: tracker mods. 57-62 (E_μ) 420
A-361 Data / MC low Q^2 sideband after fitting: tracker mods. 63-68 (E_μ) 420
A-362 Data / MC low Q^2 sideband after fitting: tracker mods. 69-74 (E_μ) 421
A-363 Data / MC low Q^2 sideband after fitting: tracker mods. 75-80 (E_μ) 421
A-364 Data / MC low Q^2 sideband after fitting: target 01 Fe (θ_μ) 422
A-365 Data / MC low Q^2 sideband after fitting: target 01 Pb (θ_μ) 423
A-366 Data / MC low Q^2 sideband after fitting: target 02 Fe (θ_μ) 423
A-367 Data / MC low Q^2 sideband after fitting: target 02 Pb (θ_μ) 424

A-368 Data / MC low Q^2 sideband after fitting: target 03 C (θ_μ) 424
A-369 Data / MC low Q^2 sideband after fitting: target 03 Fe (θ_μ) 425
A-370 Data / MC low Q^2 sideband after fitting: target 03 Pb (θ_μ) 425
A-371 Data / MC low Q^2 sideband after fitting: target 04 Pb (θ_μ) 426
A-372 Data / MC low Q^2 sideband after fitting: target 05 Fe (θ_μ) 426
A-373 Data / MC low Q^2 sideband after fitting: target 05 Pb (θ_μ) 427
A-374 Data / MC low Q^2 sideband after fitting: tracker mods. 27-32 (θ_μ) 427
A-375 Data / MC low Q^2 sideband after fitting: tracker mods. 33-38 (θ_μ) 428
A-376 Data / MC low Q^2 sideband after fitting: tracker mods. 39-44 (θ_μ) 428
A-377 Data / MC low Q^2 sideband after fitting: tracker mods. 45-50 (θ_μ) 429
A-378 Data / MC low Q^2 sideband after fitting: tracker mods. 51-56 (θ_μ) 429
A-379 Data / MC low Q^2 sideband after fitting: tracker mods. 57-62 (θ_μ) 430
A-380 Data / MC low Q^2 sideband after fitting: tracker mods. 63-68 (θ_μ) 430
A-381 Data / MC low Q^2 sideband after fitting: tracker mods. 69-74 (θ_μ) 431
A-382 Data / MC low Q^2 sideband after fitting: tracker mods. 75-80 (θ_μ) 431
B-1 Uncertainties on mis-ided DIS events: target 01 Fe (E_ν) 432
B-2 Uncertainties on mis-ided DIS events: target 02 Pb (E_ν) 433
B-3 Uncertainties on mis-ided DIS events: target 02 Fe (E_ν) 434
B-4 Uncertainties on mis-ided DIS events: target 02 Pb (E_ν) 435
B-5 Uncertainties on mis-ided DIS events: target 03 C (E_ν) 436
B-6 Uncertainties on mis-ided DIS events: target 03 Fe (E_ν) 437
B-7 Uncertainties on mis-ided DIS events: target 03 Pb (E_ν) 438
B-8 Uncertainties on mis-ided DIS events: target 04 Pb (E_ν) 439
B-9 Uncertainties on mis-ided DIS events: target 05 Fe (E_ν) 440
B-10 Uncertainties on mis-ided DIS events: target 05 Pb (E_ν) 441
B-11 Uncertainties on mis-ided DIS events: tracker mods. 27-32 (E_ν) 442
B-12 Uncertainties on mis-ided DIS events: tracker mods. 33-38 (E_ν) 443

B-13 Uncertainties on mis-ided DIS events: tracker mods. 39-44 (E_ν) 444
B-14 Uncertainties on mis-ided DIS events: tracker mods. 45-50 (E_ν) 445
B-15 Uncertainties on mis-ided DIS events: tracker mods. 51-56 (E_ν) 446
B-16 Uncertainties on mis-ided DIS events: tracker mods. 57-62 (E_ν) 447
B-17 Uncertainties on mis-ided DIS events: tracker mods. 63-68 (E_ν) 448
B-18 Uncertainties on mis-ided DIS events: tracker mods. 69-74 (E_ν) 449
B-19 Uncertainties on mis-ided DIS events: tracker mods. 75-80 (E_ν) 450
B-20 Uncertainties on mis-ided DIS events: target 01 Fe (Q^2) 451
B-21 Uncertainties on mis-ided DIS events: target 01 Pb (Q^2) 452
B-22 Uncertainties on mis-ided DIS events: target 02 Fe (Q^2) 453
B-23 Uncertainties on mis-ided DIS events: target 02 Pb (Q^2) 454
B-24 Uncertainties on mis-ided DIS events: target 03 C (Q^2) 455
B-25 Uncertainties on mis-ided DIS events: target 03 Fe (Q^2) 456
B-26 Uncertainties on mis-ided DIS events: target 03 Pb (Q^2) 457
B-27 Uncertainties on mis-ided DIS events: target 04 Pb (Q^2) 458
B-28 Uncertainties on mis-ided DIS events: target 05 Fe (Q^2) 459
B-29 Uncertainties on mis-ided DIS events: target 05 Pb (Q^2) 460
B-30 Uncertainties on mis-ided DIS events: tracker mods. 27-32 (Q^2) 461
B-31 Uncertainties on mis-ided DIS events: tracker mods. 33-38 (Q^2) 462
B-32 Uncertainties on mis-ided DIS events: tracker mods. 39-44 (Q^2) 463
B-33 Uncertainties on mis-ided DIS events: tracker mods. 45-50 (Q^2) 464
B-34 Uncertainties on mis-ided DIS events: tracker mods. 51-56 (Q^2) 465
B-35 Uncertainties on mis-ided DIS events: tracker mods. 57-62 (Q^2) 466
B-36 Uncertainties on mis-ided DIS events: tracker mods. 63-68 (Q^2) 467
B-37 Uncertainties on mis-ided DIS events: tracker mods. 69-74 (Q^2) 468
B-38 Uncertainties on mis-ided DIS events: tracker mods. 75-80 (Q^2) 469
B-39 Uncertainties on mis-ided DIS events: target 01 Fe (W) 470

B-40 Uncertainties on mis-ided DIS events: target 01 Pb (W) 471
B-41 Uncertainties on mis-ided DIS events: target 02 Fe (W) 472
B-42 Uncertainties on mis-ided DIS events: target 02 Pb (W) 473
B-43 Uncertainties on mis-ided DIS events: target 03 C (W) 474
B-44 Uncertainties on mis-ided DIS events: target 03 Fe (W) 475
B-45 Uncertainties on mis-ided DIS events: target 03 Pb (W) 476
B-46 Uncertainties on mis-ided DIS events: target 04 Pb (W) 477
B-47 Uncertainties on mis-ided DIS events: target 05 Fe (W) 478
B-48 Uncertainties on mis-ided DIS events: target 05 Pb (W) 479
B-49 Uncertainties on mis-ided DIS events: tracker mods. 27-32 (W) 480
B-50 Uncertainties on mis-ided DIS events: tracker mods. 33-38 (W) 481
B-51 Uncertainties on mis-ided DIS events: tracker mods. 39-44 (W) 482
B-52 Uncertainties on mis-ided DIS events: tracker mods. 45-50 (W) 483
B-53 Uncertainties on mis-ided DIS events: tracker mods. 51-56 (W) 484
B-54 Uncertainties on mis-ided DIS events: tracker mods. 57-62 (W) 485
B-55 Uncertainties on mis-ided DIS events: tracker mods. 63-68 (W) 486
B-56 Uncertainties on mis-ided DIS events: tracker mods. 69-74 (W) 487
B-57 Uncertainties on mis-ided DIS events: tracker mods. 75-80 (W) 488
B-58 Uncertainties on mis-ided DIS events: target 01 Fe (x_{bj}) 489
B-59 Uncertainties on mis-ided DIS events: target 01 Pb (x_{bj}) 490
B-60 Uncertainties on mis-ided DIS events: target 02 Fe (x_{bj}) 491
B-61 Uncertainties on mis-ided DIS events: target 02 Pb (x_{bj}) 492
B-62 Uncertainties on mis-ided DIS events: target 03 C (x_{bj}) 493
B-63 Uncertainties on mis-ided DIS events: target 03 Fe (x_{bj}) 494
B-64 Uncertainties on mis-ided DIS events: target 03 Pb (x_{bj}) 495
B-65 Uncertainties on mis-ided DIS events: target 04 Pb (x_{bj}) 496
B-66 Uncertainties on mis-ided DIS events: target 05 Fe (x_{bj}) 497

B-67 Uncertainties on mis-ided DIS events: target 05 Pb (x_{bj}) 498
B-68 Uncertainties on mis-ided DIS events: tracker mods. 27-32 (x_{bj}) 499
B-69 Uncertainties on mis-ided DIS events: tracker mods. 33-38 (x_{bj}) 500
B-70 Uncertainties on mis-ided DIS events: tracker mods. 39-44 (x_{bj}) 501
B-71 Uncertainties on mis-ided DIS events: tracker mods. 45-50 (x_{bj}) 502
B-72 Uncertainties on mis-ided DIS events: tracker mods. 51-56 (x_{bj}) 503
B-73 Uncertainties on mis-ided DIS events: tracker mods. 57-62 (x_{bj}) 504
B-74 Uncertainties on mis-ided DIS events: tracker mods. 63-68 (x_{bj}) 505
B-75 Uncertainties on mis-ided DIS events: tracker mods. 69-74 (x_{bj}) 506
B-76 Uncertainties on mis-ided DIS events: tracker mods. 75-80 (x_{bj}) 507
B-77 Uncertainties on mis-ided DIS events: target 01 Fe (E_μ) 508
B-78 Uncertainties on mis-ided DIS events: target 01 Pb (E_μ) 509
B-79 Uncertainties on mis-ided DIS events: target 02 Fe (E_μ) 510
B-80 Uncertainties on mis-ided DIS events: target 02 Pb (E_μ) 511
B-81 Uncertainties on mis-ided DIS events: target 03 C (E_μ) 512
B-82 Uncertainties on mis-ided DIS events: target 03 Fe (E_μ) 513
B-83 Uncertainties on mis-ided DIS events: target 03 Pb (E_μ) 514
B-84 Uncertainties on mis-ided DIS events: target 04 Pb (E_μ) 515
B-85 Uncertainties on mis-ided DIS events: target 05 Fe (E_μ) 516
B-86 Uncertainties on mis-ided DIS events: target 05 Pb (E_μ) 517
B-87 Uncertainties on mis-ided DIS events: tracker mods. 27-32 (E_μ) 518
B-88 Uncertainties on mis-ided DIS events: tracker mods. 33-38 (E_μ) 519
B-89 Uncertainties on mis-ided DIS events: tracker mods. 39-44 (E_μ) 520
B-90 Uncertainties on mis-ided DIS events: tracker mods. 45-50 (E_μ) 521
B-91 Uncertainties on mis-ided DIS events: tracker mods. 51-56 (E_μ) 522
B-92 Uncertainties on mis-ided DIS events: tracker mods. 57-62 (E_μ) 523
B-93 Uncertainties on mis-ided DIS events: tracker mods. 63-68 (E_μ) 524

B-94 Uncertainties on mis-ided DIS events: tracker mods. 69-74 (E_μ) 525
B-95 Uncertainties on mis-ided DIS events: tracker mods. 75-80 (E_μ) 526
C-1 Plastic BG prediction: target 01 Fe (E_ν) 527
C-2 Plastic BG prediction: target 01 Pb (E_ν) 528
C-3 Plastic BG prediction: target 02 Fe (E_ν) 528
C-4 Plastic BG prediction: target 02 Pb (E_ν) 529
C-5 Plastic BG prediction: target 03 C (E_ν) 529
C-6 Plastic BG prediction: target 03 Fe (E_ν) 530
C-7 Plastic BG prediction: target 03 Pb (E_ν) 530
C-8 Plastic BG prediction: target 04 Pb (E_ν) 531
C-9 Plastic BG prediction: target 05 Fe (E_ν) 531
C-10 Plastic BG prediction: target 05 Pb (E_ν) 532
C-11 Plastic BG prediction: target 01 Fe (Q^2) 533
C-12 Plastic BG prediction: target 01 Pb (Q^2) 534
C-13 Plastic BG prediction: target 02 Fe (Q^2) 534
C-14 Plastic BG prediction: target 02 Pb (Q^2) 535
C-15 Plastic BG prediction: target 03 C (Q^2) 535
C-16 Plastic BG prediction: target 03 Fe (Q^2) 536
C-17 Plastic BG prediction: target 03 Pb (Q^2) 536
C-18 Plastic BG prediction: target 04 Pb (Q^2) 537
C-19 Plastic BG prediction: target 05 Fe (Q^2) 537
C-20 Plastic BG prediction: target 05 Pb (Q^2) 538
C-21 Plastic BG prediction: target 01 Fe (W) 539
C-22 Plastic BG prediction: target 02 Pb (W) 540
C-23 Plastic BG prediction: target 02 Fe (W) 540
C-24 Plastic BG prediction: target 02 Pb (W) 541
C-25 Plastic BG prediction: target 03 C (W) 541

C-26 Plastic BG prediction: target 03 Fe (W) 542
C-27 Plastic BG prediction: target 03 Pb (W) 542
C-28 Plastic BG prediction: target 04 Pb (W) 543
C-29 Plastic BG prediction: target 05 Fe (W) 543
C-30 Plastic BG prediction: target 05 Pb (W) 544
C-31 Plastic BG prediction: target 01 Fe (x_{bj}) 545
C-32 Plastic BG prediction: target 01 Pb (x_{bj}) 546
C-33 Plastic BG prediction: target 02 Fe (x_{bj}) 546
C-34 Plastic BG prediction: target 02 Pb (x_{bj}) 547
C-35 Plastic BG prediction: target 03 C (x_{bj}) 547
C-36 Plastic BG prediction: target 03 Fe (x_{bj}) 548
C-37 Plastic BG prediction: target 03 Pb (x_{bj}) 548
C-38 Plastic BG prediction: target 04 Pb (x_{bj}) 549
C-39 Plastic BG prediction: target 05 Fe (x_{bj}) 549
C-40 Plastic BG prediction: target 05 Pb (x_{bj}) 550
C-41 Data / MC of plastic BG prediction: target 01 Fe (E_ν) 551
C-42 Data / MC of plastic BG prediction: target 01 Pb (E_ν) 552
C-43 Data / MC of plastic BG prediction: target 02 Fe (E_ν) 552
C-44 Data / MC of plastic BG prediction: target 02 Pb (E_ν) 553
C-45 Data / MC of plastic BG prediction: target 03 C (E_ν) 553
C-46 Data / MC of plastic BG prediction: target 03 Fe (E_ν) 554
C-47 Data / MC of plastic BG prediction: target 03 Pb (E_ν) 554
C-48 Data / MC of plastic BG prediction: target 04 Pb (E_ν) 555
C-49 Data / MC of plastic BG prediction: target 05 Fe (E_ν) 555
C-50 Data / MC of plastic BG prediction: target 05 Pb (E_ν) 556
C-51 Data / MC of plastic BG prediction: target 01 Fe (x_{bj}) 557
C-52 Data / MC of plastic BG prediction: target 01 Pb (x_{bj}) 558

C-53 Data / MC of plastic BG prediction: target 02 Fe (x_{bj}) 558
C-54 Data / MC of plastic BG prediction: target 02 Pb (x_{bj}) 559
C-55 Data / MC of plastic BG prediction: target 03 C (x_{bj}) 559
C-56 Data / MC of plastic BG prediction: target 03 Fe (x_{bj}) 560
C-57 Data / MC of plastic BG prediction: target 03 Pb (x_{bj}) 560
C-58 Data / MC of plastic BG prediction: target 04 Pb (x_{bj}) 561
C-59 Data / MC of plastic BG prediction: target 05 Fe (x_{bj}) 561
C-60 Data / MC of plastic BG prediction: target 05 Pb (x_{bj}) 562
C-61 Uncertainty on plastic BG prediction: target 01 Fe (E_ν) 563
C-62 Uncertainty on plastic BG prediction: target 01 Pb (E_ν) 564
C-63 Uncertainty on plastic BG prediction: target 02 Fe (E_ν) 564
C-64 Uncertainty on plastic BG prediction: target 02 Pb (E_ν) 565
C-65 Uncertainty on plastic BG prediction: target 03 C (E_ν) 565
C-66 Uncertainty on plastic BG prediction: target 03 Fe (E_ν) 566
C-67 Uncertainty on plastic BG prediction: target 03 Pb (E_ν) 566
C-68 Uncertainty on plastic BG prediction: target 04 Pb (E_ν) 567
C-69 Uncertainty on plastic BG prediction: target 05 Fe (E_ν) 567
C-70 Uncertainty on plastic BG prediction: target 05 Pb (E_ν) 568
C-71 Uncertainty on plastic BG prediction: target 01 Fe (x_{bj}) 569
C-72 Uncertainty on plastic BG prediction: target 01 Pb (x_{bj}) 570
C-73 Uncertainty on plastic BG prediction: target 02 Fe (x_{bj}) 570
C-74 Uncertainty on plastic BG prediction: target 02 Pb (x_{bj}) 571
C-75 Uncertainty on plastic BG prediction: target 03 C (x_{bj}) 571
C-76 Uncertainty on plastic BG prediction: target 03 Fe (x_{bj}) 572
C-77 Uncertainty on plastic BG prediction: target 03 Pb (x_{bj}) 572
C-78 Uncertainty on plastic BG prediction: target 04 Pb (x_{bj}) 573
C-79 Uncertainty on plastic BG prediction: target 05 Fe (x_{bj}) 573

C-80 Uncertainty on plastic BG prediction: target 05 Pb (x_{bj}) 574
D-1 Migration matrix: target 01 Fe (E_ν) 575
D-2 Migration matrix: target 01 Pb (E_ν) 576
D-3 Migration matrix: target 02 Fe (E_ν) 576
D-4 Migration matrix: target 02 Pb (E_ν) 577
D-5 Migration matrix: target 03 C (E_ν) 577
D-6 Migration matrix: target 03 Fe (E_ν) 578
D-7 Migration matrix: target 03 Pb (E_ν) 578
D-8 Migration matrix: target 04 Pb (E_ν) 579
D-9 Migration matrix: target 05 Fe (E_ν) 579
D-10 Migration matrix: target 05 Pb (E_ν) 580
D-11 Migration matrix: tracker mods. 27-32 (E_ν) 580
D-12 Migration matrix: tracker mods. 33-38 (E_ν) 581
D-13 Migration matrix: tracker mods. 39-44 (E_ν) 581
D-14 Migration matrix: tracker mods. 45-50 (E_ν) 582
D-15 Migration matrix: tracker mods. 51-56 (E_ν) 582
D-16 Migration matrix: tracker mods. 57-62 (E_ν) 583
D-17 Migration matrix: tracker mods. 63-68 (E_ν) 583
D-18 Migration matrix: tracker mods. 69-74 (E_ν) 584
D-19 Migration matrix: tracker mods. 75-80 (E_ν) 584
D-20 Migration matrix: target 01 Fe (x_{bj}) 585
D-21 Migration matrix: target 01 Pb (x_{bj}) 586
D-22 Migration matrix: target 02 Fe (x_{bj}) 586
D-23 Migration matrix: target 02 Pb (x_{bj}) 587
D-24 Migration matrix: target 03 C (x_{bj}) 587
D-25 Migration matrix: target 03 Fe (x_{bj}) 588
D-26 Migration matrix: target 03 Pb (x_{bj}) 588

D-27 Migration matrix: target 04 Pb (x_{bj}) 589
D-28 Migration matrix: target 05 Fe (x_{bj}) 589
D-29 Migration matrix: target 05 Pb (x_{bj}) 590
D-30 Migration matrix: tracker mods. 27-32 (x_{bj}) 590
D-31 Migration matrix: tracker mods. 33-38 (x_{bj}) 591
D-32 Migration matrix: tracker mods. 39-44 (x_{bj}) 591
D-33 Migration matrix: tracker mods. 45-50 (x_{bj}) 592
D-34 Migration matrix: tracker mods. 51-56 (x_{bj}) 592
D-35 Migration matrix: tracker mods. 57-62 (x_{bj}) 593
D-36 Migration matrix: tracker mods. 63-68 (x_{bj}) 593
D-37 Migration matrix: tracker mods. 69-74 (x_{bj}) 594
D-38 Migration matrix: tracker mods. 75-80 (x_{bj}) 594
D-39 Bin by bin migtation: target 01 Fe (E_ν) 595
D-40 Bin by bin migtation: target 01 Pb (E_ν) 596
D-41 Bin by bin migtation: target 02 Fe (E_ν) 596
D-42 Bin by bin migtation: target 02 Pb (E_ν) 597
D-43 Bin by bin migtation: target 03 C (E_ν) 597
D-44 Bin by bin migtation: target 03 Fe (E_ν) 598
D-45 Bin by bin migtation: target 03 Pb (E_ν) 598
D-46 Bin by bin migtation: target 04 Pb (E_ν) 599
D-47 Bin by bin migtation: target 05 Fe (E_ν) 599
D-48 Bin by bin migtation: target 05 Pb (E_ν) 600
D-49 Bin by bin migtation: tracker mods. 27-32 (E_ν) 600
D-50 Bin by bin migtation: tracker mods. 33-38 (E_ν) 601
D-51 Bin by bin migtation: tracker mods. 39-44 (E_ν) 601
D-52 Bin by bin migtation: tracker mods. 45-50 (E_ν) 602
D-53 Bin by bin migtation: tracker mods. 51-56 (E_ν) 602

D-54 Bin by bin migtation: tracker mods. 57-62 (E_ν) 603
D-55 Bin by bin migtation: tracker mods. 63-68 (E_ν) 603
D-56 Bin by bin migtation: tracker mods. 69-74 (E_ν) 604
D-57 Bin by bin migtation: tracker mods. 75-80 (E_ν) 604
D-58 Bin by bin migtation: target 01 Fe (x_{bj}) 605
D-59 Bin by bin migtation: target 01 Pb (x_{bj}) 606
D-60 Bin by bin migtation: target 02 Fe (x_{bj}) 606
D-61 Bin by bin migtation: target 02 Pb (x_{bj}) 607
D-62 Bin by bin migtation: target 03 C (x_{bj}) 607
D-63 Bin by bin migtation: target 03 Fe (x_{bj}) 608
D-64 Bin by bin migtation: target 03 Pb (x_{bj}) 608
D-65 Bin by bin migtation: target 04 Pb (x_{bj}) 609
D-66 Bin by bin migtation: target 05 Fe (x_{bj}) 609
D-67 Bin by bin migtation: target 05 Pb (x_{bj}) 610
D-68 Bin by bin migtation: tracker mods. 27-32 (x_{bj}) 610
D-69 Bin by bin migtation: tracker mods. 33-38 (x_{bj}) 611
D-70 Bin by bin migtation: tracker mods. 39-44 (x_{bj}) 611
D-71 Bin by bin migtation: tracker mods. 45-50 (x_{bj}) 612
D-72 Bin by bin migtation: tracker mods. 51-56 (x_{bj}) 612
D-73 Bin by bin migtation: tracker mods. 57-62 (x_{bj}) 613
D-74 Bin by bin migtation: tracker mods. 63-68 (x_{bj}) 613
D-75 Bin by bin migtation: tracker mods. 69-74 (x_{bj}) 614
D-76 Bin by bin migtation: tracker mods. 75-80 (x_{bj}) 614
E-1 DIS signal and CH background: target 01 Fe (E_ν) 615
E-2 DIS signal and CH background: target 01 Pb (E_ν) 616
E-3 DIS signal and CH background: target 02 Fe (E_ν) 616
E-4 DIS signal and CH background: target 02 Pb (E_ν) 617

E-5 DIS signal and CH background: target 03 C (E_ν) 617
E-6 DIS signal and CH background: target 03 Fe (E_ν) 618
E-7 DIS signal and CH background: target 03 Pb (E_ν) 618
E-8 DIS signal and CH background: target 04 Pb (E_ν) 619
E-9 DIS signal and CH background: target 05 Fe (E_ν) 619
E-10 DIS signal and CH background: target 05 Pb (E_ν) 620
E-11 DIS Signal: tracker mods. 27-32 (E_ν) 620
E-12 DIS Signal: tracker mods. 33-38 (E_ν) 621
E-13 DIS Signal: tracker mods. 39-44 (E_ν) 621
E-14 DIS Signal: tracker mods. 45-50 (E_ν) 622
E-15 DIS Signal: tracker mods. 51-56 (E_ν) 622
E-16 DIS Signal: tracker mods. 57-62 (E_ν) 623
E-17 DIS Signal: tracker mods. 63-68 (E_ν) 623
E-18 DIS Signal: tracker mods. 69-74 (E_ν) 624
E-19 DIS Signal: tracker mods. 75-80 (E_ν) 624
E-20 DIS signal and CH background: target 01 Fe (E_{had}) 625
E-21 DIS signal and CH background: target 01 Pb (E_{had}) 626
E-22 DIS signal and CH background: target 02 Fe (E_{had}) 626
E-23 DIS signal and CH background: target 02 Pb (E_{had}) 627
E-24 DIS signal and CH background: target 03 C (E_{had}) 627
E-25 DIS signal and CH background: target 03 Fe (E_{had}) 628
E-26 DIS signal and CH background: target 03 Pb (E_{had}) 628
E-27 DIS signal and CH background: target 04 Pb (E_{had}) 629
E-28 DIS signal and CH background: target 05 Fe (E_{had}) 629
E-29 DIS signal and CH background: target 05 Pb (E_{had}) 630
E-30 DIS Signal: tracker mods. 27-32 (E_{had}) 630
E-31 DIS Signal: tracker mods. 33-38 (E_{had}) 631

E-32 DIS Signal: tracker mods. 39-44 (E_{had}) 631
E-33 DIS Signal: tracker mods. 45-50 (E_{had}) 632
E-34 DIS Signal: tracker mods. 51-56 (E_{had}) 632
E-35 DIS Signal: tracker mods. 57-62 (E_{had}) 633
E-36 DIS Signal: tracker mods. 63-68 (E_{had}) 633
E-37 DIS Signal: tracker mods. 69-74 (E_{had}) 634
E-38 DIS Signal: tracker mods. 75-80 (E_{had}) 634
E-39 DIS signal and CH background: target 01 Fe (Q^2) 635
E-40 DIS signal and CH background: target 01 Pb (Q^2) 636
E-41 DIS signal and CH background: target 02 Fe (Q^2) 636
E-42 DIS signal and CH background: target 02 Pb (Q^2) 637
E-43 DIS signal and CH background: target 03 C (Q^2) 637
E-44 DIS signal and CH background: target 03 Fe (Q^2) 638
E-45 DIS signal and CH background: target 03 Pb (Q^2) 638
E-46 DIS signal and CH background: target 04 Pb (Q^2) 639
E-47 DIS signal and CH background: target 05 Fe (Q^2) 639
E-48 DIS signal and CH background: target 05 Pb (Q^2) 640
E-49 DIS Signal: tracker mods. 27-32 (Q^2) 640
E-50 DIS Signal: tracker mods. 33-38 (Q^2) 641
E-51 DIS Signal: tracker mods. 39-44 (Q^2) 641
E-52 DIS Signal: tracker mods. 45-50 (Q^2) 642
E-53 DIS Signal: tracker mods. 51-56 (Q^2) 642
E-54 DIS Signal: tracker mods. 57-62 (Q^2) 643
E-55 DIS Signal: tracker mods. 63-68 (Q^2) 643
E-56 DIS Signal: tracker mods. 69-74 (Q^2) 644
E-57 DIS Signal: tracker mods. 75-80 (Q^2) 644
E-58 DIS signal and CH background: target 01 Fe (W) 645

E-59 DIS signal and CH background: target 01 Pb (W) 646
E-60 DIS signal and CH background: target 02 Fe (W) 646
E-61 DIS signal and CH background: target 02 Pb (W) 647
E-62 DIS signal and CH background: target 03 C (W) 647
E-63 DIS signal and CH background: target 03 Fe (W) 648
E-64 DIS signal and CH background: target 03 Pb (W) 648
E-65 DIS signal and CH background: target 04 Pb (W) 649
E-66 DIS signal and CH background: target 05 Fe (W) 649
E-67 DIS signal and CH background: target 05 Pb (W) 650
E-68 DIS Signal: tracker mods. 27-32 (W) 650
E-69 DIS Signal: tracker mods. 33-38 (W) 651
E-70 DIS Signal: tracker mods. 39-44 (W) 651
E-71 DIS Signal: tracker mods. 45-50 (W) 652
E-72 DIS Signal: tracker mods. 51-56 (W) 652
E-73 DIS Signal: tracker mods. 57-62 (W) 653
E-74 DIS Signal: tracker mods. 63-68 (W) 653
E-75 DIS Signal: tracker mods. 69-74 (W) 654
E-76 DIS Signal: tracker mods. 75-80 (W) 654
E-77 DIS signal and CH background: target 01 Fe (x_{bj}) 655
E-78 DIS signal and CH background: target 01 Pb (x_{bj}) 656
E-79 DIS signal and CH background: target 02 Fe (x_{bj}) 656
E-80 DIS signal and CH background: target 02 Pb (x_{bj}) 657
E-81 DIS signal and CH background: target 03 C (x_{bj}) 657
E-82 DIS signal and CH background: target 03 Fe (x_{bj}) 658
E-83 DIS signal and CH background: target 03 Pb (x_{bj}) 658
E-84 DIS signal and CH background: target 04 Pb (x_{bj}) 659
E-85 DIS signal and CH background: target 05 Fe (x_{bj}) 659

E-86 DIS signal and CH background: target 05 Pb (x_{bj}) 660
E-87 DIS Signal: tracker mods. 27-32 (x_{bj}) 660
E-88 DIS Signal: tracker mods. 33-38 (x_{bj}) 661
E-89 DIS Signal: tracker mods. 39-44 (x_{bj}) 661
E-90 DIS Signal: tracker mods. 45-50 (x_{bj}) 662
E-91 DIS Signal: tracker mods. 51-56 (x_{bj}) 662
E-92 DIS Signal: tracker mods. 57-62 (x_{bj}) 663
E-93 DIS Signal: tracker mods. 63-68 (x_{bj}) 663
E-94 DIS Signal: tracker mods. 69-74 (x_{bj}) 664
E-95 DIS Signal: tracker mods. 75-80 (x_{bj}) 664
E-96 DIS signal and CH background: target 01 Fe (E_μ) 665
E-97 DIS signal and CH background: target 01 Pb (E_μ) 666
E-98 DIS signal and CH background: target 02 Fe (E_μ) 666
E-99 DIS signal and CH background: target 02 Pb (E_μ) 667
E-100 DIS signal and CH background: target 03 C (E_μ) 667
E-101 DIS signal and CH background: target 03 Fe (E_μ) 668
E-102 DIS signal and CH background: target 03 Pb (E_μ) 668
E-103 DIS signal and CH background: target 04 Pb (E_μ) 669
E-104 DIS signal and CH background: target 05 Fe (E_μ) 669
E-105 DIS signal and CH background: target 05 Pb (E_μ) 670
E-106 DIS Signal: tracker mods. 27-32 (E_μ) 670
E-107 DIS Signal: tracker mods. 33-38 (E_μ) 671
E-108 DIS Signal: tracker mods. 39-44 (E_μ) 671
E-109 DIS Signal: tracker mods. 45-50 (E_μ) 672
E-110 DIS Signal: tracker mods. 51-56 (E_μ) 672
E-111 DIS Signal: tracker mods. 57-62 (E_μ) 673
E-112 DIS Signal: tracker mods. 63-68 (E_μ) 673

E-113 DIS Signal: tracker mods. 69-74 (E_μ) 674
E-114 DIS Signal: tracker mods. 75-80 (E_μ) 674
E-115 Event yield uncertainties before CH subtraction: target 01 Fe (E_ν) 675
E-116 Event yield uncertainties before CH subtraction: target 021Pb (E_ν) 676
E-117 Event yield uncertainties before CH subtraction: target 02 Fe (E_ν) 677
E-118 Event yield uncertainties before CH subtraction: target 02 Pb (E_ν) 678
E-119 Event yield uncertainties before CH subtraction: target 03 C (E_ν) 679
E-120 Event yield uncertainties before CH subtraction: target 03 Fe (E_ν) 680
E-121 Event yield uncertainties before CH subtraction: target 03 Pb (E_ν) 681
E-122 Event yield uncertainties before CH subtraction: target 04 Pb (E_ν) 682
E-123 Event yield uncertainties before CH subtraction: target 05 Fe (E_ν) 683
E-124 Event yield uncertainties before CH subtraction: target 05 Pb (E_ν) 684
E-125 Event yield uncertainties: tracker mods. 27-32 (E_ν) 685
E-126 Event yield uncertainties: tracker mods. 33-38 (E_ν) 686
E-127 Event yield uncertainties: tracker mods. 39-44 (E_ν) 687
E-128 Event yield uncertainties: tracker mods. 45-50 (E_ν) 688
E-129 Event yield uncertainties: tracker mods. 51-56 (E_ν) 689
E-130 Event yield uncertainties: tracker mods. 57-62 (E_ν) 690
E-131 Event yield uncertainties: tracker mods. 63-68 (E_ν) 691
E-132 Event yield uncertainties: tracker mods. 69-74 (E_ν) 692
E-133 Event yield uncertainties after CH subtraction: tracker mods. 75-80 (E_ν) . 693
E-134 Event yield uncertainties before CH subtraction: target 01 Fe (E_{had}) 694
E-135 Event yield uncertainties before CH subtraction: target 01 Pb (E_{had}) 695
E-136 Event yield uncertainties before CH subtraction: target 02 Fe (E_{had}) 696
E-137 Event yield uncertainties before CH subtraction: target 02 Pb (E_{had}) 697
E-138 Event yield uncertainties before CH subtraction: target 03 C (E_{had}) 698
E-139 Event yield uncertainties before CH subtraction: target 03 Fe (E_{had}) 699

E-140 Event yield uncertainties before CH subtraction: target 03 Pb (E_{had}) 700
E-141 Event yield uncertainties before CH subtraction: target 04 Pb (E_{had}) 701
E-142 Event yield uncertainties before CH subtraction: target 05 Fe (E_{had}) 702
E-143 Event yield uncertainties before CH subtraction: target 05 Pb (E_{had}) 703
E-144 Event yield uncertainties: tracker mods. 27-32 (E_{had}) 704
E-145 Event yield uncertainties: tracker mods. 33-38 (E_{had}) 705
E-146 Event yield uncertainties after: tracker mods. 39-44 (E_{had}) 706
E-147 Event yield uncertainties: tracker mods. 45-50 (E_{had}) 707
E-148 Event yield uncertainties: tracker mods. 51-56 (E_{had}) 708
E-149 Event yield uncertainties: tracker mods. 57-62 (E_{had}) 709
E-150 Event yield uncertainties: tracker mods. 63-68 (E_{had}) 710
E-151 Event yield uncertainties: tracker mods. 69-74 (E_{had}) 711
E-152 Event yield uncertainties: tracker mods. 75-80 (E_{had}) 712
E-153 Event yield uncertainties before CH subtraction: target 01 Fe (Q^2) 713
E-154 Event yield uncertainties before CH subtraction: target 01 Pb (Q^2) 714
E-155 Event yield uncertainties before CH subtraction: target 02 Fe (Q^2) 715
E-156 Event yield uncertainties before CH subtraction: target 02 Pb (Q^2) 716
E-157 Event yield uncertainties before CH subtraction: target 03 C (Q^2) 717
E-158 Event yield uncertainties before CH subtraction: target 03 Fe (Q^2) 718
E-159 Event yield uncertainties before CH subtraction: target 03 Pb (Q^2) 719
E-160 Event yield uncertainties before CH subtraction: target 04 Pb (Q^2) 720
E-161 Event yield uncertainties before CH subtraction: target 05 Fe (Q^2) 721
E-162 Event yield uncertainties before CH subtraction: target 05 Pb (Q^2) 722
E-163 Event yield uncertainties: tracker mods. 27-32 (Q^2) 723
E-164 Event yield uncertainties: tracker mods. 33-38 (Q^2) 724
E-165 Event yield uncertainties: tracker mods. 39-44 (Q^2) 725
E-166 Event yield uncertainties: tracker mods. 45-50 (Q^2) 726

E-167 Event yield uncertainties: tracker mods. 51-56 (Q^2) 727
E-168 Event yield uncertainties: tracker mods. 57-62 (Q^2) 728
E-169 Event yield uncertainties: tracker mods. 63-68 (Q^2) 729
E-170 Event yield uncertainties: tracker mods. 69-74 (Q^2) 730
E-171 Event yield uncertainties: tracker mods. 75-80 (Q^2) 731
E-172 Event yield uncertainties before CH subtraction: target 01 Fe (W) 732
E-173 Event yield uncertainties before CH subtraction: target 01 Pb (W) 733
E-174 Event yield uncertainties before CH subtraction: target 02 Fe (W) 734
E-175 Event yield uncertainties before CH subtraction: target 02 Pb (W) 735
E-176 Event yield uncertainties before CH subtraction: target 03 C (W) 736
E-177 Event yield uncertainties before CH subtraction: target 03 Fe (W) 737
E-178 Event yield uncertainties before CH subtraction: target 03 Pb (W) 738
E-179 Event yield uncertainties before CH subtraction: target 04 Pb (W) 739
E-180 Event yield uncertainties before CH subtraction: target 05 Fe (W) 740
E-181 Event yield uncertainties before CH subtraction: target 05 Pb (W) 741
E-182 Event yield uncertainties: tracker mods. 27-32 (W) 742
E-183 Event yield uncertainties: tracker mods. 33-38 (W) 743
E-184 Event yield uncertainties: tracker mods. 39-44 (W) 744
E-185 Event yield uncertainties: tracker mods. 45-50 (W) 745
E-186 Event yield uncertainties: tracker mods. 51-56 (W) 746
E-187 Event yield uncertainties: tracker mods. 57-62 (W) 747
E-188 Event yield uncertainties: tracker mods. 63-68 (W) 748
E-189 Event yield uncertainties: tracker mods. 69-74 (W) 749
E-190 Event yield uncertainties: tracker mods. 75-80 (W) 750
E-191 Event yield uncertainties before CH subtraction: target 01 Fe (x_{bj}) 751
E-192 Event yield uncertainties before CH subtraction: target 01 Pb (x_{bj}) 752
E-193 Event yield uncertainties before CH subtraction: target 02 Fe (x_{bj}) 753

E-194 Event yield uncertainties before CH subtraction: target 02 Pb (x_{bj}) 754
E-195 Event yield uncertainties before CH subtraction: target 03 C (x_{bj}) 755
E-196 Event yield uncertainties before CH subtraction: target 03 Fe (x_{bj}) 756
E-197 Event yield uncertainties before CH subtraction: target 03 Pb (x_{bj}) 757
E-198 Event yield uncertainties before CH subtraction: target 04 Pb (x_{bj}) 758
E-199 Event yield uncertainties before CH subtraction: target 05 Fe (x_{bj}) 759
E-200 Event yield uncertainties before CH subtraction: target 05 Pb (x_{bj}) 760
E-201 Event yield uncertainties: tracker mods. 27-32 (x) 761
E-202 Event yield uncertainties: tracker mods. 33-38 (x_{bj}) 762
E-203 Event yield uncertainties: tracker mods. 39-44 (x_{bj}) 763
E-204 Event yield uncertainties: tracker mods. 45-50 (x_{bj}) 764
E-205 Event yield uncertainties: tracker mods. 51-56 (x_{bj}) 765
E-206 Event yield uncertainties: tracker mods. 57-62 (x_{bj}) 766
E-207 Event yield uncertainties: tracker mods. 63-68 (x_{bj}) 767
E-208 Event yield uncertainties: tracker mods. 69-74 (x_{bj}) 768
E-209 Event yield uncertainties: tracker mods. 75-80 (x_{bj}) 769
E-210 Event yield uncertainties before CH subtraction: target 01 Fe (E_μ) 770
E-211 Event yield uncertainties before CH subtraction: target 01 Pb (E_μ) 771
E-212 Event yield uncertainties before CH subtraction: target 02 Fe (E_μ) 772
E-213 Event yield uncertainties before CH subtraction: target 02 Pb (E_μ) 773
E-214 Event yield uncertainties before CH subtraction: target 03 C (E_μ) 774
E-215 Event yield uncertainties before CH subtraction: target 03 Fe (E_μ) 775
E-216 Event yield uncertainties before CH subtraction: target 03 Pb (E_μ) 776
E-217 Event yield uncertainties before CH subtraction: target 04 Pb (E_μ) 777
E-218 Event yield uncertainties before CH subtraction: target 05 Fe (E_μ) 778
E-219 Event yield uncertainties before CH subtraction: target 05 Pb (E_μ) 779
E-220 Event yield uncertainties: tracker mods. 27-32 (E_μ) 780

E-221 Event yield uncertainties: tracker mods. 33-38 (E_μ) 781
E-222 Event yield uncertainties: tracker mods. 39-44 (E_μ) 782
E-223 Event yield uncertainties: tracker mods. 45-50 (E_μ) 783
E-224 Event yield uncertainties: tracker mods. 51-56 (E_μ) 784
E-225 Event yield uncertainties: tracker mods. 57-62 (E_μ) 785
E-226 Event yield uncertainties: tracker mods. 63-68 (E_μ) 786
E-227 Event yield uncertainties: tracker mods. 69-74 (E_μ) 787
E-228 Event yield uncertainties: tracker mods. 75-80 (E_μ) 788
E-229 DIS Signal: target 01 Fe (E_ν) 789
E-230 DIS Signal: target 01 Pb (E_ν) 790
E-231 DIS Signal: target 02 Fe (E_ν) 790
E-232 DIS Signal: target 02 Pb (E_ν) 791
E-233 DIS Signal: target 03 C (E_ν) 791
E-234 DIS Signal: target 03 Fe (E_ν) 792
E-235 DIS Signal: target 03 Pb (E_ν) 792
E-236 DIS Signal: target 04 Pb (E_ν) 793
E-237 DIS Signal: target 05 Fe (E_ν) 793
E-238 DIS Signal: target 05 Pb (E_ν) 794
E-239 DIS Signal: target 01 Fe (x_{bj}) 795
E-240 DIS Signal: target 01 Pb (x_{bj}) 796
E-241 DIS Signal: target 02 Fe (x_{bj}) 796
E-242 DIS Signal: target 02 Pb (x_{bj}) 797
E-243 DIS Signal: target 03 C (x_{bj}) 797
E-244 DIS Signal: target 03 Fe (x_{bj}) 798
E-245 DIS Signal: target 03 Pb (x_{bj}) 798
E-246 DIS Signal: target 04 Pb (x_{bj}) 799
E-247 DIS Signal: target 05 Fe (x_{bj}) 799

E-248 DIS Signal: target 05 Pb (x_{bj}) 800
E-249 Event yield uncertainties after CH subtraction: target 01 Fe (E_ν) 801
E-250 Event yield uncertainties after CH subtraction: target 01 Pb (E_ν) 802
E-251 Event yield uncertainties after CH subtraction: target 02 Fe (E_ν) 803
E-252 Event yield uncertainties after CH subtraction: target 02 Pb (E_ν) 804
E-253 Event yield uncertainties after CH subtraction: target 03 C (E_ν) 805
E-254 Event yield uncertainties after CH subtraction: target 03 Fe (E_ν) 806
E-255 Event yield uncertainties after CH subtraction: target 03 Pb (E_ν) 807
E-256 Event yield uncertainties after CH subtraction: target 04 Pb (E_ν) 808
E-257 Event yield uncertainties after CH subtraction: target 05 Fe (E_ν) 809
E-258 Event yield uncertainties after CH subtraction: target 05 Pb (E_ν) 810
E-259 Event yield uncertainties after CH subtraction: target 01 Fe (x_{bj}) 811
E-260 Event yield uncertainties after CH subtraction: target 01 Pb (x_{bj}) 812
E-261 Event yield uncertainties after CH subtraction: target 02 Fe (x_{bj}) 813
E-262 Event yield uncertainties after CH subtraction: target 02 Pb (x_{bj}) 814
E-263 Event yield uncertainties after CH subtraction: target 03 C (x_{bj}) 815
E-264 Event yield uncertainties after CH subtraction: target 03 Fe (x_{bj}) 816
E-265 Event yield uncertainties after CH subtraction: target 03 Pb (x_{bj}) 817
E-266 Event yield uncertainties after CH subtraction: target 04 Pb (x_{bj}) 818
E-267 Event yield uncertainties after CH subtraction: target 05 Fe (x_{bj}) 819
E-268 Event yield uncertainties after CH subtraction: target 05 Pb (x_{bj}) 820
F-1 Unfolded DIS Signal: target 01 Fe (E_ν) 821
F-2 Unfolded DIS Signal: target 01 Pb (E_ν) 822
F-3 Unfolded DIS Signal: target 02 Fe (E_ν) 822
F-4 Unfolded DIS Signal: target 02 Pb (E_ν) 823
F-5 Unfolded DIS Signal: target 03 C (E_ν) 823
F-6 Unfolded DIS Signal: target 03 Fe (E_ν) 824

F-7 Unfolded DIS Signal: target 03 Pb (E_ν) 824
F-8 Unfolded DIS Signal: target 04 Pb (E_ν) 825
F-9 Unfolded DIS Signal: target 05 Fe (E_ν) 825
F-10 Unfolded DIS Signal: target 05 Pb (E_ν) 826
F-11 Unfolded DIS Signal: tracker mods. 27-32 (E_ν) 826
F-12 Unfolded DIS Signal: tracker mods. 33-38 (E_ν) 827
F-13 Unfolded DIS Signal: tracker mods. 39-44 (E_ν) 827
F-14 Unfolded DIS Signal: tracker mods. 45-50 (E_ν) 828
F-15 Unfolded DIS Signal: tracker mods. 51-56 (E_ν) 828
F-16 Unfolded DIS Signal: tracker mods. 57-62 (E_ν) 829
F-17 Unfolded DIS Signal: tracker mods. 63-68 (E_ν) 829
F-18 Unfolded DIS Signal: tracker mods. 69-74 (E_ν) 830
F-19 Unfolded DIS Signal: tracker mods. 75-80 (E_ν) 830
F-20 Unfolded DIS Signal: target 01 Fe (x_{bj}) 831
F-21 Unfolded DIS Signal: target 01 Pb (x_{bj}) 832
F-22 Unfolded DIS Signal: target 02 Fe (x_{bj}) 832
F-23 Unfolded DIS Signal: target 02 Pb (x_{bj}) 833
F-24 Unfolded DIS Signal: target 03 C (x_{bj}) 833
F-25 Unfolded DIS Signal: target 03 Fe (x_{bj}) 834
F-26 Unfolded DIS Signal: target 03 Pb (x_{bj}) 834
F-27 Unfolded DIS Signal: target 04 Pb (x_{bj}) 835
F-28 Unfolded DIS Signal: target 05 Fe (x_{bj}) 835
F-29 Unfolded DIS Signal: target 05 Pb (x_{bj}) 836
F-30 Unfolded DIS Signal: tracker mods. 27-32 (x_{bj}) 836
F-31 Unfolded DIS Signal: tracker mods. 33-38 (x_{bj}) 837
F-32 Unfolded DIS Signal: tracker mods. 39-44 (x_{bj}) 837
F-33 Unfolded DIS Signal: tracker mods. 45-50 (x_{bj}) 838

F-34 Unfolded DIS Signal: tracker mods. 51-56 (x_{bj}) 838
F-35 Unfolded DIS Signal: tracker mods. 57-62 (x_{bj}) 839
F-36 Unfolded DIS Signal: tracker mods. 63-68 (x_{bj}) 839
F-37 Unfolded DIS Signal: tracker mods. 69-74 (x_{bj}) 840
F-38 Unfolded DIS Signal: tracker mods. 75-80 (x_{bj}) 840
F-39 Unfolded Event yield uncertainties after CH subtraction: target 01 Fe (E_ν) 841
F-40 Unfolded Event yield uncertainties after CH subtraction: target 01 Pb (E_ν) 842
F-41 Unfolded Event yield uncertainties after CH subtraction: target 02 Fe (E_ν) 843
F-42 Unfolded Event yield uncertainties after CH subtraction: target 02 Pb (E_ν) 844
F-43 Unfolded Event yield uncertainties after CH subtraction: target 03 C (E_ν) 845
F-44 Unfolded Event yield uncertainties after CH subtraction: target 03 Fe (E_ν) 846
F-45 Unfolded Event yield uncertainties after CH subtraction: target 03 Pb (E_ν) 847
F-46 Unfolded Event yield uncertainties after CH subtraction: target 04 Pb (E_ν) 848
F-47 Unfolded Event yield uncertainties after CH subtraction: target 05 Fe (E_ν) 849
F-48 Unfolded Event yield uncertainties after CH subtraction: target 05 Pb (E_ν) 850
F-49 Unfolded Event yield uncertainties after CH subtraction: tracker mods. 27-32 (E_ν) 851
F-50 Unfolded Event yield uncertainties after CH subtraction: tracker mods. 33-38 (E_ν) 852
F-51 Unfolded Event yield uncertainties after CH subtraction: tracker mods. 39-44 (E_ν) 853
F-52 Unfolded Event yield uncertainties after CH subtraction: tracker mods. 45-50 (E_ν) 854
F-53 Unfolded Event yield uncertainties after CH subtraction: tracker mods. 51-56 (E_ν) 855
F-54 Unfolded Event yield uncertainties after CH subtraction: tracker mods. 57-62 (E_ν) 856

F-55 Unfolded Event yield uncertainties after CH subtraction: tracker mods. 63-68 (E_ν) 857
F-56 Unfolded Event yield uncertainties after CH subtraction: tracker mods. 69-74 (E_ν) 858
F-57 Unfolded Event yield uncertainties after CH subtraction: tracker mods. 75-80 (E_ν) 859
F-58 Unfolded Event yield uncertainties after CH subtraction: target 01 Fe (x_{bj}) 860
F-59 Unfolded Event yield uncertainties after CH subtraction: target 01 Pb (x_{bj}) 861
F-60 Unfolded Event yield uncertainties after CH subtraction: target 02 Fe (x_{bj}) 862
F-61 Unfolded Event yield uncertainties after CH subtraction: target 02 Pb (x_{bj}) 863
F-62 Unfolded Event yield uncertainties after CH subtraction: target 03 C (x_{bj}) 864
F-63 Unfolded Event yield uncertainties after CH subtraction: target 03 Fe (x_{bj}) 865
F-64 Unfolded Event yield uncertainties after CH subtraction: target 03 Pb (x_{bj}) 866
F-65 Unfolded Event yield uncertainties after CH subtraction: target 04 Pb (x_{bj}) 867
F-66 Unfolded Event yield uncertainties after CH subtraction: target 05 Fe (x_{bj}) 868
F-67 Unfolded Event yield uncertainties after CH subtraction: target 05 Pb (x_{bj}) 869
F-68 Unfolded Event yield uncertainties after CH subtraction: tracker mods. 27-32 (x_{bj}) 870
F-69 Unfolded Event yield uncertainties after CH subtraction: tracker mods. 33-38 (x_{bj}) 871
F-70 Unfolded Event yield uncertainties after CH subtraction: tracker mods. 39-44 (x_{bj}) 872
F-71 Unfolded Event yield uncertainties after CH subtraction: tracker mods. 45-50 (x_{bj}) 873
F-72 Unfolded Event yield uncertainties after CH subtraction: tracker mods. 51-56 (x_{bj}) 874

F-73 Unfolded Event yield uncertainties after CH subtraction: tracker mods. 57-62 (x_{bj}) 875
F-74 Unfolded Event yield uncertainties after CH subtraction: tracker mods. 63-68 (x_{bj}) 876
F-75 Unfolded Event yield uncertainties after CH subtraction: tracker mods. 69-74 (x_{bj}) 877
F-76 Unfolded Event yield uncertainties after CH subtraction: tracker mods. 75-80 (x_{bj}) 878
G-1 Overall efficiency: target 02 Fe (E_ν) 879
G-2 Overall efficiency: target 01 Pb (E_ν) 880
G-3 Overall efficiency: target 02 Fe (E_ν) 881
G-4 Overall efficiency: target 02 Pb (E_ν) 882
G-5 Overall efficiency: target 03 C (E_ν) 883
G-6 Overall efficiency: target 03 Fe (E_ν) 884
G-7 Overall efficiency: target 03 Pb (E_ν) 885
G-8 Overall efficiency: target 04 Pb (E_ν) 886
G-9 Overall efficiency: target 05 Fe (E_ν) 887
G-10 Overall efficiency: target 05 Pb (E_ν) 888
G-11 Overall efficiency: tracker mods. 27-32 (E_ν) 889
G-12 Overall efficiency: tracker mods. 33-38 (E_ν) 890
G-13 Overall efficiency: tracker mods. 39-44 (E_ν) 891
G-14 Overall efficiency: tracker mods. 45-50 (E_ν) 892
G-15 Overall efficiency: tracker mods. 51-56 (E_ν) 893
G-16 Overall efficiency: tracker mods. 57-62 (E_ν) 894
G-17 Overall efficiency: tracker mods. 63-68 (E_ν) 895
G-18 Overall efficiency: tracker mods. 69-74 (E_ν) 896
G-19 Overall efficiency: tracker mods. 75-80 (E_ν) 897

G-20 Overall efficiency: target 01 Fe (x_{bj}) 898
G-21 Overall efficiency: target 01 Pb (x_{bj}) 899
G-22 Overall efficiency: target 02 Fe (x_{bj}) 900
G-23 Overall efficiency: target 02 Pb (x_{bj}) 901
G-24 Overall efficiency: target 03 C (x_{bj}) 902
G-25 Overall efficiency: target 03 Fe (x_{bj}) 903
G-26 Overall efficiency: target 03 Pb (x_{bj}) 904
G-27 Overall efficiency: target 04 Pb (x_{bj}) 905
G-28 Overall efficiency: target 05 Fe (x_{bj}) 906
G-29 Overall efficiency: target 05 Pb (x_{bj}) 907
G-30 Overall efficiency: tracker mods. 27-32 (x_{bj}) 908
G-31 Overall efficiency: tracker mods. 33-38 (x_{bj}) 909
G-32 Overall efficiency: tracker mods. 39-44 (x_{bj}) 910
G-33 Overall efficiency: tracker mods. 45-50 (x_{bj}) 911
G-34 Overall efficiency: tracker mods. 51-56 (x_{bj}) 912
G-35 Overall efficiency: tracker mods. 57-62 (x_{bj}) 913
G-36 Overall efficiency: tracker mods. 63-68 (x_{bj}) 914
G-37 Overall efficiency: tracker mods. 69-74 (x_{bj}) 915
G-38 Overall efficiency: tracker mods. 75-80 (x_{bj}) 916
G-39 Uncertainty on overall efficiency: target 01 Fe (E_ν) 917
G-40 Uncertainty on overall efficiency: target 01 Pb (E_ν) 918
G-41 Uncertainty on overall efficiency: target 02 Fe (E_ν) 919
G-42 Uncertainty on overall efficiency: target 02 Pb (E_ν) 920
G-43 Uncertainty on overall efficiency: target 03 C (E_ν) 921
G-44 Uncertainty on overall efficiency: target 03 Fe (E_ν) 922
G-45 Uncertainty on overall efficiency: target 03 Pb (E_ν) 923
G-46 Uncertainty on overall efficiency: target 04 Pb (E_ν) 924

G-47 Uncertainty on overall efficiency: target 05 Fe (E_ν) 925
G-48 Uncertainty on overall efficiency: target 05 Pb (E_ν) 926
G-49 Uncertainty on overall efficiency: tracker mods. 27-32 (E_ν) 927
G-50 Uncertainty on overall efficiency: tracker mods. 33-38 (E_ν) 928
G-51 Uncertainty on overall efficiency: tracker mods. 39-44 (E_ν) 929
G-52 Uncertainty on overall efficiency: tracker mods. 45-50 (E_ν) 930
G-53 Uncertainty on overall efficiency: tracker mods. 51-56 (E_ν) 931
G-54 Uncertainty on overall efficiency: tracker mods. 57-62 (E_ν) 932
G-55 Uncertainty on overall efficiency: tracker mods. 63-68 (E_ν) 933
G-56 Uncertainty on overall efficiency: tracker mods. 69-74 (E_ν) 934
G-57 Uncertainty on overall efficiency: tracker mods. 75-80 (E_ν) 935
G-58 Uncertainty on overall efficiency: target 01 Fe (x_{bj}) 936
G-59 Uncertainty on overall efficiency: target 01 Pb (x_{bj}) 937
G-60 Uncertainty on overall efficiency: target 02 Fe (x_{bj}) 938
G-61 Uncertainty on overall efficiency: target 02 Pb (x_{bj}) 939
G-62 Uncertainty on overall efficiency: target 03 C (x_{bj}) 940
G-63 Uncertainty on overall efficiency: target 03 Fe (x_{bj}) 941
G-64 Uncertainty on overall efficiency: target 03 Pb (x_{bj}) 942
G-65 Uncertainty on overall efficiency: target 04 Pb (x_{bj}) 943
G-66 Uncertainty on overall efficiency: target 05 Fe (x_{bj}) 944
G-67 Uncertainty on overall efficiency: target 05 Pb (x_{bj}) 945
G-68 Uncertainty on overall efficiency: tracker mods. 27-32 (x_{bj}) 946
G-69 Uncertainty on overall efficiency: tracker mods. 33-38 (x_{bj}) 947
G-70 Uncertainty on overall efficiency: tracker mods. 39-44 (x_{bj}) 948
G-71 Uncertainty on overall efficiency: tracker mods. 45-50 (x_{bj}) 949
G-72 Uncertainty on overall efficiency: tracker mods. 51-56 (x_{bj}) 950
G-73 Uncertainty on overall efficiency: tracker mods. 57-62 (x_{bj}) 951

G-74 Uncertainty on overall efficiency: tracker mods. 63-68 (x_{bj}) 952
G-75 Uncertainty on overall efficiency: tracker mods. 69-74 (x_{bj}) 953
G-76 Uncertainty on overall efficiency: tracker mods. 75-80 (x_{bj}) 954

Abstract of Dissertation Presented to the Graduate School
of the University Of Florida in Partial Fulfillment of the
Requirements for the Degree of Doctor of Philosophy

FIRST SEARCH FOR THE EMC EFFECT AND NUCLEAR SHADOWING IN NEUTRINO NUCLEUS DEEP INELASTIC SCATTERING AT MINERVA

By

Joel A. Mousseau

August 2015

Chair: Heather Ray
Major: Physics

Decades of research in electron-nucleus deep inelastic scattering (DIS) have provided a clear picture of nuclear physics at high momentum transfer. While these effects have been clearly demonstrated by experiment, the theoretical explanation of their origin in some kinematic regions has been lacking. Particularly, the effects in the intermediate regions of Bjorken-x, anti-shadowing and the EMC effect have no universally accepted quantum mechanical explanation. In addition, these effects have not been measured systematically with neutrino-nucleus deep inelastic scattering, due to experiments lacking multiple heavy targets.

The MINERνA (Main Injector Experiment ν-A) experiment, located in the Neutrinos at the Main Injector (NuMI) facility at Fermilab, is designed explicitly to measure these kind of effects with neutrinos. MINERνA is equipped with solid targets of graphite, iron, lead and plastic scintillator. The plastic scintillator region provides excellent particle tracking capabilities, and the MINOS (Main Injector Neutrino Oscillation Search) near detector is used as a downstream muon spectrometer. The exposure of multiple nuclear targets to an identical neutrino beam allows for a systematic study of these nuclear effects.

An analysis of the MINERνA DIS data on carbon, iron, lead and plastic scintillator has been conducted in the energy region $5 \leq E_\nu < 50$ GeV and $\theta_\mu < 17°$. The data are

presented as ratios of the total cross section ($\sigma(E_\nu)$) as well as the differential cross section with respect to Bjorken-x ($\frac{d\sigma}{dx_{bj}}$) of carbon, iron and lead to scintillator. The total cross section data is useful for deciphering gross nuclear effects which effect neutrino energy reconstruction. No significant differences between simulation and MINERνA DIS data are observed in the total cross section. The ratios of the x_{bj} differential ratios however, may provide clues for decoding long standing questions about the EMC effect. The MINERνA data tend to support no difference in the strength of the EMC effect from charged lepton scattering. There is a suggestion of additional nuclear shadowing, not predicted by simulation, in the ratio of lead to scintillator.

CHAPTER 1
INTRODUCTION

1.1 Neutrinos and the Standard Model

The Standard Model is the fundamental theory of particle physics. Developed and tested over the past fifty years, the Standard Model provides a tool kit of particles, forces and conservation laws physicists may use to describe the universe at its' most basic level. Qualitatively, the Standard Model consists of seventeen particles and their antiparticles, as well as three fundamental forces [1]. The seventeen particles which make up the standard model are divided into two classes depending on the intrinsic spin of the particle, as illustrated in Figure 1-1. Bosons are particles with integer spin and act as carriers of the three fundamental forces the Standard Model describes. These three fores are, in order of strength, the electromagnetic (EM), the strong nuclear force, and the weak nuclear force. The boson which mediates the electromagnetic force is the massless photon, and the gluon mediates the strong nuclear force. The weak nuclear force is mediated by three bosons, W^+, W^- and Z^0. The final boson, the Higgs boson, bestows mass on all the other particles by coupling them to the Higgs field. Fermions are particles with spins which are an odd multiple of $\frac{1}{2}$, and comprise most of the everyday world.

The twelve fermions are further divided into hadrons and leptons depending on their sensitivity to the strong nuclear force. Hadrons are sensitive to the strong nuclear force through their coupling to gluons. These hadrons, called quarks, make up familiar nucleons such as protons and neutrons. Quarks come in three mass generations, with each generation containing a quarks and anti-quark pair. In contrast leptons do not feel the strong nuclear force and are insensitive to gluons. Leptons come in three generations: e, μ, and τ. Each lepton generation contains one massive charged particle and one light neutral particle, the neutrino.

[1] Gravity, which is immeasurably weak at the mass scale of particle physics is not explained by the Standard Model

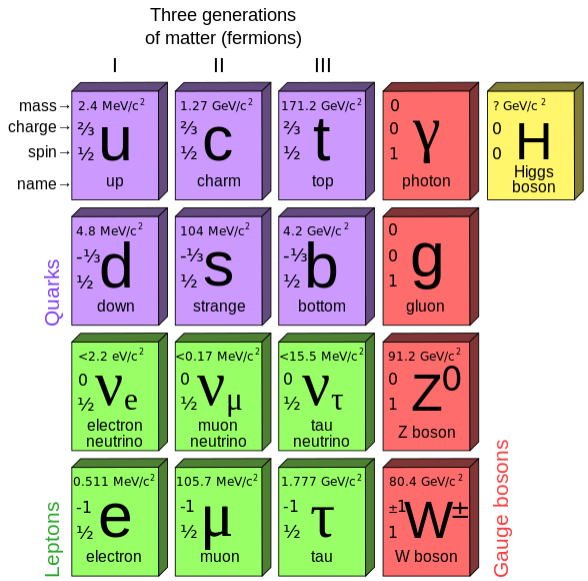

Figure 1-1. The standard model of particle physics, with the 12 fermions on the left and the 5 bosons on the right. As the absolute mass of neutrinos are yet unmeasured, only upper limits on the neutrino masses are listed. Figure is from Ref [1].

Of all of the particles which make up the menagerie which is the Standard Model, the neutrino is arguably the most elusive. For starters, its' rest mass is incredibly small, < 10 eV. Having no electric charge and no color charge makes it is completely invisible to everything except the weak nuclear force. These two qualities of neutrinos make them especially difficult to detect. So much so in fact that Wolfgang Pauli once quipped he had done "a very bad thing" by predicting a particle which could not be detected [2].

The impetus of Pauli's naughtiness can be traced back to beta decay experiments conducted during the 1920s. At the time, physicists described the beta decay of neutrons as a two-body decay into a proton and a negatively charged beta particle, or an electron: $n \rightarrow p^+ + e^-$. However, the measured energy spectrum of the outgoing electron was inconsistent with a two-body decay as can be seen in Figure 1-2. If beta decay was truly a two-body decay, the outgoing electron would be mono-energetic with an energy equal to the mass difference between the parent and daughter nuclei. The problem of the

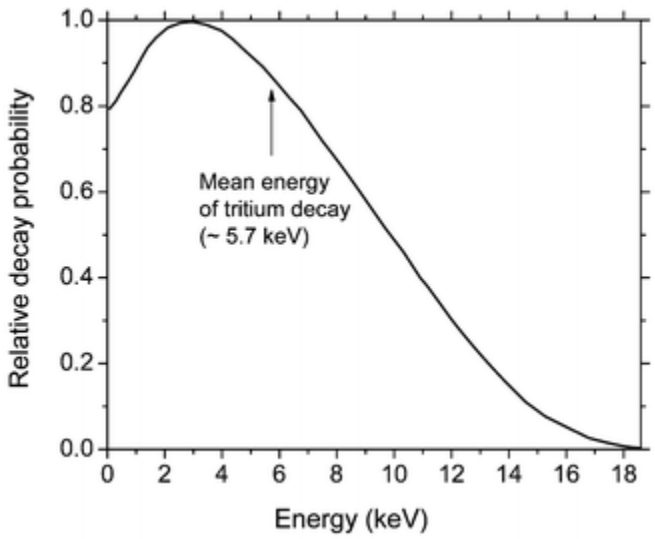

Figure 1-2. Kinetic energy of electrons observed from the decay $^3\mathrm{H} \rightarrow {}^3\mathrm{He} + \mathrm{e}^- + \overline{\nu}_e$. In the absence of neutrinos, ^{3}H decay would be a two-body decay with an outgoing e^- kinetic energy equal to 18 keV. Figure is from Ref [3].

continuous beta decay spectrum was so bad that contemporary physicists were ready to abandon the concept of energy conservation entirely.

Pauli's "desperate remedy" was to add a third particle to the right side of the beta decay equation to carry the additional energy the beta particle lacked. Enrico Fermi named this particle the "neutrino, or little neutral one in Italian. While Pauli lamented his particle could never be detected, the neutrino was indeed detected a scant 30 years after its' prediction.

When Pauli predicted the neutrino, the only sources of neutrinos predicted to be intense enough to be detected originated from nuclear fission or fusion. These could in theory originate from the sun in the case of nuclear fusion, or a nuclear power generating reactor or a nuclear weapon in the case of fission. The Savannah River nuclear power station in South Carolina was selected by Clyde Cowan and Fredrick Reines to conduct the first successful direct neutrino detection experiment. The Reines and Cowan experiment used a large tank of cadmium enriched water to act as a target for inverse beta decay of the anti-neutrinos escaping the reactor's core. Inverse beta decay, which is summarized by

the reaction $\overline{\nu}_e + p \rightarrow e^+ + n$, yields a positron and neutron in the final state. The positron soon annihilates with a electron in the tank creating two photons. The neutron is subsequently captured by the cadmium nuclei, also emitting a photon. The resulting photons interact with scintillator surrounding the water tank and are detected by photomultiplier tubes (PMTs). This creates a very clean signature for neutrino events consisting of two prompt photon signals followed by a delayed single photon [4].

Recall that in the Standard Model leptons exist in three generations: e, μ and τ. The neutrinos Reines and Cowan detected were neutrinos of the electron anti-neutrino flavor, since they created positrons after interacting with the target protons. The muon neutrino, or ν_μ was first detected at Brookhaven National Lab in 1962 [5], while the tau neutrino, ν_τ was discovered in 2001 at Fermilab [6].

1.2 Neutrino Oscillations

If neutrinos were truly massless, this would be the end of the story. The Standard Model would predict 3 generations of leptons, and each generation would have a massive, charged partner and a massless, neutral neutrino. However, if neutrinos do indeed have mass, no matter how tiny, their mass and flavor eigenstates may not be the same. If we assume the flavor eigenstate of a neutrino is $|\nu_i\rangle$, and the mass eigenstate is $|\nu_\alpha\rangle$, then:

$$|\nu_i\rangle = \sum_\alpha U_{i\alpha} |\nu_\alpha\rangle , \tag{1-1}$$

where U is the unitary mixing matrix which defines the relative mixture of each mass eigenstate to a particular flavor α, and the sum is preformed over each of the mass eigenstates. Quantum mechanics tells us that if we want to evolve a particular state in time, we can do so using the Hamiltonian operator H of the system. Under the assumption that the neutrino is existing in vacuum,

$$H |\nu_\alpha\rangle = e^{-i(E+m_i^2/2E)t} |\nu_\alpha\rangle ,^{2} \tag{1-2}$$

[2]Unless otherwise indicated, this manuscript uses natural units, where factors of h, $\hbar$ and $c = 1$

where E is the energy of the neutrino, t is the propagation time, and m_i is the eigenvalue of the mass eigenstate. Because the mass of neutrinos are so small, a good approximation is to assume they travel at the speed of light and t in Equation 1-2 is equal to the distance traveled x. This gives:

$$H\left|\nu_\alpha\right\rangle = e^{-i(E+m_i^2/2E)x}\left|\nu_\alpha\right\rangle. \tag{1-3}$$

Plugging this into Equation 1-1 shows something remarkable. The flavor eigenstate of a neutrino changes as it propagates in space, with a frequency proportional to its' energy and mass, and an amplitude proportional to the parameters of the matrix U. This means a neutrino which begins its' life as a electron neutrino, for example, may be detected several meters later as a tau or muon neutrino. As the cross-section of neutrino interactions with everyday matter is very small ($\approx 10^{-38}$ cm^2 [1]), detecting these oscillations would require a very intense source of neutrinos, a very massive detector, or both.

Fortunately, such a source of neutrinos exists nearby: the sun. The flux of solar neutrinos at the sun's core is very well described by models of nuclear fusion, and any variance in this flux detected on earth would be evidence of neutrino oscillations as described previously. The Homestake Mine experiment was set up in an abandon gold mine in North Dakota. This experiment measured the ν_μ flux from the sun using a perchloroethylene (C_2Cl_4) target using a similar inverse beta decay signal as the original Reines and Cowan experiment: $\nu_e + {}^{37}\mathrm{Cl} \rightarrow {}^{37}\mathrm{Ar} + \mathrm{e}^-$. However the number of ν_μs measured was a factor of three lower than what was predicted from solar nuclear fusion [7]. This provided the first clear experimental evidence of neutrino *disappearance*, and provided hints of the neutrino oscillations predicted by Equation 1-3.

The Homestake Mine experiment and the disappearance of solar neutrinos lead to a thirty year search into the "solar puzzle" [8]. The Sudbury Neutrino Observatory (SNO) provided the first definitive proof that ν_μs from the sun oscillated into ν_e and ν_τs [9]. SNO employed a novel technique to separate the solar neutrino flux into neutral current (NC)

and charged current (CC) neutrino interactions [3]. NC interactions in SNO were sensitive to all species of neutrinos through the interactions:

$$\nu_i + n \rightarrow n + \nu_i, \tag{1-4}$$

and:

$$\nu_i + p \rightarrow p + \nu_i. \tag{1-5}$$

The energies of solar neutrinos in SNO's sensitivity range was too small to produce muons and taus. This means the charged current interaction, which produces a neutrino's charged lepton partner, was only accessible to the electron neutrino:

$$\nu_e + n \rightarrow p + e^-. \tag{1-6}$$

SNO used a spherical tank of salinated heavy water (D_2O) surrounded by 91 PMTs. Neutral current interactions on the deuteron ejected a neutron, which was subsequently captured by another D or Na atom. Each of these captures would subsequently release a 6.25 MeV photon in the case of n + D capture, and a 8.6 MeV photon in the case of n + Na [9]. These photons would primarily Compton scatter, creating electrons above Cherenkov threshold. Charged current interactions in SNO produced an electron, also above Cherenkov threshold, and an undetected proton. Both types of electrons were detectable through characteristic Cherenkov "rings" by the PMTs. Electrons from the CC interaction were produced very far forward, while the Compton electrons from photons were mainly isotropic. It was thus possible for SNO to distinguish a CC from NC reaction by reconstructing the direction of the Cherenkov cone, and observing its' alignment relative to the sun.

[3] The difference between charged and neutral current interactions is discussed further in Chapter 2

By subtracting the charged current flux, consisting solely of ν_es, from the neutral current flux, SNO was able to unambiguously show a flux of ν_μs and ν_τs originating from the sun. This provided the first definitive evidence of neutrino oscillations. The results of SNO and a similar experiment Super-Kamiokande are presented in Figure 1-3.

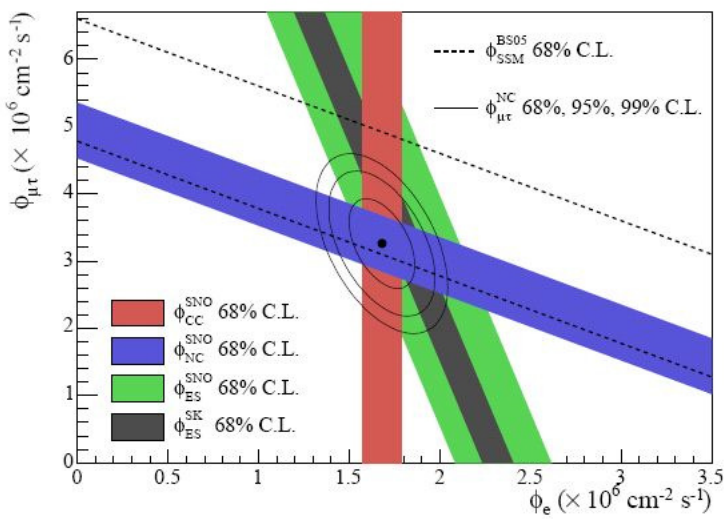

Figure 1-3. Results of the SNO experiment. The y-axis is the measured ν_μ and ν_τ flux, and the x-axis is the measured ν_e flux. The best fit point along with the 68%, 95% and 99% confidence intervals are drawn. Figure is from Ref [9].

Fundamentally SNO measured the amplitude of the ν_e to ν_μ ν_τ oscillations. Recall that the amplitude of the oscillation is equal to the $U_{i\alpha}^{th}$ element of the mixing matrix. U is presumed to be a unitary matrix, and as a result it's elements may be expressed as a series of mixing angles and phases. As the Standard Model predicts three flavors of neutrinos, the mixing matrix connecting the flavor and mass eigenstates must be a 3×3 matrix. This matrix, coined the Pontecorvo-Maki-Nakagawa-Sakata (PMNS) matrix, has the terms [10]:

$$U_{i\alpha} = \begin{pmatrix} c_{12}c_{13} & s_{12}c_{13} & s_{13}e^{-i\delta} \\ -s_{12}c_{23} - c_{12}s_{23}s_{13}e^{-i\delta} & c_{12}s_{23} - s_{12}s_{23}s_{13}e^{-i\delta} & s_{23}c_{13} \\ s_{12}c_{23} - c_{12}c_{23}s_{13}e^{-i\delta} & -c_{12}s_{23} - s_{12}c_{23}s_{13}e^{-i\delta} & c_{23}c_{13} \end{pmatrix}, \tag{1-7}$$

where c and s represent the cosine and sine of the three different mixing angles. In this case δ is a charge-parity (CP) violating phase of the oscillation which has yet to be measured.

With this matrix, the full picture of neutrino oscillations in Dirac notation can be written by substituting Equation 1-3 into Equation 1-1:

$$|\nu_i(x)\rangle = \sum_\alpha U^*_{\alpha i} e^{-i\left(E+m_i^2/2E\right)x} |\nu_\alpha\rangle . \tag{1-8}$$

To find the probability of a flavor j oscillating to a flavor i, $|\nu_\alpha\rangle$ must be expressed in terms of its' mass flavor eigenstates:

$$|\nu_\alpha\rangle = \sum_j U_{j\alpha} |\nu_j\rangle . \tag{1-9}$$

Plugging Equation 1-9 into 1-10 leads to:

$$|\nu_i(x)\rangle = \sum_\alpha \left(\sum_k U^*_{\alpha i} e^{-i\left(E+m_i^2/2E\right)x} |\nu_k\rangle U_{j\alpha} \right) |\nu_j\rangle . \tag{1-10}$$

The probability of a neutrino with a flavor i oscillating into a neutrino of flavor j after traveling length of L is given by the expression:

$$P(x = L) = |\langle \nu_i(L)|\nu_j(L)\rangle|^2, \tag{1-11}$$

which is equal to:

$$P_{i\to j}(L) = \sum_{\alpha\beta} U^*_{i\alpha} U_{j\alpha} U_{i\beta} U^*_{j\beta} \exp\left(-i\frac{\Delta m^2_{\alpha\beta} L}{2E}\right) . \tag{1-12}$$

The factors of L, E and Δm^2 in Equation 1-12 effect the wavelength of oscillations, while the elements of U effect the amplitude. L is tunable by an experiment by adjusting the distance between a neutrino source and a detector, while E is tunable for accelerator and reactor created neutrinos. An experimenter selects the best L/E ratio based on what element of the PMNS matrix, or what particular $\Delta m^2_{\alpha\beta}$ he or she would like to measure.

Recall that the α and β are the different mass eigenstates, and $\Delta m^2_{\alpha\beta}$ are the differences in the square of the masses between the states.

Outside of SNO, a litany of other experiments with differing sources of neutrinos and different detection techniques have come to the same conclusion; that neutrino flavors oscillate as they propagate through space. Decades of experimental work have identified three mass splittings, which determine the wavelength of oscillations, and three mixing angles which determine the amplitude. These are, in no particular order [1]:

- $\Delta m^2_{12} = 7.59 \times 10^{-5}$ eV^2. This mass splitting is given the nickname "solar" neutrino mixing. SNO is sensitive to this mass splitting.

- $\Delta m^2_{23} = 2.43 \times 10^{-3}$ eV^2. This so called "atmospheric" mixing was detected from neutrinos produced by the decay of cosmic ray muons created in the upper atmosphere.

- Δm^2_{13} is degenerate with the first two mass splitting due to the relationship $|\Delta m^2_{13}| = |\Delta m^2_{12} \pm \Delta m^2_{23}|$. The $\pm$ symbol refers to the hierarchy problem in neutrino physics. Since the absolute mass of any neutrino has not been measured, only the relative masses of the flavor eigenstates are known (see Figure 1-4). This is discussed further in Section 1.3.

- $\frac{\theta_{12}}{2} = 34.06°$ the solar mixing angle. This angle couples the mass eigenstates 1 and 2 in the mixing matrix U. The factor of $\frac{1}{2}$ reflects that experiments typically measure 2θ. The PMNS matrix contains many products of sines and cosines, which can be condensed to one sine using the relationship: $2sin(\theta)cos(\theta) = sin(2\theta)$.

- $\frac{\theta_{23}}{2} = 45°$ the atmospheric mixing angle.

- $\frac{\theta_{13}}{2} = 0.092°$. Unlike the solar and atmospheric angle, θ_{13} is tiny compared to the near maximal values of of θ_{12} and θ_{23}.

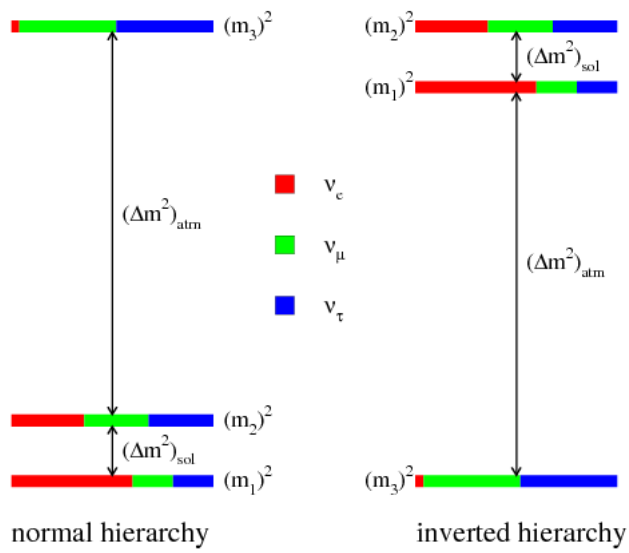

Figure 1-4. The different mass eigenstates of neutrinos, along with the different mass splittings for normal hierarchy (left) and inverted hierarchy (right). The colored regions of mass eigenstate represent the relative flavor components, and are related to the mixing angles mentioned previously.

Neutral particle oscillations are not restricted to neutrinos in the standard model. Neutral kaons and B-mesons oscillate between their mass and intrinsic strangeness (or intrinsic beauty in the case of B-mesons) eigenstates [11]. However, unlike neutrino oscillations, kaons and B oscillations are governed by the weak force. The oscillations observed are a result of $W^{\pm}$ emission and absorption of the s and b quarks. Neutrino oscillations cannot be governed by the weak force (or any other force known in the standard model), because the weak force conserves lepton number in the Standard Model. Neutrino oscillations patently violate lepton number conservation.

1.3 Neutrino Masses and the Hierarchy Problem

Neutrinos remain the sole particle in the standard model without an exact rest mass measurement. Only the square of the differences between neutrino mass eigenstates have been measured directly. Because of this, the order of the mass eigenstates is presently unknown. While it is known that there is one "small" ($\Delta m^2_{12} \approx 7.59 \times 10^{-5}$) and one

"large" splitting ($\Delta m^2_{23} \approx 2.43 \times 10^{-3}$), the order in which nature sorts these splittings is still a mystery.

Figure 1-4 illustrates the different mass orderings. In a "normal hierarchy," the mass eigenstates 1 and 2 make up the lowest mass neutrinos, with the eigenstate 3 being separated by the larger splitting Δm^2_{23}. "Inverted Hierarchy" is the opposite situation, where nature prefers mass eigenvalues 1 and 2 to be larger than 3. With the current data available there is no way to distinguish the different mass hierarchies. Determining the correct mass hierarchy is a goal of next generation neutrino experiments described in Section 1.5.

Related to the question of the mass hierarchy is the question of the absolute mass of the neutrino. The most promising avenue for measuring the neutrino's mass is in beta decay, the very same channel which prompted its' prediction in the first place. The allowable energy of the daughter e^- in a beta decay is equal to the mass difference of the parent and daughter nuclei (M_N) minus the neutrino and electron rest mass (M_ν and M_e). As a result, the electron kinetic energy spectrum will have a cutoff energy equal to $M_N - M_\nu - M_e$. Since the *total* mass of all three neutrino eigenstates is constrained to be less than 0.5 eV from cosmological measurements [12], experiments need to search for an energy difference on the order of 0.1 eV.

Future experiments designed to measure this mass tend to use tritium (^{3}H) as a beta decay source, and then have a large magnetic mass spectrometer to make a high resolution energy measurement of the daughter electron. This is the strategy behind the upcoming Karlsruhe Tritium Neutrino Experiment (KATRIN), diagrammed in Figure 1-5.

1.4 Majorana Neutrinos

While the question of whether or not neutrinos are massive particles is definitely answered by the observation of neutrino oscillations, the question of how they obtain that mass is still open. If neutrinos are typical fermions, similar to an electron for example, then

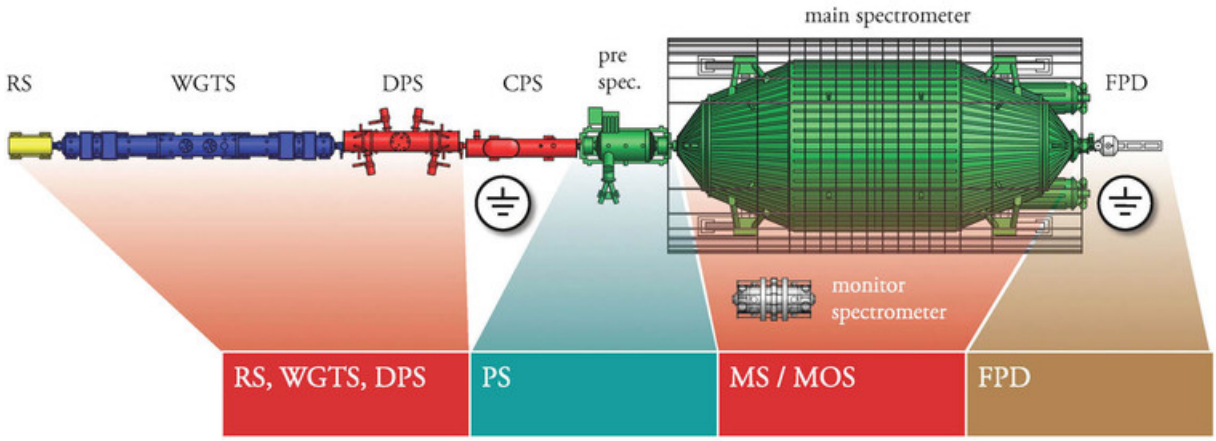

Figure 1-5. Diagram of the KATRIN experiment. The main spectrometer of the region is responsible for measuring the energies of the electrons from beta decay. The remainder of the apparatus is used for purifying and focusing the electron beam prior to entry into the spectrometer. Figure is from Ref [13].

neutrinos obtain mass by coupling to the Higgs field in the same way as other fermions. However, this formalism has a serious flaw.

All fermions in the Standard Model exist as solutions to the Dirac equation. These solutions are superpositions of two states of "handedness," which are two different components of a Weyl spinor:

$$\begin{pmatrix} \psi_R \\ \psi_L \end{pmatrix}. \tag{1-13}$$

Physically, handedness can be interpreted as the Lorentz invariant analog of helicity (λ), the dot product of a particles spin along its' momentum vector:

$$\lambda = \frac{\vec{S} \cdot \vec{p}}{|p|}. \tag{1-14}$$

A particle's handedness can also be written as a sum of two different helicity states. For a spin $\frac{1}{2}$ fermion, such as a neutrino, there are two possible helicity states, $\pm\frac{1}{2}$:

$$\psi_R \propto \left|\nu_{1/2}\right\rangle + \frac{m}{E}\left|\nu_{-1/2}\right\rangle,$$
$$\psi_L \propto \left|\nu_{-1/2}\right\rangle + \frac{m}{E}\left|\nu_{1/2}\right\rangle, \tag{1-15}$$

where m and E are the particle's mass and energy respectively. Interaction with the Higgs field, responsible for giving particles mass in the Standard Model, changes a particle's handedness by two units (from right to left or left to right):

$$\psi_L + H^0 \rightarrow \psi_R. \tag{1-16}$$

However neutrinos have only ever been observed in a single handedness. Neutrinos are always left handed, and anti-neutrinos are always right handed. This was measured experimentally by C. S. Wu in 1956, who investigated the beta decay: ${}^{80}\mathrm{Co}_{27} \rightarrow {}^{60}\mathrm{Ni}_{28} + \mathrm{e}^- + \overline{\nu}_e$ [14]. In order for this decay to simultaneously conserve linear and angular momenta, the outgoing e^- and $\overline{\nu}_e$ must have opposite helicity states. The spin and helicity of the e^- was measured in a magnetic field, and found to always be left-handed. By momentum conservation, the $\overline{\nu}_e$ is always right handed.

The single-handedness of the neutrino has been confirmed by multiple experiments. This has lead some theories to predict that neutrinos are not normal Dirac particles like all other fermions, but instead Majorana particles which only appear as one handedness. Majorana neutrinos would explain the apparent paradox with the Higgs mechanism. A low-mass left handed neutrino interacts with the Higgs field to create a right handed, high-mass right handed neutrino. This violates energy conservation, and as a result the right handed neutrino quickly re-interacts into the low-mass left handed neutrino. This formalism is commonly referred to as the "seesaw mechanism."

By definition, Majorana particles are their own anti-particles. Modern experiments attempting to deduce the Dirac or Majorana nature of neutrinos exploit this fact by

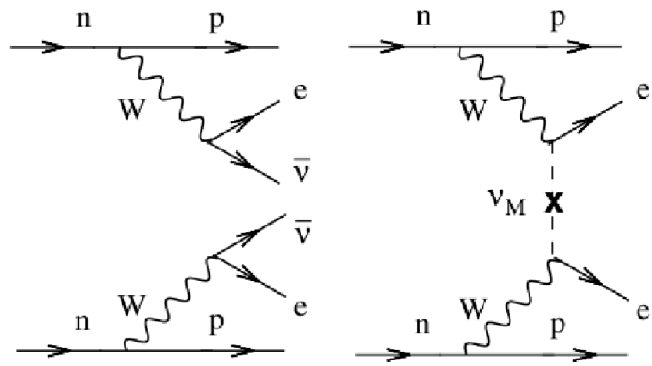

Figure 1-6. A normal double beta decay (left) vs. a neutrinoless double decay (right). Neutrinoless double beta decay is only possible if a neutrino is its' own anti-particle. Figure is from Ref [15].

searching for neutrinoless double beta decay. As the name implies, neutrinoless double beta decay is a typical double beta decay interaction, $nn \rightarrow e^- e^- pp$, where the two $\overline{\nu}_e$ are absent. On the surface, this decay violates lepton number conservation. Digging deeper though, if the $\overline{\nu}_e$ were in fact its' own anti-particle, then it is possible for the ν_e $\overline{\nu}_e$ pair to annihilate before exiting the nucleus. A Feynman diagram of this process is in 1-6.

Numerous experiments have searched for neutrinoless double beta decay, so far without success [16]. The current best limit for the half-life ($t_{\frac{1}{2}}$) of the process $nn \rightarrow e^- e^- pp$ is $t_{\frac{1}{2}} > 10^{24}$ years [17].

1.5 Sources of Neutrinos

As the cross-section of neutrino interactions on matter is very small, experiments which detect neutrinos rely on intense sources. Detectors must likewise be built to be very massive and often times constructed of high density material. These two factors have driven the design considerations of neutrino experiments since the original Savannah River experiment. The largest sources of neutrinos used in neutrino experiments are:

- Neutrinos from nuclear fission reactions in commercial power generating nuclear reactors.
- Neutrinos from nuclear fusion reactions which take place in the core of the sun.

- Neutrinos from particle decays of cosmic ray interactions in the upper atmosphere.
- Man-made neutrinos from particle accelerators.

Other sources of neutrinos exist, including neutrinos from supernovae, however these sources are generally not sufficiently prolific to be used in experiments. The creation of neutrinos via particle accelerators is discussed in more detail in Chapter 4. Roughly speaking, accelerator sources make use of the particle decay: $\pi^+ \rightarrow \mu^+ + \nu_\mu$ by producing a larger flux of pions from accelerated protons.

Future accelerator based experiments such as NuMI Off-axis ν_e Appearance Experiment (NOvA) and Deep Underground Neutrino Experiment (DUNE) will measure the CP violating phase of the PMNS matrix (δ), as well as the mass hierarchy, in the near future [18]. Accelerator neutrino sources have been selected for these experiments because they allow precise control over the $\frac{L}{E}$ of the neutrino beam, which in turn allows control over the location of oscillation peaks described by Equation 1-12. Solving Equation 1-12 for the mass hierarchy and δ simultaneously requires measurement of the flavor oscillating probabilities $P_{\mu\rightarrow e}$ and $P_{\overline{\mu}\rightarrow\overline{e}}$. Figure 1-7 is an illustration of this technique. Future detectors will require the ability to differentiate between electrons and muons with high confidence.

The energy of accelerator created neutrinos for long baseline experiments like DUNE and NOvA are typically in the 1 to 10 GeV range. This happens to be an area of neutrino scattering theory with many uncertainties, as many different processes with complicated physics are contributing. In the past, man made and natural neutrino beams did not have sufficient intensity to create high statistics neutrino data sets. As a result, ignorance of the underlying cross section was not a major concern because the systematic uncertainty would always be smaller than the statistical uncertainties. Modern accelerator based neutrino sources, however, will be powerful enough such that future experiments will not be statistics limited. Future experiments will need improved cross-section measurements to resolve the puzzles presented in this chapter.

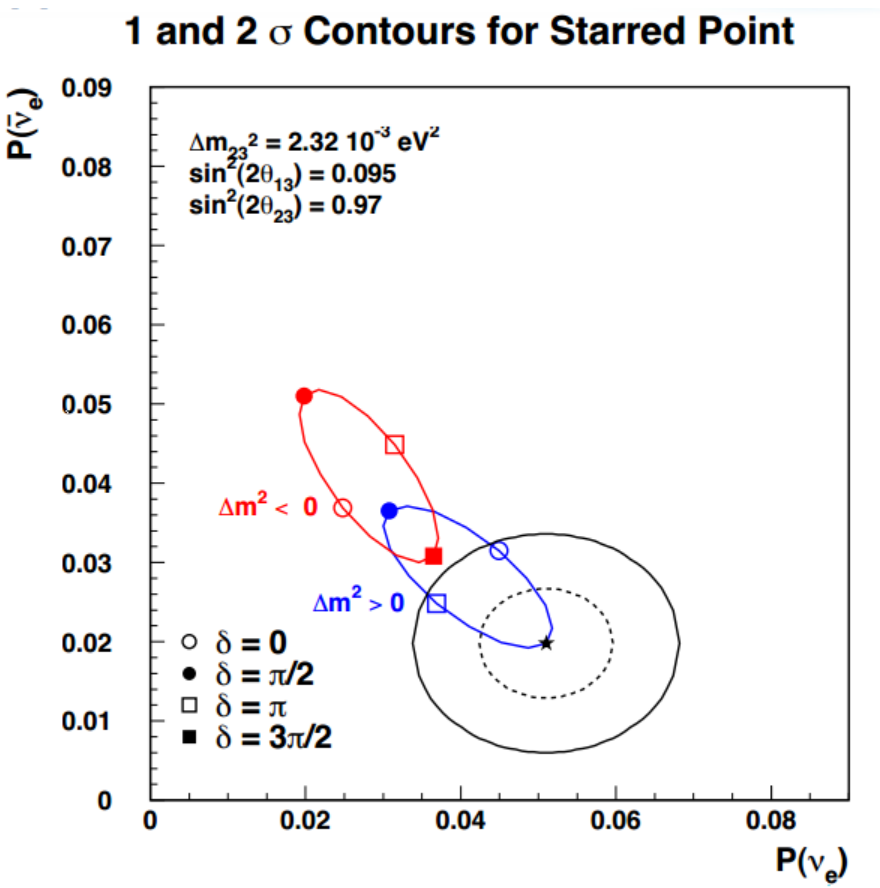

Figure 1-7. A demonstration of multiple possible δ and mass hierarchy measurements of the NOvA experiment. The y-axis reprsents possible $\overline{\nu}_e \rightarrow \overline{\nu}_\mu$ probabilities, and the x-axis different $\nu_e \rightarrow \nu_\mu$ probabilities. The blue elipse maps the possible δ values if the neutrino mass hierarchy is normal, and the red elipse is for inverted hierachy. By making a measurement of $P(\nu_\mu \rightarrow \nu_e)$ and $P(\overline{\nu}_\mu \rightarrow \overline{\nu}_e)$, NOvA will be able to pinpoint δ on one of the elipses. The assumed values for δm^2_{23}, $sin^2(\theta_{13})$ and $sin^2(\theta_{23})$ are given in the top left. Figure is from Ref [19].

CHAPTER 2
THEORY

In some ways, the theory of neutrino scattering is the simplest that can exist in particle physics. Neutrinos are only sensitive to one of the four forces, are point-like objects which do not decay, and posses such small rest mass that they are essentially always relativistic particles. As a consequence of the first property of neutrinos, the only bosons which are capable of mediating the interaction between an incoming neutrino and *any* target are the $W^{\pm}$ and the Z^0.

2.1 Neutral Current Interactions

In the case of an interaction mediated by the Z^0, no charge is exchanged between the incoming neutrino and the target particle. As a consequence, these interactions are referred to as *neutral current*. In a neutral current interaction, the incoming neutrino is identical in flavor to the outgoing neutrino, because flavor changing neutral current interactions are prohibited by the standard model and have never been detected experimentally. Another consequence of this is the target of the neutrino is likewise the same flavor before and after. The target of a neutral current interaction is any particle which is sensitive to the weak nuclear force. In practice these targets are restricted to electrons and protons, as these particles are stable at rest. Neutrons bound inside a nucleus are another potential, stable target for neutral current interactions.

An example of a neutral current interaction is the scattering of a neutrino off of a free electron at rest. The Feynman diagram for this interaction is shown in Figure 2-1. Both the neutrino and electron retain their respective flavors in the final state of the interaction. Only the outgoing energy and momentum of the particles have changed. This process can be calculated *exactly* in the Standard Model. In principal, this makes neutral current scattering off electrons an excellent channel to study the flux of a neutrino source [20], but in practice the very small cross section of this process makes the measurement difficult.

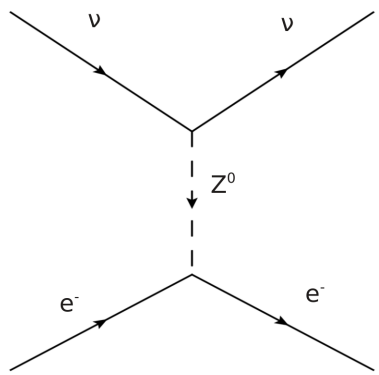

Figure 2-1. Diagram of neutrino neutral current scattering off an electron. The type of neutrino is not identified in the diagram, because the interaction is identical for all flavors of neutrino.

2.2 Charged Current Interactions

Charged current neutrino interactions begin to dominate the total neutrino cross-section once the neutrino has sufficient energy to produce its' charged lepton partner. Unlike neutral current, the charged current interaction is mediated by the $W^{\pm}$ bosons, and charged current interactions are allowed to change the flavor of the target. However, the flavor of the final state lepton is always the same flavor as the incoming neutrino, since lepton number is always conserved in the Standard Model.

All charged current interactions are of the form:

$$\nu_l + X \rightarrow l^{\pm} + Y, \tag{2-1}$$

where l is the charged lepton partner of the incoming neutrino. The charge of l is determined by the type of incoming neutrino. If the neutrino is an anti-particle, then the final state lepton will be an anti-lepton and have a positive charge. This Chapter describes the theory of muon neutrino scattering and it will consider the final state lepton to always be a μ^-.

Charged current interactions are sorted into four different broad categories depending on the final state of the event. These categories are, in order of the energy range

in which their cross sections dominate, charged current quasi-elastic (CCQE), charged current resonant production (CCRES), the inelastic transition region, and charged current deep inelastic scattering (DIS). A fifth type of interaction, where the target nucleus remains in a ground state but produces a pion in the final state, is called coherent production. While evidence for charged current coherent pion production in the 1 to 20 GeV range exists [21], the cross section is small compared to the other three channels and is not discussed further.

2.2.1 Charged Current Quasi Elastic (CCQE)

In CCQE interactions, the target nucleus remains mostly intact after the interaction. A proton is ejected from the nucleus, however the momentum of this proton is assumed to be small compared to the momentum of the outgoing muon. CCQE events have the general form of:

$$\nu_\mu + n \rightarrow \mu^- + p. \tag{2-2}$$

CCQE events are popular signal events for neutrino oscillation experiments [22]. This is because the event signature, a moderate to high energy muon with a low energy hadron, is easy to identify with modern particle detectors. In addition, the energy of the incoming neutrino can in some cases be well approximated by measuring the energy and angle of the outgoing muon.

2.2.2 Charged Current Resonance (CCRES)

Charged current resonant events involve the creation of a delta resonance (Δ) inside the nucleus. The delta creation is induced by the exchange of a W^+ between the neutrino and a proton or neutron bound inside the nucleus. In principal a number of different delta resonances can be created provided the energy of the neutrino contains sufficient center-of-mass energy. In practice, resonant production refers to the production of Δ^+ resonances, which are produced abundantly at neutrino energies above about 3 GeV, when the CCQE cross section begins to shrink.

The lifetime of delta resonances is too short to allow the delta to escape the nucleus, and as a result deltas are never directly observed in experiments. The decay products of the delta, a pion and a nucleon, are ultimately measured. Experiments typically search for a single pion in the final state. This signature is a potential background to CCQE events, since the outgoing pion can be mis-reconstructed as a muon [23]. In addition, the pion may be absorbed by the nucleus as it exits.

2.2.3 Inelastic Transition Region

Resonant and quasi-elastic interactions always posses final state hadrons with characteristic masses. For example, the final state of a quasi-elastic event is always a proton. Resonant events likewise leave a final state of a nucleon and pions consistent with the mass of the delta (≈ 1.2 GeV). Increasing the energy of the incoming neutrino increases the masses of the final state hadrons. There is a transition from the resonant to deep inelastic regime characterized by a breakdown of perturbative quantum chromodynamics (QCD). This transition region is inelastic, as there is significant transfer of energy to the final state hadrons. However it is not formally *deeply* inelastic as the momentum transfered is not large enough to resolve the individual quarks inside the nucleon.

2.3 Charged Current Deep Inelastic Scattering (DIS)

As incoming neutrino energy increases, the amount of momentum transferred to the nucleon from the incoming neutrino increases as well. There is a gradual transition from resonant events, in which the nucleon remains mostly intact, to a more inelastic region where the nucleon is destroyed by the neutrino. When the four momentum transfer becomes large enough such that the neutrino is probing individual quarks inside the nucleons as opposed to the nucleons as a whole, deep inelastic scattering (DIS) begins to take effect.

2.3.1 Definition of DIS

A DIS event is experimentally defined as a neutrino event with an outgoing muon, plus a final state of multiple hadrons. Unlike CCQE or resonant events, in MINERνA no

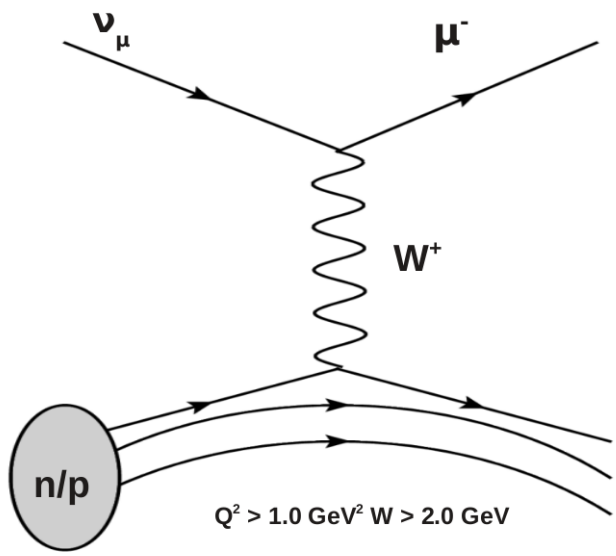

Figure 2-2. Feynman diagram of ν_μ nucleon (proton or neutron) deep inelastic scattering. Of the three quarks present in the nucleon, 2 of them are spectators and do not interact with the exchanged W. The final state of a DIS interaction is not classified by any specific particles, but is instead reconstructed as a shower of hadrons.

attempt is made to identify the particular type of particle found in the final state DIS events. It is assumed that the target quark has been ejected from the nucleon by the incoming neutrino, and what is being measured is the result of various fragmentation processes which occur as the quarks reform into hadrons. The invariant mass of this final state hadronic system turns out to be important, and is given the symbol W (not to be confused with the $W^\pm$ boson.)

A Feynman diagram of a DIS event can be seen in Figure 2-2. The four-momenta of the incoming neutrino, initial state nucleus, final state muon and final state hadron shower are noted as P_ν, P_N, P_μ and P_X respectively. Conservation of four momentum demands:

$$P_\nu + P_N = P_\mu + P_X. \tag{2-3}$$

The four-momentum transferred to the nucleus is equal to $P_\nu - P_\mu$. This variable has the name q in terms of Mandelstahm invariants. The quantity $-q^2$ turns out to be important

for DIS, and is called Q^2. If the energy of the neutrino is E_ν, and the energy and angle of the outgoing muon are E_μ, and θ respectively, then:

$$Q^2 = 4E_\nu E_\mu sin^2\left(\frac{\theta}{2}\right), \tag{2-4}$$

and

$$W^2 = P_X^2 = (P_\nu + P_N - P_\mu)^2. \tag{2-5}$$

Expanding W^2 yields:

$$P_\nu^2 + P_\nu \cdot P_N - P_\nu \cdot P_\mu + P_N \cdot P_\nu + P_N^2 - P_N \cdot P_\mu - P_\mu \cdot P_\nu - P_\mu \cdot P_N + P_\mu^2, \tag{2-6}$$

or

$$|P_\nu - P_\mu|^2 + P_\nu \cdot P_N + P_N \cdot P_\nu + P_N^2 - P_N \cdot P_\mu - P_\mu \cdot P_N. \tag{2-7}$$

Assuming the target nucleon is at rest in the lab frame and has a rest mass of M_N, expansion of the four-vector products result in:

$$-Q^2 + 2E_\nu M_N + M_N^2 - 2E_\mu M_N. \tag{2-8}$$

The total energy of the final hadronic final state must be $E_\nu - E_\mu$ by energy conservation. Setting $E_\nu - E_\mu = E_{had}$ gives:

$$W^2 = 2M_N E_{had} + M_N^2 - Q^2. \tag{2-9}$$

W^2 and Q^2 are the fundamental variables of DIS. An interaction with sufficiently high Q^2 has enough momentum to probe the deep quark structure of the nucleus.

Similarly, an interaction with sufficiently high W^2 imparts enough energy to the nucleon to interact with a constituent quark and create a truly inelastic collision. While the necessary values of Q^2 and W^2 for an event to be DIS are debatable, the general accepted quantities are $Q^2 \geq 1$ GeV^2 and $W^2 \geq 4$ GeV^2 (or $W \geq 2.0$ GeV).

The cross section for neutrino DIS is derived from quantum field theory by contracting together the leptonic tensor, described by electroweak dynamics, and the hadronic tensor of the nucleus, described by QCD. The differential cross section can be expressed in terms of any Lorentz invariant, and related to any other variable using a Jacobian matrix. The cross section expressed in terms of the two Lorentz invariants y and x_{bj} is [10]:

$$\frac{d^2\sigma}{dx_{bj}dy} = \frac{G_F^2}{2\pi} s \left(1 + \frac{Q^2}{m_W^2}\right)^{-2} \left(x_{bj} y^2 F_1 + \left(1 - y - \frac{M x_{bj} y}{E_\nu}\right) F_2 + y(1 - \frac{y}{2}) x_{bj} F_3\right), \quad (2\text{-}10)$$

where x_{bj} is a Lorentz invariant equal to:

$$x_{bj} = \frac{-q^2}{2P_N \cdot q}, \quad (2\text{-}11)$$

and y is equal to:

$$y = \frac{P_N \cdot q}{P_N \cdot P_\nu}. \quad (2\text{-}12)$$

G_F is the Fermi constant, s is the center-of-mass energy of the interaction, m_W is the W$^+$ mass, F_1, F_2, and F_3 are form factors which describe the structure of the nucleon. Theoretically, these form factors are calculated by QCD, while experimentally they are measured by a detector. Each structure function is a function of Q^2 and the dimensionless variable x_{bj}.

In the lab frame, the target nucleon is assumed to be at rest. Equation 7-3 may then be written as:

$$x_{bj} = \frac{Q^2}{2M_N E_{had}}, \tag{2-13}$$

where $E_{had} = P_X^0$. By energy conservation, $E_{had} = E_\nu - E_\mu$, where E_ν is the energy of the incoming neutrino, and E_μ is the energy of the outgoing muon. The physical interpretation of y is clearer after expanding the four-vector product in Equation 2-12. Assuming the target nucleon is at rest in the lab frame:

$$y = \frac{E_{had}}{E_\nu}. \tag{2-14}$$

y is called the *inelasticity* of the event. It is a measurement of how much of the incident neutrino's energy is transfered to the hadronic system. y is defined on the interval $0 \leq y \leq 1.0$.

2.3.2 Scaling and Bjorken-x

If the structure functions were only a function of the dimensionless variable: $F_i(x_{bj})$ and not $F_i(x_{bj},Q^2)$, then that would imply that additional momentum transferred to the hadronic system does not change the form factors of the target nucleon. The fact that F_i have strong a dependence on x_{bj} but a very weak dependence on Q^2 is referred to as scaling, and indicates that there is some point-like structure inside the nucleon [24]. This structure is point-like because it is unchanged by additional momentum transfer, which should be able to resolve finer distances due to the uncertainty principle. This theory of scaling was first proposed by Bjorken in 1968, and experimentally confirmed by the SLAC group in 1967 by directly measuring F_1 and F_2 and showing each was only weakly dependent on Q^2, but strongly dependent on the scaling variable x_{bj} [25]. This in turn, provided direct evidence of nucleons being constructed of point-like particles, or what Murray Gell-Mann referred to as quarks [26].

The Lorentz invariant defined in Equation 7-3 is named Bjorken-x in honor of Bjorken. A physical interpretation of x_{bj} can be derived by boosting into a reference frame where the energy part of q is 0, so $q = (0, \vec{q})$. According to Equation 7-3:

$$x_{bj} = \frac{|\vec{q}|^2}{-2\vec{p}_N \cdot \vec{q}}, \tag{2-15}$$

or equivalently

$$\vec{q} = -2x_{bj}\vec{p}_N. \tag{2-16}$$

The conditions for DIS ($Q^2 \geq 1.0$ GeV^2 $W \geq 2.0$ GeV) imply that the individual quarks inside the nucleon are receiving a large amount of energy from the neutrino. QCD predicts that quarks are asymptotically free, and at sufficiently high energies the strong nuclear force is irrelevant. Under this assumption, the initial four momentum (P_i) and final four momentum (P_f) of the target quark are related by:

$$P_i + q = P_f. \tag{2-17}$$

Recall that the quarks are in a boosted frame where $q^0 = 0$ by definition. In this case, Equation 2-17 breaks down into:

$$\begin{aligned} p_i^0 &= p_f^0, \\ \vec{p_i} + \vec{q} &= \vec{p_f}. \end{aligned} \tag{2-18}$$

Assuming the masses of the quarks are much smaller than their energy, the first half of Equation 2-18 reduces to $|\vec{p_i}| = |\vec{p_f}|$. The quarks also have negligible transverse momentum. These two assumptions imply that the momentum vectors of the initial and final state quarks are either identical, or differ from each other by a sign (the momentum vectors are

back to back). As $\vec{q} \neq 0$ in this frame, the only possible configuration of quark momenta is $\vec{p_i} = -\vec{p_f}$. With this information, the second expression in Equation 2-18 reduces to:

$$\vec{p_i} = \frac{-\vec{q}}{2}. \tag{2-19}$$

Substituting the definition of $\vec{q}$ from Equation 2-19 into Equation 2-16 yields:

$$\vec{p_i} = x_{bj}\vec{p_N}. \tag{2-20}$$

According to Equation 2-20, the physical interpretation of x_{bj} in the quark model is the fraction of the nucleon's total momentum carried by the quark interacting with the W^+ boson. Assuming Bjorken scaling holds in the DIS region, $F(x_{bj}, Q^2) \approx F(x_{bj})$. This means the structure functions in Equation 2-10 describe the distribution of quarks inside the nucleon as a function of their fractional momenta. Nucleons are composed of valence quarks that carry most of the nucleons momentum, sea quarks, and finally gluons which carry fractionally less momentum. All of this information can be combined into *parton distribution functions* (PDFs). PDFs describe the makeup of the nucleon in terms of valence and sea quarks. For a given structure function F_2 for example [27]:

$$F_2(x_{bj}, Q^2) \approx F_2(x_{bj}) = \sum_i k_i x_{bj}(q_+(x_{bj}) + q_-(x_{bj}) + \bar{q}_+(x_{bj}) + \bar{q}_-(x_{bj})), \tag{2-21}$$

where the sum is preformed over each quark flavor i, k_i is the color charge of each flavor, $q_\pm$ is the quark distribution function for spins aligned (misaligned) with the nucleon, and $\bar{q}_\pm$ is the anti-quark distribution function for spins aligned (misaligned) with the nucleon. Valence quarks, which make up the majority of a nucleon's quarks and thus make up a majority of the nucleon's momentum, dominate at large values of x_{bj}. Conversely, sea quarks, which carry very little of the nucleon's momentum, appear at small values of x_{bj}.

It should be noted that some of the assumptions used to define x_{bj} as the quark's fractional momentum are in general *not* true. As an example, quarks are not massless and this "target mass" effect warps the scaling of quarks from x_{bj} to a different scaling variable. QCD should be able to predict the distribution of quarks within the nucleon regardless of the Q^2 of the interaction. The derivation of DIS assumes a significantly large Q^2 such that higher powers of Q do not contribute to the perturbative expansion of QCD. There are however, QCD effects as powers of $\frac{1}{Q^4}$ and $\frac{1}{Q^6}$. These "higher twist" effects become important when trying to extend the DIS formalism to lower Q^2 and W values. There is some discussion on these subjects in Section 3.

2.4 Nuclear Effects in DIS

If nucleons were free particles which did not bind into nuclei the story would be complete. Equation 2-10 would completely describe all DIS interactions in terms of three structure functions F_1, F_2 and F_3, which are different for protons and neutrons due to the different valence quark content. However, the universe contains nuclei of protons and neutrons bound together by the strong nuclear force. This nuclear binding is not taken into account in deriving Equation 2-10, which is derived for free nucleons.

2.4.1 Non-Isoscalarity

The most obvious way to extend Equation 2-10 to calculate the *nuclear* cross section of a nucleus with atomic mass A would be to take a linear combination of the proton and neutron differential cross sections $\frac{d\sigma^P}{dxdQ^2}$ and $\frac{d\sigma^N}{dxdQ^2}$:

$$Z\frac{d\sigma^P}{dx_{bj}dy} + (A-Z)\frac{d\sigma^N}{dx_{bj}dy}, \tag{2-22}$$

where Z is the charge of the nucleus.

The proton piece of Equation 2-22 is smaller than the neutron piece. The ν_μ must convert to a μ^- in a charged current interaction as it must be interacting with a d quark to conserve charge. The cross-section of the ν_μ + neutron should therefore be larger than ν_μ + proton because the neutron contains two d quarks. For nuclei with an equal number of

protons and neutrons (isoscalar) this difference is not meaningful for a cross section averaged over all nucleons. However, heavier elements such as iron and lead contain an uneven number of protons and neutrons. This means a per-nucleon total cross section will contain more ν_μ + neutron events in lead compared to carbon. As a result, when taking the lead to carbon cross section ratio, one expects the lead cross section to be higher even when calculating a per nucleon cross section. Valence quarks tend to dominate at large values of Bjorken-x. As a result non-isoscalar effects tend to be larger at higher values of x_{bj}. They also become more prominent as A increases, and the ratio of neutrons to protons in the nucleus increases.

Non-isoscalarity persists for all x_{bj} values of DIS interactions. The effect is stronger at high x_{bj}, but it is present at low x_{bj}. The remaining nuclear effects discussed have a very strong x_{bj} dependence, and the size of the effect has a strong correlation with the x_{bj} of the event. Recalling that x_{bj} is the fraction of the total nucleon momentum carried by the target quark, x_{bj} dependent nuclear effects thus correspond to effects stemming from sea and valence quark distributions.

2.4.2 Nuclear Structure Functions

The next way to extend Equation 2-10 for bound nucleons is to substitute the free nucleon structure functions F_1, F_2, and F_3 with *nuclear* structure functions F_1^A, F_2^A, and F_3^A. These nuclear structure functions are related to the free nucleon structure functions by a function $f(x_{bj}, Q^2)$:

$$F_i^A(x_{bj}, Q^2) = f_i(x_{bj}, Q^2) F_i(x_{bj}, Q^2). \tag{2-23}$$

$f_i(x_{bj}, Q^2)$ may be different for different structure functions and different nuclei. The factor of Q^2 in f allows f to parametrize the target mass and higher twist effects discussed earlier. Since these effects are not explicitly discussed in the text, f_i is only a function of x_{bj} and 2-24 reduces to:

$$F_i^A(x_{bj}) = f_i(x_{bj})F_i(x_{bj}), \tag{2-24}$$
$$f_i(x_{bj}) = \frac{F_i^A(x_{bj})}{F_i(x_{bj})}.$$

The most common parameterization of f is derived from electron + nucleus DIS scattering experiments. As targets of truly free nuclei are difficult to use, ^{2}H is commonly used as the denominator in Equation 2-24. Figure 2-3 shows a parameterization of $f(x_{bj})$ (solid line) along with data from different charged lepton DIS experiments. There are four features in this parameterization stemming from x_{bj} dependent nuclear effects:

- Nuclear shadowing: a depletion in the bound nucleon structure function relative to the free for $x_{bj} < 0.1$.
- Anti-shadowing: an enhancement in the bound nucleon structure function relative to the free for $0.1 < x_{bj} < 0.3$.
- The EMC effect: a second depletion in the bound nucleon structure function relative to the free for intermediate x_{bj} values $0.3 < x_{bj} < 0.75$.
- Fermi motion: a sharp rise in the bound nucleon structure function as x_{bj} increases past $x_{bj} > 0.7$.

Each of these effects will be discussed in detail in the subsequent sections.

2.4.3 Nuclear Shadowing

Nuclear shadowing is caused by hadronic fluctuations of the intermediate boson. In the case of ν_μ DIS, this boson is a W^+. The fluctuated hadrons multiple scatter off surface nucleons, but are invisible to the nucleons bound deeper in the nucleus. This leads to an interference term in the cross section, which in turn reduces the bound nucleon structure functions.

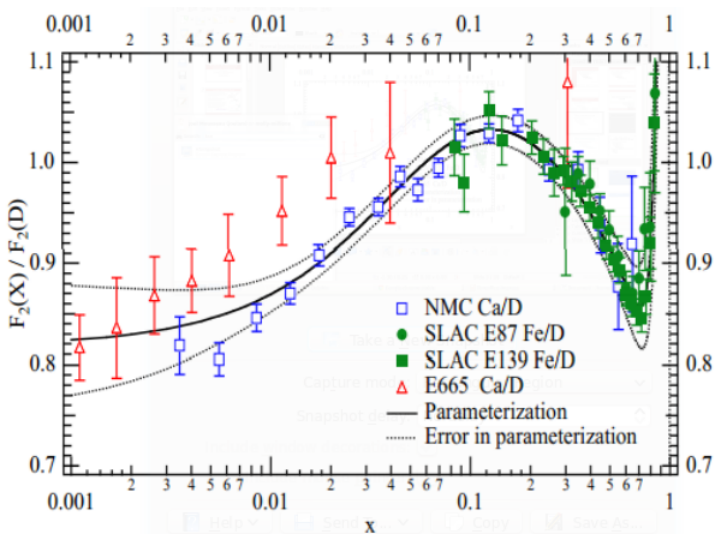

Figure 2-3. A sample parameterization of $f(x_{bj})$ (solid line), along with data from various experiments (points). The dashed line is the uncertainty on the parameterization. Figure is from Ref [28].

Nuclear shadowing occurs at low x_{bj} because there is a coherence length associated with the hadronic fluctuations of the boson. Derivation of this coherence length is beyond the scope of this thesis, however it can be estimated dimensionally by:

$$l \approx \frac{E_{had}}{Q^2 + m^2}, \tag{2-25}$$

where m^2 is the effective mass of the hadronic fluctuation. As l is directly proportional to the E_{had} of the event, low E_{had} events will not have a long enough coherence length for the hadronic fluctuation to interact with the nucleus. High E_{had} events are primarily low x_{bj} by Equation 2-13, hence shadowing may only occur at low x_{bj} [29].

It should be noted that the mass term in 2-25 can be very different for neutrinos and charged leptons. Charged lepton DIS is dominated by the vector current, which leads to effective mass terms on the order of 1 GeV^2. Neutrinos however have a contribution from the axial vector current which pushes the effective mass closer to the pion mass ($\approx$ 100 MeV^2). As a result, shadowing in neutrino scattering may occur with a longer coherence length and thus, larger values of x_{bj}.

2.4.4 Anti-Shadowing

Anti-shadowing is the converse of shadowing. An enhancement of the bound nucleon structure function is observed beyond the x_{bj} range of shadowing. Anti-shadowing was predicted shortly after shadowing was confirmed, and has been observed conclusively by muon scattering DIS experiments [30]. While shadowing suppresses the cross section of sea quarks inside the nucleon, anti-shadowing compensates for the missing quarks by enhancing the cross section at intermediate x_{bj} values.

2.4.5 The EMC Effect

The EMC effect is the depletion of the bound nucleon structure functions in the intermediate x_{bj} region of $0.3 < x_{bj} < 0.7$. It is named for the European Muon Collaboration, which first observed the effect experimentally in 1983. Prior to EMC, a gradual rise in the bound nucleon structure functions was expected beyond the anti-shadowing range. However, EMC clearly observed the opposite [31]. Because the EMC effect occurs in the intermediate x_{bj} regime, the effect originates from the valence quarks of the nucleon.

There is currently no universally accepted cause of the EMC effect [32]. Numerous theories have been proposed, including modifying the free nucleon pdfs with nuclear wave functions to derive nuclear pdfs phenomenologically [33]. It is known that the EMC effect is a strong function of the local nuclear density. Larger nuclei exhibit a stronger EMC effect relative to deuterium than lighter nuclei, as shown in Figure 2-4.

To date, the EMC effect has never been measured in neutrinos. A systematic measurement of the EMC effect with neutrinos would require multiple nuclear targets exposed to the same neutrino beam. Otherwise, systematic uncertainties from different fluxes and detector smearing effects would completely wash out any differences. MINERνA was equipped with multiple nuclear targets precisely to investigate this effect.

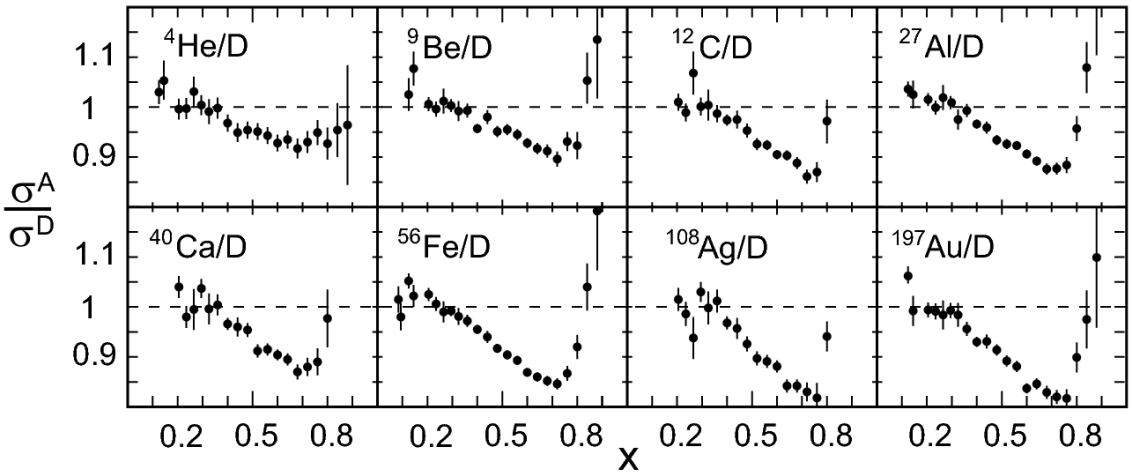

Figure 2-4. Size of the EMC effect for multiple nuclei. The heavier elements (gold, silver) show a sharper drop in the x_{bj} range of $0.5 < x_{bj} < 0.8$. Figure is from Ref [34] with data from Ref [35] and [36] .

2.4.6 Fermi Motion

As x_{bsj} increases above 0.7 the valence quarks begin to dominate the structure functions. In addition, the bound nucleon structure functions begin to grow much larger relative to the free nucleon structure functions. This effect, called Fermi Motion, is caused by the fact that any nucleon bound inside a nucleus may have an x_{bj} up to $x_{bj} = A$, where A is the number of nucleons inside the nucleus. As a consequence nucleons bound in a heavy nucleus A have access to a larger x_{bj} than those bound in a lighter nucleus a.

Fermi motion is difficult to observe in DIS events except at very high Q^2. This can be seen by setting $x_{bj} = 1$. In that case:

$$Q^2 = 2M_N E_{had}. \tag{2-26}$$

substituting Equation 2-26 into the definition of W^2 gives:

$$W = \sqrt{M_N^2 + 2M_N E_{had} - 2M_N E_{had}},$$
$$W = M_N. \tag{2-27}$$

$W = M_N$ implies the event is elastic, because the mass of the nucleon remains unchanged after the neutrino interaction. Increasing x_{bj} therefore pushes $W \to M_N$. This patently violates one of the assumptions of DIS that enough energy and momentum have been transfered to the nucleon that the individual partons may be resolved. Large x_{bj} values are possible in DIS events if the Q^2 is very large. In practice any experiment has a limit on the maximum available Q^2 because the beam energy and angular acceptance are both limited.

CHAPTER 3
EVENT SIMULATION

Processes in particle physics are fundamentally governed by probabilities that predict different outcomes of interactions. Simulating these processes is thus challenging, as on an individual event level the process is not deterministic. A realistic simulation of DIS events, or any neutrino interaction event, must simulate large numbers of events in order to fully capture all possible outcomes. This process of simulating a large number of events randomly based on input probabilities is referred to as the *Monte Carlo* (MC) technique [37]. Because Monte Carlo simulation is so ubiquitous in particle physics, it is common to describe any distribution based on the simulation as the Monte Carlo, or MC.

3.1 The GENIE Event Generator

MINERνA uses the GENIE event generator (Generates Events for Neutrino Interaction Experiment) [38] to simulate neutrino interaction events using the Monte Carlo technique. GENIE begins any event generation by first calculating the total cross section of a process as a function of E_ν. This is accomplished by integrating over the differential cross section for a specific process. The manner in which GENIE calculates this differential cross section is covered in the next section, and is not relevant to the current discussion.

Integrating the cross section is a computationally intensive process. GENIE only integrates this calculation once for a given material description and neutrino flux distribution, and stores that calculation in a spline file. In the case of resonant and DIS events, GENIE makes another simplifying assumption that the total nuclear cross section as a function of E_ν is simply the sum of the free nucleon cross sections. That is:

$$\sigma_A = Z\sigma_p + (A - Z)\sigma_n, \tag{3-1}$$

where A is an arbitrary nucleus of charge Z. This implies that GENIE does not include any nuclear effects in its calculation of the total cross section for DIS events. The integrated total cross section is stored on disk as a spline file. This spline file is accessed

during subsequent event generation, and the total cross section is only computed once per GENIE version.

Once GENIE has the total cross sections in place it still requires an input flux and detector geometry. In the case of MINERνA, the flux is input as a simulation of the neutrino energy beam explained in Chapter 4. The geometry is a description of the MINERνA detector described in Chapter 5. The first thing GENIE does is simulate a neutrino energy and flavor from the input flux. Since this Chapter is concerned with ν_μ DIS interactions, it is assumed that the incoming neutrino is a ν_μ of arbitrary energy E_ν which interacts with a nucleon N with mass M_N.

GENIE then propagates the neutrino through the detector geometry. The type of interaction is dictated by the total cross section as a function of neutrino energy of each of the different interactions GENIE is capable of simulating. Interactions with a higher cross section have a higher probability of being generated. At the conclusion of this step, GENIE has determined a process for the $\nu_\mu + N$ interaction. The most common processes observed in MINERνA are charged current quasi elastic, resonance production, and deep inelastic scattering.

3.2 GENIE's Model for DIS

Any process GENIE simulates is governed by some underlying model. A given model requires some input in order to calculate the differential cross section it is attempting to simulate. GENIE begins generating the initial state by randomly selecting a value (or set of values) the model requires to calculate a differential cross section. This value respects the phase space of the $\nu_\mu + N$ interaction, otherwise the event is marked unphysical and discarded. DIS events require a generated x_{bj} and y. The cross section is then calculated from Equation 2-10 using the generated x_{bj} and y.

GENIE's calculation of structure functions is based on the Bodek-Yang model [38], specifically the 2003 version. The Bodek-Yang model computes cross-sections at the partonic $\nu_\mu + N$ level using GRV98nlo pdfs. Bodek-Yang accounts for nuclear mass

modification and higher twist effects by calculating the nucleon pdfs as a function of an updated scaling variable ξ [28]:

$$\xi = F(x_{bj}, Q^2). \tag{3-2}$$

It should be noted that GENIE's definition of DIS is *not* the definition of DIS described in Section 2.3. GENIE uses the Bodek-Yang model to simulate events in a W range of $W > 1.3$ GeV, which is below the traditional accepted W of $W \geq 2.0$ GeV. This is one reason for the Q^2 dependence of ξ, the Q^2 dependence is tuned to account for higher twist effects which appear outside the DIS region. As a consequence, $\xi \to x_{bj}$ as $Q^2 \to \infty$.

Additionally, GENIE makes an ξ dependent correction event by event to the differential cross section $\frac{d\sigma}{dydx_{bj}}$ to account for x_{bj} dependent nuclear effects from charged lepton scattering. The modification made to the event is applied identically to all elements heavier than helium. The DIS analysis presented in this thesis analyzes carbon, polystyrene (CH), iron, and lead. As a consequence, no differences are expected in the differential cross-sections of these materials once mass, target number, and non-isoscalar effects are taken into account. This was tested empirically by running the MINERνA build of GENIE on free nucleons (protons and neutrons) as well as the heavy nuclei found in the detector (C, CH, Fe and Pb). The details of this study may be found in [39], however the conclusions were the nuclear effects simulated be GENIE are identical in C, CH, Fe and Pb.

As a reference, the function GENIE uses to parameterize the nuclear effects is:

$$\begin{aligned} f(\xi) =& 0.985 * (1. + 0.422\xi - 2.745\xi^2 + 7.570\xi^3 - 10.335\xi^4 + 5.422\xi^5) \\ & * (1.096 - 0.364\xi - 0.278e^{-21.94\xi} + 2.722\xi^{14.417}). \end{aligned} \tag{3-3}$$

This scaling effects all GENIE generated DIS events, and is valid up to an $\xi = 0.75$. Above an ξ of 0.75, GENIE "freezes" the calculation so that $\xi = 0.75$:

$$f(\xi > 0.75) = f(\xi = 0.75). \tag{3-4}$$

3.3 Final State Interactions

Final state interactions (FSI) in GENIE encompass a large class of reactions in which a meson or hadron interacts with surrounding nucleons as it moves through the nucleus. Broadly speaking, GENIE divides the total cross section of intranuclear reactions (σ_{tot}) into elastic and reactive, where $\sigma_{tot} = \sigma_{elas} + \sigma_{reac}$. GENIEs treatment of FSI is based around the Intranuclear Cascade Model (INC) [40].

When particles are generated inside the nucleus, GENIE steps them through the nucleus in steps of 0.1 fm. At each step, it calculates the probability of an interaction proportional to the mean free path of the nucleus:

$$\lambda(E, \vec{r}) = \frac{1}{\rho(\vec{r})\sigma_{tot}(E)}, \tag{3-5}$$

where ρ is the density of the nucleus and $\vec{r}$ is the position vector of the particle. GENIE continues this calculation until reaching an $r = 4r_0$, where r_0 is the radius of the nucleus.

If GENIE simulates an interaction at any given step, the interaction type is selected from the list of intranuclear reactions. These interactions are cataloged in Table 3-1. The relative cross section of each interaction is tuned to a sample of external data. Models are used to calculate the number of particles, as well as the energy distribution of the final state particles after the intranuclear reaction. This distribution respects the phase space of the event. After GENIE has propagated the intermediate state particles through the nucleus, it completes the event by recording all particles and their states to an event record.

GENIE's event record is then input into the simulation of the MINERνA detector and electronics, where it can subsequently can be reconstructed and analyzed in the same

Table 3-1. Different "fates" of an intermediate state particle as it travels through the nucleus. Note that the fate of a particle is determined by the relative cross section of the interaction to the total cross section.

Interaction Type	GENIE Name
Elastic	elas
Charge Exchange	cex
Inelastic	inelas
Absorption	abs
π^+ or π^- creation	PiProd$\pm$

manner as data. This simulation is described in detail in Section 5.3. The reconstruction of data and simulation is described in Chapter 6.

CHAPTER 4
NEUTRINO BEAMLINE

4.1 Overview

Chapter 1 introduced the idea of man-made neutrinos from a particle accelerator as a source for neutrino oscillation experiments. This chapter will expand on that idea, and explain the challenges of theoretically modeling such a beam.

The source of neutrinos for MINERνA is the Neutrinos at the Main Injector (NuMI) beamline. The NuMI beamline began operation in 2004, with the MINOS experiment as the prime consumer. Since then, many other experiments have utilized the beam including ArgoNeuT [41], NOvA [42], and of course MINERνA.

The NuMI beam produces neutrinos primarily through the decays of π and K mesons resulting from p + C collisions. The majority of neutrinos are produced through the decay $\pi^+ \rightarrow \mu^+ + \nu_\mu$. Anti-neutrinos are produced via $\pi^- \rightarrow \mu^- + \overline{\nu}_\mu$. NuMI is equipped with magnetic horns used to sign select π^+ or π^- depending on if the experiments require neutrinos or anti-neutrinos (see Section 4.3). ν_e appear in the beam as a product of the semi-leptonic decays of Kaons, however they only make up $\approx 1\%$ of the neutrino content.

4.2 The Fermilab Accelerator Complex and Main Injector

All of protons used to create the neutrinos observed by MINERνA begin their lives as ^{1}H atoms at the Fermilab pre-accelerator. The atoms are ionized into H^- by a charged cesium plate at the final stage of a 750 kV Cockroft Walton accelerator. H^- ions are loaded into a linear accelerator ("linac") after exiting the Cockroft Walton. The linac accelerates the ions to an energy of 400 MeV using an alternating electric field.

Upon exiting the linac, dipole magnets in a "dogleg" configuration steer the H^- into the ring of the Fermilab booster. This dipole deflects the incoming H^- ions in the opposite direction as the already circulating protons from previous linac extractions. A carbon foil located downstream of the dipole strips the H^- of it's electrons. The Fermilab booster is a synchrotron composed of 17 radio frequency (RF) accelerating cavities and 24 quadropole

magnets in a focusing defocusing array (FODO). The booster accelerates the now pure proton beam to 8 GeV over 20,000 turns at a frequency of 37.77 MHz at proton injection, and 52.81 MHz at extraction [43]. The operating parameters of the booster are given in Figure 4-1.

Booster Parameters

Circumference.....2π x 74.47 meters
Injection energy.....400 Mev (kinetic)
Extraction energy.....8 Gev (kinetic)
Cycle time.....1/15 sec
Harmonic number, h.....84
Transition gamma.....5.45
Injection Frequency.....37.77 Mhz
Extraction Frequency.....52.81 Mhz
Maximaum RF voltage.....0.86 MV
Longitudinal emittance.....0.25 eV sec
Horizontal β max.....33.7 meters
Vertical β max.....20.5 meters
Maximum dispersion.....3.2 meters
Tune υx = υy.....6.7
Transverse emittance(normailized).....12π mm rad
Bend magnet length.....2.9 meters
Standard cell length.....19.76 meters
Bend magnets per cell 4
Bend magnets total.....96
Typical bunch intensity.....3 x 10e10
Phase advance per cell.....96 degs
Cell type.....FOFDOOD (DOODFOF)

Figure 4-1. Operating parameters of the Fermilab booster. Figure is from Ref [43].

The injection and extraction frequencies of the booster differ because once the protons have been accelerated to 8 GeV in the booster, they must be transfered to the Fermilab main injector, a larger cyclotron operating at 52.81 MHz. This extraction is accomplished using "kicker" magnets to vertically deflect the proton beam into the main injector aperture. The main injector accelerates the protons to 120 GeV and groups them into batches roughly 1.5 μs wide [44]. During the operation of the Fermilab Tevatron, the NuMI beam would utilize 5 of these bunches. After the decommissioning of the Tevatron in

2012 the main injector no longer needed to stack and store anti-protons, and 6 bunches were delivered to NuMI. A typical time profile of the NuMI beam is plotted in Figure 4-3.

4.3 Neutrinos at the Main Injector

Protons from the main injector are extracted every 2 seconds at an energy of 120 GeV for use by NuMI. The main injector protons are extracted first with a horizontal and then vertical displacement to bend the proton beam down toward the target hall. Each extraction results in approximately 10^{13} protons per pulse (ppp). Finally, the proton beam is collimated and focused magnetically to match the cross sectional area of the graphite target [45].

The NuMI graphite target is actually a series of small pellets ("fins"), each $20 \times 15 \times 6.4$ mm. The target contains 48 fins which make up a total of two proton-carbon hadronic interaction lengths. This thin fin design optimizes the p + C cross section, while likewise minimizing the rate secondary of π and K interactions in the carbon. The fins are housed snugly in an aluminum canister running parallel to two water lines used for cooling. The entire target assembly rests inside a magnetic focusing horn. Figure 4-3 shows a diagram of the target assembly [46].

Two magnetic focusing horns are used to focus and defocus the resulting mesons via a 30 kG toroidal field. Each horn "chirp" is 200 kA and 30 kG triggered with the proton pulse [48]. In forward horn current mode (FHC) the horns pulses a negative current to focus π^+. This leads to a beam primarily of ν_μ from the decay channel $\pi^+ \to \mu^+ + \nu_\mu$. The current can be reversed to instead focus π^-, which leads to an anti-neutrino enhanced beam from the channel $\pi^- \to \mu^- + \overline{\nu}_\mu$. In practice the intensity of antineutrinos will always be smaller than neutrinos because the $p + C \to \pi^-$ rate is smaller than $p + C \to \pi^+$ due to charge conservation.

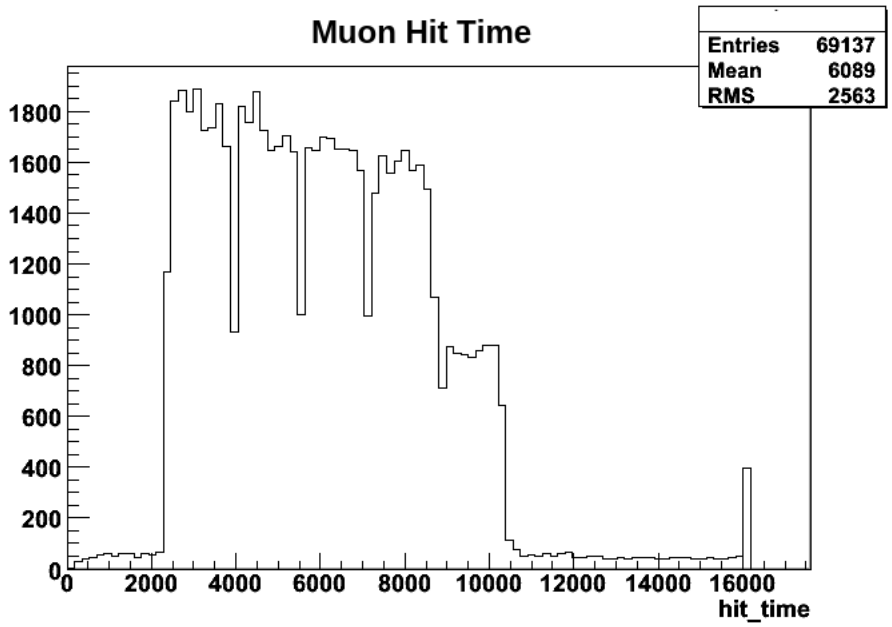

Figure 4-2. Typical time structure of the main injector during Tevatron running illustrated as the hit times of rock muons detected by the MINERνA detector. The units of the x-axis are ns. Five different bunches can be observed, each approximately 1.5 μs wide.

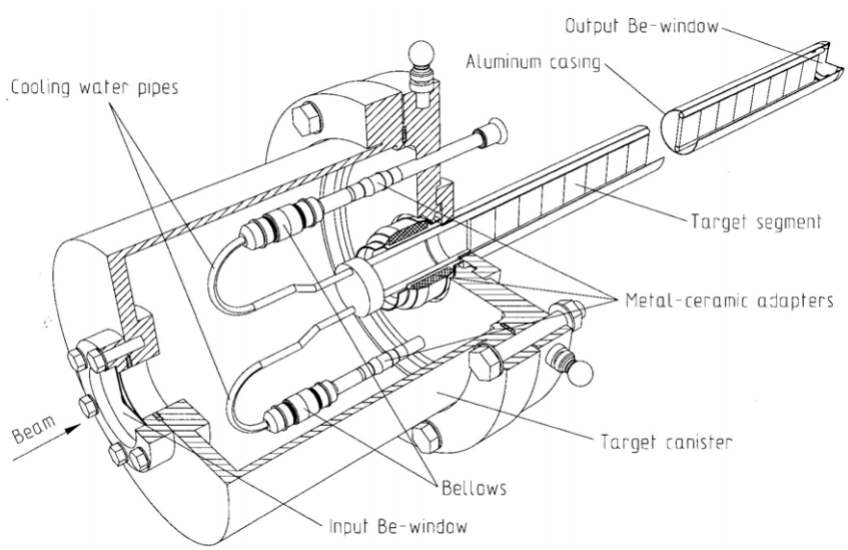

Figure 4-3. Schematic of the NuMI proton target. The cermaic adapters are used to electrically isolate the different metallic components of the assembly. Figure is from Ref [46].

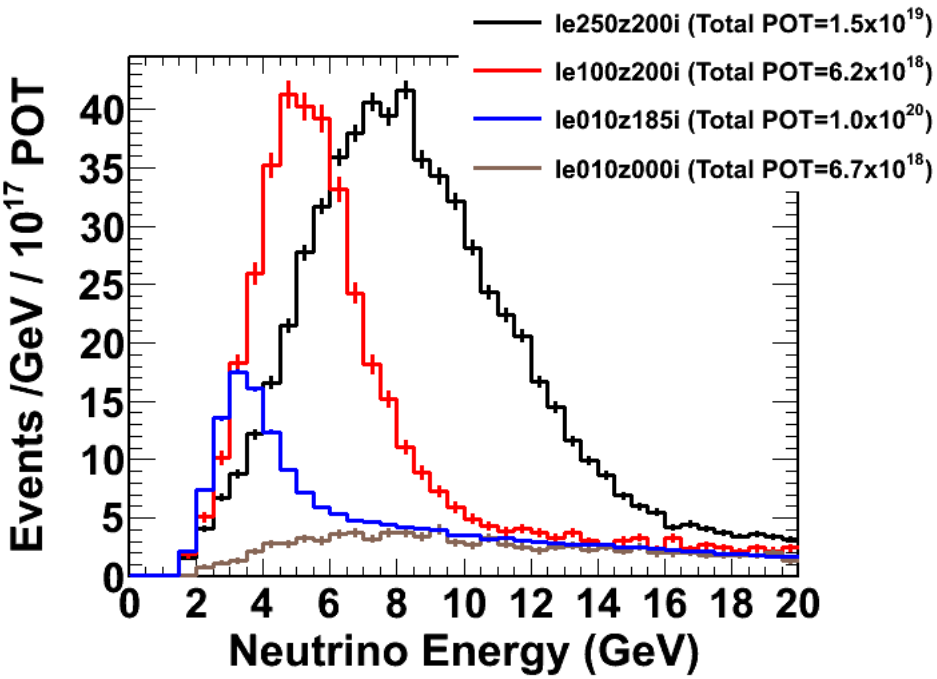

Figure 4-4. Observed neutrino flux in MINERνA for different horn currents and target positions. The black plot represents a run where the target is pulled almost entirely out of the horn. The brown plot represents a run where the horn is turned off, and no meson focusing is conducted. Figure is from Ref [47].

The NuMI target is mounted on rails which allow the longitudinal position of the target to move relative to the horns. This creates a different production, and thus focusing angle for the outgoing mesons. Higher energy pions have a shallower production angle due to the Lorentz boost. Pulling the target partially out of the magnetic horn will force higher angle, lower energy, pions away from the inner conductor of the horn. As a result, they will not be focused into the decay pipe and do not contribute neutrinos to the beam. This creates a higher average neutrino energy. Figure 4-4 gives an illustration of these runs.

All of the products from the target, including the pions decaying into neutrinos, from the target travel through an evacuated decay pipe for 675 m, which is equivalent to the decay length of a 10 GeV pion. The pipe terminates at a steel absorber, directly downstream of a ionization chamber used for beam monitoring [48]. The absorber is thick enough to stop all hadrons which have not decayed, leaving a beam of muons and

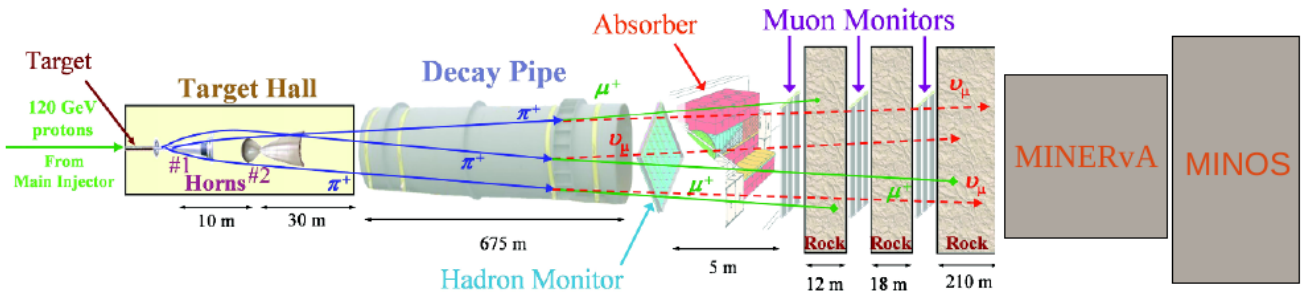

Figure 4-5. Diagram of the NuMI beamline. The distance from the proton source to the MINOS near detector is approximately 1 km. The MINERνA and MINOS detectors are not drawn to scale. Figure is from Ref [49].

neutrinos. The remaining muons range out in roughly 300 m of rock upstream of MINERνA and MINOS. Interspersed with the rock are additional ionization chambers placed in caves parallel to the beam direction. These chambers monitor the muon energy and provide additional diagnostic information as well the ability to constrain the relative beam flux. Figure 4-5 shows all of the components of the NuMI beam line.

4.4 Neutrino Flux Modeling

An essential ingredient for any cross-section experiment is an accurate description of the number of incoming particles, typically as a function of energy and possibly a function of transverse position and angle. For beams of a charged particle, this measurement is straightforward using magnetic toroids or striplines. Neutrino beams unfortunately do not allow live monitoring since the only detectable neutrino interactions destroy the particle in the process. As a result, techniques to estimate this flux theoretically have been developed over the past 20 years. Broadly speaking, an accurate prediction of the incoming neutrino flux consists of three components [50]:

- Modeling of particle production from the primary p + C collision.
- Modeling of the secondary and tertiary interactions of hadrons inside the target and target casing.

- Modeling of the horn's magnetic field produced by current pulse.

The remainder of this chapter consists of remarks on these three topics.

4.4.1 Primary Hadron Production

Production of mesons from the primary p + C collision is simulated in NuMI by the GEANT package [51]. GEANT contains different physics lists, which incorporate the different possible hadronic interactions, their probabilities, and the products of the interactions. The difference in flux predicted by physics lists can be as large as 10% in the peak of the energy spectrum [50]. This translates directly to a systematic uncertainty on the flux prediction, so constraining these models using data is highly desirable.

Incorporating external data into hadron production is often times non-trivial. As a case in point, the kinematics of external experiments rarely coincide with the kinematics of the proton beam used to produce neutrinos. Most hadron production experiments consist of a a primary beam, a production target and some apparatuses downstream of the interaction point for particle detection [52]. These apparatuses have limited acceptance, and as a result the full phase space of the hadron production cannot be measured. This means some kind of extrapolation between energy ranges is necessary.

One can accomplish this by building dimensionless scaling variables such as Feynman scaling [53]:

$$x_F = \frac{2p_L}{\sqrt{s}}, \tag{4-1}$$

where p_L is the longitudinal momentum of the particle, and $\sqrt{s}$ is the center of mass energy of the collision. Using Feynman scaling, the MINERνA experiment may use data taken from the NA49 hadron production experiment [54] to constrain different hadron production models. Figure 4-6 gives an illustration of this process where NA49 data is used to parametrize the Bertini physics list of GEANT.

Future planned constraints of the NuMI flux will take advantage of the NA61 experiment, which has a beam energy closer to the 120 GeV protons of NuMI [55]. In addition, data from the Main Injector Particle Production experiment (MIPP) will be included [56]. These future data sets will be able to cover additional values of x_F and transverse momentum (p_T) that NA49 does not.

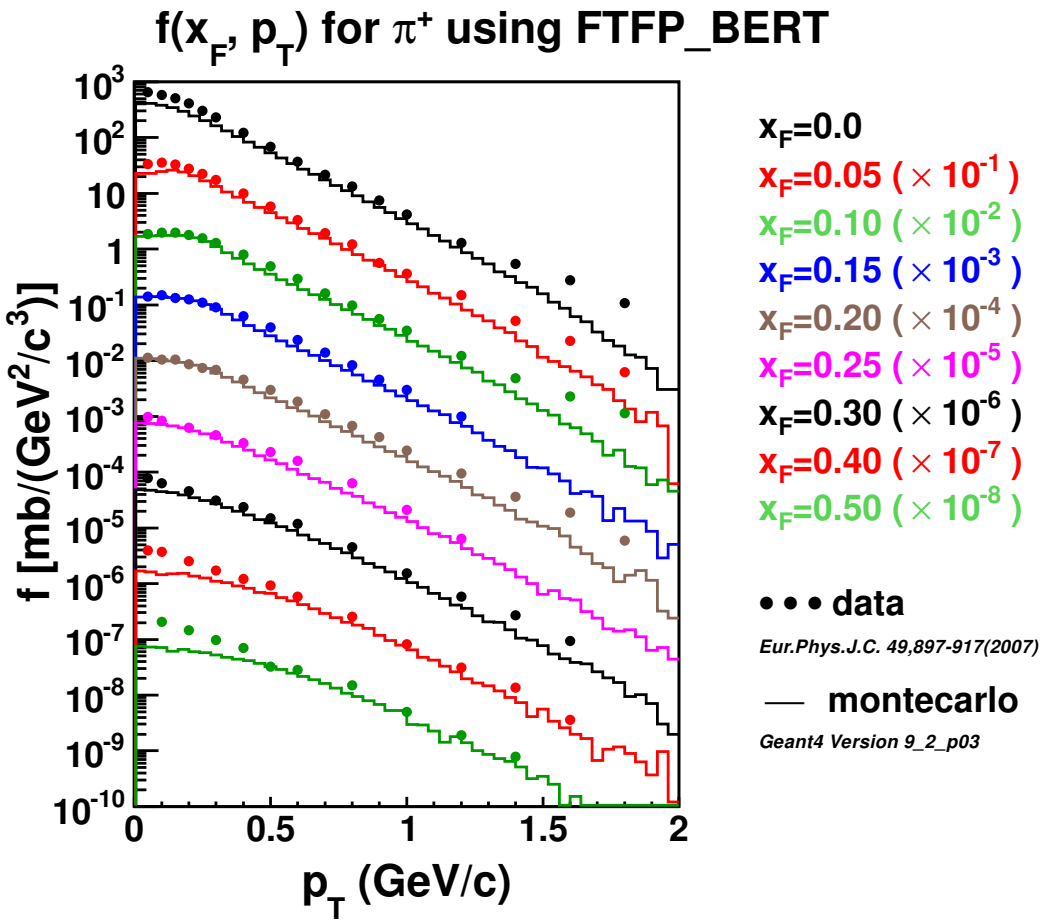

Figure 4-6. NA49 data (points) vs. the predicted production of π^+ from GEANT's FTFP Bertini physics list in different bins of Feynman x, defined in Equation 4-1. The y-axis is the π^+ production cross-section in units of milibarns per GeV per momentum bin. Figure is from Ref [57].

4.4.2 Secondary and Tertiary Hadron Production

Secondary and tertiary hadron production attempts to model the interactions of the mesons (particularly pions) as they exit the target cannister. This may include π + C or π + Al interactions. As with the primary hadrons, interactions of secondary and tertiary hadrons are simulated by GEANT. In principle, these simulations are constrained with the same data as the primary hadron production, since any particle production experiment cannot distinguish between primary and secondary hadrons. In practice however this re-interaction rate is dependent on the size and geometry of targets, meaning the most powerful data are taken with replica targets. Unfortunately, MINERνA does not have a data set available with a replica NuMI target at present. The NA61 experiment is planning to run with a replica NuMI target in the near future [55].

4.4.3 Magnetic Field and Target Modeling

Uncertainties in the magnetic field modeling tend to be smaller than those of hadron production at most energies. They do however, tend to dominate in the focusing peak of the neutrino beam where most events originate. This is shown in Figure 4-7.

While a calculation of the magnetic field of the horn as a function of radial distance is relatively straightforward, the trajectory of a particle traveling through the field is complicated. This is because the source of the mesons (the NuMI target) is *not* a point source and a meson may be generated at any point along the target. Particles may also travel through the horn itself, where they may not only multiple scatter but are subject to skin depth effects since the horn is not a perfect conductor [58]. The NuMI beam simulation accounts for these effects.

There is an inherent uncertainty in this simulation because the simulation does not perfectly replicate the reality of the target-horns configuration. For instance, the magnetic horn in reality is not a perfect conductor and contains some surface currents which change the horn's focusing parameters. Mis-alignments between the graphite target, magnetic

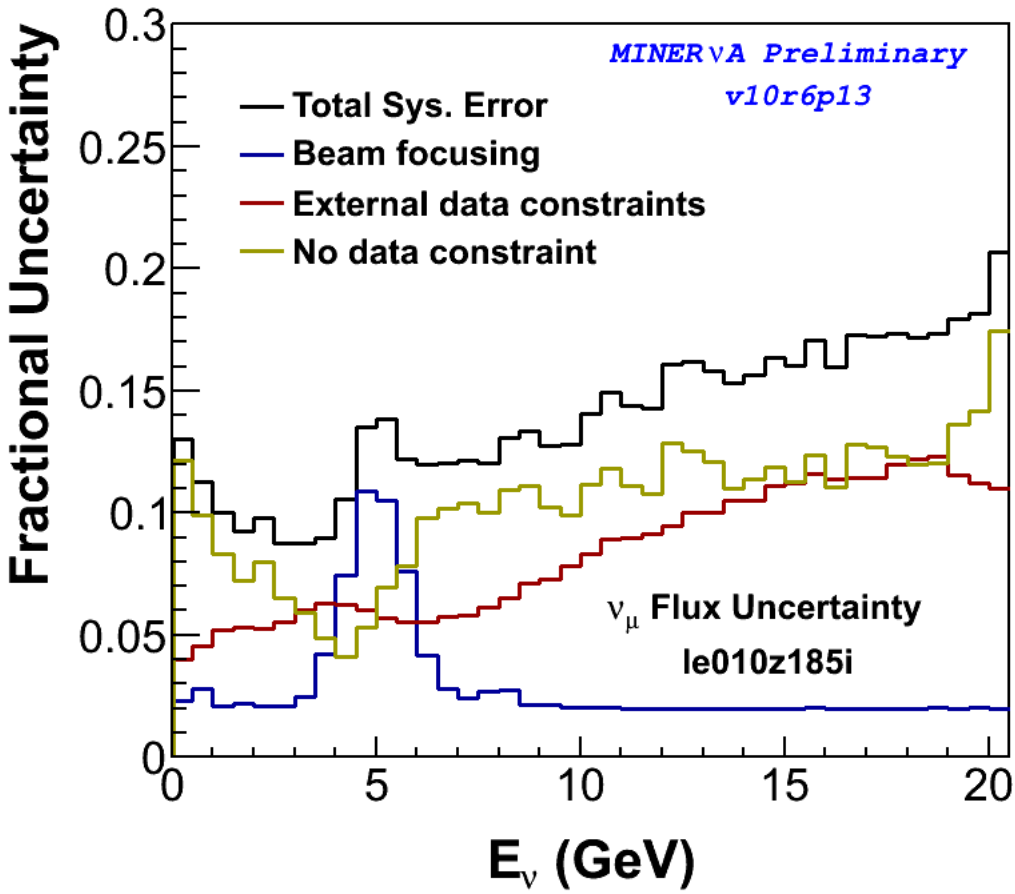

Figure 4-7. Uncertainty on the MINERνA ν_μ flux calculation, broken down by data constrained simulation uncertainties (red), non-constrained simulation uncertainties (gold), and uncertainties in the horn's magnetic filed (blue). Figure is from Ref [59].

horns and the proton beam are also not perfectly modeled in the simulation. All of these factors will alter the predicted neutrino flux spectrum from reality.

Fortunately in the case of magnetic field modeling and target position, the number of parameters in the simulation is finite enough that it is possible to simply re-run beam simulations with different parameters, and directly observe the difference in a detector simulation. Note that this method is *not* possible for estimating the hadron production uncertainty previously mentioned, since that simulation contains thousands of parameters.

Table 4-1. A sample of focusing uncertainties and their magnitudes. Values are from Ref [58].

Source	Uncertainty
Number of POT	2.0%
Horn misalignment (transverse)	1.0 mm
Horn tilt	0.2 mrad
Horn current mis-calibration	1.0%
p + baffle interactions	0.25%
Misalignment of shielding blocks	1.0 cm
Graphite density	2.0%

Calculations of the focusing uncertainties were preformed by the MINOS collaboration for the NuMI beam [58]. A summary of the uncertainties are in Table 4-1.

4.5 Summary

The production of neutrinos via accelerators seems simple on paper. A beam of mesons is produced and sign-selected with a series of magnets. These mesons, primarily π^+ or π^- depending on magnetic field, decay into a neutrinos. However, the details of the pion production, transport, and decay make this process complicated. Cross-checking this calculation with dedicated hadron production experiments provides the most direct way to improve neutrino flux predictions. The MINERνA experiment, however, lacks access to this data in the high energy tail of the neutrino spectrum. This happens to the be the energy region with a large number of DIS events. In order to probe this region with good precision, it becomes necessary to measure ratios of DIS cross sections of different materials. Since the different materials in MINERνA are exposed to the same neutrino beam, the importance of accurately modeling of this beam diminishes significantly, as the neutrino flux dependence will be removed from the ratio.

CHAPTER 5
THE MINERνA DETECTOR AND SIMULATION

5.1 Detector Hardware

5.1.1 Construction and Description

MINERνA is located in the MINOS near detector cavern at Fermi National Accelerator Laboratory in Batavia, IL. The cavern is located approximately 330 feet underground, which serves to reduce the number of cosmic rays detected by the MINERνA and MINOS detectors. The detector is located approximately 1 km away from the neutrino source described in Chapter 4.

The MINERνA detector was constructed to measure neutrino nucleus cross sections on a variety of nuclei with very high precision. To accomplish this goal, the detector must have superior energy, timing, and position resolution. The MINERνA detector is composed of five different regions. The most upstream region contains the veto walls and the liquid helium target. This is followed by the nuclear target region, which contains nuclear targets of solid graphite, iron, and lead as well as a liquid water target. Downstream of the target region, along the beam direction, is the scintillator tracker. The tracker is the largest portion of the MINERνA detector by volume. Following the tracker is the downstream electromagnetic calorimeter (ECAL), and finally the downstream hadronic calorimeter (HCAL). The MINOS near detector lies 2.0 m behind the MINERνA detector, and is used for measuring the energy of escaping muons. A schematic view of the MINERνA detector, as well as the masses of the different sub detectors, is in Figure 5-1.

Central to the construction of MINERνA are detector modules. Each module is built from a hexagonal steel frame which surrounds and supports the inner detector components. The steel frames contain bars of the same scintillator as the inner detector, and act as an outer detector for side exiting particles. The composition of the interior of a module differs depending on its' location in the detector. All of the modules in the inner detector are composed of two types of planes. The nuclear target modules contain one

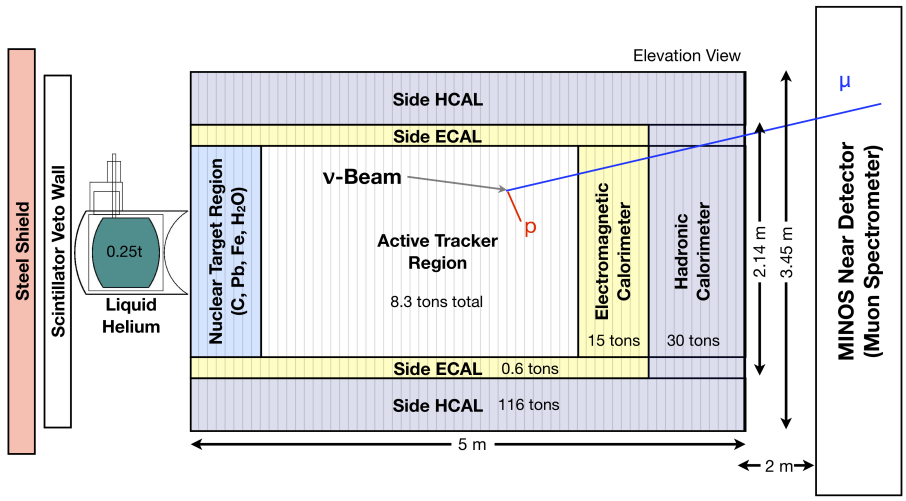

Figure 5-1. Schematic of the MINERνA detector, with all sub-detectors and their masses labeled. Figure is from Ref [60].

plane of passive material and one plane of scintillator. All modules in the tracker and ECAL are composed of two planes of scintillator, however the ECAL modules also contain a 0.2 cm (0.35 electron radiation lengths) wide sheet of lead in front of the two planes. HCAL modules contain one 2.54 cm thick (0.25 neutron interaction lengths) plane of steel and one plane of scintillator [61]. Each module is oriented perpendicular to the neutrino beam and is supported by struts on both sides of the module which rest on a horizontal rail. Modules are stacked one in front of the other with consistent spacing by using uniformly sized bolts. Figure 5-2 shows a diagram of a MINERνA module.

Every MINERνA scintillator plane is composed of individual triangle strips. Each strip is 1.7 cm tall by 3.3 cm wide, and 127 strips are arranged to make one plane. The bottom of each individual strip is coated with a reflective coating of TiO_2, which reflects light before it escapes. The triangular design of the strips allows for finer position resolution based on charge sharing between neighboring strips. The measured position

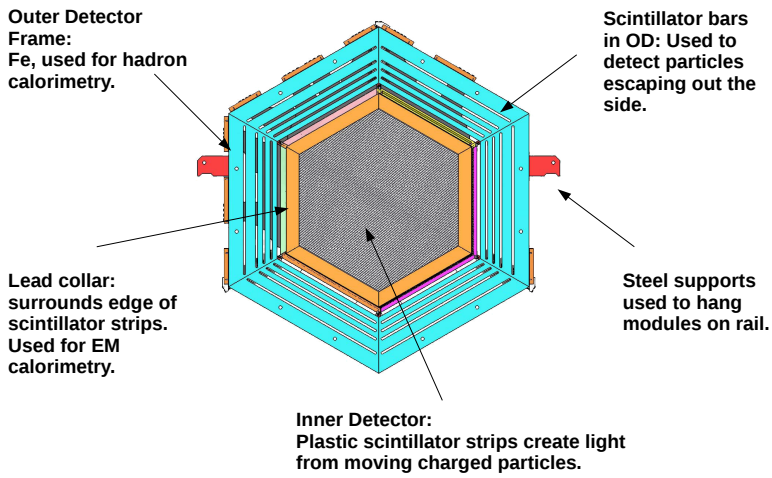

Figure 5-2. A MINERνA module, with the relevant elements labeled. Figure adapted from Ref [60].

resolution transverse to the neutrino beam is 2.0 mm [60]. Each alternating plane of scintillator is rotated $\pm 60°$ with respect to the vertical axis to obtain three different detector views (X, U, V), and provide three-dimensional event reconstruction. Figure 5-3 illustrates the X, U and V view. The scintillating strips themselves are composed of 99% polystyrene (CH) doped with 0.9% 2,5-diphenyloxazole ($C_{15}H_{11}NO$) [62] and 0.1% 1,4-bis(5-phenyloxazol-2-yl) benzene ($C_{24}H_{16}N_2O_2$) [63] to increase scintillating light output [61].

Each scintillator strip contains a green wavelength shifting (WLS) fiber running throughout the center of the strip. These fibers terminate at the end of the strip, and are optically coupled to a clear optic fiber which routes the signal into a 64 anode Hamamatsu photomultiplier tube (PMT). Strips adjacent to each other in the detector are routed to non-adjacent pixels on the face of the PMT. This reduces the cross talk between adjacent detector channels. Each PMT pixel corresponds to one scintillator strip, or one detector channel.

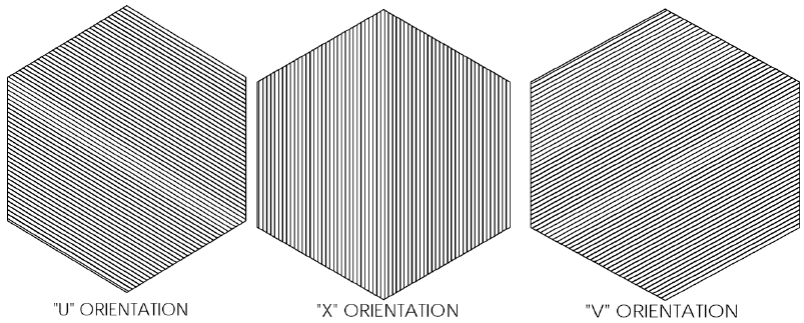

Figure 5-3. The three different detector views constructed in MINERνA. The top of the figure corresponds to the top of the detector, and the beam direction is into the page. Figure is from Ref [61].

5.1.2 The MINERνA Coordinate System

Modules are placed along the z axis of MINERνA, with increasing z along the beam direction toward the MINOS near detector, and decreasing z being in the opposite direction toward the veto wall. Modules are numbered with modules at higher z having larger numbers. The tracker begins with module 23 at $z = 5810.45$ mm, and ends with module 84 at $z = 8614.65$ mm. The y axis of MINERνA points in the opposite direction of gravity, with larger y values being "up," away from the floor. The x axis is oriented such that the (x, y, z) coordinate system is right handed. Positive x is therefore toward the top of Figure 5-1, roughly in the west direction.

5.1.3 Veto Wall and Helium Target

The most upstream sub-detector of MINERνA is the veto wall. The veto wall is composed of two walls of scintillator counters. Each wall contains six 10' x 2.5' counters stacked vertically such that each wall entirely covers the front-face of the MINERνA main detector. The primary job of the veto wall is to identify charged particles which are created by neutrino interactions with the surrounding rock of the MINERνA detector hall. These particles, in particular muons, could be mis-identified as originating from neutrino events in the main detector. Each wall is preceded upstream by a plane of 1 inch thick steel. The

purpose of the steel is to stop low energy particles and photons, as well as forcing higher energy particles to shower before they enter the main detector [64].

Directly downstream of the veto wall is the helium target. Helium is the lightest target material in the MINERνA detector, and is the target with the fewest number of nucleons per nucleus. The helium is kept in a liquid state by a cryogenic refrigerator. The entire cryostat is mounted on elevated rails such that the geometric center of the cryostat is in line with the geometric center of the main detector. The MINERνA cryostat contains no active detection such as a time projection chamber, and is entirely dependent on the veto wall to discriminate neutrino-helium events from particles created in the rock surrounding the detector.

5.1.4 Nuclear Targets

The main MINERνA detector begins immediately following the liquid helium target. The first 30 modules of the main detector are classified as the nuclear target region, and contain five nuclear target modules as described in Section 5.1.1. The other 25 modules are identical to tracker modules. Figure 5-4 shows the layout of the target and tracker modules, along with the liquid helium and water target. The targets are numbered 1 through 5, with target 1 being the most upstream and target 5 being the most downstream. Targets 1, 2 and 5 are composed of iron and lead. Target 3 is constructed of iron, lead and graphite, and target 4 is pure lead. The fiducial masses of each target and material are listed in Table 5-1.

Table 5-1. Fiducial mass of the different target materials of the MINERνA detector, along with the number of protons and neutrons per material. Table is from Ref [65].

Material	Mass (kg)	Number of Protons ($\times 10^{28}$)	Number of Neutrons ($\times 10^{28}$)
C	159	4.8	4.8
Fe	941	26.4	30.4
Pb	961	22.87	34.91
CH	5476	176.0	1534.0

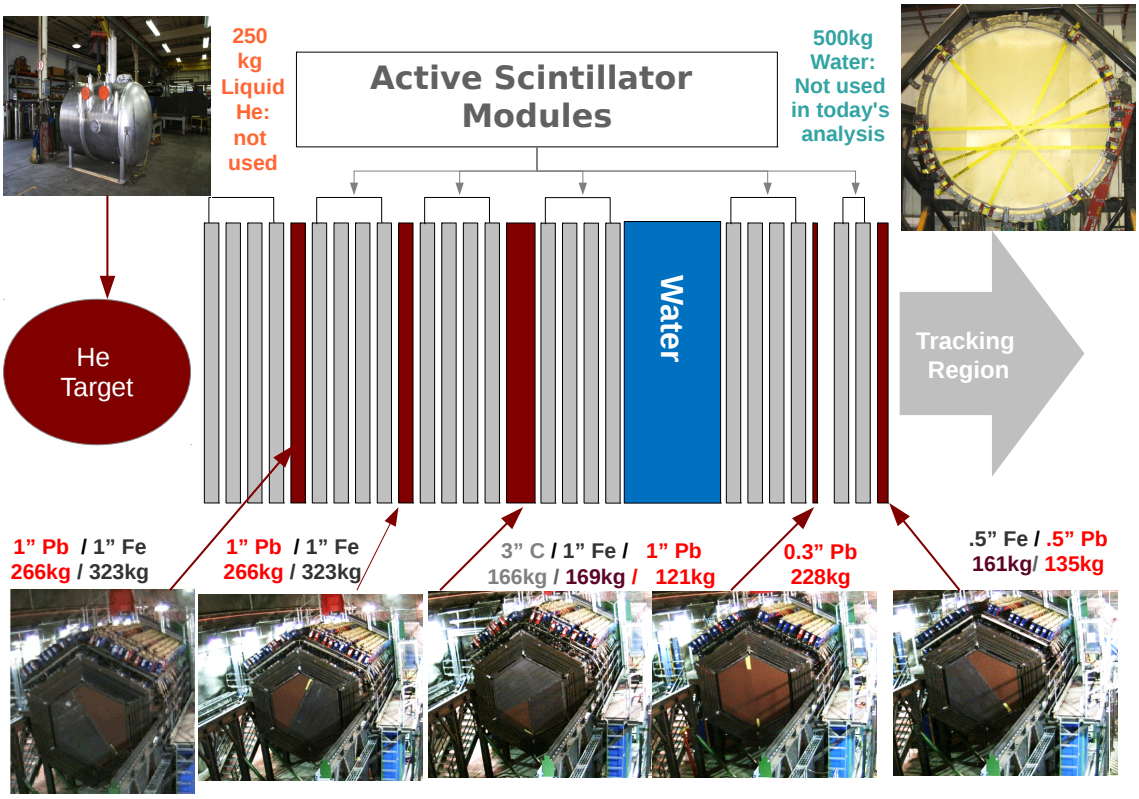

Figure 5-4. Nuclear targets present in the MINERνA detector, with the fiducial masses of the 4 downstream targets listed. The gray boxes are modules identical to MINERνA tracker modules. The alternating pattern of passive nuclear target modules and active tracker modules allow particles to be tracked as they propagate through the nuclear target region, as well as identify the correct origin of neutrino events in the passive targets. Photographs are courtsey of the MINERνA collaboration.

5.1.5 Tracker and Calorimeters

Following the nuclear target region is the tracker. As it's name implies, the tracker's main responsibility is to reconstruct tracks of charged particles as they travel through the detector. Charged particles moving through the detector ionize the scintillator as they travel. Electrons de-ionize and release photons. These photons travel to the central WLS fiber, where their wavelength is shifted to the visible spectrum before being carried to the PMTs. As a result, an illuminated row of strips is indicative of a track of a charged particle. The tracker can also partially reconstruct hadronic and electromagnetic showers, however the total mass of the tracker is too small to contain most showers.

The electromagnetic and hadronic calorimeters are located downstream of the tracker. This construction provides the maximum probability that electronic and hadronic showers are completely contained in the detector and no energy is lost. Muons with energy greater than roughly 2 GeV will not be stopped in the MINERνA main detector. In order to determine the energy and electric charge of these muons, the MINOS near detector is used. The MINOS near detector is composed of alternating layers of steel and scintillator strips similar to MINERνA. One important difference is that the steel portion is magnetized by a 1.28 T toroidal electromagnet [66]. This enables the MINOS detector to measure the momentum and charge of muons by their curvature.

Each MINERνA plane is surrounded by a lead collar 0.2 cm thick, 15 cm from the edge of the plane [60]. This collar was installed to assist with calorimetry of side exiting particles. The outer detector is likewise instrumented with scintillator bars between layers of iron, and may also be used to measure side exiting showers.

5.2 Readout Electronics

The average load of the readout electronics for MINERνA is modest by high energy physics standards. The incoming neutrino beam has a period of about 2 seconds, and each spill is about 10 microseconds in length. Each spill will create about 1 MB worth of

hit-data in the MINERνA detector. This eliminates the need for MINERνA to do any live-time triggering.

Each MINERνA PMT connects to a front end electronics board (FEB) which digitizes the analog signal of the PMTs. Each FEB contains 64 pixels to digitize 64 detector channels. This digitization is done via pipeline ADCs using Application-Specific Integrated Circuit (ASIC) chips (TriP-t). Each TriP-t chip is connected to 16 pixels. Each TriP-t has a programmable threshold voltage that acts as a discriminator for the ADC.

When a signal is detected above discriminator threshold, the TriP begins integrating charge in a 16 ns window. At the end of this window, the entire pulse height and timing information is "pushed" from pairs of TriP-ts to the on board memory of the FEB. After each push, the TriP-t pair requires as 20 ns reset time, where the pixels are effectively dead to incoming signal. Each FEB can store seven of these pushes in a single 15 microsecond integration gate. The integration gate is set longer than the beam gate to measure the decay products of long-lived particles, such as Michel electrons from muons. Sixteen FEBs are connected in series using commercial CAT-5 cable to form a chain of boards which feed into a Chain Readout Controller or CROC. The readout from each FEB is done bucket brigade style along the chain, so the readout information from FEB 16 is passed to FEB 15, which adds its' information and sends it to FEB 14 etc., until the CROC receives the data.

Similarly, instructions to each FEB are written in series by the CROC. Before each beam spill the Fermilab accelerator division sends a signal to all of the CROCs in the MINERνA detector via a timing module. The CROCs then send a signal to the FEBs, telling them to begin reading out charge and to open their discriminator latches. The CROCs then deliver a signal telling the FEBs that the integration window is closed, and to send all of their pipeline ADC data to the CROC. This makes up the largest bit of atomized time in MINERνA, and is called a "gate." Integration gates in MINERνA are set longer than the width of the beam spill in order to capture hits from long living particles in the detector.

The CROCs are connected to an event transfer PC using a VME backplane. The PC is responsible for persistently storing the data immediately after the VME backplane receives the packaged data from the CROCs. In addition, a backup PC is connected to the VME backplane in case the primary machine malfunctions.

The MINERνA DAQ has the capability to run calibration gates between beam gates, as the time between individual pulses is rather long (≈ 2 seconds). Light injection calibration data, described in Section 5.4.2, is taken after roughly every other beam gate, and pedestal data is taken after every 30 beam gates. In this way, the MINERνA detector is always active [67].

5.3 MINERνA Detector Simulation

Neutrino interactions in MINERνA are simulated using Monte Carlo (MC) simulation techniques. This simulation begins with the GENIE event generator, which is described in detail in Section 3.1. GENIE is responsible for the simulation of neutrino-nucleus interactions, as well as the propagation of intermediate state particles through the nucleus. GENIE returns a record of all of these final state particles, along with their four momenta to be used in later stages of the simulation.

Particle trajectories and interactions in the MINERνA detector are simulated by the GEANT software package [51]. GEANT simulates interactions of particles with matter including ionization, radiation, and nuclear reactions. This simulation occurs in discrete steps, and at each step GEANT selects an interaction based on internal physics models. The four momenta of all particles at each step are calculated, and then propagated further based on the updated trajectories.

The charged particles simulated and generated by GEANT are transformed into the number of photons produced in the MINERνA scintillator by an approximation known as Birks' law [68]:

$$N_\gamma \propto \frac{dE}{1 + k_B dE/dx}, \tag{5-1}$$

where N_γ is the number of photons produced, dE is the amount of energy deposited in a length of scintillator dx, and k_B is Birk's constant. Birk's constant is a function of the scintillator creating the photons, and is set to 0.133 mm/MeV in the MINERνA simulation.

Photons created by Birk's law are propagated through the WLS and clear fiber cables. The simulation accounts for the attenuation in each fiber. A time dependent correction derived from the data is used to simulate scintillator aging. The photons are converted into a number of photo-electrons at the simulated PMT cathode according to a Poisson distribution [69].

The remainder of the MINERνA simulation models the electronic readout of the detector. This model latches a discriminator and integrates simulated charge in a simulated TriP-T chip exactly as described in Section 5.2. This simulation takes into account the dead time of each TriP-T chip.

5.4 Detector Calibration

Precision experiments such as MINERνA rely on accurate, sophisticated calibrations in order to take full advantage of their technology. This section explains how the MINERνA detector is calibrated.

5.4.1 Module Mapper

Before any module is installed in the detector hall, it's response to a radioactive source is measured using a custom made module mapper. The mapper is composed of a Cesium-137 source encased in a steel box. The box is mounted to two beams which can move independently on different tracks. The mapper maneuvers the Cs-137 source to the geometric center of each strip of a module's plane. A separate data acquisition and electronic readout, identical to the MINERνA main detector, reads the light output of each PMT pixel as the mapper illuminates each strip. The result is a map of the response of each strip to the radioactive source. This map serves to not only identify bad scintillator strips before the modules are installed, but it also measures the attenuation of light in each

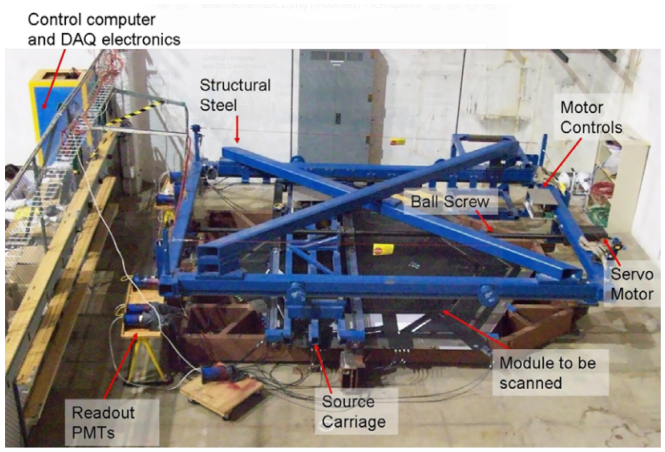

Figure 5-5. A photograph of the MINERνA module mapper, with the relevant elements labeled. The computer on the left side of the photograph controls the mapper's motors, and thus which particular strip will be illuminated by the Cs-137 source. Photograph is courtesy of Robert Flight. Reproduced from Ref [60].

strip of the detector. A photograph of the mapper, with the important components labeled, is shown in Figure 5-5.

5.4.2 PMT Gains

The remaining MINERνA calibrations take place *in situ*, that is, they are made while the detector has been installed in its' final location. The start of any calibration chain is to measure the dark noise, or pedestal of each of the MINERνA PMTs. The pedestal is measured by triggering the detector while the incoming neutrino beam is not active. Since the rate of cosmic rays in the MINERνA detector hall is very small, and the neutrino beam has a long frequency of 0.5 Hz, these triggers are taken in between beam spills. Each PMT has a separate pedestal distribution which is stored in an offline database. When beam data is analyzed the pedestal of each PMT is subtracted.

Each PMT, in addition to a characteristic pedestal, has a characteristic gain and quantum efficiency. The quantum efficiency of a PMT is the proportion between the number of photons which contact the photocathode to the number of electrons which are emitted from the cathode. The gain, on the other hand, is the proportion of electrons added to the photoavalanche at the end of the PMT dynode chain to the number of

electrons emitted from the cathode. Physically the gain is a function of the voltage difference between the beginning and the end of the dynode chain, while the quantum efficiency is a property of the PMT's filament.

While the quantum efficiency and gain have different sources, they are calibrated in the same way and from a analysis standpoint can be rolled into one calibration factor. This overall calibration factor is referred to as the "gain" of the PMT in this document. Both factors are calibrated *in situ* using a custom made light injection box. The light injection (LI) box contains 20 blue LEDs which are connected to an onboard control card. This control card can be set up to accept external start signals, or the LEDs may be triggered internally by the control card. When a trigger is received, all 20 LEDs flash for $\approx 1.0\mu$s long pulse. The light from the LEDs is distributed along a hexagonal grid of fiber optic cables. Each fiber optic cable is routed to a PMT box on the MINERνA main detector. The cables are grouped in bundles of 64, each LED provides light to 64 cables. Each MINERνA PMT box has two LI fibers attached, so one LED provides light for 32 PMTs.

The LEDs are configured to deliver a uniform amount of light to each PMT. During LI pulses, each of the MINERνA PMTs are illuminated by the LI system. The data from these pulses are analyzed, and using the fact that the light delivered to each PMT is roughly uniform, the gain of each PMT can be determined. The MINERνA detector is calibrated such that each PMT has the same gain by tuning the operating voltage of each PMT. The gain of the MINERνA PMTs as a function of time are plotted in Figure 5-6.

5.4.3 Detector Alignment

The remaining calibrations of the MINERνA are calculated using a sample of rock muons. Rock muons are muons created by neutrino interactions in the rock upstream of the detector. Rock muons used for calibration transverse the entire range of the MINERνA detector, and typically hits are seen in every detector plane. These muons are used to calibrate the alignment, individual strip response, and absolute energy scale of the detector. The alignment calibration uses the MINERνA muon tracking algorithm, described in

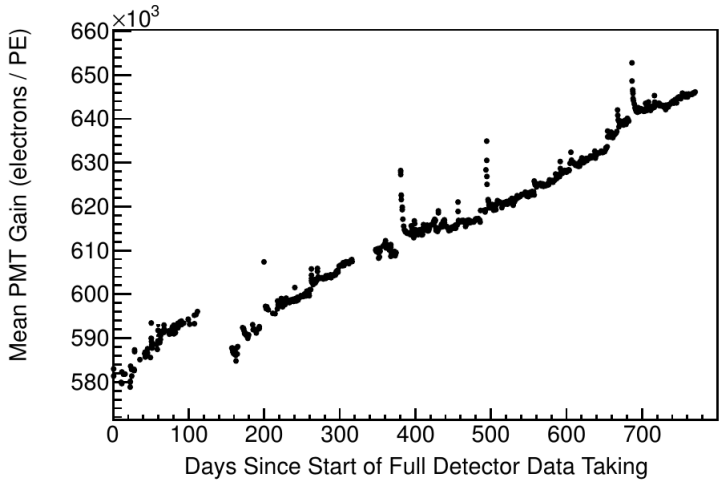

Figure 5-6. The gain of MINERνA PMTs as a function of time. Large jumps in the gain are caused by the high voltage being reset after detector shutdowns. The overall slope in the gain reflects the degredation of the scintillator light output over time. Figure is from Ref [60].

Section 6.4, to project tracks of rock muons downstream along the axis of the detector. Translations perpendicular to the strip position, as well as rotations about the beam axis, can be measured by comparing the projected track to the location of hits in the strips. Rotations perpendicular to the beam axis are measured by comparing the projected track trajectory to the peak of the energy of hits along the base of a strip. The strip positions are shifted such that the peak of the energy distribution is best fit to the center of the strip.

After applying the alignment calibration the residual of the plane position and plane angle are < 1 mm and < 1 mrad respectively.

5.4.4 Strip to Strip Normalization

The individual scintillator strips which make up the planes of MINERνA are calibrated to have uniform light output using a "strip-to-strip" correction. The strip-to-strip correction is calculated by measuring the path length averaged peak energy of through going rock muons in each scintillator strip. Initially this peak energy is normalized across the detector in a first iteration. A second iteration identifies dead strips, and in a 3rd pass the peak energies are normalized plane by plane instead of strip by strip to obtain

necessary statistics. The product of these three constants makes up the overall strip to strip calibration. These constants are normalized so the average constant across the inner detector is 1.0.

5.4.5 Absolute Energy Calibration

Once the individual strips are corrected, the absolute energy scale may be determined. The amount of energy deposited by a through going muon in each strip is roughly constant in one strip, since the muon is a minimum ionizing particle at the energies observed by MINERνA. This energy deposited post gain and strip-to-strip calibration is called a "muon energy unit, or MEU. MEUs are calibrated from time-dependent samples of rock muon events. Each rock muon sample is a continuous set of detector runs taken over a period of time. The period is large enough to contain sufficient statistics to calibrate all channels in the detector, but small enough such that the differences in MEUs over time due to scintillator aging can be measured.

The MEU calibration begins with a trial MEU factor which is used to compare the distribution of collections of energy in the scintillator strips (called clusters) between data and the Monte Carlo simulation. The peak of the data and MC are fitted using a fifth order polynomial. A final MEU factor is computed from the difference between the data and simulation after the MC is fit to data. This difference is fit to a linear equation as demonstrated in Figure 5-7. The slope of this equation is multiplied by the trial MEU factor to arrive at a final MEU factor.

The absolute energy scale of the detector can be cross-checked and monitored using Michel electrons. Michel electrons are electrons arising from the decay of muons inside the MINERνA detector from the following reaction:

$$\mu^- \rightarrow \mathrm{e}^- + \nu_\mu + \overline{\nu}_e. \tag{5-2}$$

The decay of muons is very well described by the standard model, and thus the energy spectrum of the electrons is very well modeled. The comparison between data and

simulation of Michel electrons in MINERνA is shown in Figure 5-8. The average between the data and MC agree to the 3% level, demonstrating the robustness of the calibration.

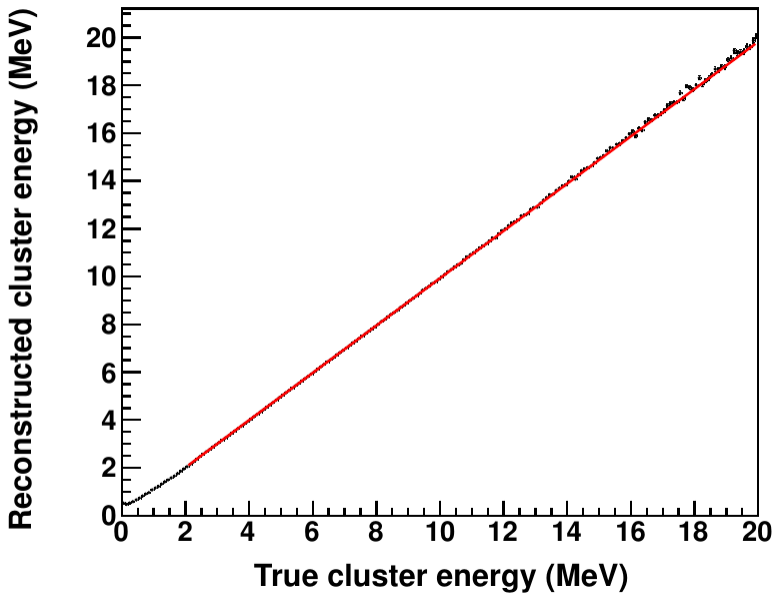

Figure 5-7. Reconstructed energy of hits in MINERνA (clusters) vs. the true energy of hits from simulation. Figure is from Ref [60].

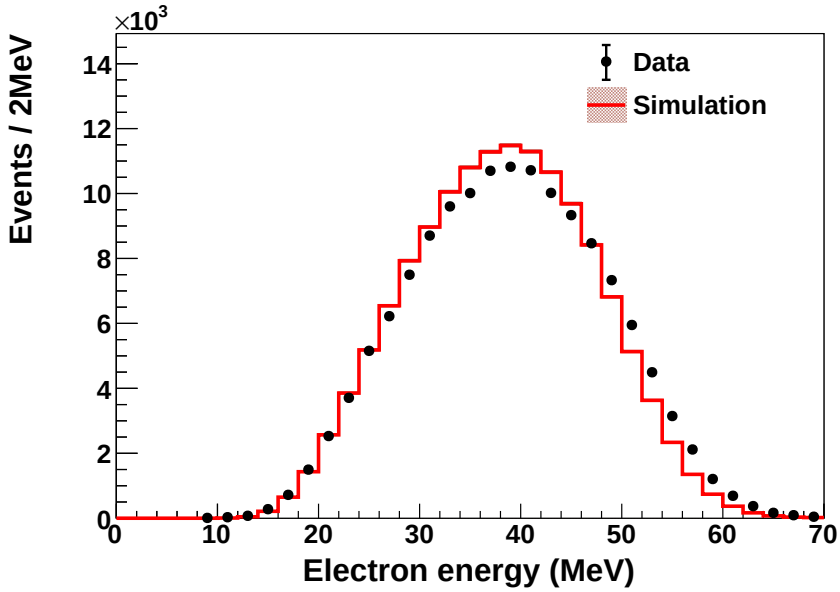

Figure 5-8. Reconstructed energy of Michel electrons in simulation (red line) and data (black points). Figure is from Ref [60].

CHAPTER 6
EVENT RECONSTRUCTION

6.1 Goals of Event Reconstruction

Event reconstruction is necessary to transform quantities the detector records such as energy of hits, location of hits, and time of hits into physics quantities. These quantities may be, for example, the mass of the particle traveling through the detector, the particle's momentum, or the charge of the particle. Knowledge of these physics quantities allow an experimenter to classify events and quantify interactions.

Identifying and reconstructing a DIS event requires measuring the muon energy and angle, as well as the energy of the final state hadronic system. Particle identification is necessary to identify or "tag" the primary muon. Identifying the particle type of the final state hadrons is in general not necessary. The physics quantities of interest are the energy (E_{had}) and invariant mass (W) of the final state hadrons, neither of which depend on the details of the hadrons masses' or charges'.

The energy of the primary muon (E_μ), the outgoing angle of the primary muon (θ_μ), and the energy of all of the final state hadrons (E_{had}) of the event is sufficient information to determine the entire kinematics of a charged current event. The mass of the target nucleon (M_N) cannot be determined event by event in a DIS event. Hence, the average of the proton and neutron mass is used to approximate M_N. A few kinematic quantities of interest (not exhaustive) as functions of E_μ, θ_μ, E_{had} and M_N are:

- The energy of the incoming neutrino E_ν. By energy conservation, $E_\nu = E_{had} + E_\mu$.
- The square of the four momentum transfer Q^2. $Q^2 = 4E_\nu E_\mu sin^2\left(\frac{\theta}{2}\right)$.
- The invariant mass of the final state hadronic shower W.
  $W = \sqrt{M_N^2 + 2E_{had}M_N - Q^2}$.
- The Bjorken-x of the event. $x_{Bj} = \frac{Q^2}{2M_N E_{had}}$.

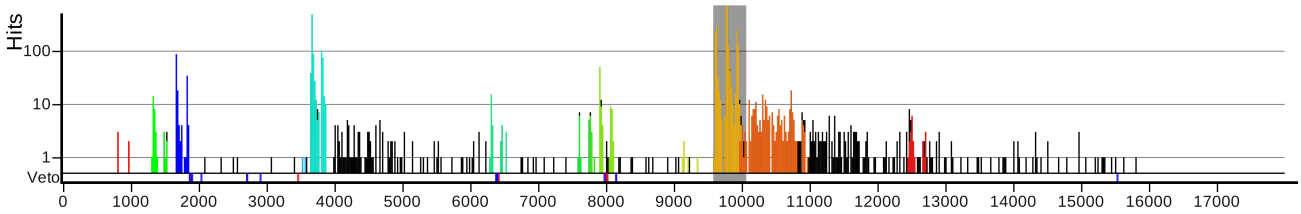

Figure 6-1. Histogram of hit times in the MINERνA detector. Each colored peak represents one time slice, found by the time slicing algorithm. This Figure has been produced using the MINERνA Arachne event display described in Ref [70].

6.2 Time Slicing

Due to the intensity of the NuMI beamline, particles resulting from multiple neutrino interactions are often observed in a single readout gate. Often, these are superfluous interactions from the rock surrounding the detector, but it is not uncommon for there to be multiple neutrino interactions in MINERνA in a single gate. As a result, the first step of the MINERνA reconstruction is to group hits in the detector into separate groups in time ("time slices").

Time slicing is preformed by an offline algorithm. It is not done real time as data is being taken. The time slicing algorithm sorts all hits in the MINERνA detector by time. If multiple hits are found with a sum or more than 10 photoelectrons within 80 ns, a time slice is created. The algorithm searches for other hits in the readout gate and adds them to the slice if they occur no later than 50 ns of the latest hit in the slice, and no earlier than 30 ns of the earliest hit in the slice. This process continues until no hits are found within the allowed time window, or no hits above 10 photoelectrons are found. Figure 6-1 shows a sample time profile of a MINERνA readout gate, along with the time slices highlighted [71].

6.3 Hit Clustering

After hits are sorted in time using time slicing, they are next sorted in space by a clustering algorithm. Clustering searches for proximal hits by looking for hits on adjacent strips on one plane. All hits in the MINERνA detector are promoted to clusters, even if

there are no other hits adjacent. As a result, one hit clusters are possible. The clusters are divided into different types depending on their size and total energy [72]:

- Cross Talk: Clusters with low photoelectrons which are likely due to optical cross talk in the PMTs.
- Trackable Clusters: Clusters that are consistent with a minimum ionizing muon. The cluster must be at most four hits wide, and must have a total energy between 1 and 12 MeV.
- Heavy Ionizing Clusters: Clusters that are likely due to ionization energy of a heavier particle, such as a proton. They are identical to trackable clusters, except there is no requirement on maximum energy.
- Superclusters: Clusters consistent with a hadronic or electromagnetic shower. Any cluster wider than 4 hits is automatically classified as a supercluster.
- Low Activity Clusters: Clusters with less than 1 MeV of total energy which have not been classified as cross talk.

The time of each cluster is assigned to be the time of the highest energy hit. The position of the cluster along the plane is determined by taking the energy-weighted average position. Since clusters in MINERνA are restricted to one plane, all position information is strictly one-dimensional.

6.4 Tracking

Tracks in MINERνA are built from clusters. Tracking takes place in two stages. In the first stage, only the longest track in the detector is formed. The start point of this track is used as an "anchor," which dictates how other tracks in the time slice will be built.

Anchor tracking begins by sorting clusters into track seeds. A track seed is a set of three clusters in different planes, but in one detector view (X, U or V). Clusters in a seed must be in consecutive planes, and must be fit to a straight line between the three seeds.

Track seeds are then stitched together by comparing their projected slopes, and ensuring that adjacent seeds share a cluster. These proto-track objects are essentially two-dimensional trajectories called "candidates."

The next step of tracking attempts to merge track candidates from different views into three dimensional objects. 3D merging is done by overlapping the three different (X, U, V) 2D candidates and checking that the 3D track forms a trajectory consistent with the track seeds. If 3D merging fails, 2D merging is attempted by looking for overlapping track candidates along the beam direction (z-axis) in any two views. 2D tracks must have a consistent 3D fit as well, and this by definition means the track will contain some breaks where there are no hits present. This case is handled by a separate track-cleaning step, where clusters unused by the tracking algorithm are used to fill gaps in the track [73].

Reconstructed tracks are fit for their slope and position cluster by cluster by a Kalman filter [74]. This filter allows for multiple scattering via a covariance matrix [75]. This completes the creation of the anchor track. The performance of the longer tracker is measured by calculating the difference between the actual position of each cluster and the projected position of the cluster as determined by the tracker. This is found to have a resolution of a few mm as illustrated in Figure 6-2. The (x, y, z) start point of the anchor track is the initial event vertex hypothesis. All clusters used to make the anchor track are flagged and are not used during the second tracking iteration, or further reconstruction. [73].

The anchor point serves as a start point to search for additional long tracks in the event. These tracks are reconstructed using the same algorithm as the anchor track.

6.5 Vertex Reconstruction

The vertexing algorithm calculates the vertex using multiple tracks and a closest-approach algorithm if multiple tracks are available. The vertex position measurement is improved with a second adaptive Kalman fit [76]. Single track vertices are assigned a vertex equal to the first node of the track.

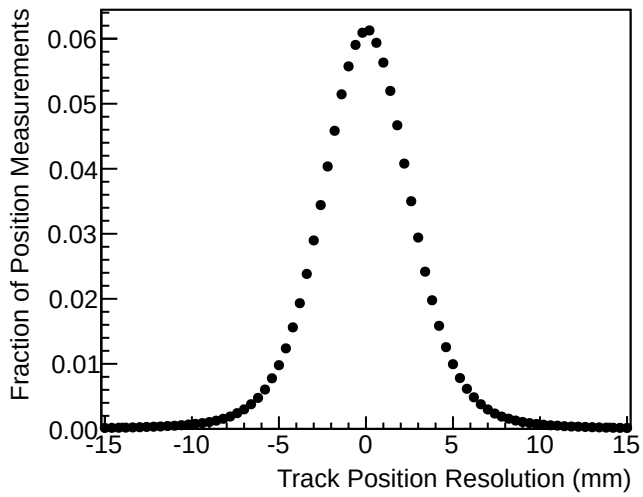

Figure 6-2. Residual of muon track clusters in MINERνA. Figure is from Ref [60].

6.6 Muon Reconstruction

Any track exiting the rear of the MINERνA detector is most likely the primary muon. A primary muon is the muon the ν_μ produced after emitting a W^+ boson. Other particles potentially produced by neutrino events, such as pions and protons, will be stopped in the MINERνA electromagnetic or hadronic calorimeters described in Chapter 5. Additional muons in the event, which could be due to the decay of other particles, are classified as hadronic recoil energy explained in Section 6.7 and are not reconstructed in the same manner as the primary muon.

6.6.1 Muon Energy

Since the primary muon escapes MINERνA by definition, it is necessary to reconstruct the energy and charge of that muon in the MINOS near detector. Muons are matched in the MINOS near detector by matching outgoing muon tracks in MINERνA to tracks in MINOS. The MINERνA track is projected to the front face of the MINOS near detector. Candidate tracks in MINOS within 200 ns of the MINERνA track are projected

toward MINERνA detector. If the residual between these matches is less than 30 cm, the track is considered matched to MINOS [73].

Muons which enter MINOS have their energy measured by range or curvature. In a range measurement, the muon stops in the MINOS near detector. The energy of the muon can be measured by the Bethe-Block formula [77] and the distance the muon traveled before stopping. The majority of the MINOS near detector is composed of steel, and thus posses more stopping power than the MINERνA detector, which is primarily composed of scintillator.

MINOS only contains enough mass to stop muons of about 10 GeV [78]. Muons with more than 10 GeV of momentum will exit the rear of MINOS, and their range energy cannot be measured. Additionally, not all muons will stop in MINOS and many may escape out the sides of the detector. These muons have their energies measured by detecting the curvature of the muon as it travels through the MINOS magnetic field. Since curvature measurements tend to have poorer resolution than range measurements, the energy determined by range is used unless the muon escapes the detector. The radius of curvature (R) is related to the momentum of the muon (p), charge (Q), and MINOS B field by:

$$\frac{1}{R} = \frac{0.3BQ}{p}. \tag{6-1}$$

As a result, higher momentum muons have a larger radius of curvature. The sign of Q in Equation 6-1 may be determined by comparing the direction of the muon's curvature to the sign of the MINOS B field. As the DIS analysis studies ν_μ DIS, the reconstruction requires $Q < 0$ as defined by MINOS. This cut is made if the muon is reconstructed by range or curvature.

The reconstruction of high energy (> 20 GeV) muons was not sufficiently studied by the MINOS collaboration, so a separate study was conducted. The conclusion of this study was that muons with a curvature significance of less than 5 are poorly reconstructed by the MINOS near detector. Additionally, events which terminate within 210 mm or outside of

2500 mm of the MINOS magnetic coil were not reconstructed satisfactorily [79]. As a consequence, these events are removed from the analysis.

After the energy of the muon in MINOS is determined, the energy at the interaction vertex is calculated by walking the muon track upstream. At each step, energy is added to the track depending on the material the track intersected, assuming the muon is a minimum ionizing particle. This uses the same Bethe-Block equation as described in Ref [77]. All muons used in the DIS analysis must be matched to MINOS. Muons stopping in the MINERνA detector may easily be confused as pions due to their similar mass and ionization profile. Since all charged-current DIS events require a muon in the final state, this effectively means all DIS events analyzed have a MINOS matched muon.

6.6.2 Muon Angle

Once the initial energy of the muon is measured, it is trivial to calculate the three components of the muon's momentum vector using the long trackers slope information. The components of the momentum vector can then be used to find the angle of the muon with respect to the incoming neutrino. The MINERνA coordinate system does not lie exactly on top of the beam axis. The beam axis has a downward slope, as it was designed to intersect the MINOS far detector in Soudan Minnesota. As a result, some transformation needs to be made to align the longitudinal momentum of the muon with the beam axis.

If θ_b is the angle of the neutrino beam, and p_x, p_y and p_z are the three components of the muon's momentum, then the angle of the muon with respect to the beam axis is given by this formula:

$$\theta_\mu = arccos\left(\frac{cos(\theta_b)p_z + sin(\theta_b)p_y}{\sqrt{\rho}}\right), \tag{6-2}$$

where

$$\rho = p_x^2 + (-sin(\theta_b)p_z + cos(\theta_b)p_y)^2 + (cos(\theta_b)p_z + sin(\theta_b)p_y)^2. \tag{6-3}$$

6.7 Hadron Energy Reconstruction

The energy of the primary muon in a DIS interaction is only half of the story of a neutrino DIS interaction. There is still a large fraction of the neutrino's energy that is transfered to the nucleus and results in a number of final state particles from the breakup of the nucleon. By energy conservation, the total energy of the neutrino, E_ν must be equal to the energy of the primary muon, E_μ plus the sum energy of the final state hadrons E_{had}:

$$E_\nu = E_\mu + E_{had}. \tag{6-4}$$

Recall that the Bjorken-x of the event defined in Chapter 2 also depends on E_{had}. E_{had} is not only important for reconstructing the neutrino energy, it is also necessary to calculate x_{Bj}.

In a deep inelastic scattering event, there is a large amount of energy transfered to the nucleus by definition. This means DIS events have very high energy hadronic final states. Measuring the hadronic final state accurately is thus very important for obtaining an accurate measurement of neutrino energy, since the majority of that neutrino's energy ends up in the hadronic system.

6.7.1 Definition of Recoil Energy

The first step in determining the hadronic energy of an event is to sum the recoil energy in each event. Calculating the recoil energy begins during the tracking stage. A separate track cleaning algorithm is run after long tracking, which breaks clusters off tracks if the clusters appear to have originated from two different particles. This determination is made based on if the cluster is consistent with the dE/dx of a minimum ionizing muon. If the cluster energy is inconsistent with a minimum ionizing muon, it is broken into two clusters: one cluster with one mip of energy and one cluster with the remainder energy. This procedure is especially powerful at isolating muons from hadron showers when the muon travels through hadron showers. Clusters which break off of tracks are flagged as not being part of the track [73].

A second algorithm searches for heavy ionizing clusters proximal to the primary muon track. As these clusters are likely δ rays from the traveling muon, they are associated with the event's muon energy, and not included in the recoil energy reconstruction.

After both of these algorithms are run, the reconstruction calculates the recoil energy of an event by summing all of the clusters in the detector within a -25 to 30 ns window of the muon vertex time, which are *not* associated with the primary muon. Clusters marked as cross-talk clusters are not included in this sum.

6.7.2 Material Correction

The sum of recoil energy measured by the detector is often a poor measurement of the total hadronic energy of the event. For example, the hadrons must travel through un-instrumented "dead" regions of the detector, especially if they are moving through one of the calorimeters. Additionally, hadron final states often contain neutral particles, such as neutrons and π^0, which will not ionize the scintillator. Energy loss in materials can be estimated from the dE/dx of passive materials, and the neutral fraction of the final state is estimated from a separate fit described in Section 6.7.3.

Energy loss in inert material is calculated by assuming each hadron is a minimum ionizing particle with normal incidence. The reconstruction adds energy to each cluster depending on the clusters proximity to the different passive elements of the detector. The dE/dx of each material in units of MeV/g cm^2 is given in Table 6-1. Studies were done to tune the energy loss in various materials using Monte Carlo, however no improvement to the hadronic energy reconstruction was observed [80]. The total recoil energy after compensating for passive material (E_m) is estimated as:

$$E_m = k_{MEU} \sum_{i}^{materials} M_i \; dE/dx_i, \tag{6-5}$$

where i is each material the hadron travels through, and M_i is the mass of that material. k_{MEU} is a factor which translates detector hits into energy deposits, and is discussed in Chapter 5.

Table 6-1. Energy loss of a minimum ionizing particle at normal incidence for various materials in MINERνA. Table is from Ref [81].

Material	dE/dx (MeV/g cm^2)
Scintillator (CH)	1.96
C	1.74
Fe	1.45
Pb	1.12

6.7.3 Energy Fits

After accounting for passive material in the detector, there are still components of the hadron system that could cause inaccuracies. These include the neutral hadrons previously mentioned, showers which are not fully contained by the detector, and the effect of final state interactions inside the nucleus. MINERνA accounts for these effects by fitting the observed material-adjusted recoil energy to the true hadronic energy, both defined by the Monte Carlo. The Monte Carlo defines a hadronic energy ν event-by-event as:

$$\nu = E_\nu - E_\mu. \tag{6-6}$$

ν is considered to be the true final state hadron energy absent of any detector or FSI effects. The factors of E_ν and E_μ in Equation 6-6 are the true neutrino energy and muon energy of the event generated by GENIE. The goal of the E_{had} reconstruction is to derive a function $f(E)$ such that:

$$\nu \approx E_{had} = f(E_m), \tag{6-7}$$

where E_m is defined by Equation 6-5.

$f(E)$ is first determined by fitting an overall calorimetric scale factor α by minimizing the error function R:

$$R = \frac{[arctan(E_m/\nu - \pi/4)]^2}{N}, \tag{6-8}$$

Table 6-2. α values used as an overall scale factor for hadron calorimetry per target. Table is from Ref [81].

Event Origin	α_j
Tracker	1.62
Target 1	1.80
Target 2	1.81
Target 3	1.71
Target 4	1.6
Target 5	1.59

where N is the number of events in the fit. Only true charged current events are included in the fit. The fits for α are preformed separately for events originating in the tracker, as well as each of the nuclear targets [80]. Table 6-2 presents the different α_j values extracted for each target j. Equation 6-5 is multiplied by α_j to arrive at a calorimetricly corrected energy E_{cal}:

$$E_{cal} = \alpha_j k_{MEU} \sum_{i}^{materials} M_i \; dE/dx_i. \tag{6-9}$$

The final step of the hadronic energy reconstruction is a per-bin correction based on the ratio of the material and calorimetric corrected energy (E_{cal}) to the true hadronic energy ν. This is calculated by measuring the mean $\Delta E/\nu$ bin-by-bin, where $\Delta E = E_{cal} - \nu$. A polyline mapping E_{cal} to E_{had} is created such that the mean of $\Delta E_{cal}/\nu = 0$ in each bin. Each (x, y) point of the polyline is defined by:

$$\begin{aligned} x(E^k_{cal}) &= \langle \nu \rangle \times (1 + \eta), \\ y(E^k_{had}) &= \langle \nu \rangle, \end{aligned} \tag{6-10}$$

where η is the difference of the mean $\Delta E_{cal}/\nu$ from 0, k is the recoil energy bin, and $\langle \nu \rangle$ is the mean, true hadronic energy of bin k. The lower and upper ends of the polyline are fixed at $(0, 0)$ GeV and $(50.0, 50.0)$ GeV respectively. A separate polyline fit is preformed

for events originating in the tracker and events originating in each nuclear target. The polyline is essentially a function (P_k) which maps E_{cal} to E_{had} based on Equation 6-10:

$$E_{had} = P_j(E_{cal}). \tag{6-11}$$

Overall the total hadronic energy is calculated as:

$$E_{had} = P_j\left(\alpha_j \sum_i M_j dE/dx_i E_i\right), \tag{6-12}$$

where α_j is the overall scale factor defined in Table 6-2, M_i is the total mass surrounding each hit, dE/dx_i is the energy loss of a minimum ionizing particle per material defined in Table 6-1, and P_j is the polyline function which maps E_{cal} onto E_{had} defined by 6-10. The summation over i is preformed over all of the recoil clusters in the detector. α_j and P_j are different depending on the event's origin.

The resolution of the hadronic energy reconstruction, δE_{had}, is equal to $\delta E_{had} = \frac{E_{had}-\nu}{\nu}$. Since one of the goals of the DIS analysis is to compare the x_{Bj} dependent cross sections between nuclear targets, it is imperative that the resolution of the hadronic energy be similar between different nuclear targets. If the resolution is very different, then one does not know if any difference measured in the cross section are due to different nuclear effects or a difference in resolution. This was investigated by comparing the δE_{had} resolution of events in nuclear target 2, which is very far upstream, and nuclear target 5, which has no other nuclear targets downstream of it. This comparison is presented in Figures 6-3 through 6-7 in various bins of x_{bj}. It is observed that the hadronic energy reconstruction produces a similar resolution between different nuclear targets. The resolution tends to degrade in the larger x_{bj} region as shown in Figure 6-7. This is primarily due to the hadronic shower transferring to discrete single-particle tracks at lower hadronic energy, as $x_{bj} \propto \frac{1}{E_{had}}$. The calorimetry is tuned to reconstructing large showers, and tends to overestimate the hadronic energy in the case of discrete tracks.

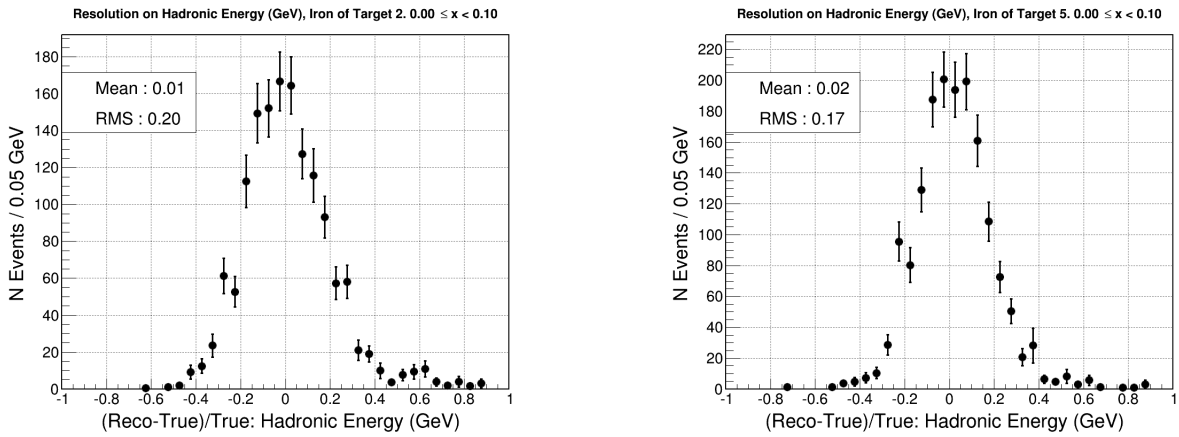

Figure 6-3. δE_{had} resolution of DIS events in the x_{bj} range $0.0 < x_{bj} < 0.1$ for nuclear target 2 (left) and nuclear target 5 (right).

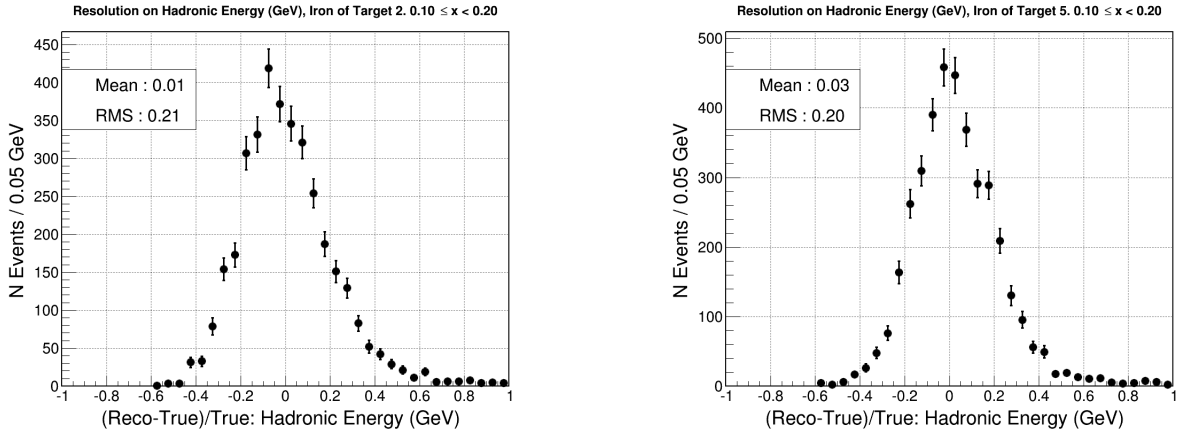

Figure 6-4. δE_{had} resolution of DIS events in the x_{bj} range $0.1 \leq x_{bj} < 0.2$ for nuclear target 2 (left) and nuclear target 5 (right).

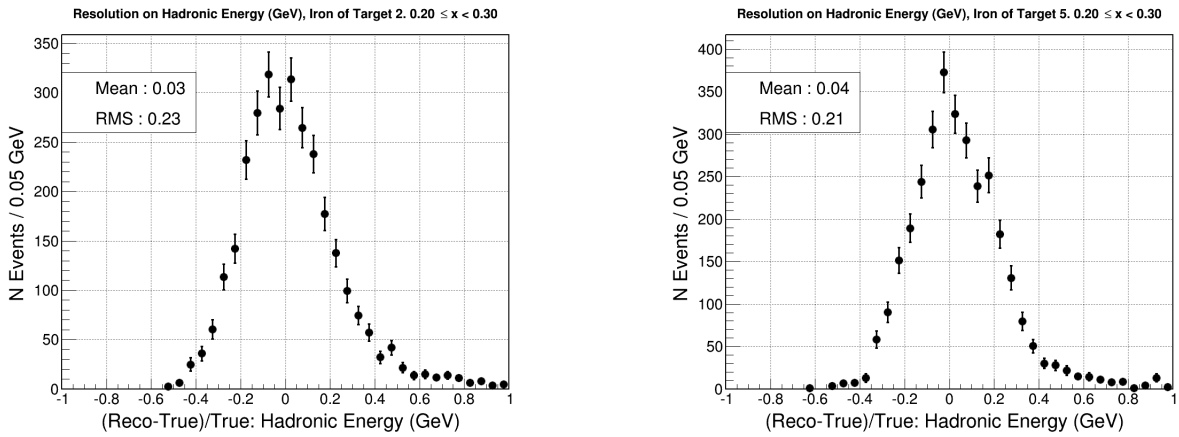

Figure 6-5. δE_{had} resolution of DIS events in the x_{bj} range $0.2 \leq x_{bj} < 0.3$ for nuclear target 2 (left) and nuclear target 5 (right).

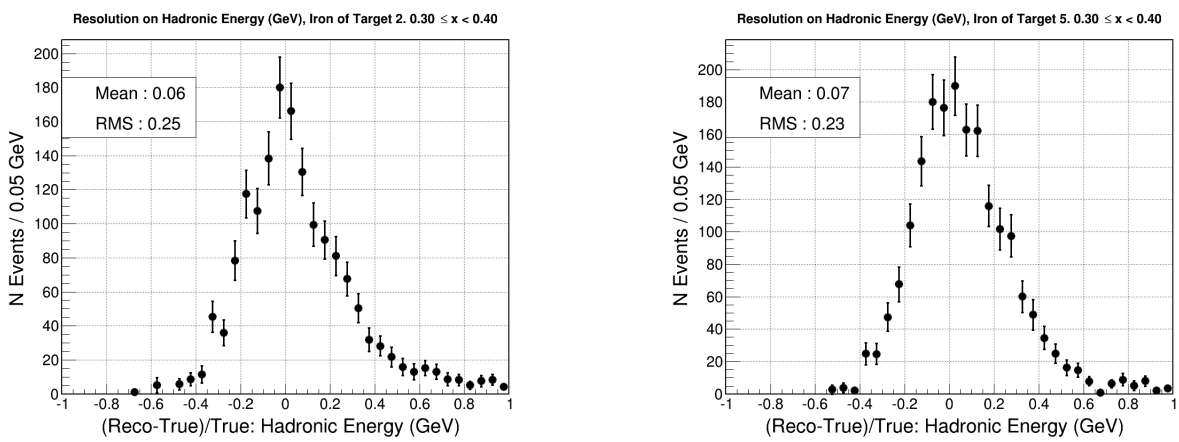

Figure 6-6. δE_{had} resolution of DIS events in the x_{bj} range $0.3 \leq x_{Bj} < 0.4$ for nuclear target 2 (left) and nuclear target 5 (right).

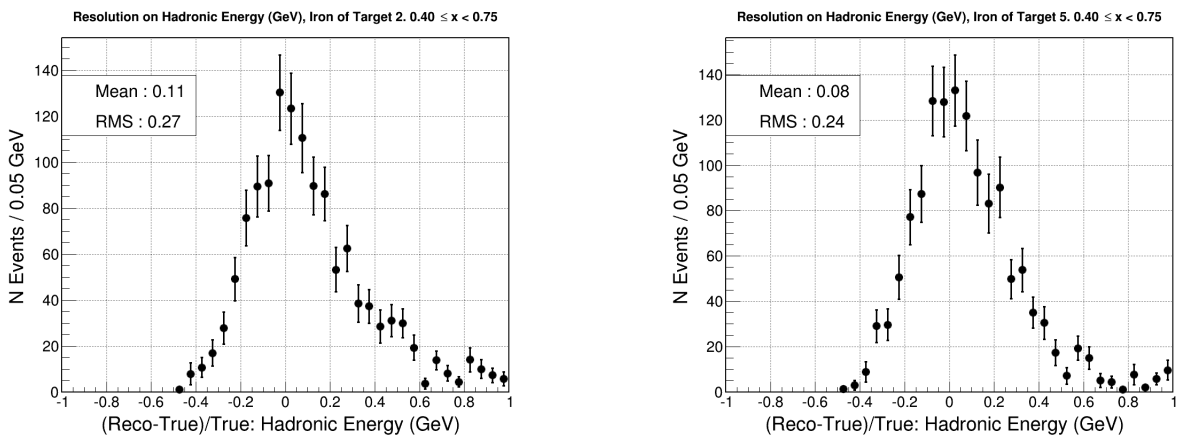

Figure 6-7. δE_{had} resolution of DIS events in the x_{bj} range $0.4 \leq x_{bj} < 0.75$ for nuclear target 2 (left) and nuclear target 5 (right).

CHAPTER 7
OVERVIEW OF THE MEASUREMENT

7.1 A Note on Units

Being a momentum transfer squared, Q^2 naturally has dimensions of momentum squared, or (length $\times$ mass / time)^2. W, being an invariant mass, has dimensions of mass. In natural units, these quantities have units of GeV^2 and GeV respectively.

The DIS analysis presented in this thesis contains many studies of backgrounds in different Q^2 and W regions than the canonical $Q^2 > 1.0$ (GeV/c)^2 and $W > 2.0$ (GeV/c^2). In order to ease confusion, the remainder of this document uses SI units to clearly distinguish if a value is a momentum transfer squared or invariant mass. This means momentum squared now has units of (GeV/c)^2 and mass has units of (GeV/c^2). This convention is persisted in the document's appendix as well.

7.2 Cross Section Formula

The total DIS cross section is measured as a function of neutrino energy (E_ν) using the standard cross-section formula:

$$\sigma_i = \frac{U_{ij}\,(d_j - b_j)}{\Delta_i\,\epsilon_i\,\Phi_i\,N}, \tag{7-1}$$

where d_j is the total number of events passing the event selection cuts in data in energy bin j, b_j is the number of background events, U_{ij} is an unsmearing matrix which transforms events reconstructed in the jth bin to their true ith bin, Δ_i is the width of bin i, ϵ_i is the total detector and event selection efficiency, Φ_i is the neutrino flux, and N is the number of scattering centers (nucleons). The differential cross section may be measured in terms of a variable x. In this case, the per-bin flux Φ_i is replaced with the integrated flux Φ:

$$\frac{d\sigma}{dx}_i = \frac{U_{ij}\,(d_j - b_j)}{\Delta_i\,\epsilon_i\,\Phi\,N}. \tag{7-2}$$

As mentioned in Section 4.5, the uncertainties on the flux calculation (Φ) are large especially in the high energy tail of the neutrino beam where most of the DIS events

originate. As a consequence, ratios of the cross section between different nuclei are measured. The DIS analysis always uses the CH of the MINERνA detector as its' denominator, and uses C, Fe and Pb as the numerator.

In the case of the scaling variable Bjorken-x (x_{bj}), ratios of the differential cross section on the nuclei C, Fe and Pb to CH provide direct evidence of x_{bj} dependent nuclear effects, which are well known in electron scattering but have not been systematically measured or observed in neutrino scattering. Physically, the scaling variable x_{bj} is the fraction of the total nucleon momentum carried by the struck quark in a DIS interaction. It is calculated based on the four-momentum transfer (Q^2), target nucleon mass (M_N), and the event's recoil energy (E_{had}):

$$x_{bj} = \frac{Q^2}{2M_N E_{had}}. \tag{7-3}$$

The goal of the DIS analysis is therefore to measure the quantities:

$$\frac{d\sigma}{dx_{bj}}^{A} / \frac{d\sigma}{dx_{bj}}^{CH} \approx \frac{U_{ij}^{A}\left(d_j^A - b_j^A\right)\epsilon_i^{CH} N^{CH}}{U_{ij}^{CH}\left(d_j^{CH} - b_j^{CH}\right)\epsilon_i^{A} N^{A}}, \tag{7-4}$$

where d, b, U, and ϵ are all functions of x_{bj} and

$$\sigma(E_\nu)^A / \sigma(E_\nu)^{CH} \approx \frac{U_{ij}^{A}\left(d_j^A - b_j^A\right)\epsilon_i^{CH} N^{CH}}{U_{ij}^{CH}\left(d_j^{CH} - b_j^{CH}\right)\epsilon_i^{A} N^{A}}, \tag{7-5}$$

where d, b, U, and ϵ are now all functions of E_ν. A = C, Fe and Pb in both equations.

CHAPTER 8
EVENT SELECTION AND EFFICIENCY

The first step in any cross section measurement is to count the number of events passing a set of signal selection cuts. These cuts attempt to isolate the DIS events from all events the detector records, and sort them into different bins of E_ν and x_{bj} based on the reconstruction. Recalling the formula for total cross section (Equation 7-1):

$$\sigma_i = \frac{U_{ij}\,(d_j - b_j)}{\Delta_i\,\epsilon_i\,\Phi_i\,N}, \tag{8-1}$$

the event selection populates d_j in the data and simulation.

8.1 Data and MC Samples Used

The nuclear target DIS analysis uses the MINERνA "Resurrection" data and MC processing. The data processed is all FHC low energy data on disk. This data comprises 3.12×10^{20} POT. The MC processed is the "Resurrection" era MC generation using GENIE version 2.6.2. This corresponds to 20.528×10^{20} POT. This is about a factor of 6.5 larger than the data sample. All of the data and MC presented in this dissertation correspond to this sample.

8.2 Pre-Cuts

The DIS nuclear target analysis inherits a set of cuts from the previously published nuclear target inclusive analysis [65]. These cuts are:

- Only muons tracks which are matched into tracks in the MINOS near detector are reconstructed and analyzed.
- As the muon travels through MINOS, it is required to have a negative curvature in the MINOS magnet field. This ensures the muon is negatively charged, and the event is a ν_μ event.
- The vertex of the event must be be located in a 85 cm apothem hexagon fiducial area in x and y.

- For the passive target sample, the vertex must have a z location between 1 plane upstream and 2 planes downstream of the nuclear targets 2, 3, 4 and 5.
- The vertex of the event must be more than 25 mm away from the barrier of materials, if the event is in targets 2, 3 or 5.
- A cut is imposed on the maximum allowed deadtime upstream of the vertex. This cut is used to reduce the rate of rock muons mis-reconstructed in the fiducial volume. Events with more than one dead TriP upstream of the projected track of the muon are rejected.
- Events with an average energy between 1.5 and 6.5 MeV for more than 7 planes upstream of the event vertex are cut. This cut is implemented to remove events where the vertexing algorithm mis-identified an event in an upstream target to a target downstream. Further details are given in Section 9.3.
- The inclusive analysis is restricted to events with a neutrino energy $2 \leq E_\nu < 20$ GeV, and a muon angle $\theta_\mu \leq 17°$. The θ_μ cut is applied because the muon acceptance into MINOS falls off rapidly at high angles. In addition, the minimum amount of energy necessary for a muon to penetrate the MINERνA nuclear target and tracker regions is approximately 2.5 GeV. Since the acceptance falls off rapidly below 2 GeV, events below this threshold are cut.

The basic DIS cuts inherit from the framework of the nuclear target analysis. However, a few modifications are necessary for the DIS analysis. First, the maximum neutrino energy is increased from 20 to 50 GeV. The larger maximum energy increases the statistics of the DIS sample by roughly 40%. In addition, the minimum energy is increased from 2 to 5 GeV. The $W \geq 2.0$ GeV/c^2 cut implies a minimum shower energy of 2 GeV in the lab frame. Combined with the ≈ 2.5 GeV threshold for matching a muon in MINOS and the minimum $Q^2 \geq 1.0$ (GeV/c)^2, the minimum accepted energy for a DIS event is ≈ 4.5 GeV.

Since the DIS analysis selects high shower energy events, the upstream energy cut was changed to account for the fact that hadronic energy from showers obscuring the muon were far more likely to cause failures in the vertexing algorithm than muon tracks which are mis-reconstructed. The number of planes allowed with upstream energy was reduced from 7 planes to 5 planes, and all events with at least 1.5 MeV of energy per plane are cut. More details of this study can be found in section 9.3.

Finally, the most upstream nuclear target, nuclear target 1 is included in the DIS analysis but not the inclusive analysis. It was found in the inclusive analysis that nuclear target 1 contained a large rock muon background which was unsimulated in the MINERνA Monte Carlo. However, the DIS W cut removes most of the rock muon background, because through going rock muons are very unlikely to leave significant recoil energy in an event. As a result, target 1 is included in the DIS analysis.

Taken all together, the set of pre-cuts used for the DIS analysis are given below. Cuts that differ from the inclusive analysis are listed in *italics*:

- Only muons which are matched into the MINOS near detector are reconstructed and analyzed.
- As the muon travels through MINOS, it is required to have a negative curvature in the MINOS magnet field. This ensures the muon is negatively charged, and the event is a ν_μ event.
- The vertex of the event must be be located in a 85 cm apothem hexagon fiducial area in x and y.
- For the passive target sample, the vertex must have a z location between 1 plane upstream and 2 planes downstream of the nuclear targets *1*, 2, 3, 4 and 5.
- The vertex of the event must be more than 25 mm away from the barrier of materials, if the event is in targets *1*, 2, 3 or 5.

- A cut is imposed on the maximum allowed deadtime upstream of the vertex. This cut is used to reduce the rate of rock muons mis-reconstructed in the fiducial volume. Events with more than one dead TriP upstream of the projected track of the muon are rejected.

- *Events with an average energy greater than 1.5 MeV for more than 5 planes upstream of the event vertex are cut. This cut is implemented to remove events where the vertexing algorithm mis-identified an event in an upstream target to a target downstream. More explanation is given in section 9.3 .*

- *Muons reconstructed by curvature in the MINOS magnetic field must have a curvature significance of at least 5* σ.

- *Muons reconstructed in MINOS must terminate at least 210 mm from the MINOS magnetic coil, but no more than 2500 mm away from the coil (*$210 < R < 2500$ *mm)* .

- *The DIS analysis is restricted to events with a neutrino energy* $5 \leq E_\nu < 50$ *GeV*, and a muon angle $\theta_\mu \leq 17°$.

A breakdown of how many events are removed by each pre-cut listed may be found in Table 8-1. In order to isolate a DIS sample from the inclusive nuclear target sample, kinematic cuts are imposed on the reconstructed Q^2 and W of the event. An event (data or MC) is considered a DIS event if the reconstructed $Q^2 \geq 1$ (GeV/c)^2 and the reconstructed $W \geq 2$ GeV/c^2. A MC event is considered to be a true DIS event if it had a true generated $Q^2 \geq 1$ (GeV/c)^2, a true generated $W \geq 2$ GeV/c^2 and a GENIE channel = 3 (i.e. DIS). The GENIE channel = 3 serves to eliminate CCQE events which produced a c quark. These events could potentially pass the Q^2 and W cuts, however they are not formally DIS. Events which pass the W and Q^2 cuts based on *reconstructed* W and Q^2 are called "reco events," events which pass based on the *true* W and Q^2 are called "true events," and events which pass both are called "true reco events." Events in data may only be reco events, or not reco events. Events in MC may be any (or all) the three types.

Table 8-1. A breakdown of event rates after each cut for the iron events in nuclear target 3. This table correpsonds to 3.12×10^{20} POT.

	Number of Events	Survival Rate (%)
Generated DIS Events	3042	100
Matched to MINOS	774	25.45
Reconstructed in Target	739	24.30
μ^-	647	21.26
85 cm Apothem	587	19.30
Target Quality Cuts	520	17.08
tdead cut	518	17.04
Upstream E	471	15.47
MINOS Quality Track	400	13.15
$5 \leq E_\nu < 50$ and $17 \geq \theta_\mu$	367	12.07
Reco DIS	247	8.11

8.3 Event Efficiencies and Purities

There are two kinds of efficiency to consider when isolating the DIS sample. The first efficiency answers how efficient the DIS cut is relative to the existing inclusive sample. This efficiency is defined as the number of events in the true material passing the reconstructed CCInclusive cuts, the reconstructed AND truth DIS cut, divided by the number of events in the true material which pass the truth DIS cut and all of the reconstructed CCInclusive cuts previously mentioned. This efficiency measures how effectively the DIS cuts isolate events from the inclusive sample. This efficiency depends on the underlying resolution of the hadronic and muon reconstruction, since Q^2 and W are calculated completely from these quantities. This efficiency is referred to as the "inelastic efficiency" in the text.

An "inelastic purity" is related to inelastic efficiency. The number of events in the true material passing the reconstructed CCInclusive cuts, the reconstructed AND truth DIS cut was divided by the number of events in the true material passing the reconstructed CCInclusive cuts and the reconstructed DIS cut. Both inelastic purity and inelastic efficiency quantify the efficacy of the DIS cuts.

Related to the inelastic efficiency is the overall efficiency. This quantity has the same numerator; the number of events in the true material passing the reconstructed CCInclusive cuts, the reconstructed AND truth DIS cut. However, the denominator is instead *all* true CC DIS events in the true fiducial volume. This quantity explains the overall efficiency of the DIS cut, the MINOS matching and the algorithm which builds vertices in the nuclear targets. Since the denominator is naturally larger in the case of overall efficiency than inelastic efficiency, the overall efficiency must be lower than the inelastic efficiency. The overall efficiency is used in the calculation of the total and differential cross-section as described in Section 12.1.

The "overall purity" is related to the overall efficiency. It is defined as the number of events in the true material passing the reconstructed CCInclusive cuts, the reconstructed AND truth DIS cut, divided by the number of events passing the reconstructed CCInclusive cuts and reconstructed DIS cut. The overall purity takes into account the loss of purity of events mis-reconstructed in the fiducial volume, while the inelastic purity does not.

Table 8-2 presents the inelastic and overall efficiencies and purities for the DIS cuts as a percentage. The errors in the table are statistical only. The inelastic efficiency is presented in table 8-3. The contamination (1 minus the inelastic purity) is given in table 8-4.

8.4 Event Sample (Data and MC)

The analysis produces histograms by running over inclusive ntuples created by the NukeCCInclusive algorithm. The NukeCCInclusive algorithm divides the entire sample into different subsamples depending on the reconstructed z vertex of the event. Each event is initially sorted by the reconstructed z position into nuclear target 1, 2, 3, 4 or 5, or the tracker, with nuclear target 1 being the most upstream and nuclear target 5 being the most downstream. An event is then classified according to its' target nuclei based on the x, y position of the vertex in each target.

Table 8-2. Inelastic and overall efficiencies and purities of the DIS cut of the five nuclear targets. These numbers are for an energy range of $5 \leq E_\nu < 50$ GeV, and correspond to 3.12×10^{20} POT.

Target / Z	Inelastic Efficiency	Inelastic Purity	Overall Efficiency	Overall Purity
1/26	$77 \pm 0.5\%$	$79 \pm 0.5\%$	$11 \pm 0.1\%$	$54 \pm 0.5\%$
1/82	$79 \pm 0.5\%$	$82 \pm 0.4\%$	$13 \pm 0.2\%$	$63 \pm 0.5\%$
2/26	$78 \pm 0.5\%$	$81 \pm 0.4\%$	$12 \pm 0.1\%$	$55 \pm 0.5\%$
2/82	$78 \pm 0.5\%$	$81 \pm 0.4\%$	$13 \pm 0.1\%$	$60 \pm 0.5\%$
3/6	$80 \pm 0.5\%$	$83 \pm 0.5\%$	$17 \pm 0.2\%$	$48 \pm 0.5\%$
3/26	$73 \pm 0.7\%$	$84 \pm 0.6\%$	$11 \pm 0.2\%$	$55 \pm 0.7\%$
3/82	$67 \pm 1\%$	$83 \pm 0.9\%$	$8 \pm 0.2\%$	$60 \pm 1\%$
4/82	$82 \pm 0.4\%$	$84 \pm 0.4\%$	$18 \pm 0.2\%$	$42 \pm 0.4\%$
5/26	$83 \pm 0.4\%$	$84 \pm 0.4\%$	$20 \pm 0.2\%$	$48 \pm 0.4\%$
5/82	$83 \pm 0.5\%$	$83 \pm 0.5\%$	$20 \pm 0.3\%$	$54 \pm 0.5\%$

Events originating in the tracker are divided into separate "faux targets" depending on the z vertex. Six tracker modules make up one "faux set." The DIS analysis uses tracker modules 27 through 80 inclusive as faux targets. This selection and division of faux targets is identical to the charged current inclusive analysis [82].

Histograms are produced target by target and material by material, so each of the 9 sets of six tracker modules (faux target sets) and 5 nuclear targets are initially analyzed separately. Figure 8-1 displays the DIS selection of reco events for data and MC as a function of neutrino energy. The MC is broken down into it's constituent channels. Each MC channel is defined in terms of *true* W and Q^2 (except for the QE channel, which is all QE events regardless of W or Q^2). The plots draw the true DIS signal as dark purple.

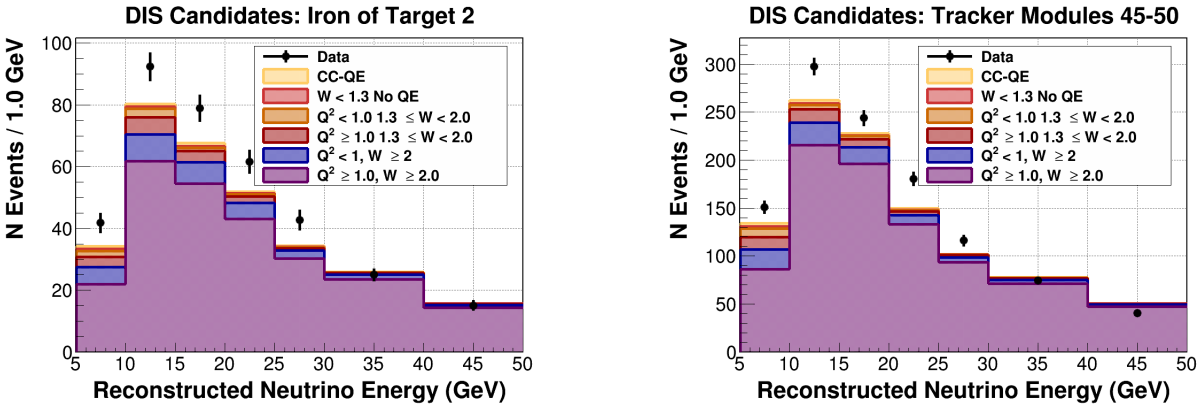

Figure 8-1. The reconstructed DIS events for data (black points) and MC (various colored bands) in the iron of target 2 (left) and tracker modules 45-50 (right). The data and MC correspond to 3.12×10^{20} POT.

Table 8-3. The number of true DIS events (True Events), the number of true DIS events passing the reconstructed DIS cuts (True Reco Events) and the inelastic efficiency of the nuclear targets. These numbers are for an energy range of $5 \leq E_\nu < 50$ GeV, and correspond to 3.12×10^{20} POT.

Target	Target Z	True Events	True Reco Events	Inelastic Efficiency (%)
1	26	1200	950	$77 \pm 0.5\%$
1	82	1100	910	$79 \pm 0.5\%$
2	26	1300	980	$78 \pm 0.5\%$
2	82	1200	960	$78 \pm 0.5\%$
3	6	940	750	$80 \pm 0.5\%$
3	26	630	460	$73 \pm 0.7\%$
3	82	360	240	$67 \pm 1\%$
4	82	1400	1200	$82 \pm 0.4\%$
5	26	1100	900	$83 \pm 0.4\%$
5	82	8700	720	$83 \pm 0.5\%$

Table 8-4. The number of reconstructed DIS events (Reco Events), the number of true DIS events passing the reconstructed DIS cuts (True Reco Events) and the non-DIS contamination of the nuclear targets. These numbers are for an energy range of $5 \leq E_\nu < 50$ GeV, and correspond to 3.12×10^{20} POT.

Target	Target Z	Reco Events	True Reco Events	Contamination (%)
1	26	1200	950	$20 \pm 0.7\%$
1	82	1100	910	$17 \pm 0.6\%$
2	26	1200	980	$17 \pm 0.7\%$
2	82	1200	960	$19 \pm 0.7\%$
3	6	910	750	$17 \pm 0.8\%$
3	26	540	460	$14 \pm 0.9\%$
3	82	290	240	$15 \pm 1\%$
4	82	1400	1200	$15 \pm 0.7\%$
5	26	1100	900	$15 \pm 0.7\%$
5	82	870	720	$15 \pm 0.7\%$

CHAPTER 9
BACKGROUNDS

The inelastic purity described in Section 8.3 indicates the DIS cuts selected events with a reconstructed $Q^2 \geq 1.0$ and $W \geq 2.0$ when in fact the true $Q^2 < 1.0$ or the true $W < 2.0$. These are contamination events which must be removed from the reconstructed DIS sample before measuring a cross section. Backgrounds in the jth bin of E_ν and x_{bj} are expressed as b_j cross section expression:

$$\sigma_i = \frac{U_{ij}\,(d_j - b_j)}{\Delta_i\,\epsilon_i\,\Phi_i\,N}. \tag{9-1}$$

The Monte Carlo is used to subtract this background, however prior to subtraction the Monte Carlo is tuned to the data using sidebands.

9.1 Non-DIS Backgrounds

Table 9-1 gives the breakdown of the different components of the contamination. The largest contribution are events with a true $Q^2 < 1.0$ and a true $W \geq 2.0$. The second largest contribution are events with a true $1.3 \leq W < 2.0$ and a true $Q^2 \geq 1.0$. Initially, two sidebands with *reconstructed* $Q^2 < 1.0$, $W \geq 2.0$ (low Q^2 sideband) and $1.3 \leq W < 2.0$, $Q^2 \geq 1.0$ (low W sideband) were selected to estimate the background present in the signal region (see Figure 9-1).

The goal of the background subtraction is to take a distribution of reconstructed DIS events that are reconstructed as originating in a nuclear target, T_r, and transform that to a distribution of true DIS events truly originating in the nuclear target, T_t. The DIS analysis contains background from events which erroneously pass the Q^2 and W cut, as well as events truly occurring in the plastic scintillator surrounding the nuclear targets. As a result the background subtraction is more complicated than most analyses, and special care has to be taken. This section presents the derivation for the background subtraction transformation used.

Table 9-1. Breakdown of contamination events which passed the reconstructed DIS cuts. The percentage quoted is the percentage of total contamination events falling into that W and Q^2 region. The W and Q^2 values are true values.

Target / Z	Quasi-Elastic	$W < 2.0$ All Q^2	$W \geq 2.0$ $Q^2 < 1.0$
1 / 26	10.9%	40.1%	48.5%
1 / 82	11%	41.8%	46.9%
2 / 26	10.2%	37.9%	51%
2 / 82	12.2%	41.3%	45.3%
3 / 6	8.96%	32.1%	58.5%
3 / 26	11.3%	33.3%	55.1%
3 / 82	9.06%	34.1%	56.2%
4 / 82	9.89%	37.7%	51.7%
5 / 26	9.22%	36.1%	54.2%
5 / 82	10%	36.2%	52.9%

The true number of DIS events, truly occurring in a nucleus N, T_N is equal to the number of true DIS events reconstructed to (but not truly) in a nucleus N, R_N minus the number of true DIS events truly in the surrounding scintillator, CH:

$$T_N = R_N - CH \tag{9-2}$$

Both R_N and CH are composed *only* of true DIS events. R_N is equal to the number of reconstructed DIS events reconstructed in nucleus N S_N, minus the true *non*-DIS events reconstructed in the nucleus N, C_N

$$R_N = S_N - C_N. \tag{9-3}$$

Similarly, the true DIS events in the surrounding scintillator CH are equal to:

$$CH = CH_r - CH_{bg}, \tag{9-4}$$

where CH_r are the events in the scintillator reconstructed as DIS, and CH_{bg} are events in the scintillator which are truly not DIS.

Putting together Equations 9-2, 9-3 and 9-4 yields:

$$T_N = (S_N - C_N) - (CH_r - CH_{bg}). \tag{9-5}$$

Both C_N and CH_{bg} are estimated from the Monte Carlo. This Monte Carlo simulation is tuned to the data following the procedure outlined later in this section. CH_r is measured separately for the data and MC, by measuring the event rate of reconstructed DIS events in downstream tracker modules ("faux targets"). The difference $(CH_r - CH_{bg})$ is extrapolated from the downstream faux targets to the nuclear region using the procedure described in section 9.2.

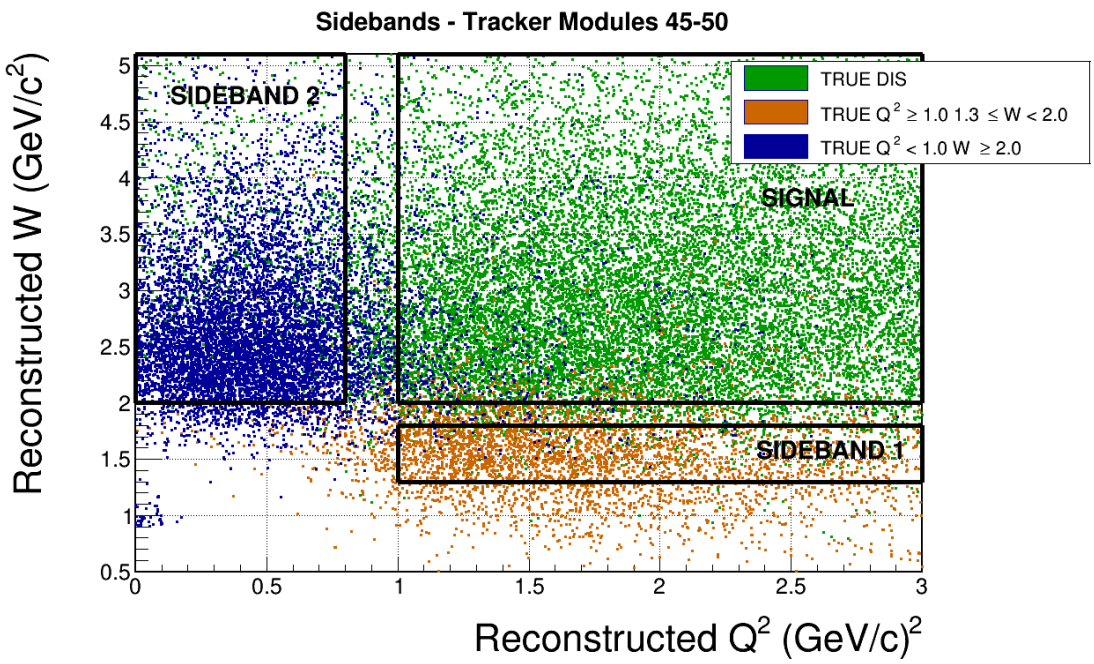

Figure 9-1. Reconstruced W vs. reconstructed Q^2, with the two sidebands labeled. The green dots are true DIS events. The blue and orange dots in the top-right box labeled signal are from non-DIS backgrounds.

9.1.1 Construction of Sidebands

The reconstructed sidebands are further tuned to reduce the amount of signal events in the sideband, while still ensuring the kinematics of the sideband sufficiently emulate the kinematics of the true non-DIS background.

Figure 9-2 shows the true content of each reconstructed sideband as a function of reconstructed Q^2 and W. In the case of W, reducing the range of the reconstructed W to $1.3 \leq W < 1.8$ reduces the amount of true signal in the sideband by 80%. Similarly, reducing the range of the reconstructed Q^2 to $Q^2 < 0.7$ reduces the amount of true signal by 50%.

The low Q^2 sideband is further tuned to determine the lowest Q^2 boundary where the kinematics of the sideband still resemble the kinematics of the true contamination. In this study, the upper Q^2 bound of the low Q^2 sideband is lowered to $Q^2 = 0.35$. The shape between this sample ($Q^2 < 0.35$ $W \geq 2.0$) is compared to the shape of the backgrounds. It is concluded that the shape of the backgrounds in W of the $Q^2 < 0.35$ $W \geq 2.0$ events closely resembles the shape of the W of the true contamination sufficiently below $Q^2 < 0.35$, and the Q^2 cut of the sideband may be lowered to $Q^2 = 0$. This is demonstrated in Figure 9-3.

Plots of the POT normalized data and MC of each sideband as a function of E_ν, x_{bj}, Q^2, E_μ and θ_μ may be found in Figures 9-4 and 9-5 as well as Appendix A.1 and A.4. The MC is separated into each of the different true components. The reconstructed low Q^2 band contains between 20 and 30 % true DIS events, and the low W band contains approximately 5 % true DIS events. The MC templates were fit using two different methods. In the first method, the true signal template was fixed at the default GENIE prediction. In the second, the fit was allowed to change the amount of signal. That is, the true signal was treated as a separate MC template. In both cases, the values extracted for the two background templates were similar as demonstrated by Table 9-2. As a result, it is sufficient to subtract the true DIS content from the data prior to fitting in both cases.

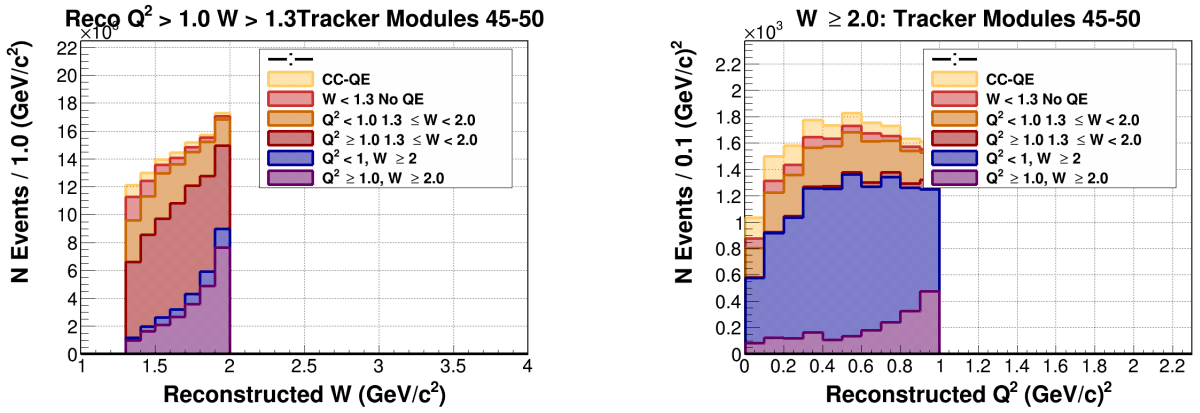

Figure 9-2. Plots of the true contribution of each reconstructed sideband as a function of Q^2 and W, before tuning to data. The upper value of each sideband was tuned to minimize the amount of true signal in each sideband, while simultaneously preserving sufficient statistics in each sideband to make a convincing fit to the data.

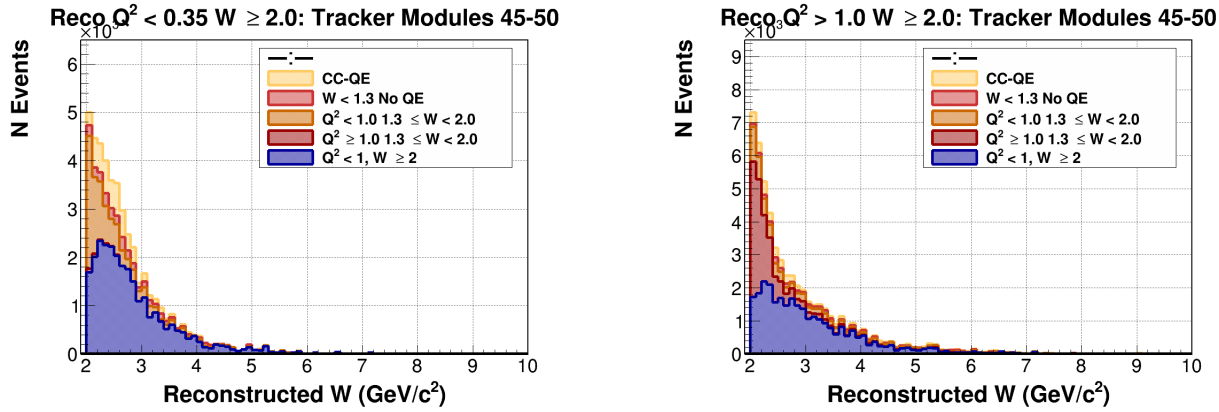

Figure 9-3. Plots of the true contribution of events with a reconstructed $Q^2 < 0.35$, $W \geq 2.0$ (left), and reconstructed $Q^2 \geq 1.0$, $W \geq 2.0$ (right), before tuning to data. The true DIS component is suppressed in each plot. As the shape in W is similar between the two plots, it was concluded that $Q^2 < 0.35$ (and thus $Q^2 < 0.8$) is a valid region for background tuning.

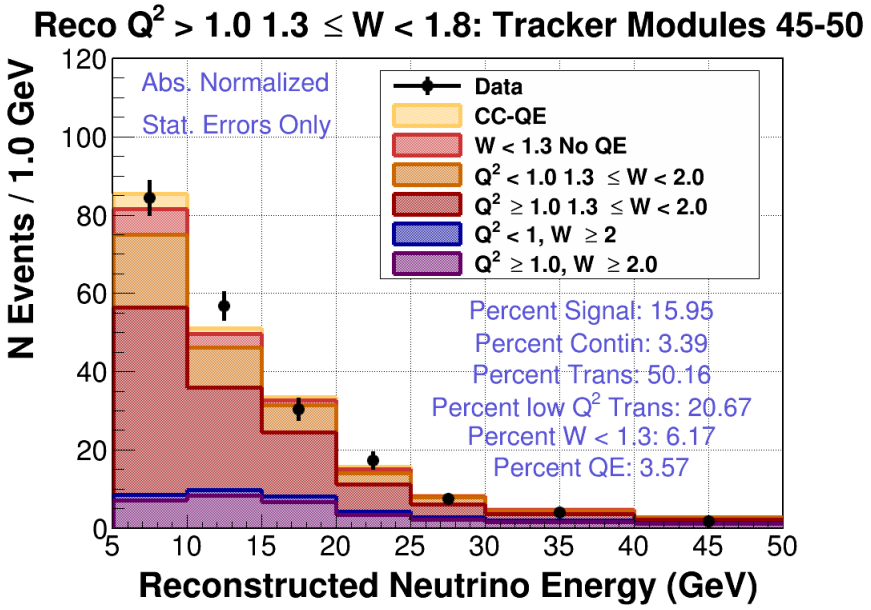

Figure 9-4. Data and MC for events with a reconstructed $Q^2 \geq 1.0$ and $1.3 \leq W < 1.8$ for CH events in tracker modules 45 - 50 prior to fitting to data. The relative content of each MC process is listed on the plot.

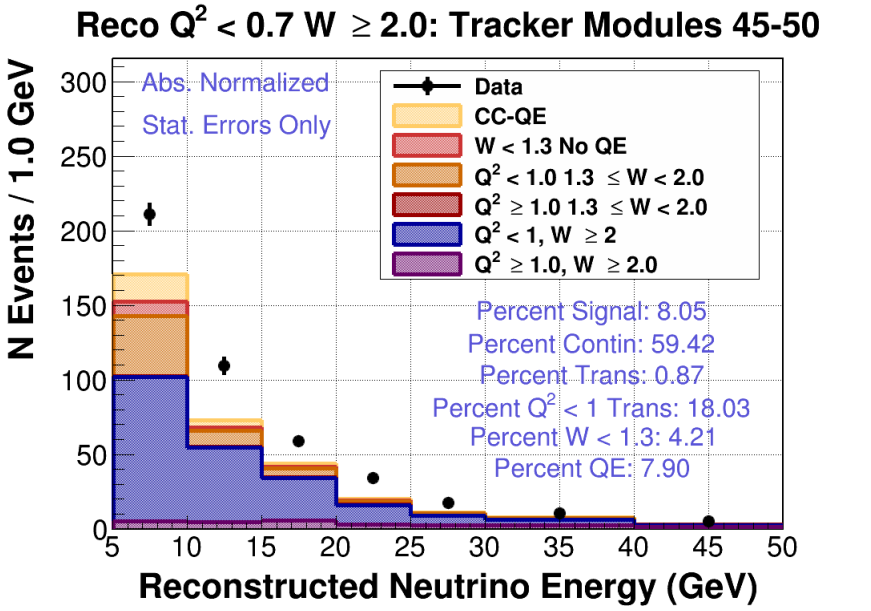

Figure 9-5. Data and MC for events with a reconstructed $Q^2 < 0.8$ and $2.0 \geq W$ for CH events in tracker modules 45 - 50 prior to fitting to data. The relative content of each MC process is listed on the plot.

Table 9-2. Scale factors of the two templates derived from data and Monte Carlo tuning for each nuclues analyzed when the true signal is held constant (first two columns), and when the signal is allowed to change with the fit (last three columns). The errors quoted are statistical errors.

	DIS NOT Included in Fit		DIS Included in Fit		
A	low W	low Q^2	low W	low Q^2	DIS
CH	0.94 ± 0.01	1.57 ± 0.01	0.93 ± 0.02	1.57 ± 0.02	1.07 ± 0.06
C	0.90 ± 0.08	1.58 ± 0.11	0.84 ± 0.12	1.59 ± 0.1	1.24 ± 0.35
Fe	0.99 ± 0.04	1.58 ± 0.05	0.98 ± 0.05	1.59 ± 0.05	1.03 ± 0.2
Pb	0.95 ± 0.03	1.36 ± 0.05	0.92 ± 0.05	1.36 ± 0.05	1.09 ± 0.2

9.1.2 Fitting Prescription

After subtracting the true DIS events from each sideband, two MC background templates are fit to the data. The first template (template 1) consists of the sum of all events with $W < 2.0$ and QE events. The second template (template 2) consists of all events with $W \geq 2.0$ but $Q^2 < 1.0$. The two templates are fit simultaneously to the data in both sidebands using a χ^2 minimization technique, with χ^2 defined as:

$$\chi^2 = \sum^{i} \frac{(N_{data} - N_{MC})^2}{\sigma^2_{data}}, \tag{9-6}$$

for each energy bin i.

The fits are performed for each passive target/material combination and each faux target set over the energy range $5 \leq E_\nu < 50$ GeV. The results of the fits for each target are two scale factors α and β which are used to scale template 1 and template 2 respectively.

Since each sideband is statistics limited, it is preferable to combine targets / materials to obtain a more precise measurement of each scale factor. In order to prove the fits to each target individually were consistent with a fit to the sum, a statistical analysis was preformed for each material with multiple targets (CH, Fe and Pb). This analysis compares the consistency of α ($W < 2.0$) and β ($W \geq 2.0$, $Q^2 < 1.0$) of each target/material combination to the error-weighted mean α and β of each material.

In all but two cases, the average and individual scale factors did not differ by more than 1 σ. Plots of the individual scale factors may be found in Appendix A.2 and A.5. The two special cases occurred for β, the low Q^2 scale factor, in the CH and the Pb.

The scale factors β extracted for each faux module set appear to exhibit a slope in z position, as demonstrated in Figure 9-6. This slope had a roughly 2.1 σ significance. The consistency of the individual scale factors is presented in Figure 9-7. This slope is driven by the most upstream tracker modules, faux target set 1.

When the fits of β to the Pb of targets 1, 2, 3, 4 and 5 were compared to the average fit value, the scale factors extracted from targets 1 and 5 is about 2.5 σ away from the mean in opposite directions (see Figure 9-8).

The χ^2 computed between the scale factor obtained from fitting solely the lead of target 5 and the average is 6.2114. The probability of having an excursion from the mean at least this extreme by chance is 1.3%. This is a less than 3 σ effect, and is not considered a significant enough excursion to warrant decoupling the targets.

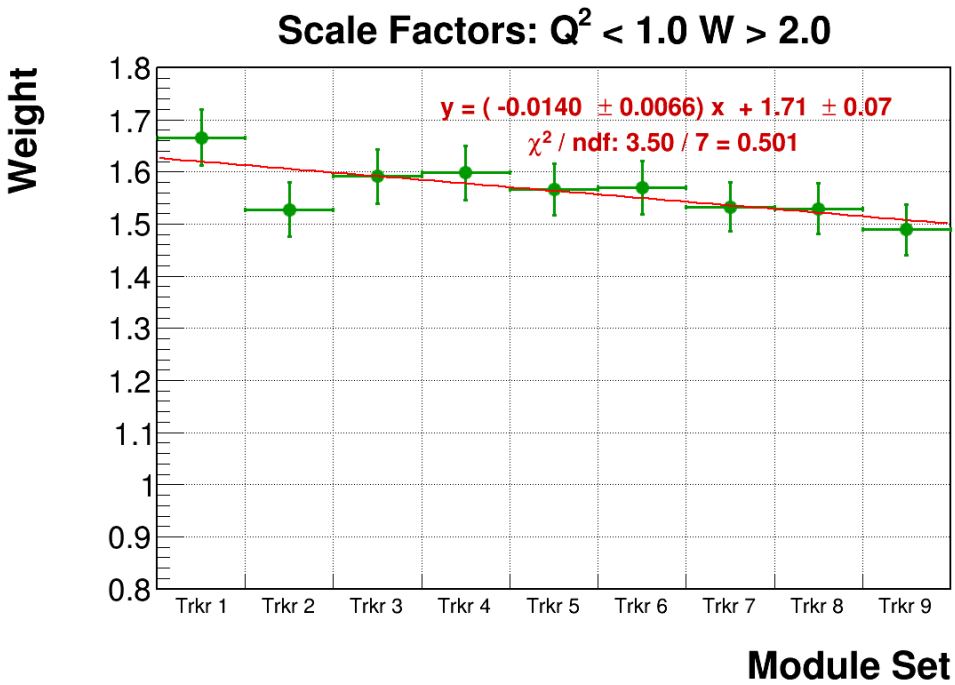

Figure 9-6. Scale factors obtained from fitting template 2 ($Q^2 < 1.0$ $W \geq 2.0$) for all 9 faux targets. The results of the fit to a line are presented on the plot.

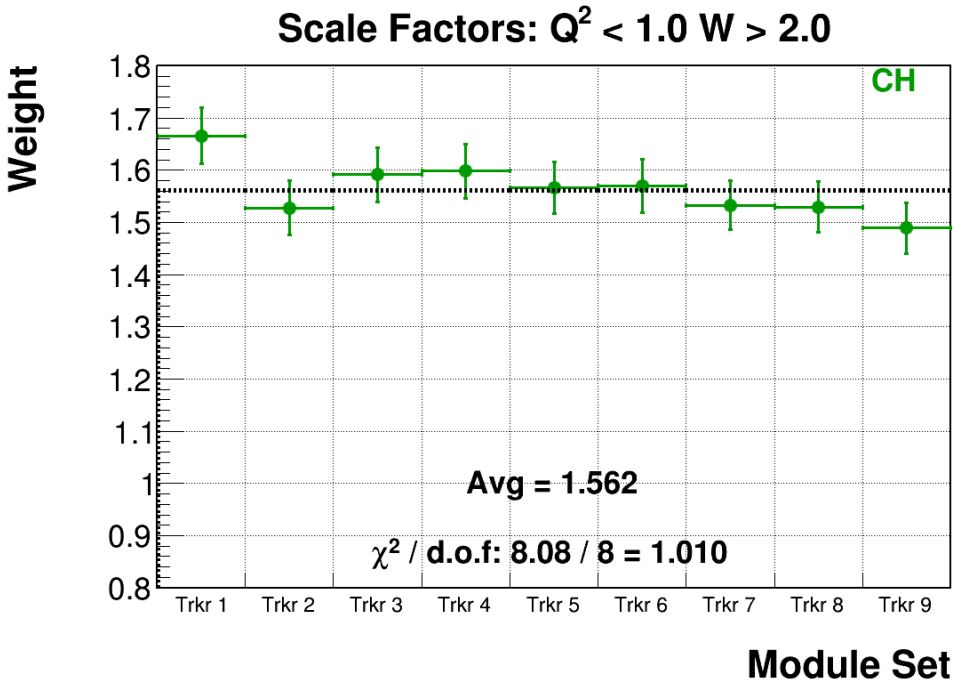

Figure 9-7. Scale factors obtained from fitting template 2 ($Q^2 < 1.0$ $W \geq 2.0$) for all 9 faux targets, as well as the error-weighted average scale factor of all 9 faux targets.

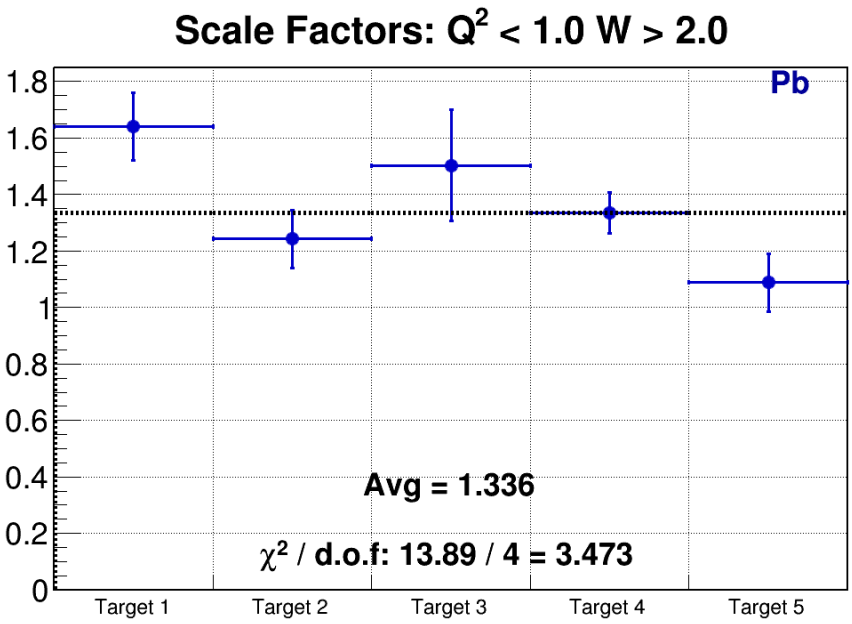

Figure 9-8. Scale factors obtained from fitting template 2 for all passive targets containing lead, as well as the error-weighted average scale factor of all lead targets.

.

9.1.3 Fit Results

After summing targets of identical materials, scale factors were derived for each material and each MC template. The extracted scale factors can be found in Table 9-3.

Table 9-3. Scale factors of the two templates, derived from data and Monte Carlo tuning for each material analyzed. The errors quoted in the table are statistical errors.

Material	low W scale (α)	low Q^2 scale (β)
CH	0.94 ± 0.01	1.57 ± 0.02
C	0.90 ± 0.08	1.58 ± 0.11
Fe	0.99 ± 0.04	1.58 ± 0.05
Pb	0.95 ± 0.03	1.36 ± 0.05

The scale factors are applied to non-DIS events passing the DIS event selection cuts in the MC. This re-weighted MC is then subtracted from the candidate DIS events in data. The analysis preforms the non-DIS event subtraction before it preforms the CH (wrong-nuclei) background subtraction. In this sense, the plastic background predicted at each nuclear target is a DIS-only prediction. This is explained in further detail in Section 9.2.

Data to MC comparisons of selected DIS events before and after background tuning are in Figure 9-9. These plots sum the different background components into true $W < 2.0$ and true $Q^2 < 1.0$ $W \geq 2.0$.

9.2 Plastic Background Subtraction

The z-vertex selection of events in the passive nuclear targets allow 2 tracker modules (4 planes) downstream of the passive targets and 1 tracker module (2 planes) upstream to pass as nuclear target events. As a result, there is a component of the passive target sample that truly occurred in the plastic surrounding the nuclear targets. The technique for subtracting the CH background is the same technique as the inclusive analysis, and is described in detail in Ref [82]. However three important changes were made for the DIS analysis.

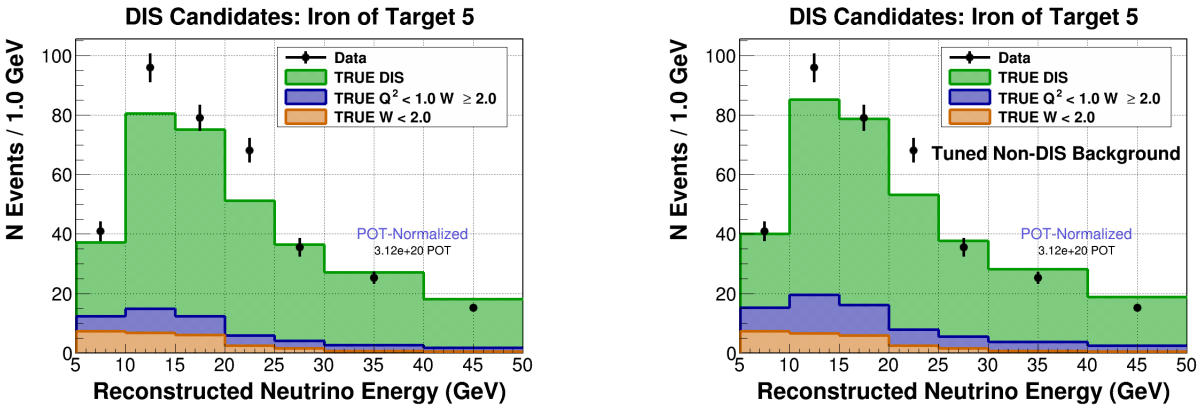

Figure 9-9. Events passing the DIS selection cuts in data (black points) as well as the MC signal (green) and background (orange and blue). The left plot is prior to the background tuning to data, and the right plot is after tuning.

First, the plastic background extracted by the procedure is a DIS-only plastic background. Initially, all of the reconstructed DIS events in the downstream faux targets are measured and weighted for their MINOS acceptance using a muon gun simulation. Prior to extrapolating a CH background prediction, the events have the non-DIS events subtracted from them. The non-DIS subtraction applies the sideband weights derived in Section 9. Mathematically in a given faux target i,

$$CH_i = a_i(N_i - w * C_i), \tag{9-7}$$

where N_i is the number of events passing the DIS selection cuts in the faux target i, C_i is the number of truly non-DIS events passing the DIS selection cuts in the faux target i, w is the sideband tuned scale factor, and $a_i(E_\mu, \theta)$ is the MINOS acceptance weight. w in Equation 9-7 depends on the MC truth information of the event. It is the α value described in Section 9 for QE events, or events with a true $W < 2.0$, or β for events with a true $W > 2.0$. The CH_i factor extracted from Equation 9-7 is extracted separately for the data and the MC. In this case of the MC extrapolation, $N_i, C_i a_i$ and w are all computed

from the MC. In the case of the data, N_i is measured from the data. However, $C_i a_i$ and w are derived from the MC.

The MINOS acceptance weights (a_i) are calculated from a muon-gun only MC, which generates muons of varying energy and angle at various (x, y, z) points in the nuclear targets and tracker. This procedure is fully described in Ref [83]. The weights applied to the DIS analysis are identical to those applied in the inclusive analysis.

In order to more accurately estimate the background, the plastic background derived from each faux target according to Equation 9-7 is scaled to the true CH background at each nuclear target. The true CH background used in the scaling subtracts the DIS contamination in the same manner as Equation 9-7:

$$k_{ij} = \frac{T_j^{reco} - w * T_j^{contam}}{CH_{ij}^{reco} - w * CH_{ij}^{contam}}, \tag{9-8}$$

where T_{reco} is the number of events passing the DIS selection cuts truly in the CH surrounding target j, T_{contam} is the number of non-true DIS events passing the selection cuts truly in the CH surrounding target j, CH_{reco} is the number background events extrapolated from faux set i passing the DIS selection cuts calculated in Equation 9-7 in target j, and CH_{contam} is the number extrapolated background events, falsely identified as DIS events, reconstructed in target j. w has the same definition in 9-7 and 9-8. All of the factors in 9-8 are derived from the MC.

The result of this procedure for MC events in the carbon of nuclear target 3 is illustrated in Figure 9-10. The y-axis is the number of DIS events predicted from the 10 different faux sets. Each dashed line on the plot shows the DIS CH background extrapolated from one set of faux targets. The red solid line is the average prediction of the eight most upstream faux targets. The black points in Figure 9-10 are *not* CH data, but instead the true DIS events truly originating in the CH surrounding target 3. Deviations from the solid line and black points in Figure 9-10 indicate imperfections in the CH background subtraction procedure.

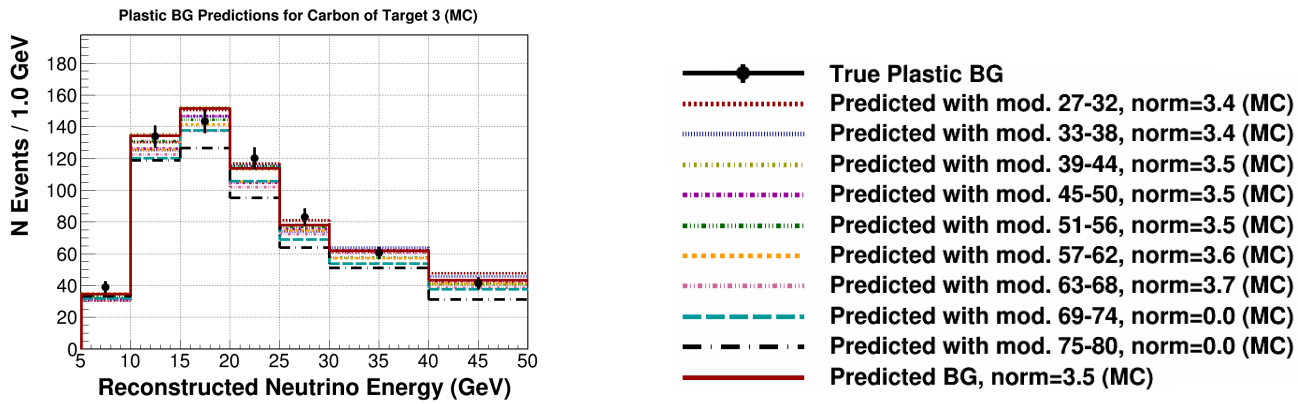

Figure 9-10. Extrapolated MC plastic background for the Carbon of target 3. Left: Plastic background predicted by each of the nine different target module sets (dashed lines) as well as the average (solid line) of the first seven faux sets (modules 27 - 68). The points are the true DIS CH events mis-reconstructed into target 3, along with the statistical error.Right: Legend of the left plot. Each of the "norm" factors are the area normalizations calculated for a different faux set for target 3 from Equation 9-8. Since the last two faux sets are not used in the DIS analysis, they are set to 0.

Each of the dashed lines in Figure 9-10 has been scaled according to Equation 9-8, and the solid line has been scaled to Equation 9-8, averaged over the seven most upstream faux targets.

A second difference from the inclusive analysis is only the first 7 sets of tracker modules are used to predict the background surrounding the nuclear targets in the DIS analysis. Removing the two most downstream sets of faux targets results in a substantial improvement to the accuracy of the background prediction as measured using the MC (see Figure 9-11).

Thirdly, the E_{had} weights used in the inclusive analysis are not used in the DIS analysis. These weights are computed from the MC, and calculated such that the ratio of predicted and true plastic background in the MC was identically equal to 1 for all E_{had}. This procedure was implemented primarily to fix deficiencies of the background subtraction at low hadronic energy, which are not present in the DIS analysis.

In contrast, the DIS analysis observes deficiencies with the plastic background subtraction at *high* hadronic energy, particularly in the Carbon sample of target 3 (see

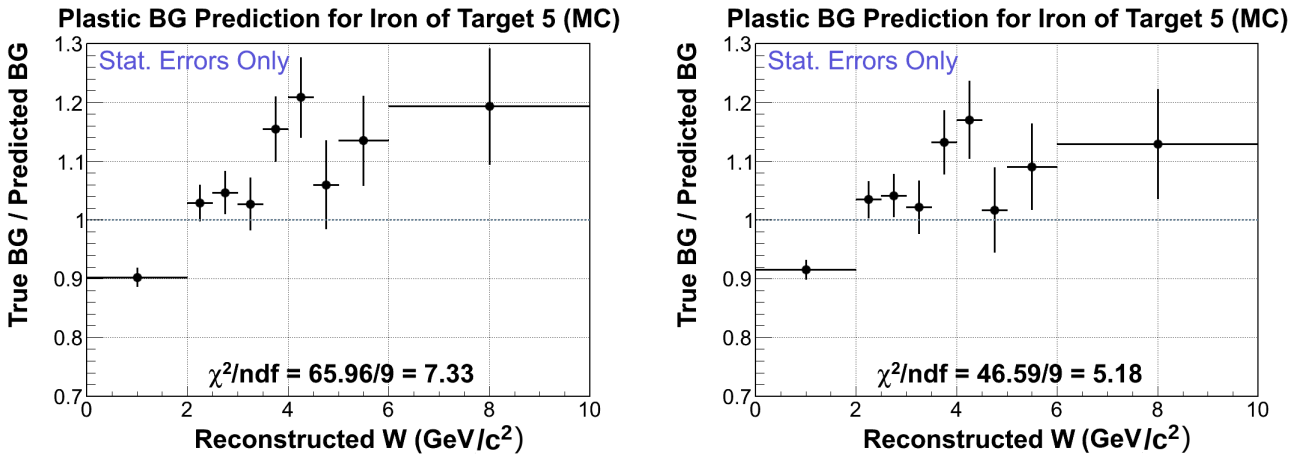

Figure 9-11. Plots of the true / predicted plastic background for events reconstructed in the iron of target 5 for MC events using all 9 faux target sets (left), and removing the two most downstream sets (right) as a function of W. The prediction improves by removing the downstream targets, especially at high W. The χ^2 improves as well. Note that these two samples are not statistically independent.

Figure 9-11). Investigating this discrepancy revealed a substantial number of events were truly occurring in upstream nuclear targets and subsequently reconstructed in downstream targets. This lead to a re-optimization of the upstream energy cuts, as detailed in Section 9.3.

Putting everything together, the final CH DIS background is calculated for each passive target by:

- Measuring the number of events passing the DIS selection cuts in each variable and each faux target set. The non-DIS events are subtracted according to Equation 9-7.
- The faux target event rate is weighted for its' acceptance in MINOS based on a muon gun MC.
- The weighed, measured event rate in each faux target is area-normalized to the true DIS CH BG in each passive target.
- The area normalized distributions (as plotted in Figure 9-10) are averaged. Only the first seven sets of faux targets are used in the average.

Each passive target j, has a DIS only CH background estimation CH_j according to:

$$CH_j = \frac{1}{7}\sum_i^7 CH'_i k_{ij}, \tag{9-9}$$

or

$$CH_j = \frac{1}{7}\sum_i^7 a_i(N_i - w * C_i) * \frac{T_j^{reco} - w * T_j^{contam}}{CH_{ij}^{reco} - w * CH_{ij}^{contam}}. \tag{9-10}$$

At the conclusion of this calculation the plastic DIS background can be predicted to about the 10% level (see Appendix C.1). Differences from 0 in the (true - predicted) arise from the fact that the nuclear target z-vertex selection erroneously includes events from neighboring, upstream nuclear targets. These events are not fully constrained by the procedure detailed in this section. An attempt was made to mitigate this upstream contamination as described in the next section.

9.3 Upstream Energy Cuts

9.3.1 z-Vertex Biases in the Nuclear Targets

The plastic background procedure outlined in the previous section reveals a significant difference in the predicted vs. true background of high W events, particularly in target 3. A large number of events that reconstruct in target 3 truly originate in the iron and lead of target 2. Failures in the z-vertex reconstruction cause this effect. Events with a large amount of shower energy (large inelasticity and W) create showers which obscure muon tracking, forcing the vertex downstream of its' true origin.

Figure 9-12 presents the true origin of events reconstructed in the Carbon of target 3 vs. reconstructed W. The green points are events which truly originate in the C of target 3. The red and blue points are iron and lead events originating upstream of target 3. Nearly 14% of the events at high W originate from a mis-identified target upstream of target 3.

While target 3 contains the largest amount of mis-identified events, the other nuclear targets contain a non-negligible number of poorly reconstructed events. This is

illustrated in Figure 9-13, which describes the true event origin of events reconstructed inside the nuclear target region of the detector. The MC used for this plot does not include the MINERνA liquid water target centered at $z \approx 525$ mm. As a result, there are large normalization differences in the tracker module directly downstream, since the water target was full during data taking. The red and blue area below the orange are events misidentified in neighboring nuclear targets, while the green events are correctly reconstructed to their respective targets. Broadly speaking target 3, the third peak, experiences the largest amount of vertex contamination from nuclear targets 1 and 2 (blue and red). However, the contamination is noticeable in other targets, particularly target 5.

9.3.2 Updated Upstream Energy Cuts

Since the genesis of the mis-identification is events with a large hadronic shower between nuclear targets, a set of cuts are adopted to remove these events from the sample. A variation of this problem existed in the inclusive analysis, where a muon track would be reconstructed to a particular nuclear target despite the fact that the track extended upstream to a different target [84]. The solution for the inclusive analysis was to cut events which contained an average between 1.5 and 8 MeV of visible energy per plane in the direction of the projected tracker, upstream of the track, for at least 8 planes. These cuts formed the basis for the upstream energy cuts of the DIS analysis.

The DIS analysis updates the upstream energy cuts by removing the 8 MeV energy ceiling, as well as reducing the minimum required number of planes from 8 to 6. The removal of the 8 MeV requirement allows hadronic showers, which deposit more energy in the detector, to contribute to the total upstream energy. The reduction from 8 planes to 6 planes reflects the fact that the event selection of each nuclear target allows events vertexed in one plane upstream of the nuclear target. Thus, the minimum number of planes between events identified in target 3, where the event contamination is the most severe, and target 2 the source of that contamination, is 7 planes. An extra plane is included in the cut so only one module is allowed to be illuminated.

It was also discovered during hand scanning of events that a number of low-energy (5 to 15 GeV) DIS events were identified as originating in target 3 with a muon track that extended back to target 2. Details of this event scan may be found in Section 9.3.3. The vertex of the event would be placed in target 3 due to a second track creating a multi-track vertex (see Figure 9-14). As a result, the DIS analysis looks upstream of the *vertex* for the purposes of accumulating upstream energy. This is in contrast to the inclusive analysis, which looks upstream of the *track endpoint*.

9.3.3 Event Scans

Prior to applying the upstream vertex cut, the consistency of the z-vertex bias and the fraction of upstream energy between the data and MC were studied. Both of these studies focused exclusively on target 3, since proximity of target 3 to nuclear target 2, only 8 planes of scintillator ($\approx$ 10 cm), caused significant event mis-identification. A hand-scan of events is used to measure the consistency of the z-vertex bias between data and MC.

The hand-scan selected a set of events reconstructed in the C, Fe and Pb of nuclear target 3 in two different energy ranges. All of the data events in C between 5 and 10 GeV of energy were scanned, along with all data events in Fe and Pb between 5 and 15 GeV. These energy bins were selected because prior to updating the upstream vertex cuts excesses in the data of target 3 were observed in the 5 to 10 GeV bin for the carbon, and in the 5 to 10 and 10 to 15 GeV bin for the iron. No excesses were observed in the lead. However since the number of lead events from 5 to 15 GeV in target 3 is on the order 100 events, it seemed prudent to do a hand scan. Scanners were asked to characterize all events as either originating in target 3, originating in a upstream nuclear target, or originating in a downstream nuclear target.

For the data scan, 7 people scanned 598 events with almost 100% overlap. Of 598 events scanned:

- 34 originated in an upstream target.
- 13 originated in a downstream target.

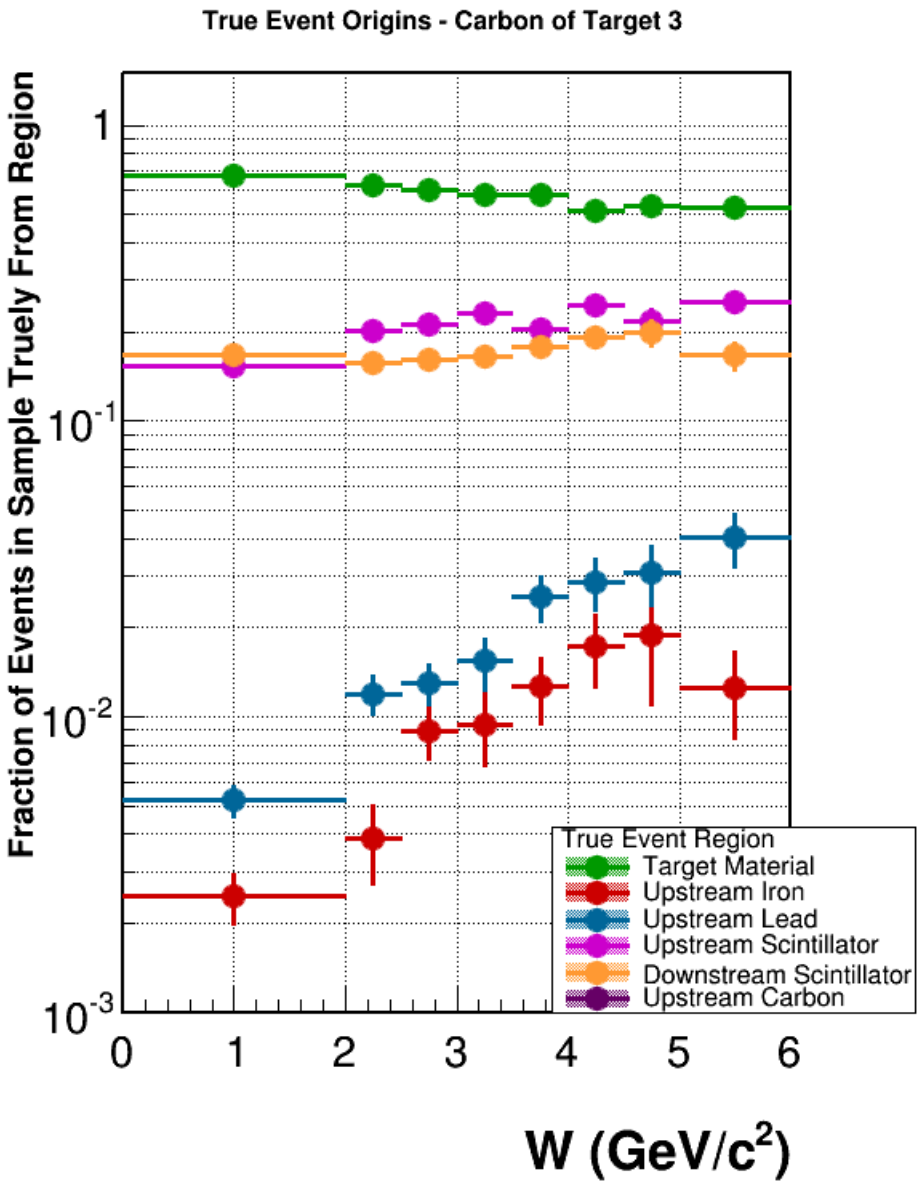

Figure 9-12. True event origins of inclusive events reconstructed in the Carbon of target 3 vs.reconstructed W.

- 19 were unknown / too close to call.
- 30 were clearly overlapping events.

In this case, "overlapping events" are events with either two distinct neutrino interactions in the same time slice, or a neutrino event taking place in the same time slice

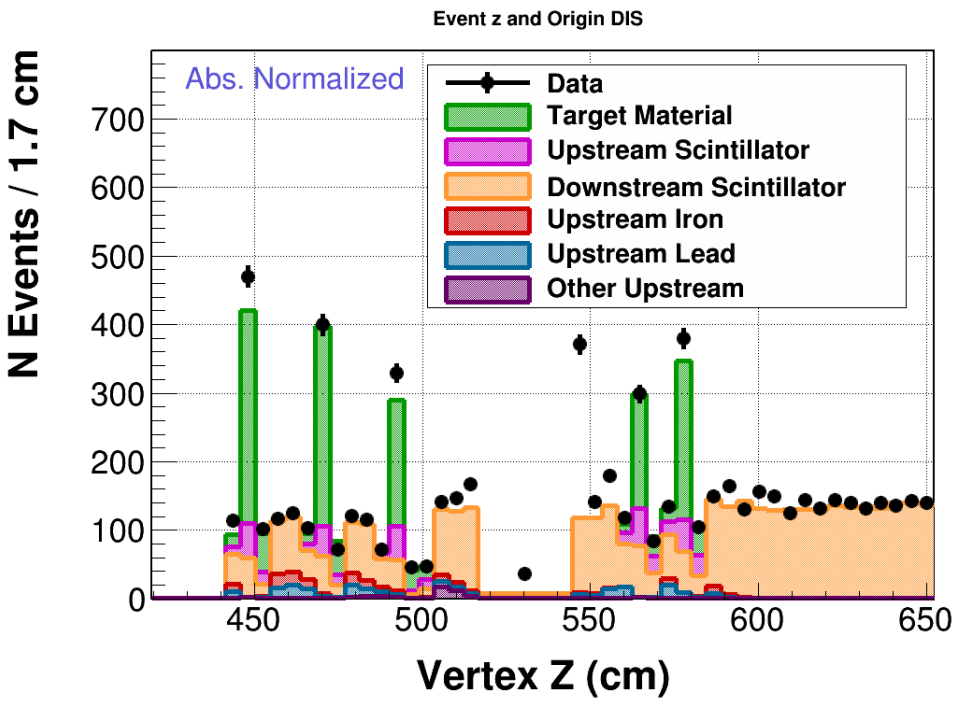

Figure 9-13. True event origin of all DIS events in the nuclear target region of MINERνA. The black points are data DIS events, and the two samples are absolutely normalized.

as a rock muon. These events cause concern, because the overlapping neutrino event or rock muon will be mis-characterized as hadronic energy by the reconstruction. These events therefore enter the sample as a background.

Table 9-4 presents the number of events tagged as "upstream" for the data events scanned per nuclei found in target 3.

A second hand scan of MC events was conducted after the data scan. The results of this scan are summarized in Table 9-5. The goals of this scan were to measure the consistency of the upstream mis-identification rate in data and MC by eye, as well as see if the overlapping event rate in MC was similar to data. In both cases, it is observed that the MC does a sufficient job of simulating z-vertex bias as well as the overlapping event rate. The MC scan consisted of 878 events in the same energy bins and nuclei as the data scan. The 878 events amounted to roughly $\frac{1}{3}$ of the total MC. Of the 878 Events:

- 49 Originated in an upstream target.

- 21 Originated in a downstream target.

- 70 were overlap events.

The rate of overlapping events in data and MC is found to be approximately 8%. Knowing this, it can be said with confidence that event overlaps which force non-DIS data events into the DIS region are well-covered by the simulation. The simulation of background events is, in addition, fit to the data using the sidebands described in Section 9. These sidebands are constructed to mimic DIS events selected by cutting on variables (Q^2, W) which are sensitive to the E_{had} of the event. As a result, the component of background due to overlapping events is strongly tied to the overlapping rate in data.

Table 9-6 shows the percentage of events tagged as upstream in data and MC, as well as the probability of the data having more events upstream than the MC based on Poisson probability. No significant differences from the data and MC are observed. In the

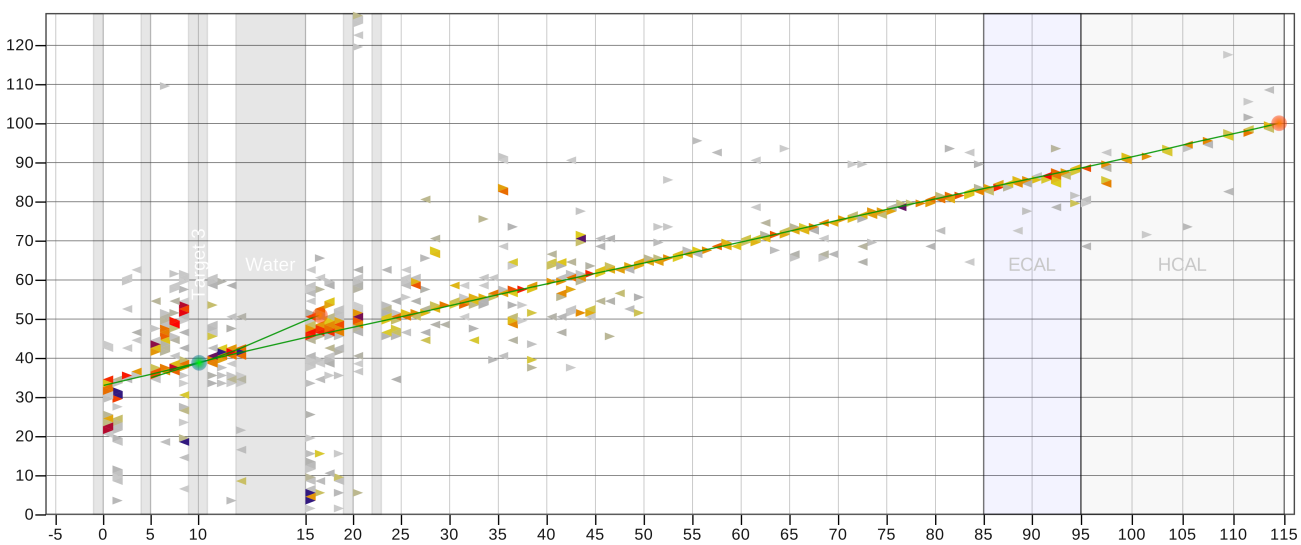

Figure 9-14. A candidate DIS event vertexed into targt 3, which clearly originated in target 2. In this case, two different tracks were built out of the single muon track, and the two tracks were used to fit the vertex (green dot). These types of events are vetoed in the data and MC in the DIS analysis by looking for energy along a line projected uptream of the muon track.

most severe case, carbon, there is a 92% chance that there are more upstream events in the data than in the MC. After completing updates to the reconstruction to look upstream of the vertex rather than the track, it was discovered the differences between the z-vertex in data and MC were not significant.

Table 9-4. The number of events tagged as originating in an upstream nuclear target (target 1 or 2) as decided by the data hand-scan.

	Total Events Scanned (data)	Upstream Events Tagged (data)	Percent Tagged
C	155	15	9.7%
Fe	307	14	4.5%
Pb	133	5	3.8%

Table 9-5. The number of events tagged as originating in an upstream nuclear target (target 1 or 2) as decided by the Monte Carlo hand-scan.

	Total Events Scanned (MC)	Upstream Events Tagged (MC)	Percent Tagged
C	237	15	6%
Fe	424	17	4%
Pb	217	17	8%

Table 9-6. Percent of events tagged as upstream in data and MC, along with the probability of the data having more upstream events than the MC based on Poisson statistics.

	Percent of Upstream Events Tagged (data)	Percent of Upstream Events Tagged (MC)	Poisson Probability
C	10%	6%	0.92
Fe	5%	4%	0.71
Pb	4%	8%	0.11

9.3.4 Upstream Energy Ratio

Recoil energy in the detector can broadly be classified into upstream and downstream energy. In this context, recoil energy is synonymous with hadronic energy, or all energy deposits in the detector not associated with the primary muon. Recoil energy is divided into upstream energy by counting the number of clusters upstream of the primary vertex according to the algorithm described in section 9.3.2. The downstream energy is defined as the total recoil energy minus the upstream energy.

The ratio of the upstream energy to downstream energy is measured in each event for the data and MC. This was done to see if the MC sufficiently modeled the energy upstream. Again, target 3 is heavily studied as this is the target with the largest amount of

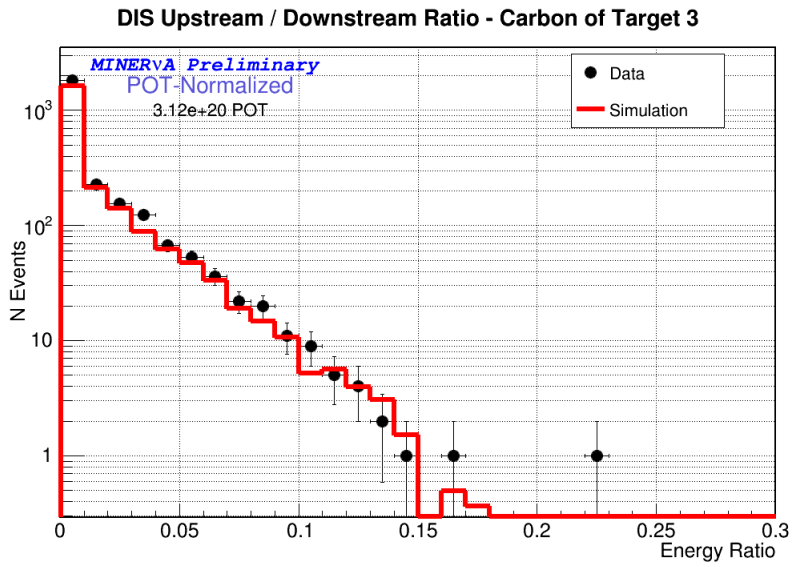

Figure 9-15. Ratio of up to downstream energy in data (black points) and simulation (red line) for the carbon of target 3. The error bars are statistical only.

upstream events originating in targets 2 and 1. This analysis is preformed prior to applying upstream energy cuts, so all DIS events are counted regardless of the amount of energy upstream in the event.

Figures 9-15 through 9-17 show the upstream energy ratio for data and MC. In each target, a large number of events contain no energy upstream of the vertex (ratio = 0). This is important, because events with 0 energy upstream will all pass the upstream energy cuts. Any event with an upstream ratio greater than 0 has some probability to be cut from the analysis, with a probability proportional to the ratio.

Initially, no significant differences are seen between the data and MC when the the ratio is greater than 0. This conclusion is more pronounced in Figures 9-18 through 9-19, which show the data / MC ratio of all nuclei in target 3. In the case of each nuclei, the ratio is roughly consistent with a difference in absolute normalization based on the $\chi^2_\nu \approx 1.0$ between the data and the fit to a constant. This indicates the shape of the upstream energy ratio is the approximately the same in data and MC.

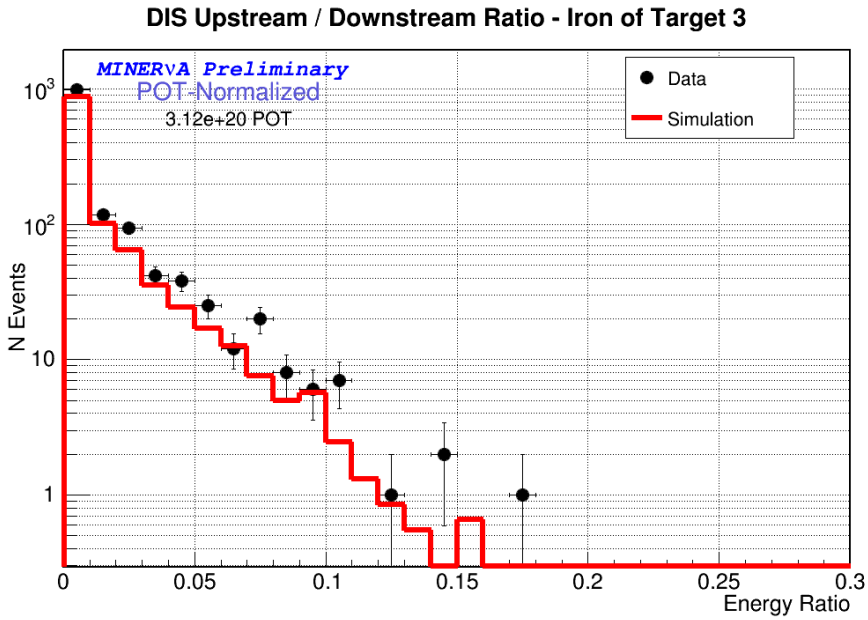

Figure 9-16. Ratio of up to downstream energy in data (black points) and simulation (red line) for the iron of target 3. The error bars are statistical only.

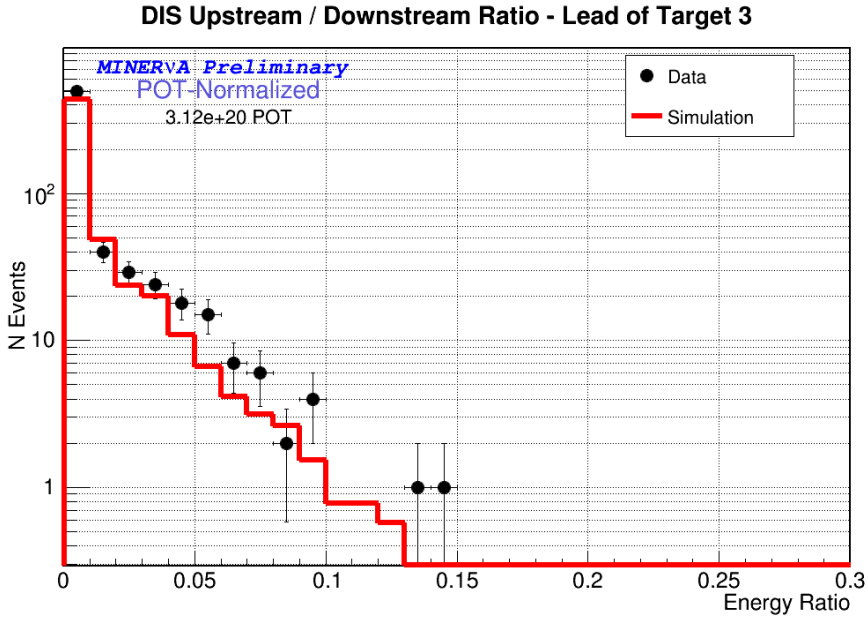

Figure 9-17. Ratio of up to downstream energy in data (black points) and simulation (red line) for the lead of target 3. The error bars are statistical only.

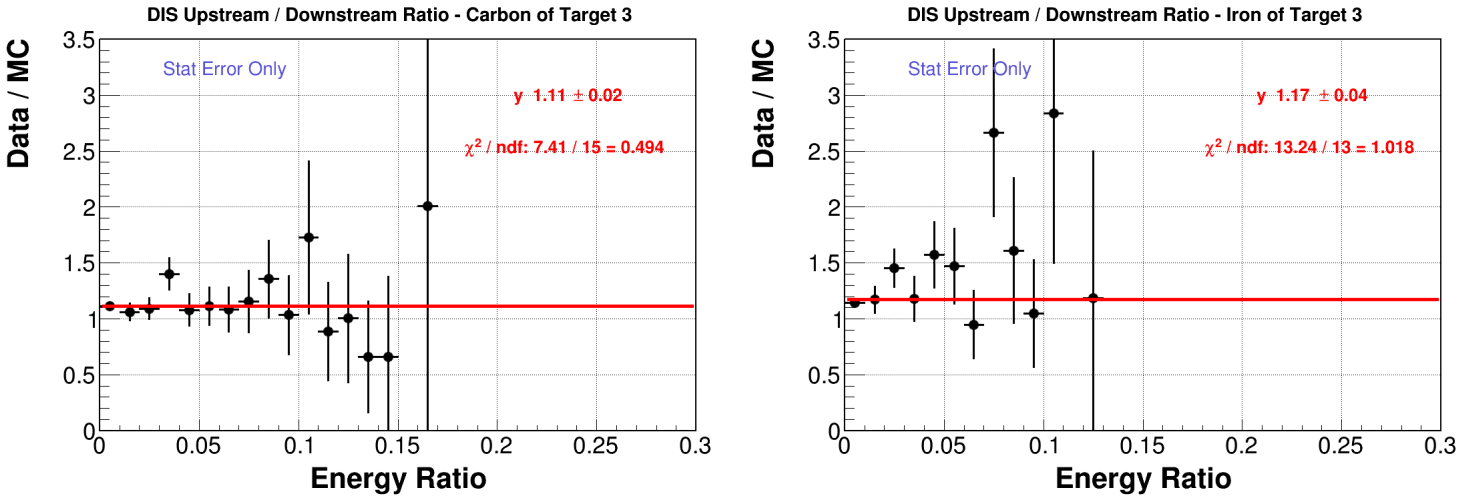

Figure 9-18. Data / MC ratio of up to downstream energy for the carbon of target 3 (left) and iron of target 3 (right). The ratio is fit to a constant factor printed in red on the plot. The error bars are statistical only.

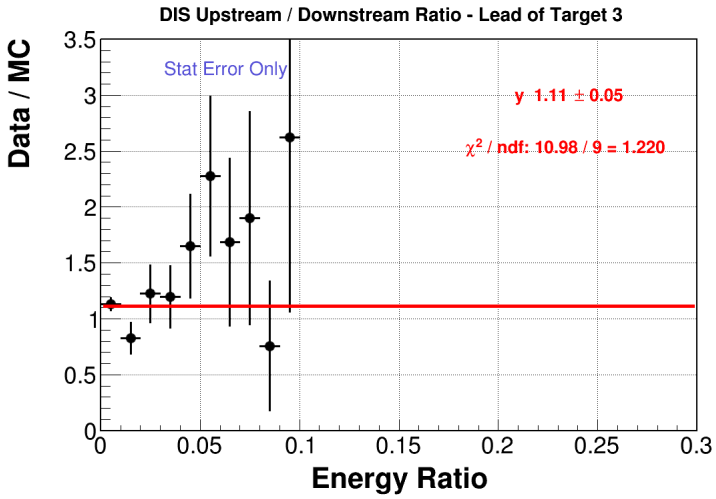

Figure 9-19. Data / MC ratio of up to downstream energy for the lead of target 3. The ratio is fit to a constant factor printed in red on the plot. The error bars are statistical only.

9.3.5 Results of Updated Upstream Energy Cuts

Figure 9-20 shows the true event origins of events reconstructed into the C of nuclear target 3 after updating the upstream energy cuts. Compared to Figure 9-12, the number of events that truly originate in upstream Fe and Pb were reduced by approximately a factor of 2 in the largest W bin. Integrated over the neutrino energy range of 5 to 50 GeV, there was about a 50% reduction of events mis-identified in upstream targets (see Tables 9-7 and 9-8).

Table 9-7. Location of DIS events truly occurring upstream of the Carbon of Target 3 broken down by target nucleus. Each cell is the percentage of total events that originated upstream. This table applies the default, inclusive era upstream energy cuts.

E_ν	% in CH	% in Fe	% in Pb
5 - 6	100 ± 0	0 ± 0	0 ± 0
6 - 8	71.2 ± 5.56	1.92 ± 1.68	26.9 ± 5.44
8 - 10	83.8 ± 2.79	3.28 ± 1.35	12.9 ± 2.54
10 - 15	76.6 ± 1.59	9.23 ± 1.09	14.2 ± 1.31
15 - 20	70.7 ± 1.68	13.3 ± 1.25	16 ± 1.35
20 - 25	65.9 ± 1.97	11.1 ± 1.31	23 ± 1.75
25 - 30	69.9 ± 2	9.72 ± 1.29	20.4 ± 1.76
30 - 40	66.3 ± 1.88	12.3 ± 1.31	21.3 ± 1.63
40 - 50	66.4 ± 2.27	11.8 ± 1.55	21.7 ± 1.98
50 - 100	63.9 ± 2.99	12.3 ± 2.04	23.8 ± 2.65
TOTAL	70.4 ± 0.735	10.8 ± 0.499	18.9 ± 0.63

Table 9-8. Location of DIS events truly occurring upstream of the Carbon of Target 3 broken down by target nucleus. Each cell is the percentage of total events that originated upstream. The updated upstream energy cuts have been applied.

E_ν	% in CH	% in Fe	% in Pb
5 - 10	91.3 ± 1.93	0.875 ± 0.638	7.84 ± 1.84
10 - 15	89.5 ± 1.31	5.21 ± 0.946	5.33 ± 0.956
15 - 20	89.2 ± 1.35	4.29 ± 0.88	6.51 ± 1.07
20 - 25	85.5 ± 1.71	4.48 ± 1	10 ± 1.46
25 - 30	85.6 ± 2	5.06 ± 1.25	9.36 ± 1.66
30 - 40	81.2 ± 1.95	7.57 ± 1.32	11.2 ± 1.57
40 - 50	84.9 ± 2.26	4.78 ± 1.35	10.3 ± 1.92
TOTAL	86.8 ± 0.653	4.86 ± 0.416	8.31 ± 0.533

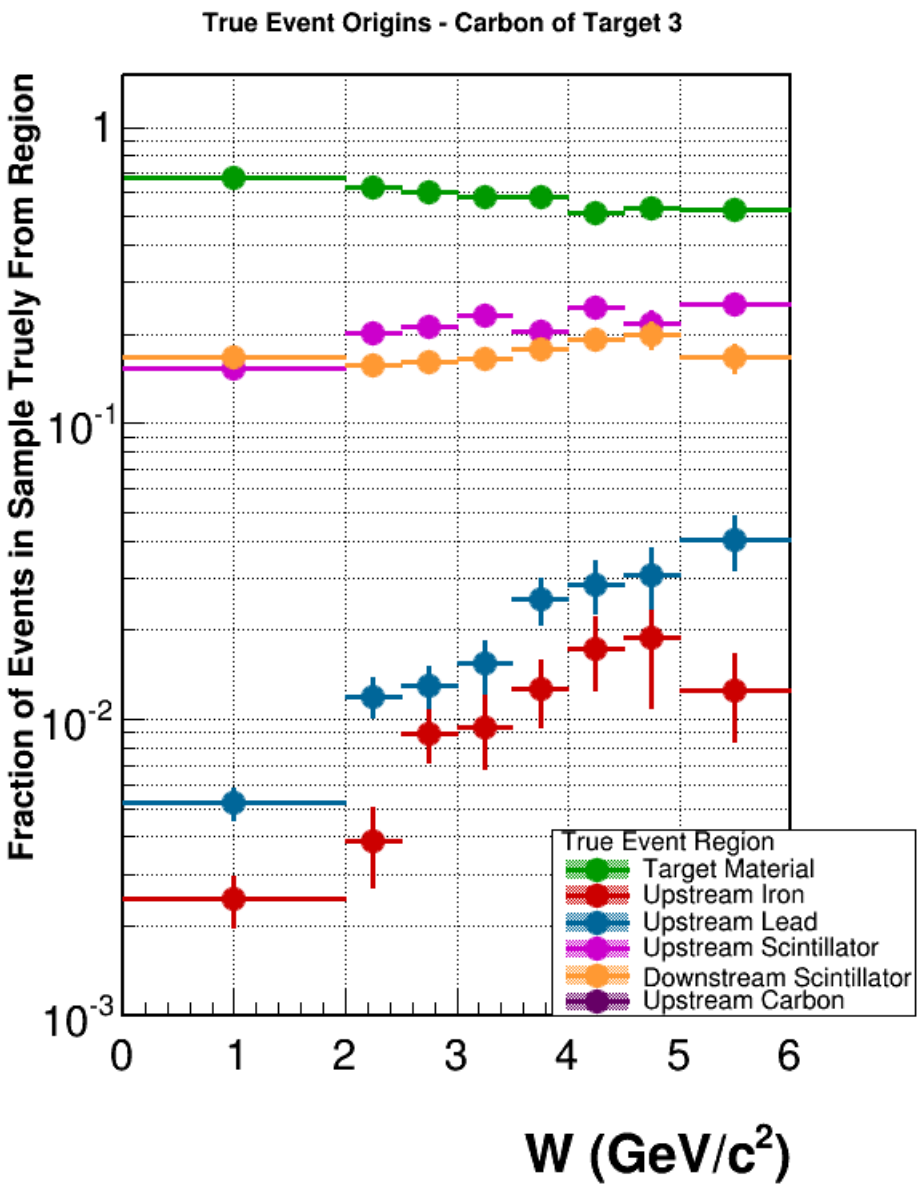

Figure 9-20. True event origins of inclusive events reconstructed in the Carbon of target 3 vs.reconstructed W. These events have the updated upstream cuts applied, which are re-tuned for the DIS analysis.

Finally, the predicted plastic background of the Carbon of target 3 is shown before and after updating the upstream cuts in Figure 9-21. The ratio of true to predicted background of the MC is greatly improved by the updated cuts. Whereas previously a drop in predicted background was observed as W increased, the updated cuts create a reasonably flat prediction in W. After applying the updated upstream energy cuts, the plastic background was accurately predicted in all targets at the 10% level.

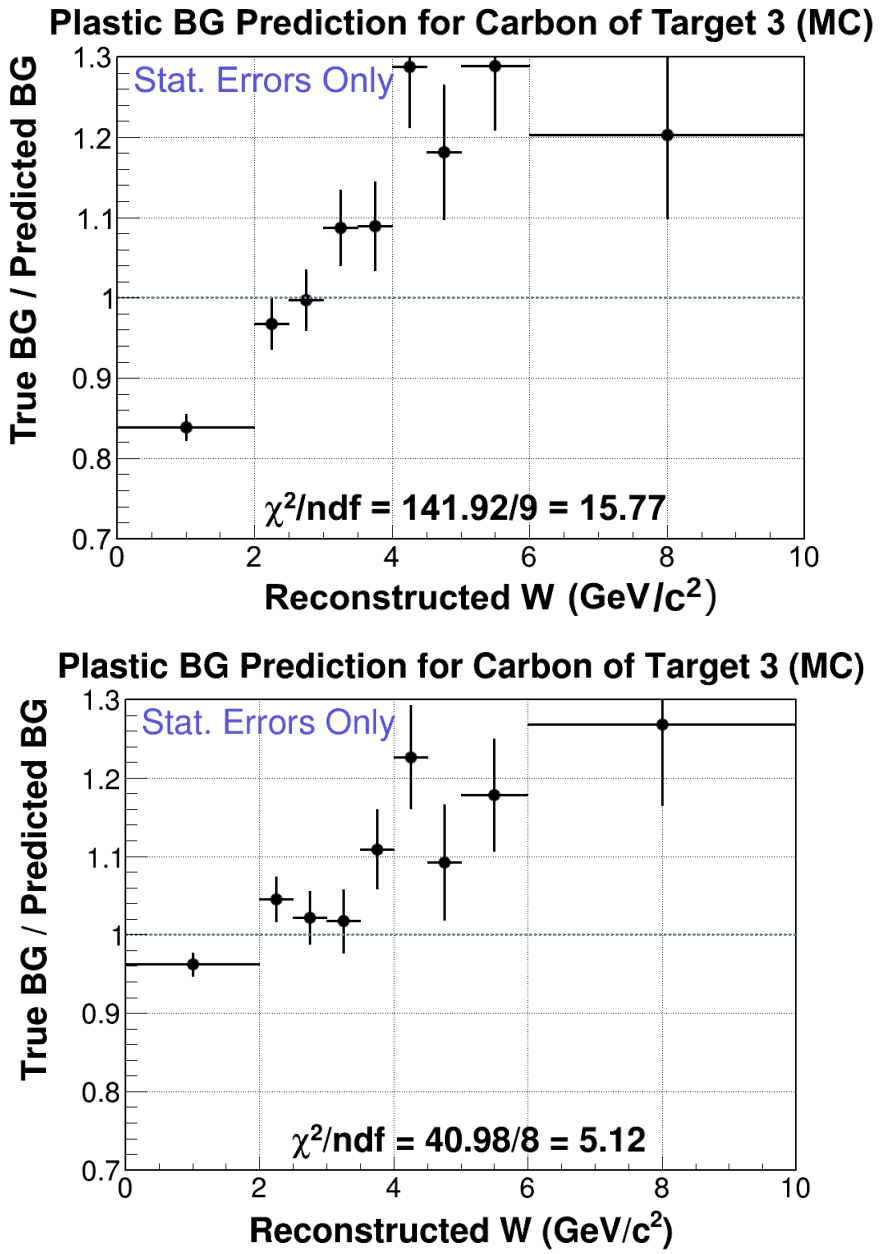

Figure 9-21. The true plastic BG / the predicted plastic background before tuning the upstream cuts (top) and after (bottom) as a function of reconstructed W.

CHAPTER 10
SYSTEMATIC UNCERTAINTIES

Systematic uncertainties reflect imperfect knowledge of assumptions that go into the cross section measurement, or inaccuracies in the manner the detector selects events. Statistical uncertainties, by contrast, are due to stochastic variations of observables over time. The DIS analysis assigns a systematic uncertainty to the predicted MC, however all systematics assigned to the MC are equally valid for the data. Statistical uncertainties are assigned to the data. The statistical uncertainty on the MC is ignored in most cases. The MC generation is large enough such that the MC statistical error is smalled compared to that of the data.

10.1 Calculating Systematic Uncertainties

The DIS analysis uses the standard MINERνA method of computing the systematic uncertainty on the distribution of any parameter x. The underlying parameters which made up the distribution were varied n times according to the 1σ variation of all of the parameters. n varied from 1 to 100, depending on the parameter in question. The n resulting distributions of x were then measured, and the spread of these distributions was then taken to be the uncertainty on x, δx. The total uncertainty was composed off the sum of all of the separate parameters taking the correlations between parameters into account when appropriate.

Plots of the uncertainties at many stages of the analysis made be found in Appendices B, C.3, E.2, E.4, F.2 and G.2. The remainder of this section is a discussion on how the various components of those uncertainties were calculated.

10.2 GENIE Uncertainties

10.2.1 Rewightable GENIE Uncertainties

The GENIE systematic reflects the uncertainties inherit to the models GENIE uses to calculate cross-sections. These uncertainties are calculated via reweighing. Two different universes are calculated using the two different pre-calculated GENIE weights which

correspond to the positive and negative σ variations in question. The spread of the two universes is the uncertainty. Details of how the GENIE weights were calculated may be found in [85]. Each GENIE knob is varied separately when calculating the uncertainty.

GENIE systematic uncertainties are evaluated on the efficiency, as well as the CH and non-DIS background events. The reconstructed signal events are not assigned a GENIE uncertainty.

10.2.2 GENIE FSI Uncertainties

FSI uncertainties originate from the final state interaction model GENIE uses after cross section calculation to transport intermediate particles through the nucleus. The FSI uncertainties are likewise calculated using re-weighting. An event is re-weighted depending on the "fate" of the particle for each step along its' mean free path through the nucleus. A brief description of the operation of GENIE'S FSI model may be found in [85].

10.2.3 Non-Rewightable GENIE Uncertainties

Certain aspects on the uncertainty of the hadronization model in GENIE are not expressible as a reweighting. In these cases, a separate generation of GENIE is necessary to evaluate the systematic uncertainties on the model. The inclusive analysis is preformed on the regenerated samples between an E_{had} of 2 and 20 GeV (see Appendix E.1). Most of the DIS events fall into this energy range, and updating this calculation to include the high energy tail is expected to have very little effect. Deriving the uncertainty involves measuring the shifted sample, and then calculating the ratio of the shifted sample to the default GENIE model in each bin of E_{had} [82]. This ratio is taken as the $\pm 1\sigma$ uncertainty. This systematic was evaluated independently for the passive and faux targets.

The alternate GENIE samples included:

- Varying Birk's parameter (Birks).
- Changing the effective radius of the interacting nucleus (ENuc).
- Altering the formation length of hadrons (hadronization).

- An alternate tuning of the hadronization model GENIE uses to simulate intermediate energy hadron showers, AGKY.

10.3 Flux

The flux error is computed by varying the underlying flux model and generating the standard 100 different flux weights for beam focusing, tertiary hadron production, and NA49 uncertainties. These weights were combined into one weight / uncertainty, because the final ratio analysis does not have a large flux uncertainty. The ratio does have a tiny dependence due to the different energy spectra seen by the different nuclear targets.

Unlike many analyses, the nuclear target DIS analysis assigns a flux uncertainty to the yield of events in each bin. This is done primarily for historical reasons. The inclusive framework the DIS analysis inherits assigns flux uncertainties to the event yield. The early days of MINERνA used inclusive analyses as a cross-check on detector calibrations and reconstruction algorithms. Hence, it was very valuable to draw the systematic uncertainty of the flux on distributions of events to see if the differences seen in normalization could be attributed to the flux model.

As the primary result of the DIS analysis is cross section ratios where the flux largely cancels, the flux uncertainty remains on distributions of event yields. This holds for the reconstructed and unfolded distributions. Dividing by the flux to calculate absolute cross sections as described in Chapter 13 thus incurs no additional uncertainty, and the uncertainties on the absolute cross section are similar to those on the event yields as a function of unfolded variables. There are small differences between the two uncertainties due to the efficiency correction.

10.4 Absolute Normalization

Uncertainty on the absolute normalization arises from the uncertainty on the detector mass, POT counting, MINOS, and MINERνA tracking efficiency. This uncertainty was unchanged from the inclusive analysis. Details of these uncertainties may

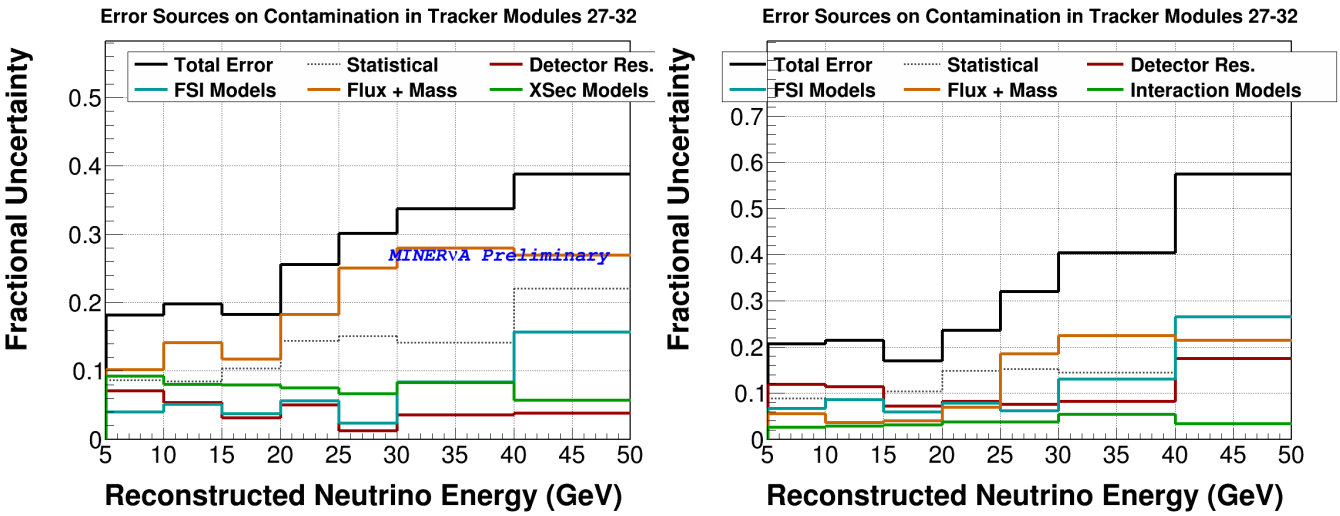

Figure 10-1. Uncertainty on the non-DIS event prediction before data tuning (left) and after data tuning (right). The majority of the improvement is below 20 GeV, where the data sidebands are well populated.

be found in [82]. Primary protons from the NuMI beam are counted using magnetic toroids, and the accuracy of this measurement is about 1%.

10.5 Non-DIS Background Subtraction

The systematic error evaluated for the non-DIS background tuning is derived by re-running the fits to the sidebands in each different universe. In the case of GENIE and FSI errors, each universe corresponds to one positive or negative knob twist of one of GENIE's reweightable parameters. In the case of flux errors, each universe corresponds to one of the shifted flux universes. The weight derived for each universe is applied to the two different sidebands described in Section 9. After applying the weights, the fit is re-run over the same data set and MC templates. In the end, a set of fit values are derived for each universe and each variation.

At the creation of each distribution of the predicted non-DIS events, each universe which made up the systematic error was scaled by the scale factor derived for that universe. In this way, each shifted universe (and the CV) of the non-DIS events is pinned to the data in some way. This procedure reduced systematic errors considerably (see Figure 10-1).

10.6 Plastic Background Subtraction

The systematic errors calculated for the non-DIS background are also calculated for the plastic background estimate. These included the same GENIE, flux and detector resolution errors previously described. Plots of the systematic uncertainty of the extracted plastic background may be found in Appendix C.3.

The accuracy of the plastic background subtraction is fundamentally limited by the statistics of the true DIS plastic background. This is because the subtraction procedure used the number of true plastic background events in the denominator of the area normalization (see Equation 9-8 in Section 9.2). The largest error on the plastic background subtraction is statistical.

The full statistical plus systematic error band does not cover the differences between the true and extrapolated CH background for some targets. As a result, an additional systematic error is added to account for the difference. This error consists of adding additional error to each E_ν and x_{bj} bin until the $\chi^2_\nu \leq 1$ for the difference between true and extrapolated MC background. In order to properly account for the anti-correlations between bins, the added uncertainty is assigned a sign based on the difference between the extrapolated and true background. In bins where the background is *overpredicted* (extrapolated - true > 0), the universe is given a positive $(+)$ weight. Bins where the background is *underpredicted* are in contrast assigned a negative $(-)$ weight. In practice, this procedure converges very quickly as the χ^2 between the true and extrapolated CH background is often small for the non-DIS subtracted case.

10.7 Detector Resolution

Uncertainties in the detector's reconstruction of E_μ, θ_μ and E_{had} lead to uncertainties on derived quantities (Q^2, W, etc.), as well as an uncertainty on the number of DIS events reconstructed. The detector resolution uncertainties use the same multiverse method as the flux uncertainties, however the number of universes used was only 60 instead of 100, since the expected excursions in each universe is smaller than expected for the flux

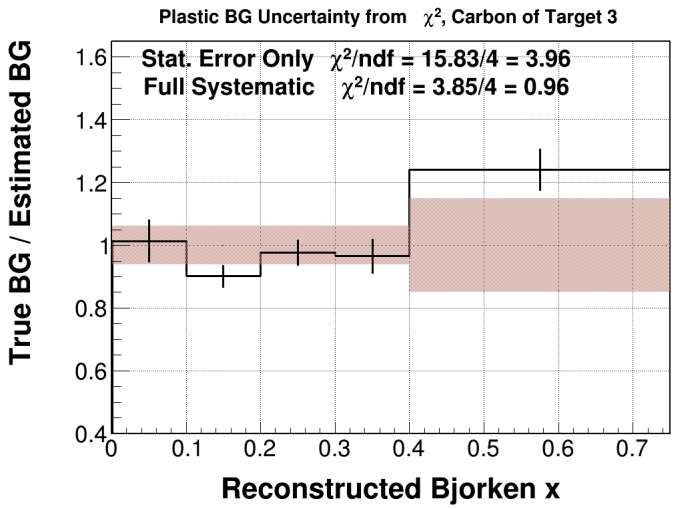

Figure 10-2. Ratio of estimated to true CH background for DIS events in the Carbon of target 3 as a function of Bjorken-x, as measured in the MC. The red band represents the additional systematic uncertainty assigned.

model. In addition, weights are not calculated for detector resolution uncertainties. Instead, each basic quantity E_μ, θ_μ and E_{had} is shifted individually according to a Gaussian random number with variance equal to the 1 σ variance of the variable in question. All the derived quantities are then re-calculated. The RMS of all shifted quantities is taken as the uncertainty.

Shifts in the derived quantities Q^2, W, and E_ν may cause an event to smear into or out of the selected DIS sample. To account for this, all CC events are initially considered part of the detector resolution error band. If the event passed the DIS cuts based on the central value universe or any of the 60 universes with a shifted Q^2, W, E_ν and θ_μ, the universe is added to the resolution band. In contrast, an event was considered as DIS in the central value universe but not in in a shifted universe is skipped when calculating the error band.

The x, y vertexing algorithm of the reconstruction is accurate to the 1 mm level, and no additional uncertainty is assigned. The z vertexing however, has a resolution of approximately 1 cm [82]. To evaluate the effect of this resolution, the analysis was re-run

by smearing the z vertex according to a Gaussian random number with a $\sigma = 1.0$. This smearing changes the number of events reconstructed in each nuclear target. The interquartile spread of this event distribution is taken as the 1σ uncertainty for each target and material combination.

CHAPTER 11
RECONSTRUCTED AND UNFOLDED EVENT YIELDS

After subtracting the backgrounds according to the methods in Chapter 9, the numerator of Equation 7-1 is almost completely known:

$$\sigma_i = \frac{U_{ij}\,(d_j - b_j)}{\Delta_i\,\epsilon_i\,\Phi_i\,N}. \tag{11-1}$$

The difference $(d_j - b_j)$ is the number of true DIS events in each E_ν and x_{bj} bin i in each nucleus A. Plots of the event yields are described in Section 11.2.

The final necessary piece of the numerator before calculating a cross-section is the unsmearing matrix U_{ij}. U_{ij} is needed to transform events from the reconstructed j bin to their true origin bin i. This process is referred to as *unfolding* and is explained in this chapter.

11.1 Unfolding

Physical quantities reconstructed and computed by the detector and reconstruction are offset form their true values due to imperfect reconstruction and detection. That is, the true value of a quantity x_i in bin i truly originated from bin j. The two quantities (measured and true) are related by the smearing matrix M_{ij}:

$$x_i = M_{ij} x_j. \tag{11-2}$$

M_{ij} is computed from the MC separately for each target. The goal of unfolding is to find the inverse of the smearing matrix, the unsmearing matrix, such that:

$$x_j = M_{ji}^{-1} x_i. \tag{11-3}$$

Smearing matrices are often times not directly invertible. In addition, directly inverting smearing matrices introduces a significant amount of model dependence into the measurement. As a result, the DIS analysis decided to use Bayesian unfolding. This

unfolding technique is described in Ref [86]. The two variables selected for unfolding were neutrino energy E_ν and Bjorken-x x_{bj}.

11.1.1 Unfolding Procedure

The smearing matrices of each target and material combination are constructed from the reconstructed and generated x_{bj} and E_ν. Each event in the smearing matrix passed all reconstruction cuts, as well as the true DIS and true material cuts. In general, the measured migrations are similar from target to target (see Figure 11-1 and 11-2). The reconstructed data from each target combination is then unfolded using the MinervaUnfold package with Bayseian unfolding. The number of unfolded iterations was tuned using fake data studies described in section 11.1.2.

11.1.2 Unfolding Tunning

A fake data study is used to tune the number of unfolding iterations, as well as to monitor any biases that may occur in unfolding. This study re-weights the non-DIS background data tuned MC, and uses the standard smearing matrices. Fake data is generated by re-weighting the MC according to a re-weighting function $f(x_{bj})$, which mimics the data / MC ratio in each bin. $f(x_{bj})$ is a smooth function, computed from a 3rd degree polynomial fit to the data / MC ratio in x_{bj} of the carbon of nuclear target 3. The choice of a 3rd degree polynomial is based on the shape of the data and MC in Figure 11-3. A 3rd degree polynomial is the least complicated function possible to approximate the shape ratio. In order to further understand the bias, 500 universes of fake data are generated, where each universe is generated by setting the number of events in each bin to a random integer generated from a Poisson distribution with a mean equal to the re-weighted value. The number of universe is set such that reasonable distributions of universes could be generated, keeping computing speed and power in mind.

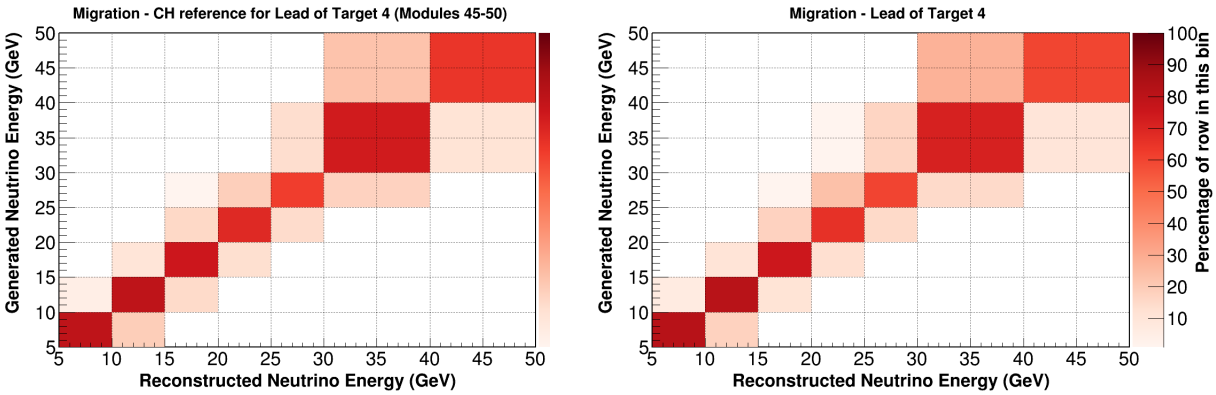

Figure 11-1. Neutrino energy migration for tracker modules 45 - 50 (left) and target 4 (right). The y-axis is generated E_ν and the x-axis is reconstructed E_ν. Each cell records the percent of true and reconstructed DIS events.

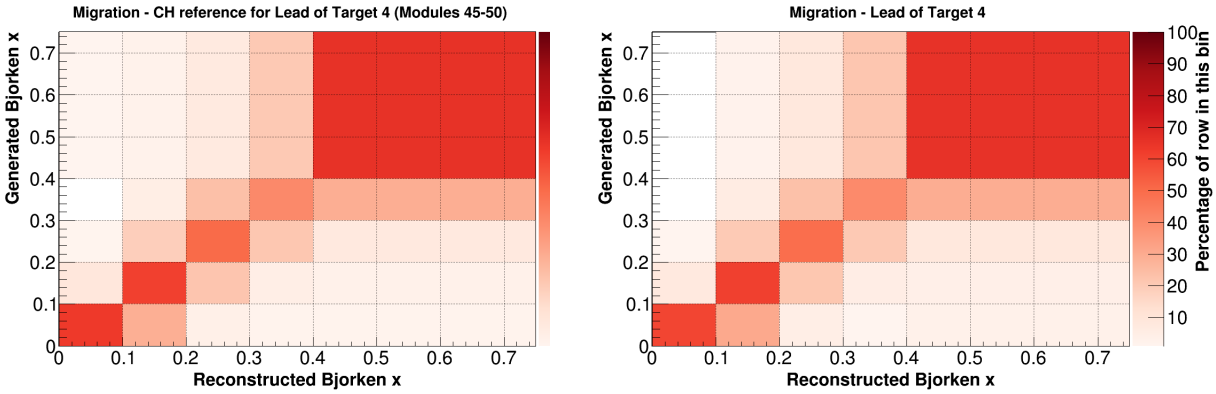

Figure 11-2. Bjorken-x migration for tracker modules 45 - 50 (left) and target 4 (right). The y-axis is generated x_{bj} and the x-axis is reconstructed x_{bj}. Each cell records the percent of true and reconstructed DIS events.

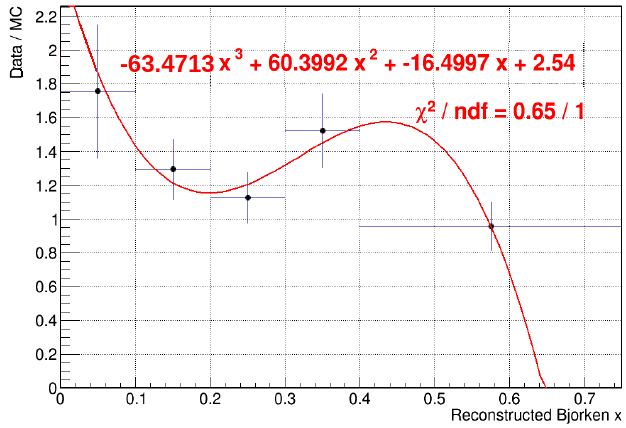

Figure 11-3. Data to MC ratio of DIS events in the carbon of target 3, as a function of Bjorken-x. The red line is a fit to a third-degree polynomial used to reweight the MC for fake data studies with unfodling. The error bars are statistical only.

An important note is the unfolding study presented in this section used a slightly different Monte Carlo sample from the main analysis. A bug in the way the nuclear target ntuples were merged and split resulted in a loss of approximately 17% of the passive target events [87]. This unfolding study was preformed before this bug was repaired. The study was partially repeated with the full MC sample, however the conclusions did not change.

Figure 11-4 shows an example of this procedure. The blue dots are the means of the fake data universes after 1 iteration of unfolding, the dashed lines are each universe, and the red line is the truth value of the MC re-weighted according to the data / MC ratio. Each MC universe, and the truth MC are scaled to data-size statistics.

The analysis generates 500 universes of fake data, and unfolds the fake data using 0 to 6 iterations. For each iteration, the difference between the mean unfolded and true number of events is calculated.

11.1.2.1 Unfolding With Predicted Backgrounds

In the initial unfolding study, the MC sample which forms a basis of the fake data contains events passing the reconstructed DIS cuts with the *predicted* non-DIS and CH events subtracted off using the procedures described in Sections 9 and 9.2. This study

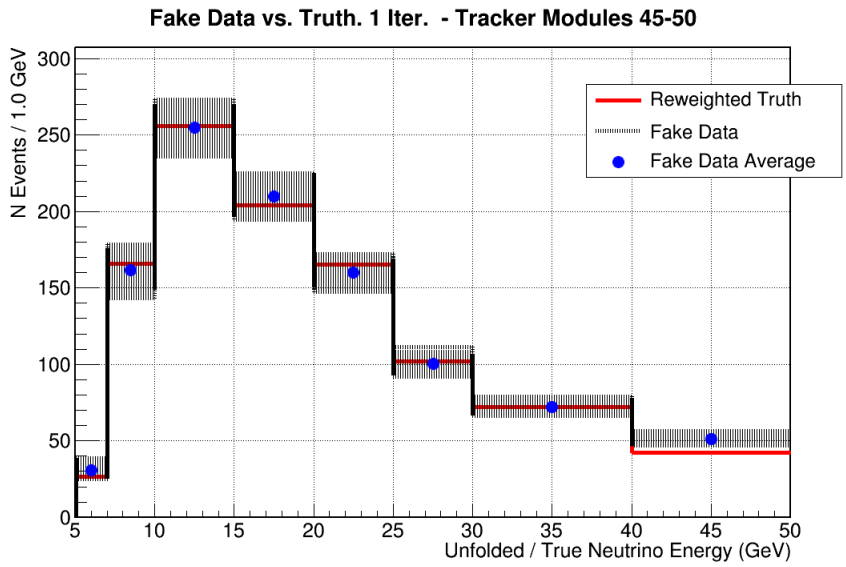

Figure 11-4. Illustration of the fake data used for unfolding. Each dashed line is an unfolded fake data universe, and the blue dots are the unfolded mean of the fake data universes.

attempts to emulate the unfolding of actual data as closely as possible, and so subtracts the background identically according to equation 9-5 in section 9:

$$T_N = (S_N - C_N) - (CH_r - CH_{bg}). \tag{11-4}$$

Figure 11-5 and 11-6 show the results of this unfolding study using MC originating in tracker modules 45 - 50. Since this study uses tracker events from the MC as input, no CH background is subtracted. Differences between the true and unfolded mean in this case are due to the changes in the DIS backgrounds created from the data tuning, as well as the underlying MC biasing the unfolding.

In the case of E_ν (Figure 11-5), 1 iteration seems sufficient to remove all biases from the MC. Similarly, x_{bj} (Figure 11-6), requires only one iteration to minimize the bias in the majority of the bins. It should be noted that some bins show pathological behavior, primarily the largest x_{bj} bin 6. In the case of x_{bj}, this bin is all events with $x_{bj} > 0.75$ which contains a tiny number of events. These low statistics cause pathologies in the unfolding.

The unfolding study is repeated on the C of target 3. Unlike tracker modules 45 - 50, the C sample contains wrong nuclei background events from the surrounding scintillator modules. This scintillator background is subtracted prior to unfolding the fake data in an attempt to measure the unfolding's performance on actual data.

Immediately based on Figure 11-7 there appear to be biases in the unfolded sample not related to the unfolding. This is evident by the fact that this bias does not change with the number of iterations, it is fairly flat for a given bin, for example bin 12. In any case, the minimization of the bias occurs at 1 iteration as was seen with the tracker modules. This fact is further emphasized in Figure 11-8. The unfolding in x_{bj} shows a greater excursion from the true MC value, especially in the largest x_{bj} bin where the migration is the most severe and the plastic background subtraction is least accurate. Again it is found that one iteration of unfolding is optimal, especially considering the divergences seen in bin $0.4 \leq x_{bj} < 0.75$ after 1 iteration.

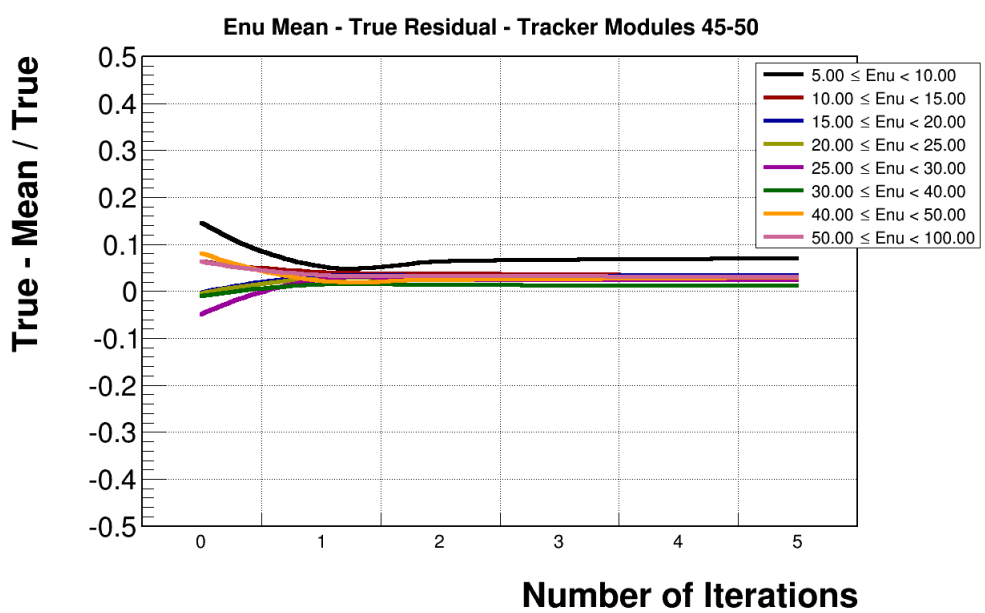

Figure 11-5. (True - Unfolded Mean) / True of each E_ν bin as a function of N iterations. The predicted non-DIS events have been subtracted from the unfolded events.

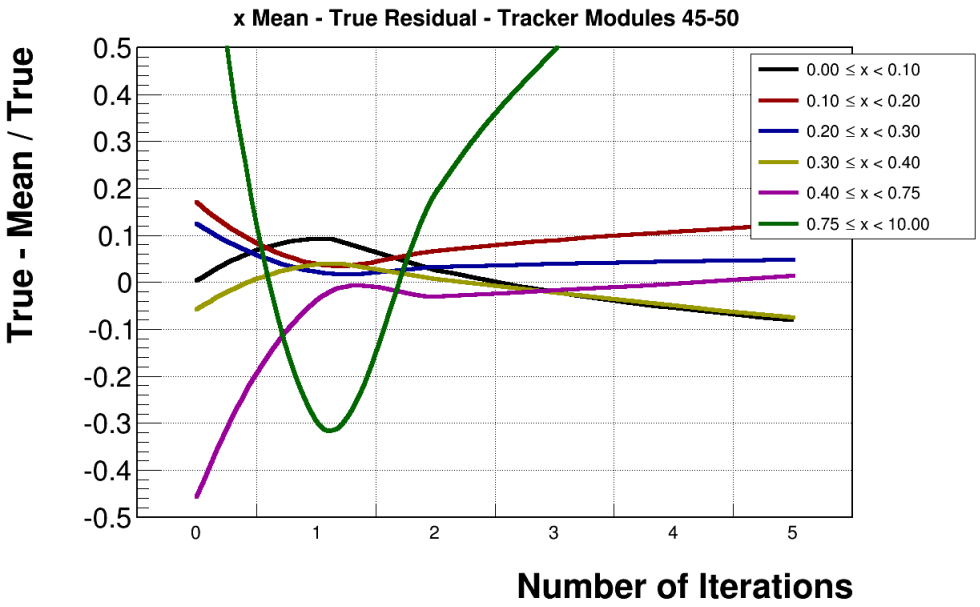

Figure 11-6. (True - Unfolded Mean) / True of each x_{bj} bin as a function of N iterations. The predicted non-DIS events have been subtracted from the unfolded events.

11.1.2.2 Unfolding True DIS Events

Since the results of the unfolding post background subtraction seem heavily biased, the study was repeated only bypassing the background subtraction steps and instead unfolding the *true* DIS events in the *true* material; only binned in reconstructed kinematics. The smearing function used for this study is identical to that of the previous study.

In this case, the unfolding shows practically no bias as can be seen in Figure 11-9, which shows the E_ν residual for tracker modules 45 - 50. Greater deviations are seen in unfolding x_{bj}, as shown in Figure 11-10. This is expected since the migration matrix for x_{bj} is less diagonal, and thus more difficult to unfold. None of these deviations is greater than 10% after one iteration.

There is significant improvement in the unfolding of the C of target 3 after bypassing the background subtraction. Comparing Figure 11-7 to 11-11 shows a dramatic decrease in the bias from $\approx 10\%$ to the few percent level. A similar effect can be seen in Figure 11-8 to

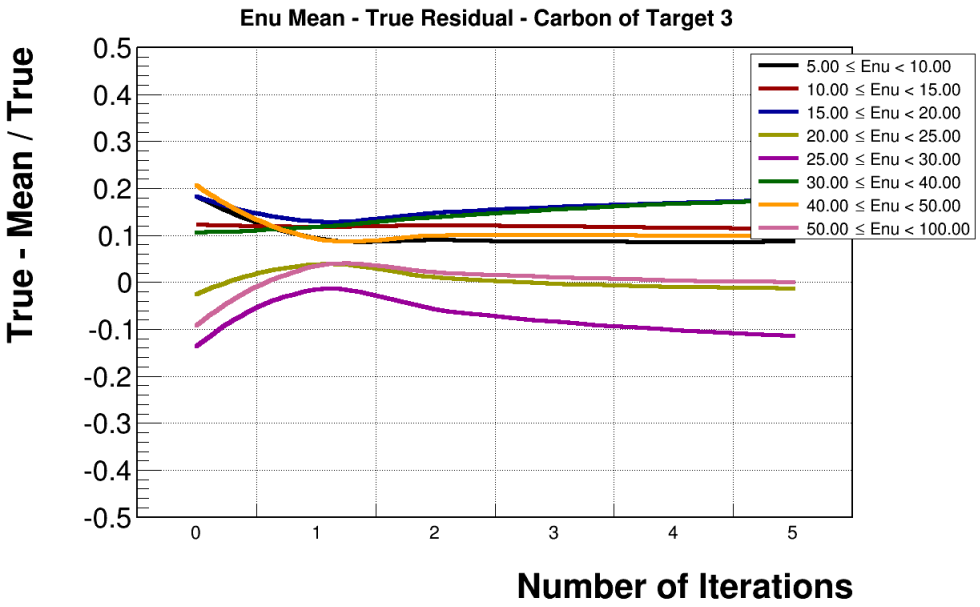

Figure 11-7. (True - Unfolded Mean) / True of each E_ν bin as a function of N iterations. The predicted CH and non-DIS events have been subtracted from the unfolded events.

Figure 11-12 where again the unfolding bias shrinks to the few percent level. In both cases, one iteration still appears sufficient to remove any existing bias between the samples.

11.1.2.3 Summary

It is found that 1 iteration is sufficient to unfold the reconstructed E_ν and x_{bj} for both the carbon of target 3 and tracker modules 45 -50. Since the migration matrix between the various targets is similar and never differs by more than 5% in a given bin, these conclusions hold for all of the target combinations used in the analysis. 1 iteration is used to unfold the E_ν and x_{bj} regardless of target.

Even after 1 iteration, biases are found when attempting to unfold the background subtracted sample. These biases by and large disappear when the true DIS and true nuclei sample are unfolded. The conclusion is the differences seen in the true and unfolded sample are due to imperfections and inconsistencies in the background subtraction methods, and NOT the unfolding machinery. As both of these background predictions are tuned to data, it is not expected that they will affect the unfolding.

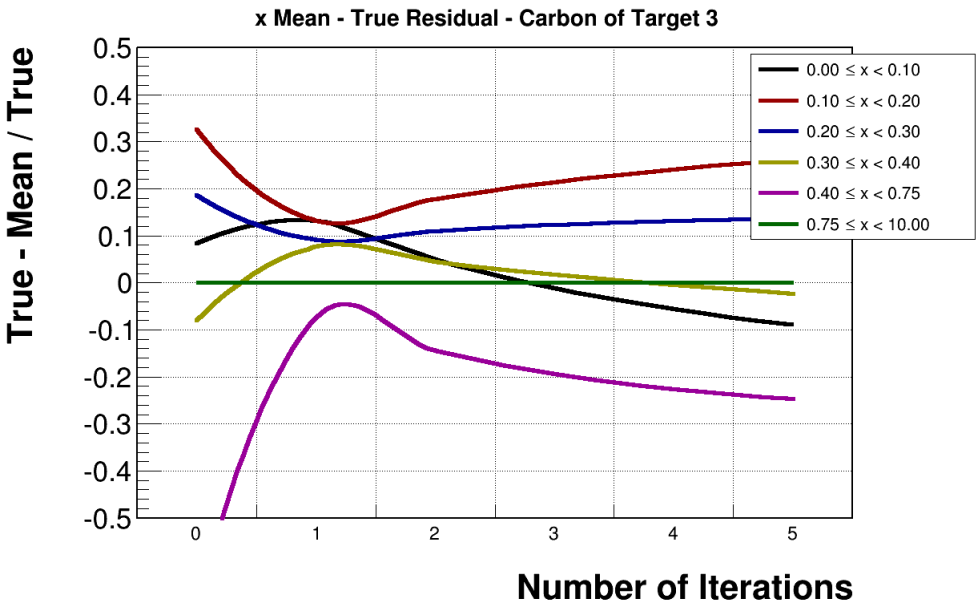

Figure 11-8. (True - Unfolded Mean) / True of each x_{bj} bin as a function of N iterations. The predicted CH and non-DIS events have been subtracted from the unfolded events.

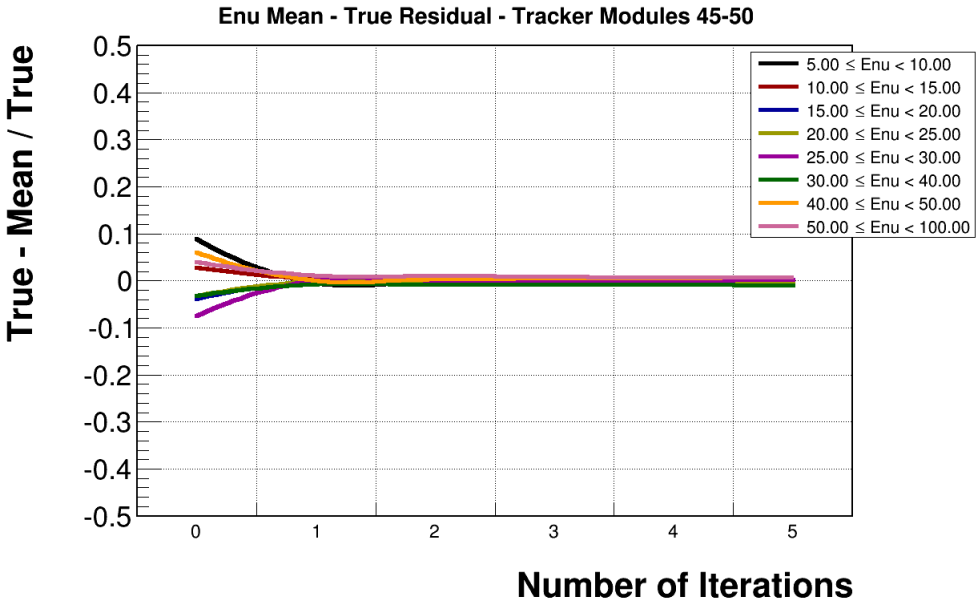

Figure 11-9. (True - Unfolded Mean) / True of each E_ν bin as a function of N iterations. The unfolded sample is *true* DIS events truly occuring in tracker modules 45 - 50, expressed in recostructed kinematics prior to warping and unfolding.

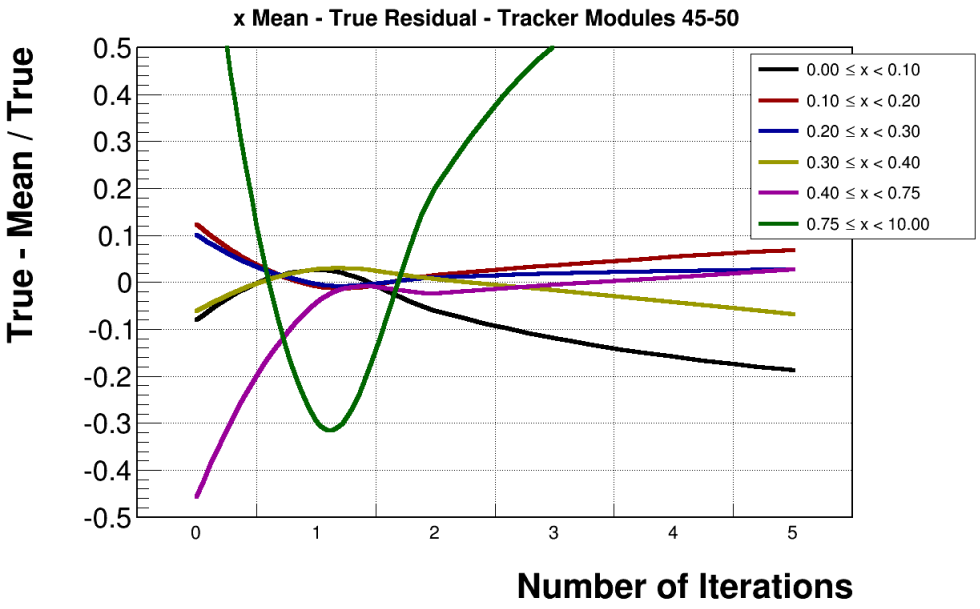

Figure 11-10. (True - Unfolded Mean) / True of each x_{bj} bin as a function of N iterations. The unfolded sample is *true* DIS events truly occuring in tracker modules 45 - 50, expressed in recostructed kinematics prior to warping and unfolding.

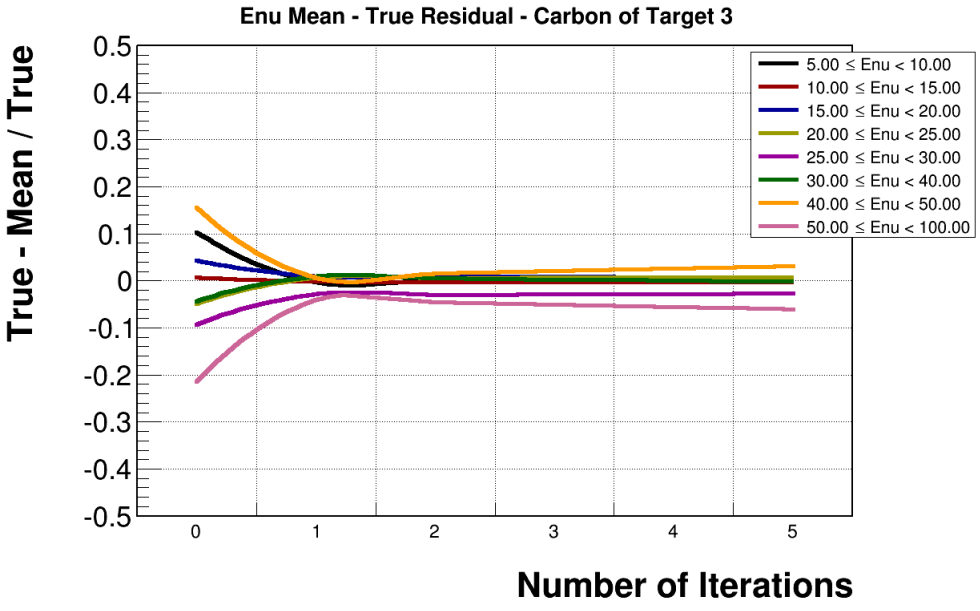

Figure 11-11. (True - Unfolded Mean) / True of each E_ν bin as a function of N iterations. The unfolded sample is *true* DIS events truly occuring in C of target 3, expressed in recostructed kinematics prior to warping and unfolding.

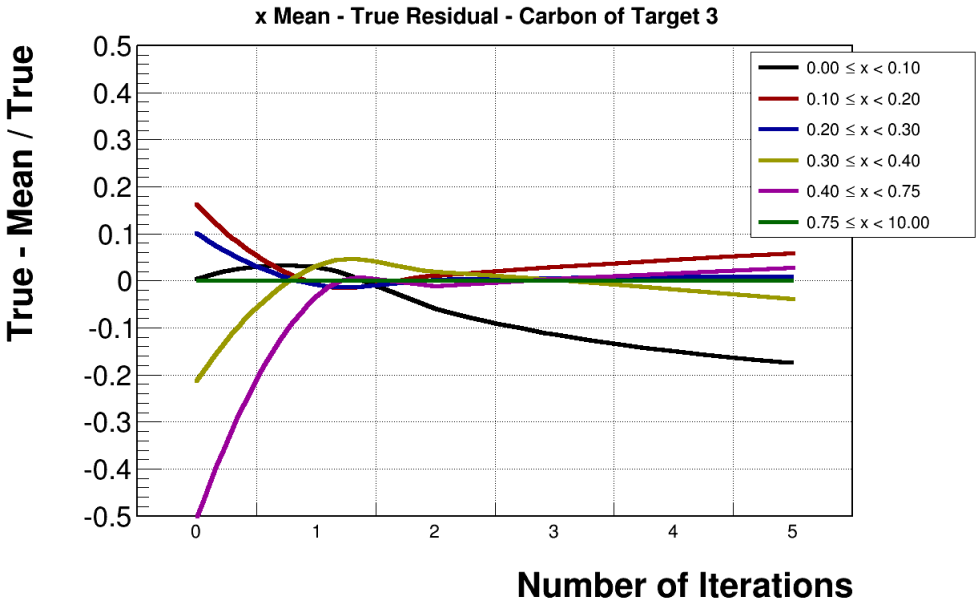

Figure 11-12. (True - Unfolded Mean) / True of each x_{bj} bin as a function of N iterations. The unfolded sample is *true* DIS events truly occuring in C of target 3, expressed in recostructed kinematics prior to warping and unfolding.

11.2 Event Yields per Nuclei

After finalizing all event selection cuts, the background estimations (CH and non-DIS), and unfolding, the analysis measures the number of DIS events per E_ν and x_{bj} for the nuclei C, CH, Fe and Pb. The targets are summed material-by-material prior to making these plots. The carbon presented originates from nuclear target 3, the iron from nuclear targets 1, 2, 3, 5, the lead from nuclear targets 1, 2, 3, 4 and 5, and the CH from tracker modules 26 through 80.

11.2.1 Reconstructed Kinematics

Figures 11-13 through 11-16 show the DIS events for C, CH, Fe and Pb vs reconstructed neutrino energy along with the extracted CH background. In each case, the non-DIS events have been subtracted using the procedure described in Section 9. In the case of CH, Figure 11-16, no CH background is subtracted.

Figures 11-17 through 11-20 show the same information, only now as a function of reconstructed Bjorken-x. In the case of CH, Figure 11-20, no CH background is subtracted.

For each nuclei C, Fe and Pb, the extracted CH is subtracted using a MINERνA specific method [88], which propagates the uncertainties by subtracting each universe of each error band. The result of the subtraction is a distribution in reconstructed x_{bj} and E_ν for each nuclei. These are plotted in Figures 11-21 through 11-26.

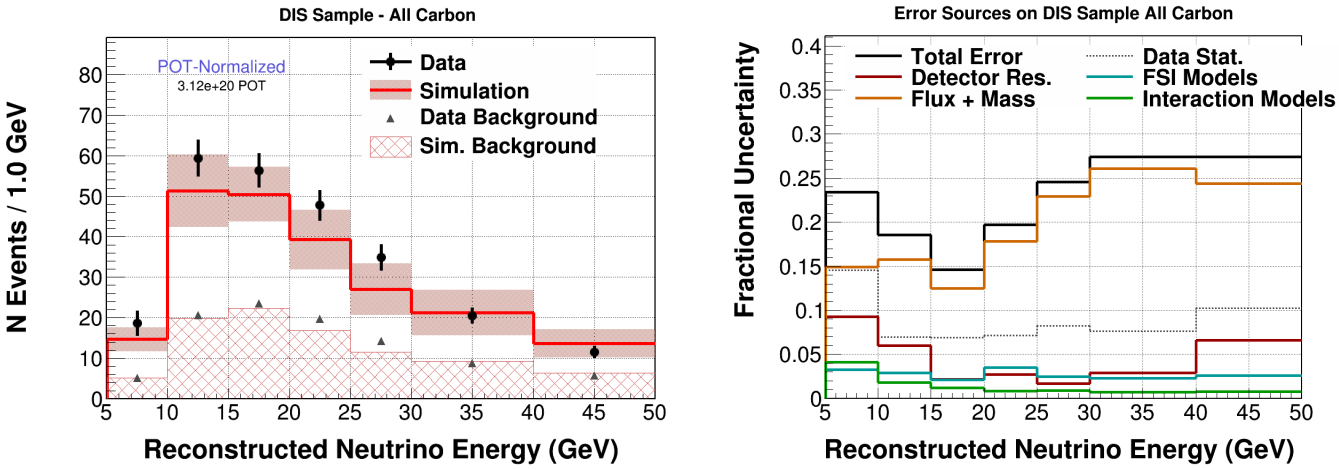

Figure 11-13. DIS events reconstructed in carbon per neutrino energy in data (black points) and Monte Carlo (red line). The pink band around the line is the systematic error displayed on the right. The extracted CH background from the data (triangles) and MC (hatched plot) are drawn as well.

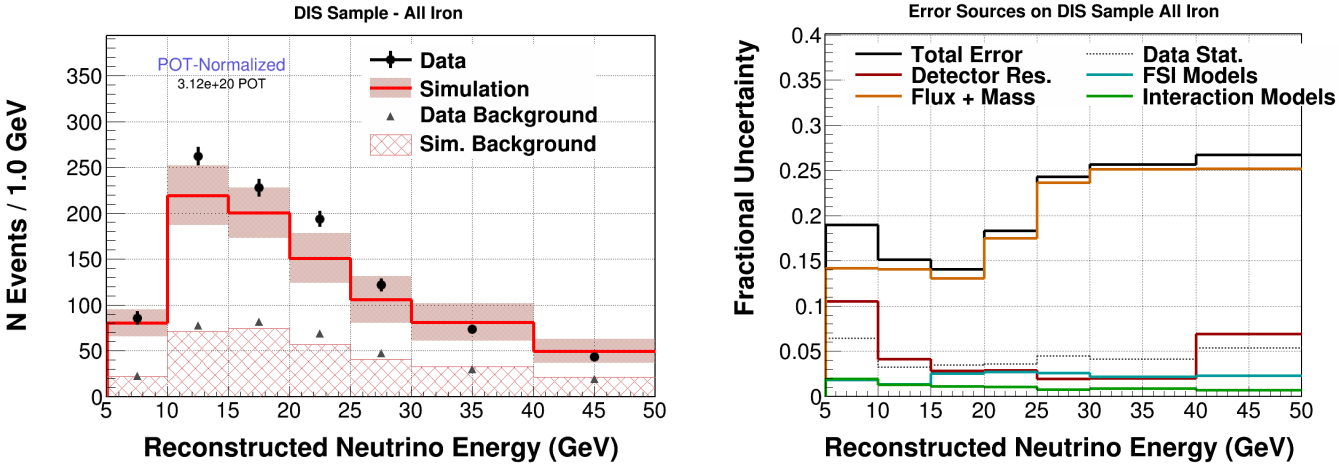

Figure 11-14. DIS events reconstructed in iron per neutrino energy in data (black points) and Monte Carlo (red line). The pink band around the line is the systematic error displayed on the right. The extracted CH background from the data (triangles) and MC (hatched plot) are drawn as well.

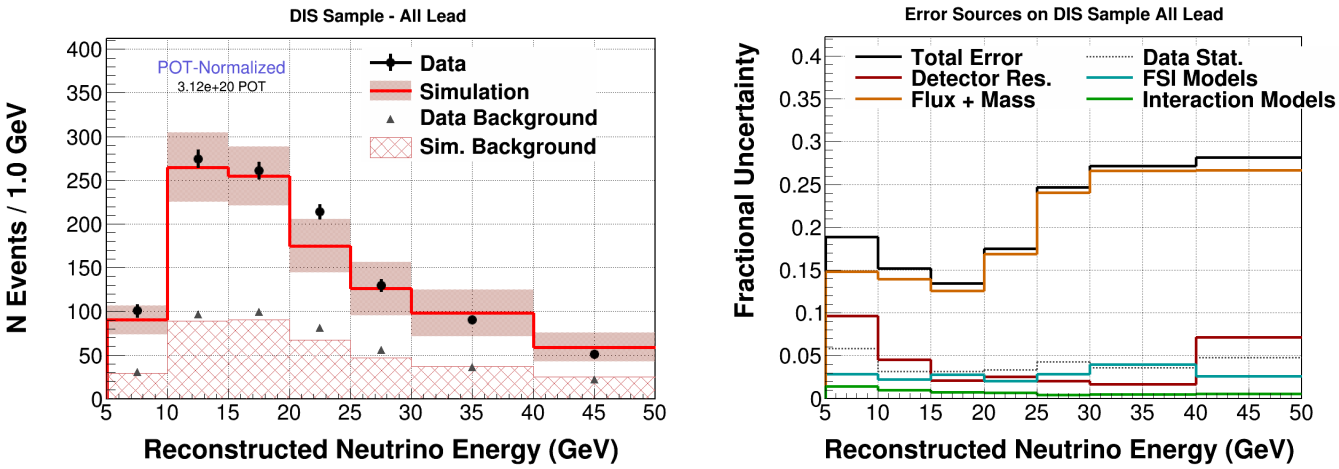

Figure 11-15. DIS events reconstructed in lead per neutrino energy in data (black points) and Monte Carlo (red line). The pink band around the line is the systematic error displayed on the right. The extracted CH background from the data (triangles) and MC (hatched plot) are drawn as well.

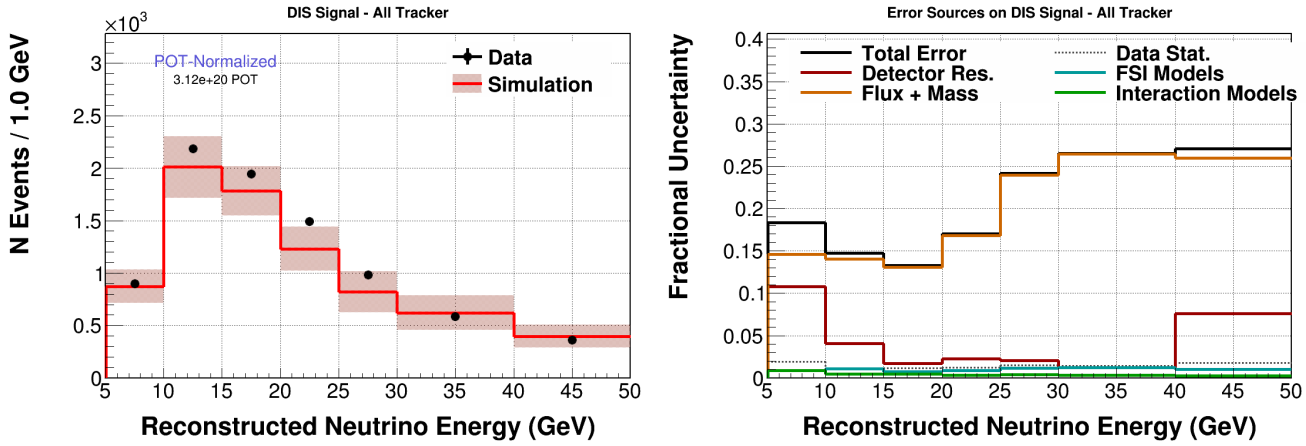

Figure 11-16. DIS events reconstructed in scintillator per neutrino energy in data (black points) and Monte Carlo (red line). The pink band around the line is the systematic error displayed on the right.

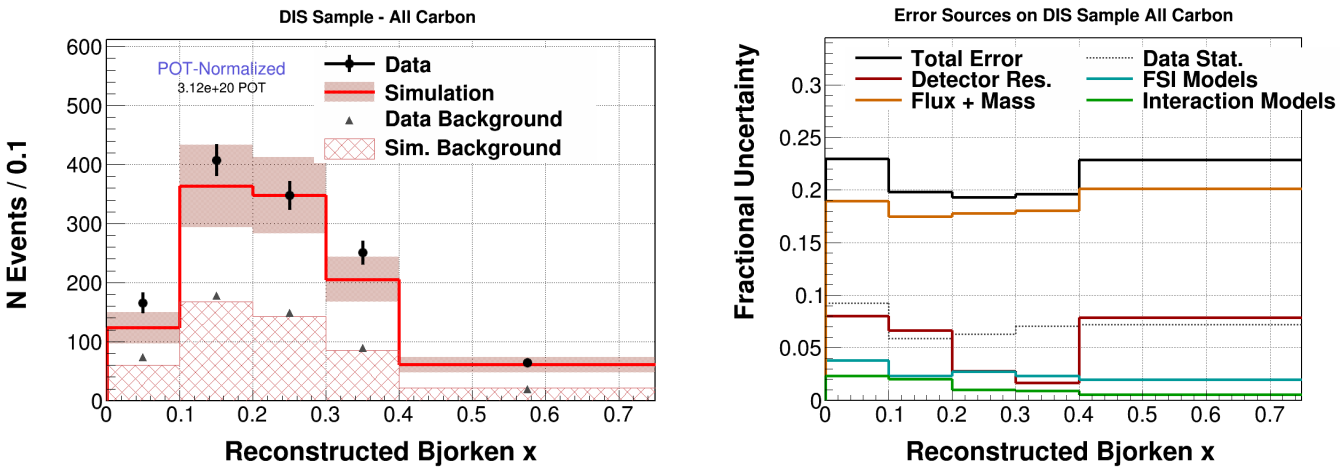

Figure 11-17. DIS events reconstructed in carbon per Bjorken-x in data (black points) and Monte Carlo (red line). The pink band around the line is the systematic error displayed on the right. The extracted CH background from the data (triangles) and MC (hatched plot) are drawn as well.

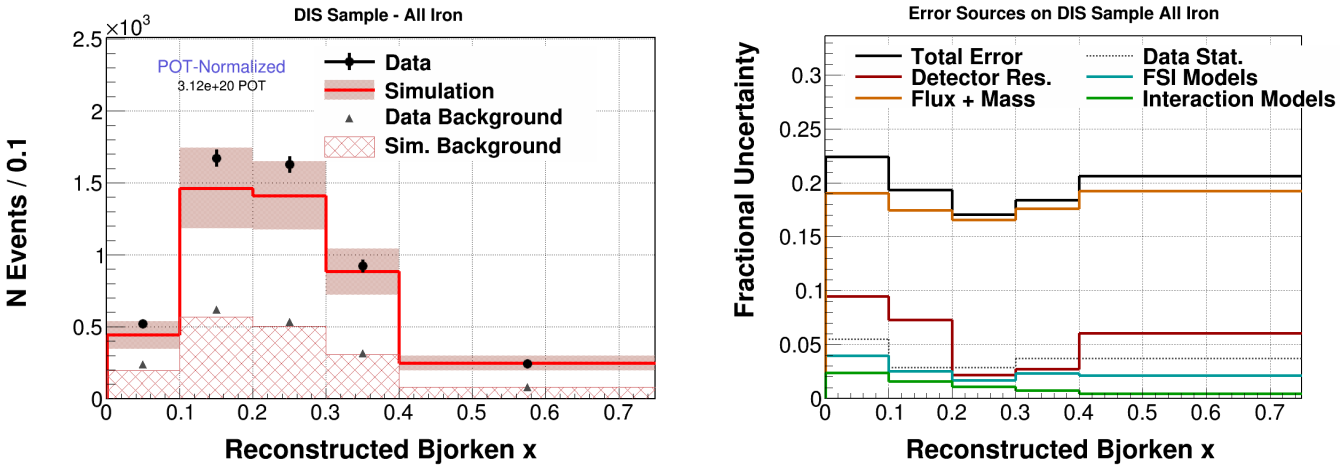

Figure 11-18. DIS events reconstructed in iron per Bjorken-x in data (black points) and Monte Carlo (red line). The pink band around the line is the systematic error displayed on the right. The extracted CH background from the data (triangles) and MC (hatched plot) are drawn as well.

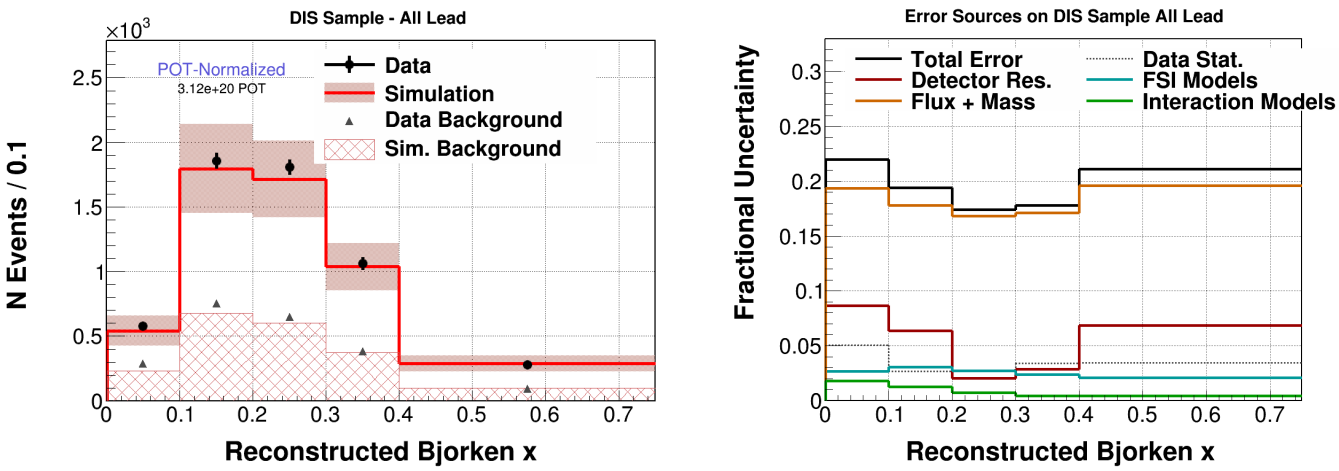

Figure 11-19. DIS events reconstructed in lead per Bjorken-x in data (black points) and Monte Carlo (red line). The pink band around the line is the systematic error displayed on the right. The extracted CH background from the data (triangles) and MC (hatched plot) are drawn as well.

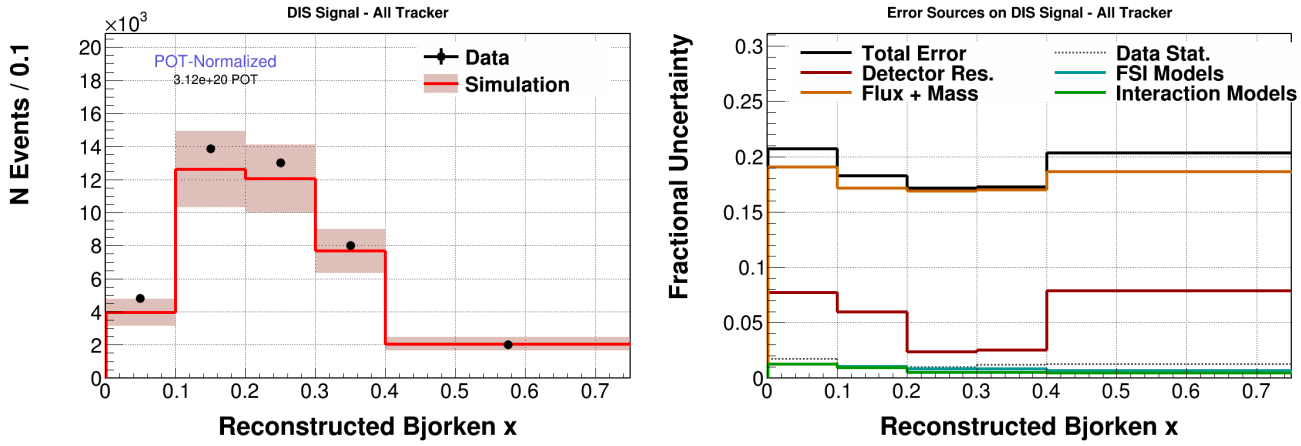

Figure 11-20. DIS events reconstructed in scintillator per Bjorken-x in data (black points) and Monte Carlo (red line). The pink band around the line is the systematic error displayed on the right

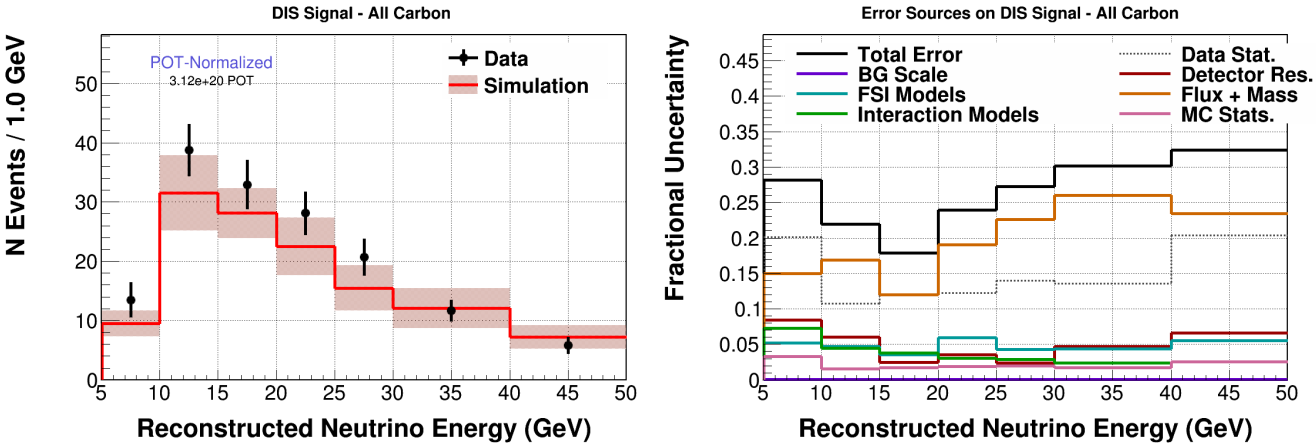

Figure 11-21. DIS events in carbon per neutrino energy in data (black points) and Monte Carlo (red line). The pink band around the line is the systematic error displayed on the right.

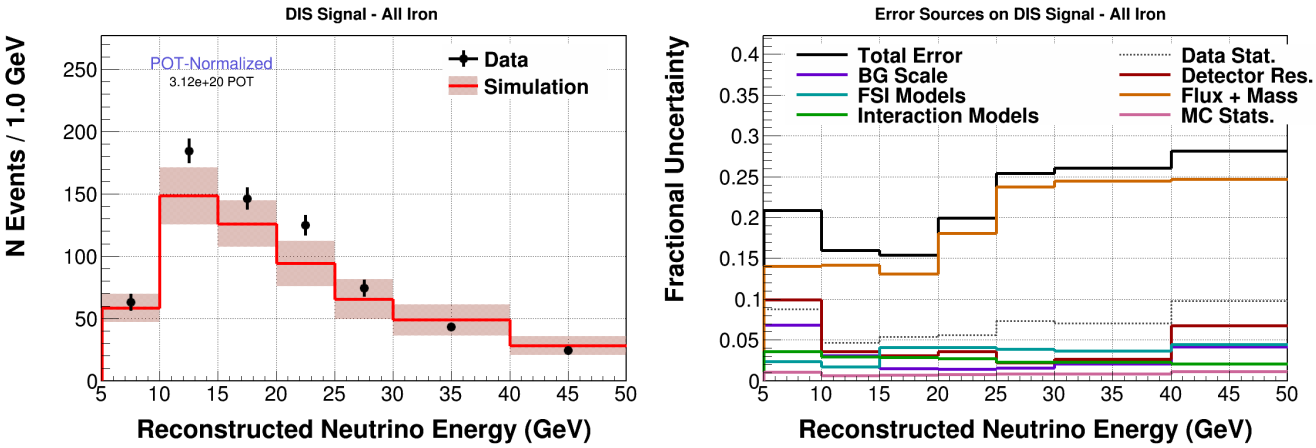

Figure 11-22. DIS events in iron per neutrino energy in data (black points) and Monte Carlo (red line). The pink band around the line is the systematic error displayed on the right.

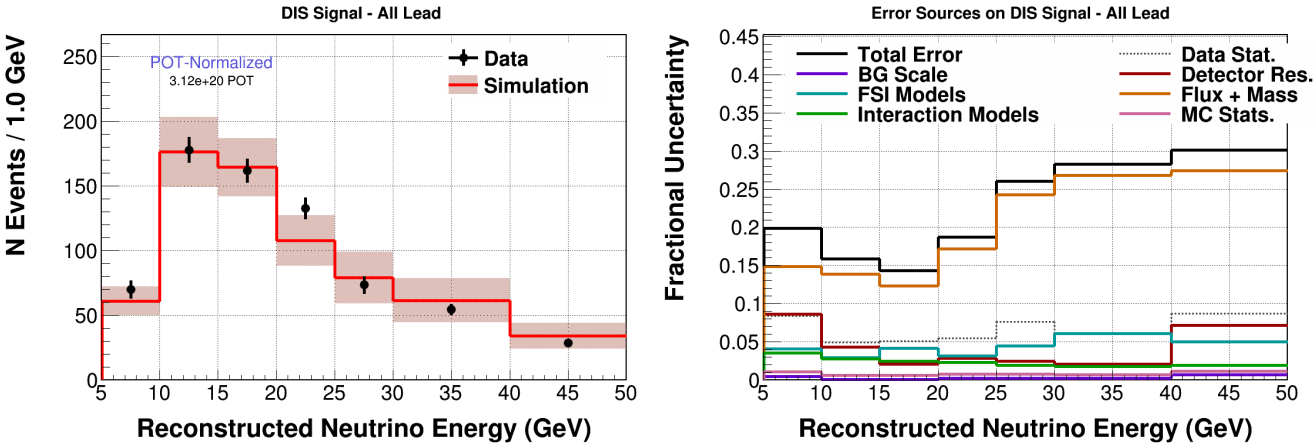

Figure 11-23. DIS events in lead per neutrino energy in data (black points) and Monte Carlo (red line). The pink band around the line is the systematic error displayed on the right.

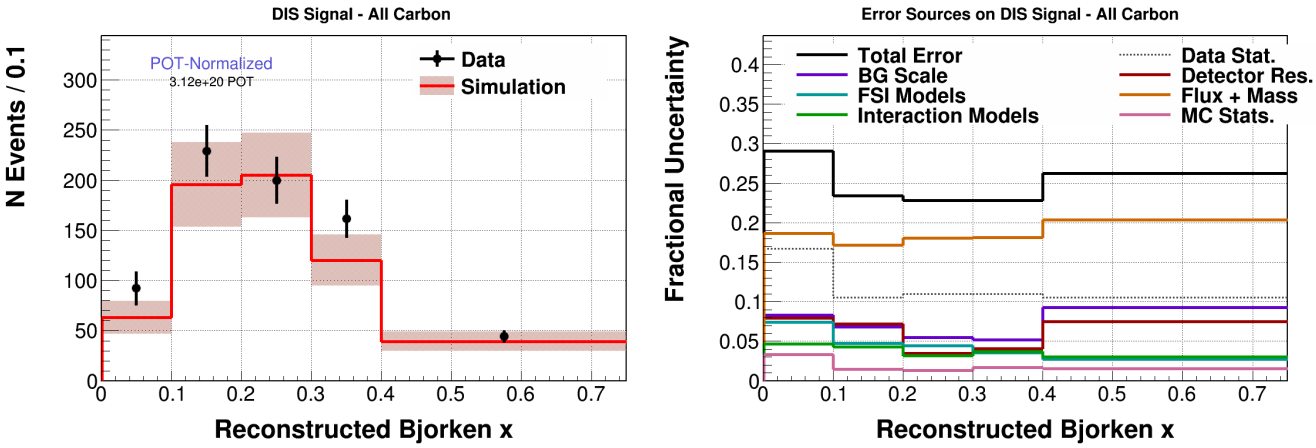

Figure 11-24. DIS events in carbon per Bjorken-x in data (black points) and Monte Carlo (red line). The pink band around the line is the systematic error displayed on the right.

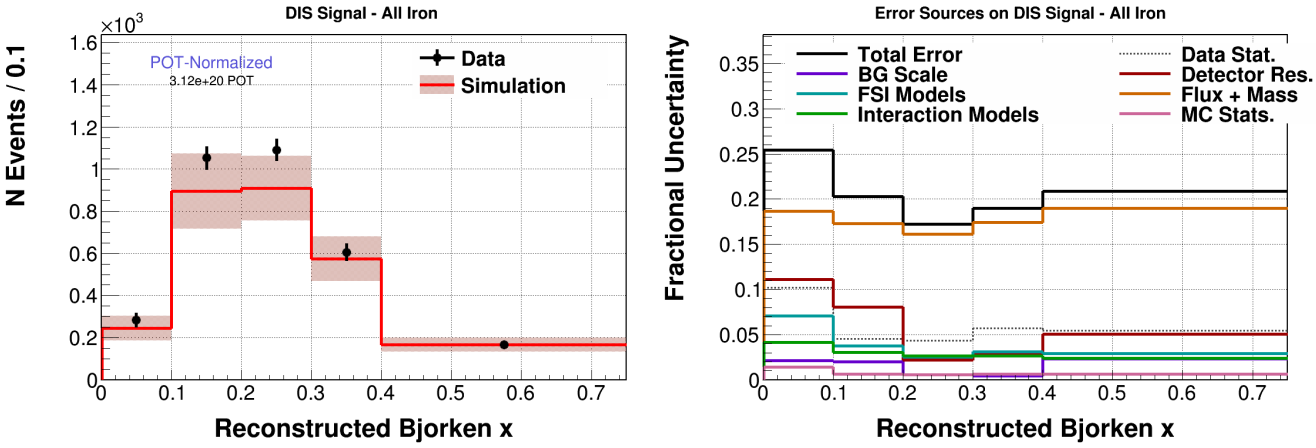

Figure 11-25. DIS events in iron per Bjorken-x in data (black points) and Monte Carlo (red line). The pink band around the line is the systematic error displayed on the right.

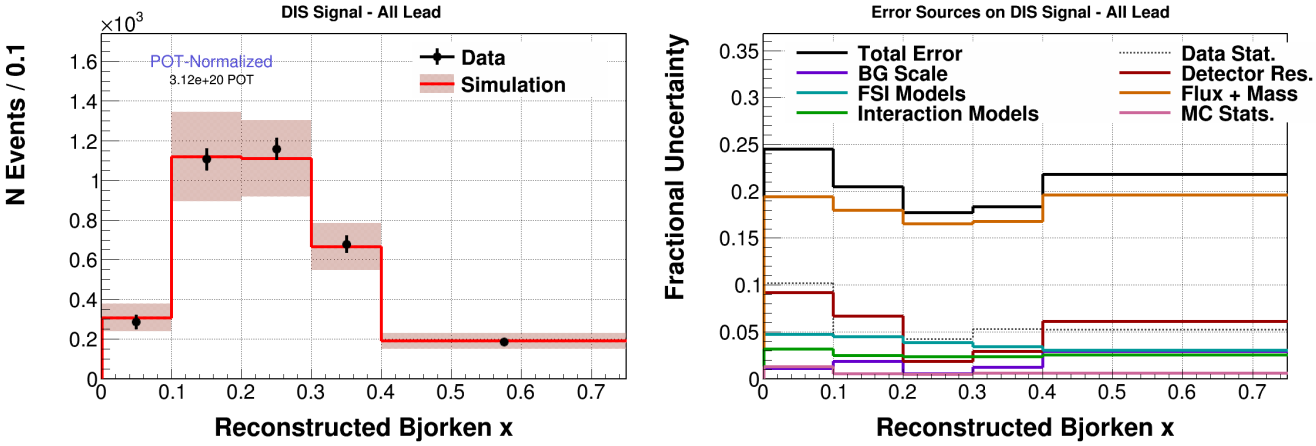

Figure 11-26. DIS events in lead per Bjorken-x in data (black points) and Monte Carlo (red line). The pink band around the line is the systematic error displayed on the right.

11.2.2 Unfolded Kinematics

Unfolding is preformed after subtracting the non-DIS and CH backgrounds. The neutrino energy and Bjorken-x distributions are unfolded separately for each target and nuclei, however for brevity only the plots of the sum of each nuclei after unfolding are presented. Plots of the unfolded variables target by target may be found in Appendix F.1.

The process of unfolding introduces correlations into the statistical uncertainty. As a result, the statistical error of the data, calculated only form the *diagonal* errors, appears to decrease post unfolding. The separate universes used in calculating the systematic uncertainties are unfolded using a separate migration matrix calculated in that universe. Migration matrices used for the central value may be found in Appendix D and D.2.

Plots of the events in C, CH, Fe, Pb as a function of unfolded neutrino energy and Bjorken-x, along with the uncertainty are displayed in Figures 11-27 through 11-34.

To gain a better understanding of the effect on unfolding, the reconstructed and unfolded versions are plotted side by side in Figures 11-35 through 11-42. Two trends are observed. In the case of E_ν the unfolding does very little. The neutrino energy distribution has large bins necessary to get sufficient statistics in each bin. These bins, at least 5 GeV wide, are much larger than the neutrino energy resolution of the event sample. As a result, there is not much smearing bin to bin in neutrino energy. In the case of x_{bj}, most events are smeared from the peak of the x_{bj} ($0.2 < x_{bj} < 0.4$) distribution to the high x_{bj} tail ($0.4 < x_{bj} < 0.75$). This effect is seen in all nuclei.

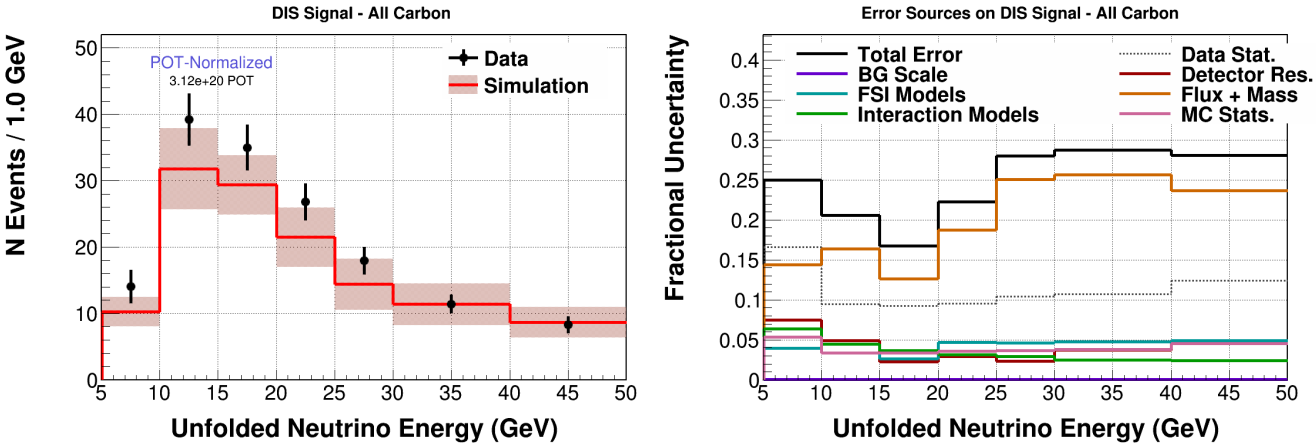

Figure 11-27. DIS events in carbon per unfolded neutrino energy in data (black points) and Monte Carlo (red line). The pink band around the line is the systematic error displayed on the right.

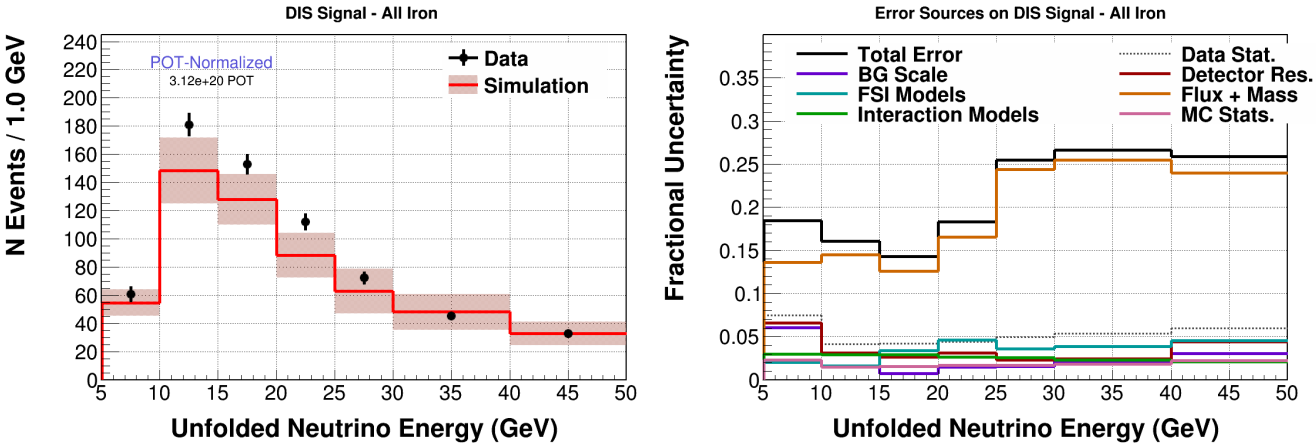

Figure 11-28. DIS events in iron per unfolded neutrino energy in data (black points) and Monte Carlo (red line). The pink band around the line is the systematic error displayed on the right.

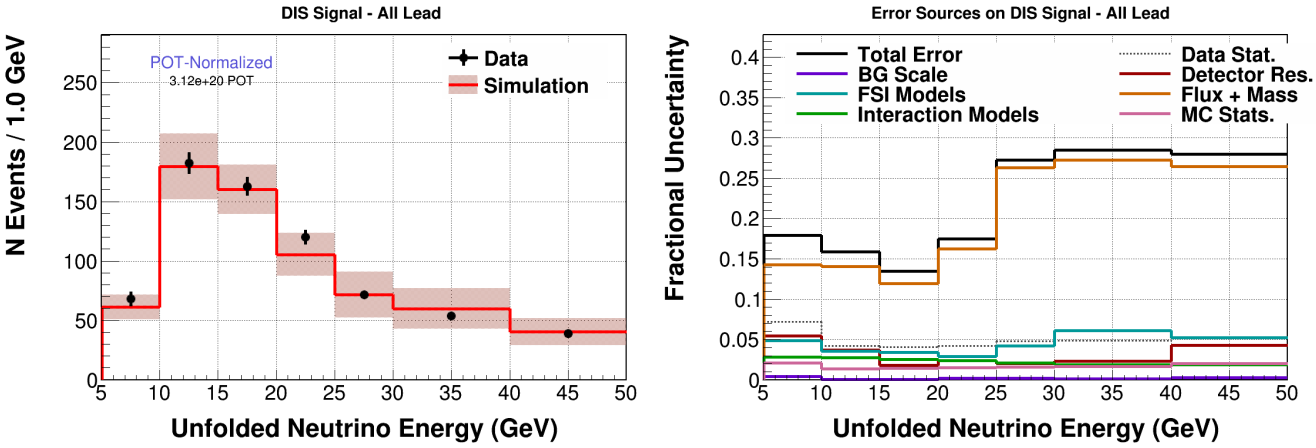

Figure 11-29. DIS events in lead per unfolded neutrino energy in data (black points) and Monte Carlo (red line). The pink band around the line is the systematic error displayed on the right.

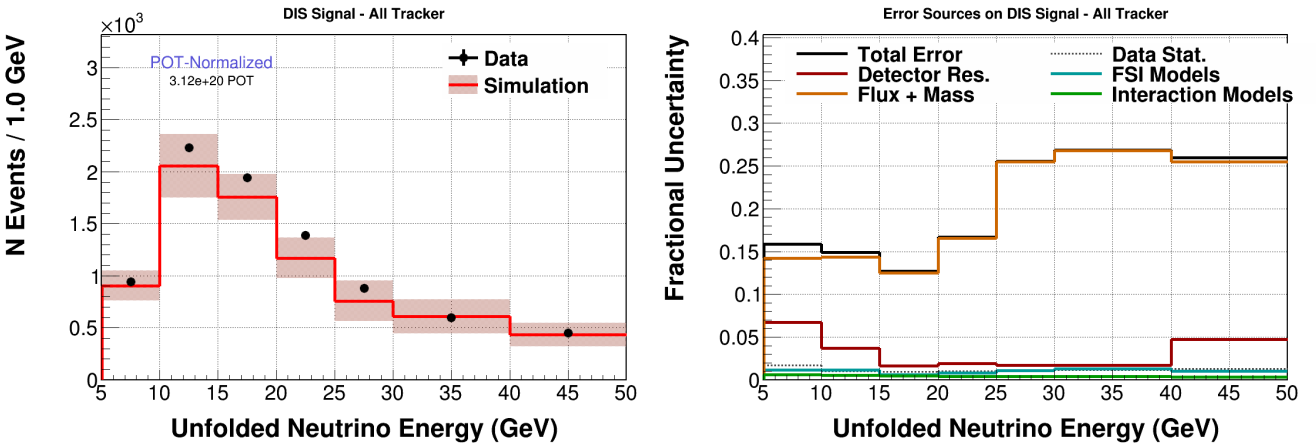

Figure 11-30. DIS events in scintillator per unfolded neutrino energy in data (black points) and Monte Carlo (red line). The pink band around the line is the systematic error displayed on the right.

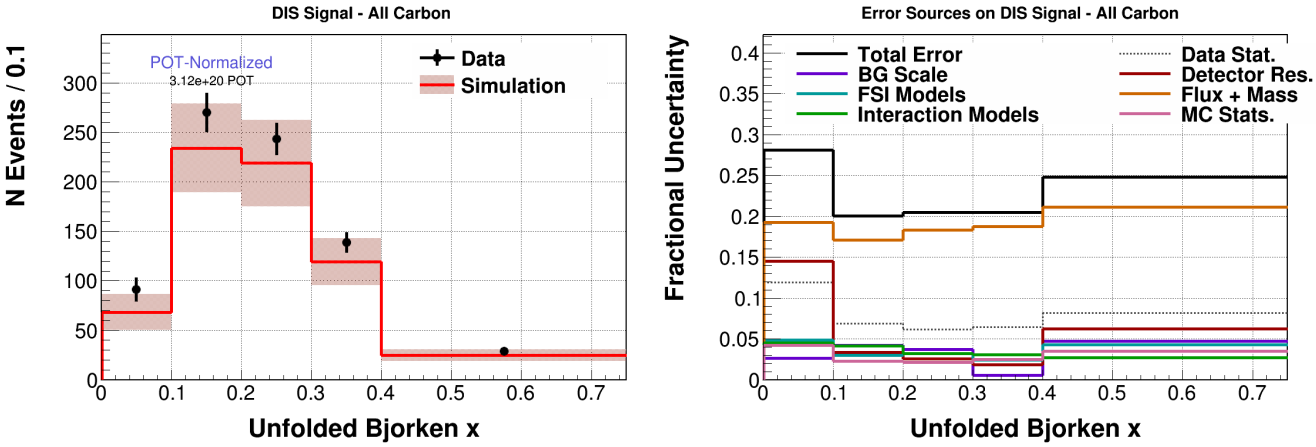

Figure 11-31. DIS events in carbon per unfolded Bjorken-x in data (black points) and Monte Carlo (red line). The pink band around the line is the systematic error displayed on the right.

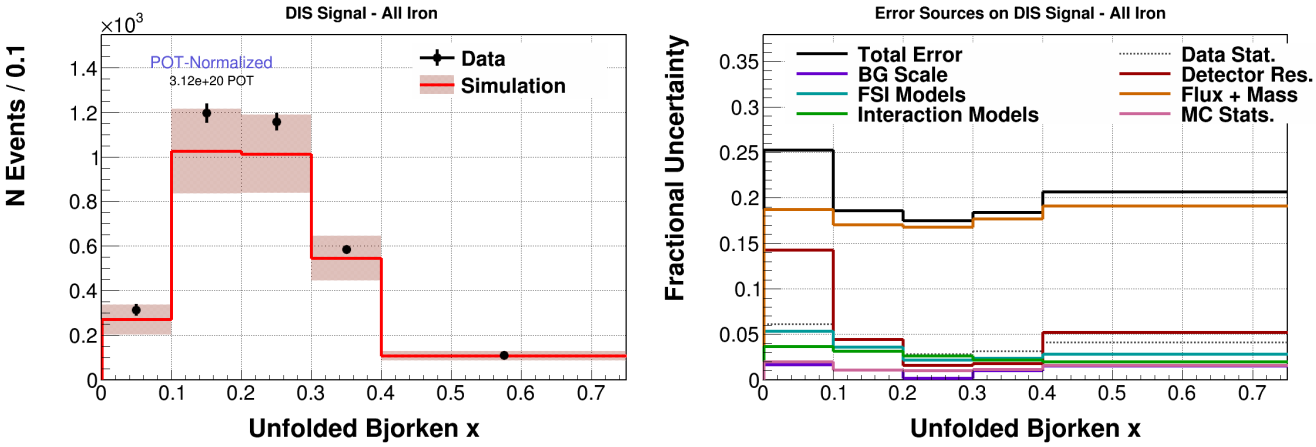

Figure 11-32. DIS events in iron per unfolded Bjorken-x in data (black points) and Monte Carlo (red line). The pink band around the line is the systematic error displayed on the right.

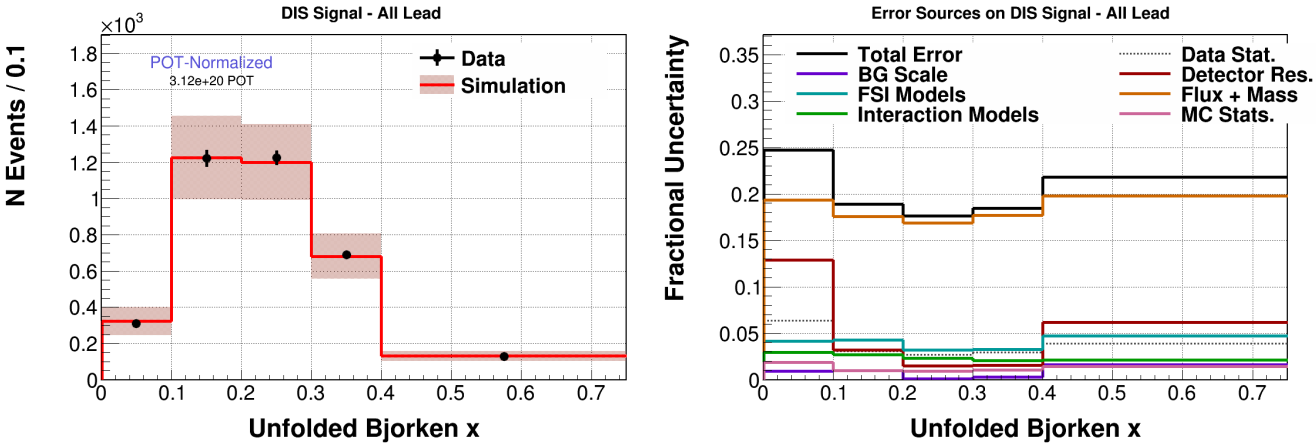

Figure 11-33. DIS events in lead per Bjorken-x in data (black points) and Monte Carlo (red line). The pink band around the line is the systematic error displayed on the right.

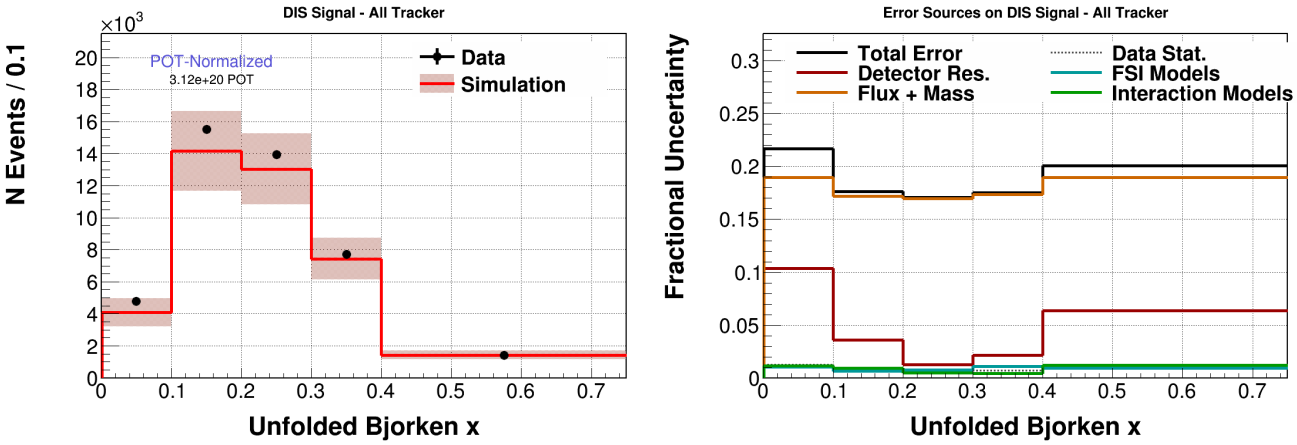

Figure 11-34. DIS events in scintillator per unfolded Bjorken-x in data (black points) and Monte Carlo (red line). The pink band around the line is the systematic error displayed on the right.

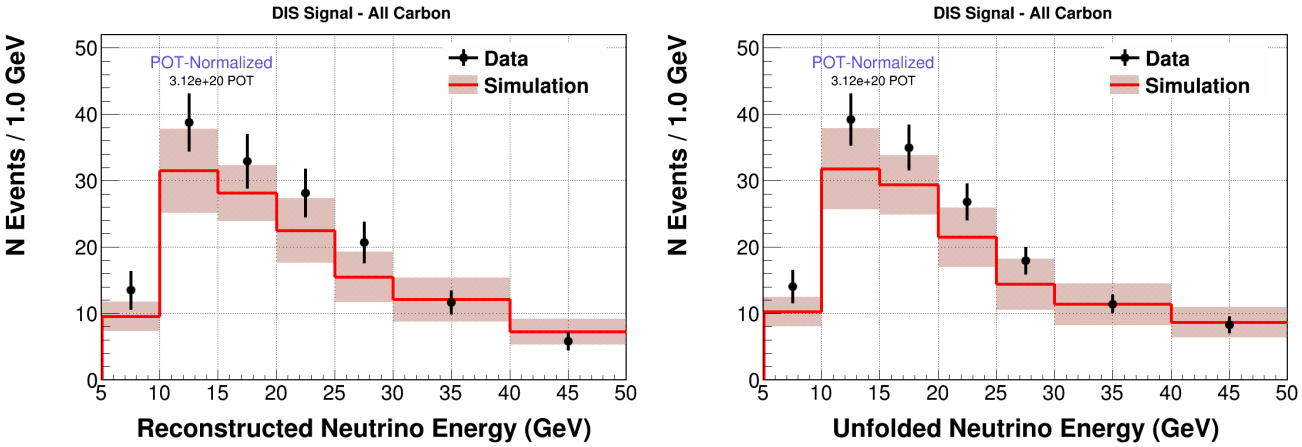

Figure 11-35. DIS events in carbon per reconstructed E_ν (left) and unfolded E_ν (right).

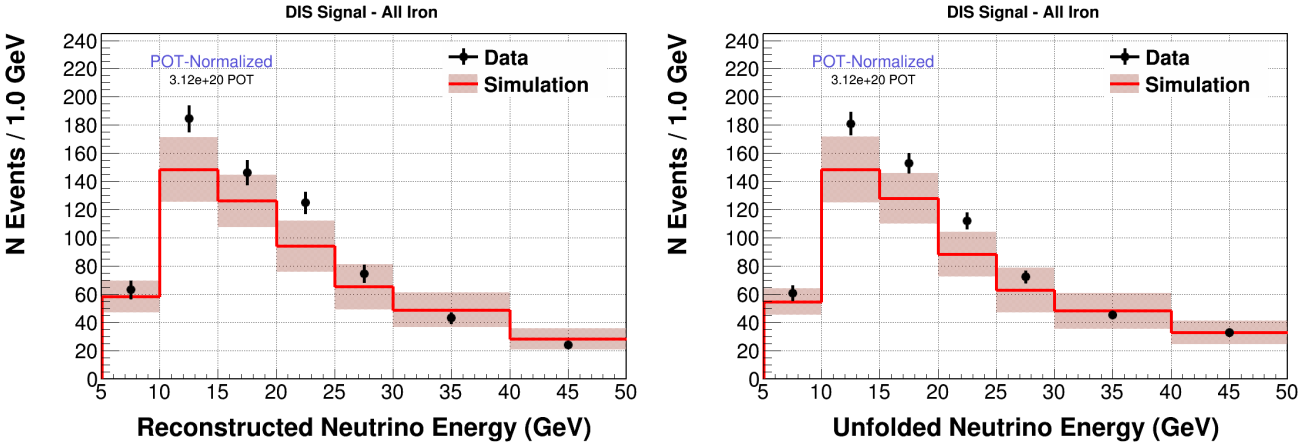

Figure 11-36. DIS events in iron per reconstructed E_ν (left) and unfolded E_ν (right).

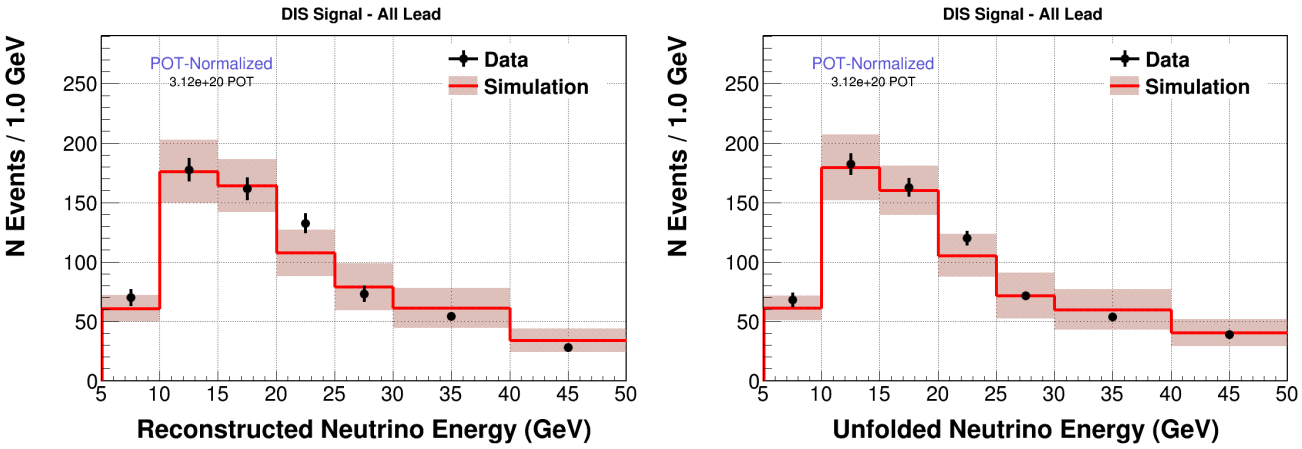

Figure 11-37. DIS events in lead per reconstructed E_ν (left) and unfolded E_ν (right).

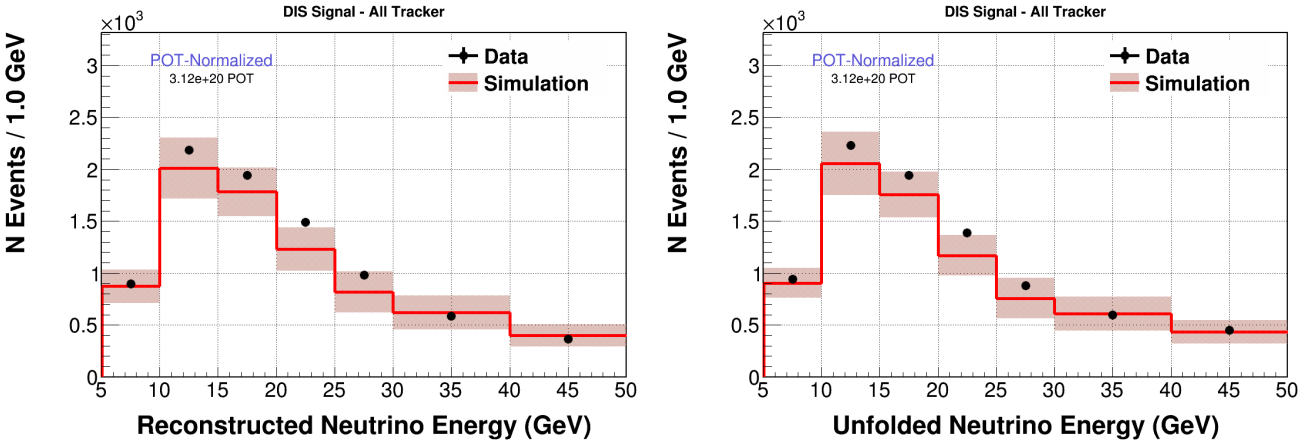

Figure 11-38. DIS events in scintillator per reconstructed E_ν (left) and unfolded E_ν (right).

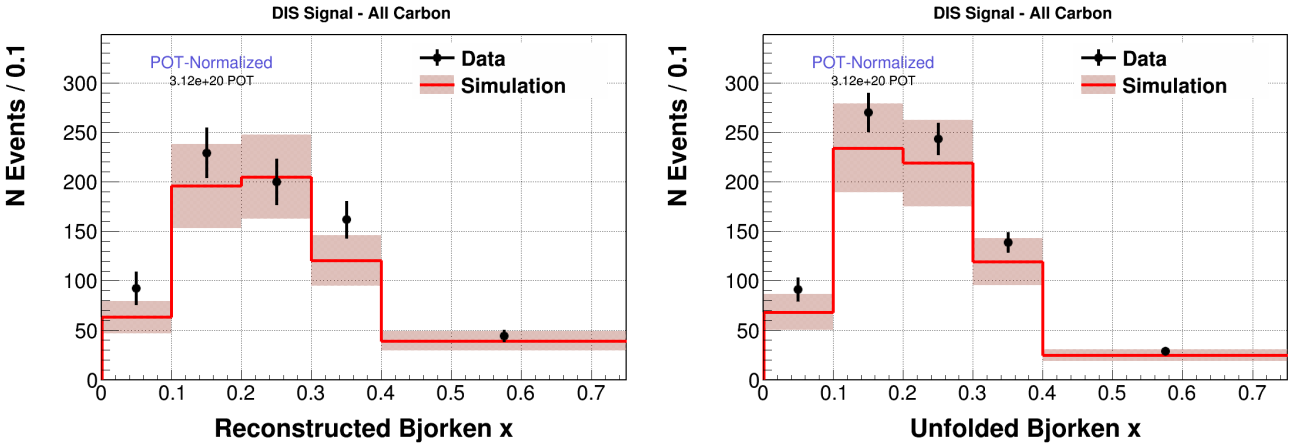

Figure 11-39. DIS events in carbon per reconstructed x_{bj} (left) and unfolded x_{bj} (right).

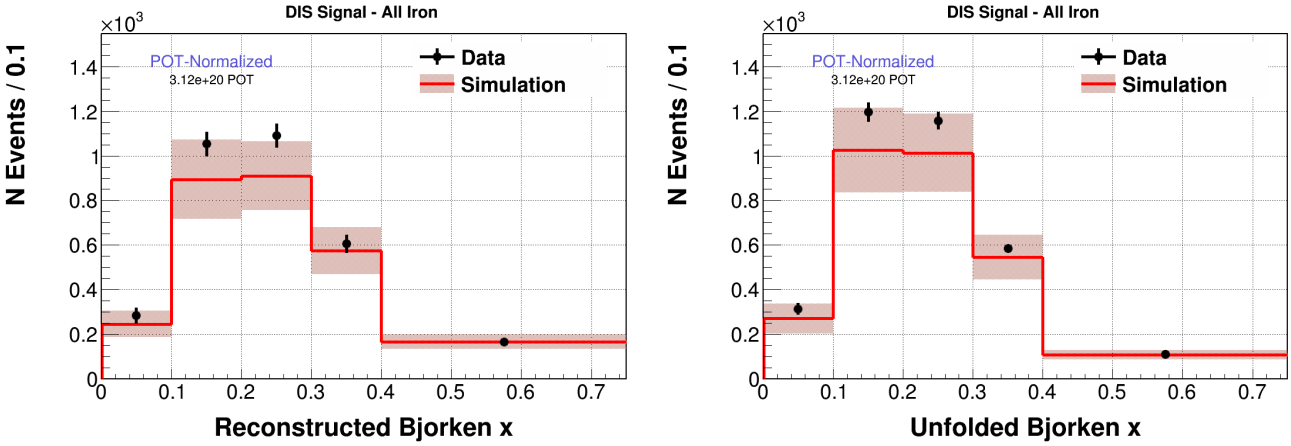

Figure 11-40. DIS events in iron per reconstructed x_{bj} (left) and unfolded x_{bj} (right).

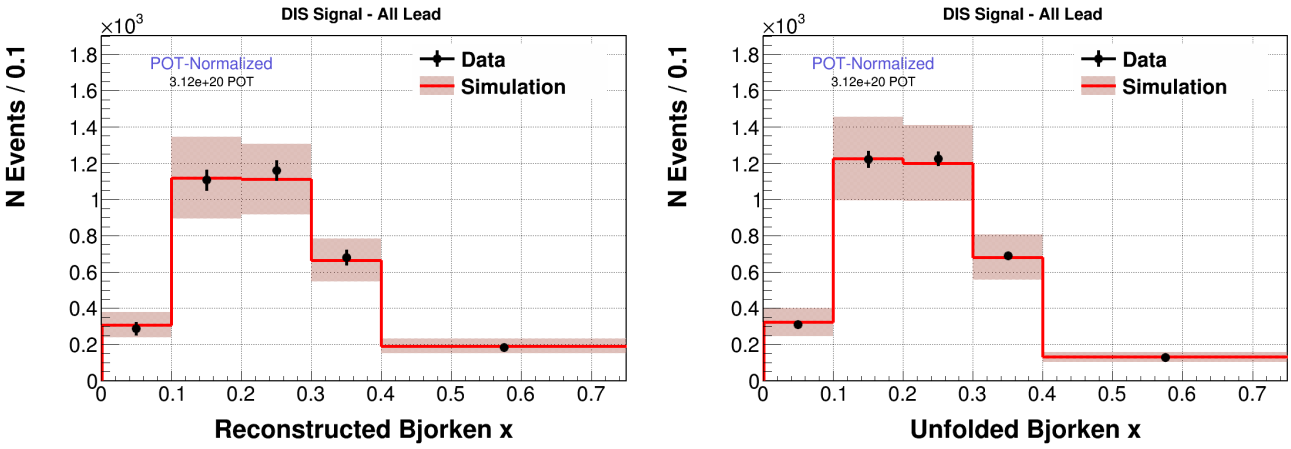

Figure 11-41. DIS events in lead per reconstructed x_{bj} (left) and unfolded x_{bj} (right).

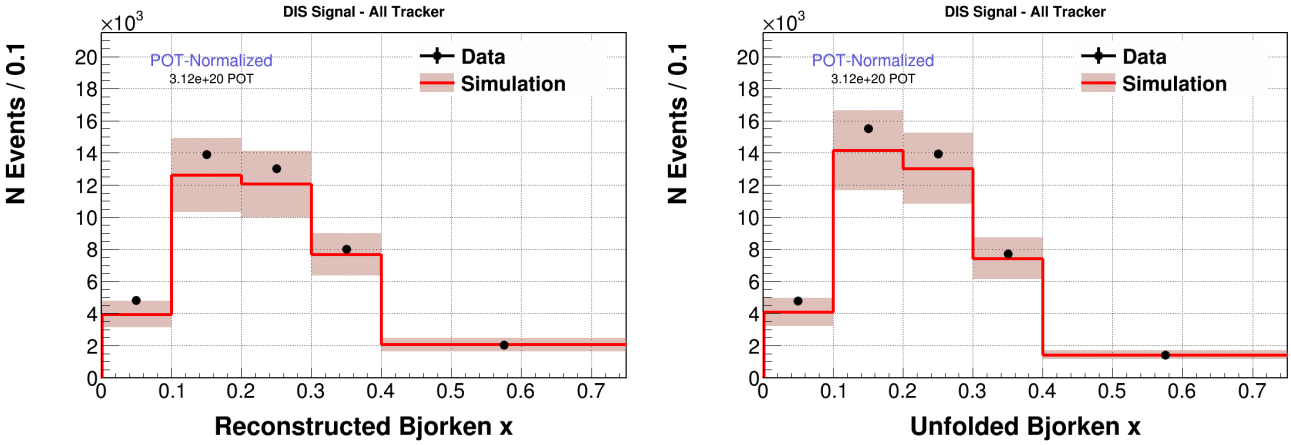

Figure 11-42. DIS events in scintillator per reconstructed x_{bj} (left) and unfolded x_{bj} (right).

CHAPTER 12
EFFICIENCY CORRECTION AND FLUX DIVISION

The final step to converting event yields to cross-sections is to divide by the flux, overall efficiency and the number of targets. In the case of the total cross section, $\sigma(E_\nu)$, the flux is *averaged* over each E_ν bin i:

$$\sigma_i = \frac{U_{ij}\,(d_j - b_j)}{\Delta_i\,\epsilon_i\,\Phi_i\,N}. \tag{12-1}$$

In contrast, the differential with respect to Bjorken-x ($\frac{d\sigma}{dx}$) is divided by the *integrated* flux over the accepted energy range:

$$\frac{d\sigma}{dx}_i = \frac{U_{ij}\,(d_j - b_j)}{\Delta_i\,\epsilon_i\,\Phi\,N}, \tag{12-2}$$

where Φ is integrated from $5 \leq E_\nu < 50$ GeV.

12.1 Efficiency Correction

12.1.1 Overall Efficiency

In order to obtain an accurate measurement of the total cross section, the inefficiency of the detector and analysis must be corrected prior to dividing by the flux. The efficiency is calculated completely from the MC, and defined exactly the same way as in Section 8.3:

Overall Efficiency 1 *Reconstructed DIS events that pass the true DIS cuts, truly in a nuclear target A / the total number of DIS events generated by the MC in nuclear target A.*

Each nuclear target A posses its' own efficiency correction as a function of true x_{bj} and E_ν. Plots of the efficiency correction, as well as the systematic error on the correction may be found in Appendix G.1 and G.2. Figure 12-1 shows the efficiency correction as a function of E_ν for the lead of target 4, as well as the uncertainty on the efficiency correction. The efficiency and its' uncertainty as a function of true W is plotted in Figure 12-2.

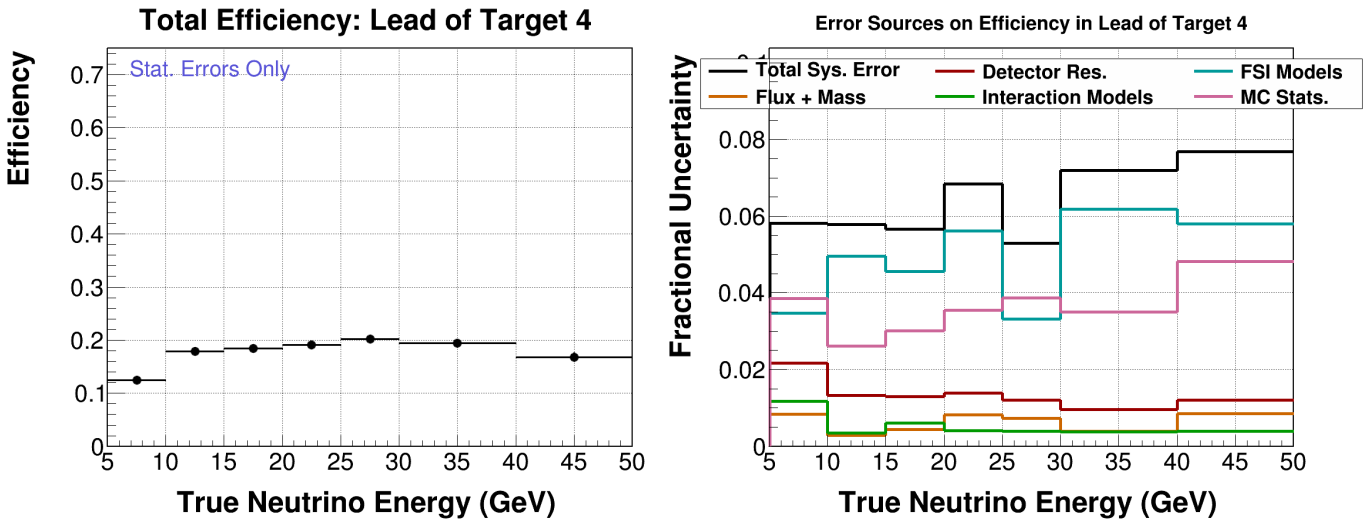

Figure 12-1. Overall efficiency of events in the lead of target 4 as a function of true E_ν (left) and the systematic uncertainty on the overall efficiency (right).

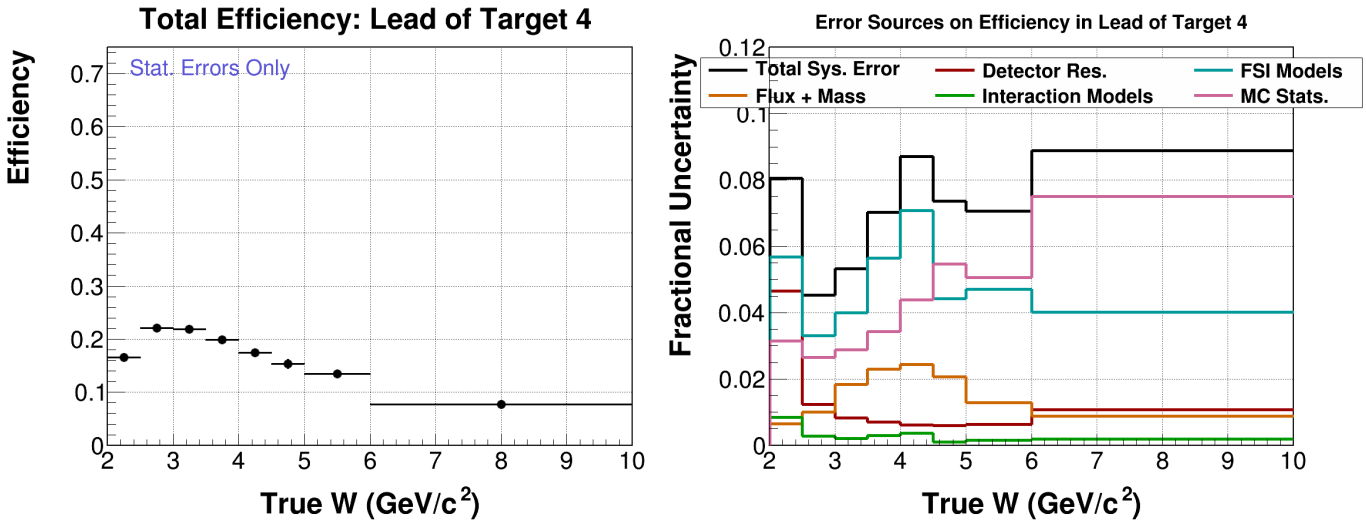

Figure 12-2. Overall efficiency of events in the lead of target 4 as a function of true W (left) and the systematic uncertainty on the overall efficiency (right).

12.1.2 FSI Uncertainties

Overall, the leading uncertainty on the efficiency correction is the uncertainty in GENIE's final state interaction model (FSI). Further analysis found the pion inelastic and pion absorption uncertainties drive the FSI uncertainty at high energies and high W as presented in Figure 12-3. This makes sense, since higher energy events will contain a larger number of intermediate pions with a dependence proportional to $ln(W)$. As a result, the uncertainties tend to build as more pions are being simulated and propagated in the event.

12.2 Flux Division

The neutrino flux is computed from the Monte Carlo. The total number of charged-current events, regardless of event type, of the entire simulated exposure are measured with no cuts other than the primary neutrino must be a ν_μ. The events are histogramed in bins of neutrino energy. This histogram is divided bin by bin by the total cross section splines GENIE uses during event generation. These are the same spline files as described in Section 3.1. As flux uncertainties are assigned to the event yields, this flux histogram has no uncertainty associated with it.

In the case of the total cross section, the flux histogram is averaged over each energy bin of the analysis prior to division. In the case of the differential cross section, the flux histogram is integrated over $5 \leq E_\nu < 50$ GeV.

12.3 Target Counting

After dividing the the efficiency and flux, the cross-sections must be divided by the number of nucleons in each nuclear target and the tracker before arriving at a per nucleon cross-section. The number of nucleons in each target is computed from the measured density of each material. This is converted into a mass by multiplying by the fiducial area and thickness of each target. As the DIS analysis is unable to distinguish between ν_μ plus proton and ν_μ plus neutron events, the total mass is divided by the total atomic mass of each nucleus. This mass is then multiplied by Avagadro's number to finally compute the total number of nucleons in each target.

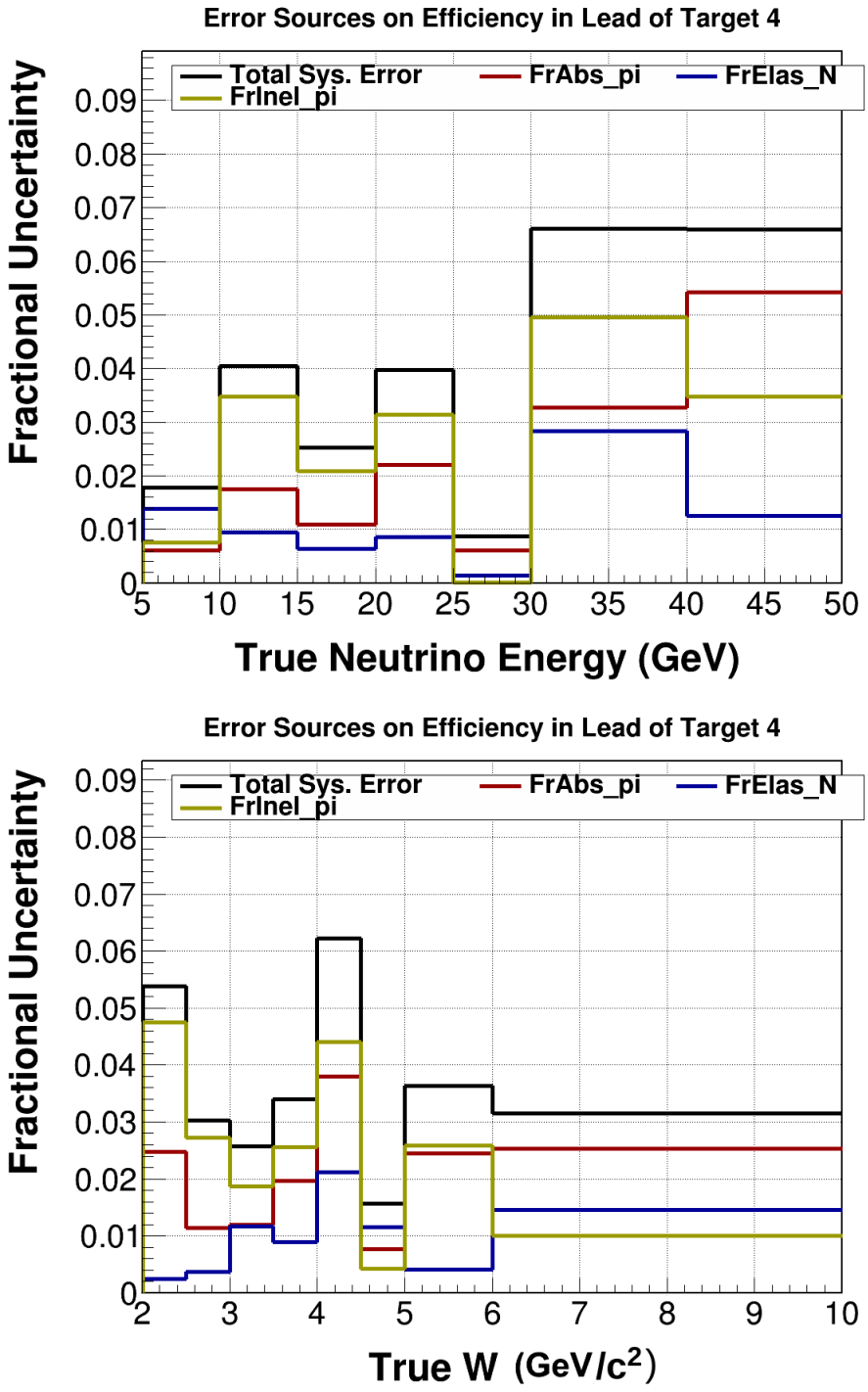

Figure 12-3. Final state interaction model uncertainties on the overall efficiency of events in the lead of target 4. The only contributions plotted are those that contribute more than 1% to the total uncertainy. The leading uncertainties are the pion inelastic probability (FrInel pi) and the pion absorption probability (FrAbs pi). Top: Uncertainty plotted as a function of E_ν. Bottom: Uncertainty plotted as a function of W.

CHAPTER 13
CROSS SECTION RESULTS

13.1 Closure Tests

Prior to measuring the data cross-sections, the internal consistency of the analysis is tested by comparing the analyzed MC to an external GENIE calculation. In this test, the MC is treated like data, and unfolded and efficiency corrected using the same unfolding matrix and efficiency correction as the data. The only distinctions between the data analysis and the MC closure test is the closure test subtracts the *true* CH background and *true* non-DIS background prior to unfolding. The expectation is that after subtracting the true background the closure test should produce the same cross-section as GENIE. The GENIE cross-section is calculated using the cross-section extraction tool described in Ref [89].

The result of this test for carbon is shown in Figure 13-1, which shows the two calculations return exactly the same value for each bin of E_ν. Figure 13-1 also displays the ratio, which is identically unity for all neutrino energy bins.

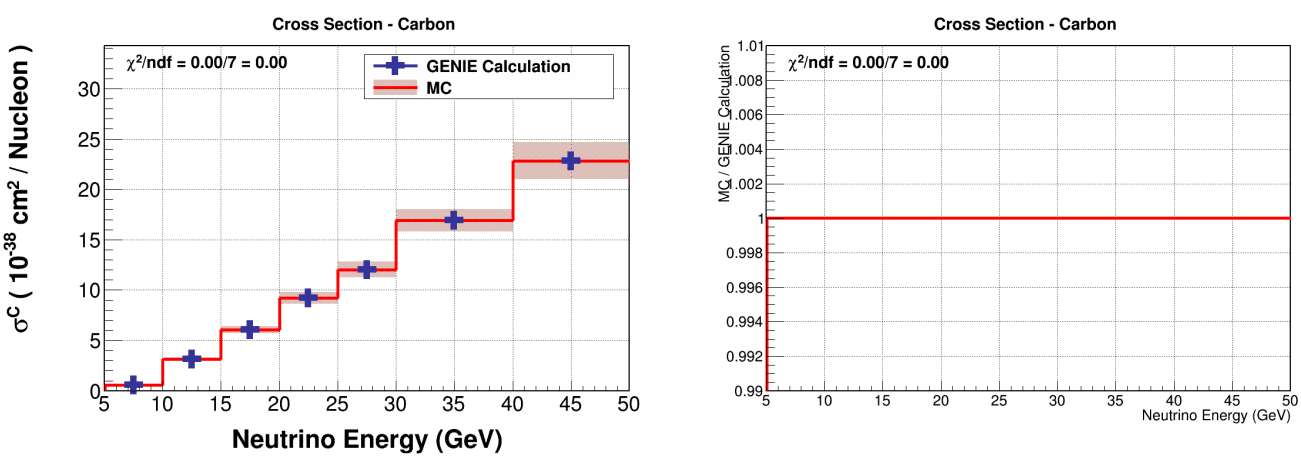

Figure 13-1. Left: Analyzed cross-section from MC, with true backgrounds subtracted (red line) vs. the cross-section extracted from GENIE (blue crosses). The error band on the MC is statistical only. Right: Ratio of the analyzed MC cross-section to the GENIE extracted cross-section.

13.2 Absolute Cross Sections

The absolute cross section per nucleon as a function of neutrino energy and Bjorken-x is calculated for C, CH, Fe and Pb. In each nuclei, the data is compared to the simulation. Each of the data points contains the statistical uncertainty on the cross section measurement. The red band surrounding the MC contains all of the systematic errors, including those on the MC statistics. The cross sections and the breakdown of uncertainties as a function of unfolded E_ν are in Figures 13-2 through 13-5. In general, the MC tends to under-predict the cross section at low energies ($E_\nu < 30$ GeV) and over-predict at high energies ($E_\nu \geq 30$ GeV). None of these differences are significant taking into account the systematic uncertainty assigned to each bin. Since this trend is observed across the different nuclei, a likely explanation is a shape-difference between the actual and predicted neutrino flux.

Figures 13-6 through 13-9 show the differential cross section as a function of Bjorken-x. No significant differences between the data and MC are observed.

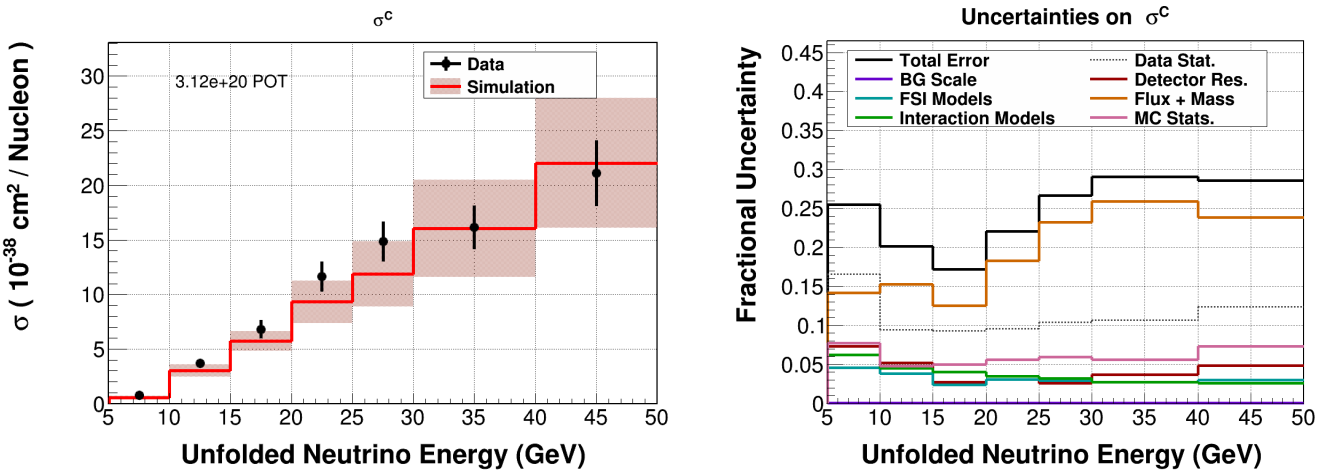

Figure 13-2. The total DIS cross section per nucleon on carbon as a function of unfolded neutrino energy for data (black points) and simulation (red line). The total systematic error is drawn as a red band around the simulation, and the breakdown of the systematic errors is drawn in the right hand plot.

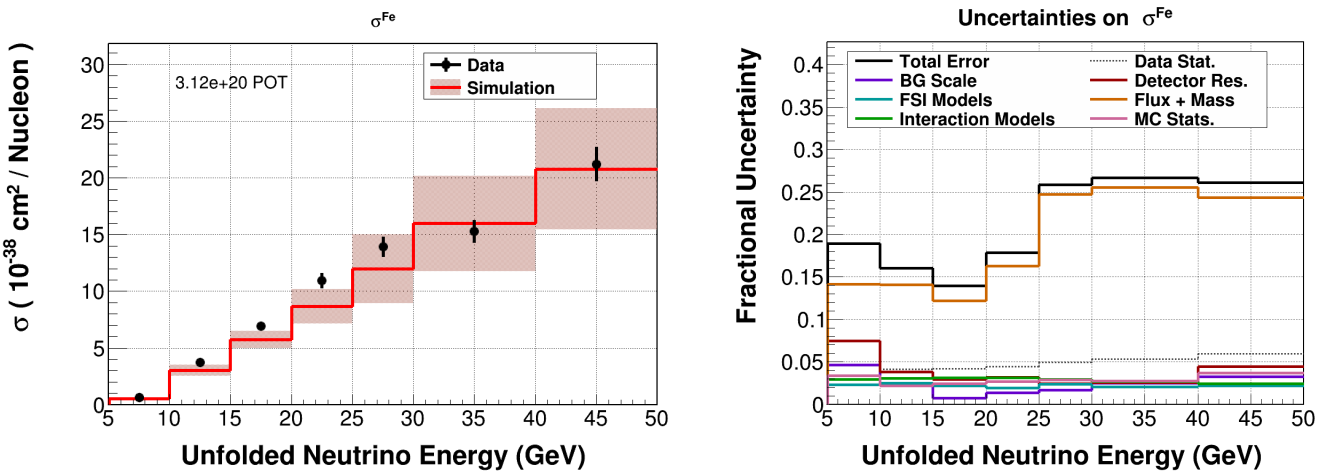

Figure 13-3. The total DIS cross section per nucleon on iron as a function of unfolded neutrino energy for data (black points) and simulation (red line). The total systematic error is drawn as a red band around the simulation, and the breakdown of the systematic errors is drawn in the right hand plot.

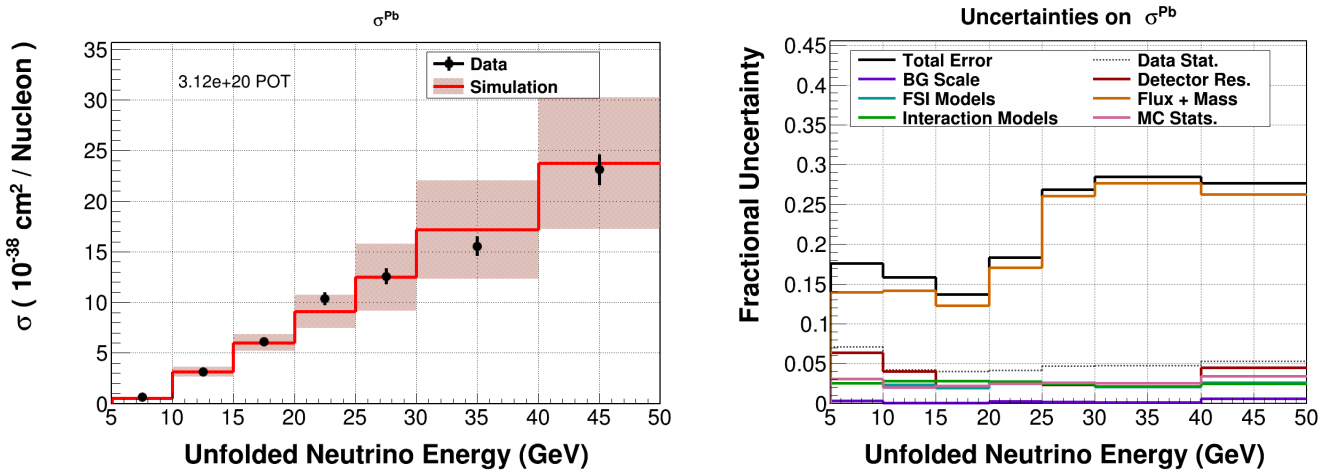

Figure 13-4. The total DIS cross section per nucleon on lead as a function of unfolded neutrino energy for data (black points) and simulation (red line). The total systematic error is drawn as a red band around the simulation, and the breakdown of the systematic errors is drawn in the right hand plot.

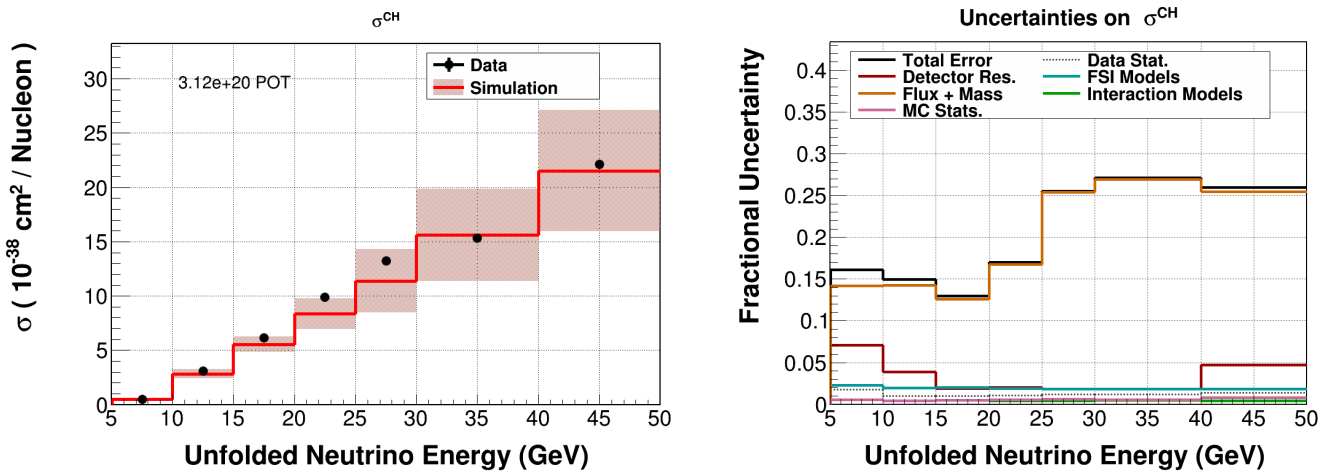

Figure 13-5. The total DIS cross section per nucleon on scintillator as a function of unfolded neutrino energy for data (black points) and simulation (red line). The total systematic error is drawn as a red band around the simulation, and the breakdown of the systematic errors is drawn in the right hand plot.

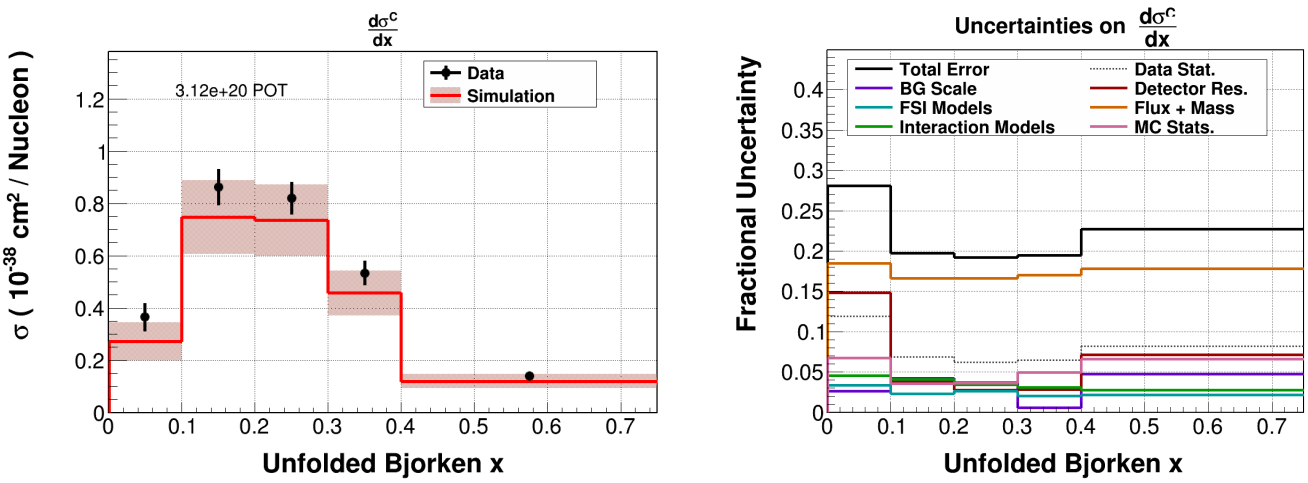

Figure 13-6. The total DIS cross section per nucleon on carbon as a function of unfolded neutrino energy for data (black points) and simulation (red line). The total systematic error is drawn as a red band around the simulation, and the breakdown of the systematic errors is drawn in the right hand plot.

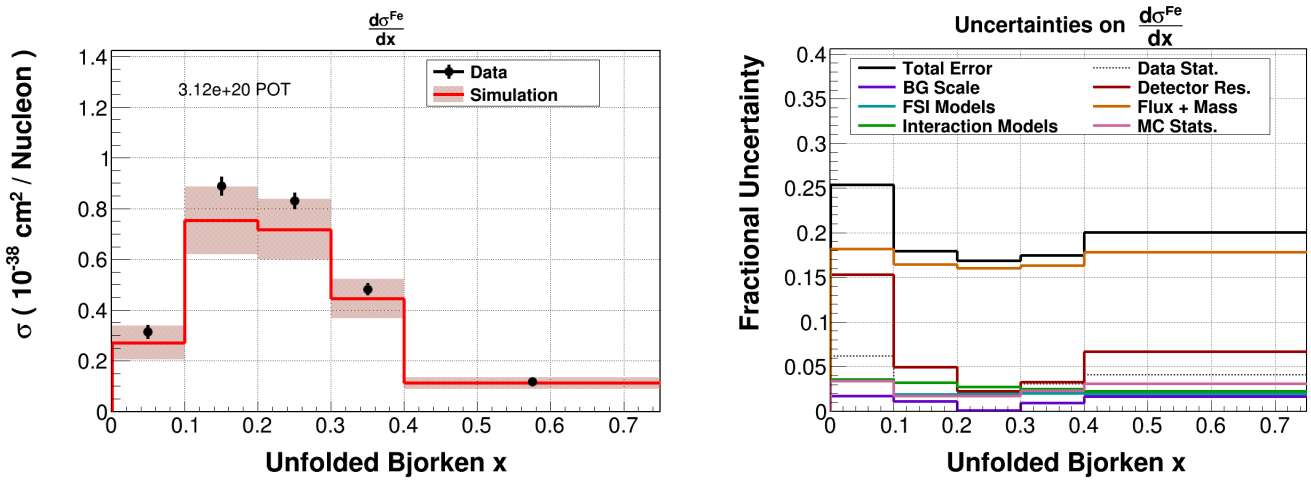

Figure 13-7. The total DIS cross section per nucleon on iron as a function of unfolded Bjorken-x for data (black points) and simulation (red line). The total systematic error is drawn as a red band around the simulation, and the breakdown of the systematic errors is drawn in the right hand plot.

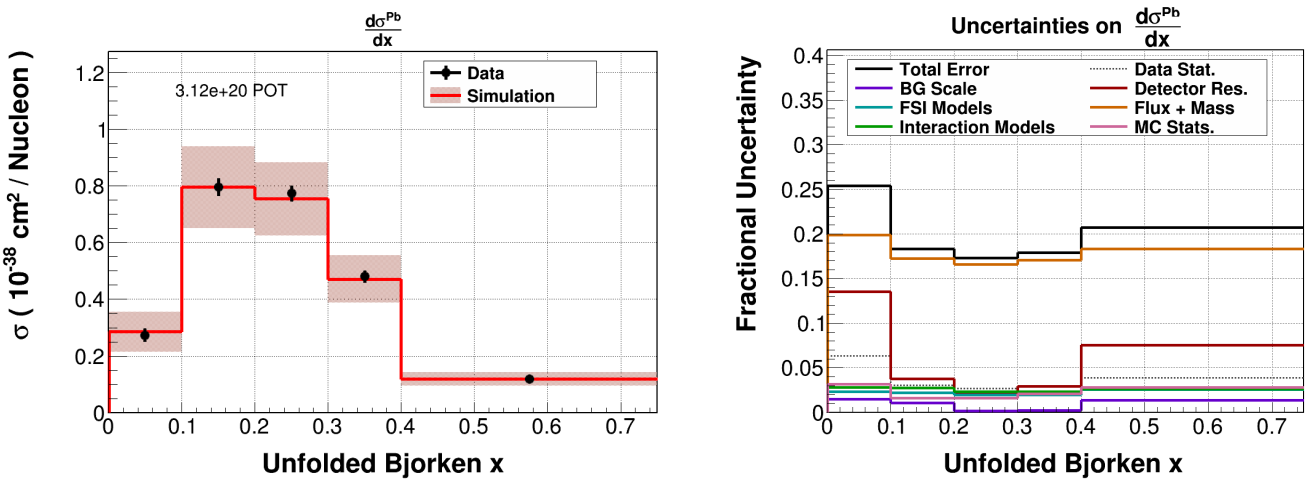

Figure 13-8. The total DIS cross section per nucleon on lead as a function of unfolded Bjorken-x for data (black points) and simulation (red line). The total systematic error is drawn as a red band around the simulation, and the breakdown of the systematic errors is drawn in the right hand plot.

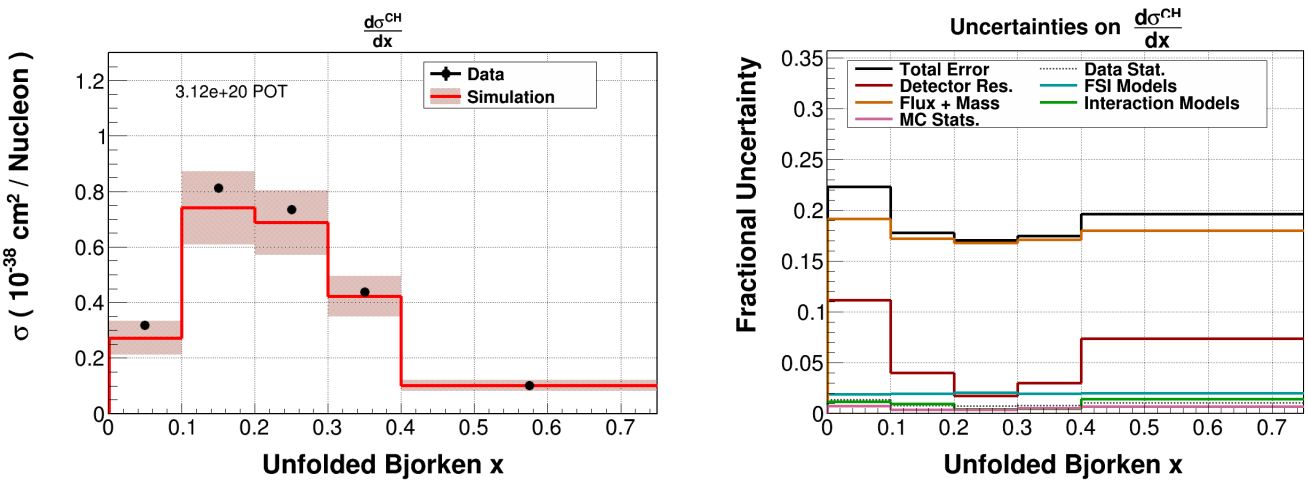

Figure 13-9. The total DIS cross section per nucleon on scintillator as a function of unfolded Bjorken-x for data (black points) and simulation (red line). The total systematic error is drawn as a red band around the simulation, and the breakdown of the systematic errors is drawn in the right hand plot.

13.3 Cross Section Ratios

In order to reduce uncertainties, especially the dominate flux uncertainty on the absolute cross sections, ratios of the total and differential cross sections are taken. The

ratios measured by the analysis are C, Fe, and Pb to CH. If the ratios of different nuclei show any differences between the data and MC, then that would be evidence of un-simulated nuclear effects.

The ratios of total cross sections of C, Fe and Pb to CH are plotted in Figures 13-10 through 13-12. In the case of total cross sections, we observe a smaller than expected ratio in one energy bin of the Pb / CH $\sigma(E_\nu)$, 20 to 25 GeV. This is consistent with a general trend of the data ratio in the heavier targets (Fe/CH and Pb/CH) being lower than the simulation at high energy. In contrast, the C to CH ratio at low energy (5 to 10 GeV) is somewhat large (1.5) with a large statistical uncertainty which is not inconsistent with the MC ratio of ≈ 1.1.

The x_{bj} differential ratios may be seen in Figures 13-13 through 13-15. In regards to the x_{bj}-differential ratios, there is a suggestion of a smaller than predicted Pb/CH ratio at low x_{bj} ($x_{bj} < 0.1$). This observation is consistent with additional nuclear shadowing in neutrino nuclear scattering. Interestingly enough, the data appear to have the same structure as the inclusive analysis; a deficit relative to the MC at low x_{bj} which vanishes as x_{bj} increases. However, the DIS analysis does not have sufficient sensitivity to say anything definite about these features.

In addition, the data excess at large x_{bj} observed by the inclusive analysis does not appear in the DIS analysis. This is due to the fact that large x_{bj} events are predominantly quasi-elastic and resonant, and fail the W and Q^2 criteria required for an event to be deeply inelastic. Instead, the data in the intermediate x_{bj} range ($0.4 < x_{bj} < 0.75$) are very consistent between the inclusive and DIS analyses.

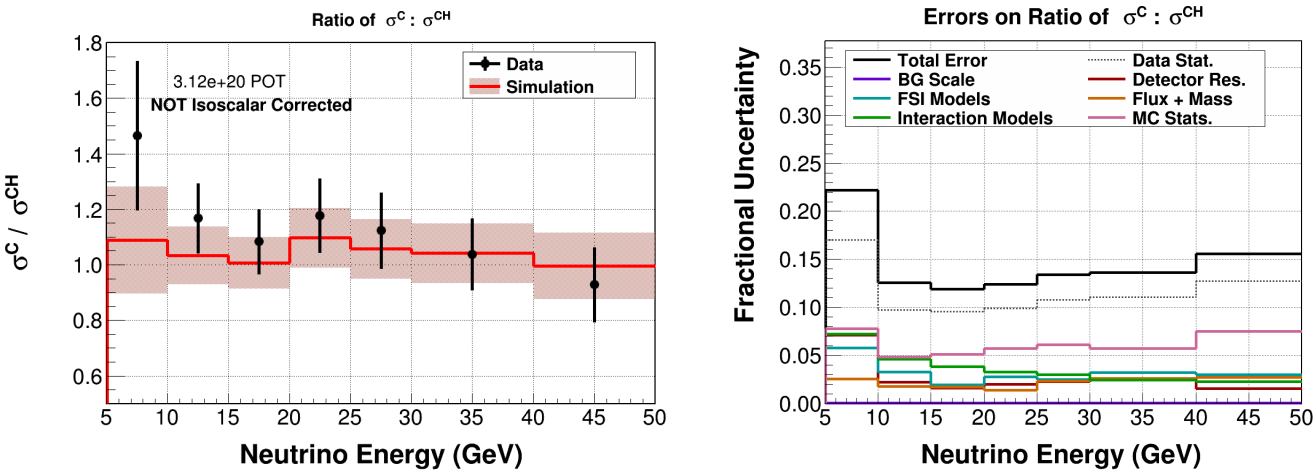

Figure 13-10. Ratio of the total DIS cross section on C divided by CH for data (black points) and simulation (red lines). The total systematic error is drawn as a red band around the simulation, and the breakdown of the systematic errors is drawn in the right hand plot.

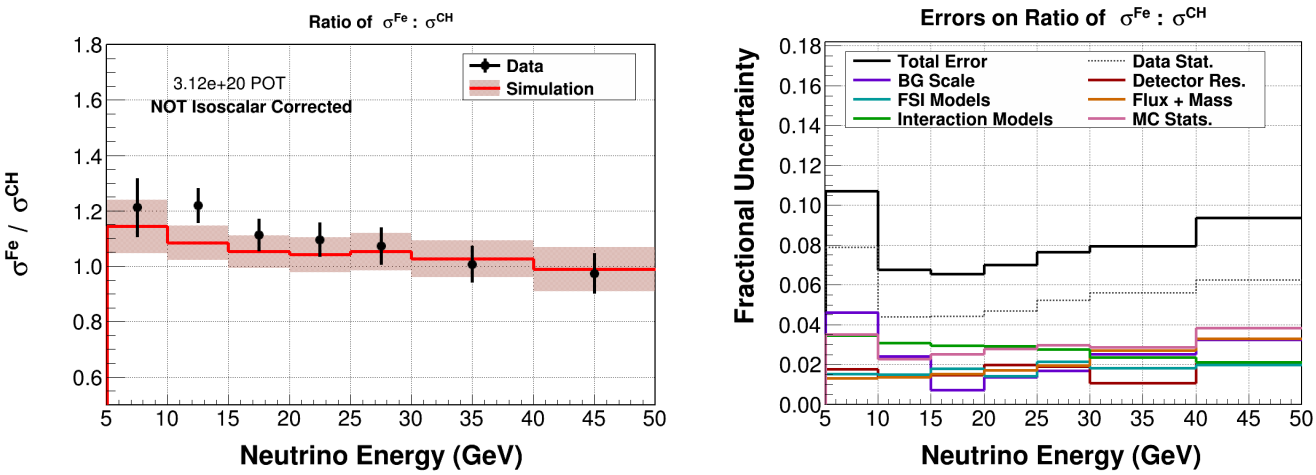

Figure 13-11. Ratio of the total DIS cross section on Fe divided by CH for data (black points) and simulation (red lines). The total systematic error is drawn as a red band around the simulation, and the breakdown of the systematic errors is drawn in the right hand plot.

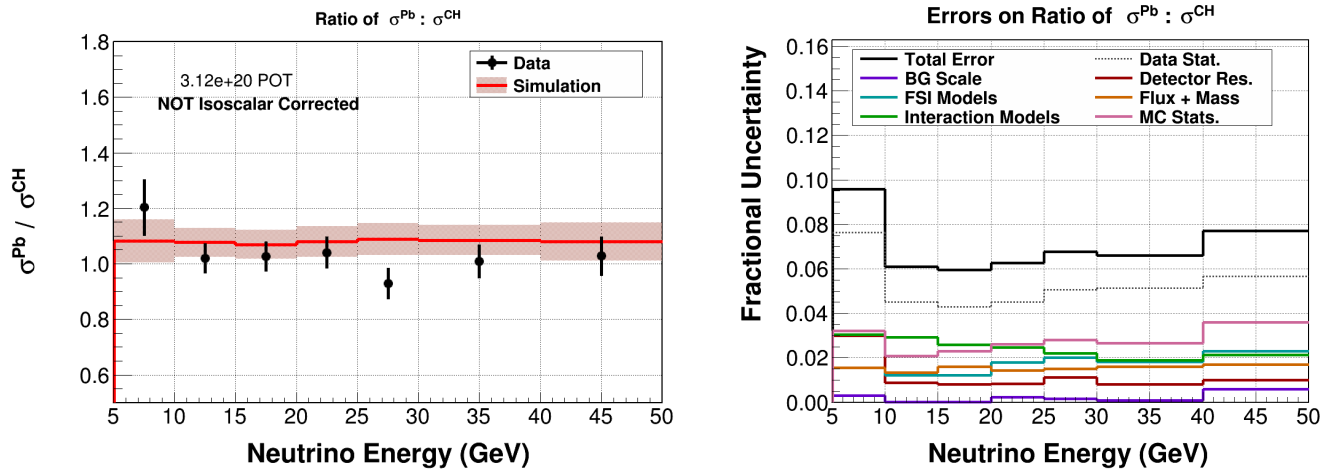

Figure 13-12. Ratio of the total DIS cross section on Pb divided by CH for data (black points) and simulation (red lines). The total systematic error is drawn as a red band around the simulation, and the breakdown of the systematic errors is drawn in the right hand plot.

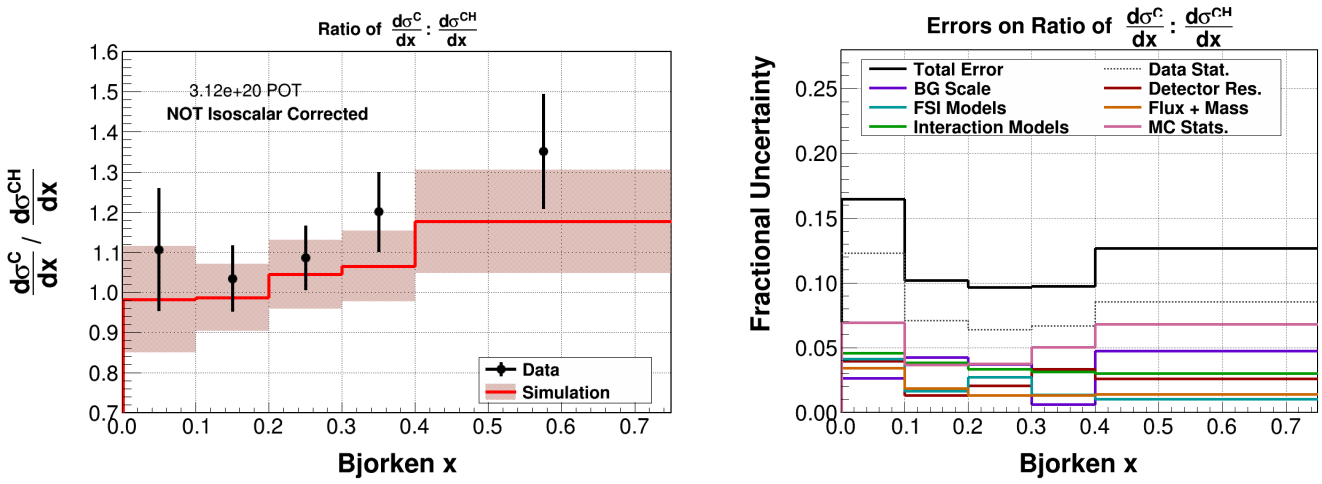

Figure 13-13. Ratio of the x_{bj}-differential DIS cross section on C divided by CH for data (black points) and simulation (red lines). The total systematic error is drawn as a red band around the simulation, and the breakdown of the systematic errors is drawn in the right hand plot.

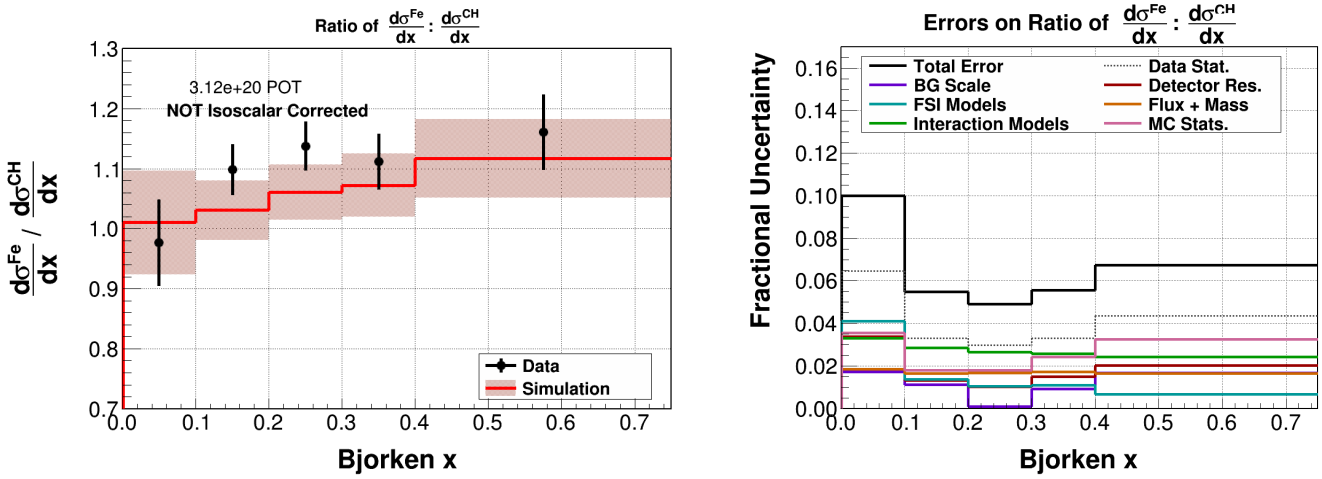

Figure 13-14. Ratio of the x_{bj}-differential DIS cross section on Fe divided by CH for data (black points) and simulation (red lines). The total systematic error is drawn as a red band around the simulation, and the breakdown of the systematic errors is drawn in the right hand plot.

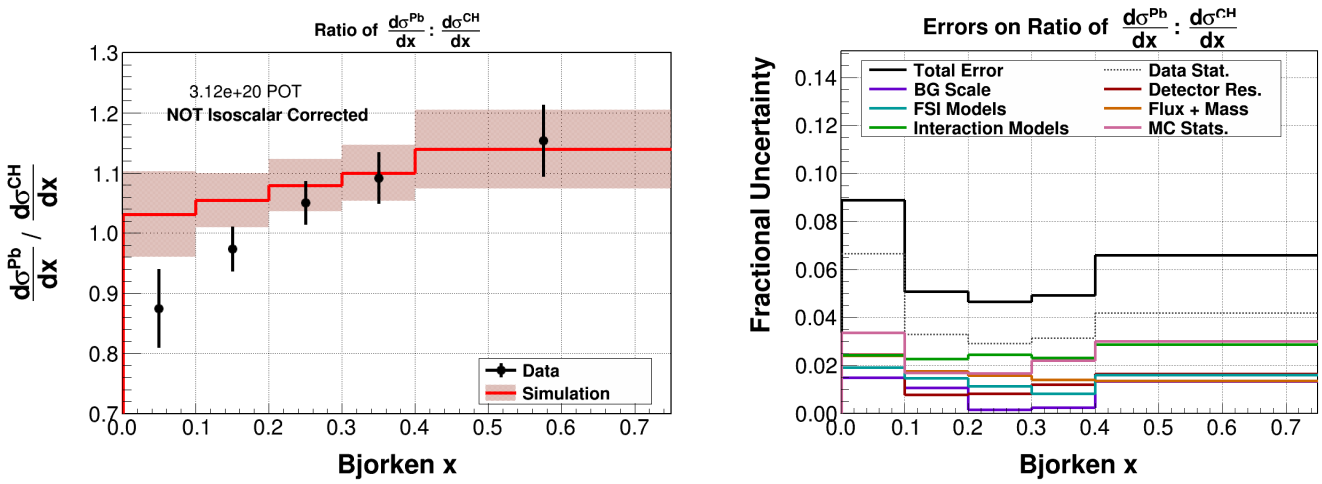

Figure 13-15. Ratio of the x_{bj}-differential DIS cross section on Pb divided by CH for data (black points) and simulation (red lines). The total systematic error is drawn as a red band around the simulation, and the breakdown of the systematic errors is drawn in the right hand plot.

CHAPTER 14
CONCLUSIONS

Starting from the nuclear charged current inclusive analysis, a deep inelastic sample is isolated by requiring reconstructed $Q^2 \geq 1.0$ (GeV/c)^2 and $W \geq 2.0$ GeV/c^2. The energy range of the analysis was extended from $2 < E_\nu < 20$ GeV to $5 < E_\nu < 50$ GeV. A series of updated MINOS and upstream energy cuts were developed to better account for the higher muon and hadronic energy DIS events. After subtracting non-DIS and plastic backgrounds, the reconstructed neutrino energy and Bjorken-x are transformed to their true quantities by using Bayesian unfolding. The unfolded distributions of C, Fe and Pb are divided by the unfolded CH distributions. This division serves to reduce the uncertainties inherent to the flux simulation.

The results of the analysis were a lower than expected Pb / CH ratio at large neutrino energy ($E_\nu > 20$ GeV) and low Bjorken-x ($x_{bj} < 0.1$). The low x_{bj} deficit is consistent with the deficit observed in the inclusive analysis [65]. This deficit is suggestive of additional nuclear shadowing in lead for neutrino-nucleon scattering versus charged lepton-nucleon scattering. The data of the other nuclei, carbon and iron, did not demonstrate any significant differences from the MC. This is the case across the x_{bj} and E_ν region.

The ratios of all three nuclei carbon, iron, and lead, display very good agreement in the largest x_{bj} bin $0.4 \leq x_{bj} < 0.75$. This bin corresponds to the region where the dominant nuclear effect is the EMC effect. As GENIE simulates the EMC effect for neutrinos identically as charged leptons, the data imply the differences between the EMC effect in charged leptons and neutrinos are minimal. At the very least, the potential differences between these two effects must be smaller than the MINERνA data can resolve.

None of the differences from the data and MC observed have significances greater than 3σ. Neutrino running in the NuMI medium energy range will provide additional statistics, and will enable future measurements of these effects with greater precision.

APPENDIX A
SIDEBAND PLOTS

A.1 Low W Sideband: $Q^2 \geq 1.0$ (GeV/c)^2 $1.3 \leq W < 1.8$ GeV/c^2 (Before Fitting)

The following plots show the population of the low W sideband ($Q^2 \geq 1.0$ (GeV/c)^2 $1.3 \leq W < 1.8$ GeV/c^2) *before* tuning to data as a function of neutrino energy (E_ν):

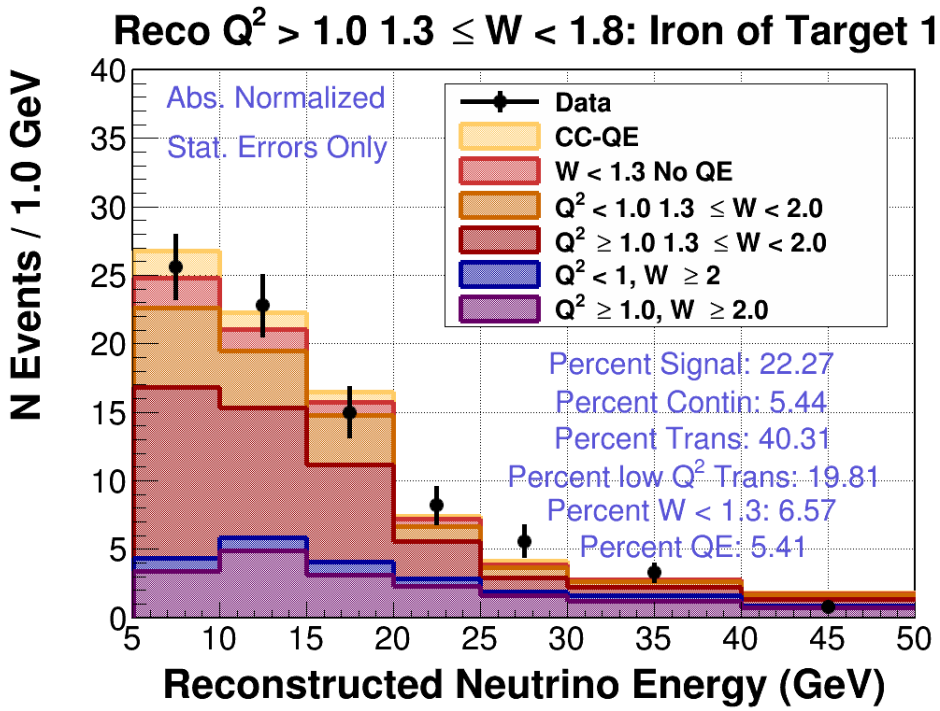

Figure A-1. Data / MC low W sideband before fitting: target 01 Fe (E_ν)

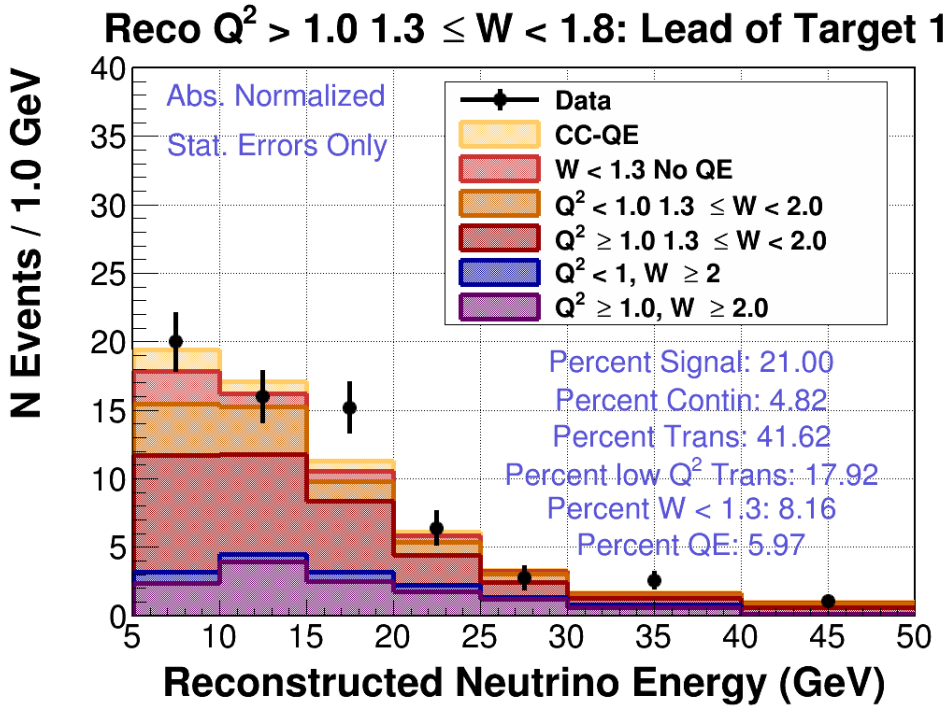

Figure A-2. Data / MC low W sideband before fitting: target 01 Pb (E_ν)

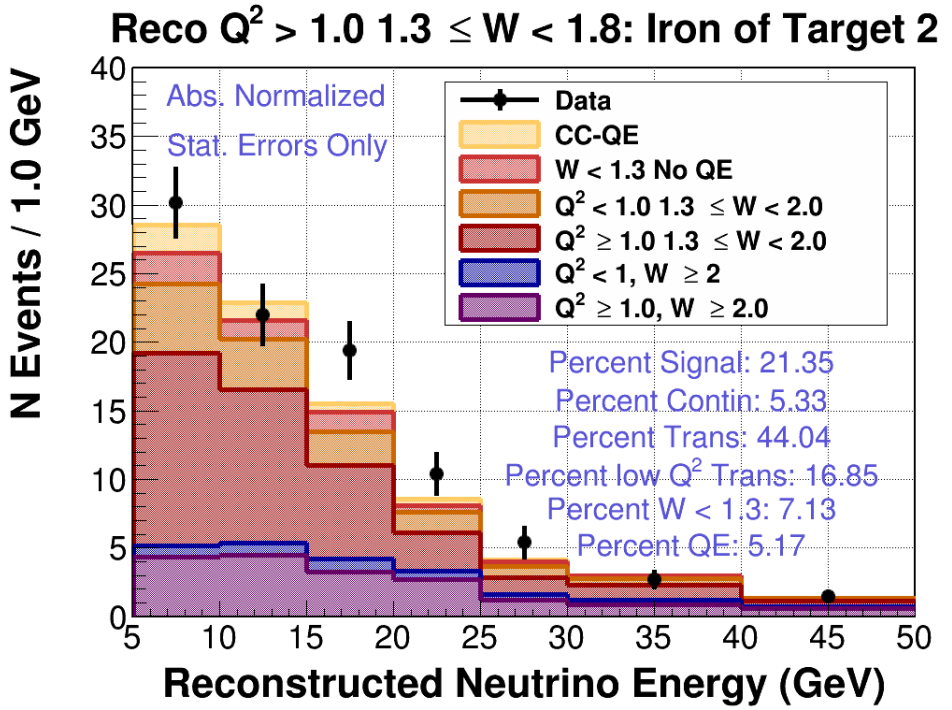

Figure A-3. Data / MC low W sideband before fitting: target 02 Fe (E_ν)

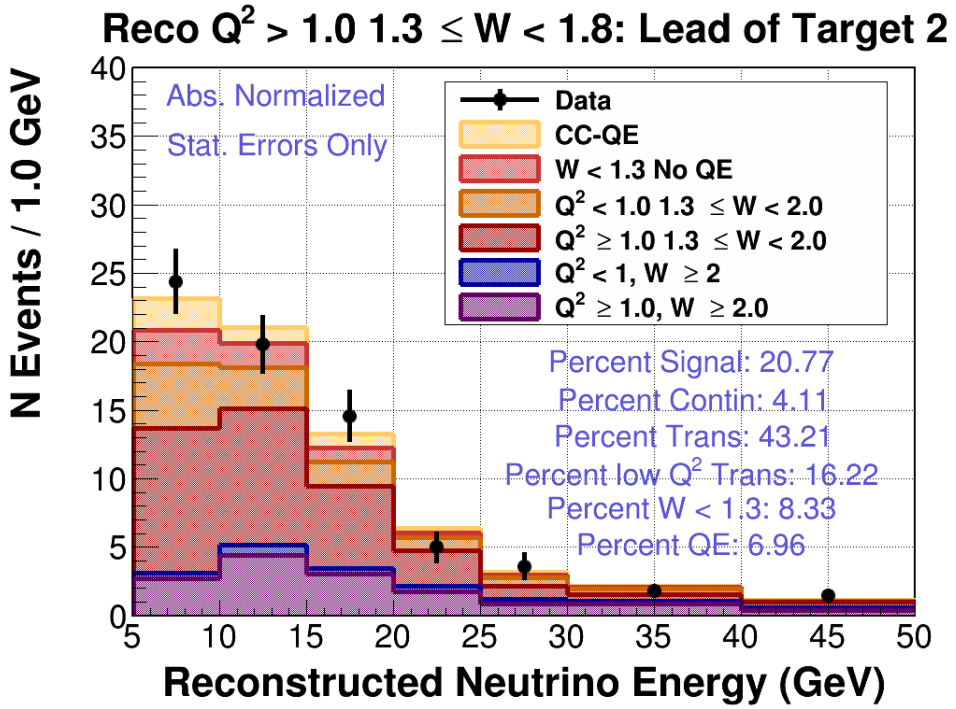

Figure A-4. Data / MC low W sideband before fitting: target 02 Pb (E_ν)

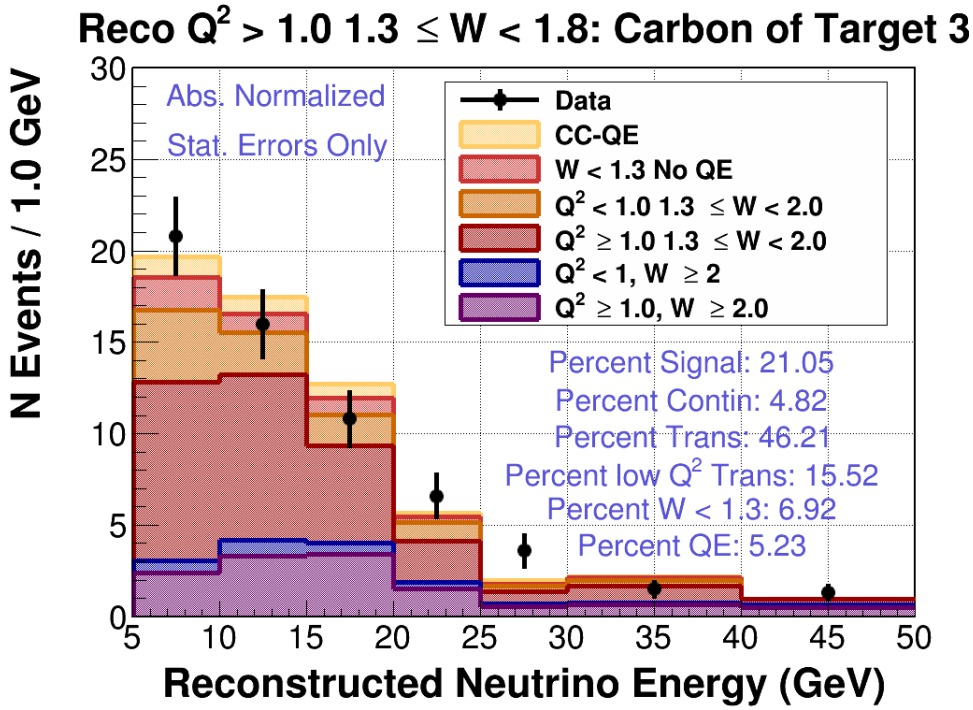

Figure A-5. Data / MC low W sideband before fitting: target 03 C (E_ν)

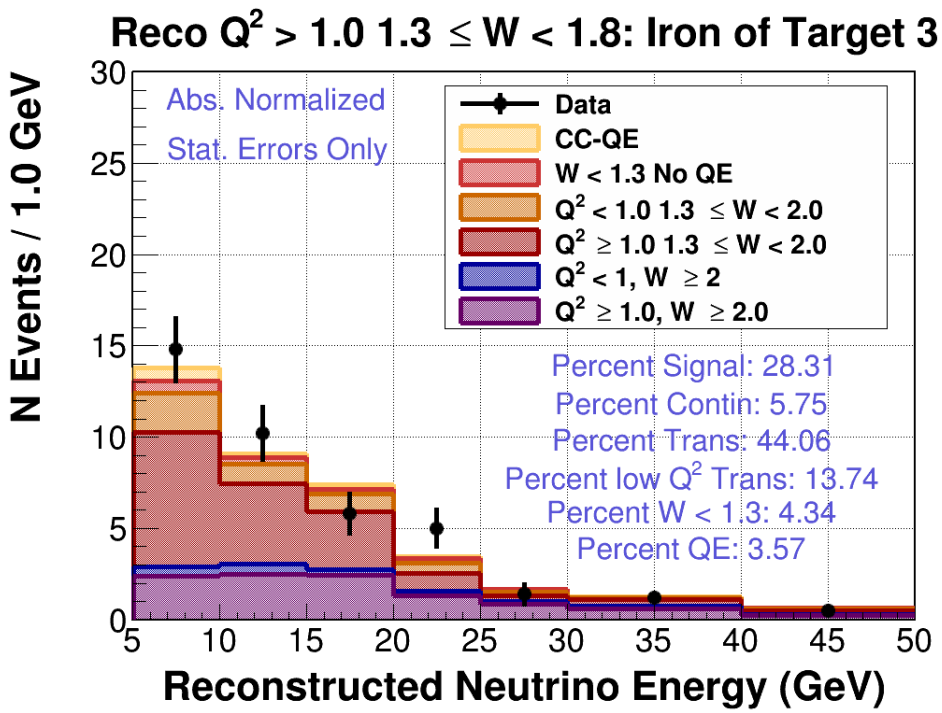

Figure A-6. Data / MC low W sideband before fitting: target 03 Fe (E_ν)

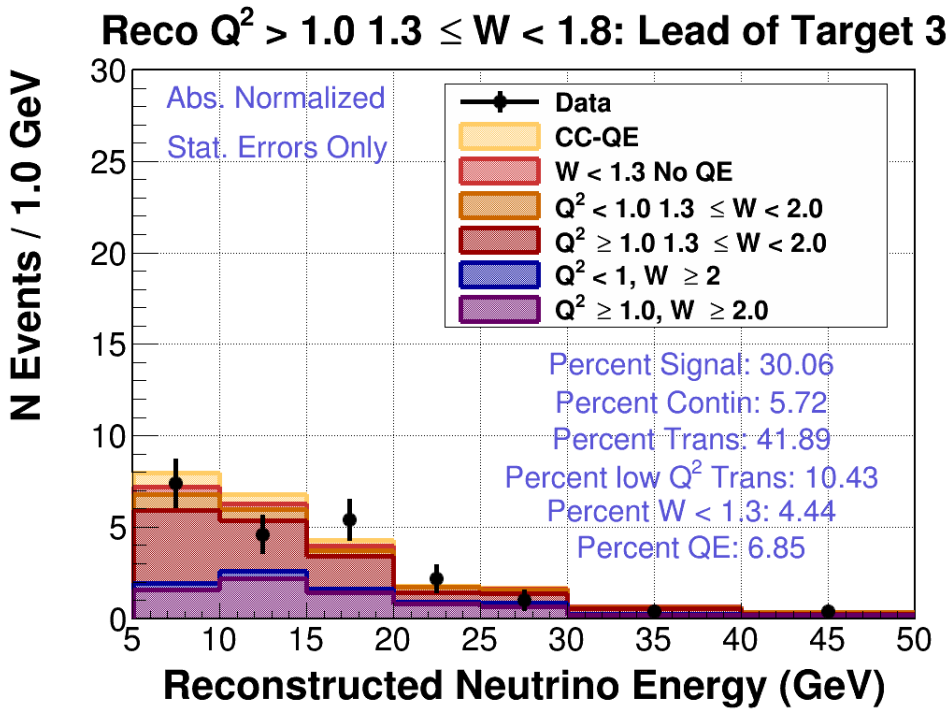

Figure A-7. Data / MC low W sideband before fitting: target 03 Pb (E_ν)

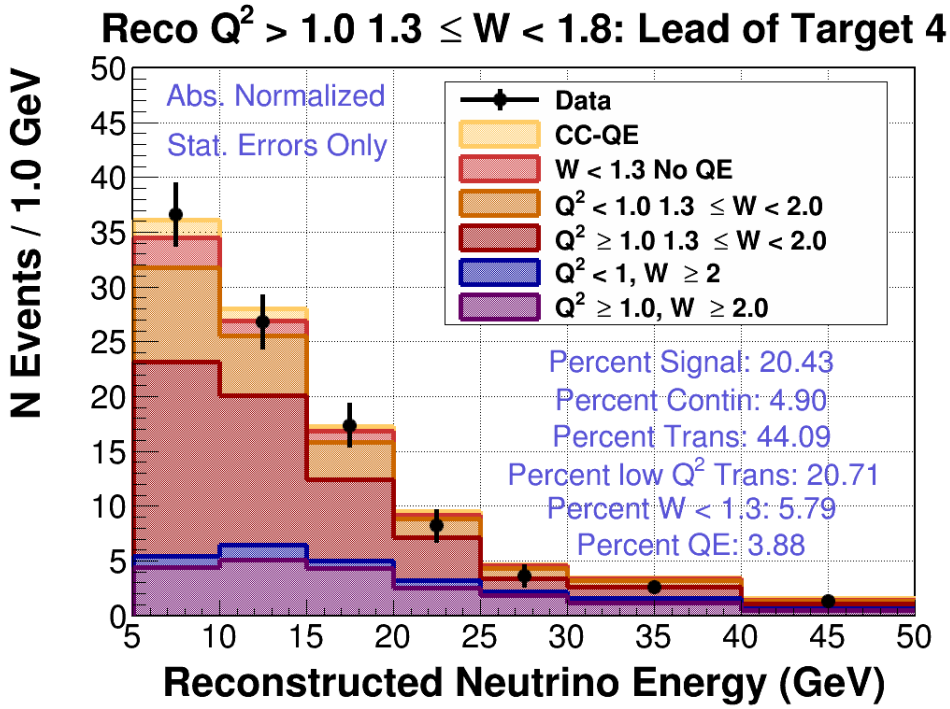

Figure A-8. Data / MC low W sideband before fitting: target 04 Pb (E_ν)

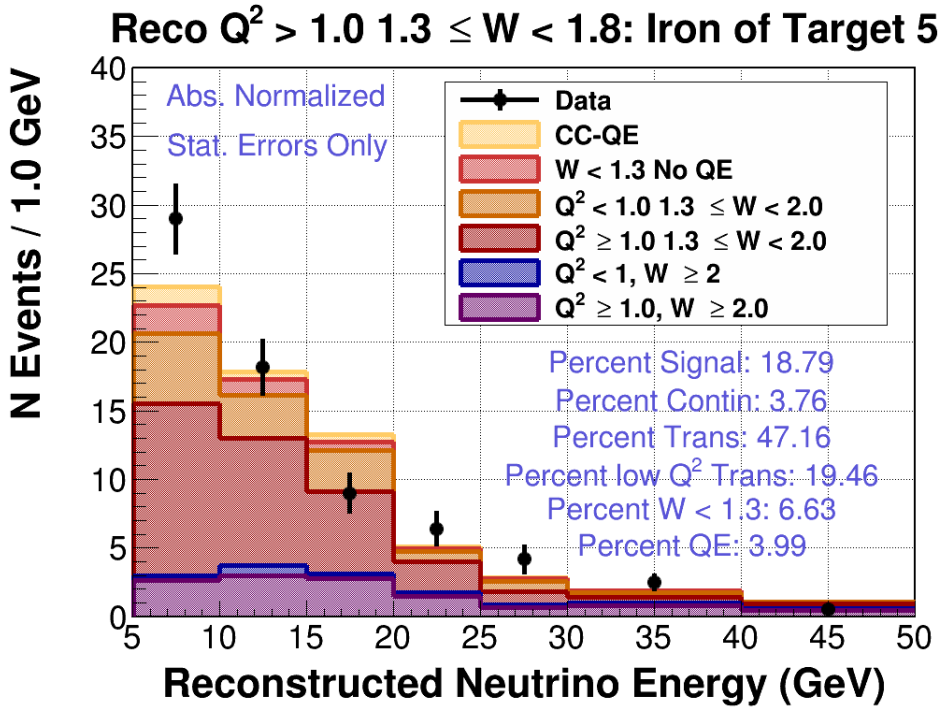

Figure A-9. Data / MC low W sideband before fitting: target 05 Fe (E_ν)

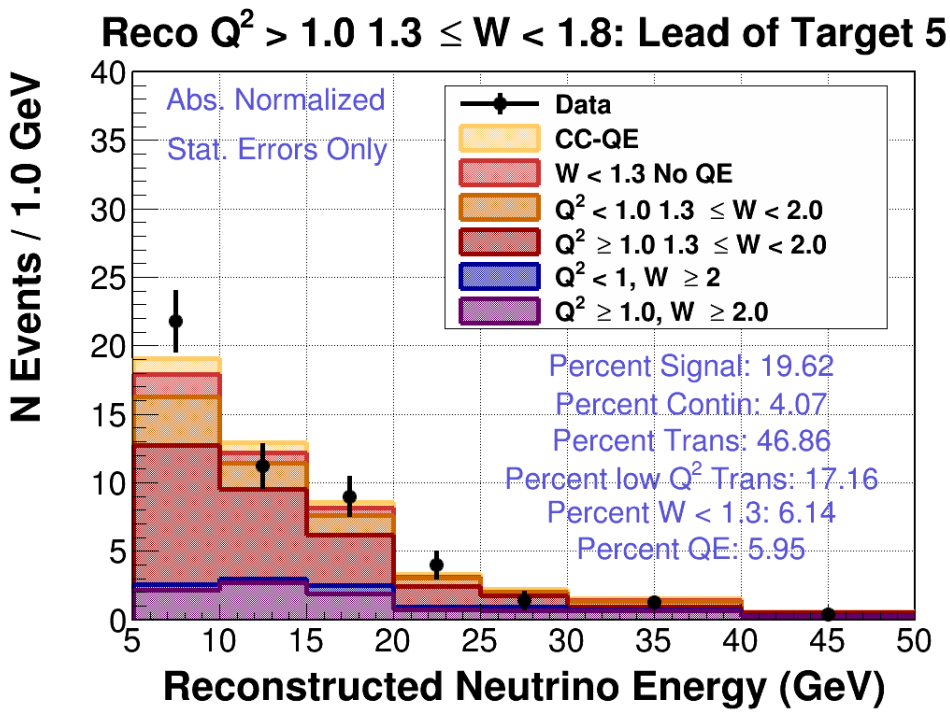

Figure A-10. Data / MC low W sideband before fitting: target 05 Pb (E_ν)

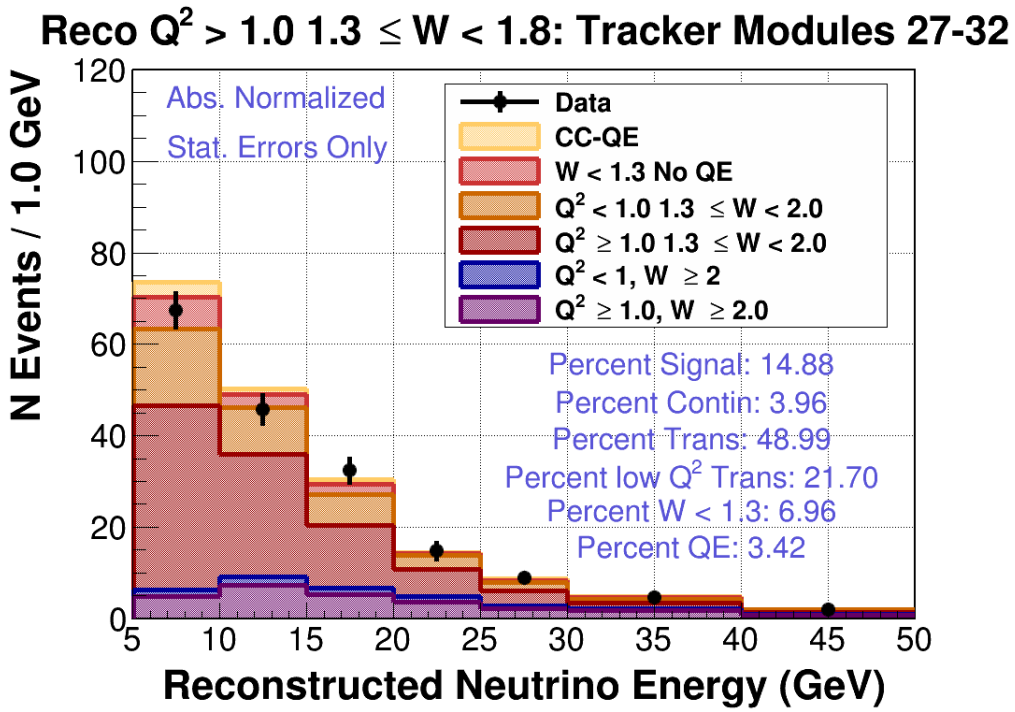

Figure A-11. Data / MC low W sideband before fitting: tracker mods. 27-32 (E_ν)

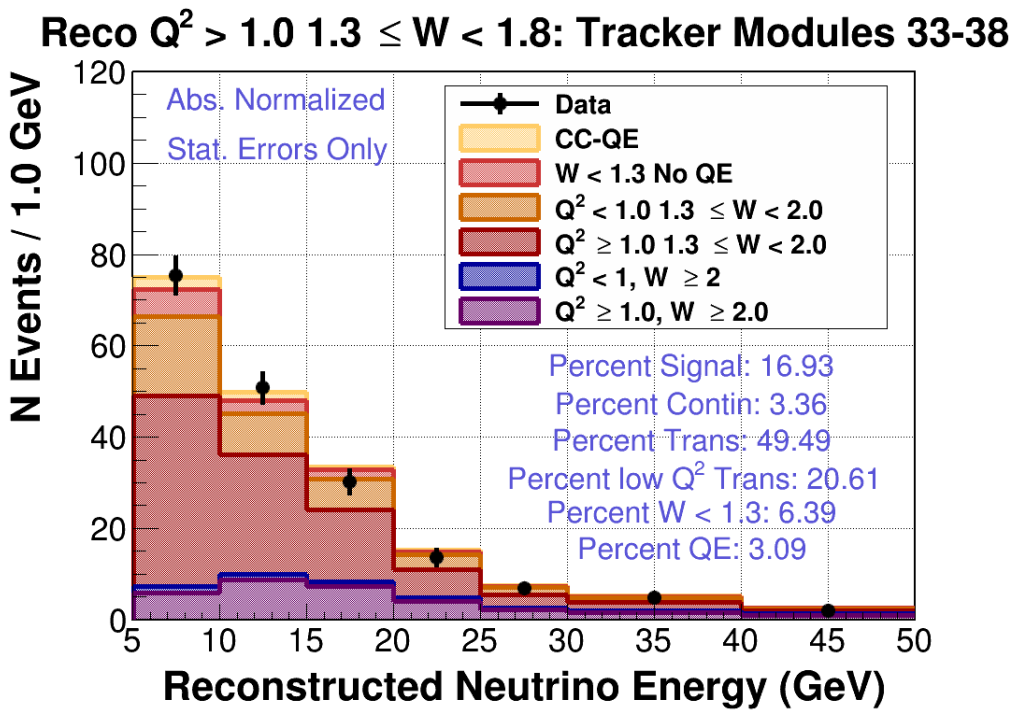

Figure A-12. Data / MC low W sideband before fitting: tracker mods. 33-38 (E_ν)

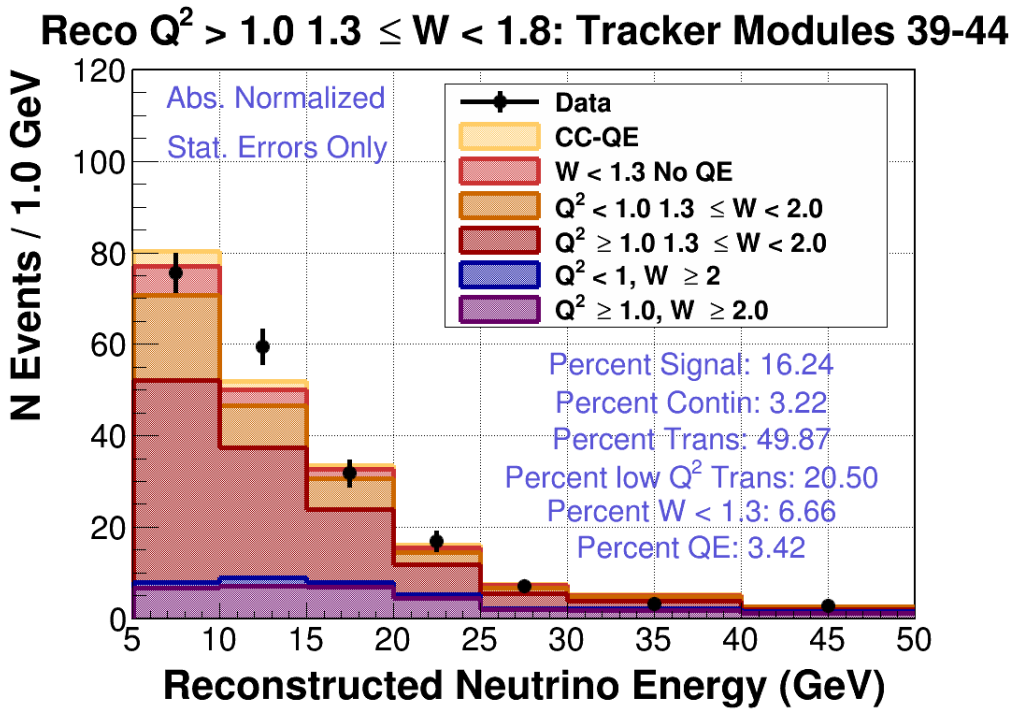

Figure A-13. Data / MC low W sideband before fitting: tracker mods. 39-44 (E_ν)

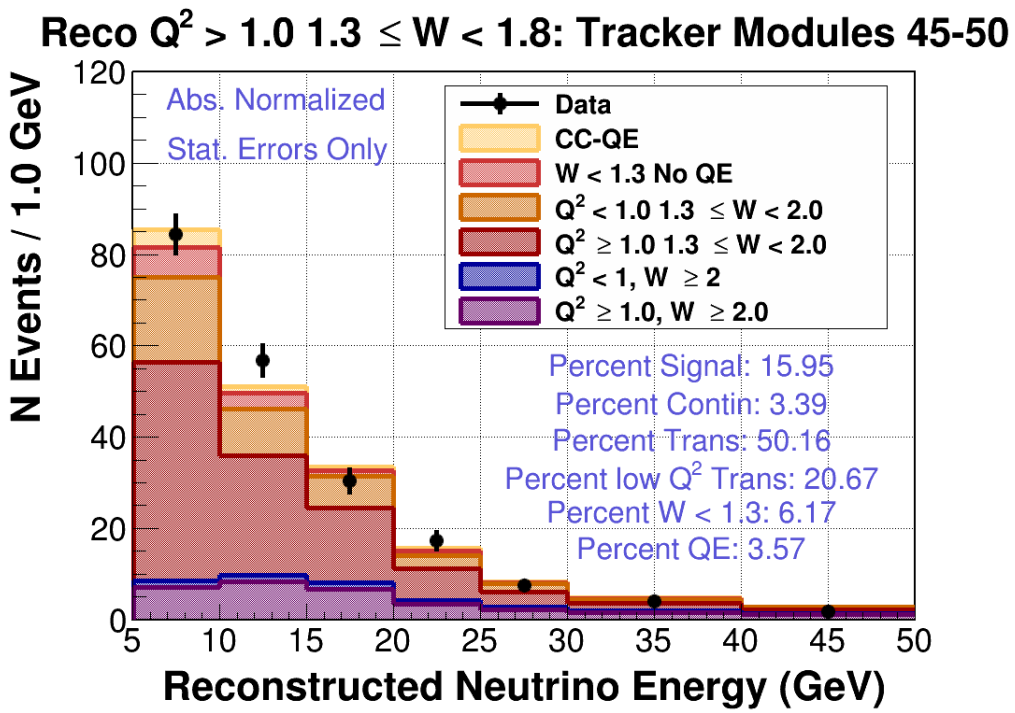

Figure A-14. Data / MC low W sideband before fitting: tracker mods. 45-50 (E_ν)

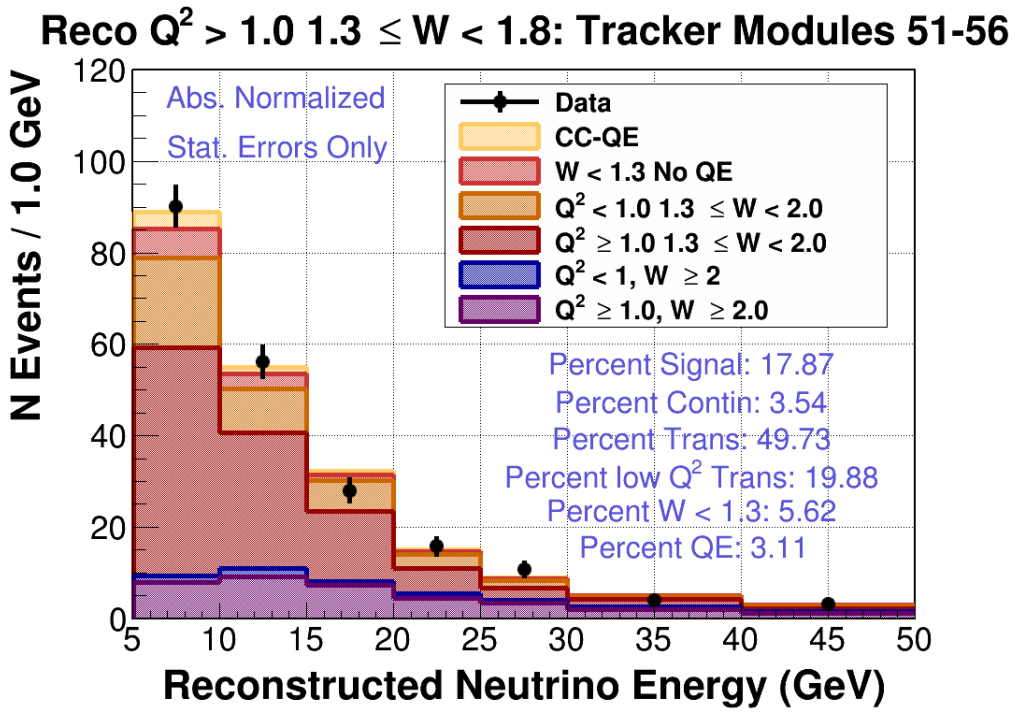

Figure A-15. Data / MC low W sideband before fitting: tracker mods. 51-56 (E_ν)

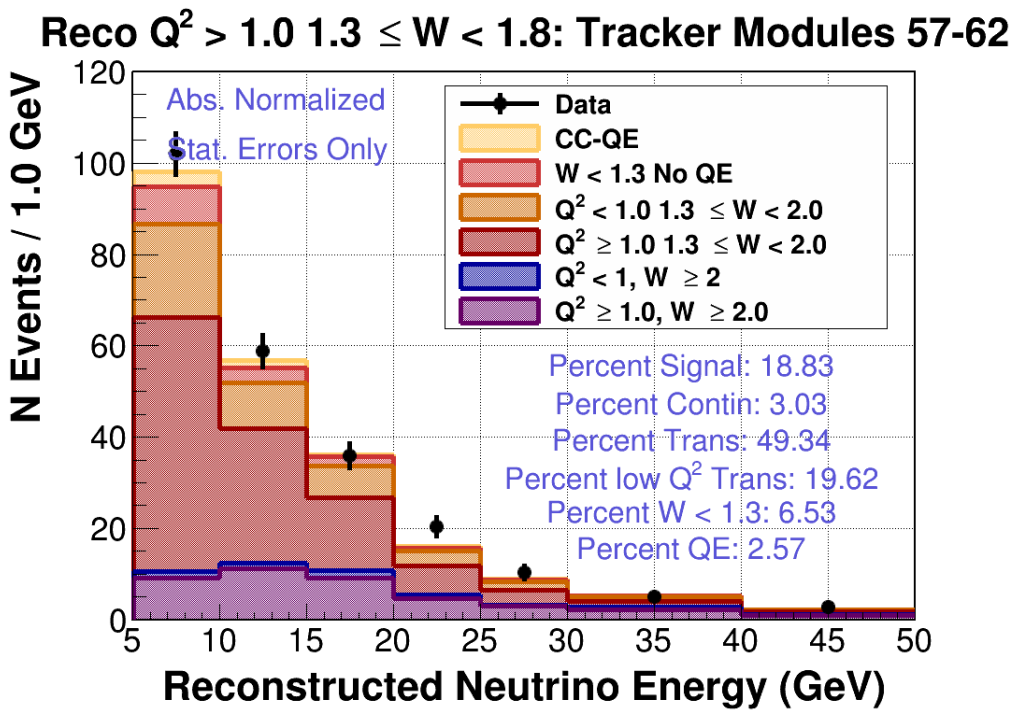

Figure A-16. Data / MC low W sideband before fitting: tracker mods. 57-62 (E_ν)

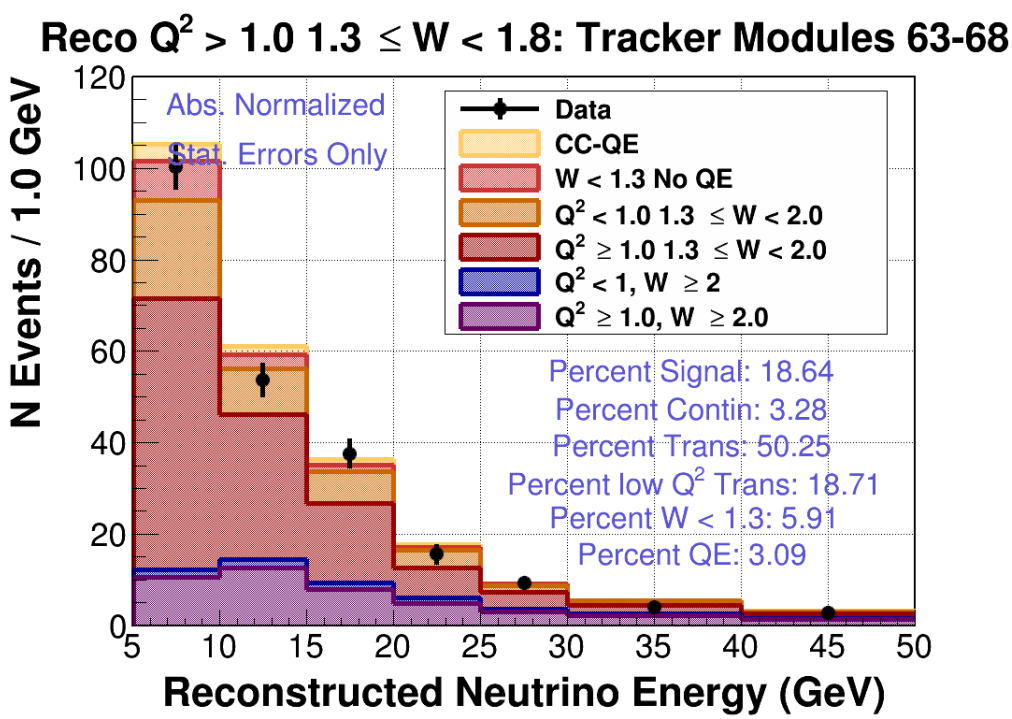

Figure A-17. Data / MC low W sideband before fitting: tracker mods. 63-68 (E_ν)

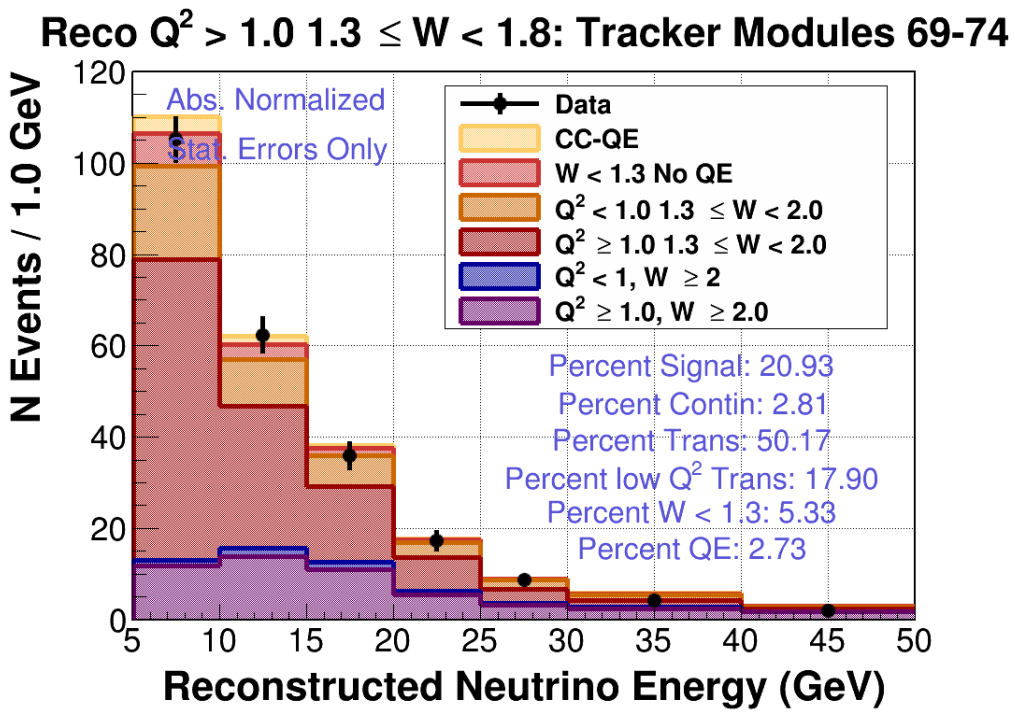

Figure A-18. Data / MC low W sideband before fitting: tracker mods. 69-74 (E_ν)

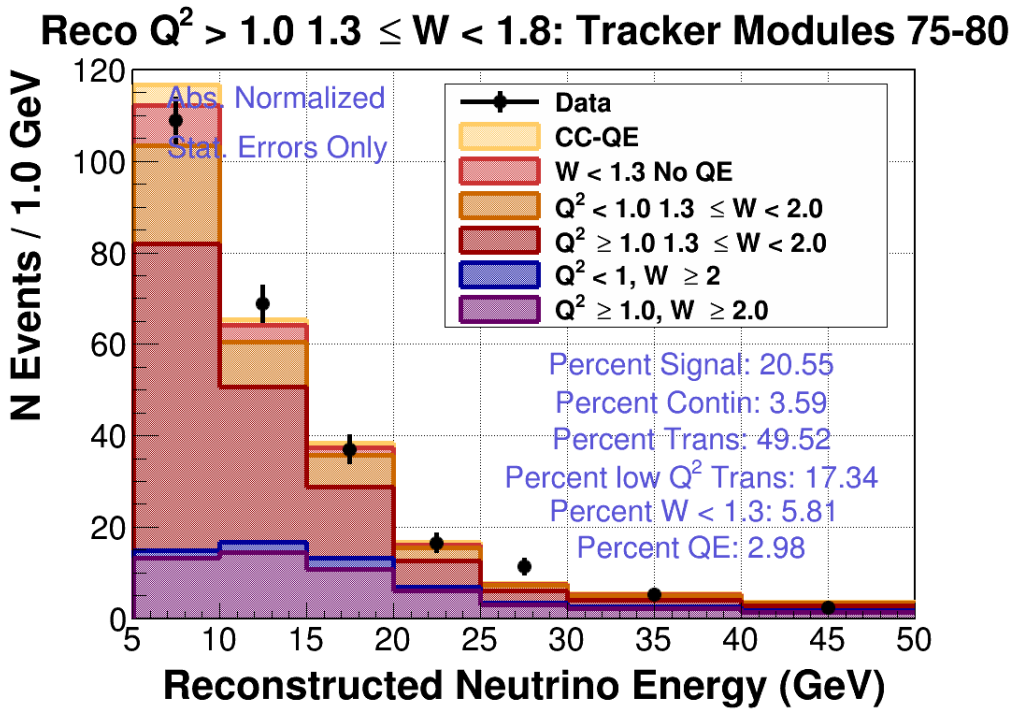

Figure A-19. Data / MC low W sideband before fitting: tracker mods. 75-80 (E_ν)

The following plots show the population of the low W sideband ($Q^2 \geq 1.0$ (GeV/c)^2 $1.3 \leq W < 1.8$ GeV/c^2) *before* tuning to data as a function of four momentum transfer squared (Q^2):

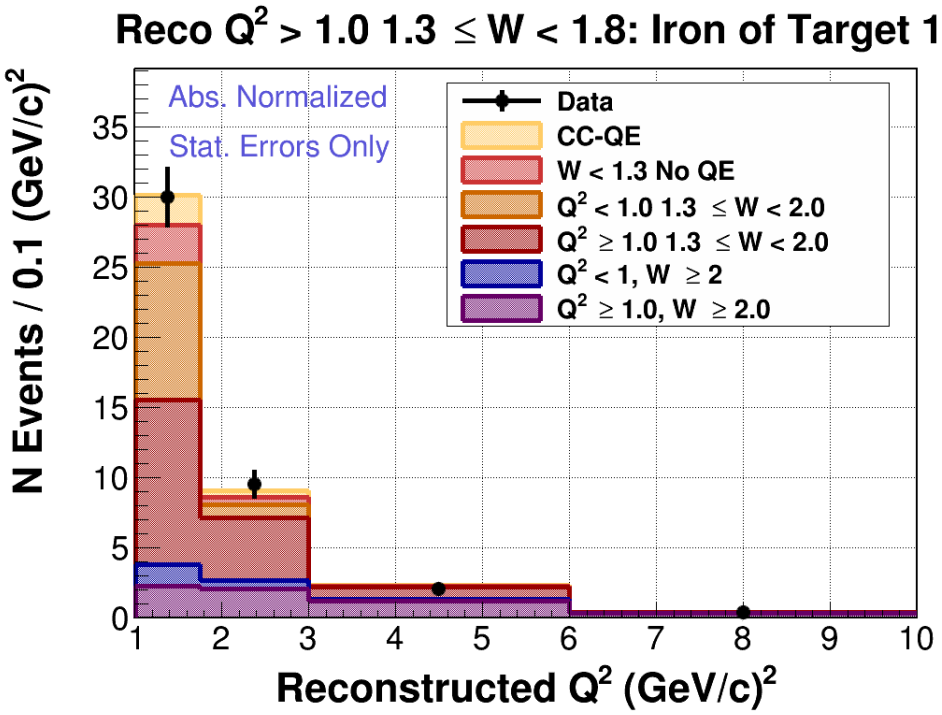

Figure A-20. Data / MC low W sideband before fitting: target 01 Fe (Q^2)

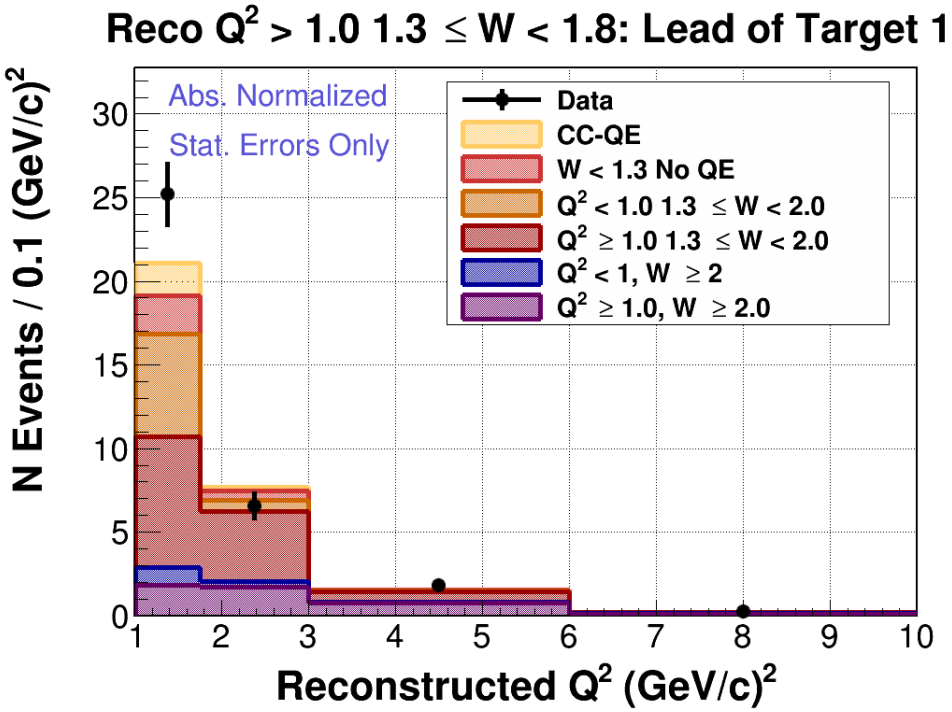

Figure A-21. Data / MC low W sideband before fitting: target 01 Pb (Q^2)

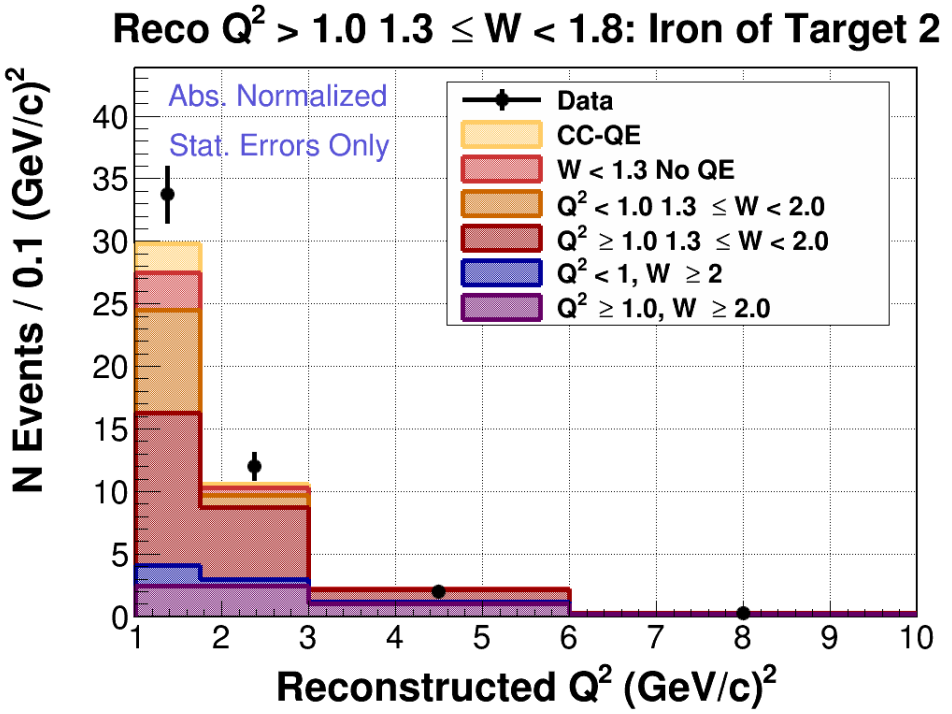

Figure A-22. Data / MC low W sideband before fitting: target 02 Fe (Q^2)

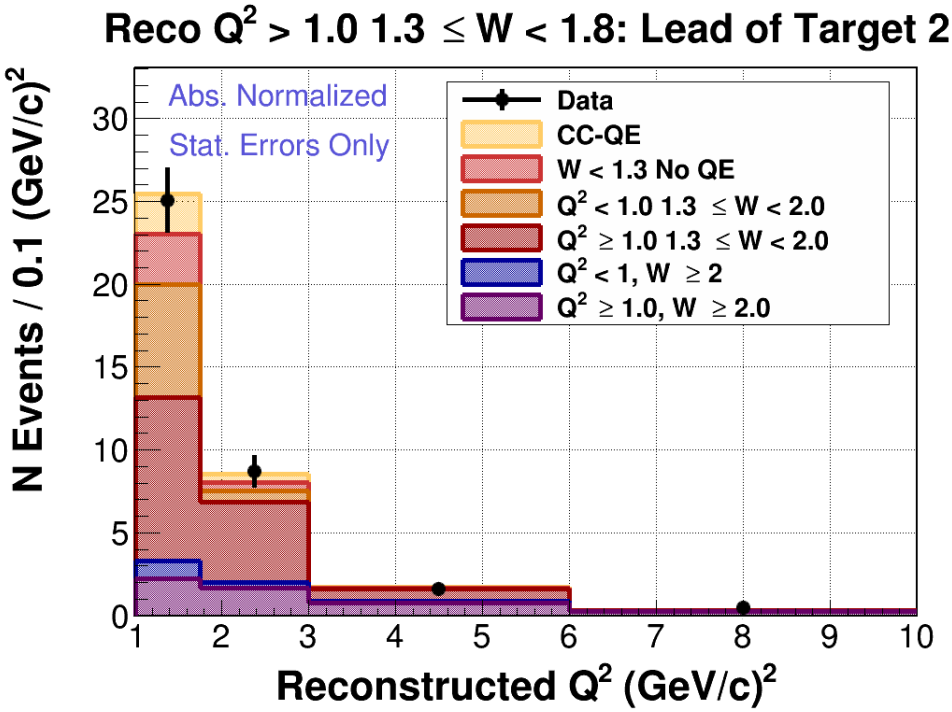

Figure A-23. Data / MC low W sideband before fitting: target 02 Pb (Q^2)

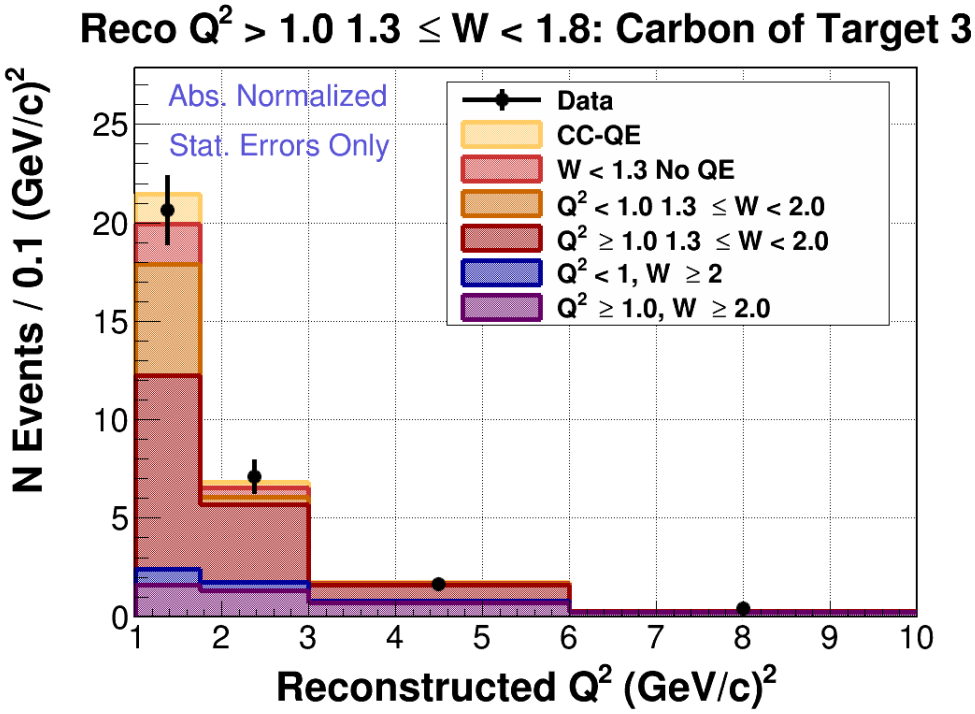

Figure A-24. Data / MC low W sideband before fitting: target 03 C (Q^2)

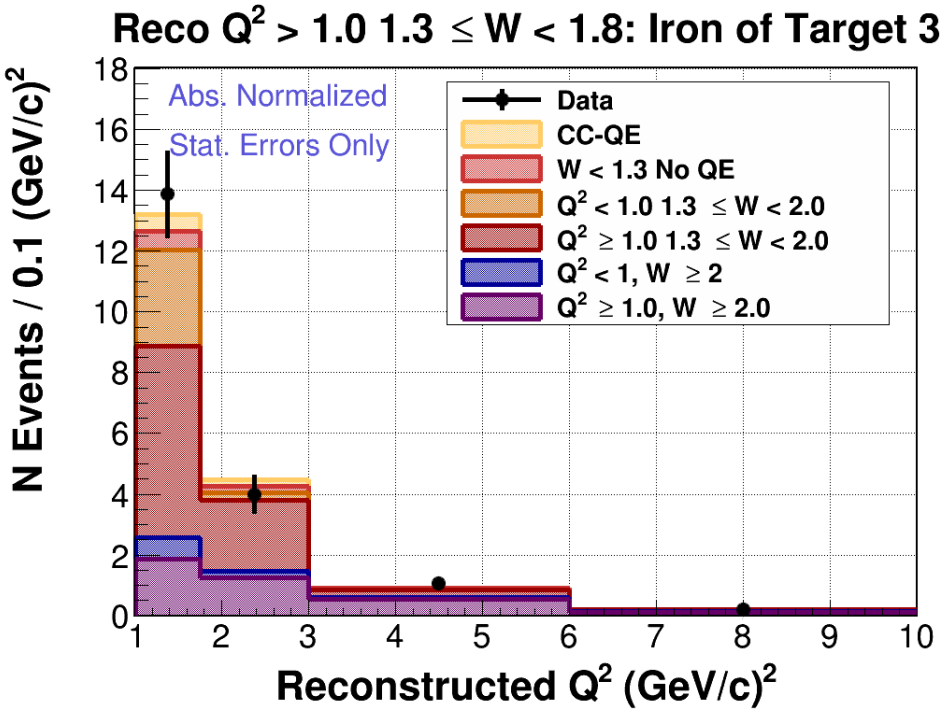

Figure A-25. Data / MC low W sideband before fitting: target 03 Fe (Q^2)

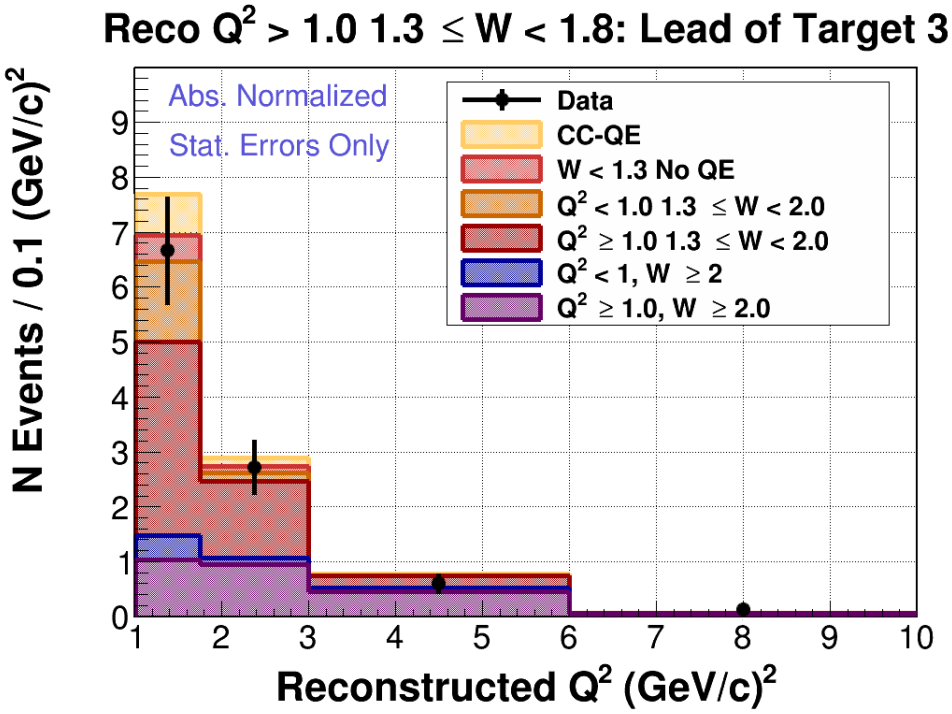

Figure A-26. Data / MC low W sideband before fitting: target 03 Pb (Q^2)

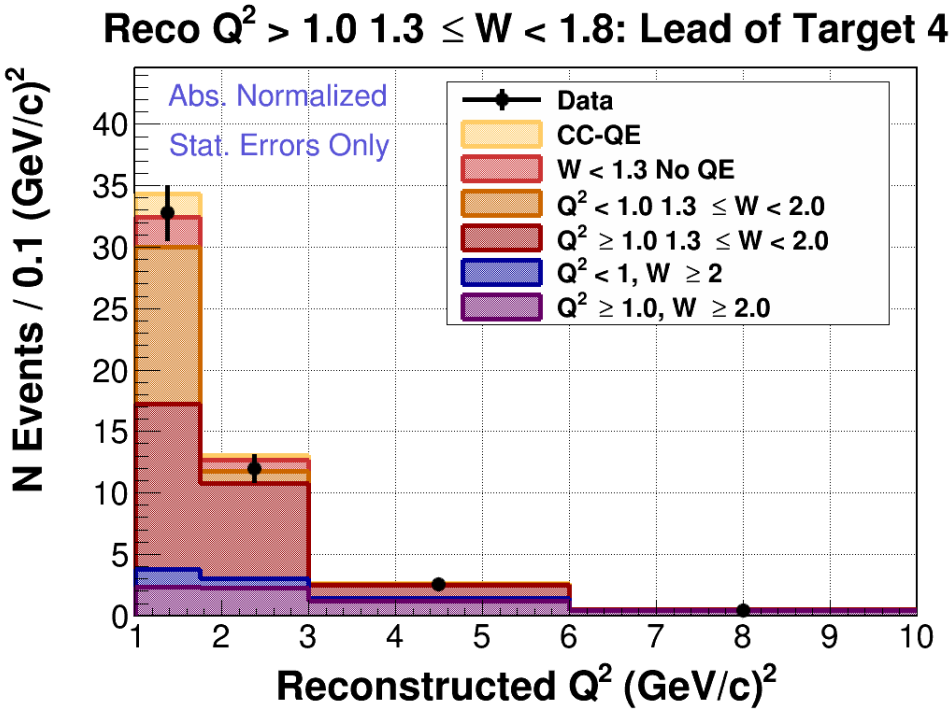

Figure A-27. Data / MC low W sideband before fitting: target 04 Pb (Q^2)

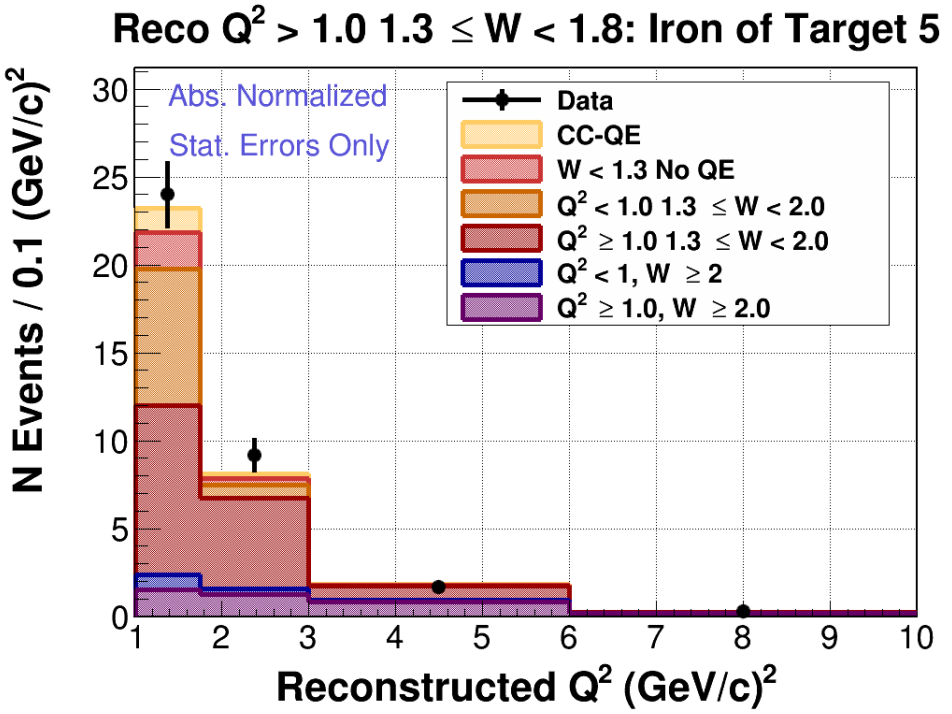

Figure A-28. Data / MC low W sideband before fitting: target 05 Fe (Q^2)

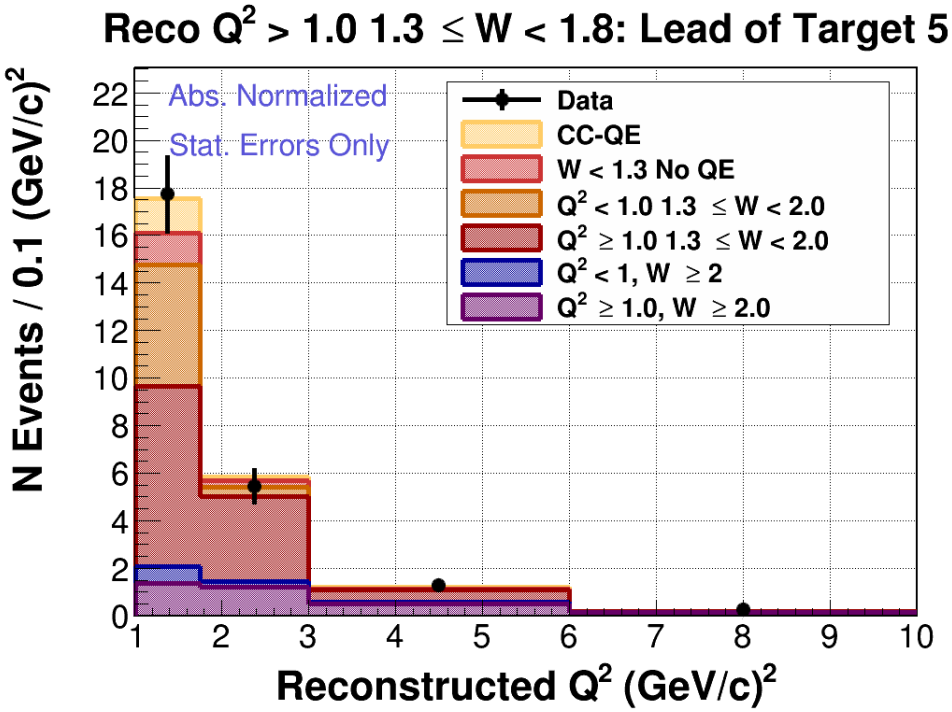

Figure A-29. Data / MC low W sideband before fitting: target 05 Pb (Q^2)

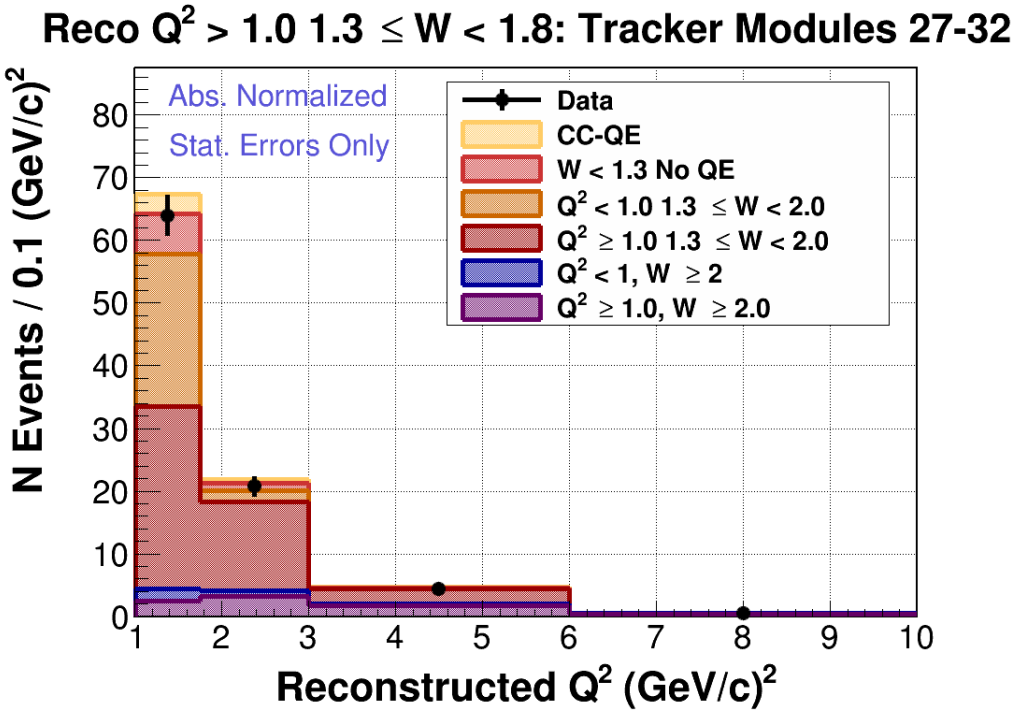

Figure A-30. Data / MC low W sideband before fitting: tracker mods. 27-32 (Q^2)

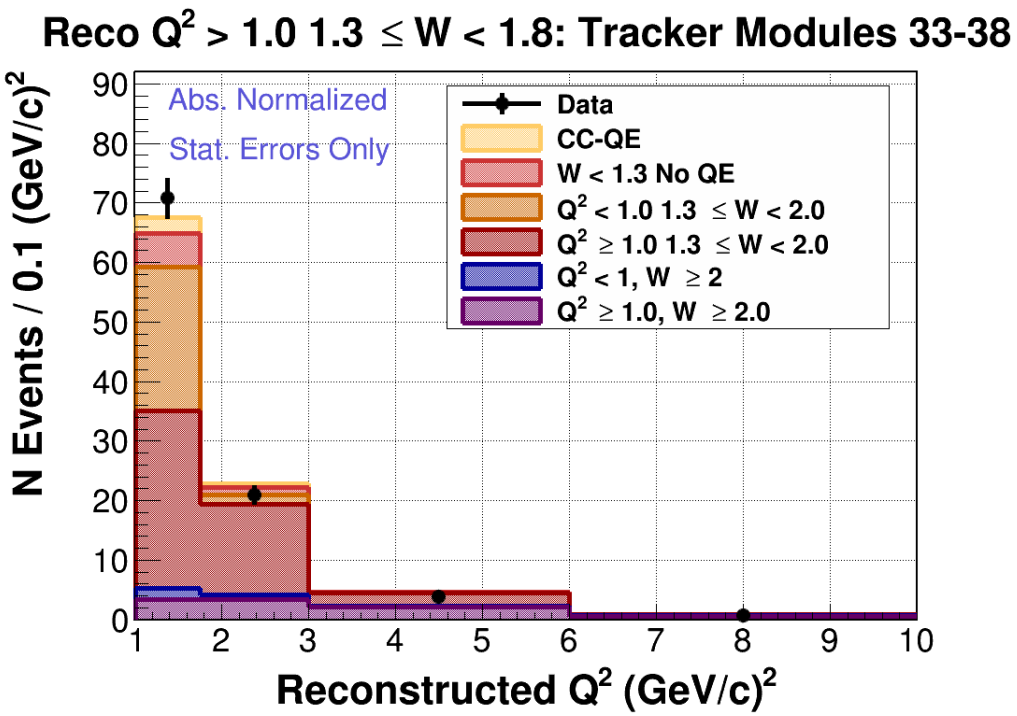

Figure A-31. Data / MC low W sideband before fitting: tracker mods. 33-38 (Q^2)

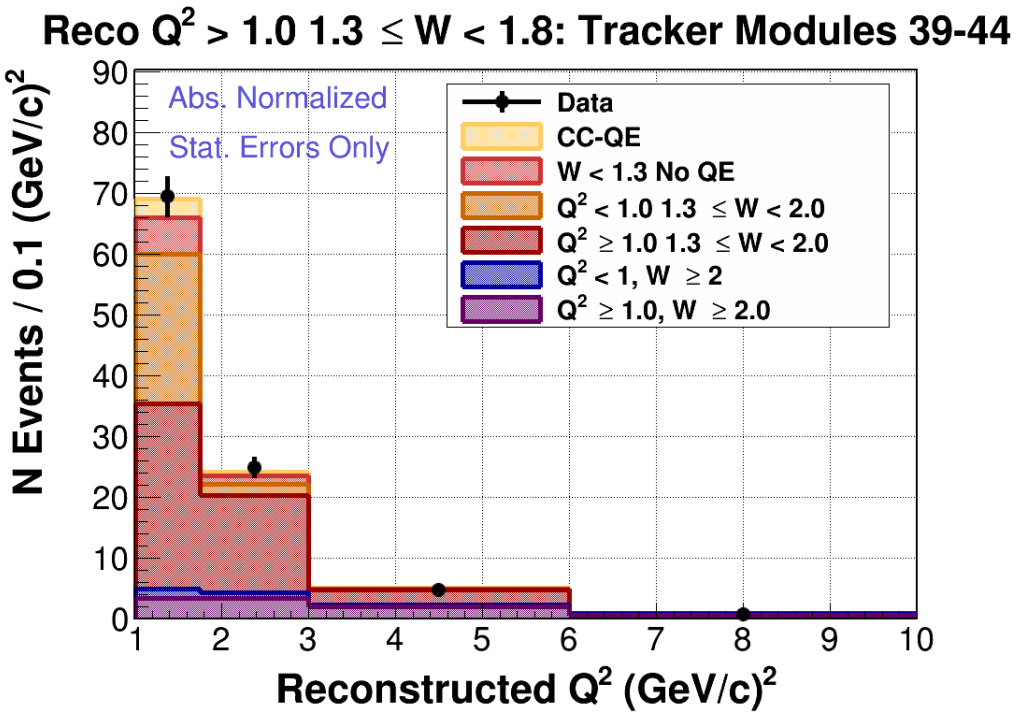

Figure A-32. Data / MC low W sideband before fitting: tracker mods. 39-44 (Q^2)

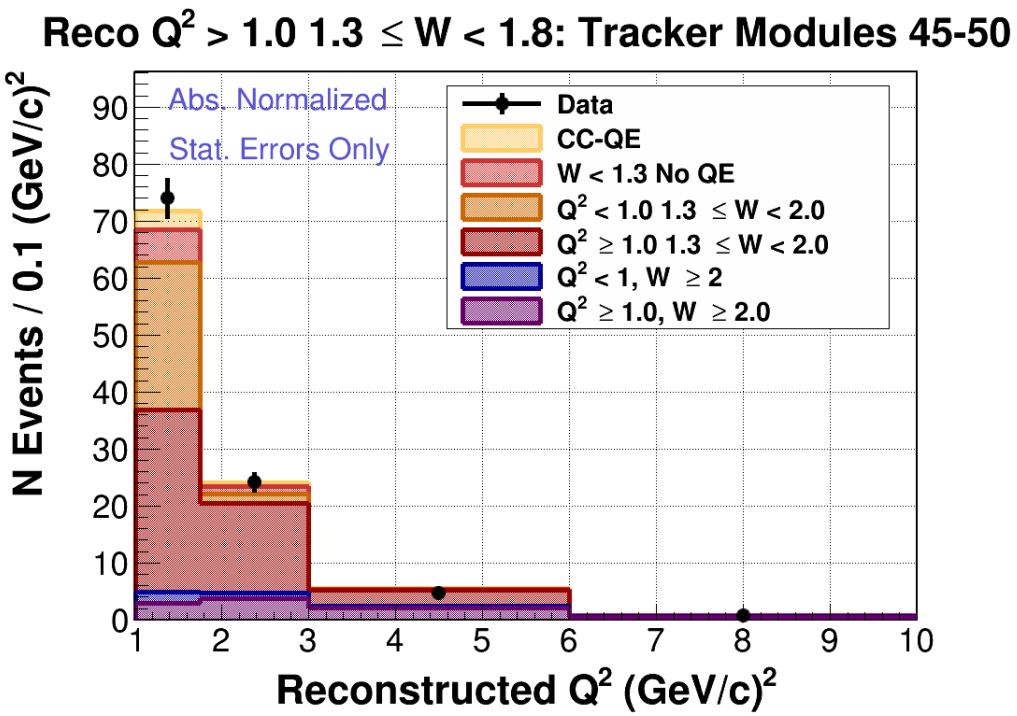

Figure A-33. Data / MC low W sideband before fitting: tracker mods. 45-50 (Q^2)

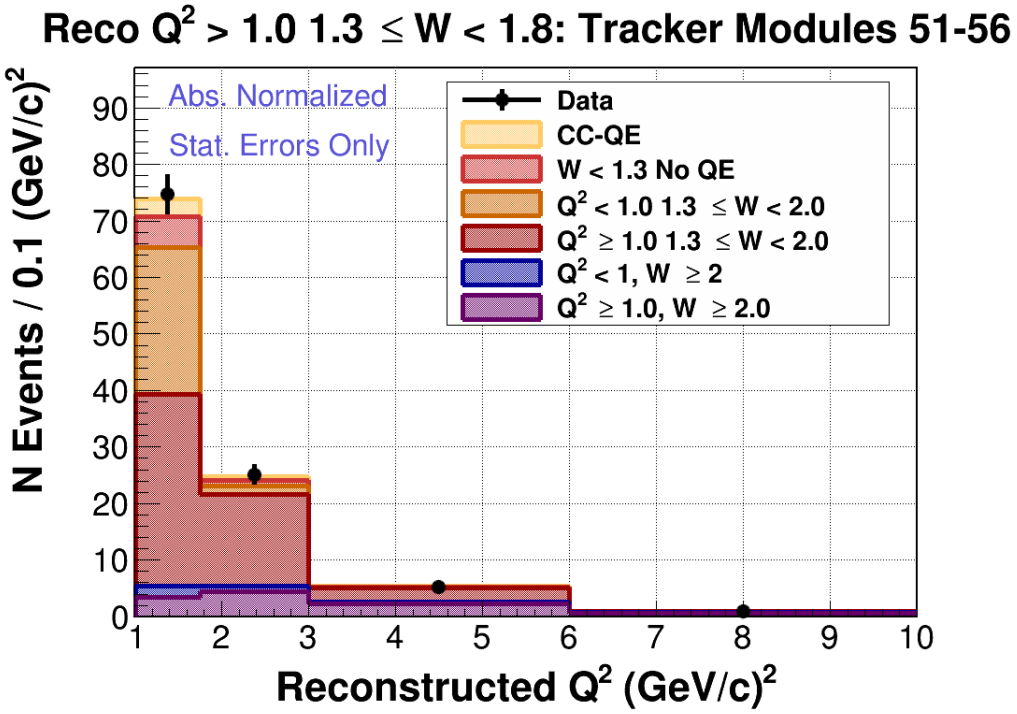

Figure A-34. Data / MC low W sideband before fitting: tracker mods. 51-56 (Q^2)

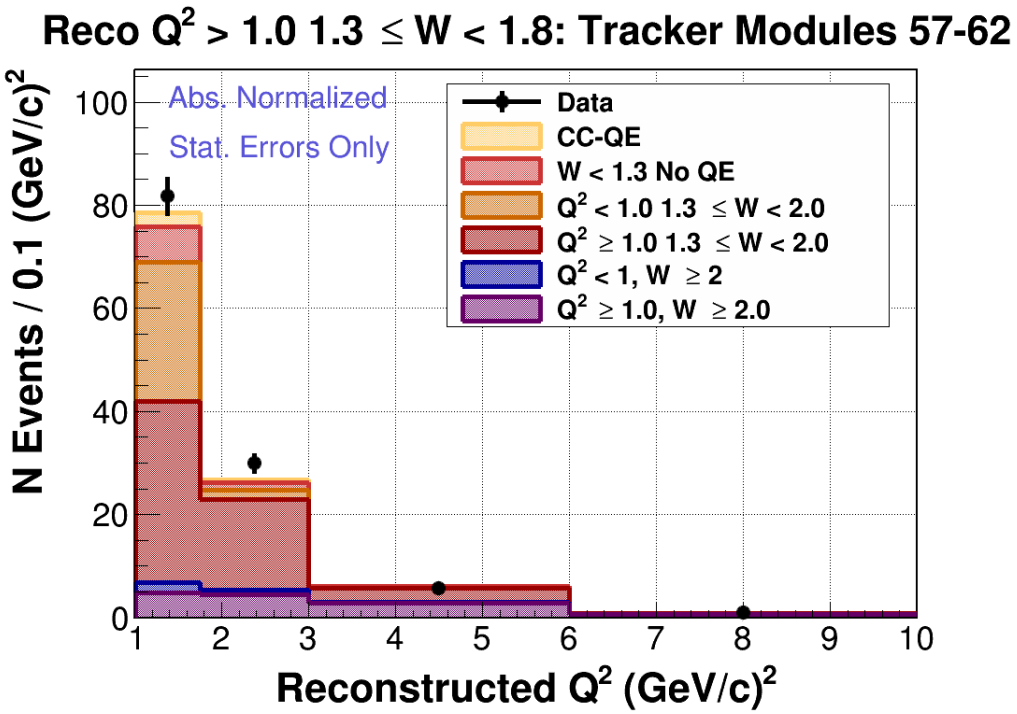

Figure A-35. Data / MC low W sideband before fitting: tracker mods. 57-62 (Q^2)

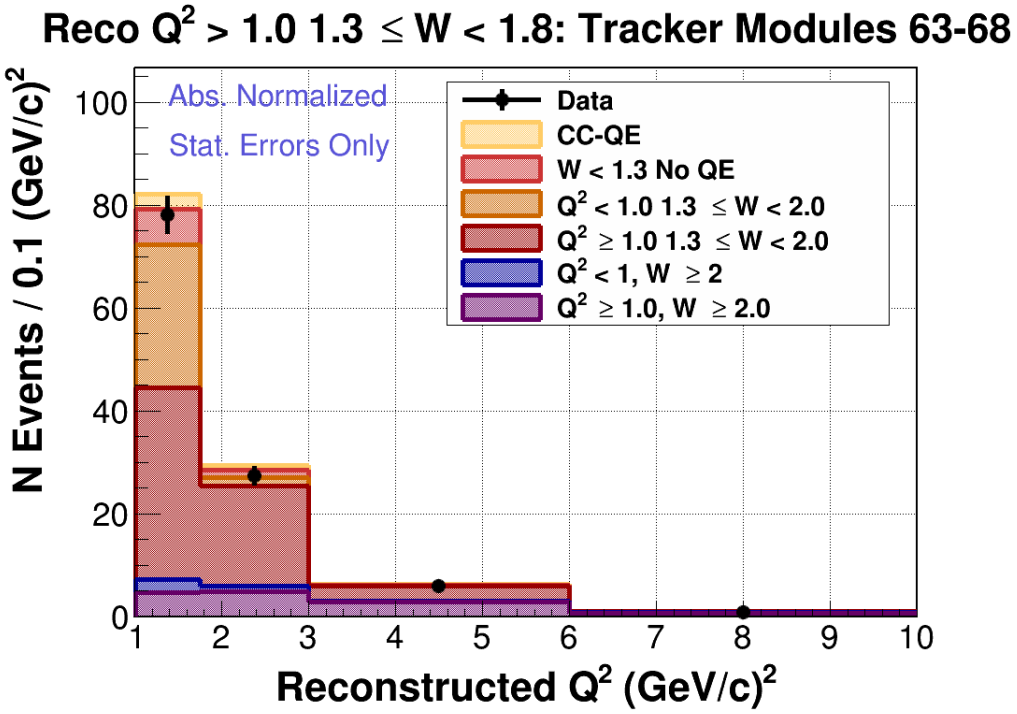

Figure A-36. Data / MC low W sideband before fitting: tracker mods. 63-68 (Q^2)

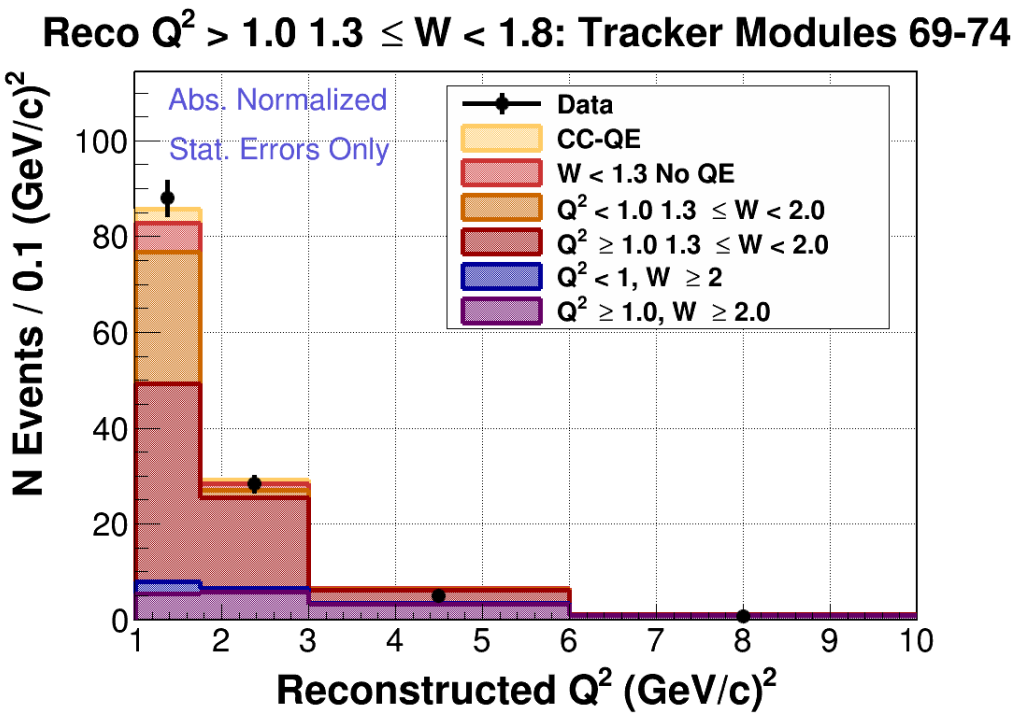

Figure A-37. Data / MC low W sideband before fitting: tracker mods. 69-74 (Q^2)

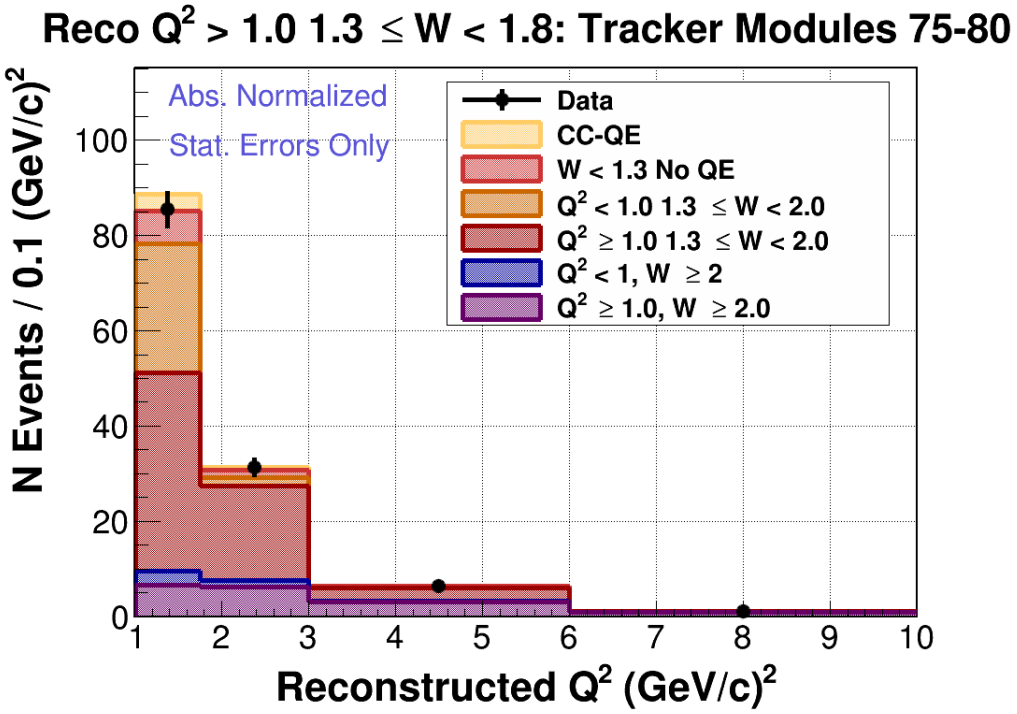

Figure A-38. Data / MC low W sideband before fitting: tracker mods. 75-80 (Q^2)

The following plots show the population of the low W sideband ($Q^2 \geq 1.0$ (GeV/c)^2 $1.3 \leq W < 1.8$) *before* tuning to data as a function of Bjorken-x (x_{bj}):

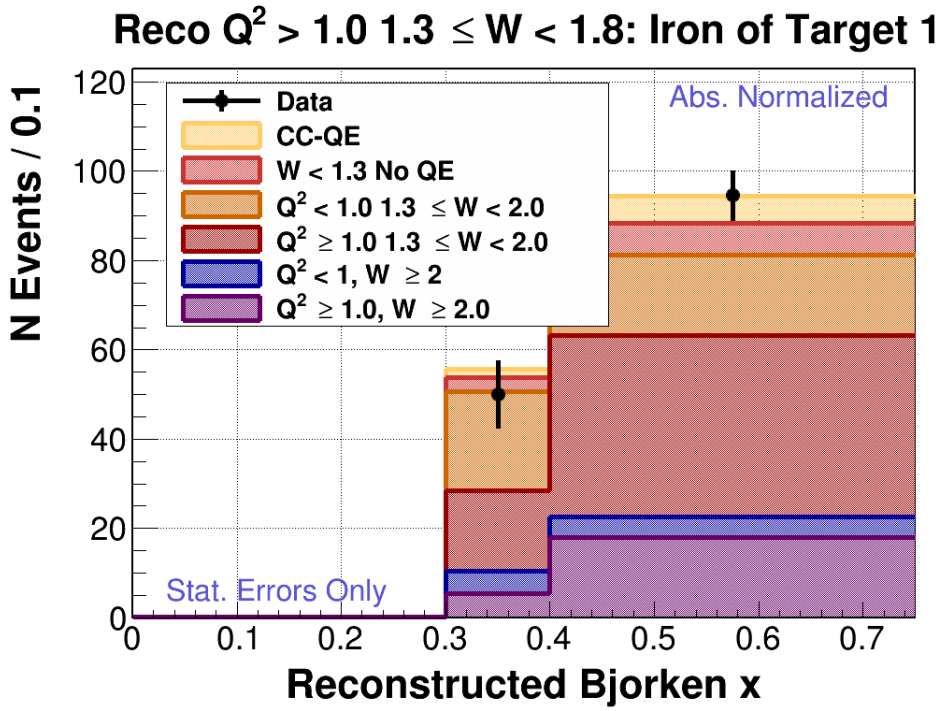

Figure A-39. Data / MC low W sideband before fitting: target 01 Fe (x_{bj})

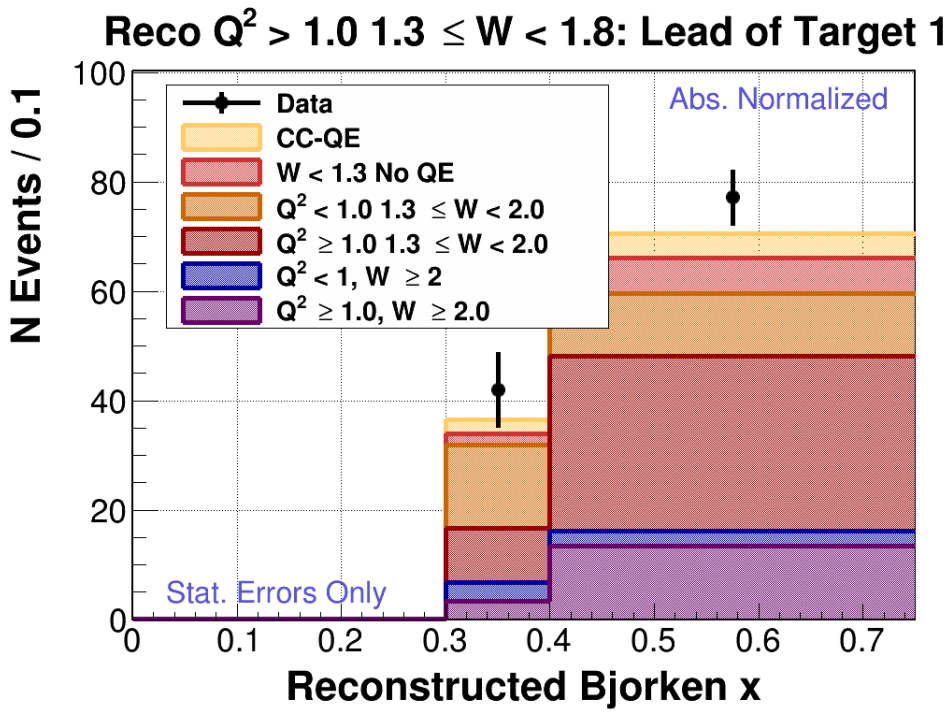

Figure A-40. Data / MC low W sideband before fitting: target 01 Pb (x_{bj})

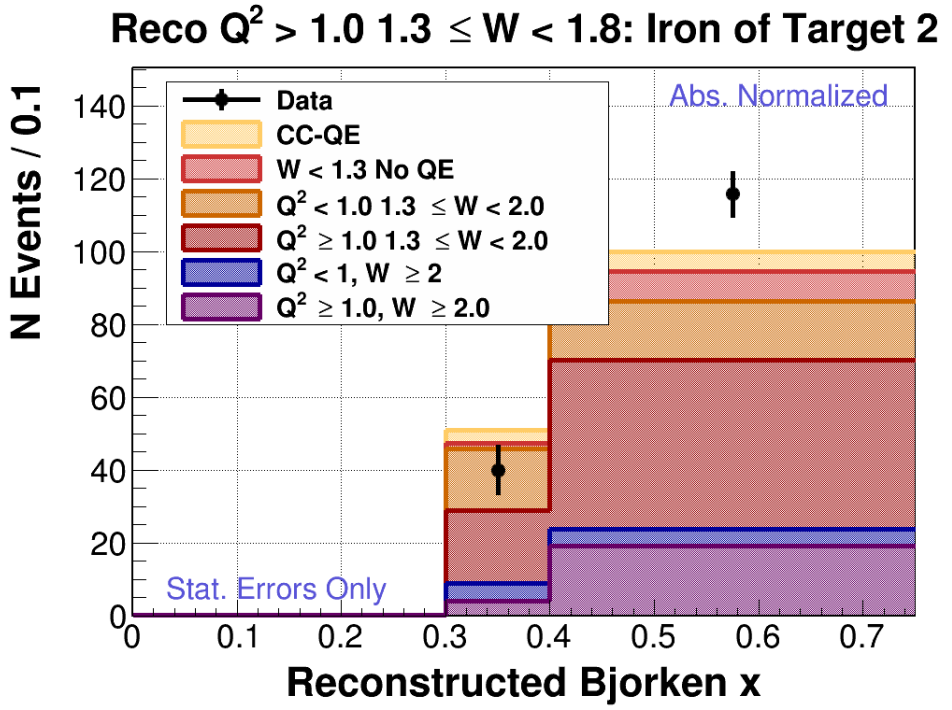

Figure A-41. Data / MC low W sideband before fitting: target 02 Fe (x_{bj})

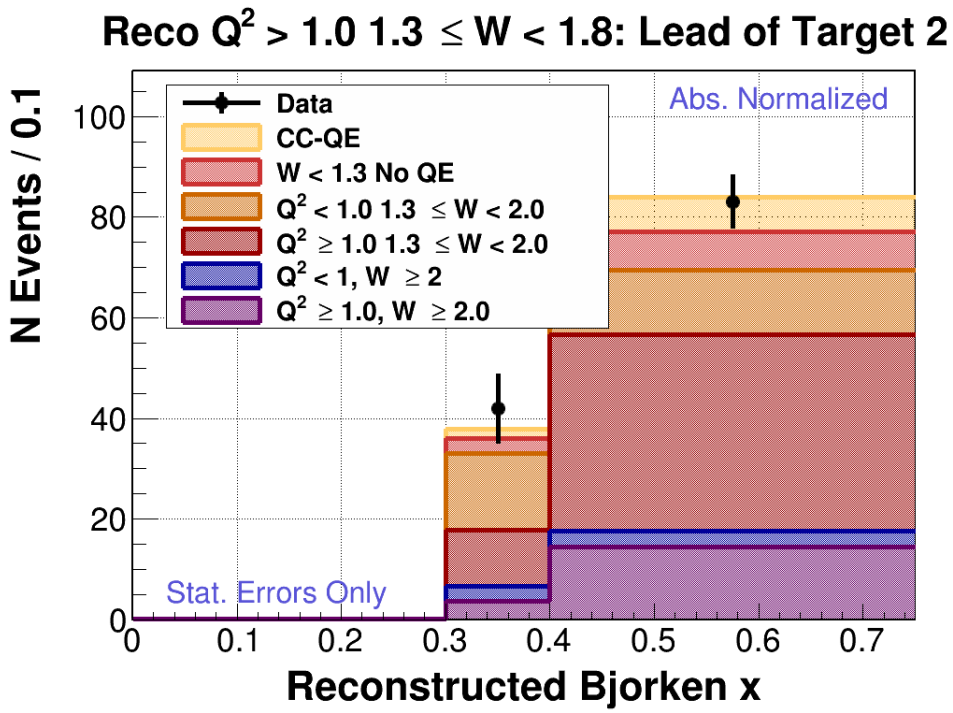

Figure A-42. Data / MC low W sideband before fitting: target 02 Pb (x_{bj})

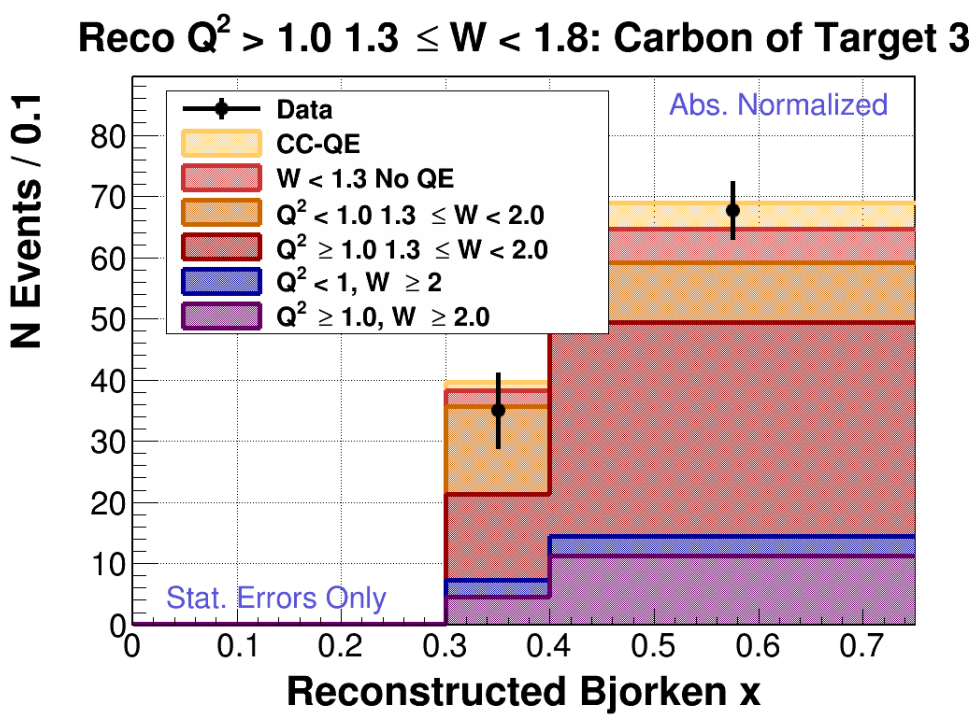

Figure A-43. Data / MC low W sideband before fitting: target 03 C (x_{bj})

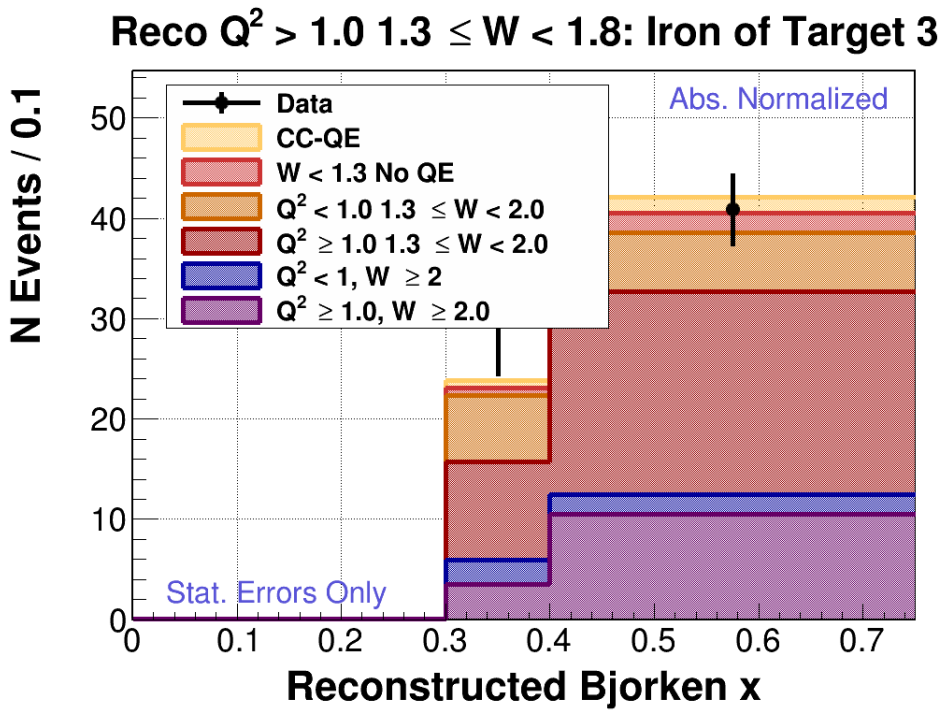

Figure A-44. Data / MC low W sideband before fitting: target 03 Fe (x_{bj})

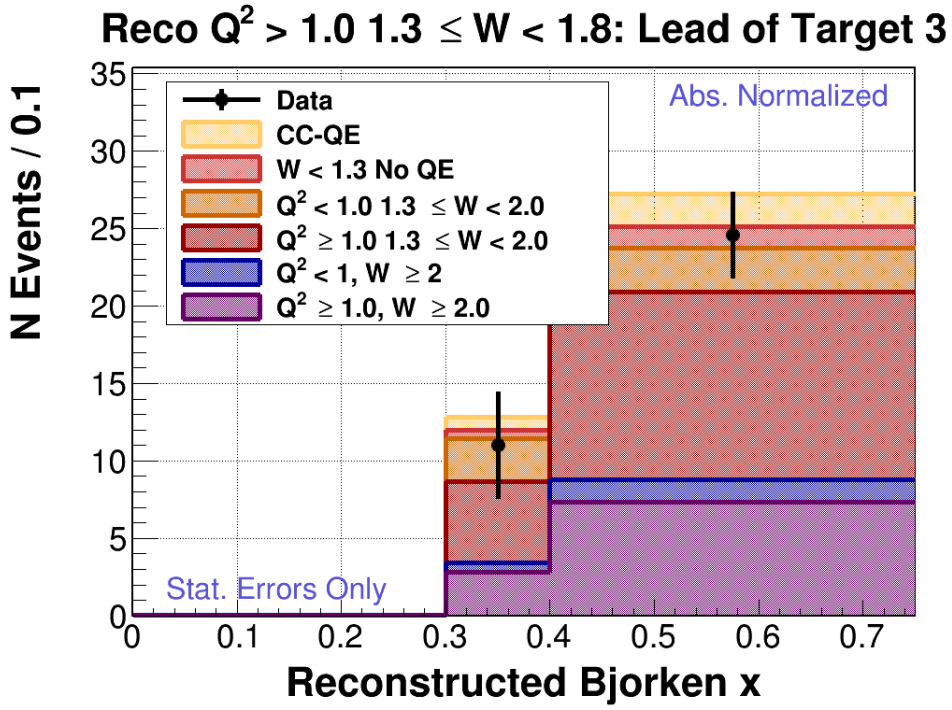

Figure A-45. Data / MC low W sideband before fitting: target 03 Pb (x_{bj})

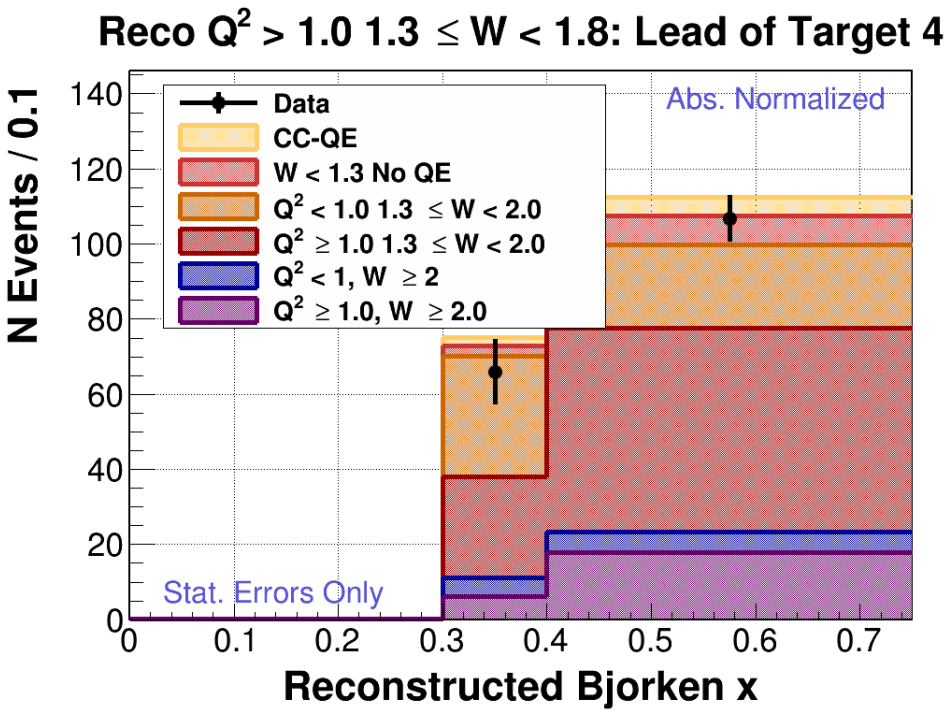

Figure A-46. Data / MC low W sideband before fitting: target 04 Pb (x_{bj})

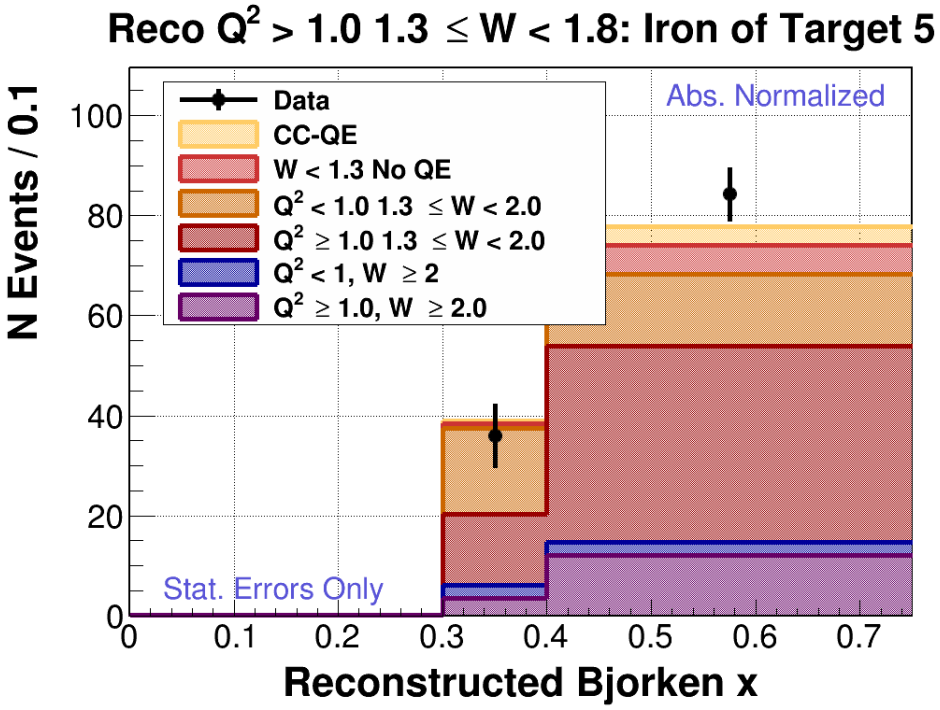

Figure A-47. Data / MC low W sideband before fitting: target 05 Fe (x_{bj})

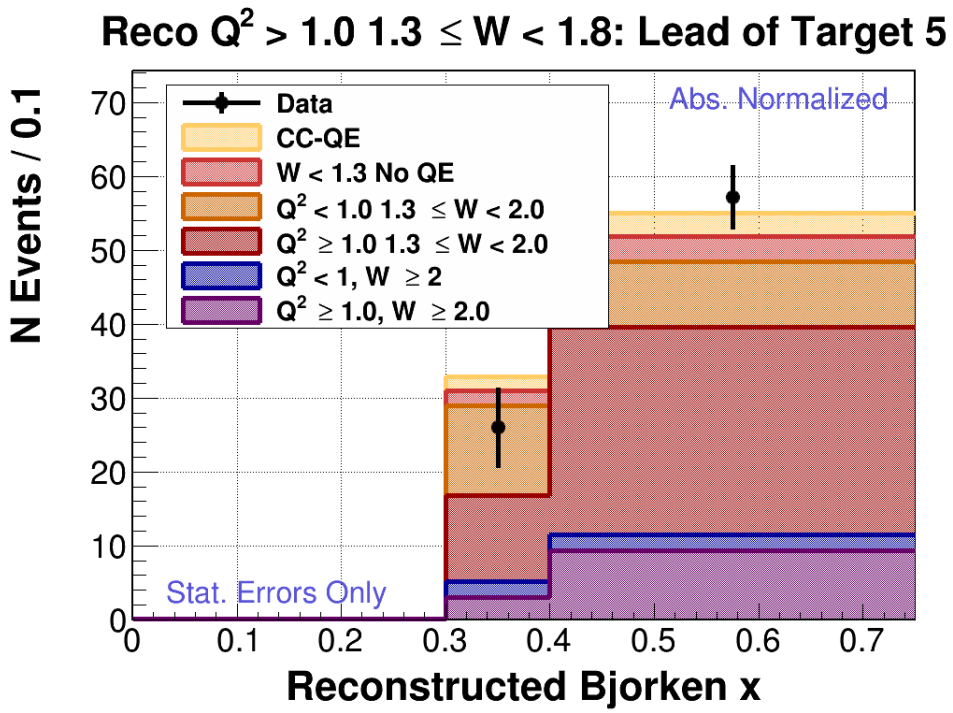

Figure A-48. Data / MC low W sideband before fitting: target 05 Pb (x_{bj})

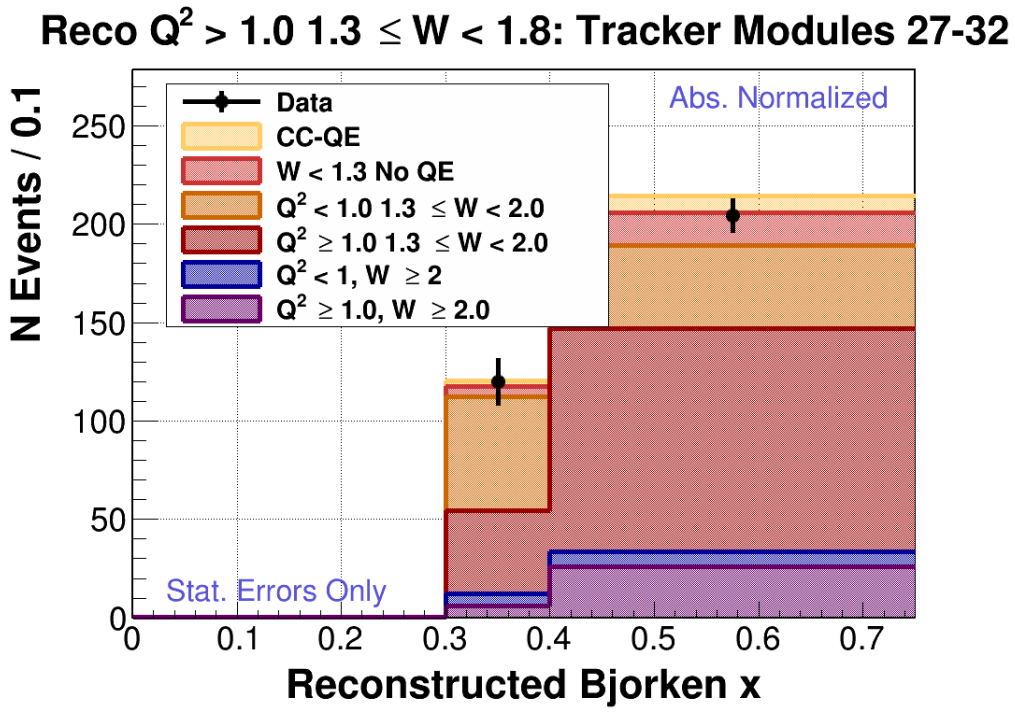

Figure A-49. Data / MC low W sideband before fitting: tracker mods. 27-32 (x_{bj})

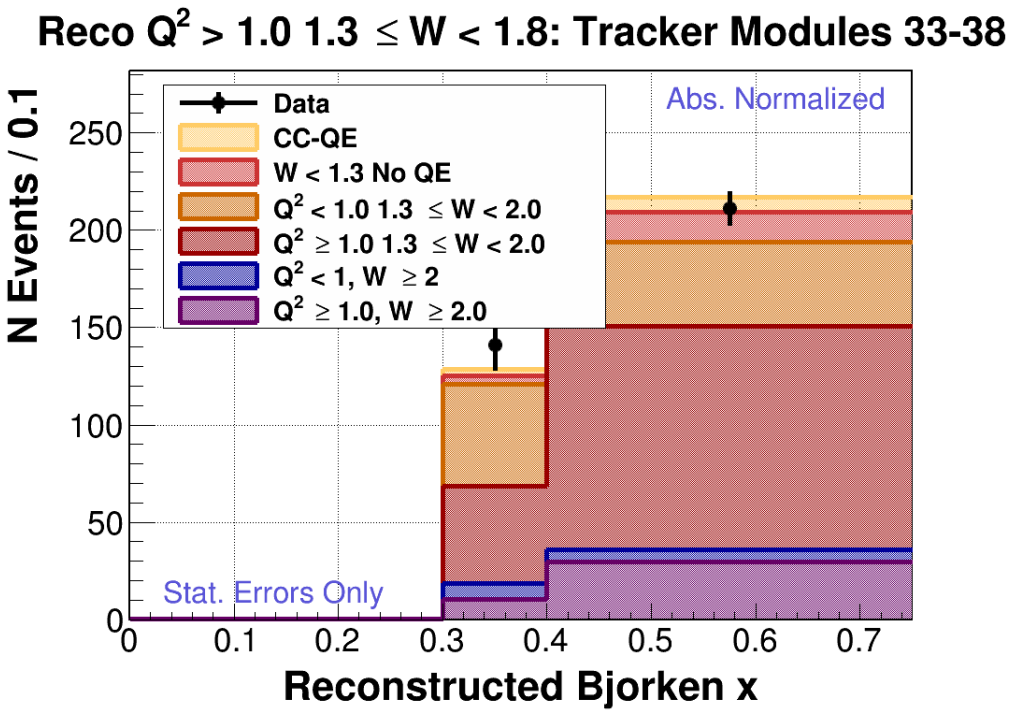

Figure A-50. Data / MC low W sideband before fitting: tracker mods. 33-38 (x_{bj})

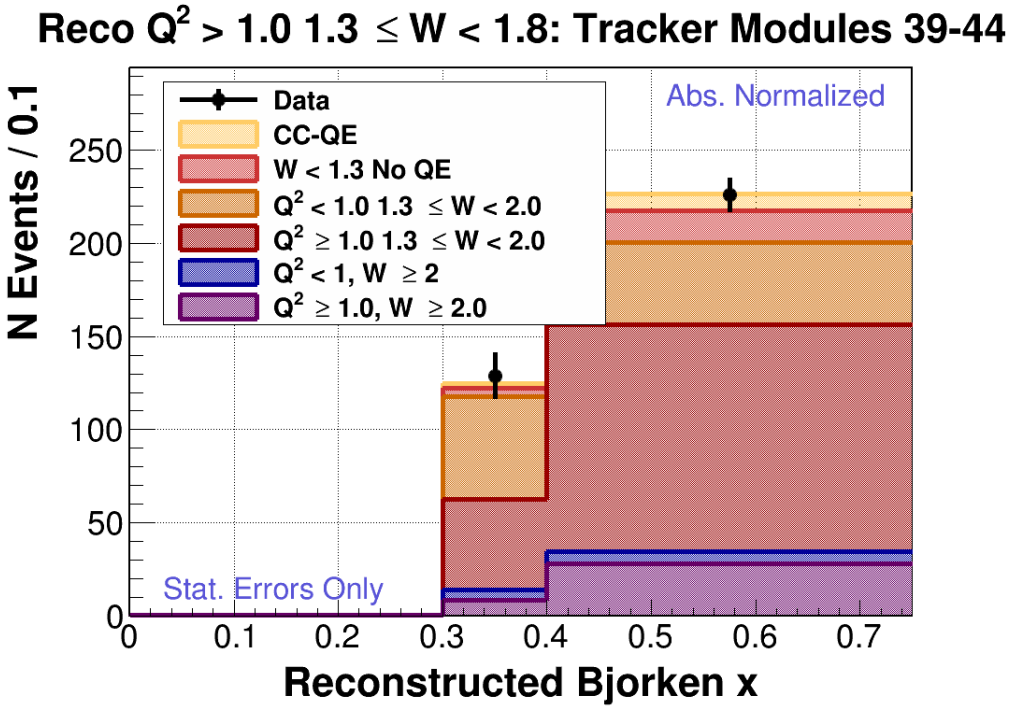

Figure A-51. Data / MC low W sideband before fitting: tracker mods. 39-44 (x_{bj})

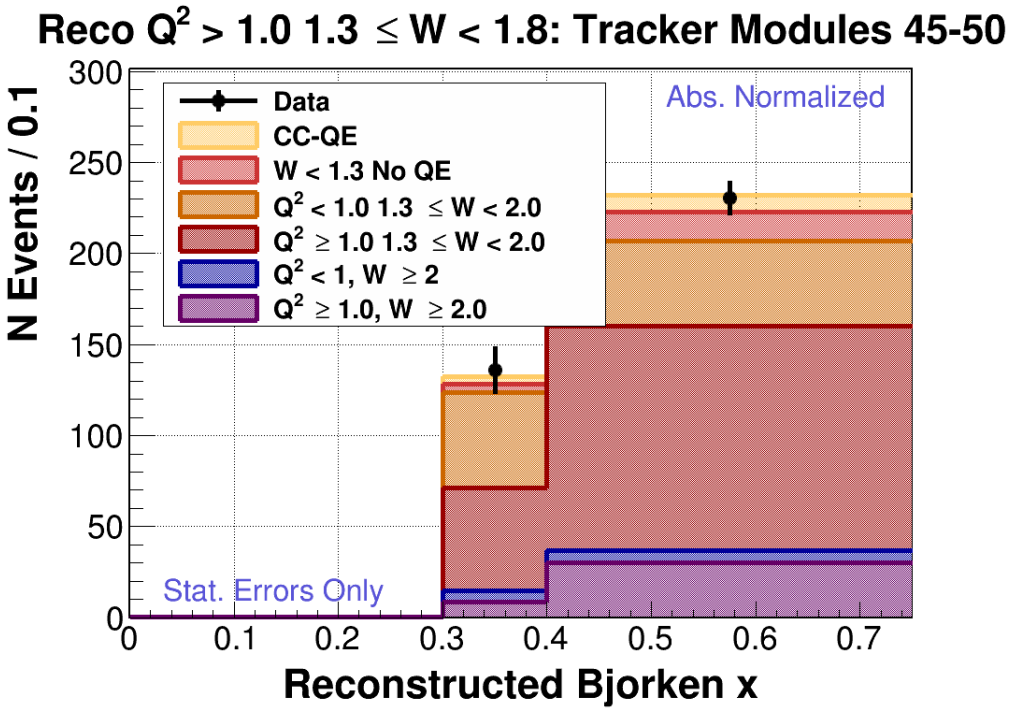

Figure A-52. Data / MC low W sideband before fitting: tracker mods. 45-50 (x_{bj})

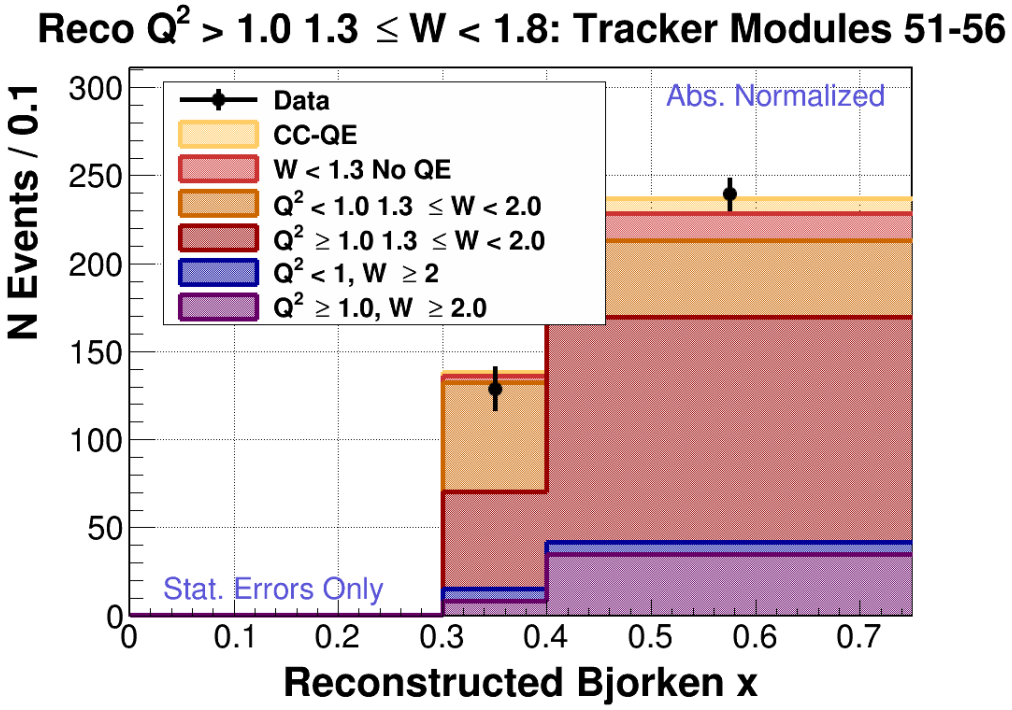

Figure A-53. Data / MC low W sideband before fitting: tracker mods. 51-56 (x_{bj})

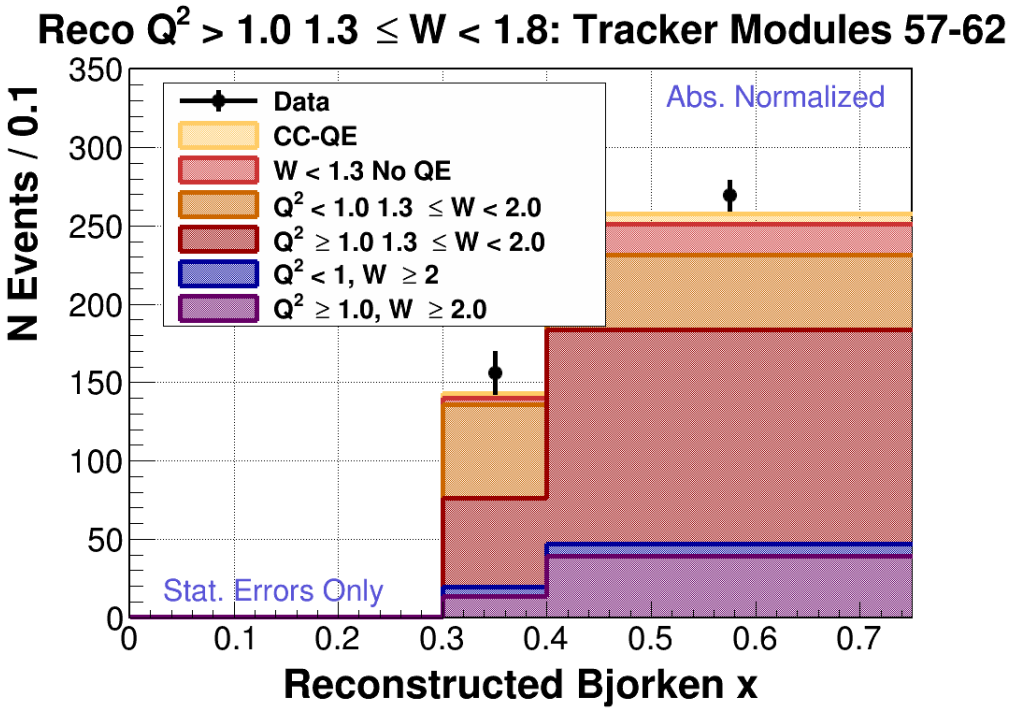

Figure A-54. Data / MC low W sideband before fitting: tracker mods. 57-62 (x_{bj})

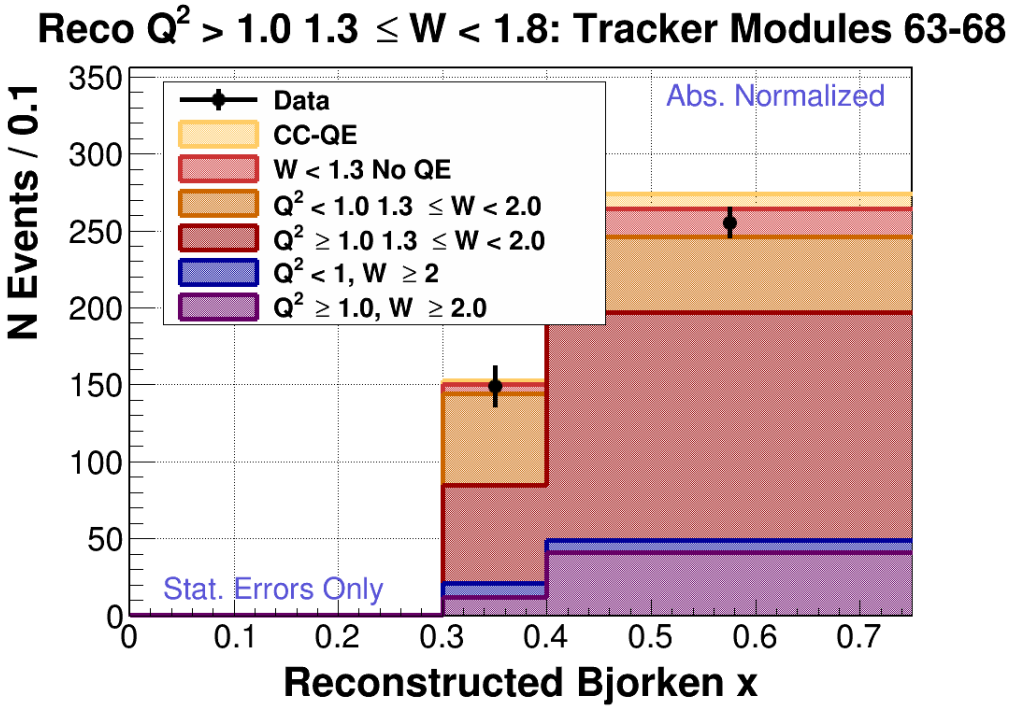

Figure A-55. Data / MC low W sideband before fitting: tracker mods. 63-68 (x_{bj})

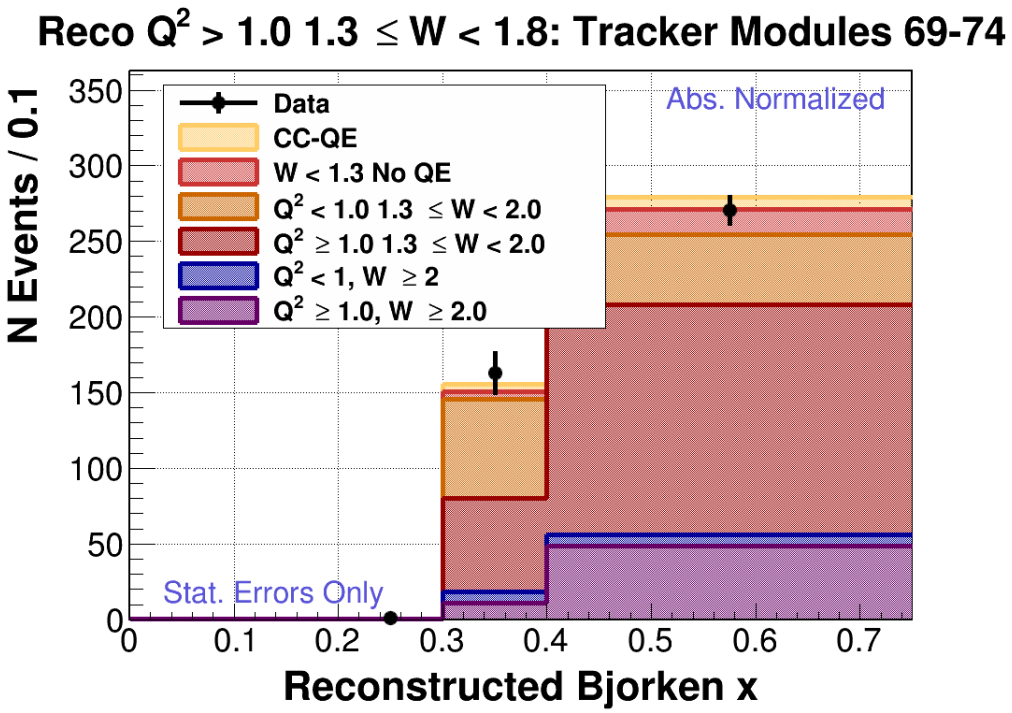

Figure A-56. Data / MC low W sideband before fitting: tracker mods. 69-74 (x_{bj})

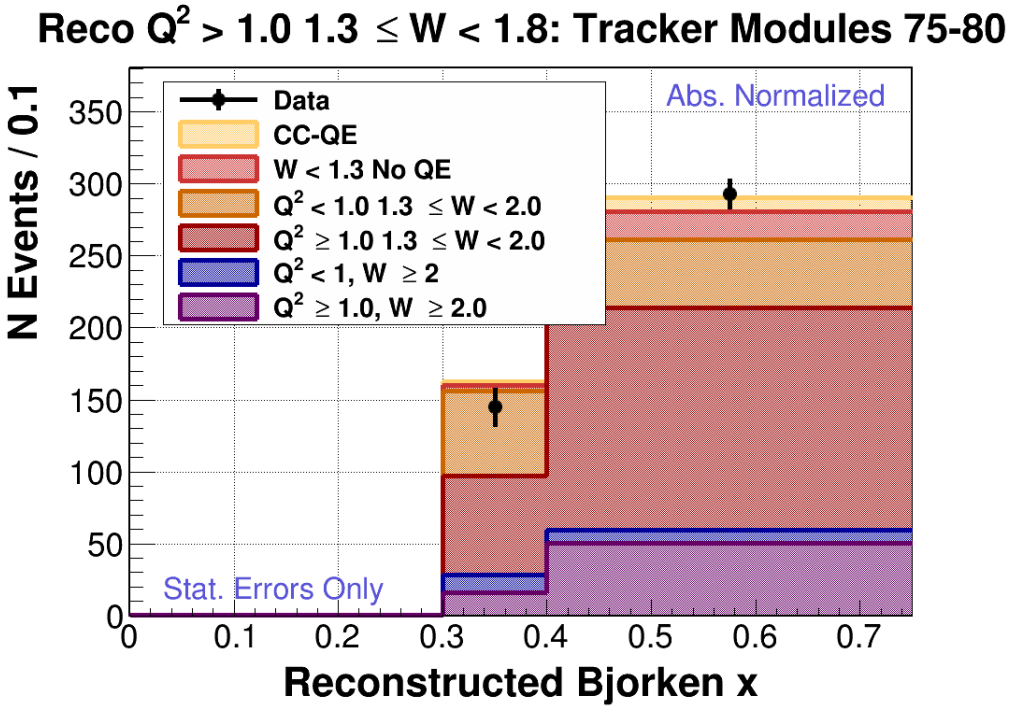

Figure A-57. Data / MC low W sideband before fitting: tracker mods. 75-80 (x_{bj})

The following plots show the population of the low W sideband ($Q^2 \geq 1.0$ (GeV/c)^2 $1.3 \leq W < 1.8$ GeV/c^2) *before* tuning to data as a function of muon energy (E_μ):

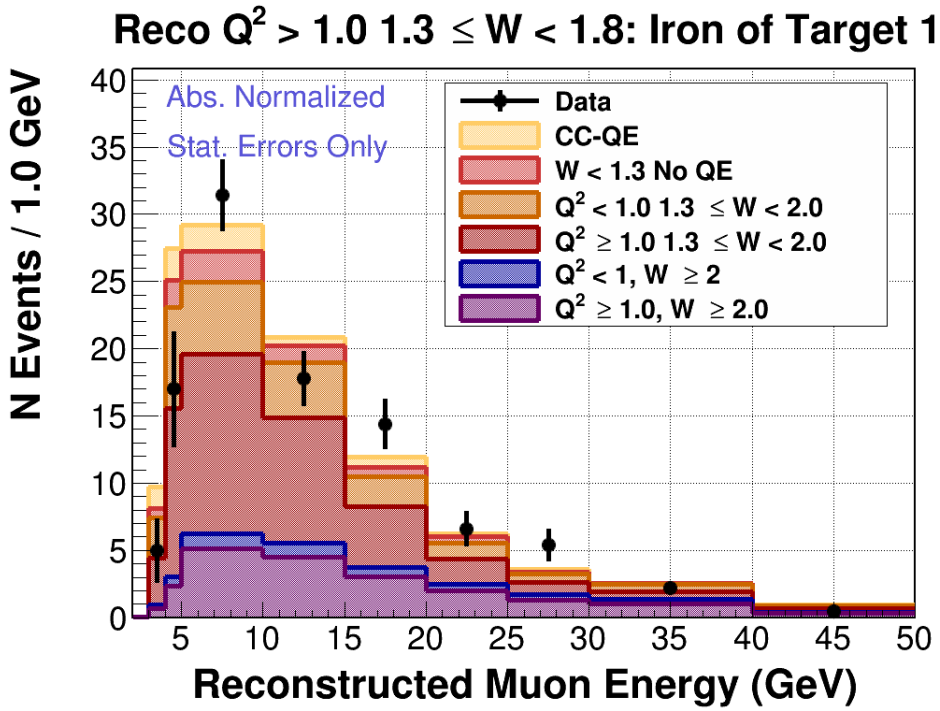

Figure A-58. Data / MC low W sideband before fitting: target 01 Fe (E_μ)

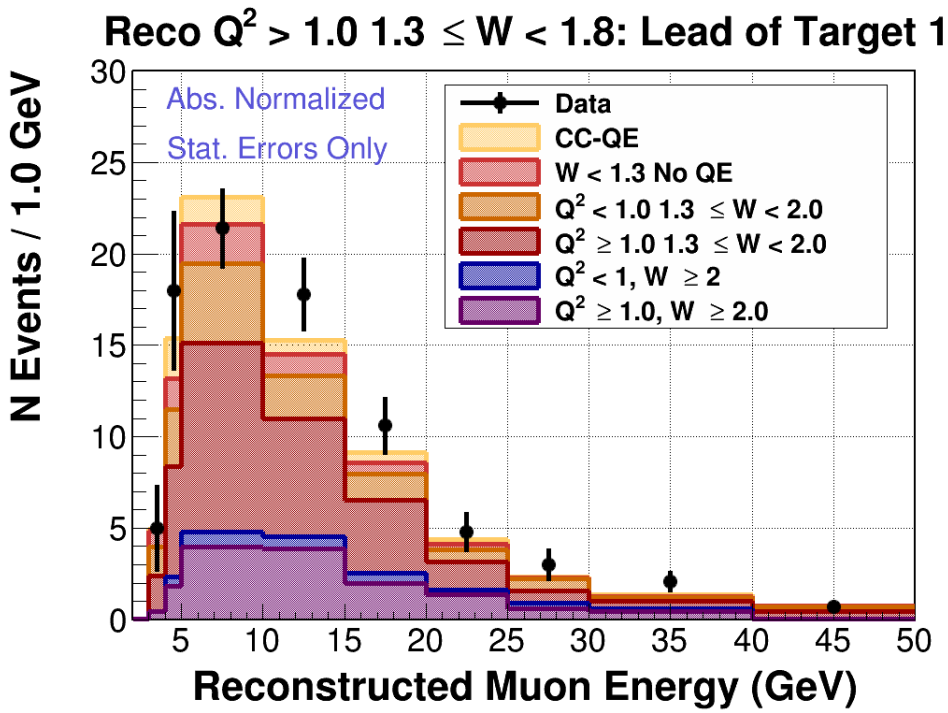

Figure A-59. Data / MC low W sideband before fitting: target 01 Pb (E_μ)

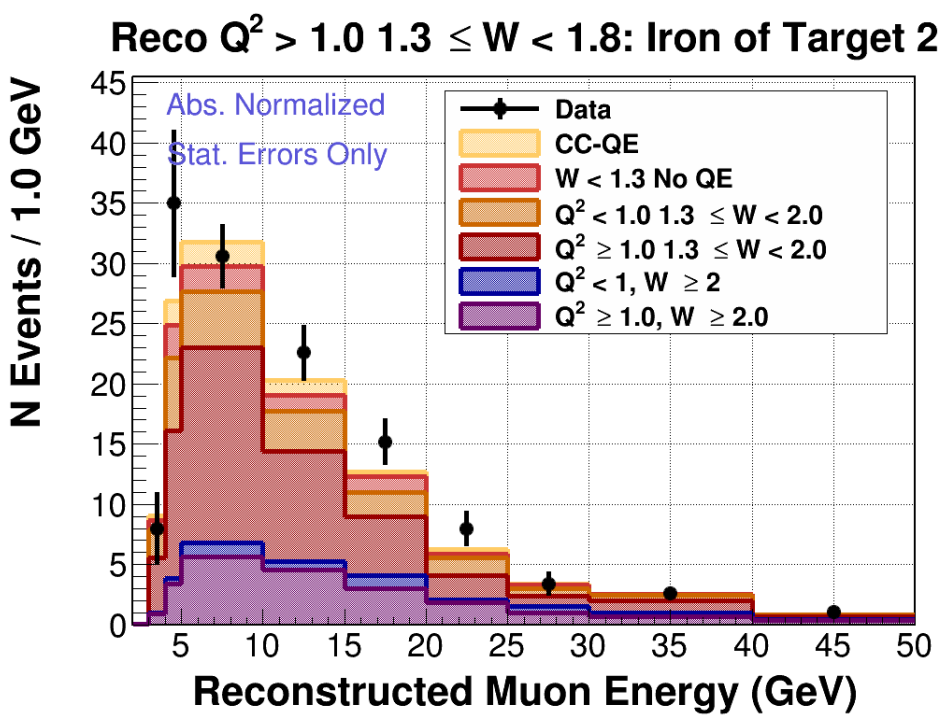

Figure A-60. Data / MC low W sideband before fitting: target 02 Fe (E_μ)

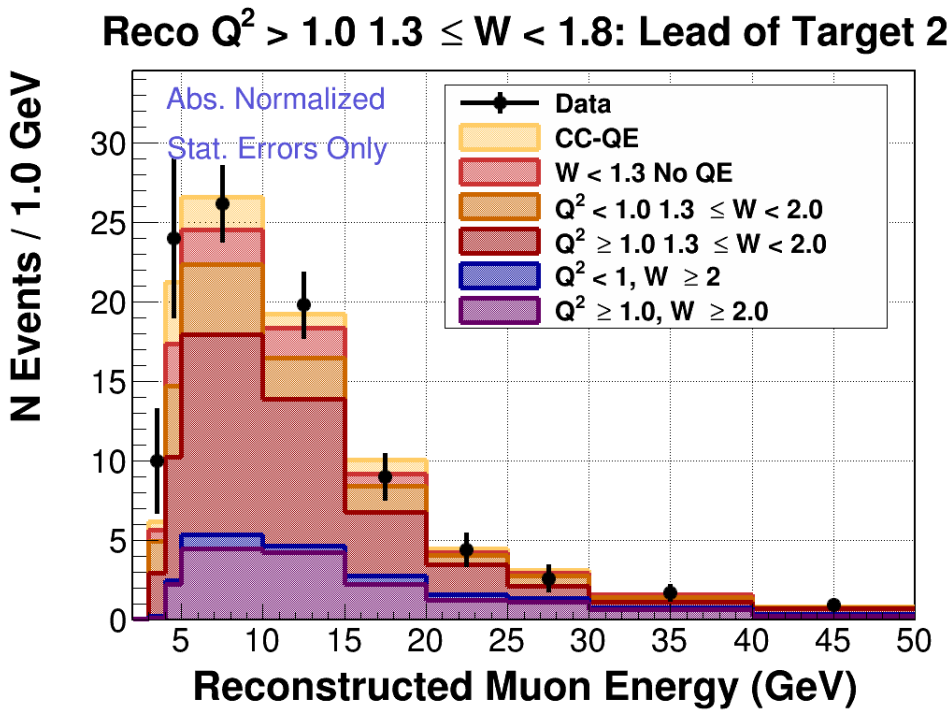

Figure A-61. Data / MC low W sideband before fitting: target 02 Pb (E_μ)

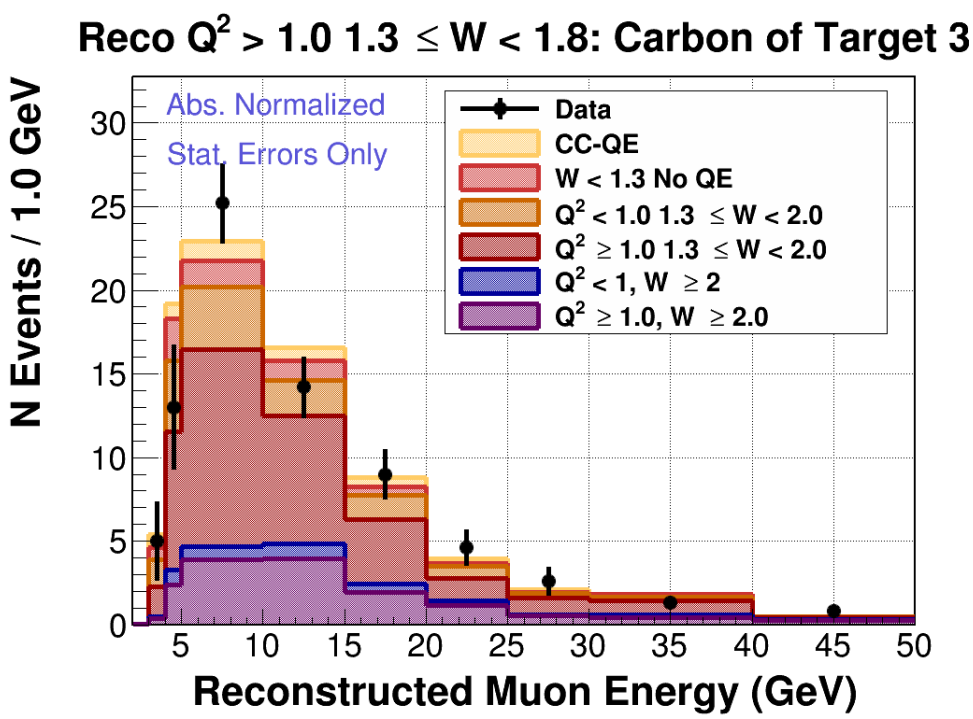

Figure A-62. Data / MC low W sideband before fitting: target 03 C (E_μ)

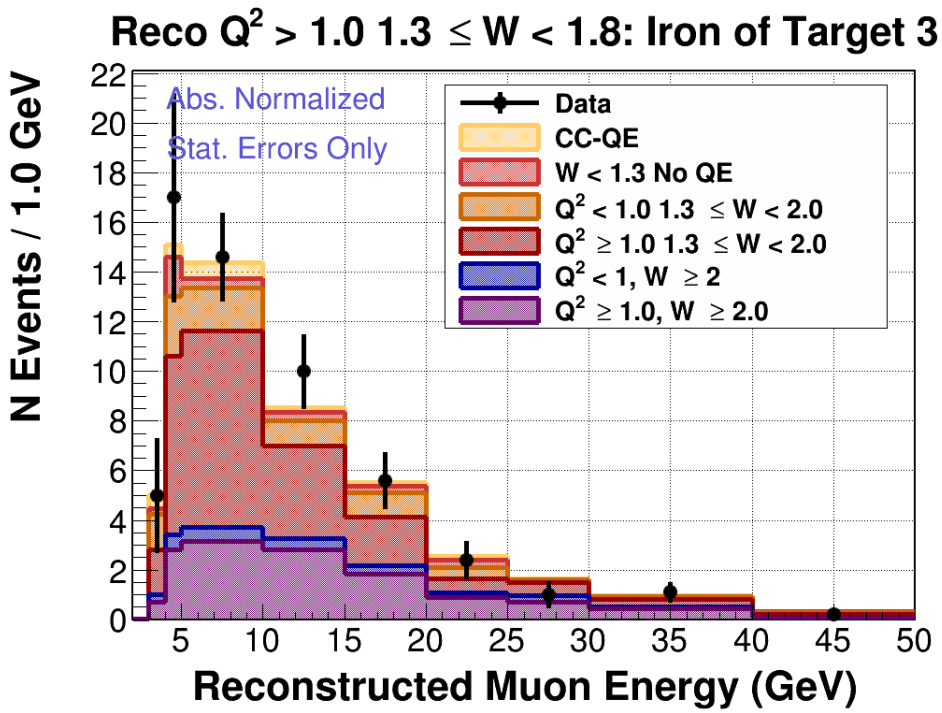

Figure A-63. Data / MC low W sideband before fitting: target 03 Fe (E_μ)

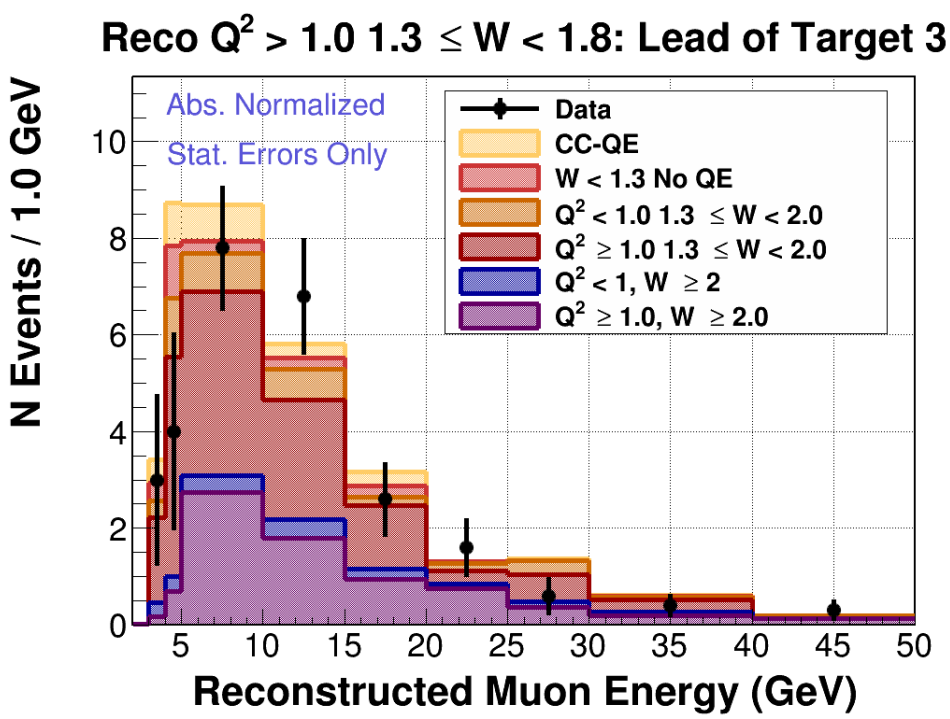

Figure A-64. Data / MC low W sideband before fitting: target 03 Pb (E_μ)

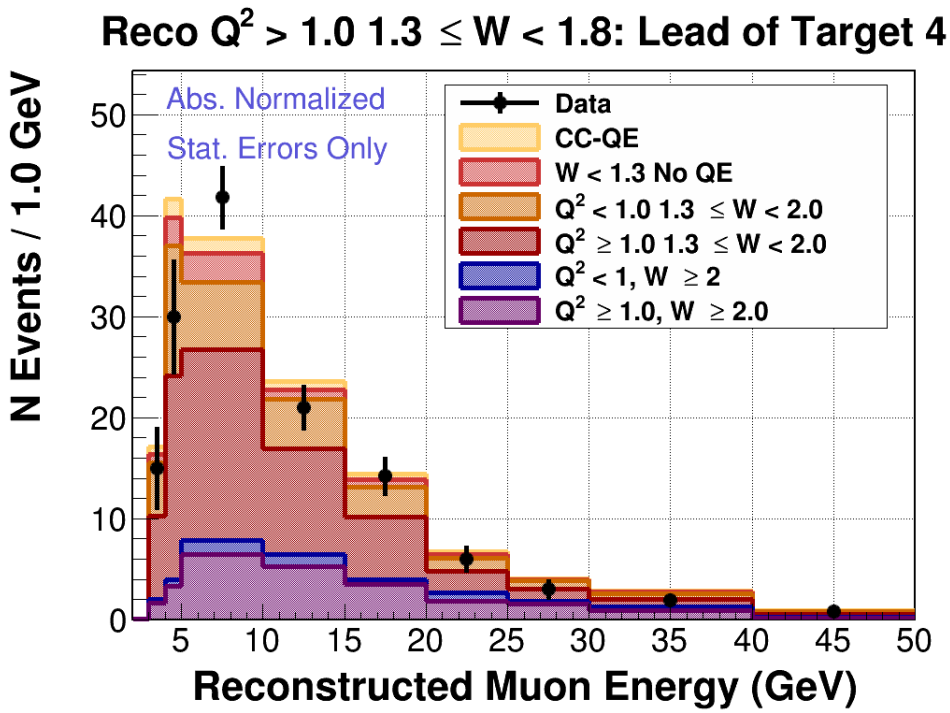

Figure A-65. Data / MC low W sideband before fitting: target 04 Pb (E_μ)

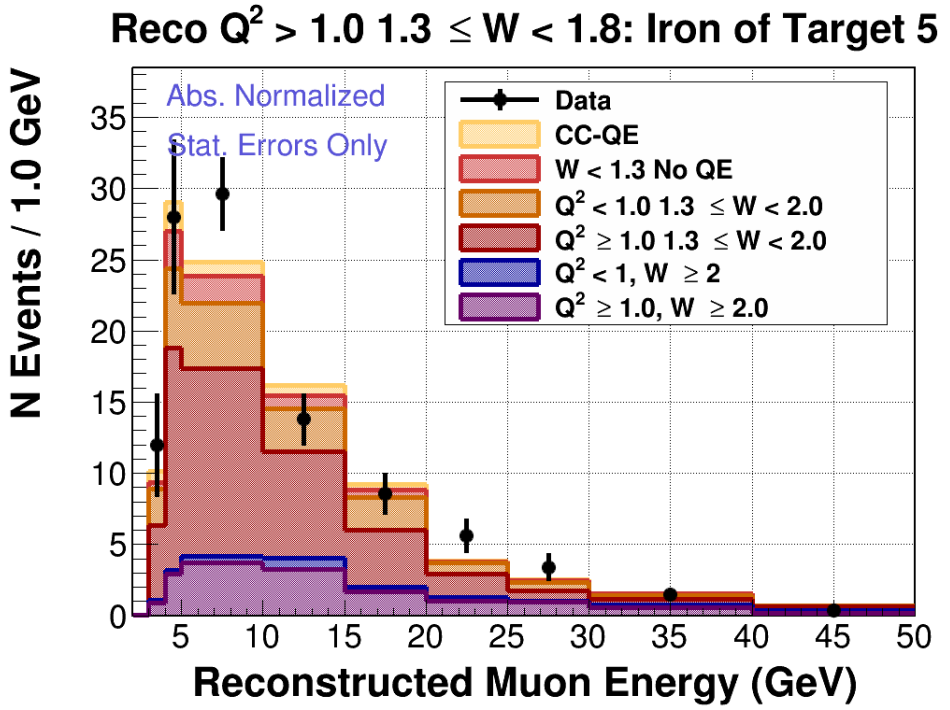

Figure A-66. Data / MC low W sideband before fitting: target 05 Fe (E_μ)

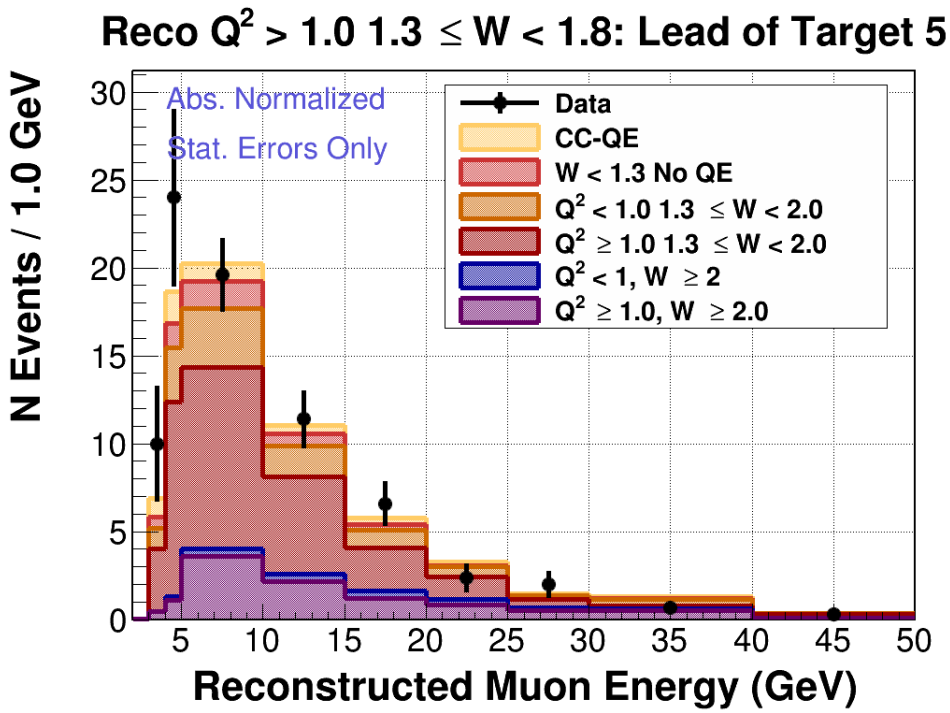

Figure A-67. Data / MC low W sideband before fitting: target 05 Pb (E_μ)

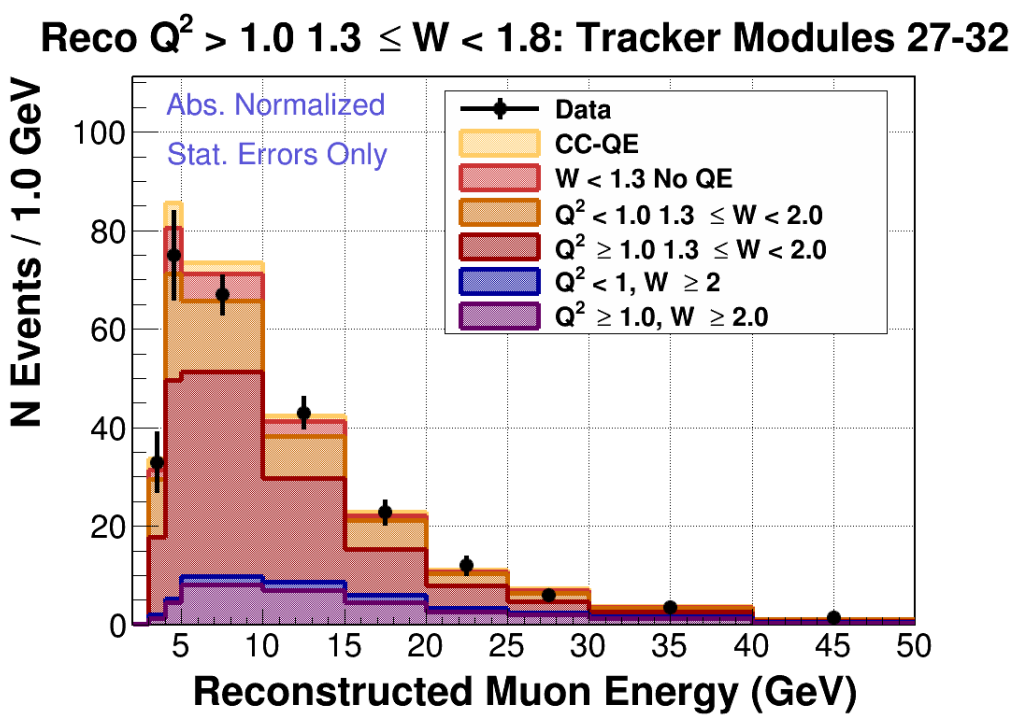

Figure A-68. Data / MC low W sideband before fitting: tracker mods. 27-32 (E_μ)

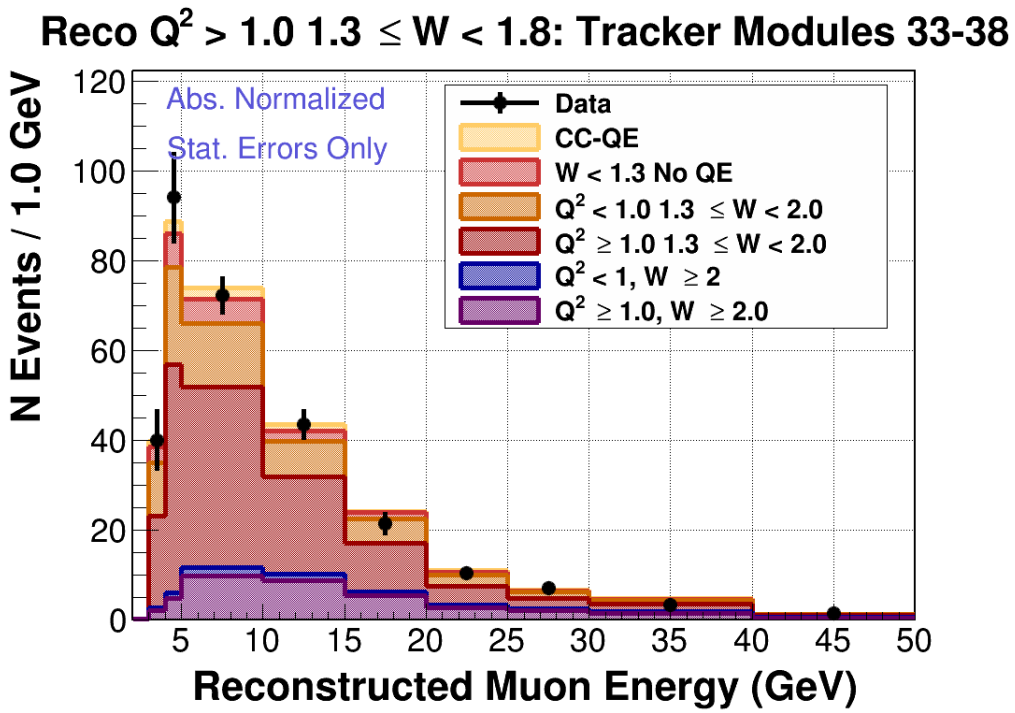

Figure A-69. Data / MC low W sideband before fitting: tracker mods. 33-38 (E_μ)

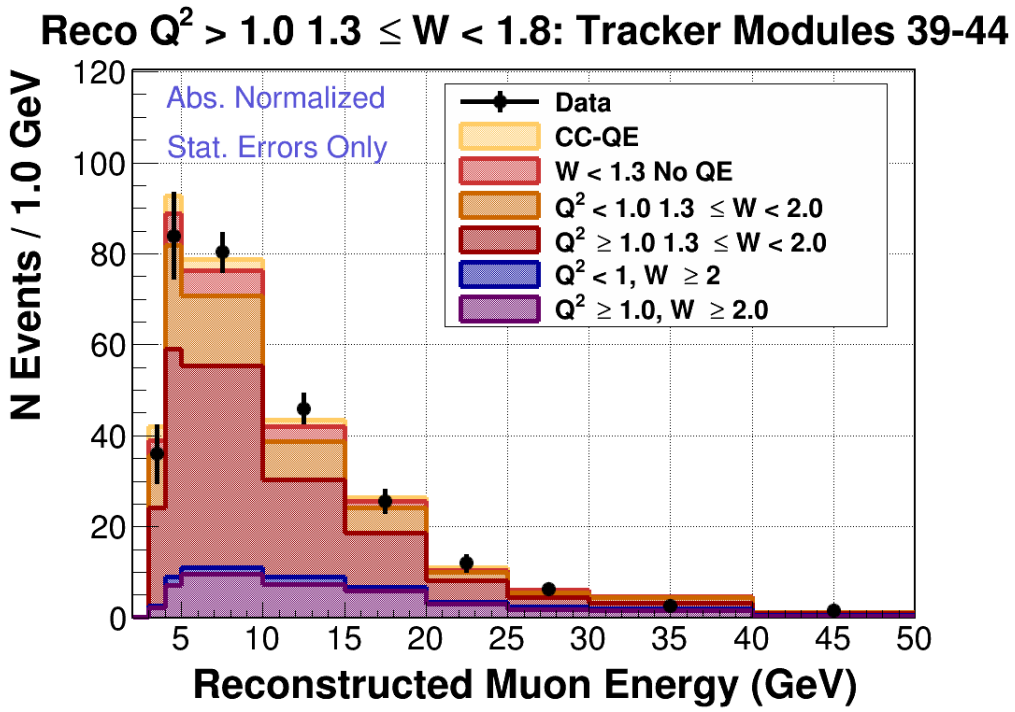

Figure A-70. Data / MC low W sideband before fitting: tracker mods. 39-44 (E_μ)

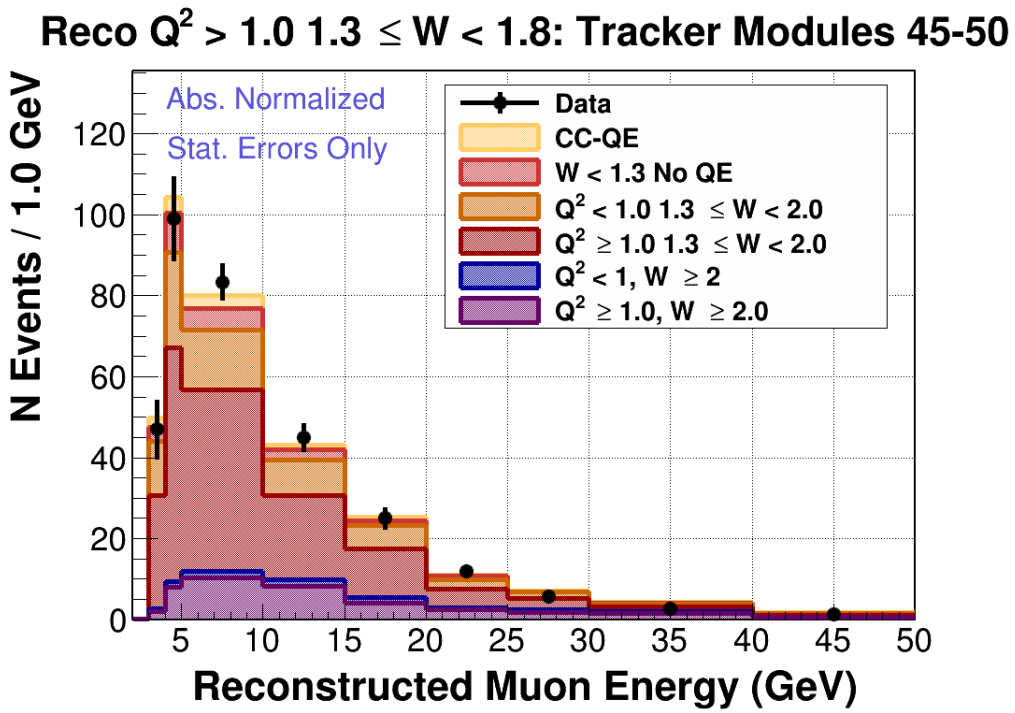

Figure A-71. Data / MC low W sideband before fitting: tracker mods. 45-50 (E_μ)

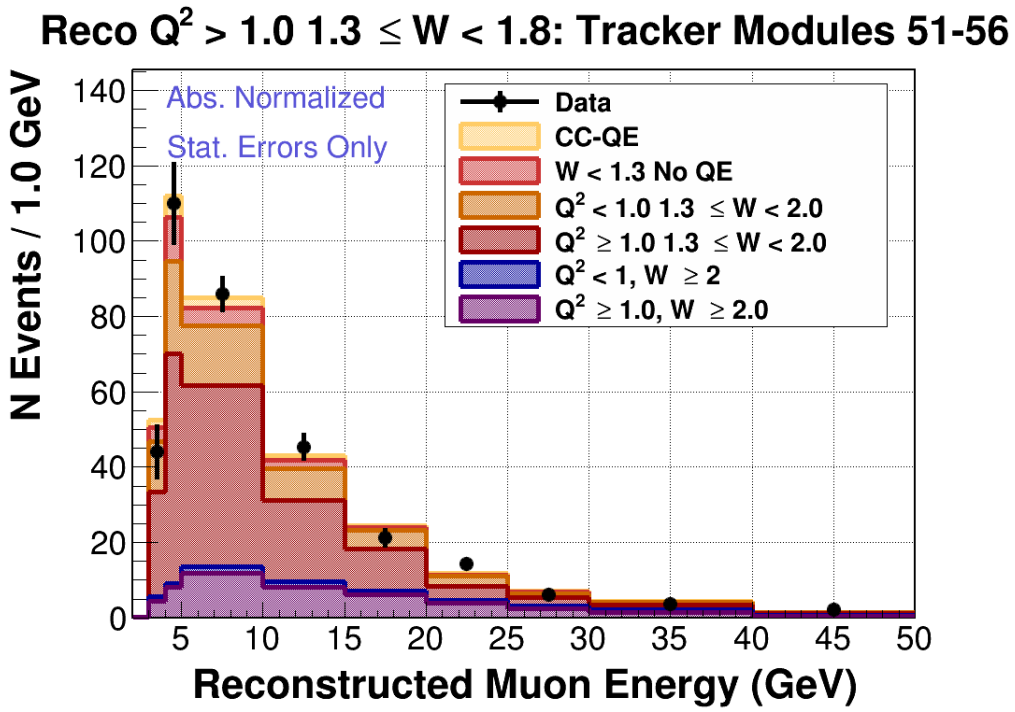

Figure A-72. Data / MC low W sideband before fitting: tracker mods. 51-56 (E_μ)

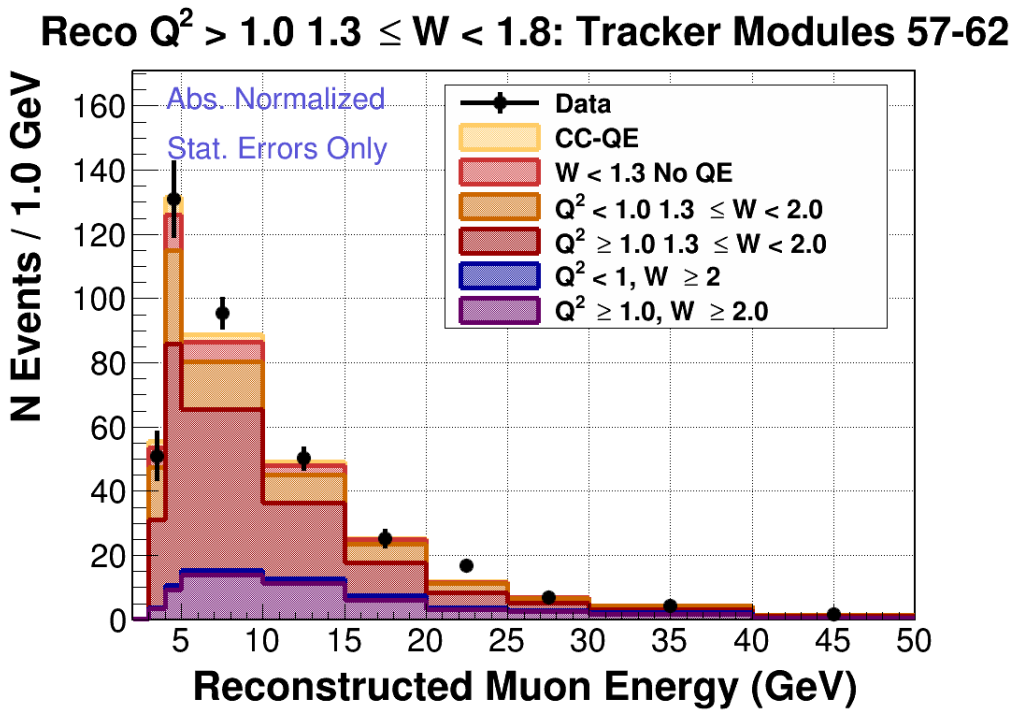

Figure A-73. Data / MC low W sideband before fitting: tracker mods. 57-62 (E_μ)

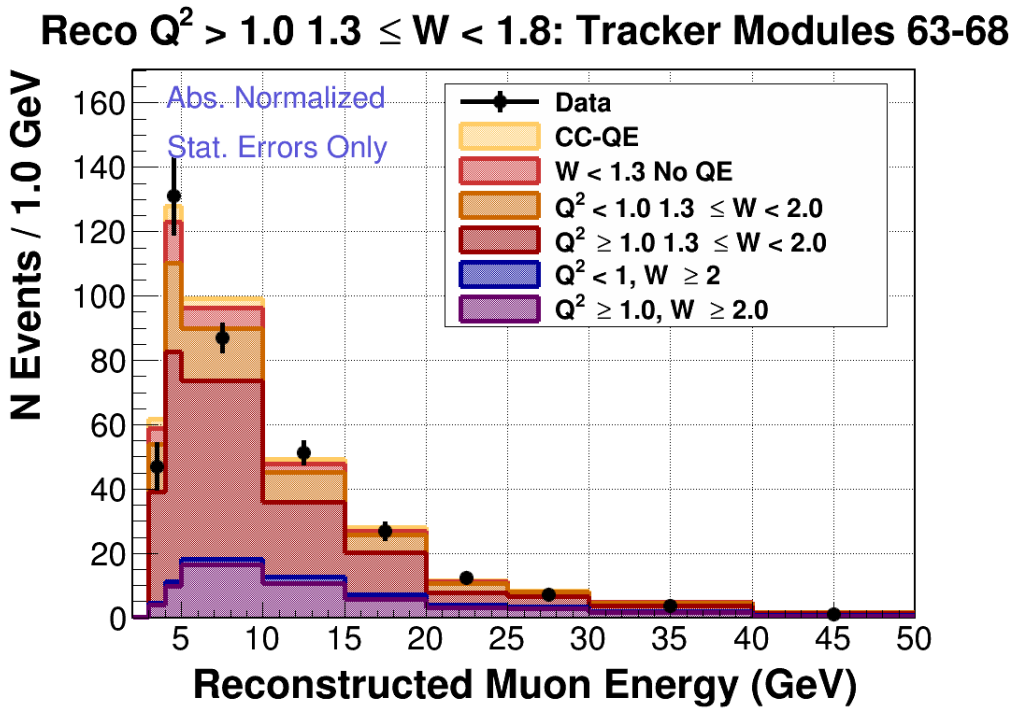

Figure A-74. Data / MC low W sideband before fitting: tracker mods. 63-68 (E_μ)

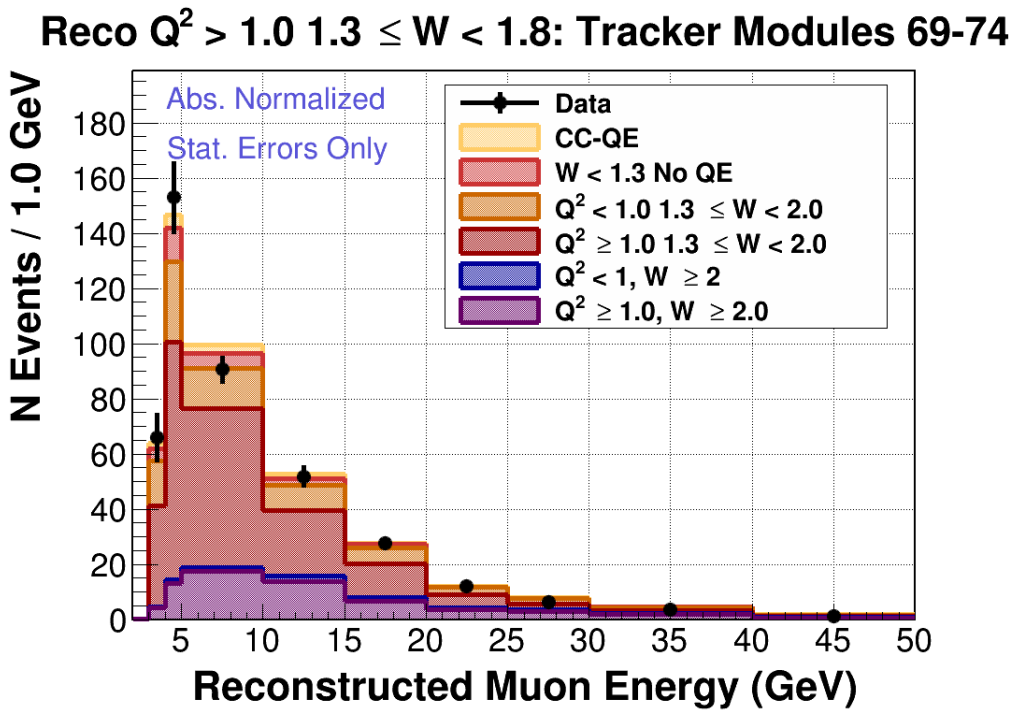

Figure A-75. Data / MC low W sideband before fitting: tracker mods. 69-74 (E_μ)

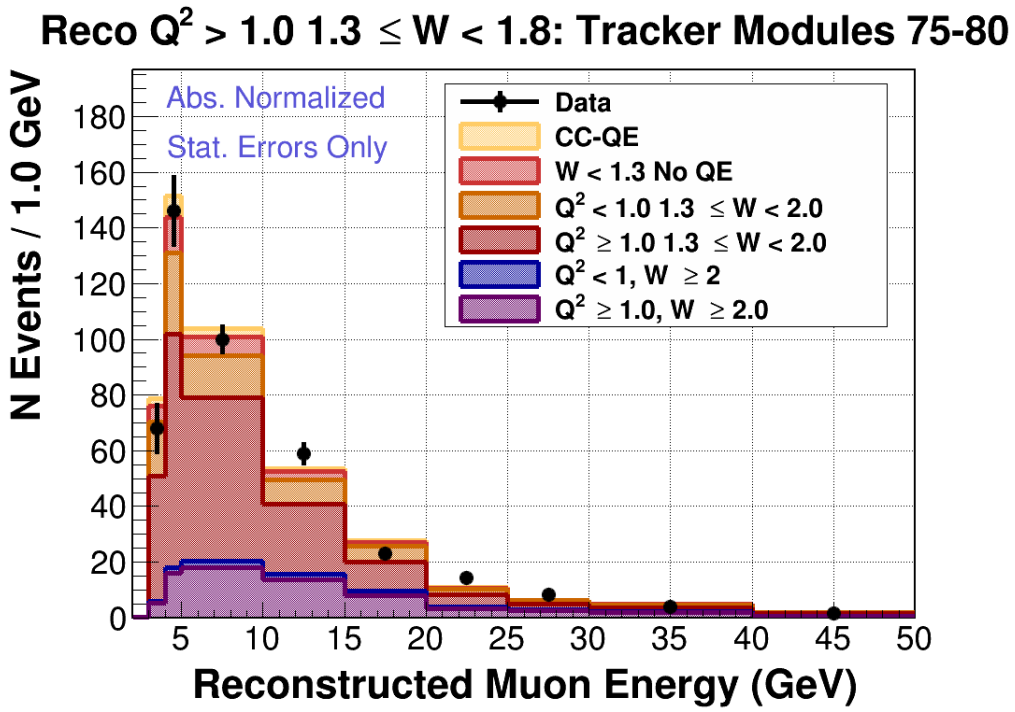

Figure A-76. Data / MC low W sideband before fitting: tracker mods. 75-80 (E_μ)

The following plots show the population of the low W sideband ($Q^2 \geq 1.0$ (GeV/c)^2 $1.3 \leq W < 1.8$) *before* tuning to data as a function of muon angle (θ_μ):

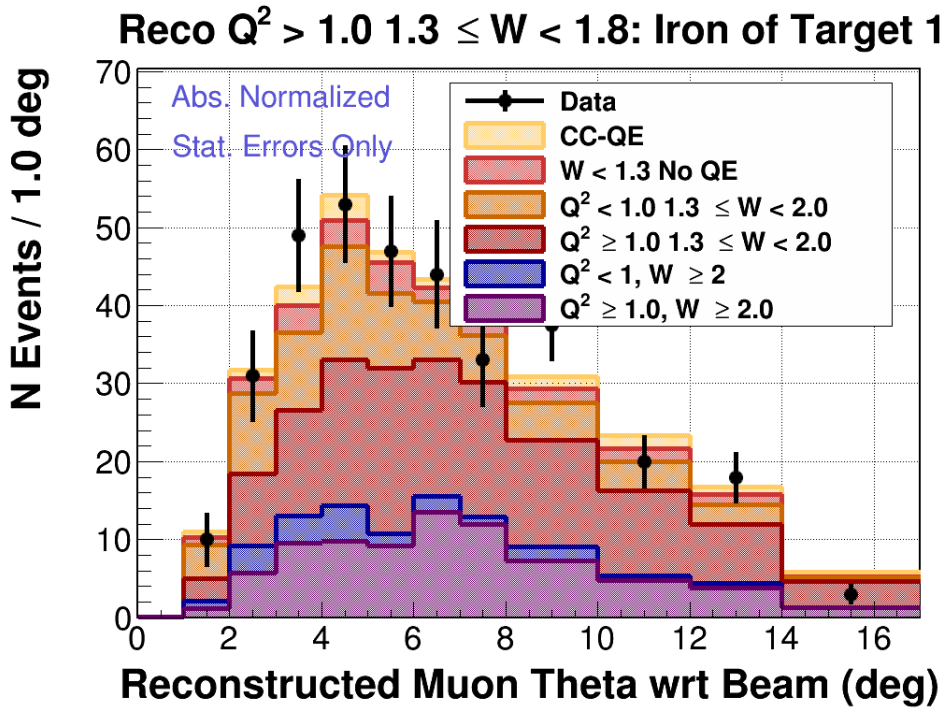

Figure A-77. Data / MC low W sideband before fitting: target 01 Fe (θ_μ)

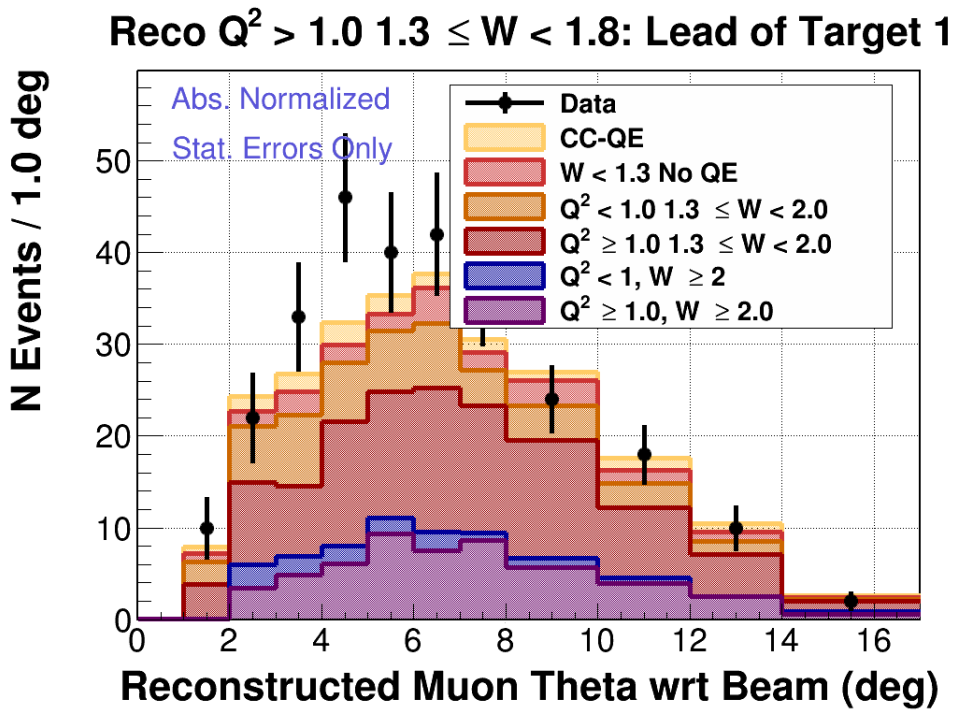

Figure A-78. Data / MC low W sideband before fitting: target 01 Pb (θ_μ)

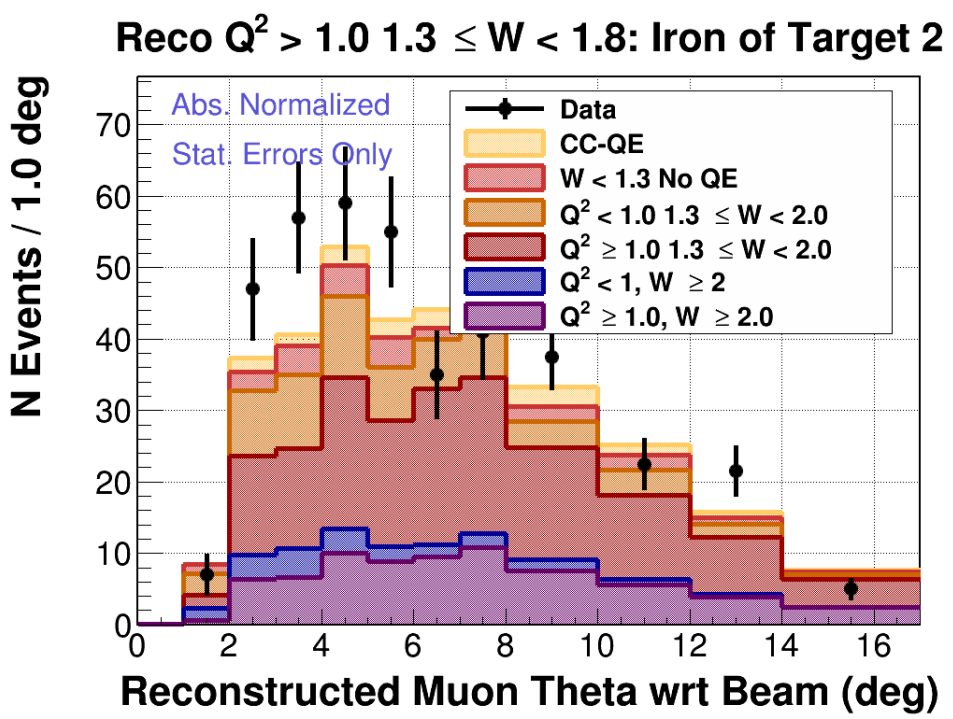

Figure A-79. Data / MC low W sideband before fitting: target 02 Fe (θ_μ)

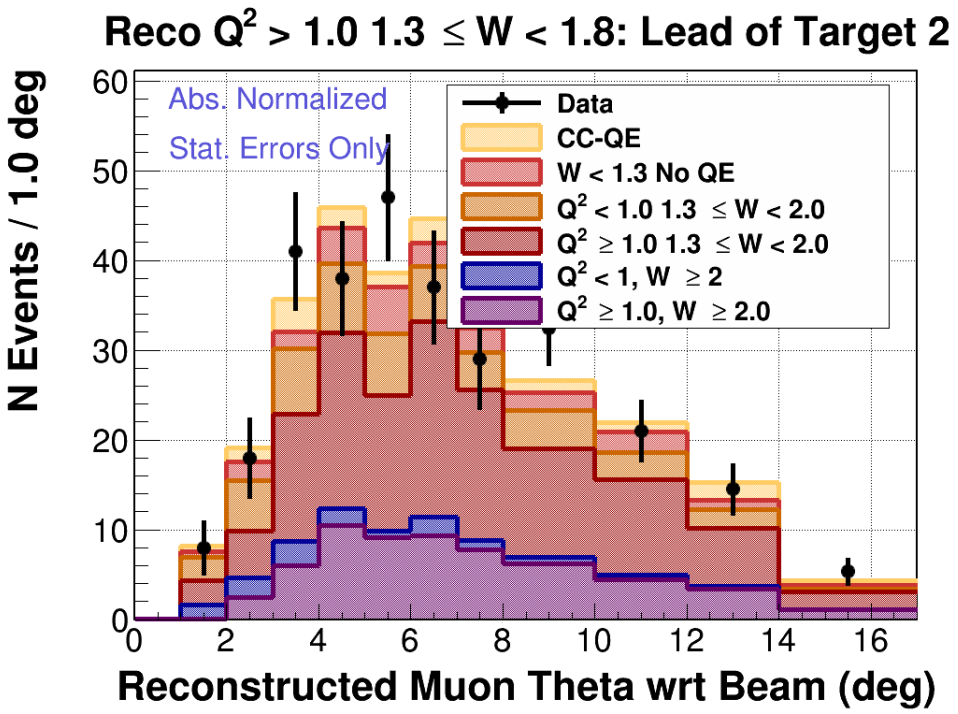

Figure A-80. Data / MC low W sideband before fitting: target 02 Pb (θ_μ)

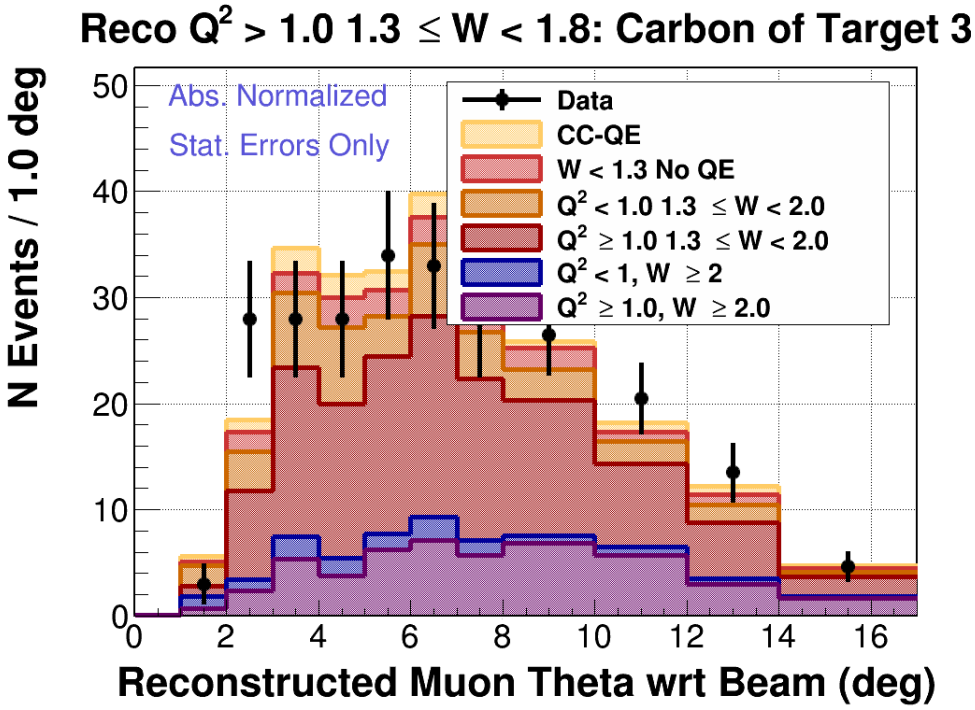

Figure A-81. Data / MC low W sideband before fitting: target 03 C (θ_μ)

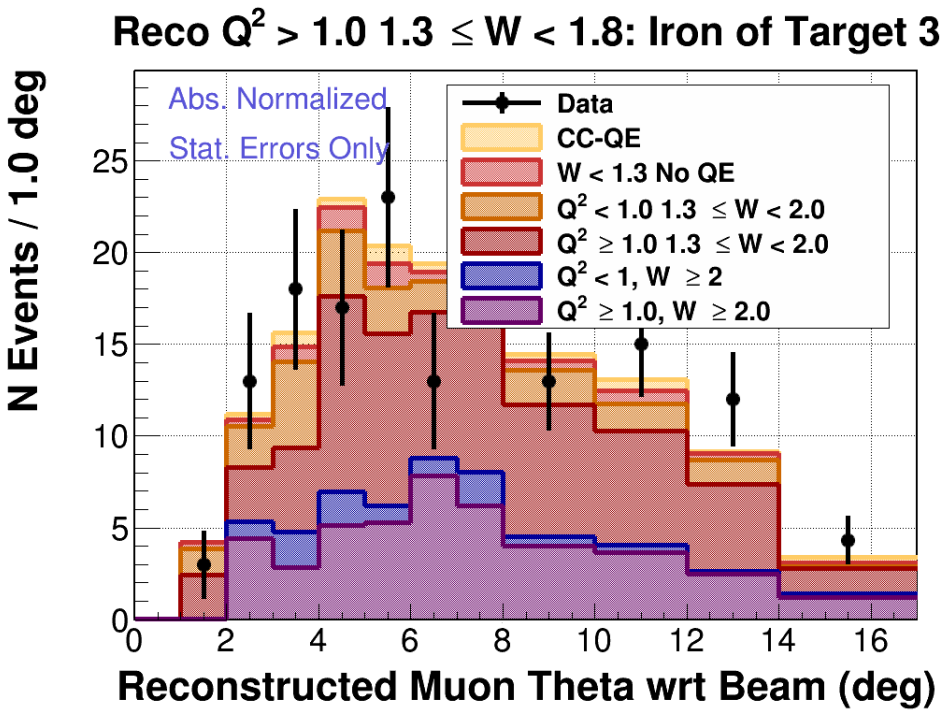

Figure A-82. Data / MC low W sideband before fitting: target 03 Fe (θ_μ)

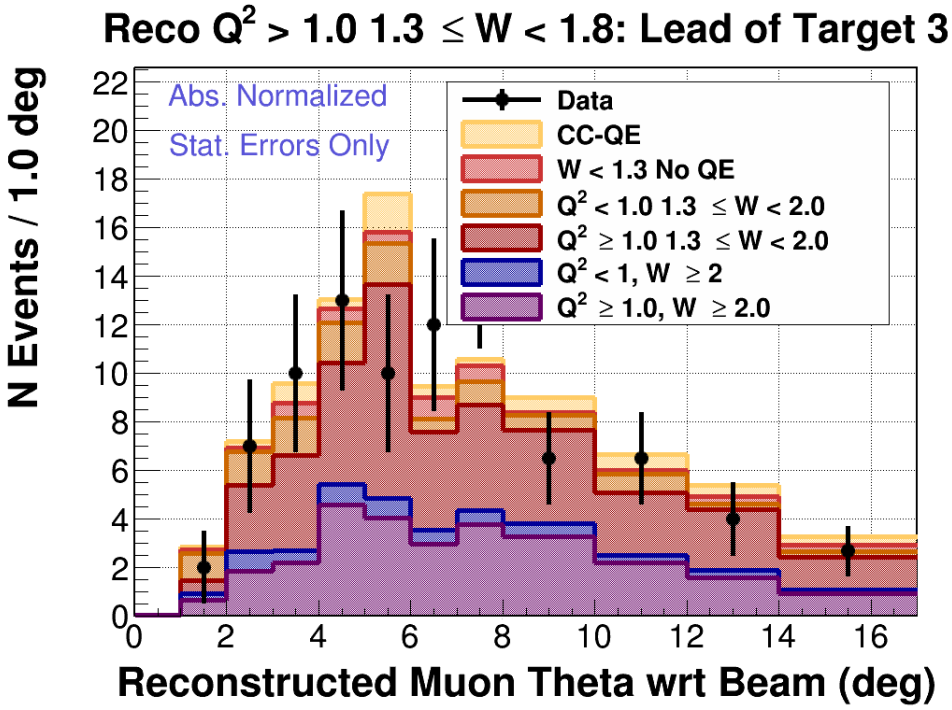

Figure A-83. Data / MC low W sideband before fitting: target 03 Pb (θ_μ)

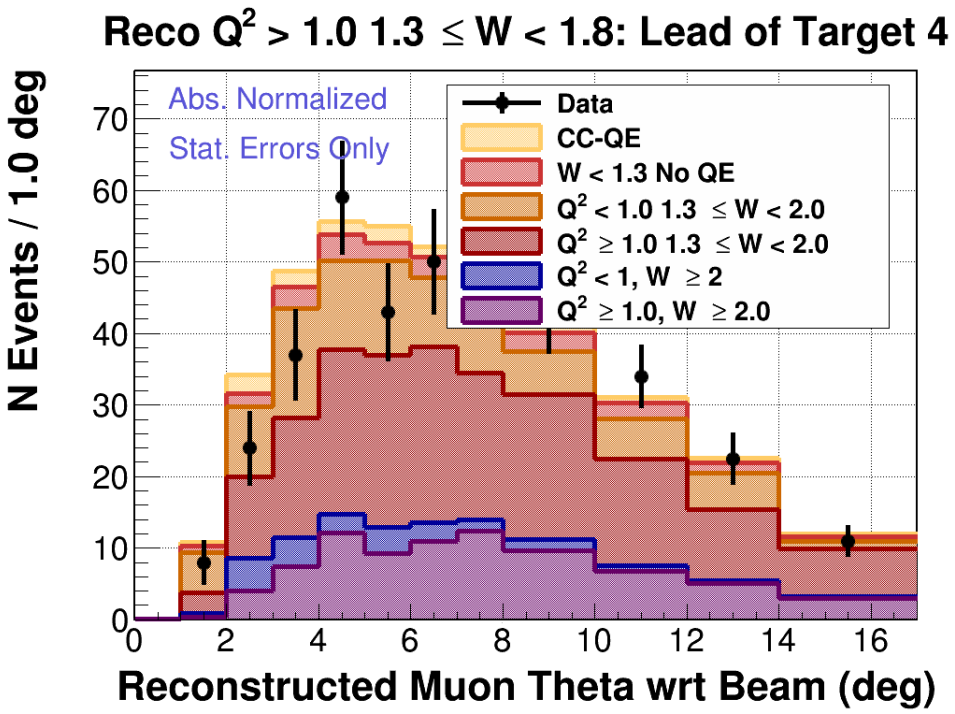

Figure A-84. Data / MC low W sideband before fitting: target 04 Pb (θ_μ)

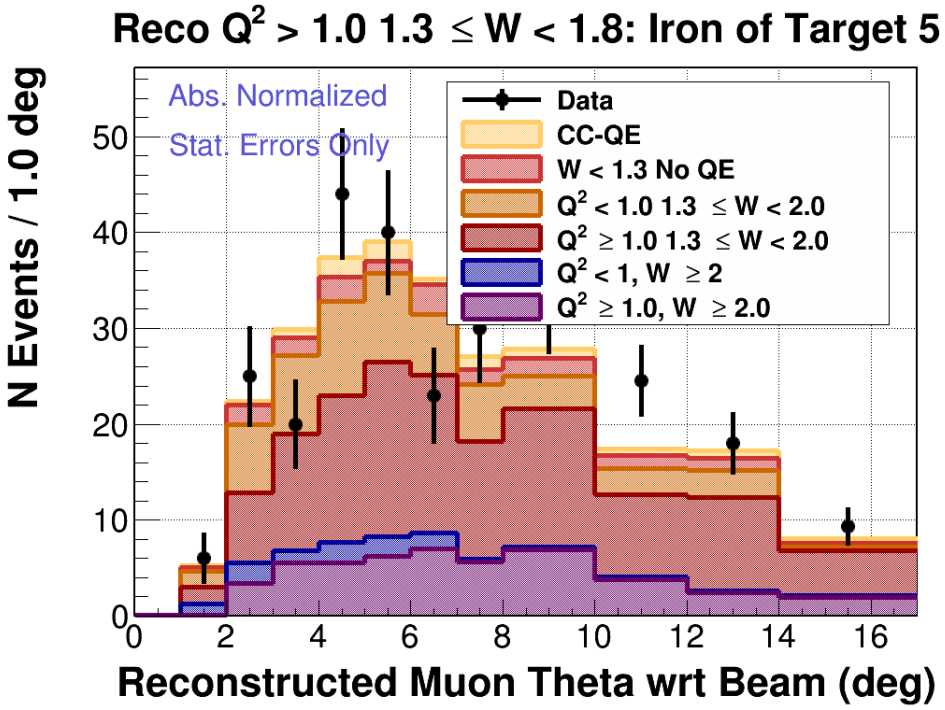

Figure A-85. Data / MC low W sideband before fitting: target 05 Fe (θ_μ)

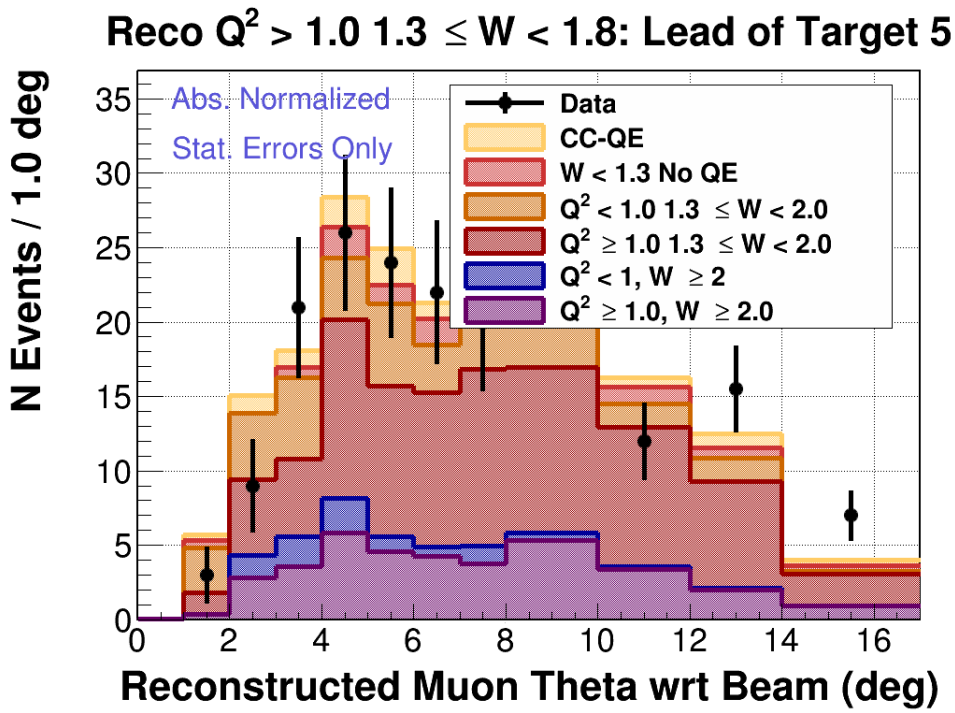

Figure A-86. Data / MC low W sideband before fitting: target 05 Pb (θ_μ)

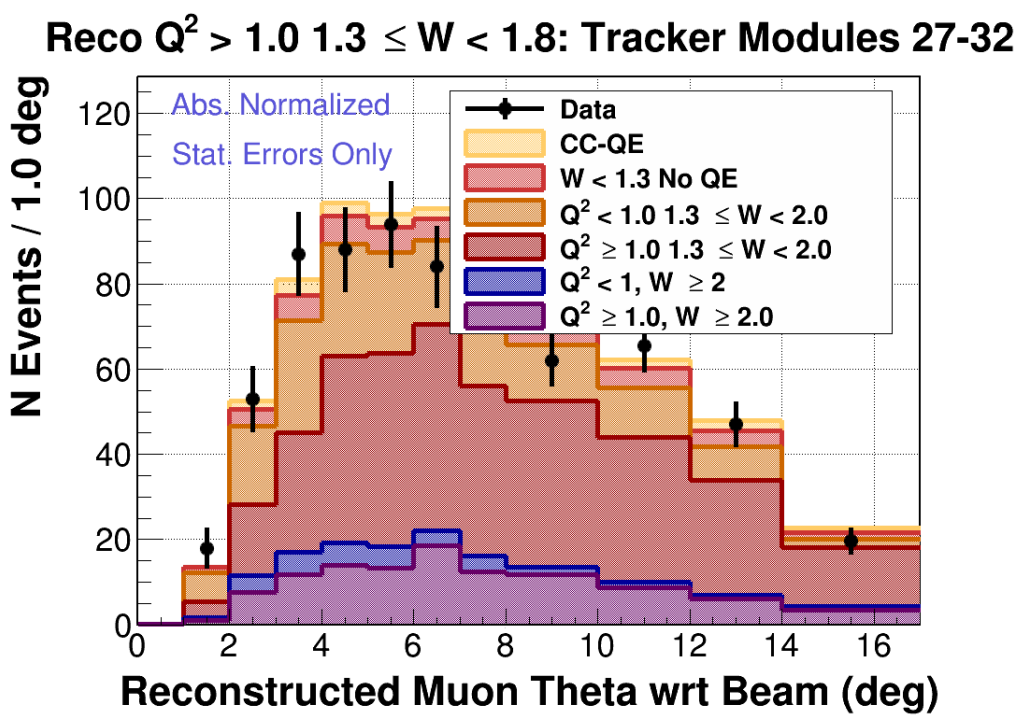

Figure A-87. Data / MC low W sideband before fitting: tracker mods. 27-32 (θ_μ)

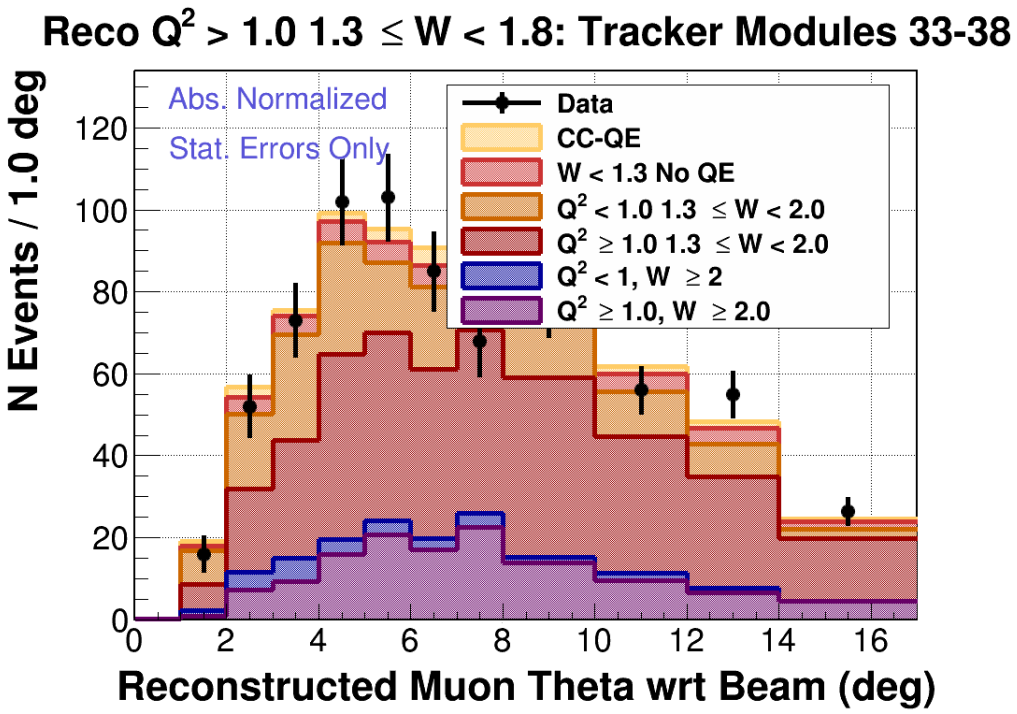

Figure A-88. Data / MC low W sideband before fitting: tracker mods. 33-38 (θ_μ)

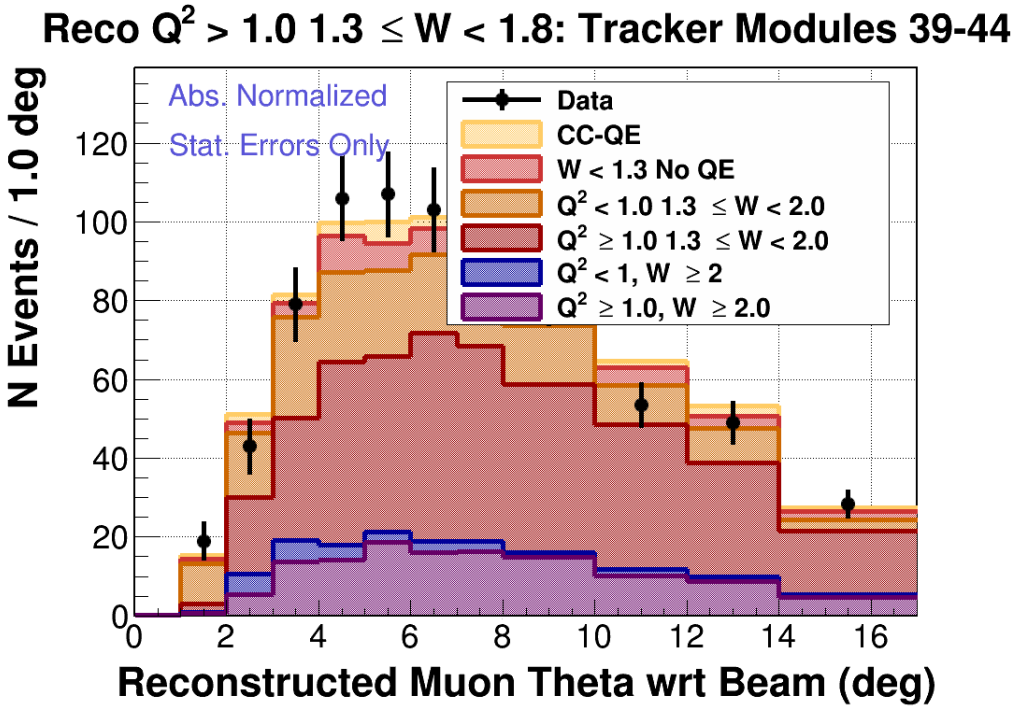

Figure A-89. Data / MC low W sideband before fitting: tracker mods. 39-44 (θ_μ)

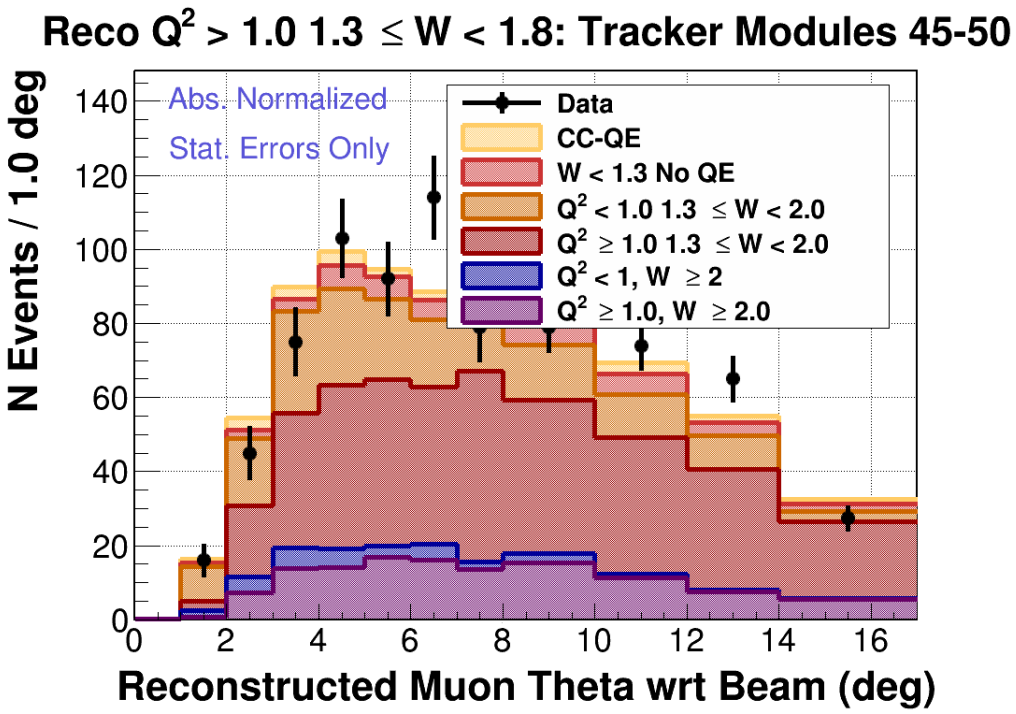

Figure A-90. Data / MC low W sideband before fitting: tracker mods. 45-50 (θ_μ)

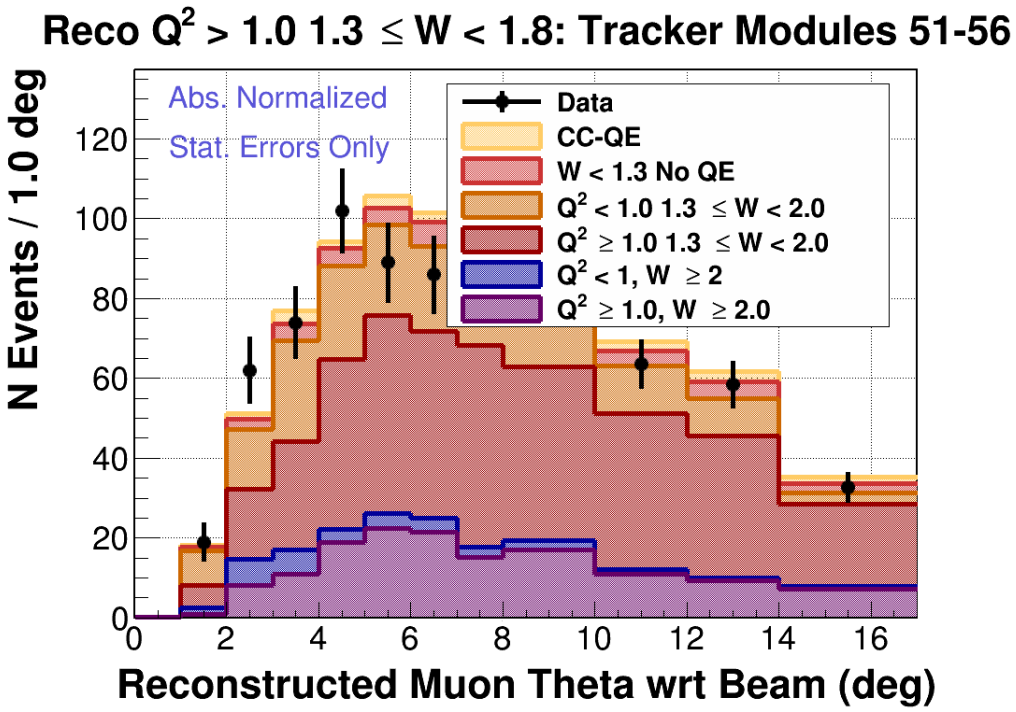

Figure A-91. Data / MC low W sideband before fitting: tracker mods. 51-56 (θ_μ)

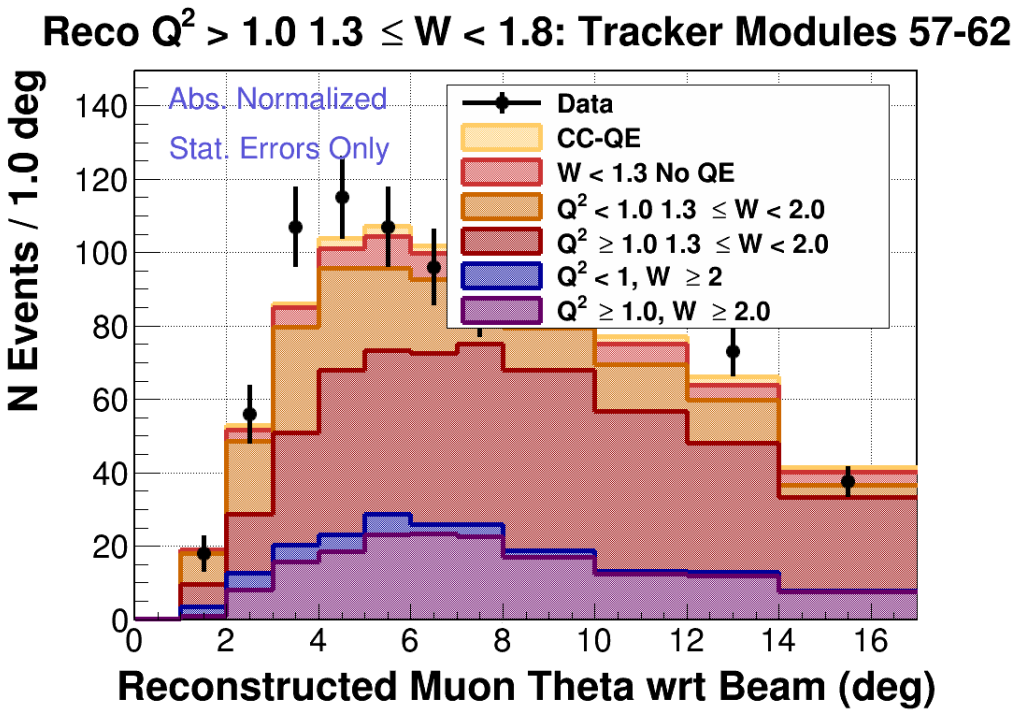

Figure A-92. Data / MC low W sideband before fitting: tracker mods. 57-62 (θ_μ)

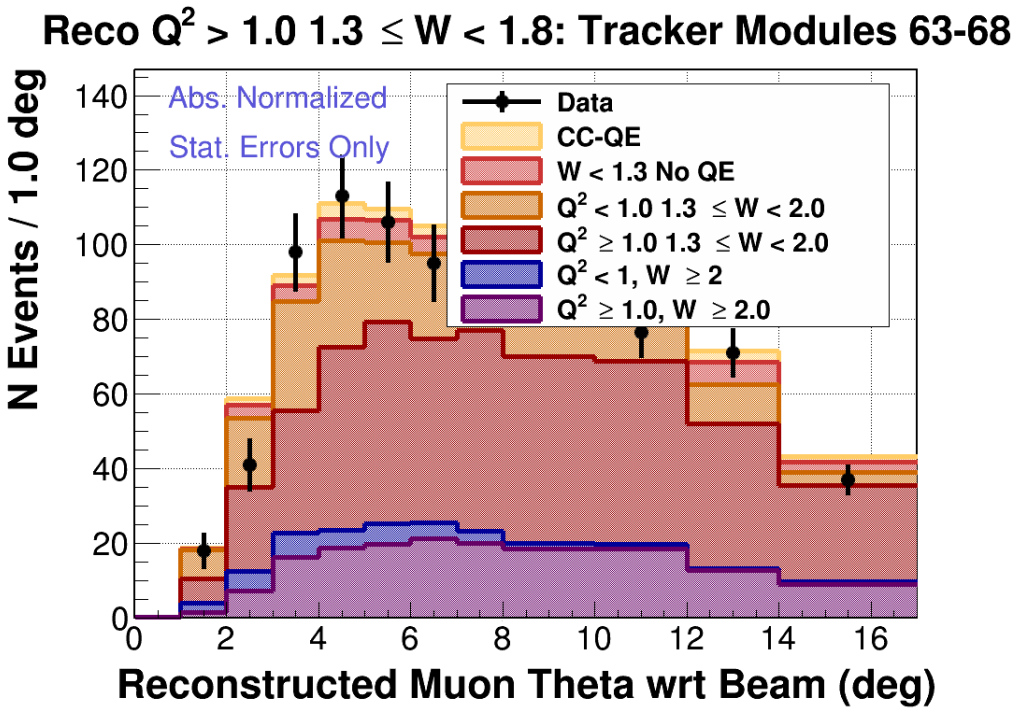

Figure A-93. Data / MC low W sideband before fitting: tracker mods. 63-68 (θ_μ)

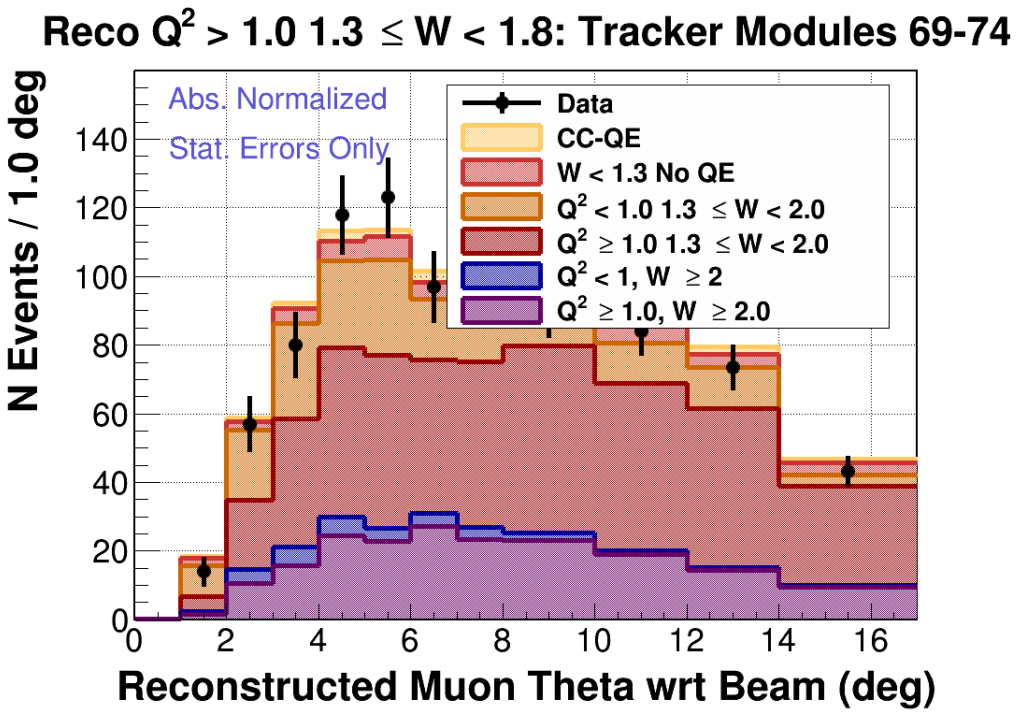

Figure A-94. Data / MC low W sideband before fitting: tracker mods. 69-74 (θ_μ)

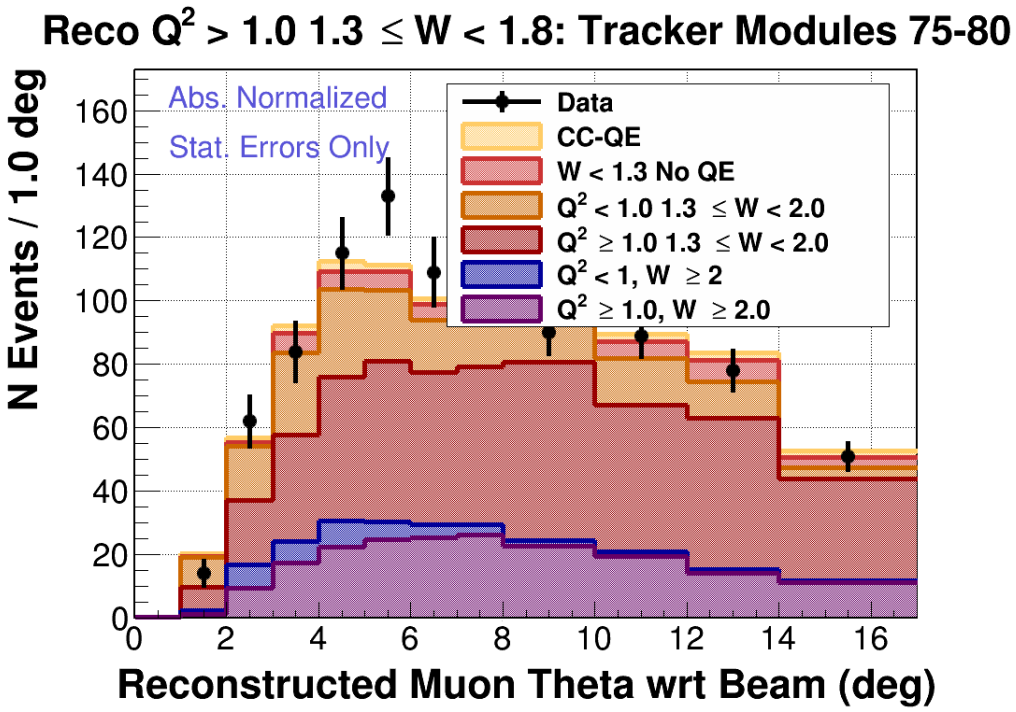

Figure A-95. Data / MC low W sideband before fitting: tracker mods. 75-80 (θ_μ)

A.2 Scale Factors derived per Target / Nucleus for the Low W Sideband:

$Q^2 \geq 1.0$ **(GeV/c)**^{2} $1.3 \leq W < 1.8$ **GeV/c**^{2}

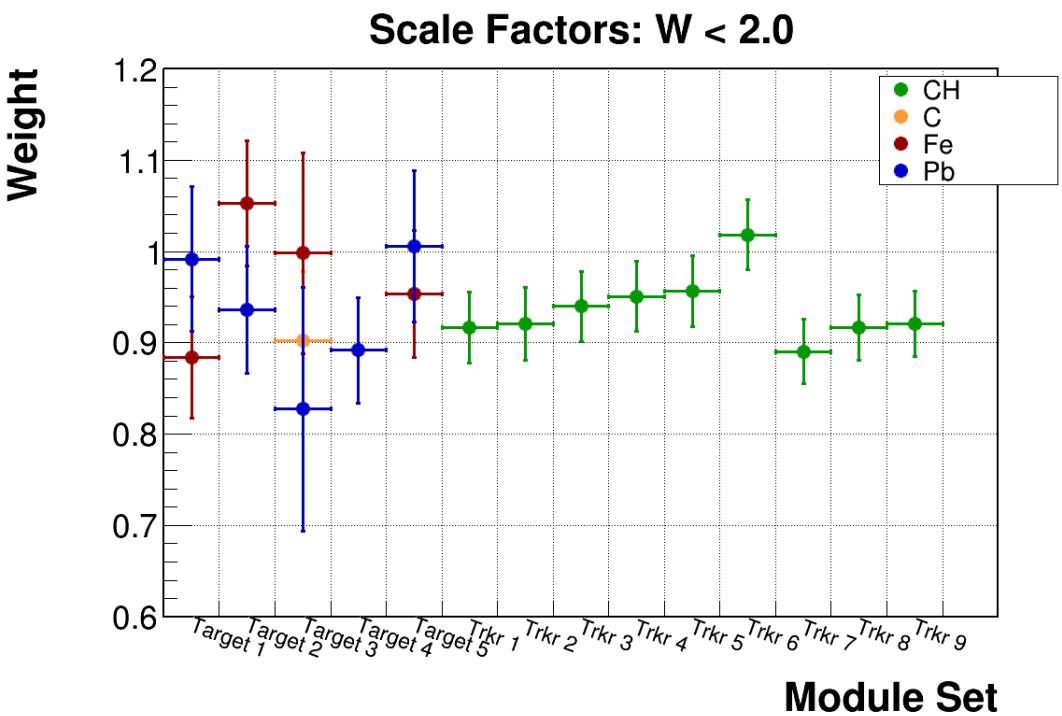

Figure A-96. Low W scale factors per target

A.3 Low W Sideband: $Q^2 \geq 1.0$ (GeV/c)^2 $1.3 \leq W < 1.8$ GeV/c^2 (After Fitting)

The following plots show the population of the low W sideband ($Q^2 \geq 1.0$ (GeV/c)^2 $1.3 \leq W < 1.8$) *after* tuning to data as a function of neutrino energy (E_ν):

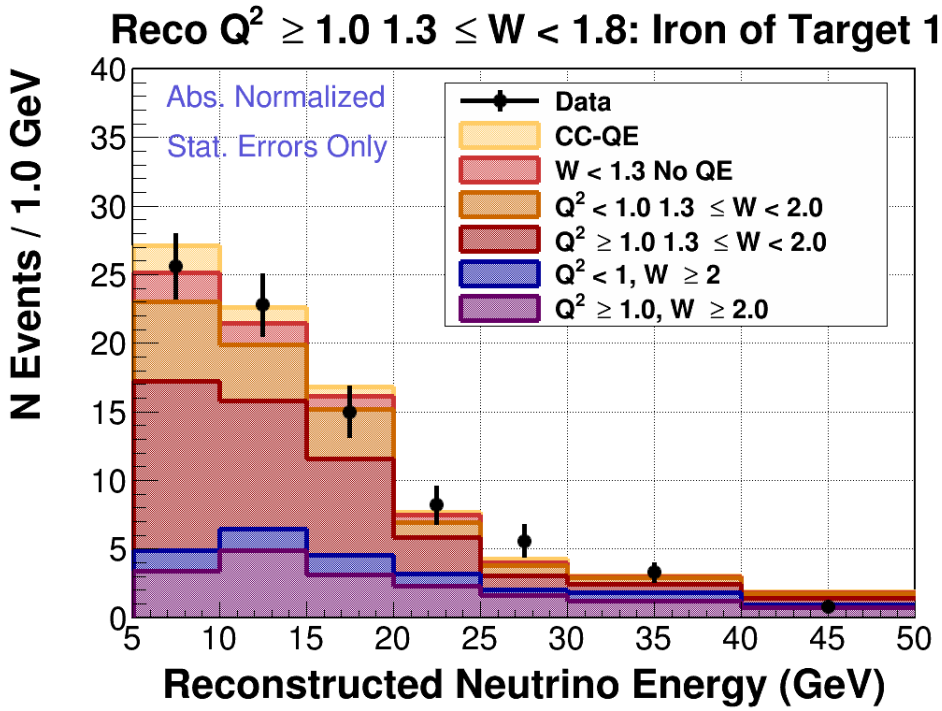

Figure A-97. Data / MC low W sideband after fitting: target 01 Fe (E_ν)

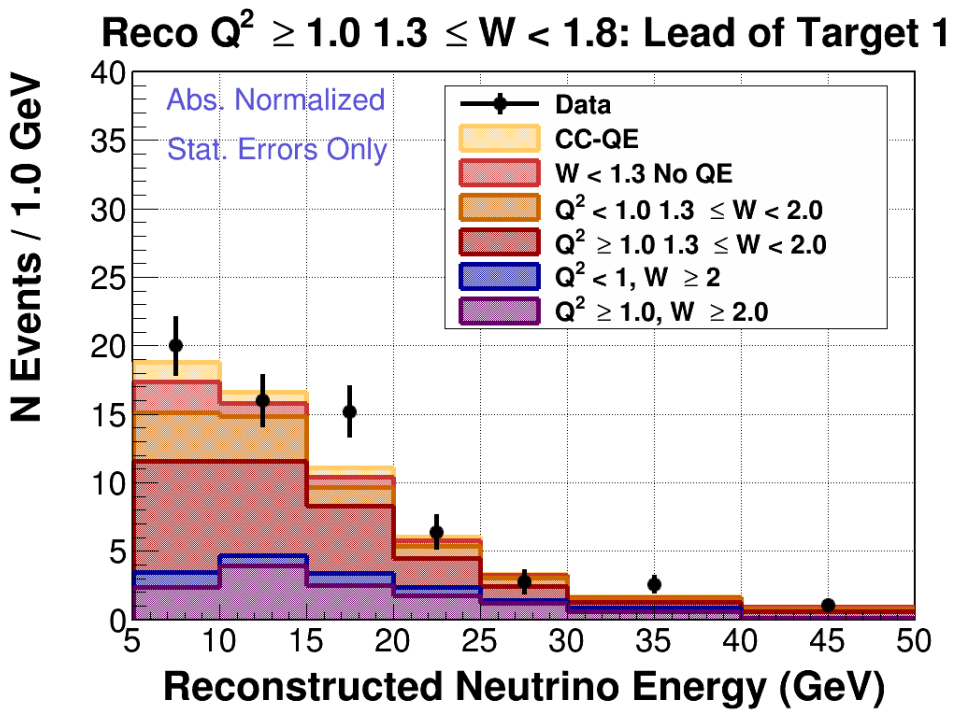

Figure A-98. Data / MC low W sideband after fitting: target 01 Pb (E_ν)

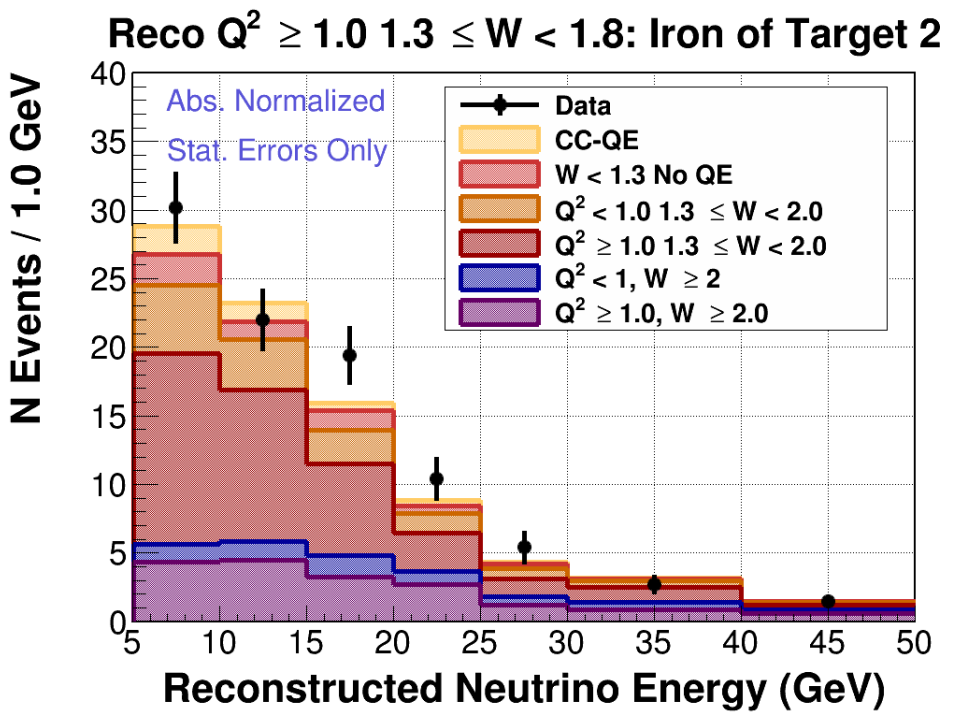

Figure A-99. Data / MC low W sideband after fitting: target 02 Fe (E_ν)

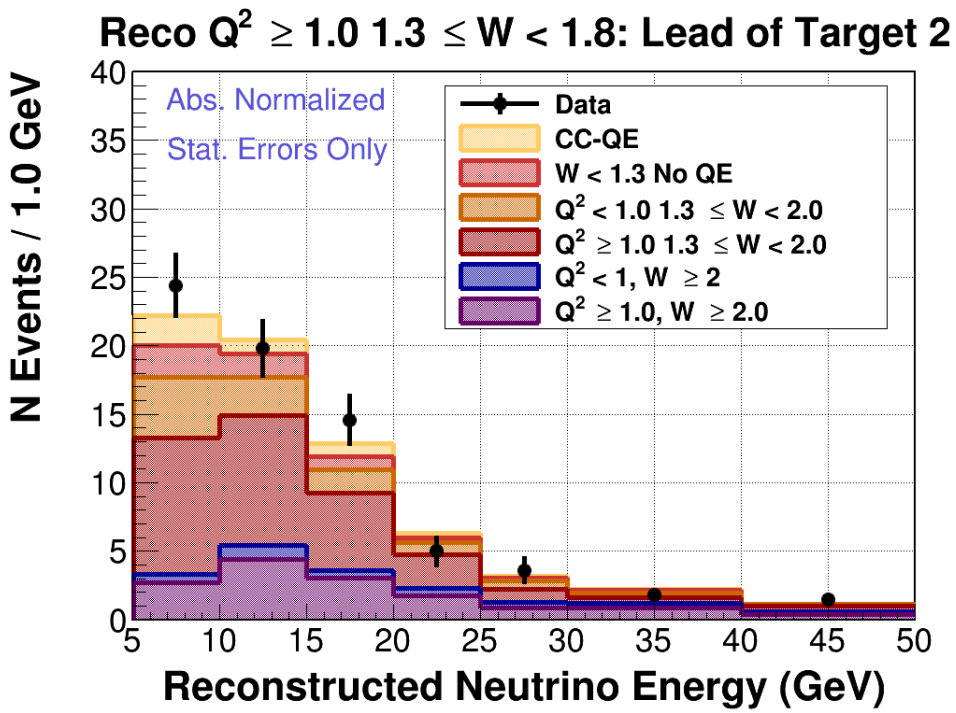

Figure A-100. Data / MC low W sideband after fitting: target 02 Pb (E_ν)

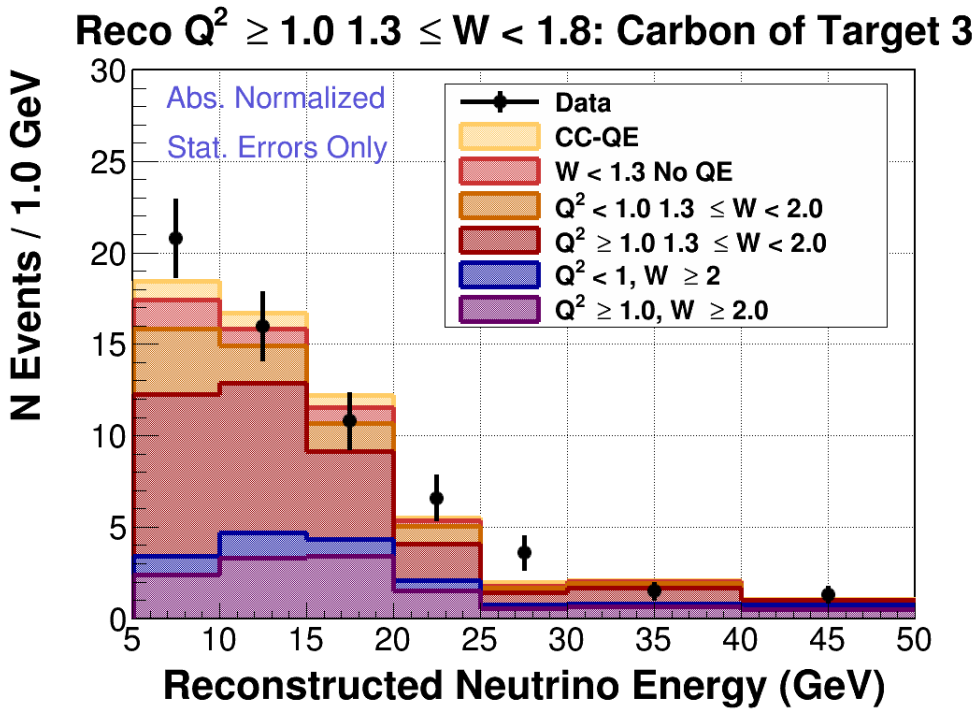

Figure A-101. Data / MC low W sideband after fitting: target 03 C (E_ν)

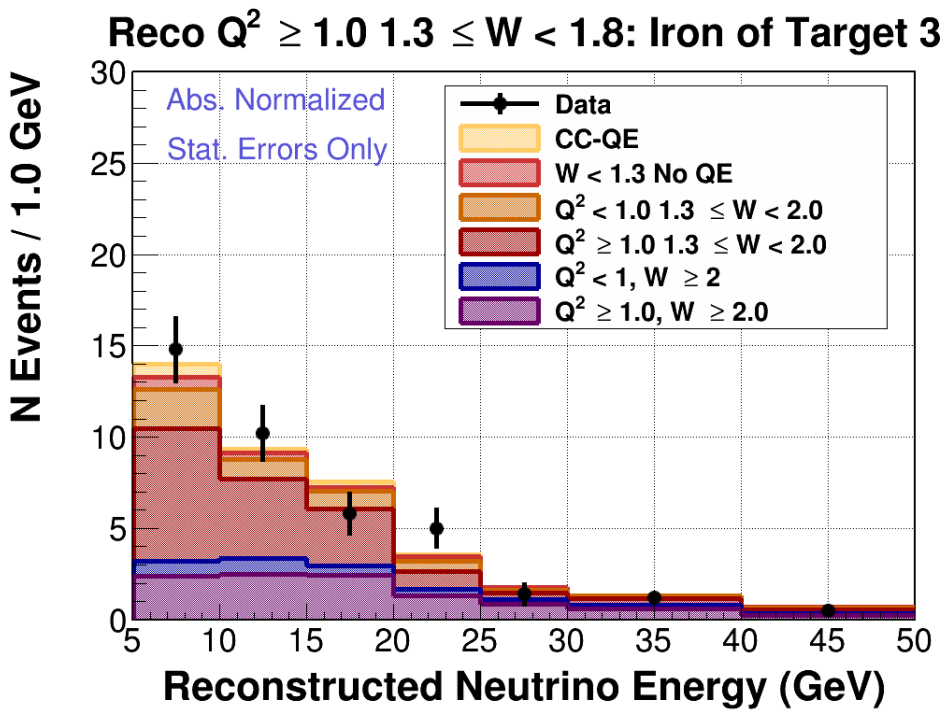

Figure A-102. Data / MC low W sideband after fitting: target 03 Fe (E_ν)

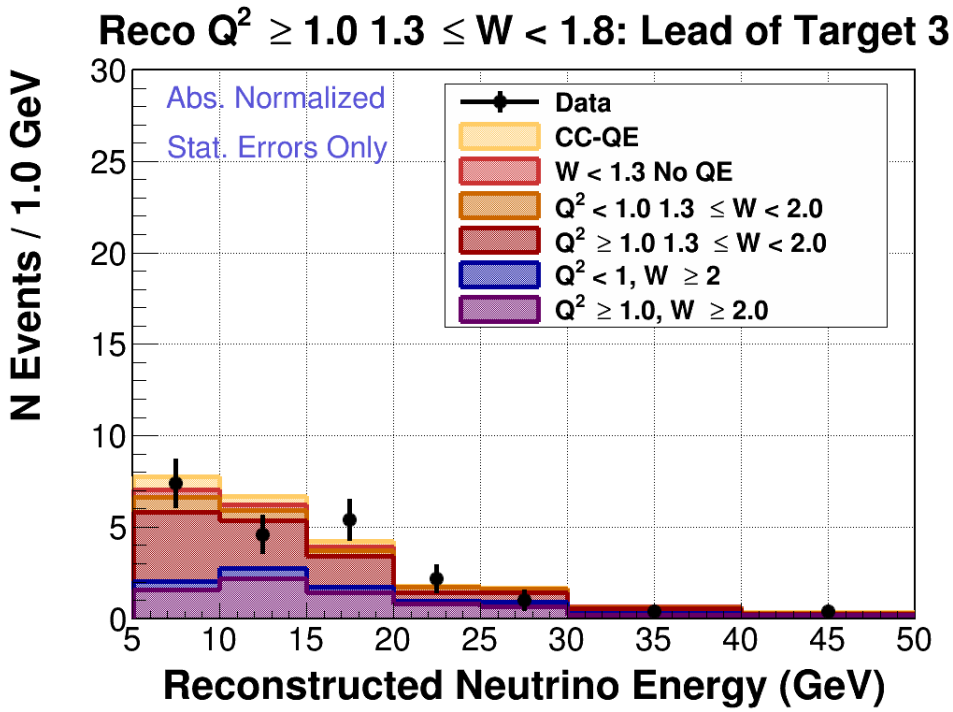

Figure A-103. Data / MC low W sideband after fitting: target 03 Pb (E_ν)

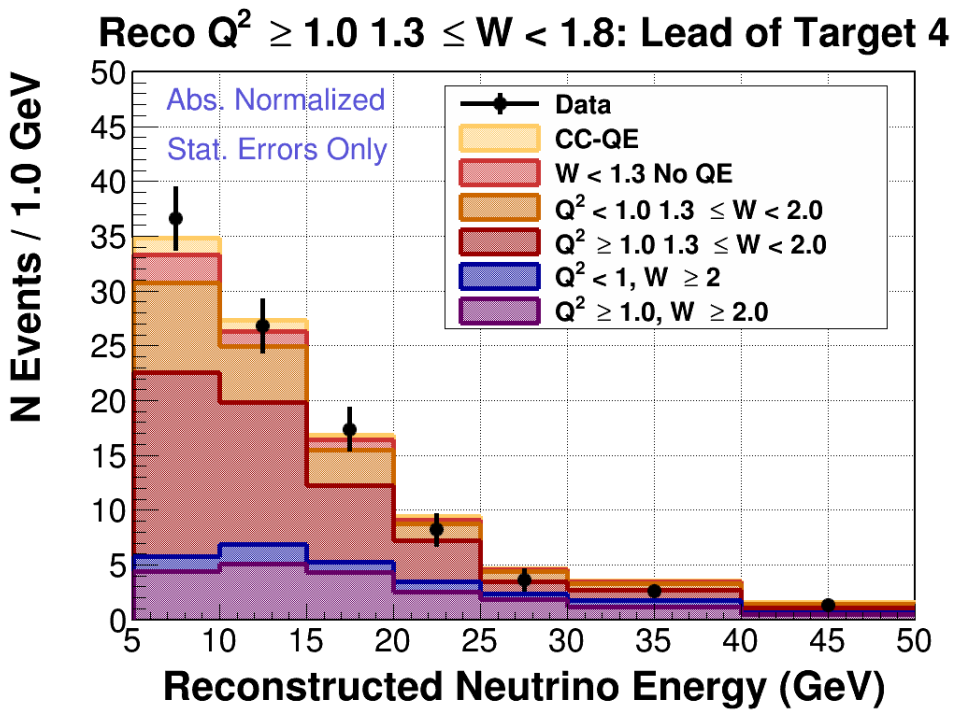

Figure A-104. Data / MC low W sideband after fitting: target 04 Pb (E_ν)

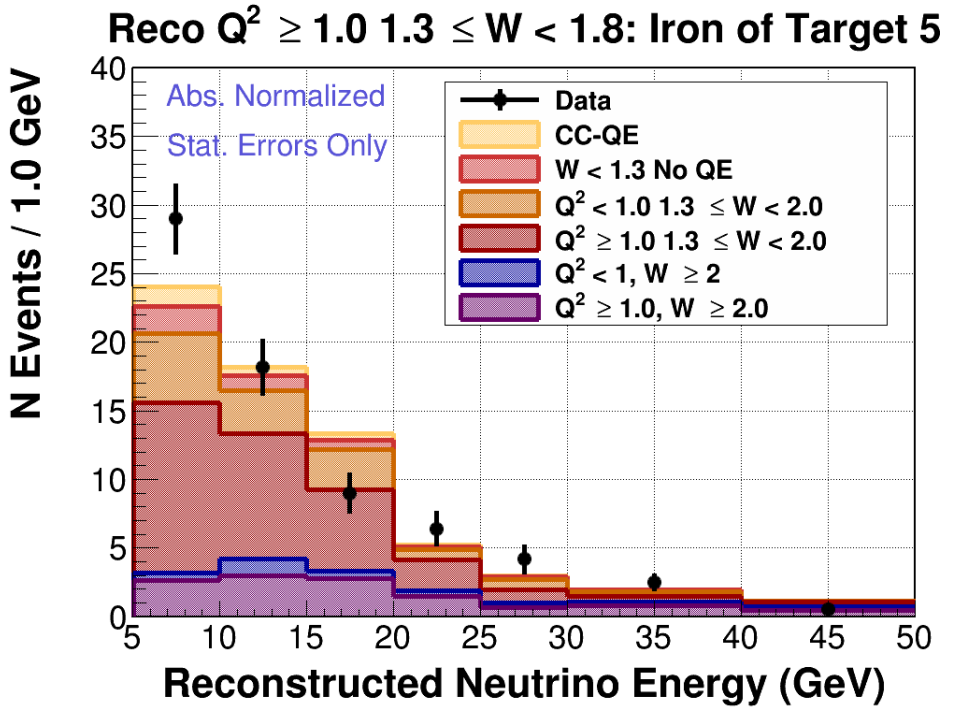

Figure A-105. Data / MC low W sideband after fitting: target 05 Fe (E_ν)

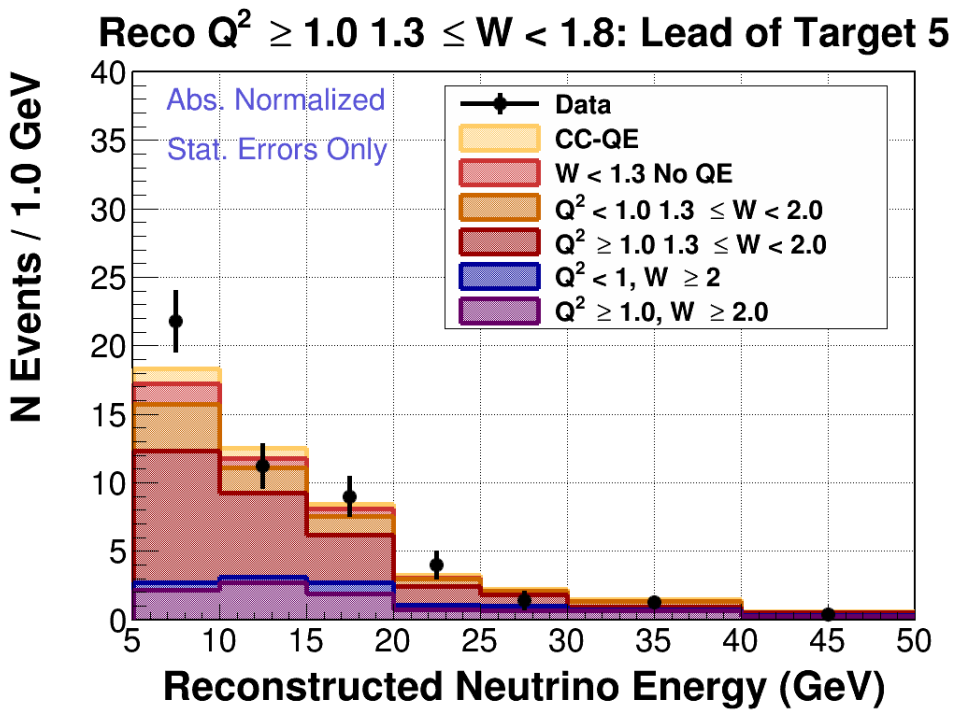

Figure A-106. Data / MC low W sideband after fitting: target 05 Pb (E_ν)

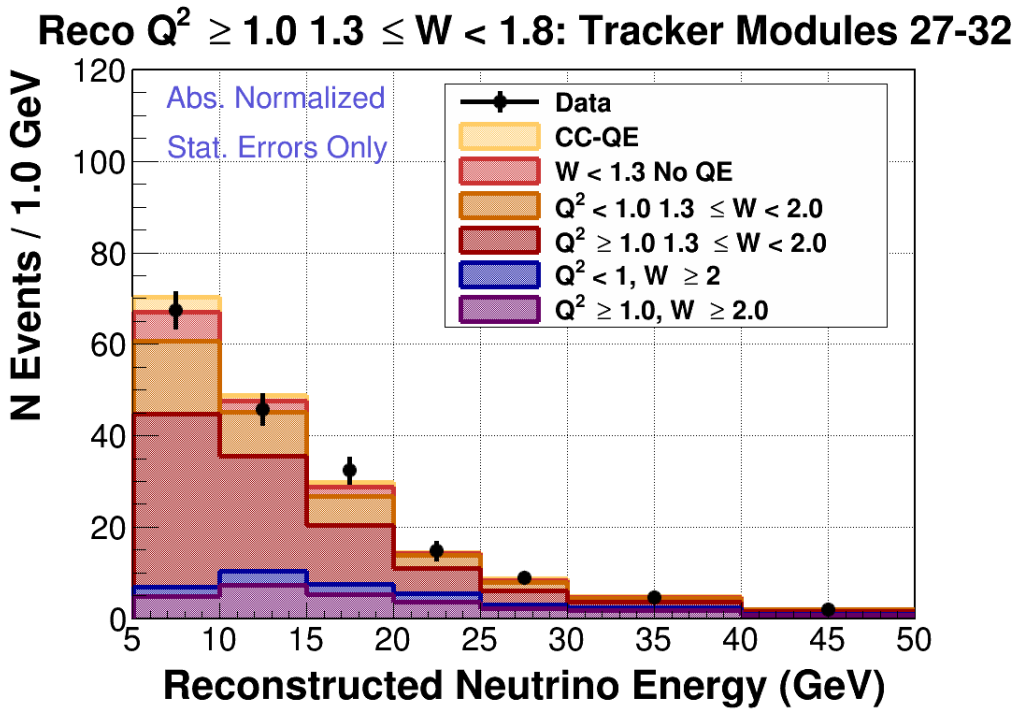

Figure A-107. Data / MC low W sideband after fitting: tracker mods. 27-32 (E_ν)

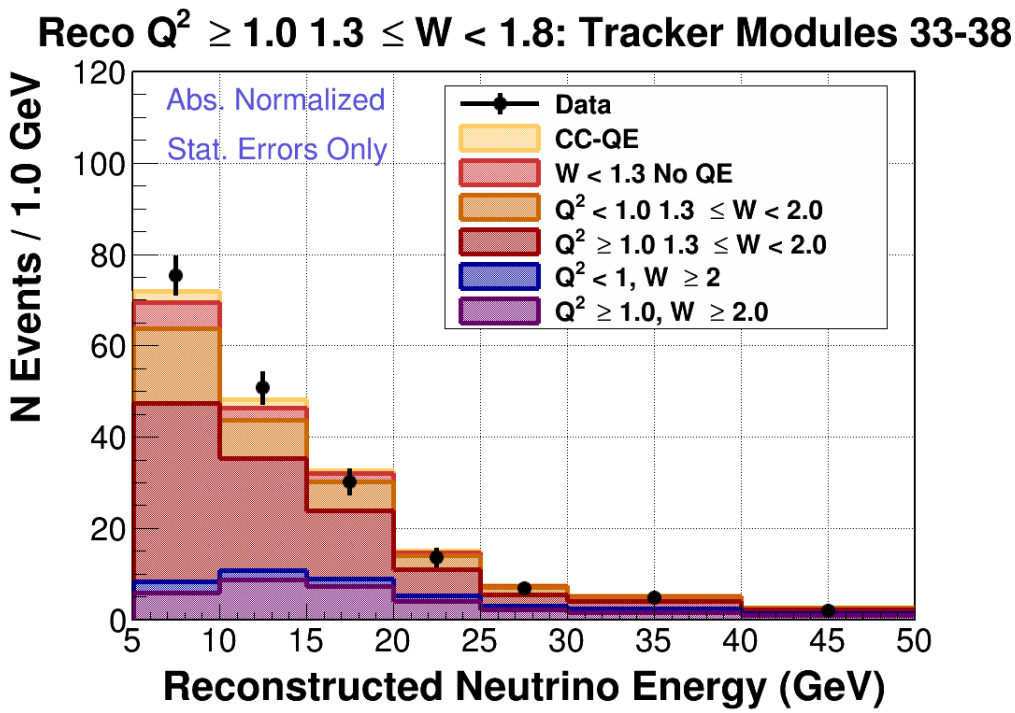

Figure A-108. Data / MC low W sideband after fitting: tracker mods. 33-38 (E_ν)

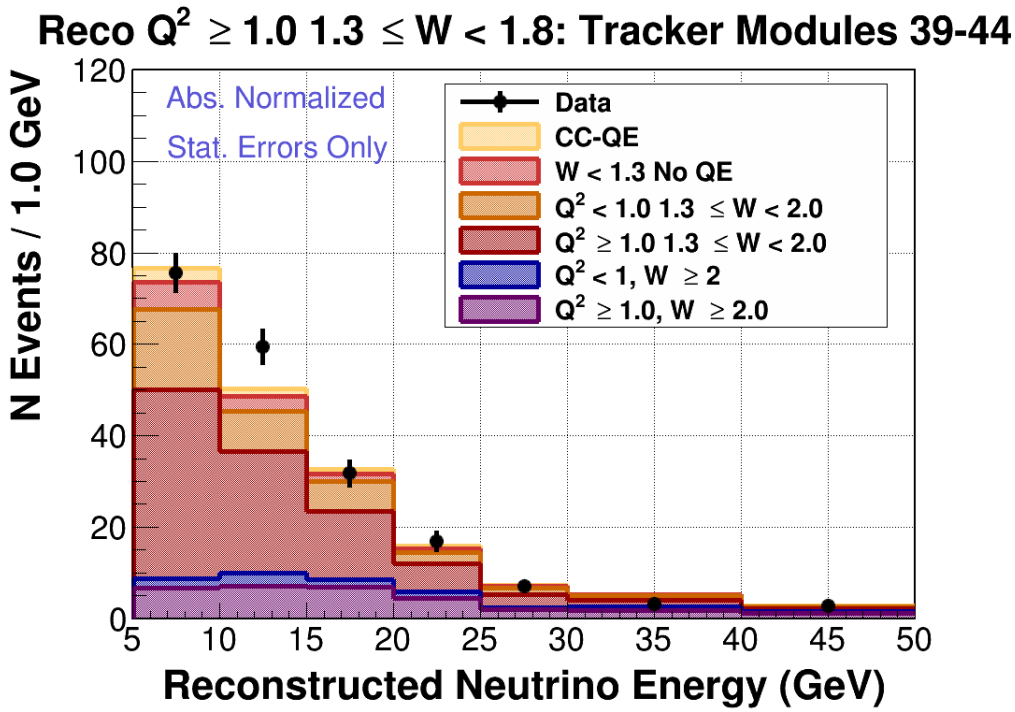

Figure A-109. Data / MC low W sideband after fitting: tracker mods. 39-44 (E_ν)

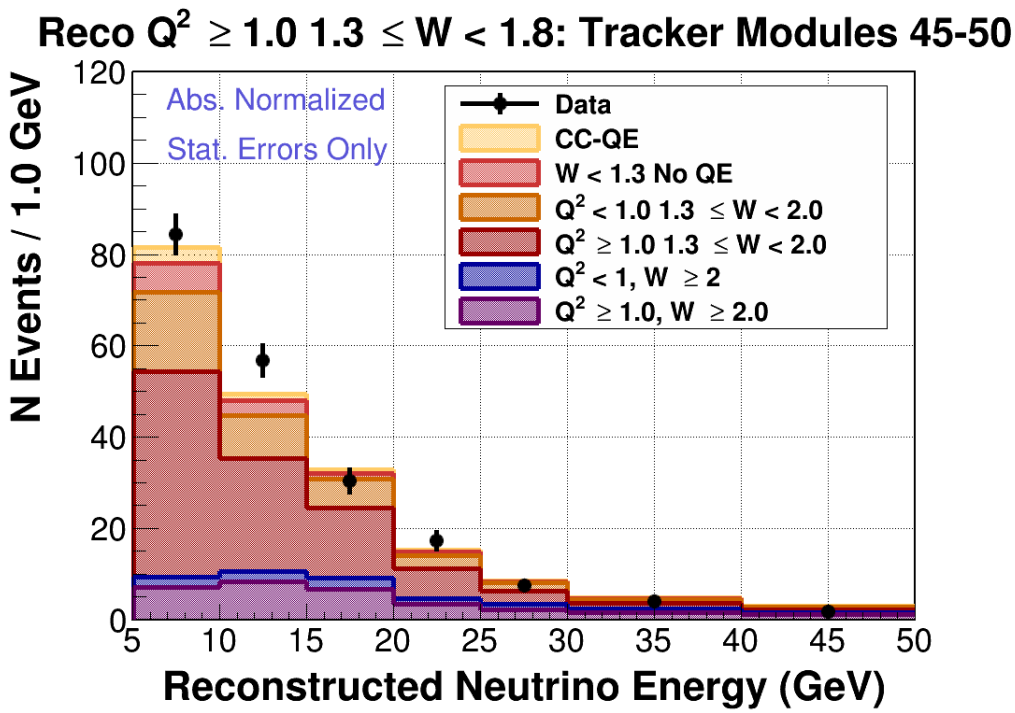

Figure A-110. Data / MC low W sideband after fitting: tracker mods. 45-50 (E_ν)

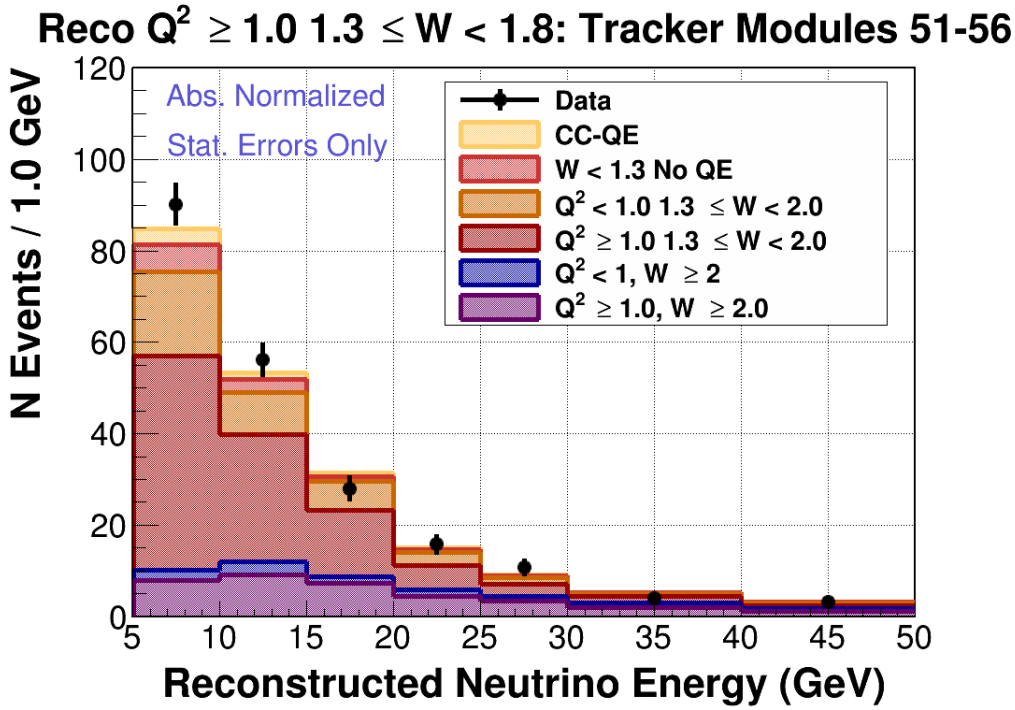

Figure A-111. Data / MC low W sideband after fitting: tracker mods. 51-56 (E_ν)

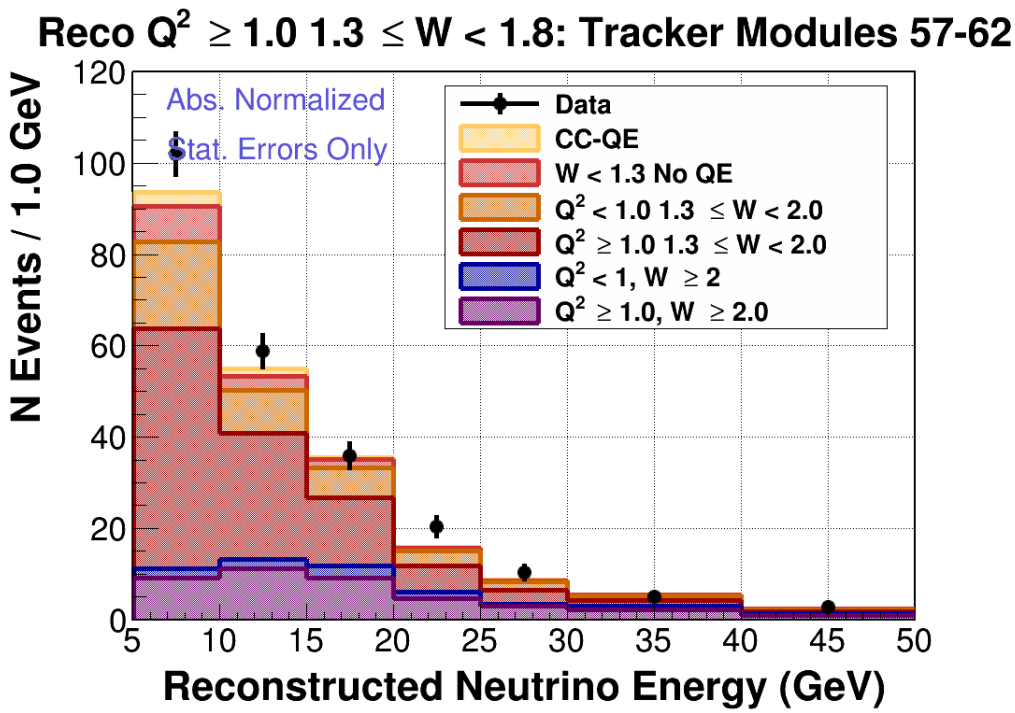

Figure A-112. Data / MC low W sideband after fitting: tracker mods. 57-62 (E_ν)

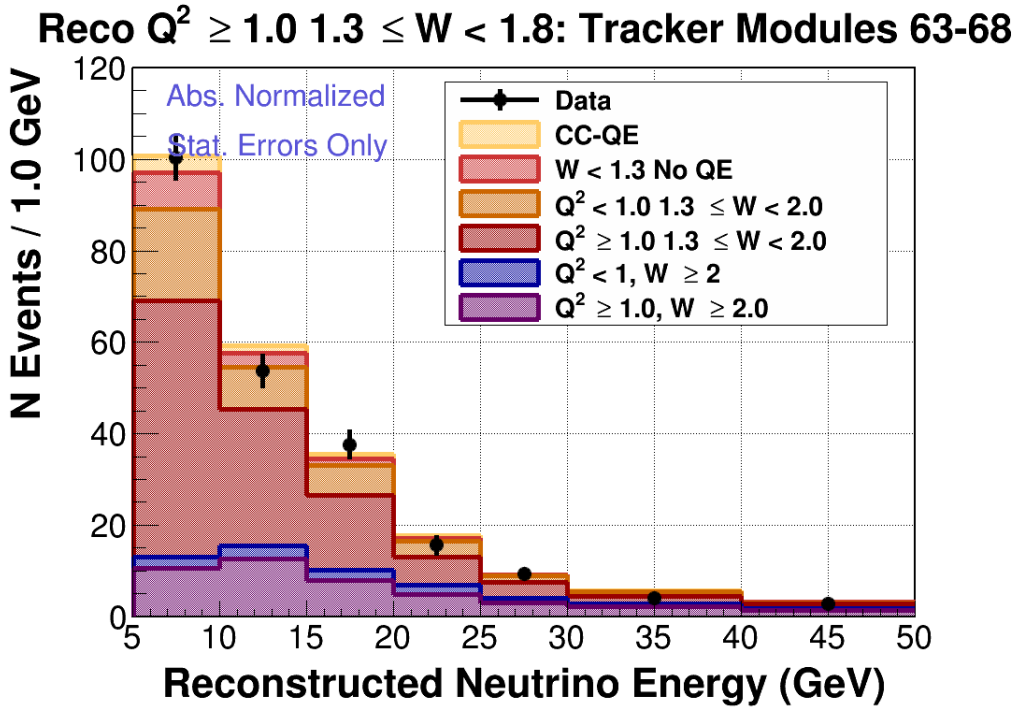

Figure A-113. Data / MC low W sideband after fitting: tracker mods. 63-68 (E_ν)

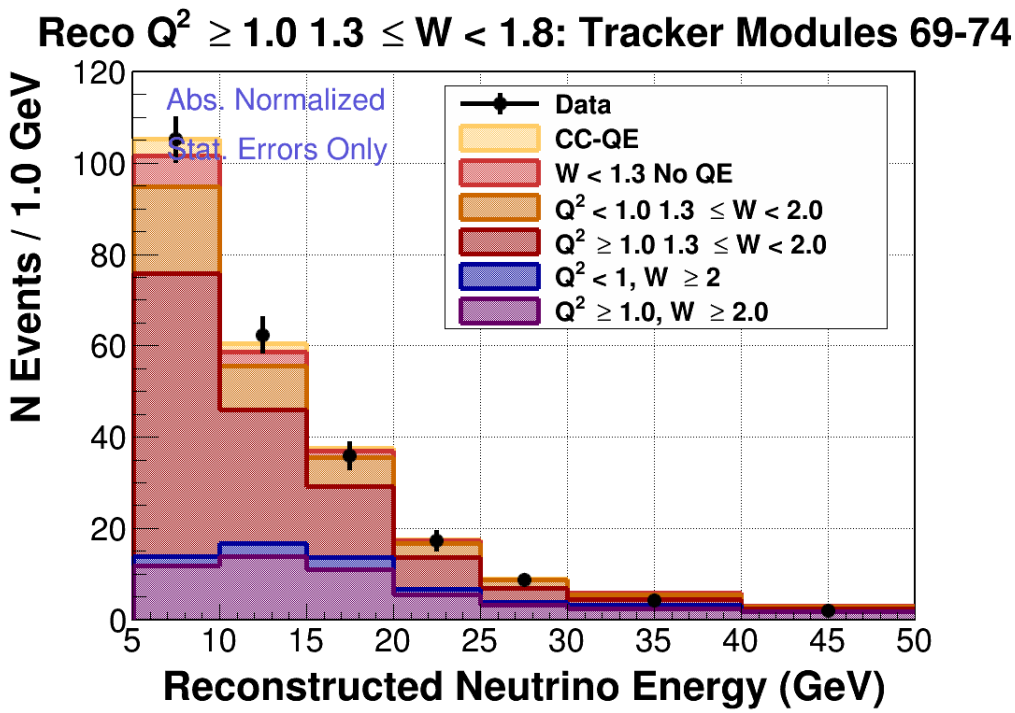

Figure A-114. Data / MC low W sideband after fitting: tracker mods. 69-74 (E_ν)

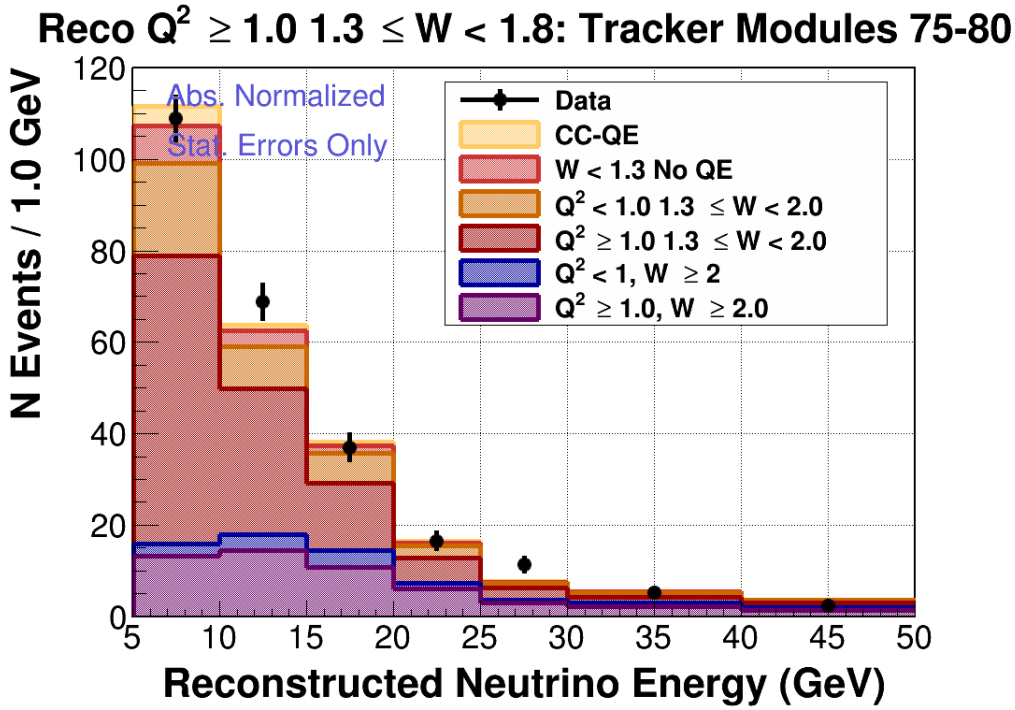

Figure A-115. Data / MC low W sideband after fitting: tracker mods. 75-80 (E_ν)

The following plots show the population of the low W sideband ($Q^2 \geq 1.0$ (GeV/c)^2 $1.3 \leq W < 1.8$ GeV/c^2) *after* tuning to data as a function of four momentum transfer squared (Q^2):

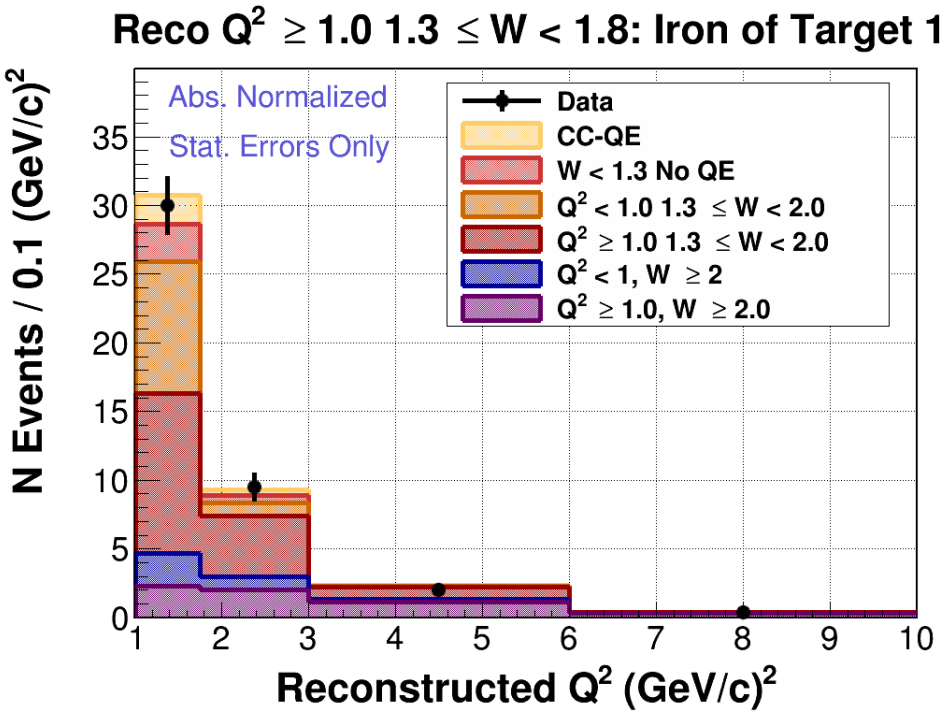

Figure A-116. Data / MC low W sideband after fitting: target 01 Fe (Q^2)

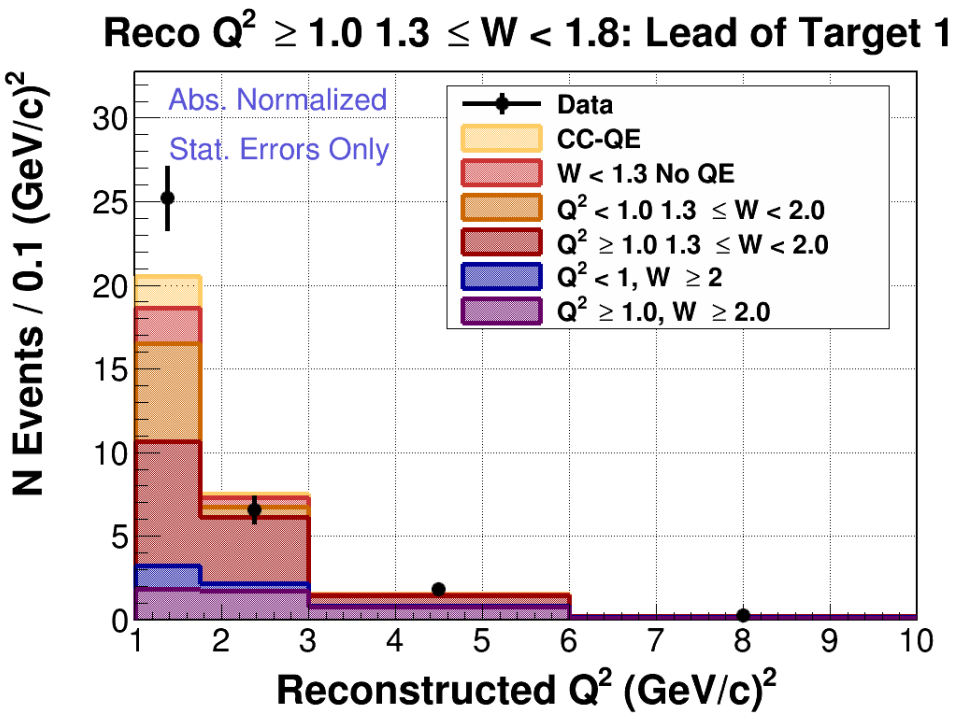

Figure A-117. Data / MC low W sideband after fitting: target 01 Pb (Q^2)

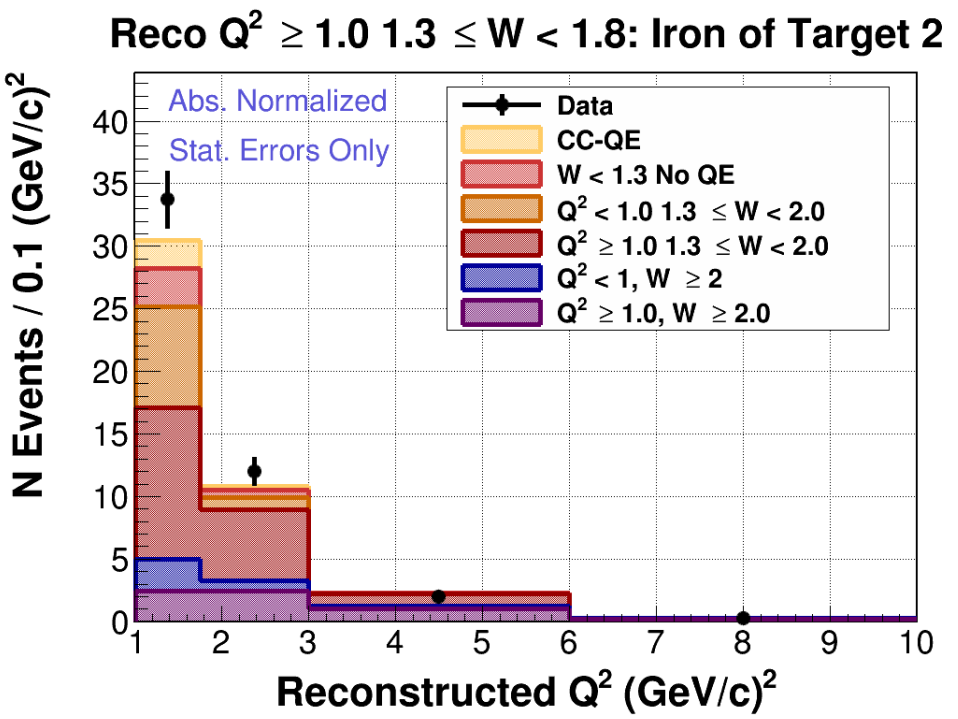

Figure A-118. Data / MC low W sideband after fitting: target 02 Fe (Q^2)

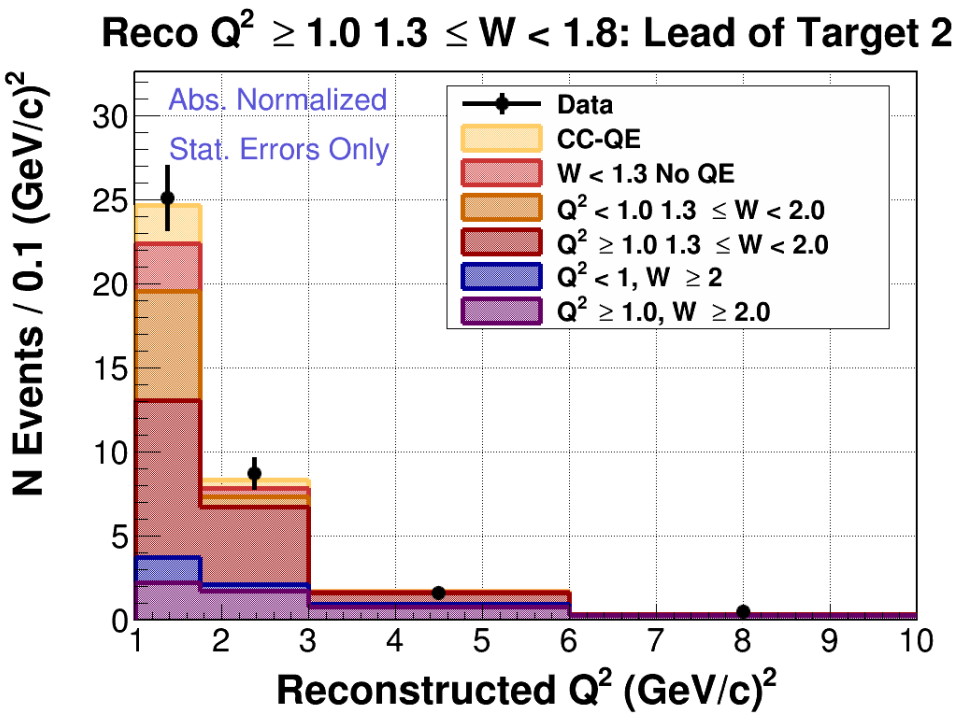

Figure A-119. Data / MC low W sideband after fitting: target 02 Pb (Q^2)

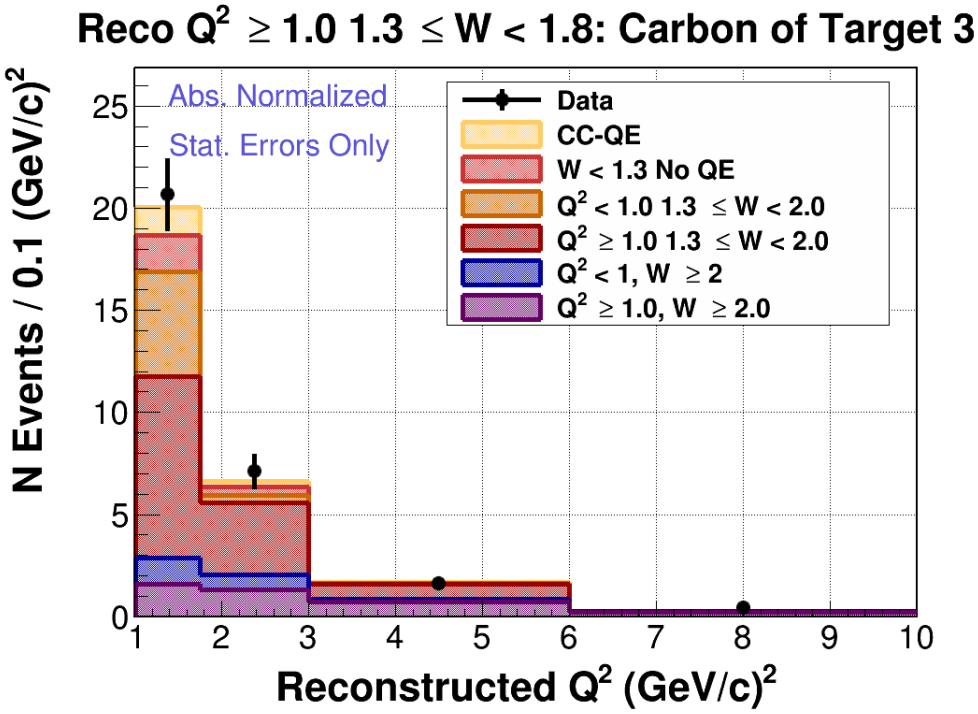

Figure A-120. Data / MC low W sideband after fitting: target 03 C (Q^2)

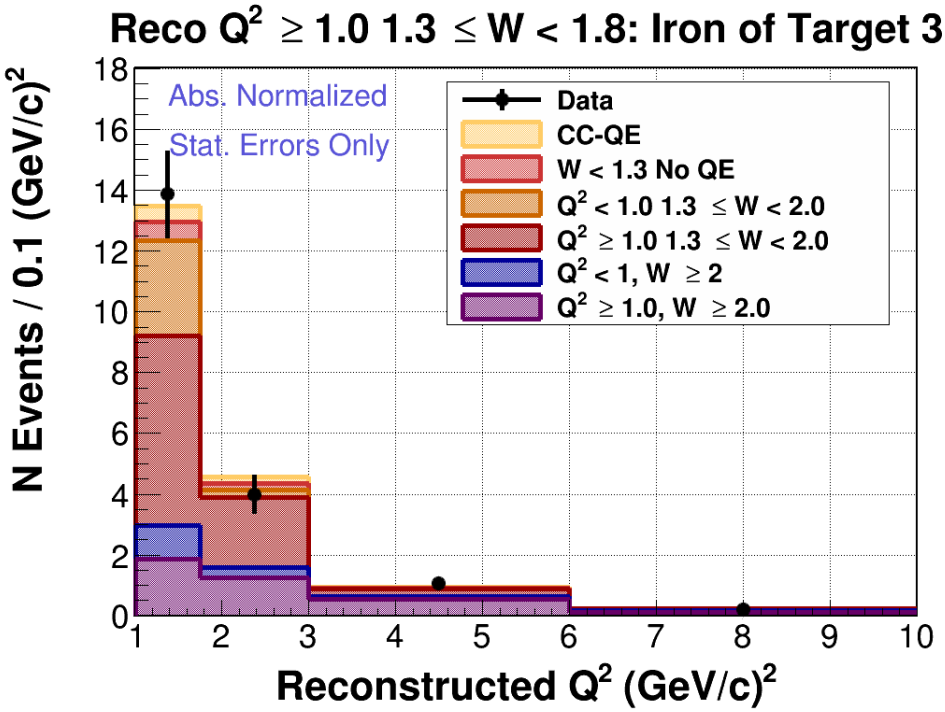

Figure A-121. Data / MC low W sideband after fitting: target 03 Fe (Q^2)

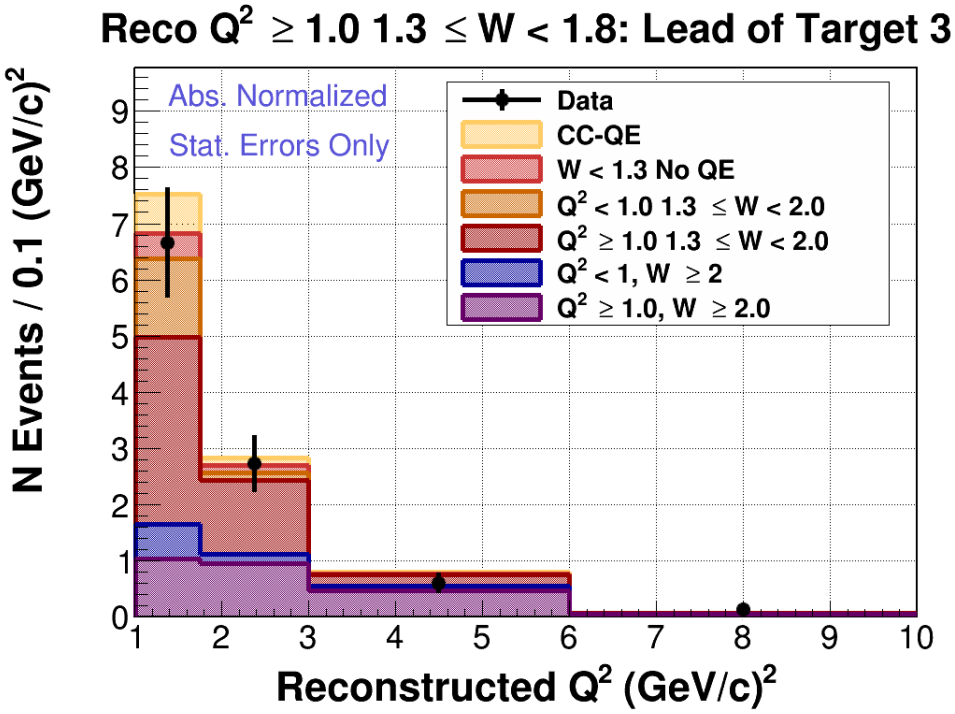

Figure A-122. Data / MC low W sideband after fitting: target 03 Pb (Q^2)

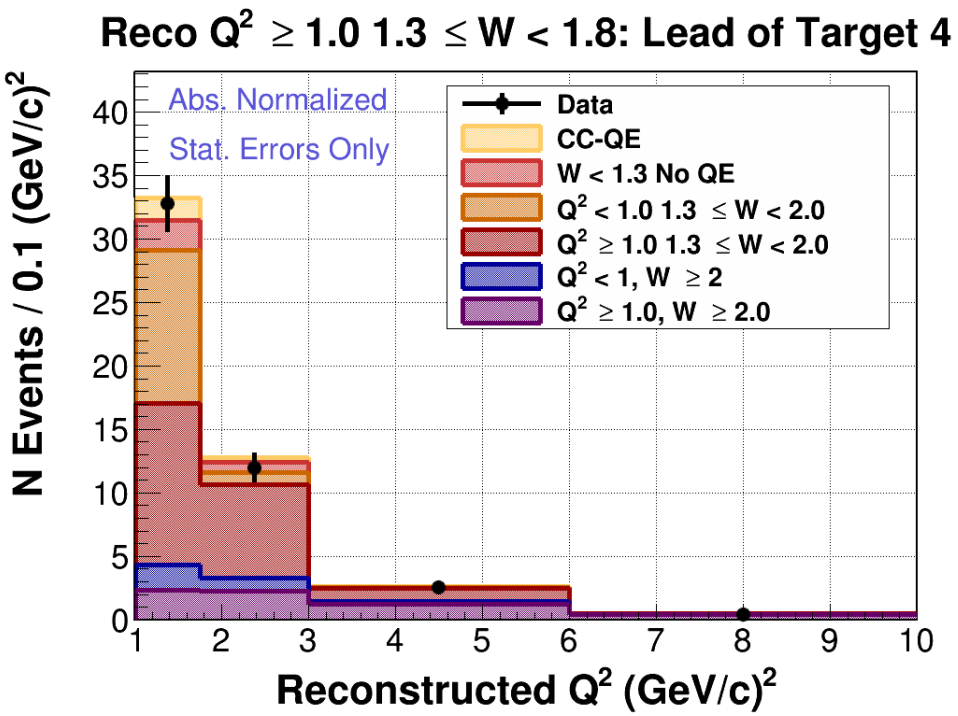

Figure A-123. Data / MC low W sideband after fitting: target 04 Pb (Q^2)

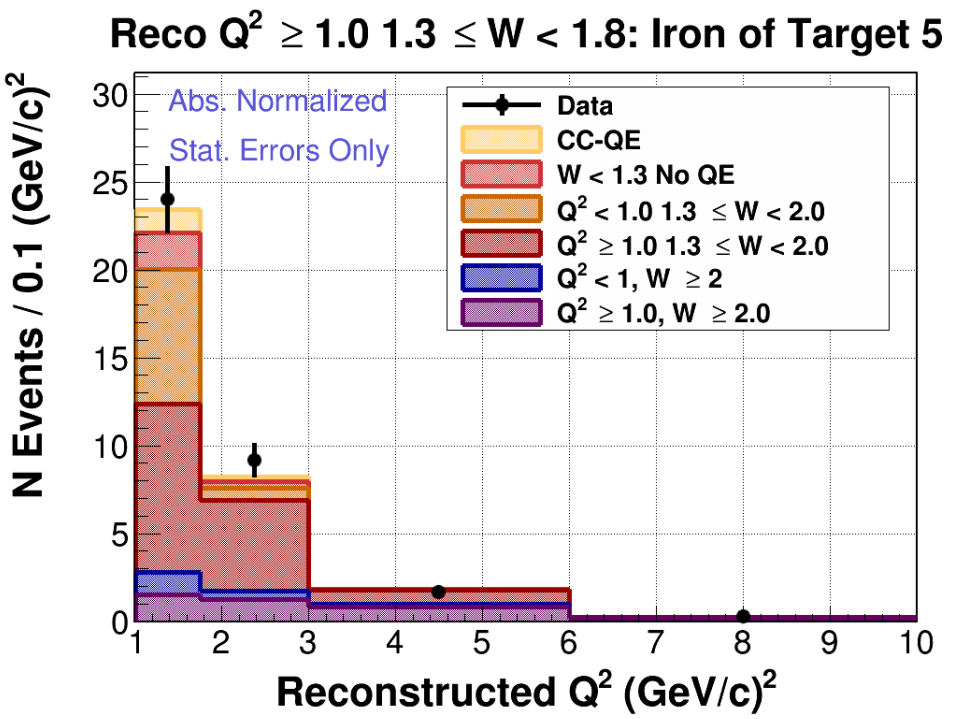

Figure A-124. Data / MC low W sideband after fitting: target 05 Fe (Q^2)

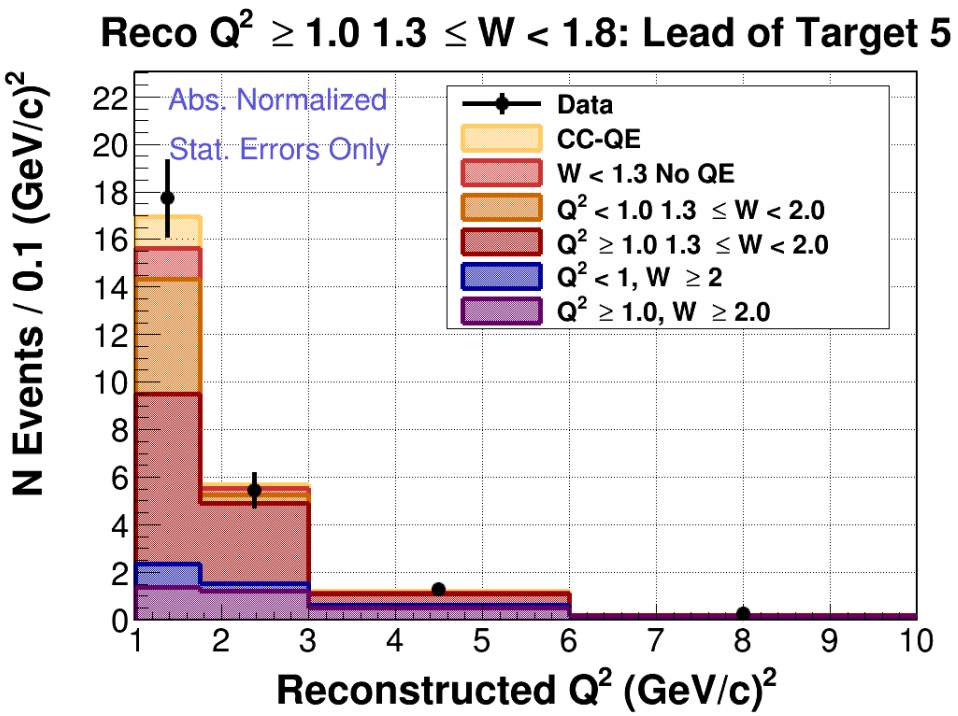

Figure A-125. Data / MC low W sideband after fitting: target 05 Pb (Q^2)

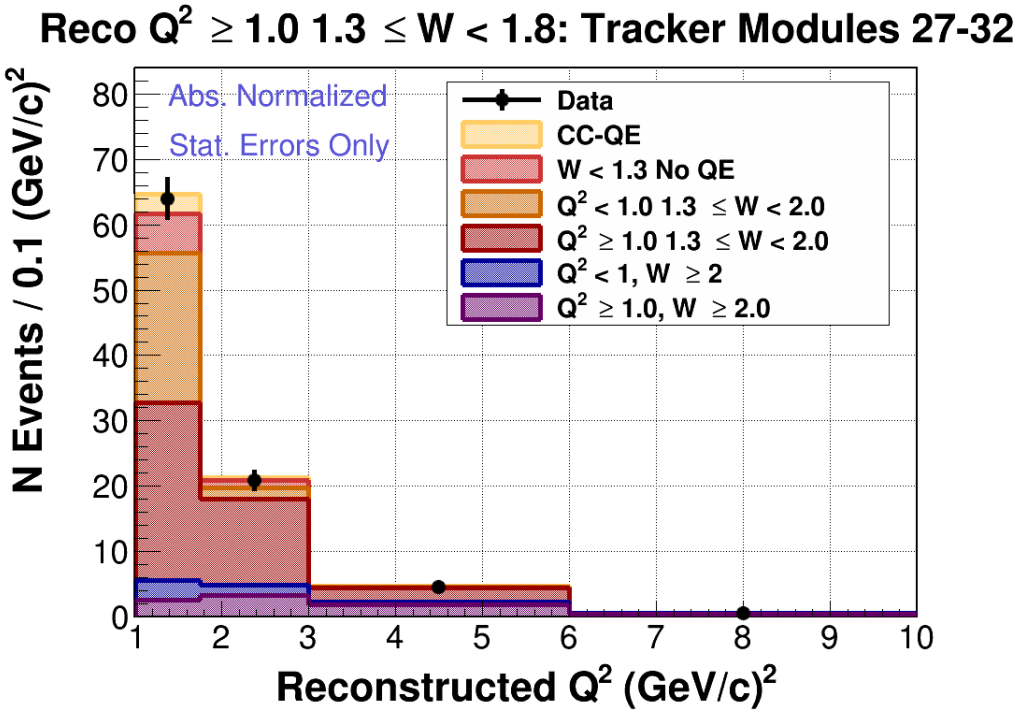

Figure A-126. Data / MC low W sideband after fitting: tracker mods. 27-32 (Q^2)

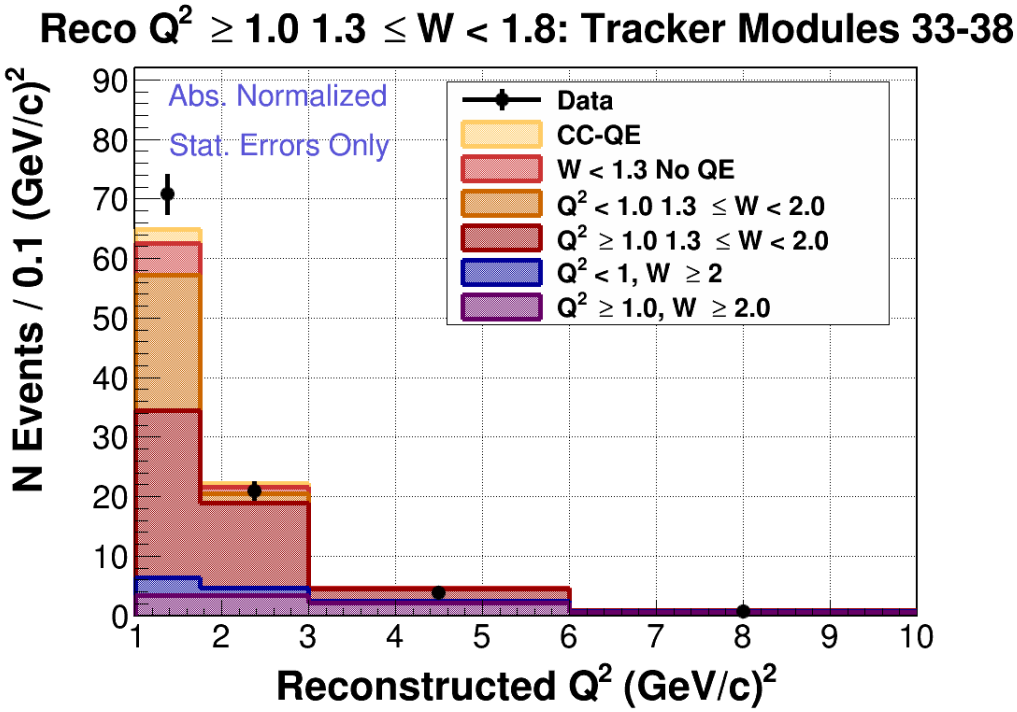

Figure A-127. Data / MC low W sideband after fitting: tracker mods. 33-38 (Q^2)

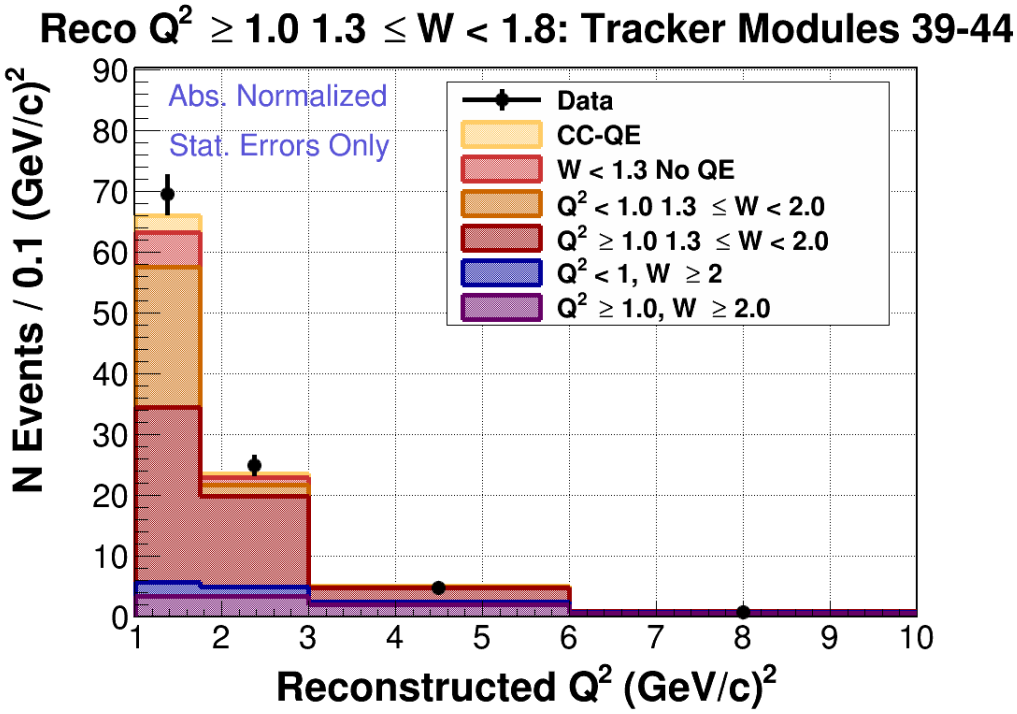

Figure A-128. Data / MC low W sideband after fitting: tracker mods. 39-44 (Q^2)

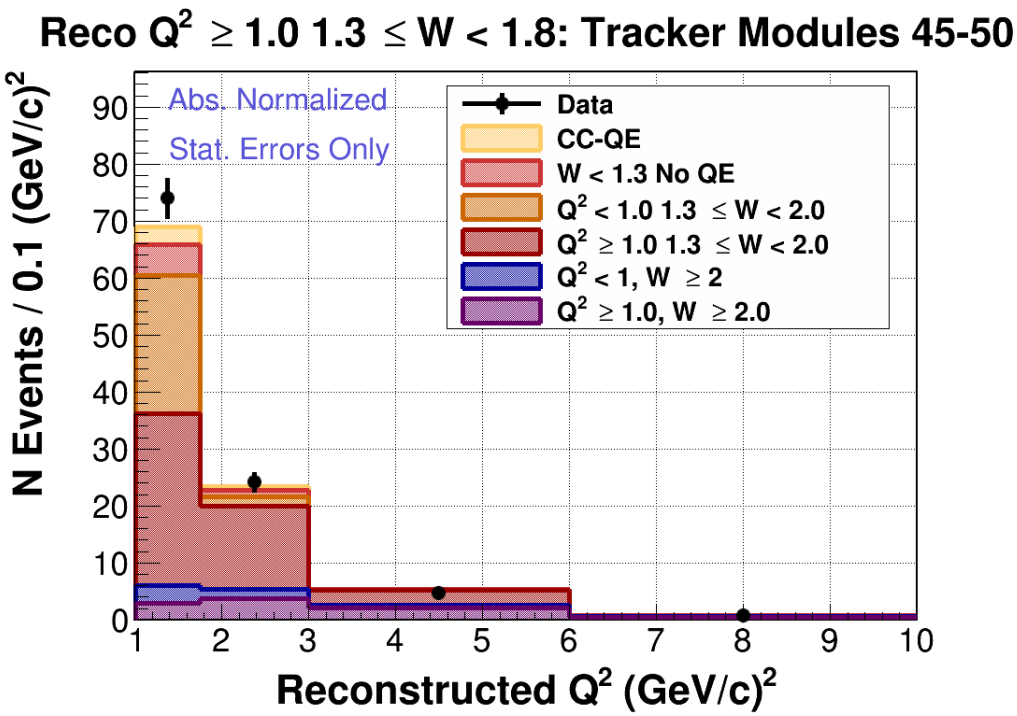

Figure A-129. Data / MC low W sideband after fitting: tracker mods. 45-50 (Q^2)

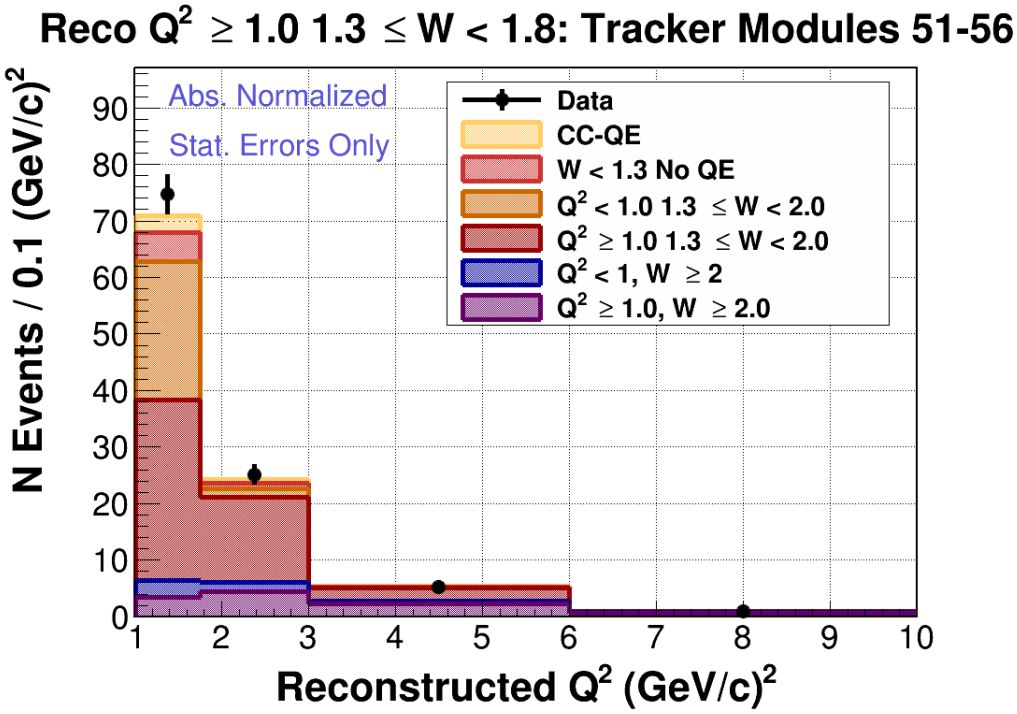

Figure A-130. Data / MC low W sideband after fitting: tracker mods. 51-56 (Q^2)

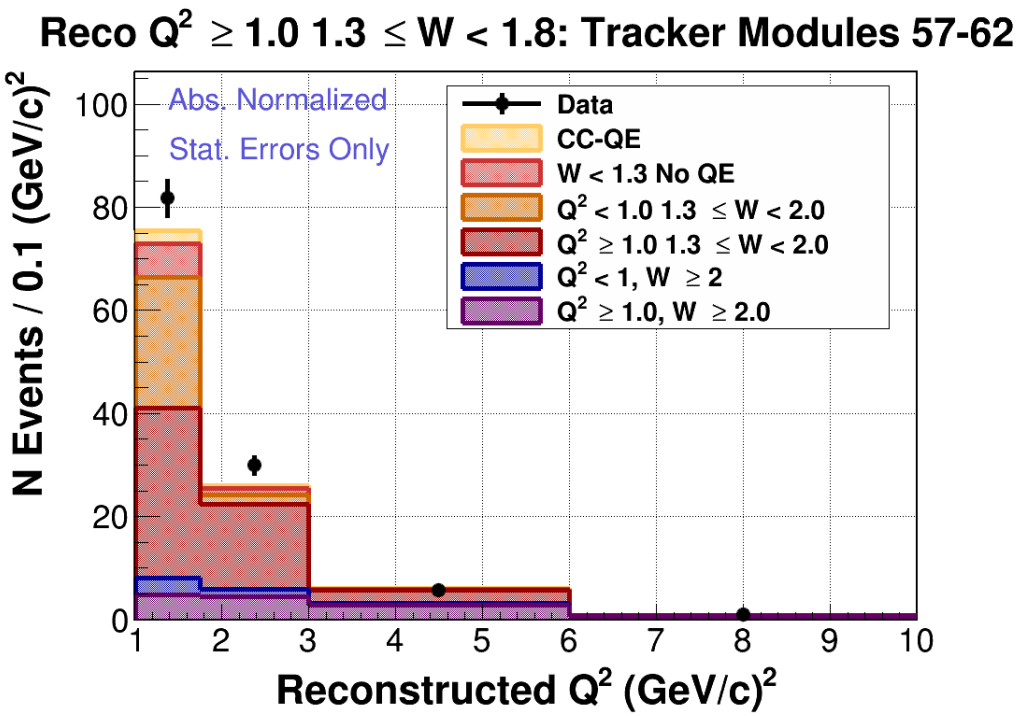

Figure A-131. Data / MC low W sideband after fitting: tracker mods. 57-62 (Q^2)

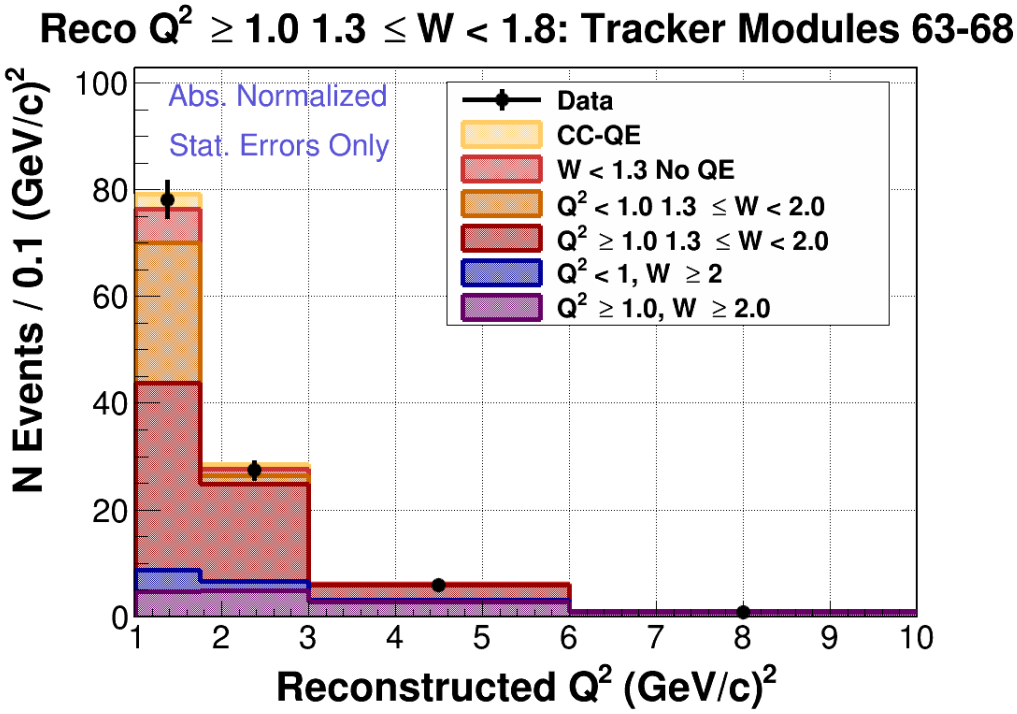

Figure A-132. Data / MC low W sideband after fitting: tracker mods. 63-68 (Q^2)

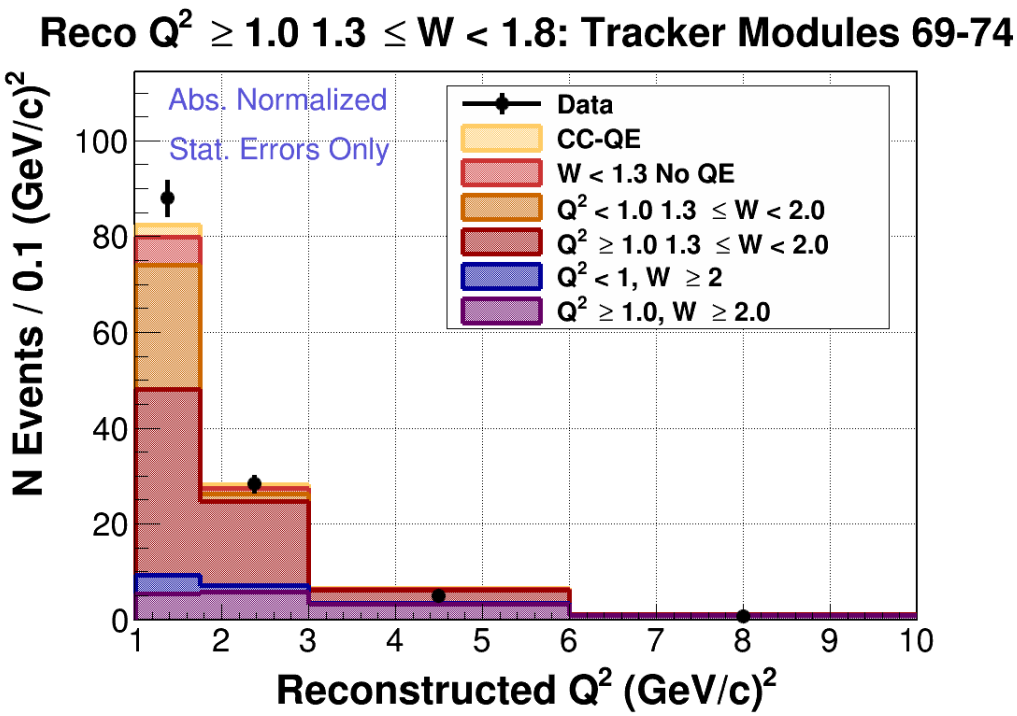

Figure A-133. Data / MC low W sideband after fitting: tracker mods. 69-74 (Q^2)

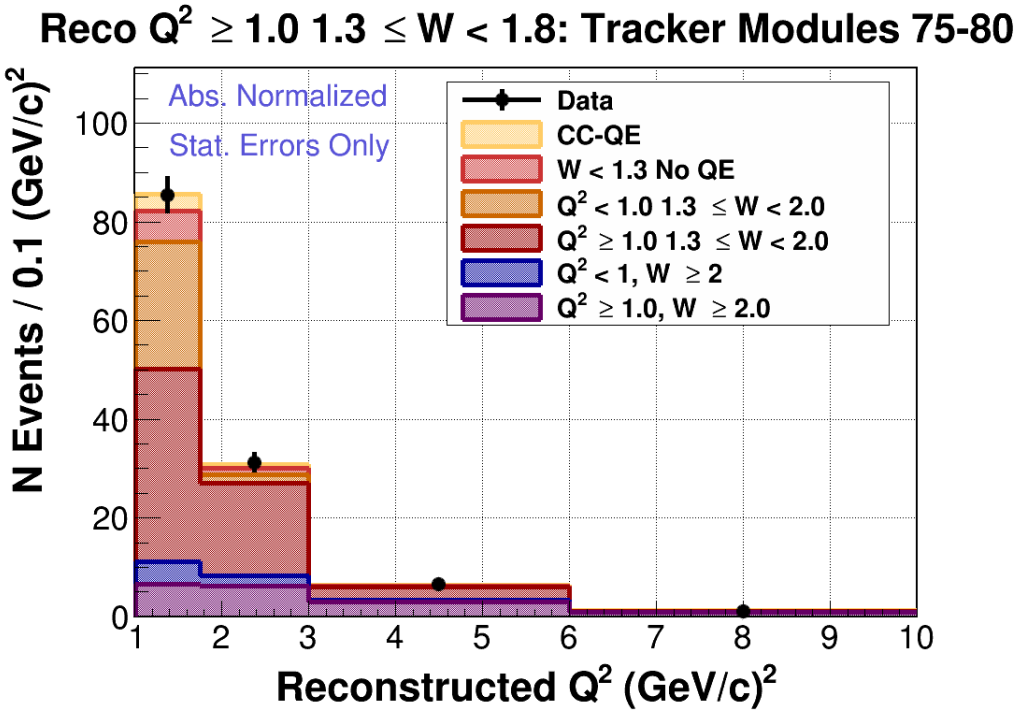

Figure A-134. Data / MC low W sideband after fitting: tracker mods. 75-80 (Q^2)

The following plots show the population of the low W sideband ($Q^2 \geq 1.0$ (GeV/c)^2 $1.3 \leq W < 1.8$ GeV/c^2) *after* tuning to data as a function of Bjorken-x (x_{bj}):

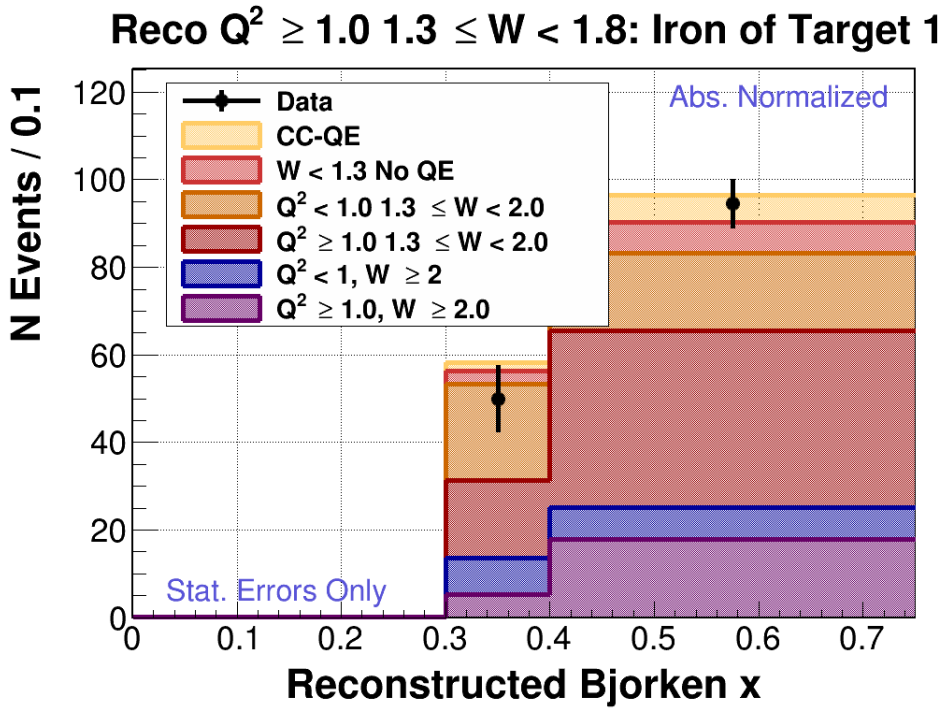

Figure A-135. Data / MC low W sideband after fitting: target 01 Fe (x_{bj})

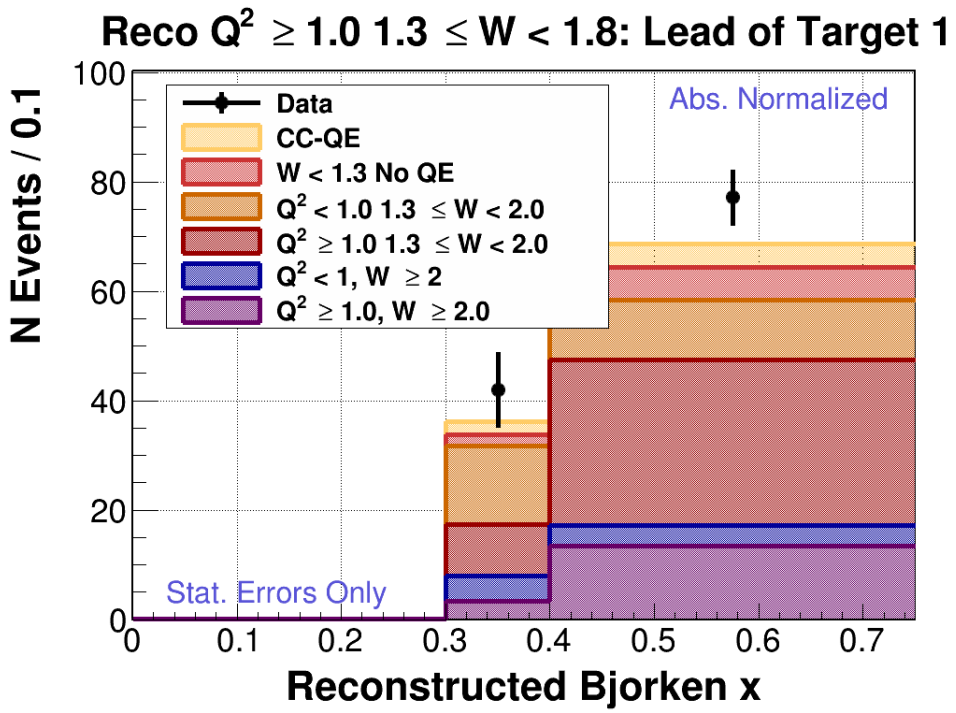

Figure A-136. Data / MC low W sideband after fitting: target 01 Pb (x_{bj})

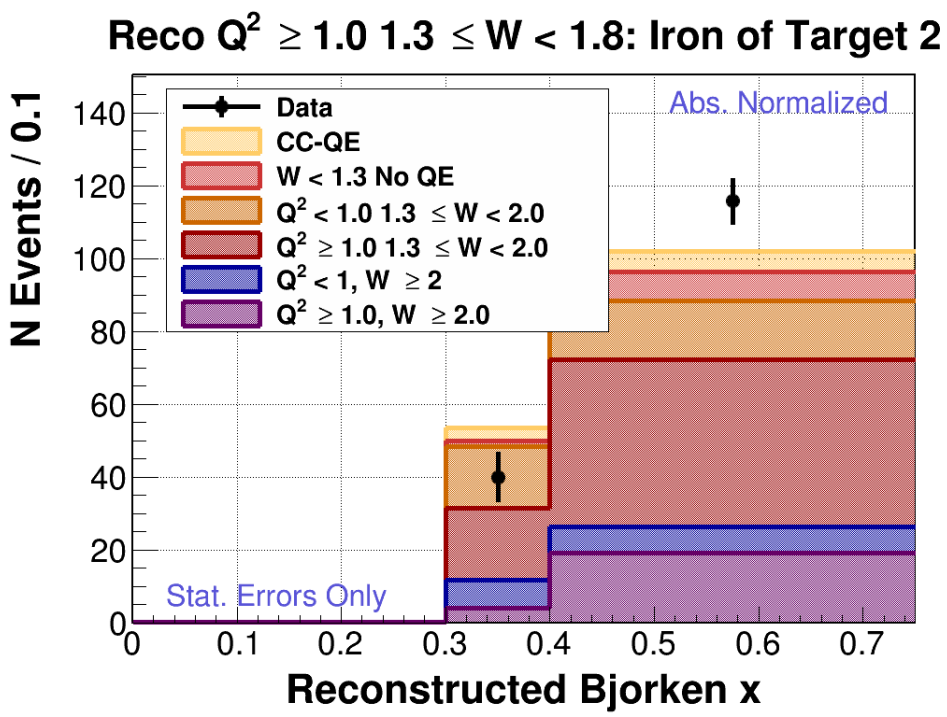

Figure A-137. Data / MC low W sideband after fitting: target 02 Fe (x_{bj})

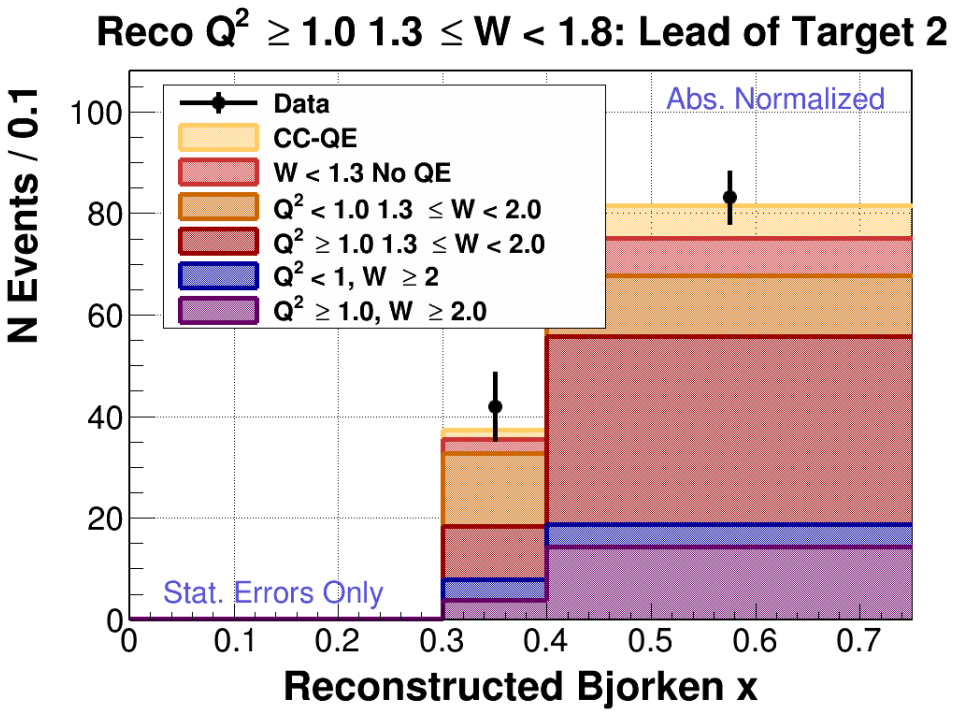

Figure A-138. Data / MC low W sideband after fitting: target 02 Pb (x_{bj})

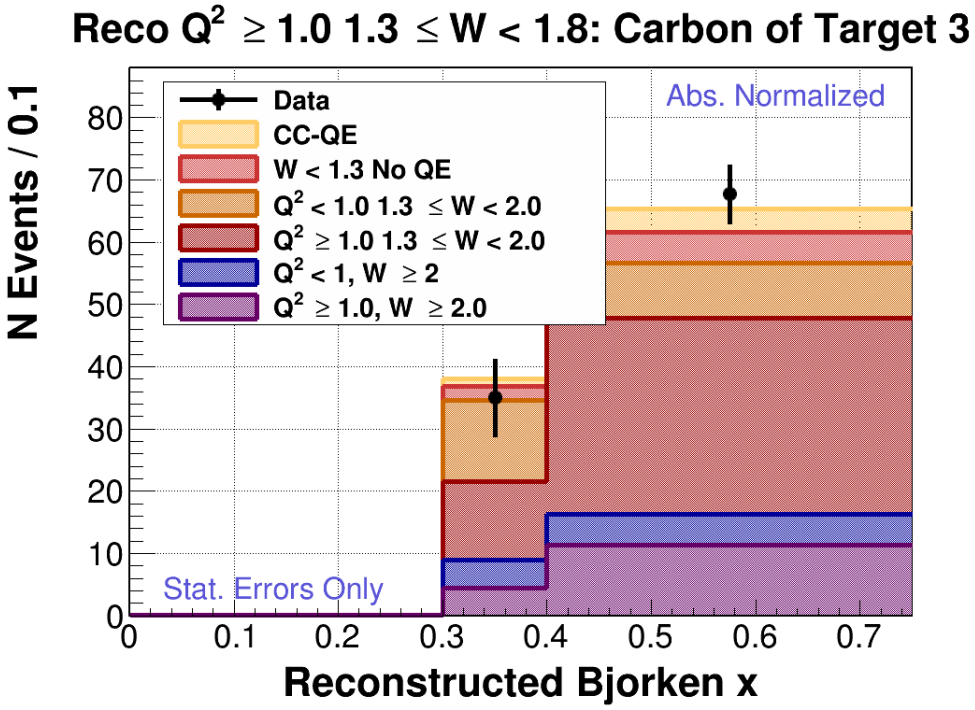

Figure A-139. Data / MC low W sideband after fitting: target 03 C (x_{bj})

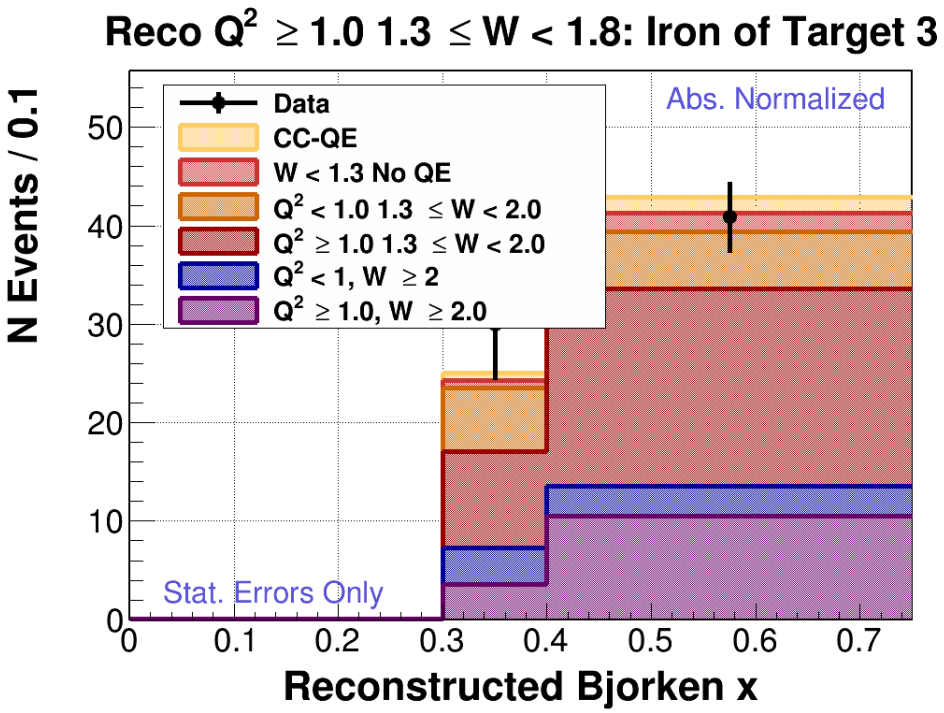

Figure A-140. Data / MC low W sideband after fitting: target 03 Fe (x_{bj})

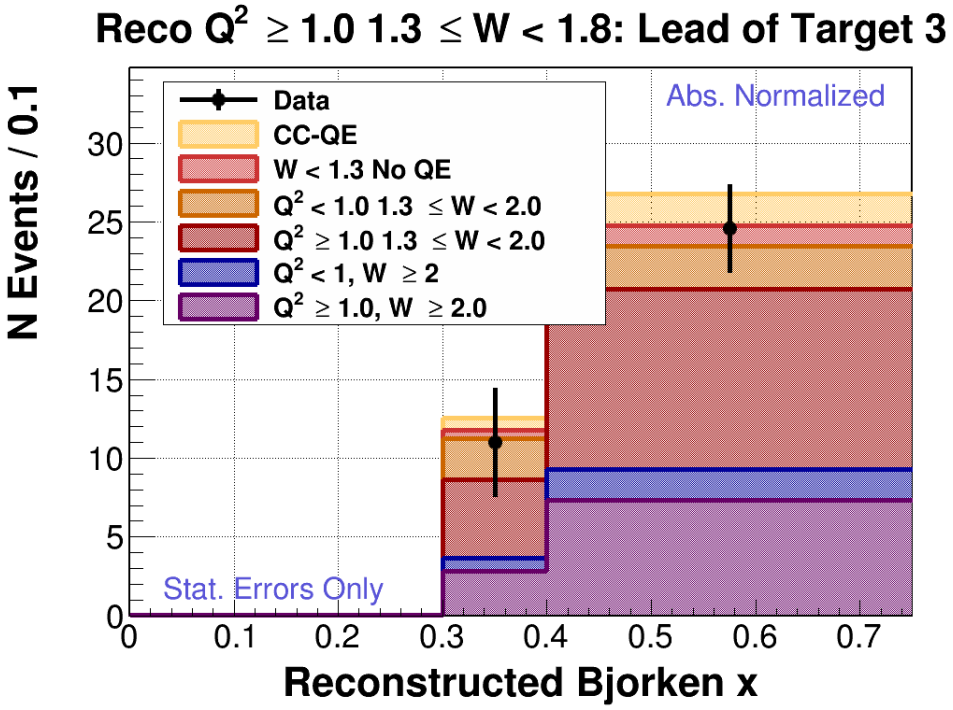

Figure A-141. Data / MC low W sideband after fitting: target 03 Pb (x_{bj})

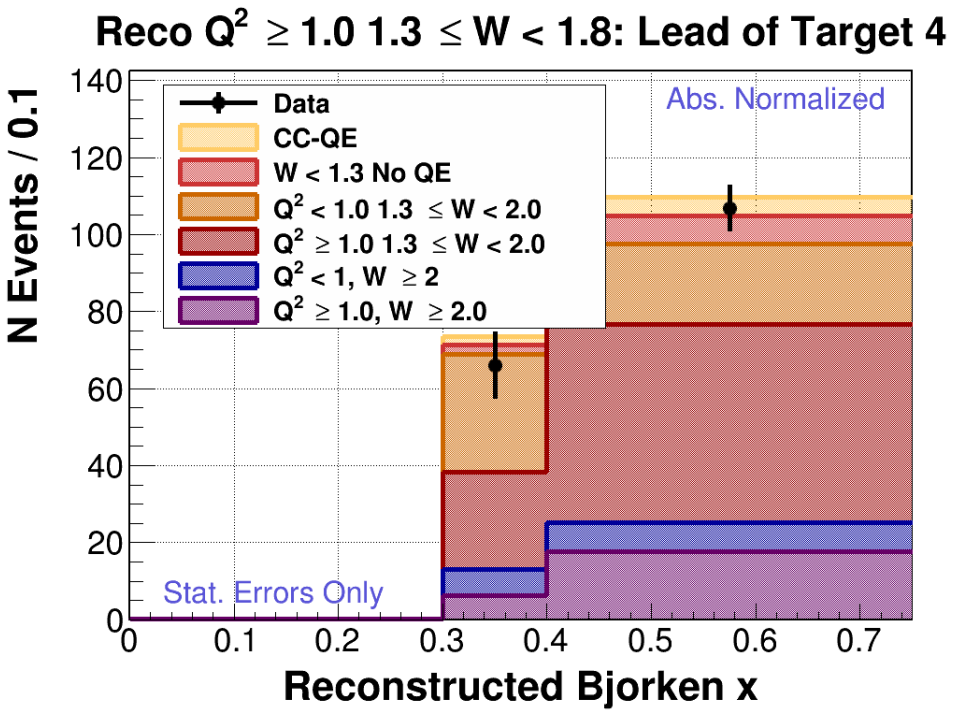

Figure A-142. Data / MC low W sideband after fitting: target 04 Pb (x_{bj})

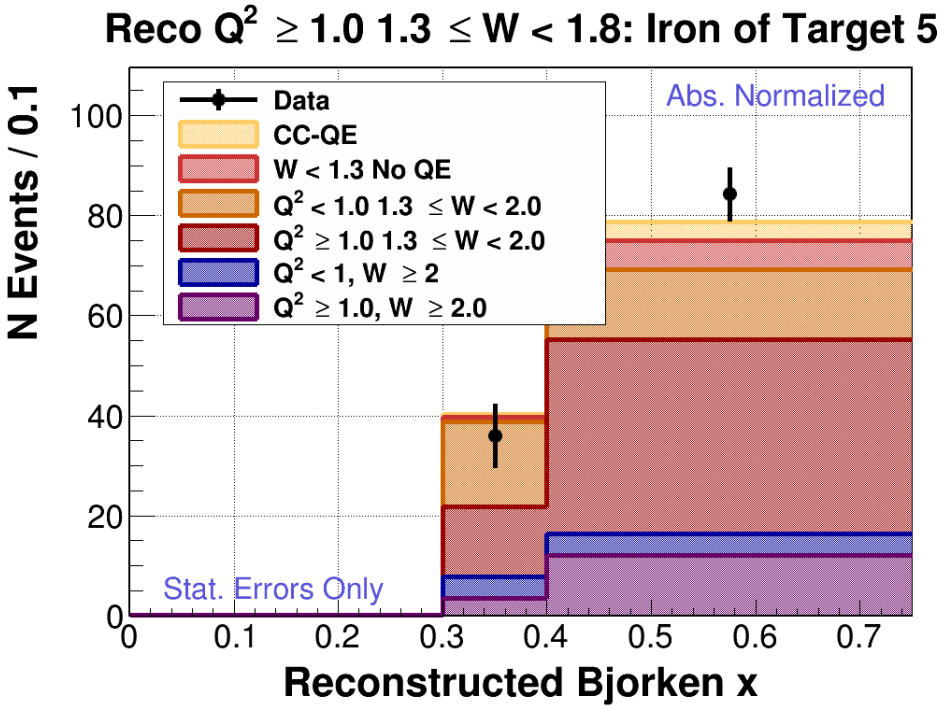

Figure A-143. Data / MC low W sideband after fitting: target 02 Fe (x_{bj})

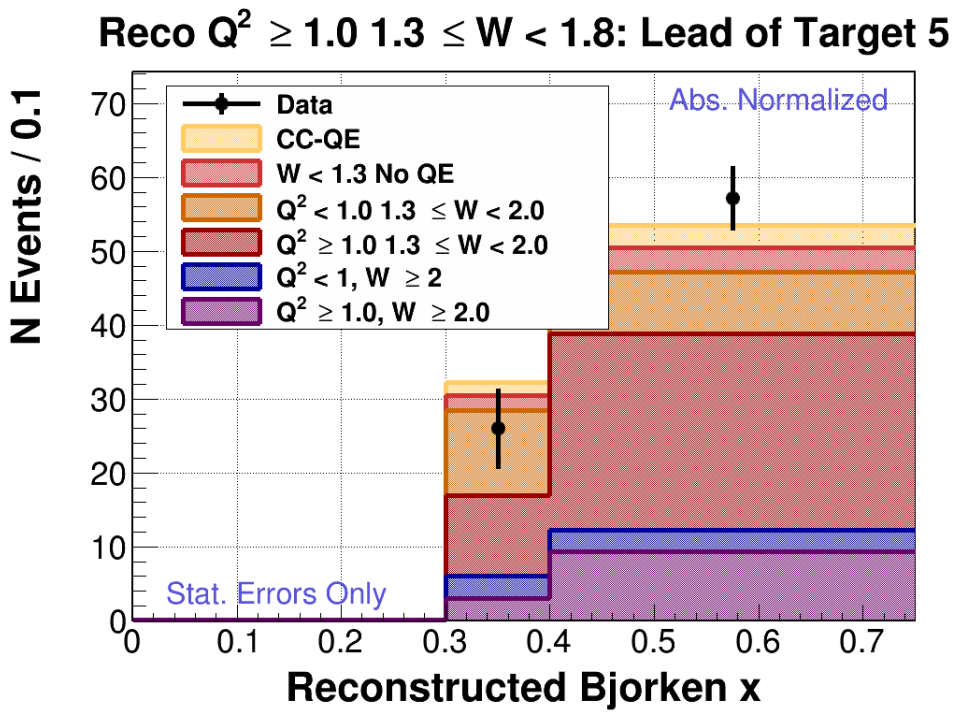

Figure A-144.

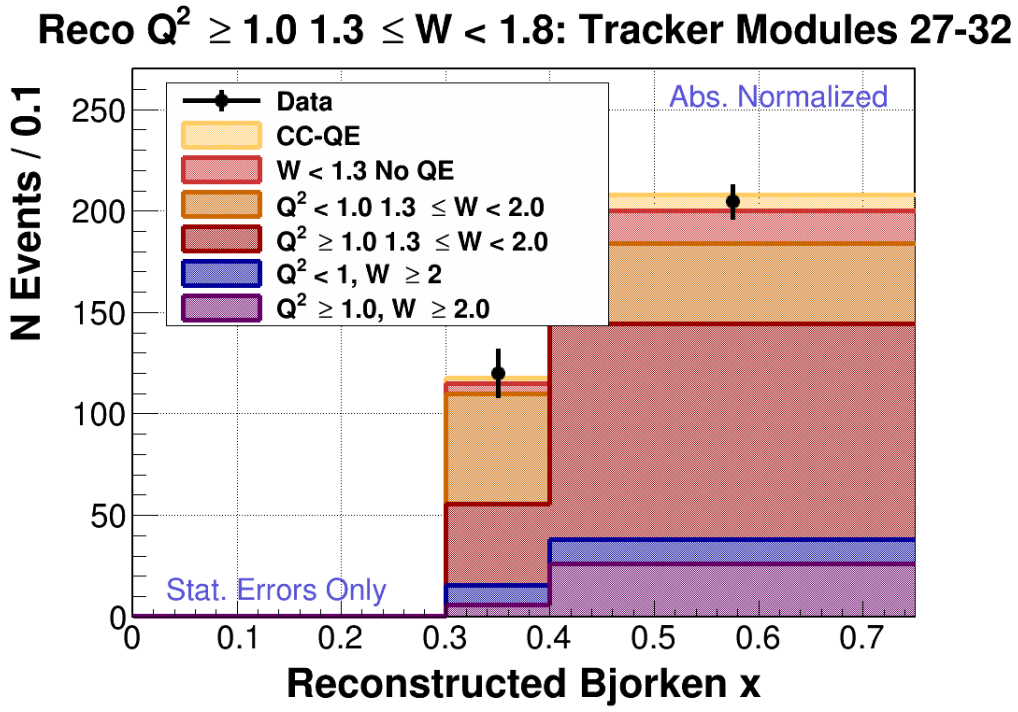

Figure A-145. Data / MC low W sideband after fitting: tracker mods. 27-32 (x_{bj})

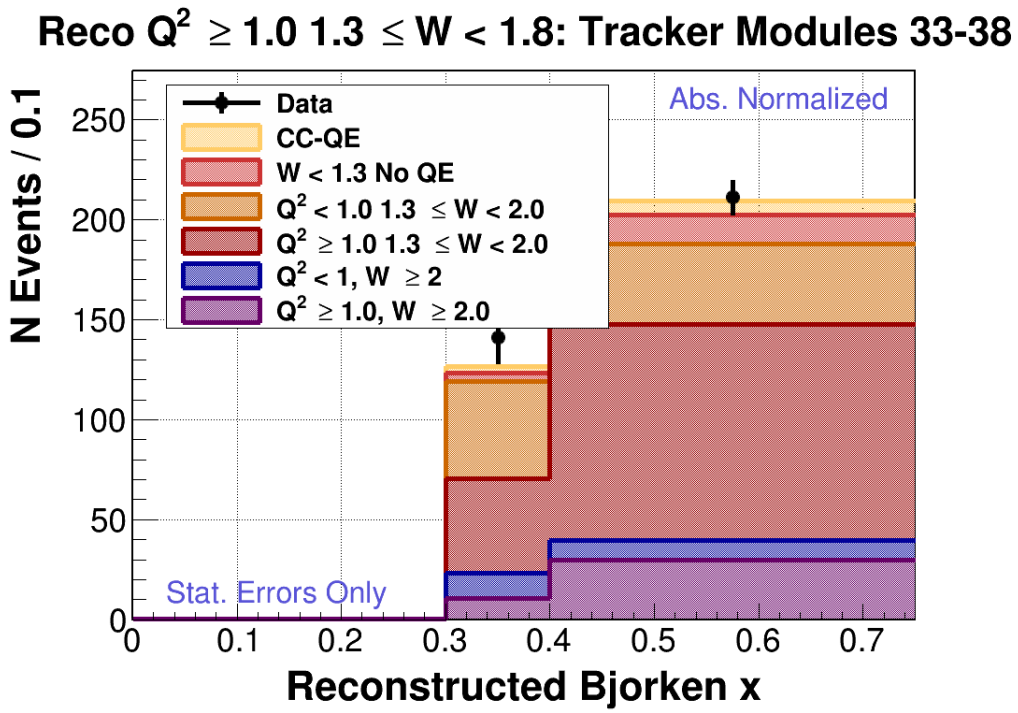

Figure A-146. Data / MC low W sideband after fitting: tracker mods. 33-38 (x_{bj})

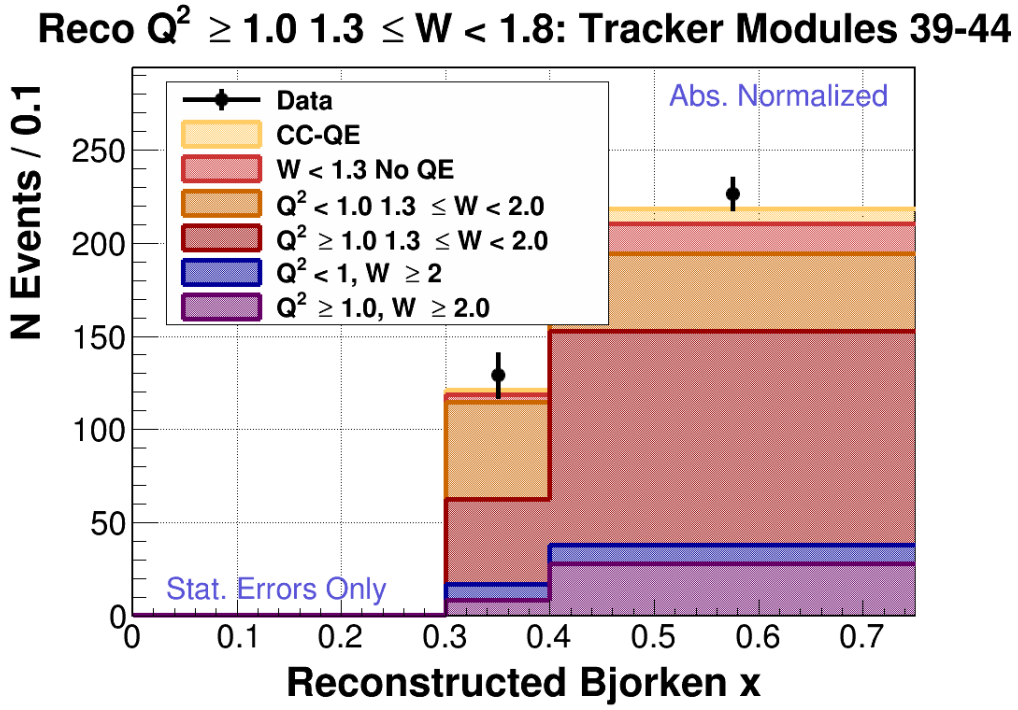

Figure A-147. Data / MC low W sideband after fitting: tracker mods. 39-44 (x_{bj})

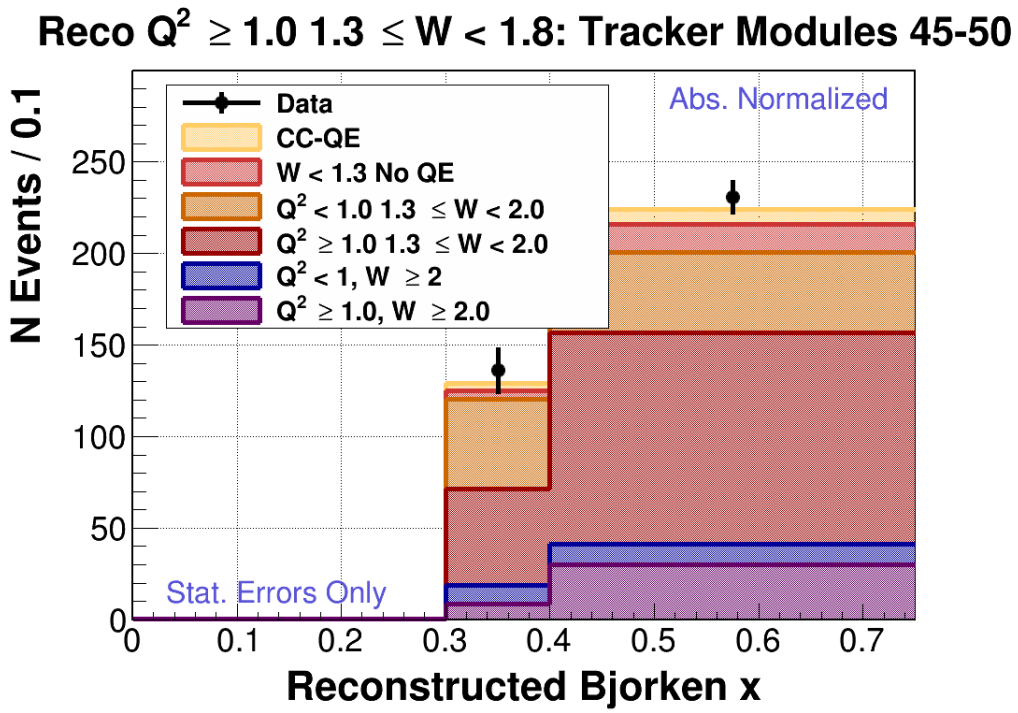

Figure A-148. Data / MC low W sideband after fitting: tracker mods. 45-50 (x_{bj})

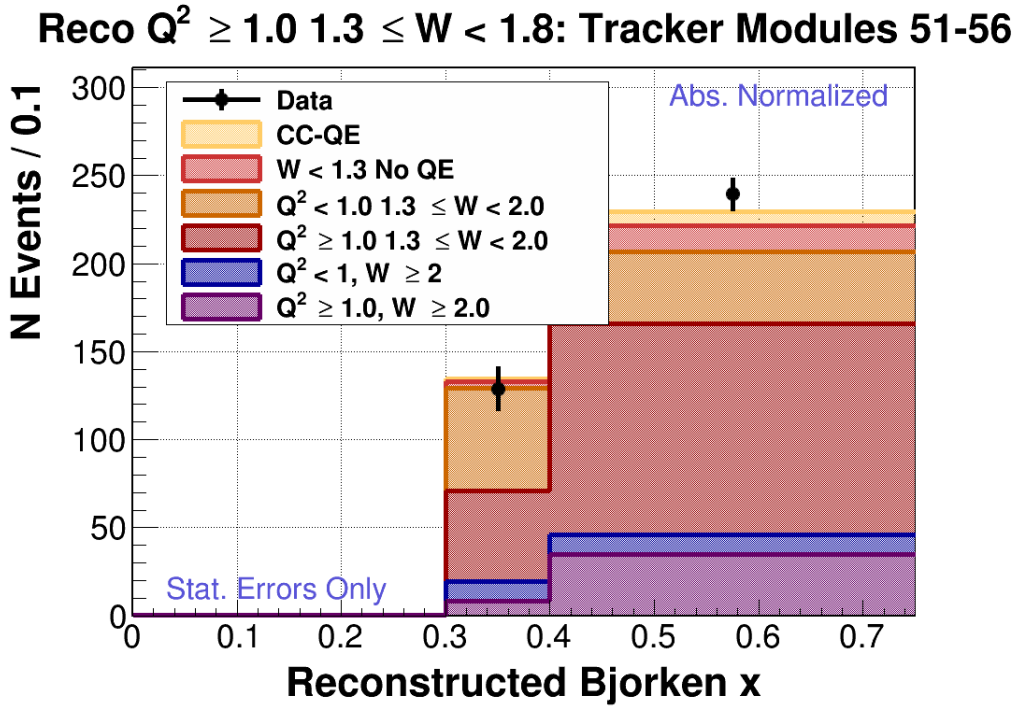

Figure A-149. Data / MC low W sideband after fitting: tracker mods. 51-56 (x_{bj})

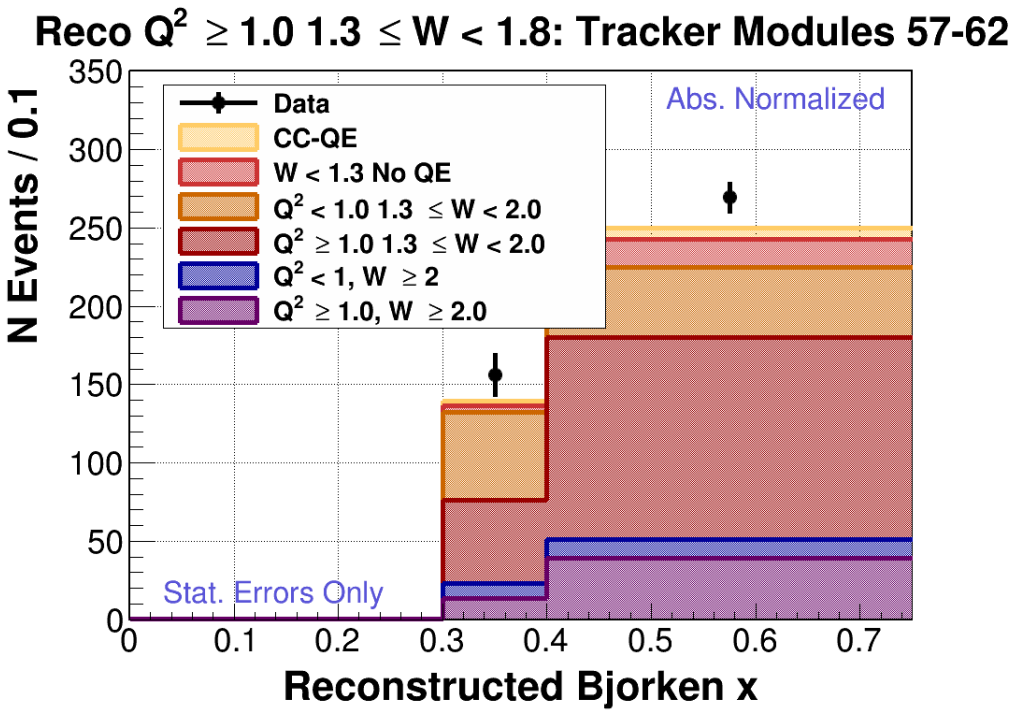

Figure A-150. Data / MC low W sideband after fitting: tracker mods. 57-62 (x_{bj})

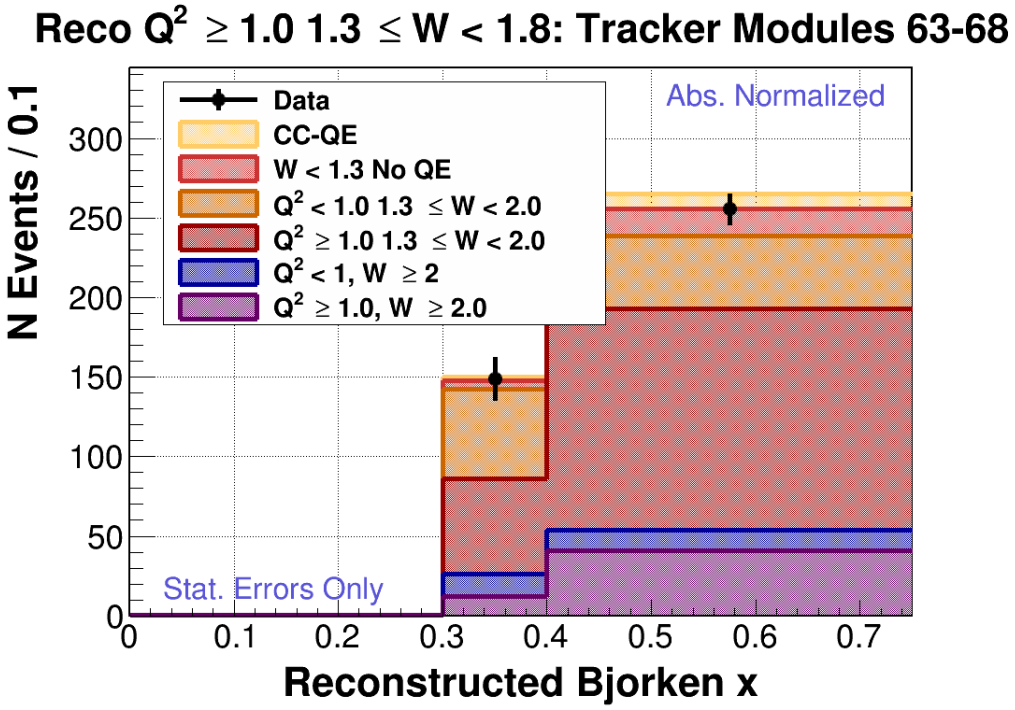

Figure A-151. Data / MC low W sideband after fitting: tracker mods. 63-68 (x_{bj})

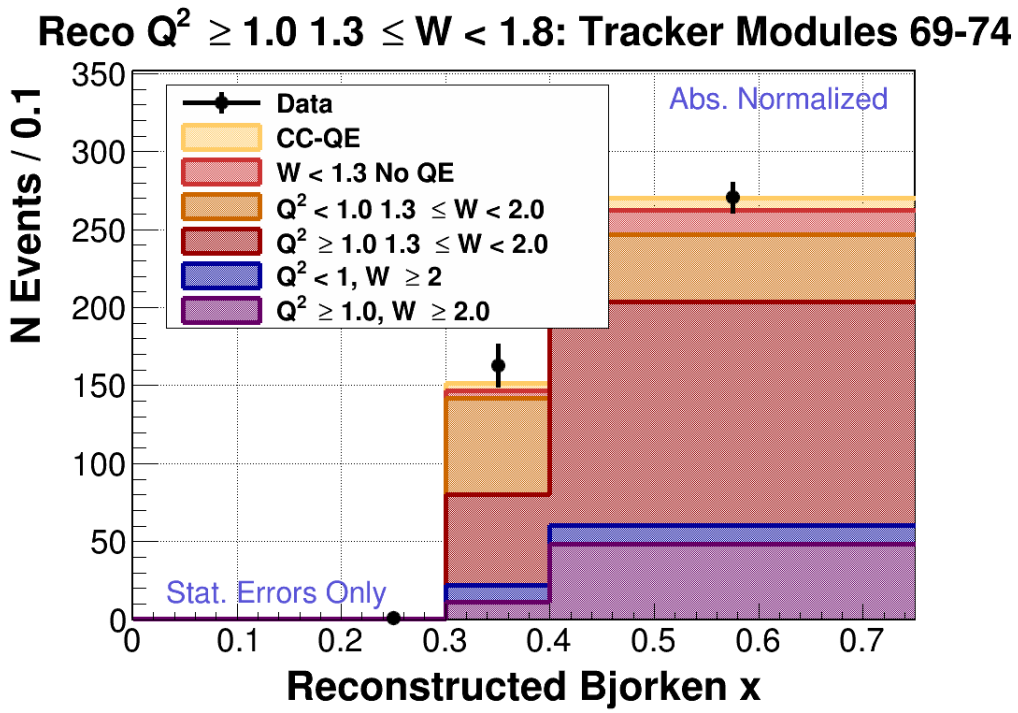

Figure A-152. Data / MC low W sideband after fitting: tracker mods. 69-74 (x_{bj})

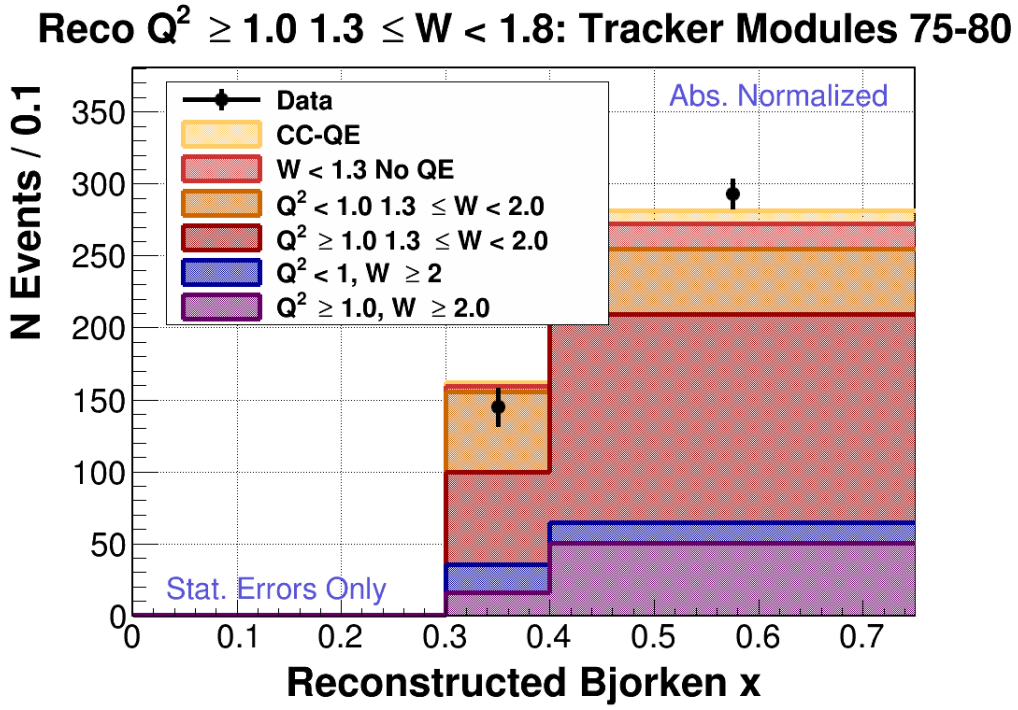

Figure A-153. Data / MC low W sideband after fitting: tracker mods. 75-80 (x_{bj})

The following plots show the population of the low W sideband ($Q^2 \geq 1.0$ (GeV/c)^2 $1.3 \leq W < 1.8$ GeV/c^2) *after* tuning to data as a function of muon energy (E_μ):

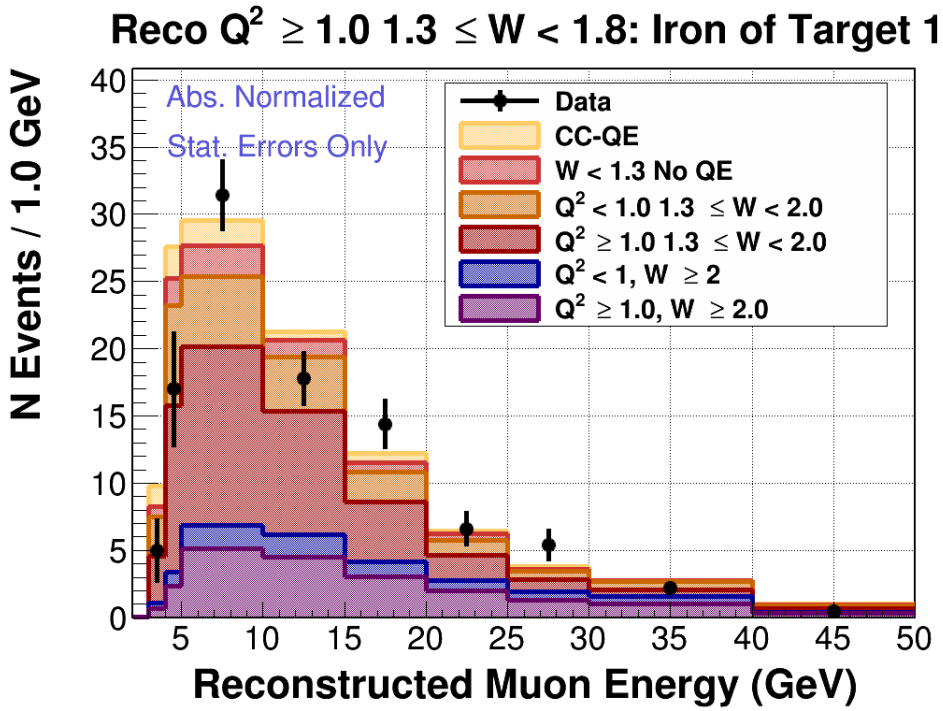

Figure A-154. Data / MC low W sideband after fitting: target 01 Fe (E_μ)

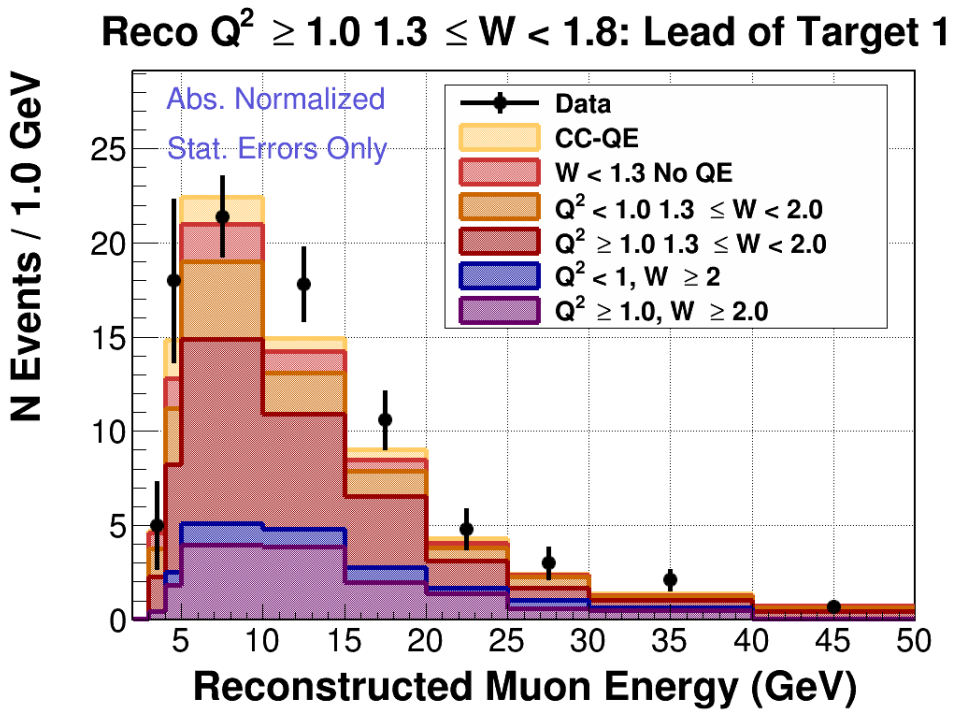

Figure A-155. Data / MC low W sideband after fitting: target 01 Pb (E_μ)

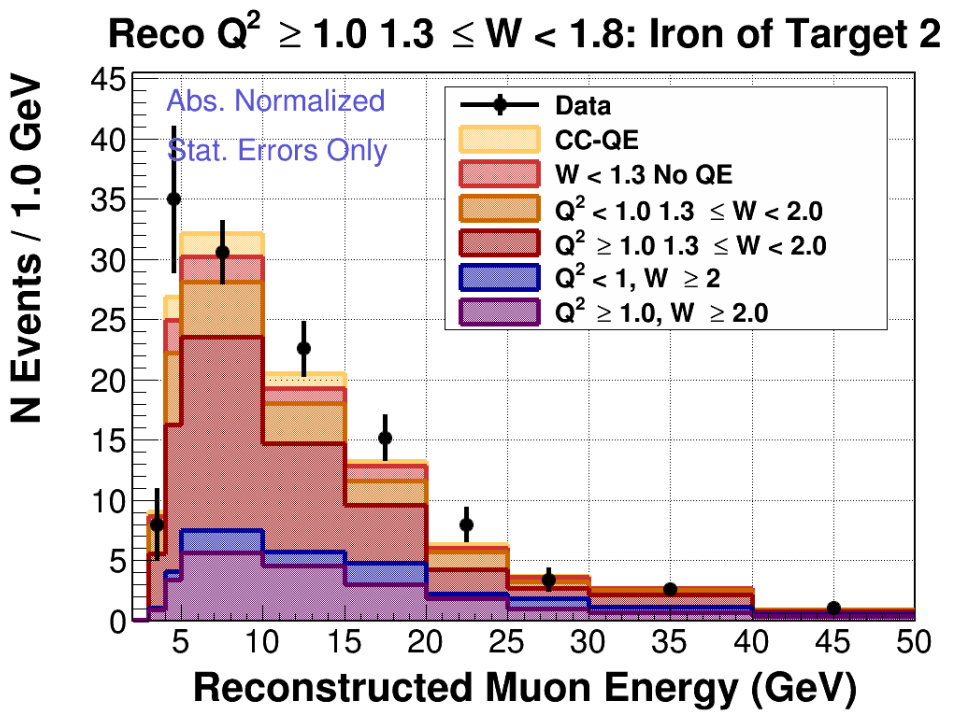

Figure A-156. Data / MC low W sideband after fitting: target 02 Fe (E_μ)

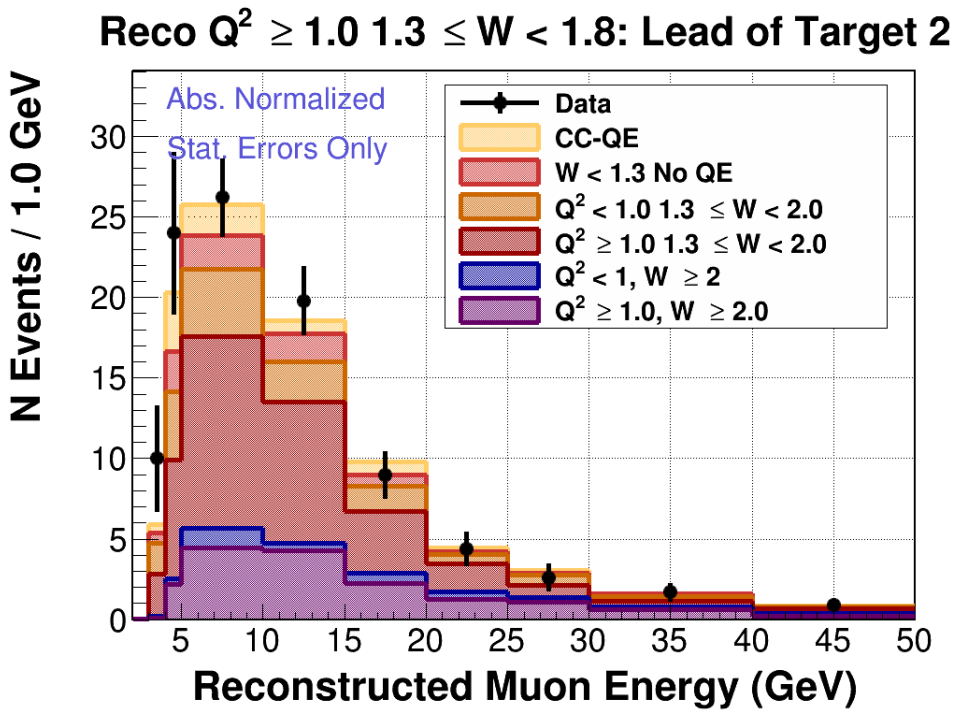

Figure A-157. Data / MC low W sideband after fitting: target 02 Pb (E_μ)

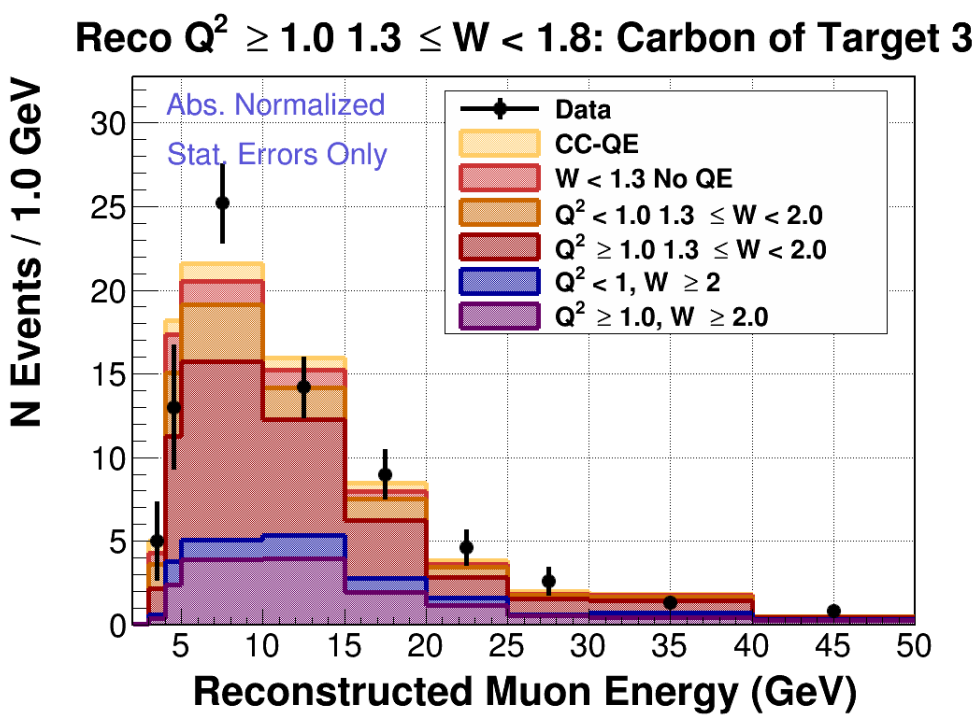

Figure A-158. Data / MC low W sideband after fitting: target 03 C (E_μ)

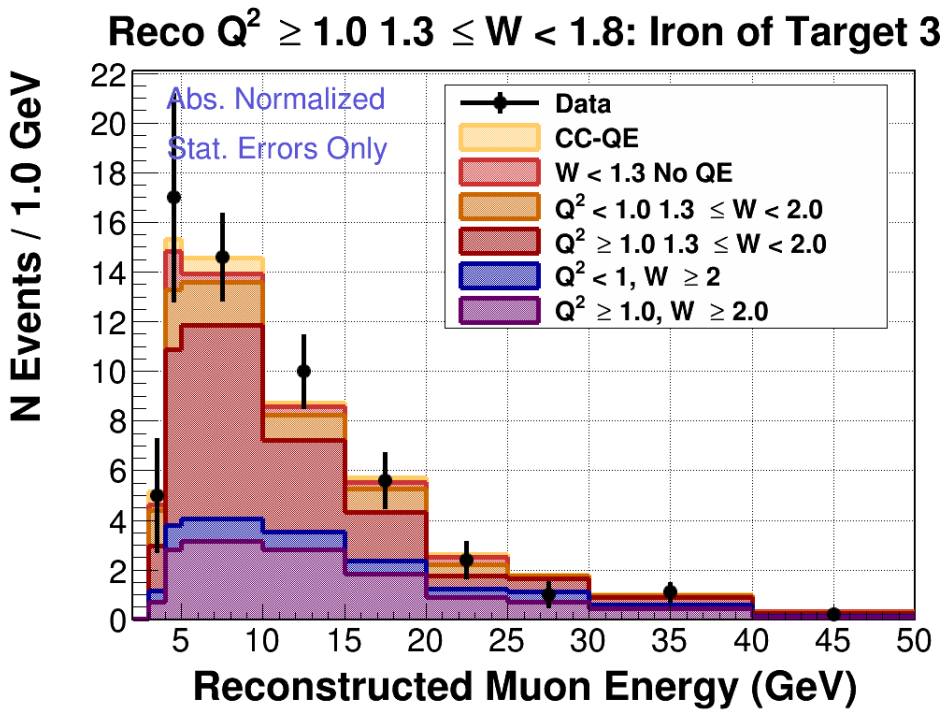

Figure A-159. Data / MC low W sideband after fitting: target 03 Fe (E_μ)

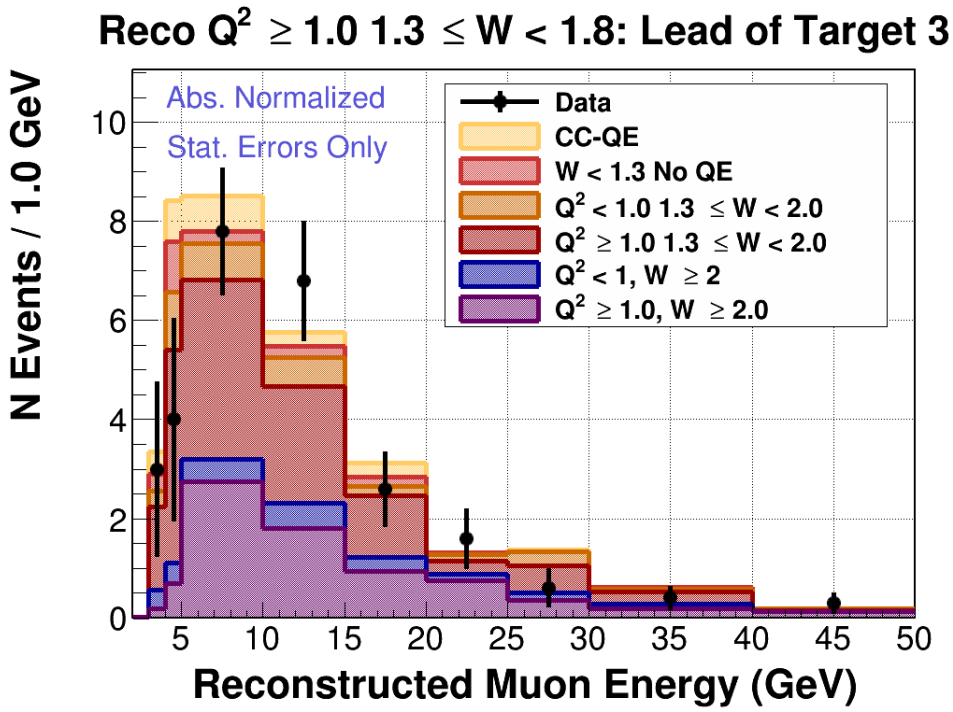

Figure A-160. Data / MC low W sideband after fitting: target 03 Pb (E_μ)

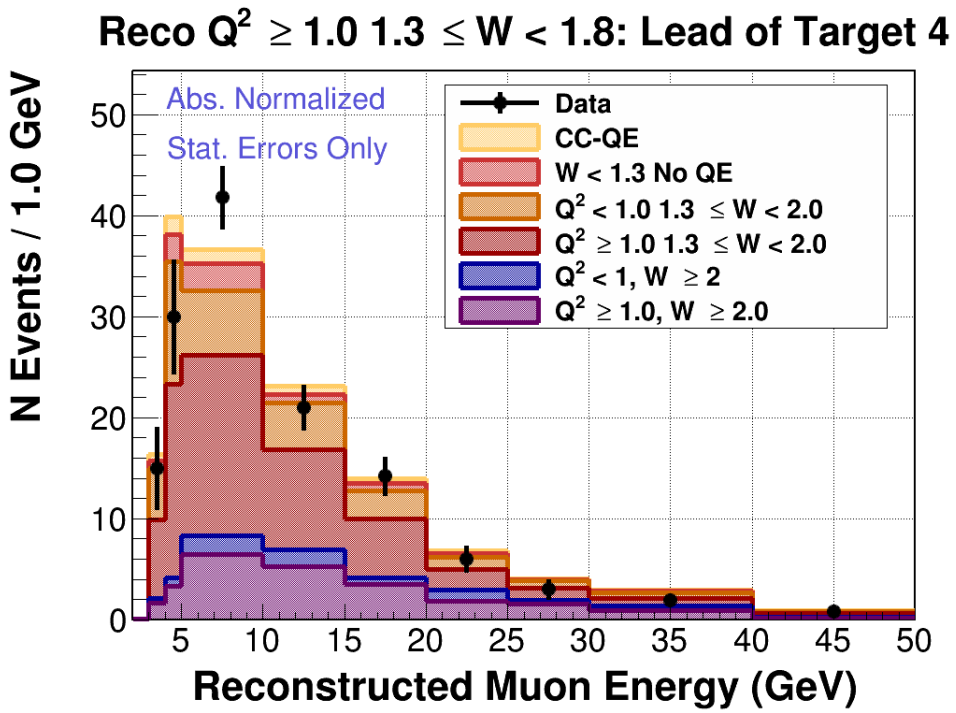

Figure A-161. Data / MC low W sideband after fitting: target 04 Pb (E_μ)

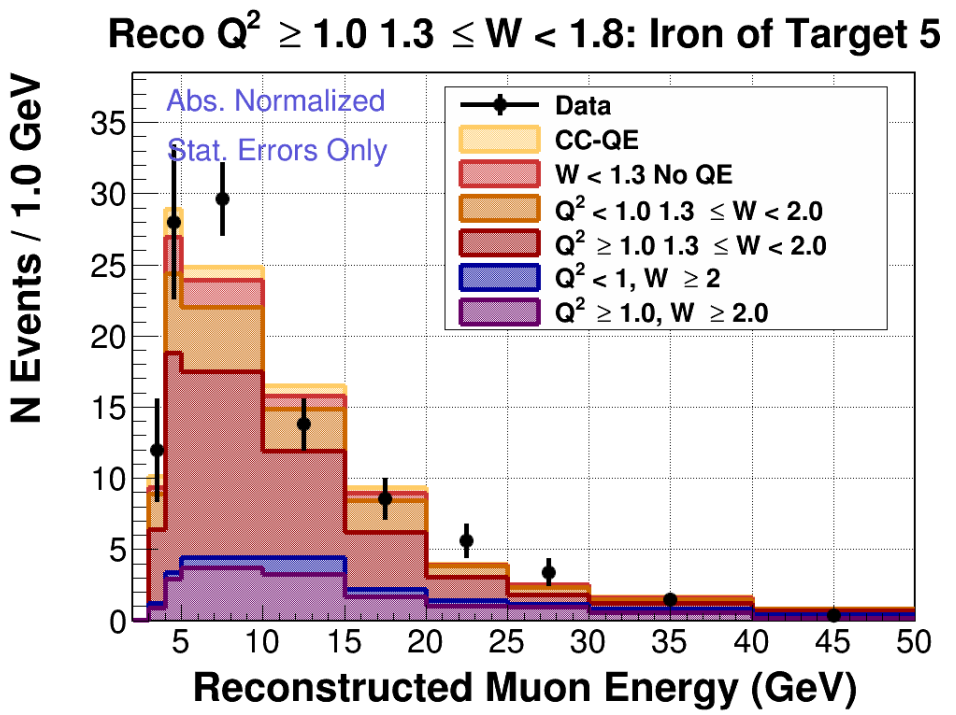

Figure A-162. Data / MC low W sideband after fitting: target 05 Fe (E_μ)

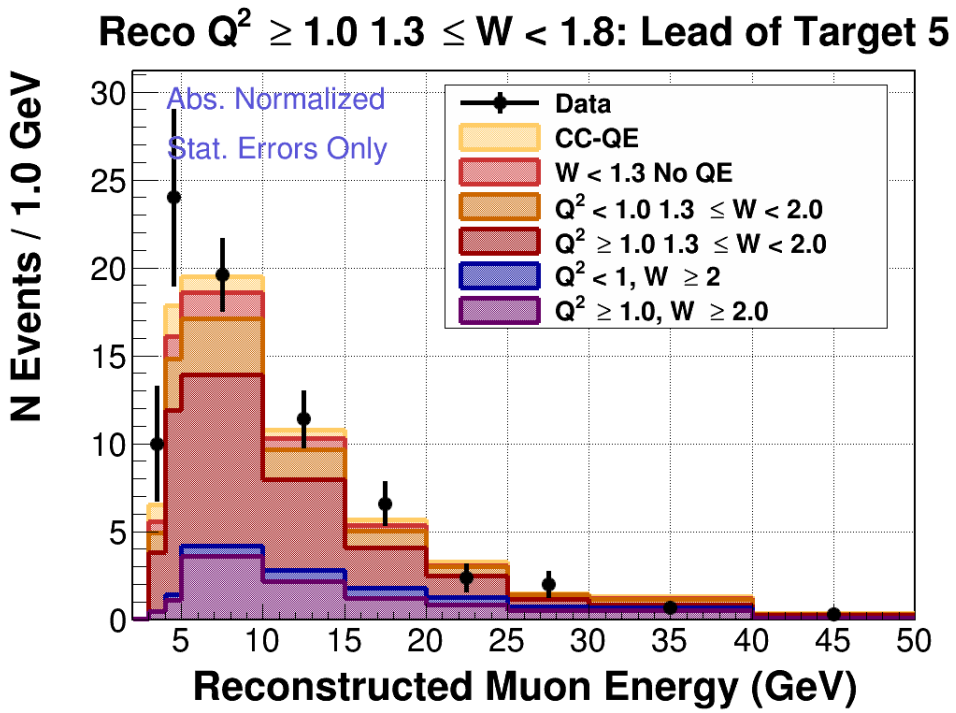

Figure A-163. Data / MC low W sideband after fitting: target 05 Pb (E_μ)

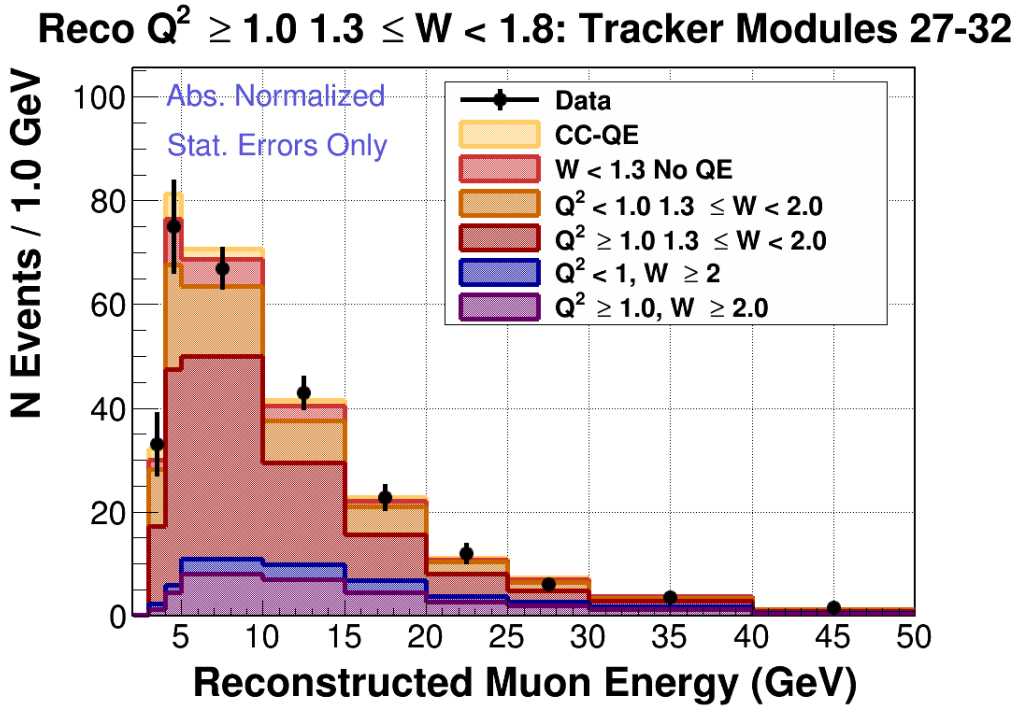

Figure A-164. Data / MC low W sideband after fitting: tracker mods. 27-32 (E_μ)

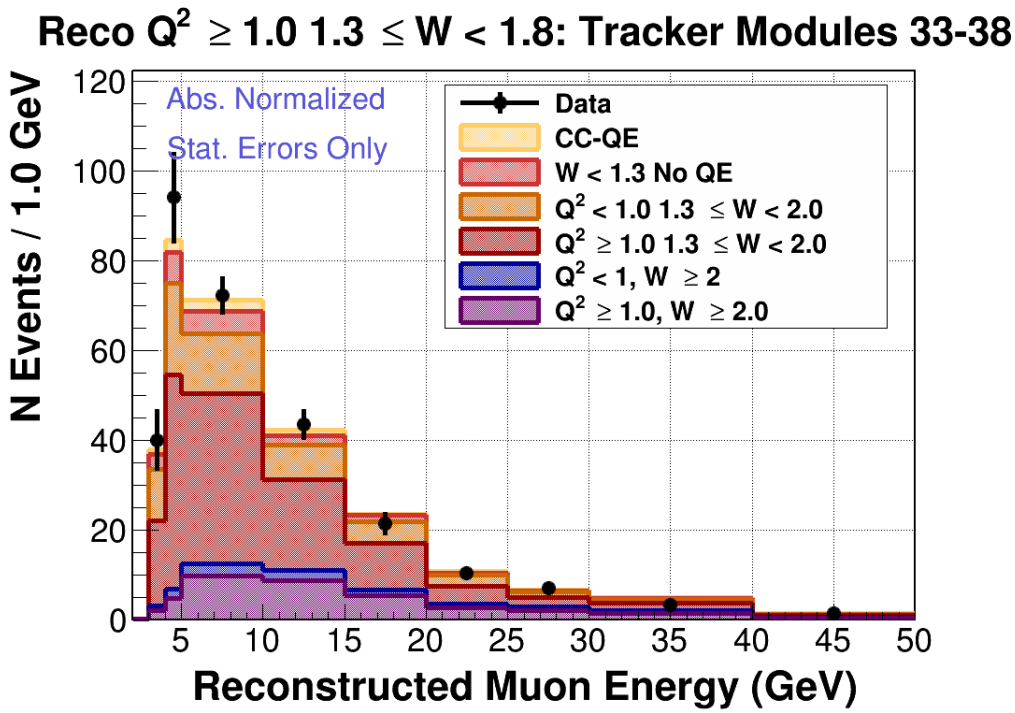

Figure A-165. Data / MC low W sideband after fitting: tracker mods. 33-38 (E_μ)

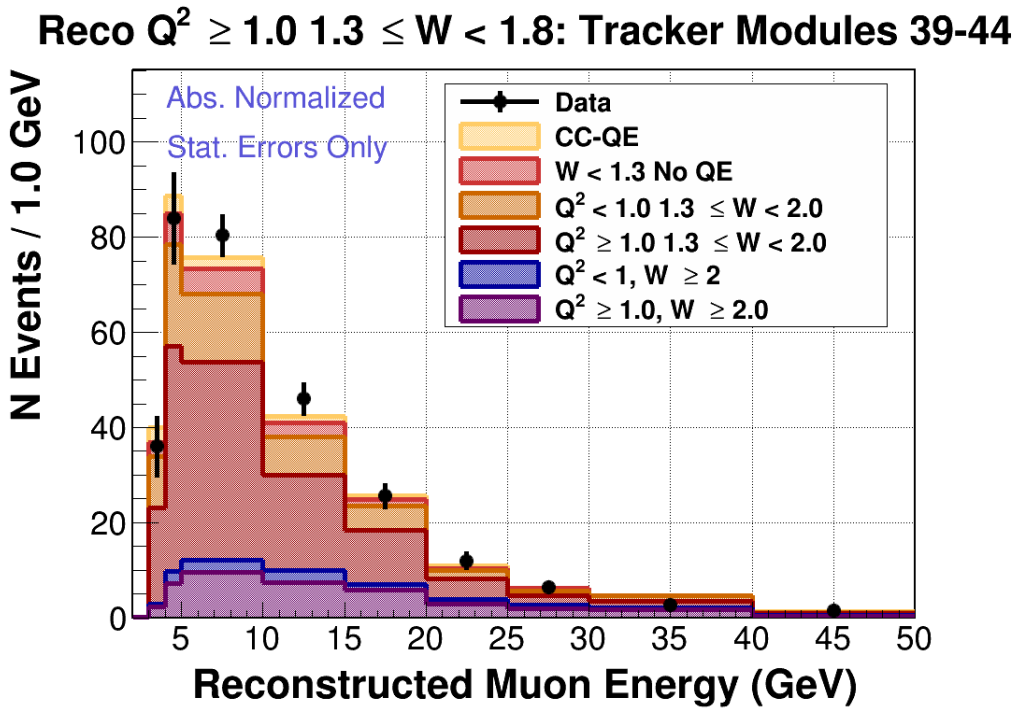

Figure A-166. Data / MC low W sideband after fitting: tracker mods. 39-44 (E_μ)

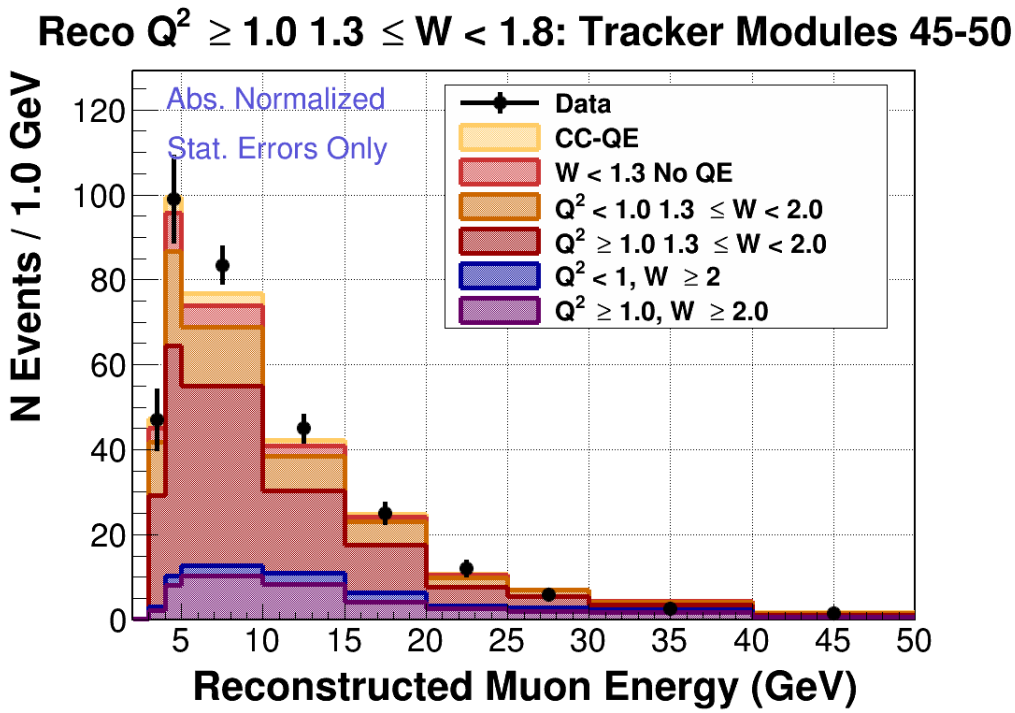

Figure A-167. Data / MC low W sideband after fitting: tracker mods. 45-50 (E_μ)

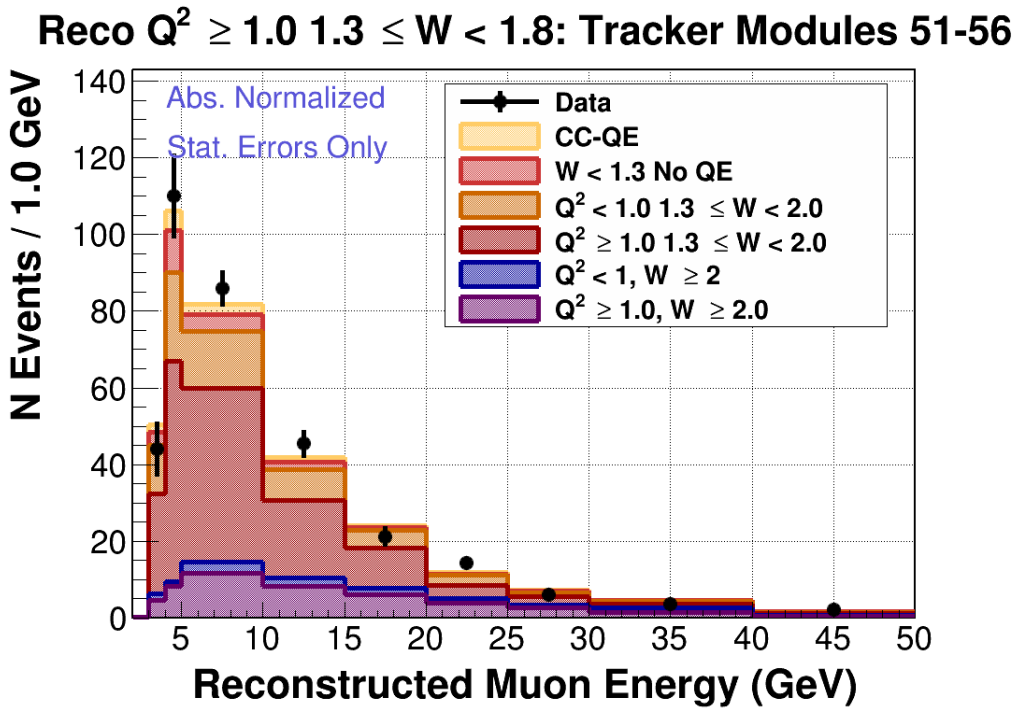

Figure A-168. Data / MC low W sideband after fitting: tracker mods. 51-56 (E_μ)

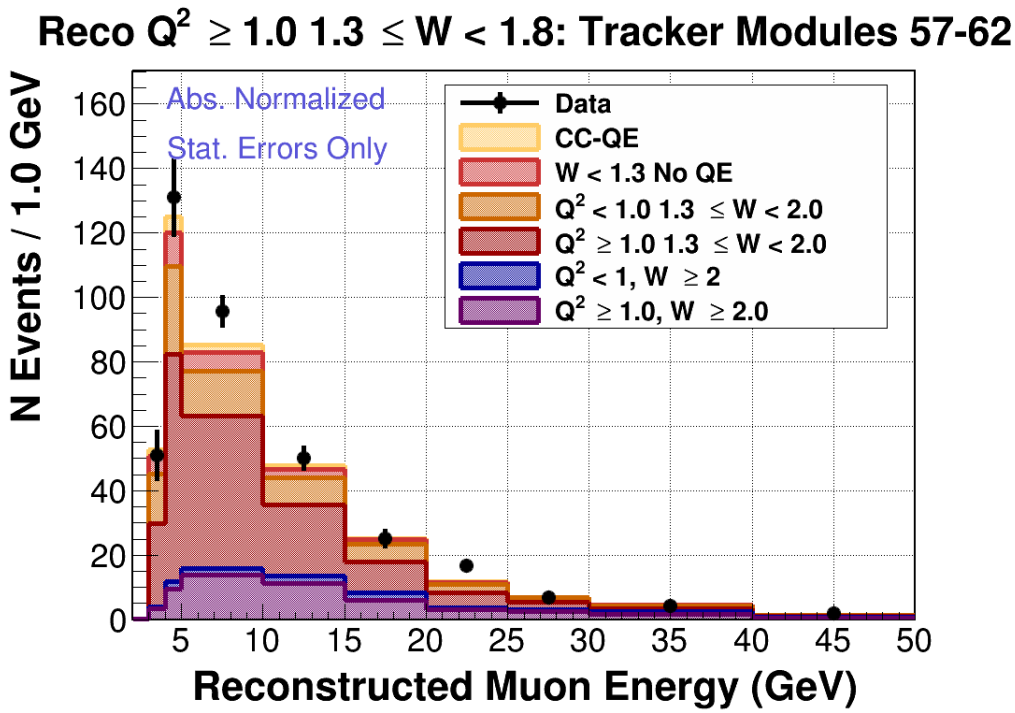

Figure A-169. Data / MC low W sideband after fitting: tracker mods. 57-62 (E_μ)

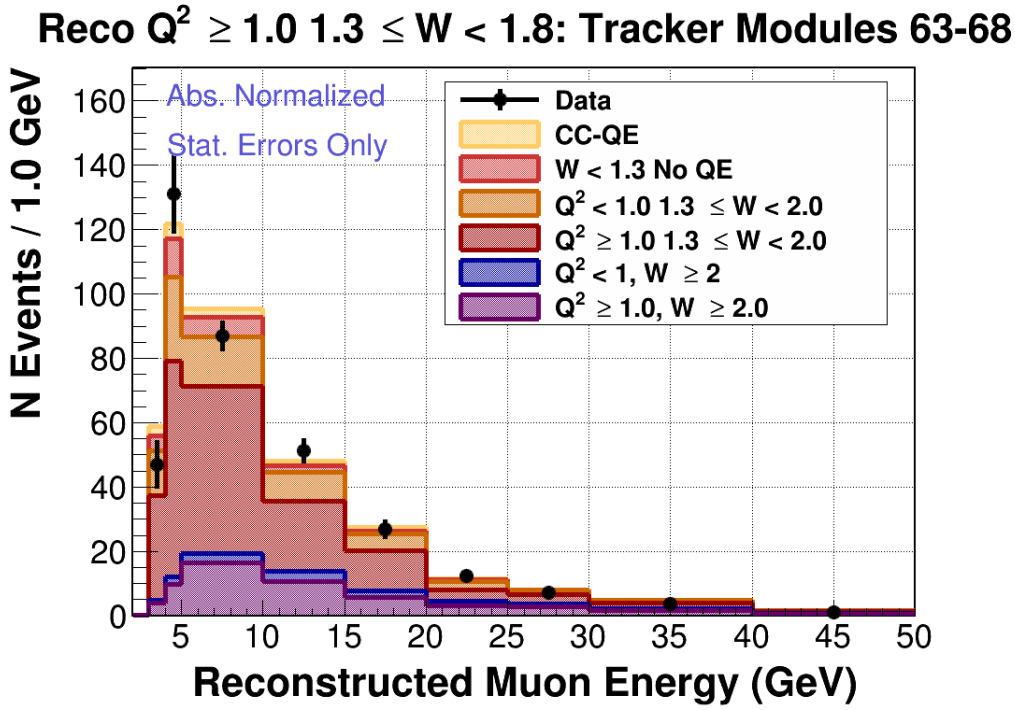

Figure A-170. Data / MC low W sideband after fitting: tracker mods. 63-68 (E_μ)

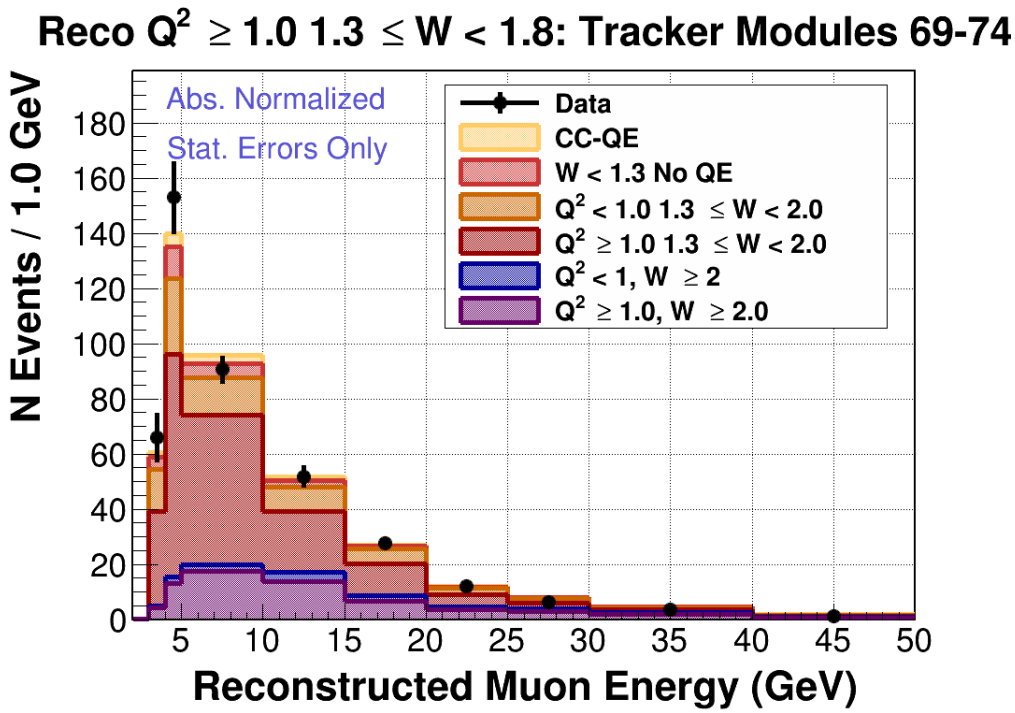

Figure A-171. Data / MC low W sideband after fitting: tracker mods. 69-74 (E_μ)

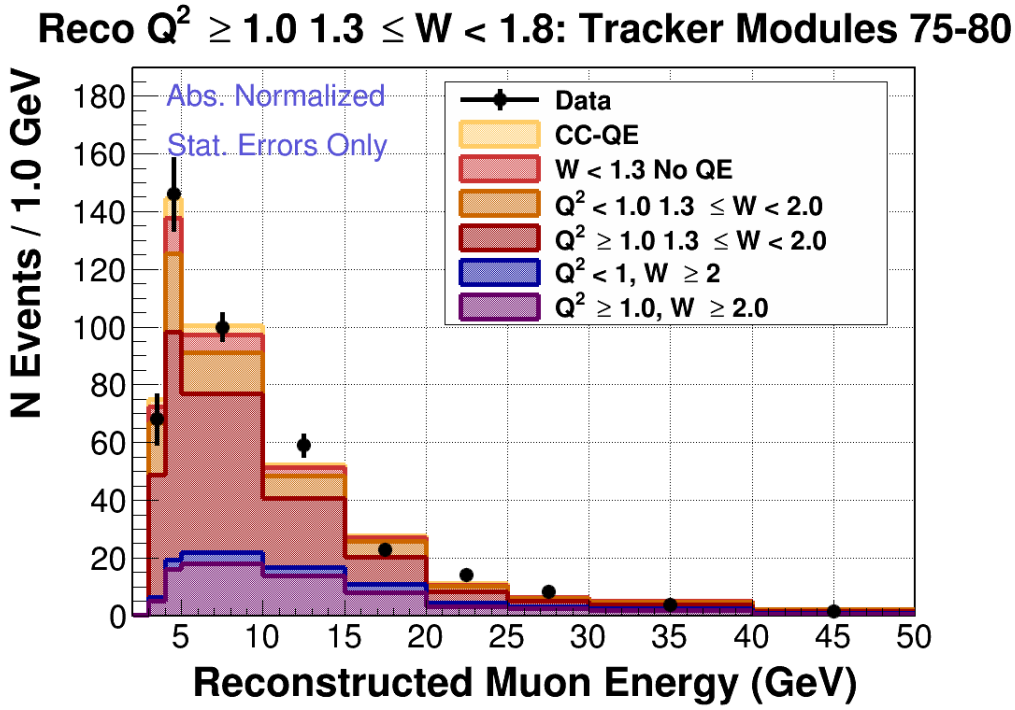

Figure A-172. Data / MC low W sideband after fitting: tracker mods. 75-80 (E_μ)

The following plots show the population of the low W sideband ($Q^2 \geq 1.0$ (GeV/c)^2 $1.3 \leq W < 1.8$ GeV/c^2) *after* tuning to data as a function of muon angle (θ_μ):

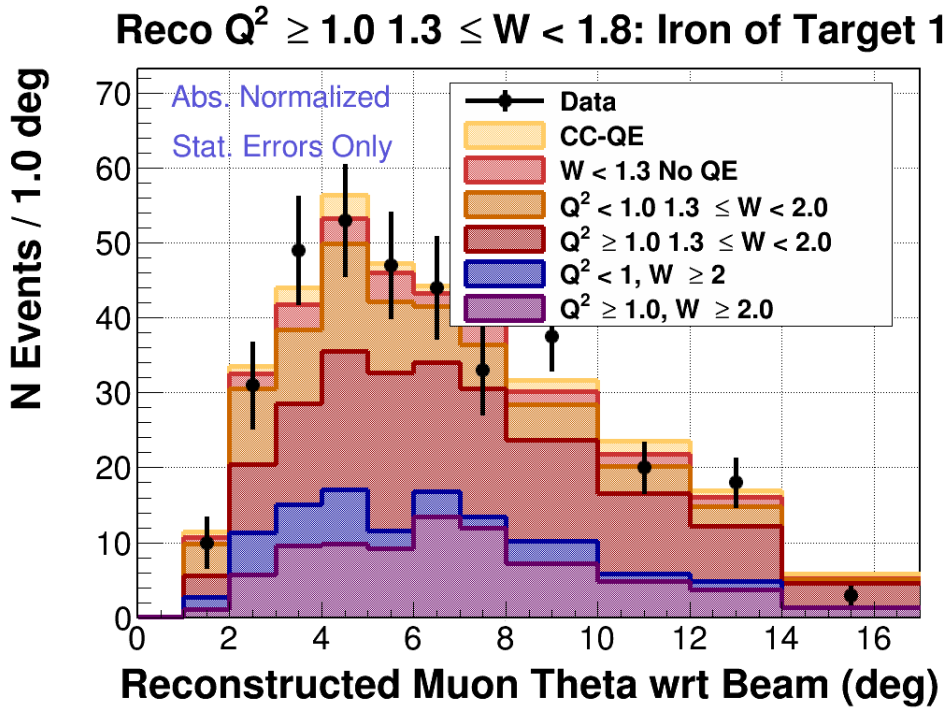

Figure A-173. Data / MC low W sideband after fitting: target 01 Fe (θ_μ)

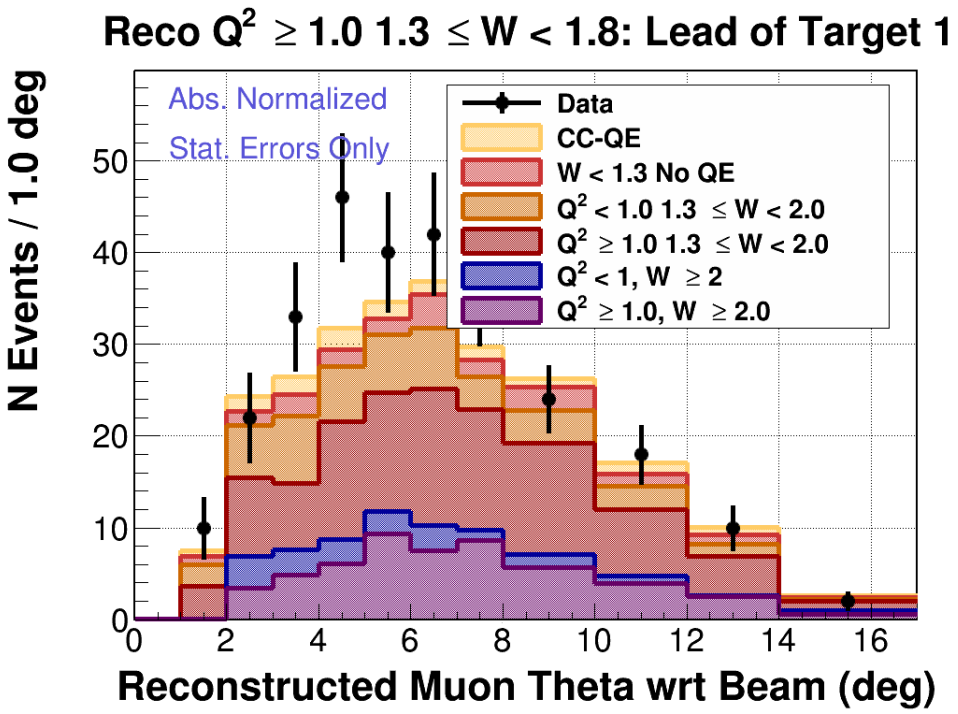

Figure A-174. Data / MC low W sideband after fitting: target 01 Pb (θ_μ)

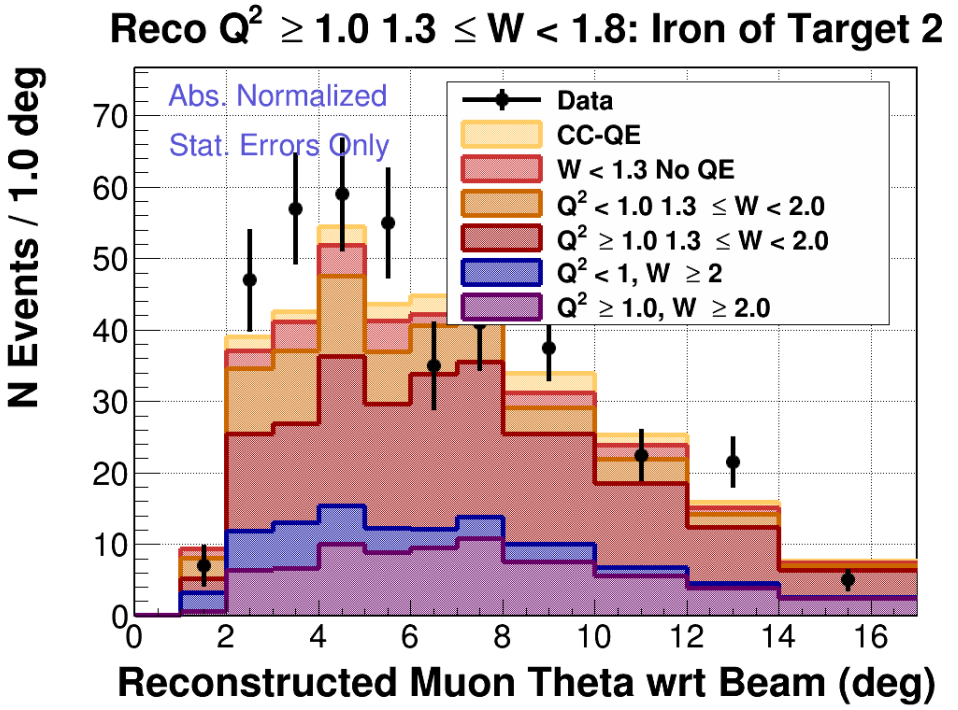

Figure A-175. Data / MC low W sideband after fitting: target 02 Fe (θ_μ)

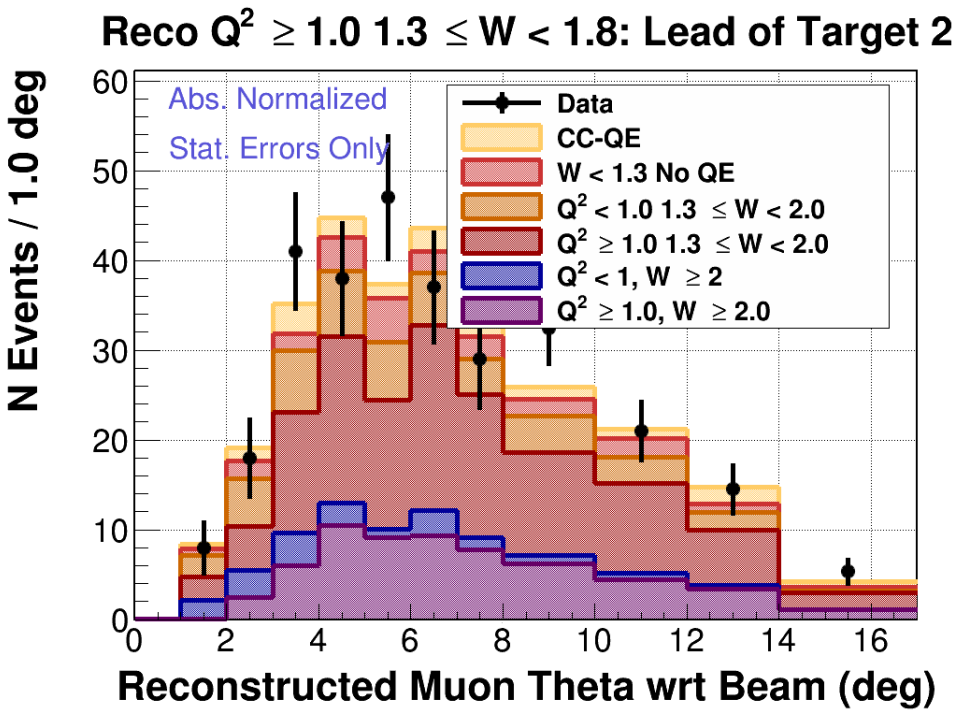

Figure A-176. Data / MC low W sideband after fitting: target 02 Pb (θ_μ)

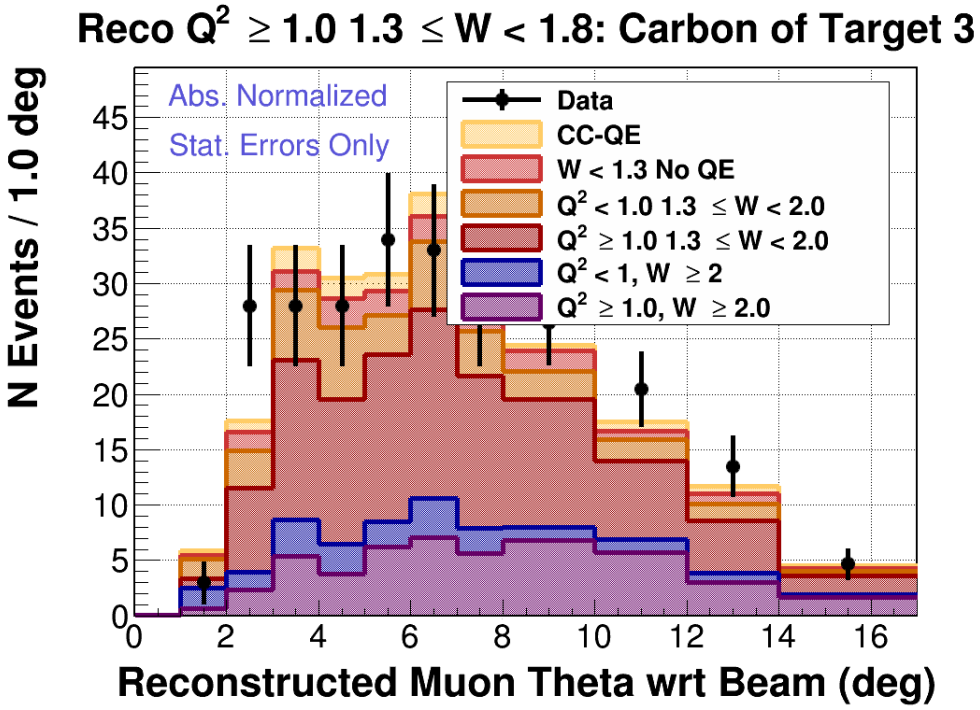

Figure A-177. Data / MC low W sideband after fitting: target 03 C (θ_μ)

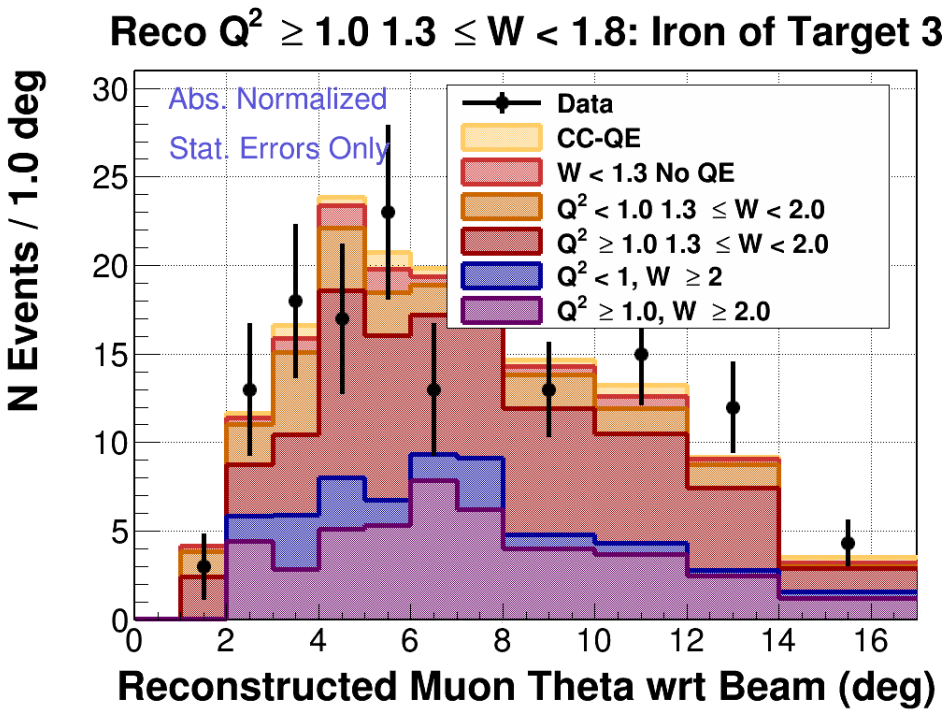

Figure A-178. Data / MC low W sideband after fitting: target 03 C (θ_μ)

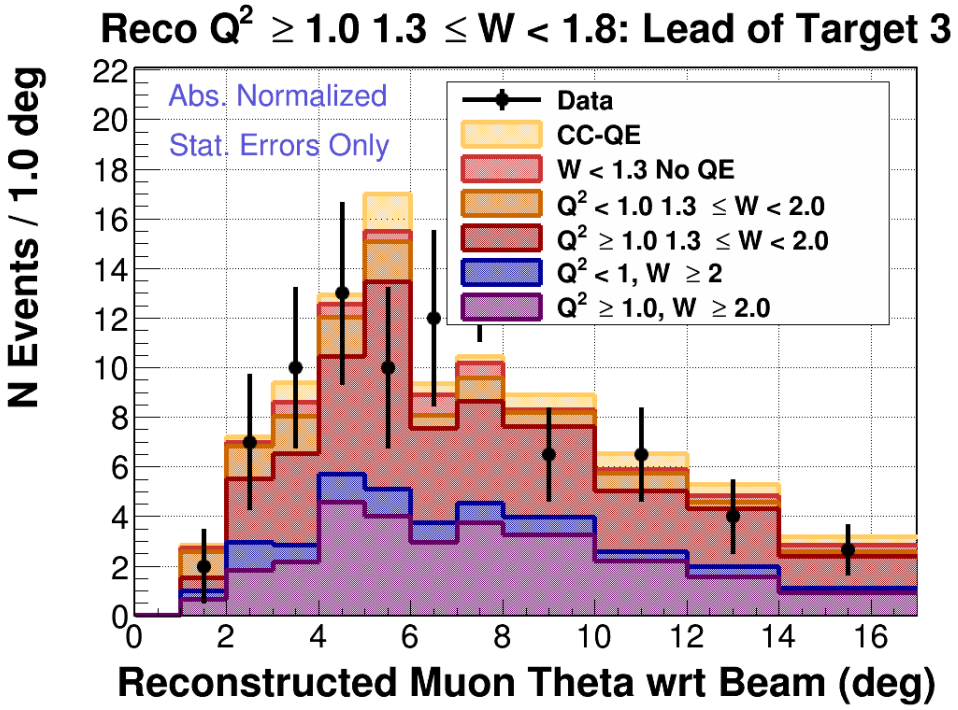

Figure A-179. Data / MC low W sideband after fitting: target 03 Pb (θ_μ)

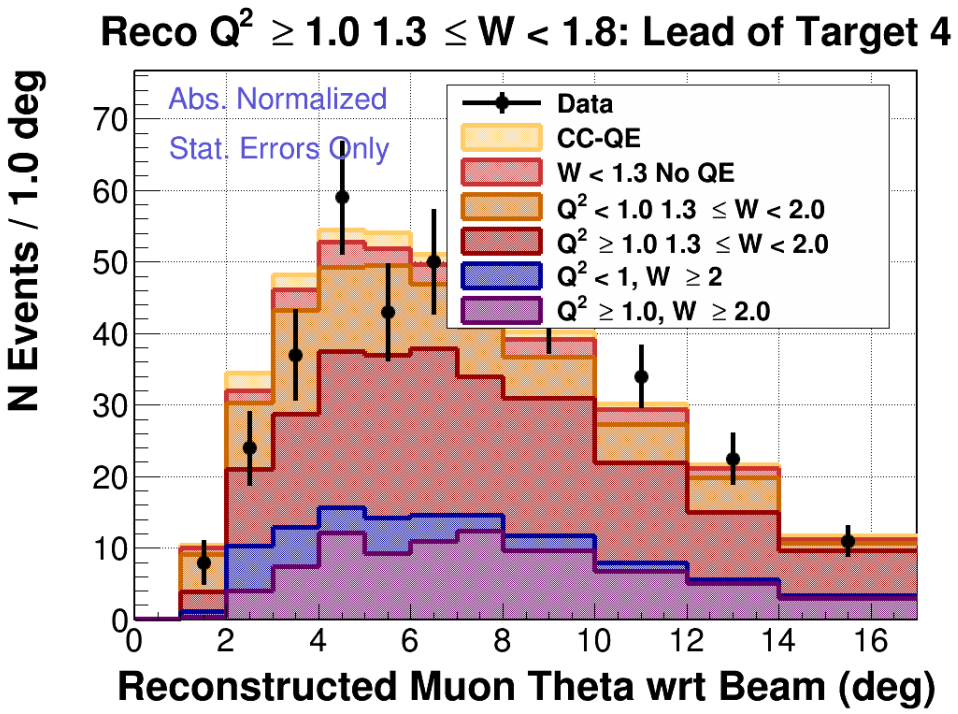

Figure A-180. Data / MC low W sideband after fitting: target 04 Pb (θ_μ)

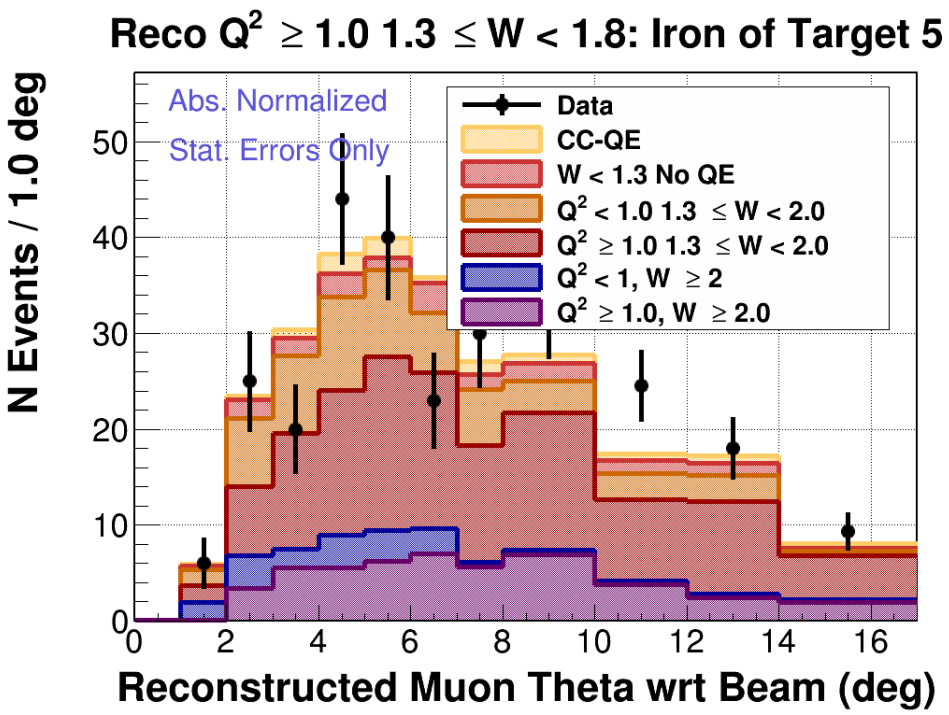

Figure A-181. Data / MC low W sideband after fitting: target 05 Fe (θ_μ)

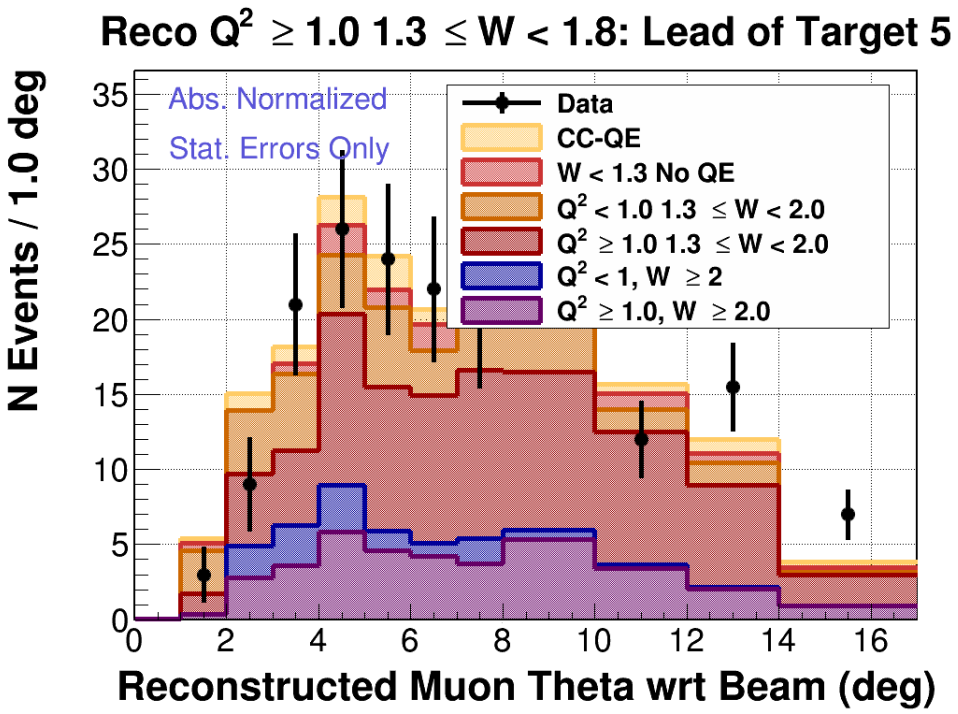

Figure A-182. Data / MC low W sideband after fitting: target 05 Pb (θ_μ)

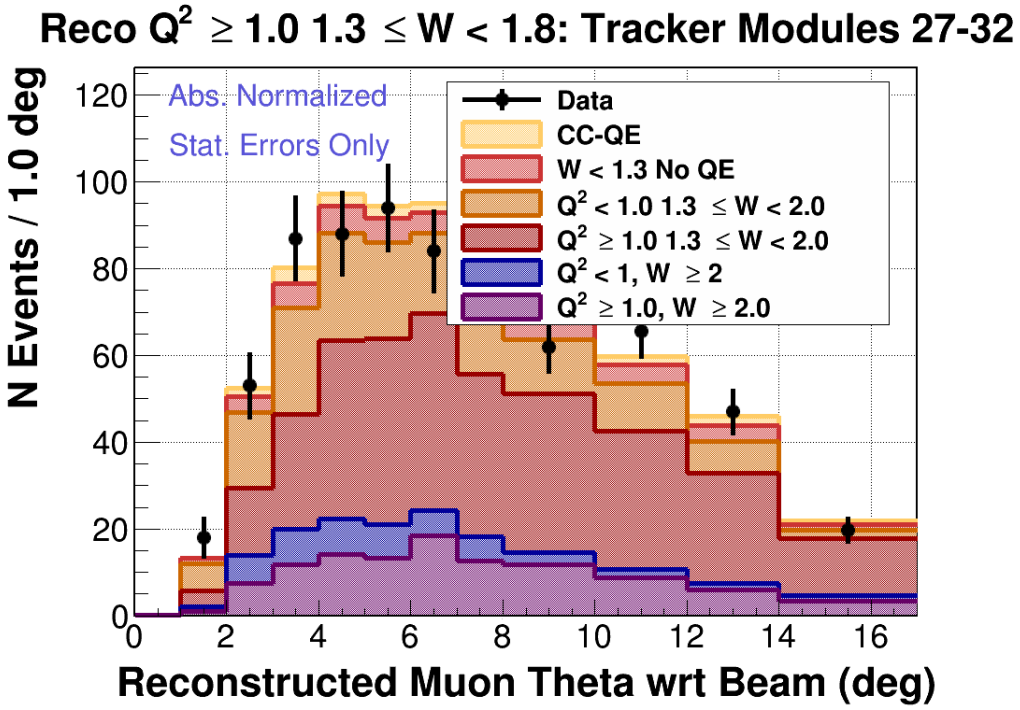

Figure A-183. Data / MC low W sideband after fitting: tracker mods. 27-32 (θ_μ)

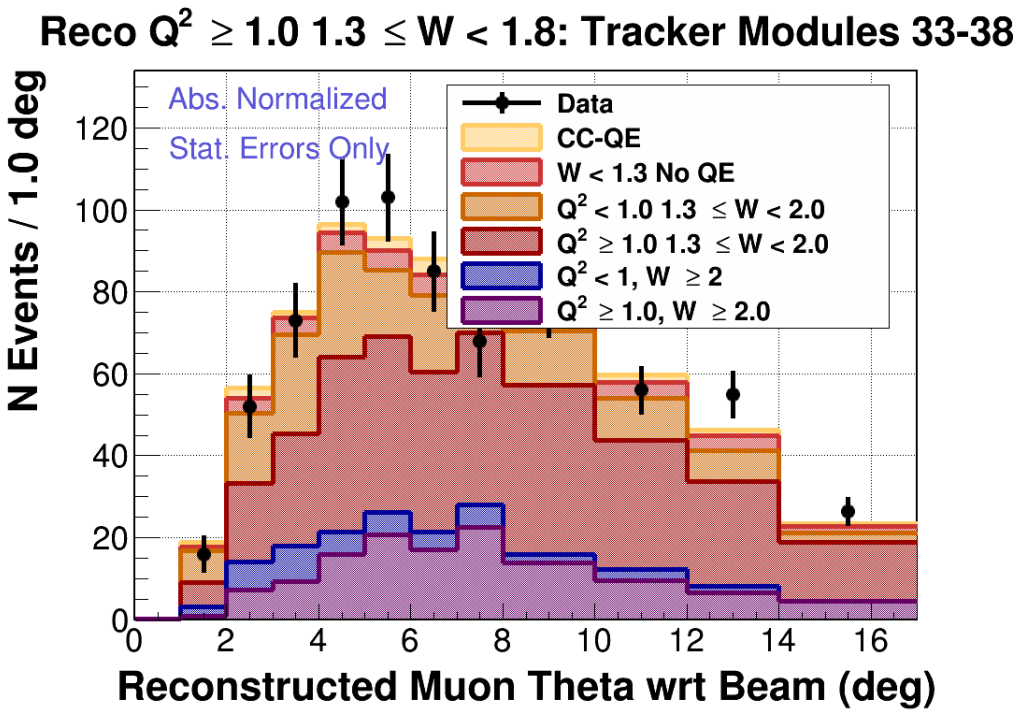

Figure A-184. Data / MC low W sideband after fitting: tracker mods. 33-38 (θ_μ)

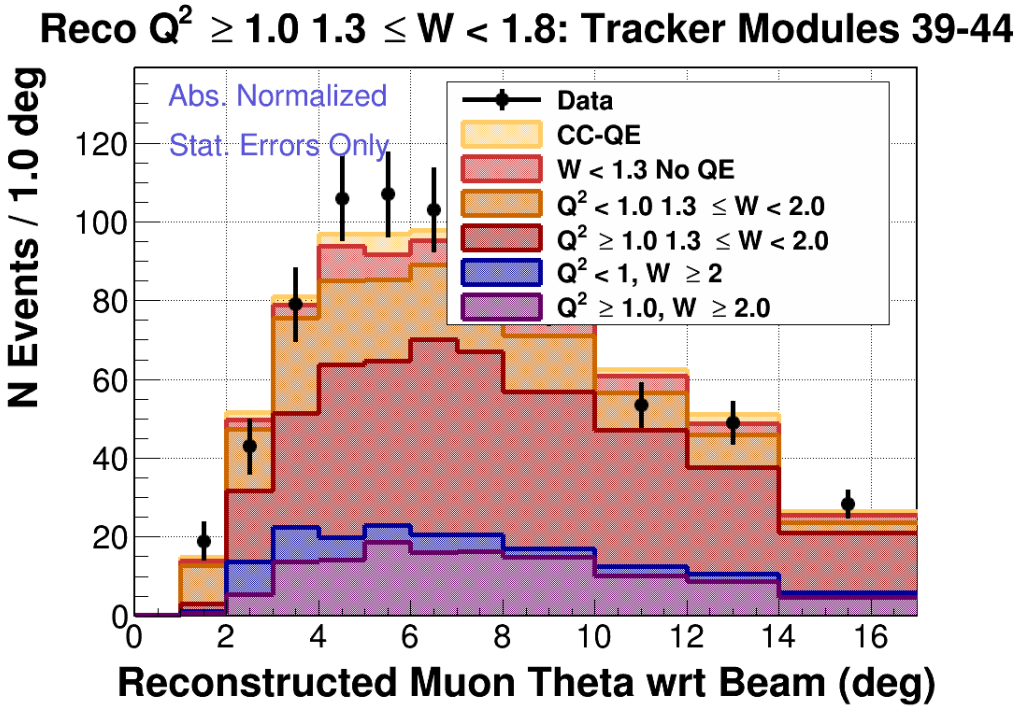

Figure A-185. Data / MC low W sideband after fitting: tracker mods. 39-44 (θ_μ)

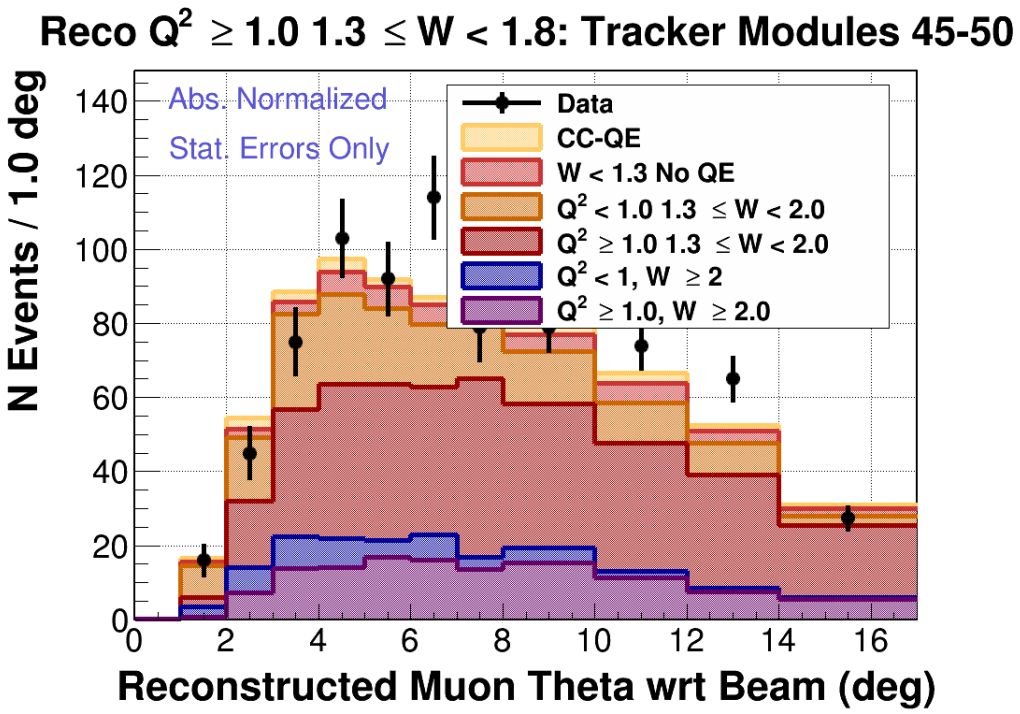

Figure A-186. Data / MC low W sideband after fitting: tracker mods. 45-50 (θ_μ)

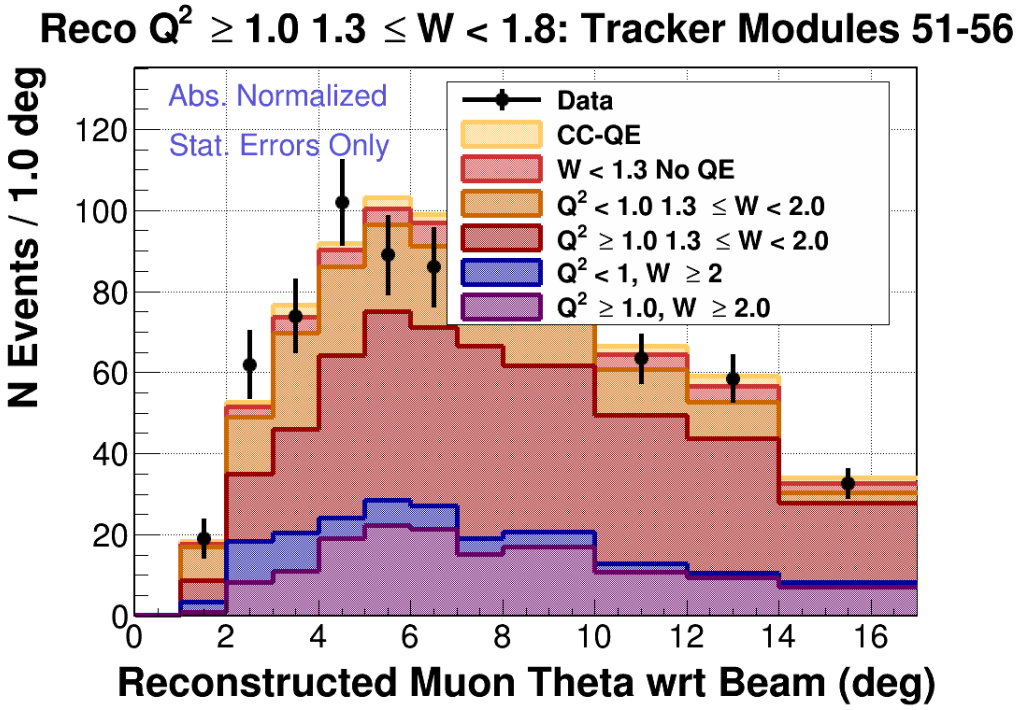

Figure A-187. Data / MC low W sideband after fitting: tracker mods. 51-56 (θ_μ)

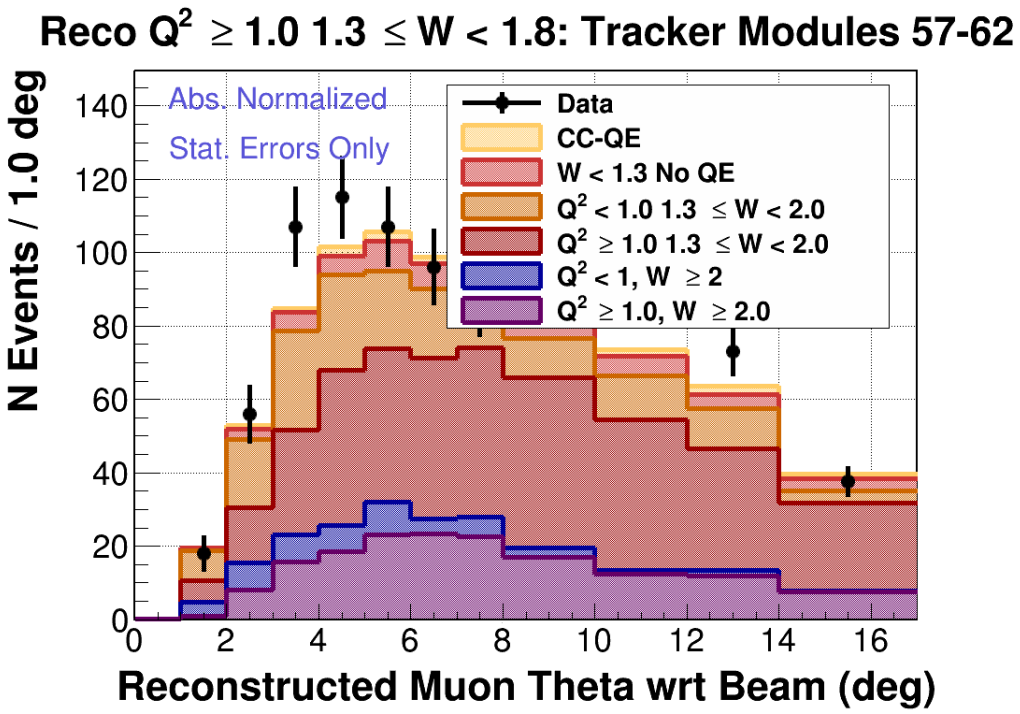

Figure A-188. Data / MC low W sideband after fitting: tracker mods. 57-62 (θ_μ)

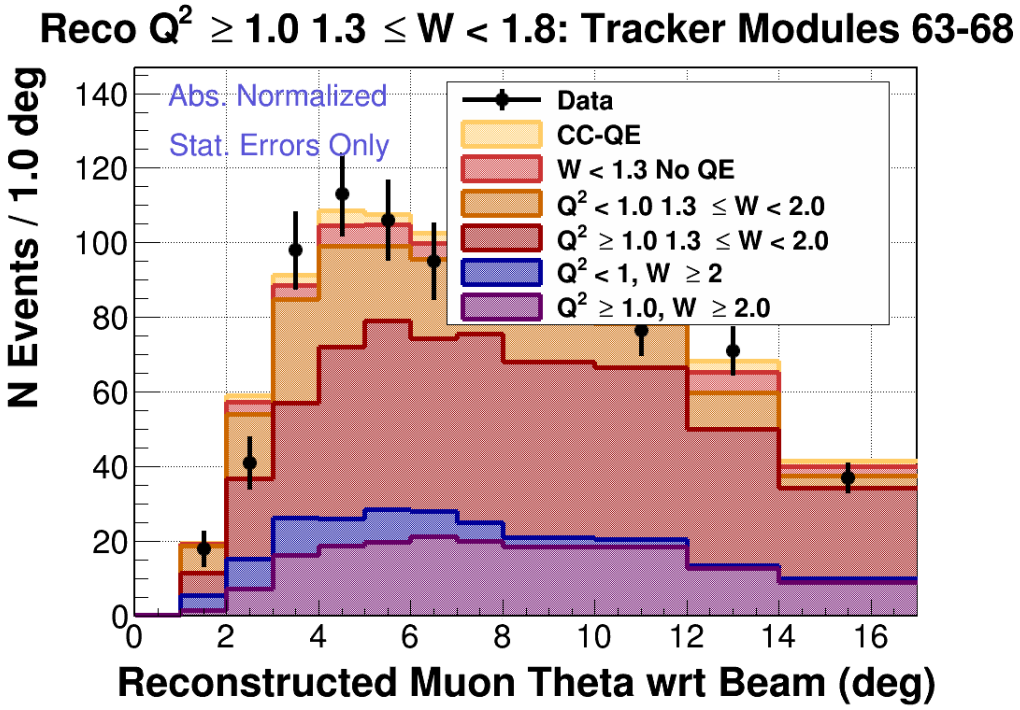

Figure A-189. Data / MC low W sideband after fitting: tracker mods. 63-68 (θ_μ)

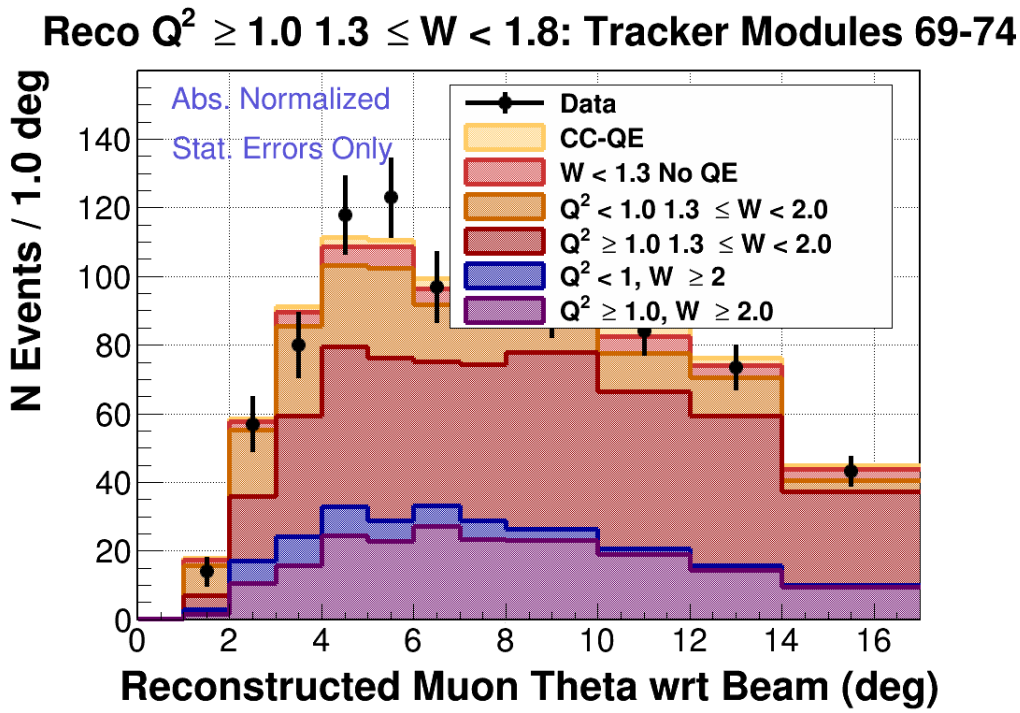

Figure A-190. Data / MC low W sideband after fitting: tracker mods. 69-74 (θ_μ)

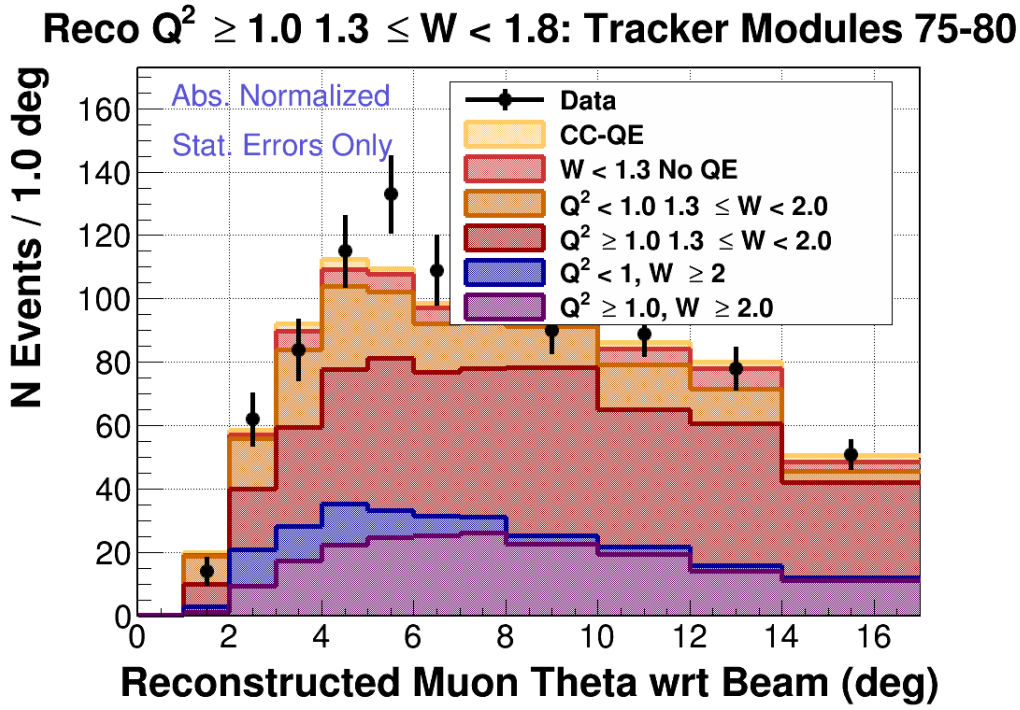

Figure A-191. Data / MC low W sideband after fitting: tracker mods. 75-80 (θ_μ)

A.4 Low Q^2 Sideband: $Q^2 < 0.8$ (GeV/c)^2 $W \geq 2.0$ GeV/c^2 (Before Fitting)

The following plots show the population of the low Q^2 sideband ($Q^2 < 0.8$ (GeV/c)^2 $W \geq 2.0$) *before* tuning to data as a function of neutrino energy (E_ν):

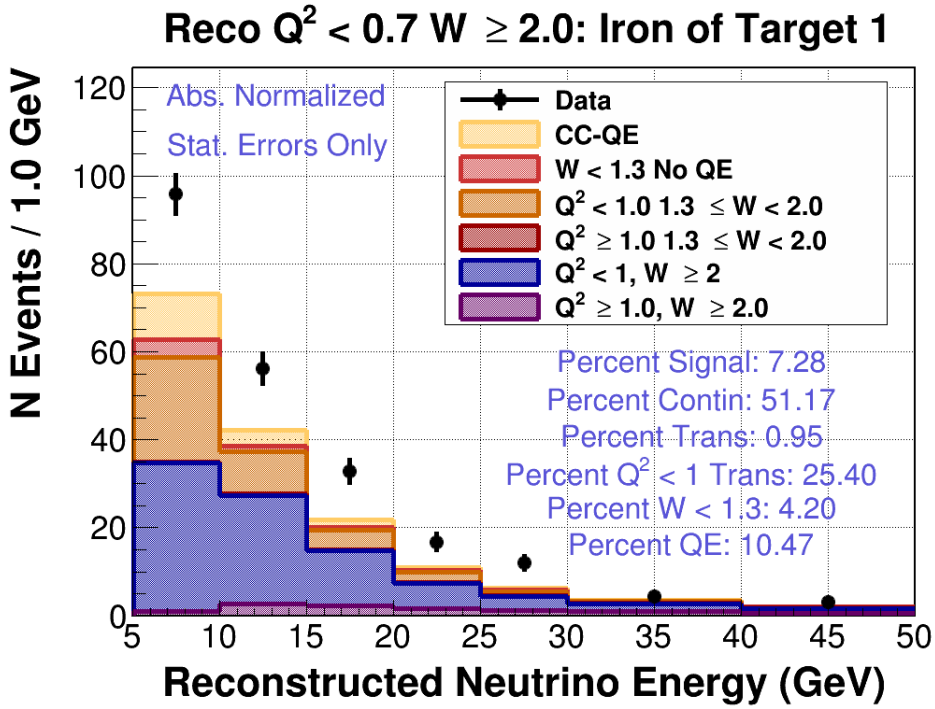

Figure A-192. Data / MC low Q^2 sideband before fitting: target 01 Fe (E_ν)

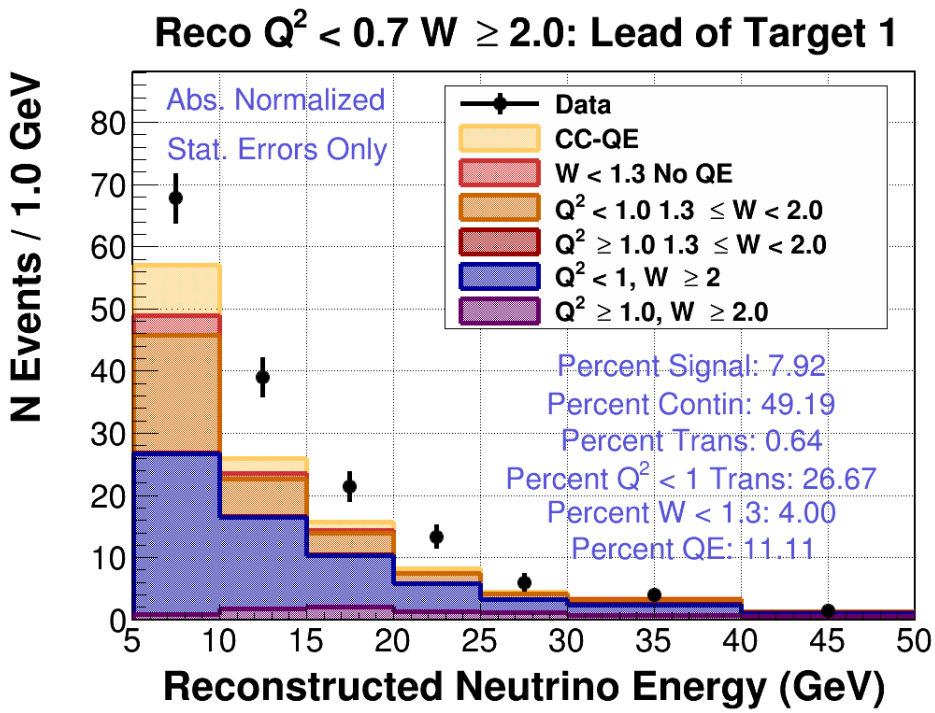

Figure A-193. Data / MC low Q^2 sideband before fitting: target 01 Pb (E_ν)

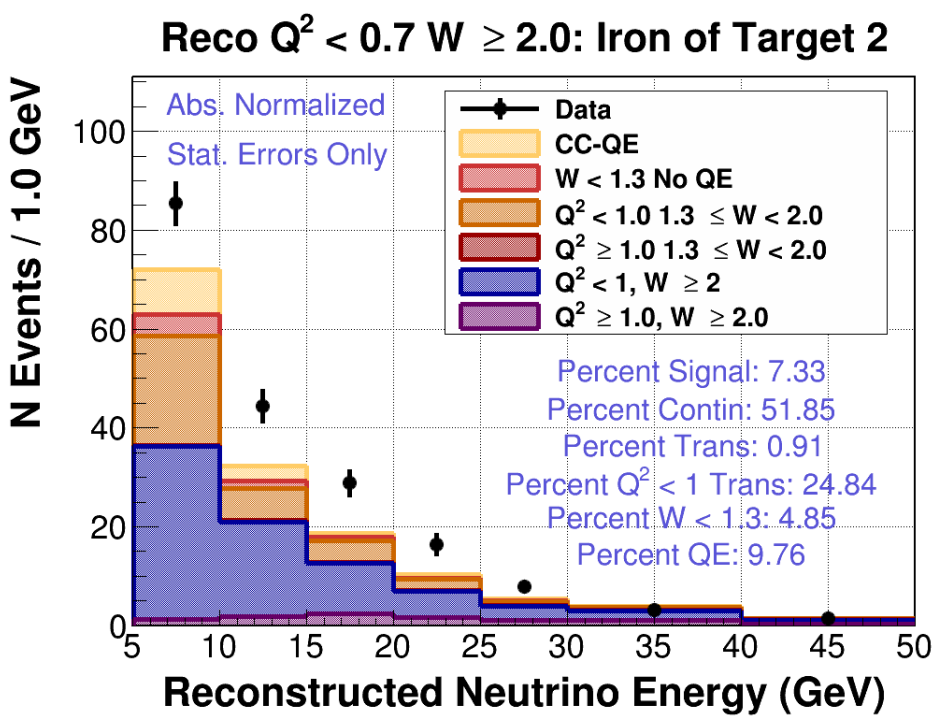

Figure A-194. Data / MC low Q^2 sideband before fitting: target 02 Fe (E_ν)

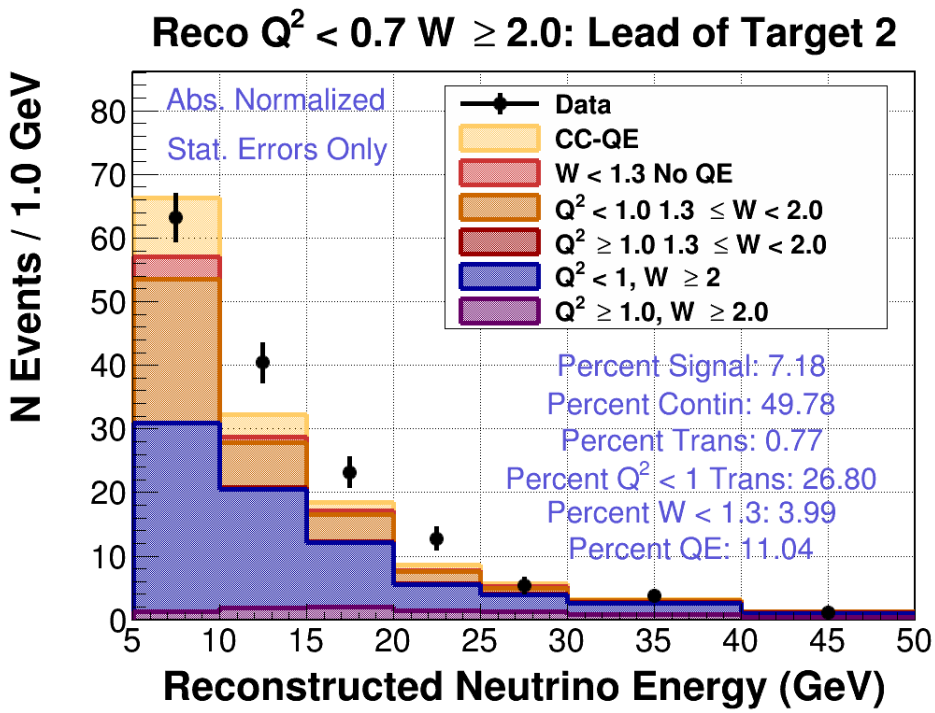

Figure A-195. Data / MC low Q^2 sideband before fitting: target 02 Pb (E_ν)

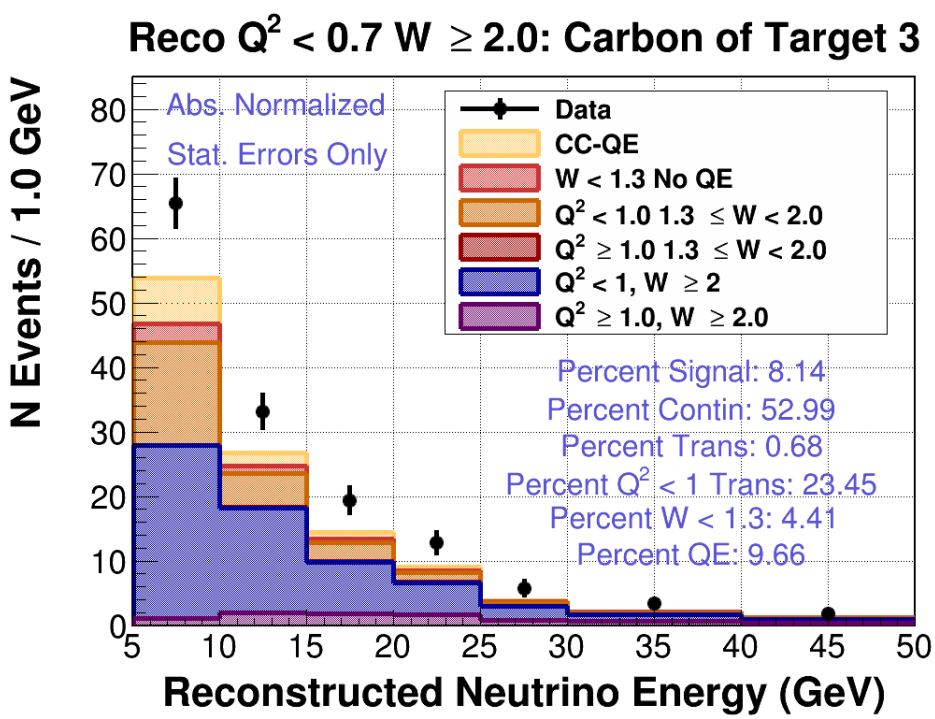

Figure A-196. Data / MC low Q^2 sideband before fitting: target 03 C (E_ν)

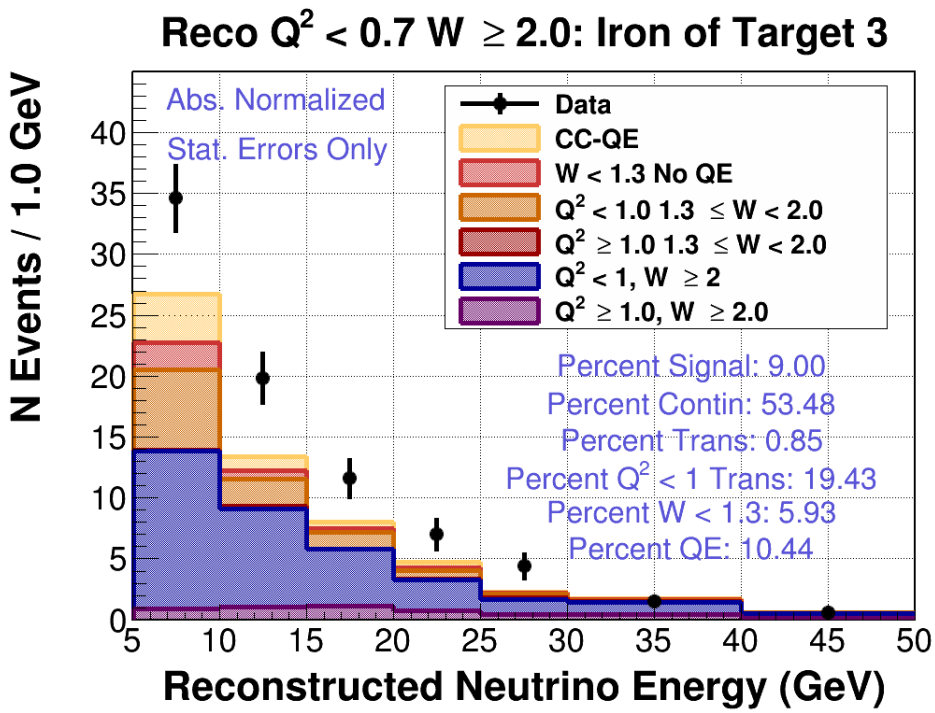

Figure A-197. Data / MC low Q^2 sideband before fitting: target 03 Fe (E_ν)

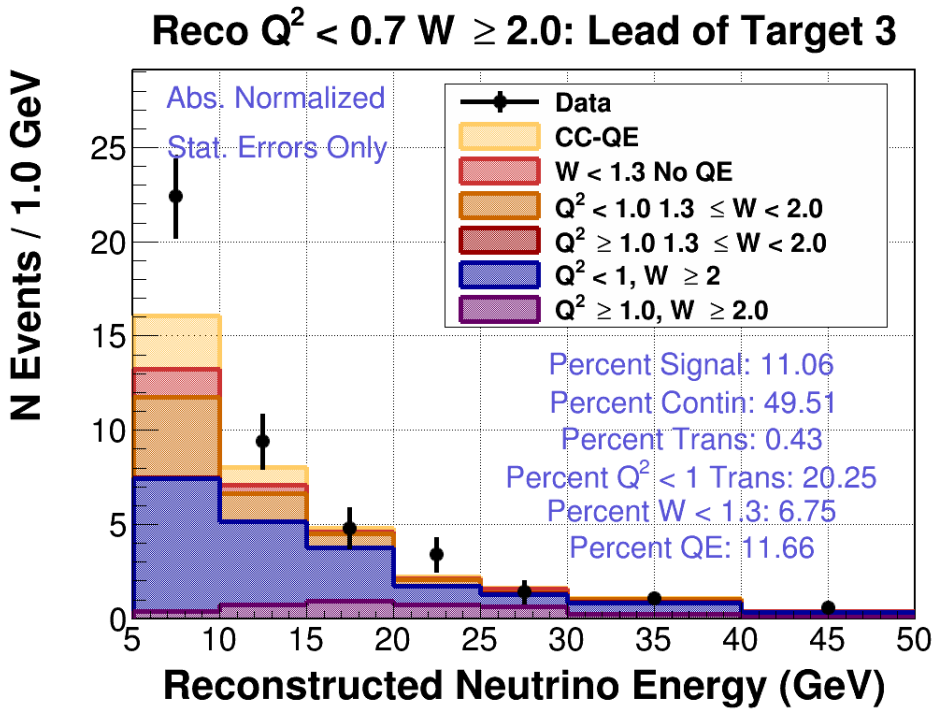

Figure A-198. Data / MC low Q^2 sideband before fitting: target 03 Pb (E_ν)

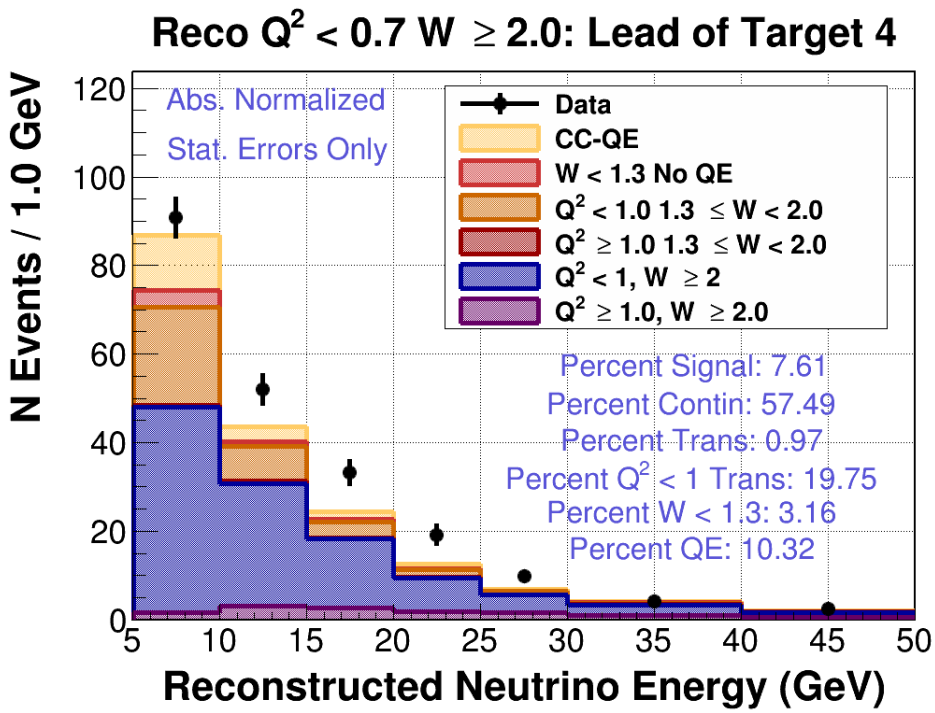

Figure A-199. Data / MC low Q^2 sideband before fitting: target 04 Pb (E_ν)

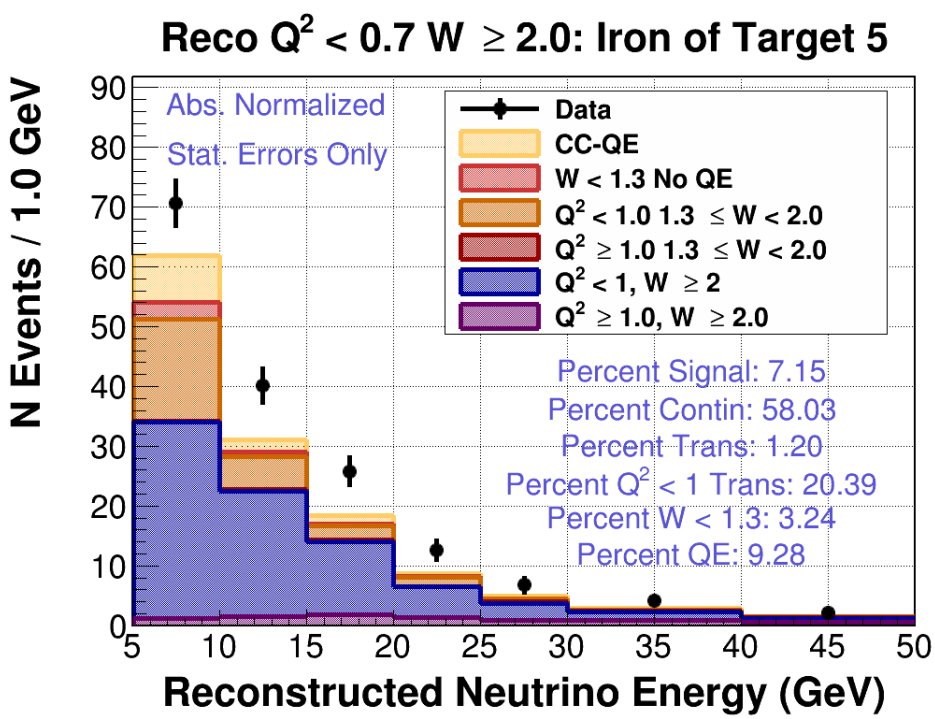

Figure A-200. Data / MC low Q^2 sideband before fitting: target 05 Fe (E_ν)

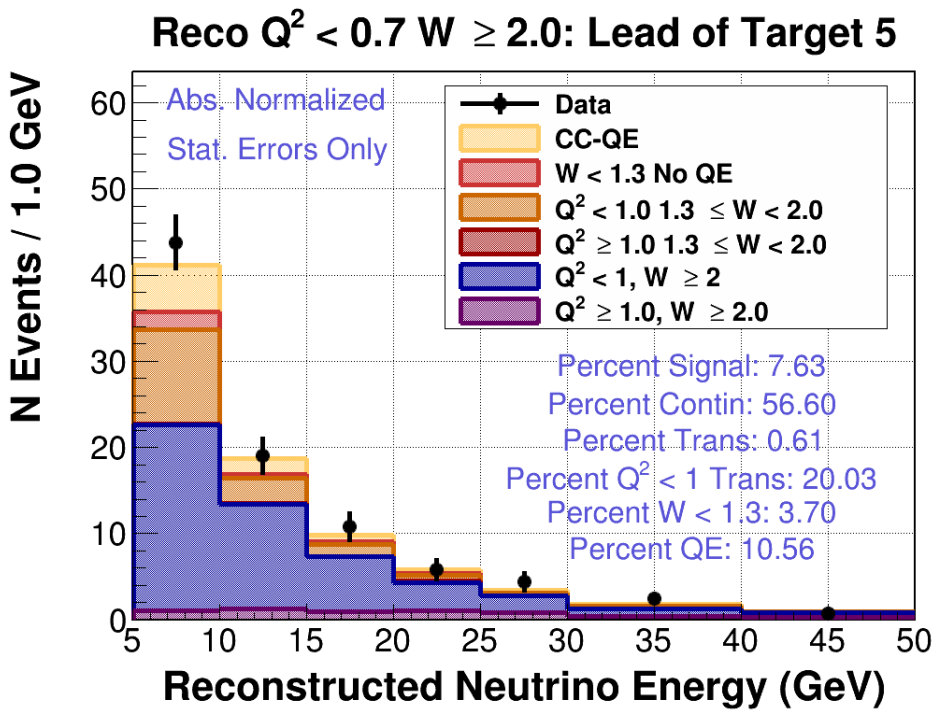

Figure A-201. Data / MC low Q^2 sideband before fitting: target 05 Pb (E_ν)

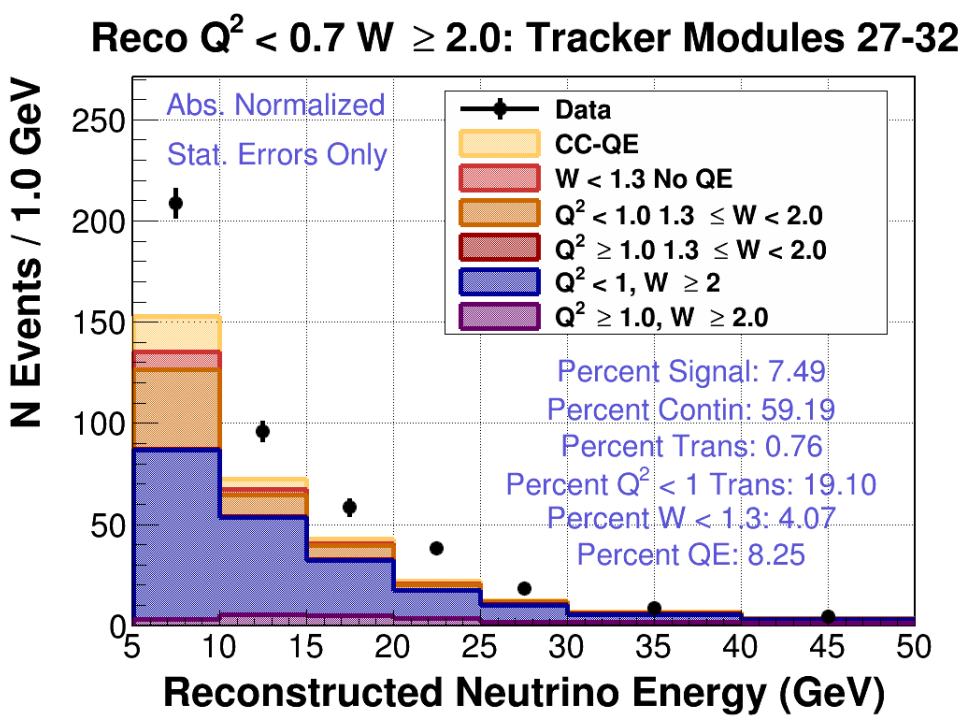

Figure A-202. Data / MC low Q^2 sideband before fitting: tracker mods. 27-32 (E_ν)

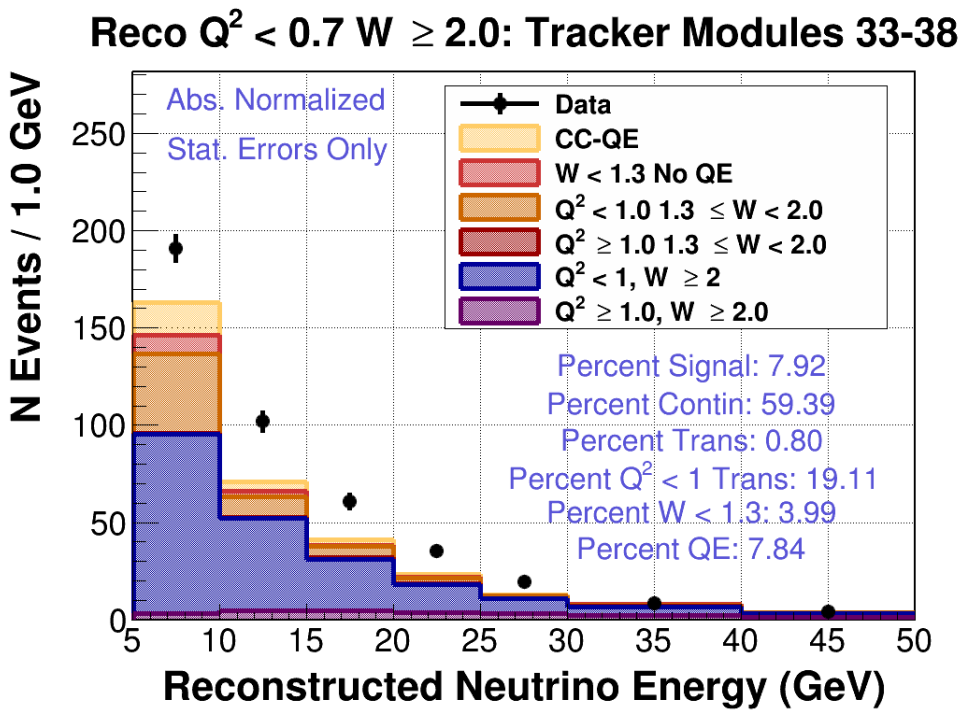

Figure A-203. Data / MC low Q^2 sideband before fitting: tracker mods. 33-38 (E_ν)

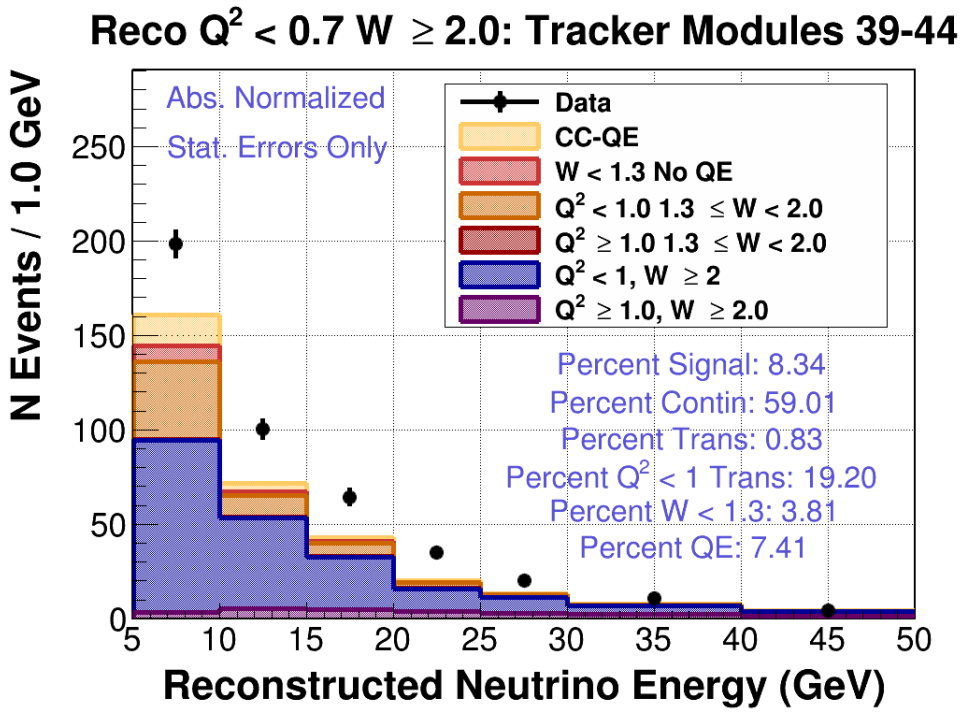

Figure A-204. Data / MC low Q^2 sideband before fitting: tracker mods. 39-44 (E_ν)

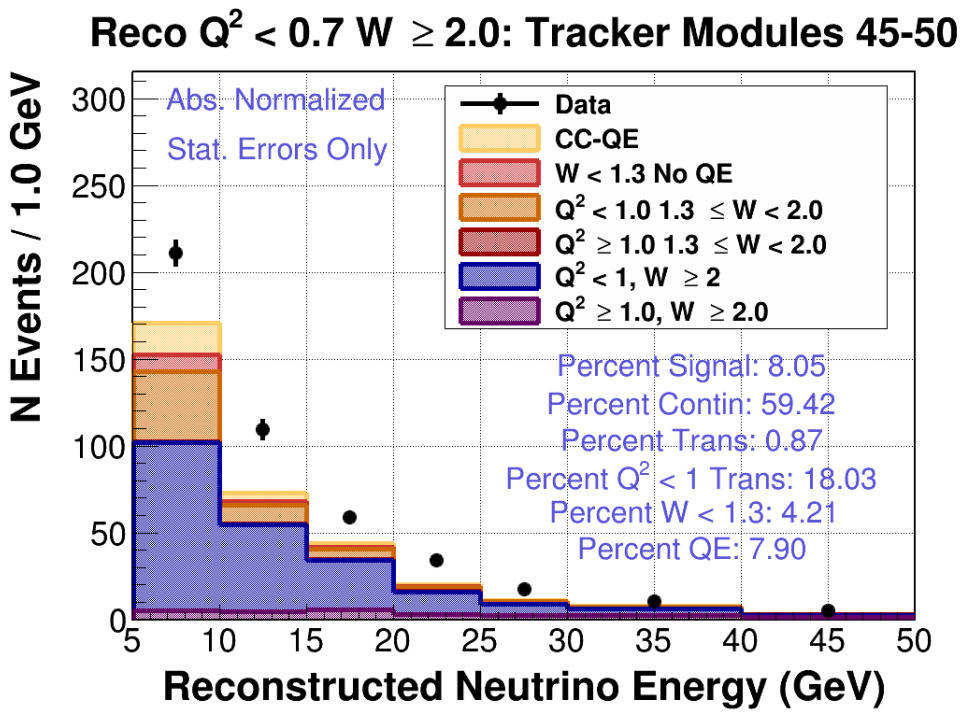

Figure A-205. Data / MC low Q^2 sideband before fitting: tracker mods. 45-50 (E_ν)

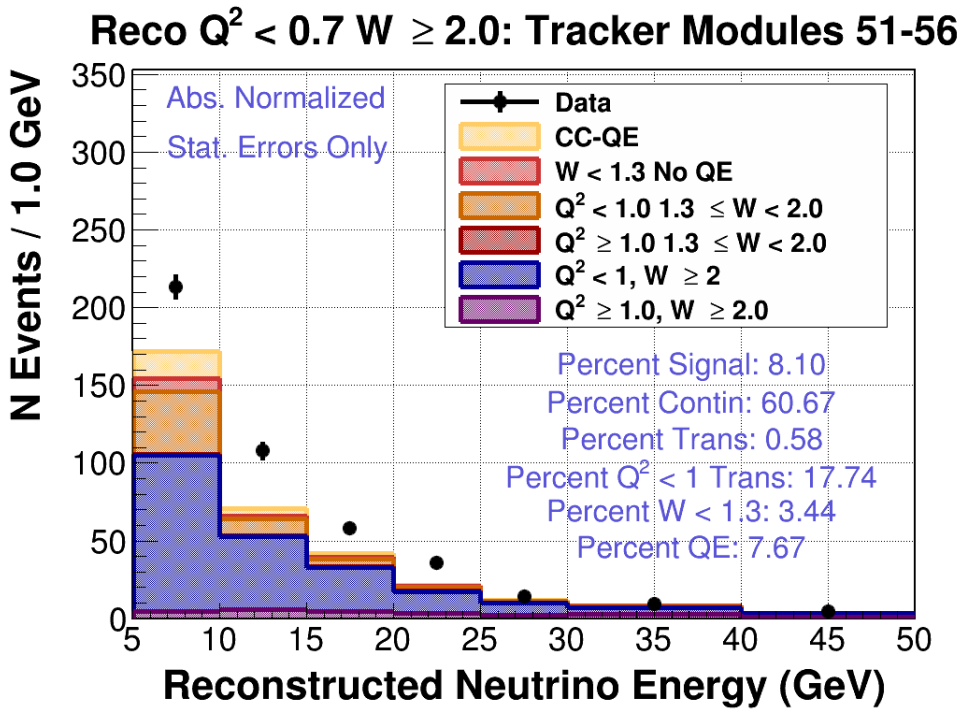

Figure A-206. Data / MC low Q^2 sideband before fitting: tracker mods. 51-56 (E_ν)

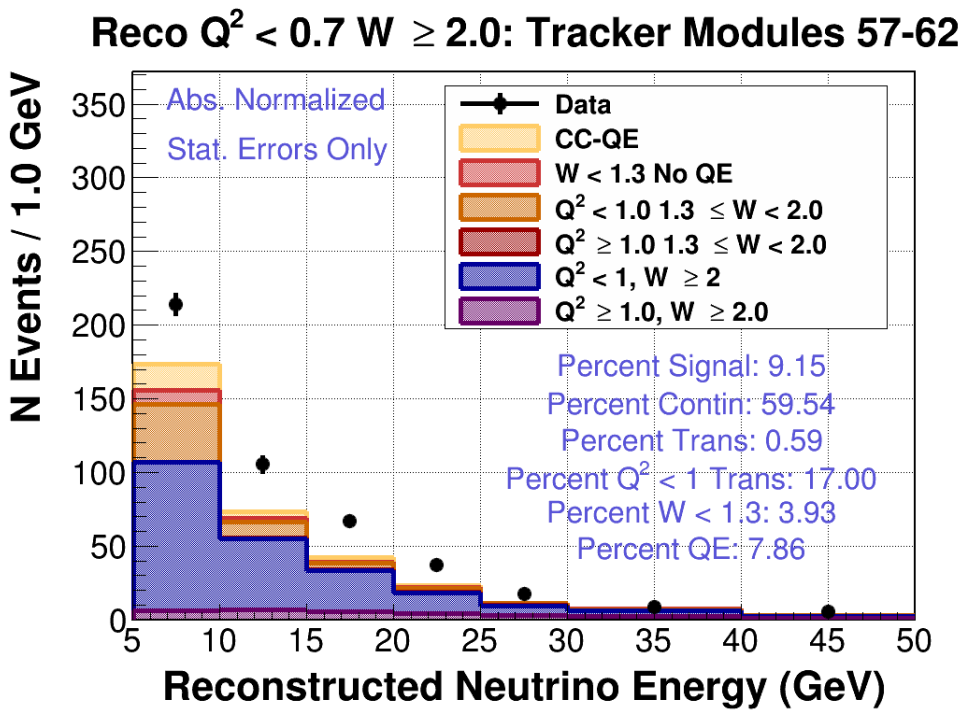

Figure A-207. Data / MC low Q^2 sideband before fitting: tracker mods. 57-62 (E_ν)

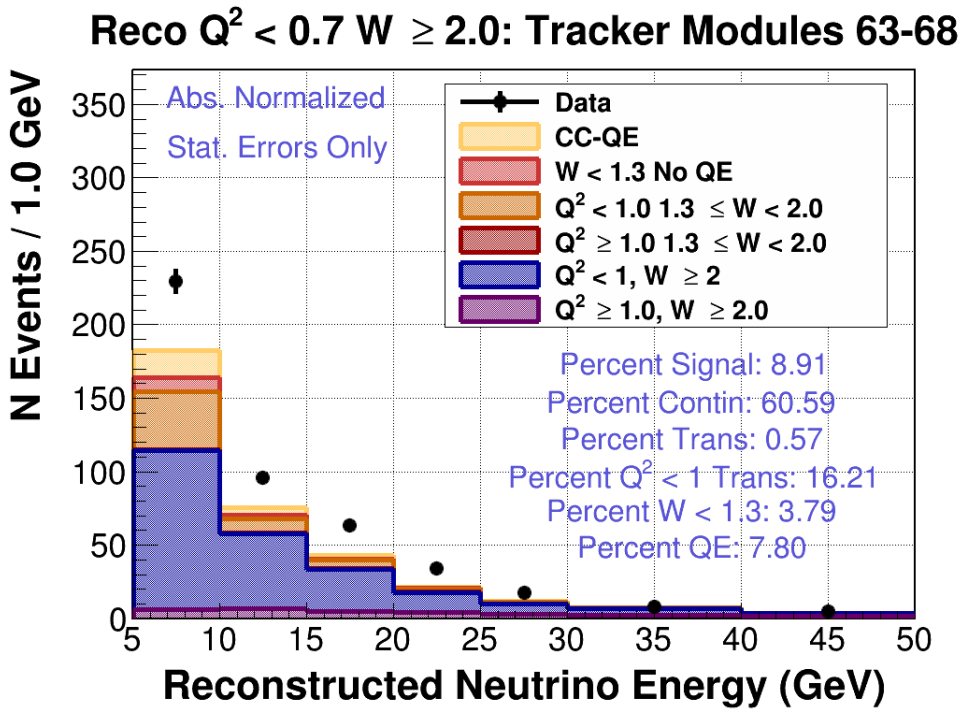

Figure A-208. Data / MC low Q^2 sideband before fitting: tracker mods. 63-68 (E_ν)

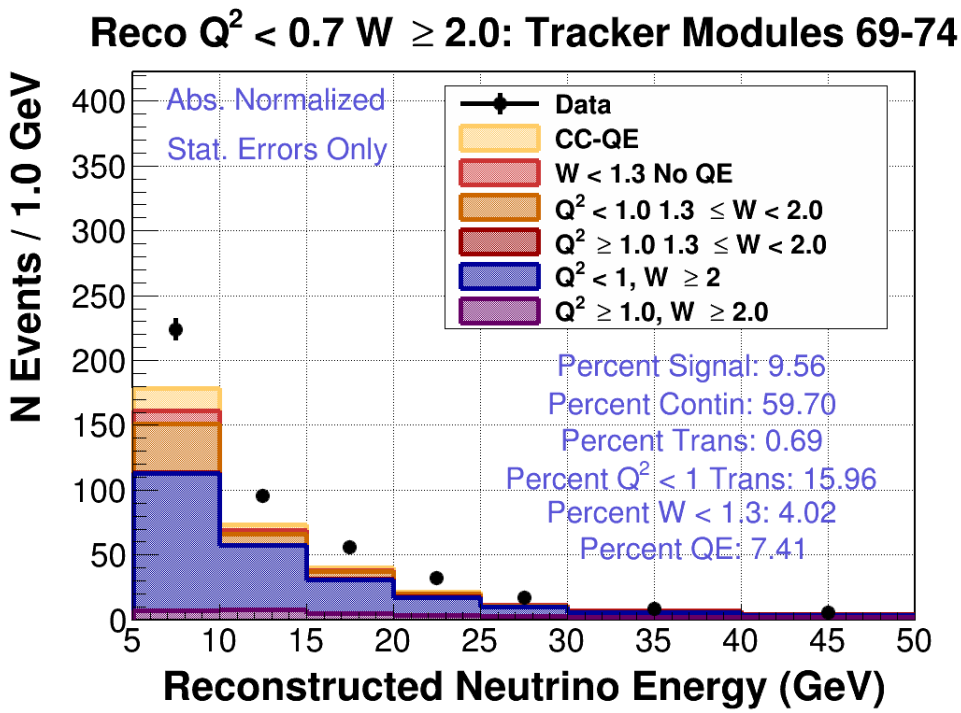

Figure A-209. Data / MC low Q^2 sideband before fitting: tracker mods. 69-74 (E_ν)

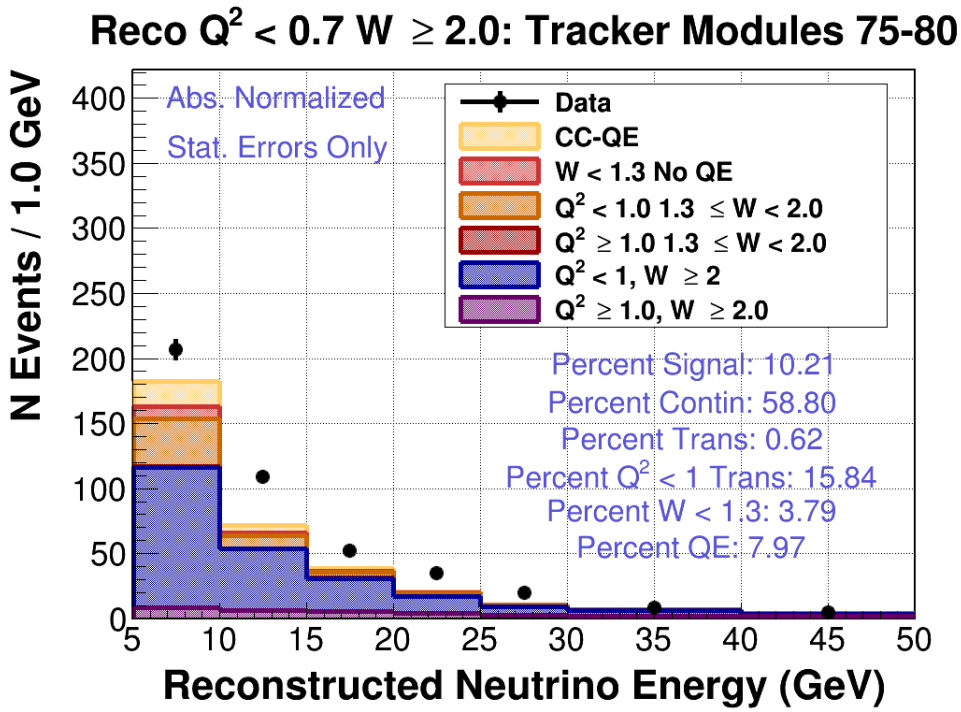

Figure A-210. Data / MC low Q^2 sideband before fitting: tracker mods. 75-80 (E_ν)

The following plots show the population of the low Q^2 sideband ($Q^2 < 0.8$ (GeV/c)^2 $W \geq 2.0$ GeV/c^2) *before* tuning to data as a function of final state hadronic shower invariant mass (W):

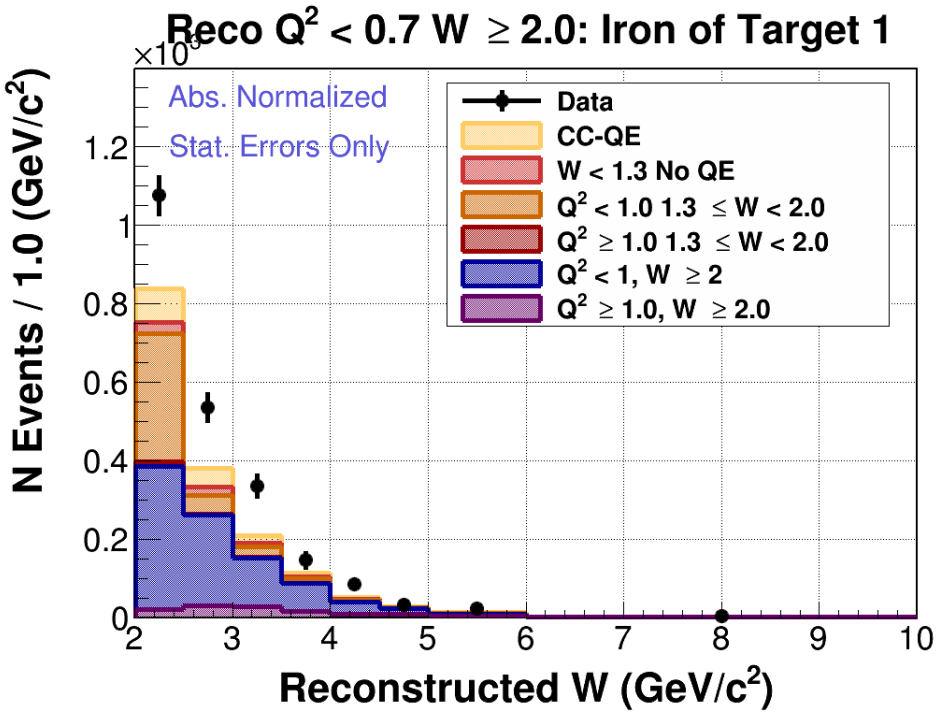

Figure A-211. Data / MC low Q^2 sideband before fitting: target 01 Fe (W)

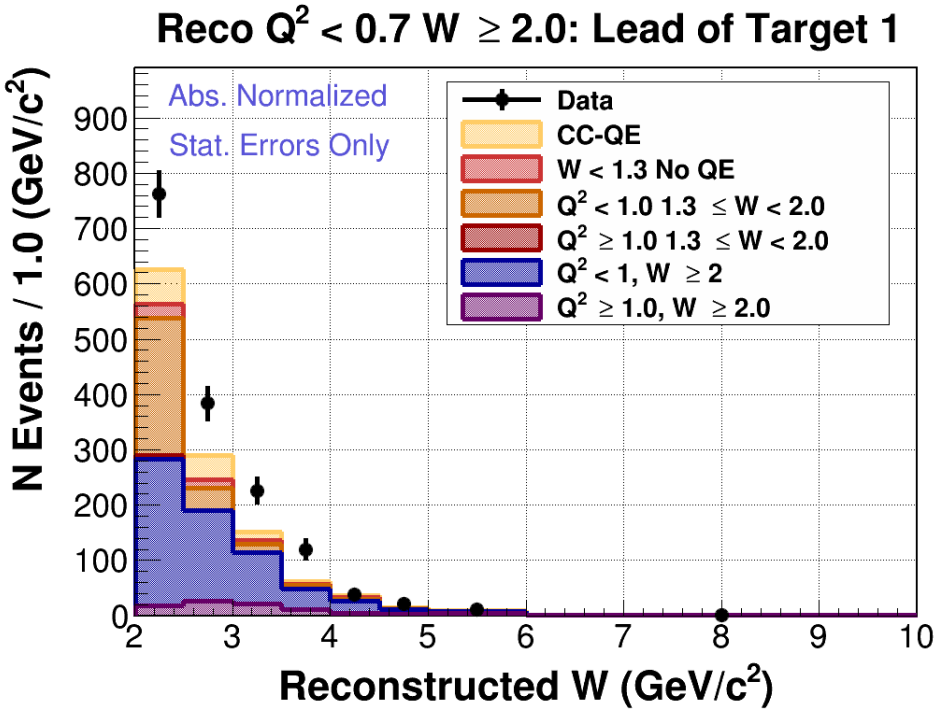

Figure A-212. Data / MC low Q^2 sideband before fitting: target 01 Pb (W)

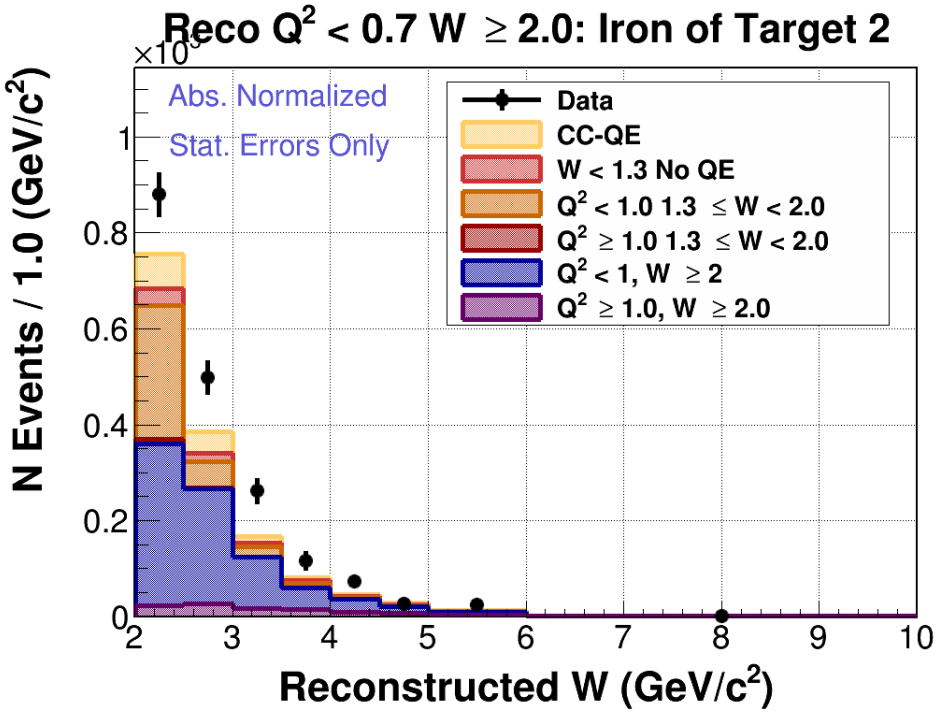

Figure A-213. Data / MC low Q^2 sideband before fitting: target 02 Fe (W)

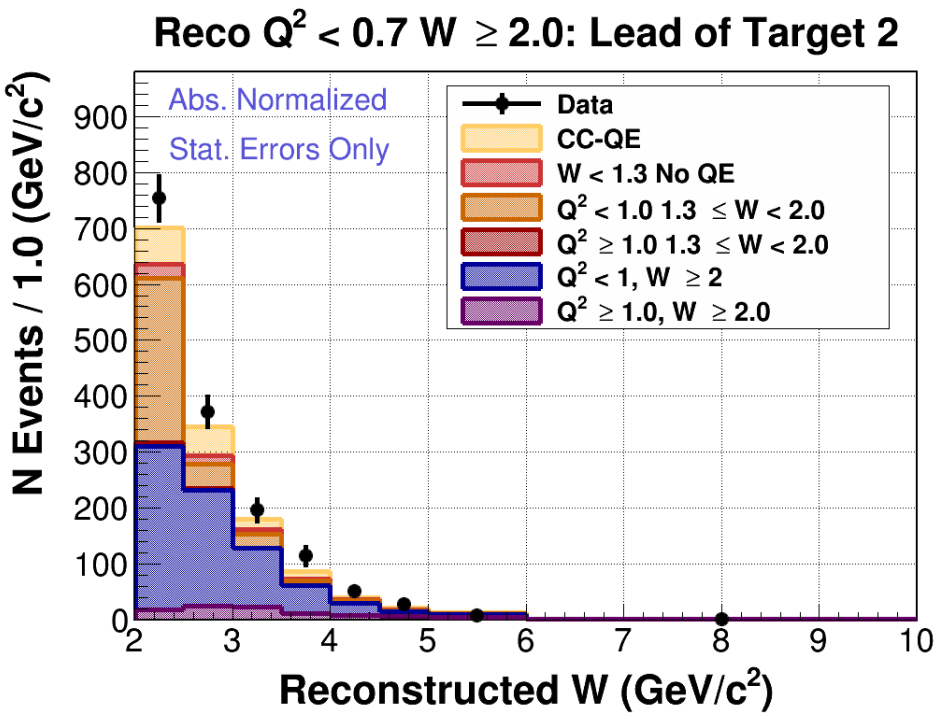

Figure A-214. Data / MC low Q^2 sideband before fitting: target 02 Pb (W)

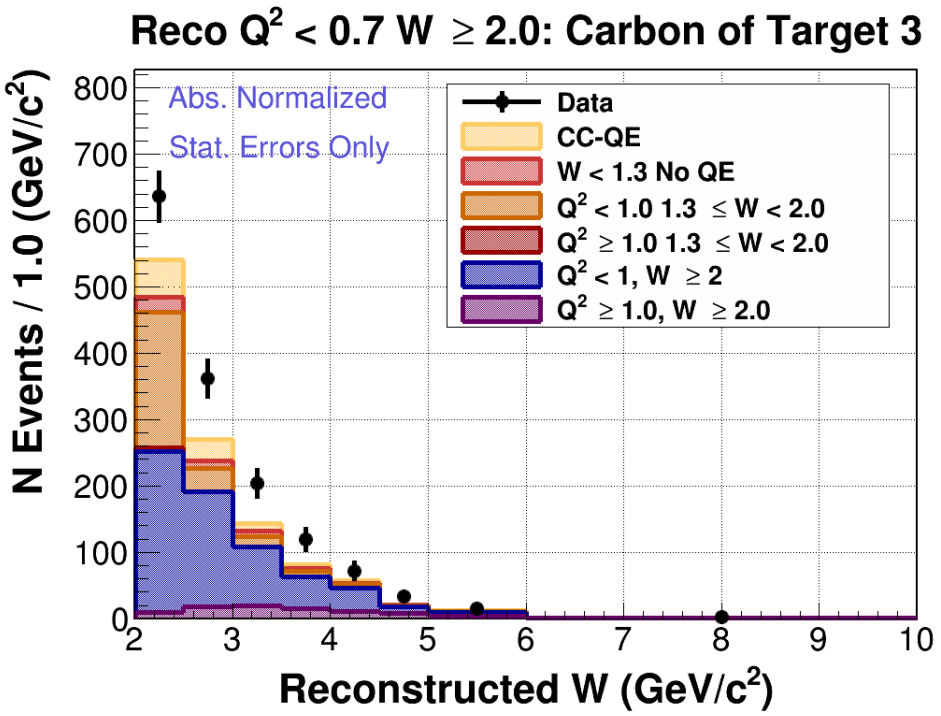

Figure A-215. Data / MC low Q^2 sideband before fitting: target 03 C (W)

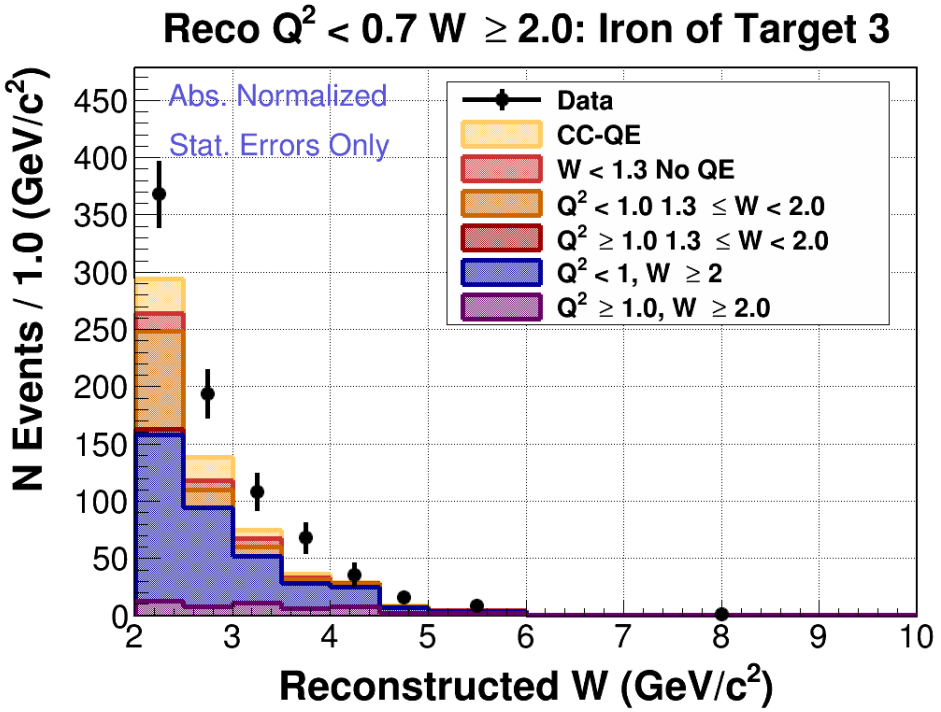

Figure A-216. Data / MC low Q^2 sideband before fitting: target 03 Fe (W)

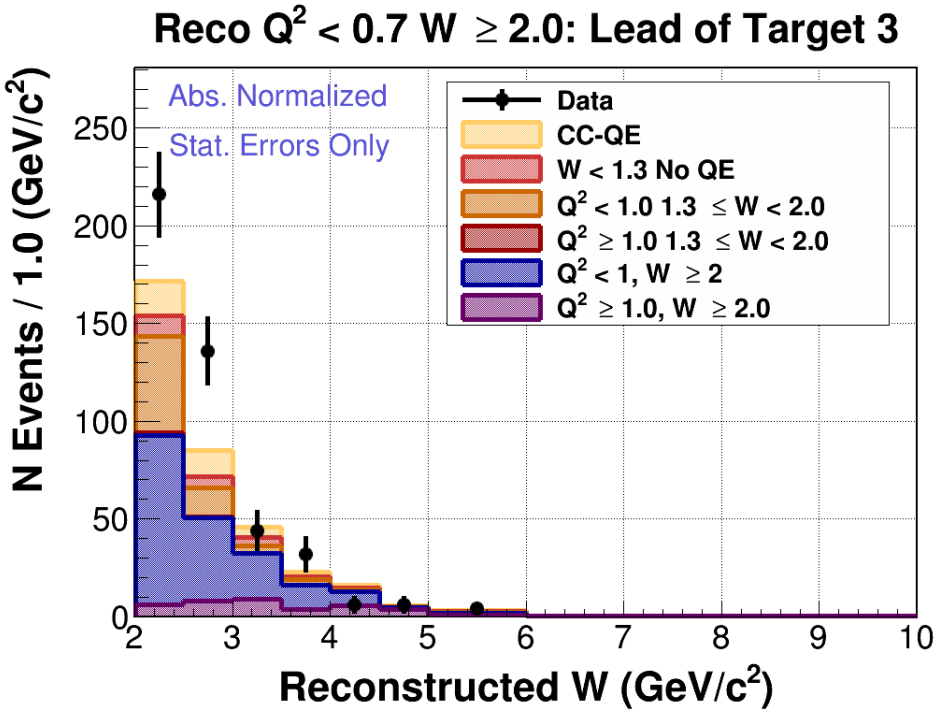

Figure A-217. Data / MC low Q^2 sideband before fitting: target 03 Pb (W)

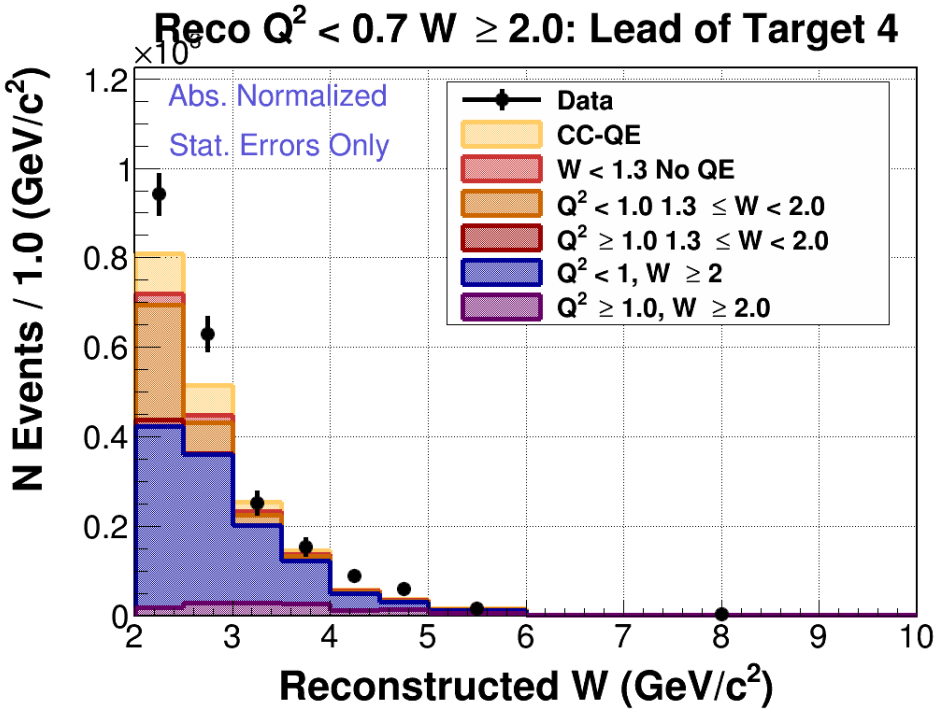

Figure A-218. Data / MC low Q^2 sideband before fitting: target 04 Pb (W)

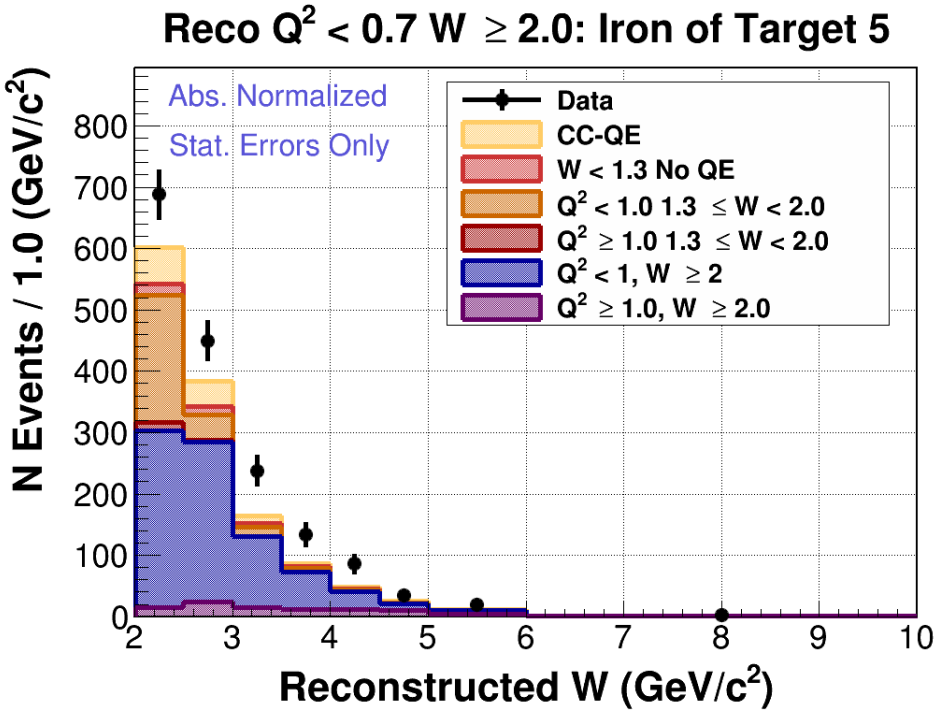

Figure A-219. Data / MC low Q^2 sideband before fitting: target 05 Fe (W)

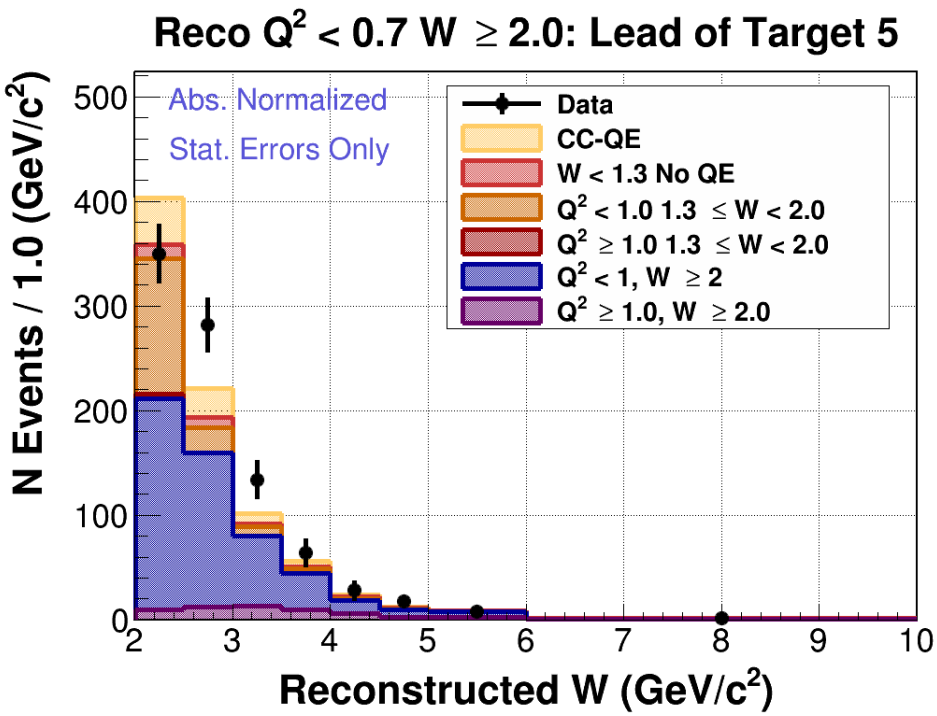

Figure A-220. Data / MC low Q^2 sideband before fitting: target 05 Pb (W)

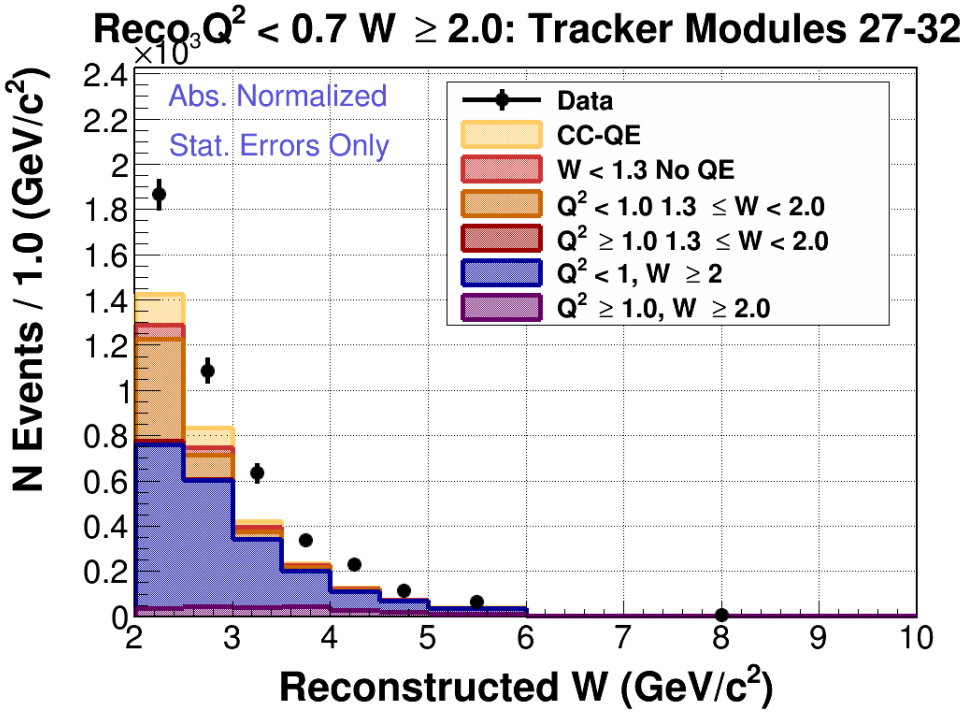

Figure A-221. Data / MC low Q^2 sideband before fitting: tracker mods. 27-32 (W)

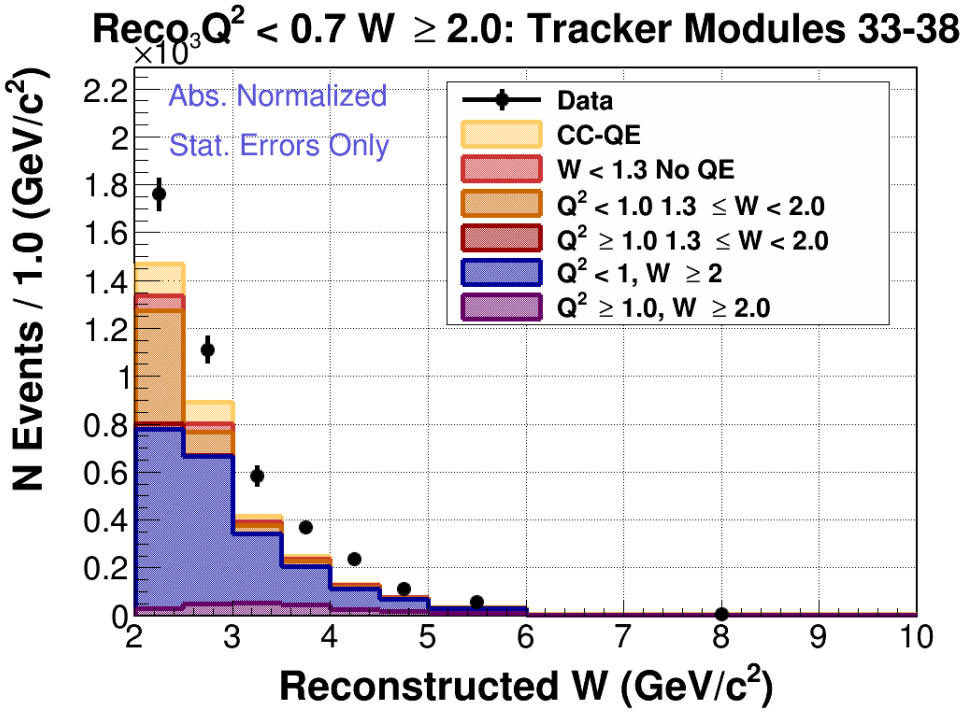

Figure A-222. Data / MC low Q^2 sideband before fitting: tracker mods. 33-38 (W)

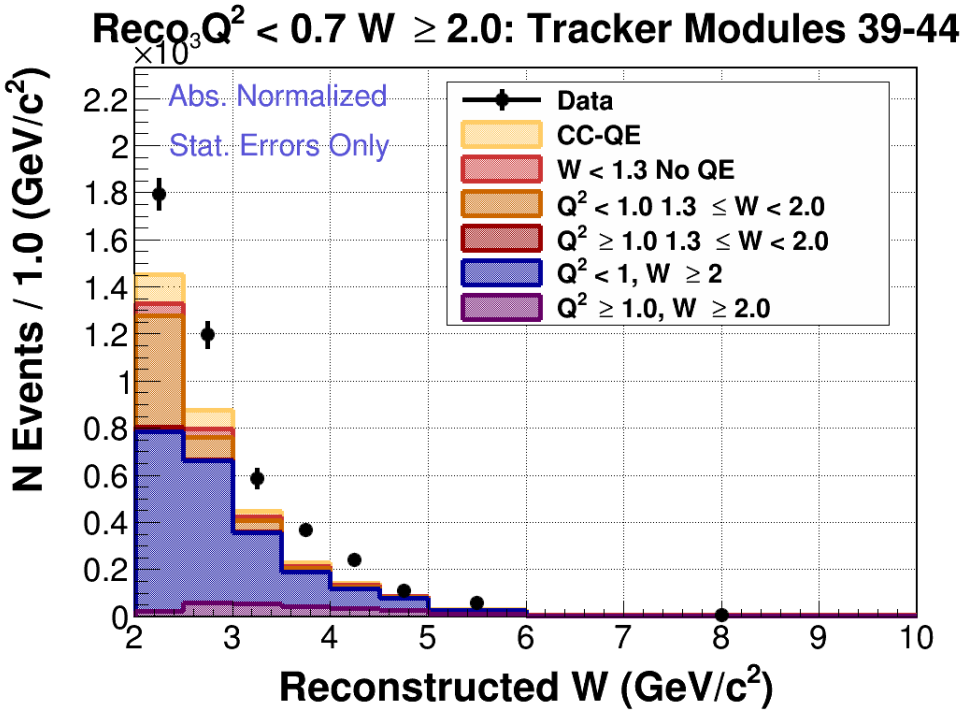

Figure A-223. Data / MC low Q^2 sideband before fitting: tracker mods. 39-44 (W)

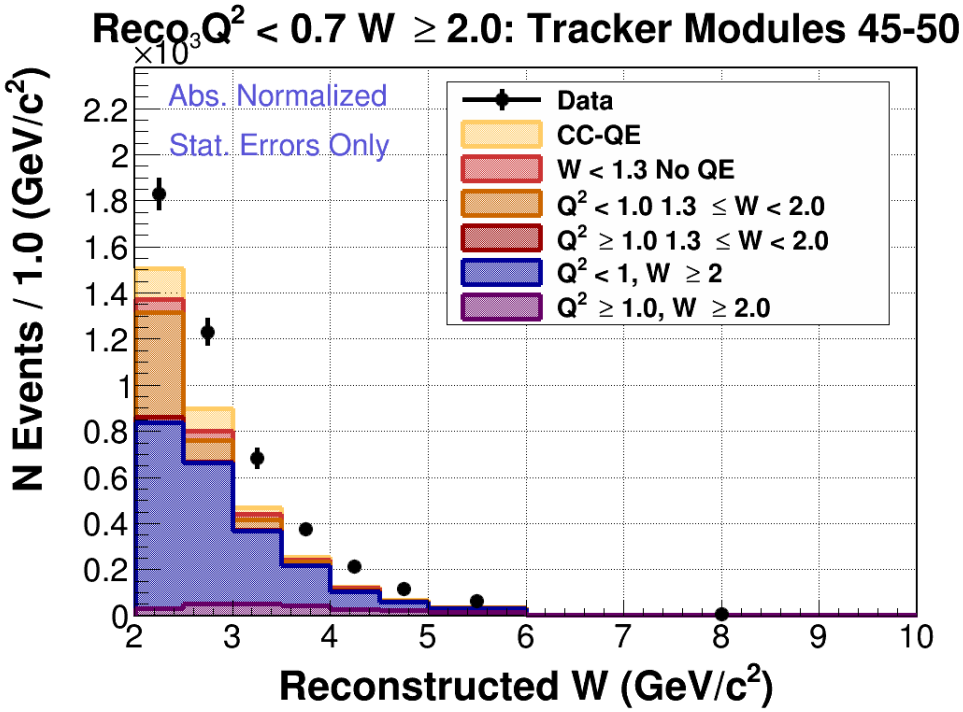

Figure A-224. Data / MC low Q^2 sideband before fitting: tracker mods. 45-50 (W)

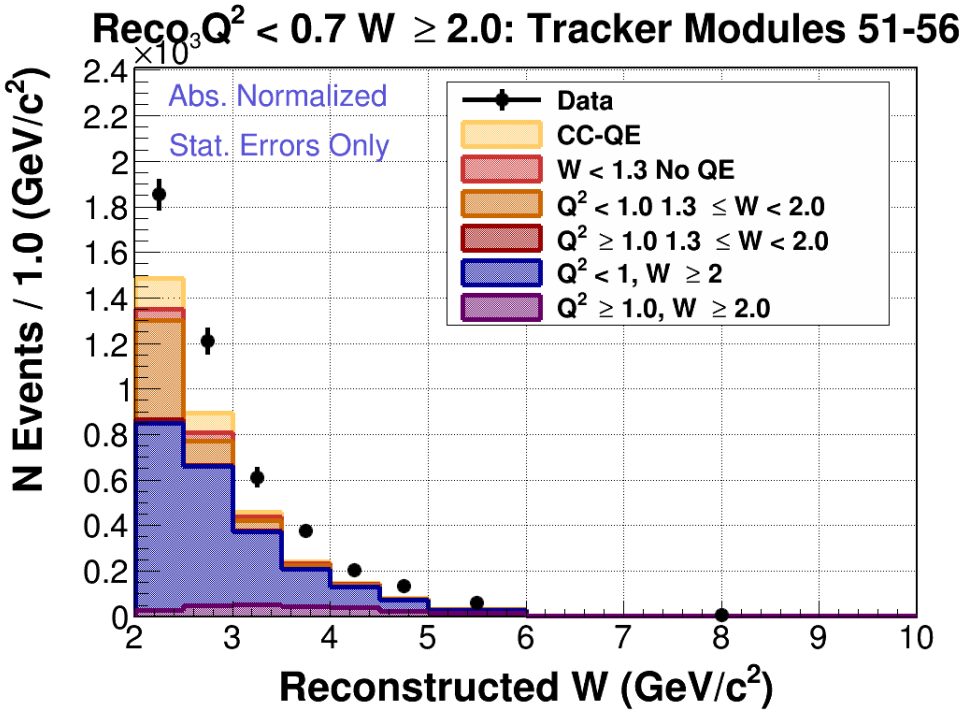

Figure A-225. Data / MC low Q^2 sideband before fitting: tracker mods. 51-56 (W)

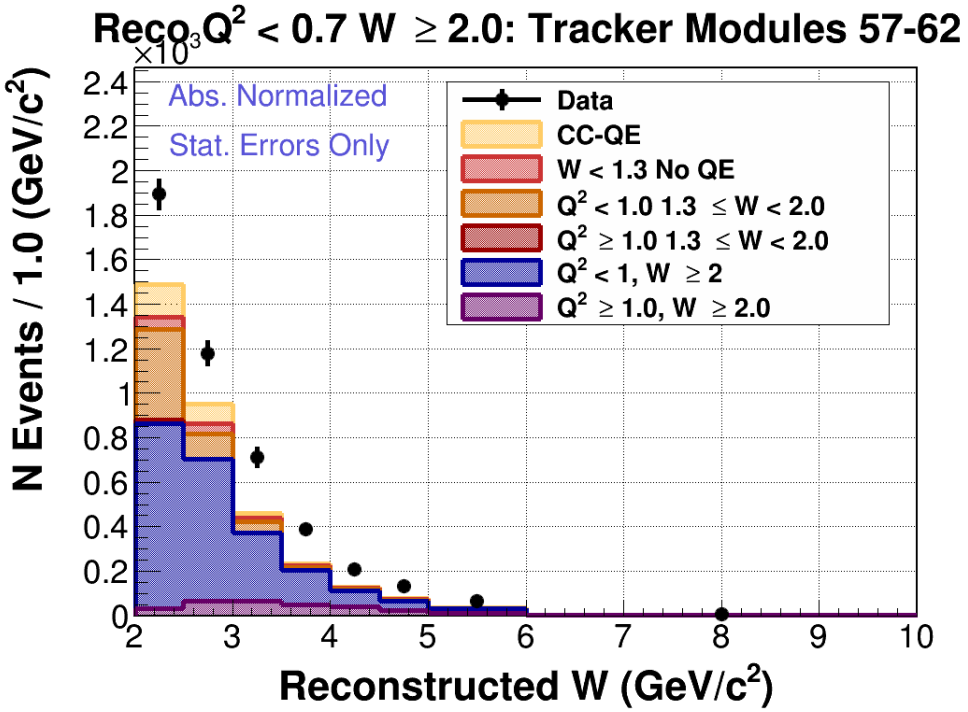

Figure A-226. Data / MC low Q^2 sideband before fitting: tracker mods. 57-62 (W)

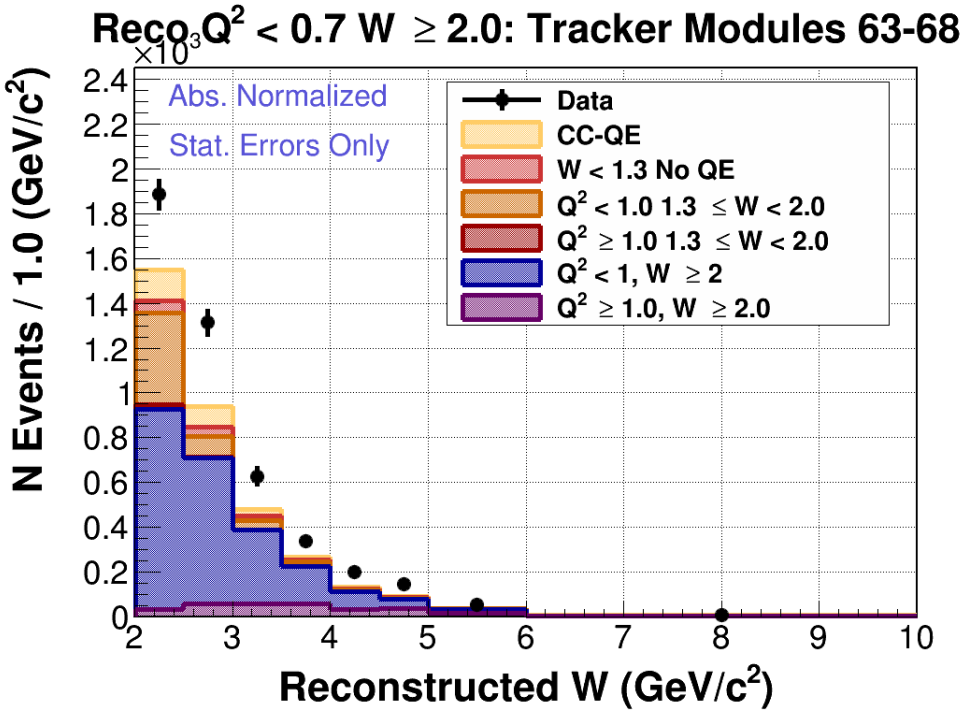

Figure A-227. Data / MC low Q^2 sideband before fitting: tracker mods. 63-68 (W)

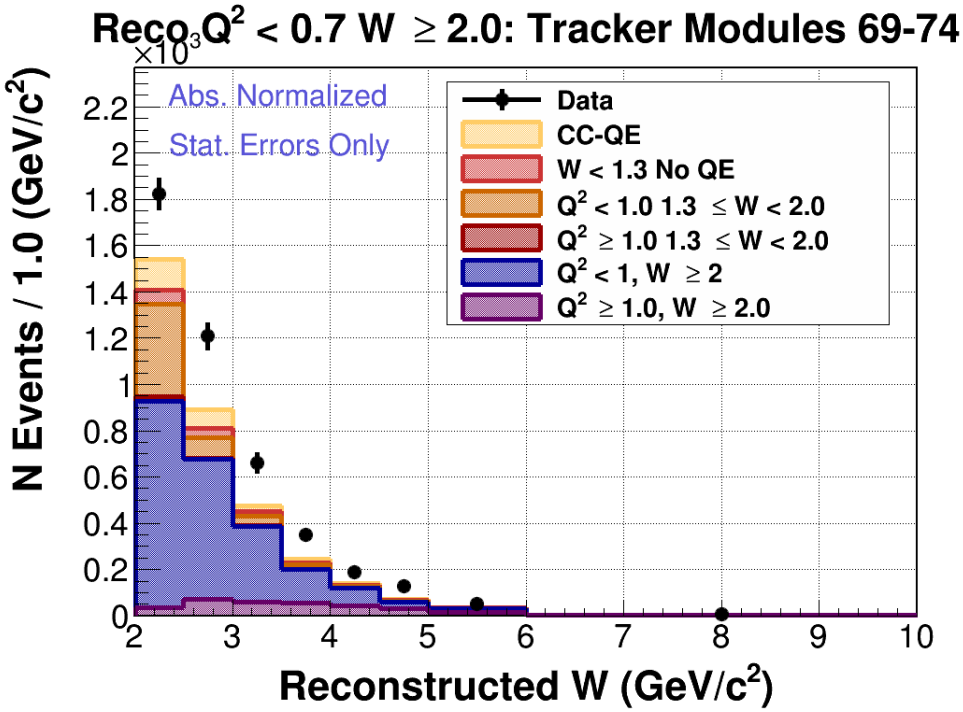

Figure A-228. Data / MC low Q^2 sideband before fitting: tracker mods. 69-74 (W)

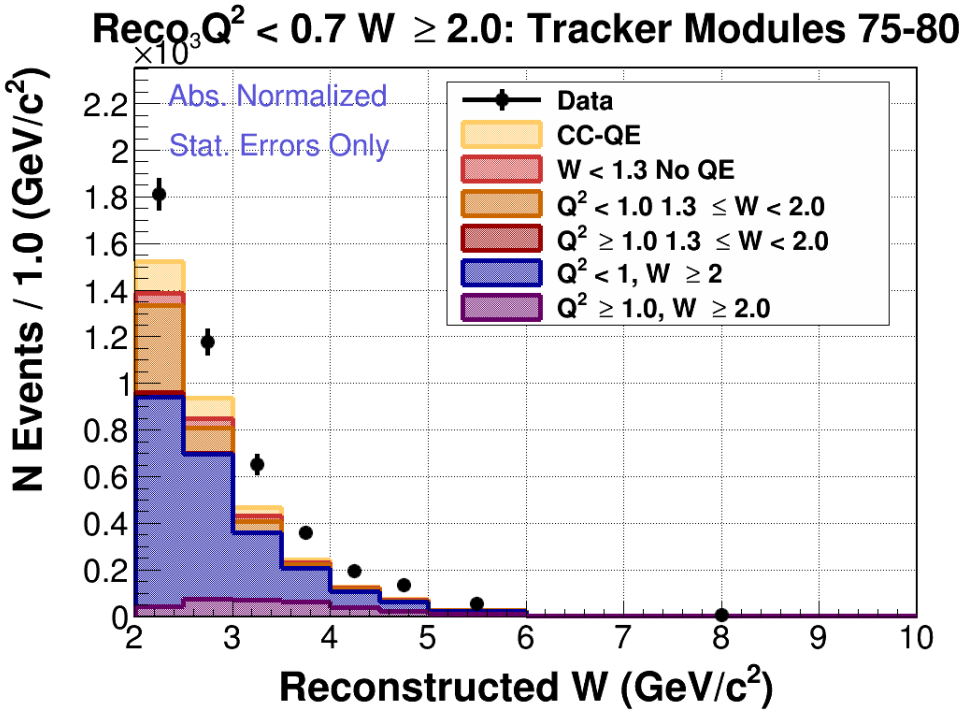

Figure A-229. Data / MC low Q^2 sideband before fitting: tracker mods. 75-80 (W)

The following plots show the population of the low Q^2 sideband ($Q^2 < 0.8$ (GeV/c)^2 $W \geq 2.0$ GeV/c^2) *before* tuning to data as a function of Bjorken-x (x_{bj}):

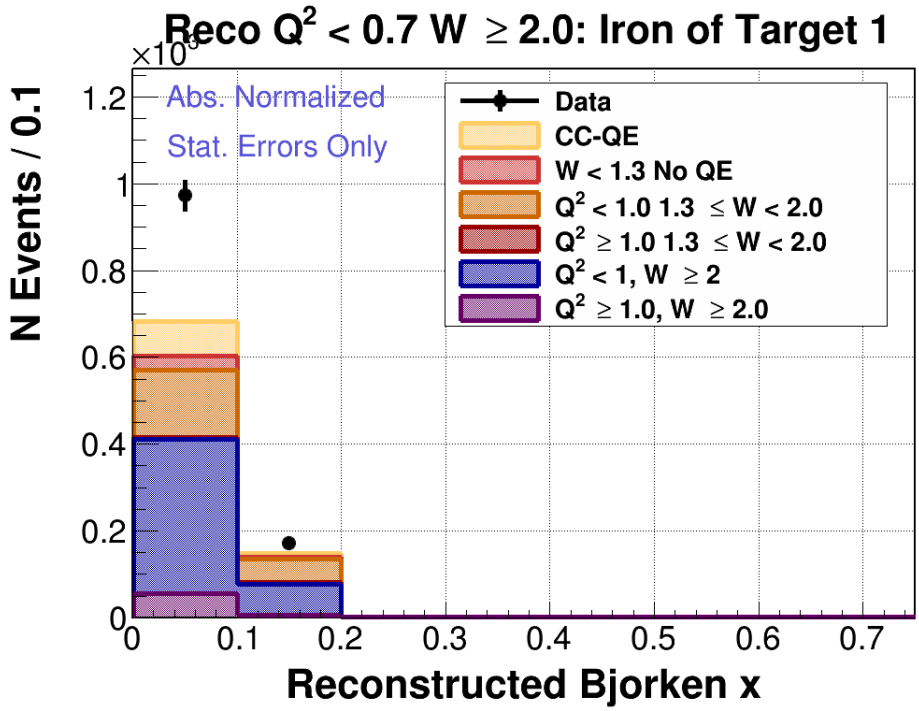

Figure A-230. Data / MC low Q^2 sideband before fitting: target 01 Fe (x_{bj})

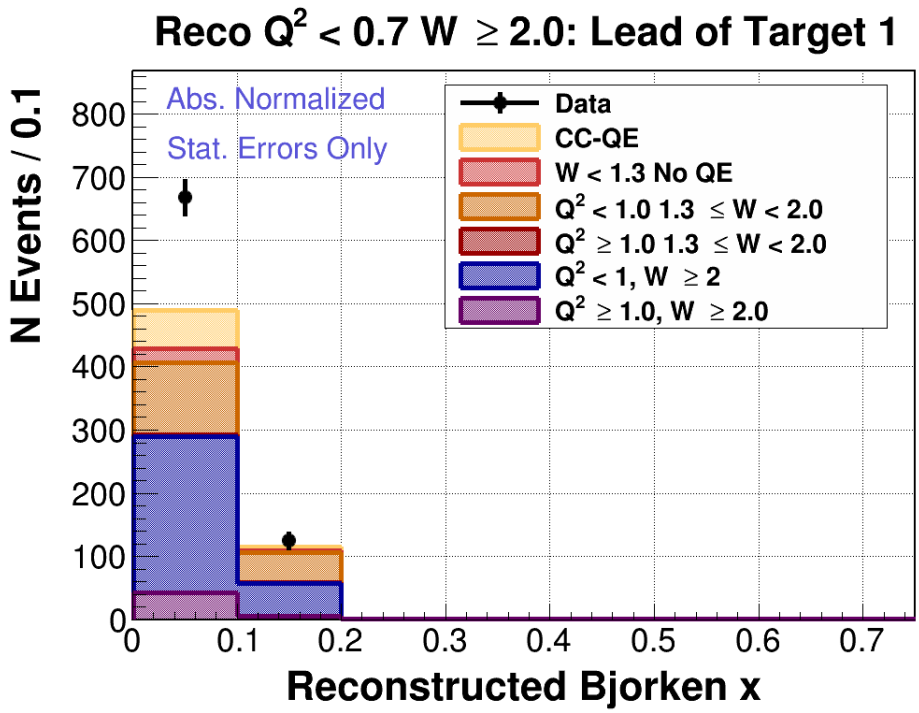

Figure A-231. Data / MC low Q^2 sideband before fitting: target 01 Pb (x_{bj})

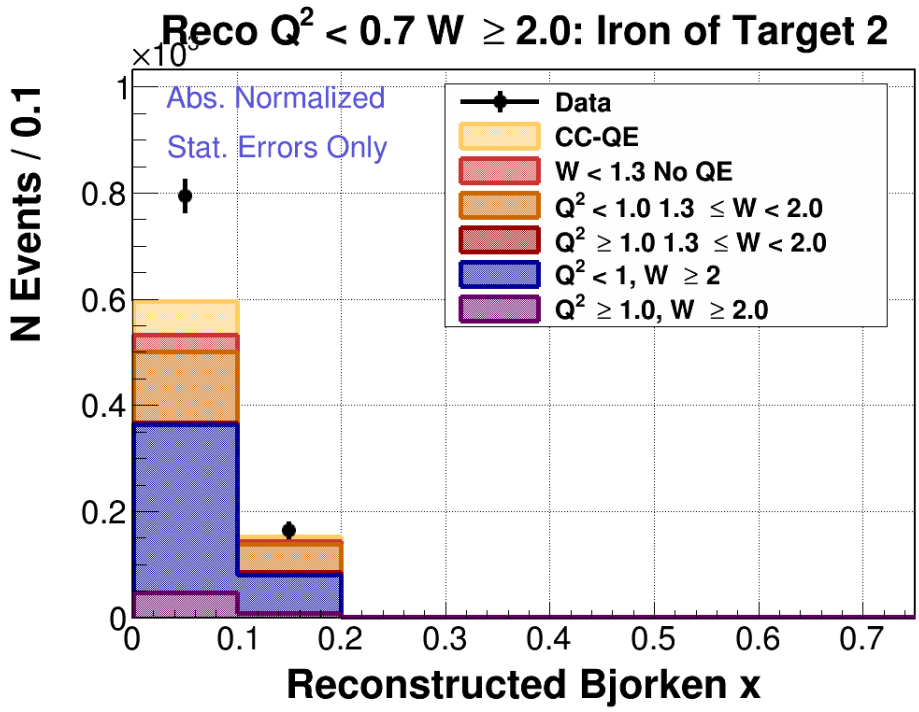

Figure A-232. Data / MC low Q^2 sideband before fitting: target 02 Fe (x_{bj})

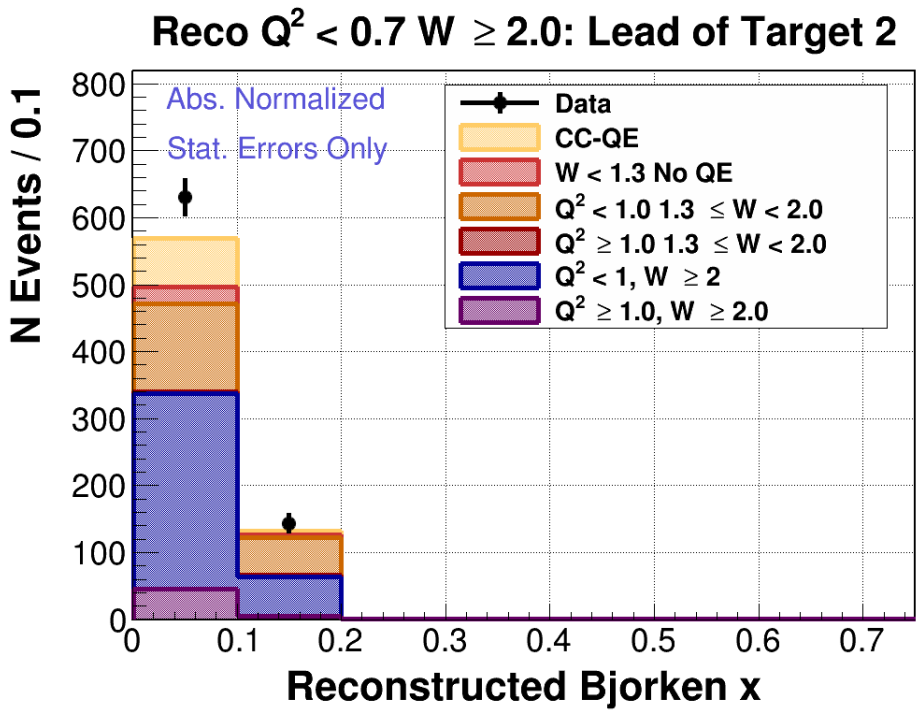

Figure A-233. Data / MC low Q^2 sideband before fitting: target 02 Pb (x_{bj})

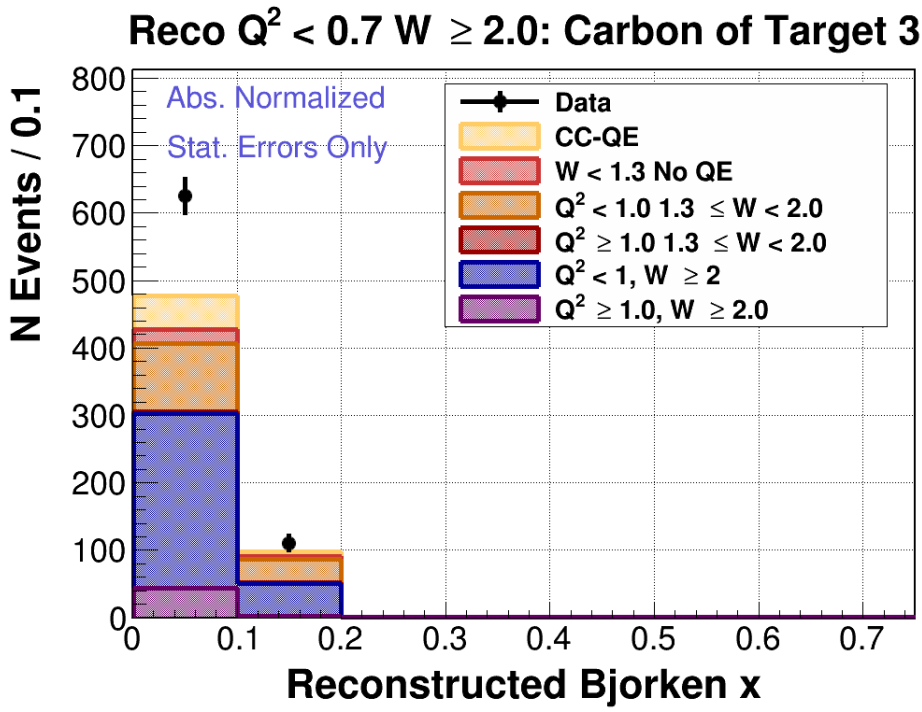

Figure A-234. Data / MC low Q^2 sideband before fitting: target 03 C (x_{bj})

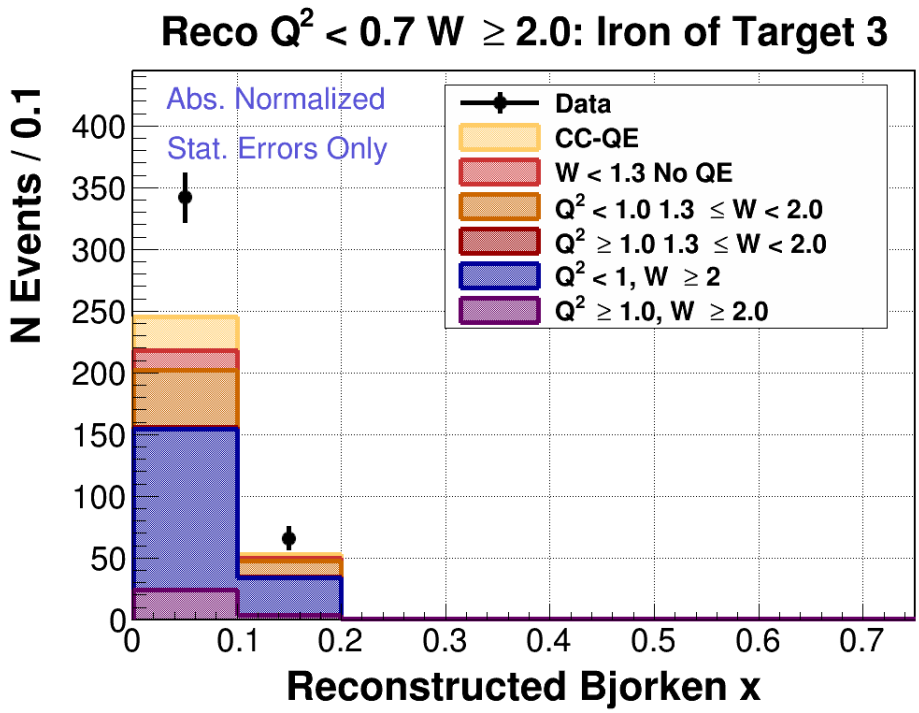

Figure A-235. Data / MC low Q^2 sideband before fitting: target 03 Fe (x_{bj})

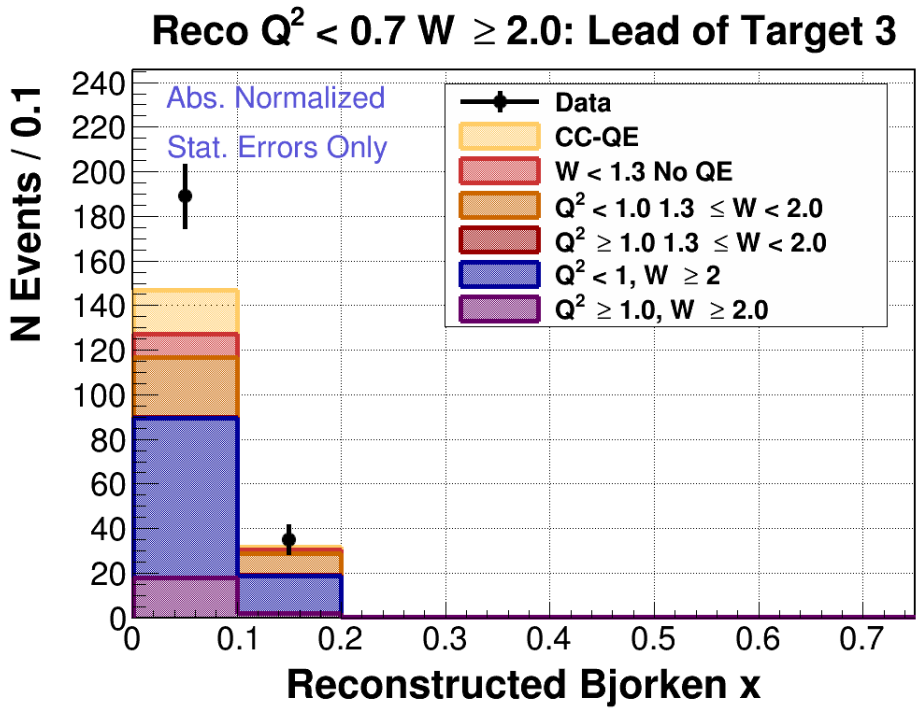

Figure A-236. Data / MC low Q^2 sideband before fitting: target 03 Pb (x_{bj})

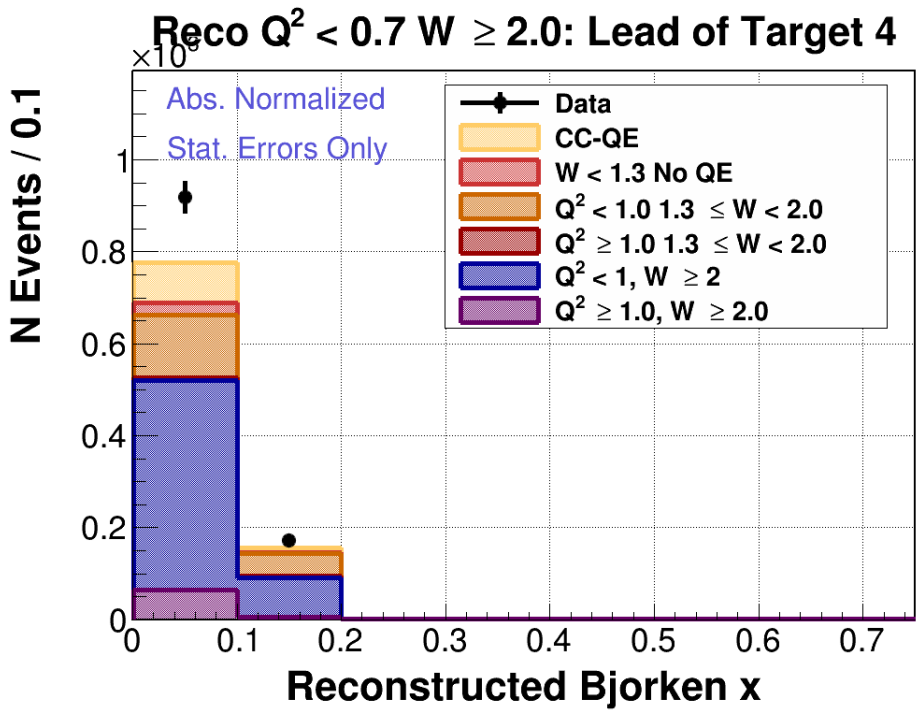

Figure A-237. Data / MC low Q^2 sideband before fitting: target 04 Pb (x_{bj})

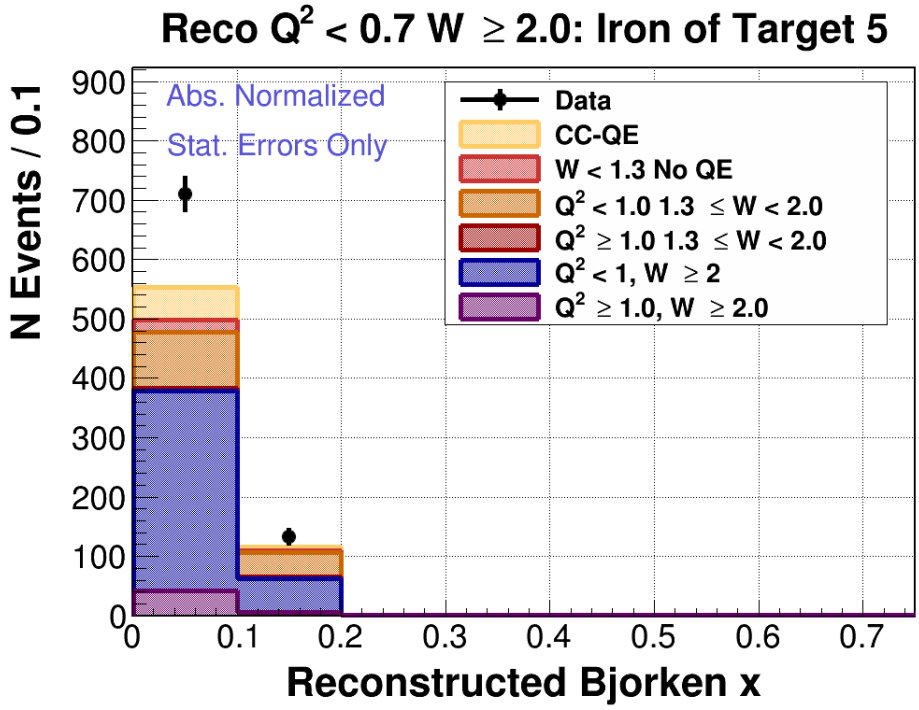

Figure A-238. Data / MC low Q^2 sideband before fitting: target 05 Fe (x_{bj})

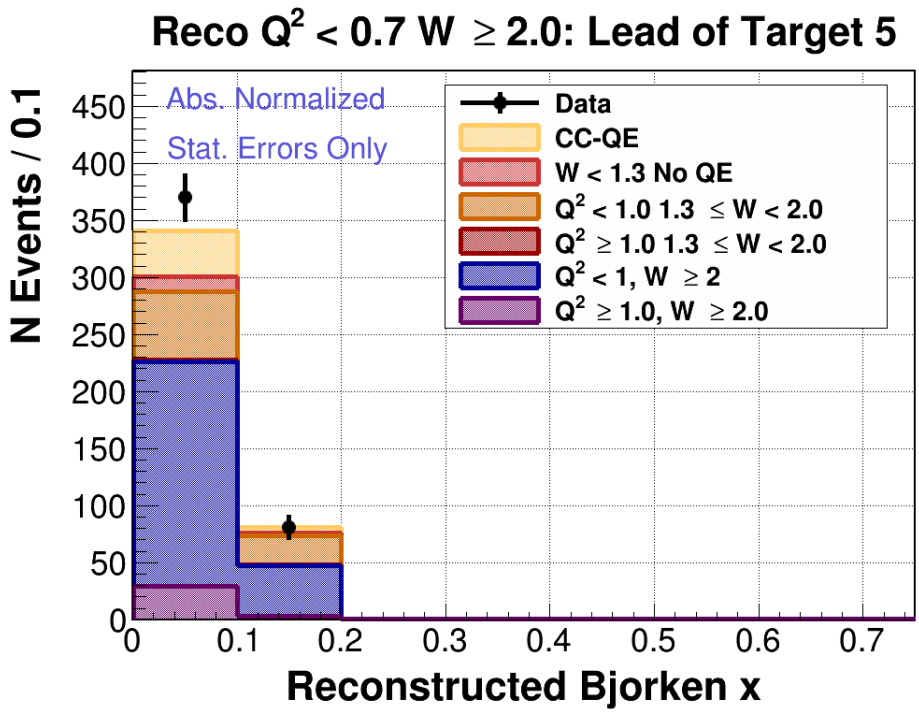

Figure A-239. Data / MC low Q^2 sideband before fitting: target 05 Pb (x_{bj})

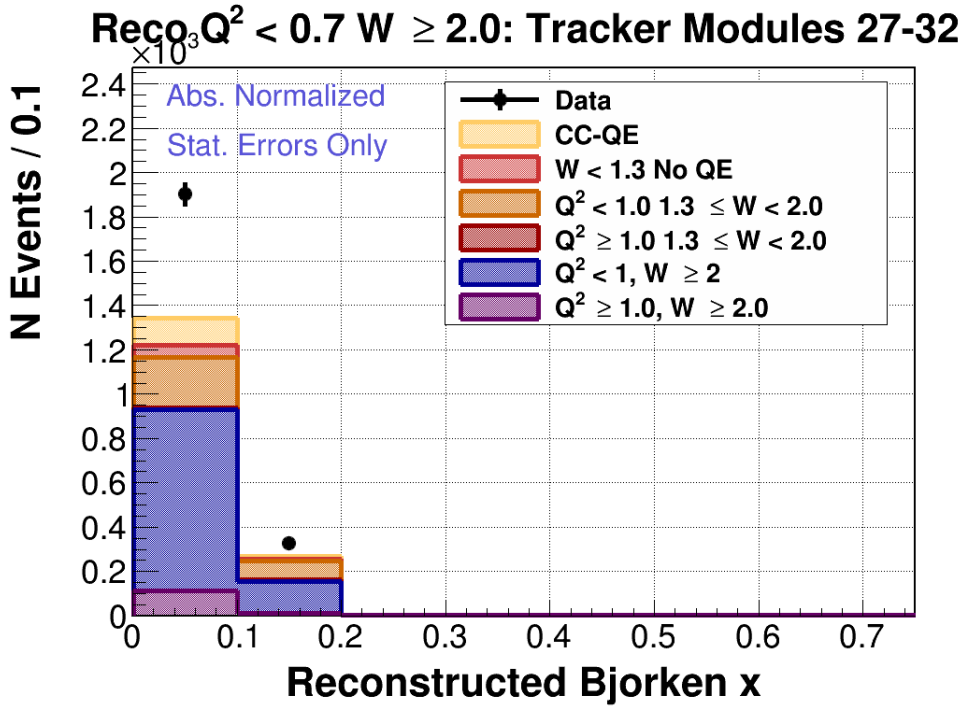

Figure A-240. Data / MC low Q^2 sideband before fitting: tracker mods. 27-32 (x_{bj})

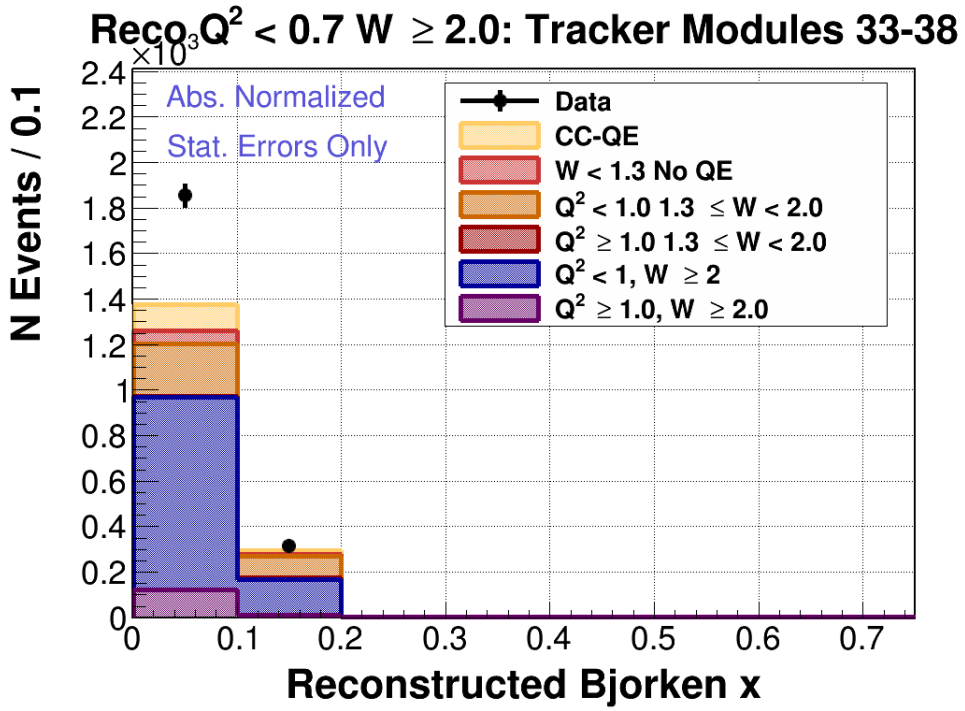

Figure A-241. Data / MC low Q^2 sideband before fitting: tracker mods. 33-38 (x_{bj})

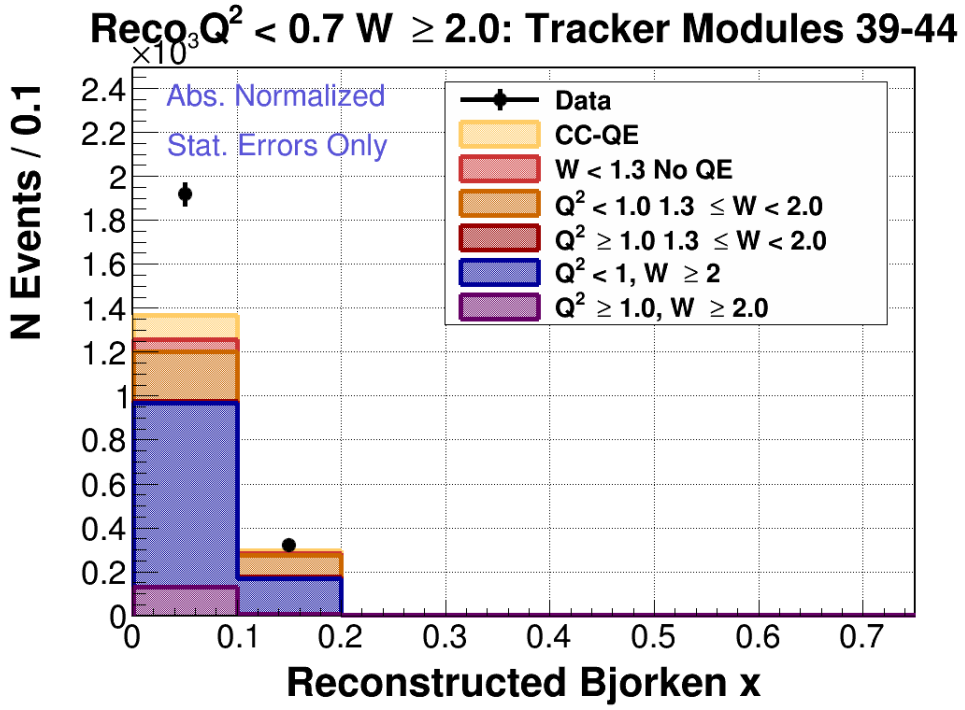

Figure A-242. Data / MC low Q^2 sideband before fitting: tracker mods. 39-44 (x_{bj})

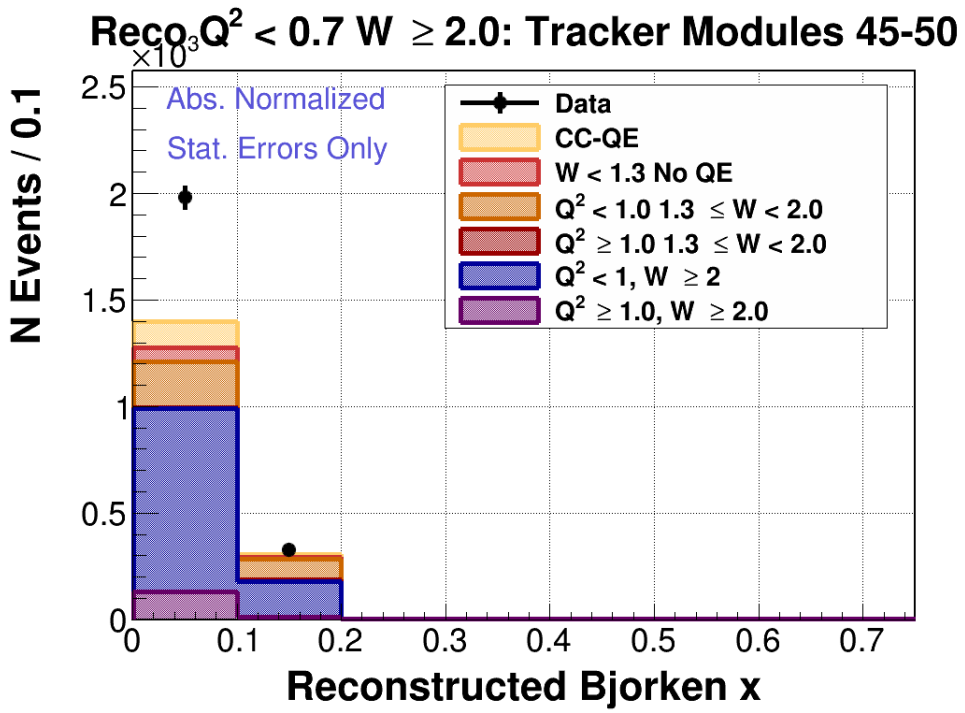

Figure A-243. Data / MC low Q^2 sideband before fitting: tracker mods. 45-50 (x_{bj})

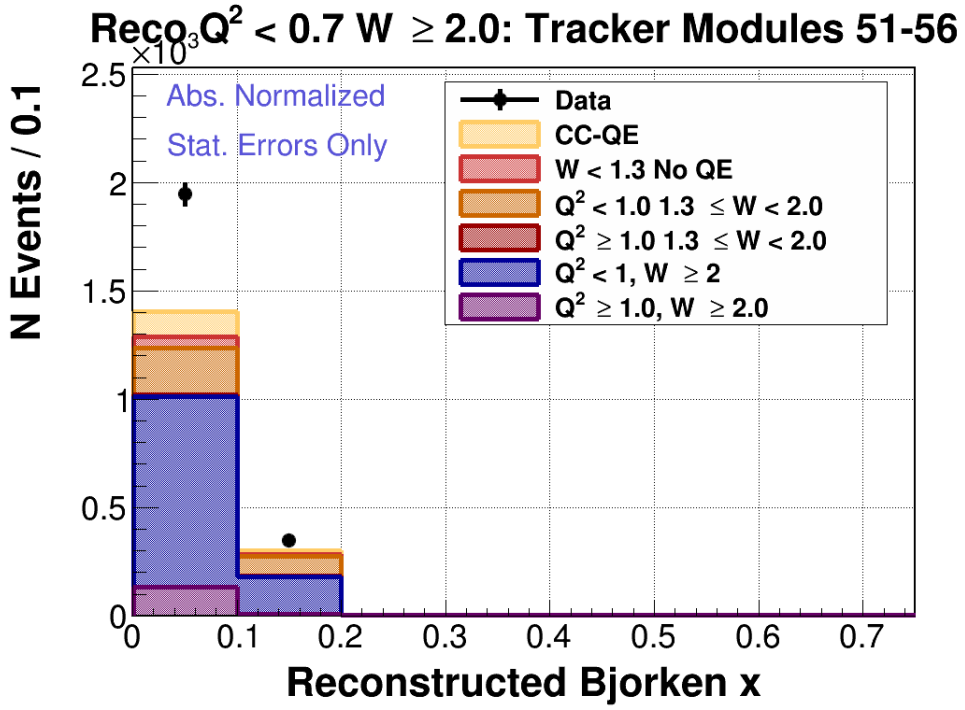

Figure A-244. Data / MC low Q^2 sideband before fitting: tracker mods. 51-56 (x_{bj})

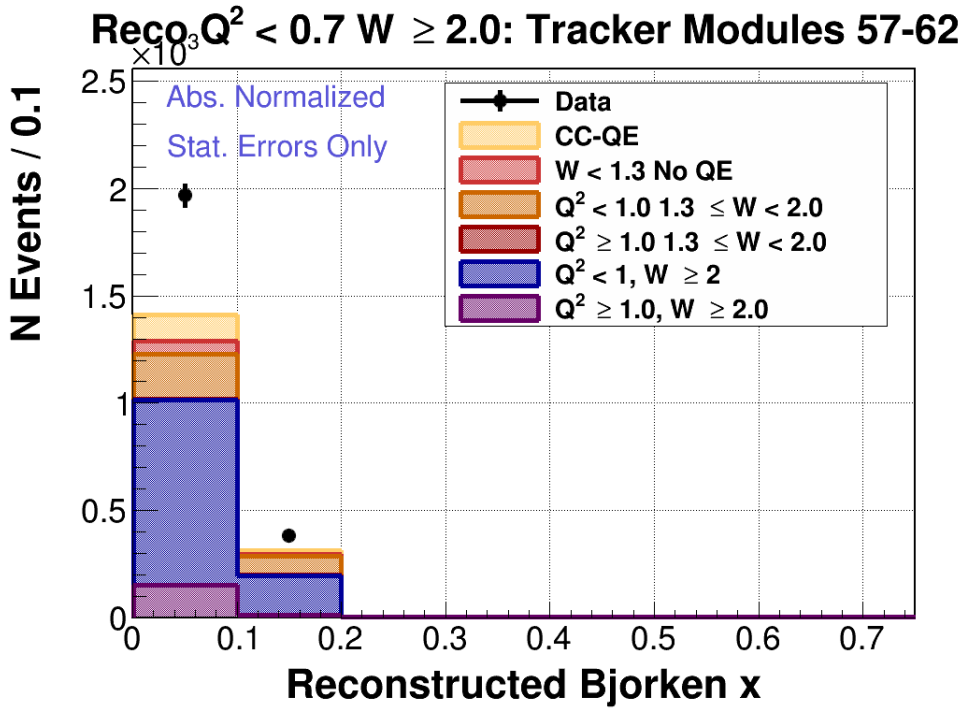

Figure A-245. Data / MC low Q^2 sideband before fitting: tracker mods. 57-62 (x_{bj})

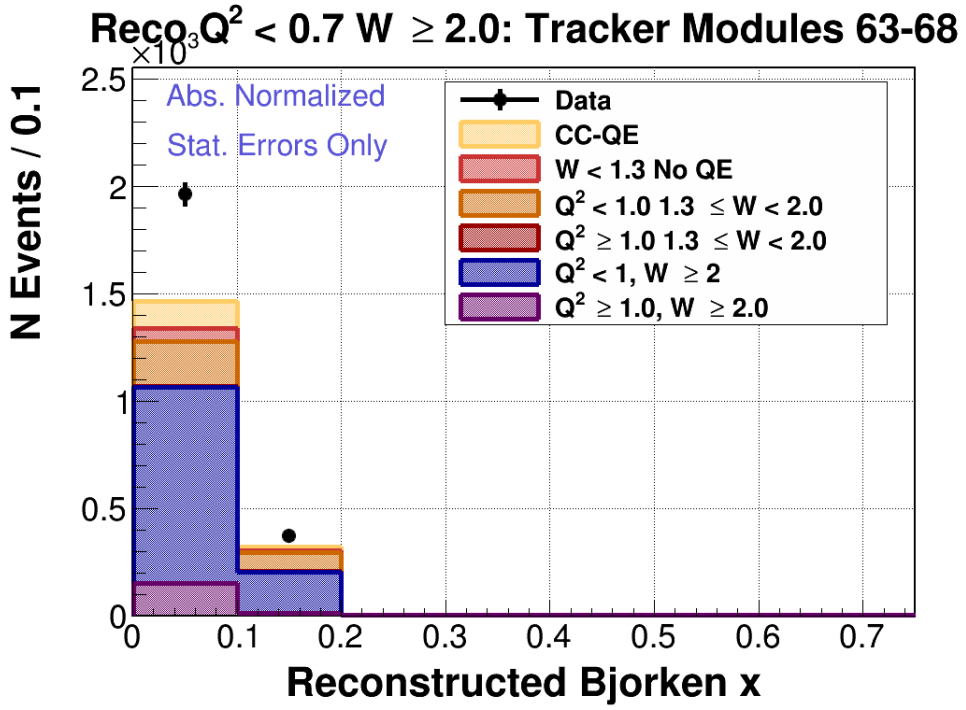

Figure A-246. Data / MC low Q^2 sideband before fitting: tracker mods. 63-68 (x_{bj})

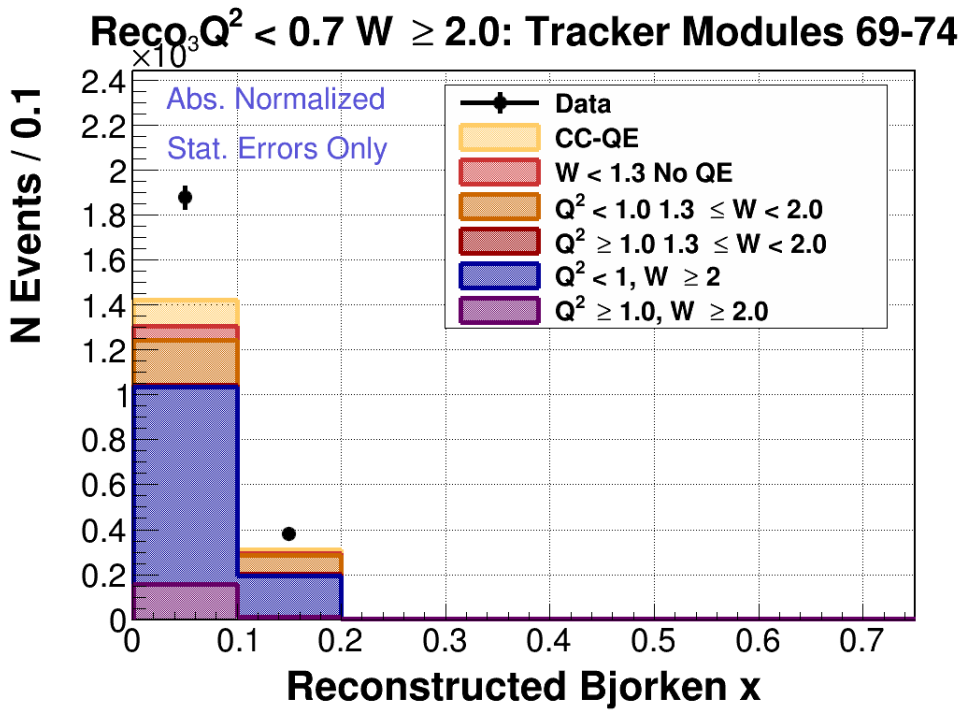

Figure A-247. Data / MC low Q^2 sideband before fitting: tracker mods. 69-74 ($_{bj}x$)

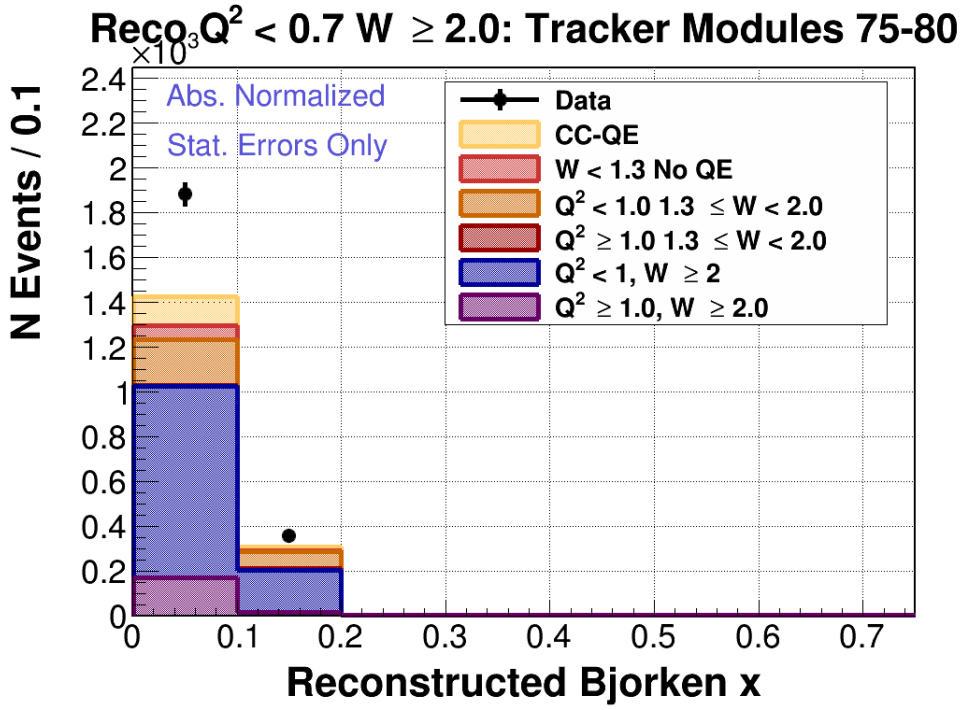

Figure A-248. Data / MC low Q^2 sideband before fitting: tracker mods. 75-80 (x_{bj})

The following plots show the population of the low Q^2 sideband ($Q^2 < 0.8$ (GeV/c)^2 $W \geq 2.0$ GeV/c^2) *before* tuning to data as a function of muon energy (E_μ):

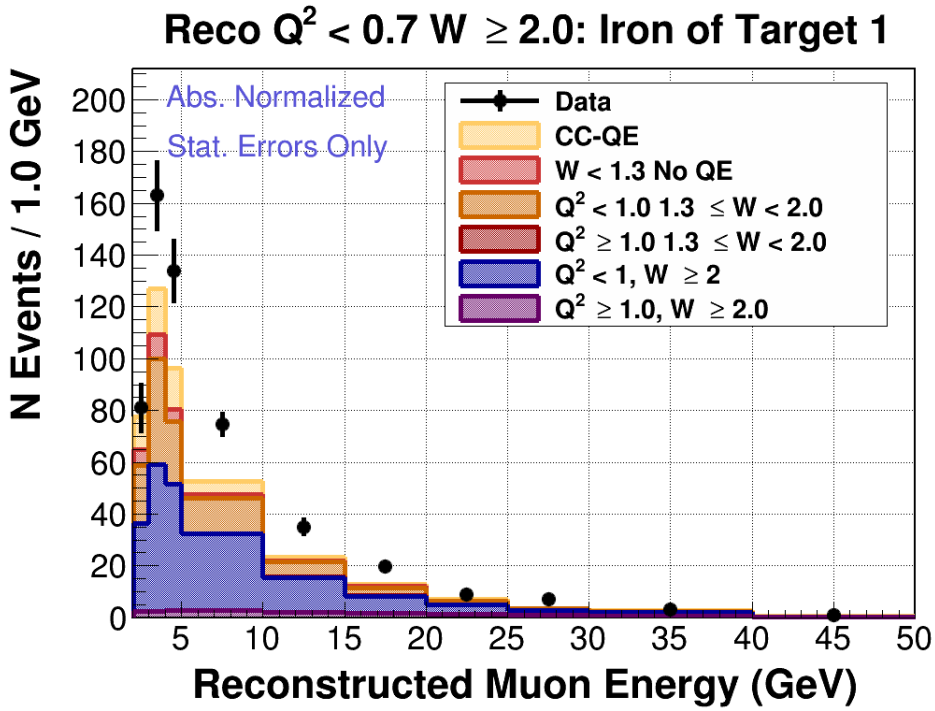

Figure A-249. Data / MC low Q^2 sideband before fitting: target 01 Fe (E_μ)

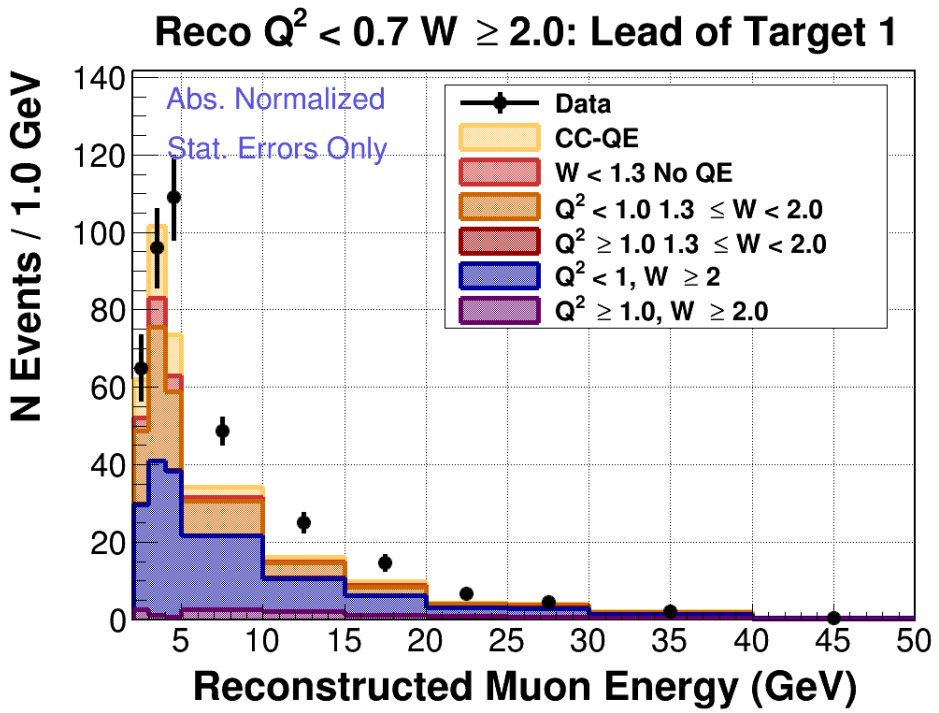

Figure A-250. Data / MC low Q^2 sideband before fitting: target 01 Pb (E_μ)

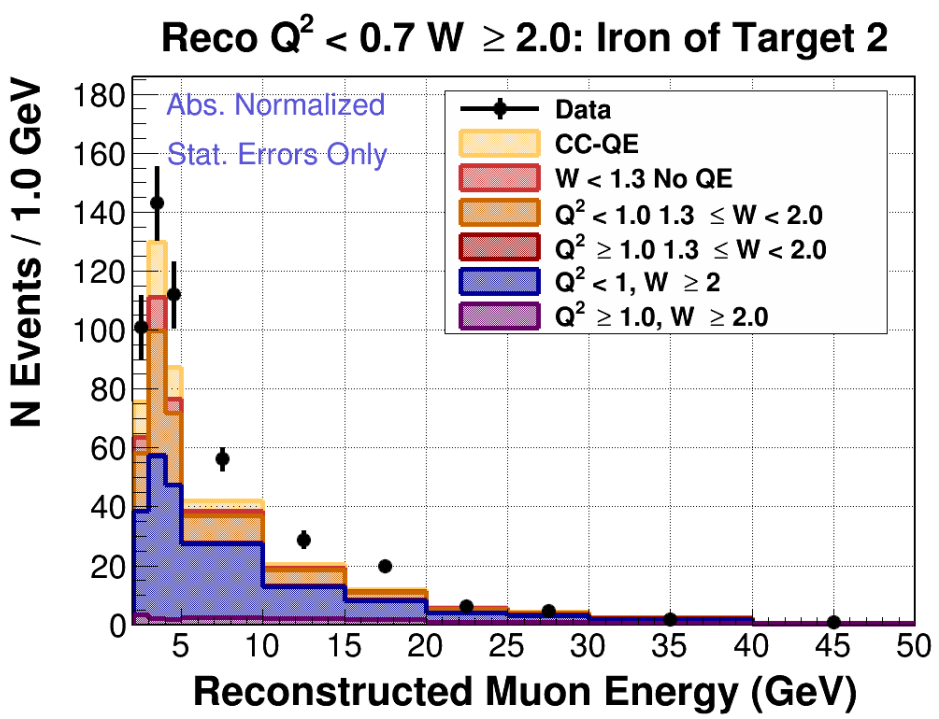

Figure A-251. Data / MC low Q^2 sideband before fitting: target 02 Fe (E_μ)

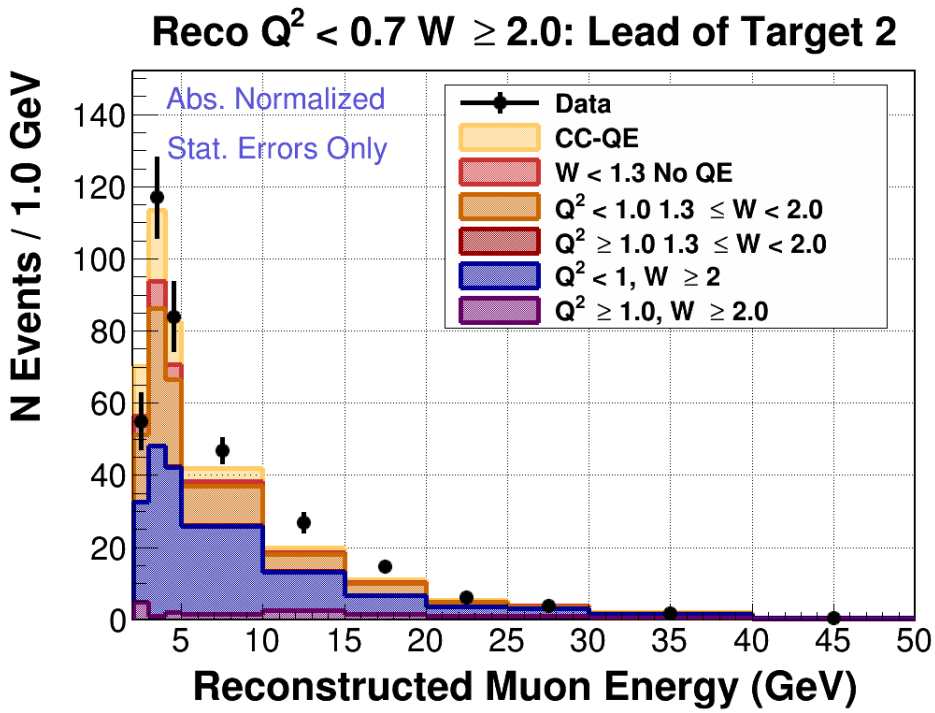

Figure A-252. Data / MC low Q^2 sideband before fitting: target 02 Pb (E_μ)

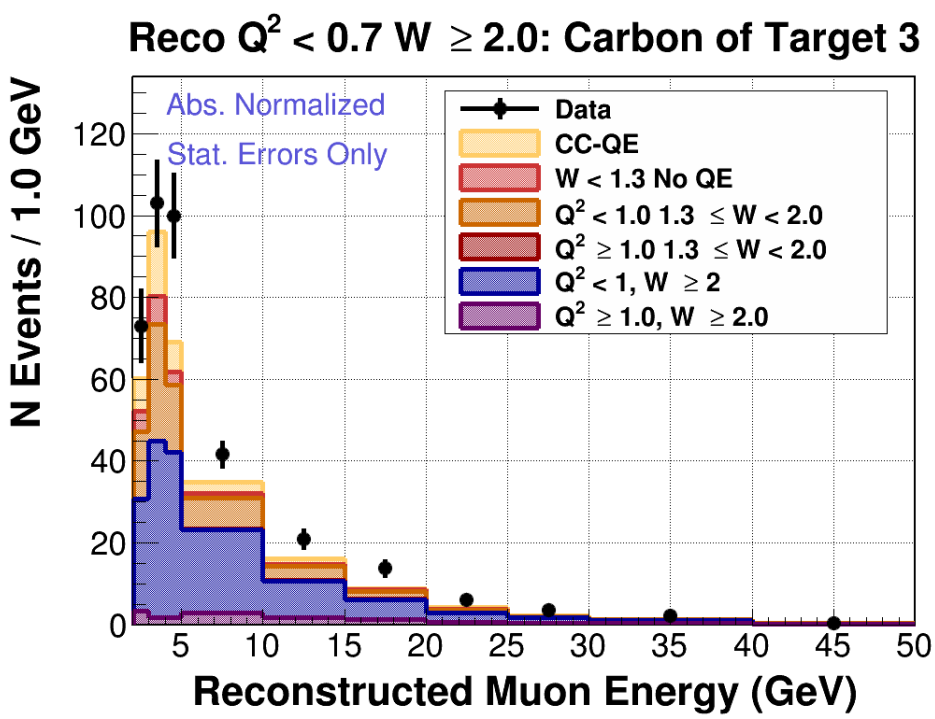

Figure A-253. Data / MC low Q^2 sideband before fitting: target 03 C (E_μ)

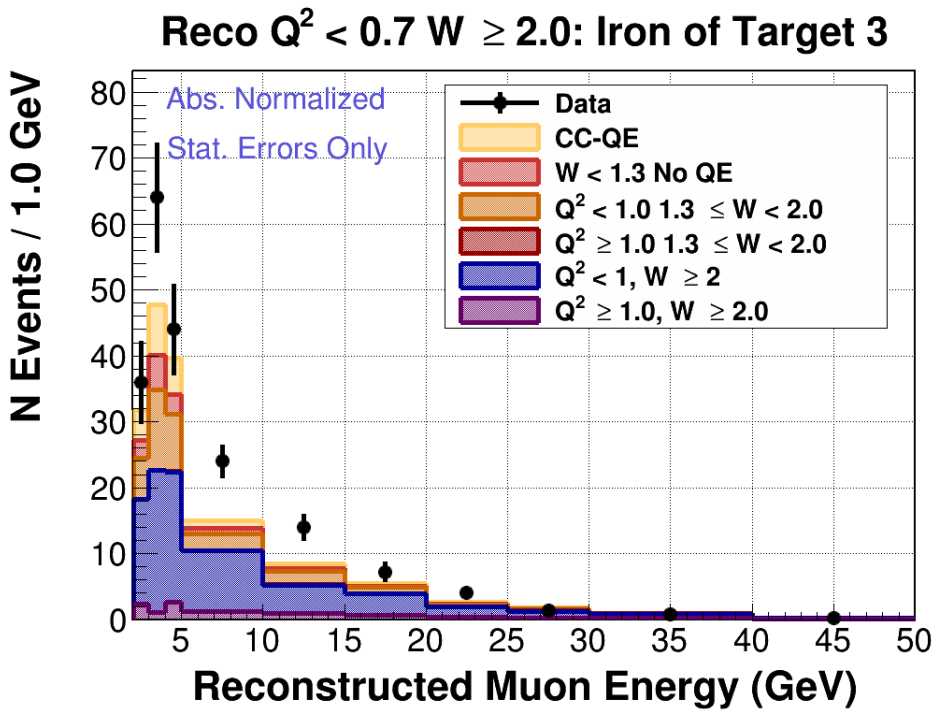

Figure A-254. Data / MC low Q^2 sideband before fitting: target 03 Fe (E_μ)

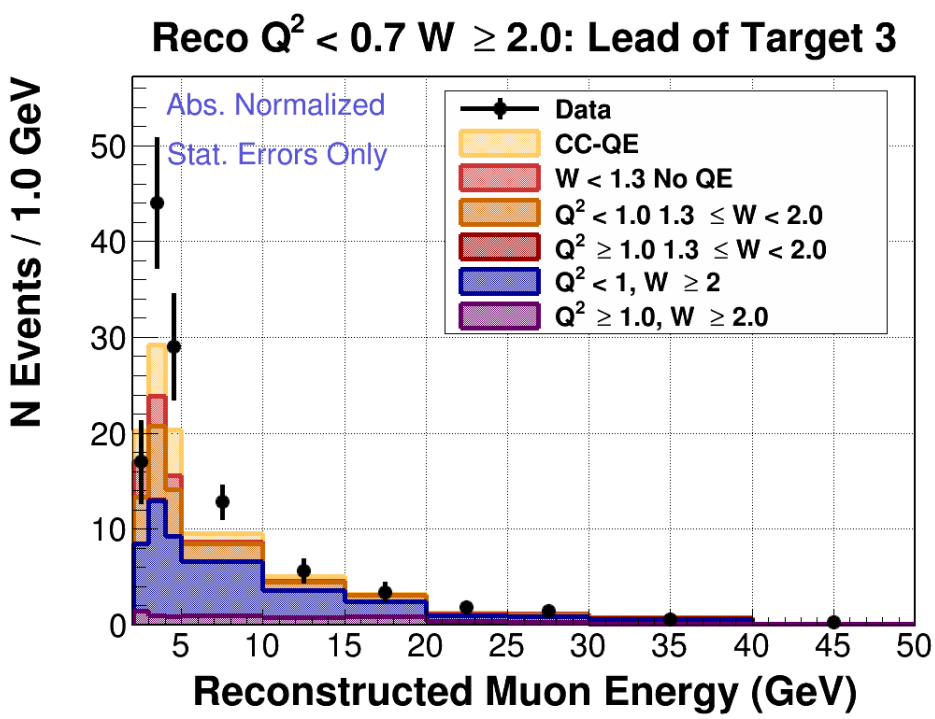

Figure A-255. Data / MC low Q^2 sideband before fitting: target 03 Pb (E_μ)

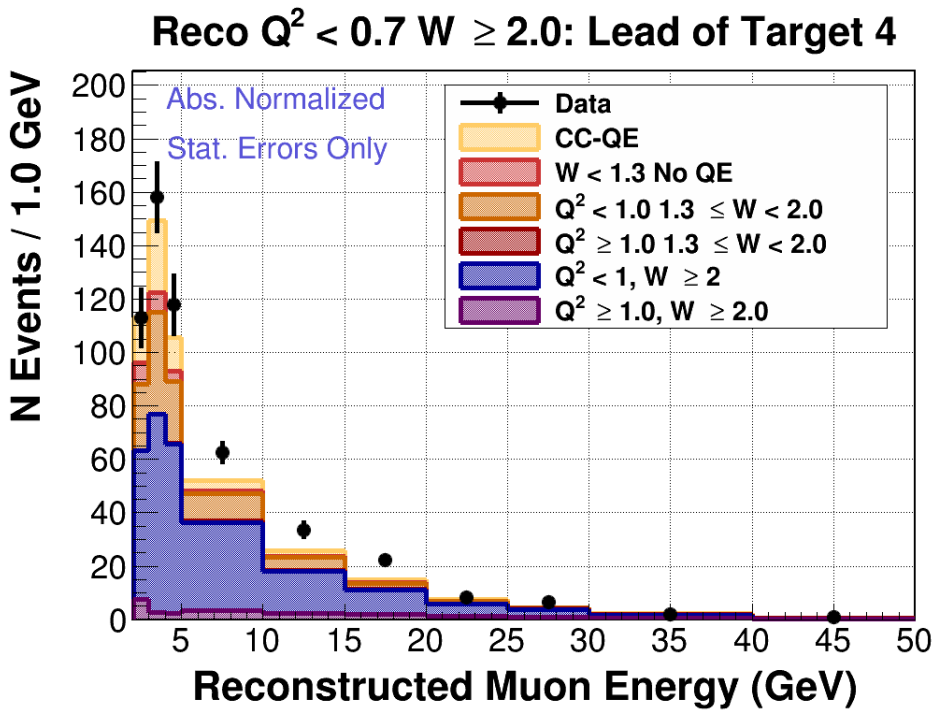

Figure A-256. Data / MC low Q^2 sideband before fitting: target 04 Pb (E_μ)

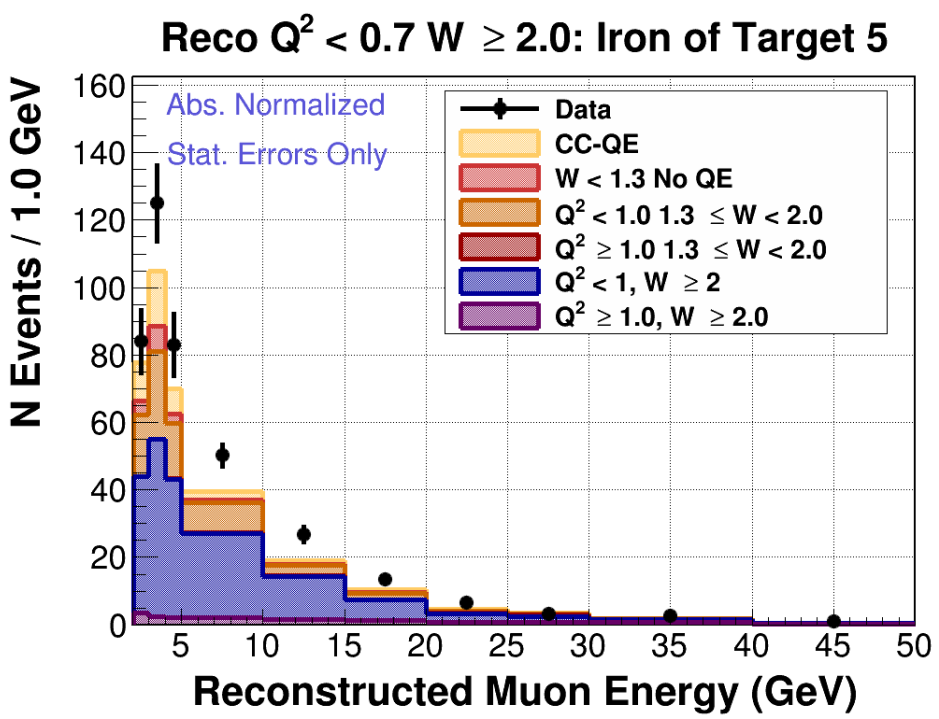

Figure A-257. Data / MC low Q^2 sideband before fitting: target 05 Fe (E_μ)

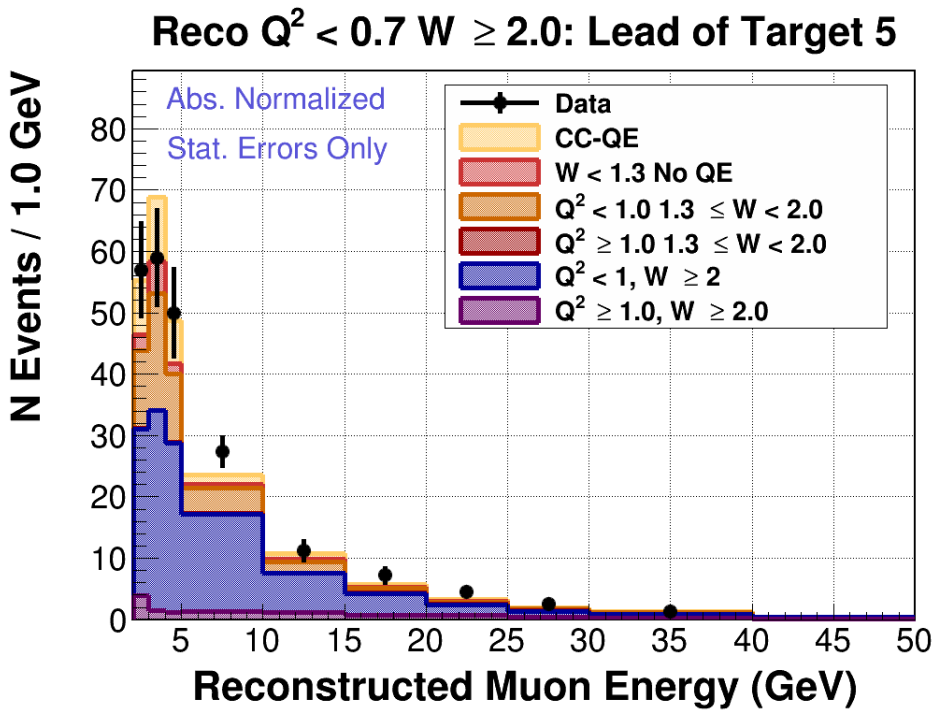

Figure A-258. Data / MC low Q^2 sideband before fitting: target 05 Pb (E_μ)

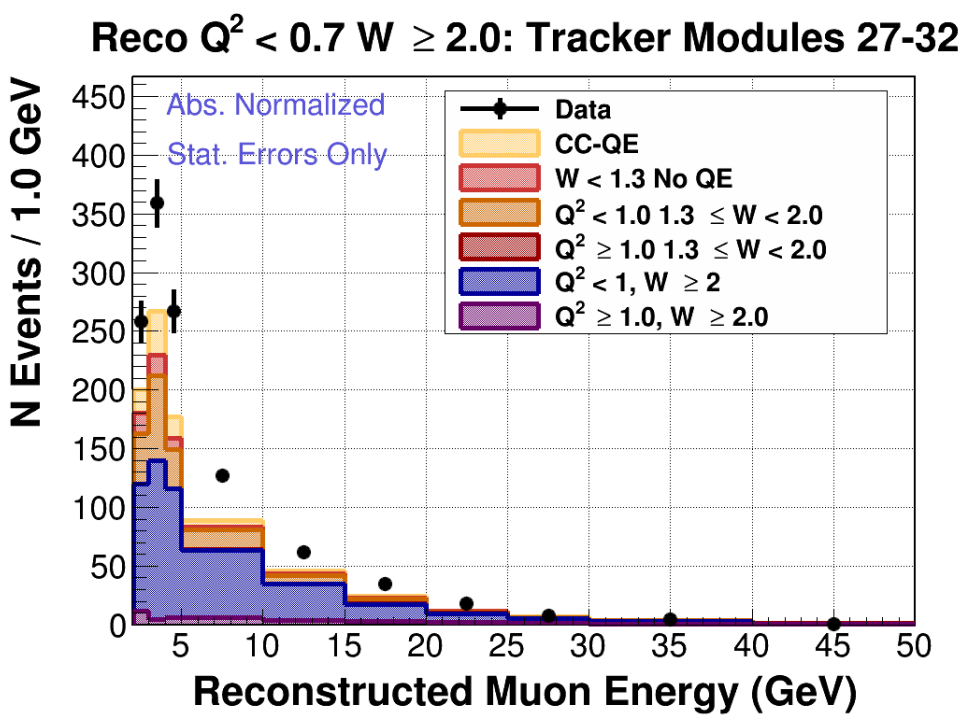

Figure A-259. Data / MC low Q^2 sideband before fitting: tracker mods. 27-32 (E_μ)

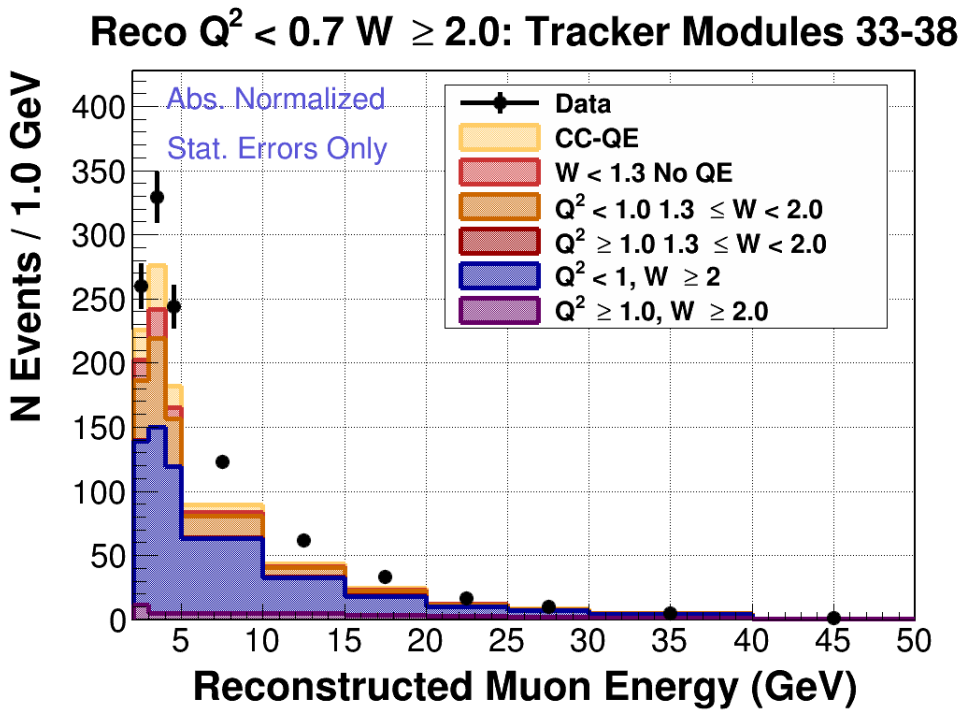

Figure A-260. Data / MC low Q^2 sideband before fitting: tracker mods. 33-38 (E_μ)

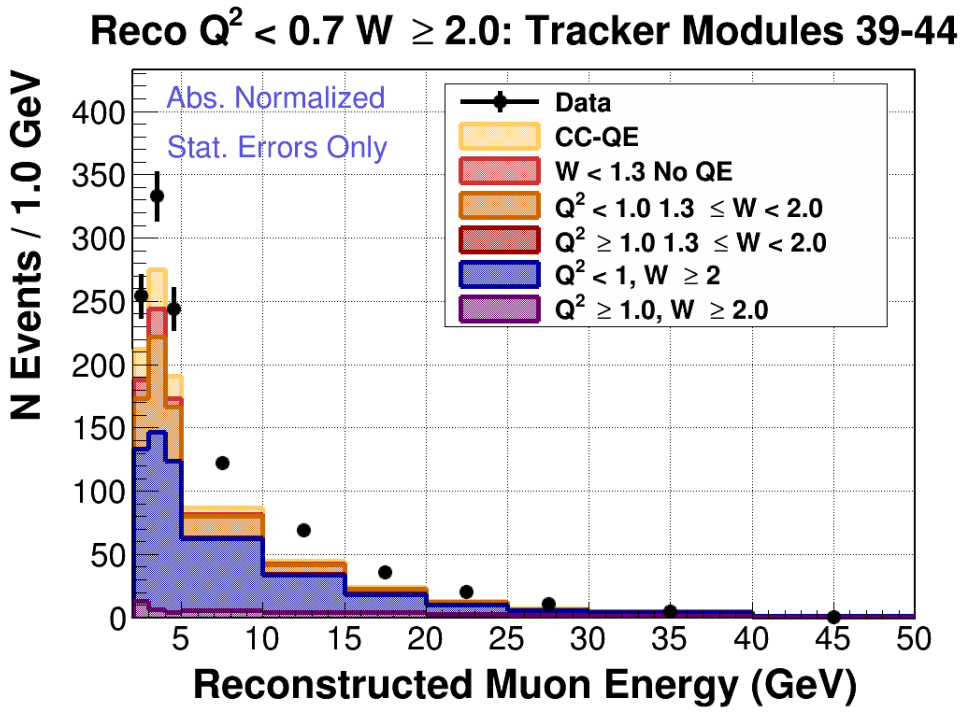

Figure A-261. Data / MC low Q^2 sideband before fitting: tracker mods. 39-44 (E_μ)

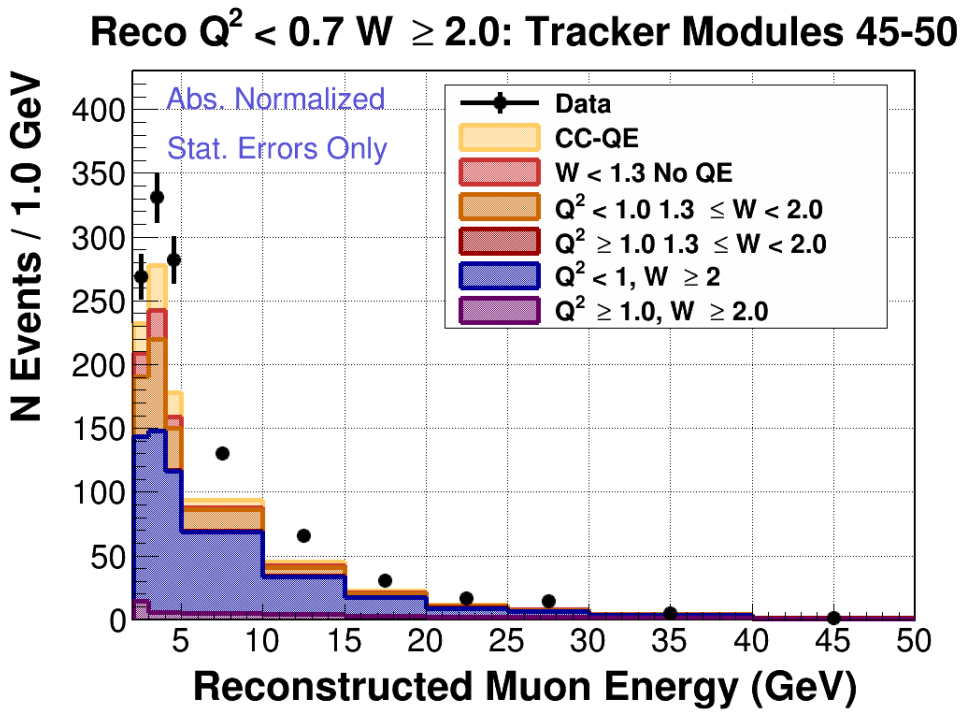

Figure A-262. Data / MC low Q^2 sideband before fitting: tracker mods. 45-50 (E_μ)

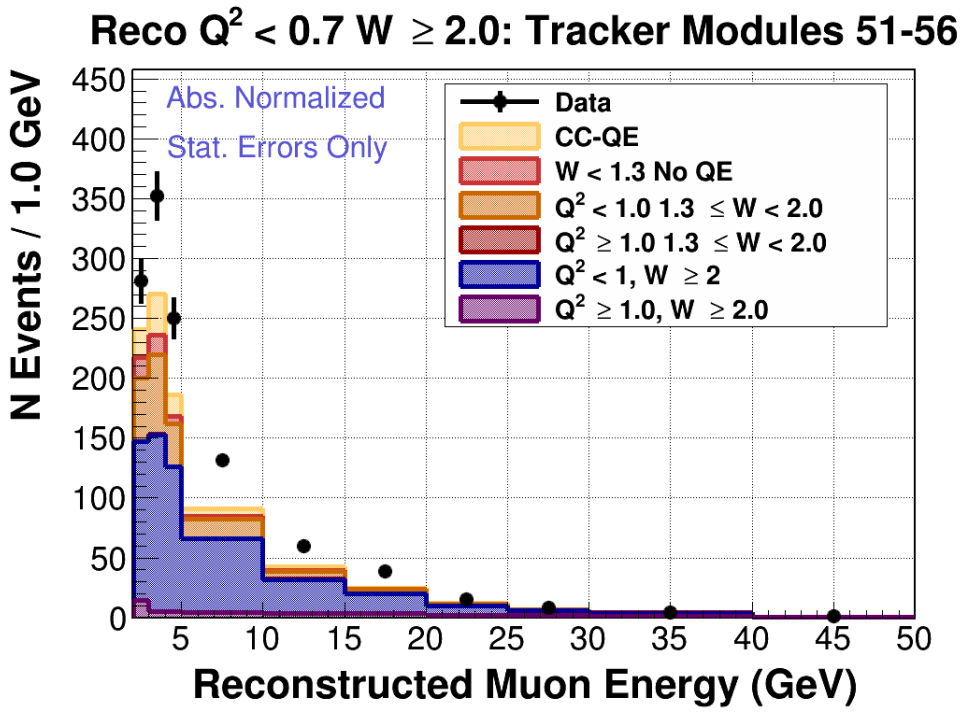

Figure A-263. Data / MC low Q^2 sideband before fitting: tracker mods. 51-56 (E_μ)

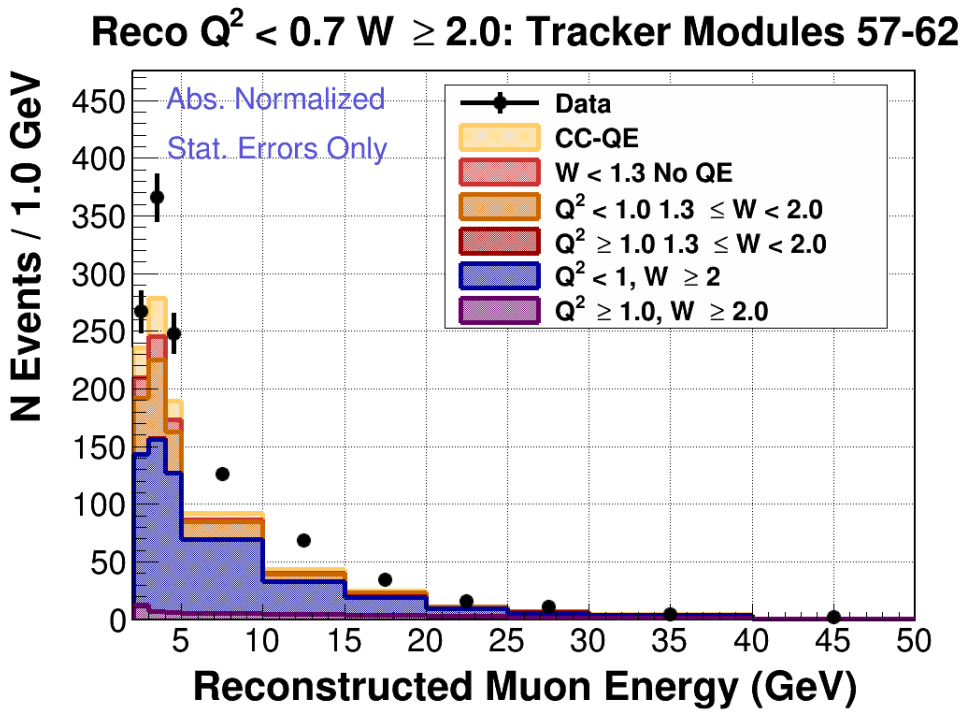

Figure A-264. Data / MC low Q^2 sideband before fitting: tracker mods. 57-62 (E_μ)

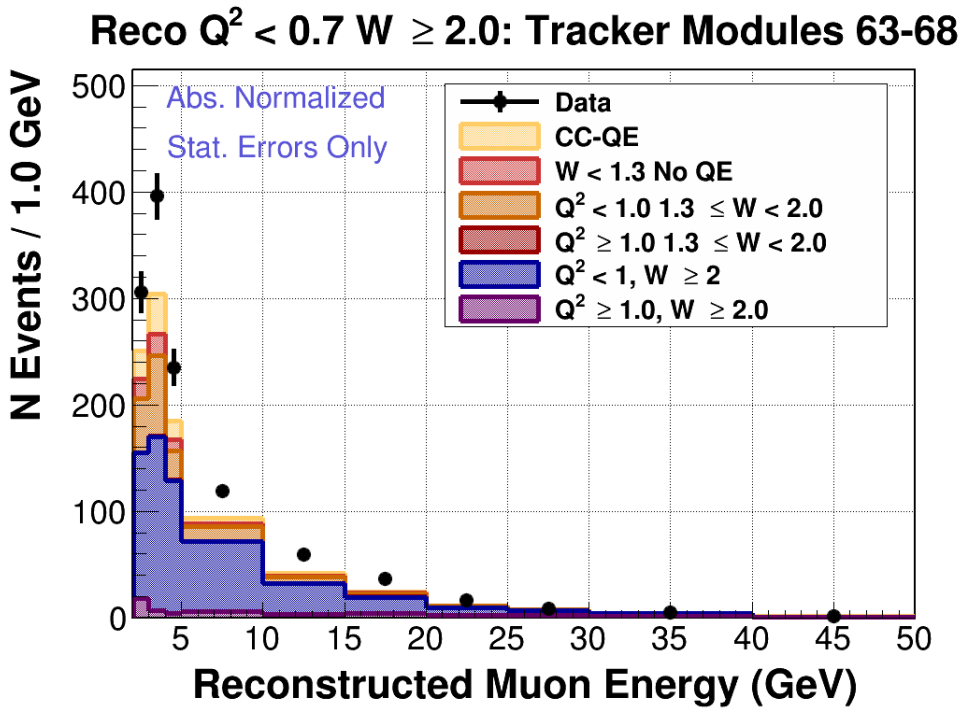

Figure A-265. Data / MC low Q^2 sideband before fitting: tracker mods. 63-68 (E_μ)

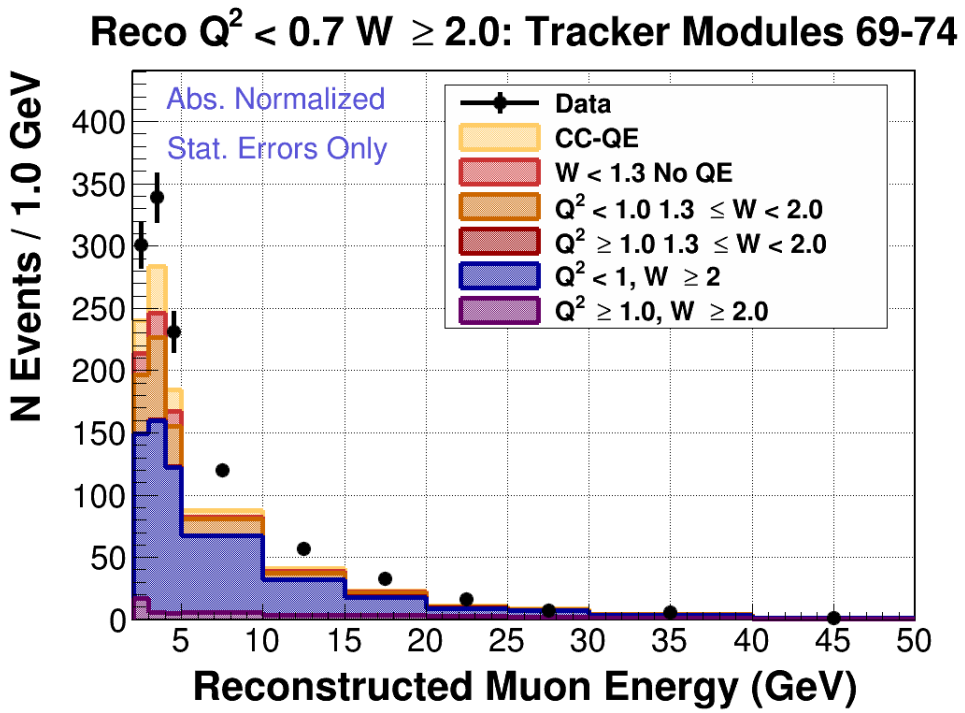

Figure A-266. Data / MC low Q^2 sideband before fitting: tracker mods. 69-74 (E_μ)

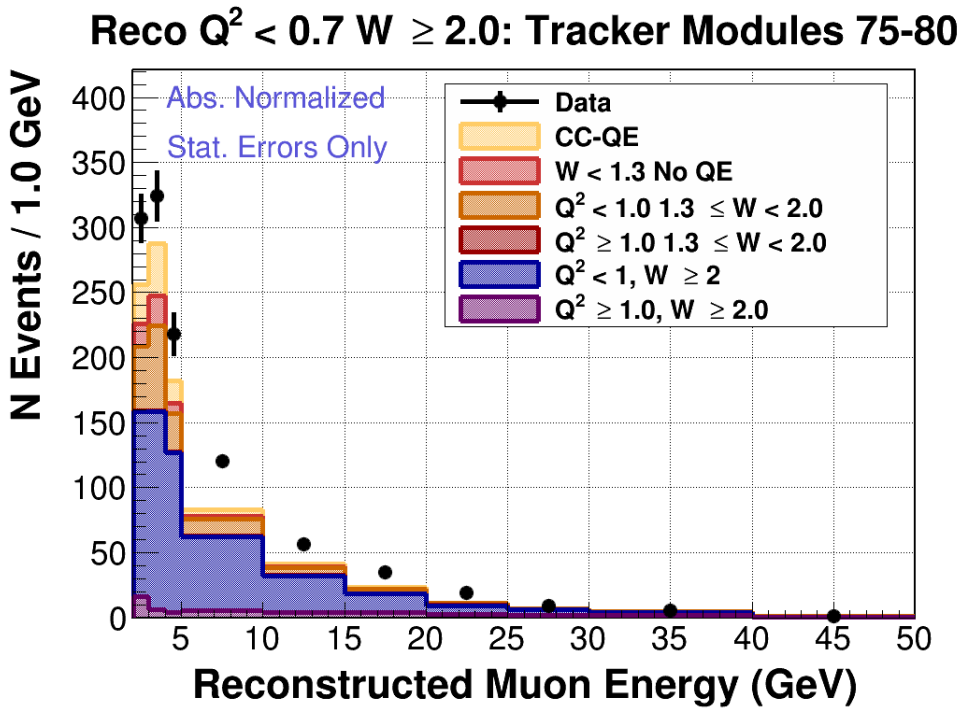

Figure A-267. Data / MC low Q^2 sideband before fitting: tracker mods. 75-80 (E_μ)

The following plots show the population of the low Q^2 sideband ($Q^2 < 0.8$ (GeV/c)^2 $W \geq 2.0$ GeV/c^2) *before* tuning to data as a function of muon angle (θ_μ):

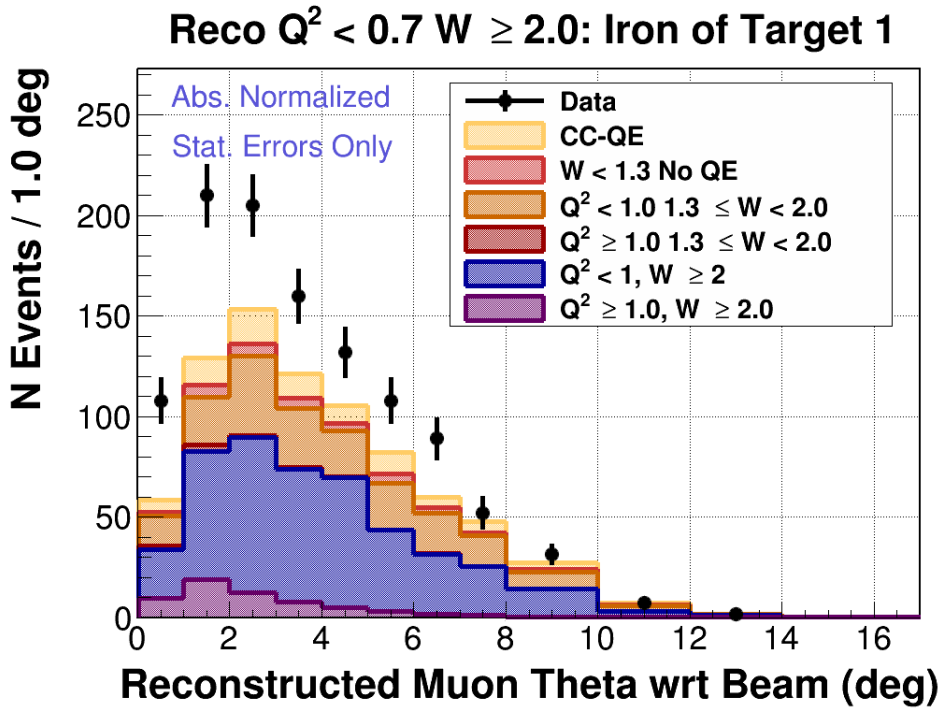

Figure A-268. Data / MC low Q^2 sideband before fitting: target 01 Fe (θ_μ)

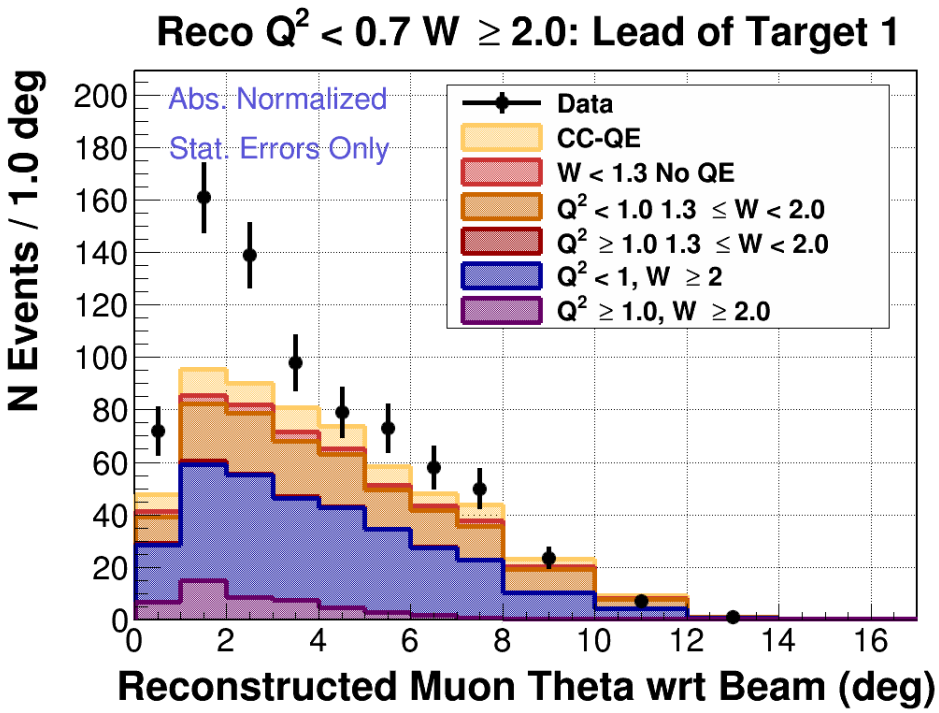

Figure A-269. Data / MC low Q^2 sideband before fitting: target 01 Pb (θ_μ)

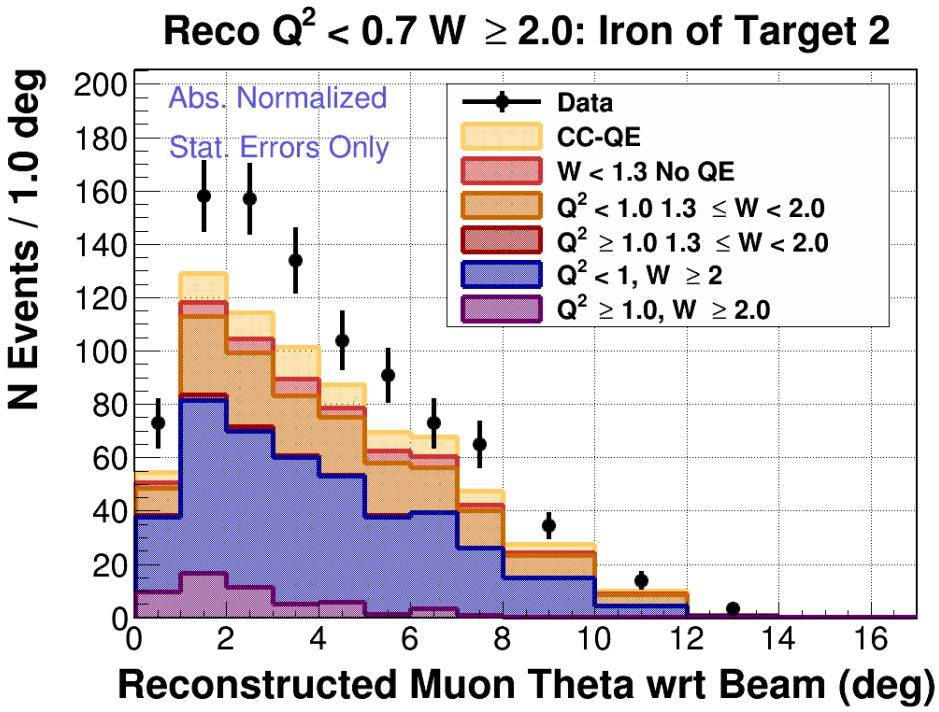

Figure A-270. Data / MC low Q^2 sideband before fitting: target 02 Fe (θ_μ)

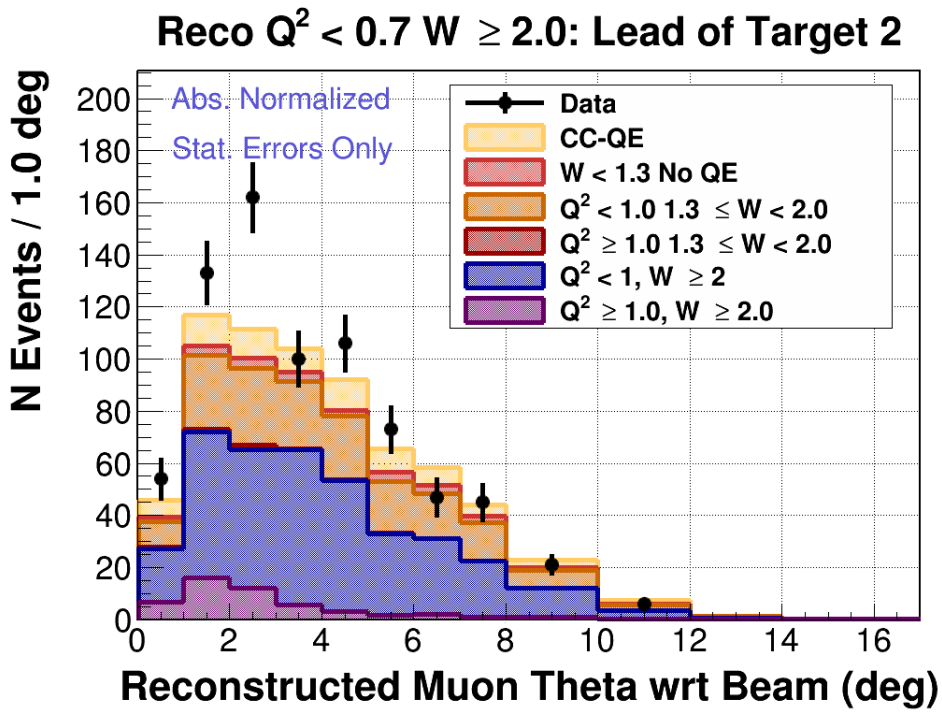

Figure A-271. Data / MC low Q^2 sideband before fitting: target 02 Pb (θ_μ)

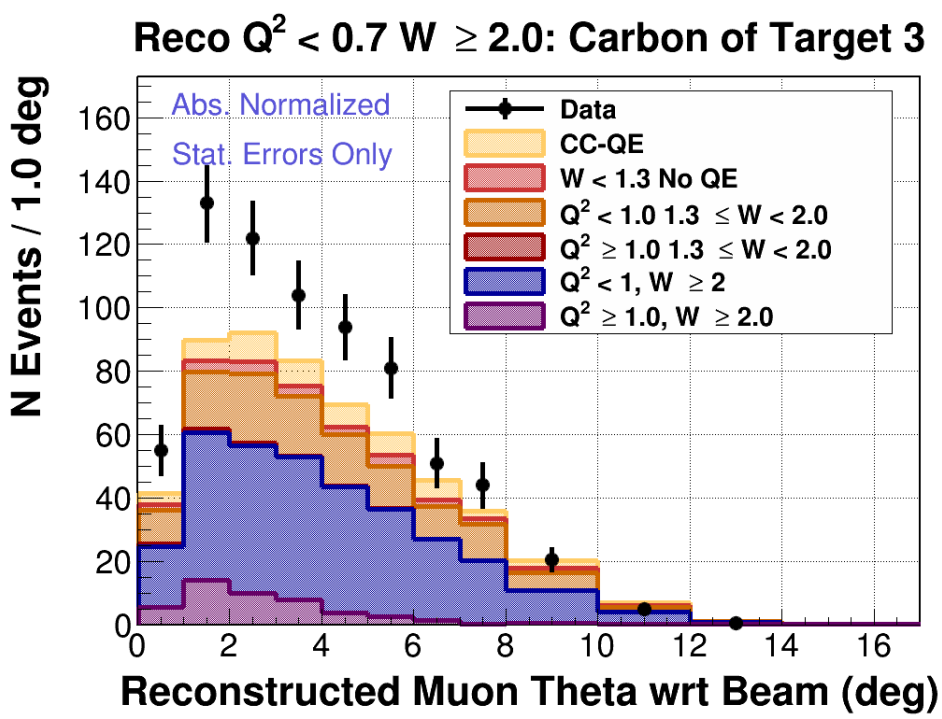

Figure A-272. Data / MC low Q^2 sideband before fitting: target 03 C (θ_μ)

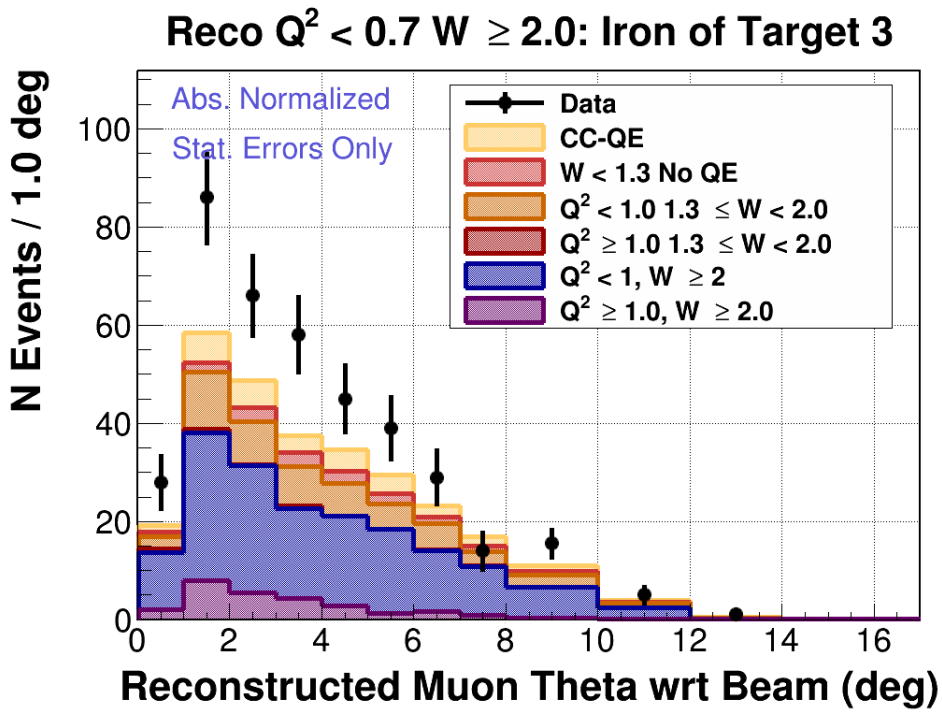

Figure A-273. Data / MC low Q^2 sideband before fitting: target 03 Fe (θ_μ)

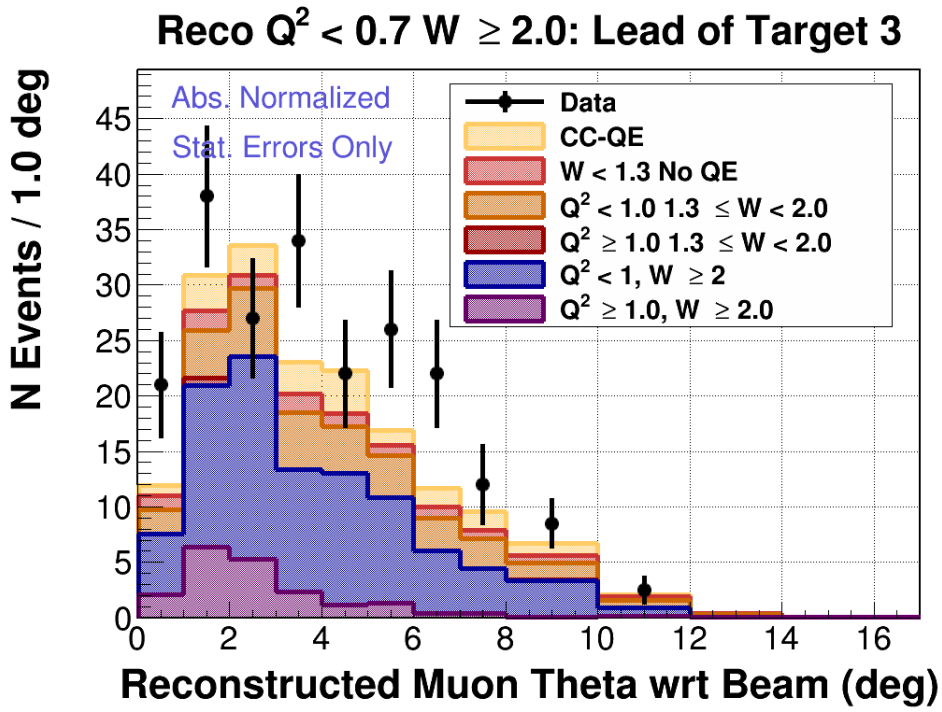

Figure A-274. Data / MC low Q^2 sideband before fitting: target 03 Pb (θ_μ)

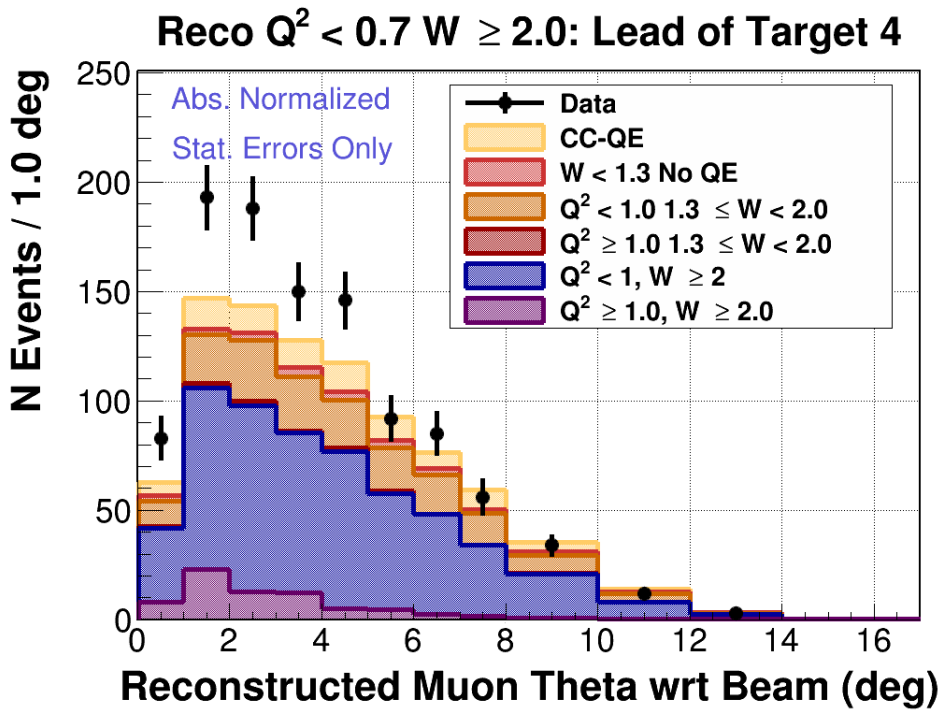

Figure A-275. Data / MC low Q^2 sideband before fitting: target 04 Pb (θ_μ)

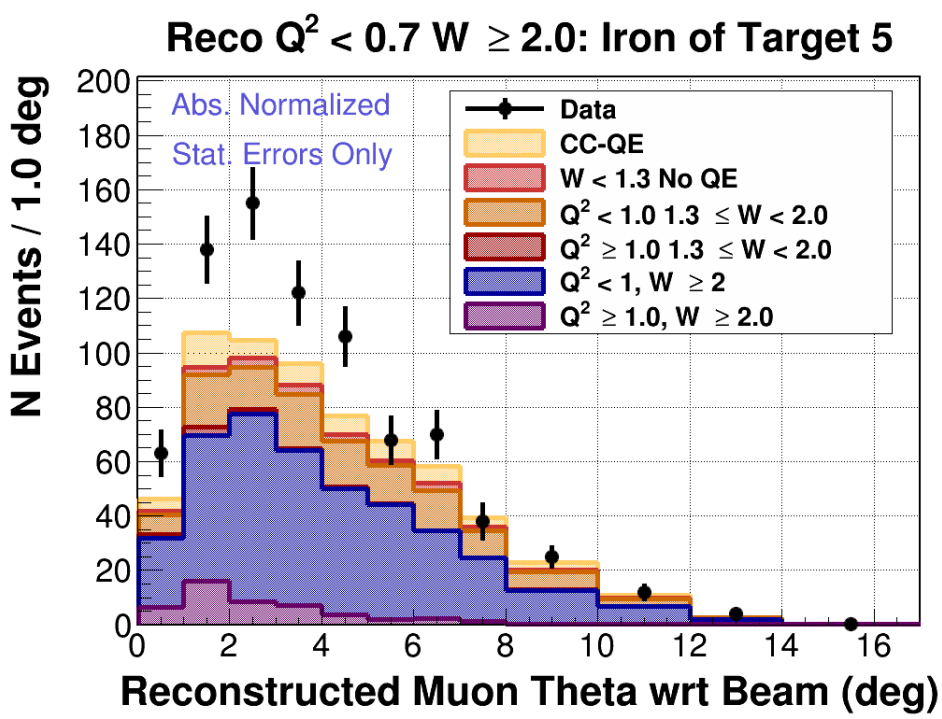

Figure A-276. Data / MC low Q^2 sideband before fitting: target 05 Fe (θ_μ)

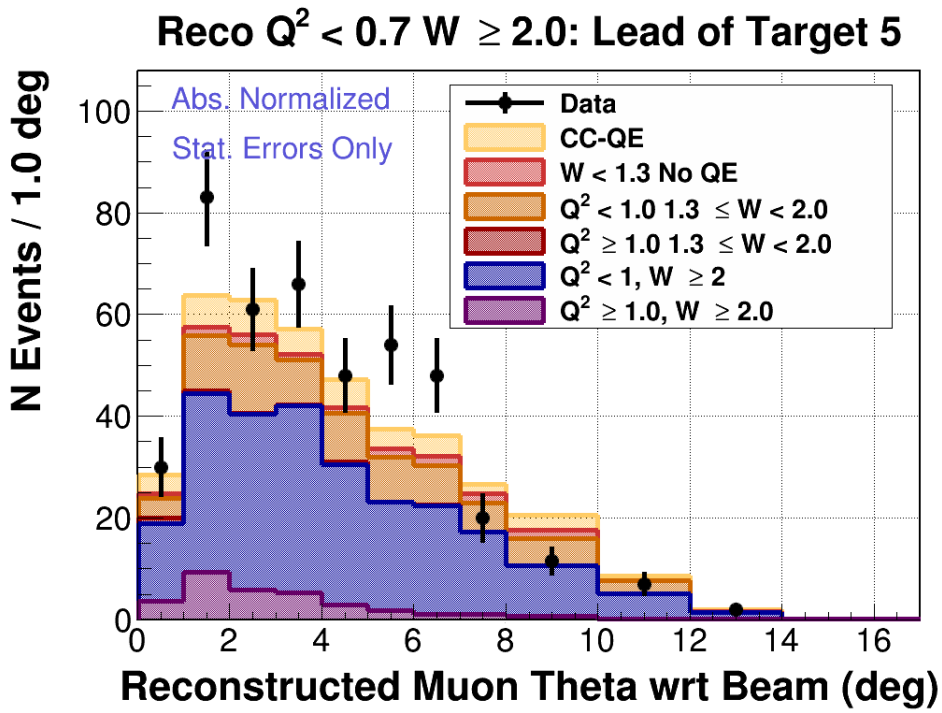

Figure A-277. Data / MC low Q^2 sideband before fitting: target 05 Pb (θ_μ)

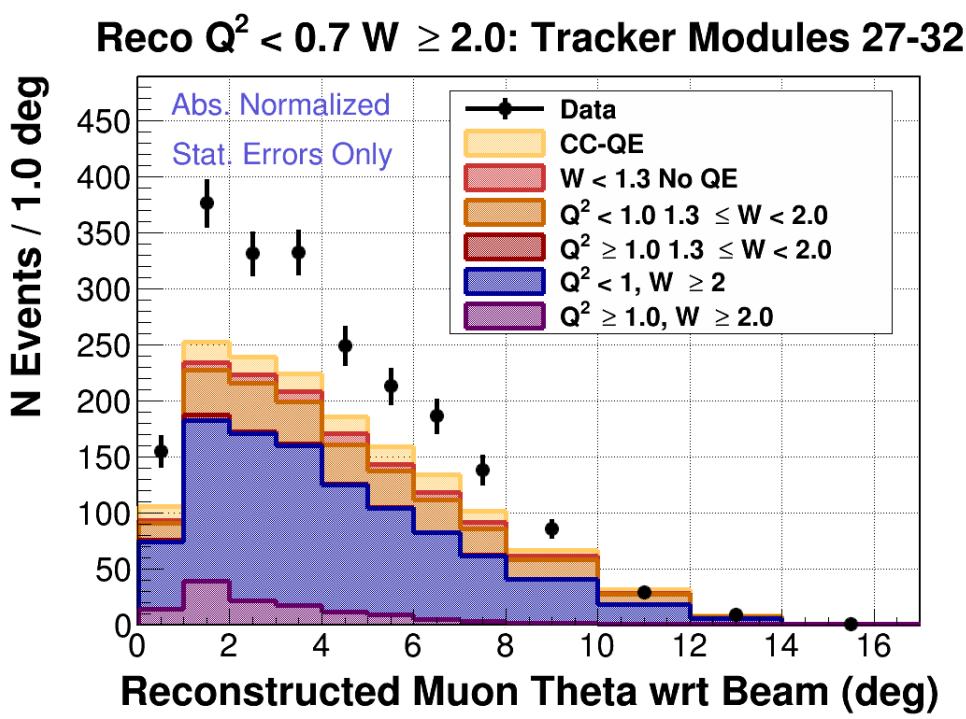

Figure A-278. Data / MC low Q^2 sideband before fitting: tracker mods. 27-32 (θ_μ)

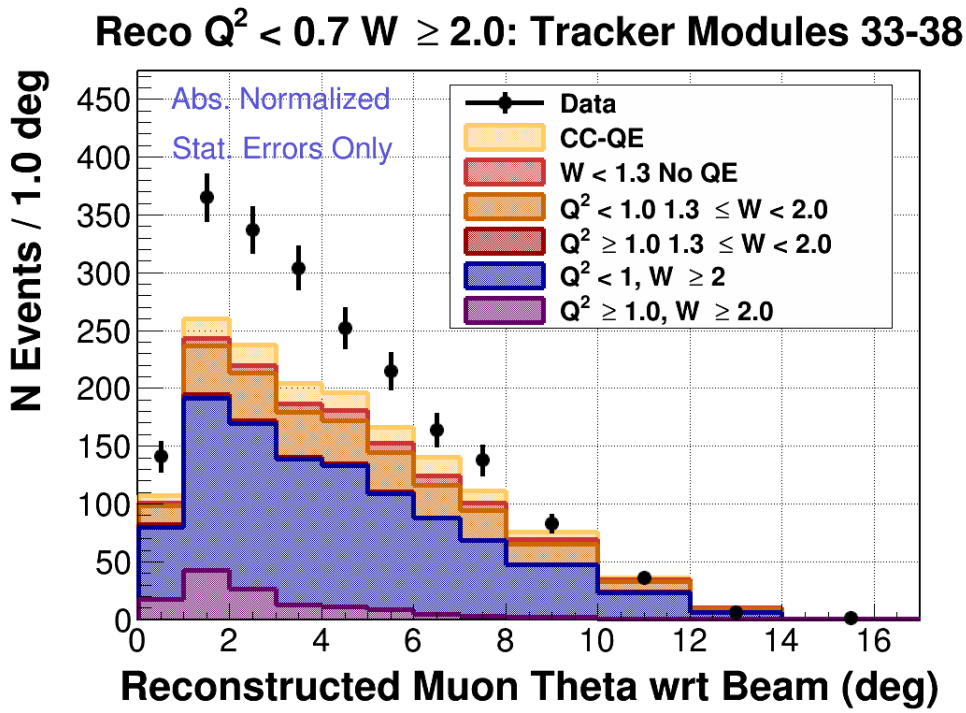

Figure A-279. Data / MC low Q^2 sideband before fitting: tracker mods. 33-38 (θ_μ)

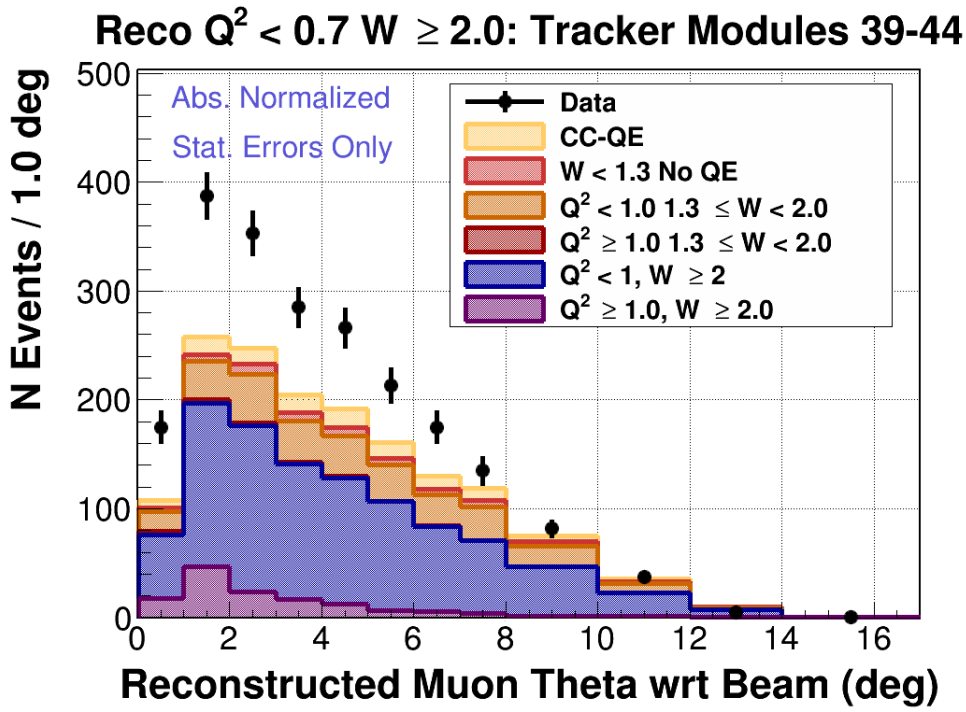

Figure A-280. Data / MC low Q^2 sideband before fitting: tracker mods. 39-44 (θ_μ)

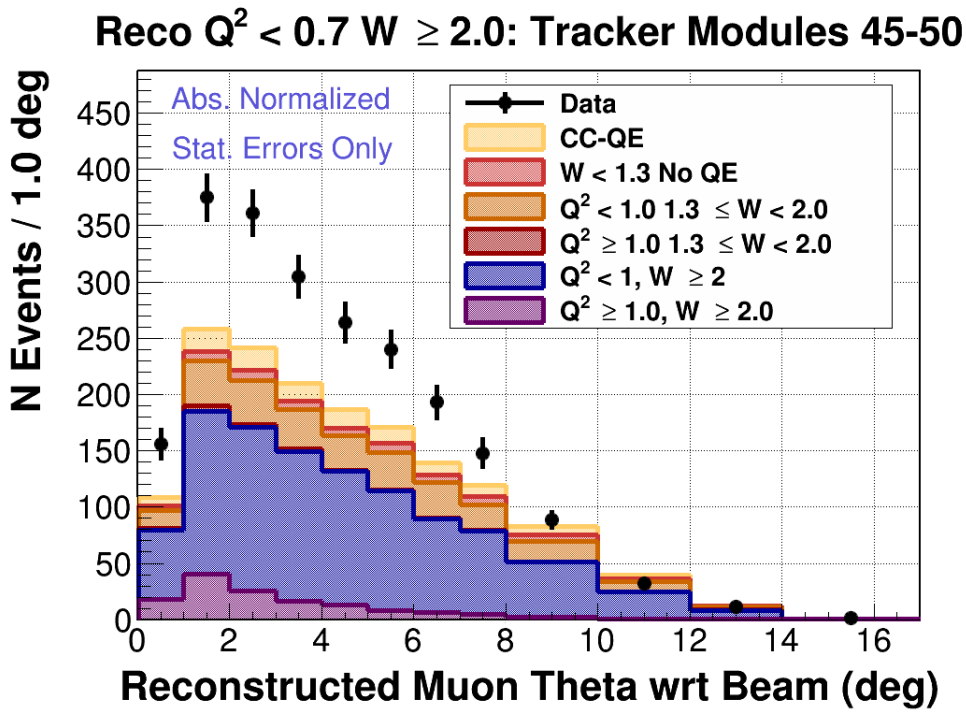

Figure A-281. Data / MC low Q^2 sideband before fitting: tracker mods. 45-50 (θ_μ)

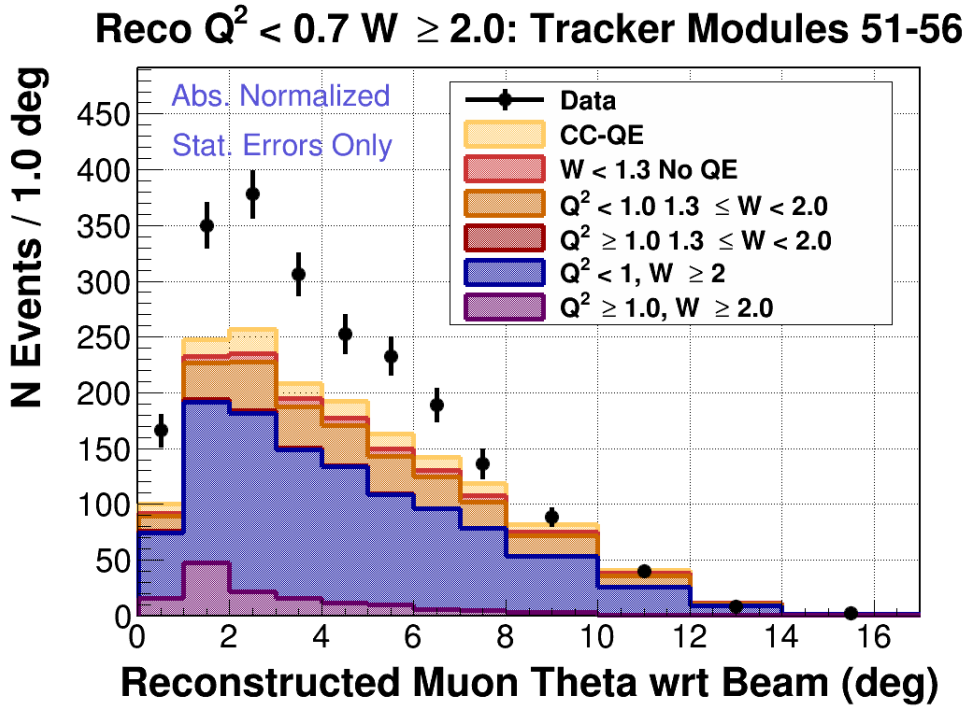

Figure A-282. Data / MC low Q^2 sideband before fitting: tracker mods. 51-56 (θ_μ)

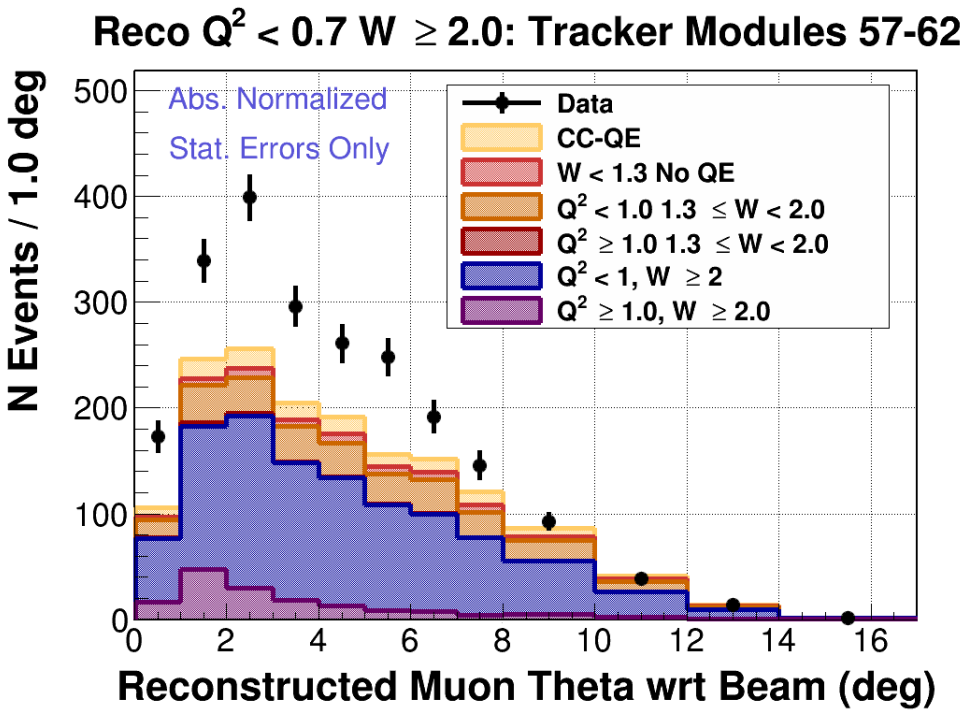

Figure A-283. Data / MC low Q^2 sideband before fitting: tracker mods. 57-62 (θ_μ)

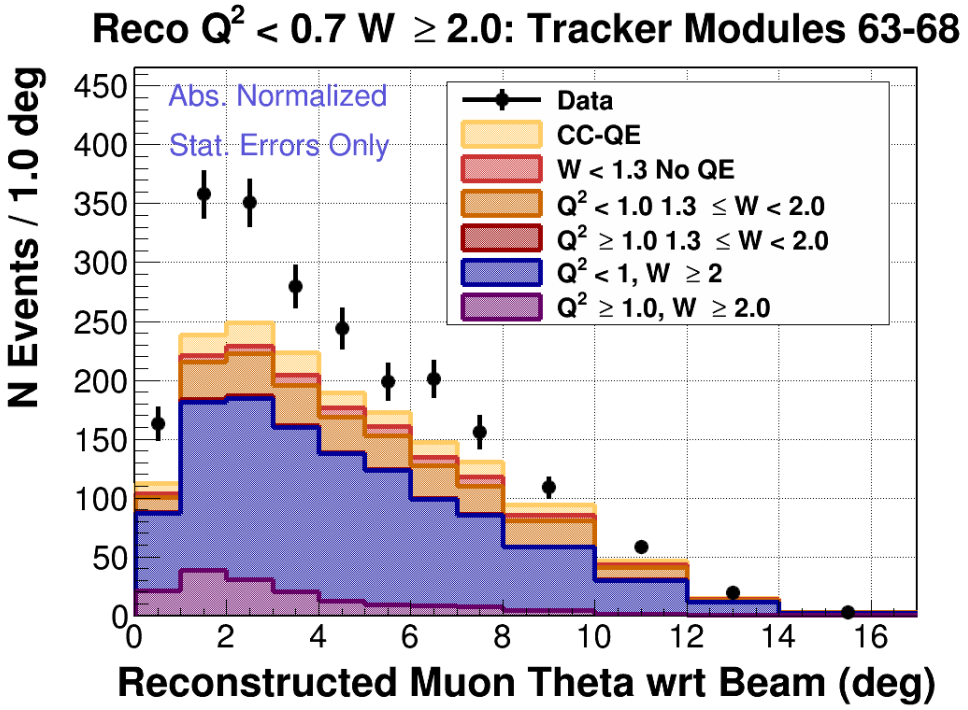

Figure A-284. Data / MC low Q^2 sideband before fitting: tracker mods. 63-68 (θ_μ)

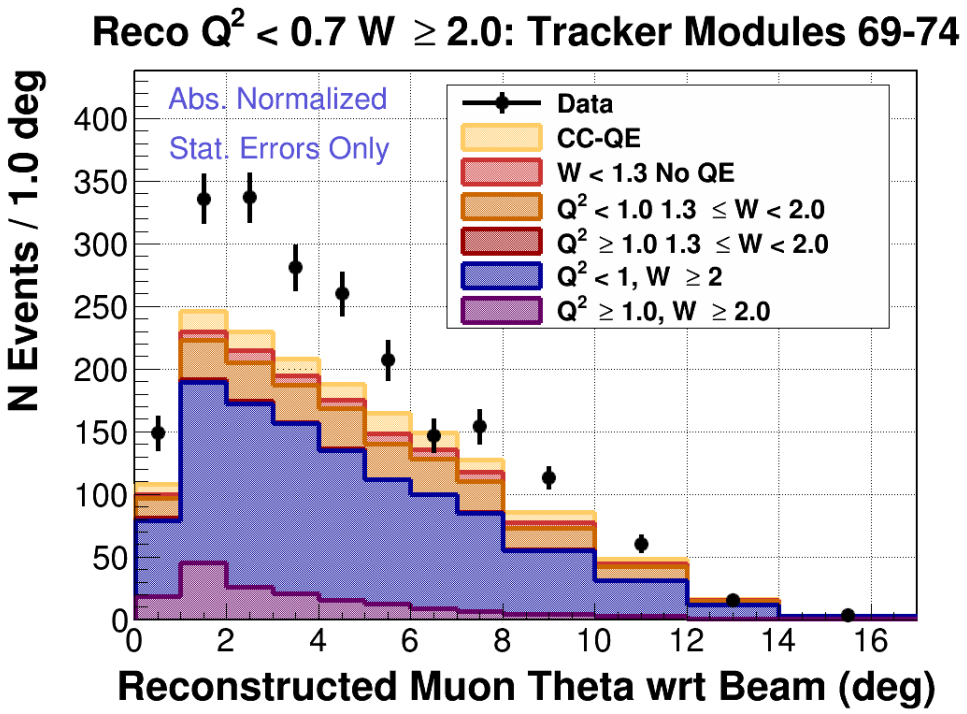

Figure A-285. Data / MC low Q^2 sideband before fitting: tracker mods. 69-74 (θ_μ)

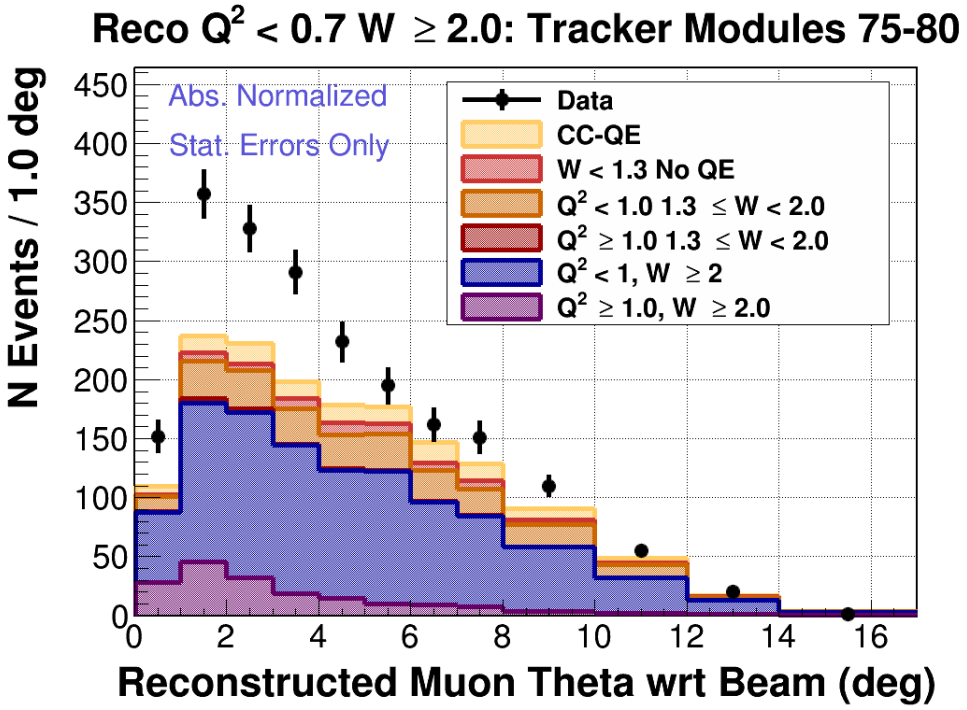

Figure A-286. Data / MC low Q^2 sideband before fitting: tracker mods. 75-80 (θ_μ)

A.5 Scale Factors derived per Target / Nucleus for the Low Q^2 Sideband: $Q^2 < 0.8$ $(\mathbf{GeV/c})^2$ $W \geq 2.0$ $\mathbf{GeV/c^2}$

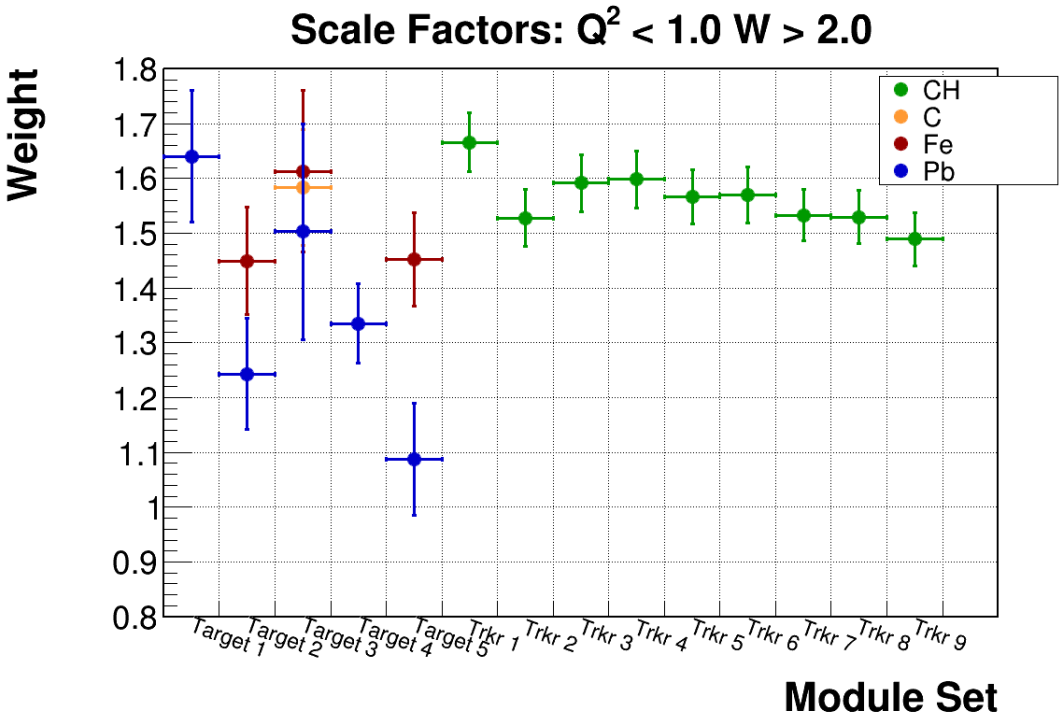

Figure A-287. Low Q^2 scale factors per target

A.6 Low Q^2 Sideband: $Q^2 < 0.8$ (GeV/c)^2 $W \geq 2.0$ GeV/c^2 (After Fitting)

The following plots show the population of the low Q^2 sideband ($Q^2 < 0.8$ (GeV/c)^2 $W \geq 2.0$ GeV) *after* tuning to data as a function of neutrino energy (E_ν):

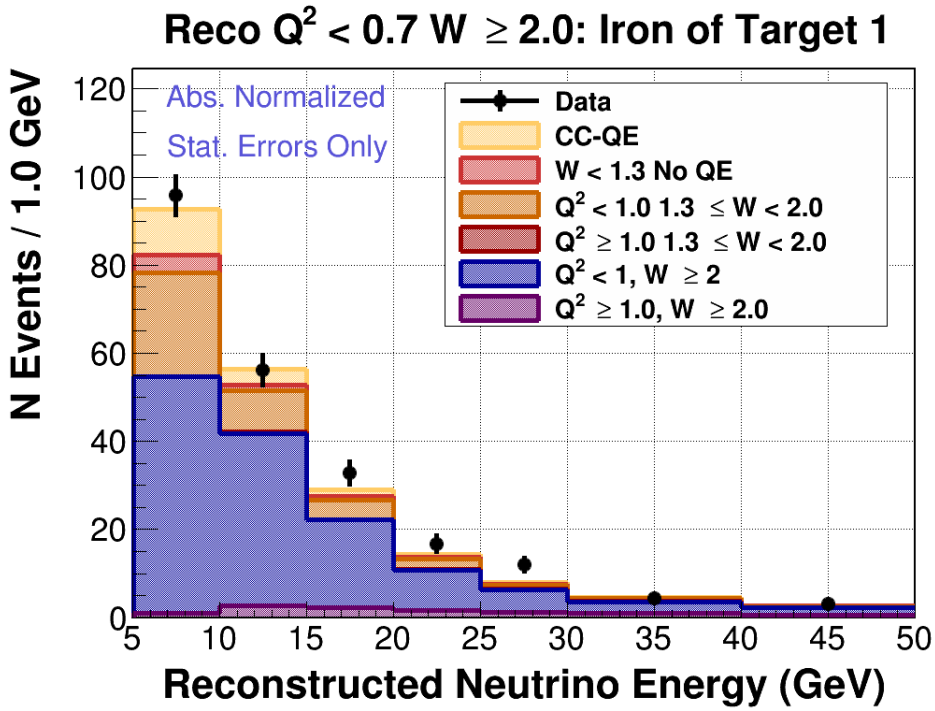

Figure A-288. Data / MC low Q^2 sideband after fitting: target 01 Fe (E_ν)

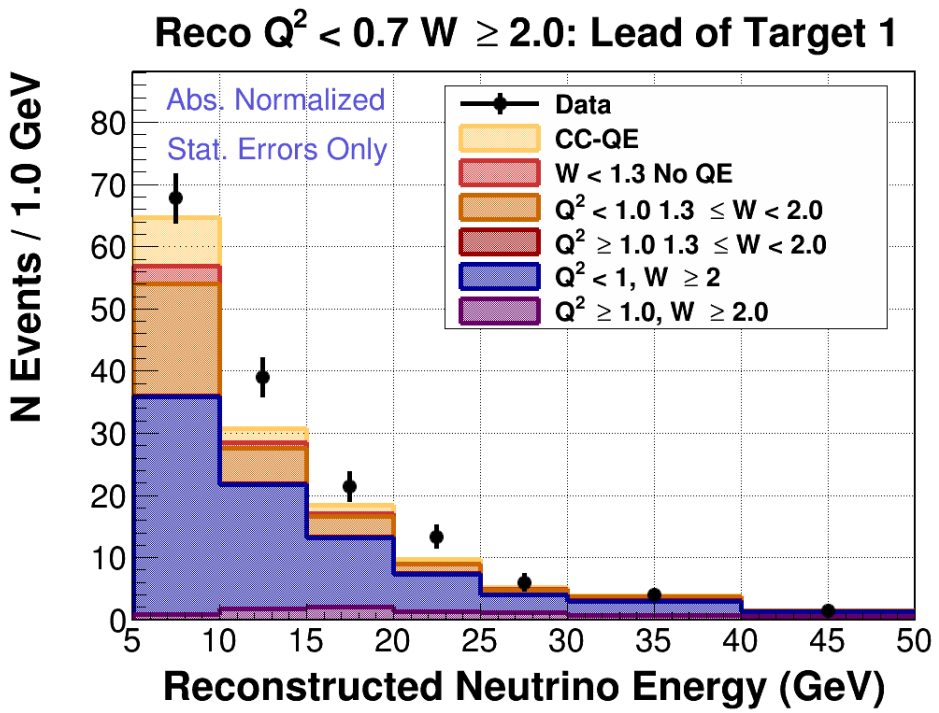

Figure A-289. Data / MC low Q^2 sideband after fitting: target 01 Pb (E_ν)

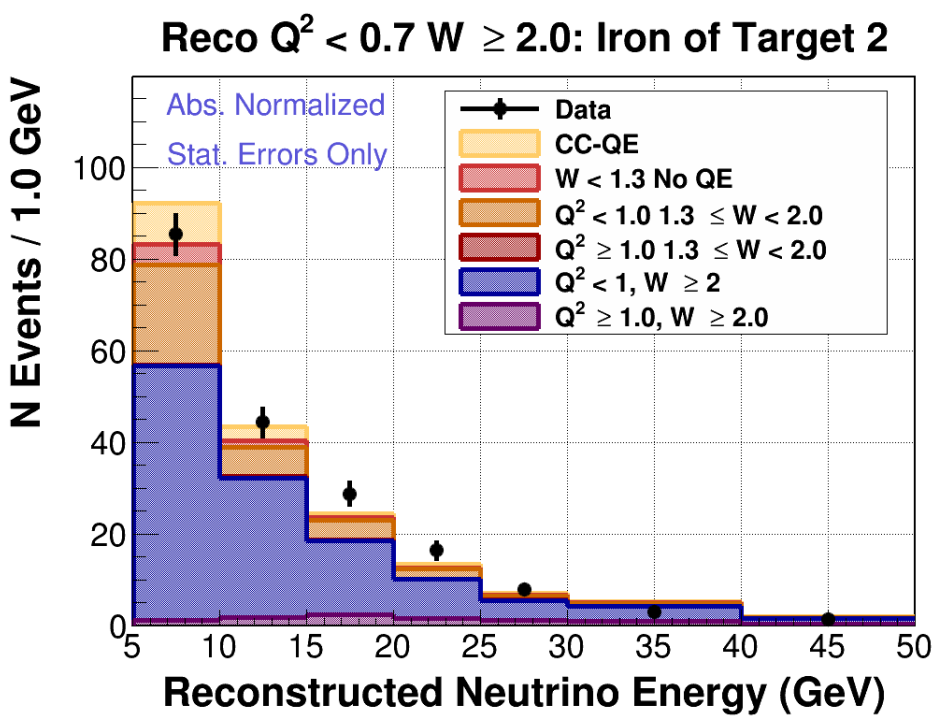

Figure A-290. Data / MC low Q^2 sideband after fitting: target 02 Fe (E_ν)

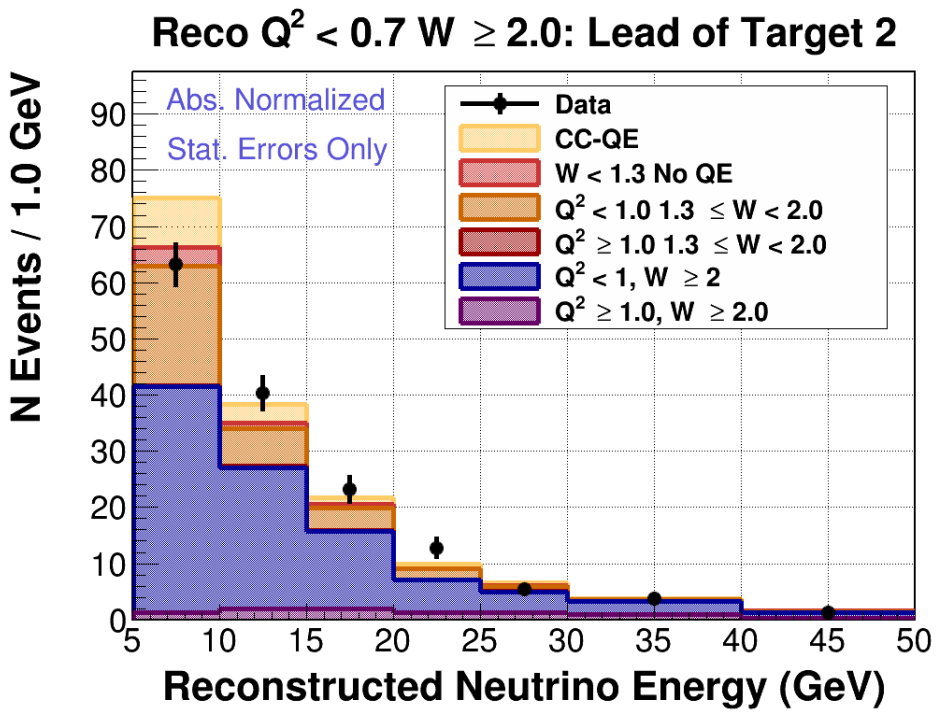

Figure A-291. Data / MC low Q^2 sideband after fitting: target 02 Pb (E_ν)

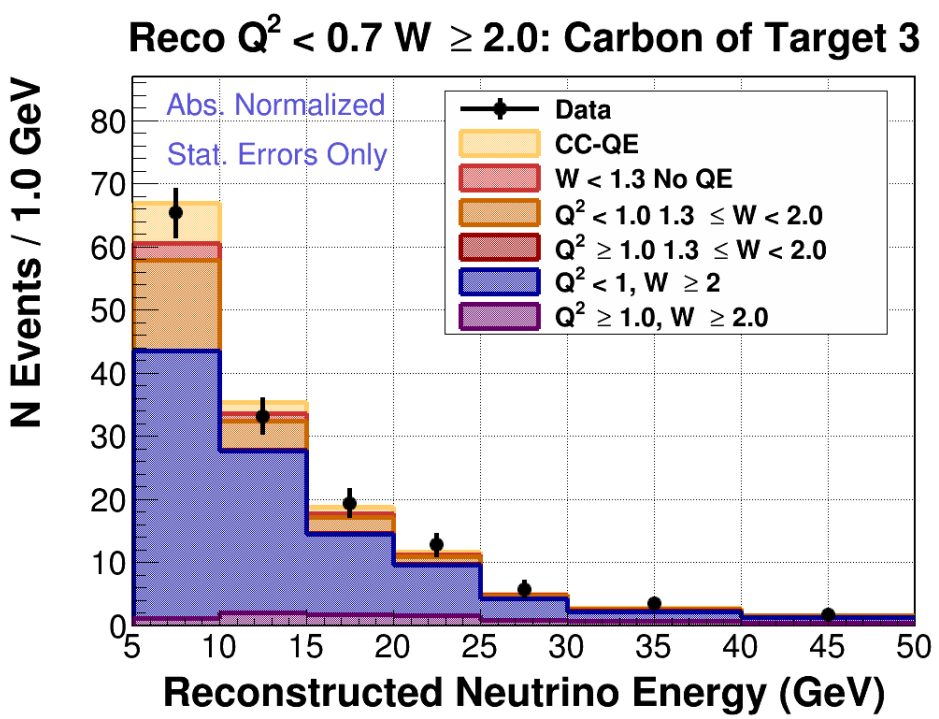

Figure A-292. Data / MC low Q^2 sideband after fitting: target 03 C (E_ν)

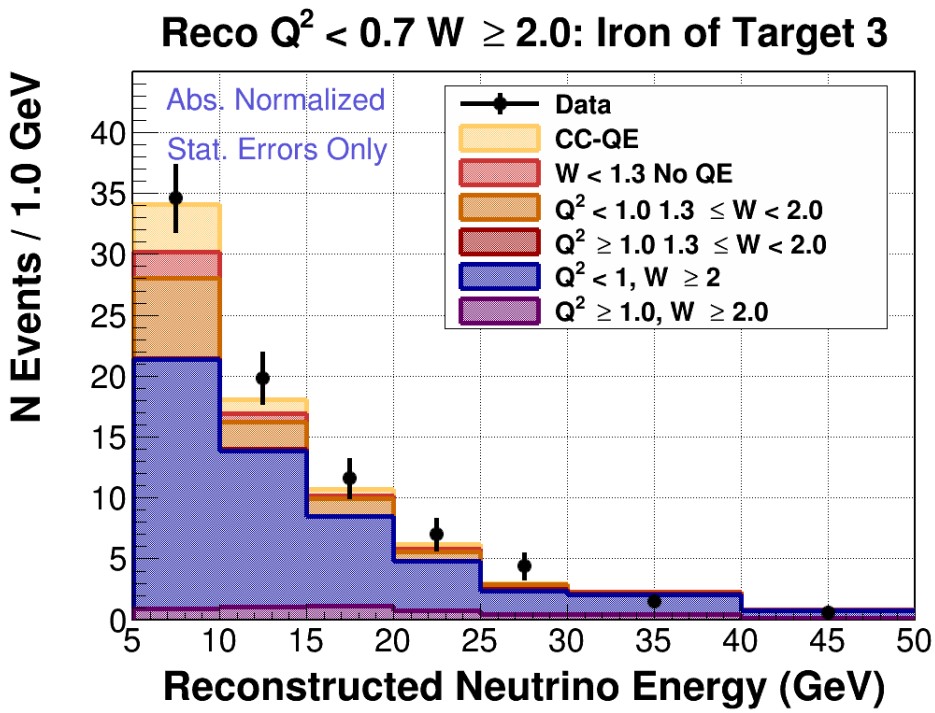

Figure A-293. Data / MC low Q^2 sideband after fitting: target 03 Fe (E_ν)

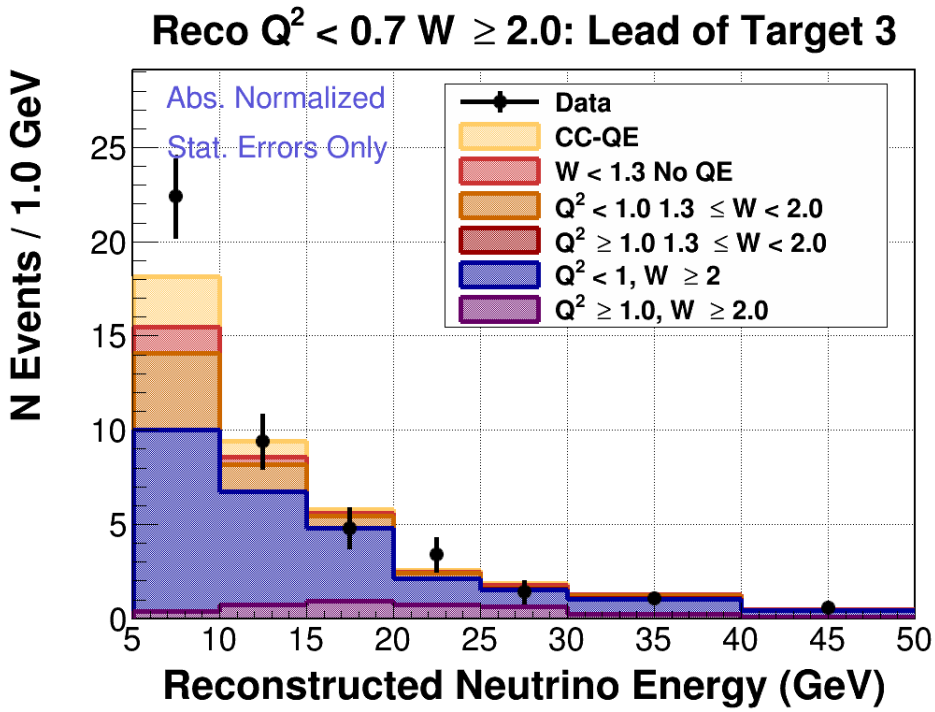

Figure A-294. Data / MC low Q^2 sideband after fitting: target 03 Pb (E_ν)

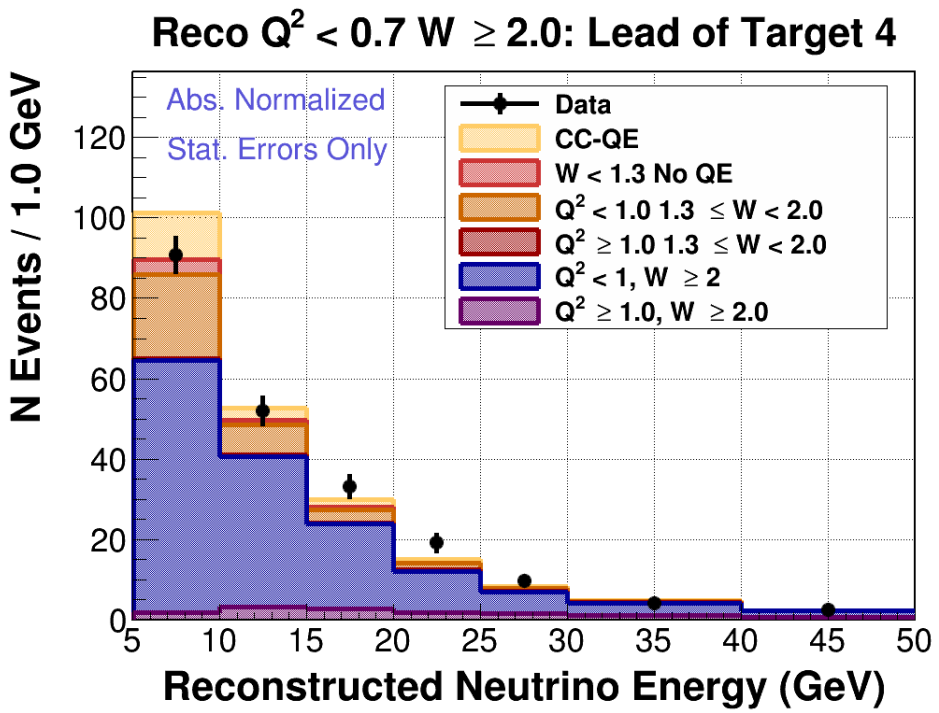

Figure A-295. Data / MC low Q^2 sideband after fitting: target 04 Pb (E_ν)

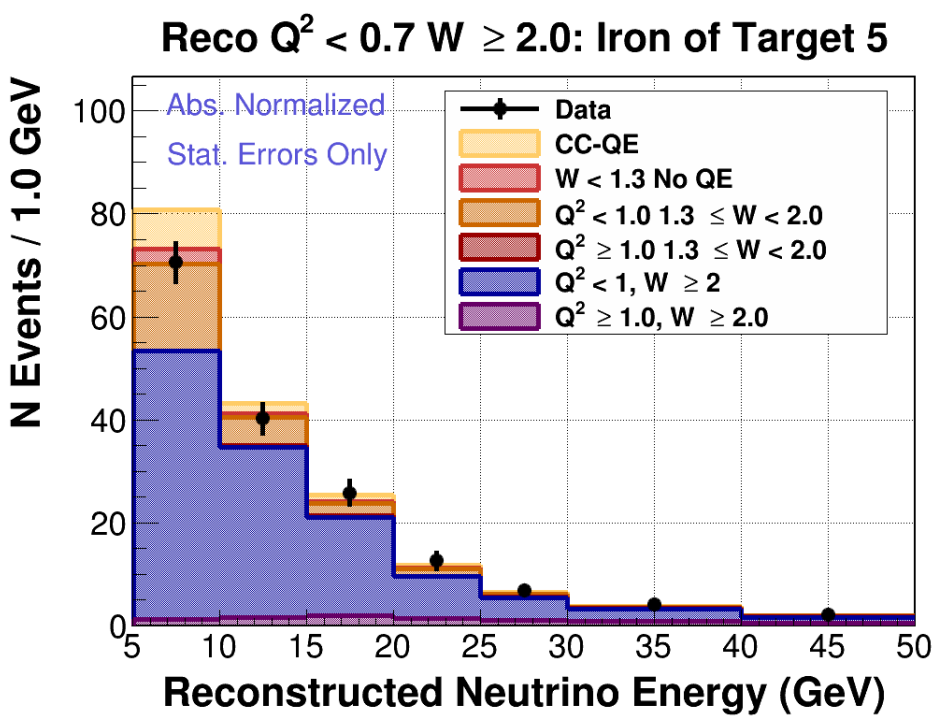

Figure A-296. Data / MC low Q^2 sideband after fitting: target 05 Fe (E_ν)

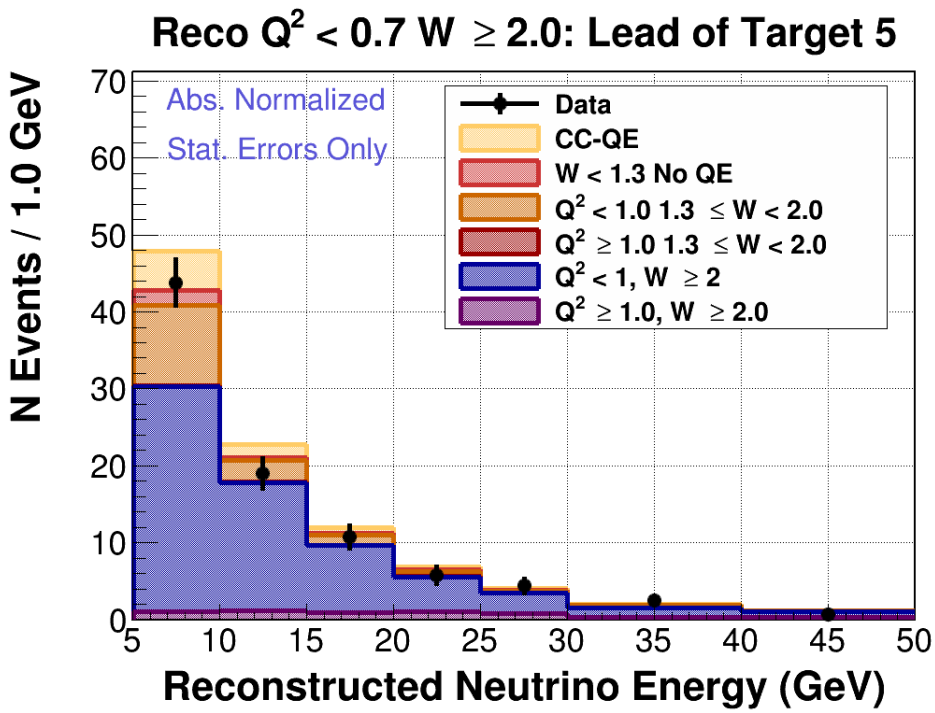

Figure A-297. Data / MC low Q^2 sideband after fitting: target 05 Pb (E_ν)

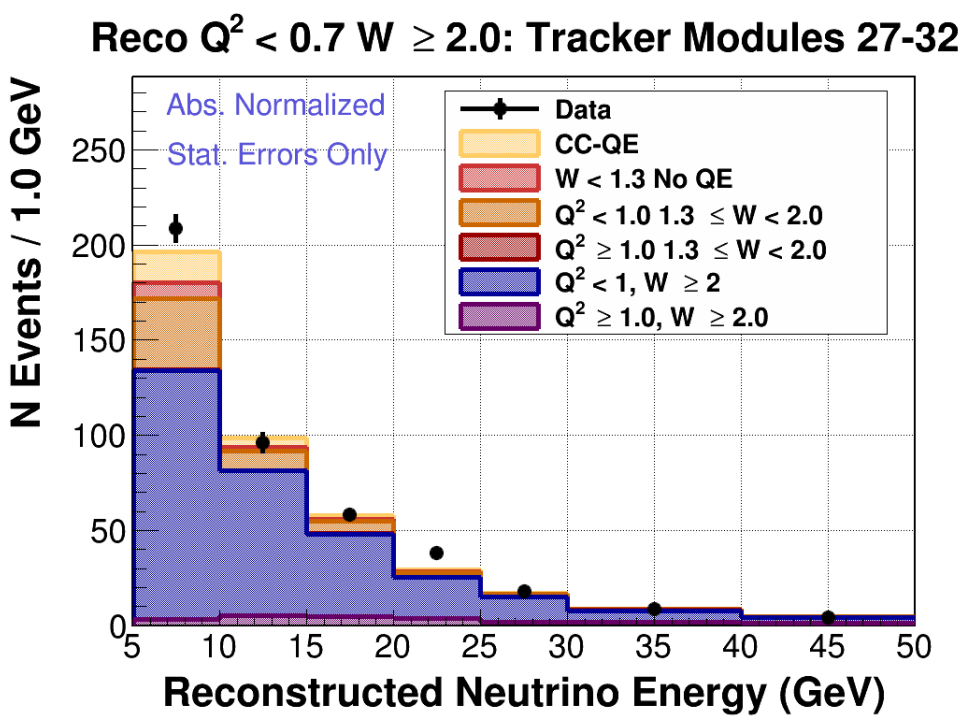

Figure A-298. Data / MC low Q^2 sideband after fitting: tracker mods. 27-32 (E_ν)

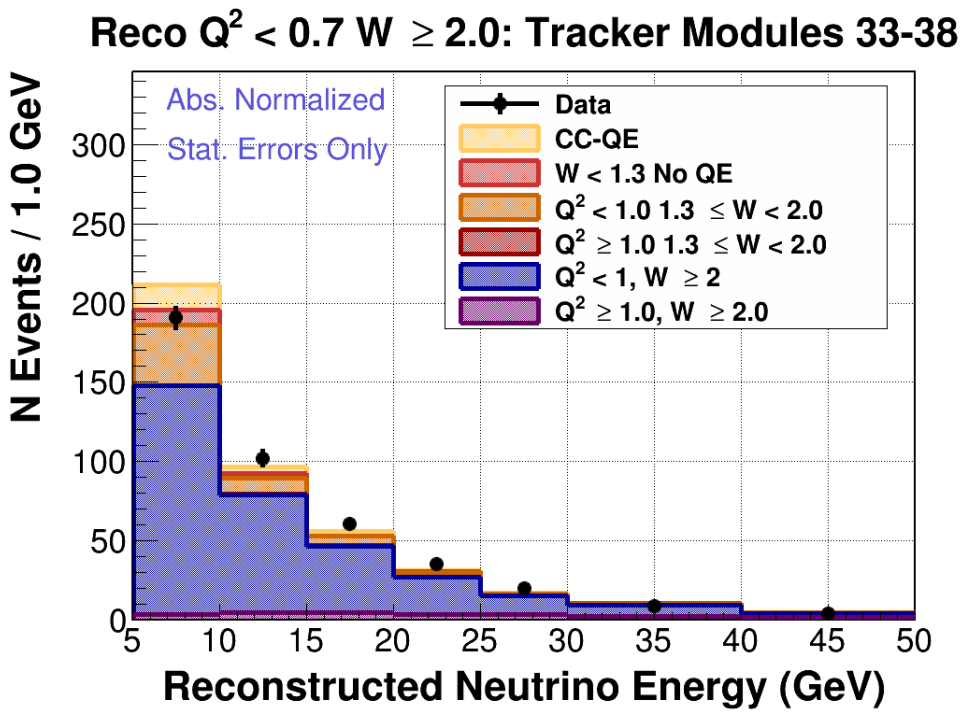

Figure A-299. Data / MC low Q^2 sideband after fitting: tracker mods. 33-38 (E_ν)

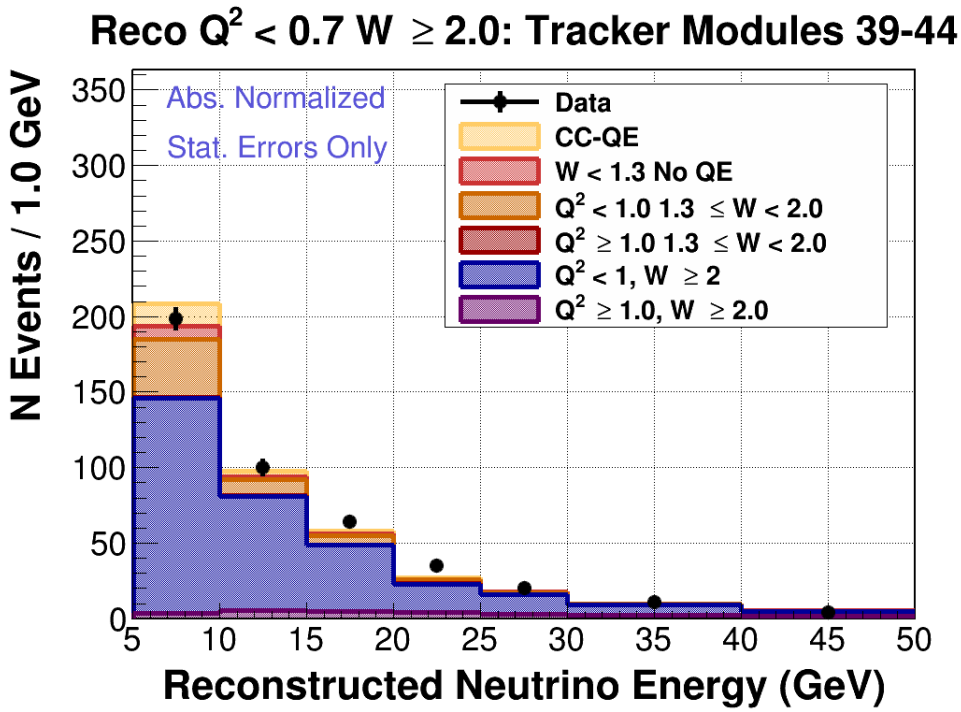

Figure A-300. Data / MC low Q^2 sideband after fitting: tracker mods. 39-44 (E_ν)

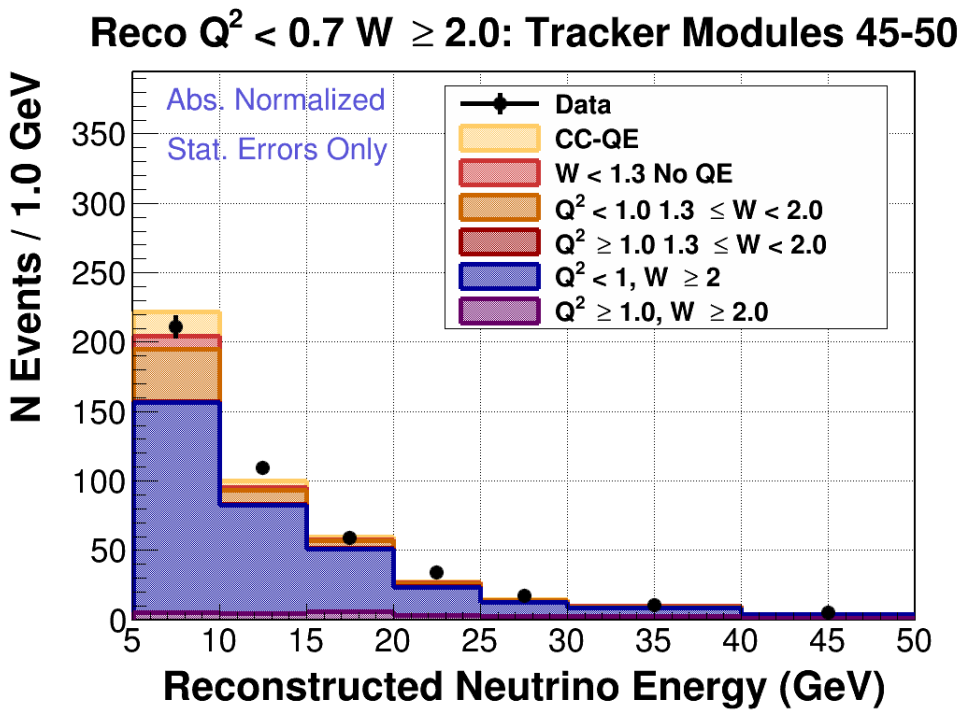

Figure A-301. Data / MC low Q^2 sideband after fitting: tracker mods. 45-50 (E_ν)

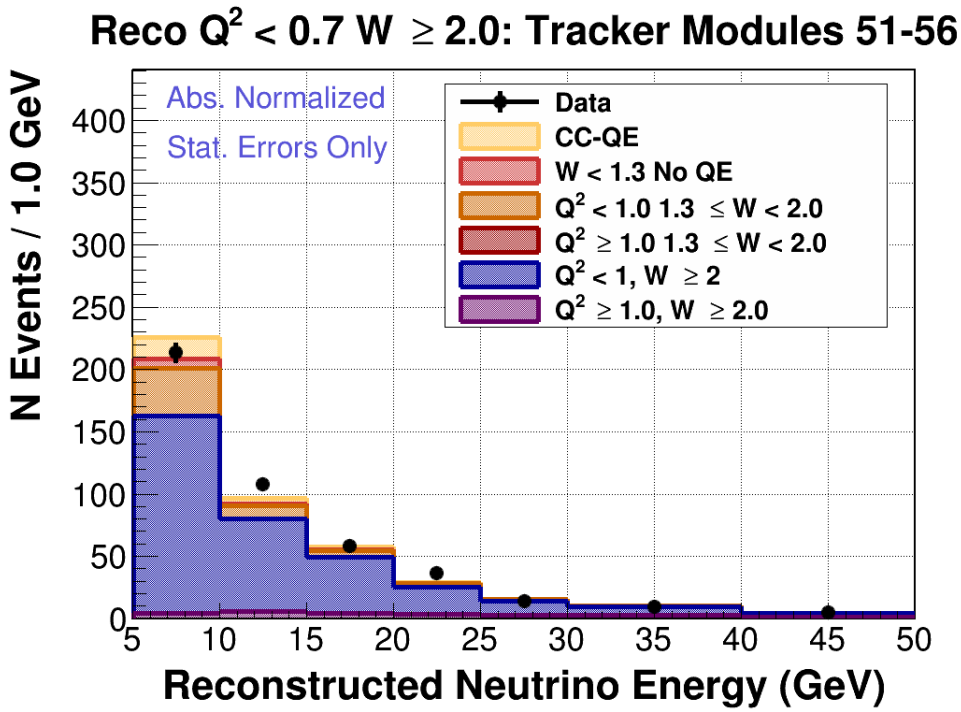

Figure A-302. Data / MC low Q^2 sideband after fitting: tracker mods. 51-56 (E_ν)

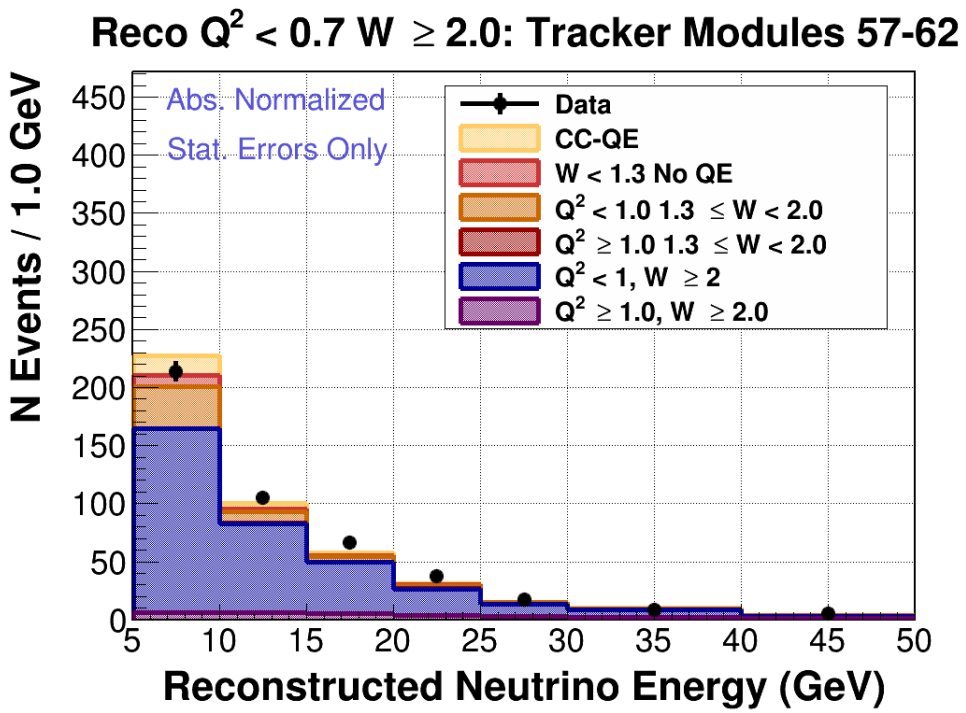

Figure A-303. Data / MC low Q^2 sideband after fitting: tracker mods. 57-62 (E_ν)

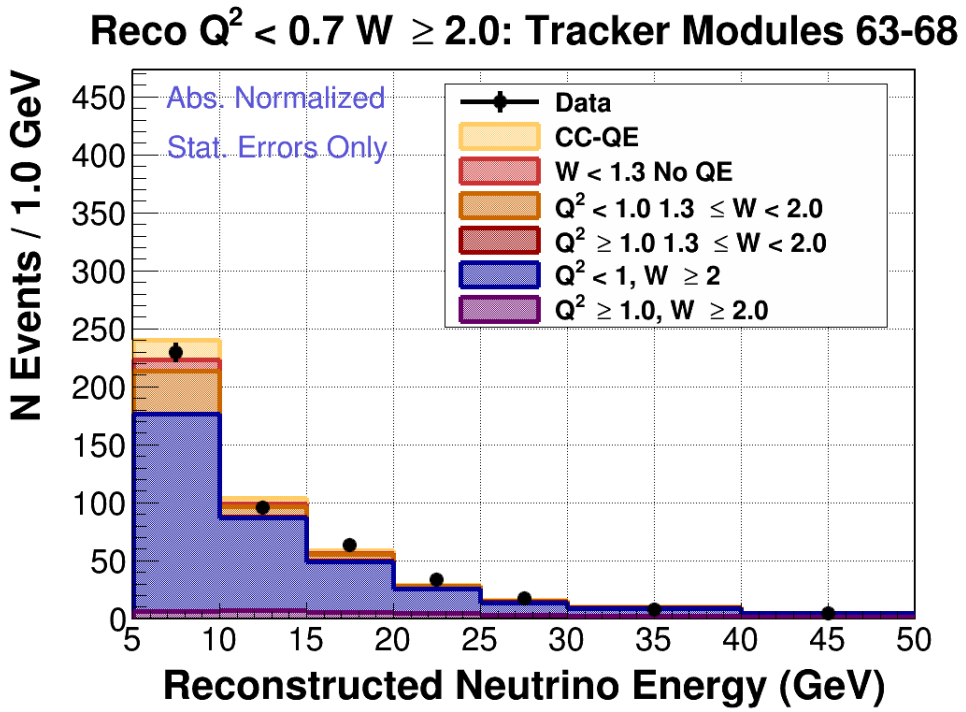

Figure A-304. Data / MC low Q^2 sideband after fitting: tracker mods. 63-68 (E_ν)

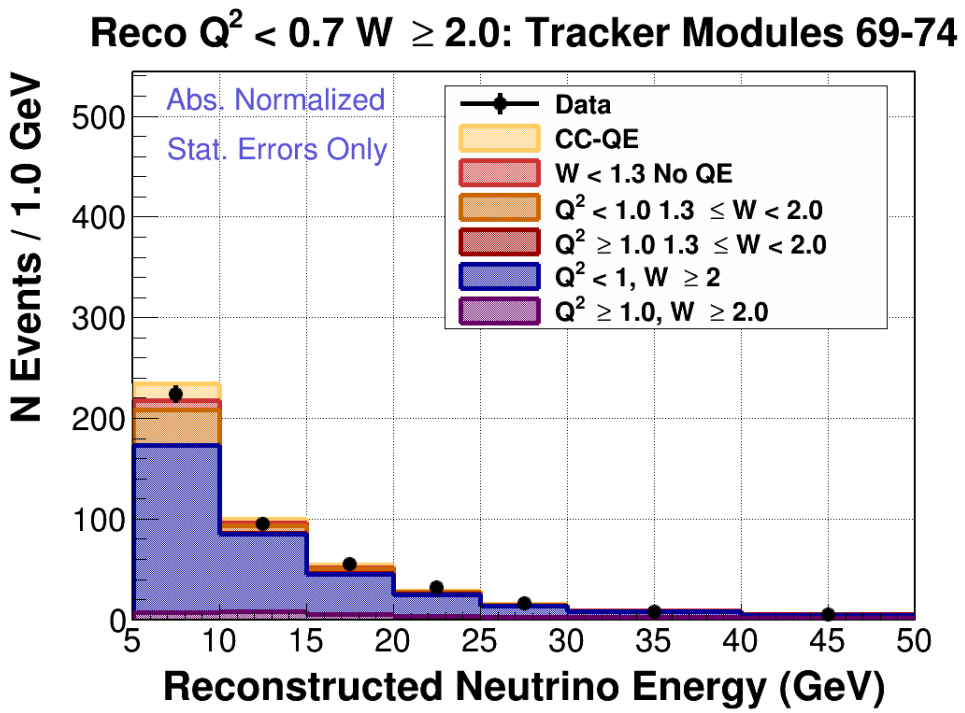

Figure A-305. Data / MC low Q^2 sideband after fitting: tracker mods. 69-74 (E_ν)

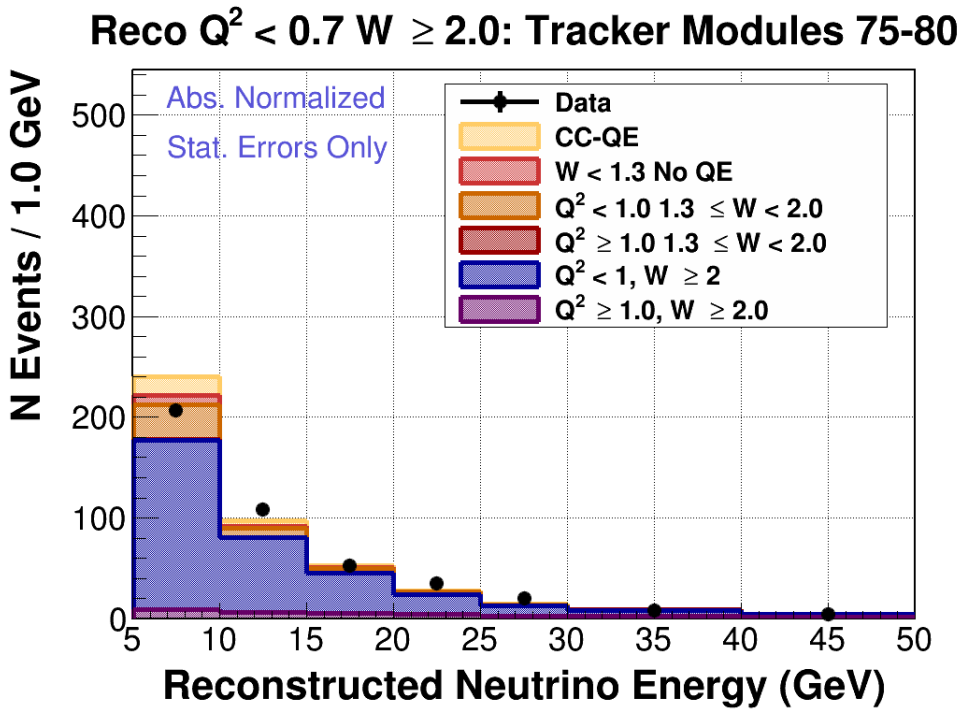

Figure A-306. Data / MC low Q^2 sideband after fitting: tracker mods. 75-80 (E_ν)

The following plots show the population of the low Q^2 sideband ($Q^2 < 0.8$ (GeV/c)^2 $W \geq 2.0$ GeV/c^2) *after* tuning to data as a function of final state hadronic shower invariant mass (W):

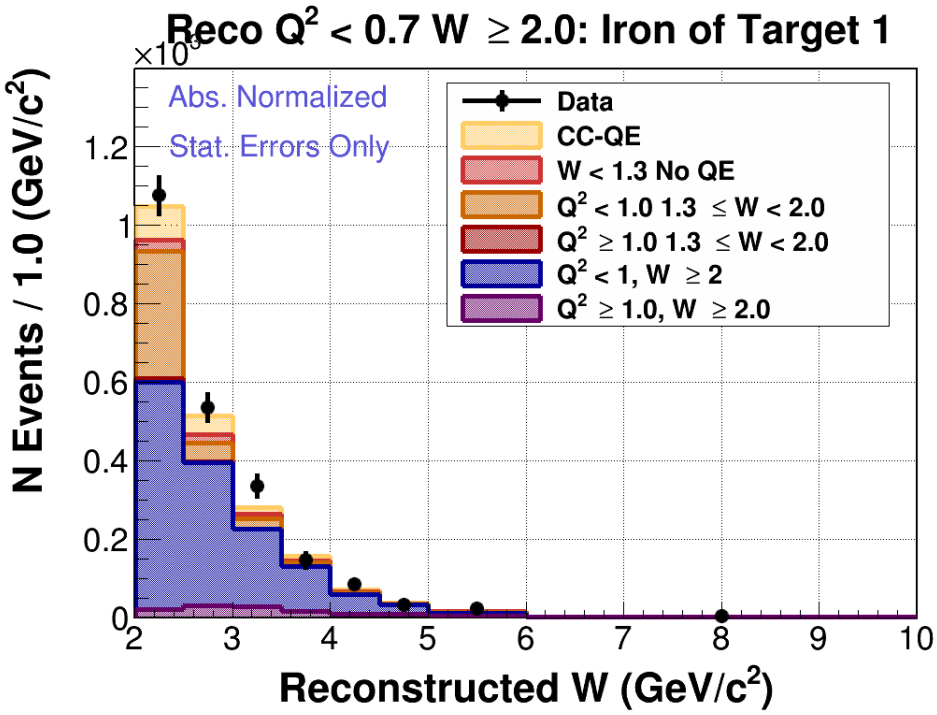

Figure A-307. Data / MC low Q^2 sideband after fitting: target 01 Fe (W)

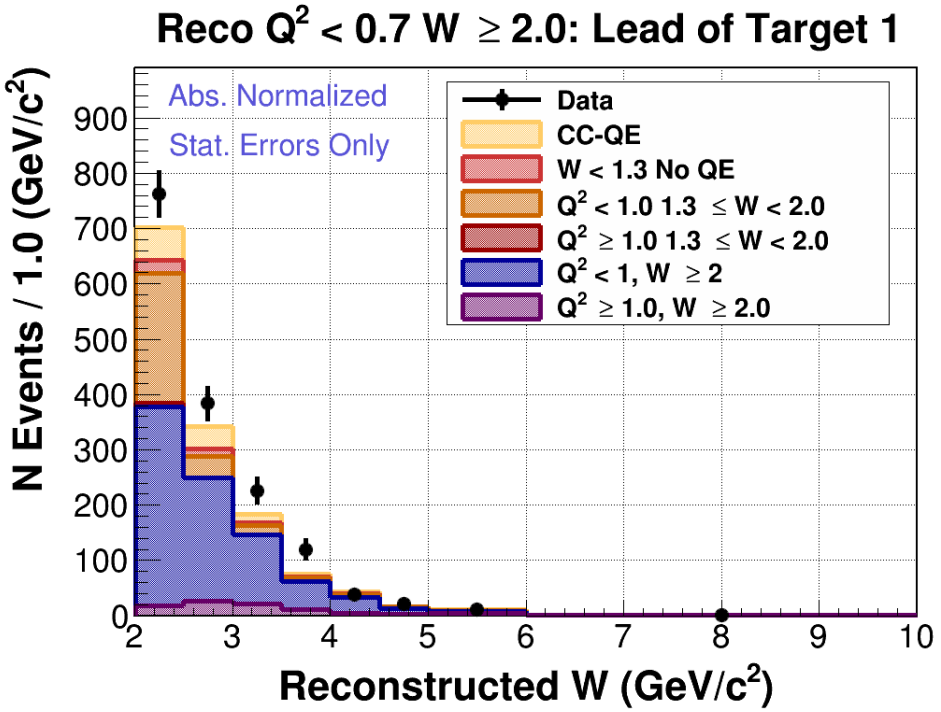

Figure A-308. Data / MC low Q^2 sideband after fitting: target 01 Pb (W)

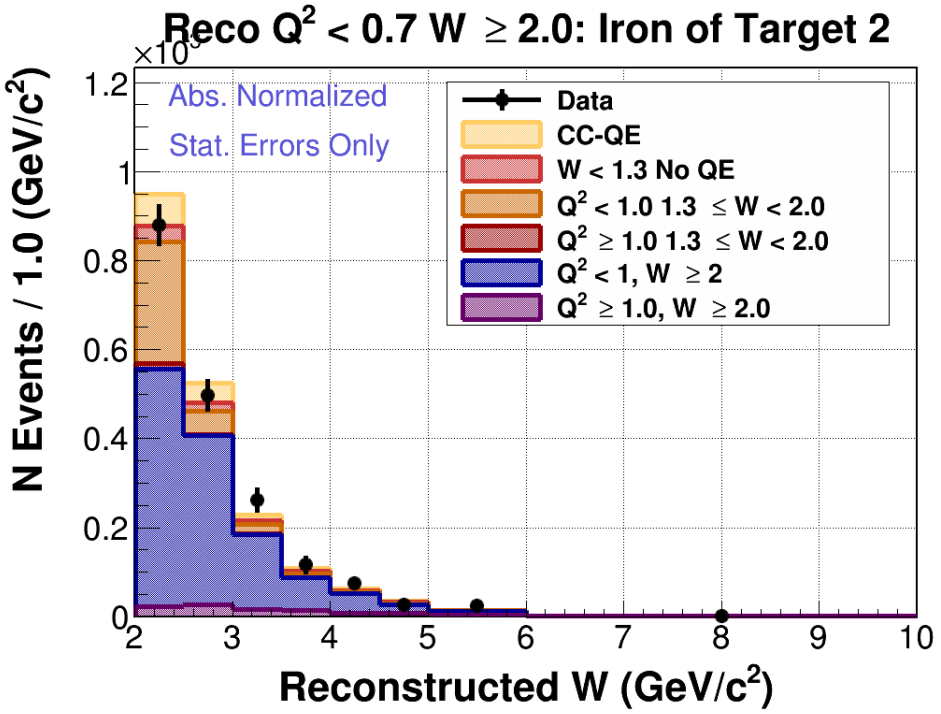

Figure A-309. Data / MC low Q^2 sideband after fitting: target 02 Fe (W)

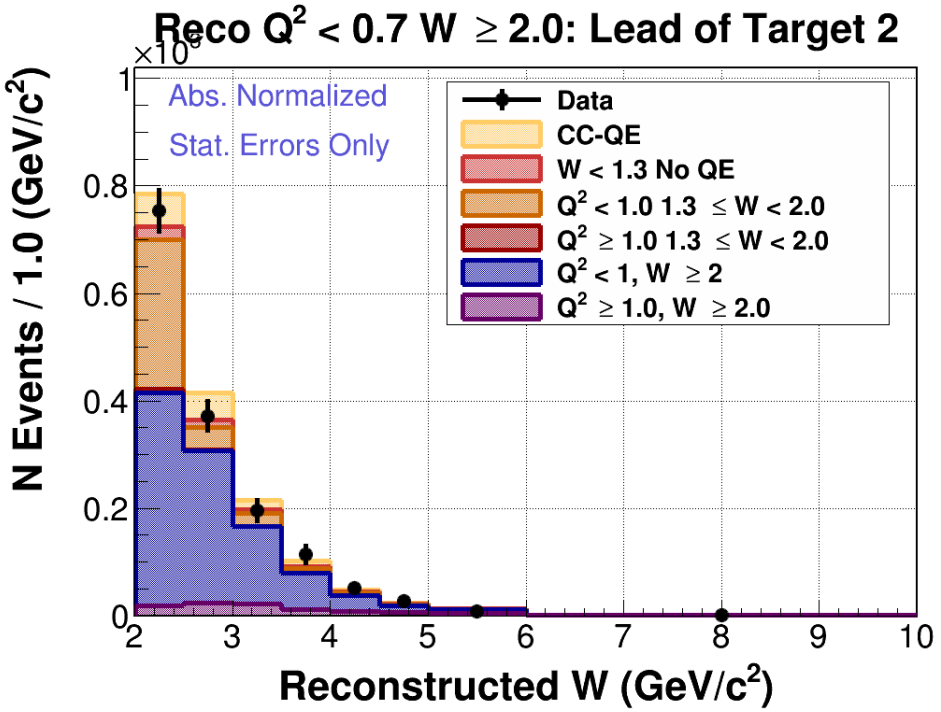

Figure A-310. Data / MC low Q^2 sideband after fitting: target 02 Pb (W)

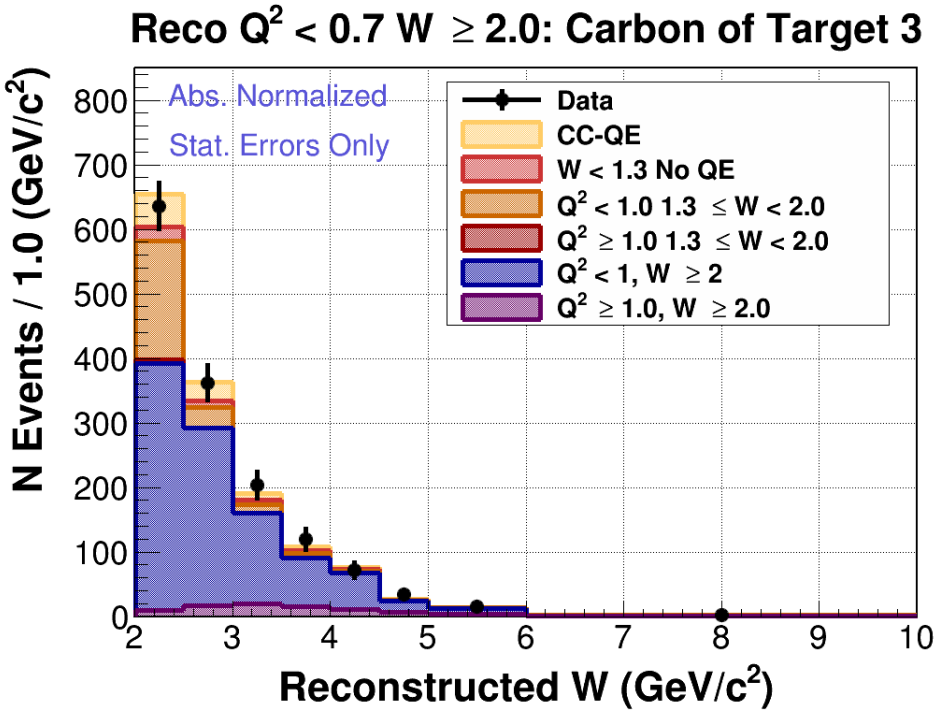

Figure A-311. Data / MC low Q^2 sideband after fitting: target 03 C (W)

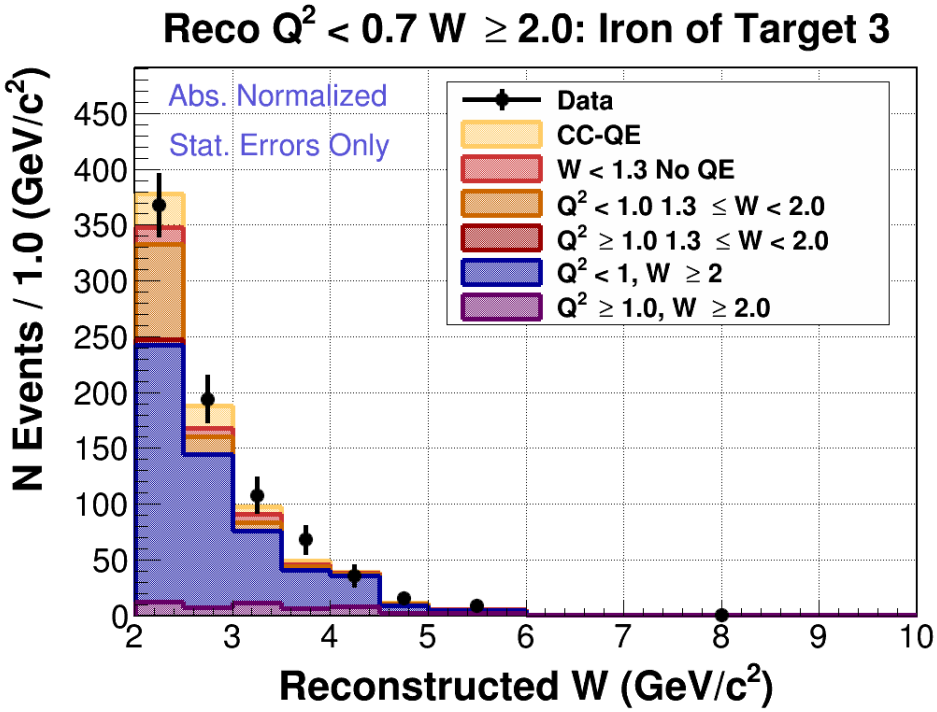

Figure A-312. Data / MC low Q^2 sideband after fitting: target 03 Fe (W)

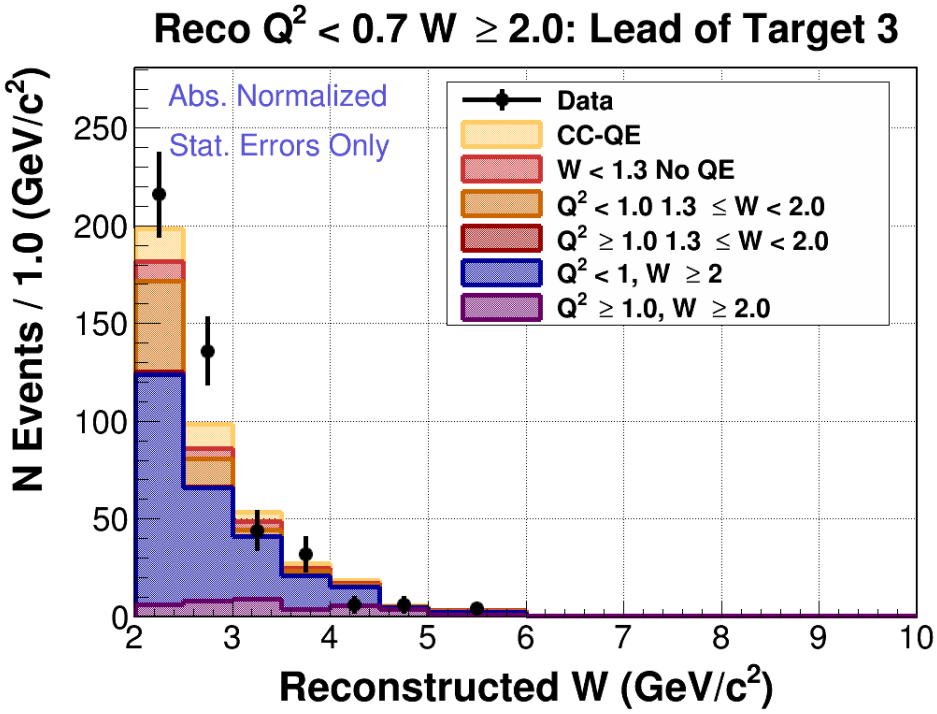

Figure A-313. Data / MC low Q^2 sideband after fitting: target 03 Pb (W)

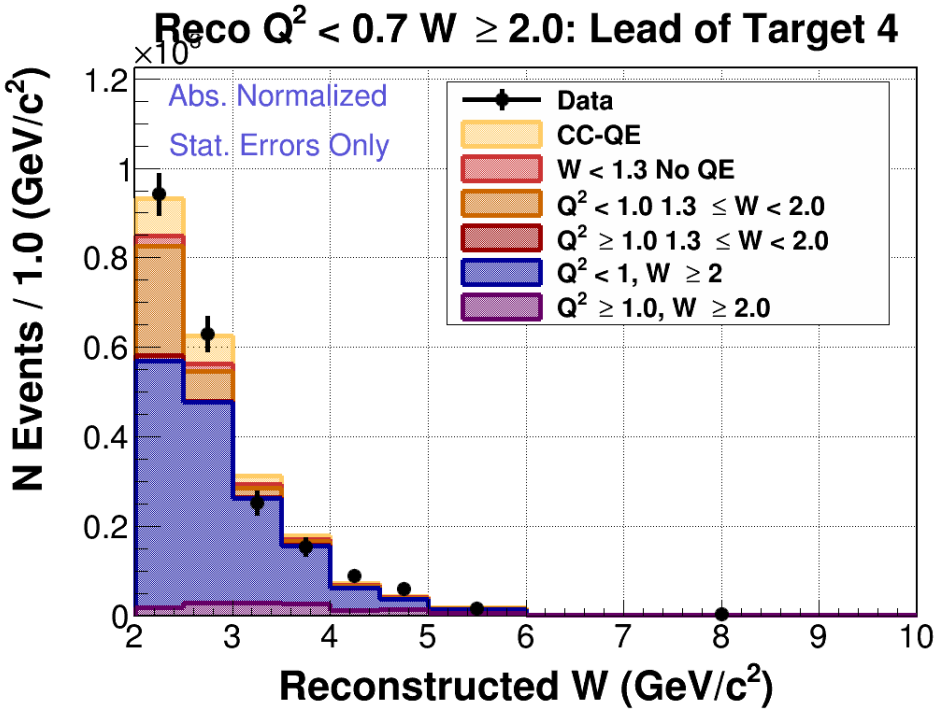

Figure A-314. Data / MC low Q^2 sideband after fitting: target 04 Pb (W)

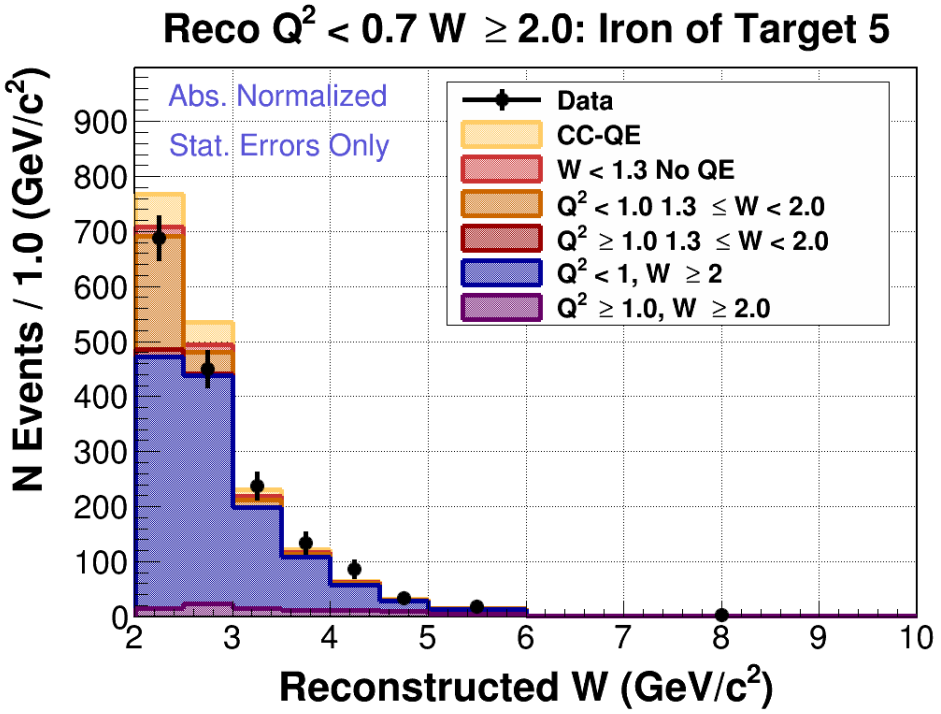

Figure A-315. Data / MC low Q^2 sideband after fitting: target 05 Fe (W)

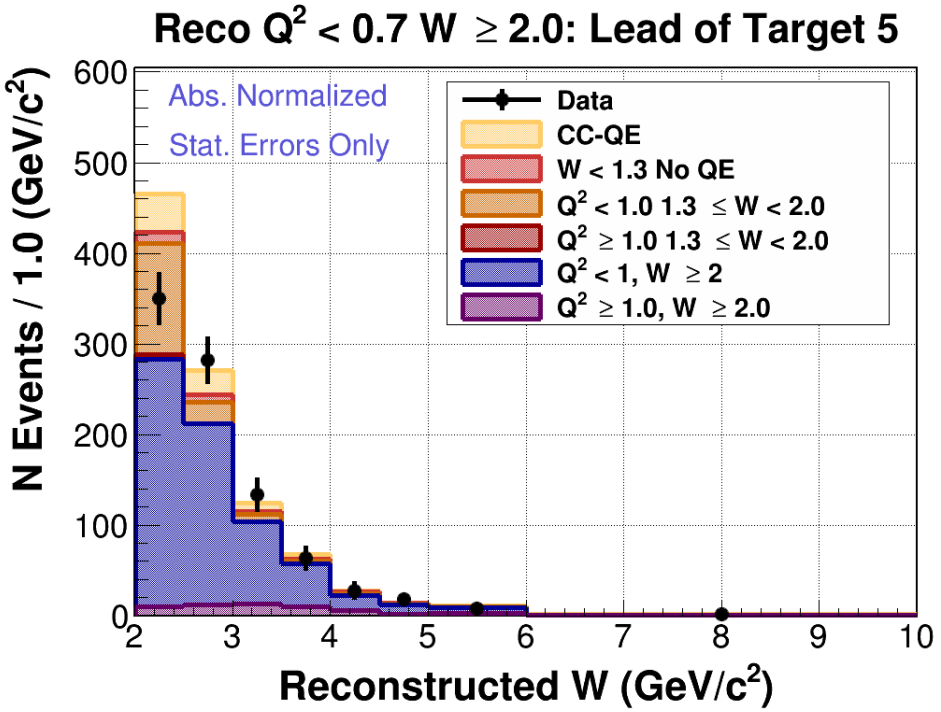

Figure A-316. Data / MC low Q^2 sideband after fitting: target 05 Pb (W)

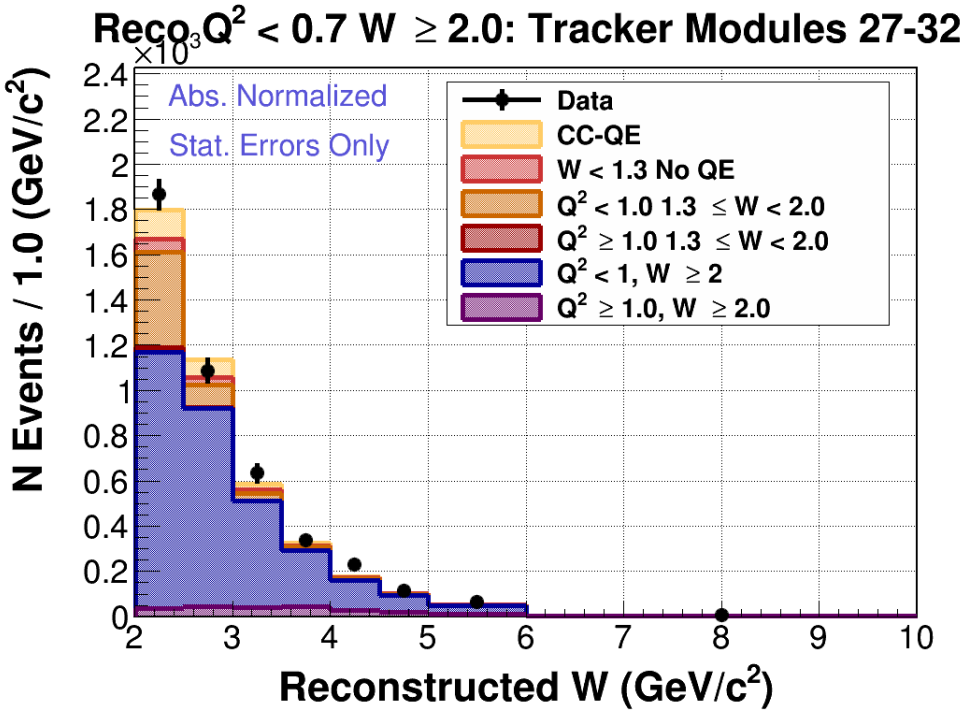

Figure A-317. Data / MC low Q^2 sideband after fitting: tracker mods. 27-32 (W)

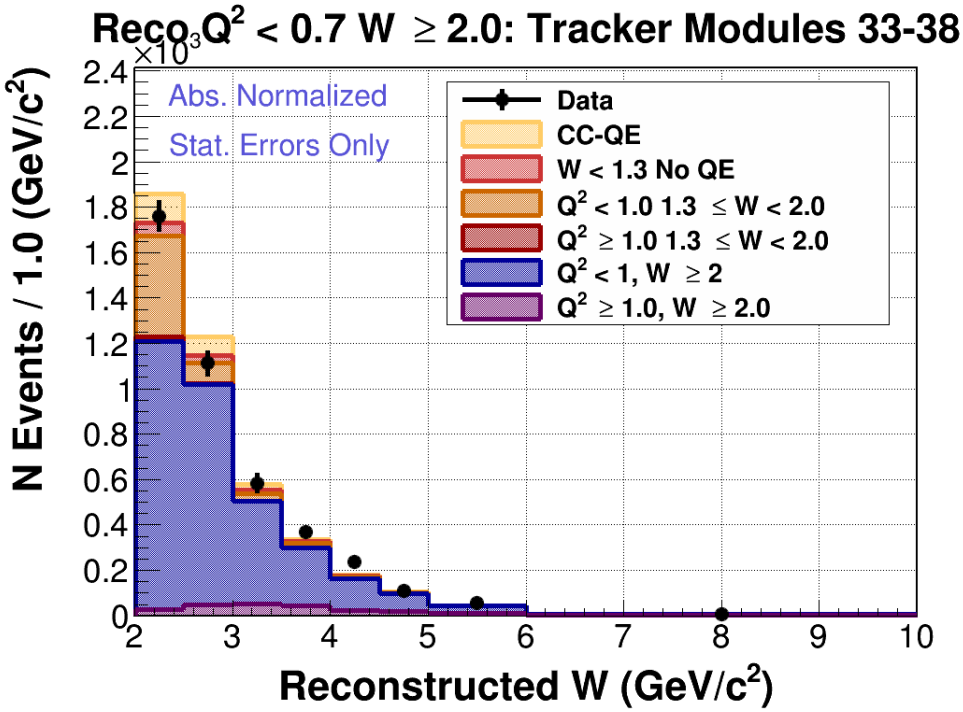

Figure A-318. Data / MC low Q^2 sideband after fitting: tracker mods. 33-38 (W)

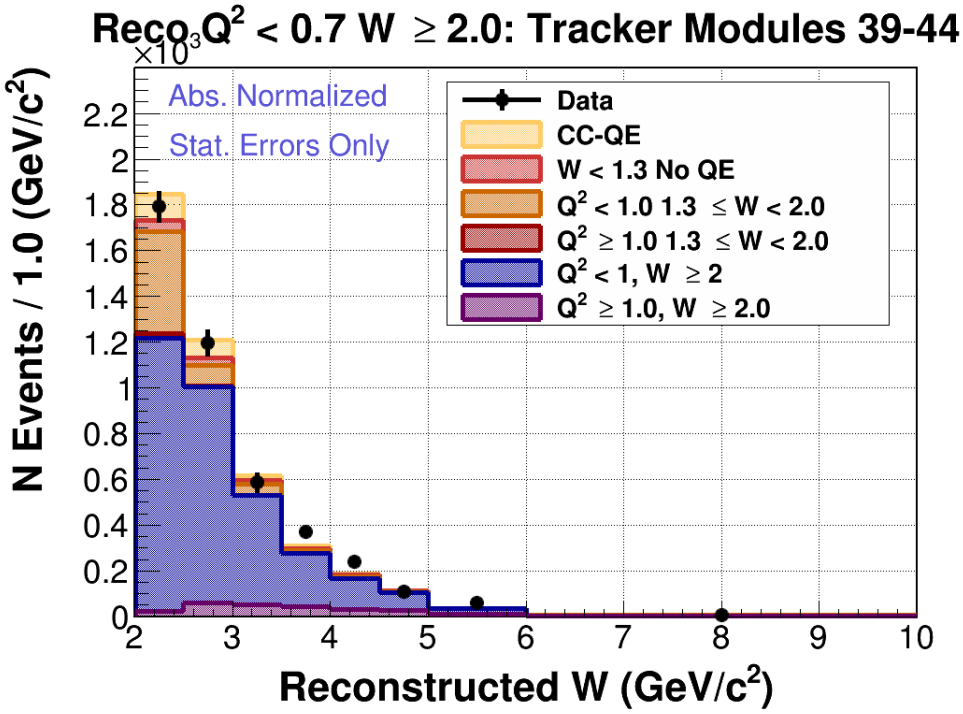

Figure A-319. Data / MC low Q^2 sideband after fitting: tracker mods. 39-44 (W)

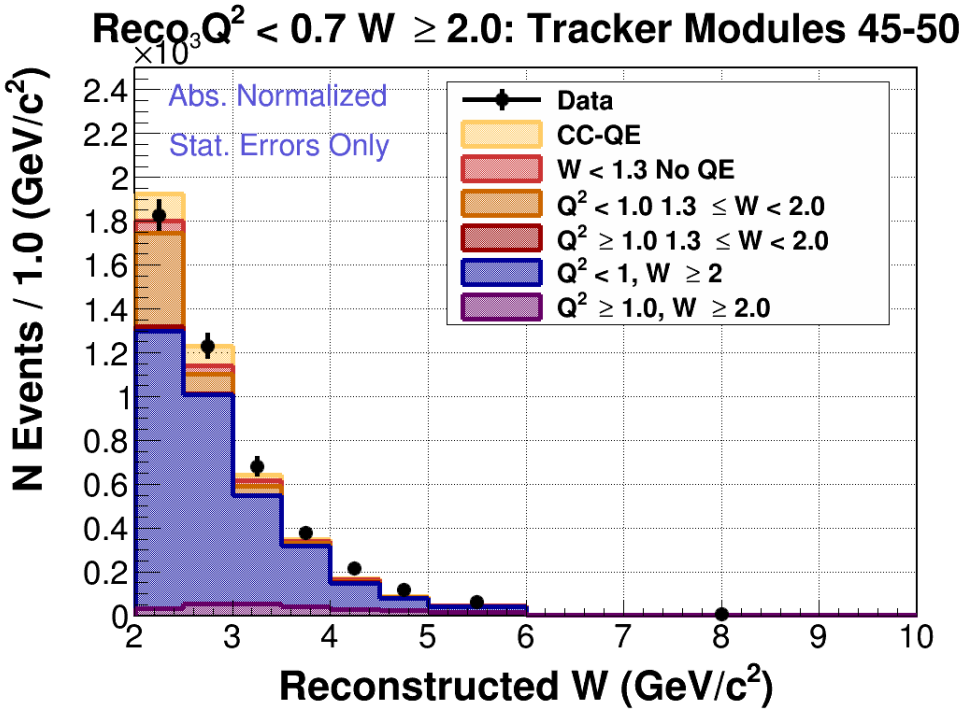

Figure A-320. Data / MC low Q^2 sideband after fitting: tracker mods. 45-50 (W)

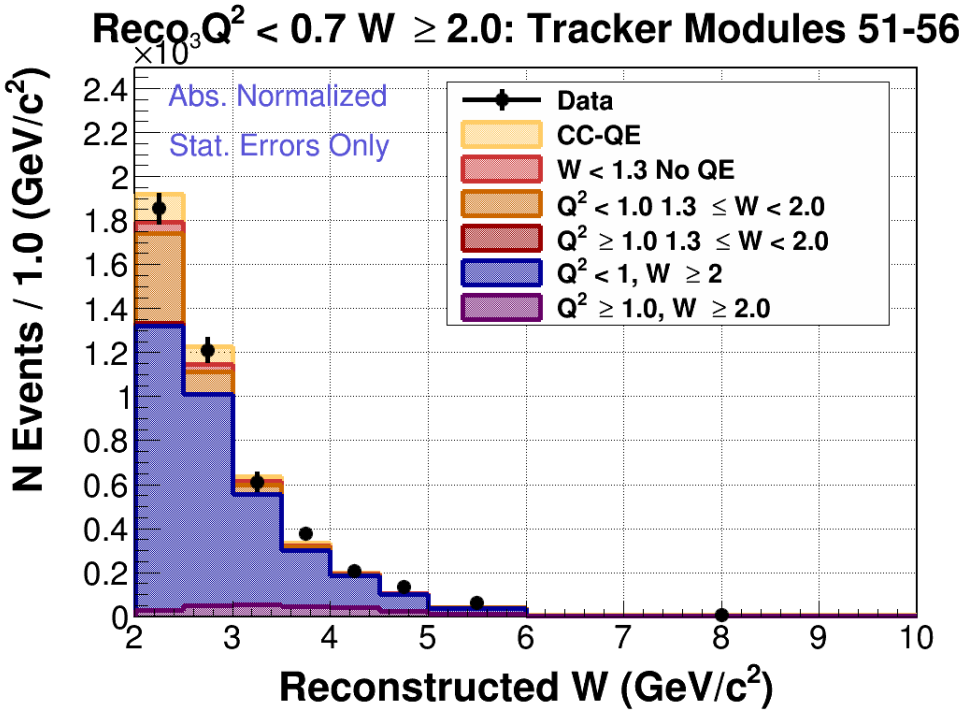

Figure A-321. Data / MC low Q^2 sideband after fitting: tracker mods. 51-56 (W)

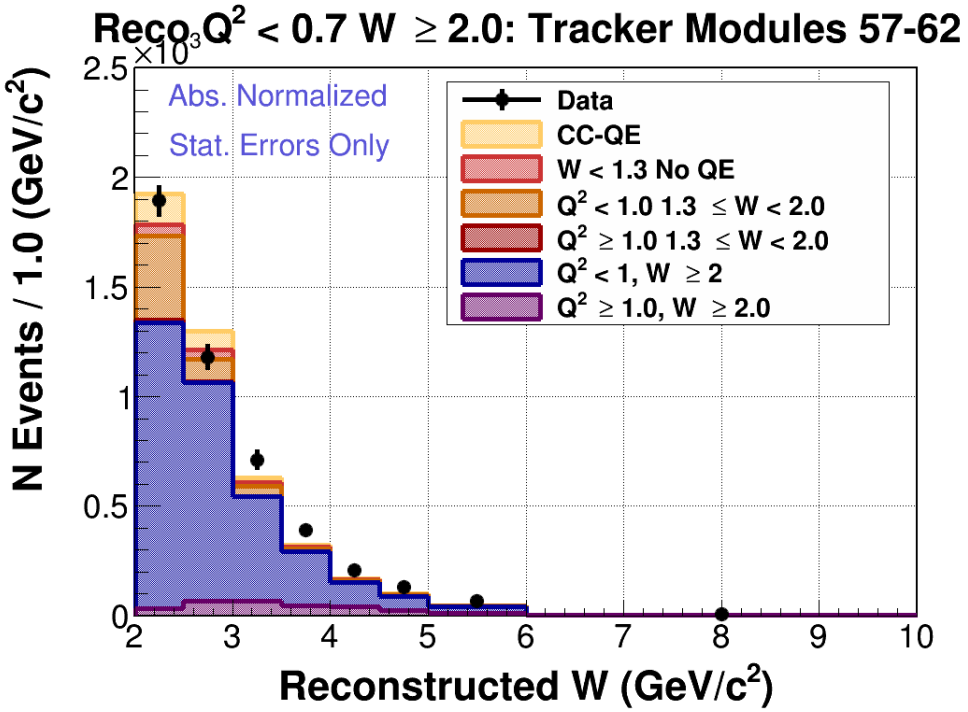

Figure A-322. Data / MC low Q^2 sideband after fitting: tracker mods. 57-62 (W)

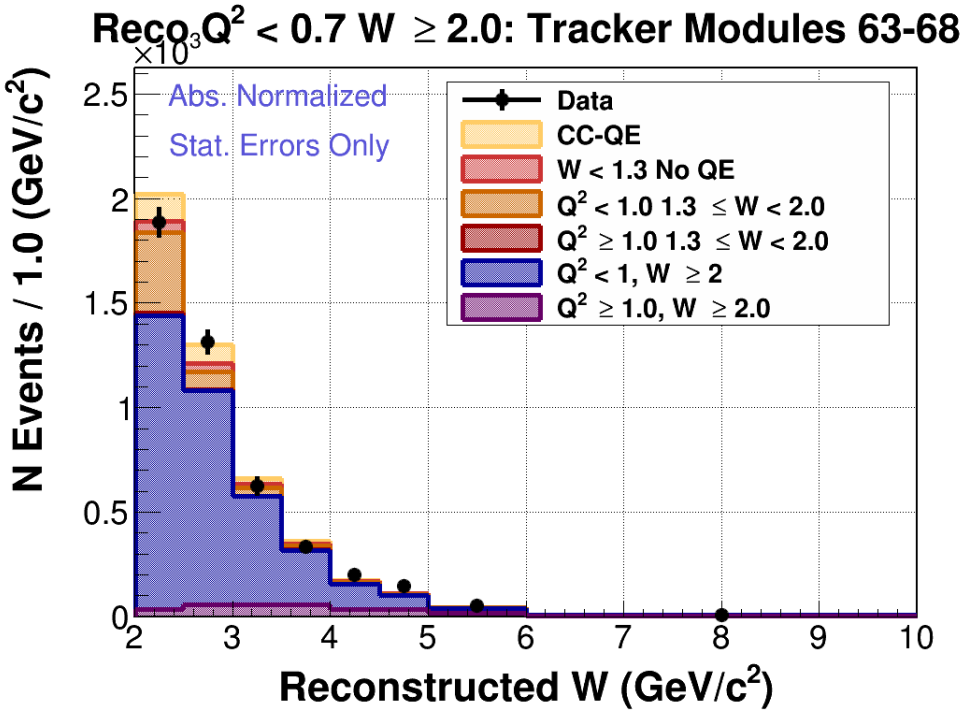

Figure A-323. Data / MC low Q^2 sideband after fitting: tracker mods. 63-68 (W)

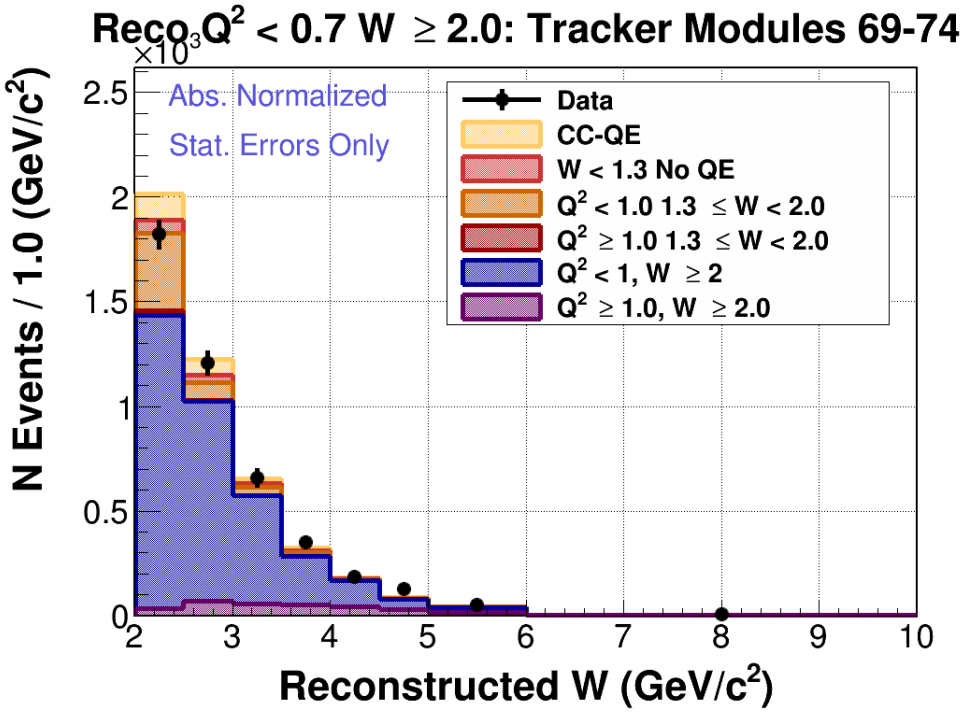

Figure A-324. Data / MC low Q^2 sideband after fitting: tracker mods. 69-74 (W)

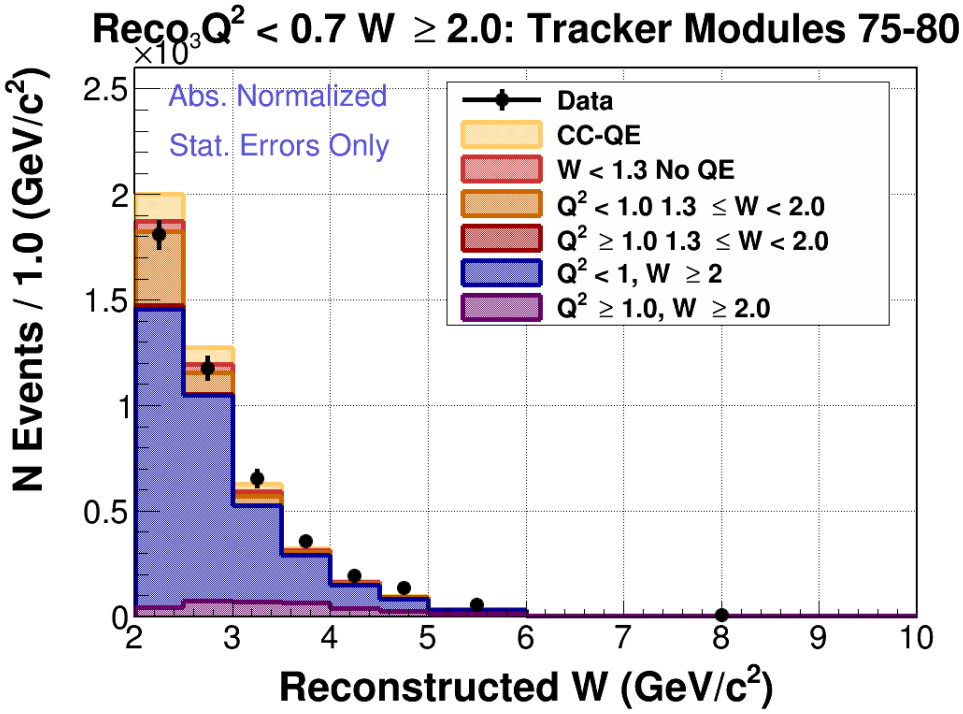

Figure A-325. Data / MC low Q^2 sideband after fitting: tracker mods. 75-80 (W)

The following plots show the population of the low Q^2 sideband ($Q^2 < 0.8$ (GeV/c)^2 $W \geq 2.0$ GeV/c^2) *after* tuning to data as a function of Bjorken-x (x_{bj}):

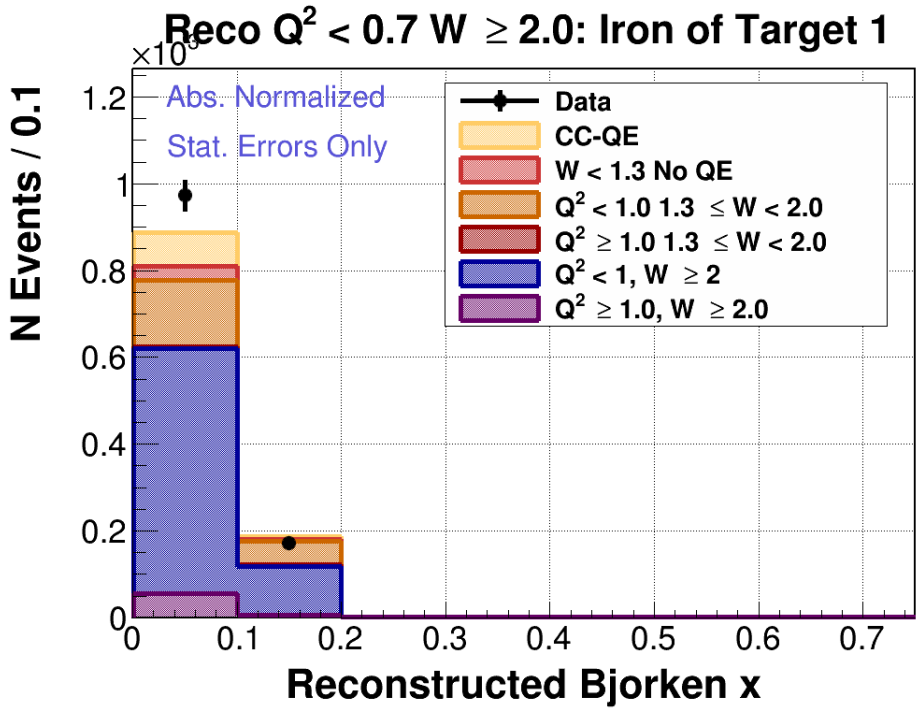

Figure A-326. Data / MC low Q^2 sideband after fitting: target 01 Fe (x_{bj})

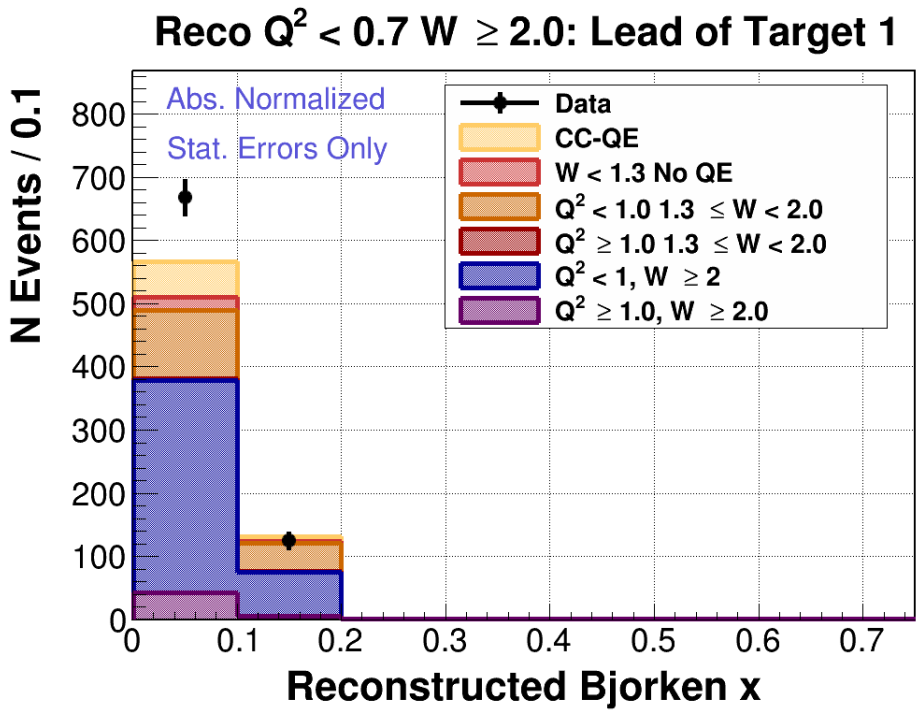

Figure A-327. Data / MC low Q^2 sideband after fitting: target 01 Pb (x_{bj})

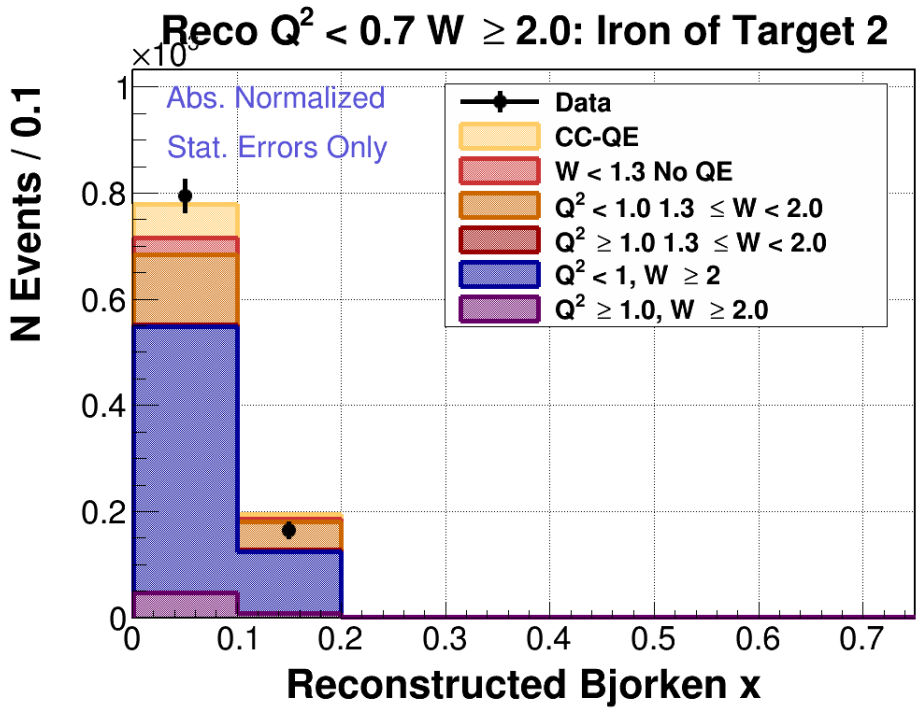

Figure A-328. Data / MC low Q^2 sideband after fitting: target 02 Fe (x_{bj})

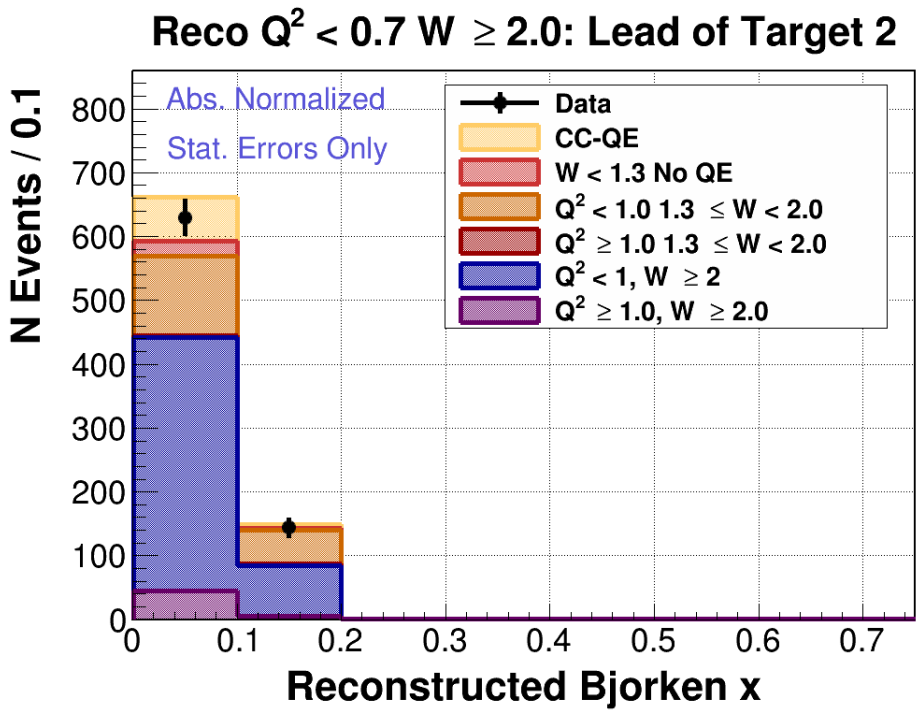

Figure A-329. Data / MC low Q^2 sideband after fitting: target 02 Pb (x_{bj})

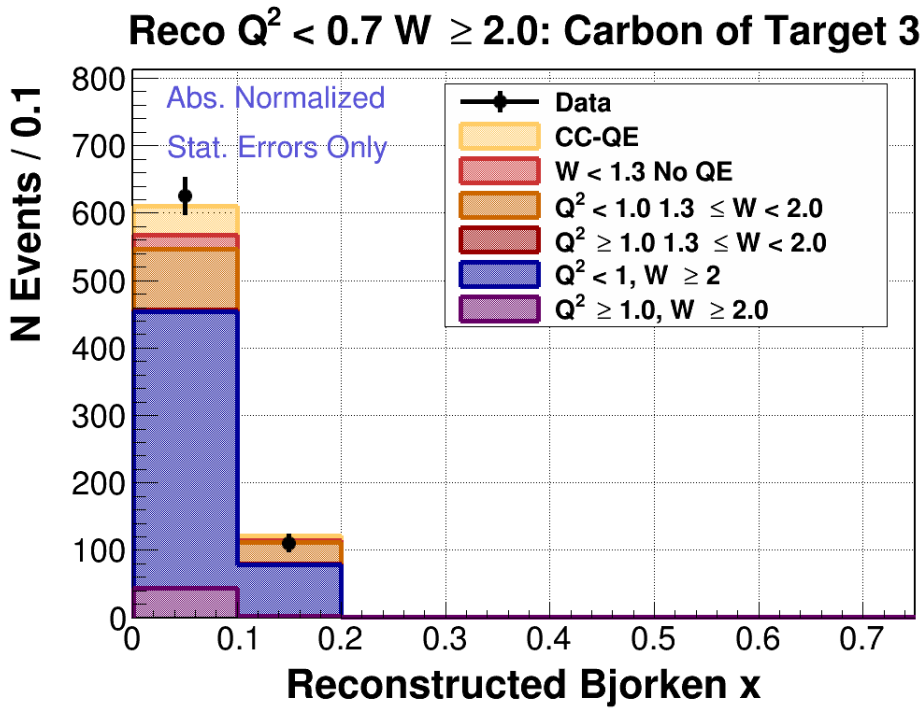

Figure A-330. Data / MC low Q^2 sideband after fitting: target 03 C (x_{bj})

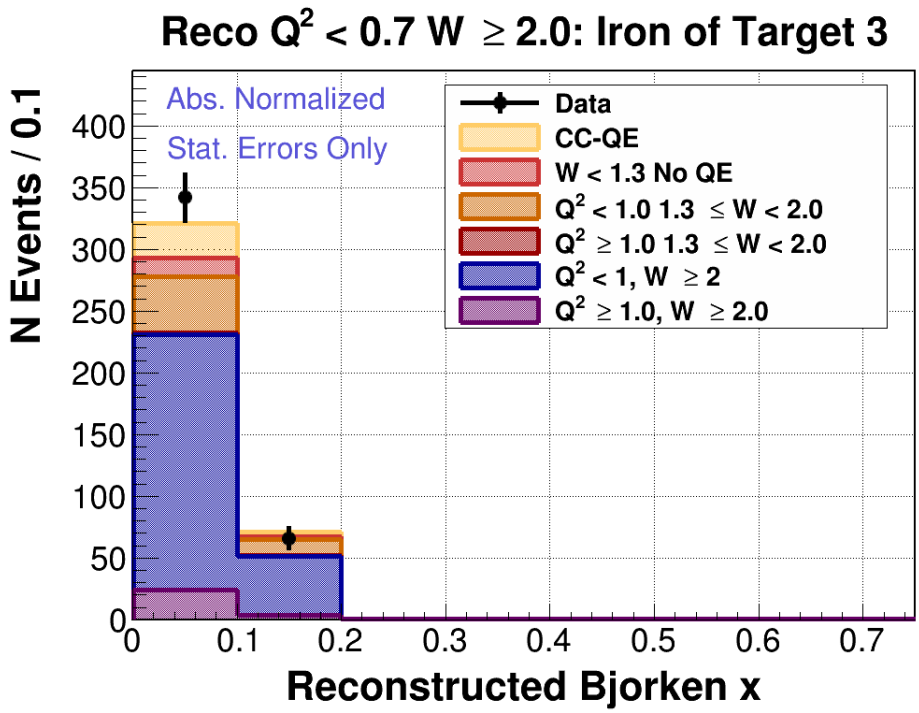

Figure A-331. Data / MC low Q^2 sideband after fitting: target 03 Fe (x_{bj})

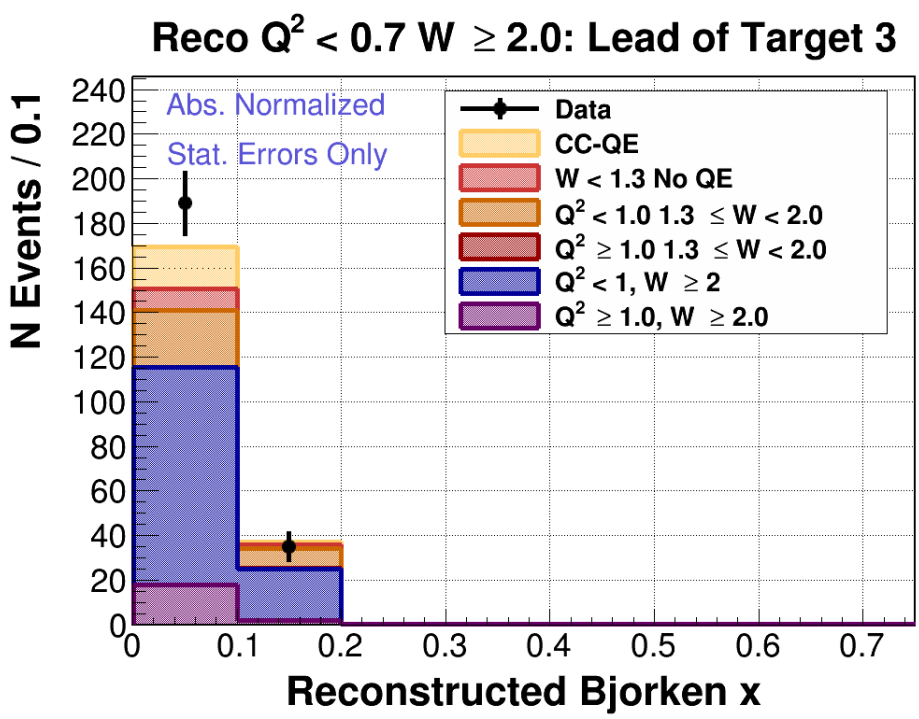

Figure A-332. Data / MC low Q^2 sideband after fitting: target 03 Pb (x_{bj})

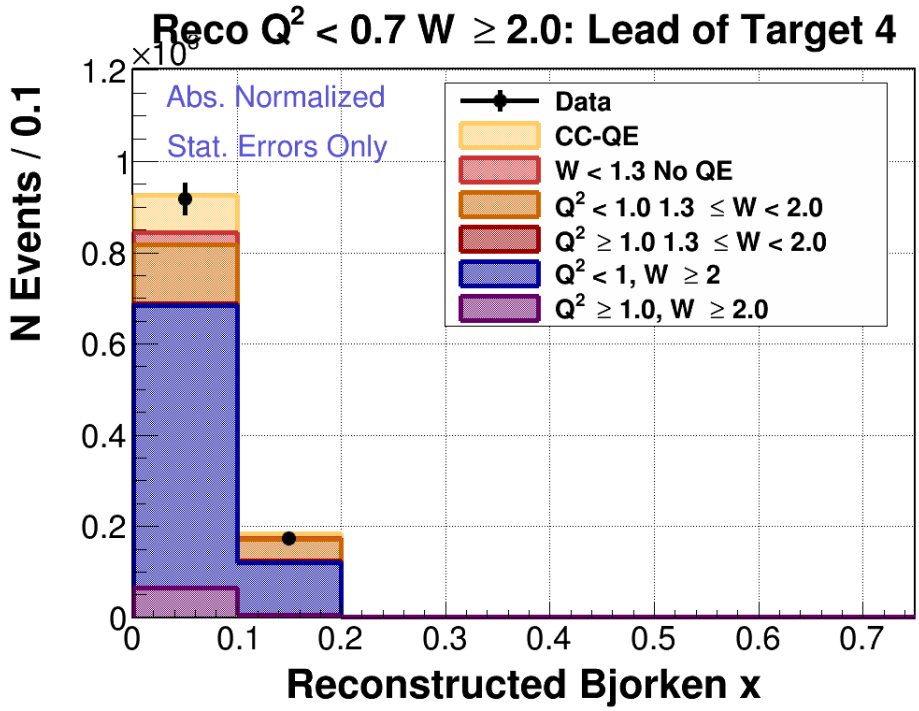

Figure A-333. Data / MC low Q^2 sideband after fitting: target 04 Pb (x_{bj})

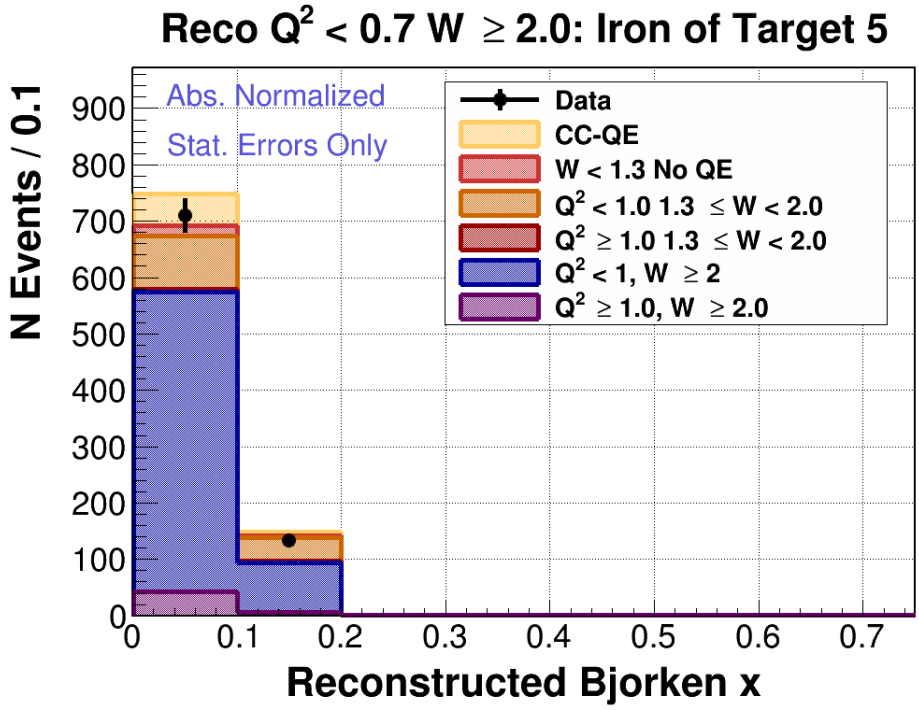

Figure A-334. Data / MC low Q^2 sideband after fitting: target 05 Fe (x_{bj})

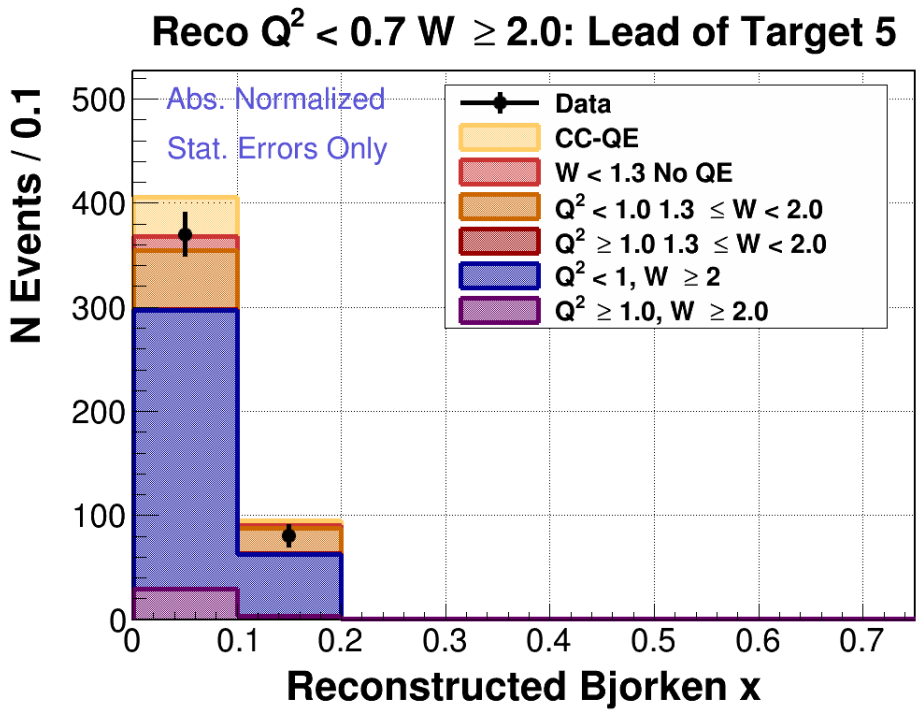

Figure A-335. Data / MC low Q^2 sideband after fitting: target 05 Pb (x_{bj})

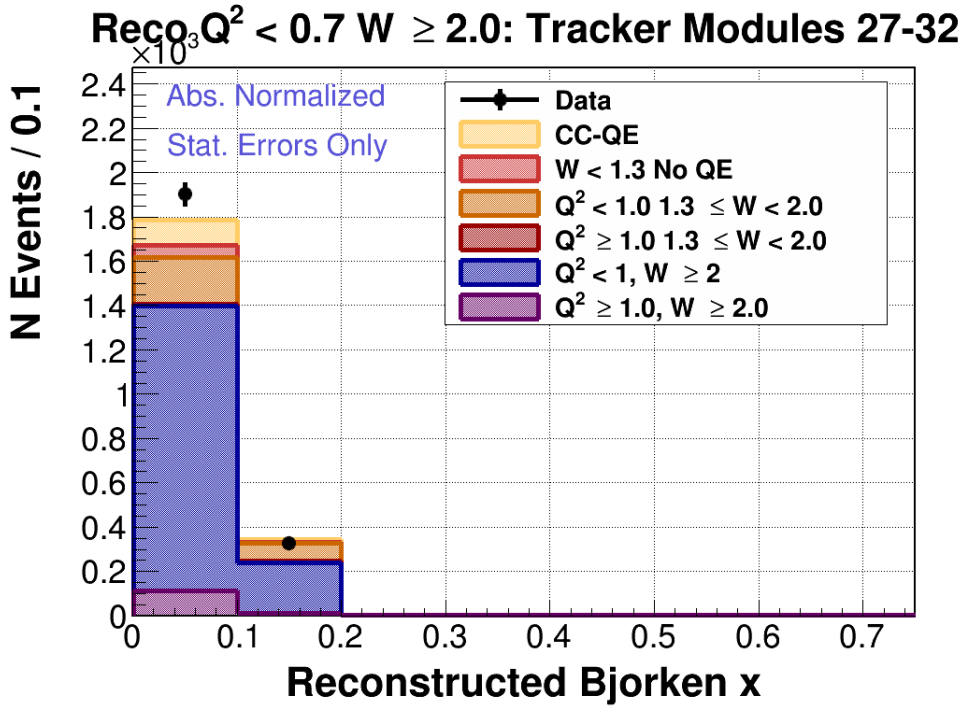

Figure A-336. Data / MC low Q^2 sideband after fitting: tracker mods. 27-32 (x_{bj})

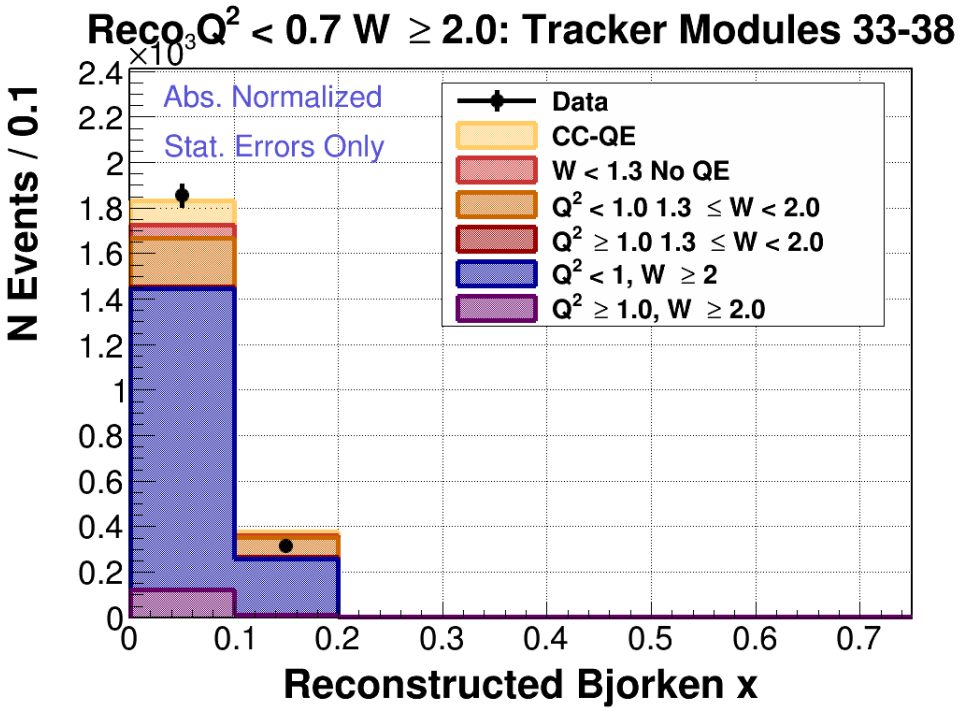

Figure A-337. Data / MC low Q^2 sideband after fitting: tracker mods. 33-38 (x_{bj})

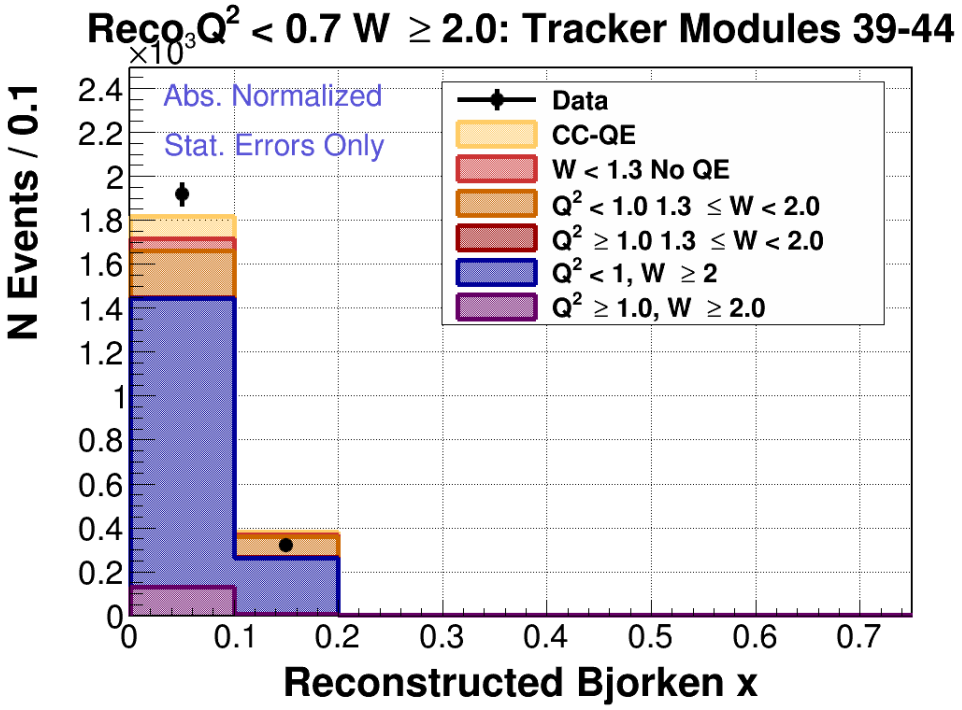

Figure A-338. Data / MC low Q^2 sideband after fitting: tracker mods. 39-44 (x_{bj})

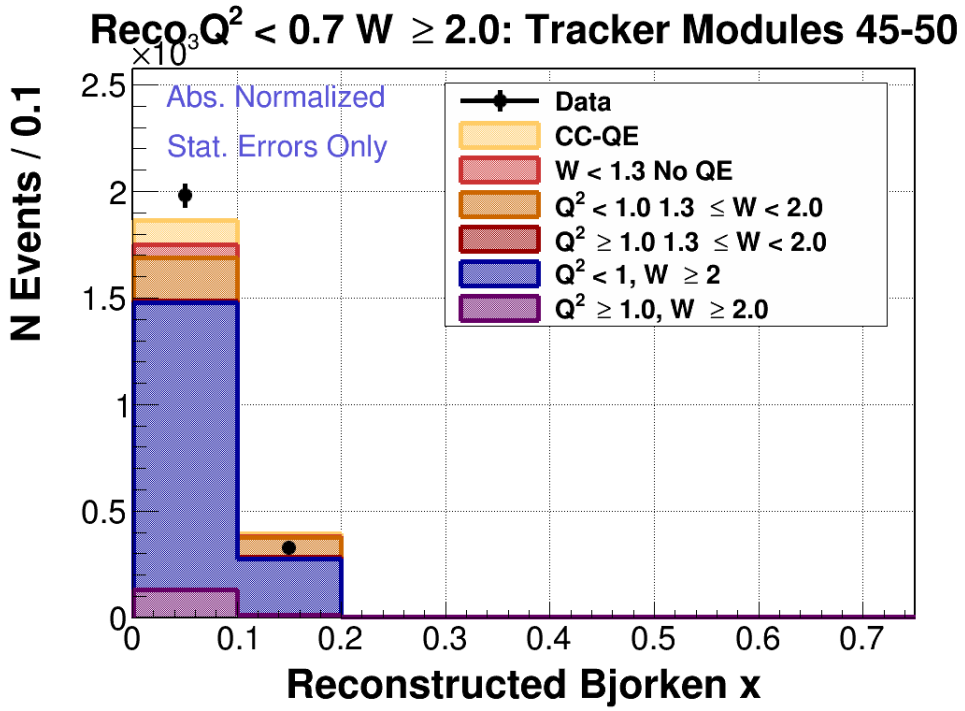

Figure A-339. Data / MC low Q^2 sideband after fitting: tracker mods. 45-50 (x_{bj})

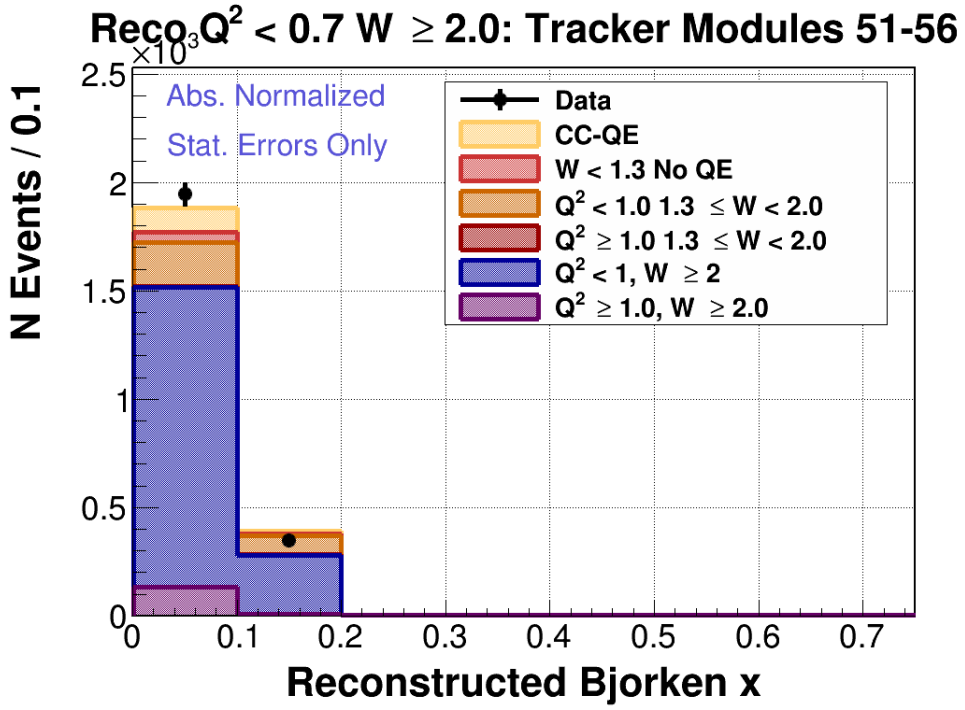

Figure A-340. Data / MC low Q^2 sideband after fitting: tracker mods. 51-56 (x_{bj})

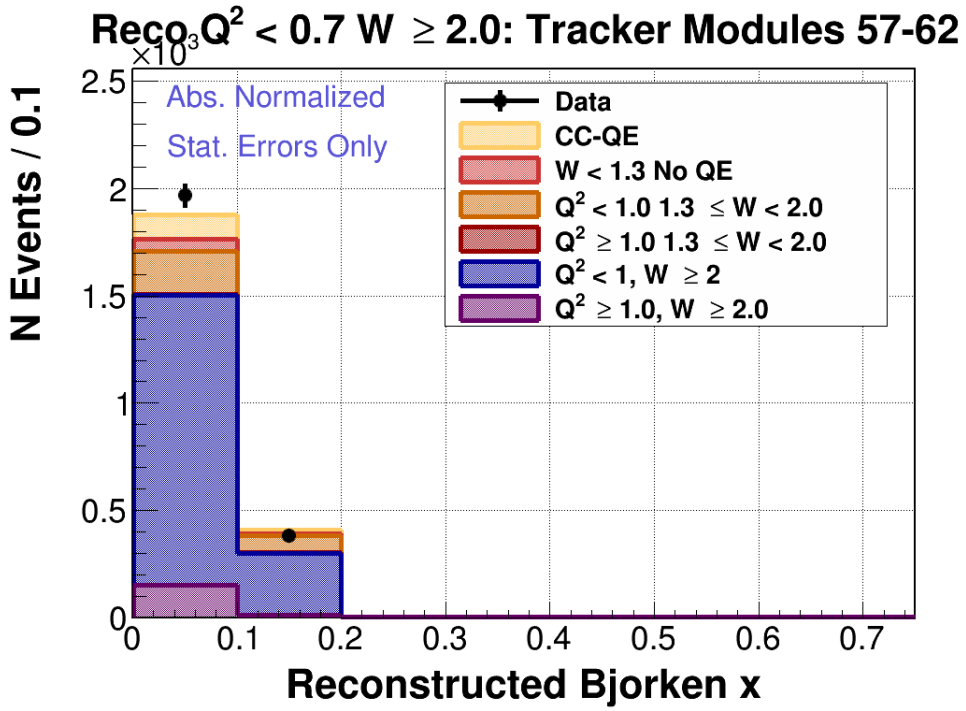

Figure A-341. Data / MC low Q^2 sideband after fitting: tracker mods. 57-62 (x_{bj})

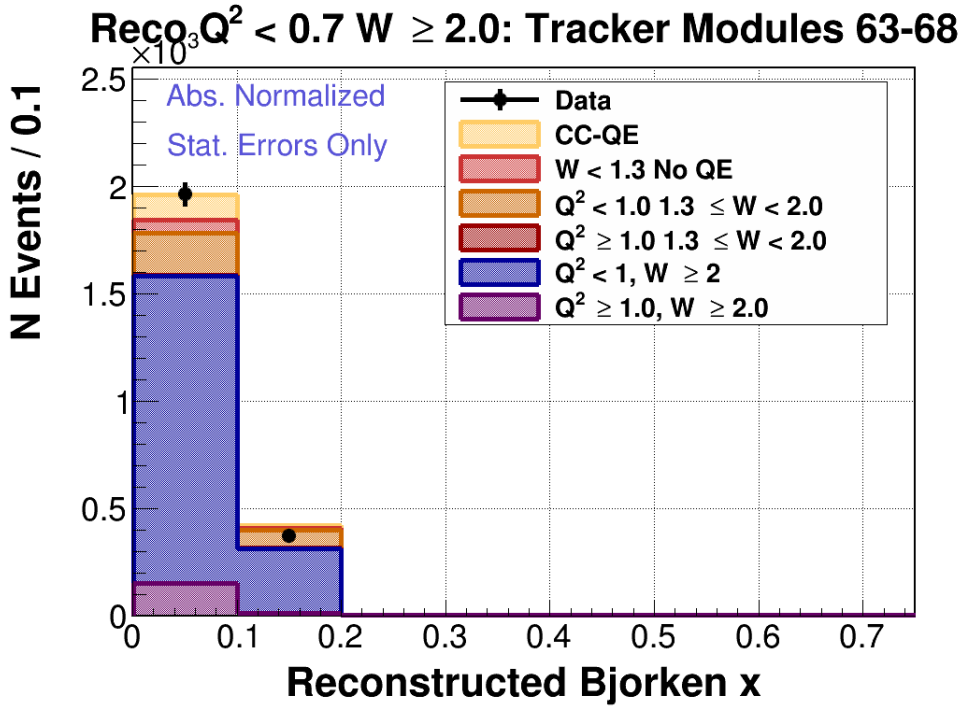

Figure A-342. Data / MC low Q^2 sideband after fitting: tracker mods. 63-68 (x_{bj})

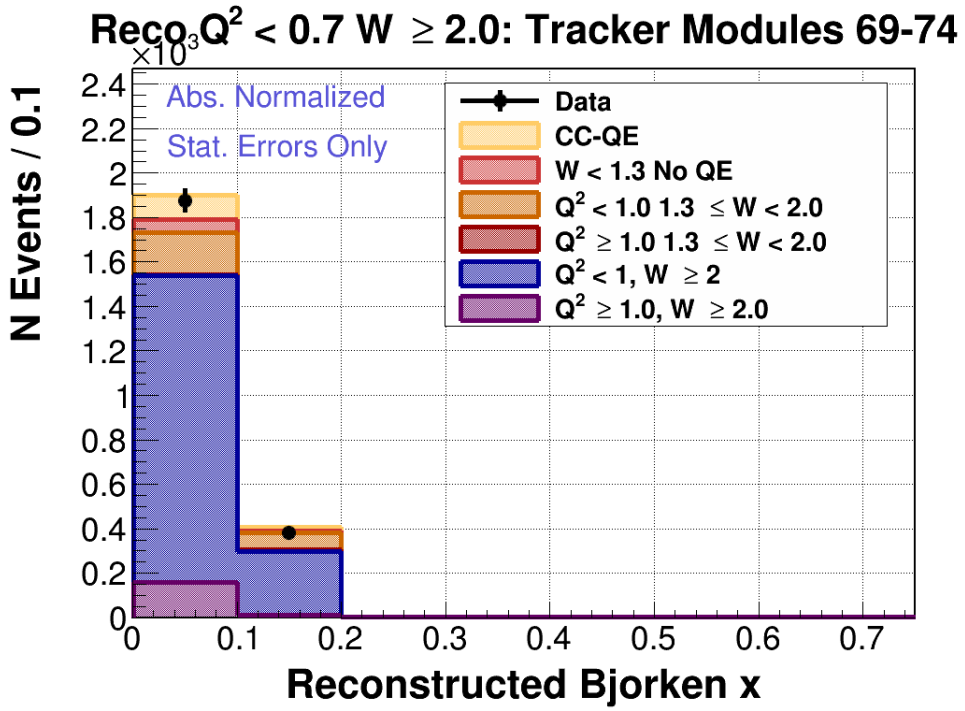

Figure A-343. Data / MC low Q^2 sideband after fitting: tracker mods. 69-74 (x_{bj})

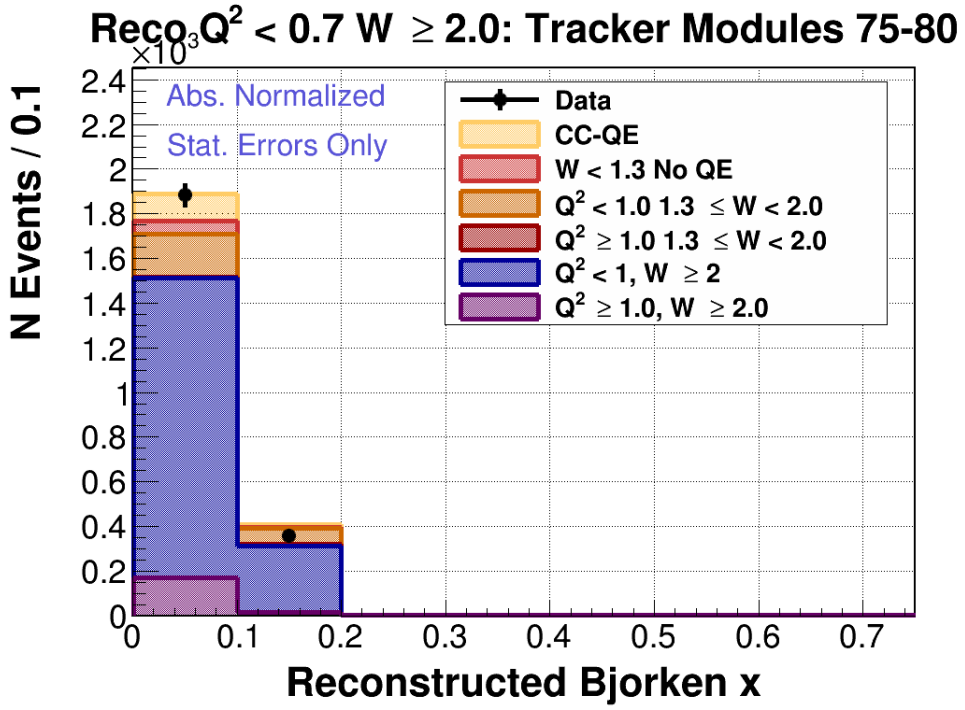

Figure A-344. Data / MC low Q^2 sideband after fitting: tracker mods. 75-80 (x_{bj})

The following plots show the population of the low Q^2 sideband ($Q^2 < 0.8$ (GeV/c)^2 $W \geq 2.0$ GeV/c^2) *after* tuning to data as a function of muon energy (E_μ):

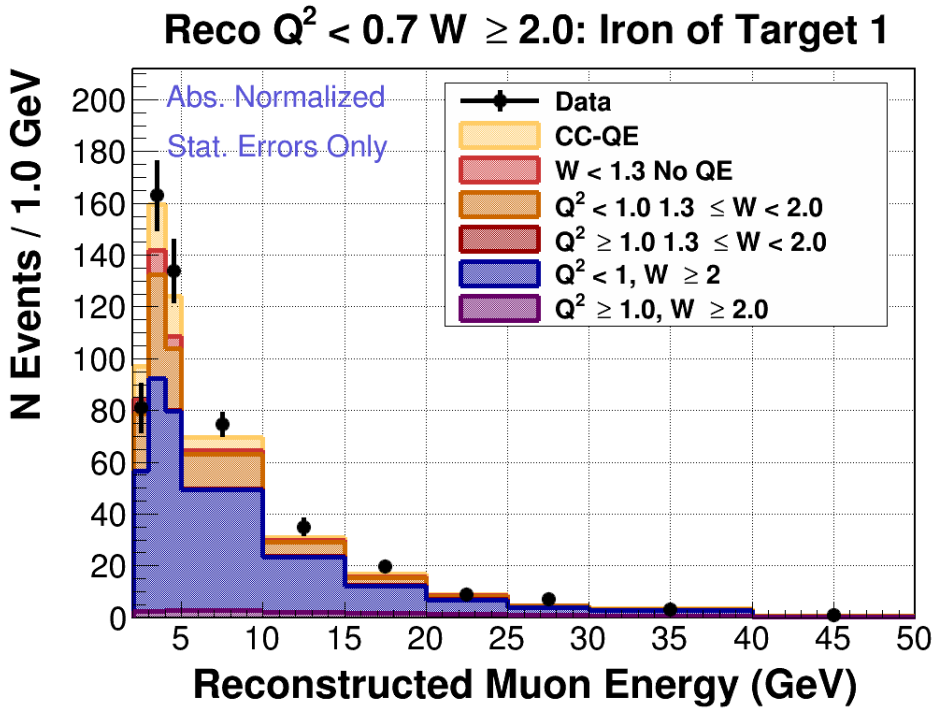

Figure A-345. Data / MC low Q^2 sideband after fitting: target 01 Fe (E_μ)

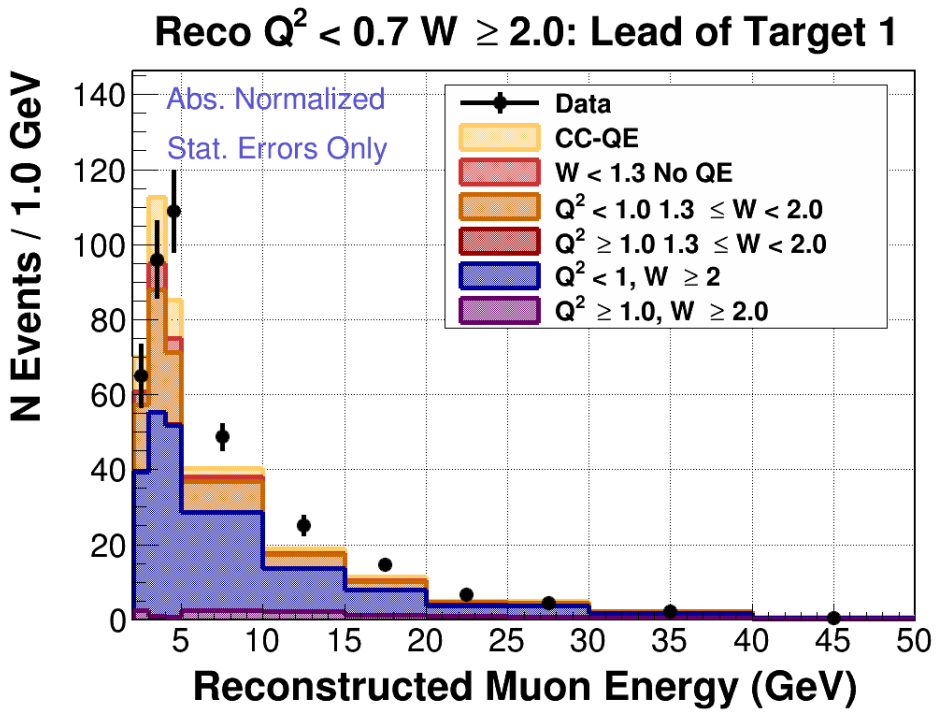

Figure A-346. Data / MC low Q^2 sideband after fitting: target 01 Pb (E_μ)

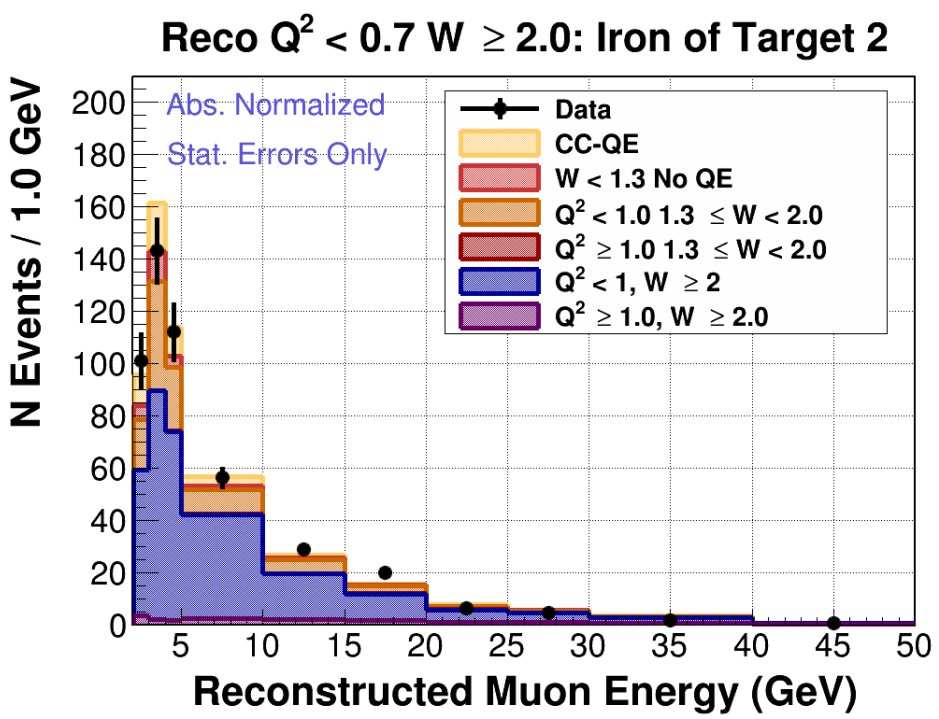

Figure A-347. Data / MC low Q^2 sideband after fitting: target 02 Fe (E_μ)

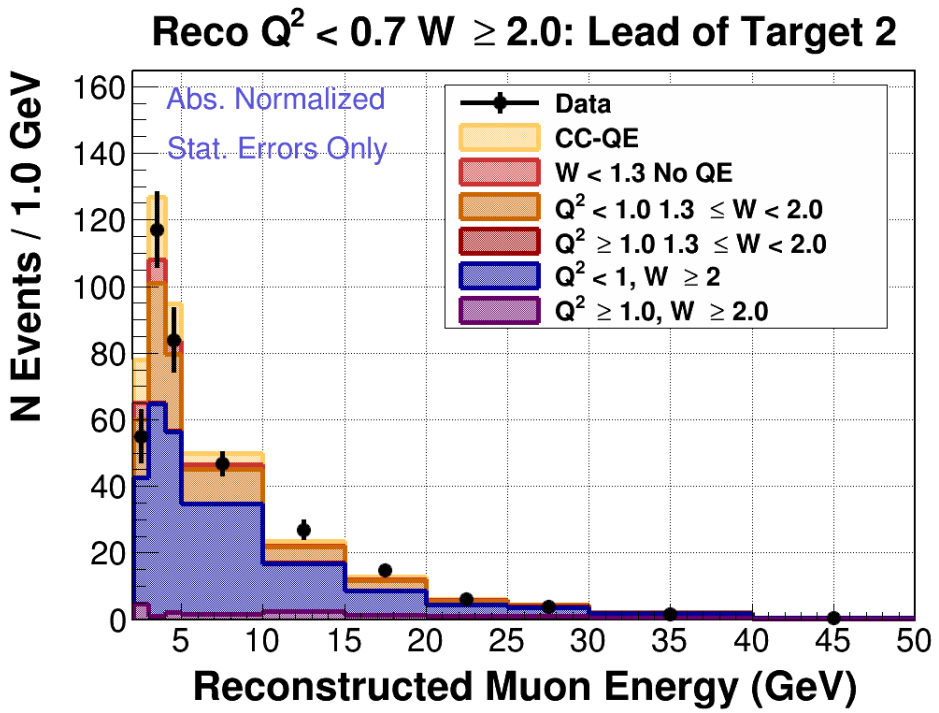

Figure A-348. Data / MC low Q^2 sideband after fitting: target 02 Pb (E_μ)

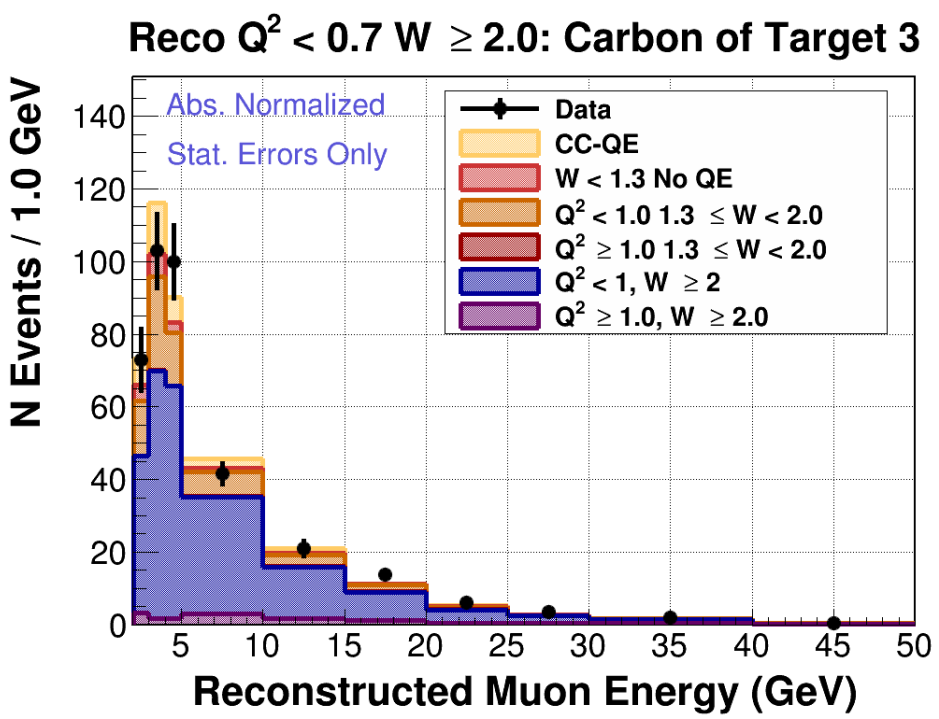

Figure A-349. Data / MC low Q^2 sideband after fitting: target 03 C (E_μ)

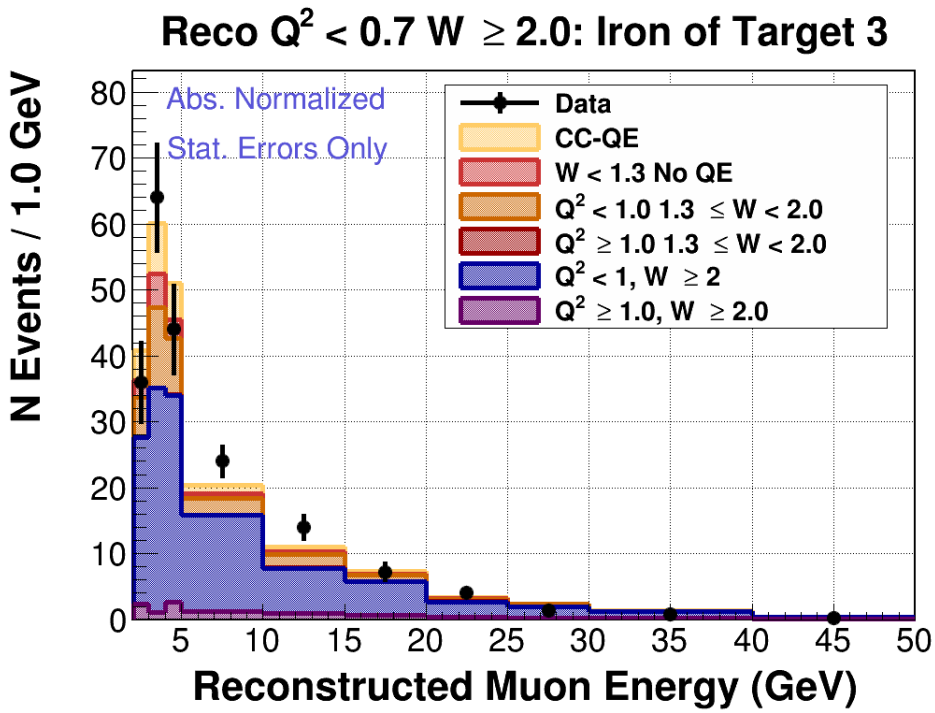

Figure A-350. Data / MC low Q^2 sideband after fitting: target 03 Fe (E_μ)

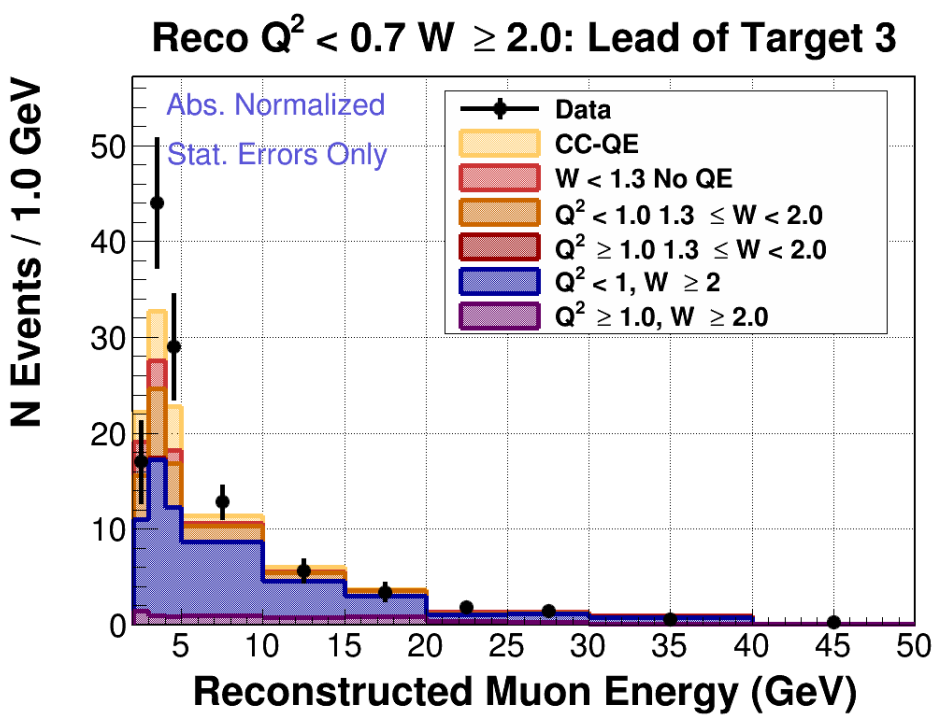

Figure A-351. Data / MC low Q^2 sideband after fitting: target 03 Pb (E_μ)

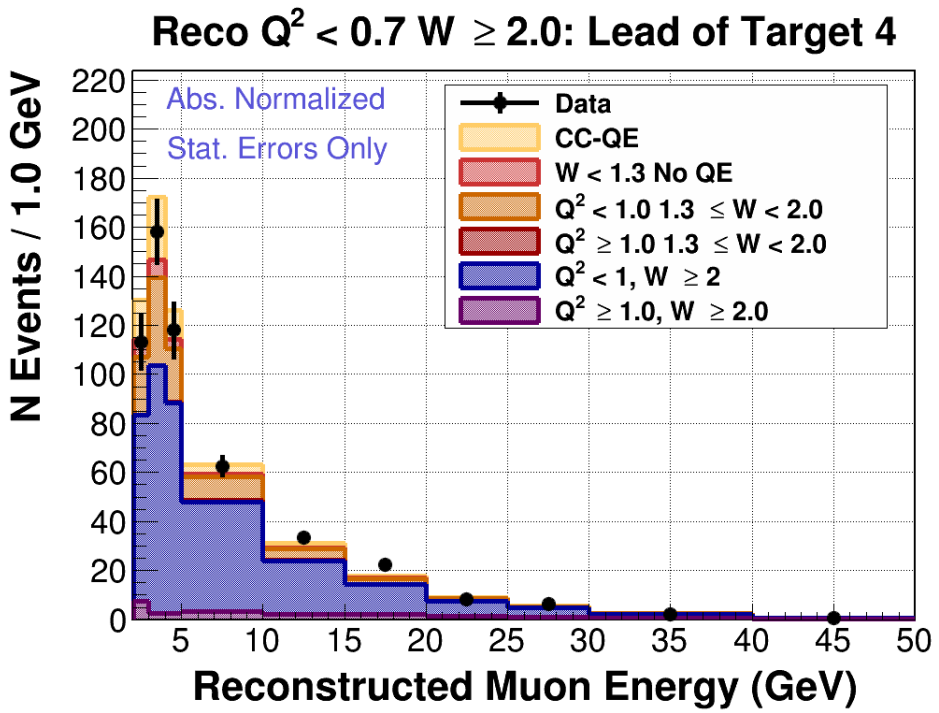

Figure A-352. Data / MC low Q^2 sideband after fitting: target 04 Pb (E_μ)

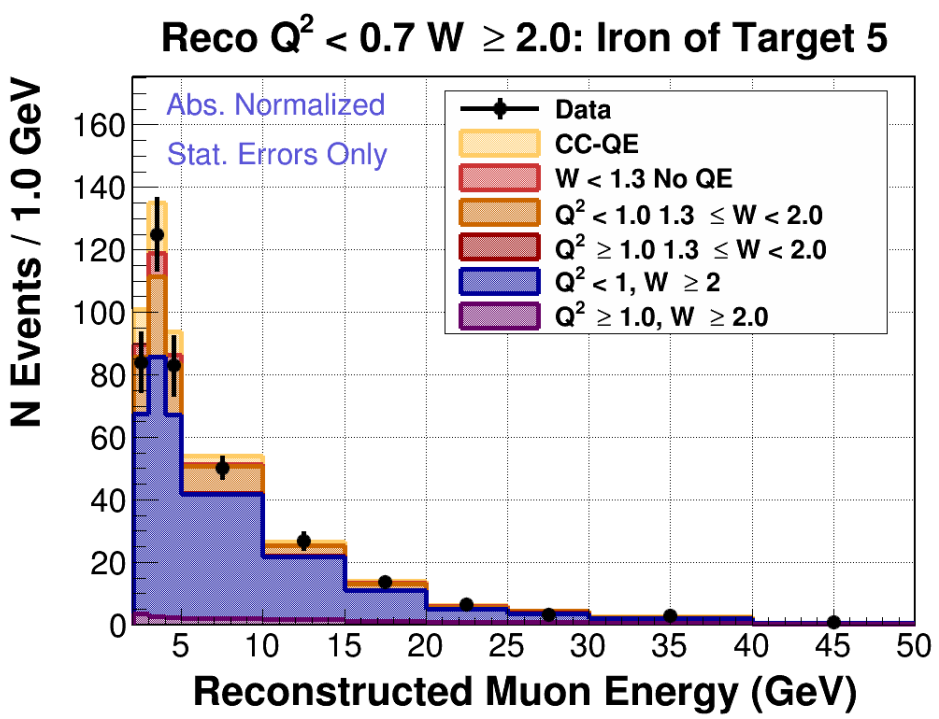

Figure A-353. Data / MC low Q^2 sideband after fitting: target 05 Fe (E_μ)

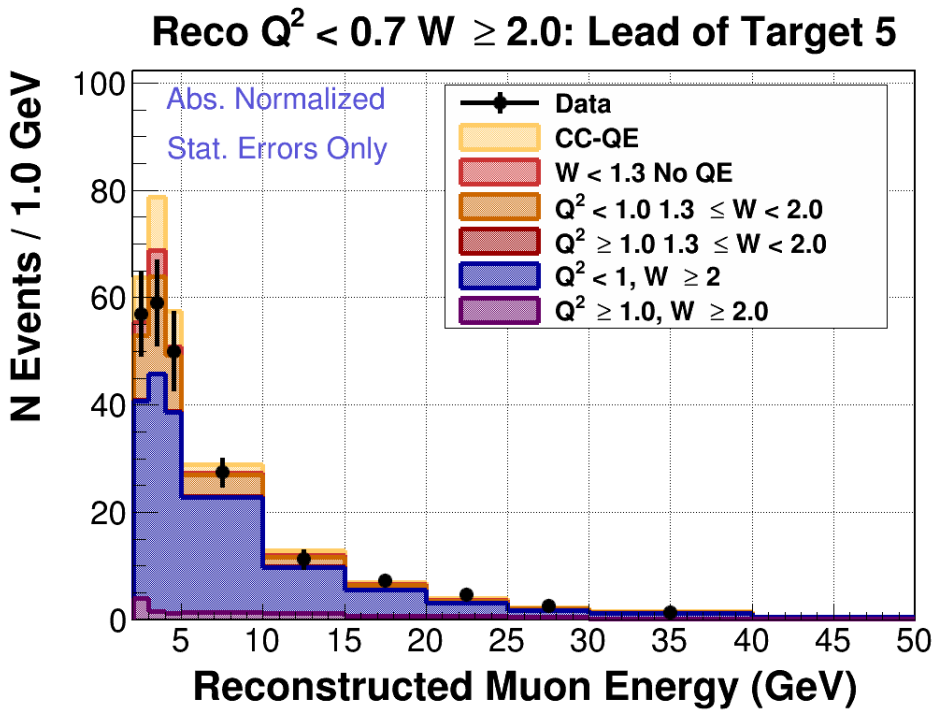

Figure A-354. Data / MC low Q^2 sideband after fitting: target 05 Pb (E_μ)

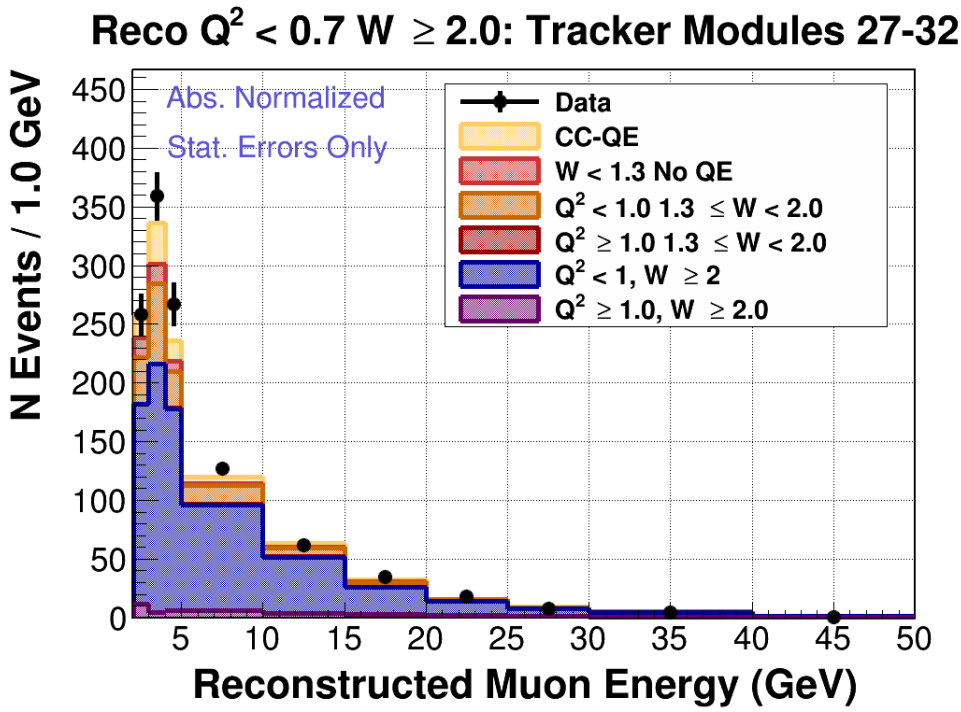

Figure A-355. Data / MC low Q^2 sideband after fitting: tracker mods. 27-32 (E_μ)

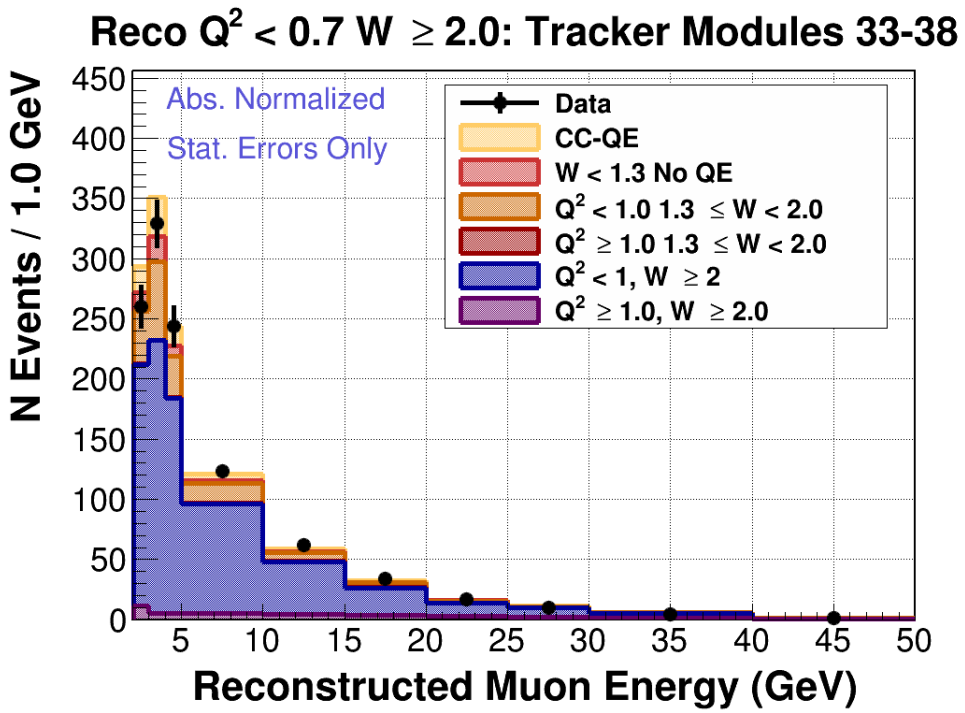

Figure A-356. Data / MC low Q^2 sideband after fitting: tracker mods. 33-38 (E_μ)

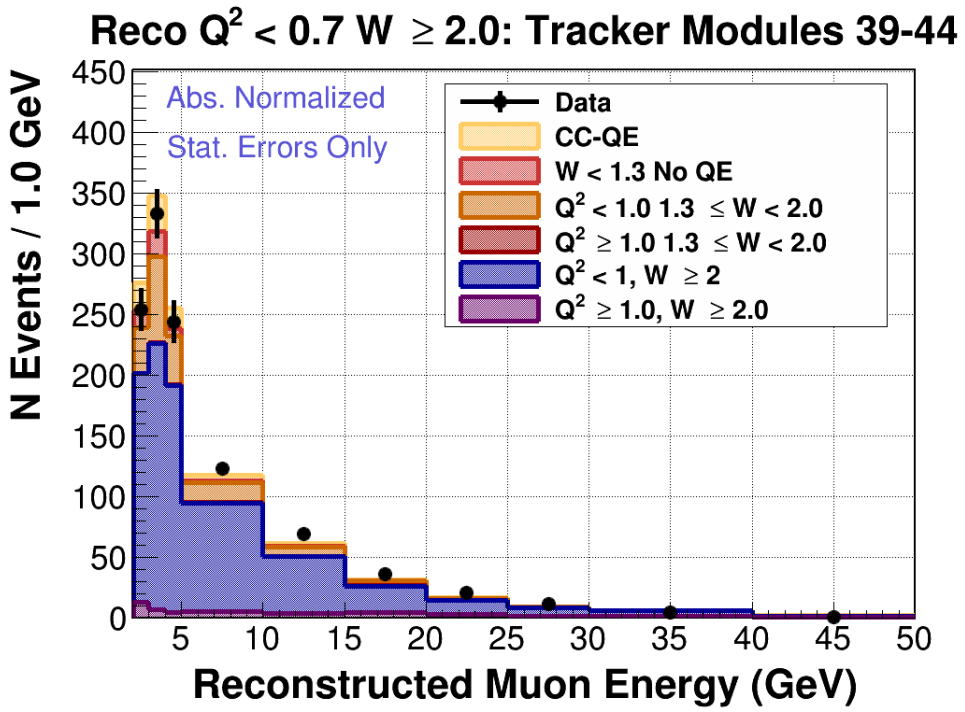

Figure A-357. Data / MC low Q^2 sideband after fitting: tracker mods. 39-44 (E_μ)

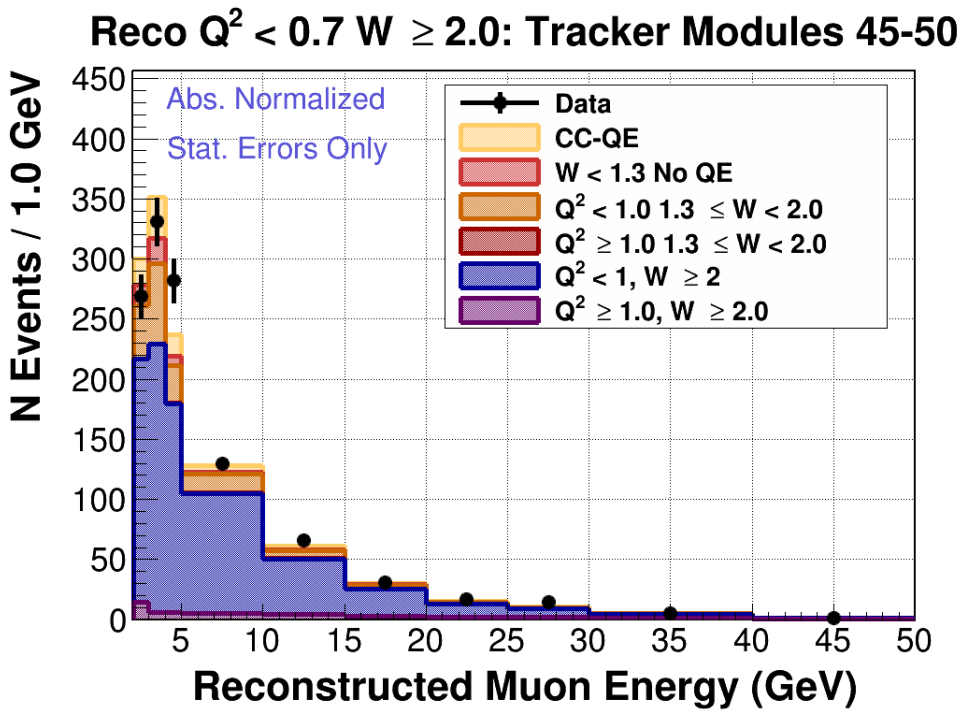

Figure A-358. Data / MC low Q^2 sideband after fitting: tracker mods. 45-50 (E_μ)

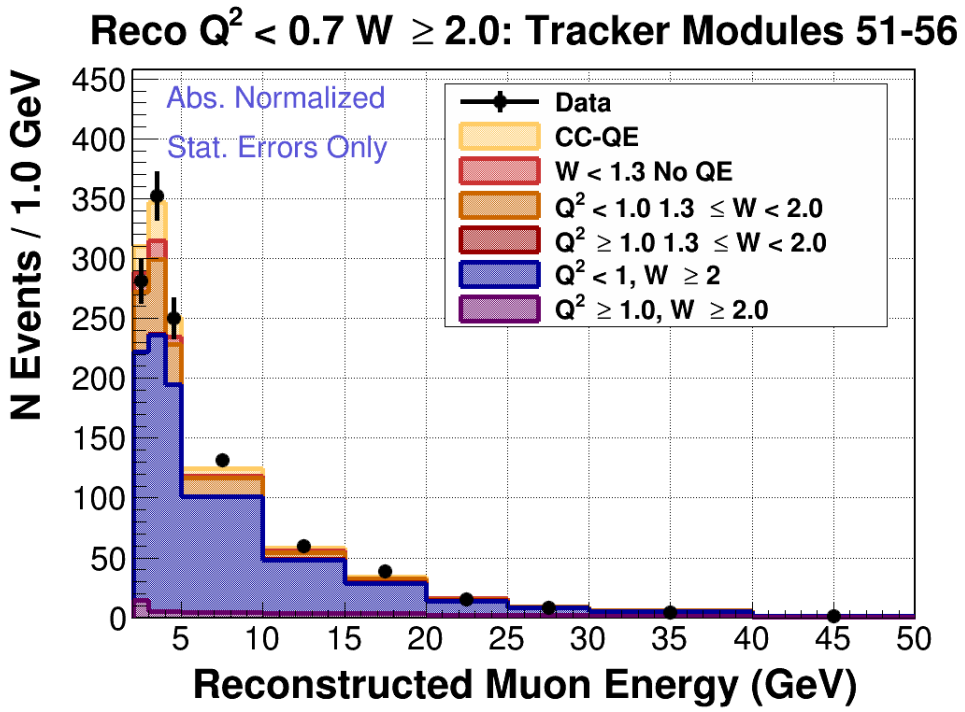

Figure A-359. Data / MC low Q^2 sideband after fitting: tracker mods. 51-56 (E_μ)

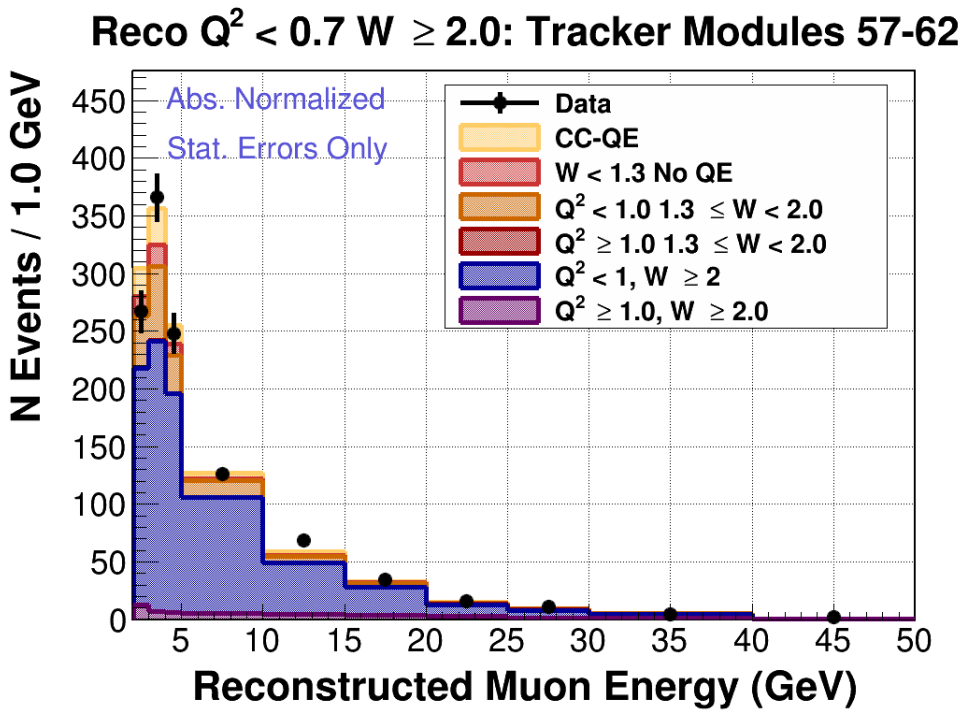

Figure A-360. Data / MC low Q^2 sideband after fitting: tracker mods. 57-62 (E_μ)

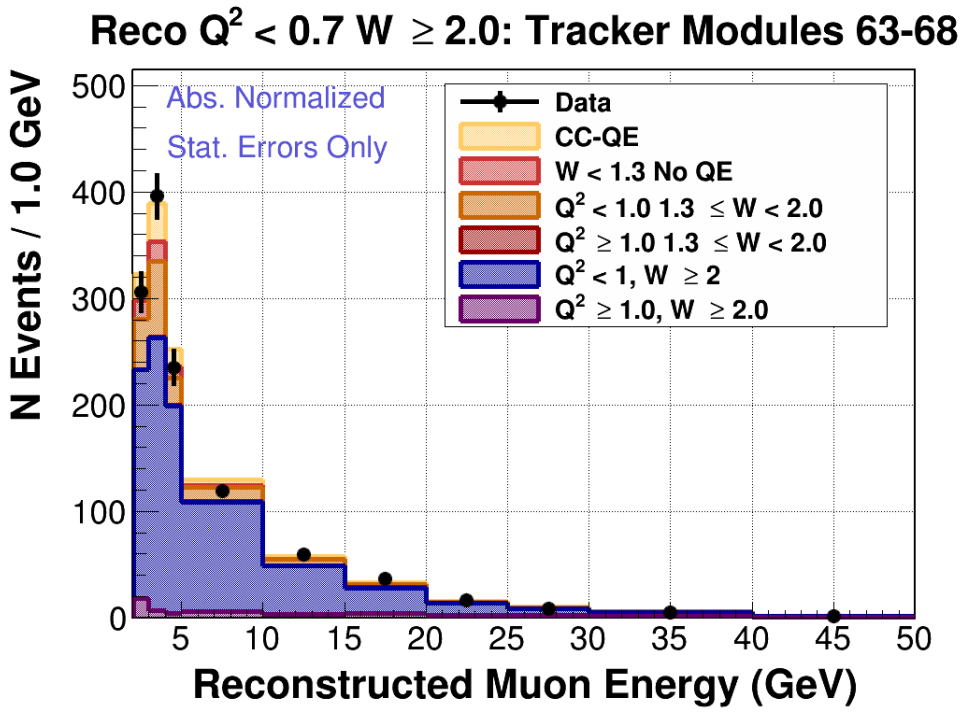

Figure A-361. Data / MC low Q^2 sideband after fitting: tracker mods. 63-68 (E_μ)

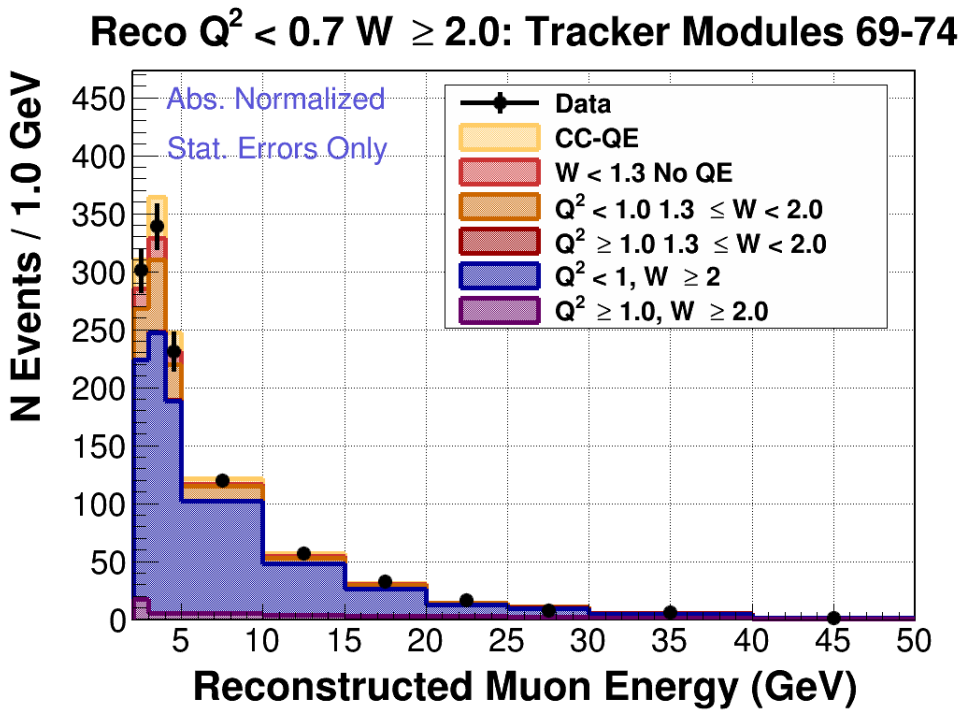

Figure A-362. Data / MC low Q^2 sideband after fitting: tracker mods. 69-74 (E_μ)

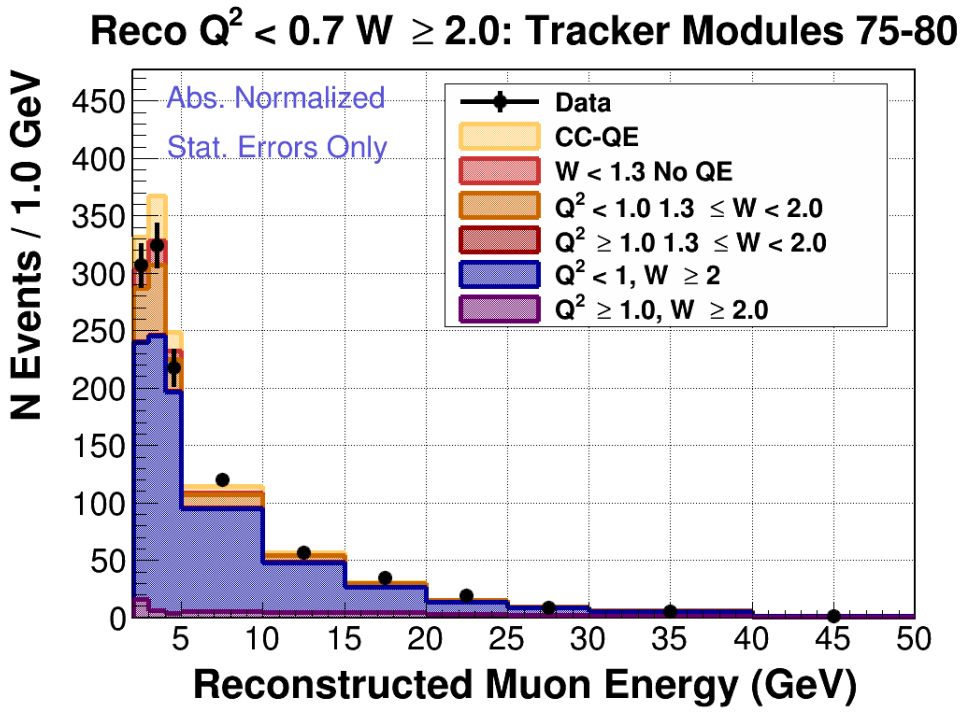

Figure A-363. Data / MC low Q^2 sideband after fitting: tracker mods. 75-80 (E_μ)

The following plots show the population of the low Q^2 sideband ($Q^2 < 0.8$ (GeV/c)^2 $W \geq 2.0$ GeV/c^2) *after* tuning to data as a function of muon angle (θ_μ):

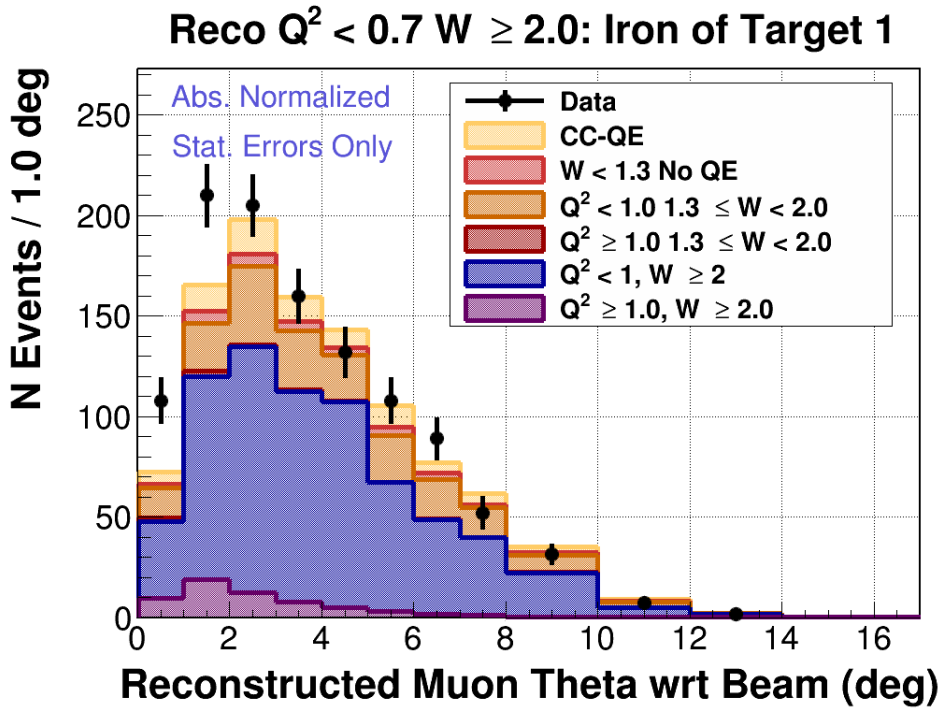

Figure A-364. Data / MC low Q^2 sideband after fitting: target 01 Fe (θ_μ)

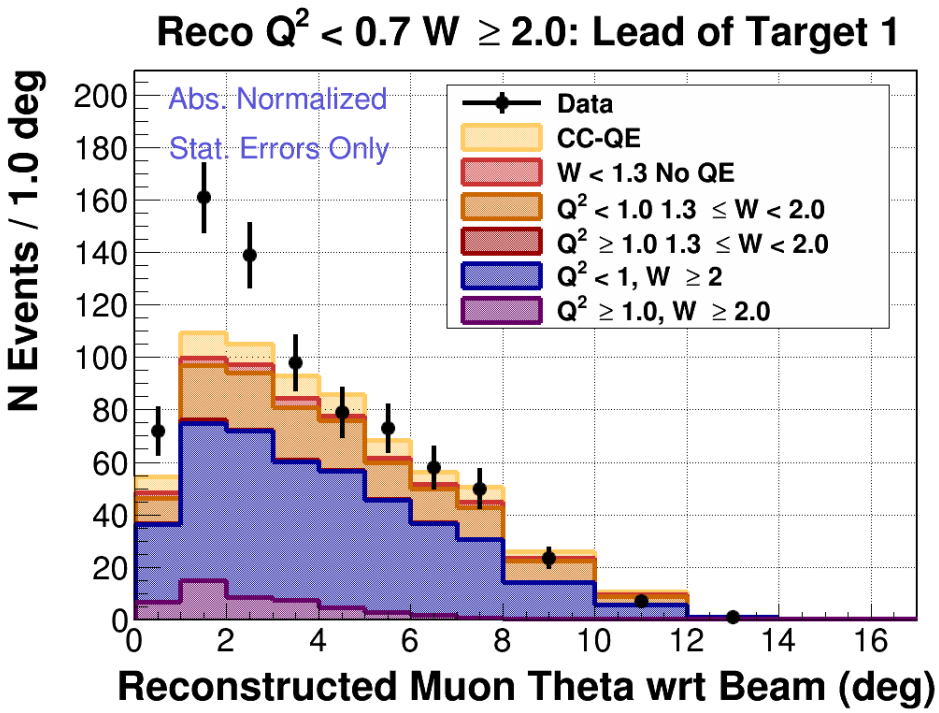

Figure A-365. Data / MC low Q^2 sideband after fitting: target 01 Pb (θ_μ)

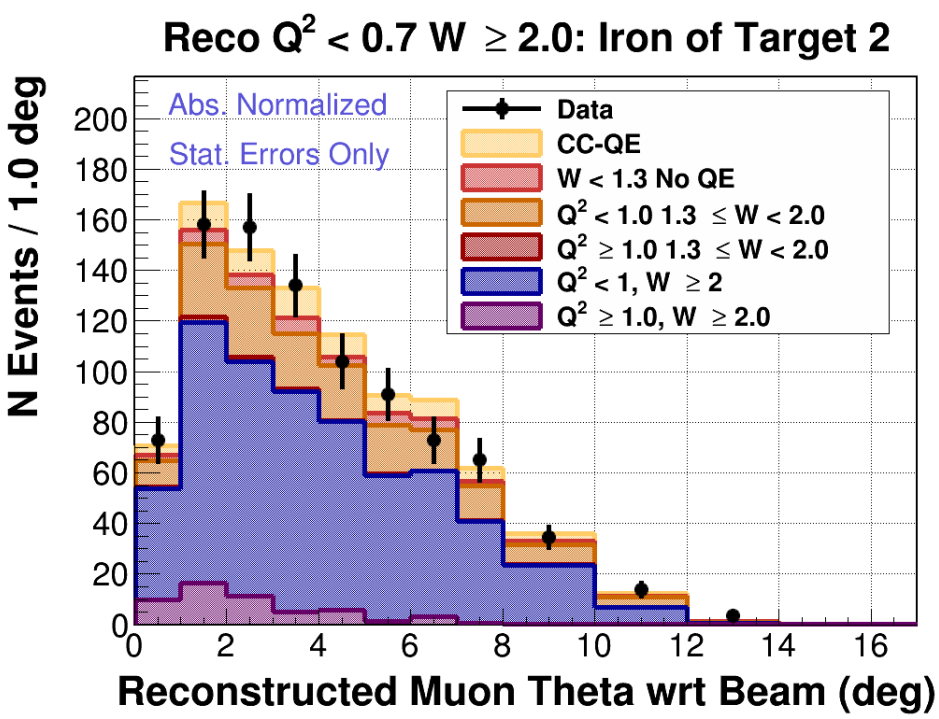

Figure A-366. Data / MC low Q^2 sideband after fitting: target 02 Fe (θ_μ)

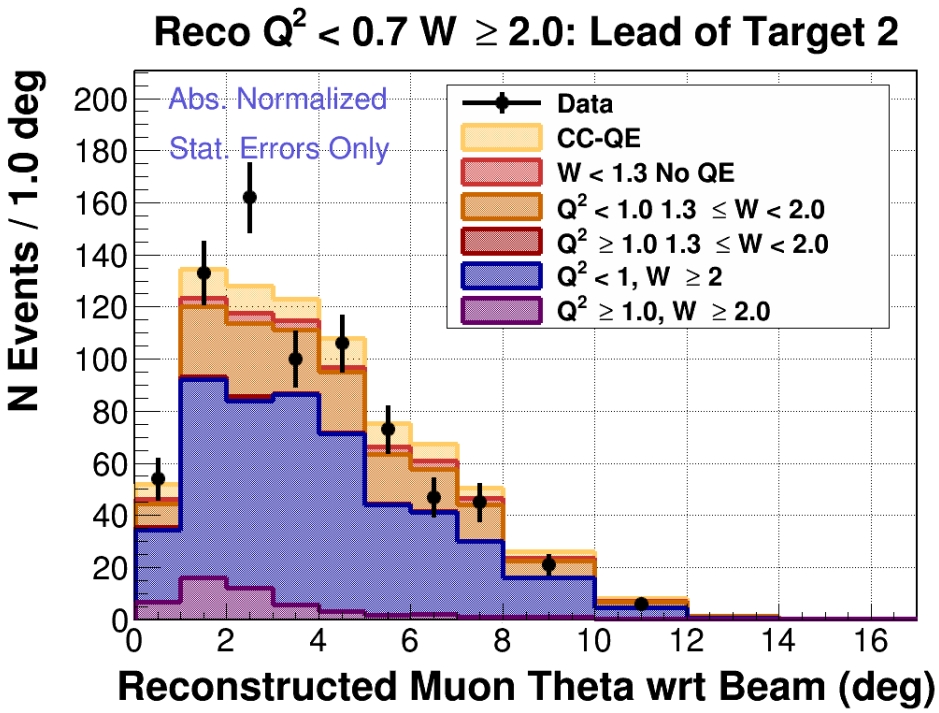

Figure A-367. Data / MC low Q^2 sideband after fitting: target 02 Pb (θ_μ)

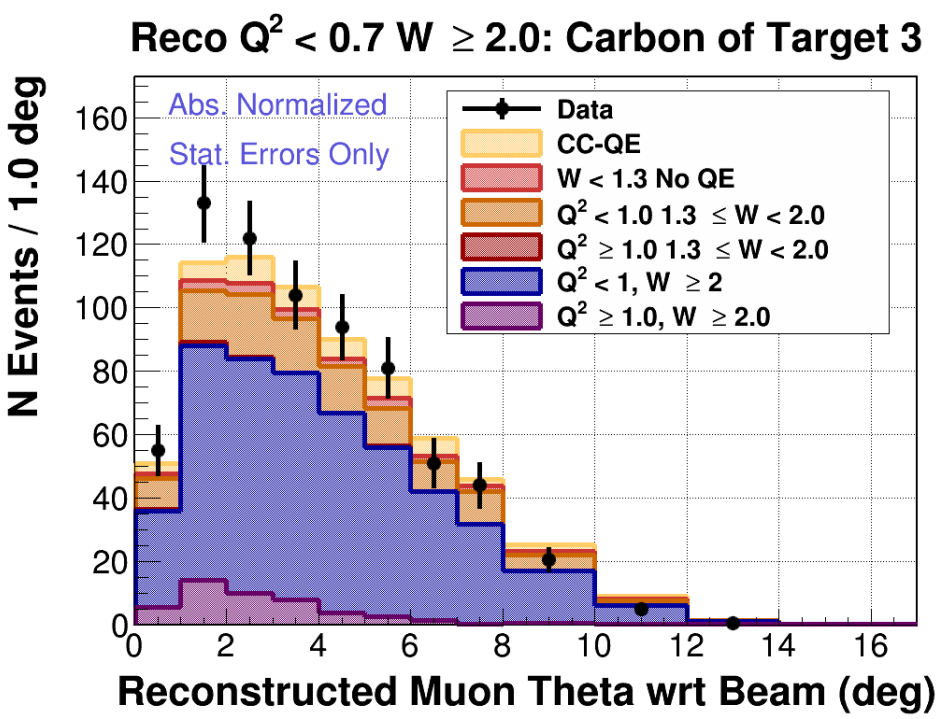

Figure A-368. Data / MC low Q^2 sideband after fitting: target 03 C (θ_μ)

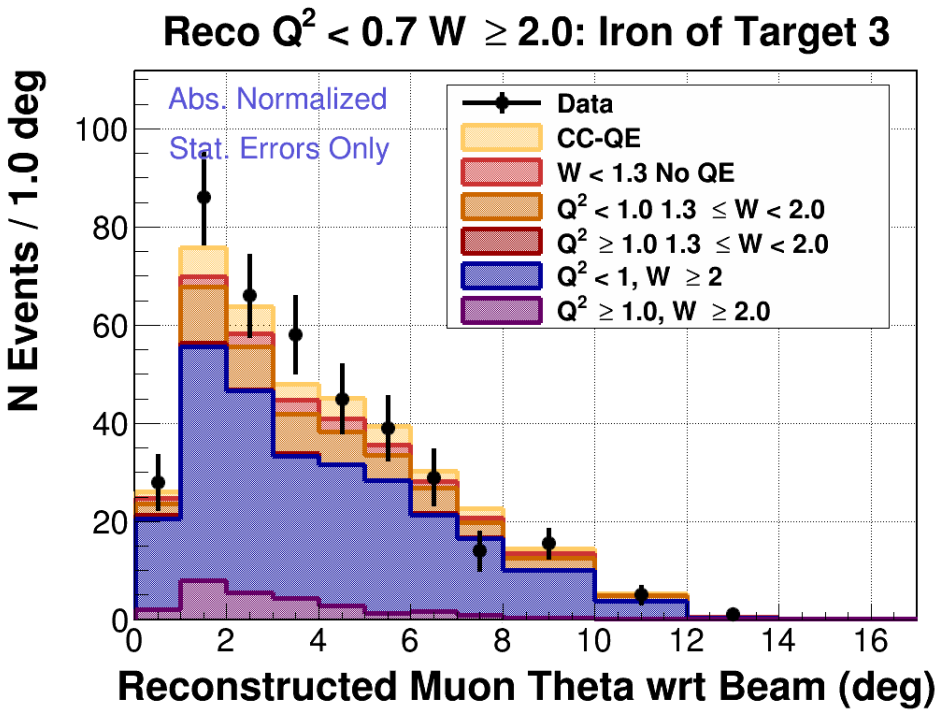

Figure A-369. Data / MC low Q^2 sideband after fitting: target 03 Fe (θ_μ)

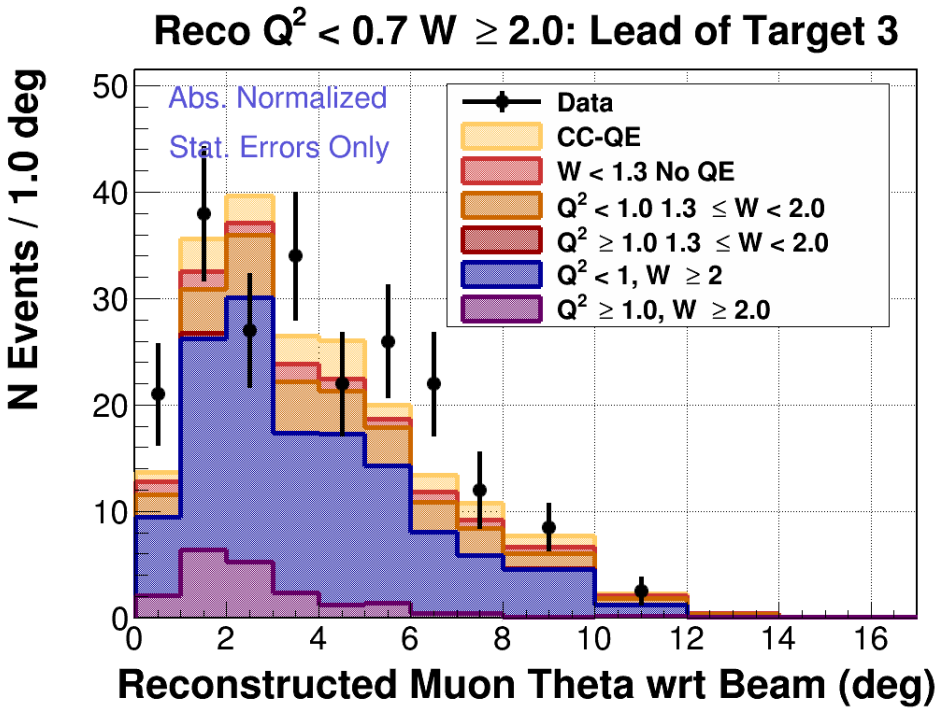

Figure A-370. Data / MC low Q^2 sideband after fitting: target 03 Pb (θ_μ)

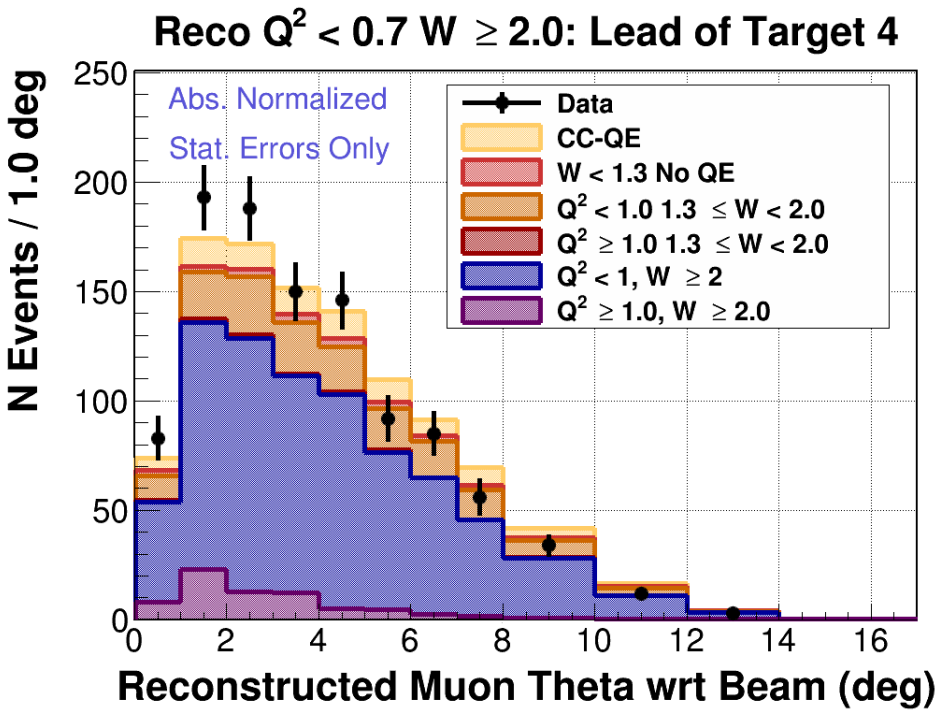

Figure A-371. Data / MC low Q^2 sideband after fitting: target 04 Pb (θ_μ)

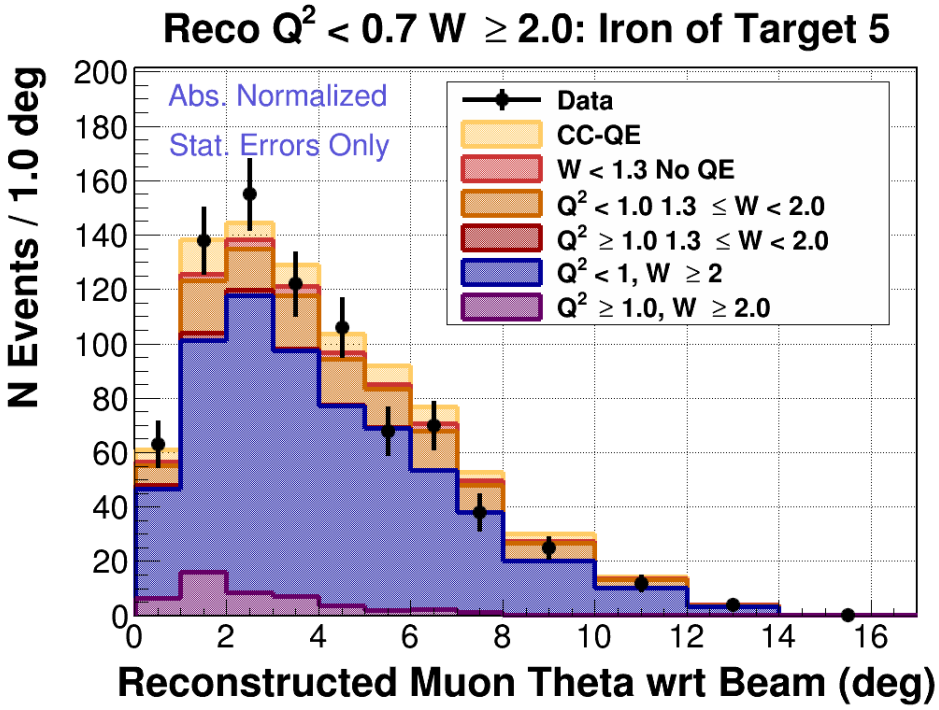

Figure A-372. Data / MC low Q^2 sideband after fitting: target 05 Fe (θ_μ)

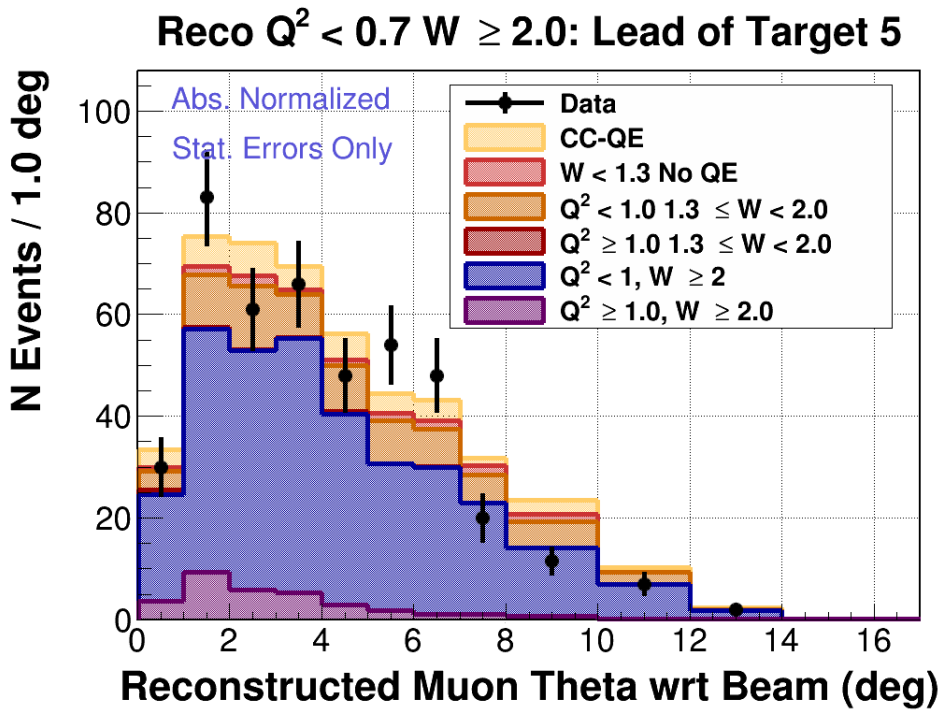

Figure A-373. Data / MC low Q^2 sideband after fitting: target 05 Pb (θ_μ)

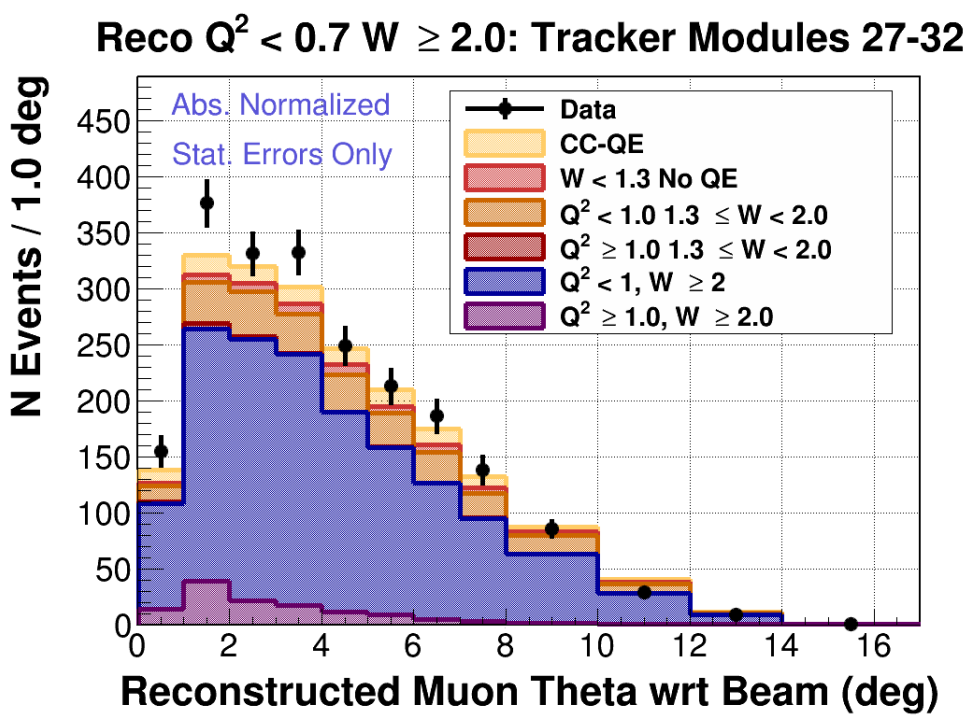

Figure A-374. Data / MC low Q^2 sideband after fitting: tracker mods. 27-32 (θ_μ)

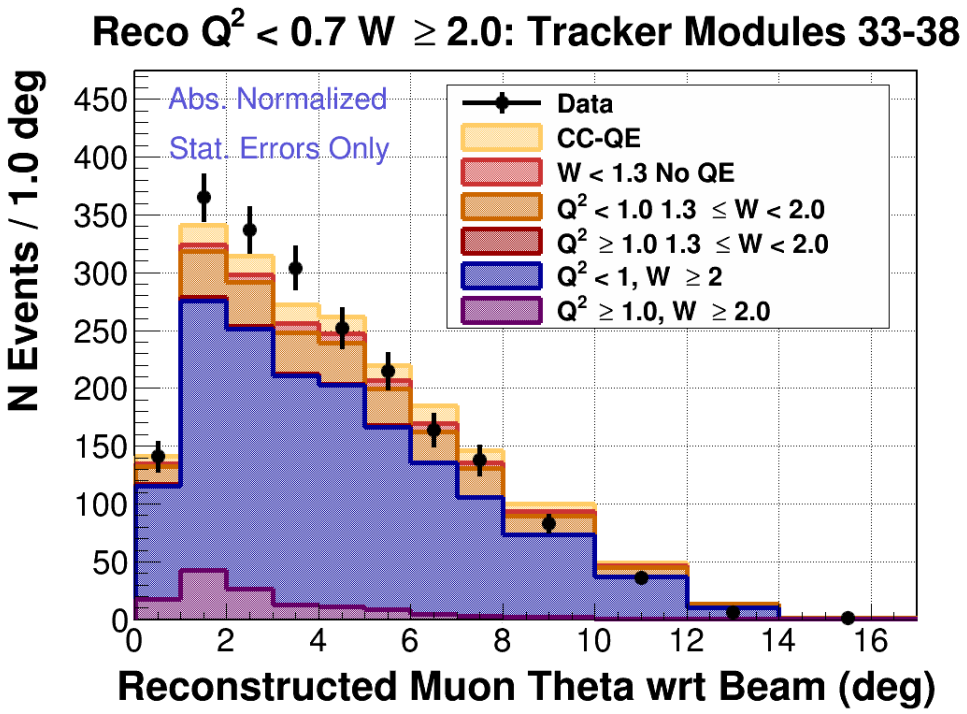

Figure A-375. Data / MC low Q^2 sideband after fitting: tracker mods. 33-38 (θ_μ)

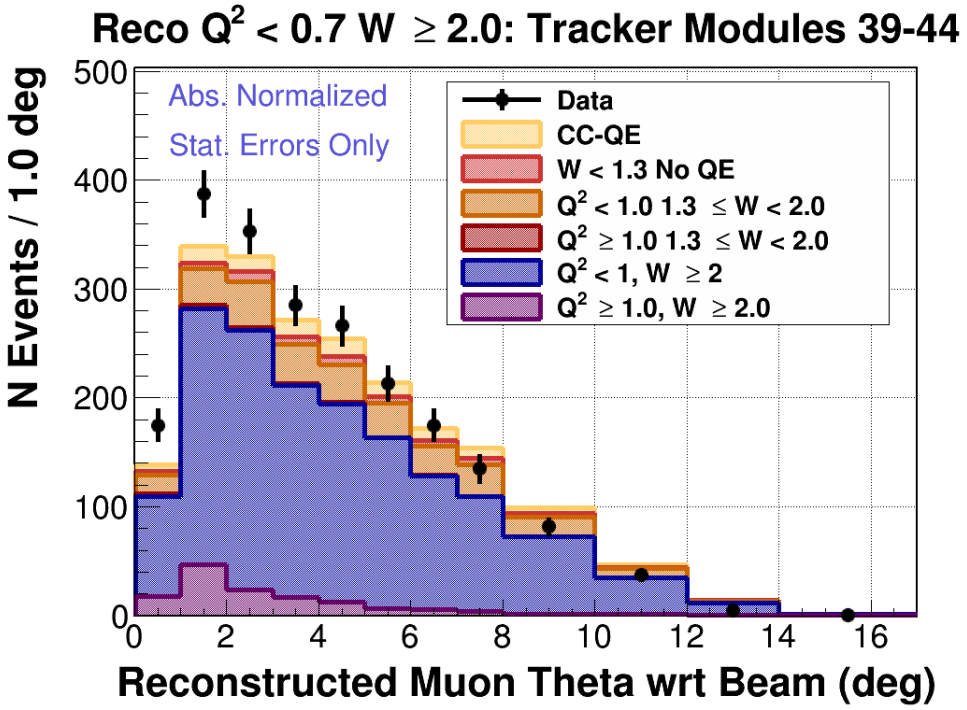

Figure A-376. Data / MC low Q^2 sideband after fitting: tracker mods. 39-44 (θ_μ)

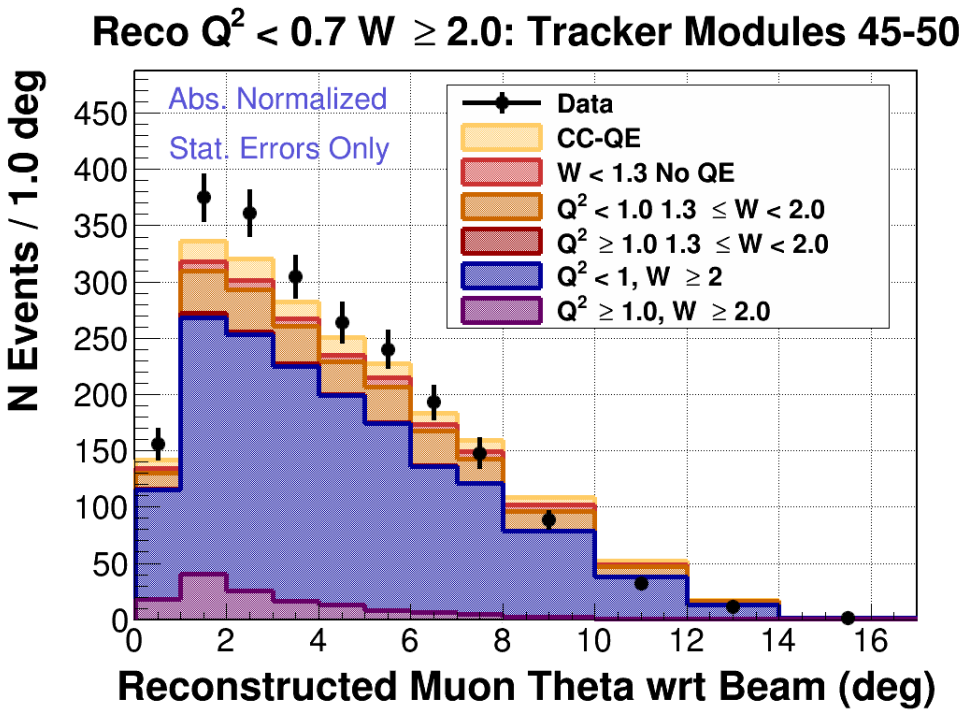

Figure A-377. Data / MC low Q^2 sideband after fitting: tracker mods. 45-50 (θ_μ)

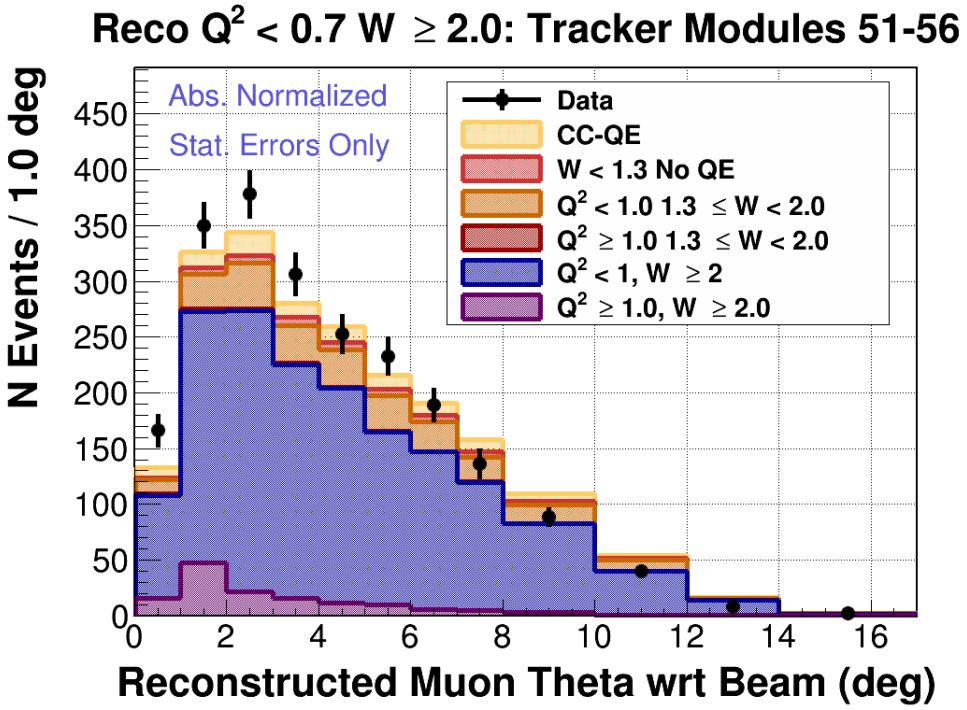

Figure A-378. Data / MC low Q^2 sideband after fitting: tracker mods. 51-56 (θ_μ)

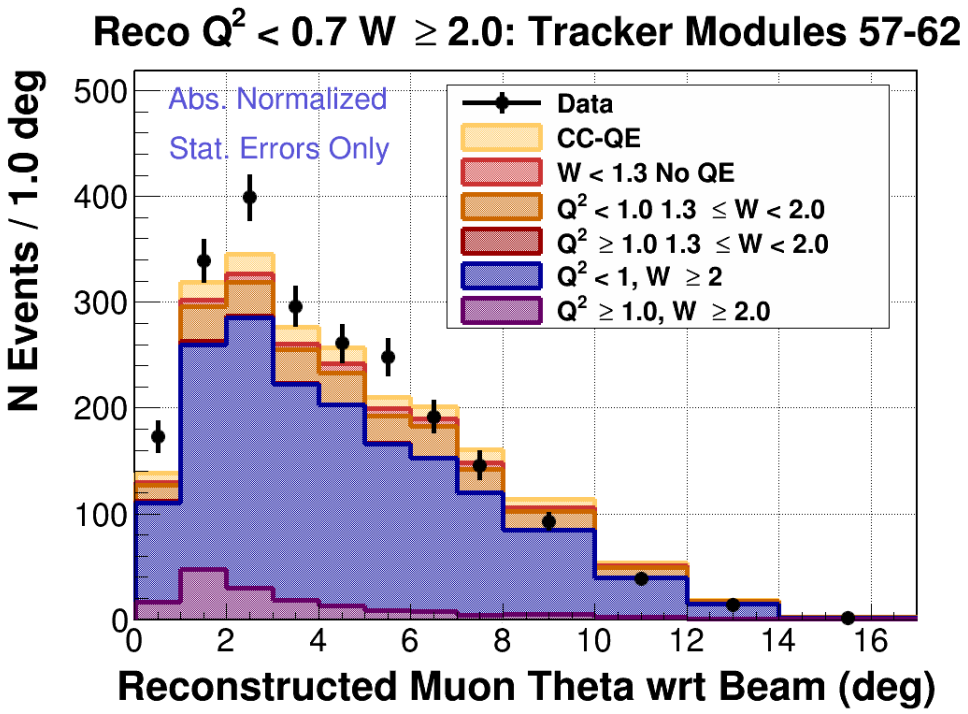

Figure A-379. Data / MC low Q^2 sideband after fitting: tracker mods. 57-62 (θ_μ)

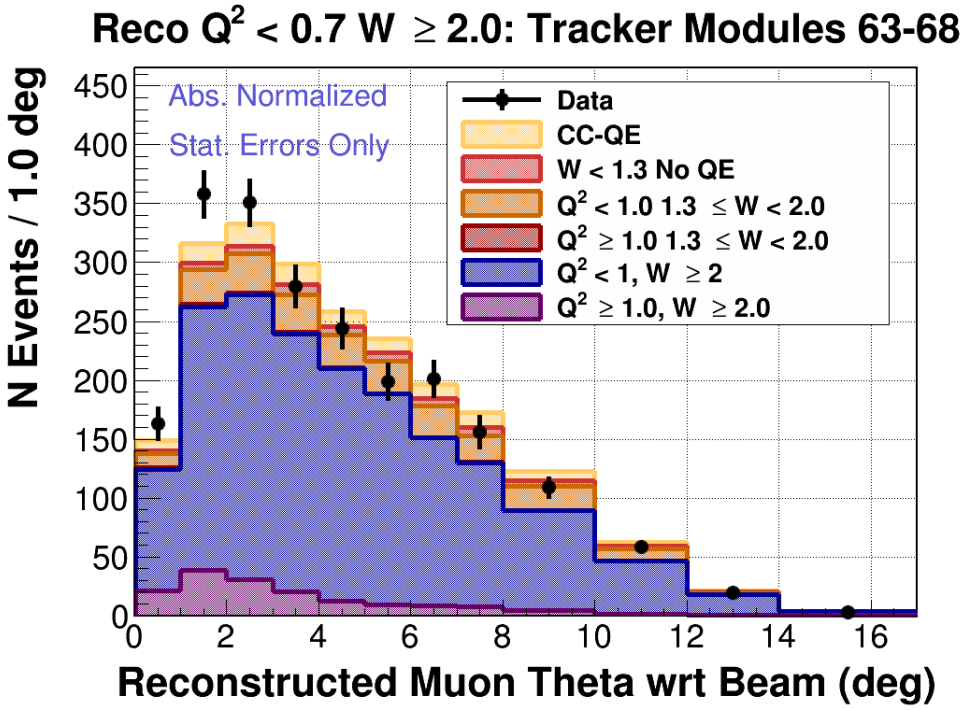

Figure A-380. Data / MC low Q^2 sideband after fitting: tracker mods. 63-68 (θ_μ)

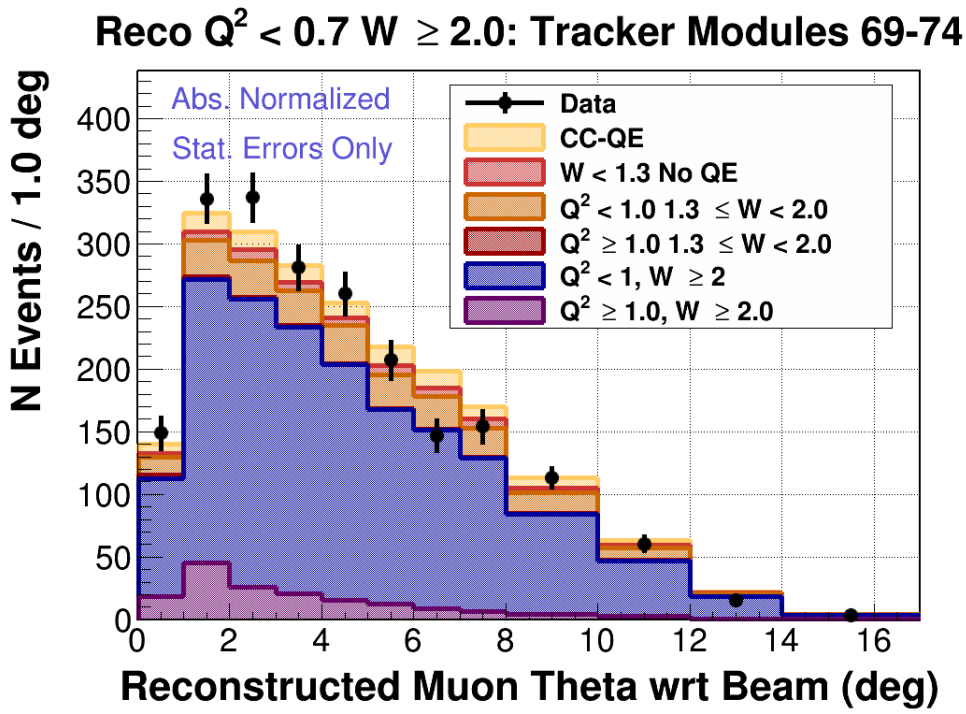

Figure A-381. Data / MC low Q^2 sideband after fitting: tracker mods. 69-74 (θ_μ)

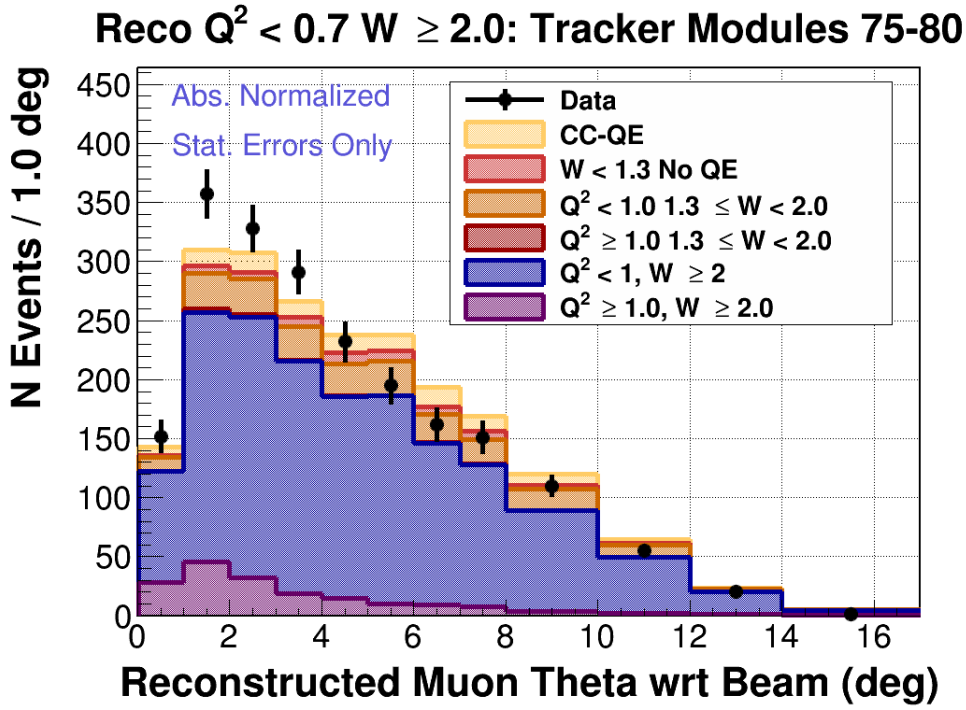

Figure A-382. Data / MC low Q^2 sideband after fitting: tracker mods. 75-80 (θ_μ)

APPENDIX B
NON-DIS EVENT UNCERTAINTIES (AFTER TUNING)

The following plots show the uncertainty on the number of truly non-DIS events which pass the DIS event selection cuts as a function of neutrino energy (E_ν):

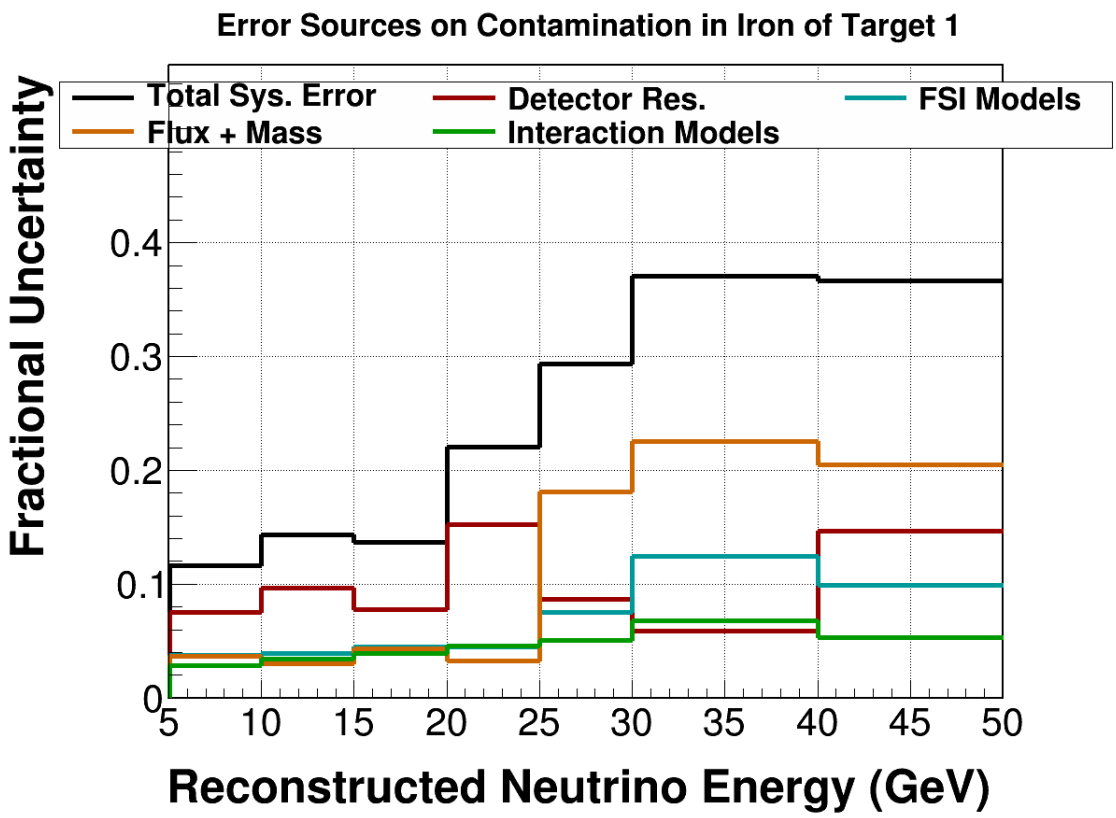

Figure B-1. Uncertainties on mis-ided DIS events: target 01 Fe (E_ν)

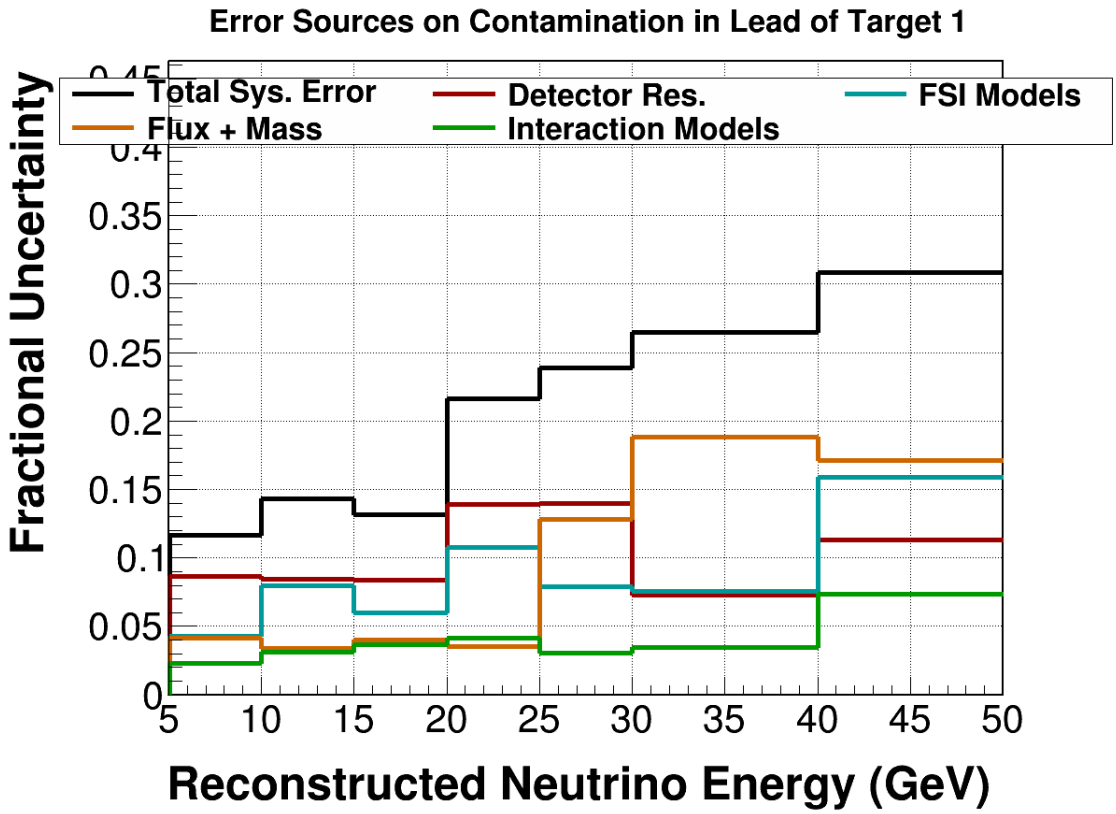

Figure B-2. Uncertainties on mis-ided DIS events: target 01 Pb (E_ν)

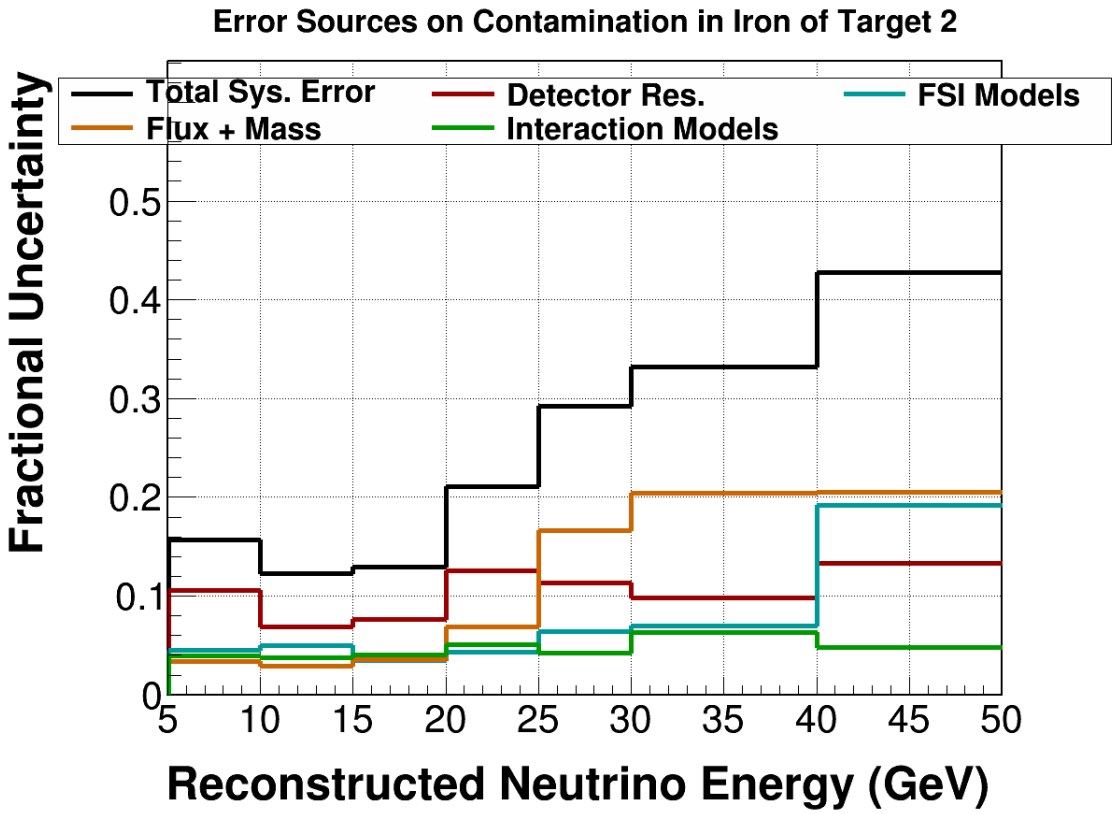

Figure B-3. Uncertainties on mis-ided DIS events: target 02 Fe (E_ν)

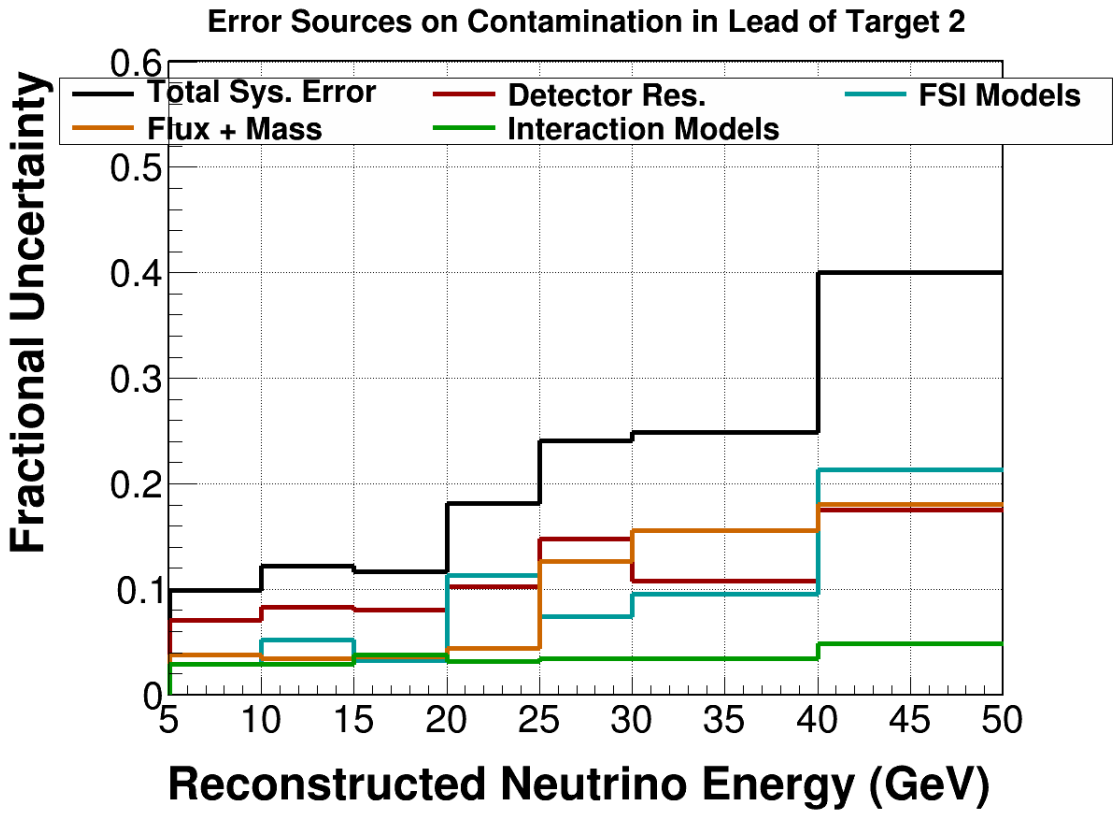

Figure B-4. Uncertainties on mis-ided DIS events: target 02 Pb (E_ν)

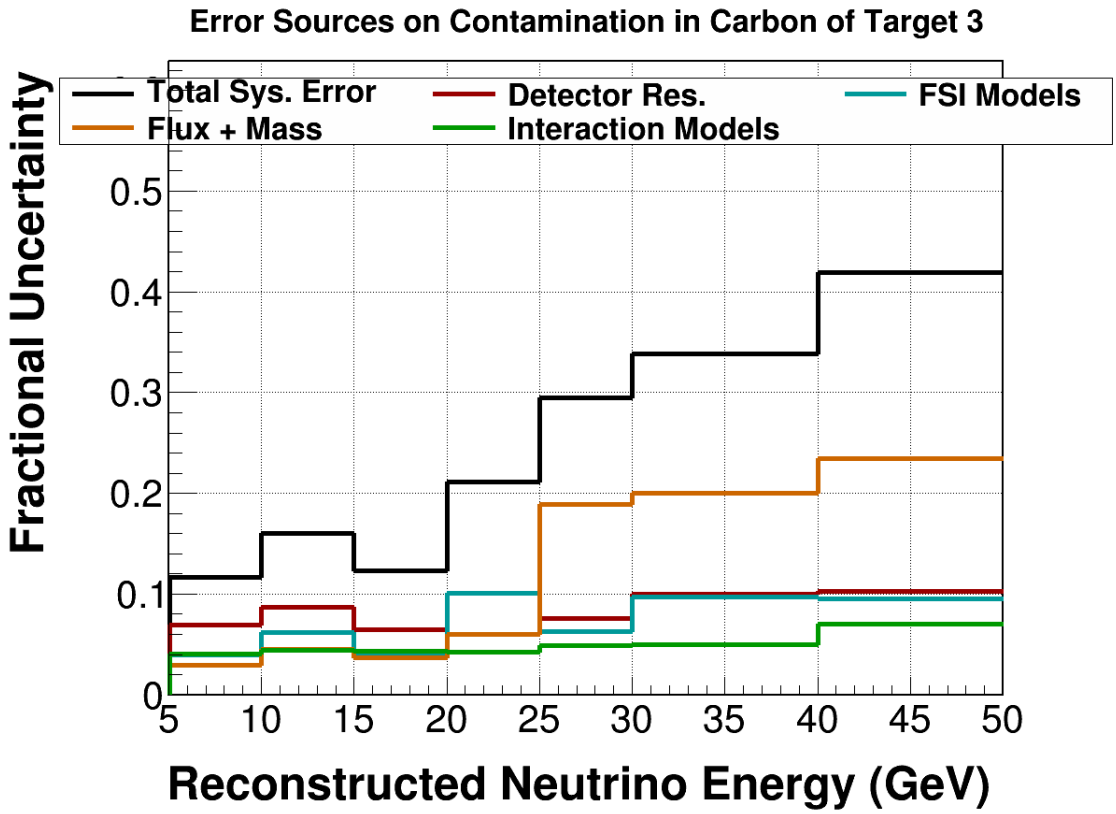

Figure B-5. Uncertainties on mis-ided DIS events: target 03 C (E_ν)

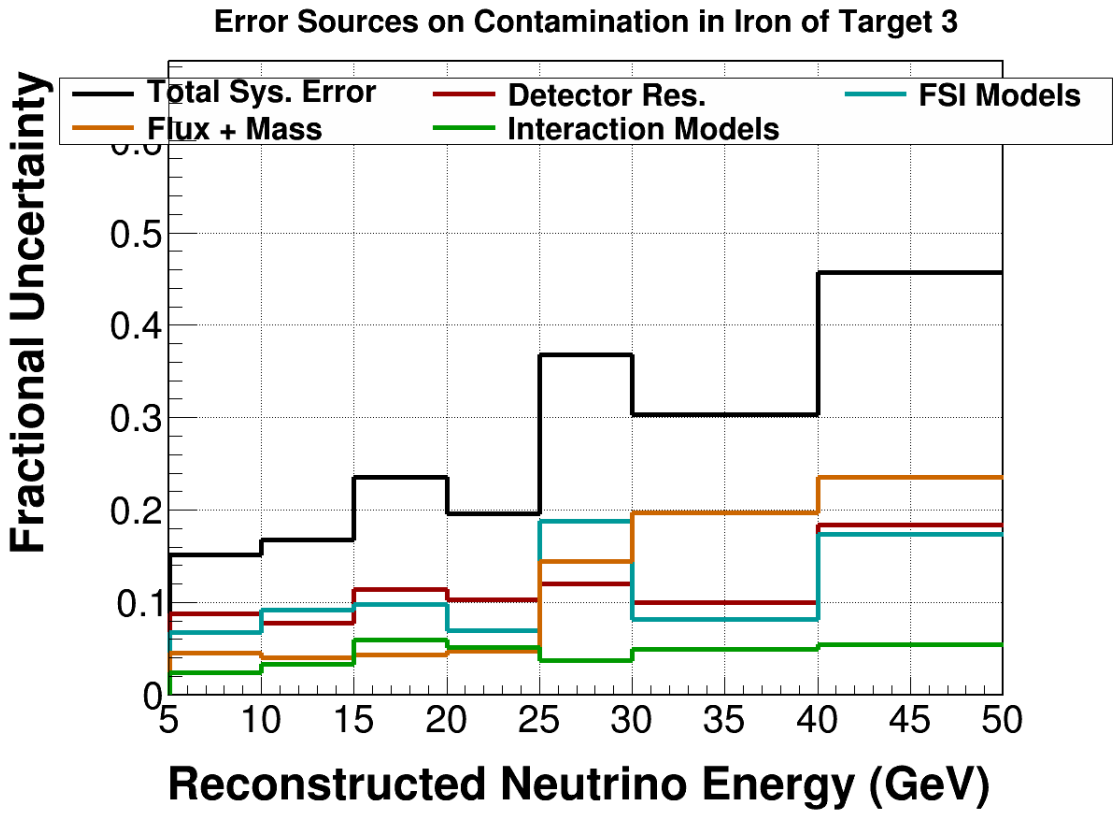

Figure B-6. Uncertainties on mis-ided DIS events: target 03 Fe (E_ν)

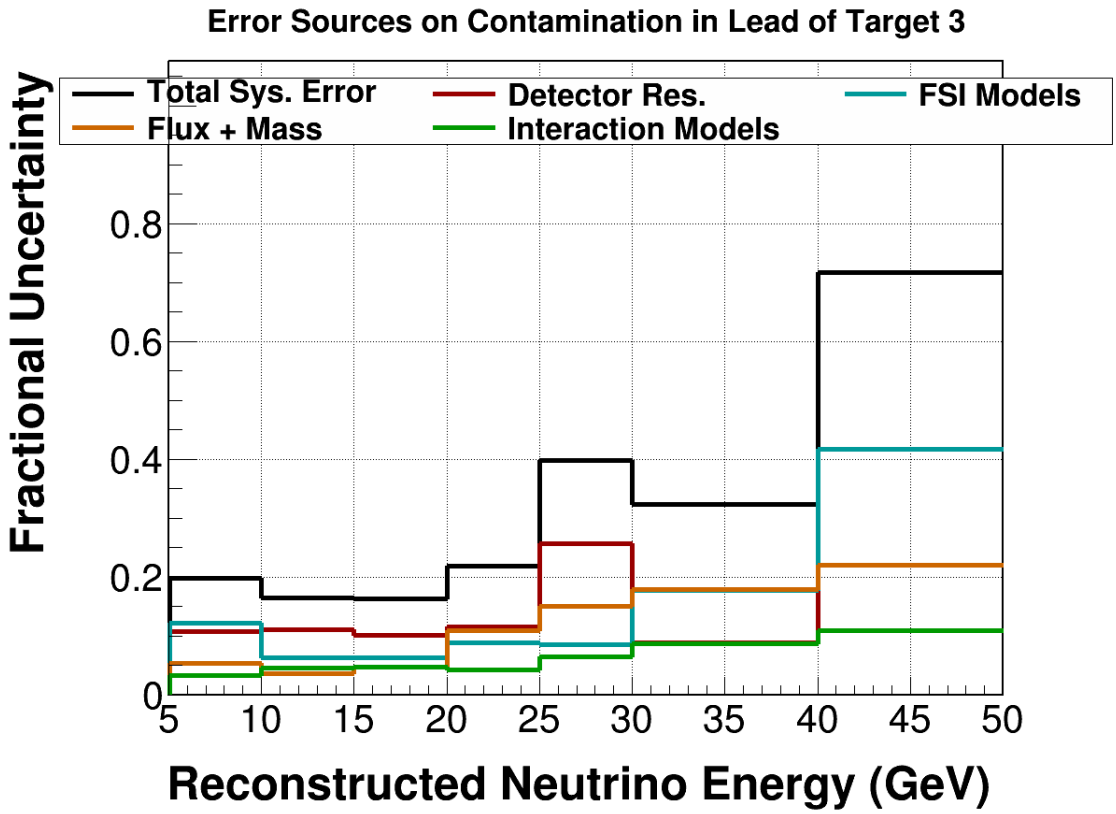

Figure B-7. Uncertainties on mis-ided DIS events: target 03 Pb (E_ν)

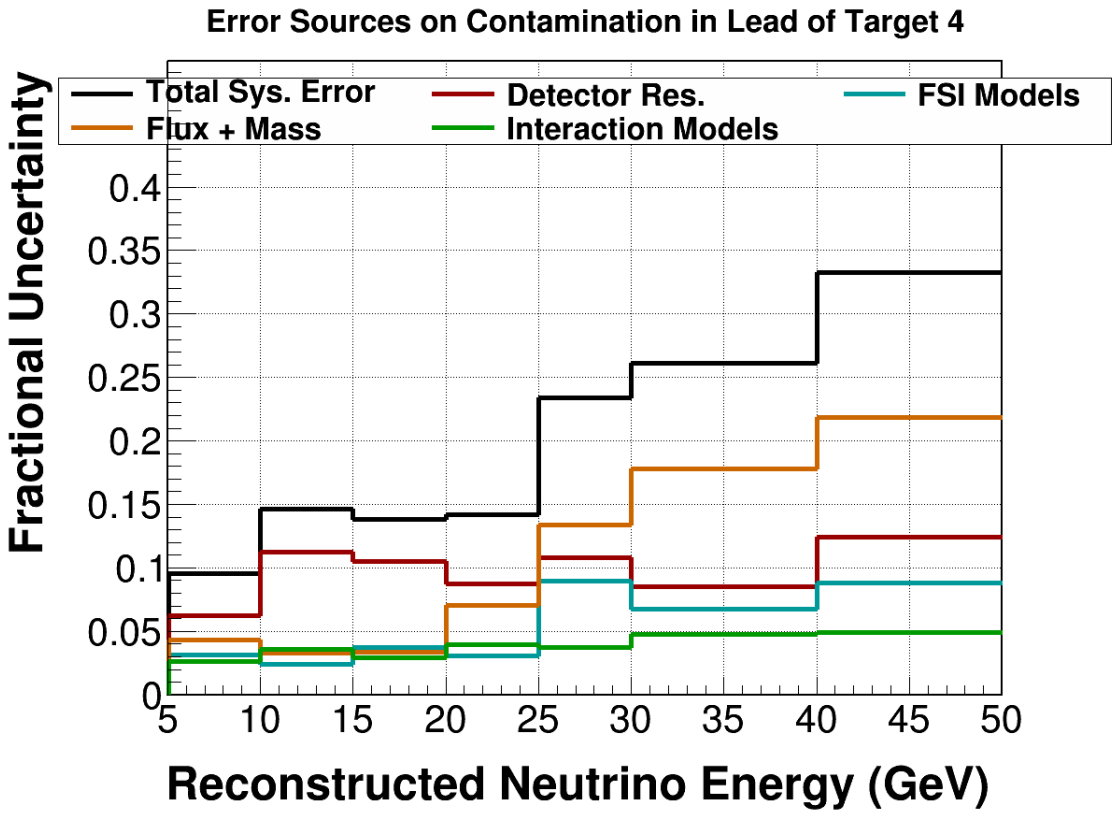

Figure B-8. Uncertainties on mis-ided DIS events: target 04 Pb (E_ν)

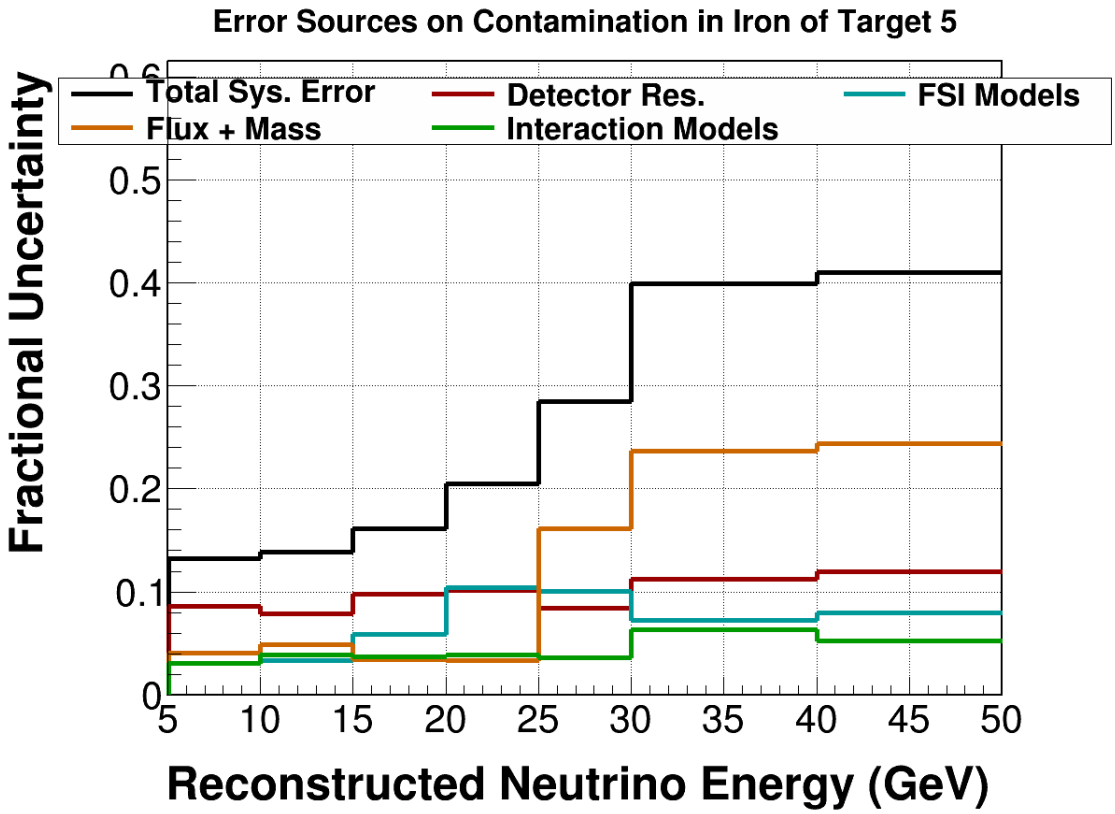

Figure B-9. Uncertainties on mis-ided DIS events: target 05 Fe (E_ν)

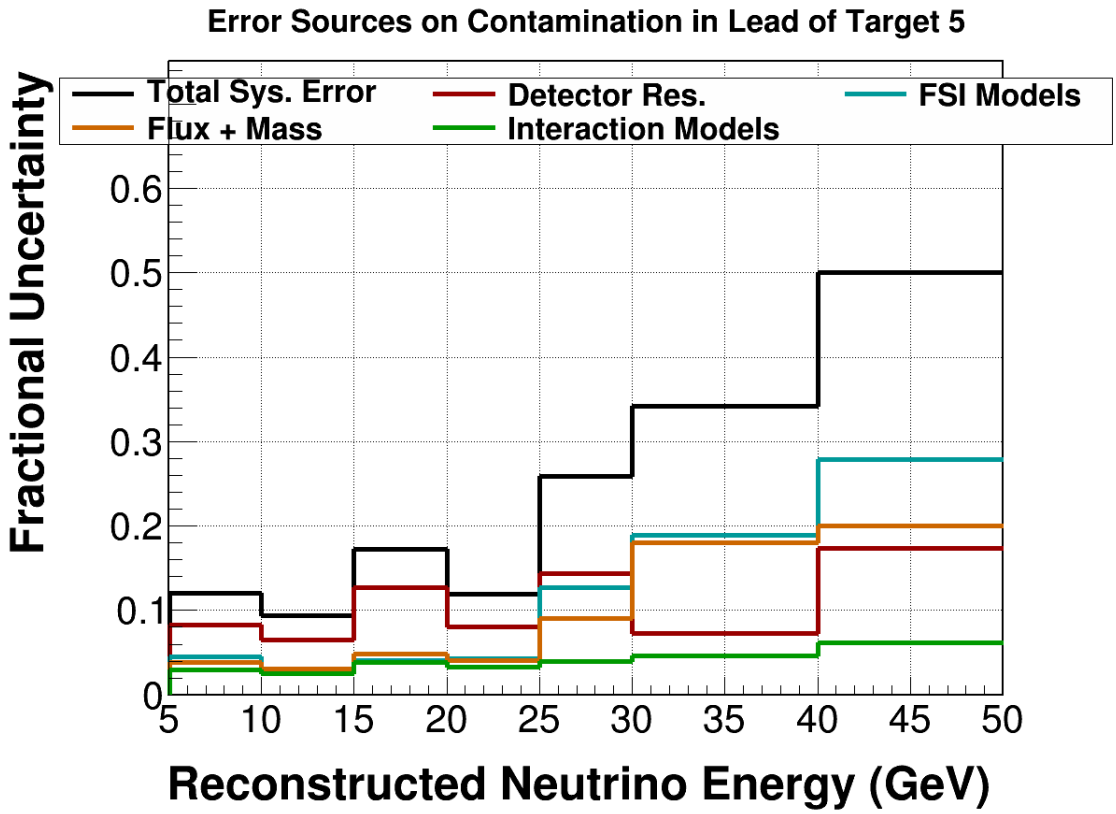

Figure B-10. Uncertainties on mis-ided DIS events: target 02 Pb (E_ν)

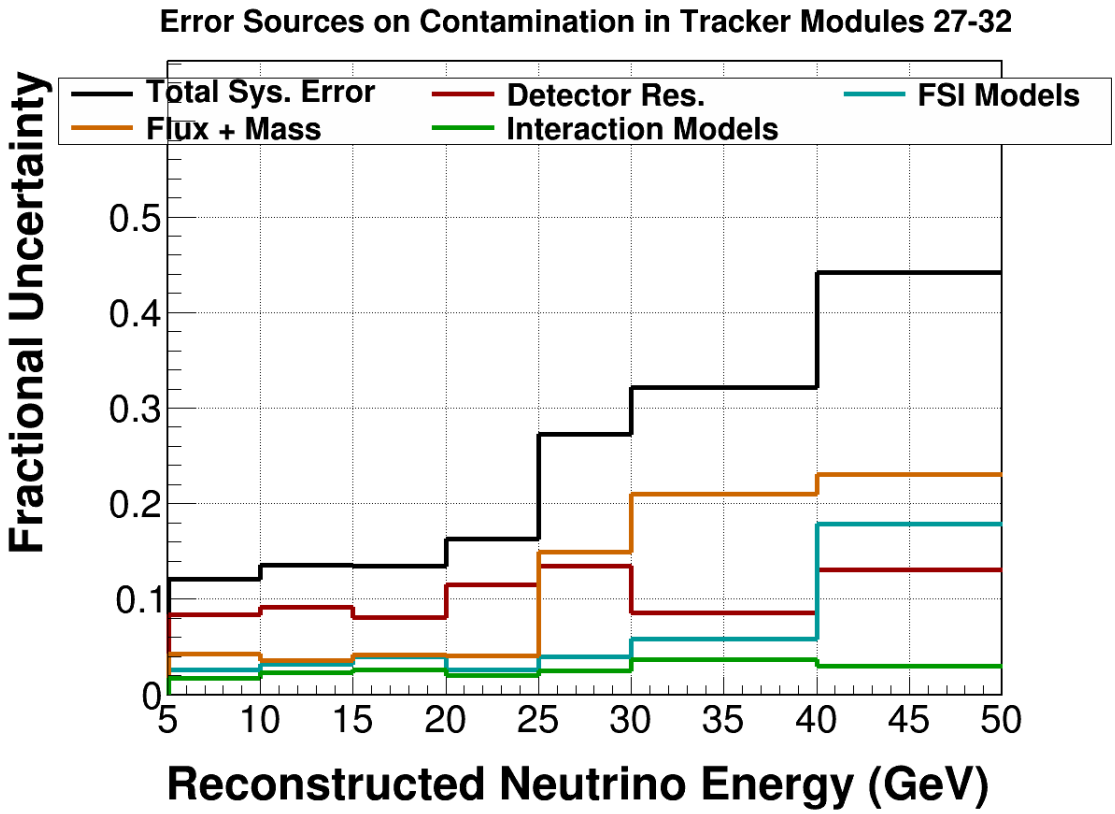

Figure B-11. Uncertainties on mis-ided DIS events: tracker mods. 27-32 (E_ν)

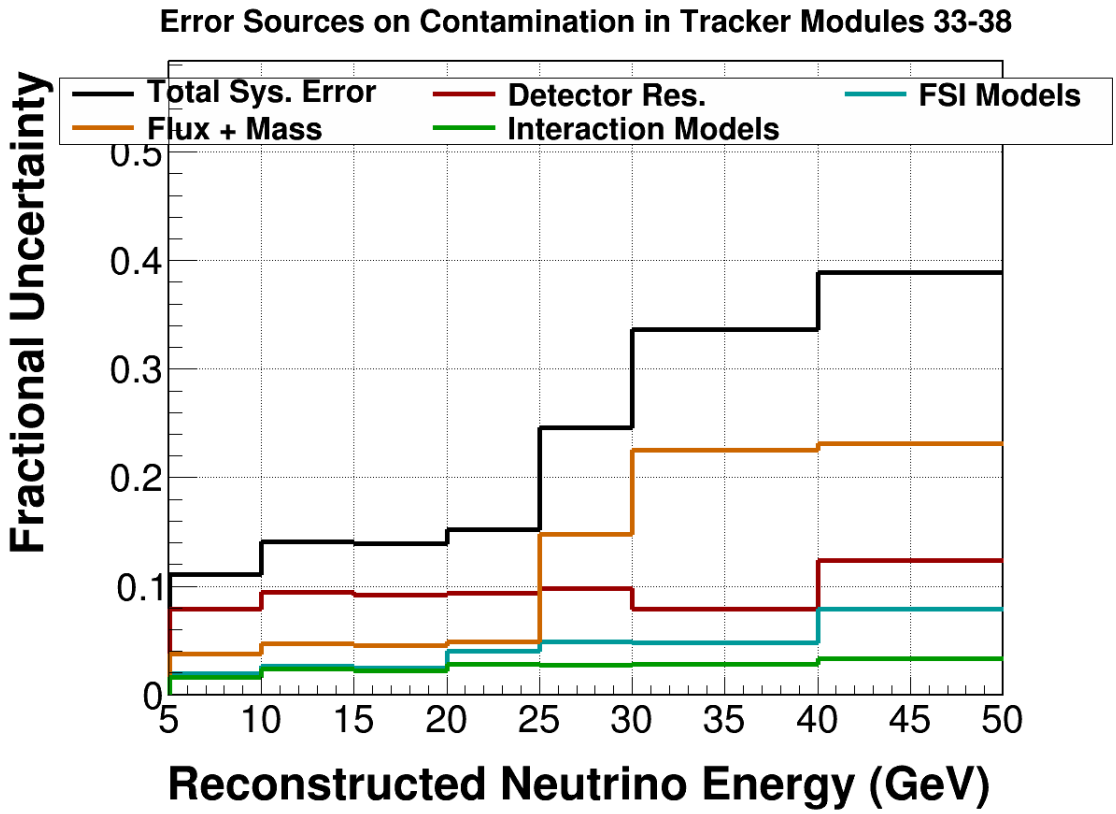

Figure B-12. Uncertainties on mis-ided DIS events: tracker mods. 33-38 (E_ν)

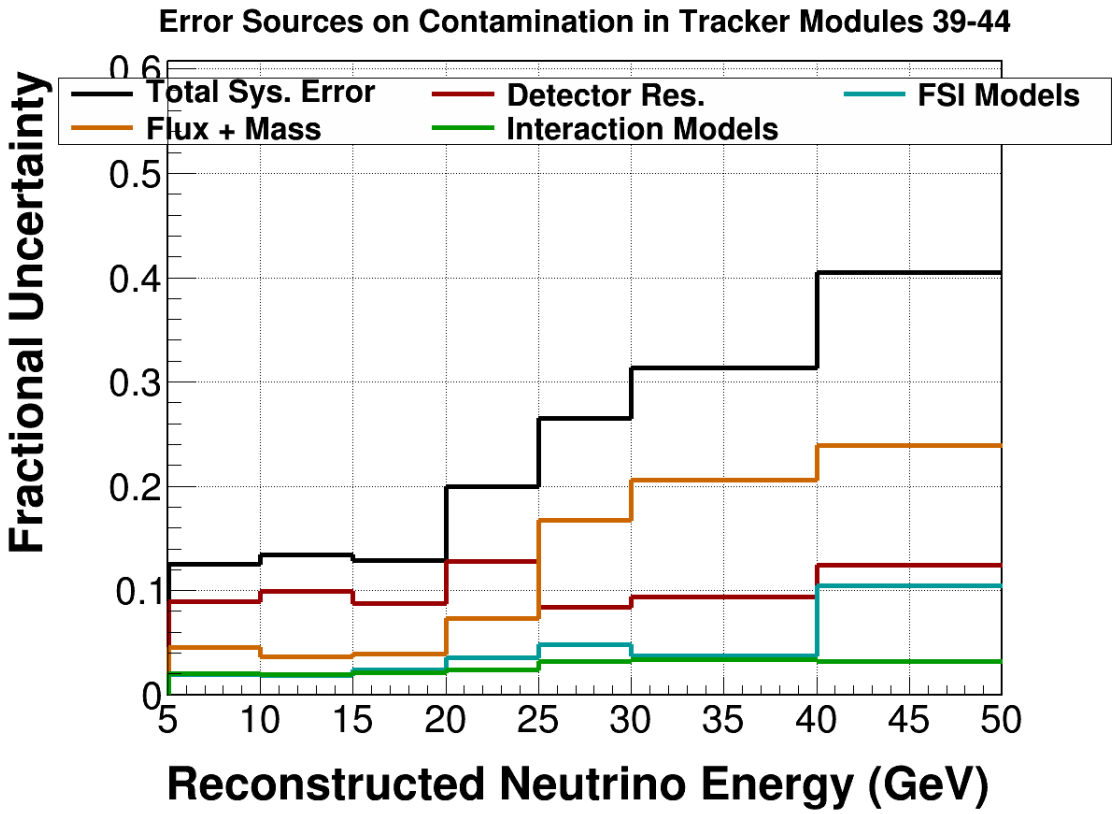

Figure B-13. Uncertainties on mis-ided DIS events: tracker mods. 39-44 (E_ν)

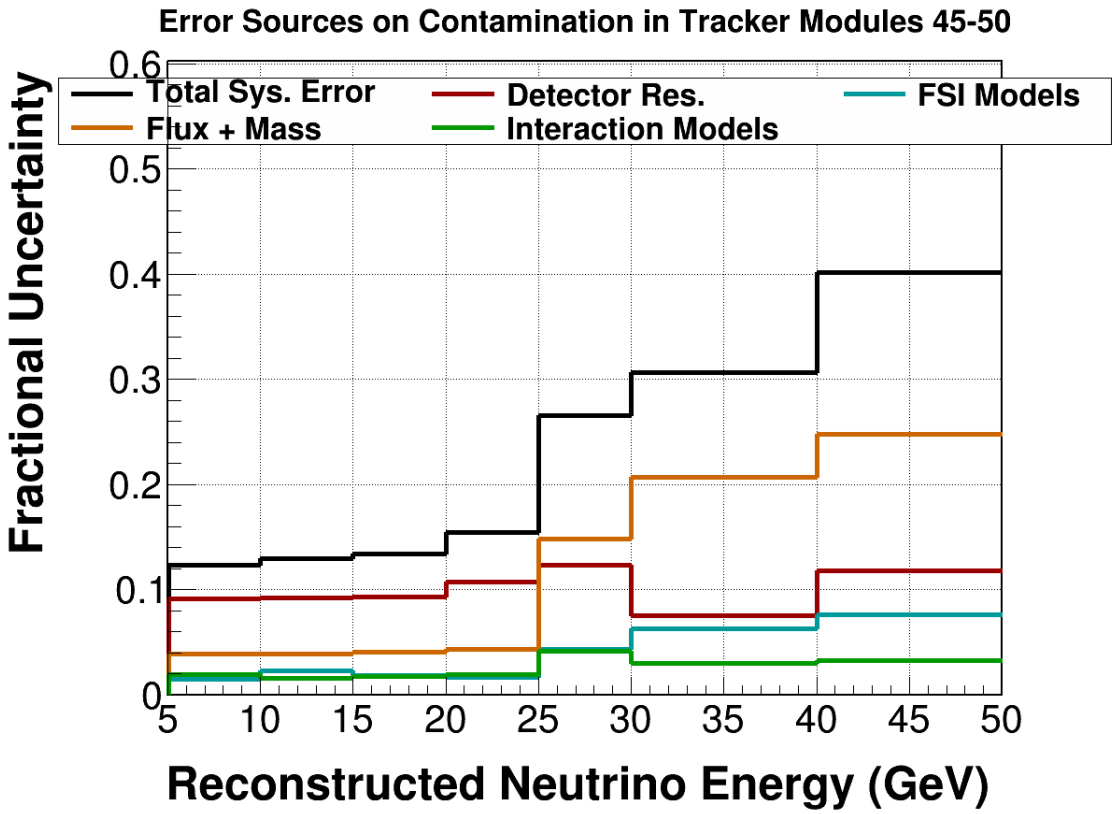

Figure B-14. Uncertainties on mis-ided DIS events: tracker mods. 45-50 (E_ν)

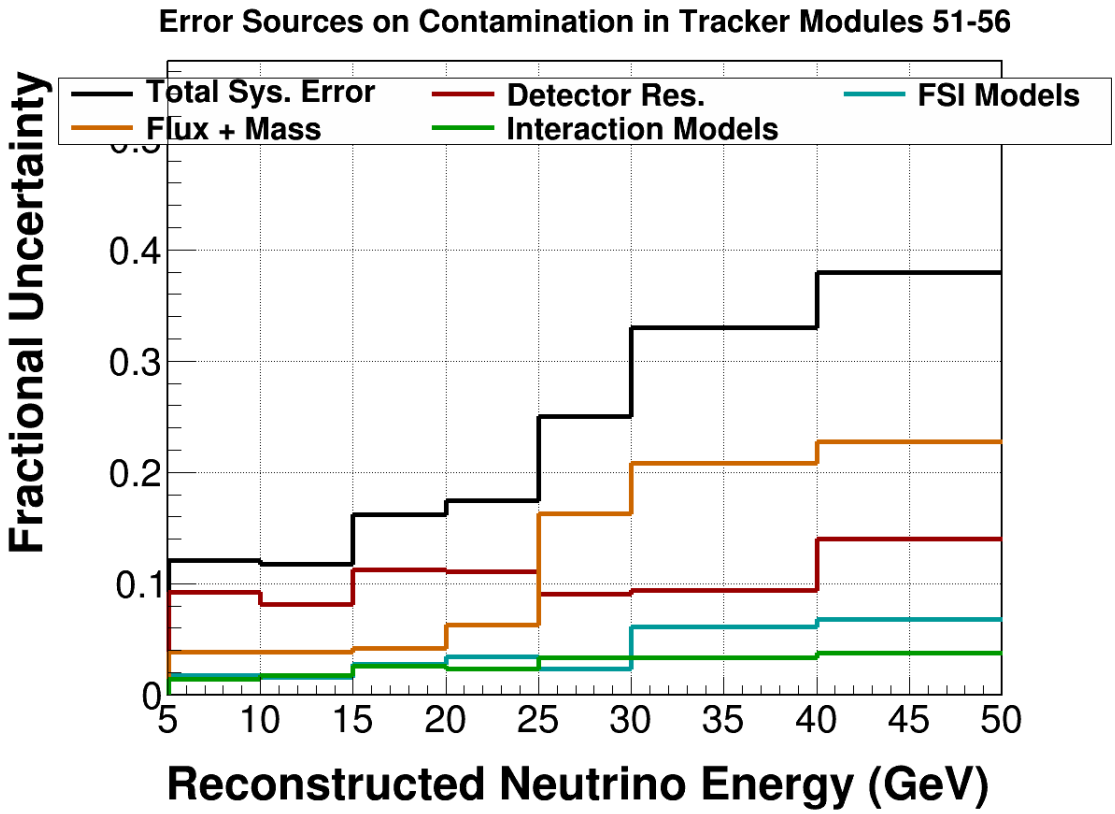

Figure B-15. Uncertainties on mis-ided DIS events: tracker mods. 51-56 (E_ν)

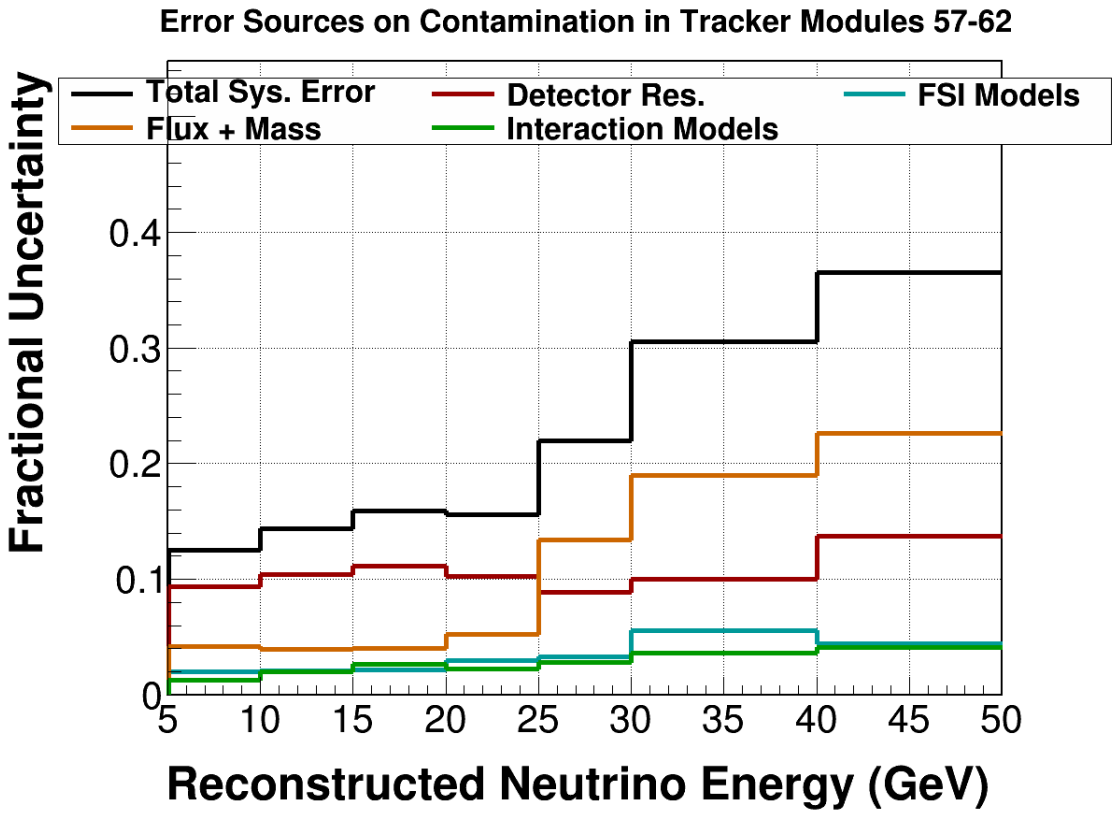

Figure B-16. Uncertainties on mis-ided DIS events: tracker mods. 57-62 (E_ν)

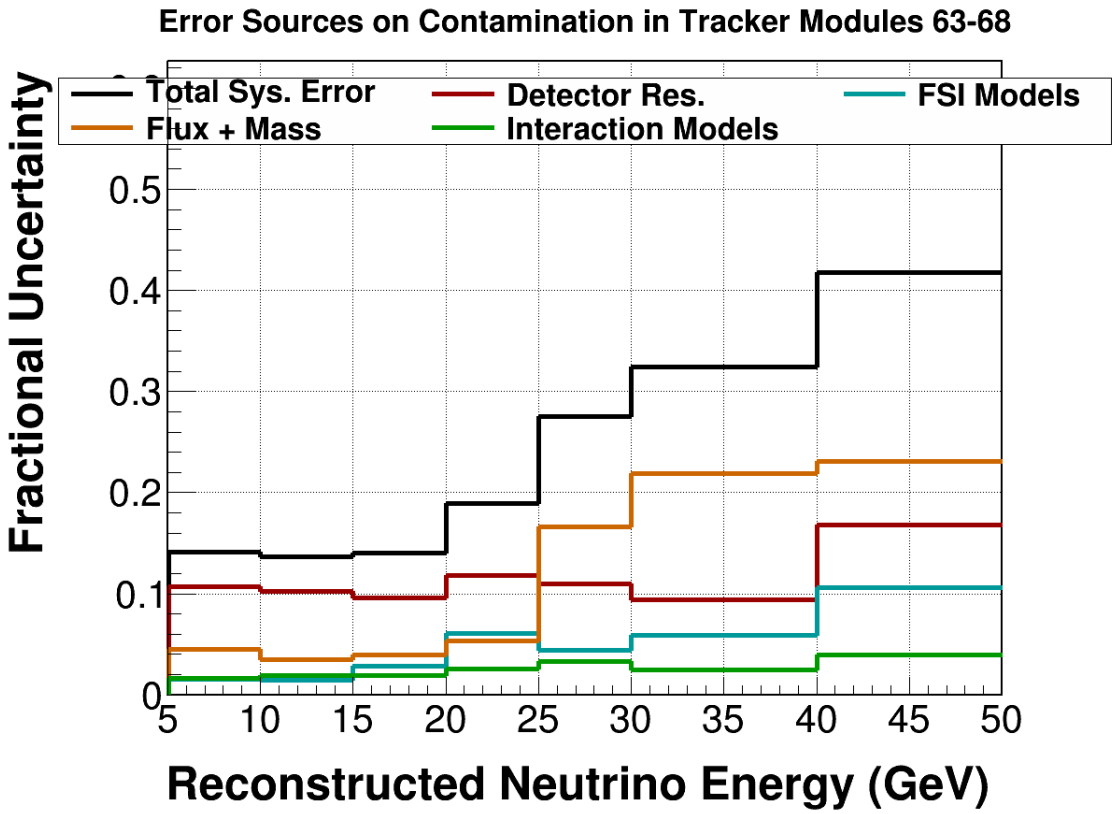

Figure B-17. Uncertainties on mis-ided DIS events: tracker mods. 63-68 (E_ν)

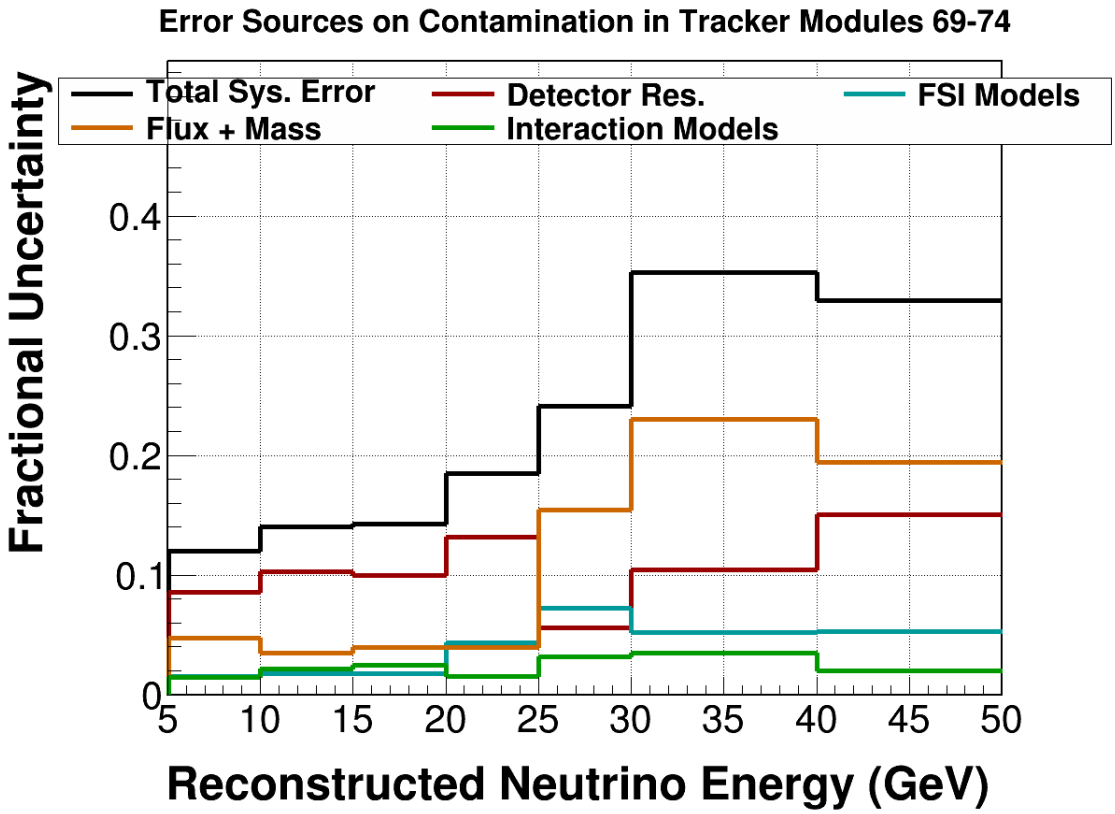

Figure B-18. Uncertainties on mis-ided DIS events: tracker mods. 69-74 (E_ν)

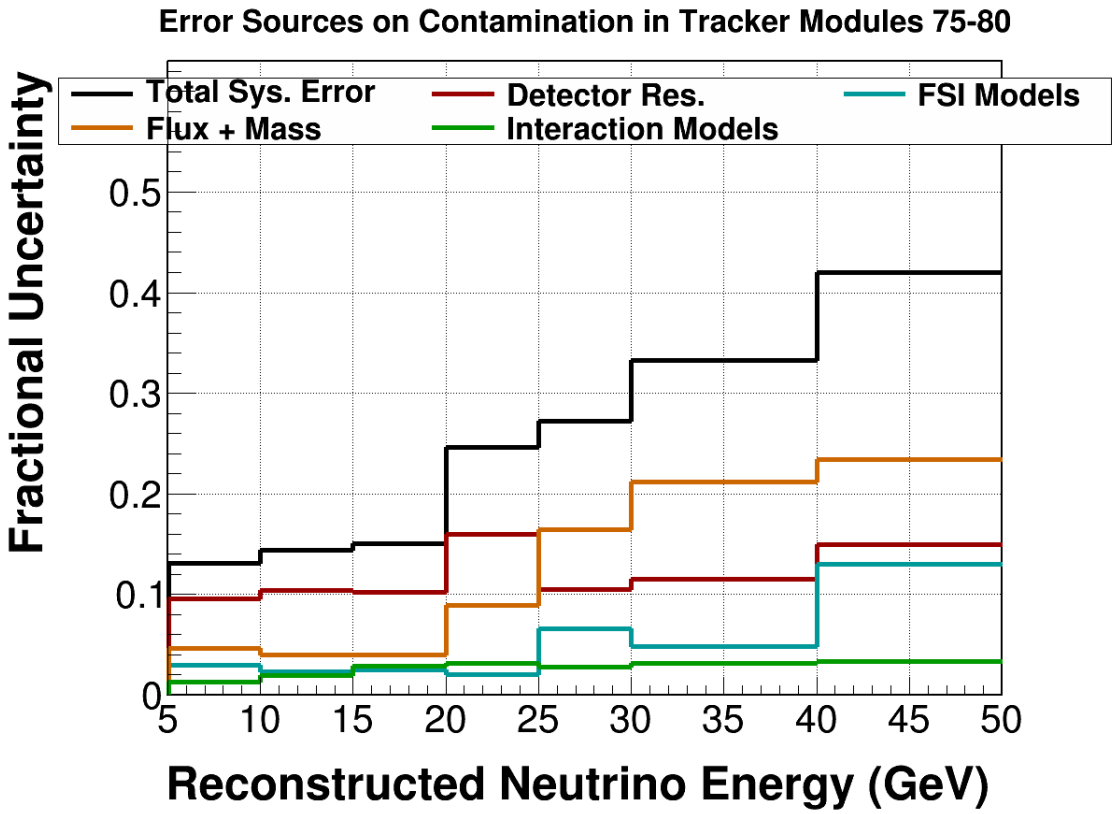

Figure B-19. Uncertainties on mis-ided DIS events: tracker mods. 75-80 (E_ν)

The following plots show the uncertainty on the number of truly non-DIS events which pass the DIS event selection cuts as a function of four momentum transfer squared (Q^2):

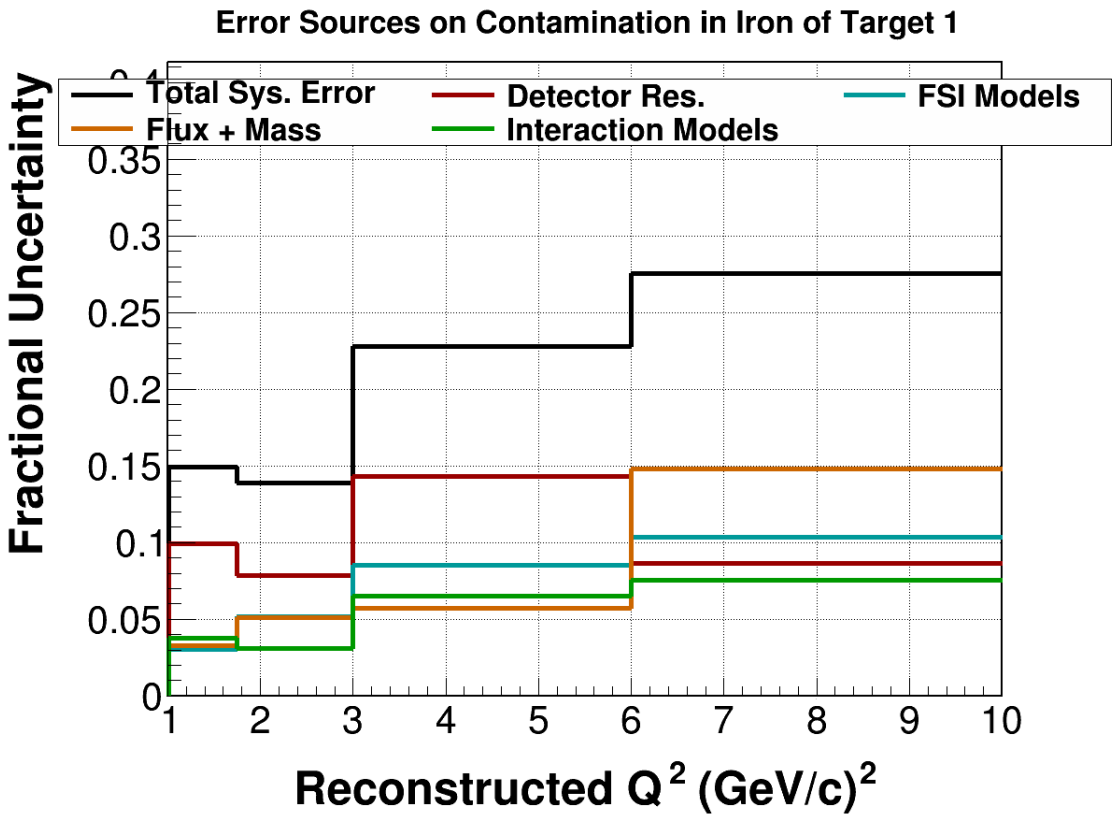

Figure B-20. Uncertainties on mis-ided DIS events: target 01 Fe (Q^2)

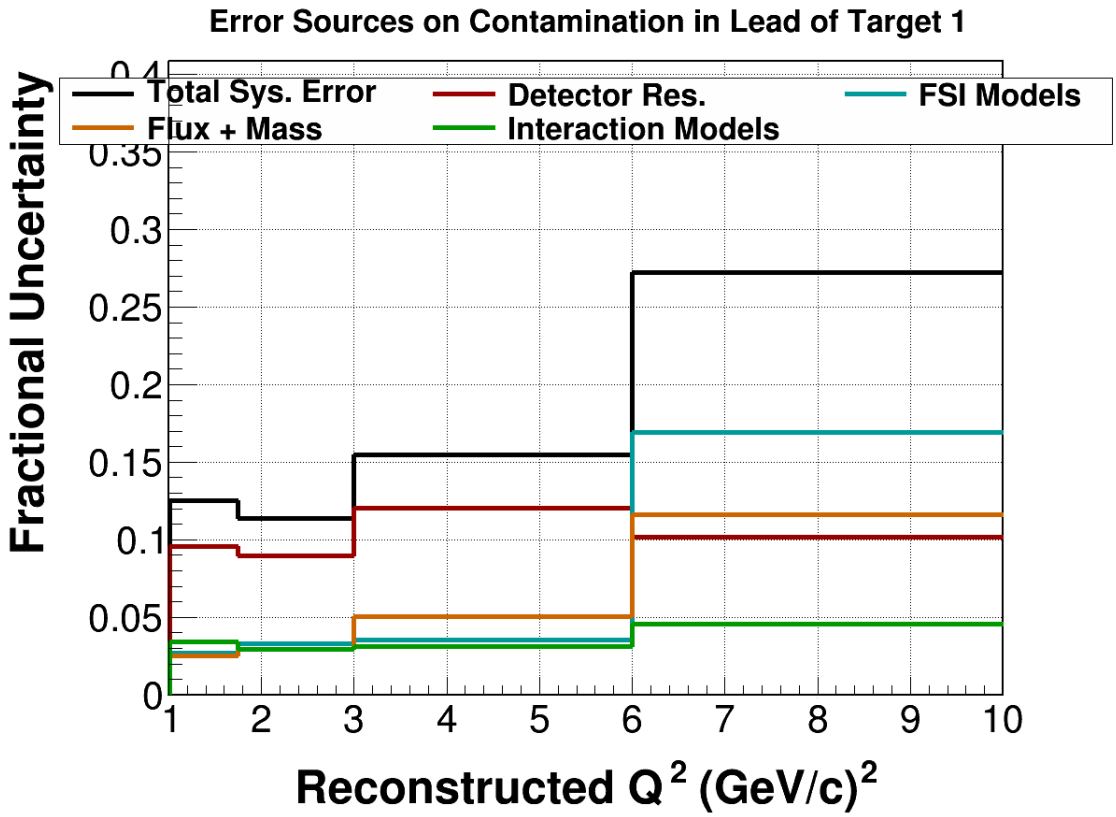

Figure B-21. Uncertainties on mis-ided DIS events: target 01 Pb (Q^2)

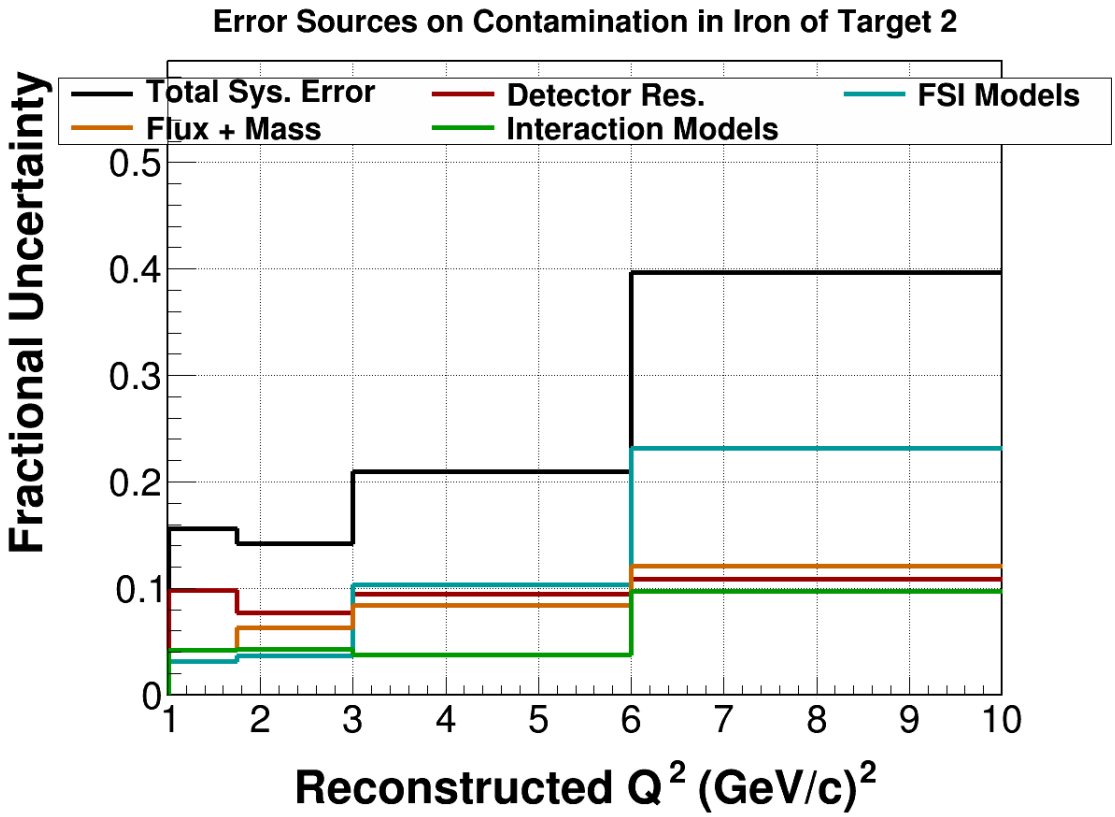

Figure B-22. Uncertainties on mis-ided DIS events: target 02 Fe (Q^2)

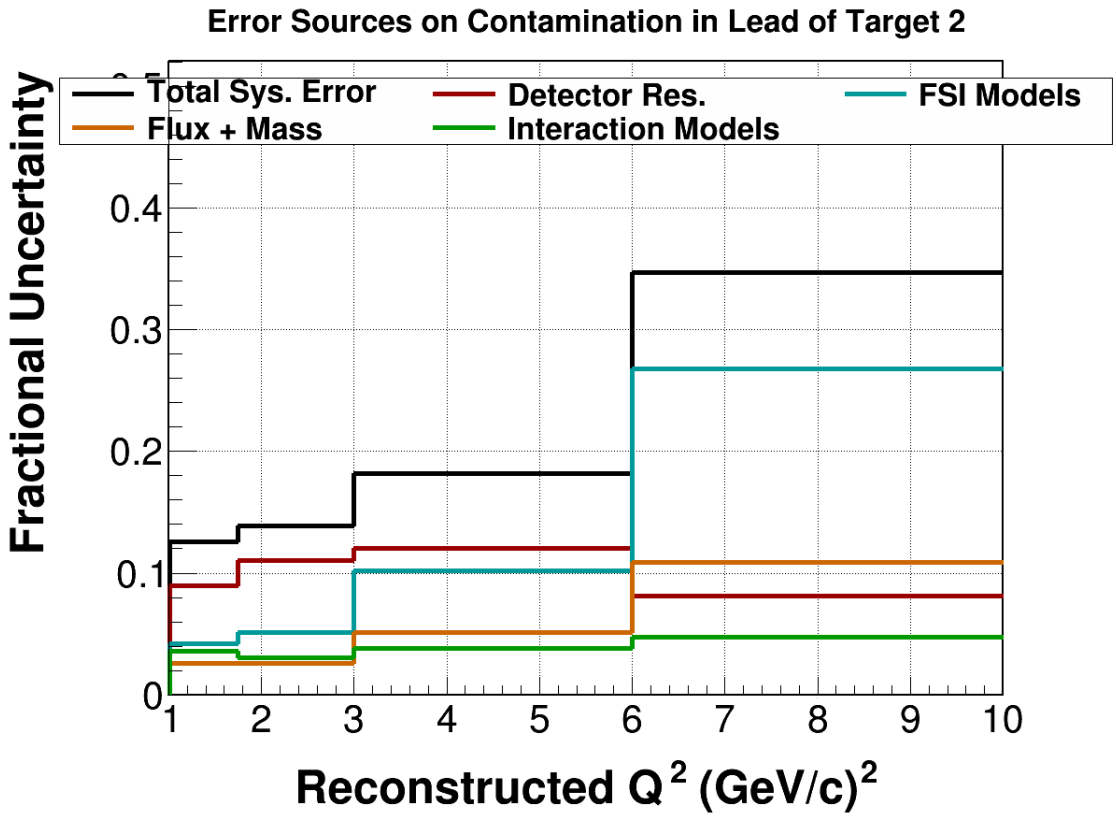

Figure B-23. Uncertainties on mis-ided DIS events: target 02 Pb (Q^2)

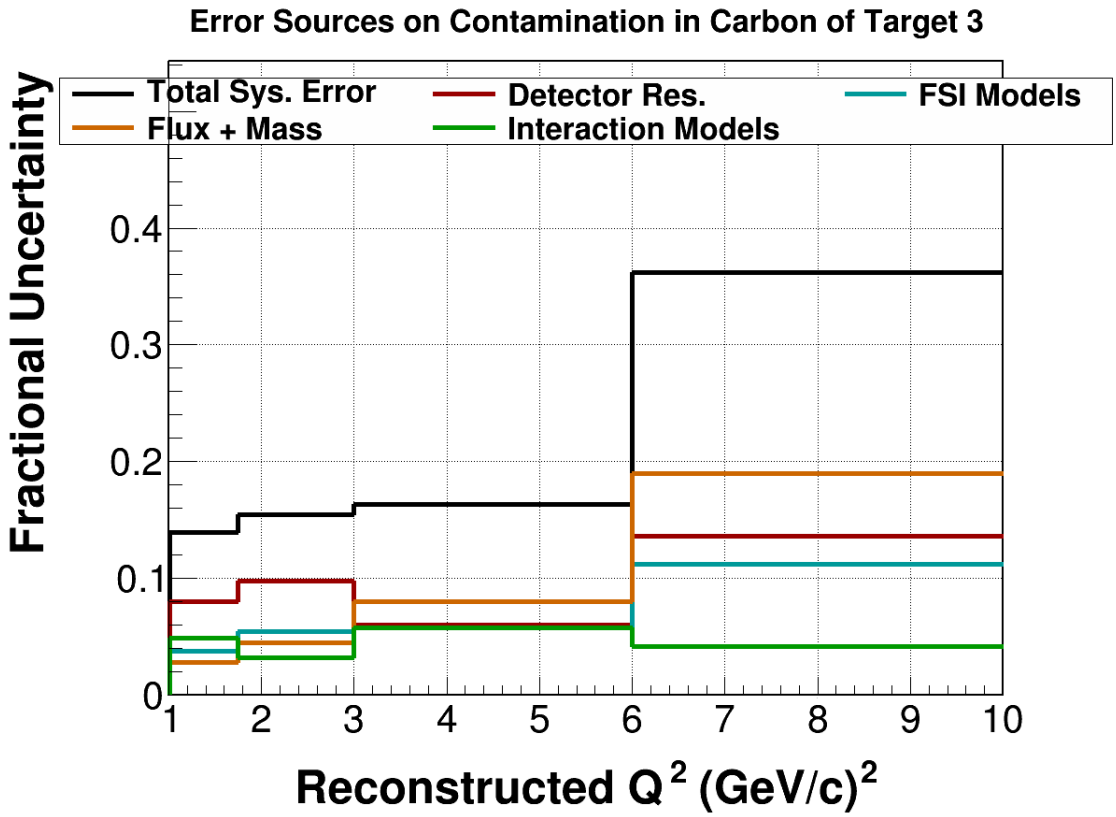

Figure B-24. Uncertainties on mis-ided DIS events: target 03 C (Q^2)

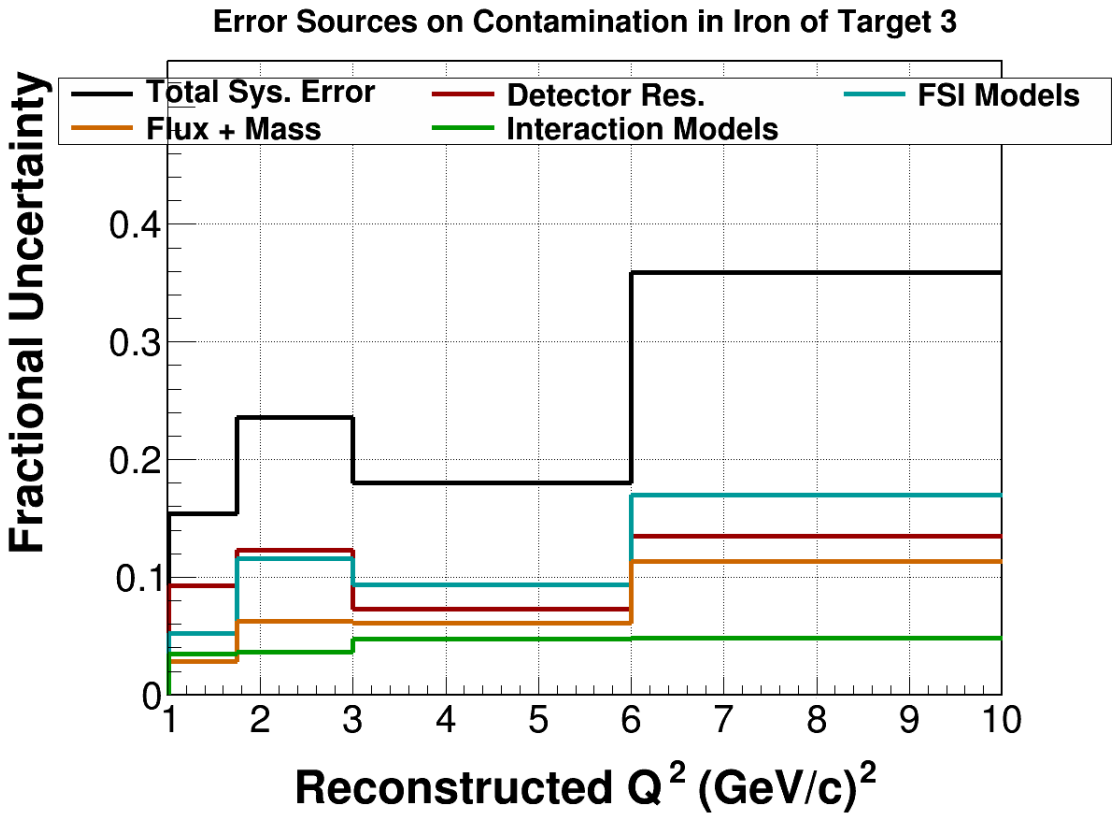

Figure B-25. Uncertainties on mis-ided DIS events: target 03 Fe (Q^2)

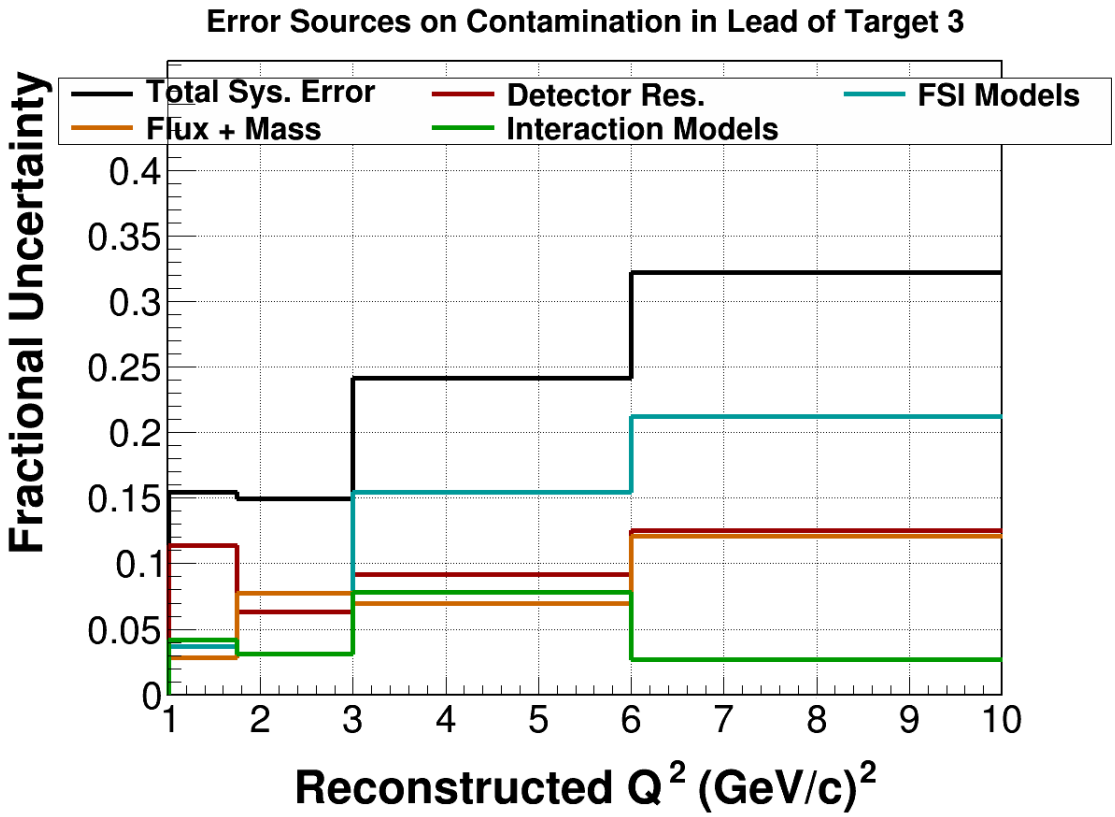

Figure B-26. Uncertainties on mis-ided DIS events: target 03 Pb (Q^2)

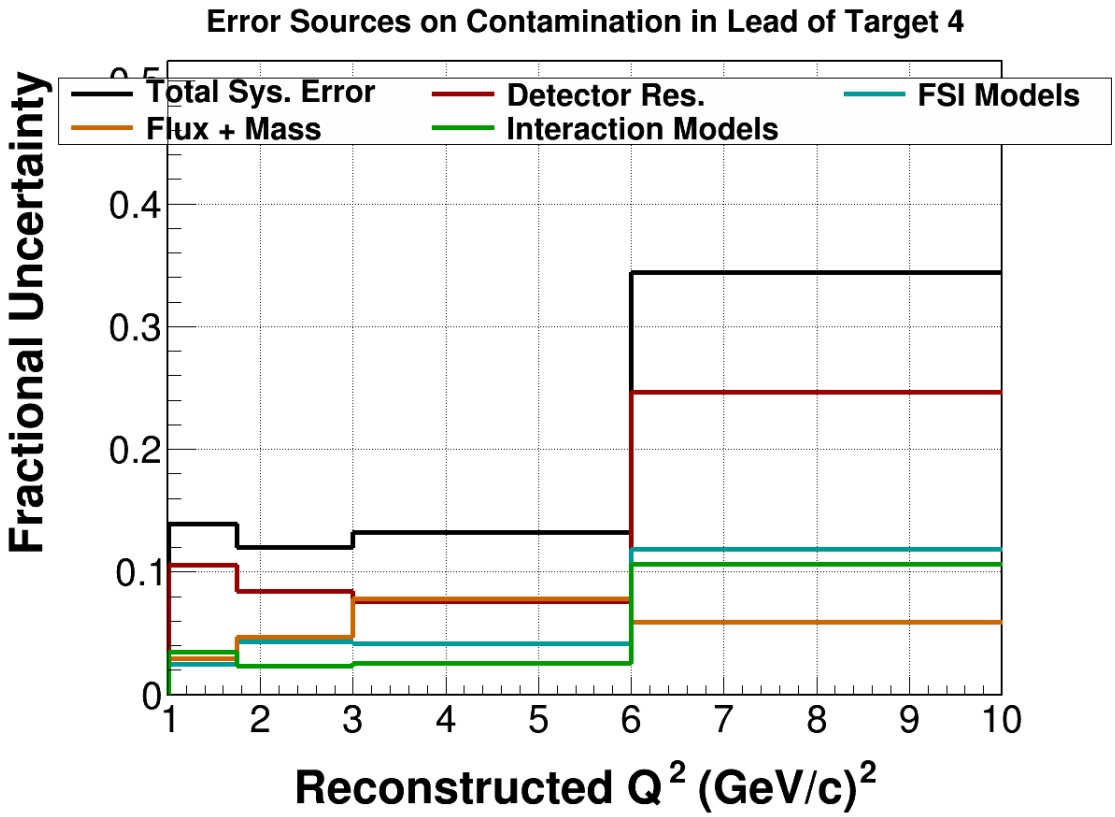

Figure B-27. Uncertainties on mis-ided DIS events: target 04 Pb (Q^2)

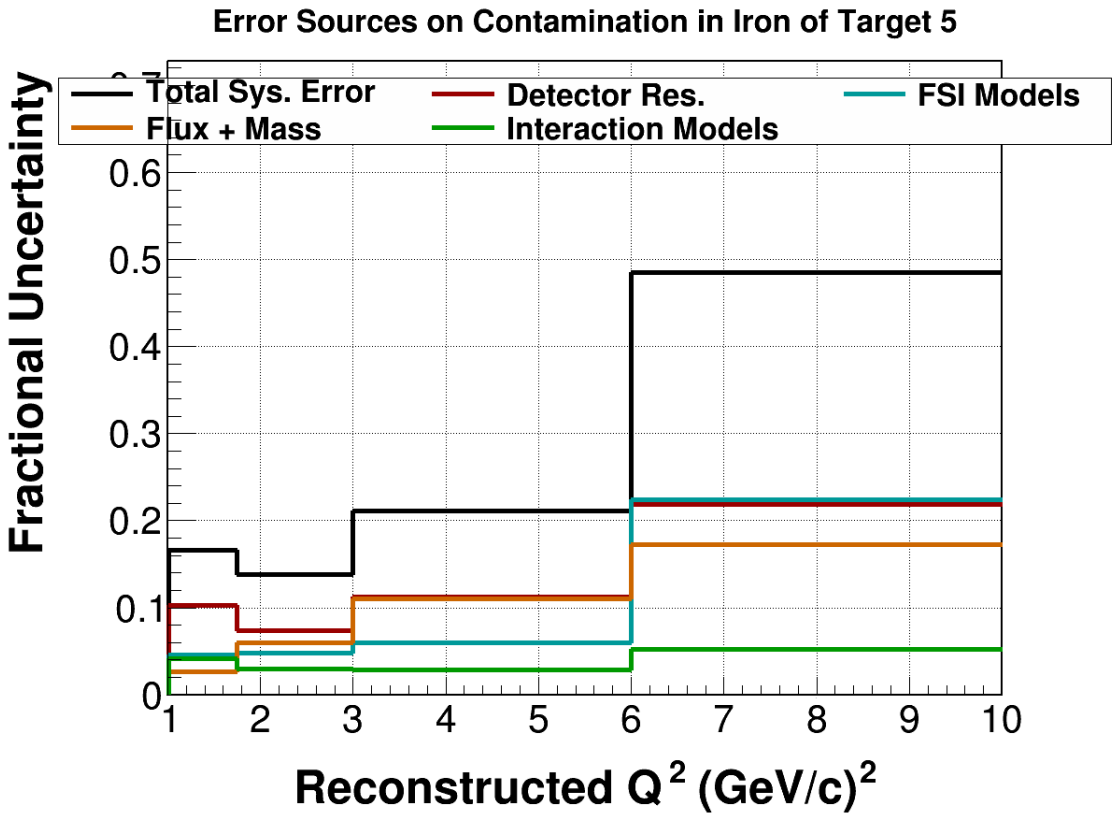

Figure B-28. Uncertainties on mis-ided DIS events: target 05 Fe (Q^2)

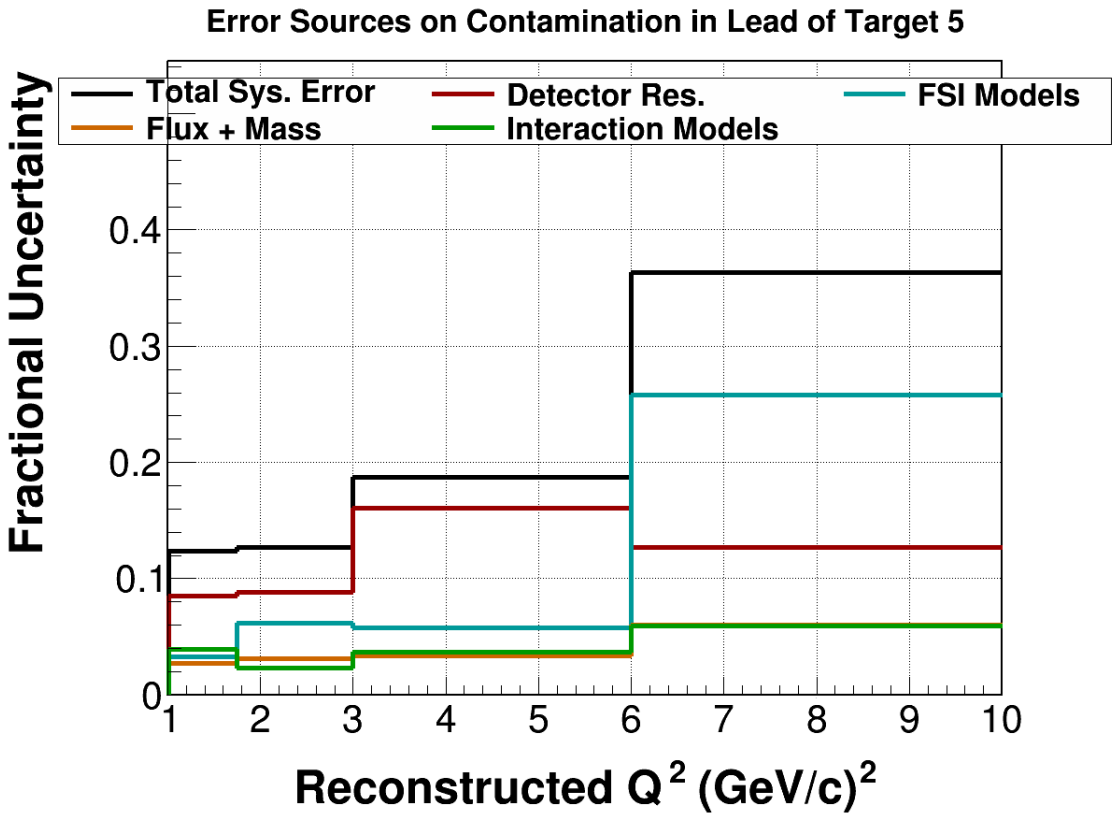

Figure B-29. Uncertainties on mis-ided DIS events: target 05 Pb (Q^2)

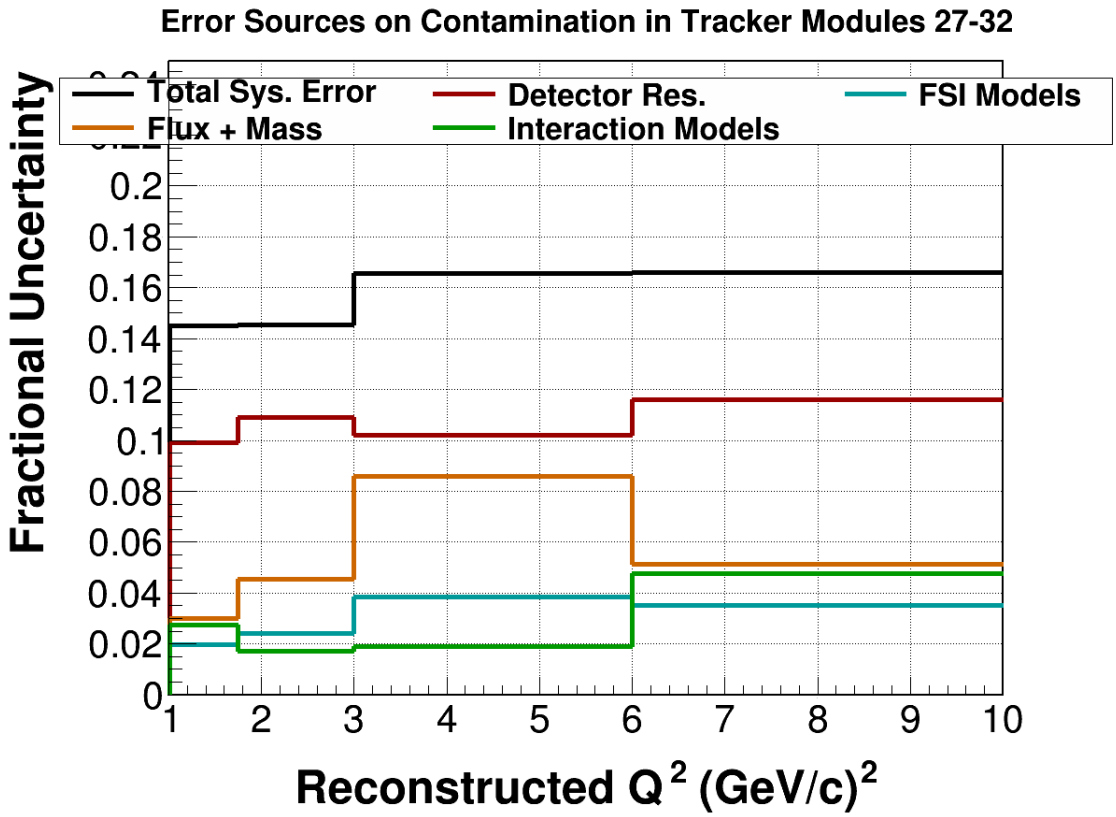

Figure B-30. Uncertainties on mis-ided DIS events: tracker mods. 27-32 (Q^2)

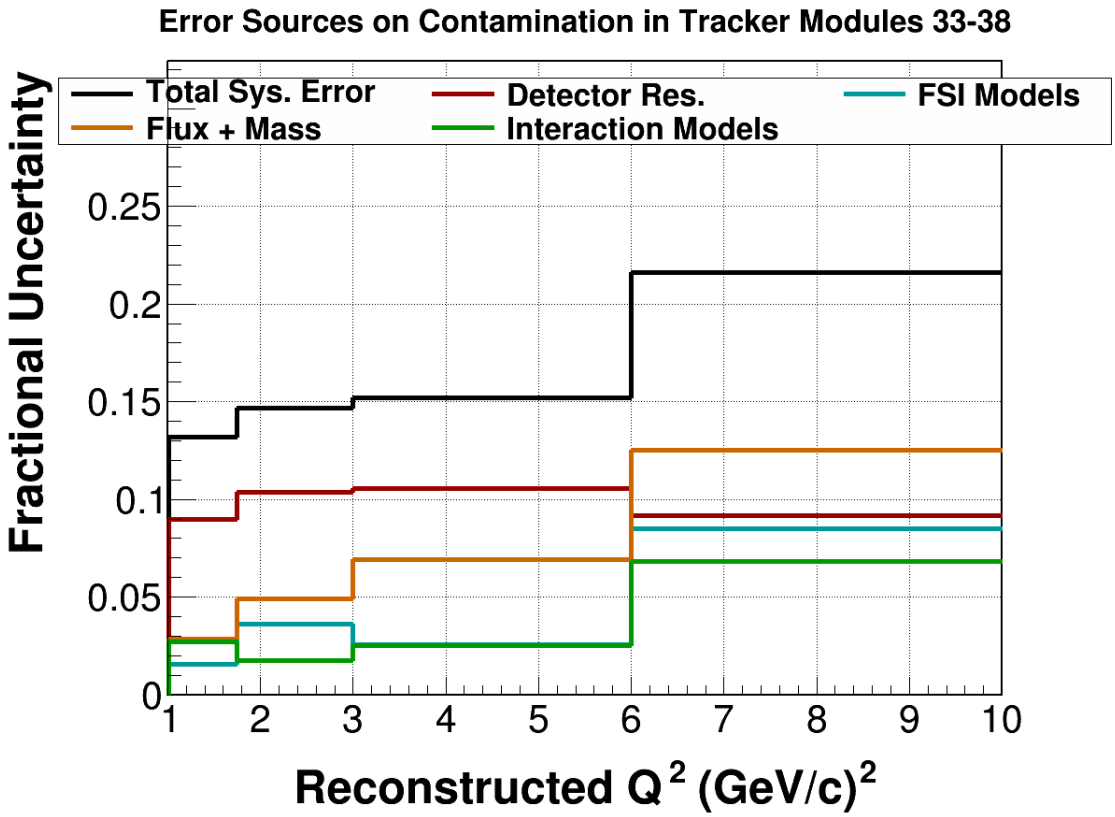

Figure B-31. Uncertainties on mis-ided DIS events: tracker mods. 33-38 (Q^2)

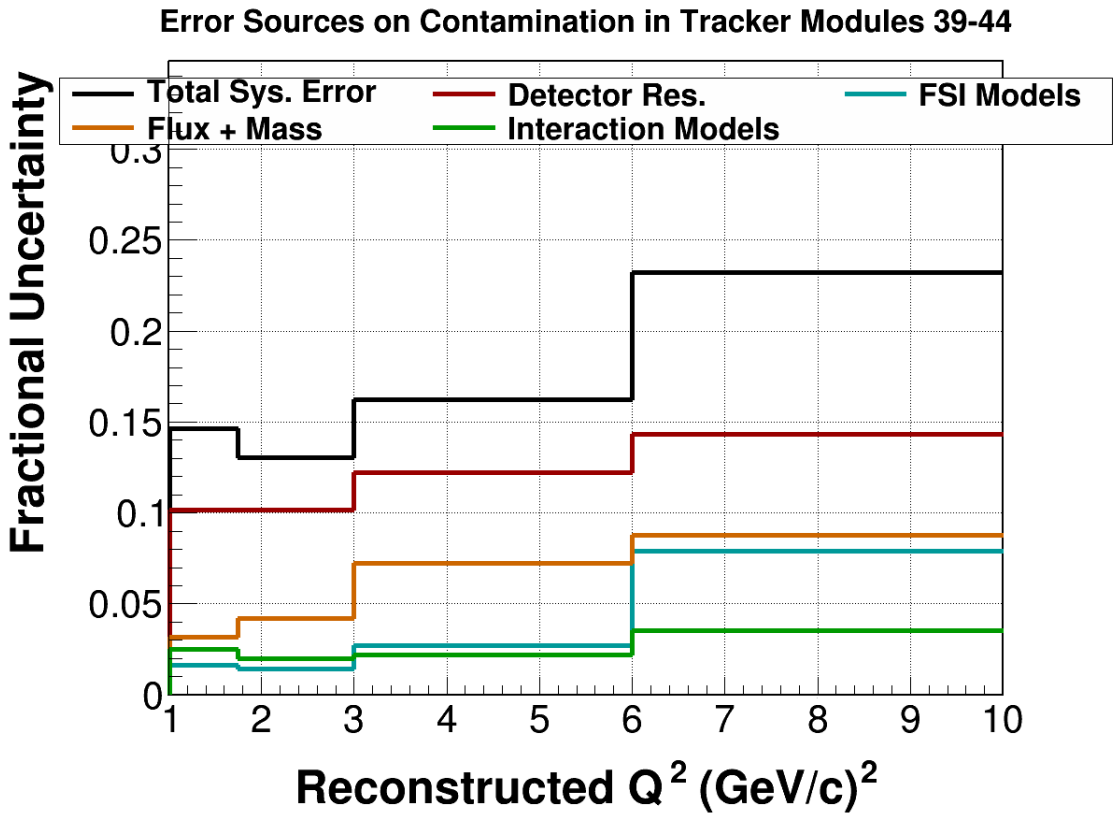

Figure B-32. Uncertainties on mis-ided DIS events: tracker mods. 39-44 (Q^2)

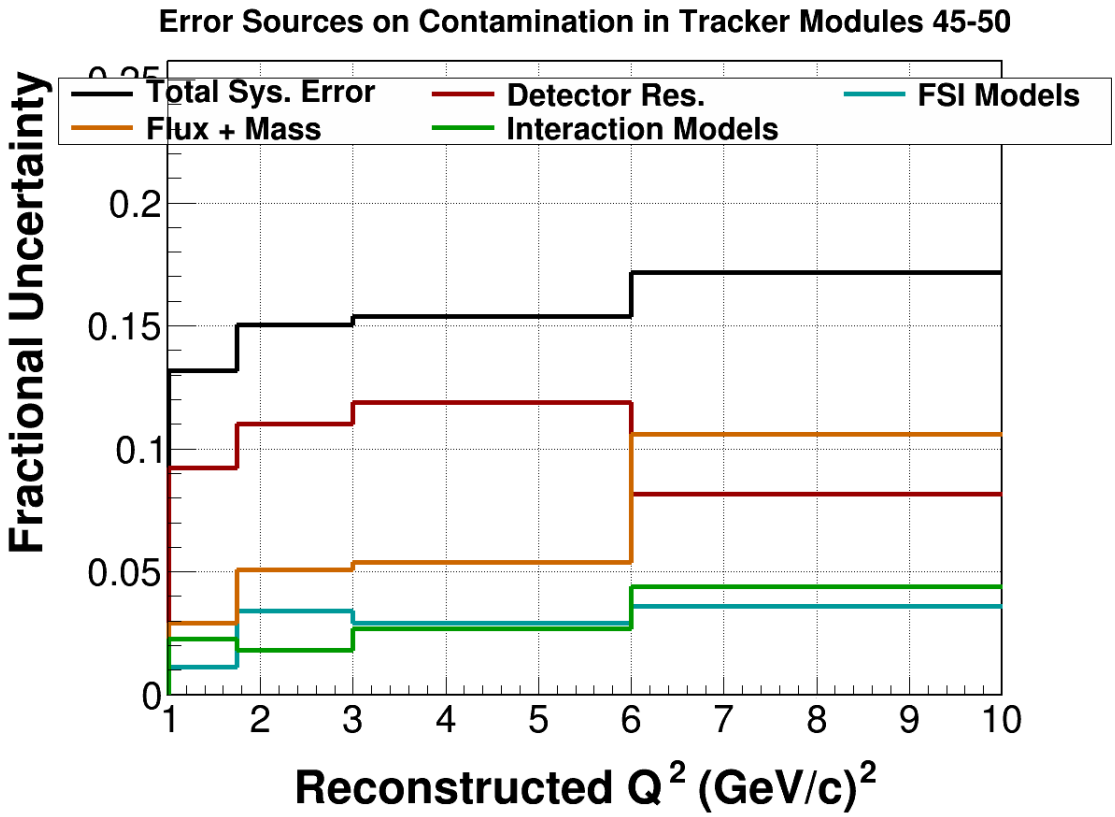

Figure B-33. Uncertainties on mis-ided DIS events: tracker mods. 45-50 (Q^2)

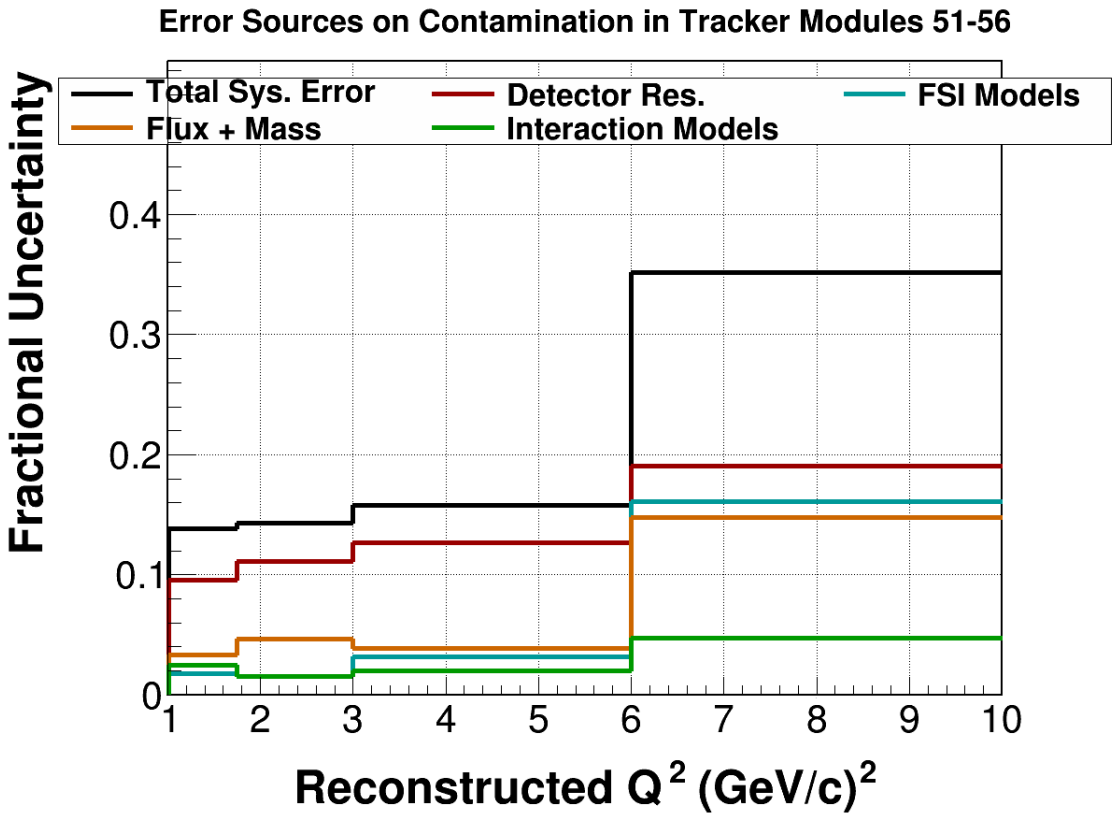

Figure B-34. Uncertainties on mis-ided DIS events: tracker mods. 51-56 (Q^2)

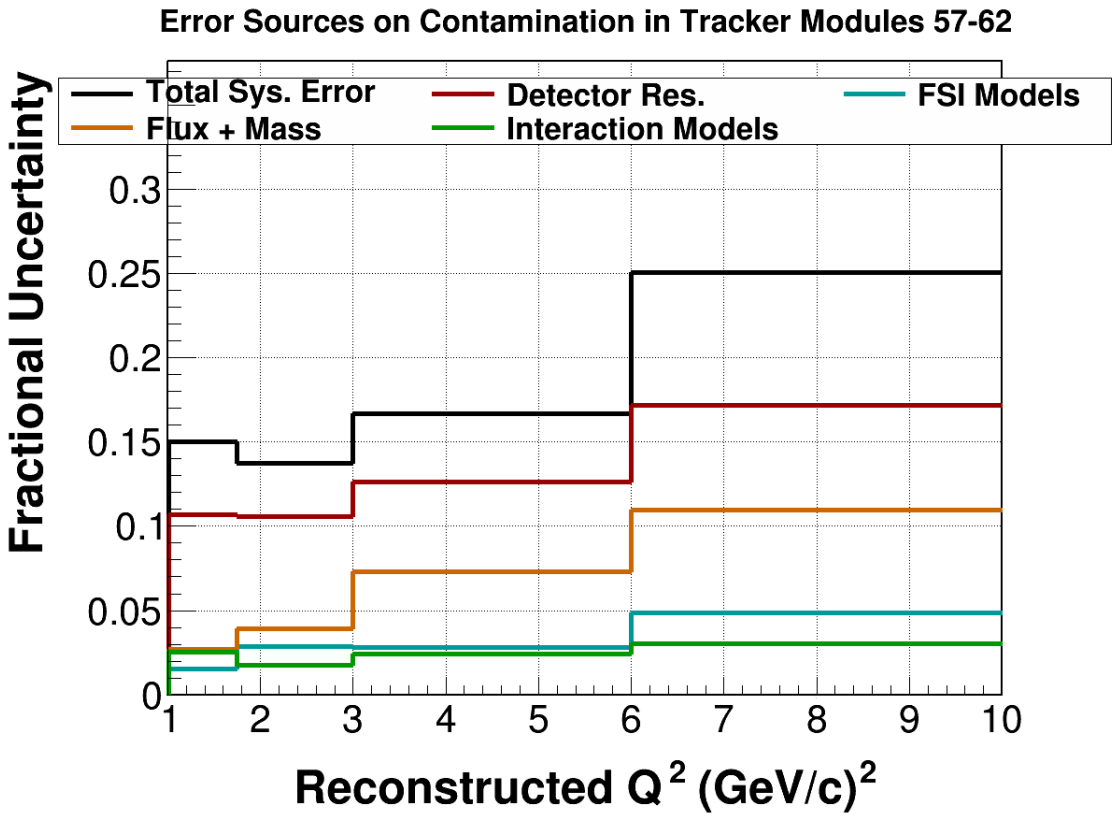

Figure B-35. Uncertainties on mis-ided DIS events: tracker mods. 57-62 (Q^2)

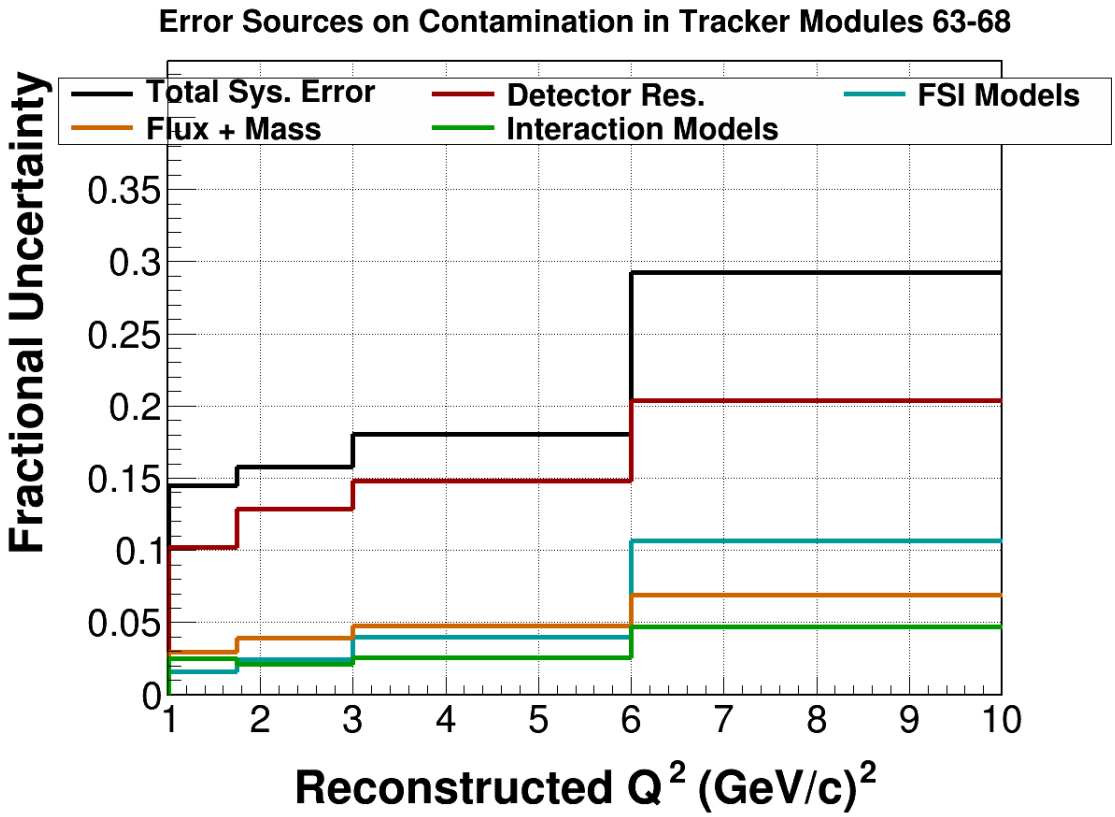

Figure B-36. Uncertainties on mis-ided DIS events: tracker mods. 63-68 (Q^2)

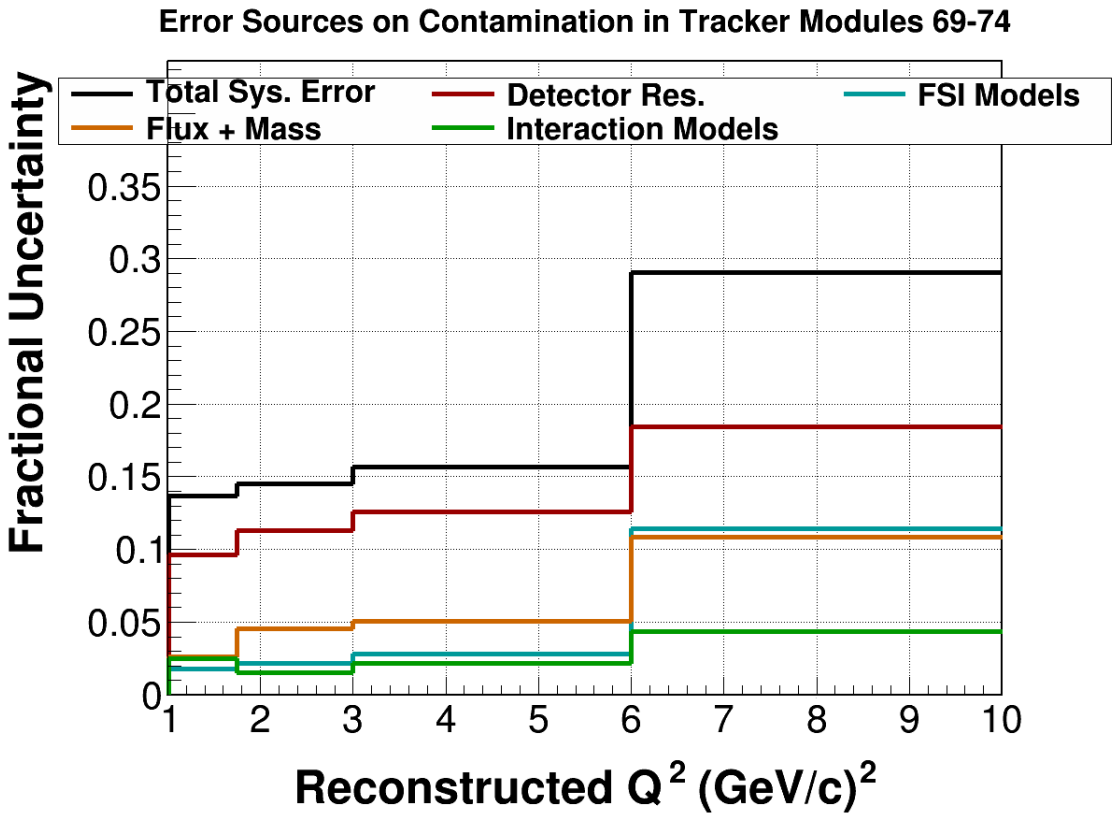

Figure B-37. Uncertainties on mis-ided DIS events: tracker mods. 69-74 (Q^2)

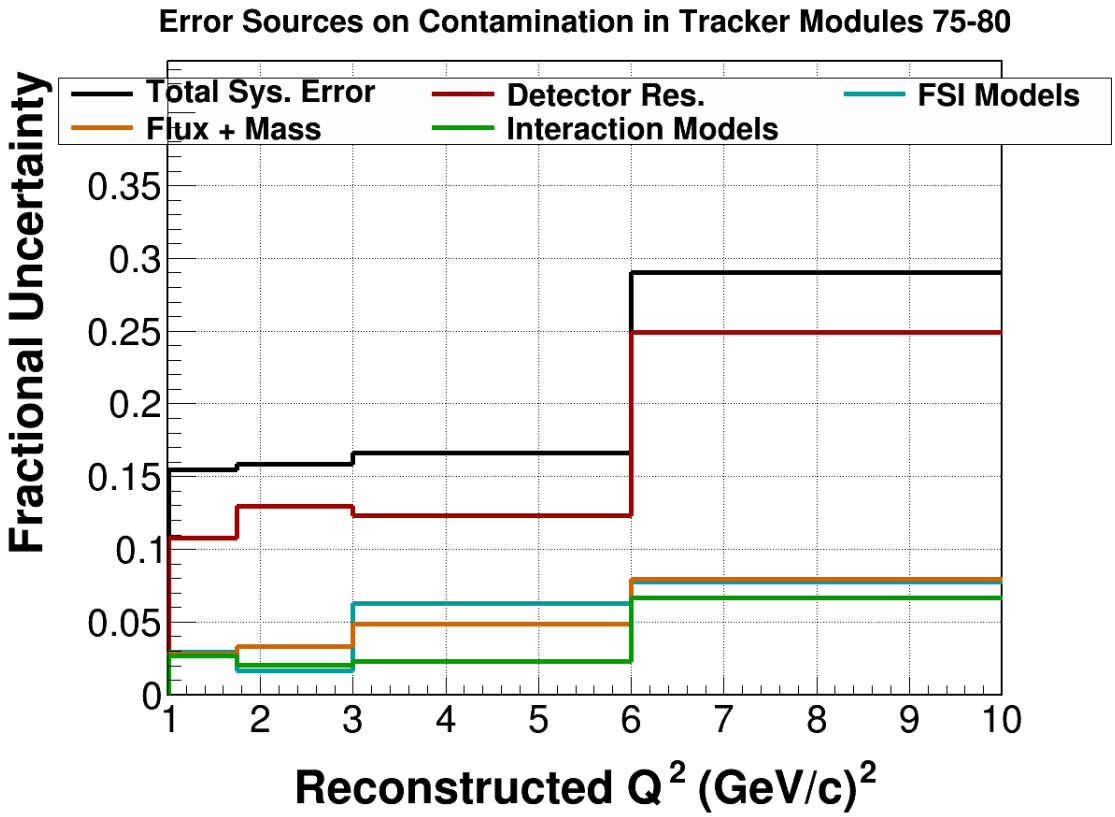

Figure B-38. Uncertainties on mis-ided DIS events: tracker mods. 75-80 (Q^2)

The following plots show the uncertainty on the number of truly non-DIS events which pass the DIS event selection cuts as a function of final state hadron shower invariant mass (W):

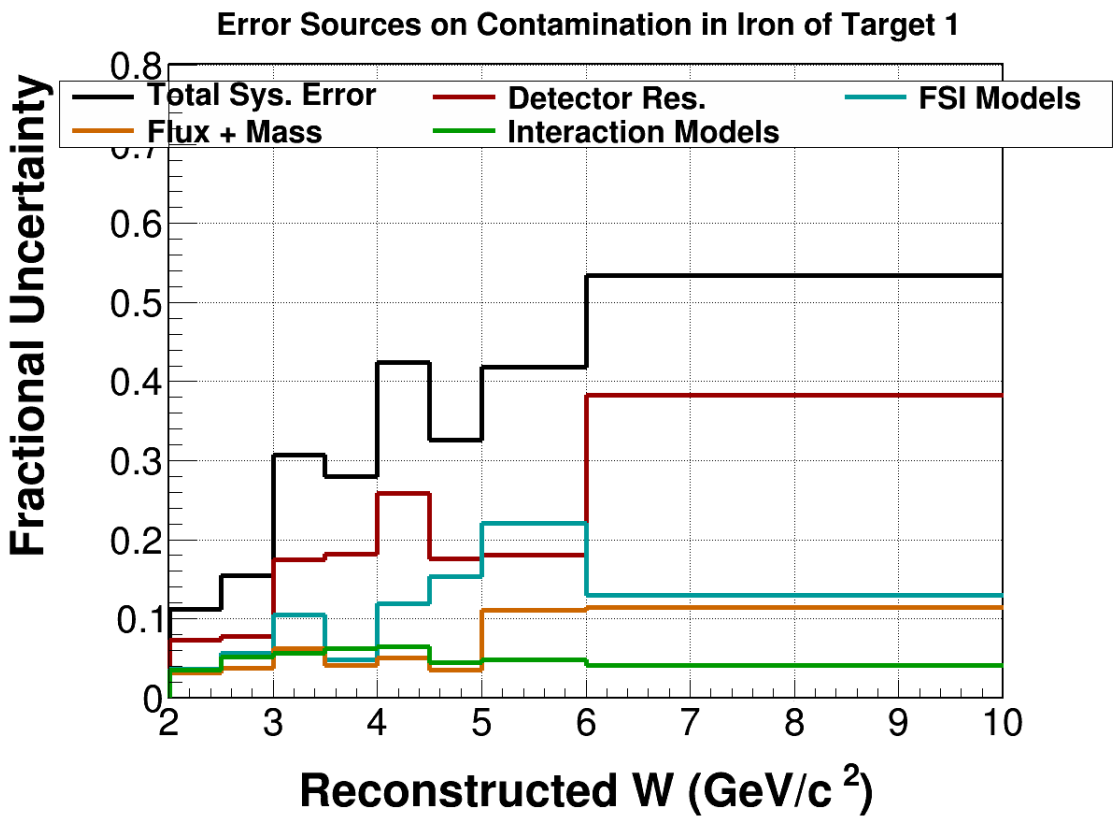

Figure B-39. Uncertainties on mis-ided DIS events: target 01 Fe (W)

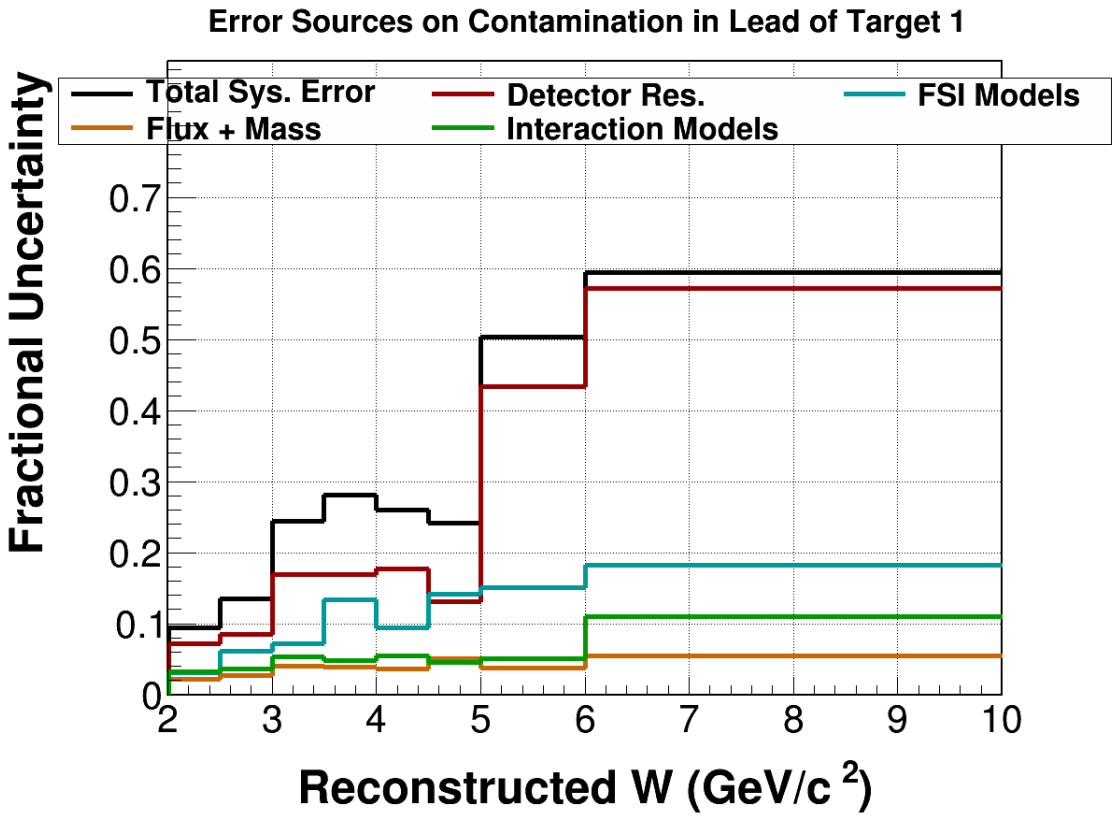

Figure B-40. Uncertainties on mis-ided DIS events: target 01 Pb (W)

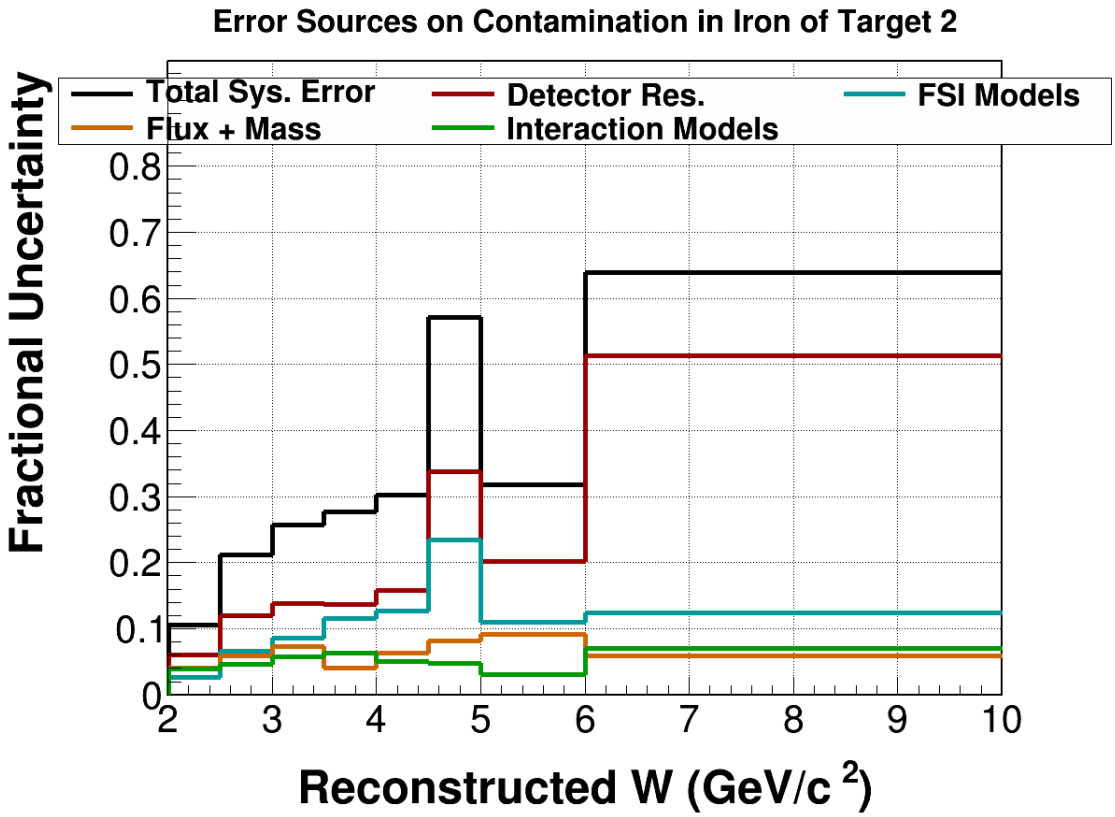

Figure B-41. Uncertainties on mis-ided DIS events: target 02 Fe (W)

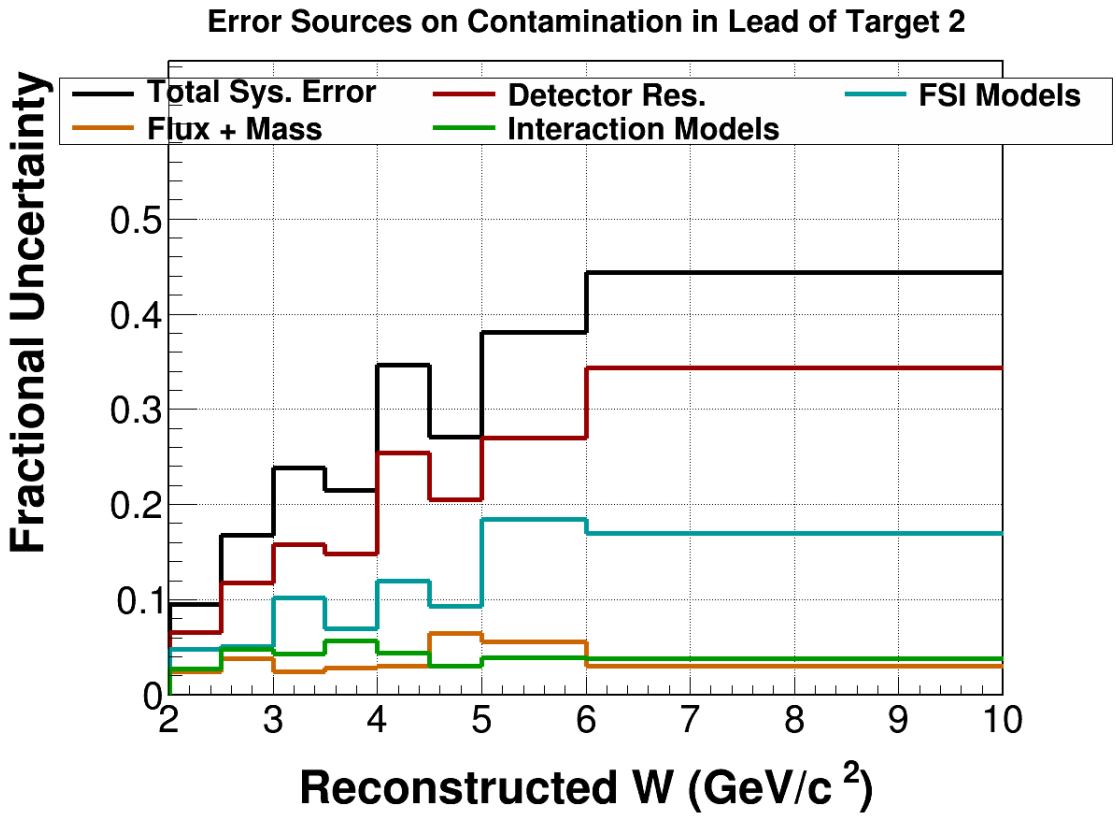

Figure B-42. Uncertainties on mis-ided DIS events: target 02 Pb (W)

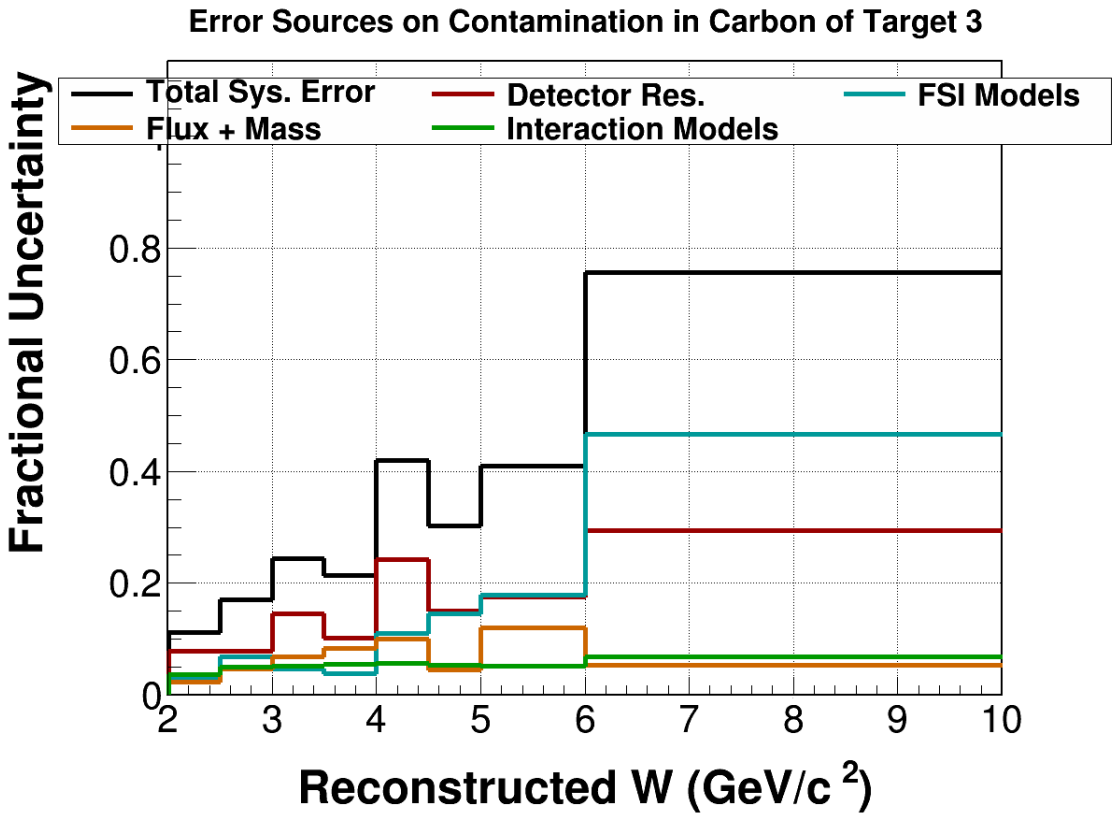

Figure B-43. Uncertainties on mis-ided DIS events: target 03 C (W)

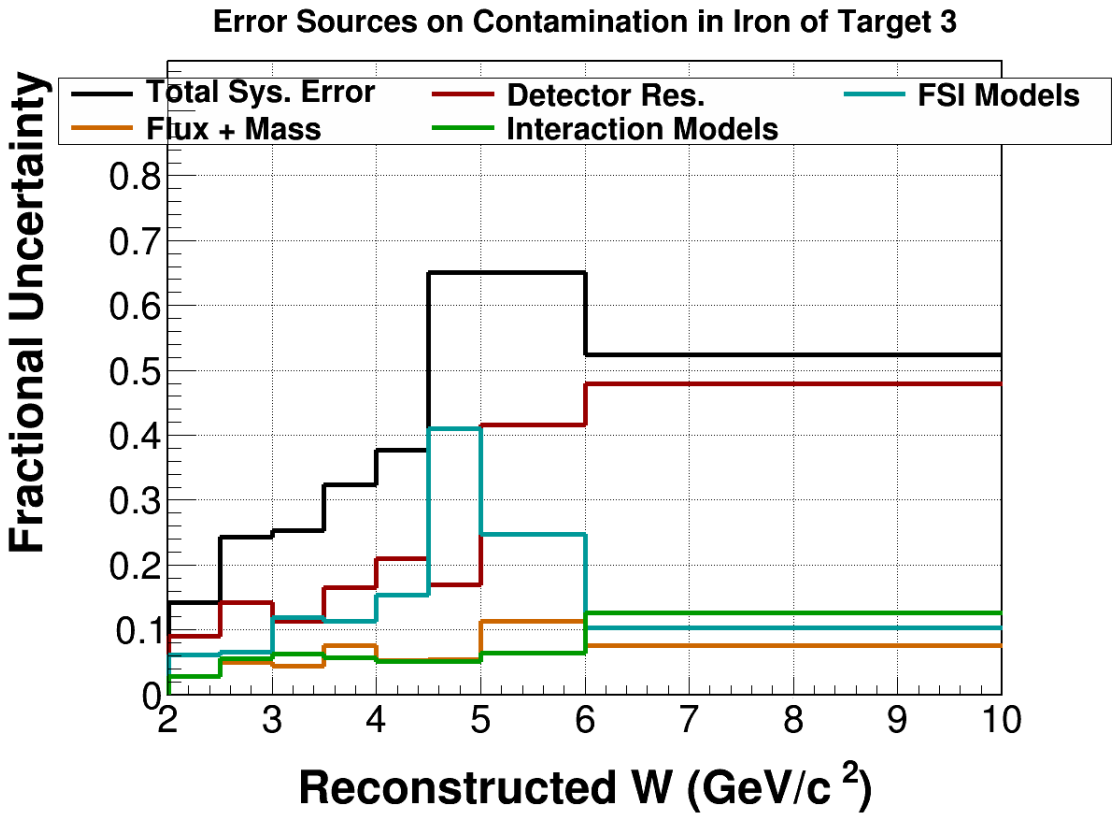

Figure B-44. Uncertainties on mis-ided DIS events: target 03 Fe (W)

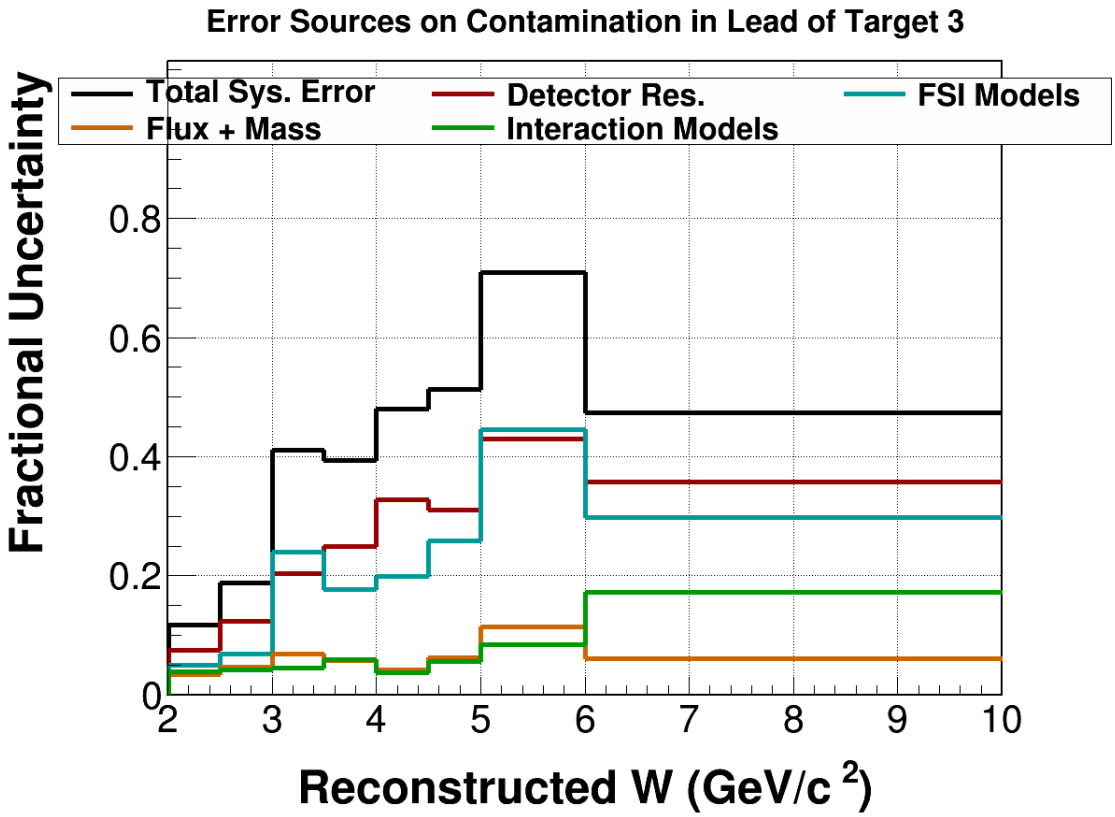

Figure B-45. Uncertainties on mis-ided DIS events: target 03 Pb (W)

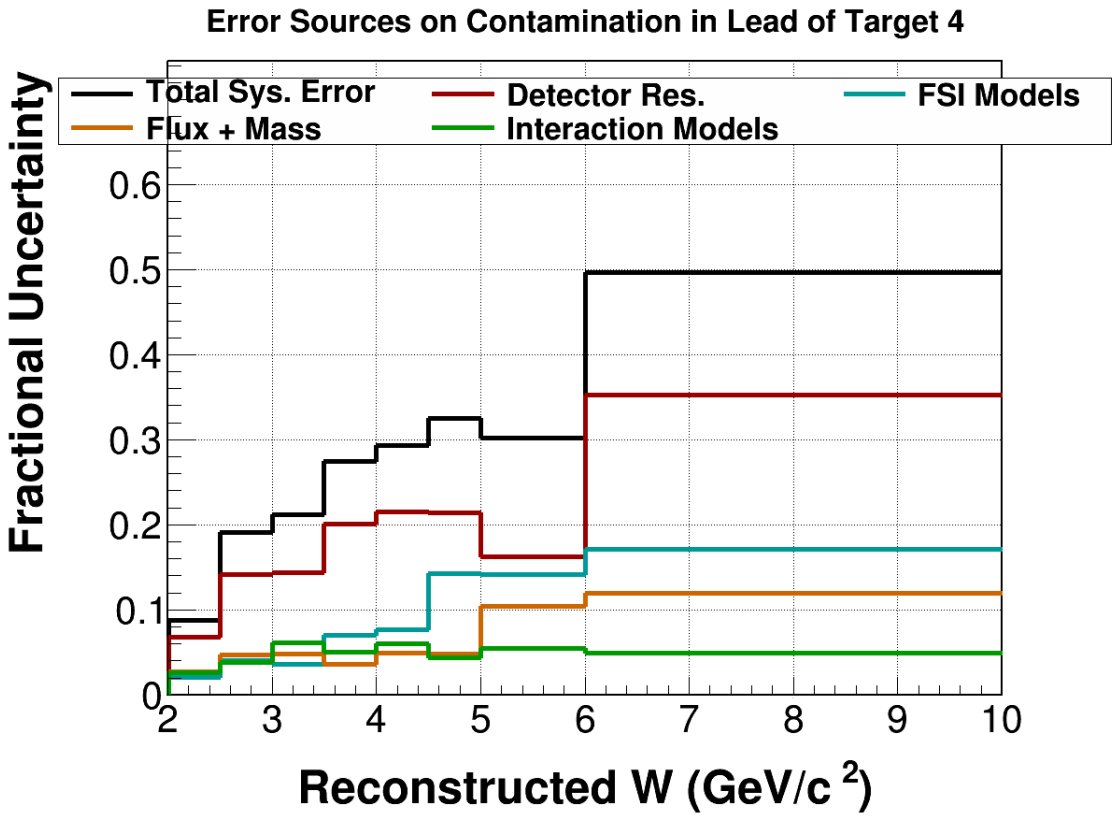

Figure B-46. Uncertainties on mis-ided DIS events: target 04 Pb (W)

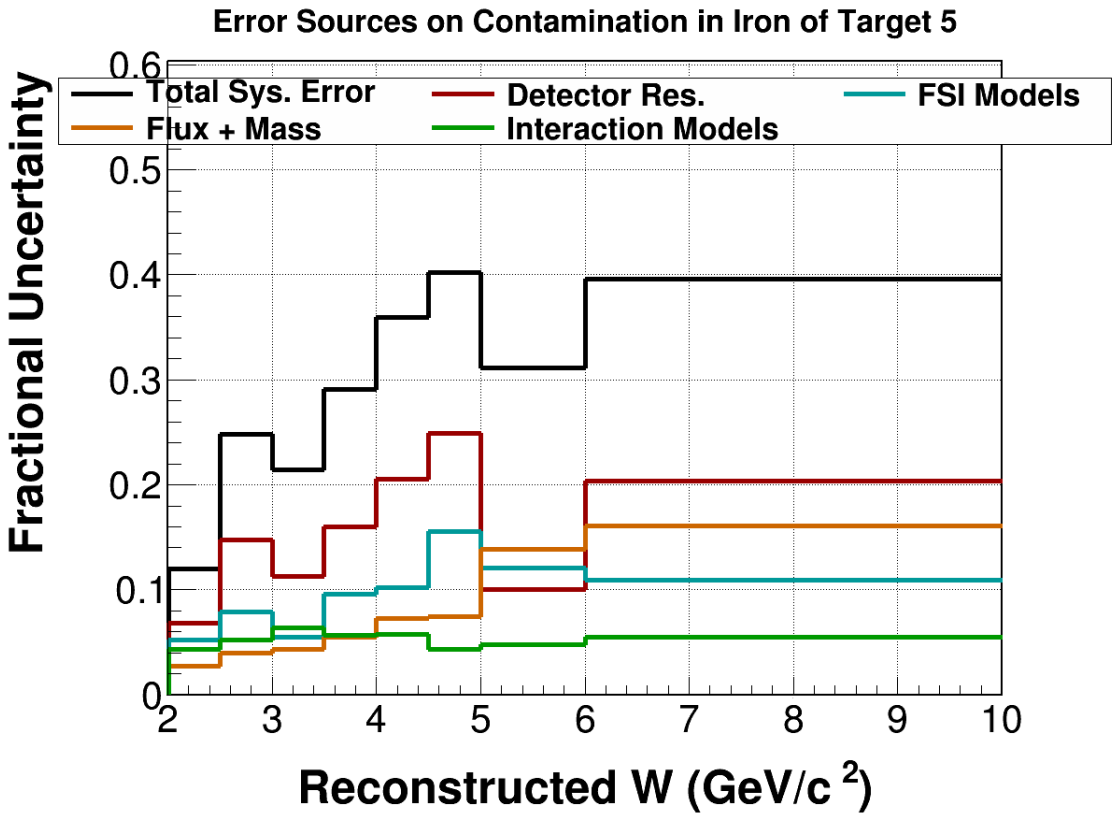

Figure B-47. Uncertainties on mis-ided DIS events: target 05 Fe (W)

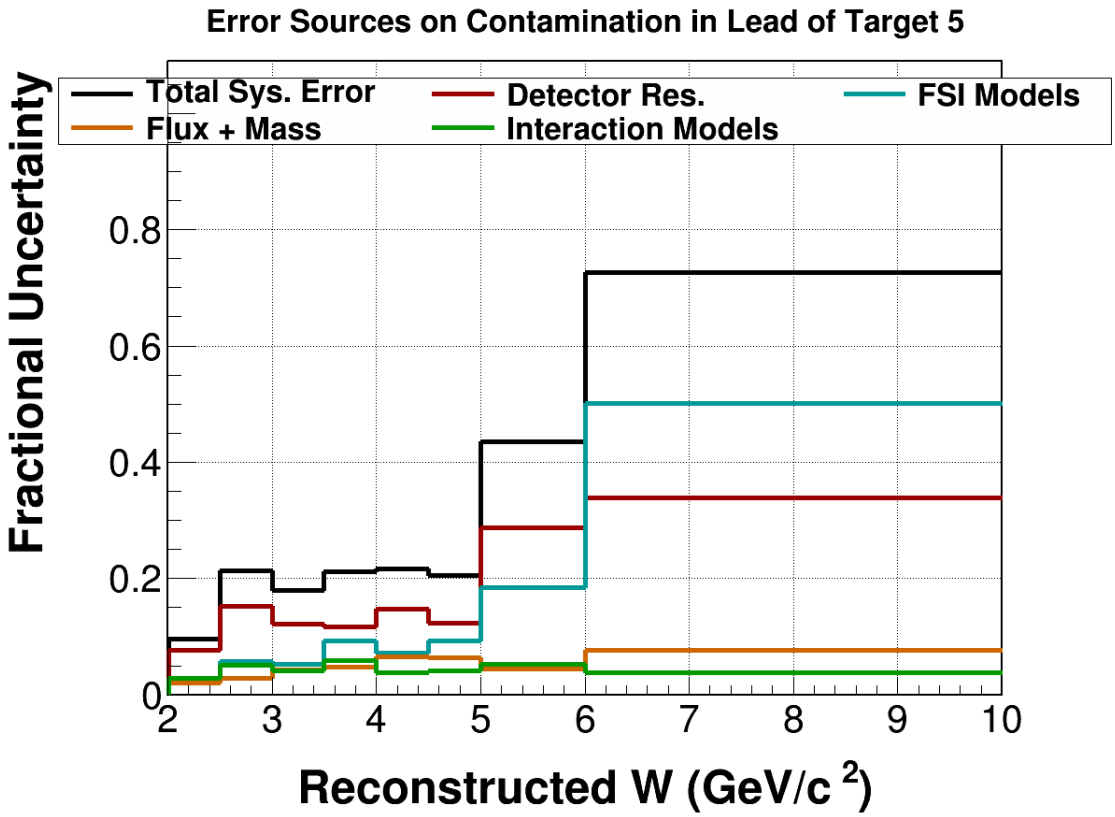

Figure B-48. Uncertainties on mis-ided DIS events: target 05 Pb (W)

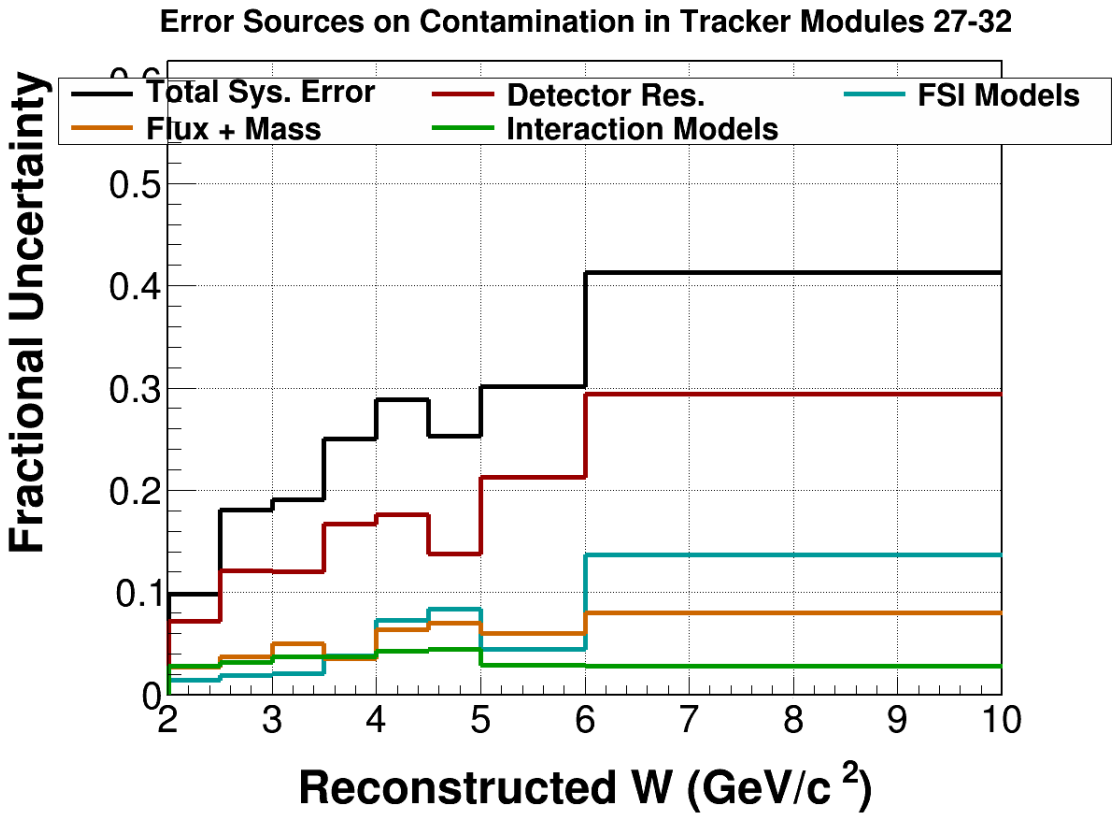

Figure B-49. Uncertainties on mis-ided DIS events: tracker mods. 27-32 (W)

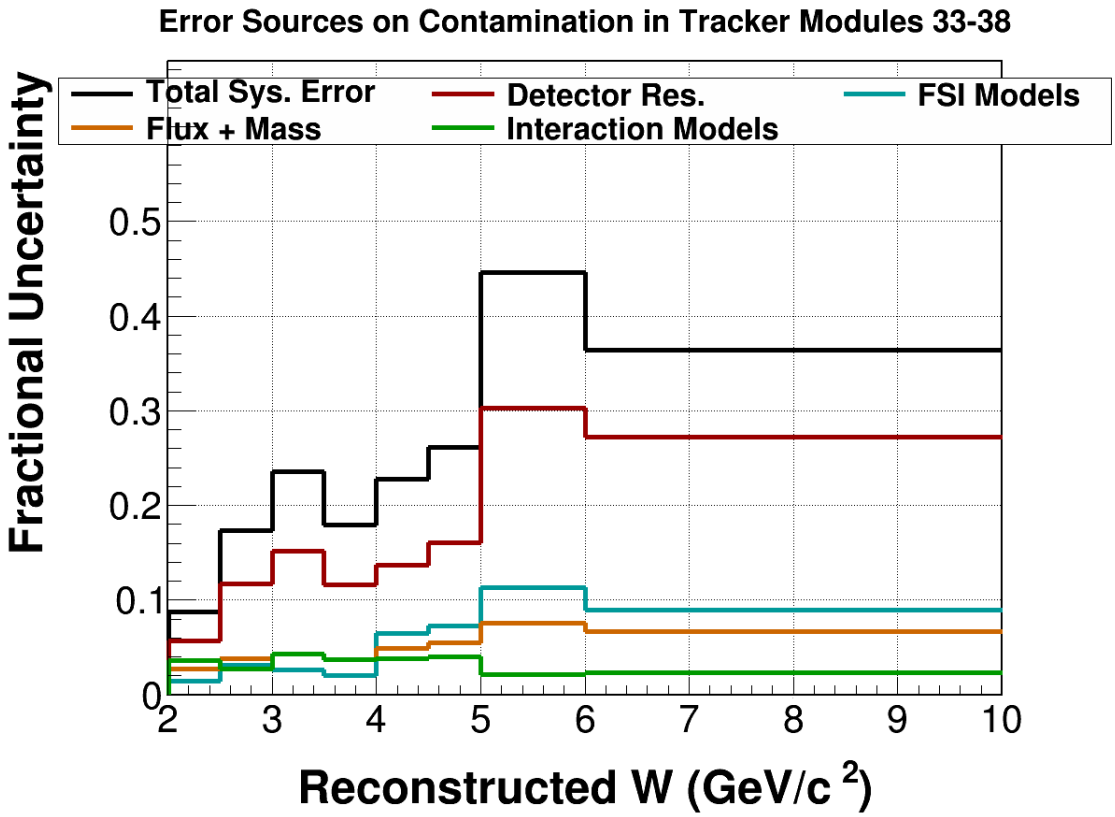

Figure B-50. Uncertainties on mis-ided DIS events: tracker mods. 33-38 (W)

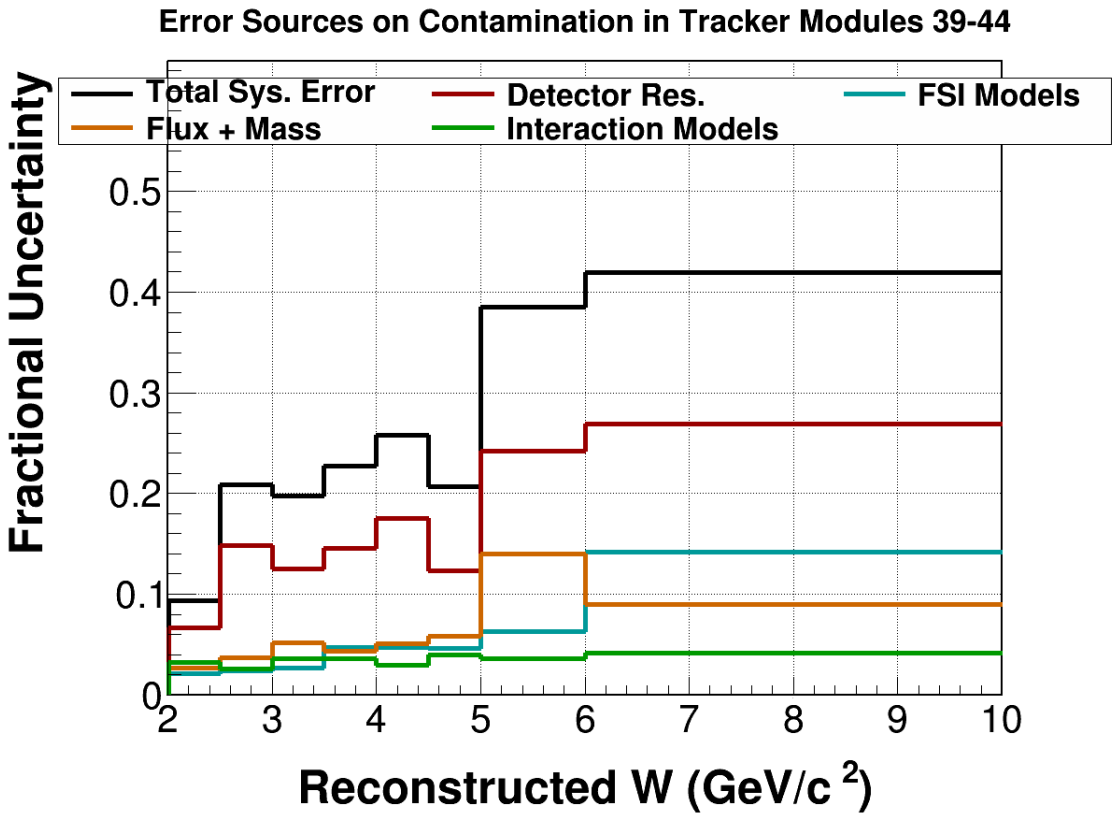

Figure B-51. Uncertainties on mis-ided DIS events: tracker mods. 39-44 (W)

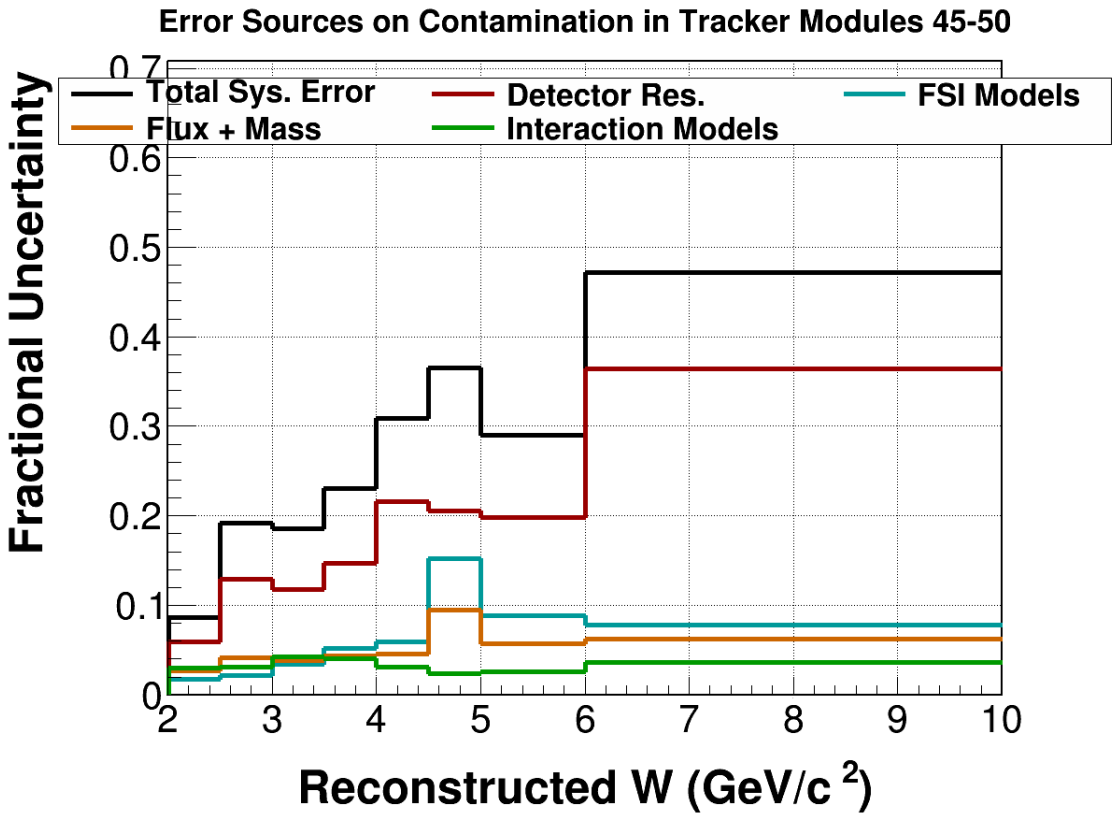

Figure B-52. Uncertainties on mis-ided DIS events: tracker mods. 45-50 (W)

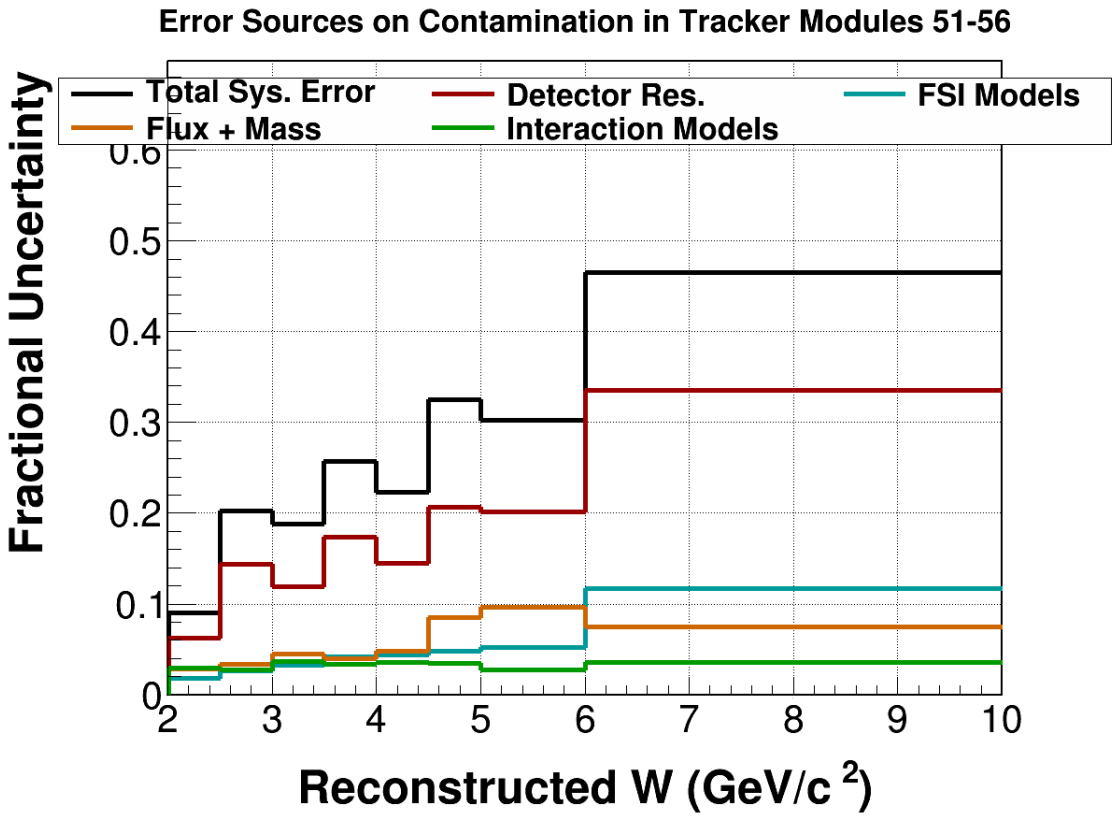

Figure B-53. Uncertainties on mis-ided DIS events: tracker mods. 51-56 (W)

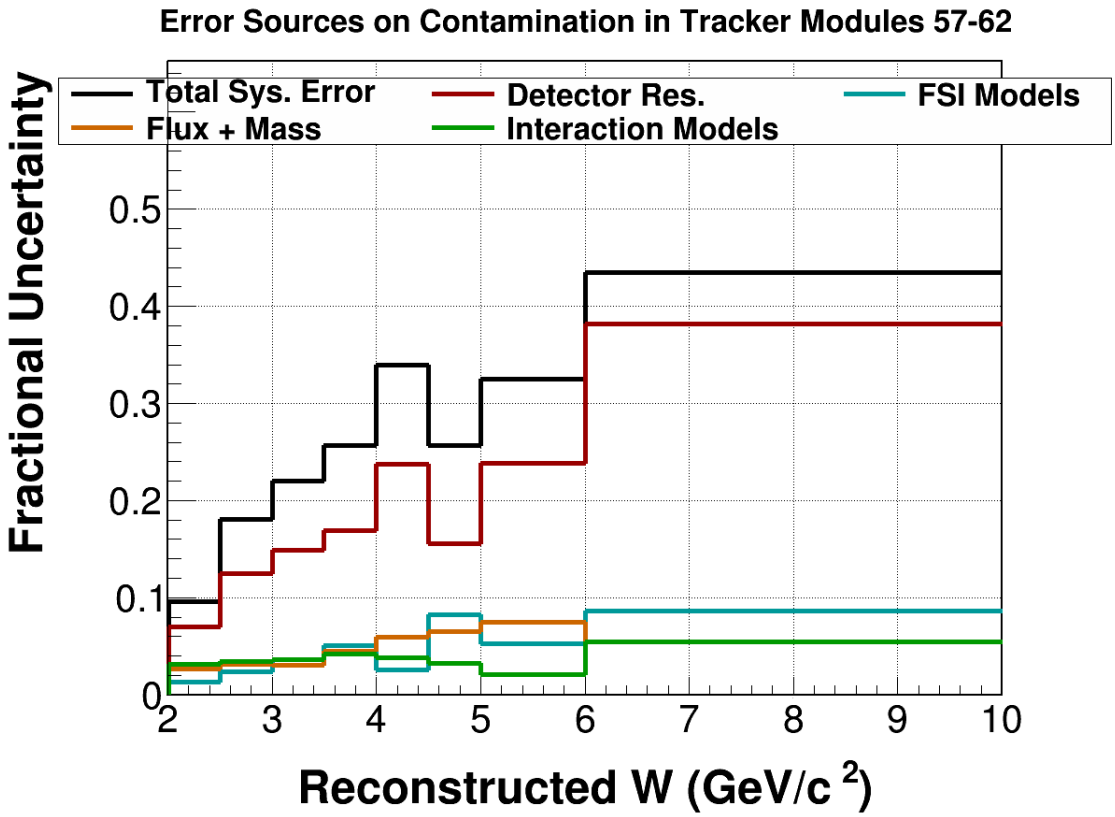

Figure B-54. Uncertainties on mis-ided DIS events: tracker mods. 57-62 (W)

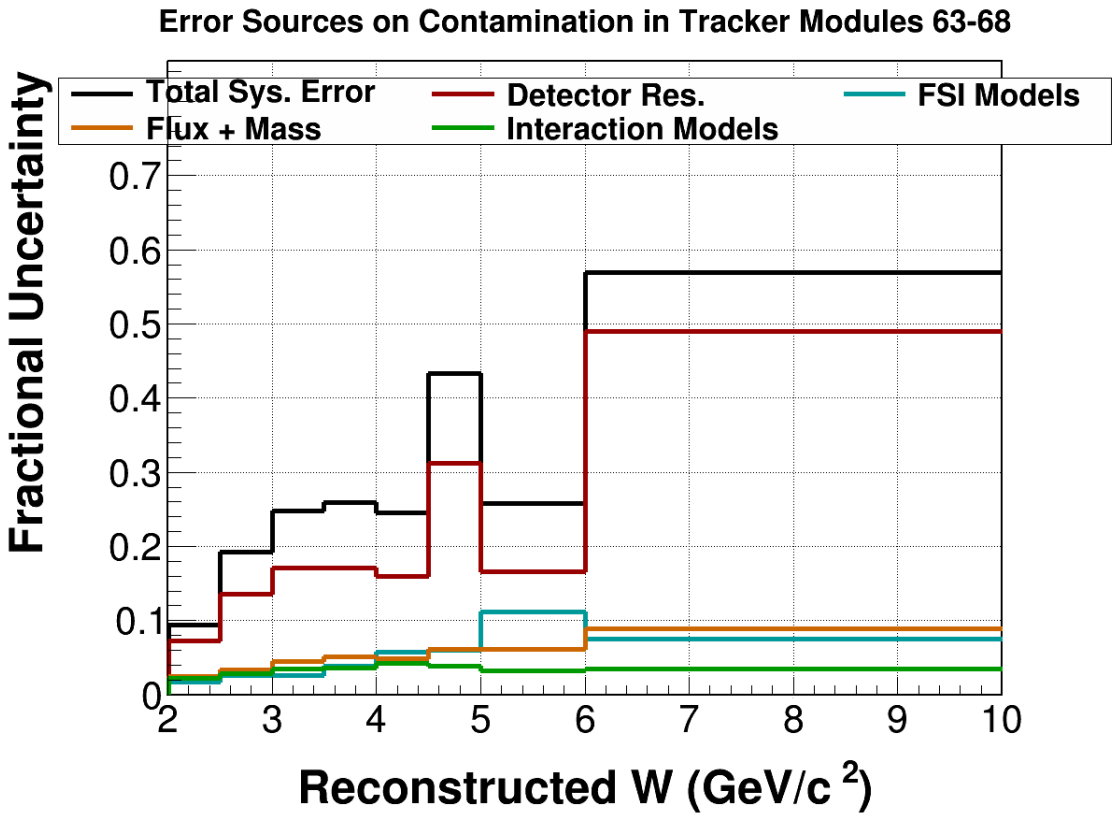

Figure B-55. Uncertainties on mis-ided DIS events: tracker mods. 63-68 (W)

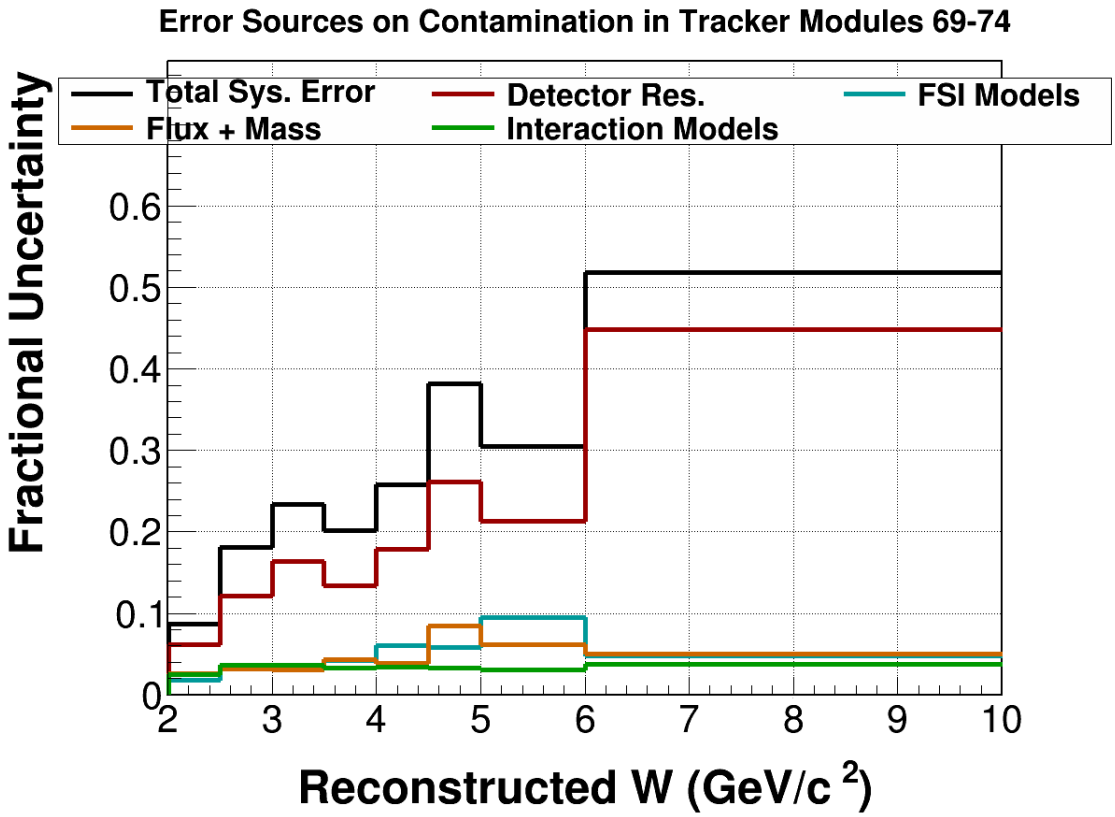

Figure B-56. Uncertainties on mis-ided DIS events: tracker mods. 69-74 (W)

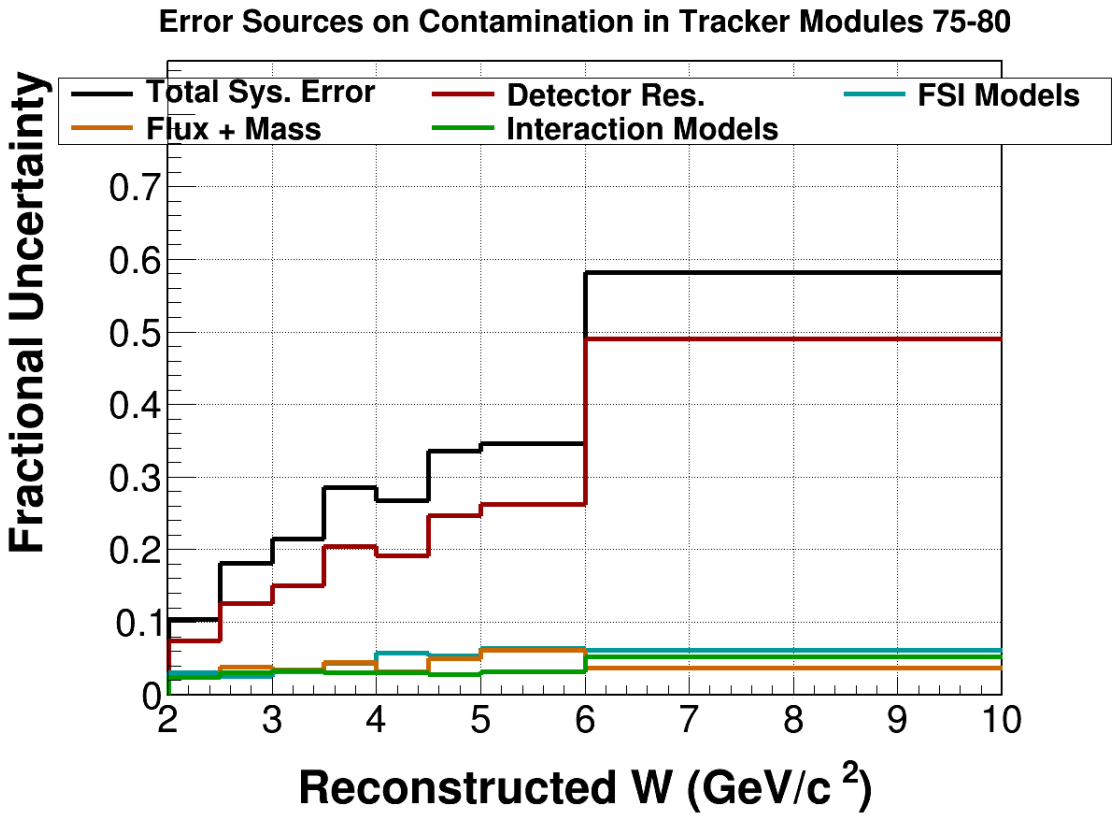

Figure B-57. Uncertainties on mis-ided DIS events: tracker mods. 75-80 (W)

The following plots show the uncertainty on the number of truly non-DIS events which pass the DIS event selection cuts as a function of Bjorken-x (x_{bj}):

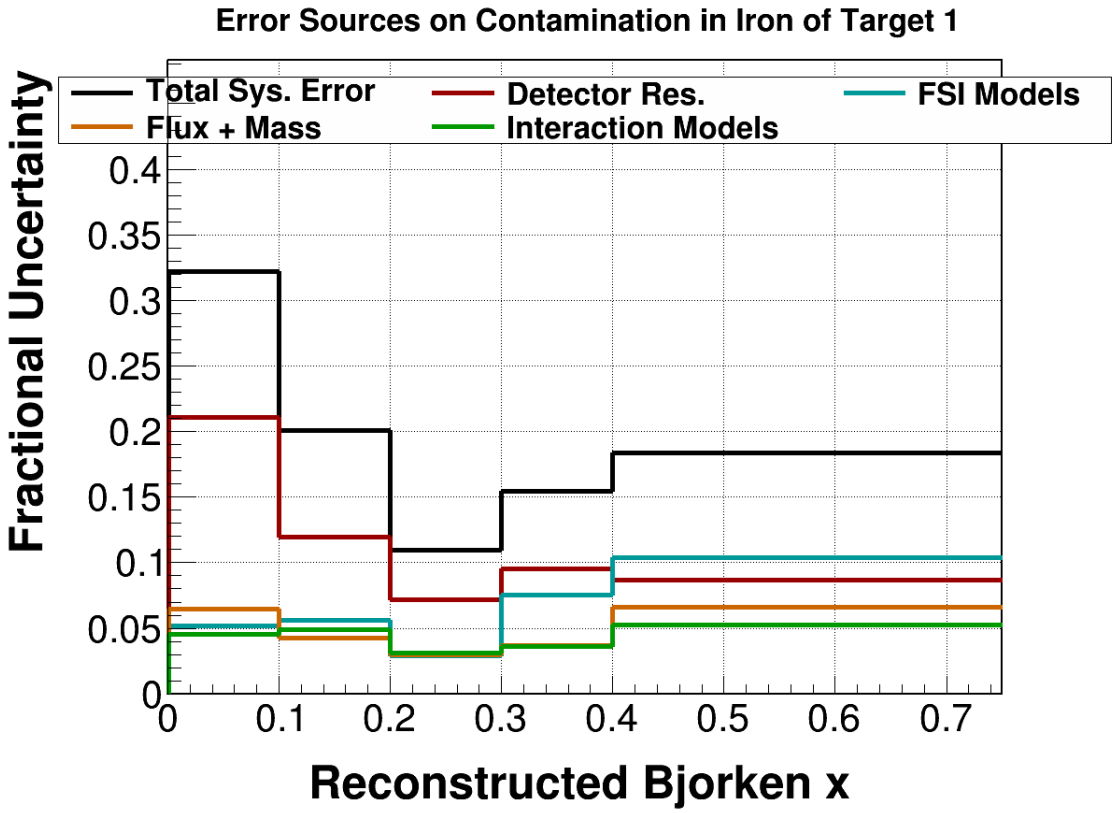

Figure B-58. Uncertainties on mis-ided DIS events: target 01 Fe (x_{bj})

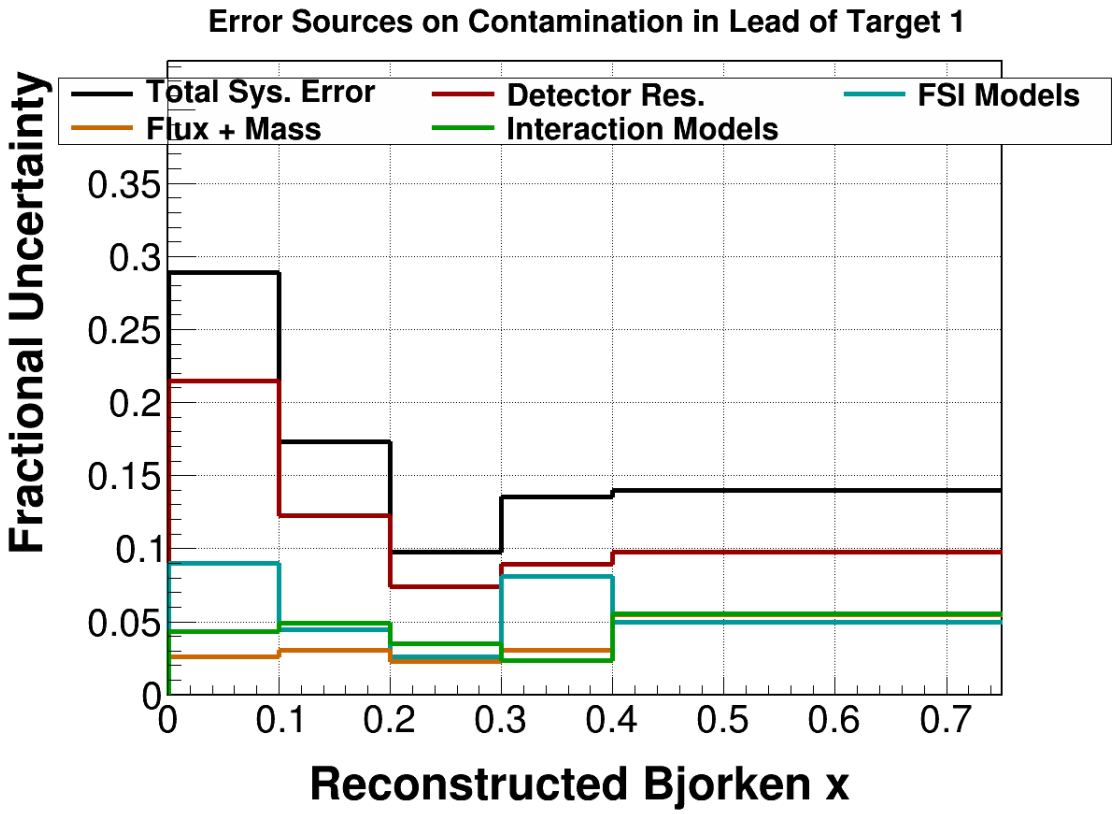

Figure B-59. Uncertainties on mis-ided DIS events: target 01 Pb (x_{bj})

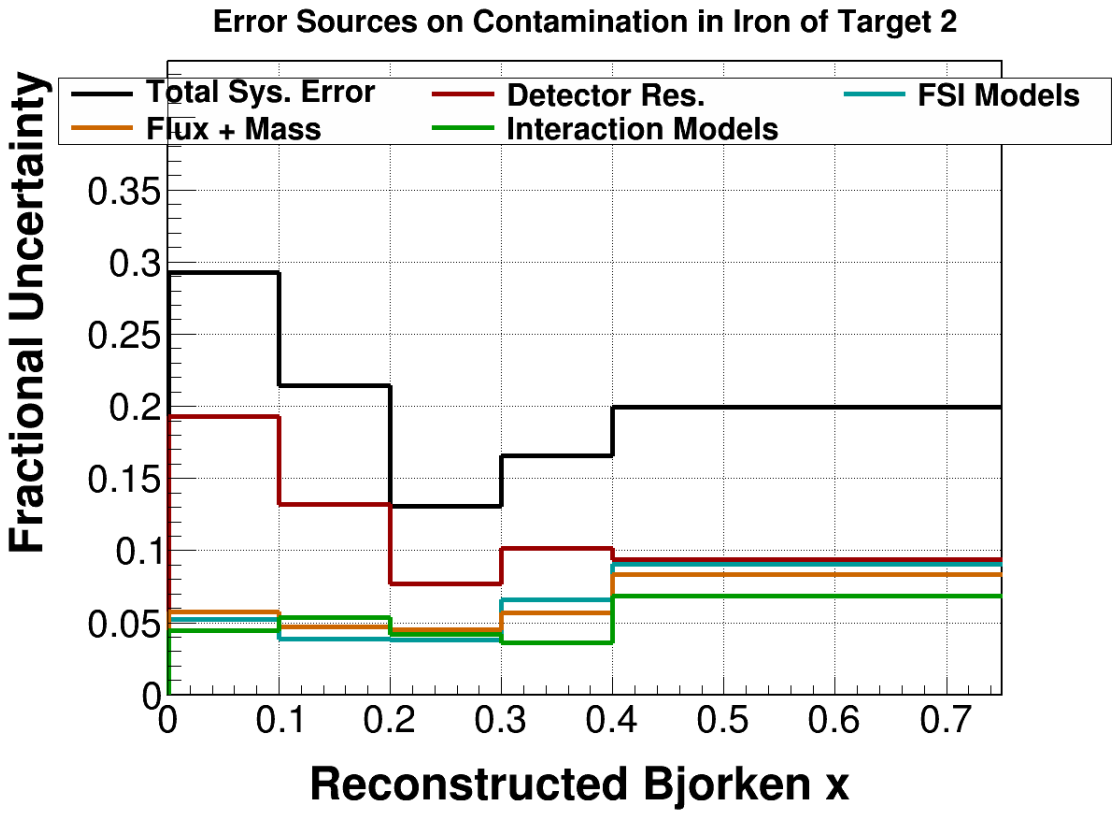

Figure B-60. Uncertainties on mis-ided DIS events: target 02 Fe (x_{bj})

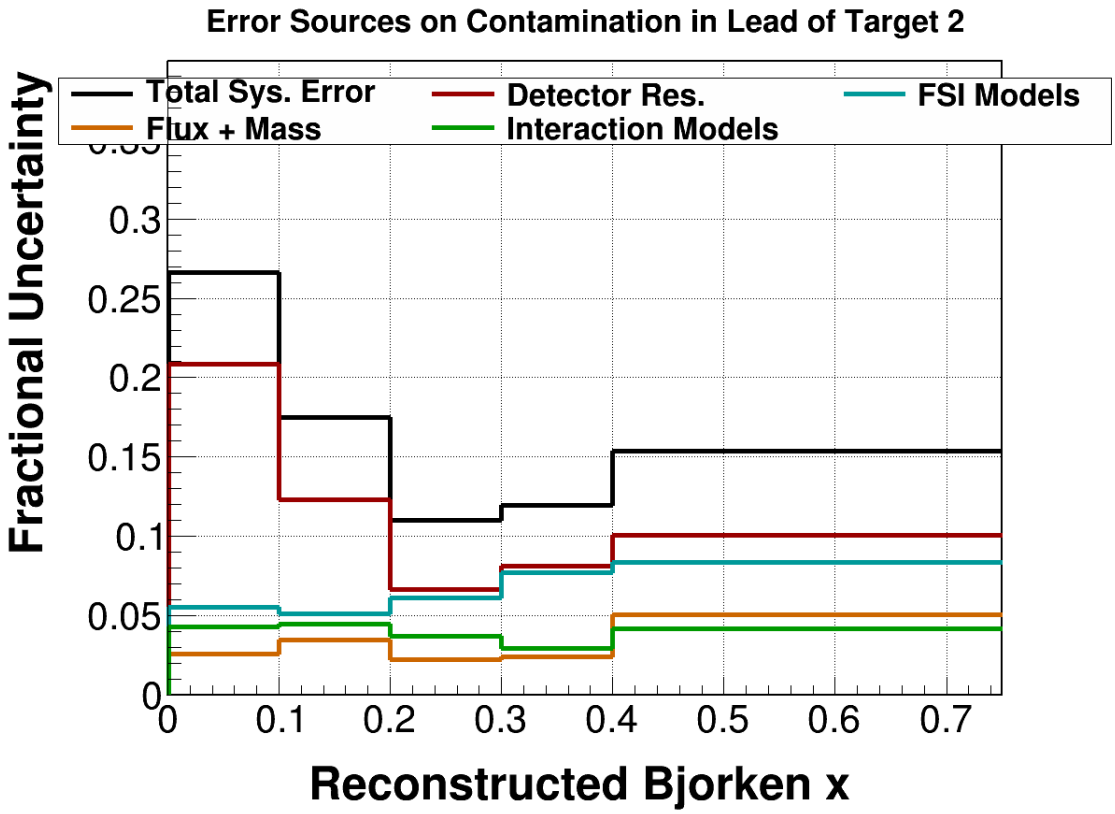

Figure B-61. Uncertainties on mis-ided DIS events: target 02 Pb (x_{bj})

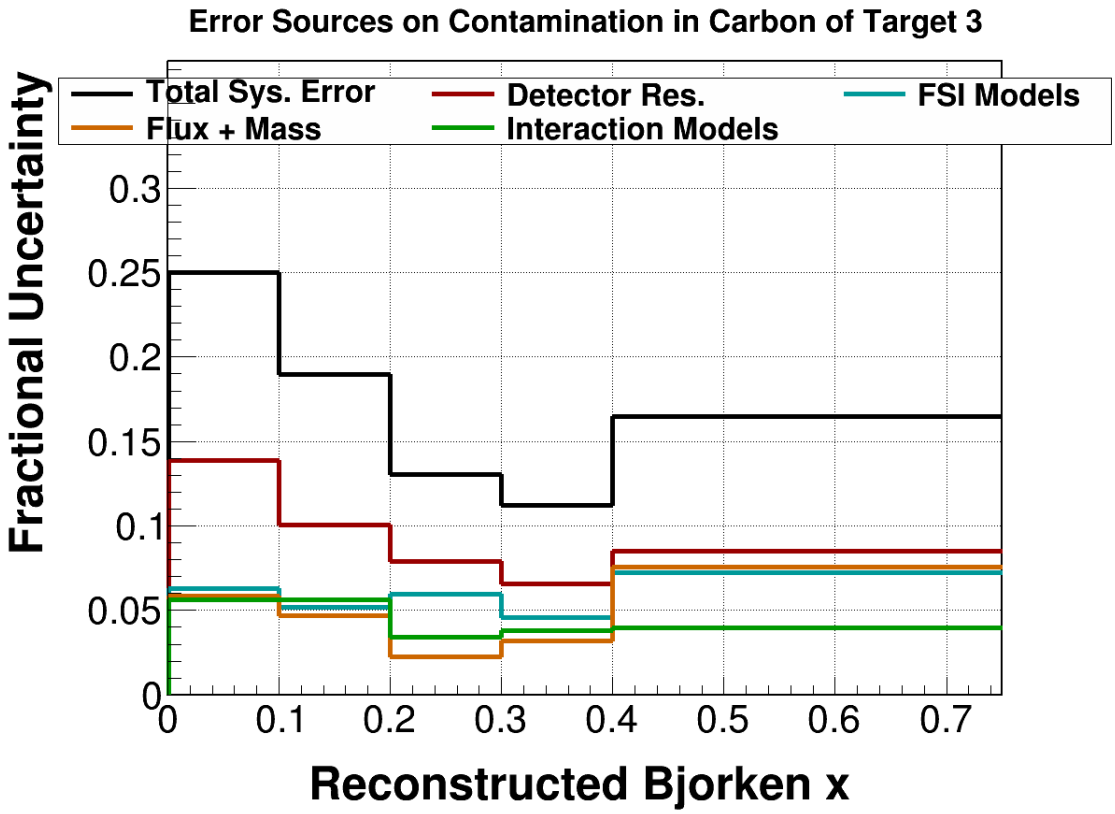

Figure B-62. Uncertainties on mis-ided DIS events: target 03 C (x_{bj})

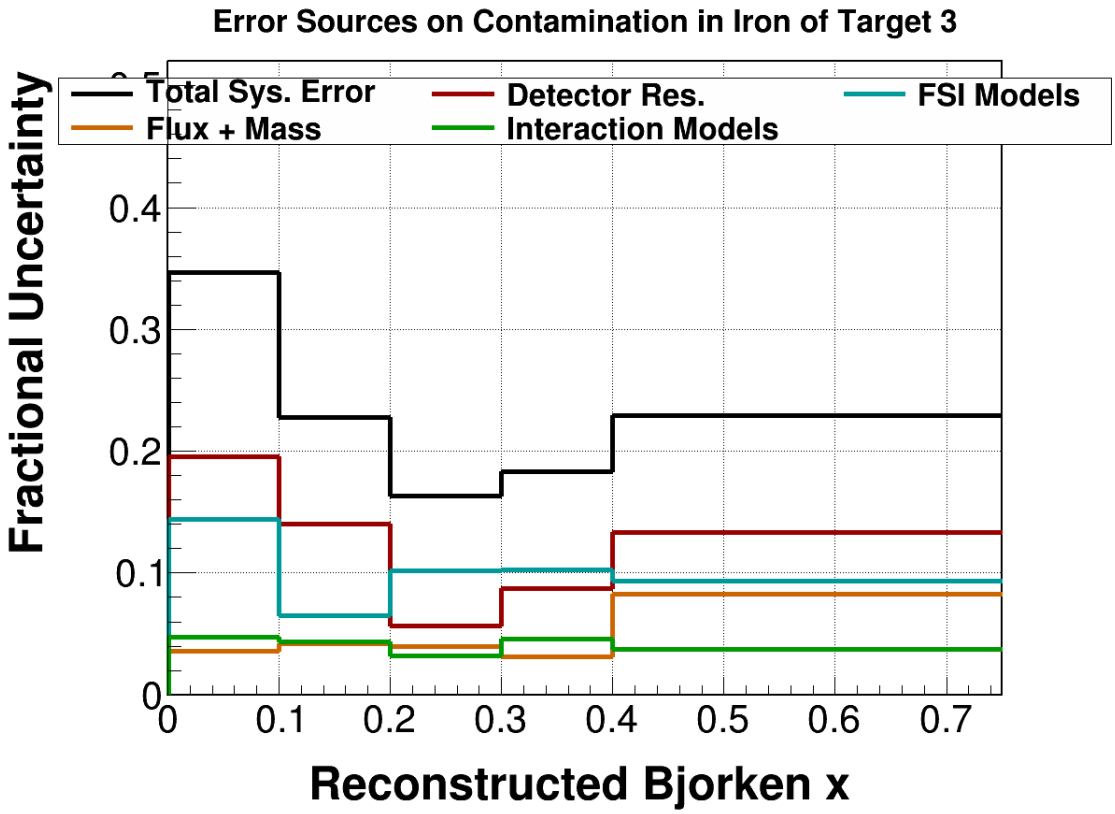

Figure B-63. Uncertainties on mis-ided DIS events: target 03 Fe (x_{bj})

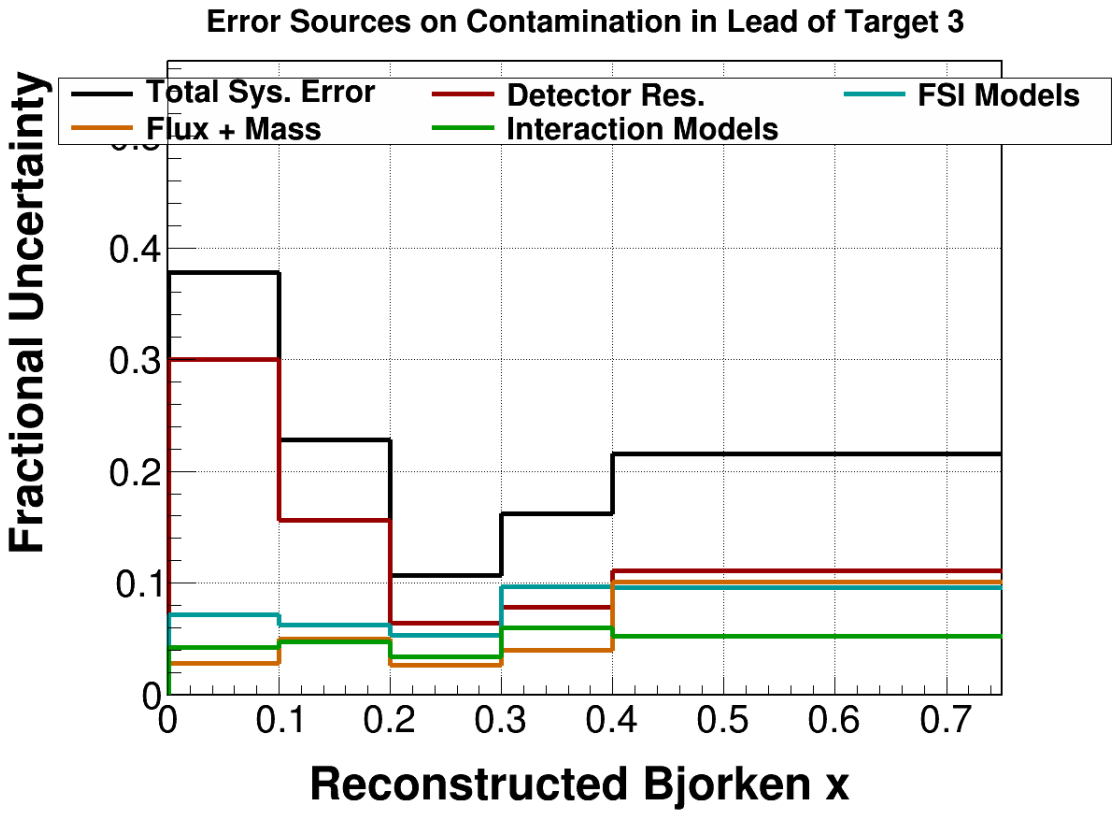

Figure B-64. Uncertainties on mis-ided DIS events: target 03 Pb (x_{bj})

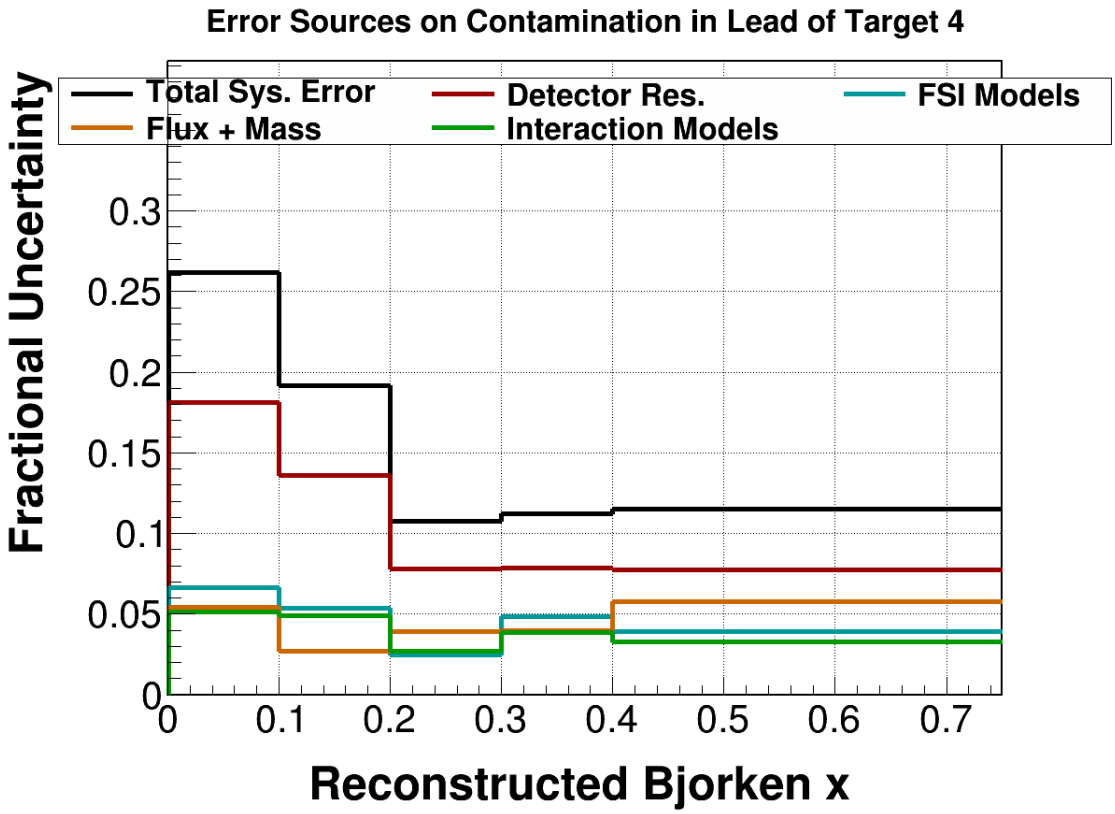

Figure B-65. Uncertainties on mis-ided DIS events: target 04 Pb (x_{bj})

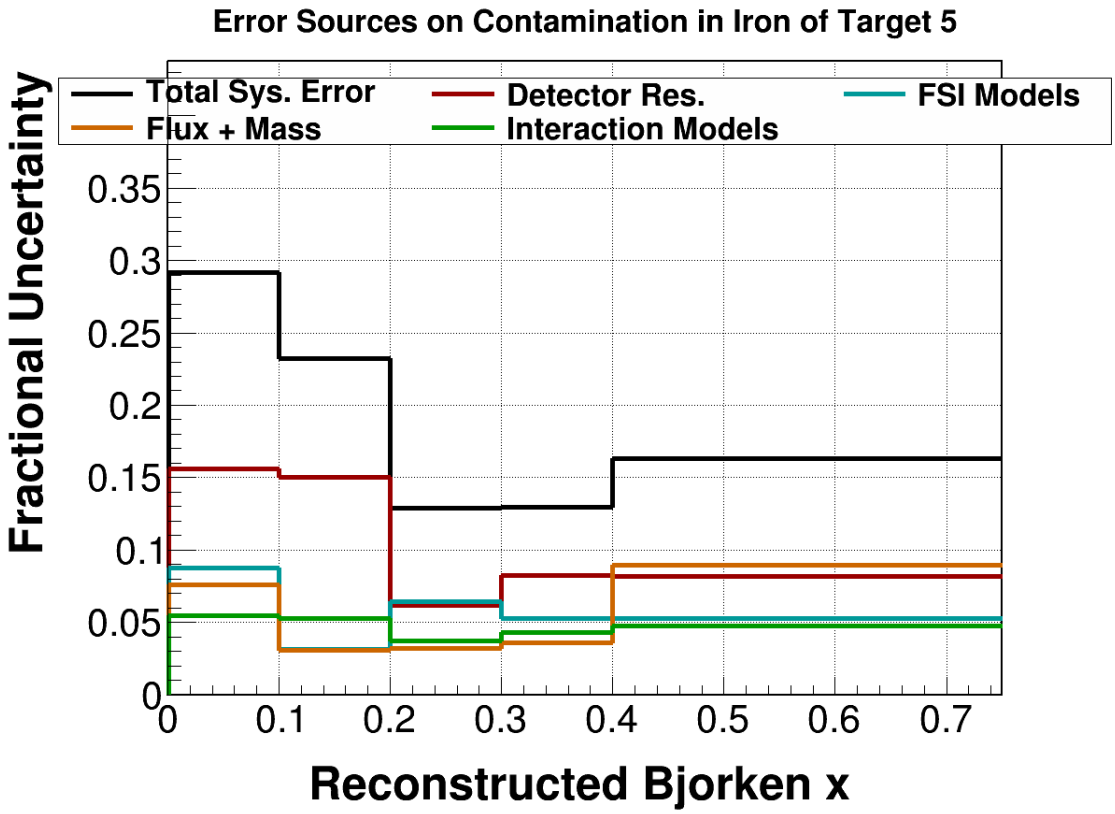

Figure B-66. Uncertainties on mis-ided DIS events: target 05 Fe (x_{bj})

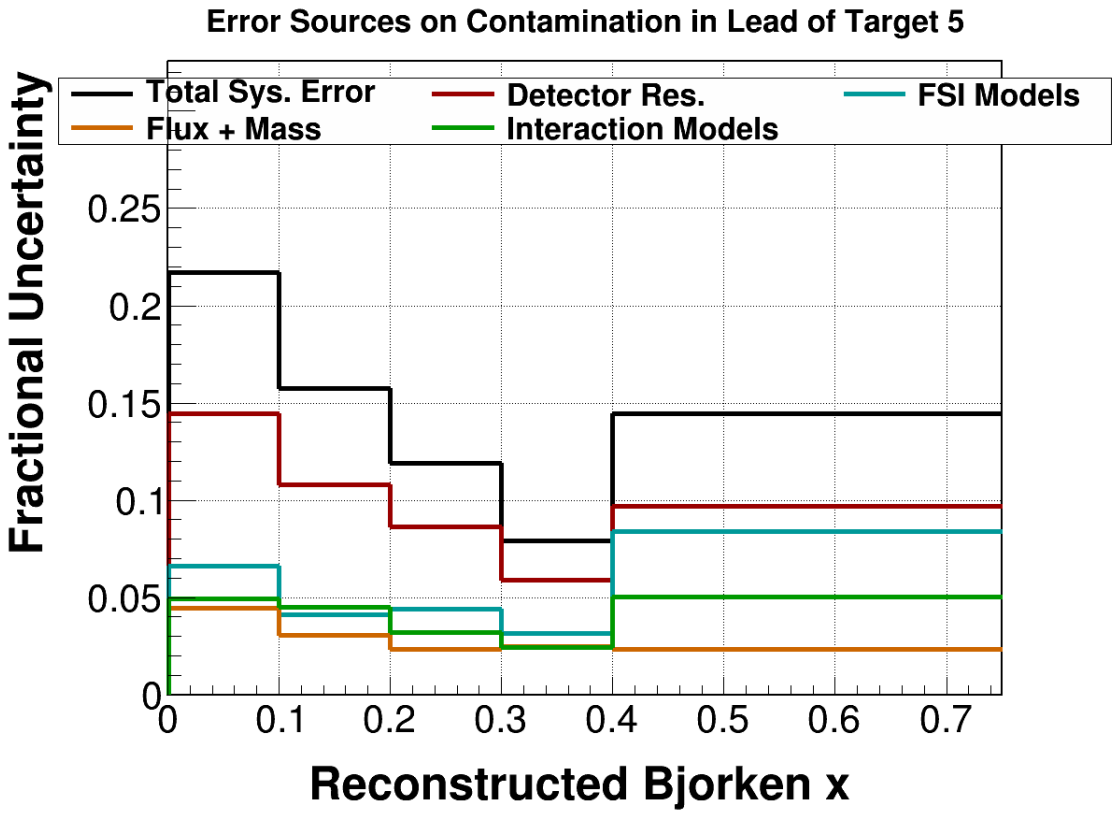

Figure B-67. Uncertainties on mis-ided DIS events: target 05 Pb (x_{bj})

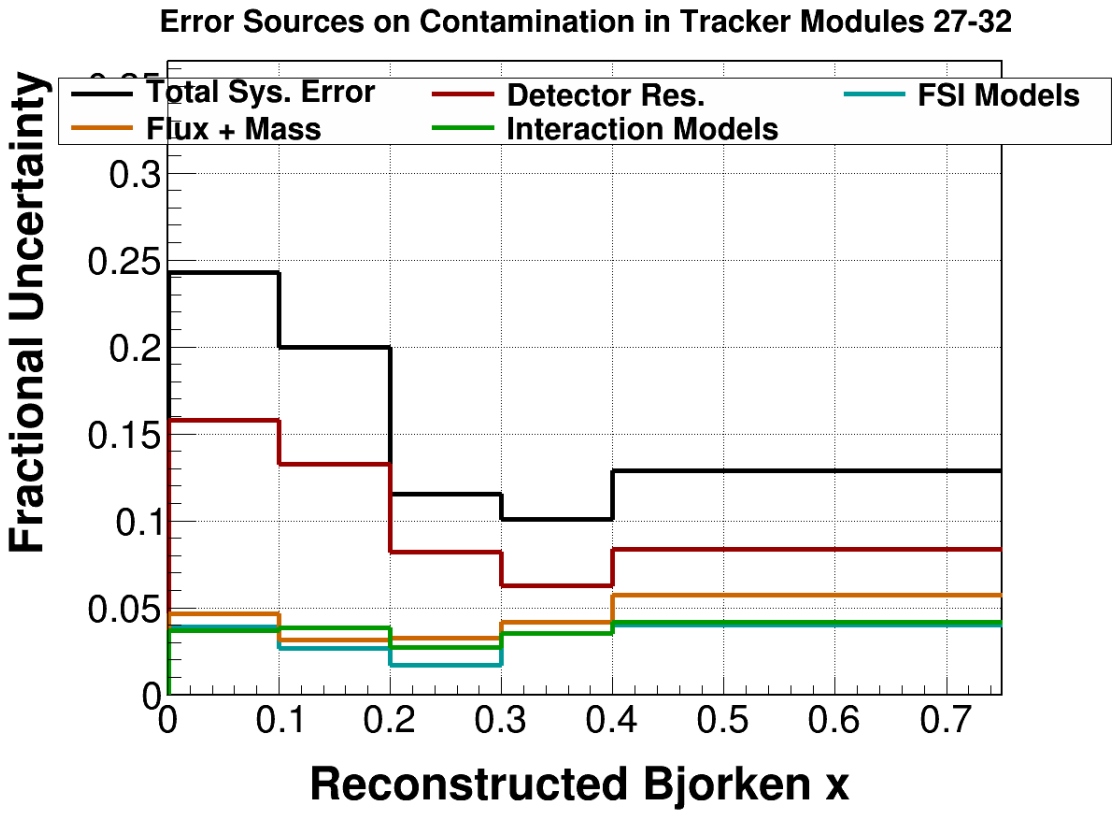

Figure B-68. Uncertainties on mis-ided DIS events: tracker mods. 27-32 (x_{bj})

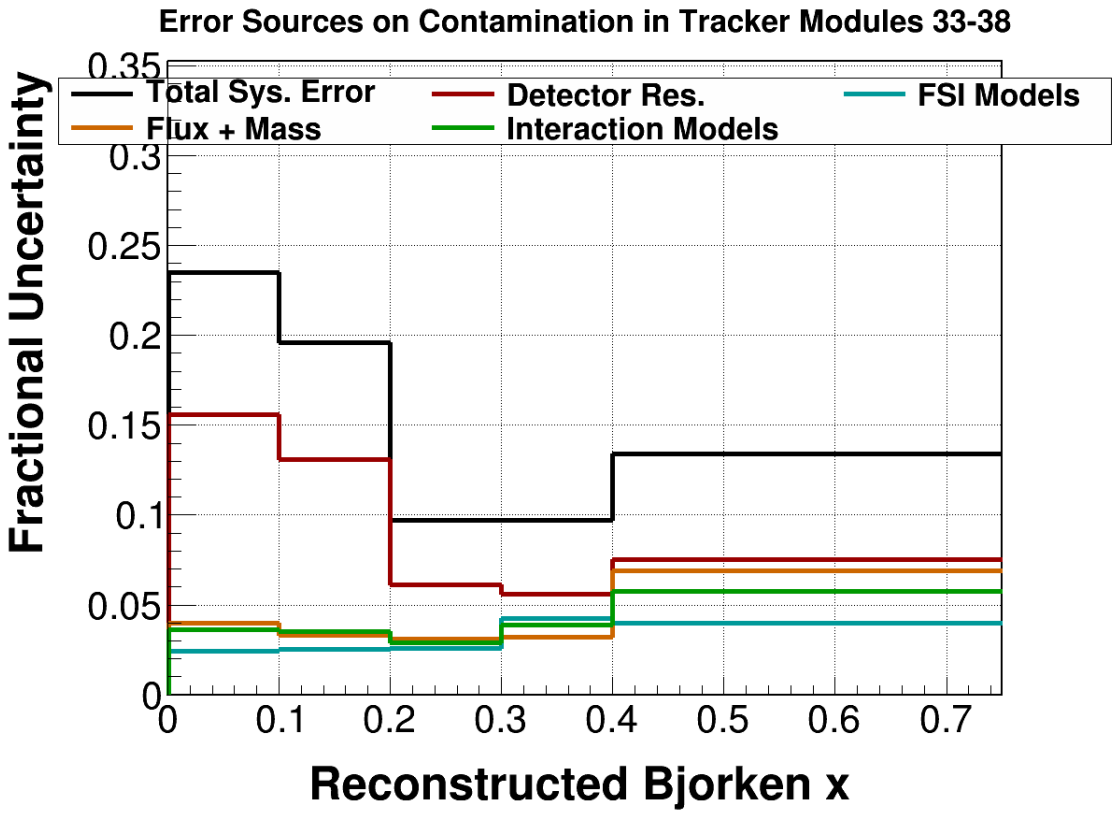

Figure B-69. Uncertainties on mis-ided DIS events: tracker mods. 33-38 (x_{bj})

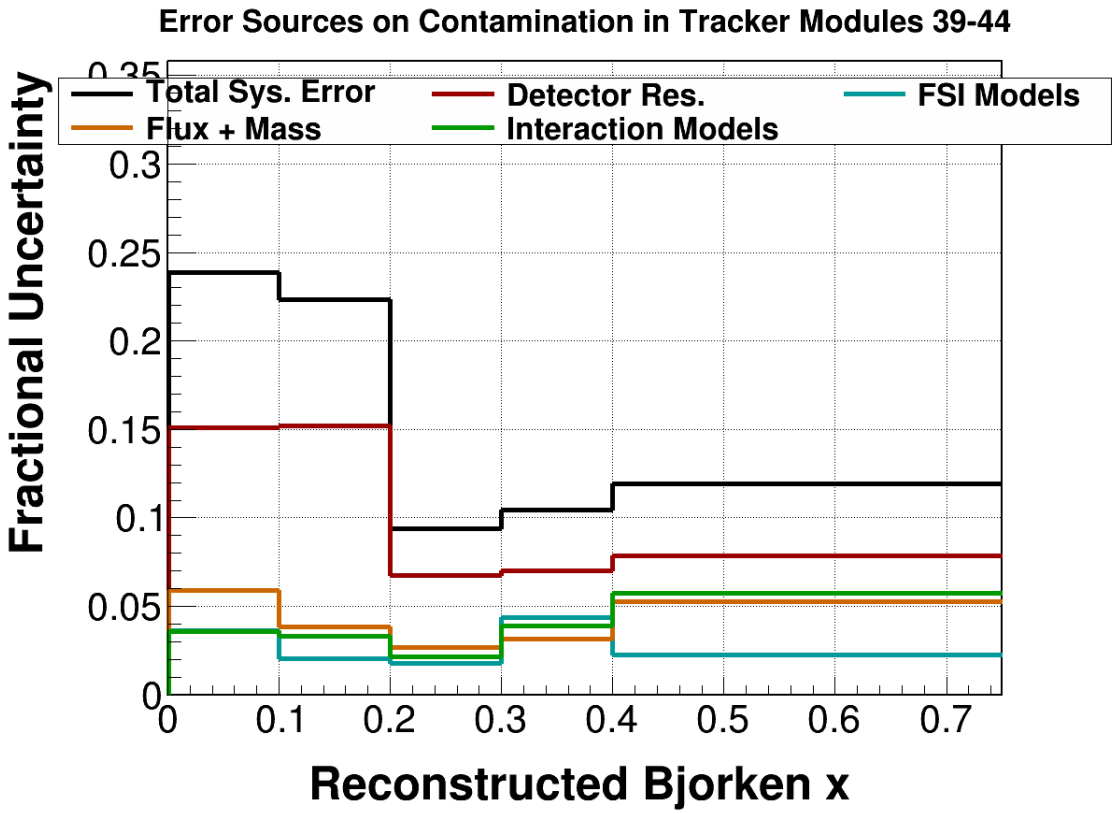

Figure B-70. Uncertainties on mis-ided DIS events: tracker mods. 39-44 (x_{bj})

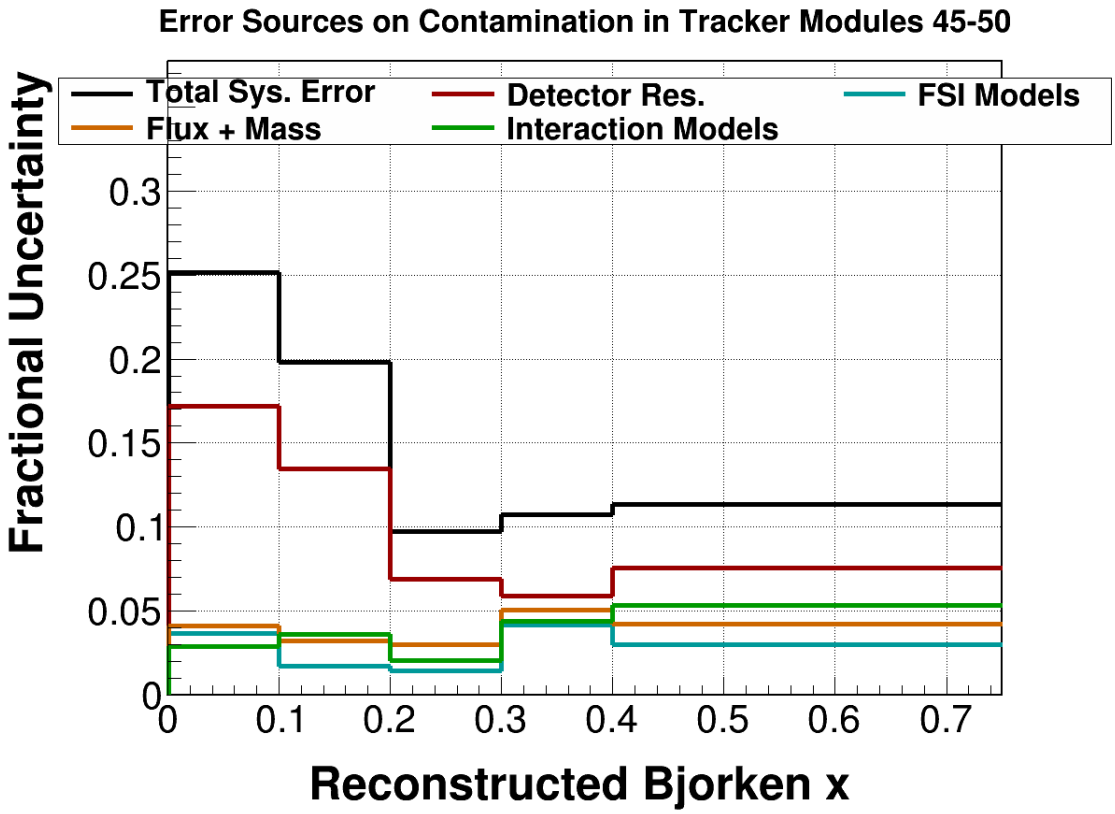

Figure B-71. Uncertainties on mis-ided DIS events: tracker mods. 45-50 (x_{bj})

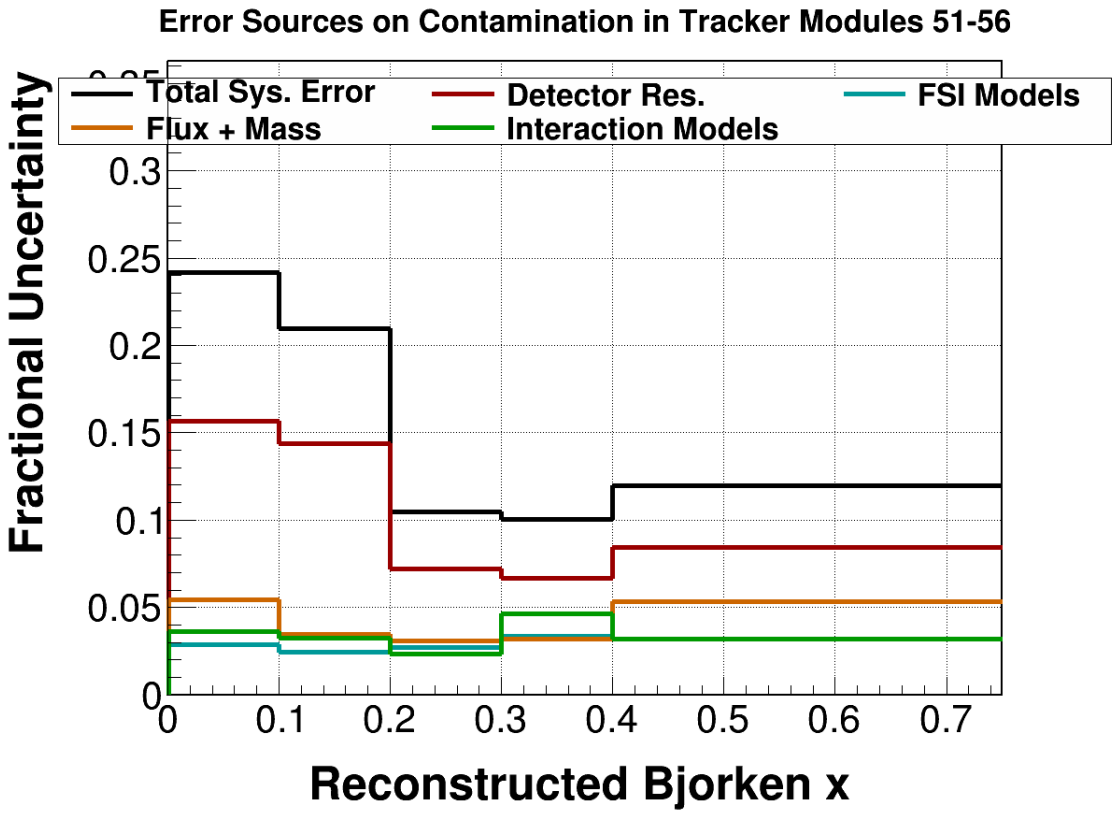

Figure B-72. Uncertainties on mis-ided DIS events: tracker mods. 51-56 (x_{bj})

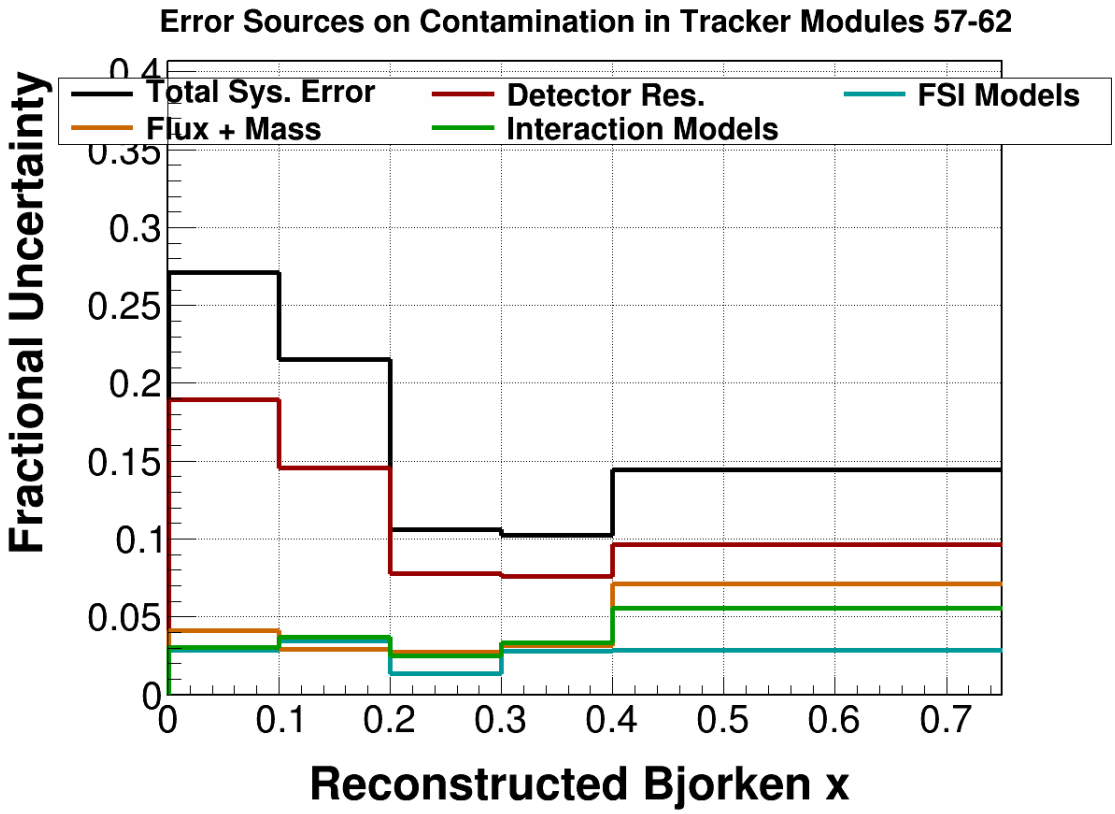

Figure B-73. Uncertainties on mis-ided DIS events: tracker mods. 57-62 (x_{bj})

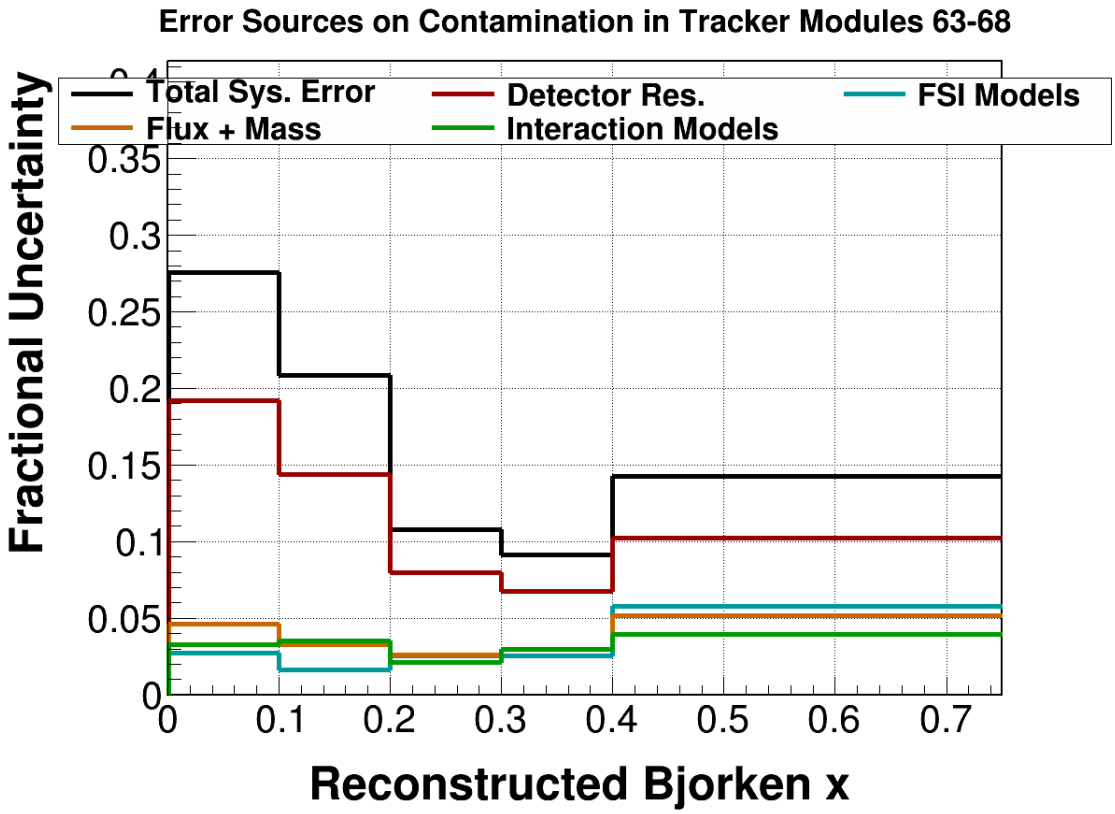

Figure B-74. Uncertainties on mis-ided DIS events: tracker mods. 63-68 (x_{bj})

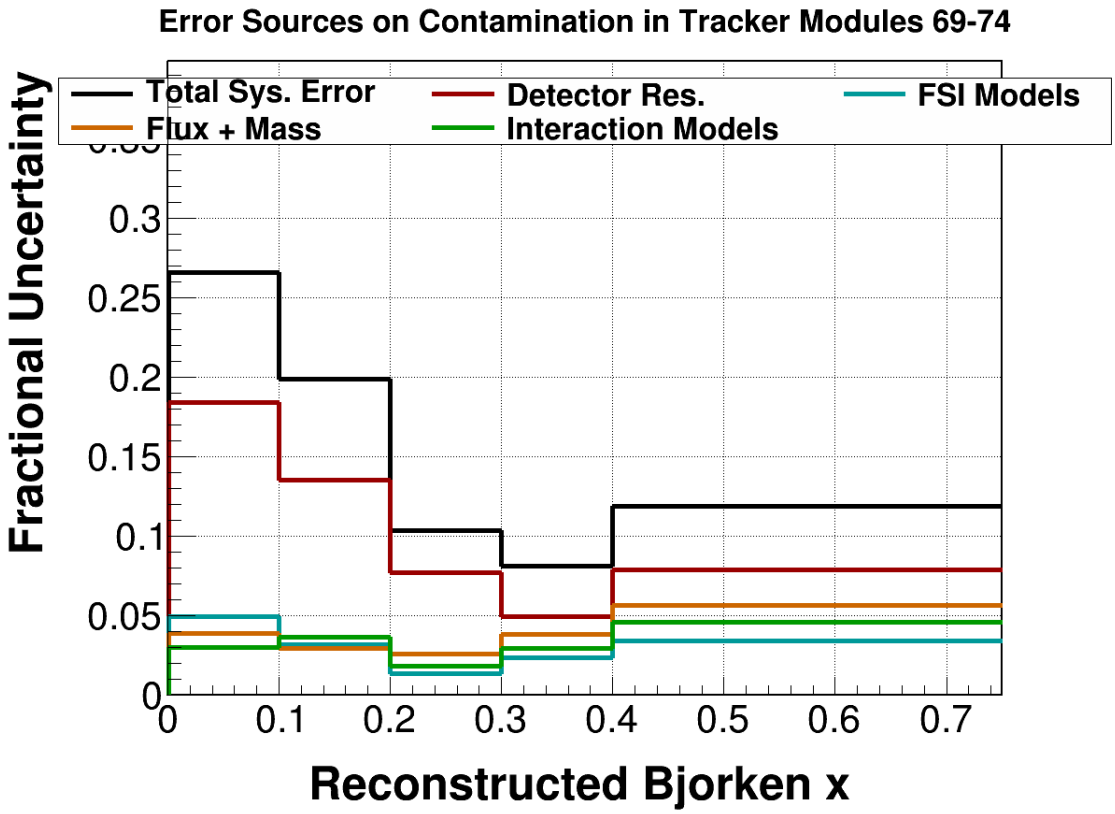

Figure B-75. Uncertainties on mis-ided DIS events: tracker mods. 69-74 (x_{bj})

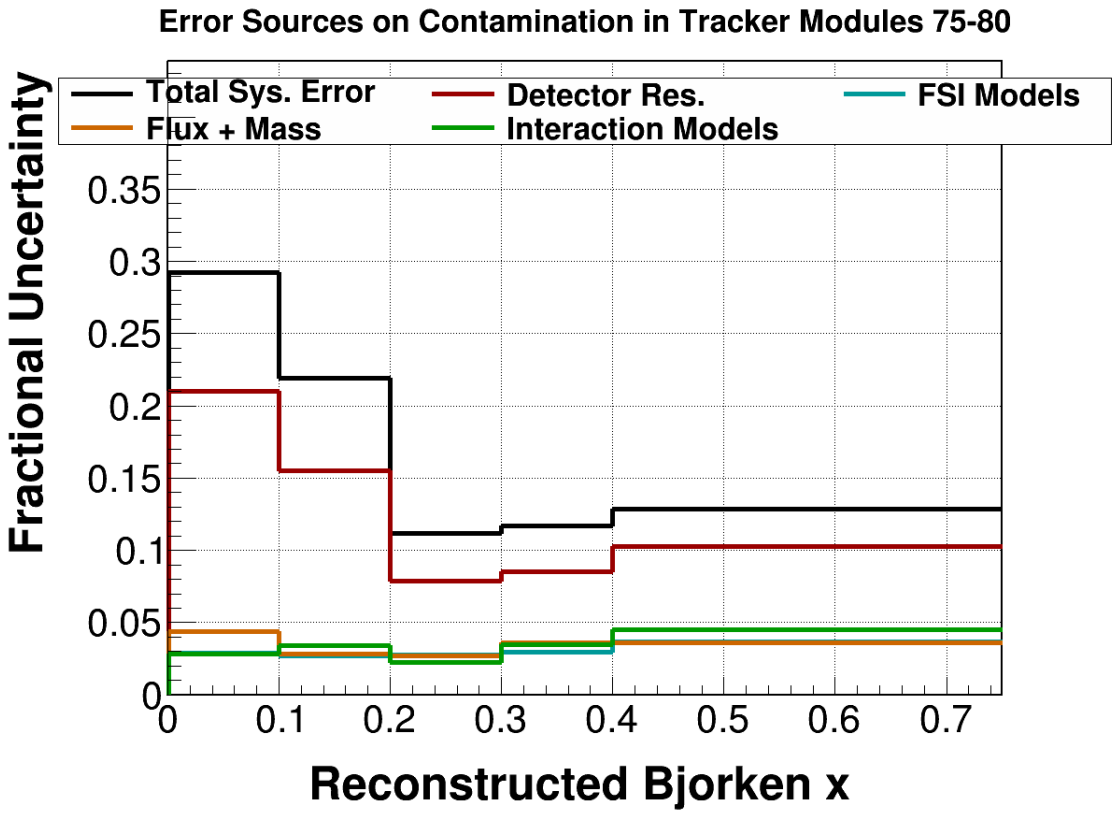

Figure B-76. Uncertainties on mis-ided DIS events: tracker mods. 75-80 (x_{bj})

The following plots show the uncertainty on the number of truly non-DIS events which pass the DIS event selection cuts as a function of muon energy (E_μ):

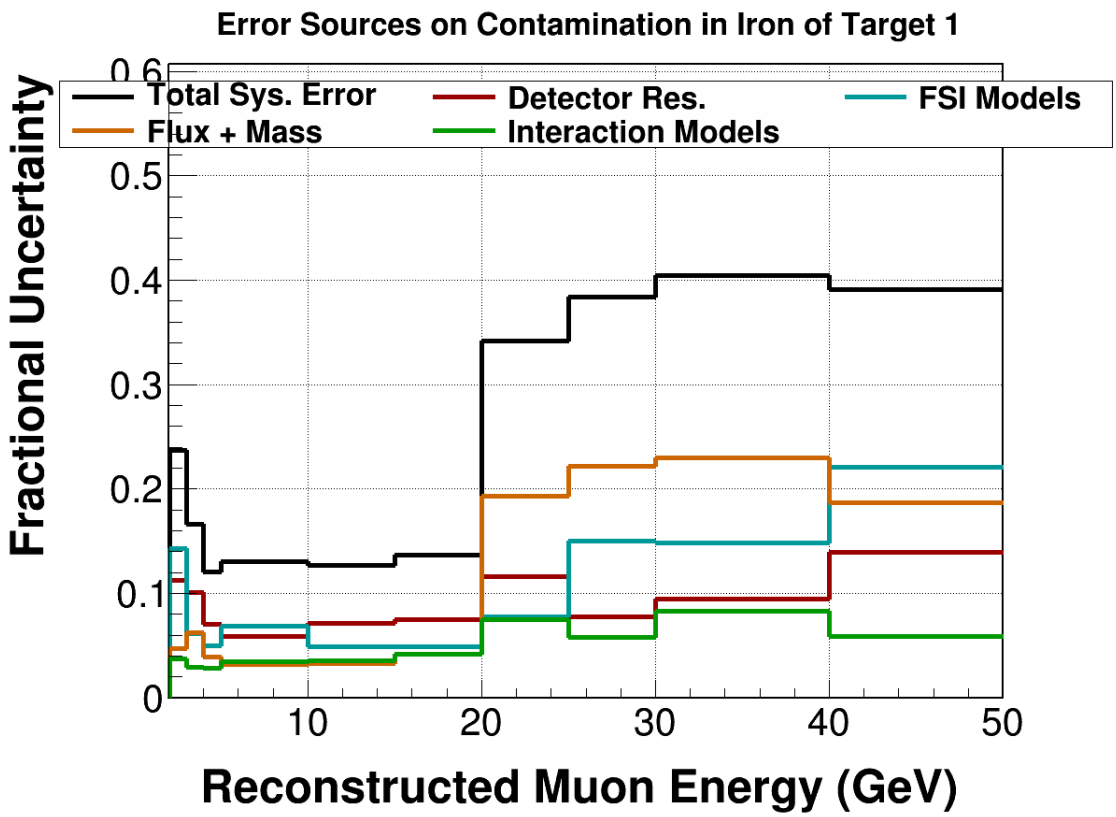

Figure B-77. Uncertainties on mis-ided DIS events: target 01 Fe (E_μ)

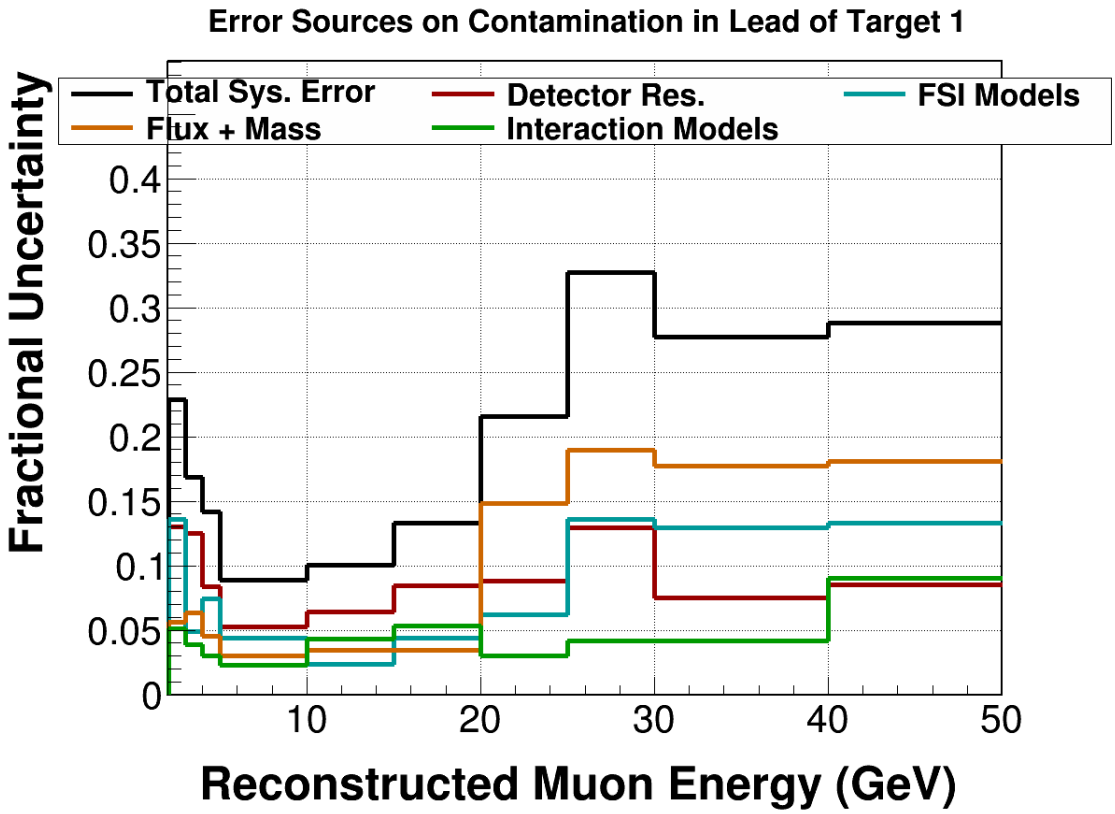

Figure B-78. Uncertainties on mis-ided DIS events: target 01 Pb (E_μ)

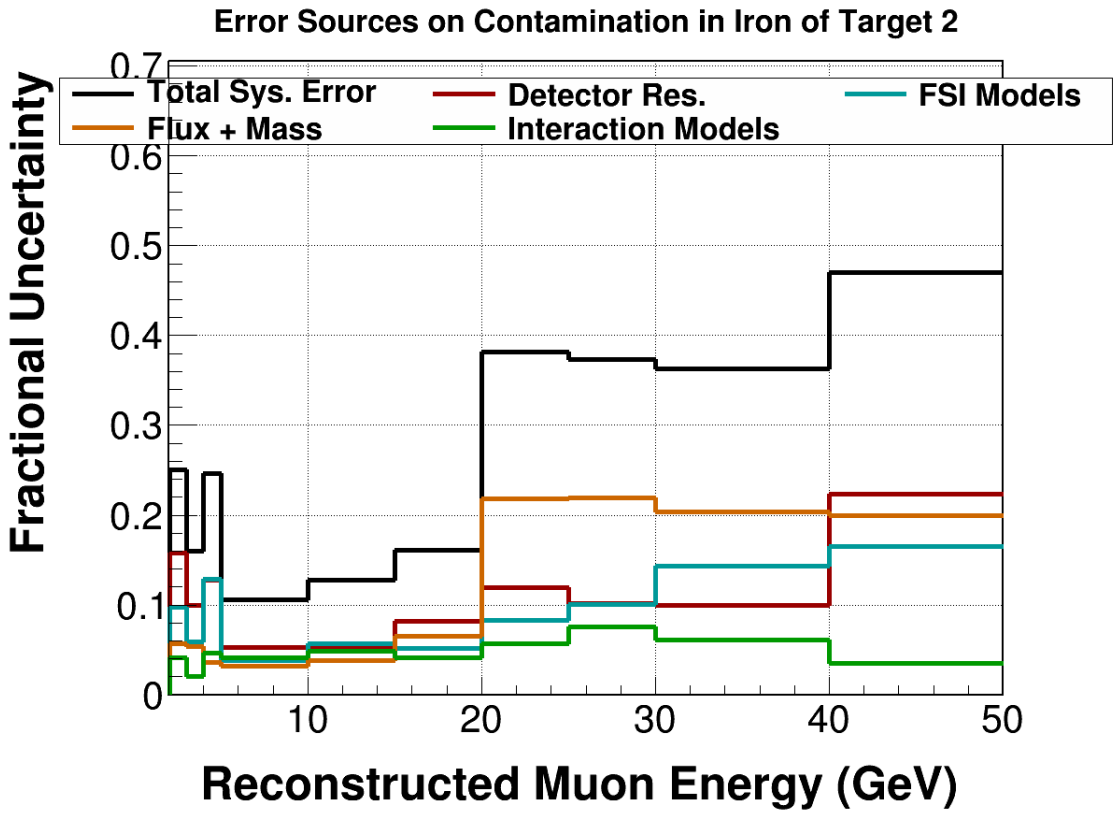

Figure B-79. Uncertainties on mis-ided DIS events: target 02 Fe (E_μ)

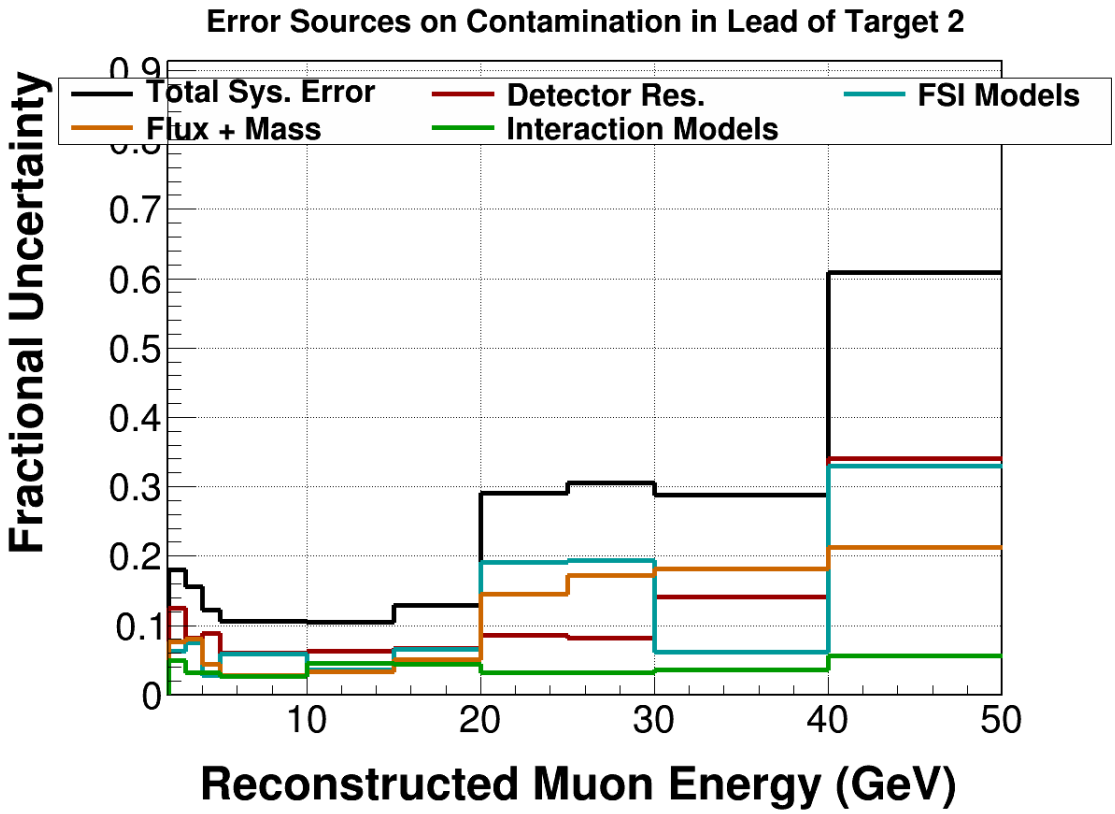

Figure B-80. Uncertainties on mis-ided DIS events: target 02 Pb (E_μ)

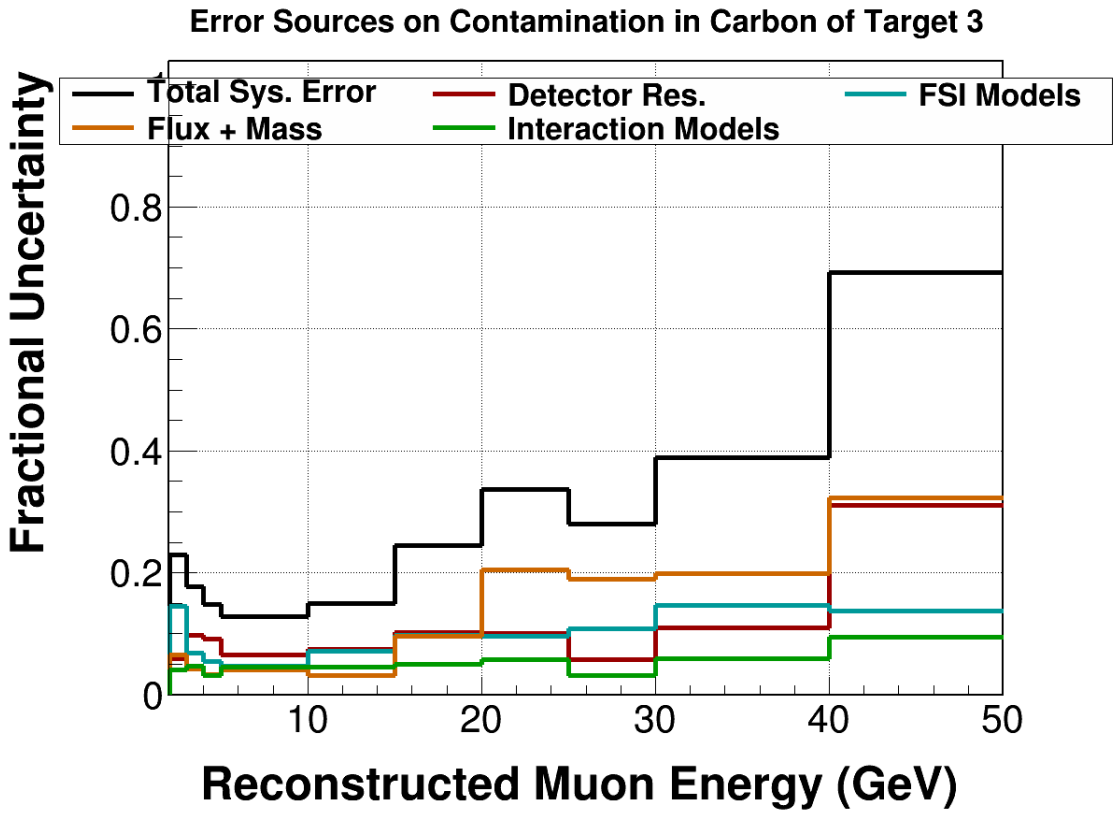

Figure B-81. Uncertainties on mis-ided DIS events: target 03 C (E_μ)

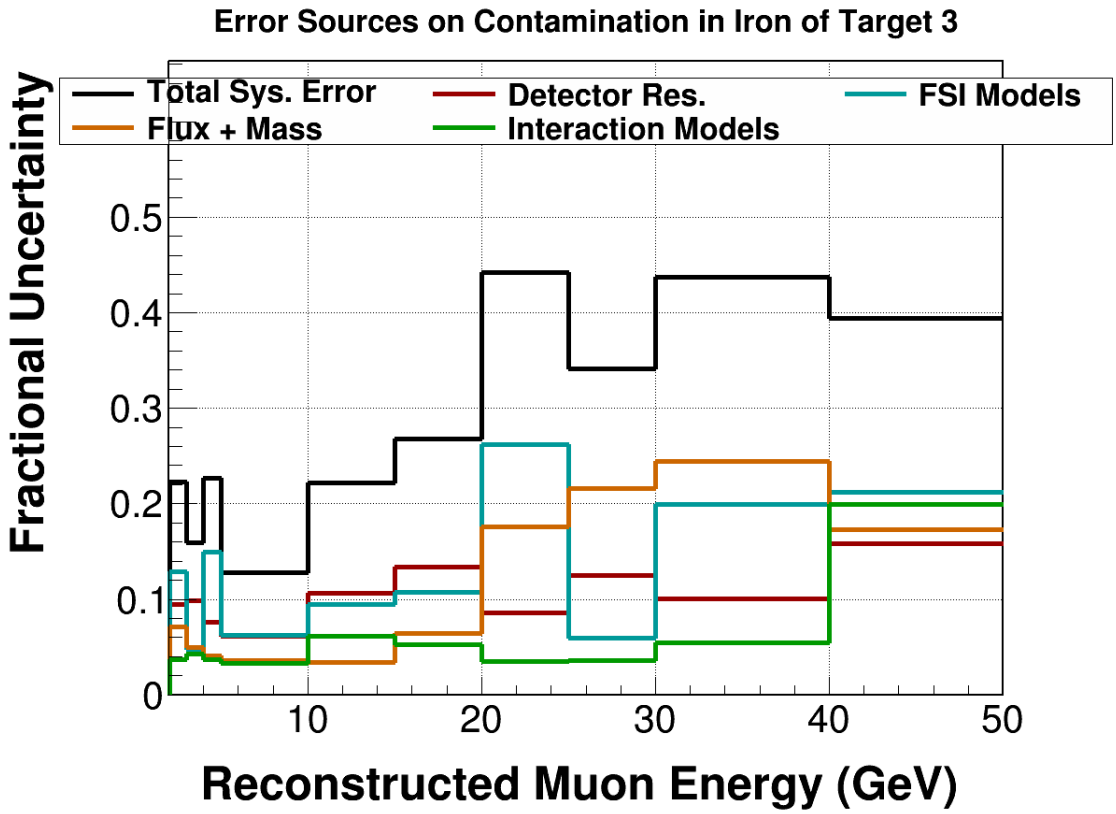

Figure B-82. Uncertainties on mis-ided DIS events: target 03 Fe (E_μ)

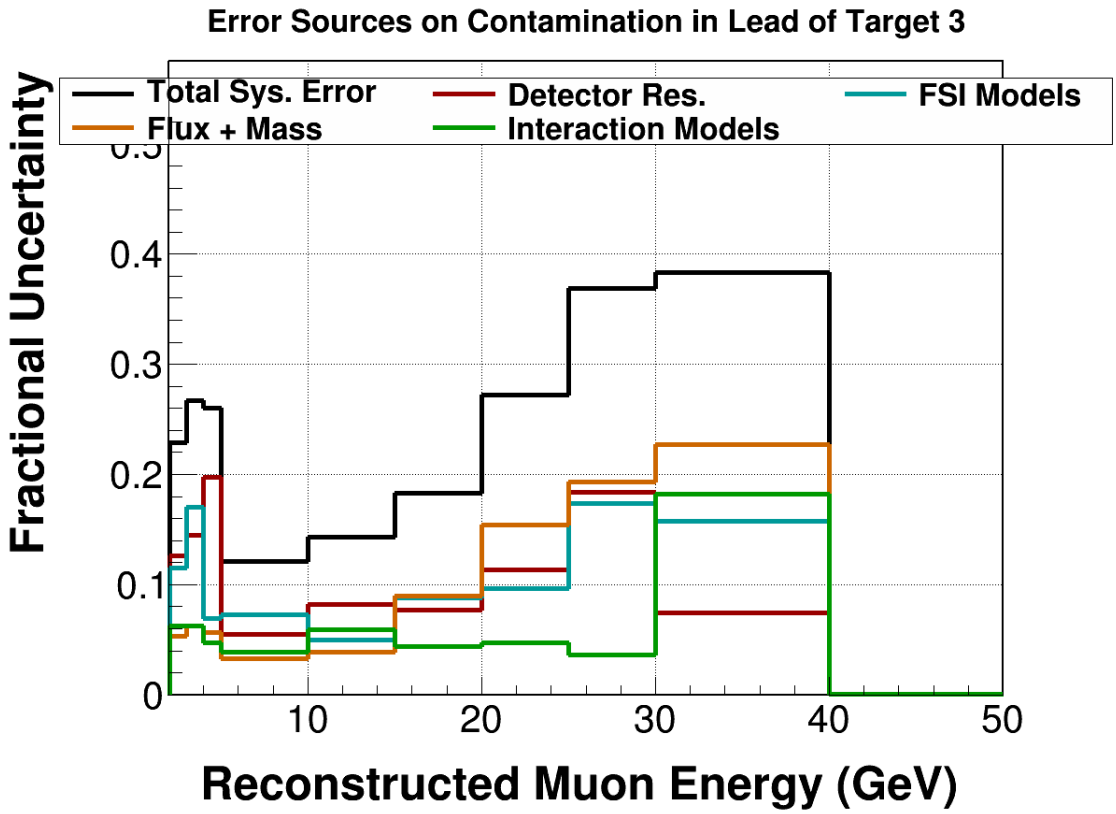

Figure B-83. Uncertainties on mis-ided DIS events: target 03 Pb (E_μ)

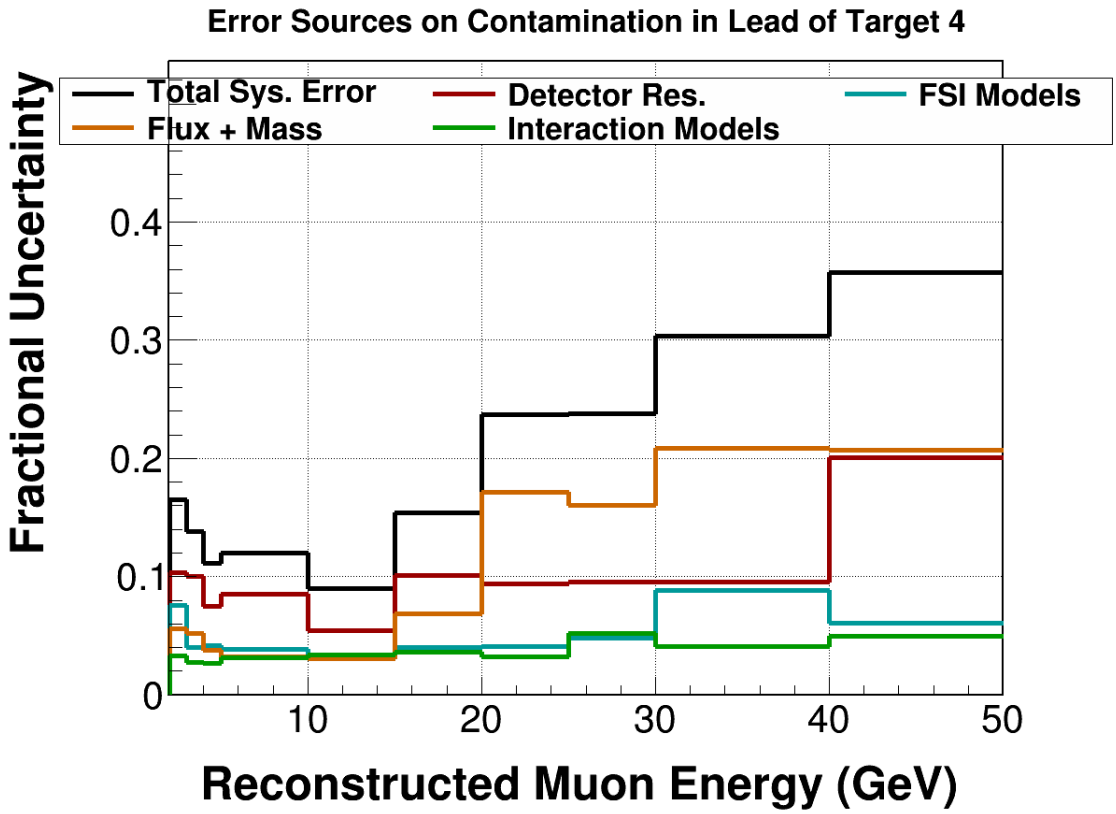

Figure B-84. Uncertainties on mis-ided DIS events: target 04 Pb (E_μ)

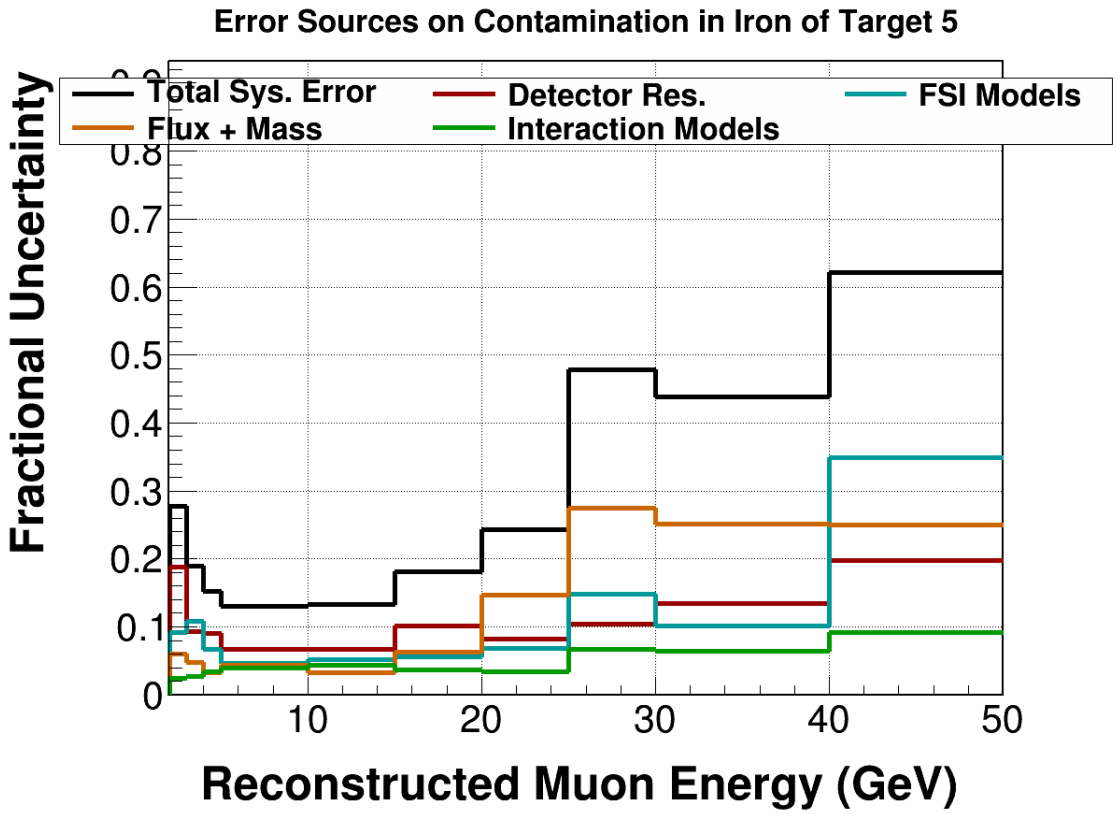

Figure B-85. Uncertainties on mis-ided DIS events: target 05 Fe (E_μ)

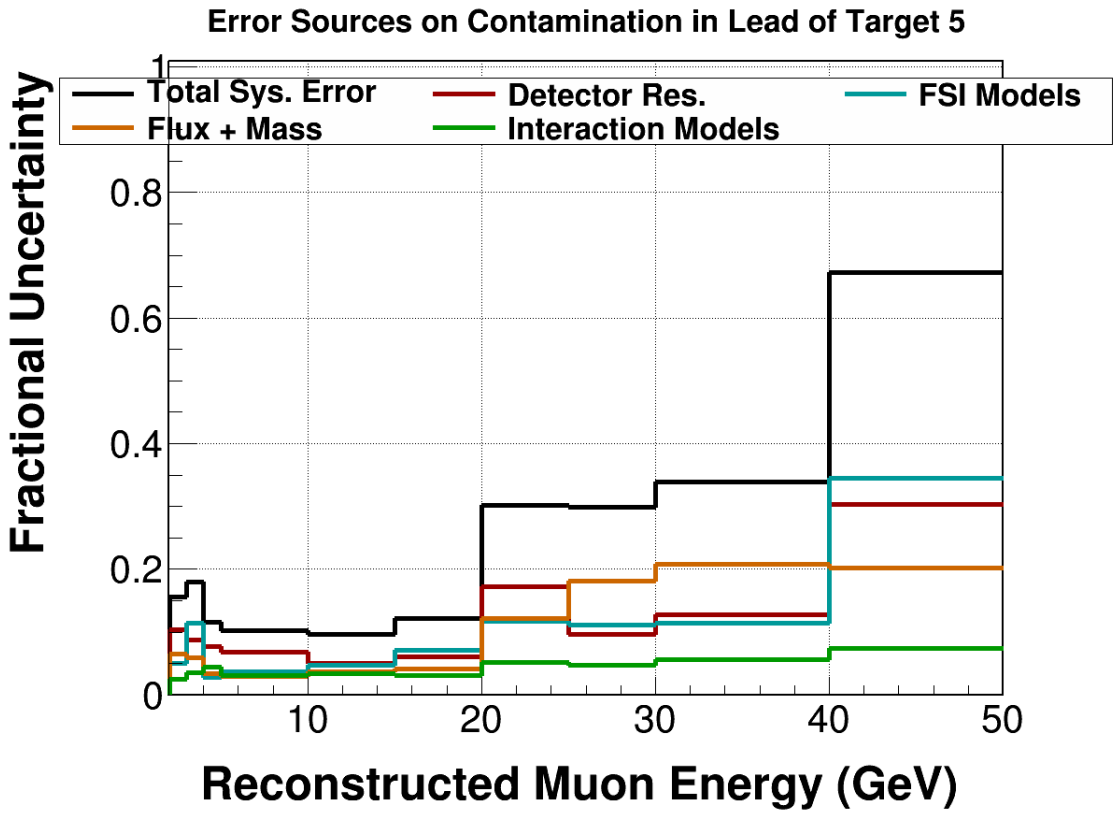

Figure B-86. Uncertainties on mis-ided DIS events: target 05 Pb (E_μ)

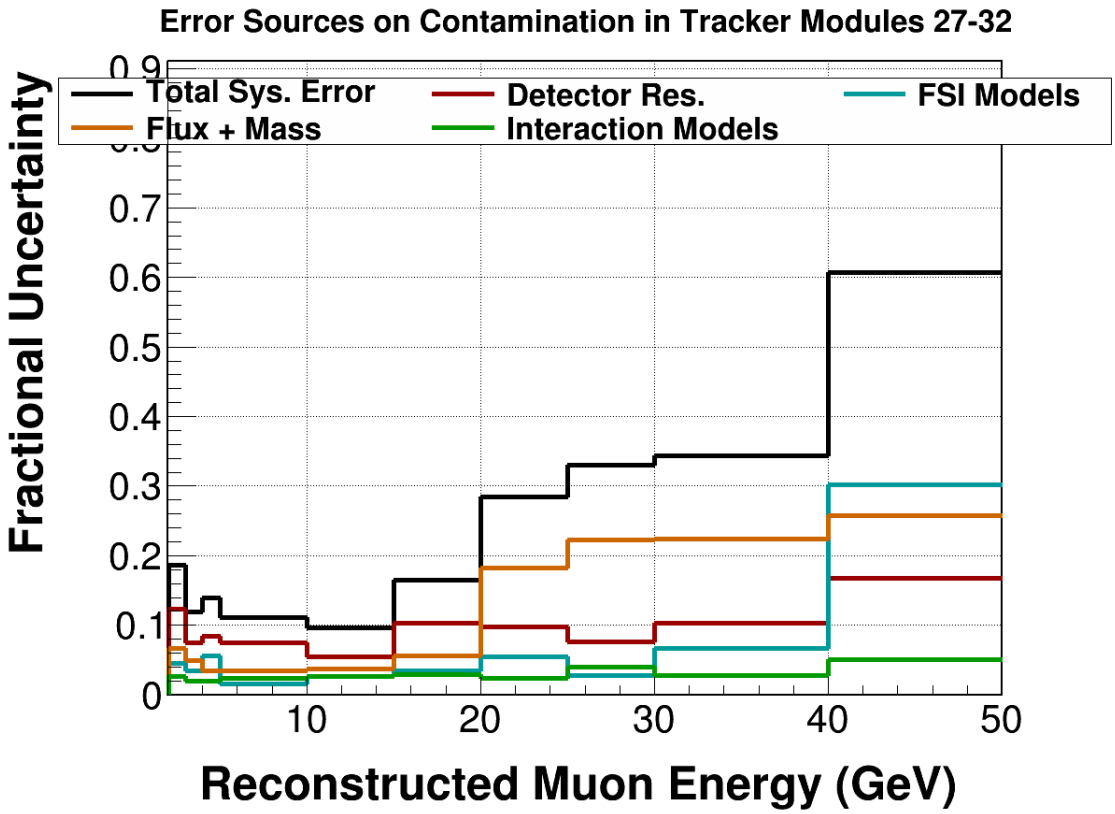

Figure B-87. Uncertainties on mis-ided DIS events: tracker mods. 27-32 (E_μ)

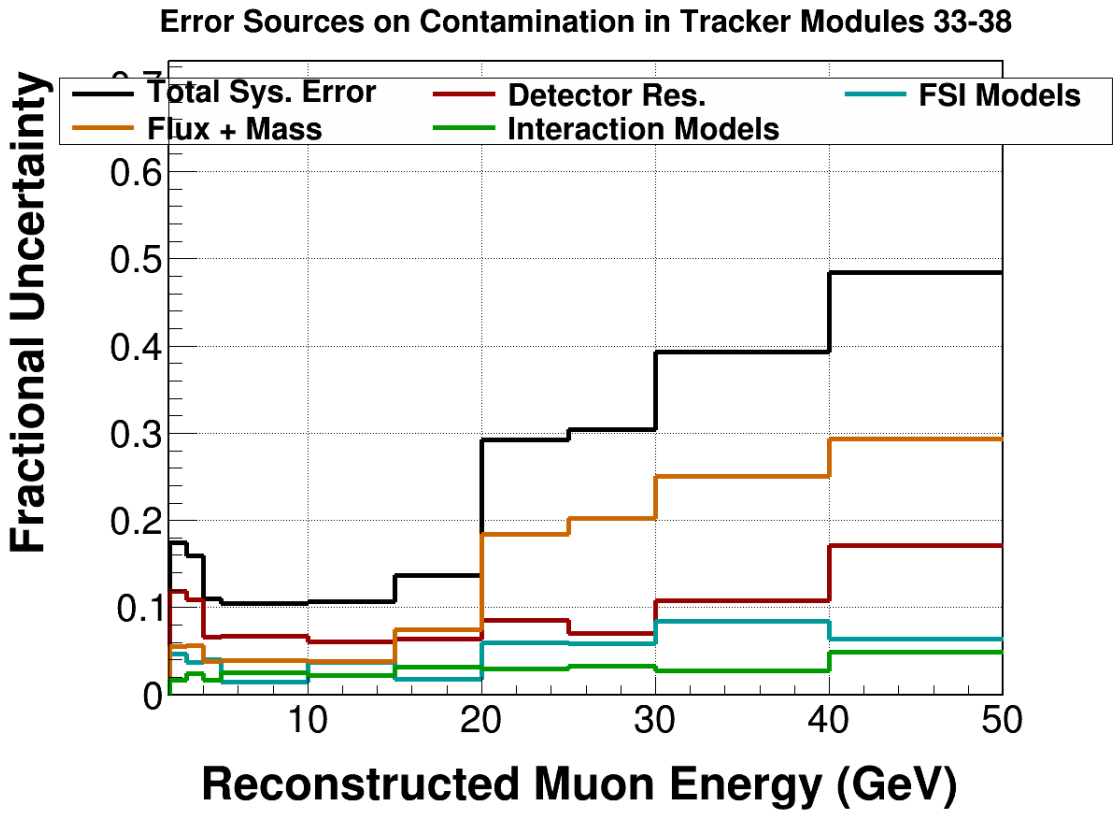

Figure B-88. Uncertainties on mis-ided DIS events: tracker mods. 33-38 (E_μ)

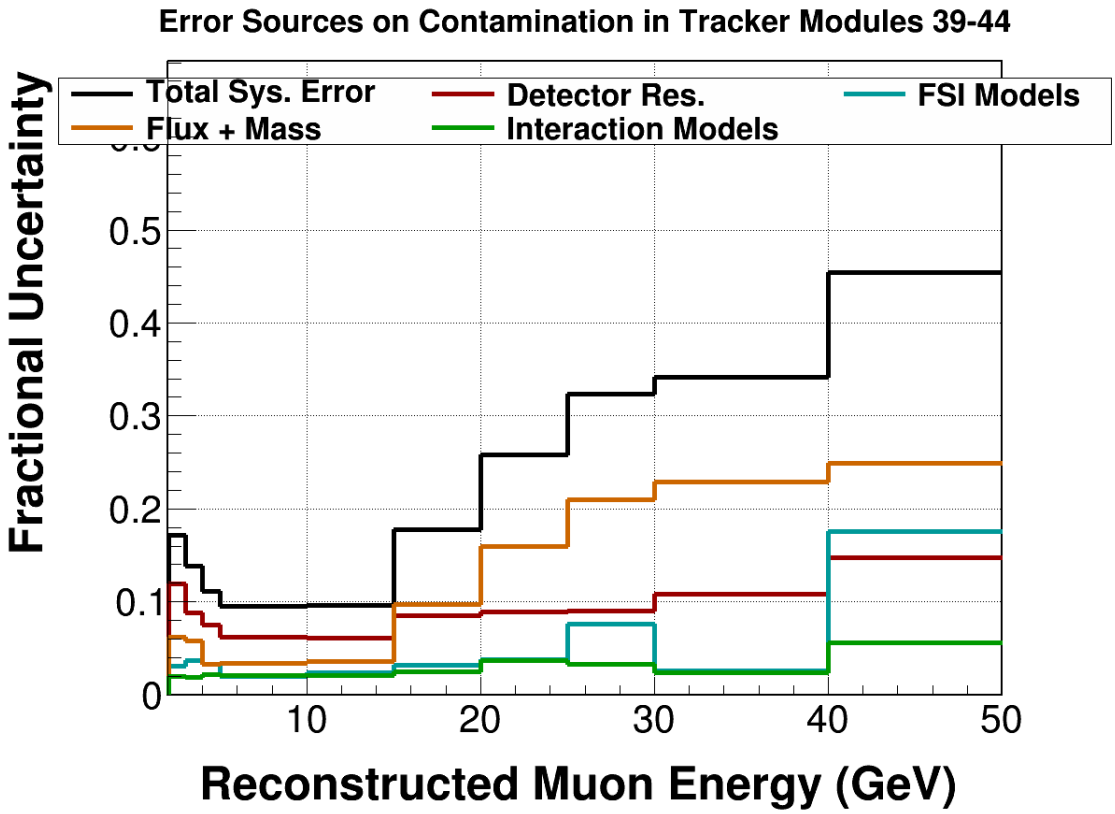

Figure B-89. Uncertainties on mis-ided DIS events: tracker mods. 39-44 (E_μ)

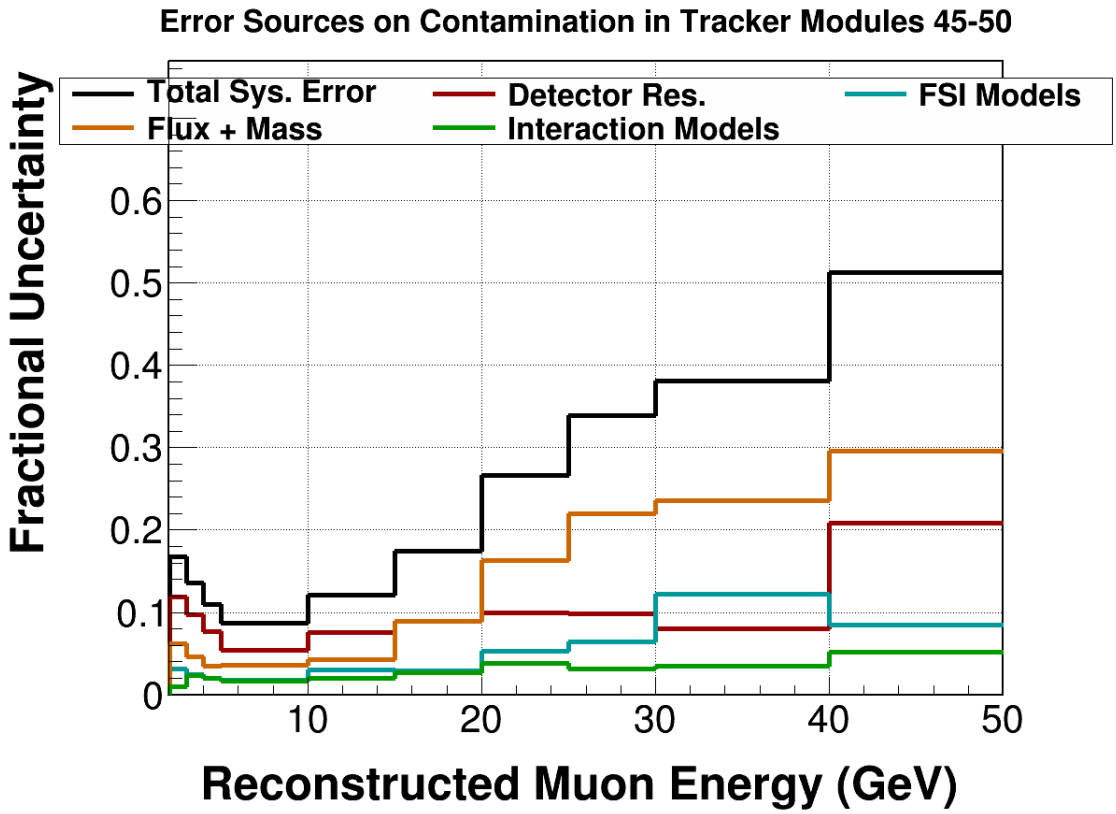

Figure B-90. Uncertainties on mis-ided DIS events: tracker mods. 45-50 (E_μ)

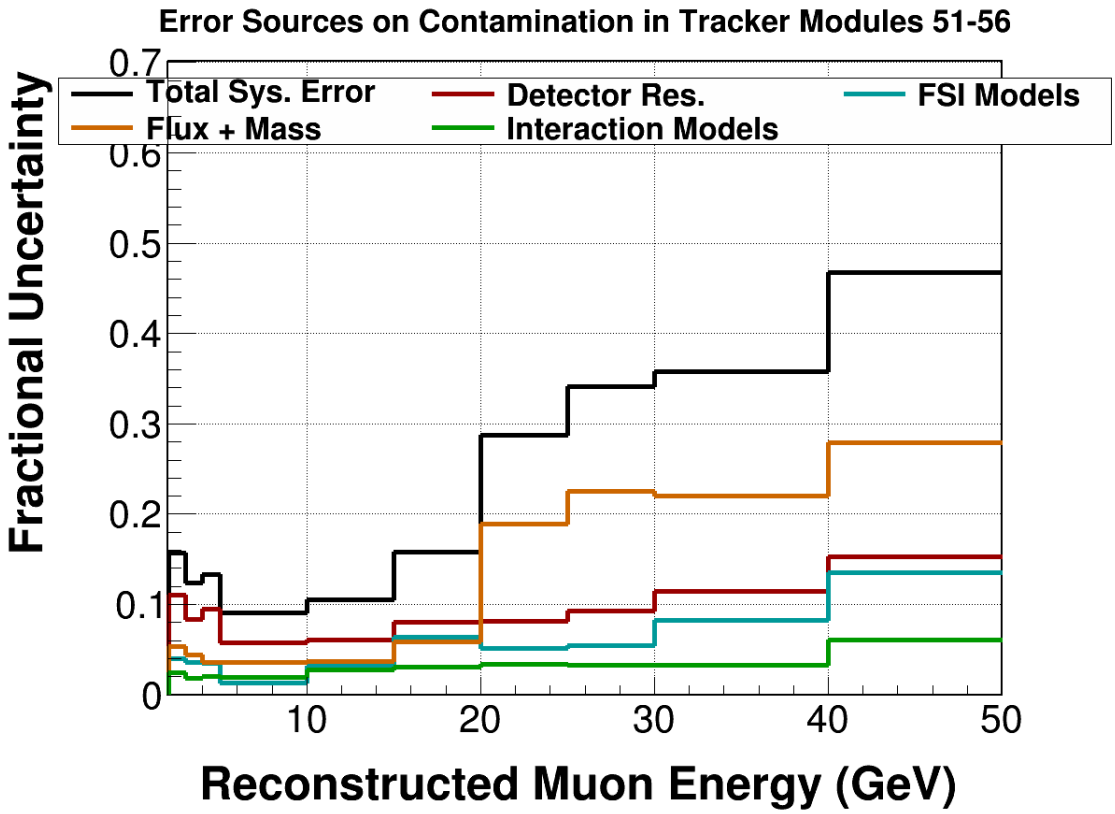

Figure B-91. Uncertainties on mis-ided DIS events: tracker mods. 51-56 (E_μ)

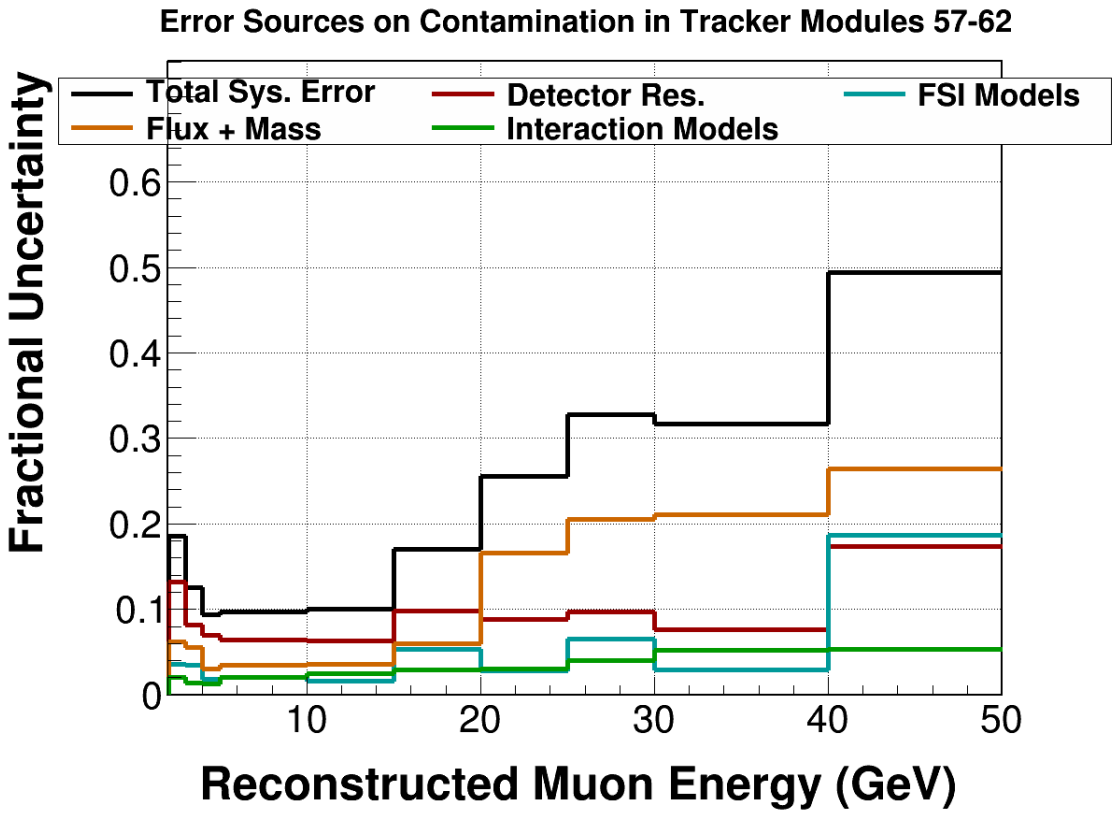

Figure B-92. Uncertainties on mis-ided DIS events: tracker mods. 57-62 (E_μ)

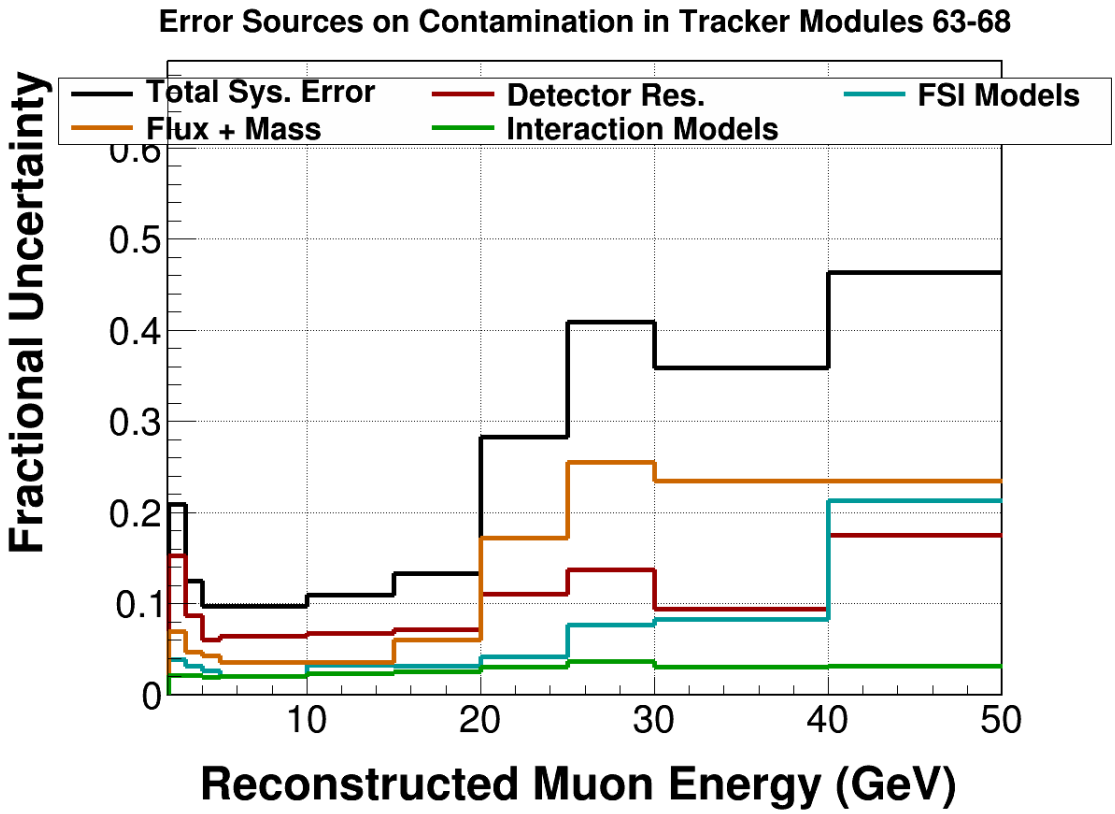

Figure B-93. Uncertainties on mis-ided DIS events: tracker mods. 63-68 (E_μ)

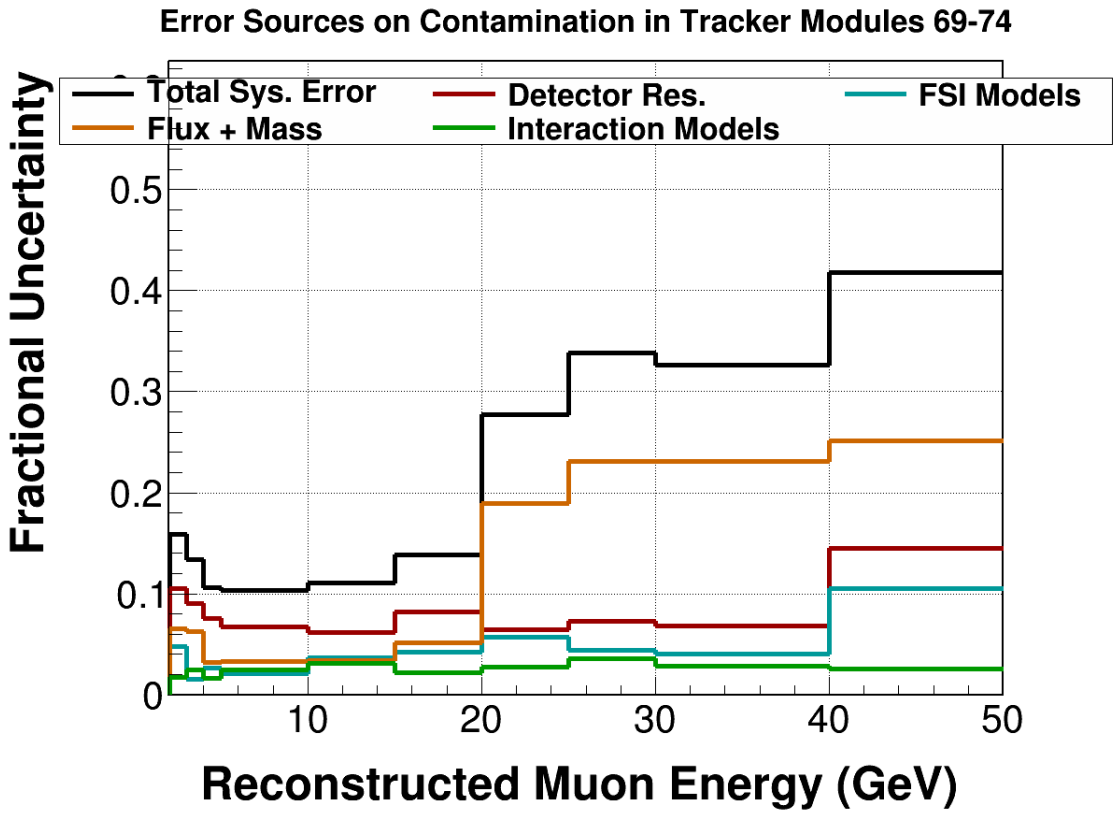

Figure B-94. Uncertainties on mis-ided DIS events: tracker mods. 69-74 (E_μ)

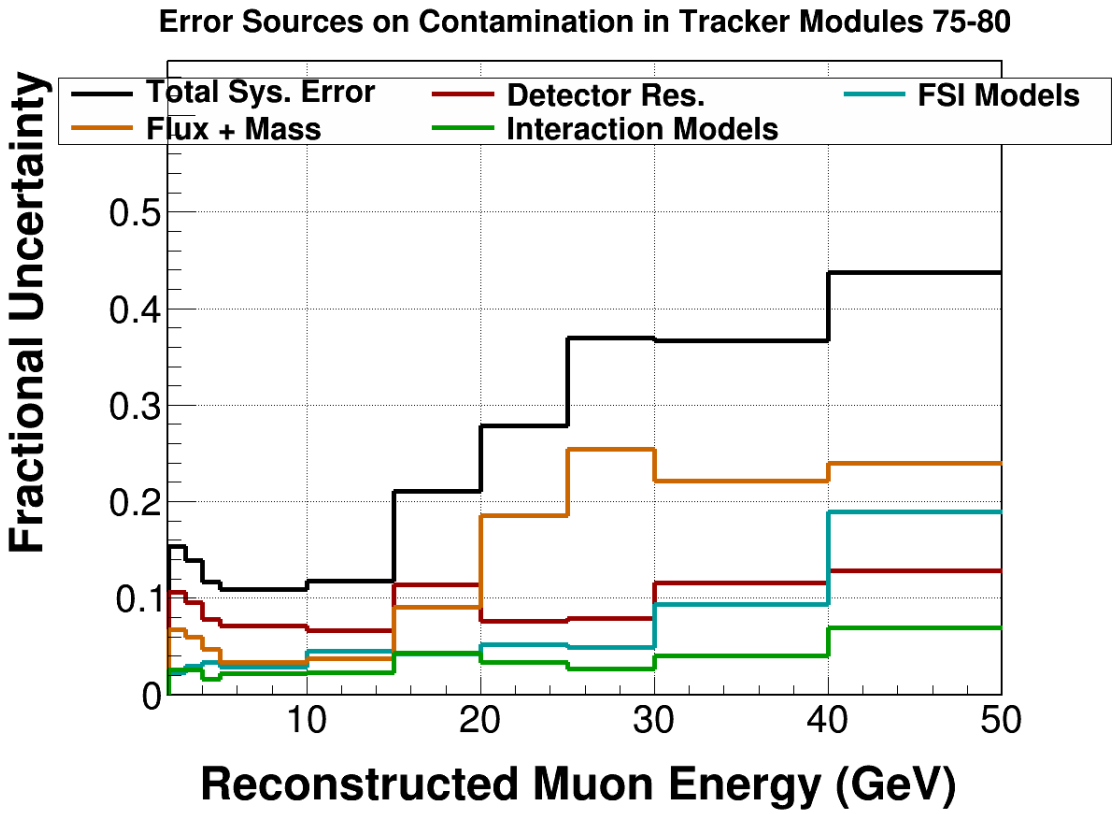

Figure B-95. Uncertainties on mis-ided DIS events: tracker mods. 75-80 (E_μ)

APPENDIX C
PLASTIC BACKGROUND SUBTRACTION

C.1 Predicted vs. True CH Background

The following plots are the true / predicted CH BG of each nuclear target, after subtracting the non-DIS events. They are plotted as a function of neutrino energy (E_ν):

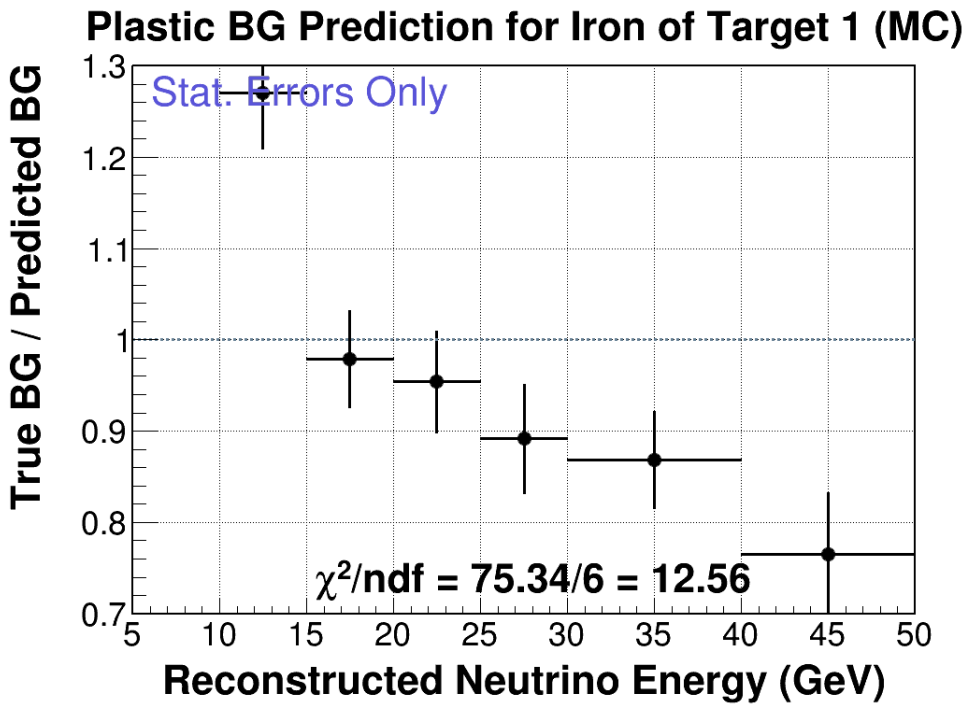

Figure C-1. Plastic BG prediction: target 01 Fe (E_ν)

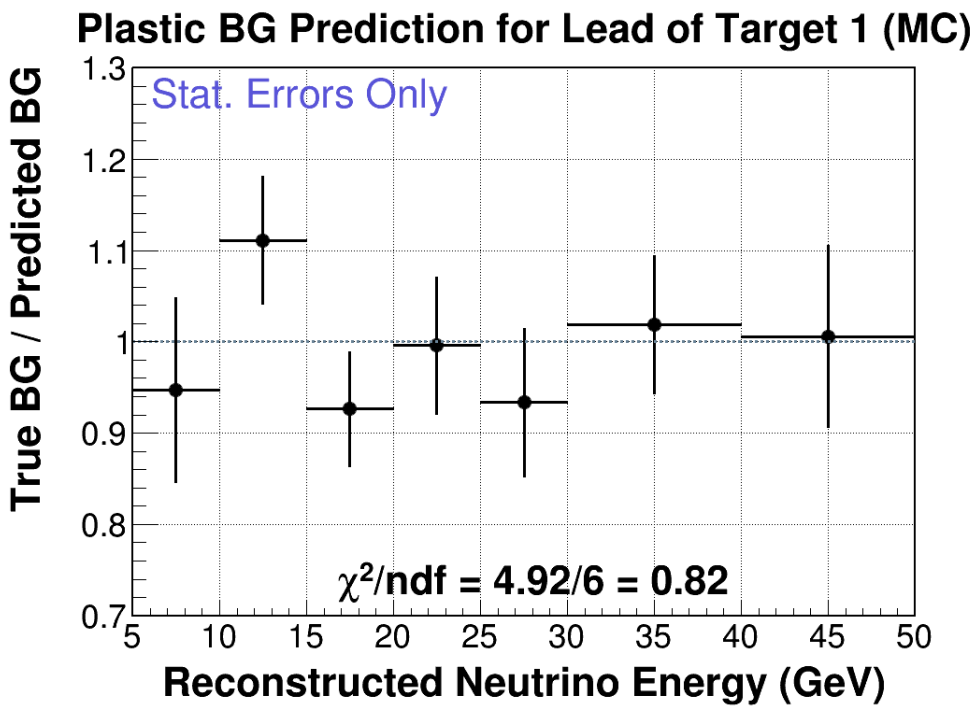

Figure C-2. Plastic BG prediction: target 01 Pb (E_ν)

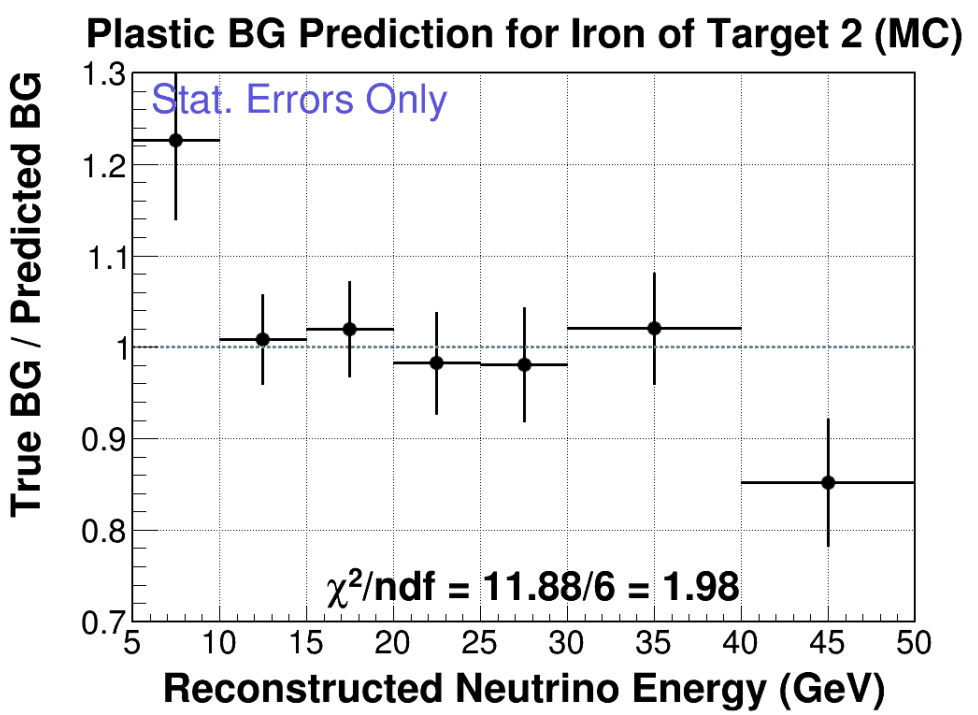

Figure C-3. Plastic BG prediction: target 02 Fe (E_ν)

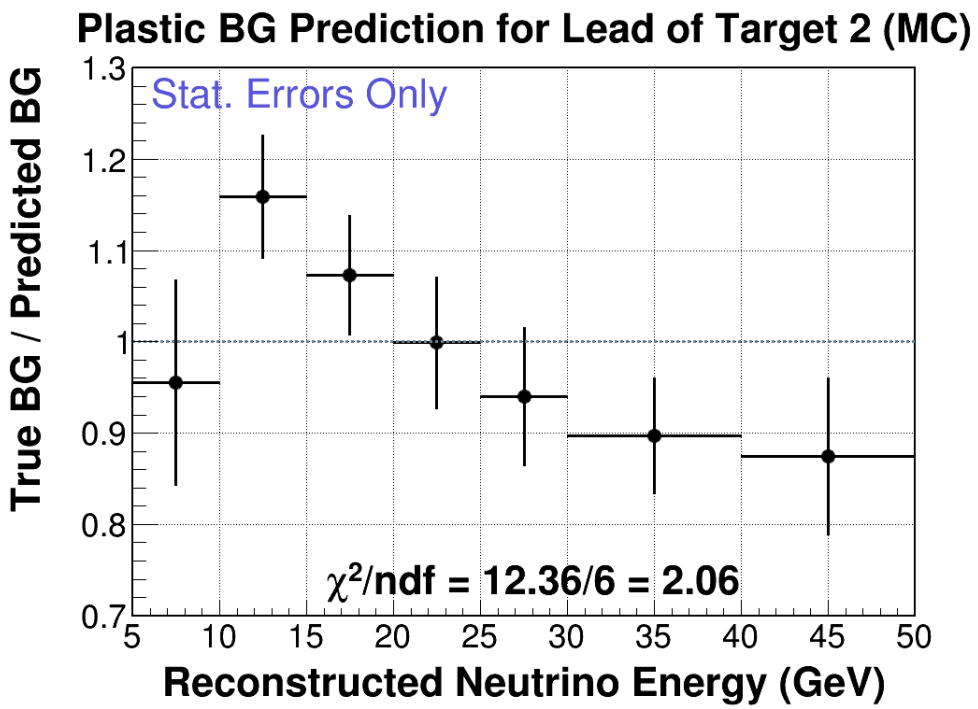

Figure C-4. Plastic BG prediction: target 02 Pb (E_ν)

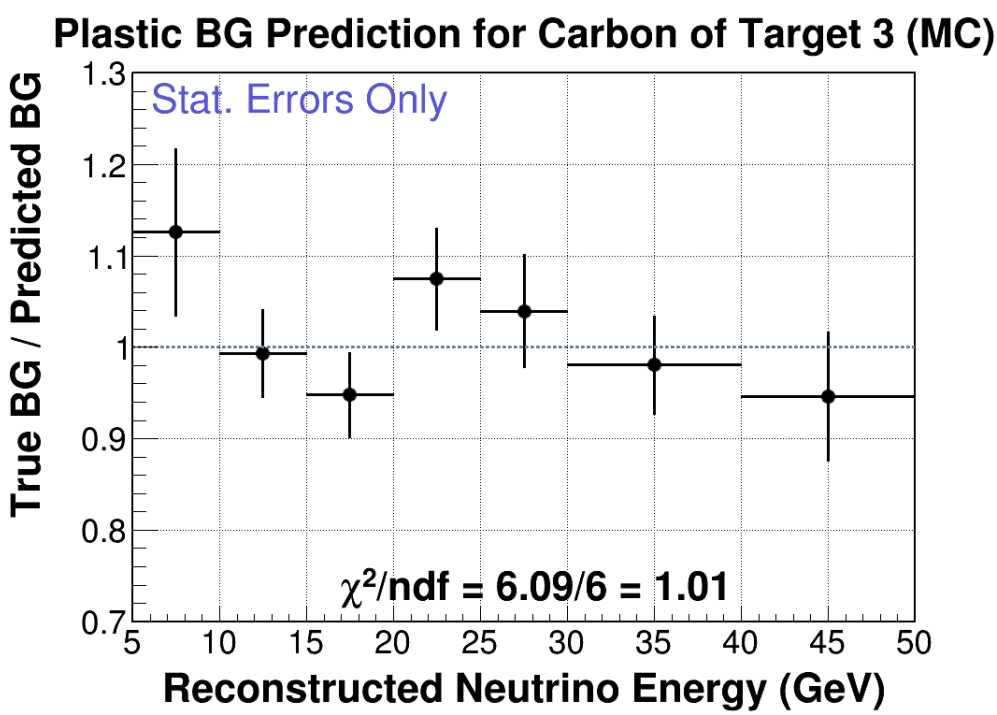

Figure C-5. Plastic BG prediction: target 03 C (E_ν)

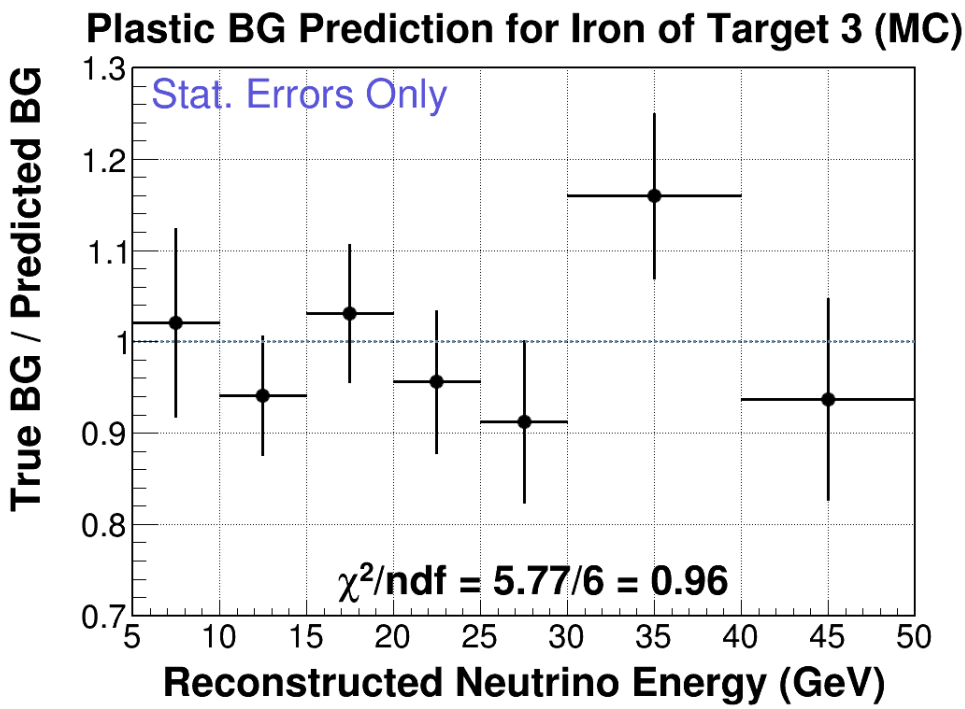

Figure C-6. Plastic BG prediction: target 03 Fe (E_ν)

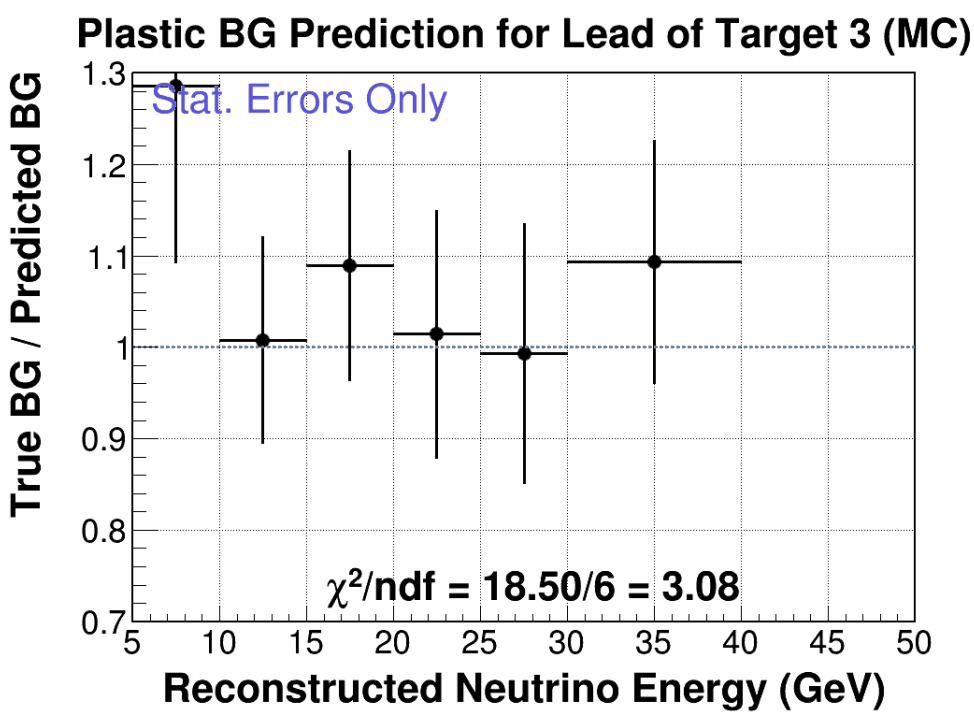

Figure C-7. Plastic BG prediction: target 03 Pb (E_ν)

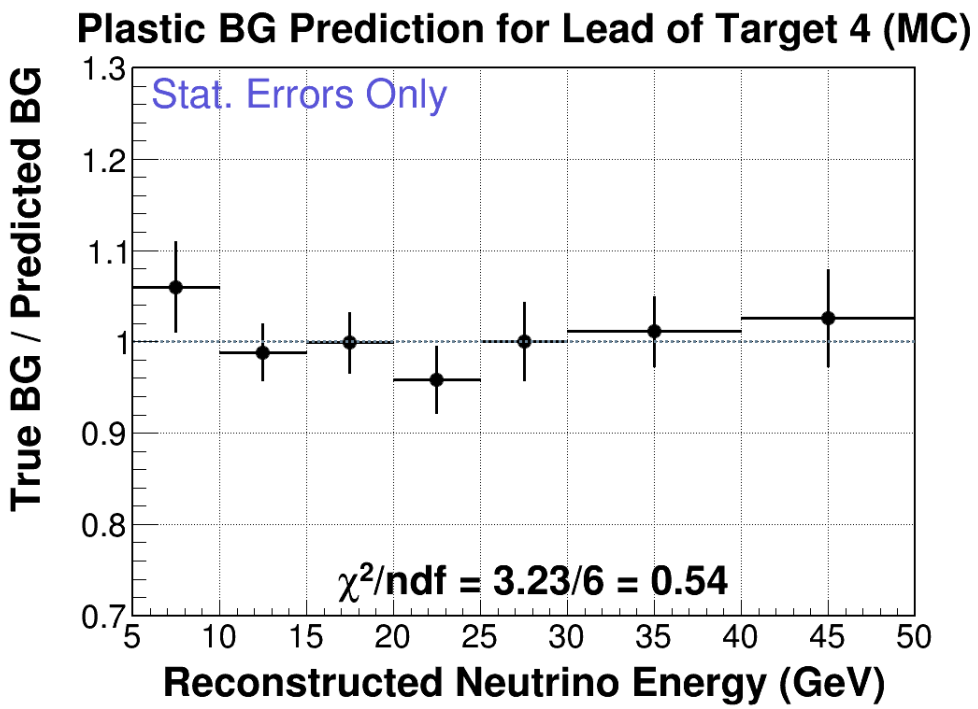

Figure C-8. Plastic BG prediction: target 04 Pb (E_ν)

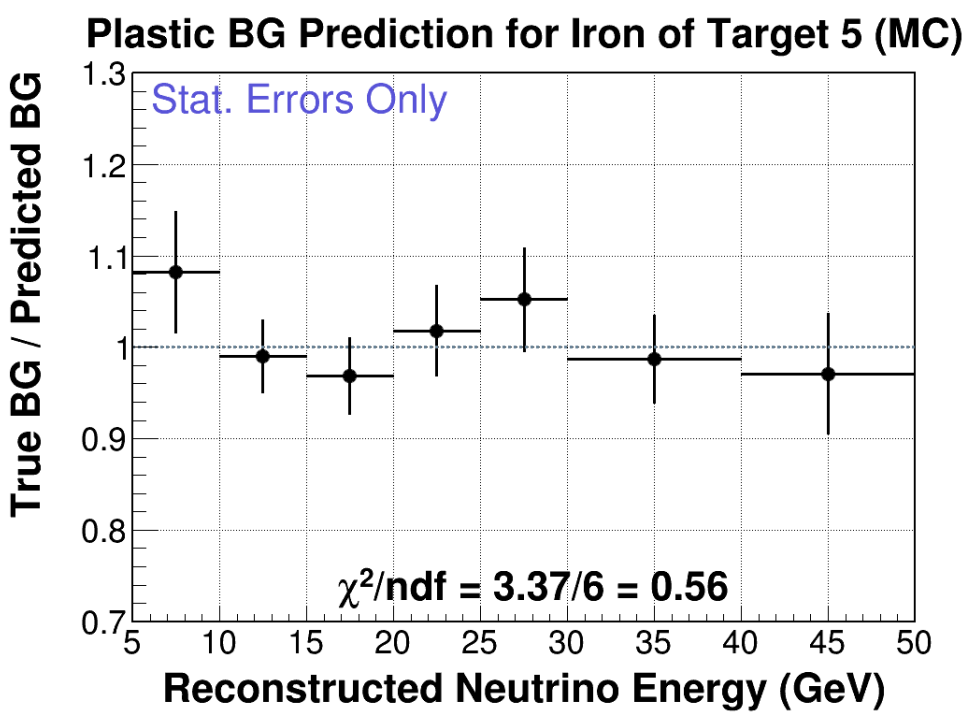

Figure C-9. Plastic BG prediction: target 05 Fe (E_ν)

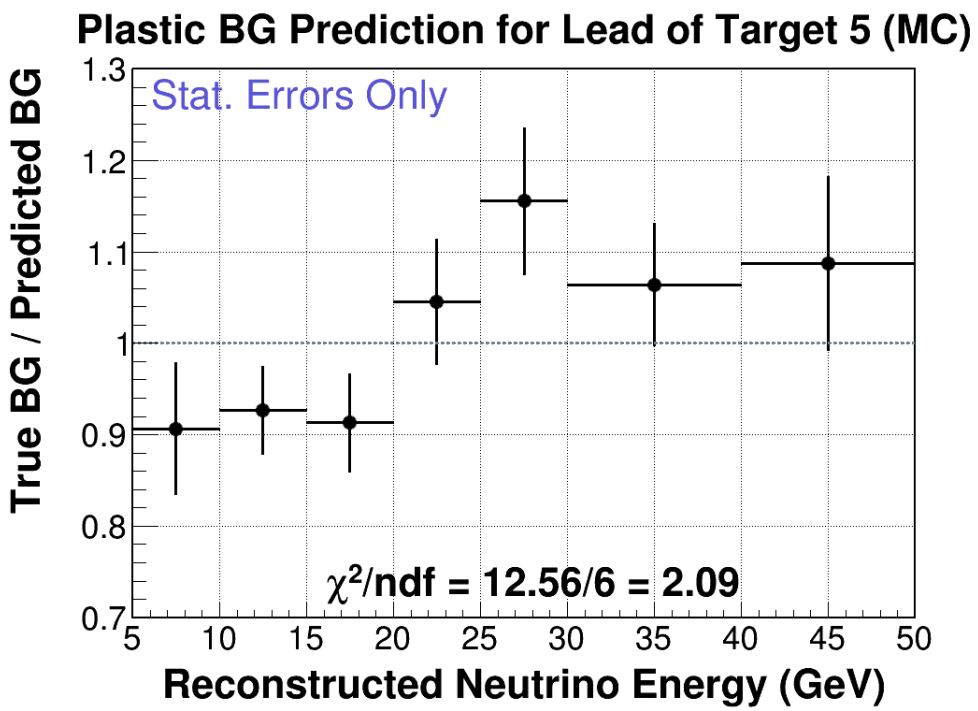

Figure C-10. Plastic BG prediction: target 05 Pb (E_ν)

The following plots are the true / predicted CH BG of each nuclear target, after subtracting the non-DIS events. They are plotted as a function of four momentum transfer squared (Q^2):

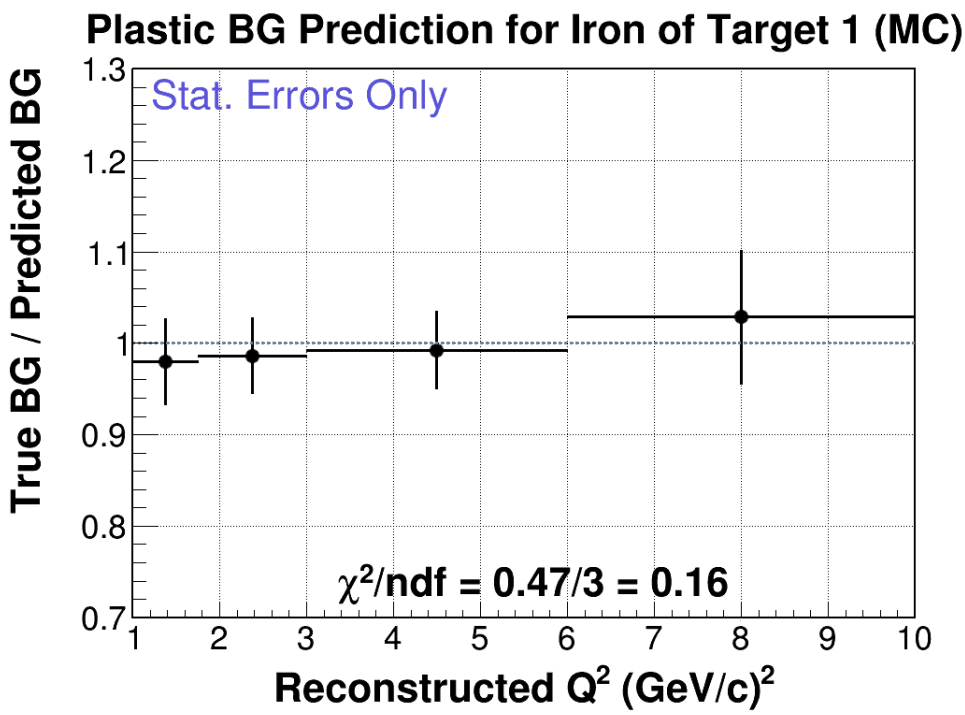

Figure C-11. Plastic BG prediction: target 01 Fe (Q^2)

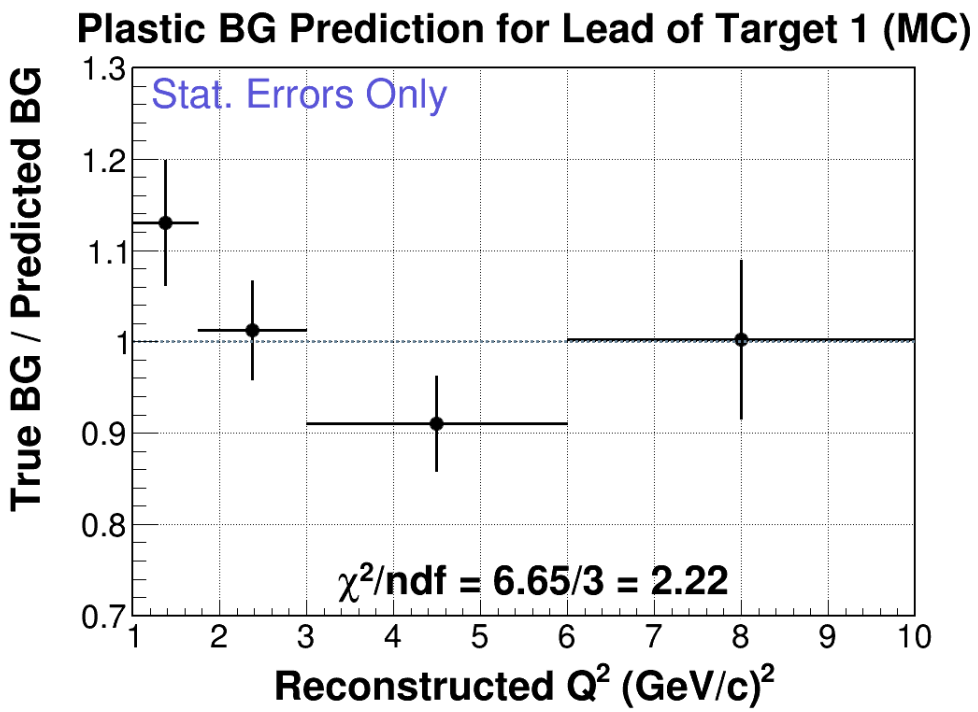

Figure C-12. Plastic BG prediction: target 01 Pb (Q^2)

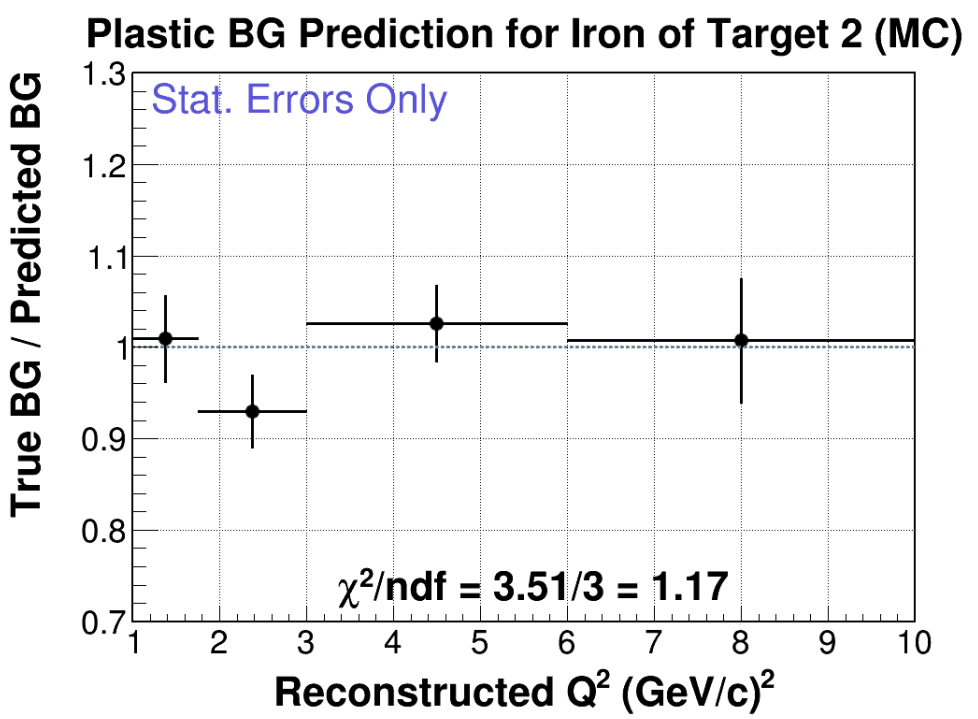

Figure C-13. Plastic BG prediction: target 02 Fe (Q^2)

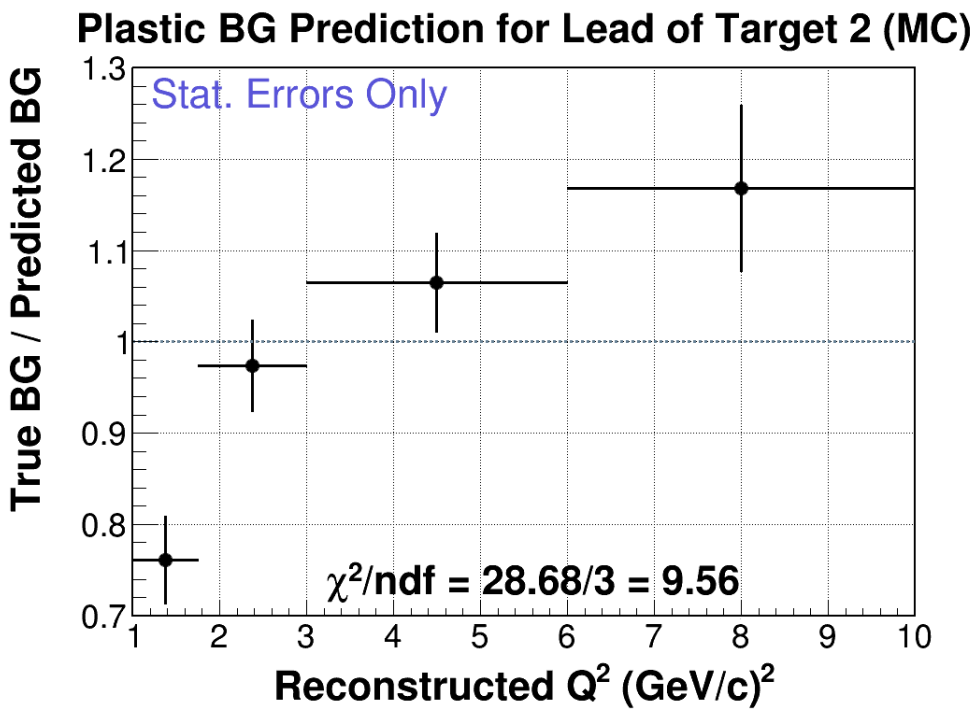

Figure C-14. Plastic BG prediction: target 02 Pb (Q^2)

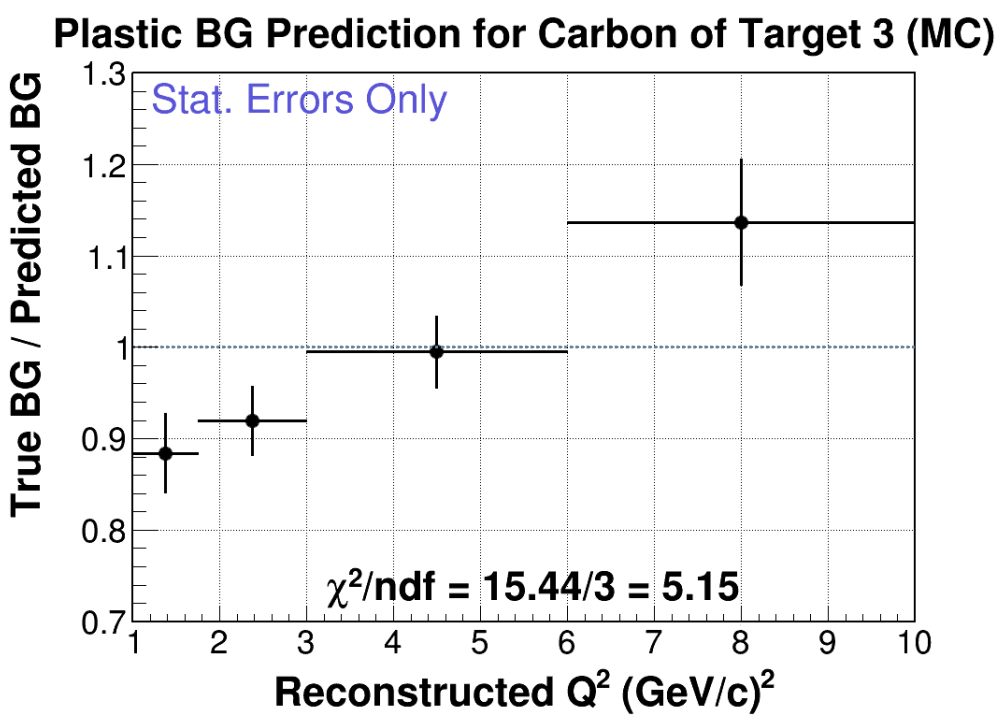

Figure C-15. Plastic BG prediction: target 03 C (Q^2)

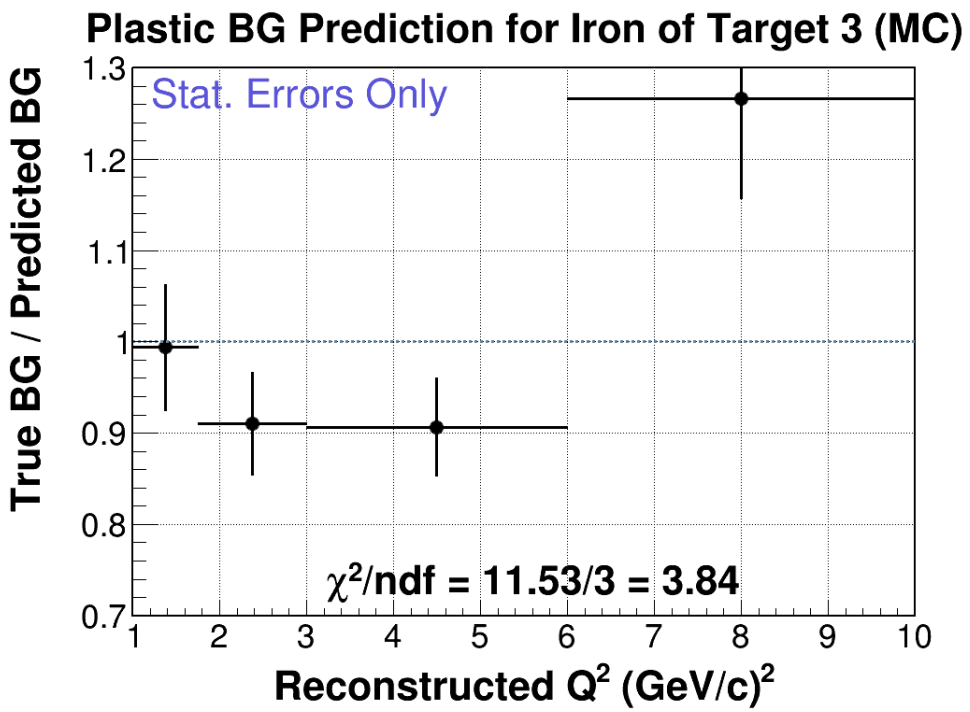

Figure C-16. Plastic BG prediction: target 03 Fe (Q^2)

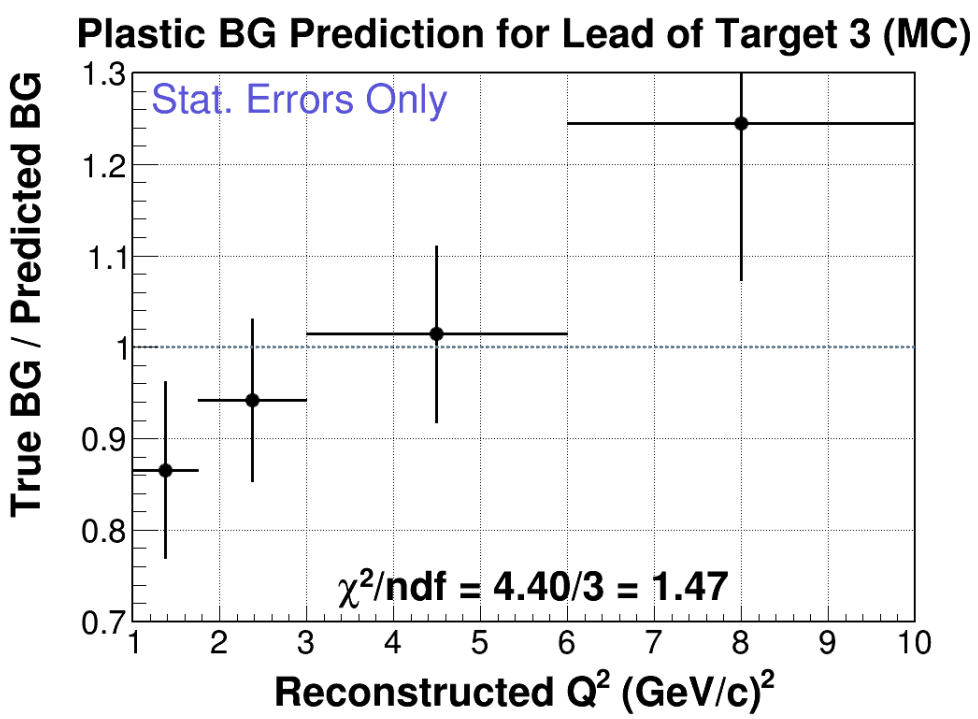

Figure C-17. Plastic BG prediction: target 03 Pb (Q^2)

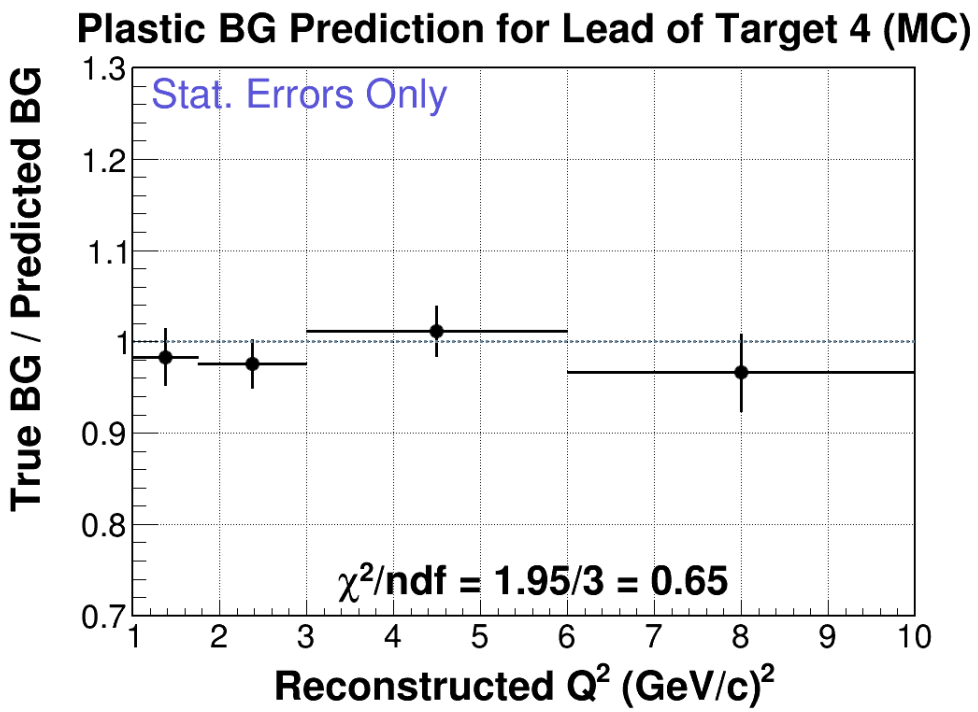

Figure C-18. Plastic BG prediction: target 04 Pb (Q^2)

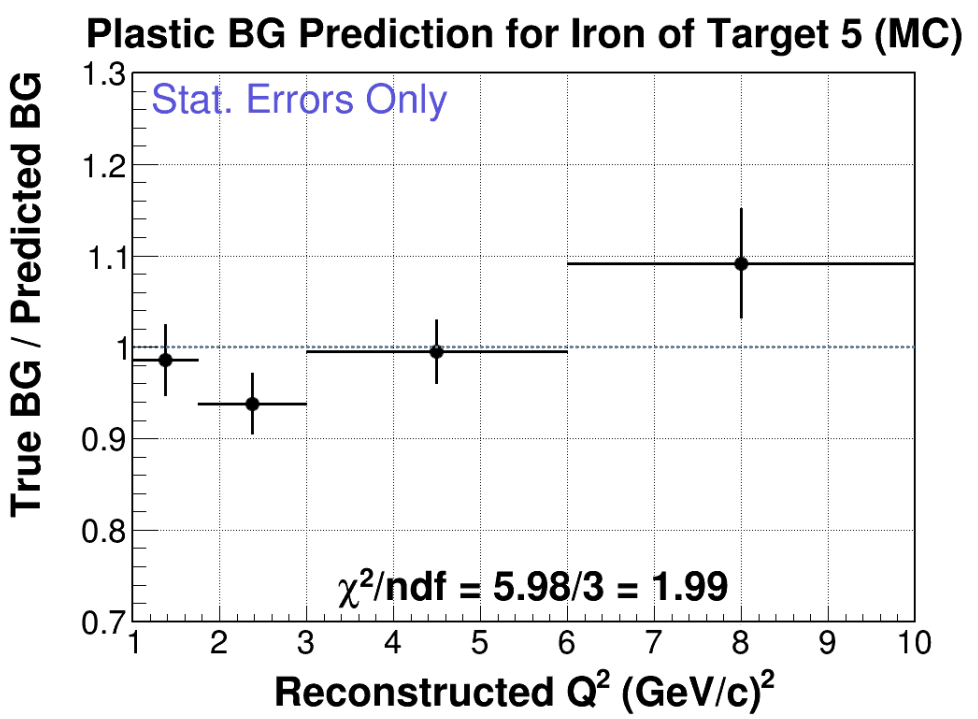

Figure C-19. Plastic BG prediction: target 05 Fe (Q^2)

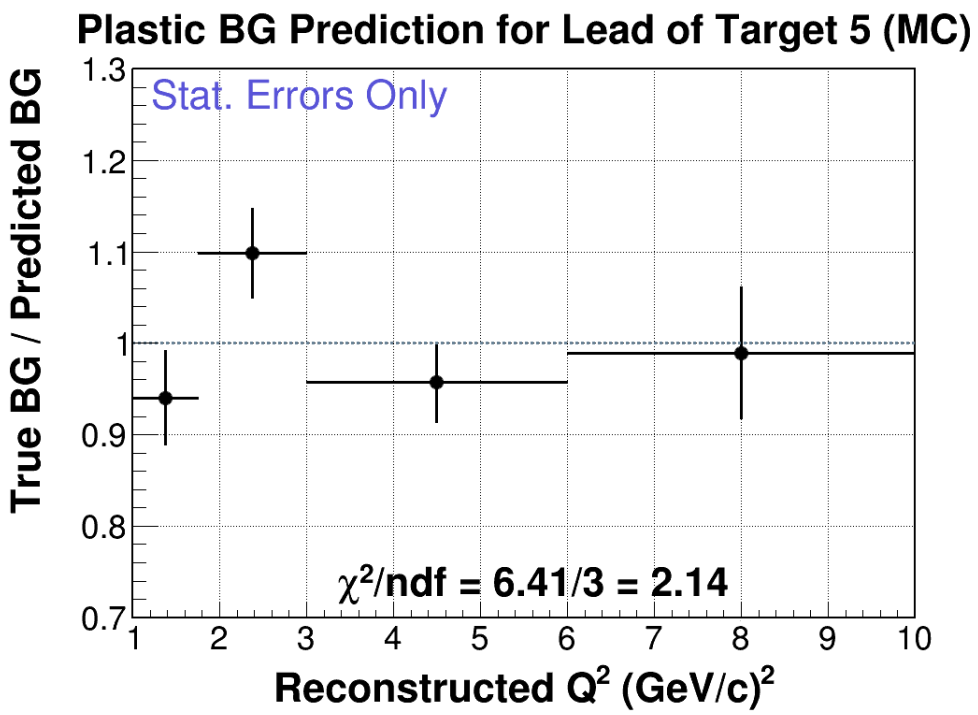

Figure C-20. Plastic BG prediction: target 05 Pb (Q^2)

The following plots are the true / predicted CH BG of each nuclear target, after subtracting the non-DIS events. They are plotted as a function of final state hadron shower invariant mass (W):

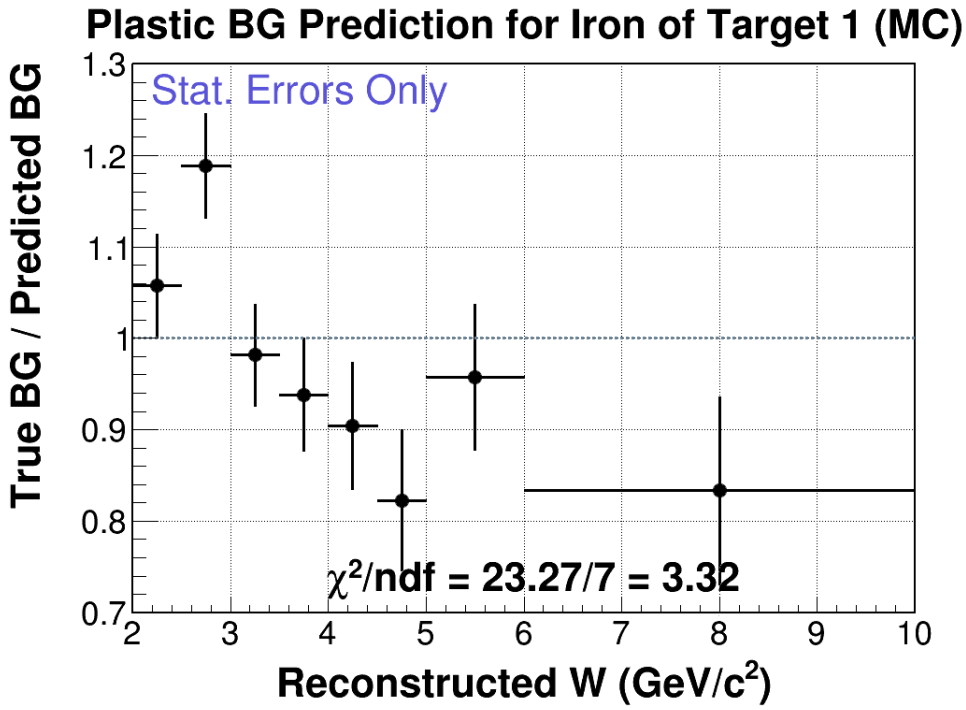

Figure C-21. Plastic BG prediction: target 01 Fe (W)

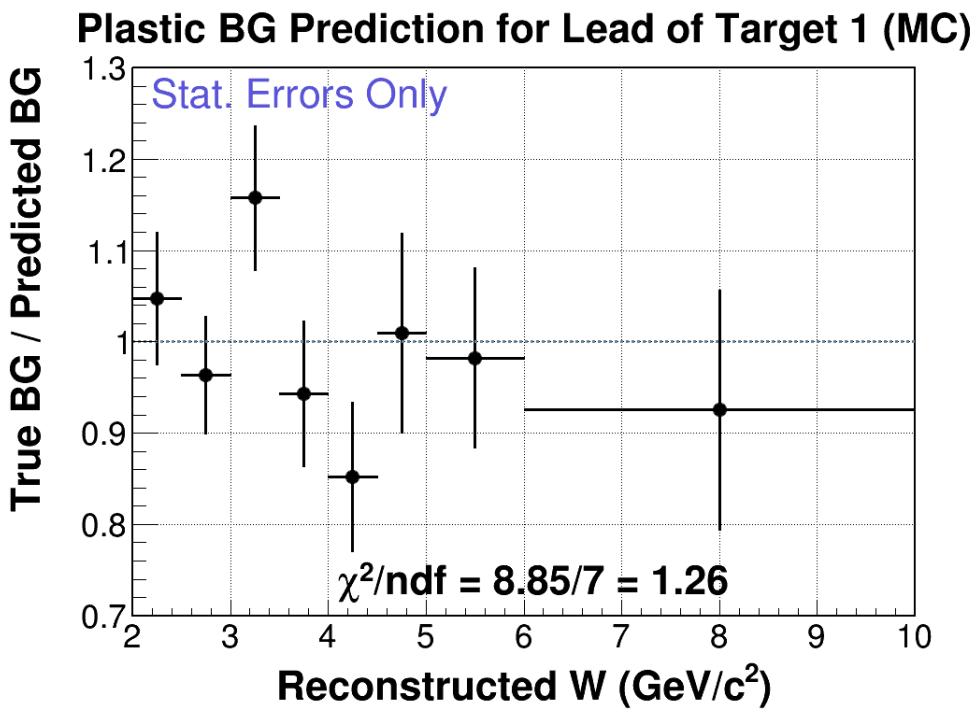

Figure C-22. Plastic BG prediction: target 01 Pb (W)

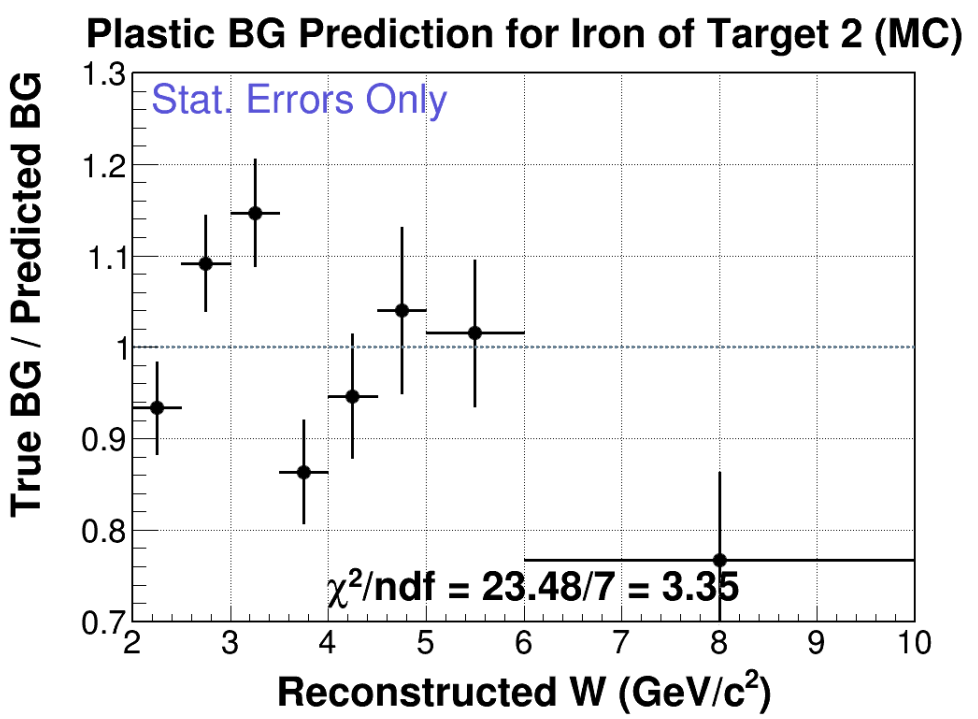

Figure C-23. Plastic BG prediction: target 02 Fe (W)

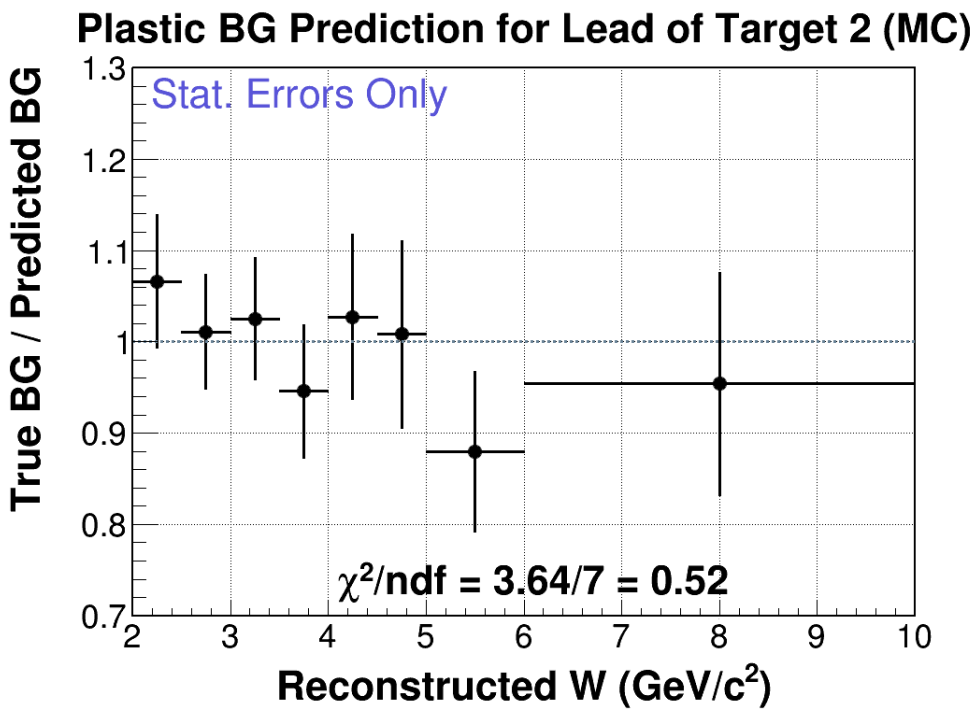

Figure C-24. Plastic BG prediction: target 02 Pb (W)

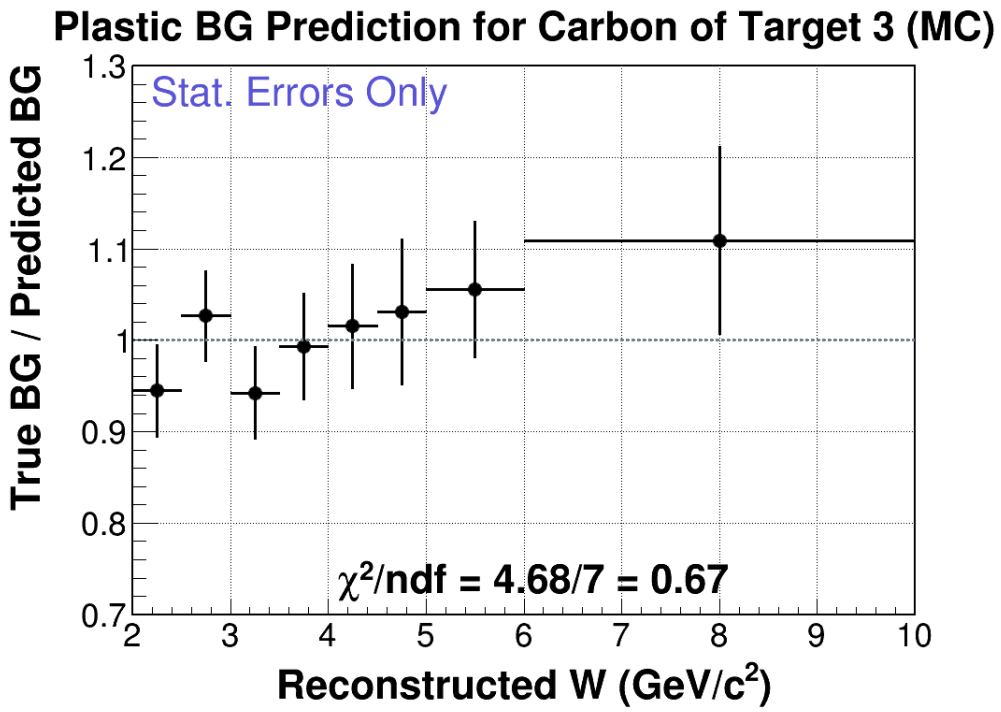

Figure C-25. Plastic BG prediction: target 03 C (W)

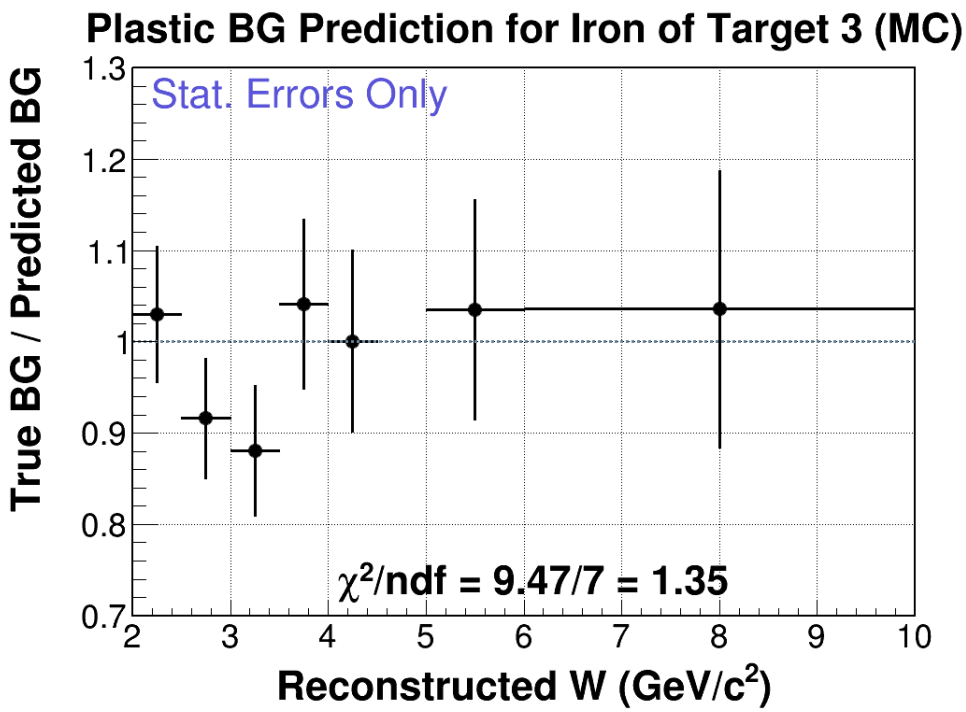

Figure C-26. Plastic BG prediction: target 03 Fe (W)

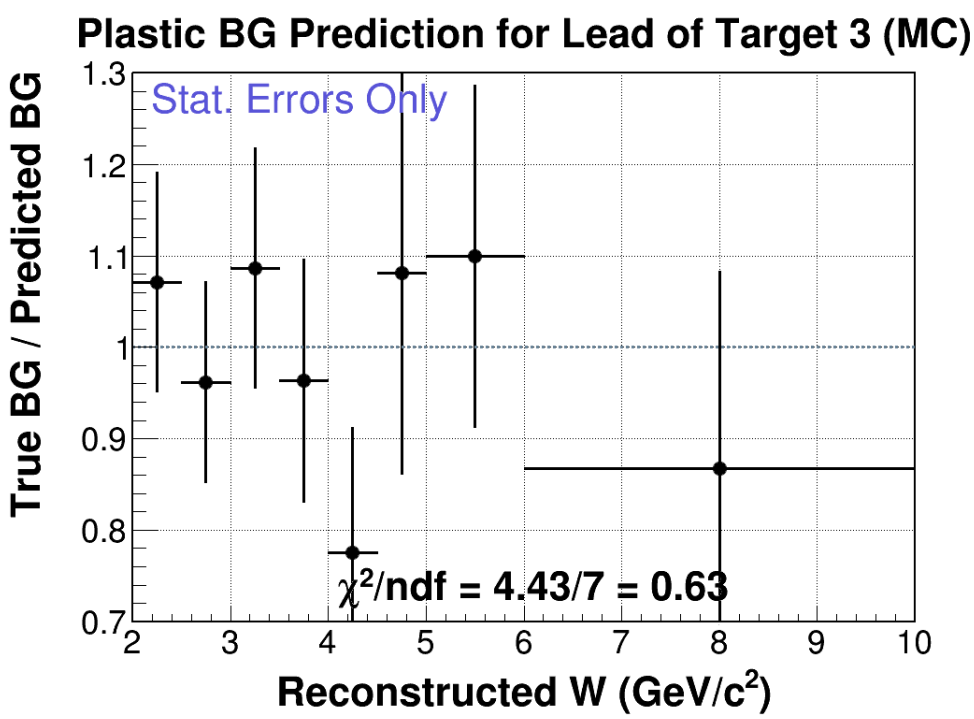

Figure C-27. Plastic BG prediction: target 03 Pb (W)

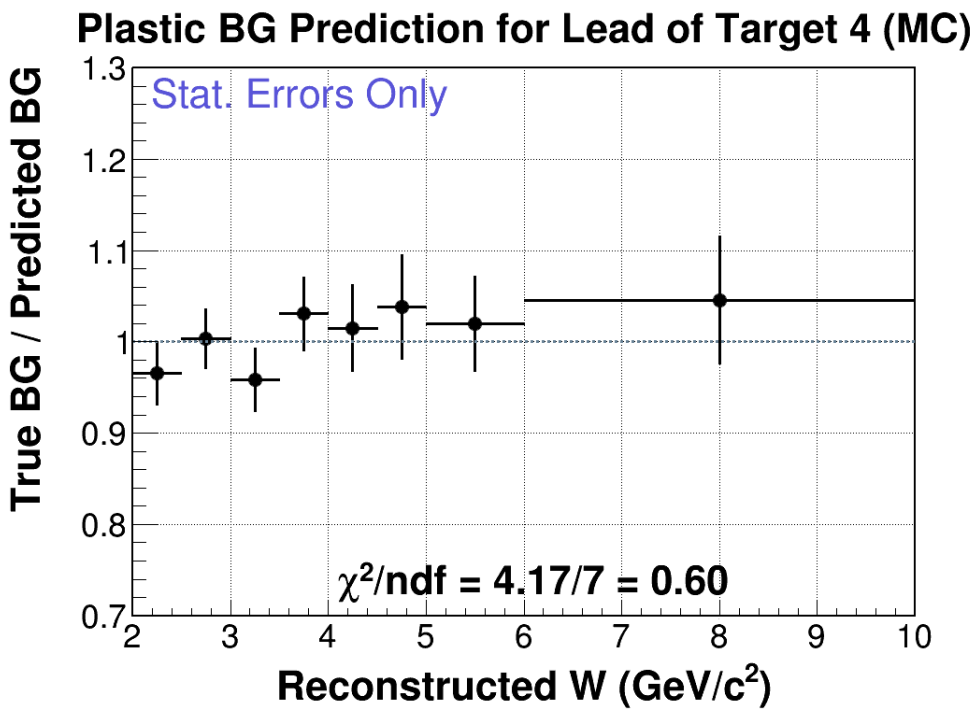

Figure C-28. Plastic BG prediction: target 04 Pb (W)

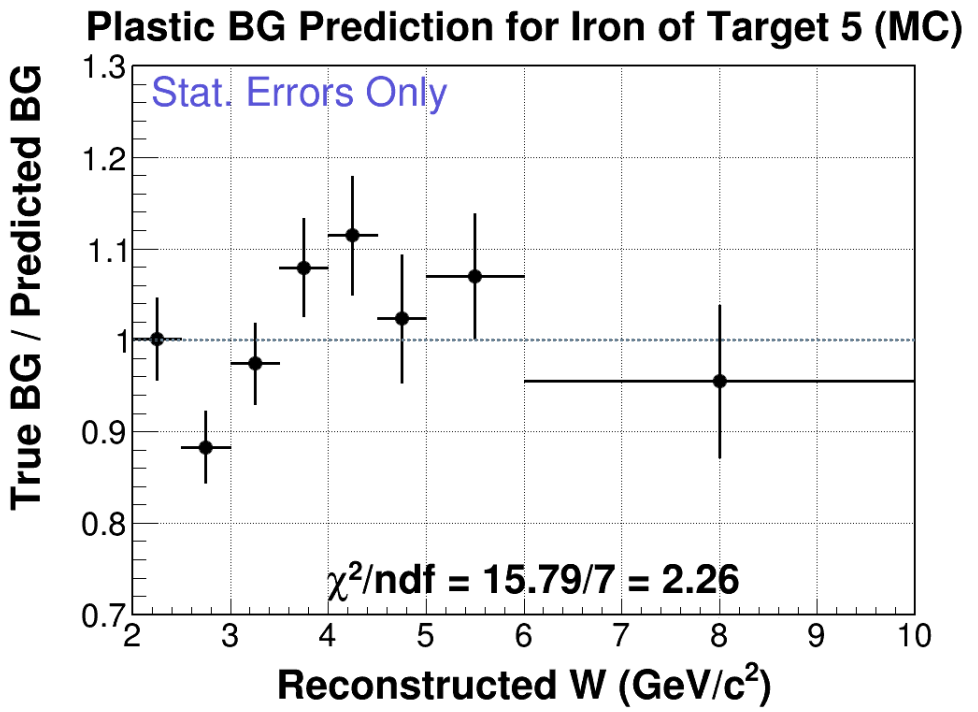

Figure C-29. Plastic BG prediction: target 05 Fe (W)

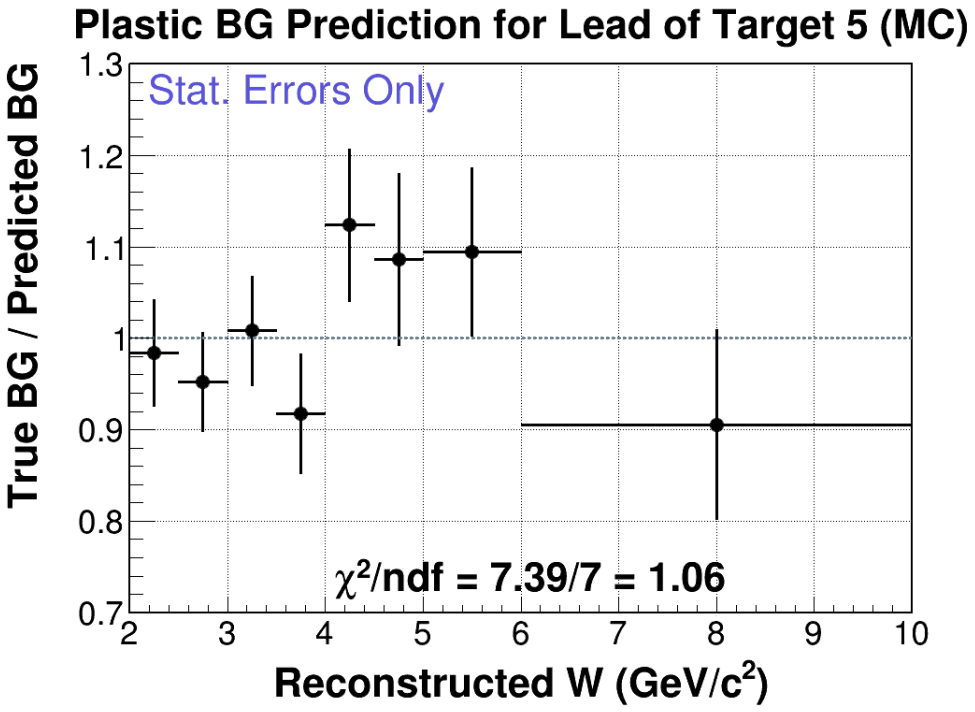

Figure C-30. Plastic BG prediction: target 05 Pb (W)

The following plots are the true / predicted CH BG of each nuclear target, after subtracting the non-DIS events. They are plotted as a function of Bjorken-x (x):

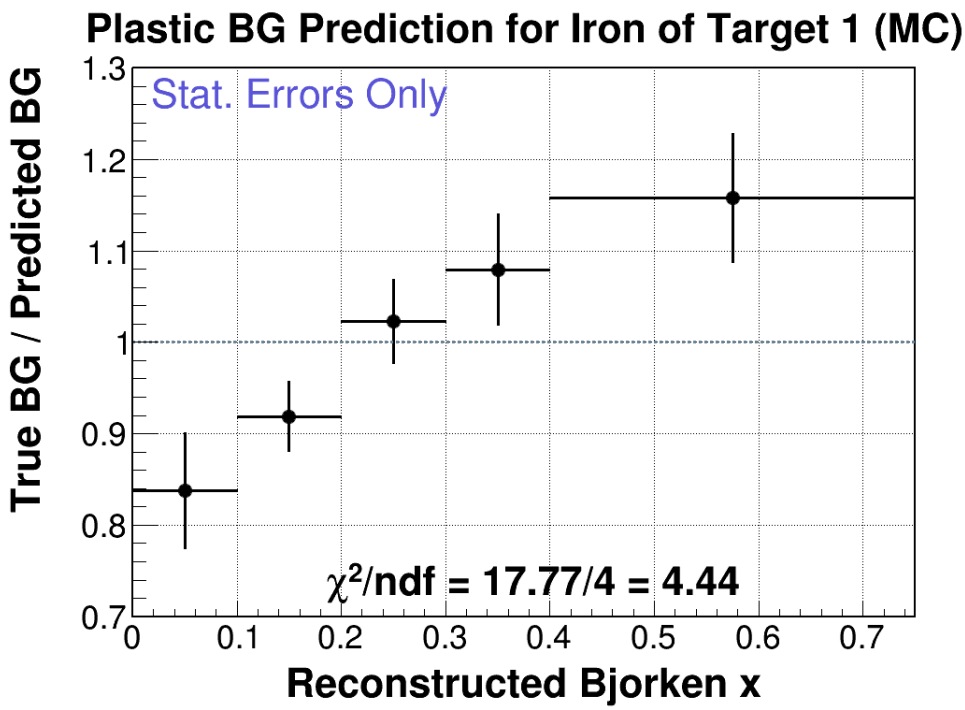

Figure C-31. Plastic BG prediction: target 01 Fe (x_{bj})

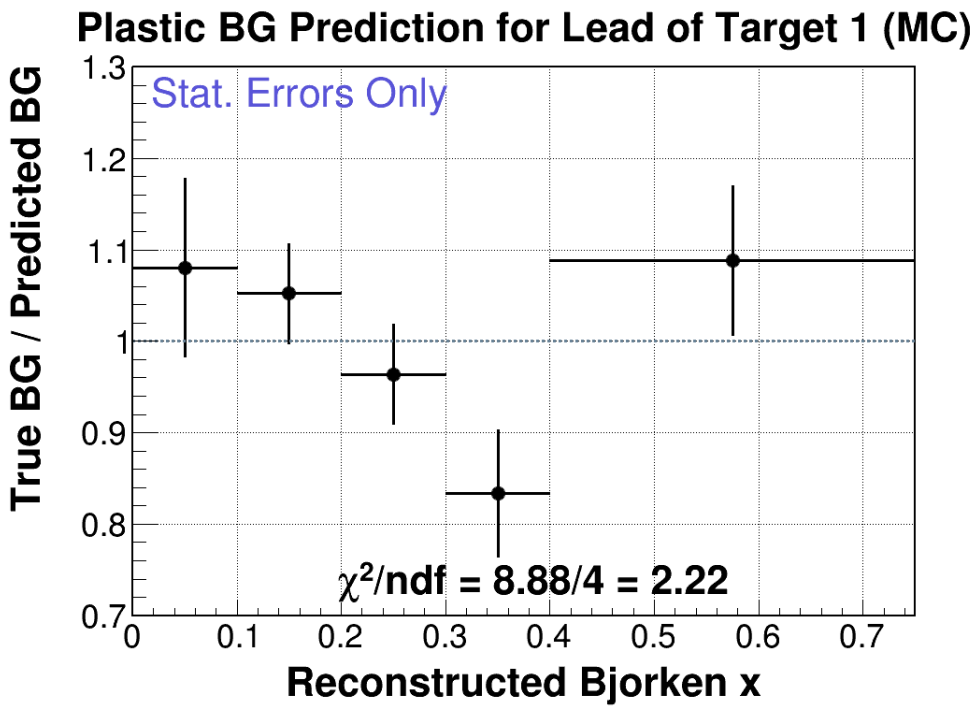

Figure C-32. Plastic BG prediction: target 01 Pb (x_{bj})

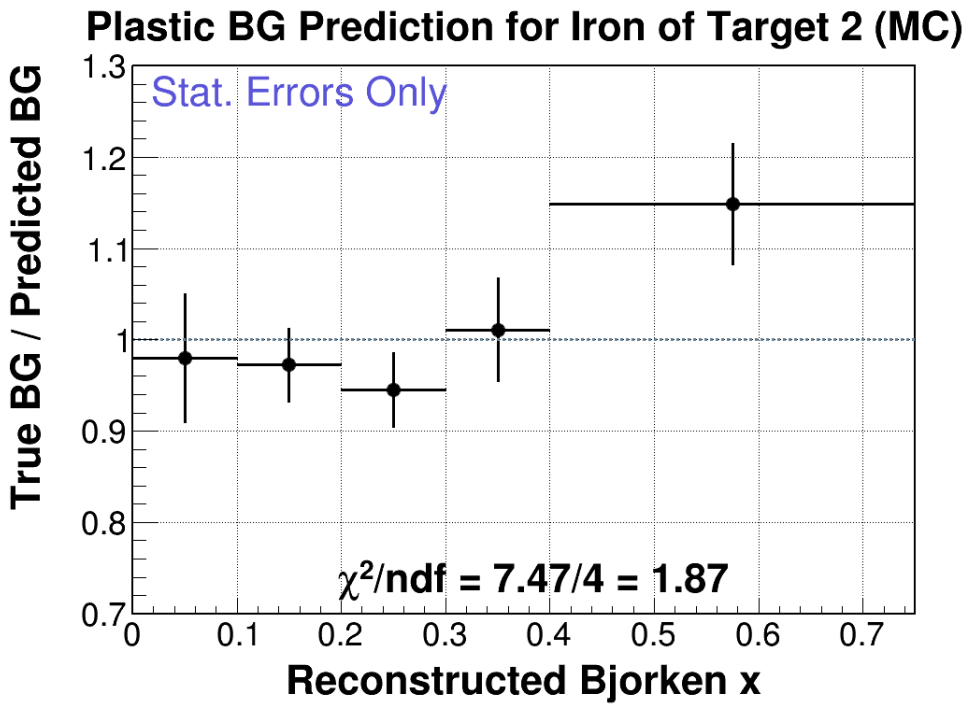

Figure C-33. Plastic BG prediction: target 02 Fe (x_{bj})

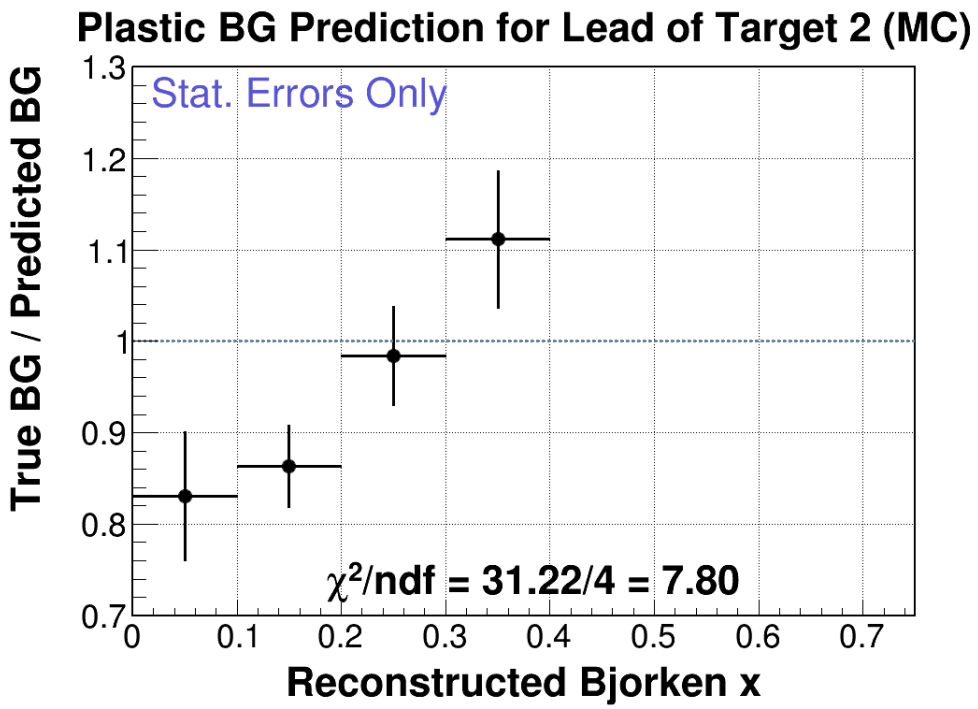

Figure C-34. Plastic BG prediction: target 02 Pb (x_{bj})

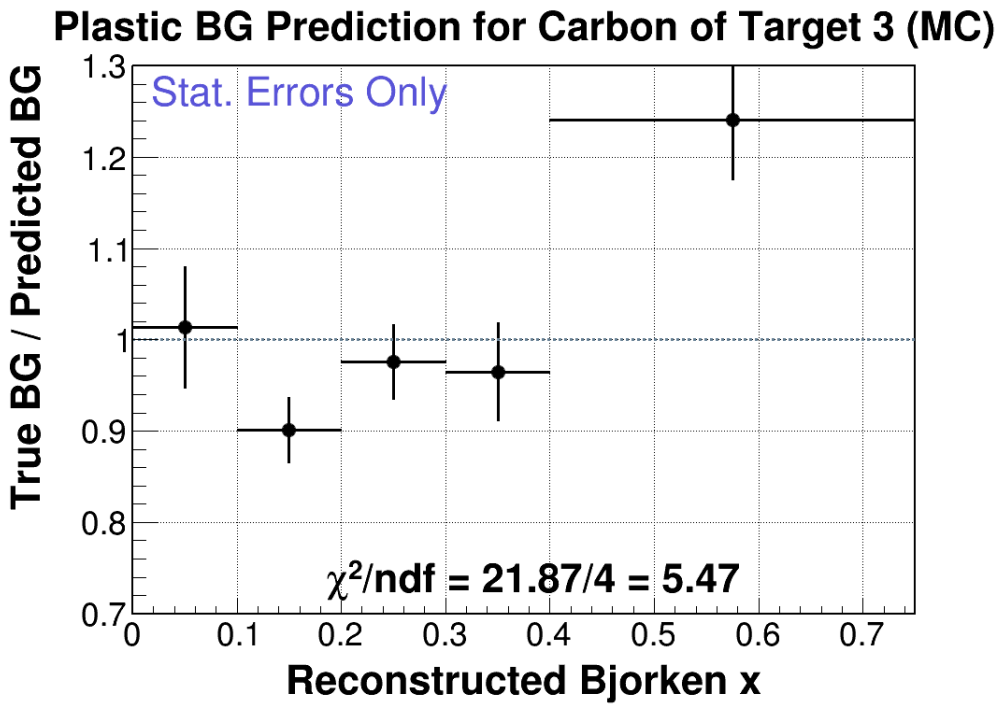

Figure C-35. Plastic BG prediction: target 03 C (x_{bj})

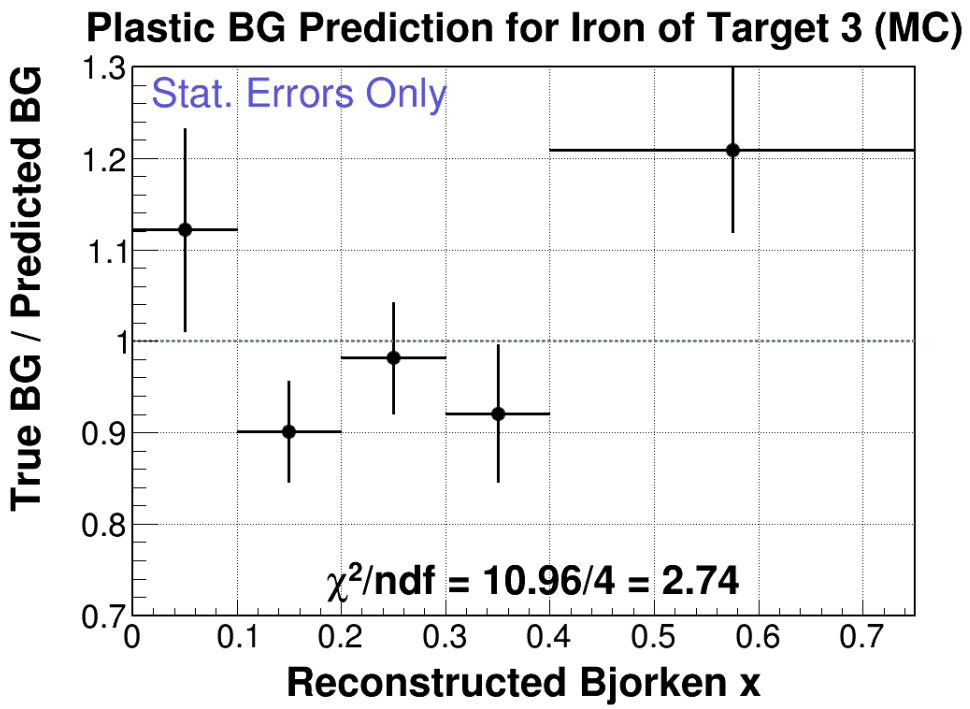

Figure C-36. Plastic BG prediction: target 03 Fe (x_{bj})

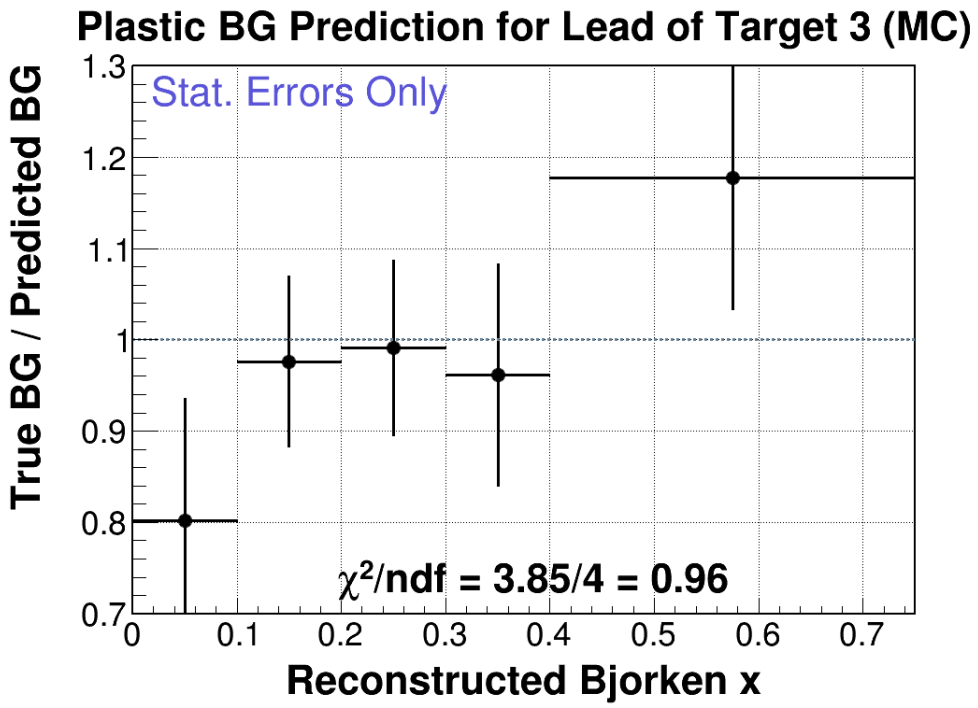

Figure C-37. Plastic BG prediction: target 03 Pb (x_{bj})

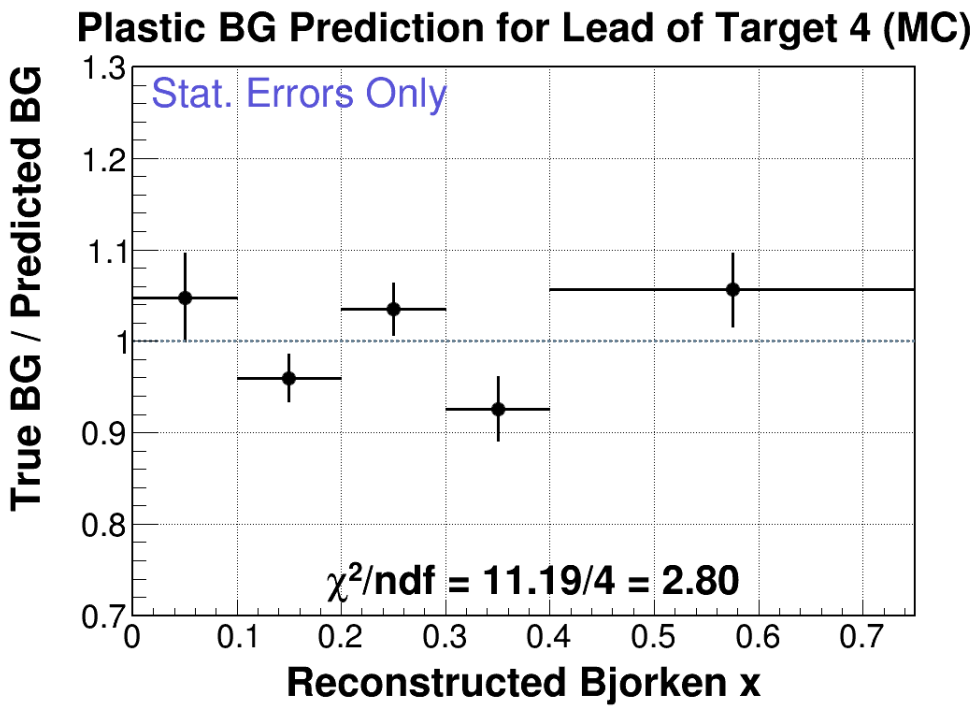

Figure C-38. Plastic BG prediction: target 04 Pb (x_{bj})

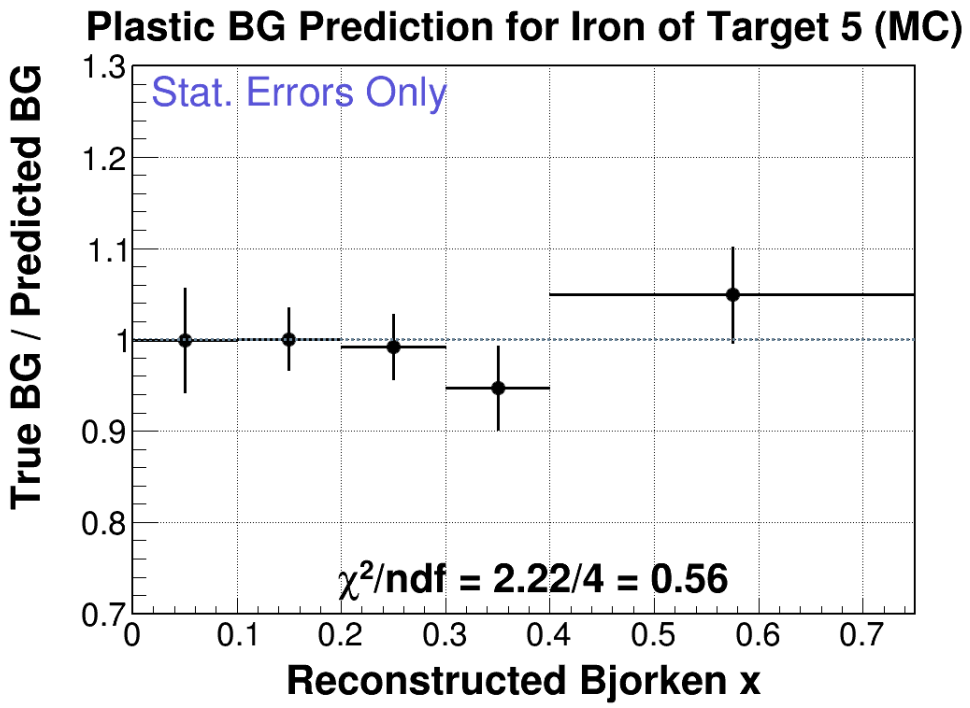

Figure C-39. Plastic BG prediction: target 05 Fe (x_{bj})

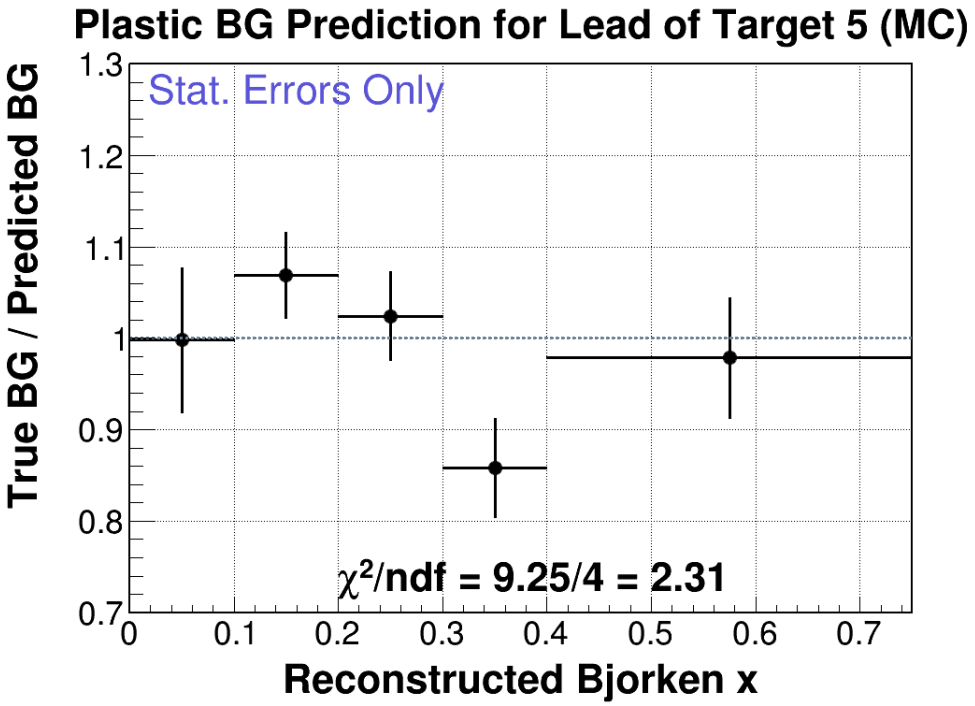

Figure C-40. Plastic BG prediction: target 05 Pb (x_{bj})

C.2 CH Background Data / MC

The following plots show the extracted CH background after, after subtracting the non-DIS events for the data (black points) and MC (red line). The band around the MC is the systematic error, plotted in Appendix C.3. They are plotted as a function of neutrino energy (E_ν):

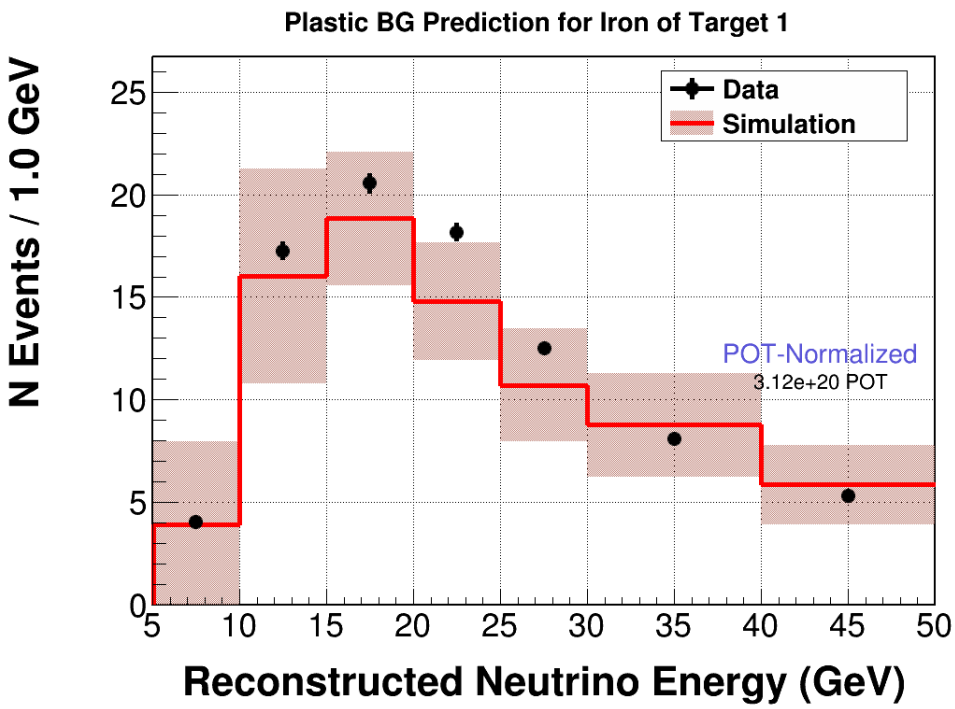

Figure C-41. Data / MC of plastic BG prediction: target 01 Fe (E_ν)

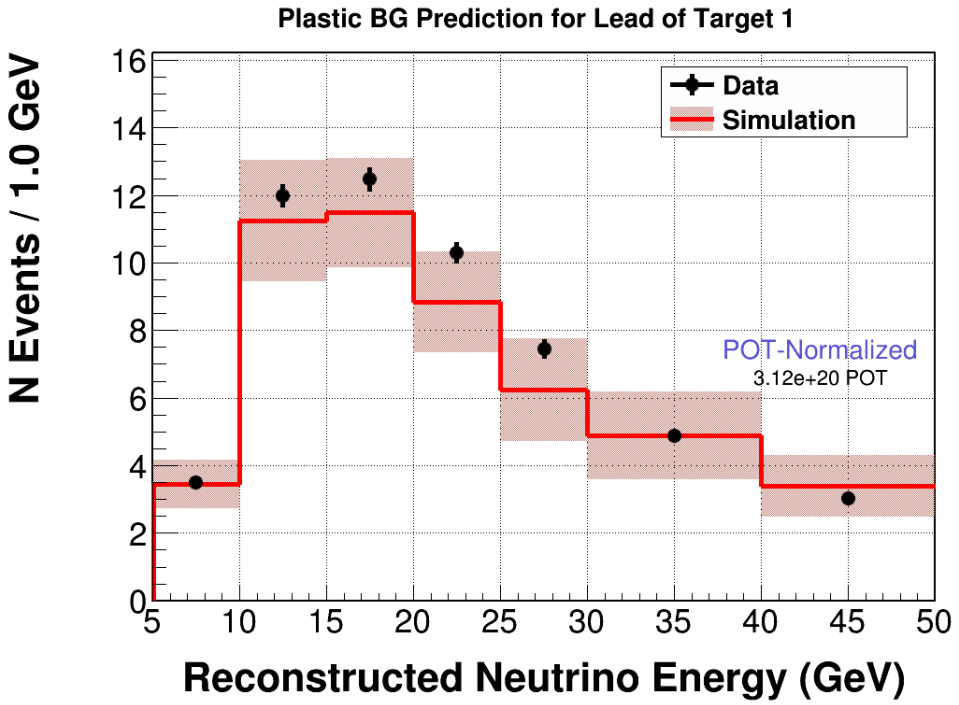

Figure C-42. Data / MC of plastic BG prediction: target 01 Pb (E_ν)

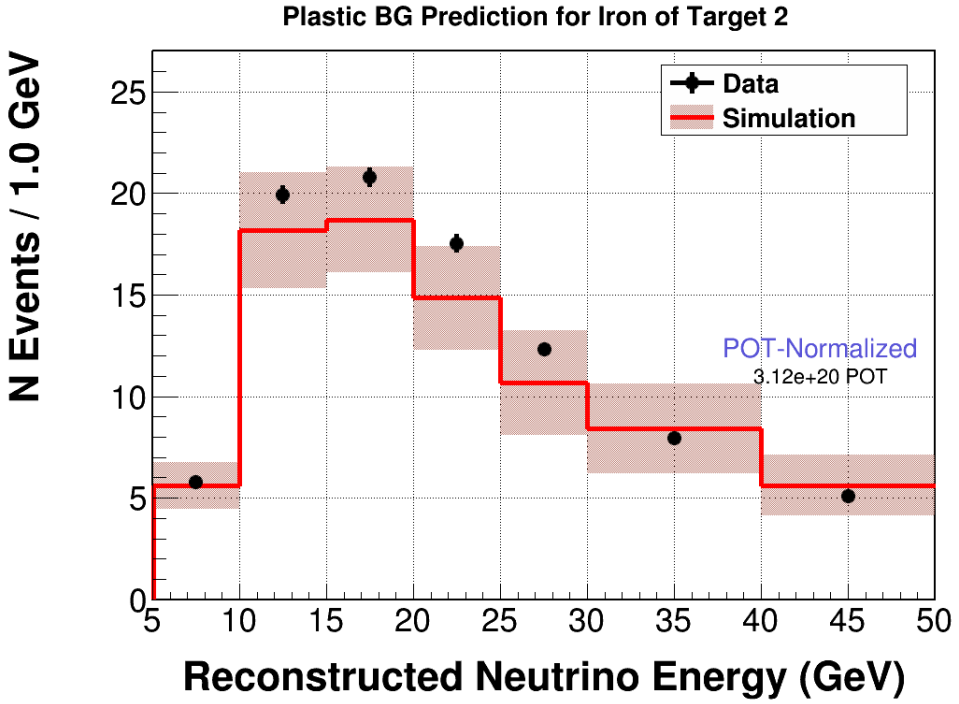

Figure C-43. Data / MC of plastic BG prediction: target 02 Fe (E_ν)

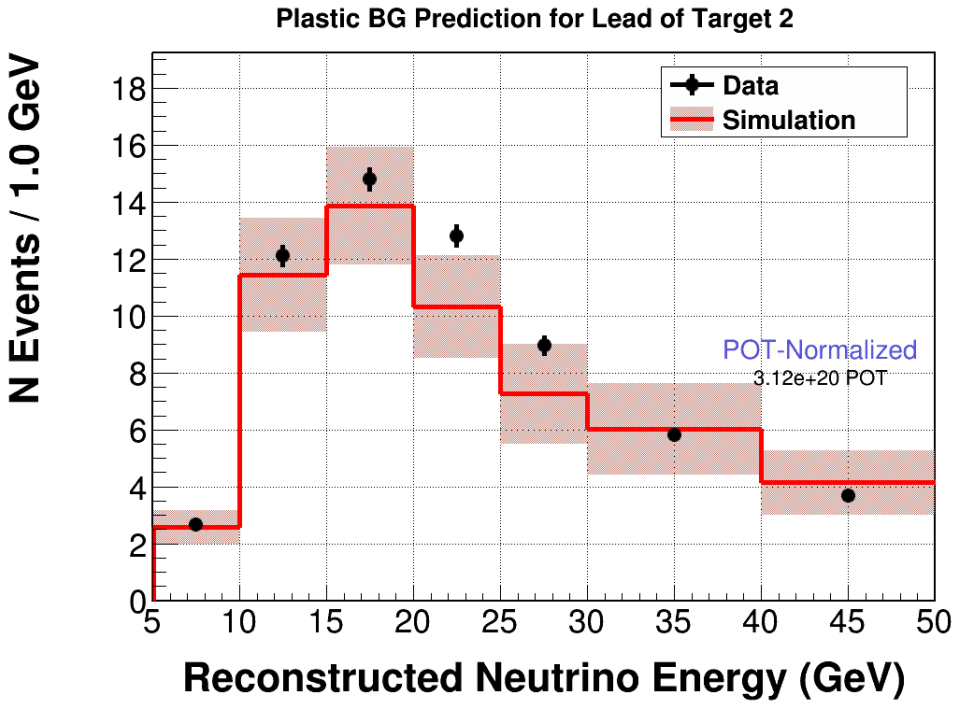

Figure C-44. Data / MC of plastic BG prediction: target 02 Pb (E_ν)

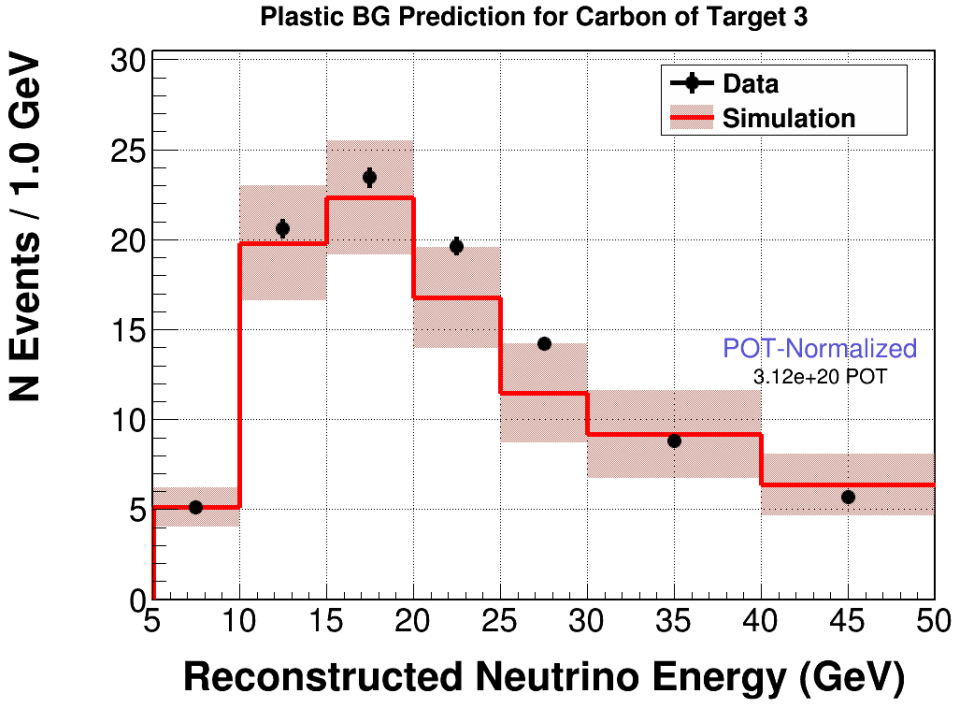

Figure C-45. Data / MC of plastic BG prediction: target 03 C (E_ν)

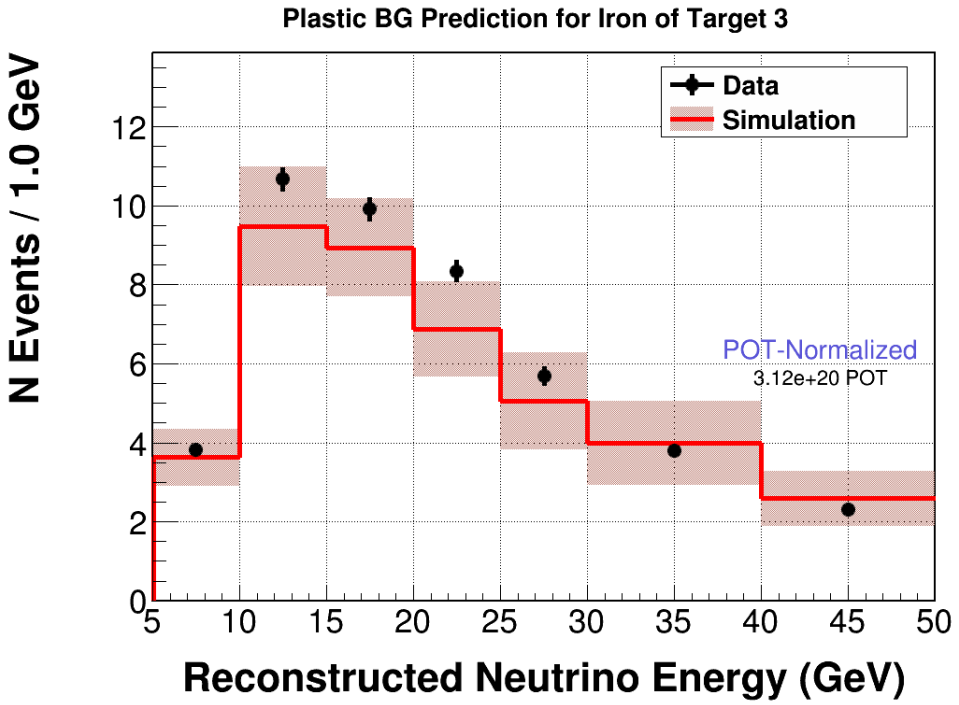

Figure C-46. Data / MC of plastic BG prediction: target 03 Fe (E_ν)

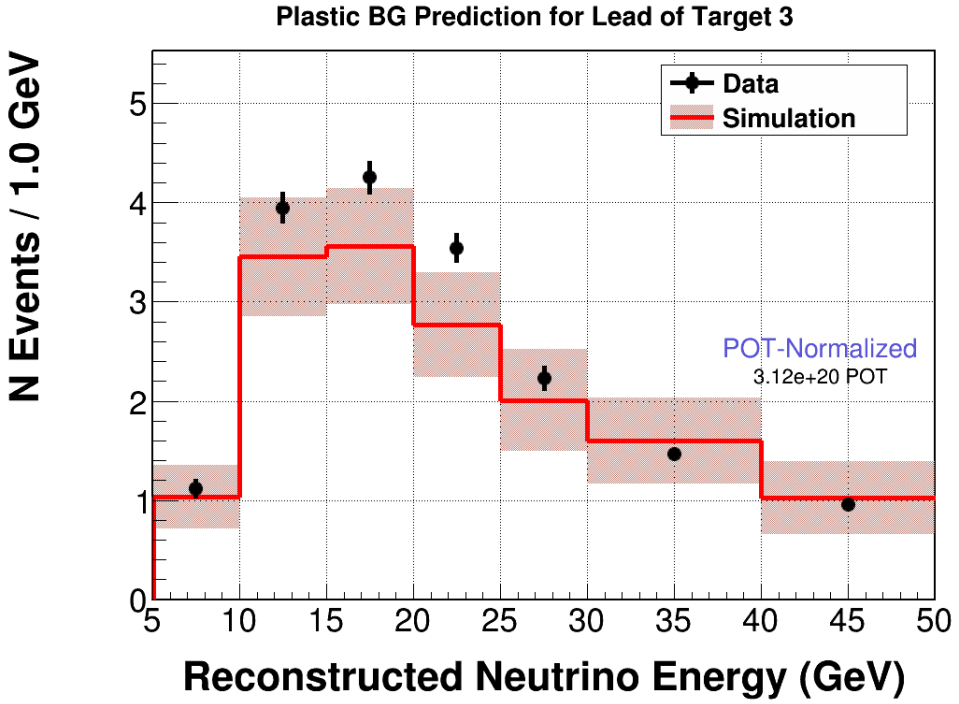

Figure C-47. Data / MC of plastic BG prediction: target 03 Pb (E_ν)

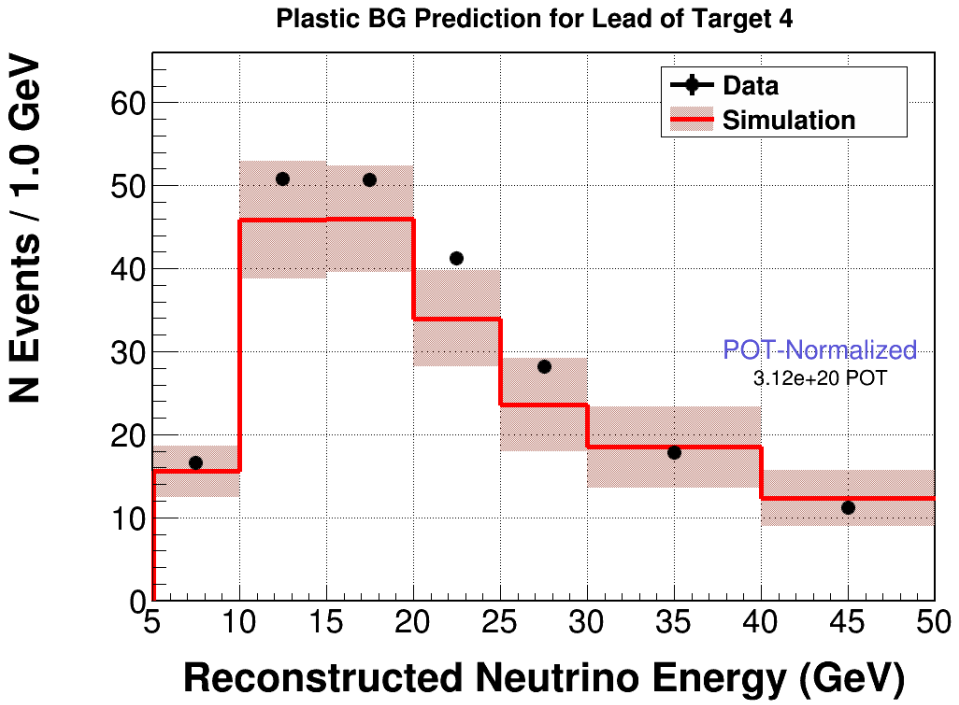

Figure C-48. Data / MC of plastic BG prediction: target 04 Pb (E_ν)

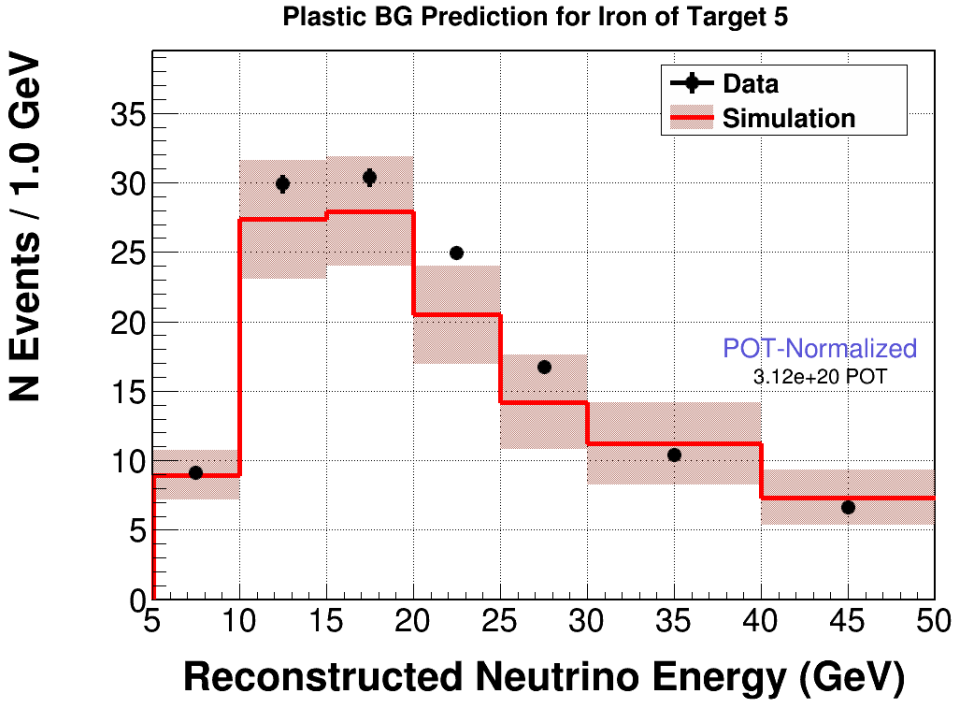

Figure C-49. Data / MC of plastic BG prediction: target 05 Fe (E_ν)

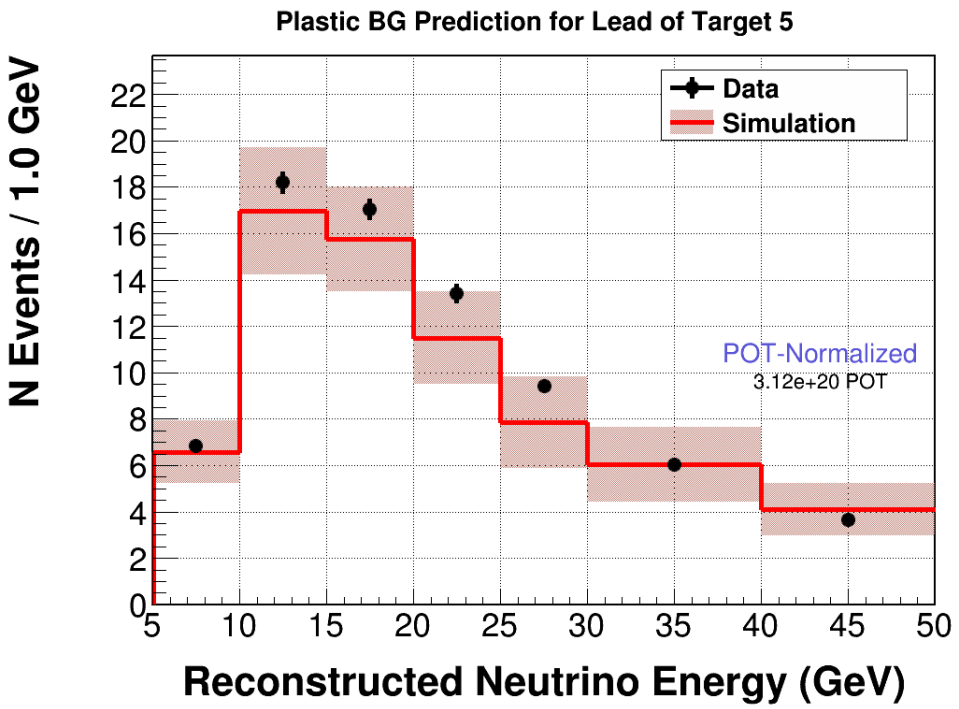

Figure C-50. Data / MC of plastic BG prediction: target 05 Pb (E_ν)

The following plots show the extracted CH background after, after subtracting the non-DIS events for the data (black points) and MC (red line). The band around the MC is the systematic error, plotted in Appendix C.3. They are plotted as a function of Bjorken-x (x_{bj}):

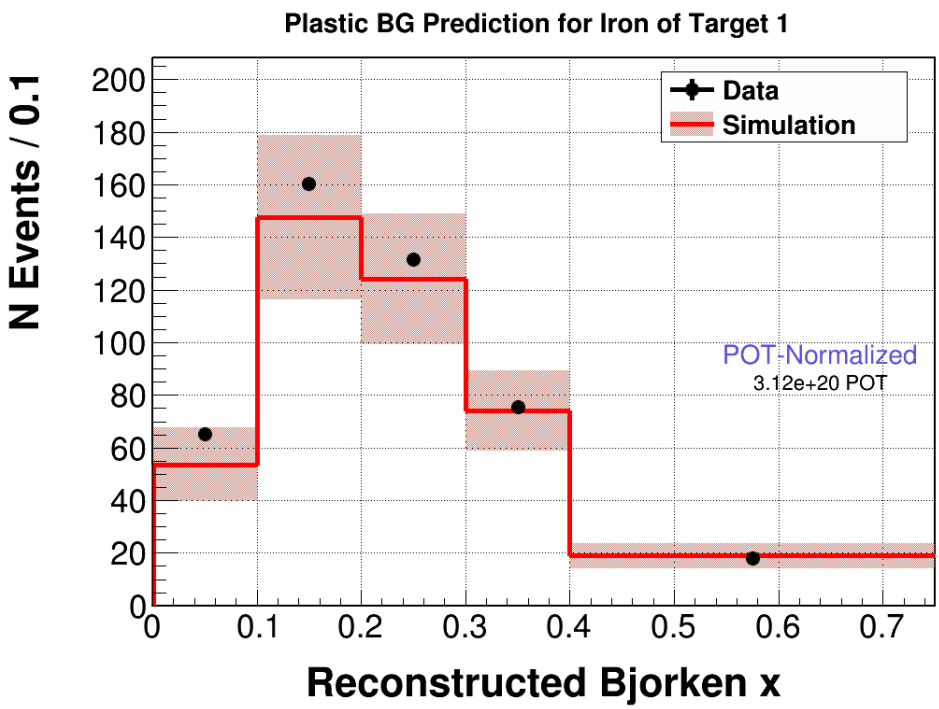

Figure C-51. Data / MC of plastic BG prediction: target 01 Fe (x_{bj})

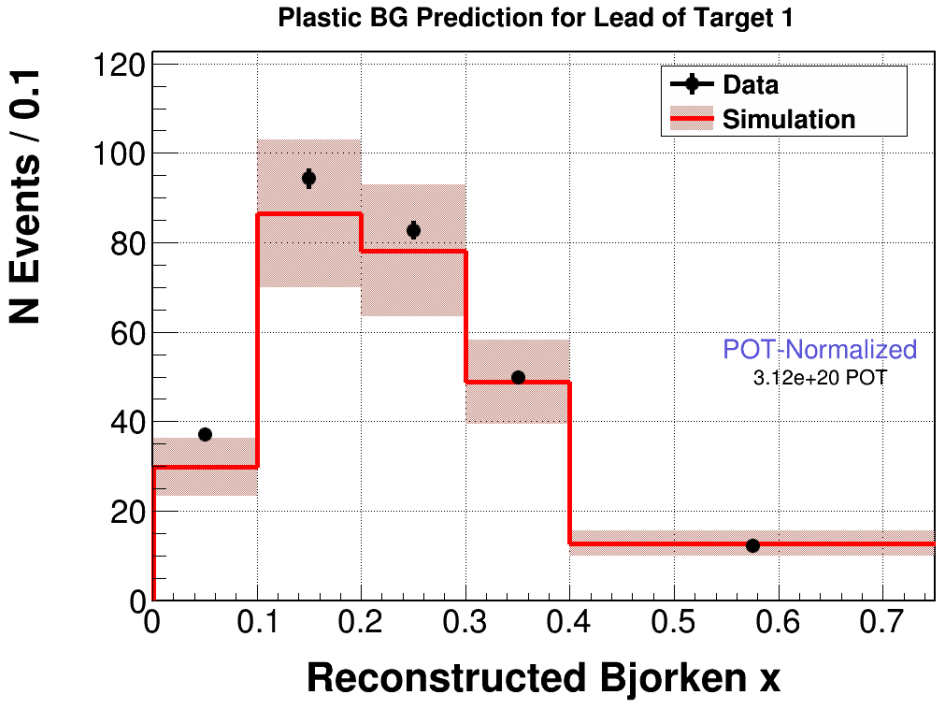

Figure C-52. Data / MC of plastic BG prediction: target 01 Pb (x_{bj})

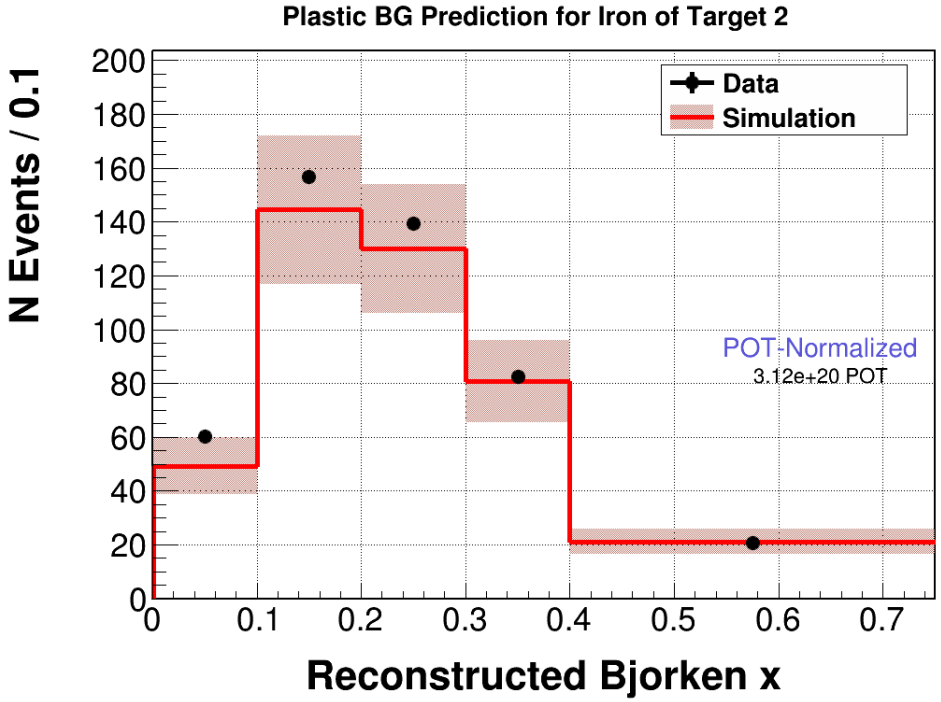

Figure C-53. Data / MC of plastic BG prediction: target 02 Fe (x_{bj})

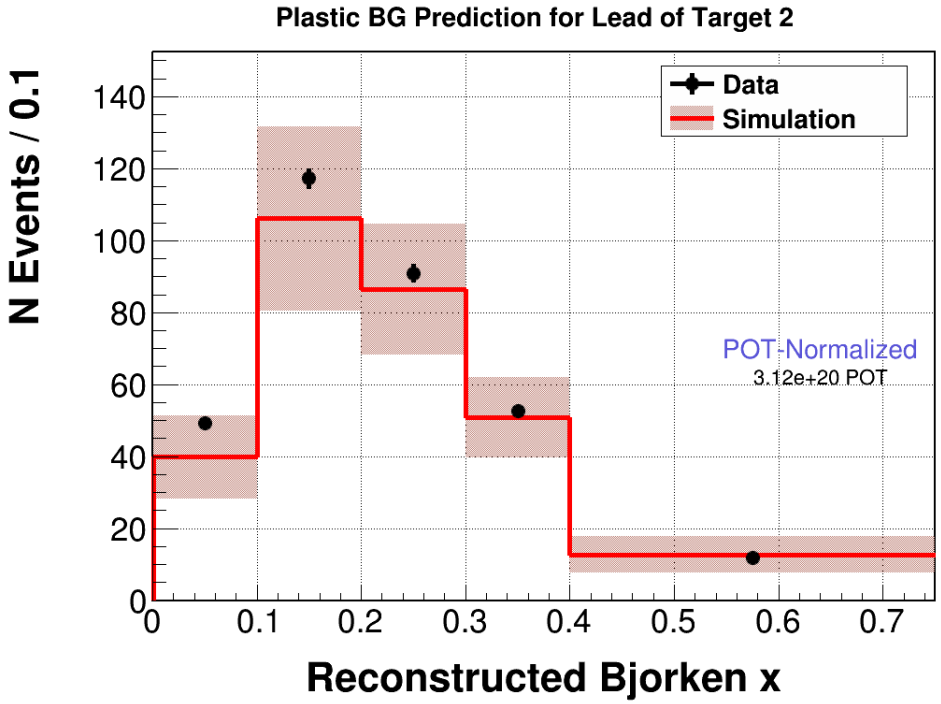

Figure C-54. Data / MC of plastic BG prediction: target 02 Pb (x_{bj})

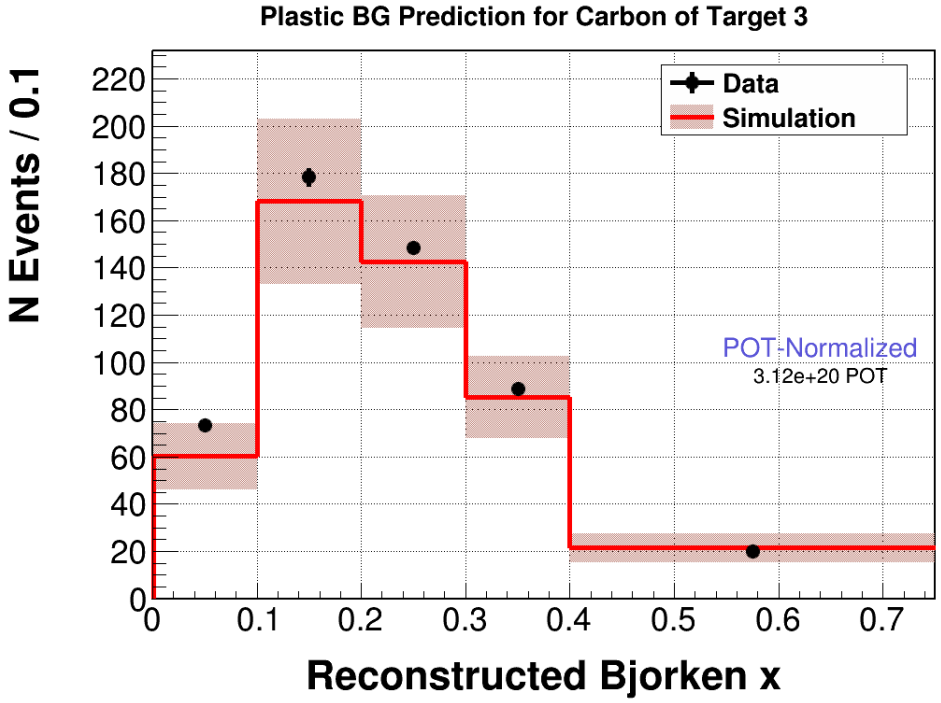

Figure C-55. Data / MC of plastic BG prediction: target 03 C (x_{bj})

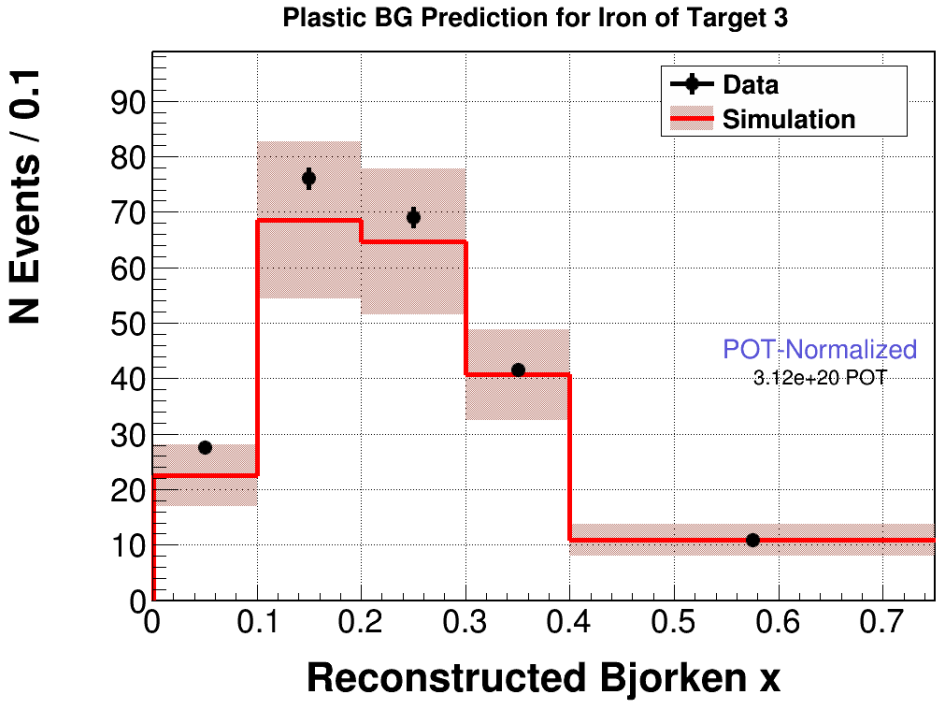

Figure C-56. Data / MC of plastic BG prediction: target 03 Fe (x_{bj})

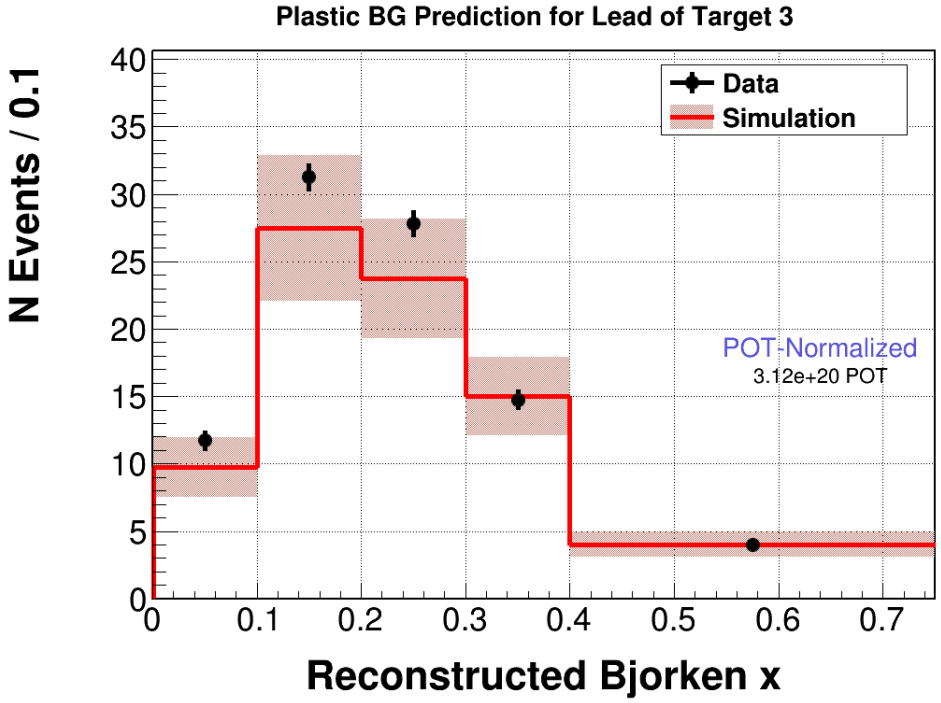

Figure C-57. Data / MC of plastic BG prediction: target 03 Pb (x_{bj})

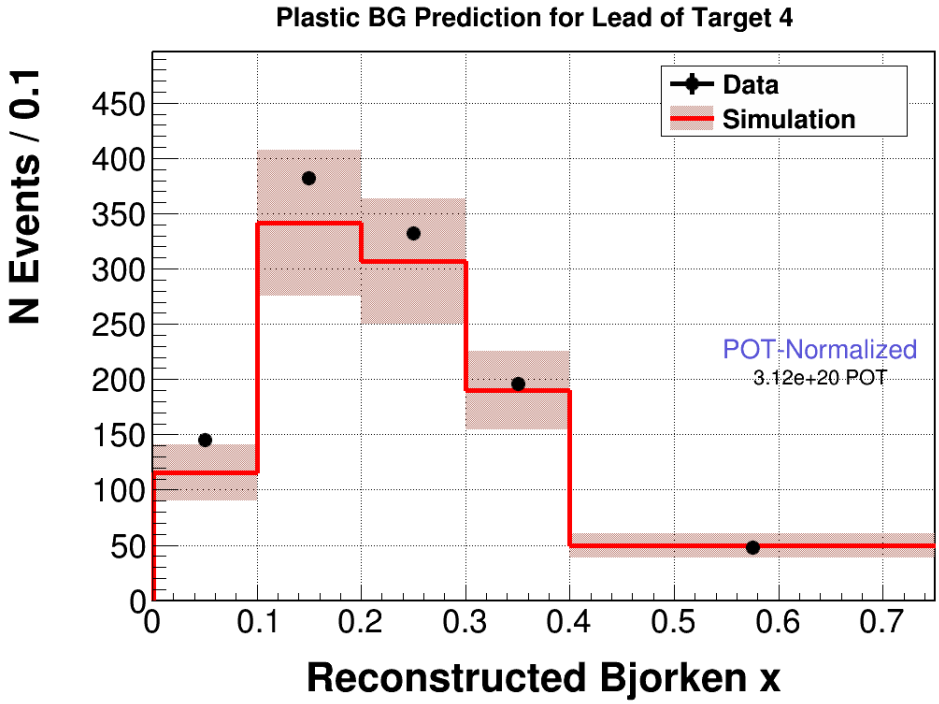

Figure C-58. Data / MC of plastic BG prediction: target 04 Pb (x_{bj})

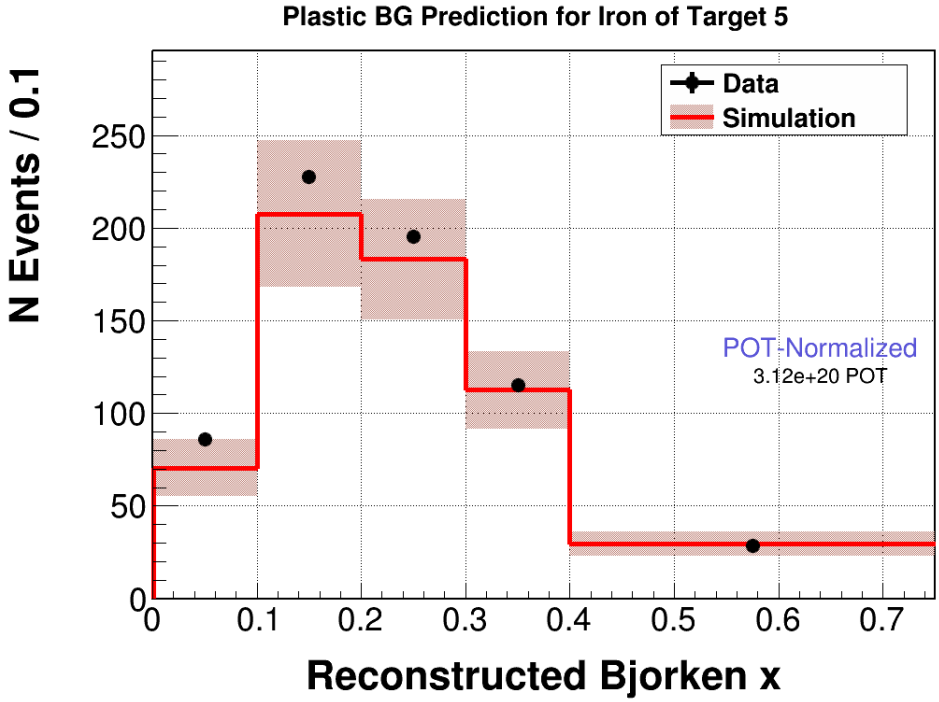

Figure C-59. Data / MC of plastic BG prediction: target 05 Fe (x_{bj})

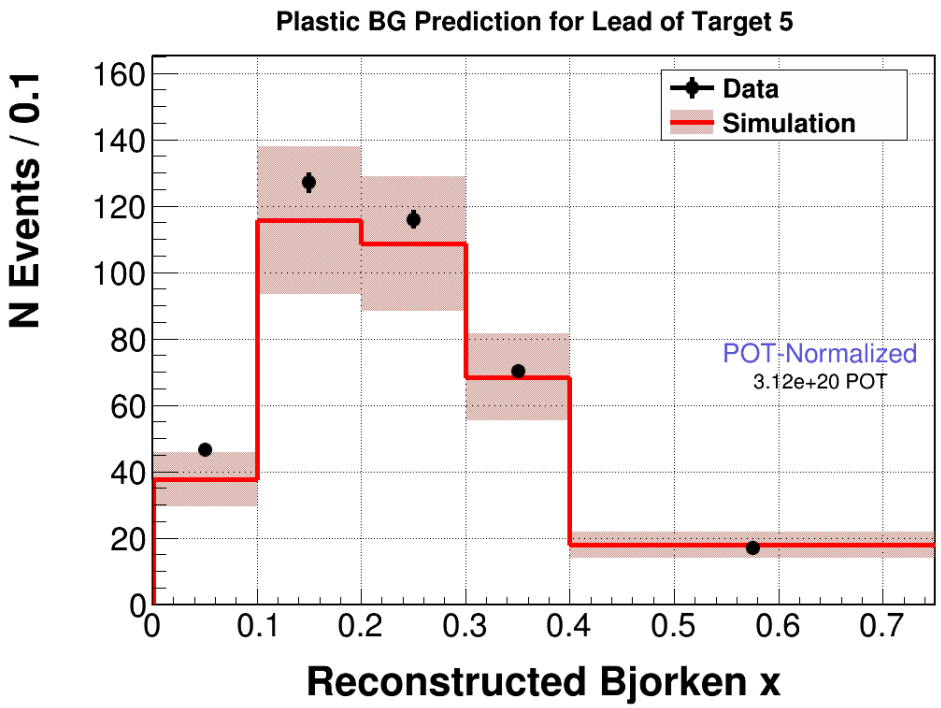

Figure C-60. Data / MC of plastic BG prediction: target 05 Pb (x_{bj})

C.3 CH Background Uncertainty Breakdown

The following plots show the uncertainty on the extracted CH background after, after subtracting the non-DIS events. They are plotted as a function of neutrino energy (E_ν):

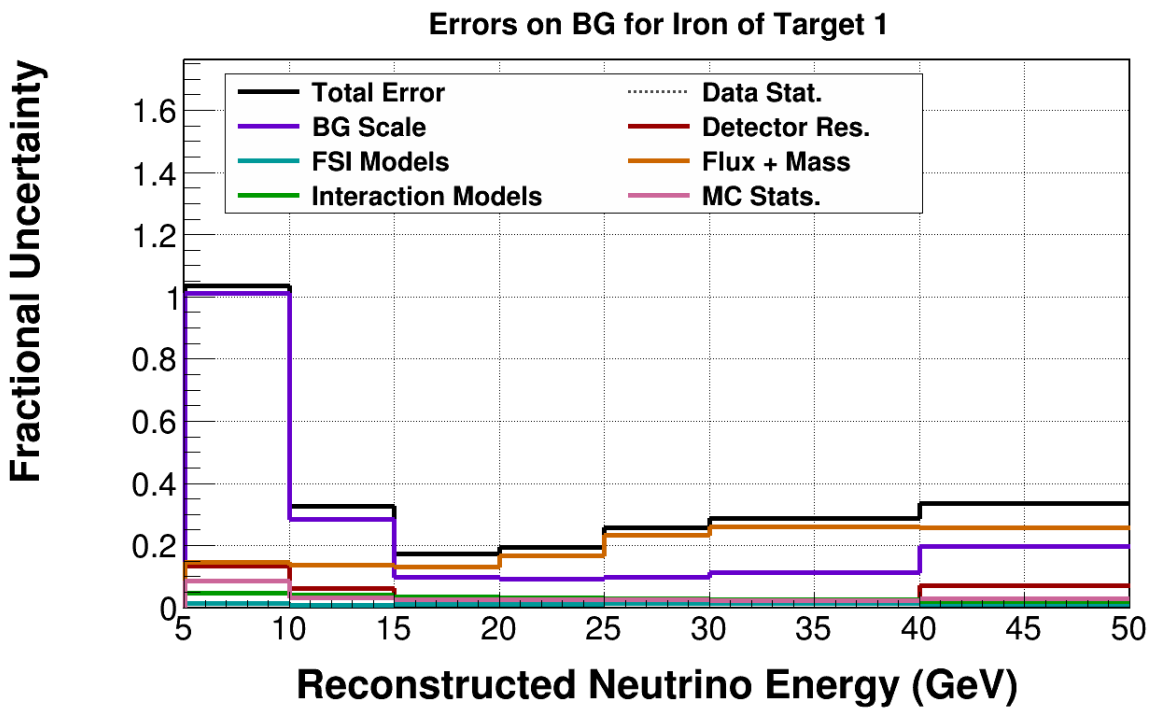

Figure C-61. Uncertainty on plastic BG prediction: target 01 Fe (E_ν)

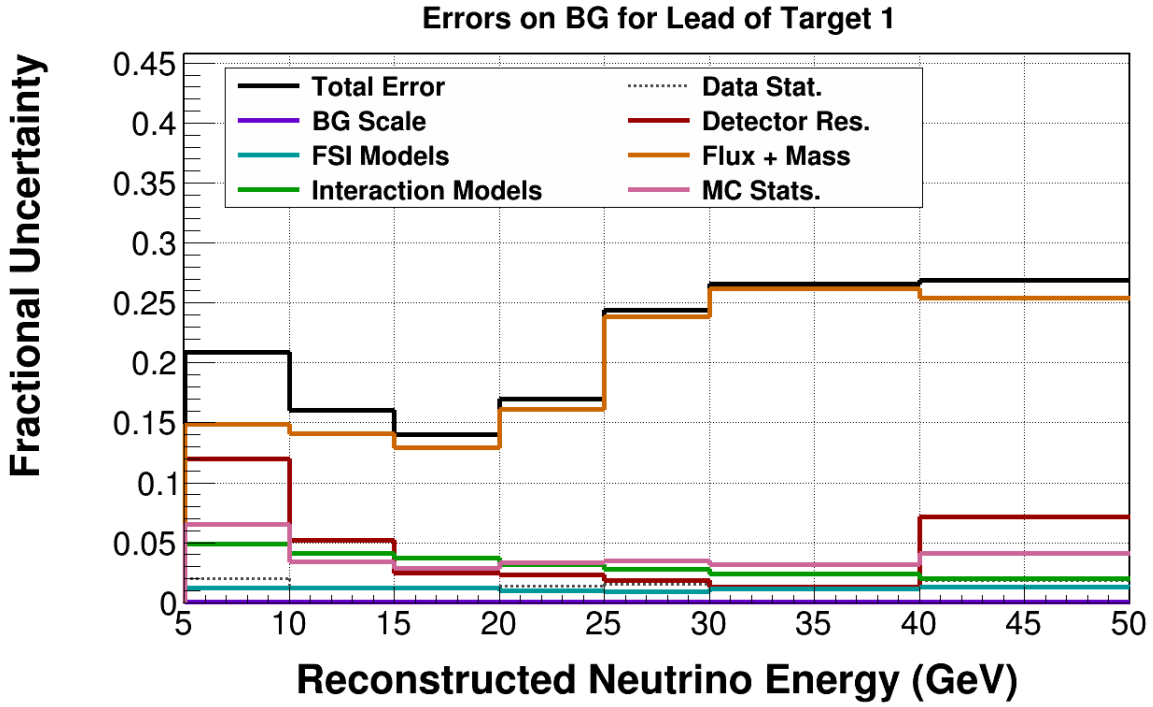

Figure C-62. Uncertainty on plastic BG prediction: target 01 Pb (E_ν)

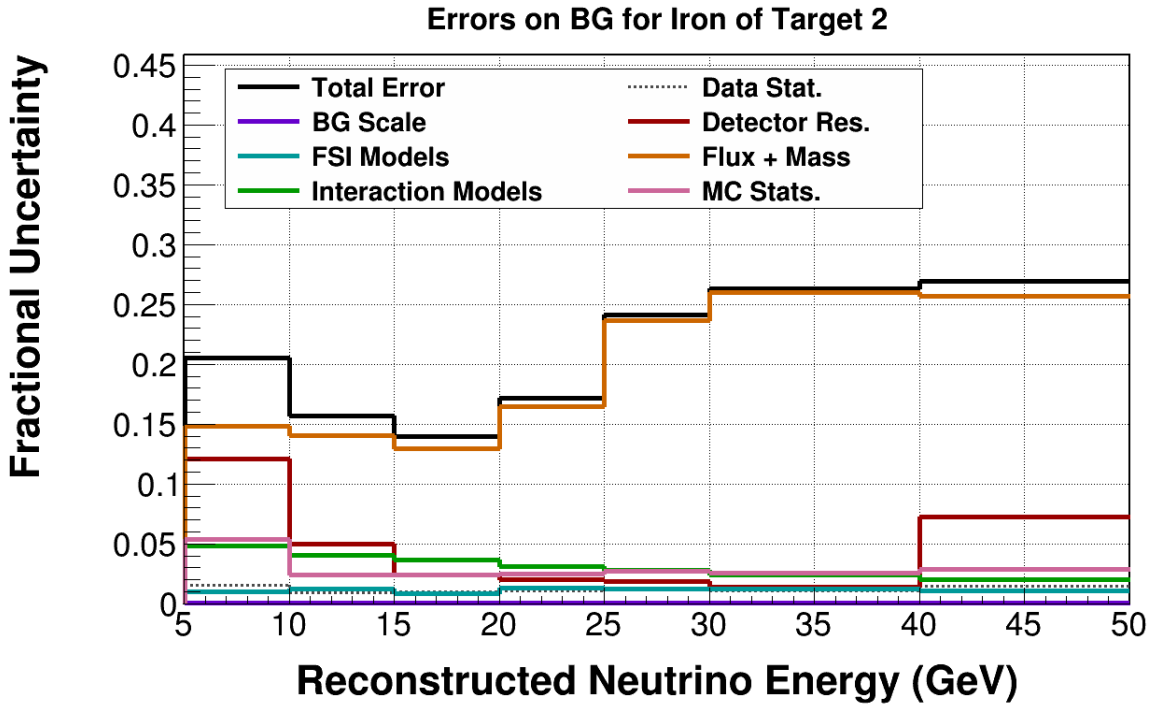

Figure C-63. Uncertainty on plastic BG prediction: target 02 Fe (E_ν)

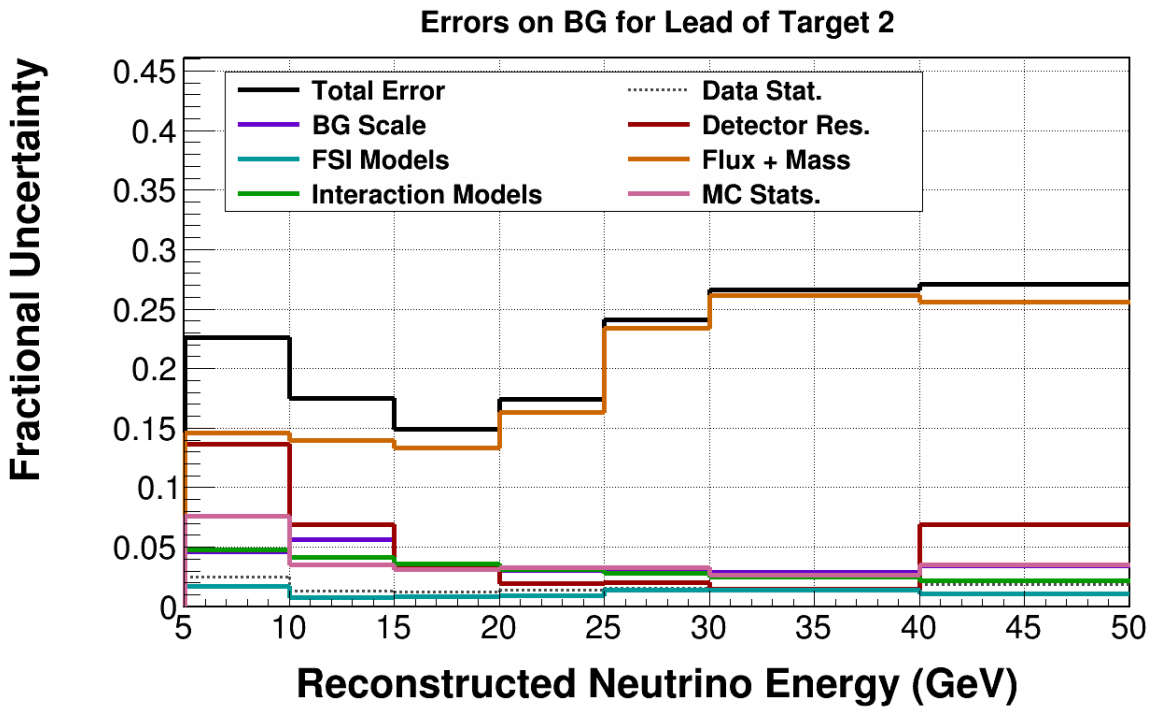

Figure C-64. Uncertainty on plastic BG prediction: target 02 Pb (E_ν)

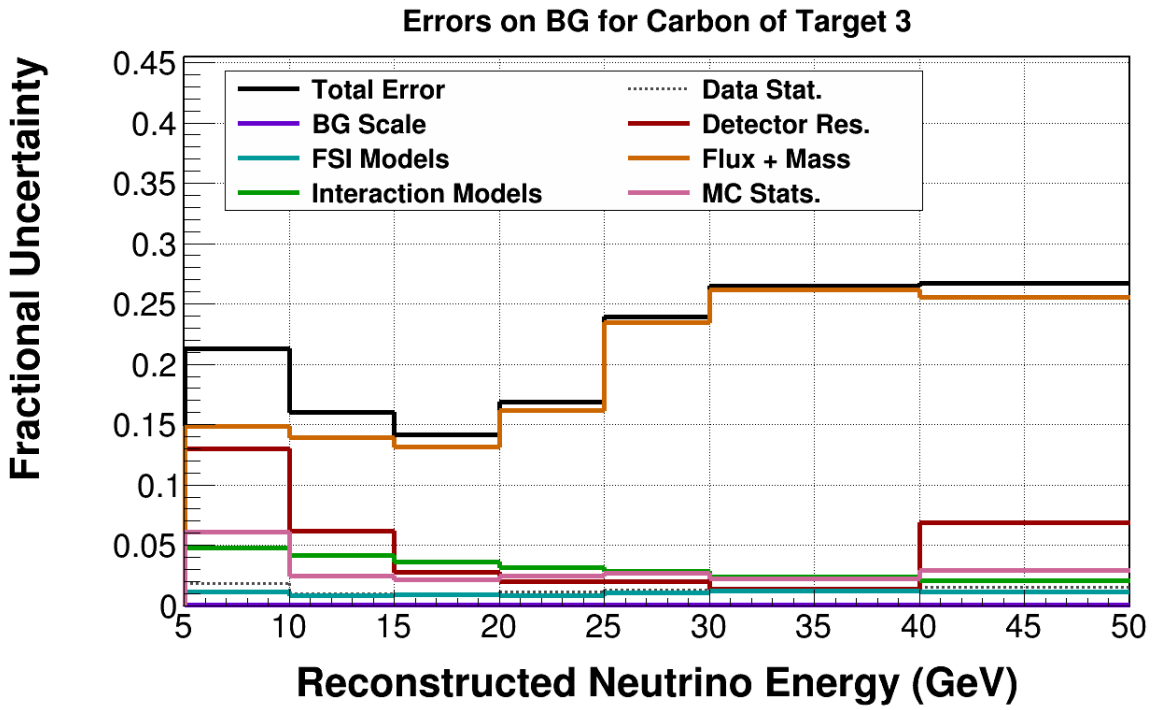

Figure C-65. Uncertainty on plastic BG prediction: target 03 C (E_ν)

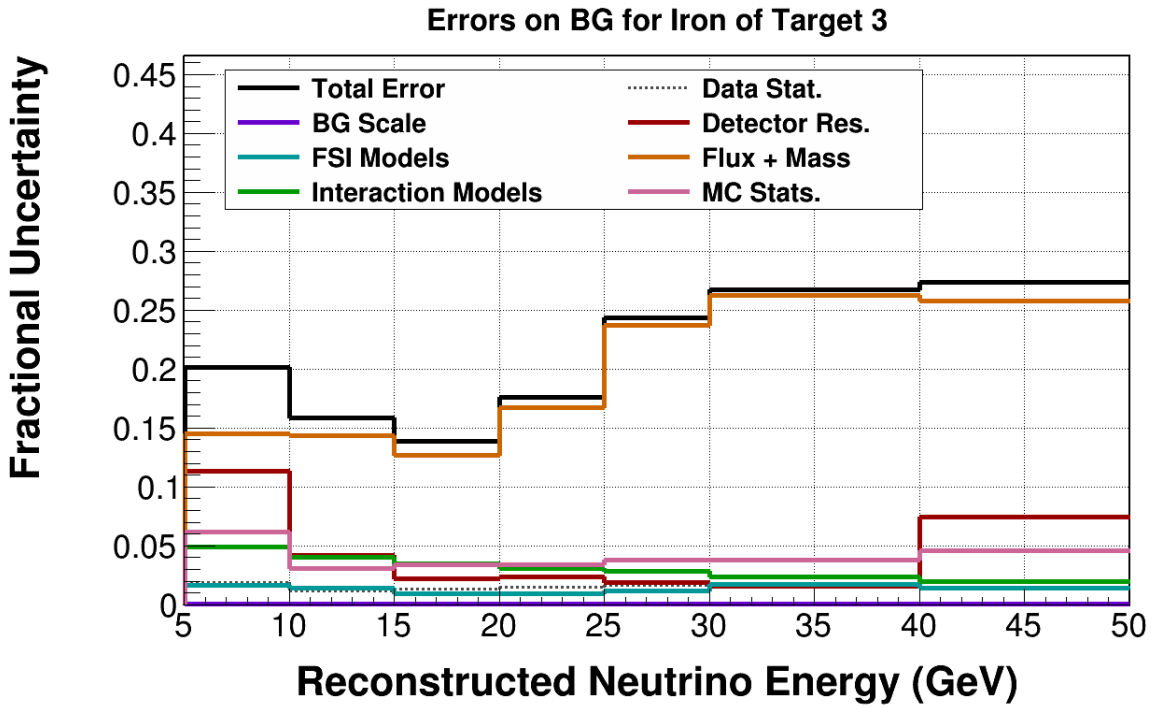

Figure C-66. Uncertainty on plastic BG prediction: target 03 Fe (E_ν)

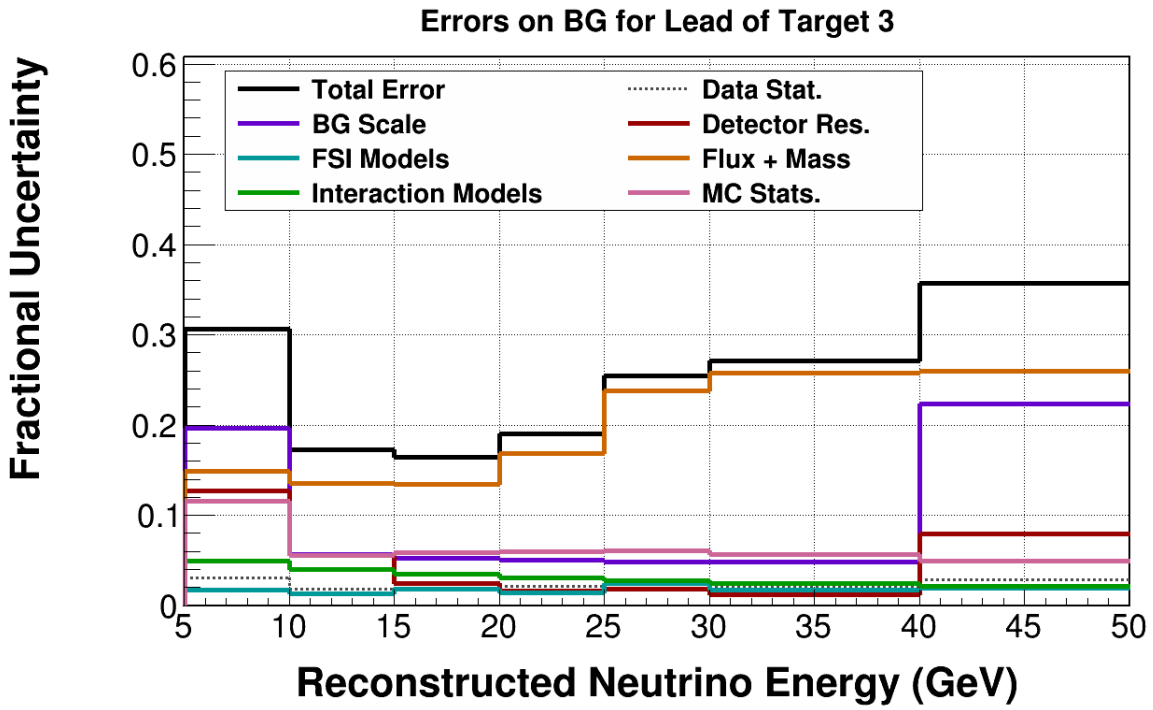

Figure C-67. Uncertainty on plastic BG prediction: target 03 Pb (E_ν)

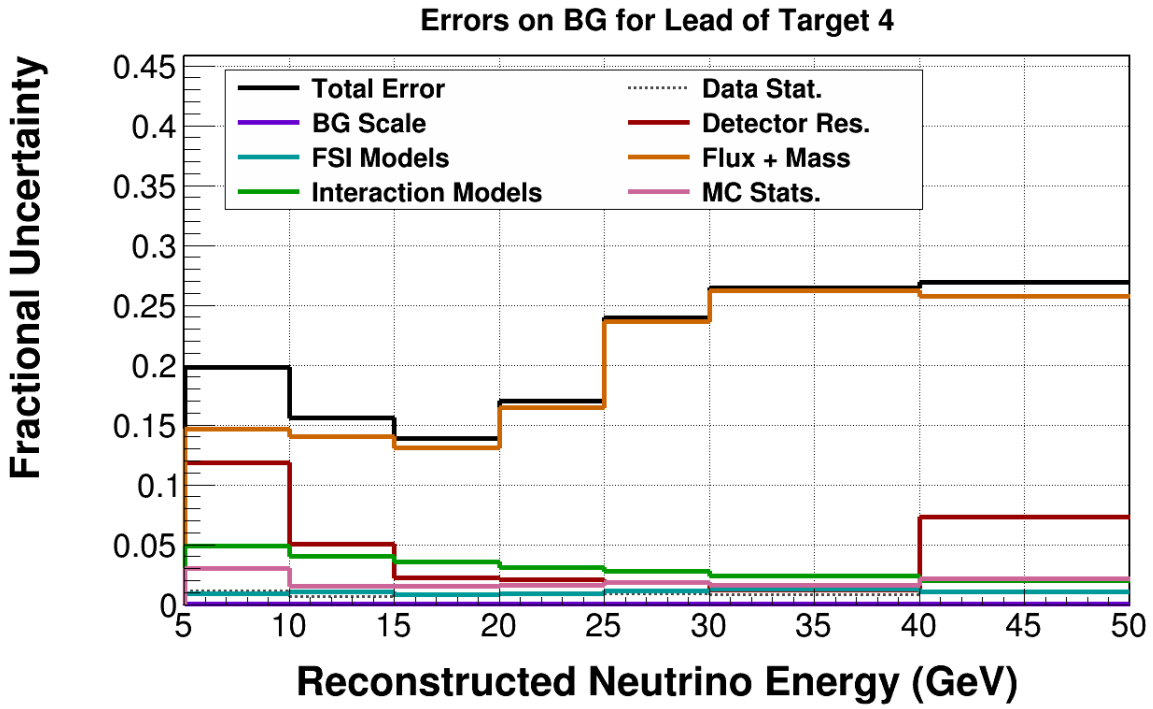

Figure C-68. Uncertainty on plastic BG prediction: target 04 Pb (E_ν)

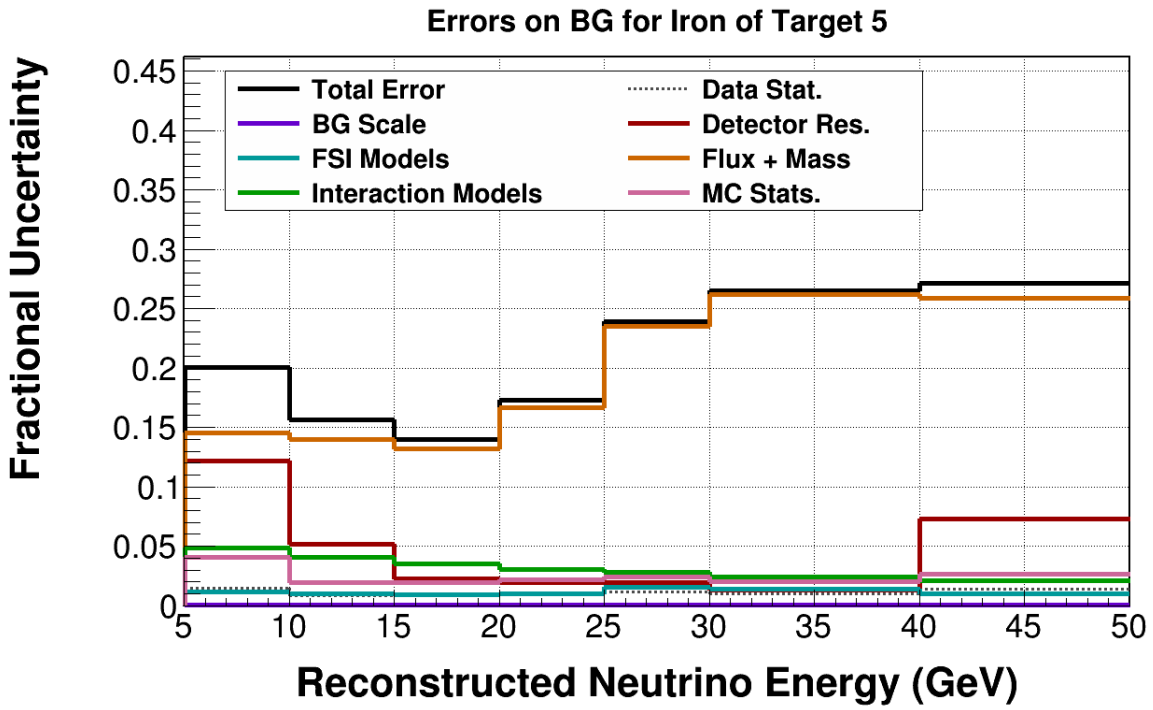

Figure C-69. Uncertainty on plastic BG prediction: target 05 Fe (E_ν)

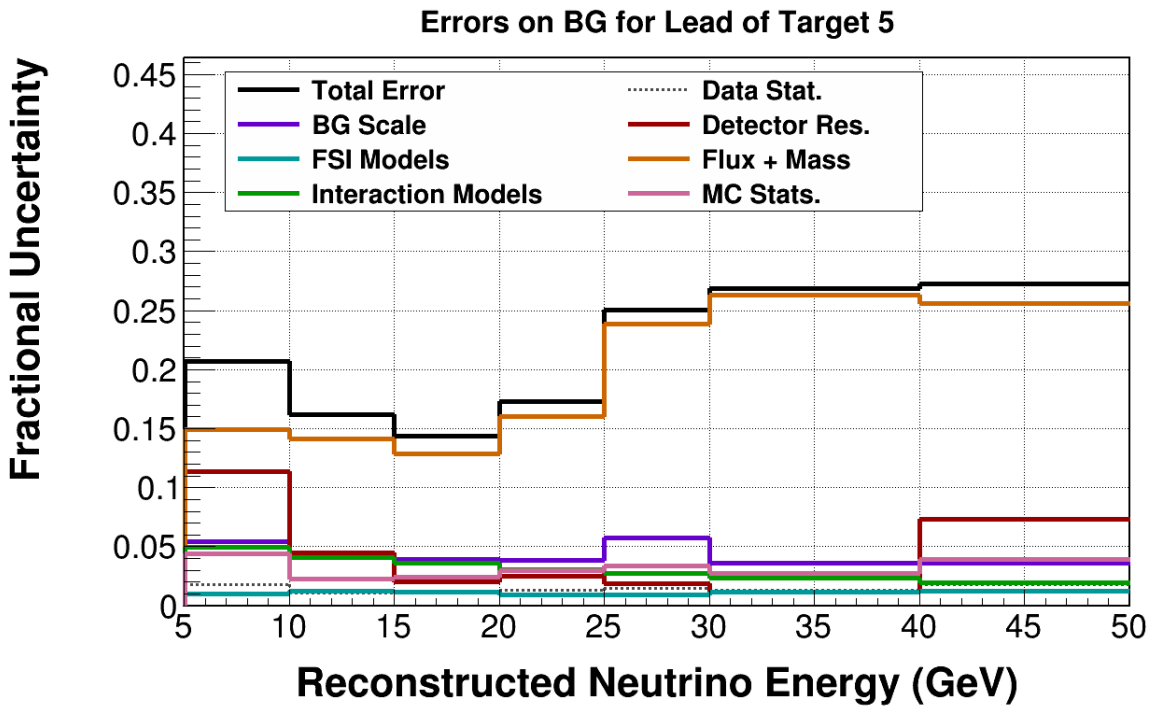

Figure C-70. Uncertainty on plastic BG prediction: target 05 Pb (E_ν)

The following plots show the uncertainty on the extracted CH background after, after subtracting the non-DIS events. They are plotted as a function of Bjorken-x (x_{bj}):

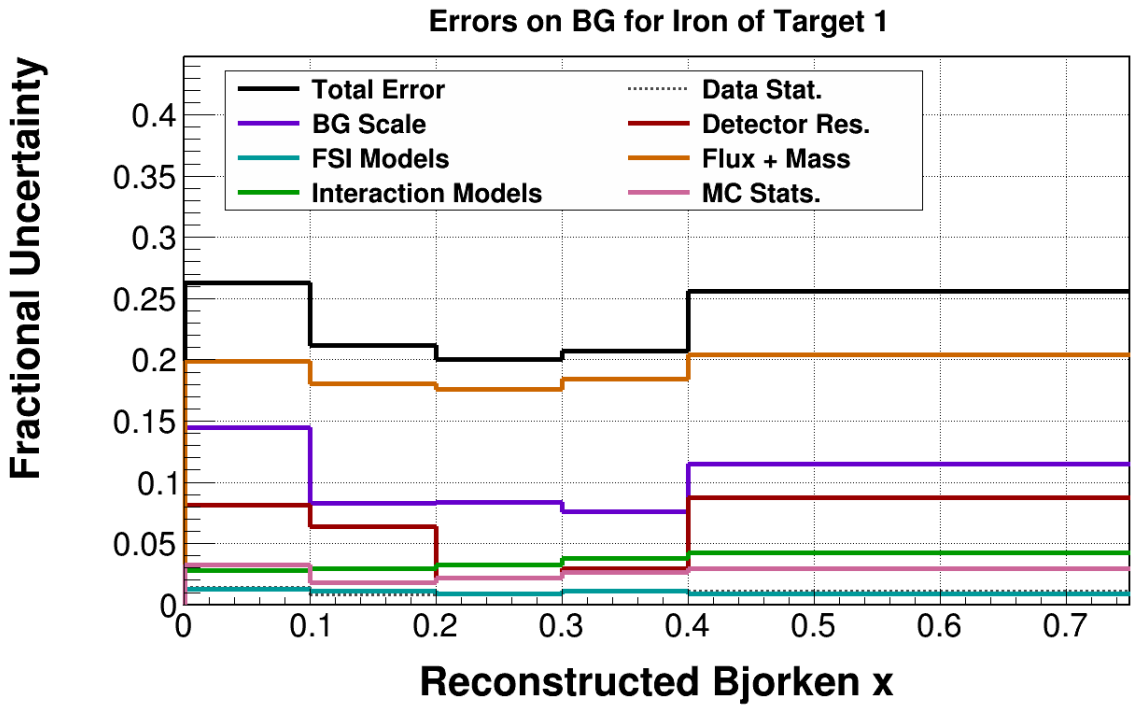

Figure C-71. Uncertainty on plastic BG prediction: target 01 Fe (x_{bj})

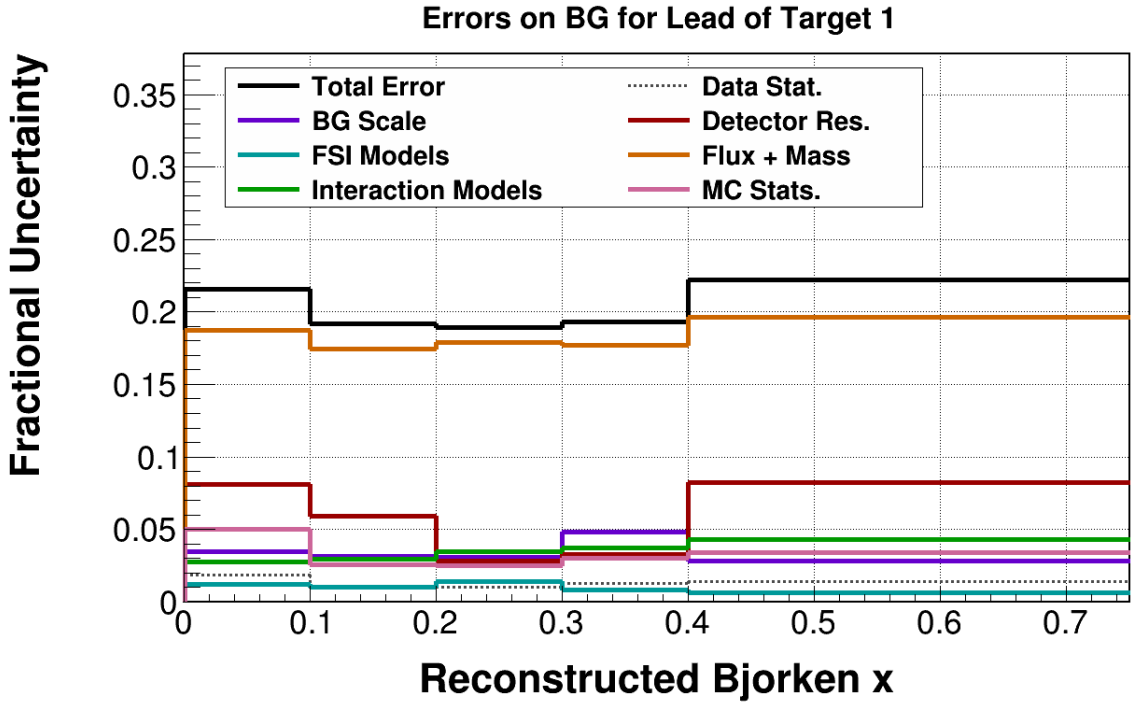

Figure C-72. Uncertainty on plastic BG prediction: target 01 Pb (x_{bj})

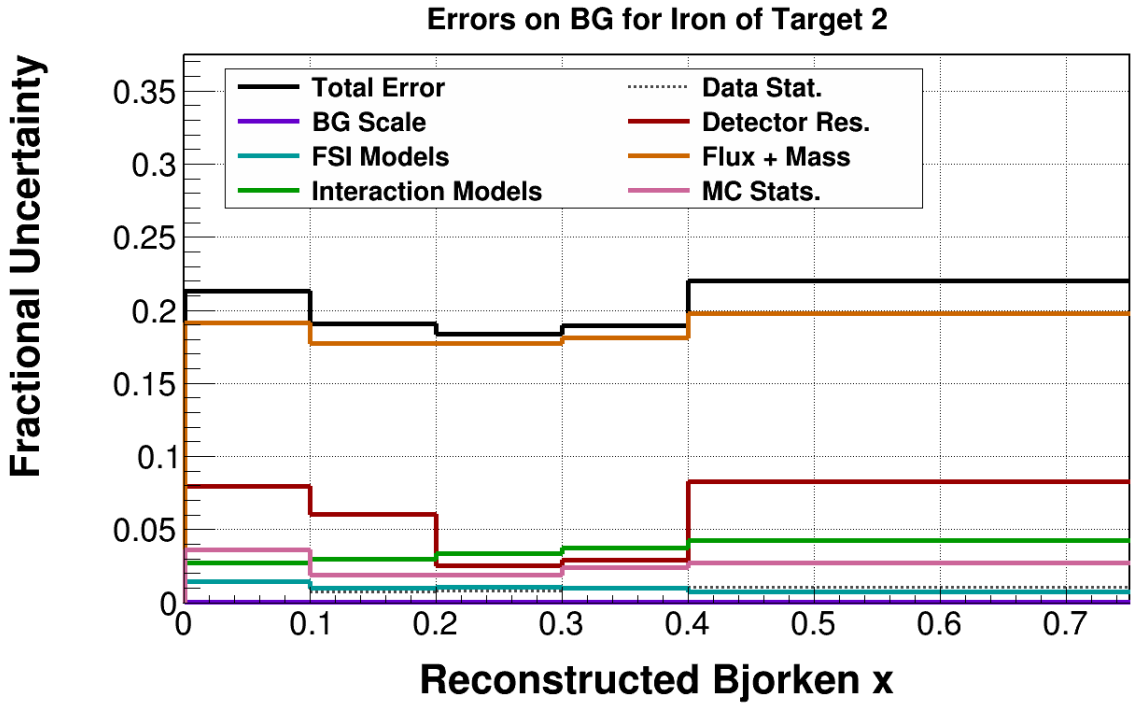

Figure C-73. Uncertainty on plastic BG prediction: target 02 Fe (x_{bj})

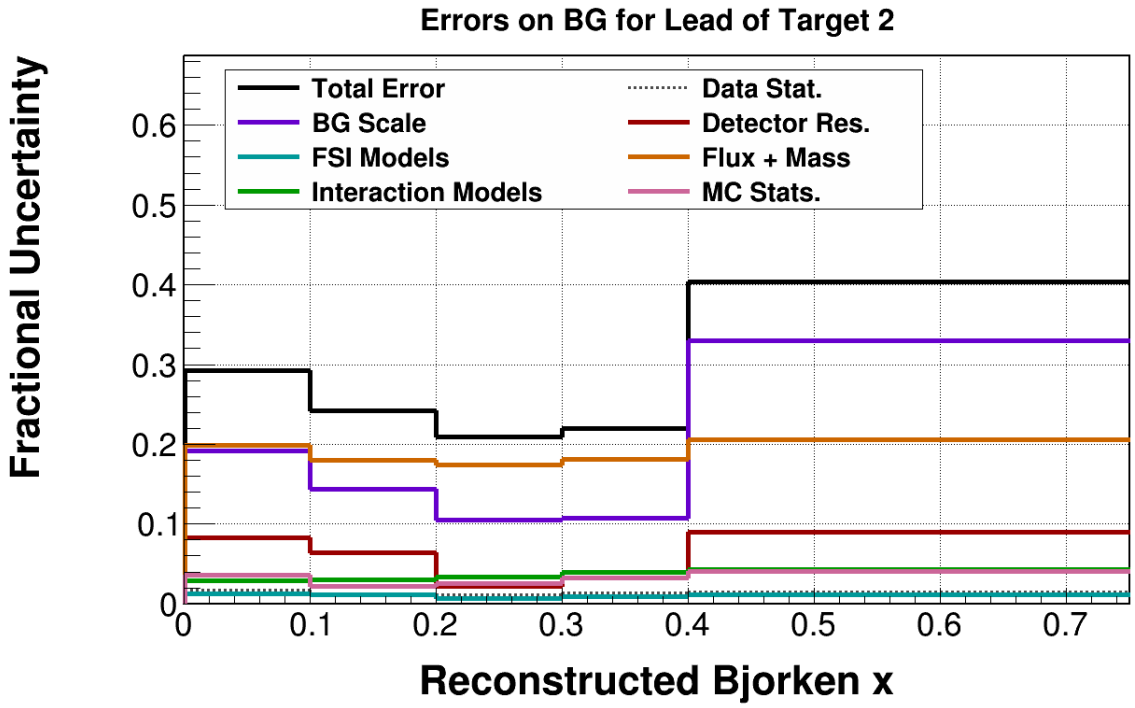

Figure C-74. Uncertainty on plastic BG prediction: target 02 Pb (x_{bj})

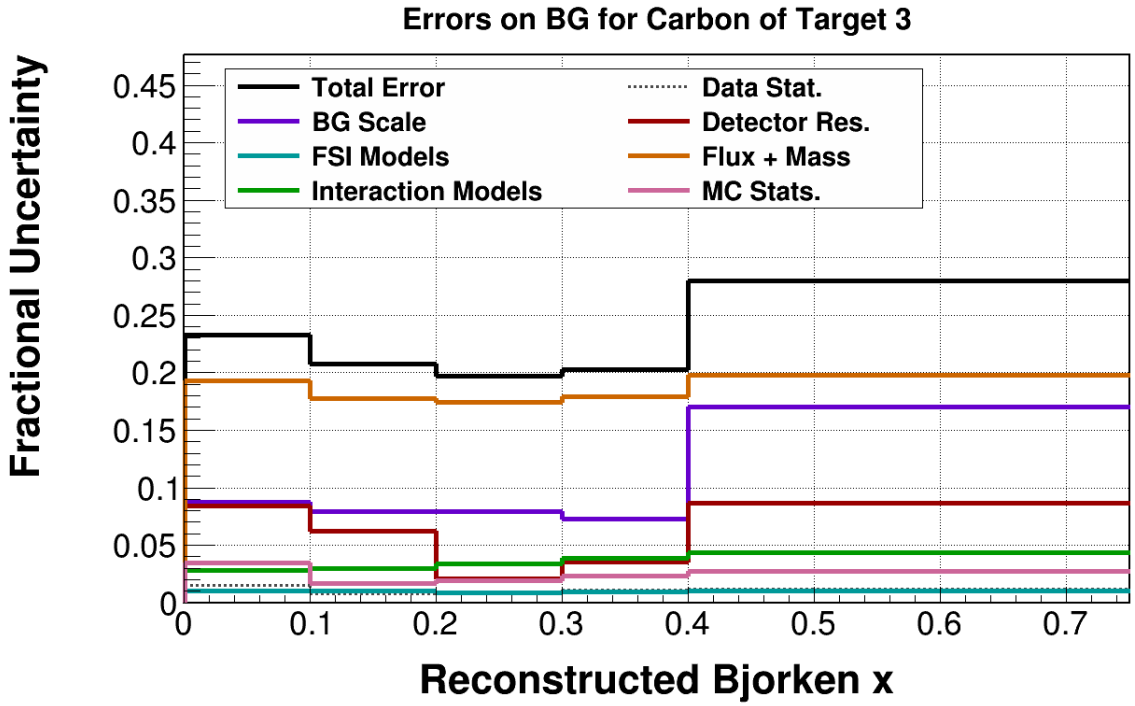

Figure C-75. Uncertainty on plastic BG prediction: target 03 C (x_{bj})

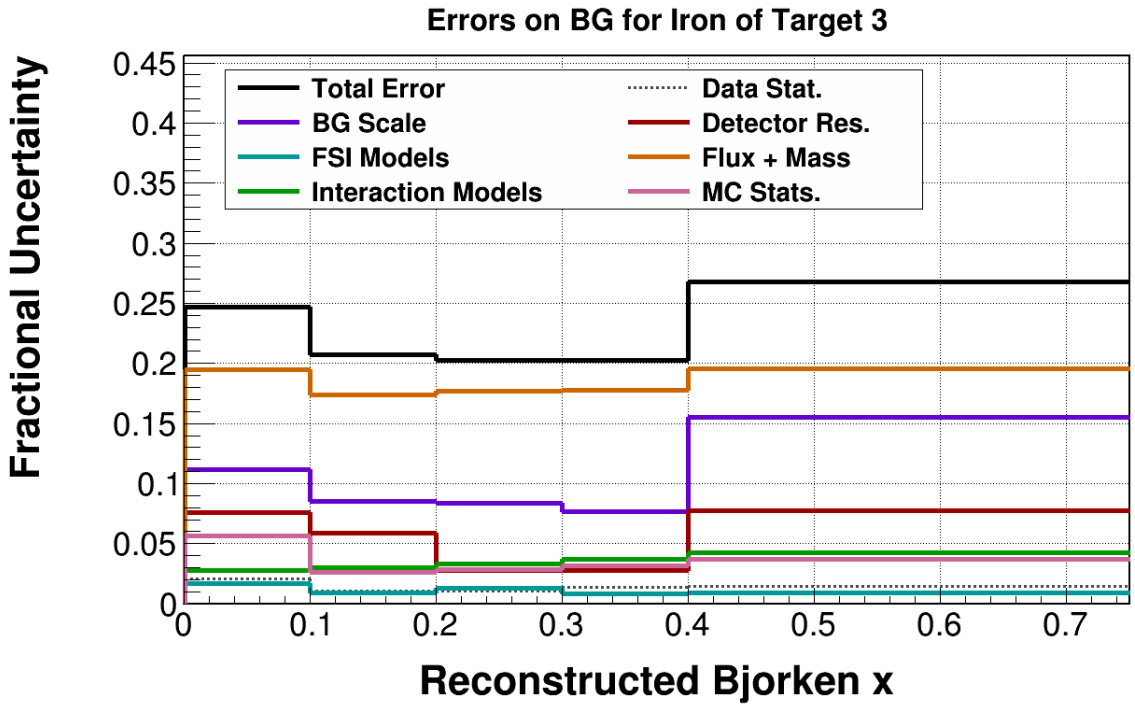

Figure C-76. Uncertainty on plastic BG prediction: target 03 Fe (x_{bj})

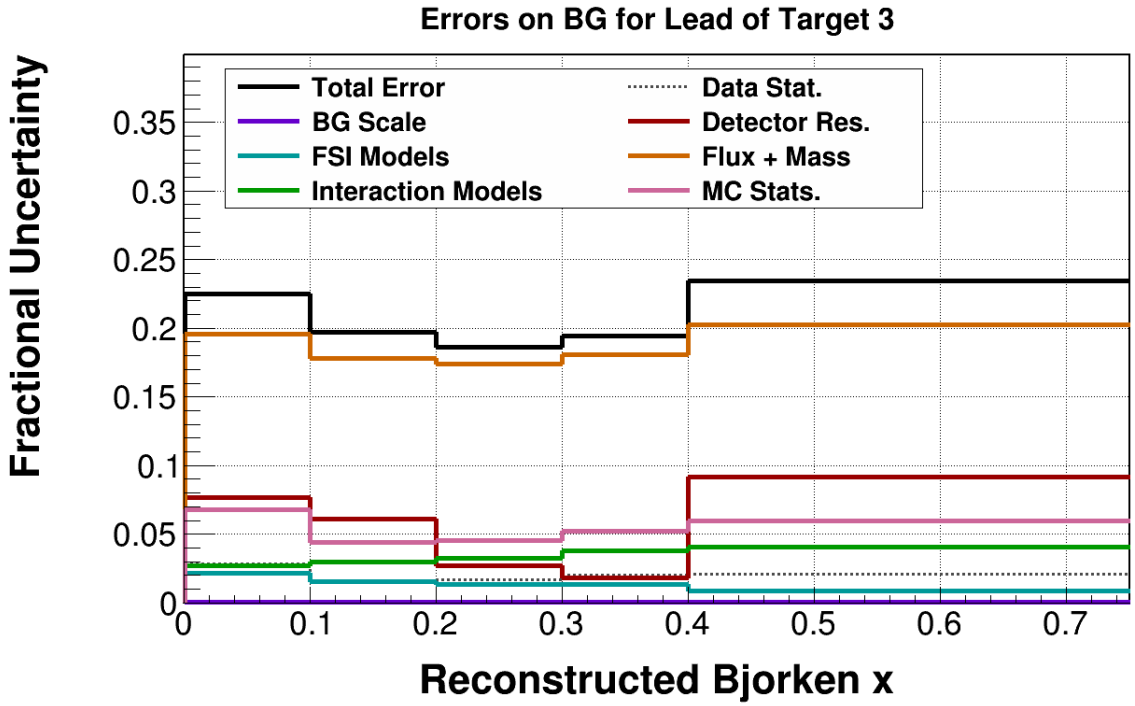

Figure C-77. Uncertainty on plastic BG prediction: target 03 Pb (x_{bj})

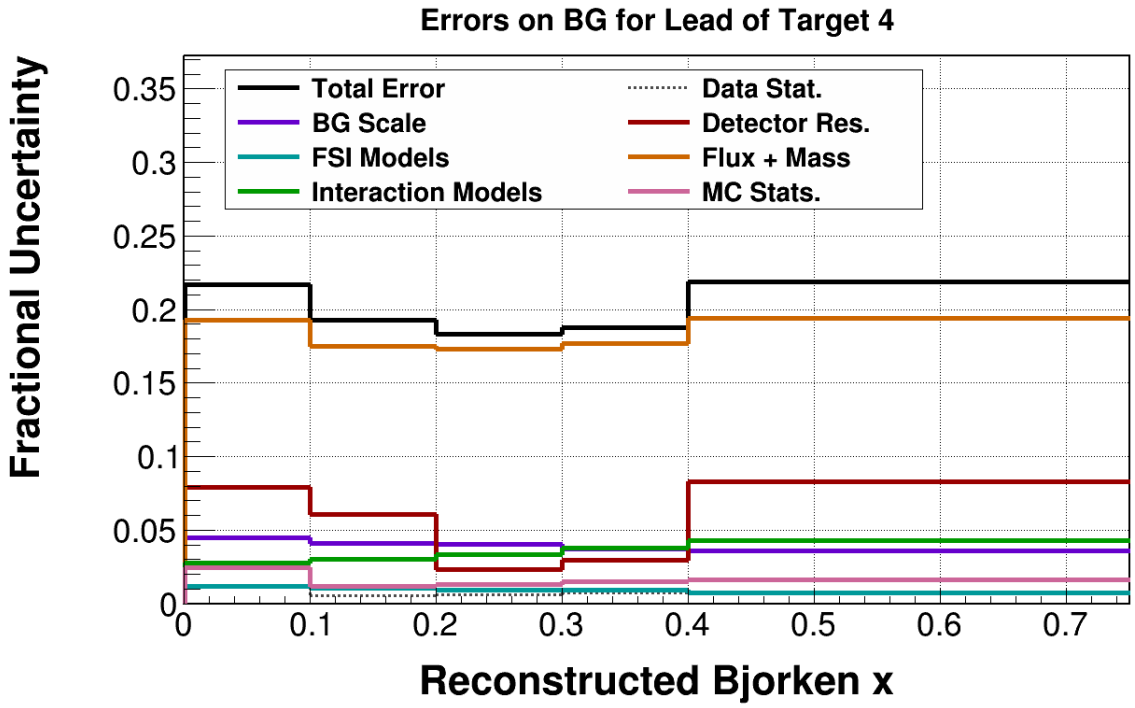

Figure C-78. Uncertainty on plastic BG prediction: target 04 Pb (x_{bj})

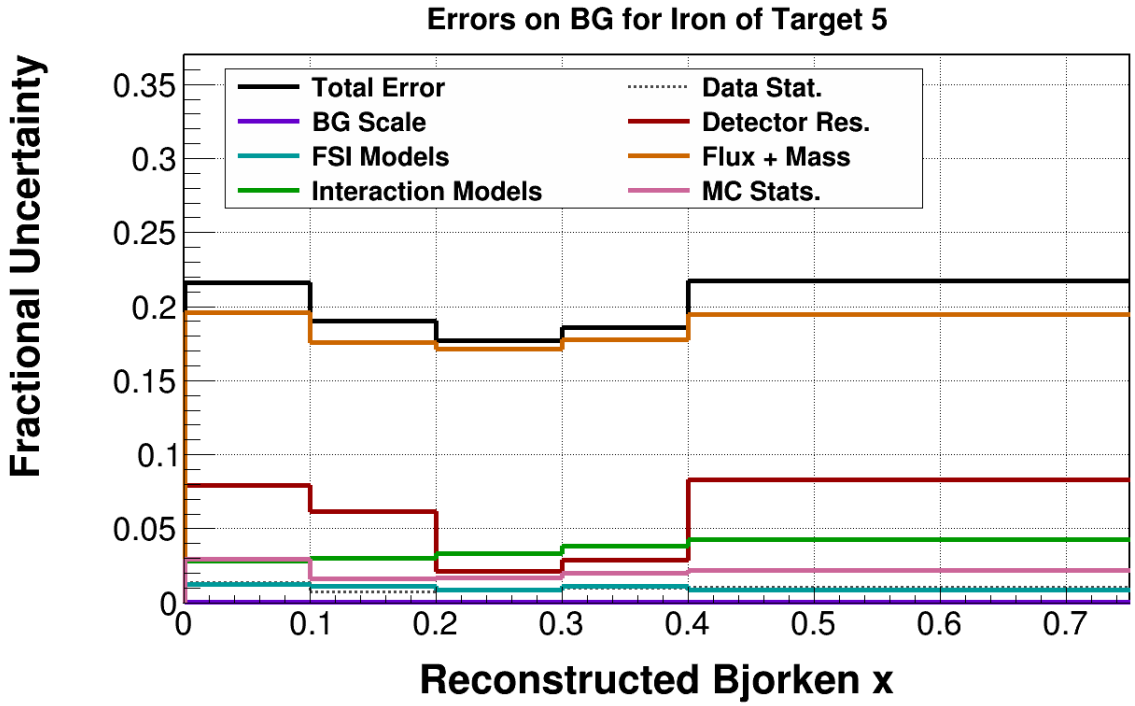

Figure C-79. Uncertainty on plastic BG prediction: target 05 Fe (x_{bj})

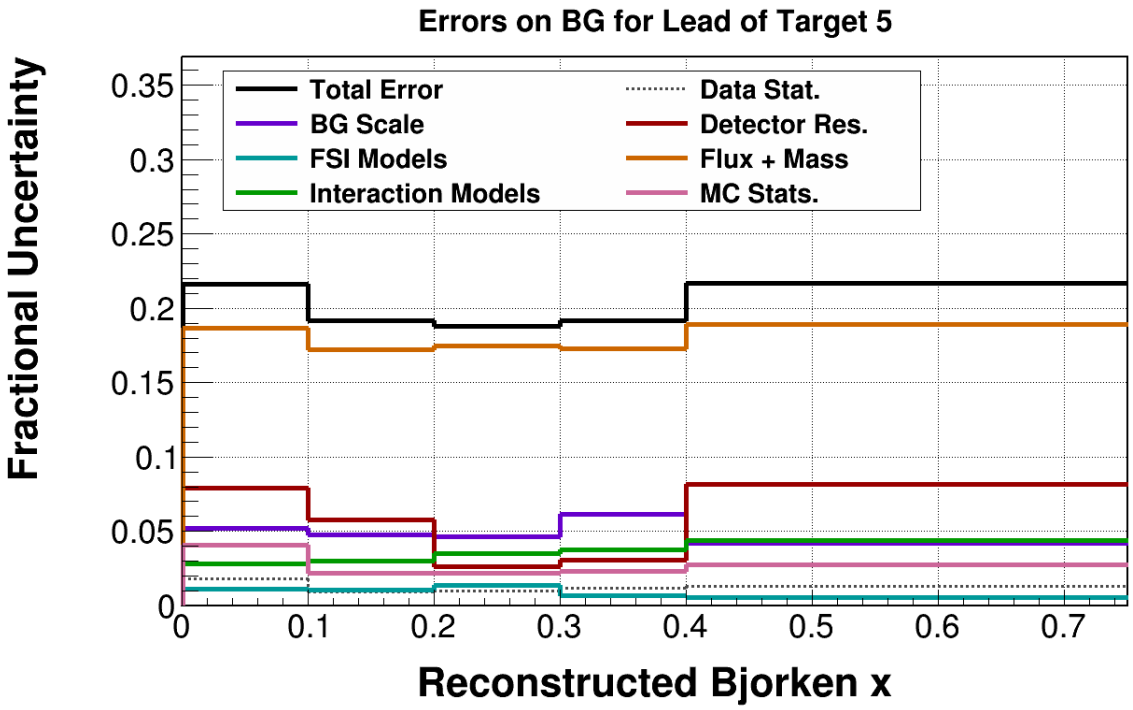

Figure C-80. Uncertainty on plastic BG prediction: target 05 Pb (x_{bj})

APPENDIX D
MIGRATION MATRICES

D.1 Migration Plots

Migration matrices are presented for neutrino energy as 2D histograms of true E_ν (y-axis) vs. reconstructed E_ν (x-axis):

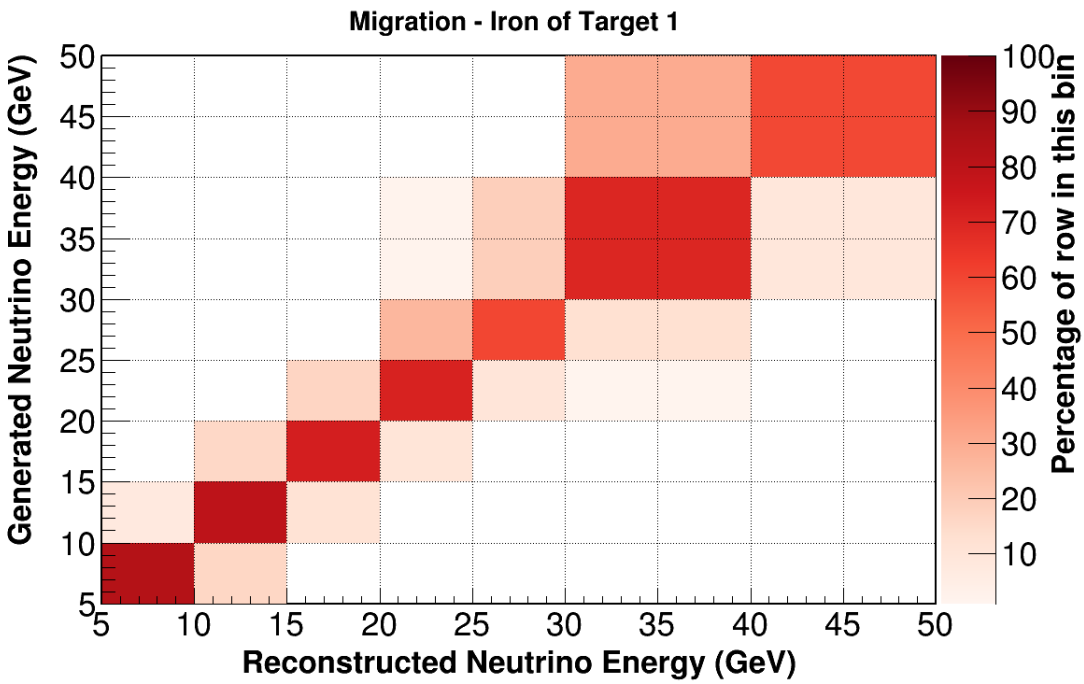

Figure D-1. Migration matrix: target 01 Fe (E_ν)

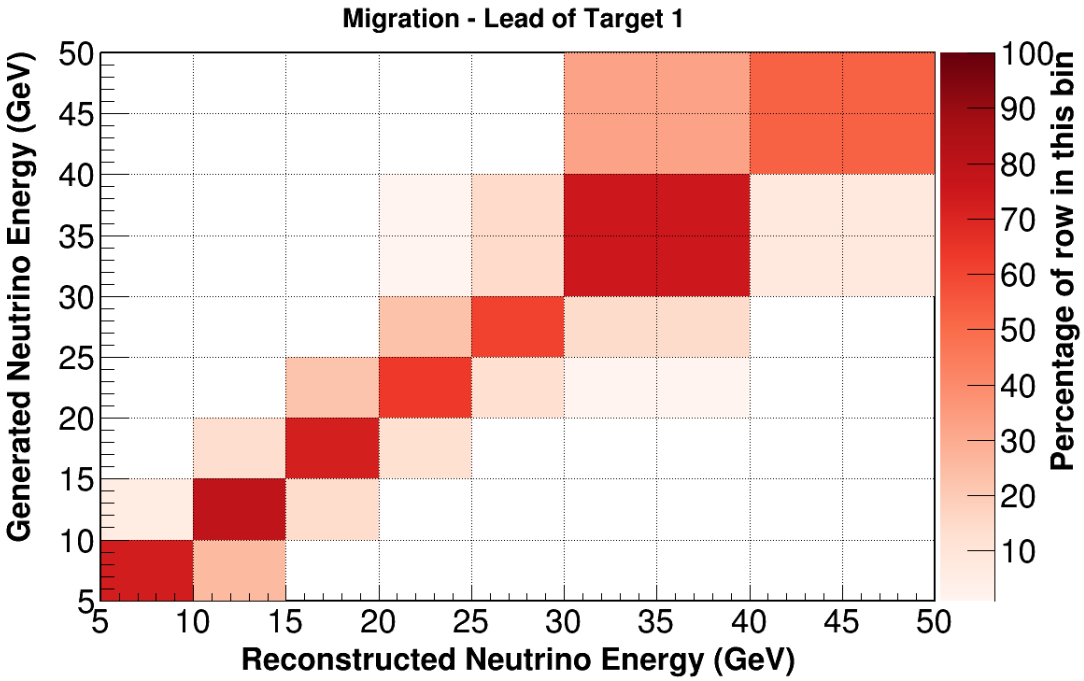

Figure D-2. Migration matrix: target 01 Pb (E_ν)

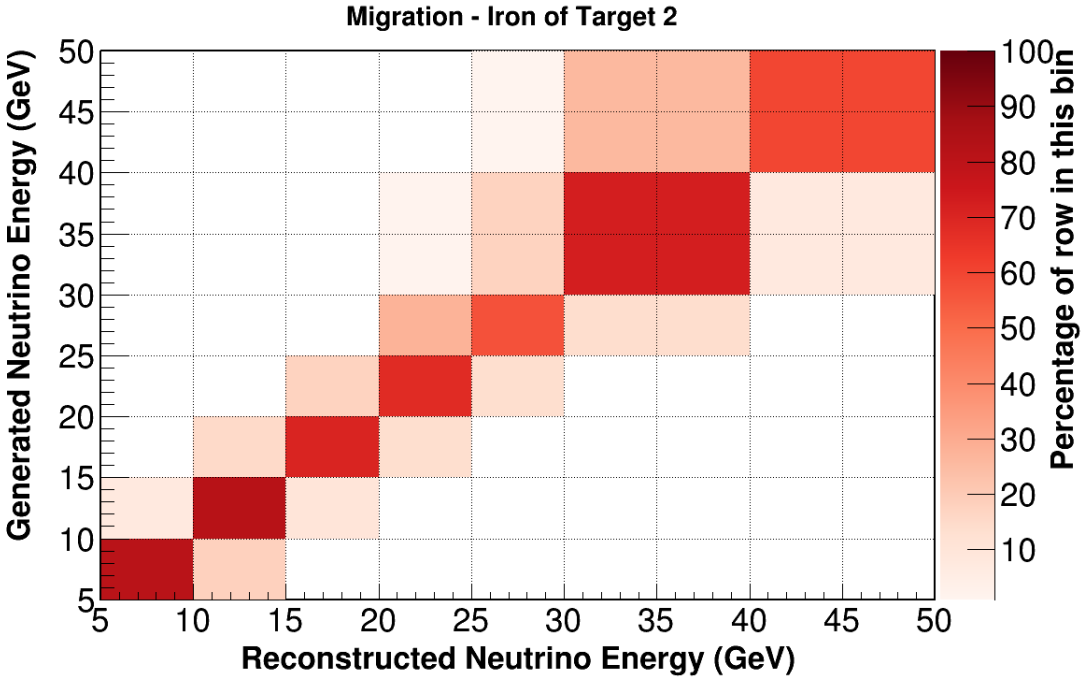

Figure D-3. Migration matrix: target 02 Fe (E_ν)

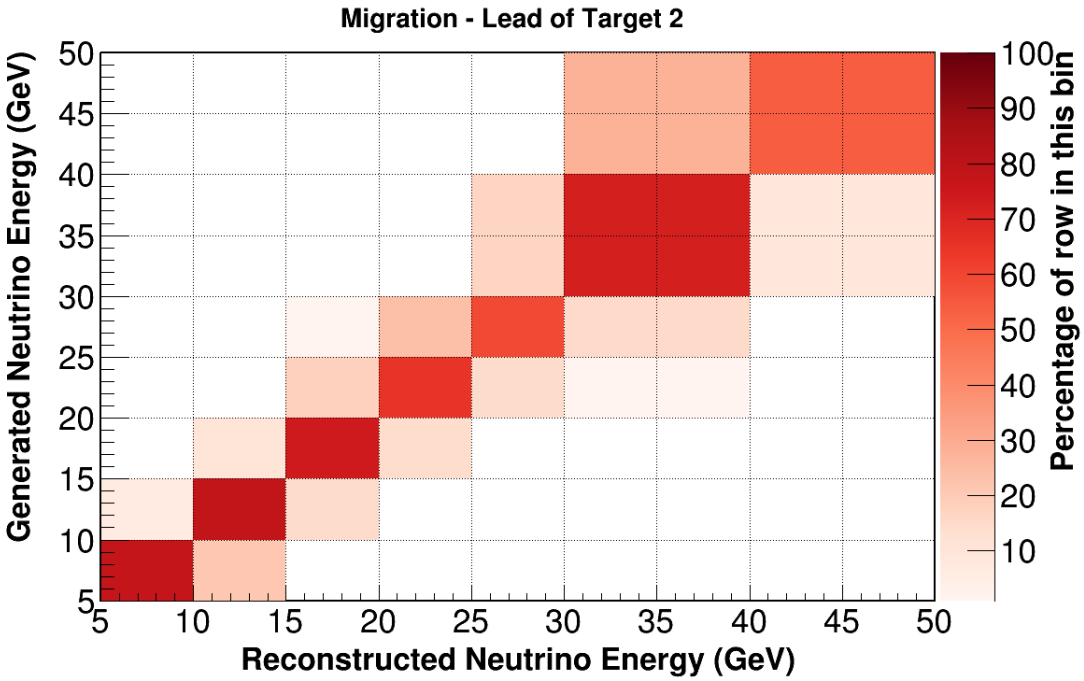

Figure D-4. Migration matrix: target 02 Pb (E_ν)

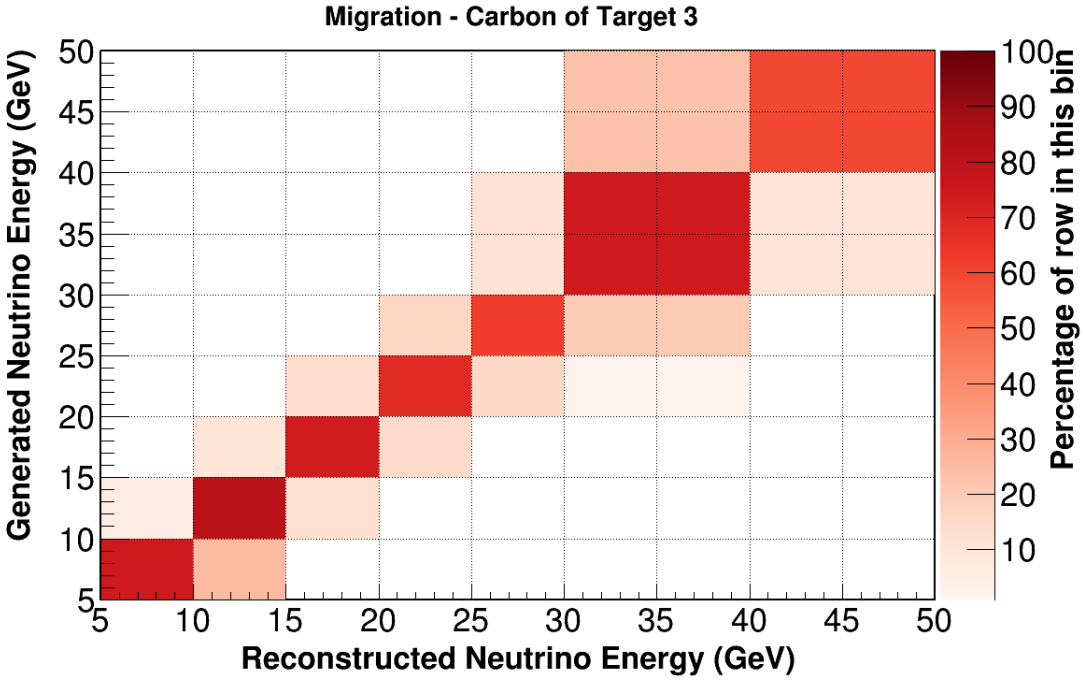

Figure D-5. Migration matrix: target 03 C (E_ν)

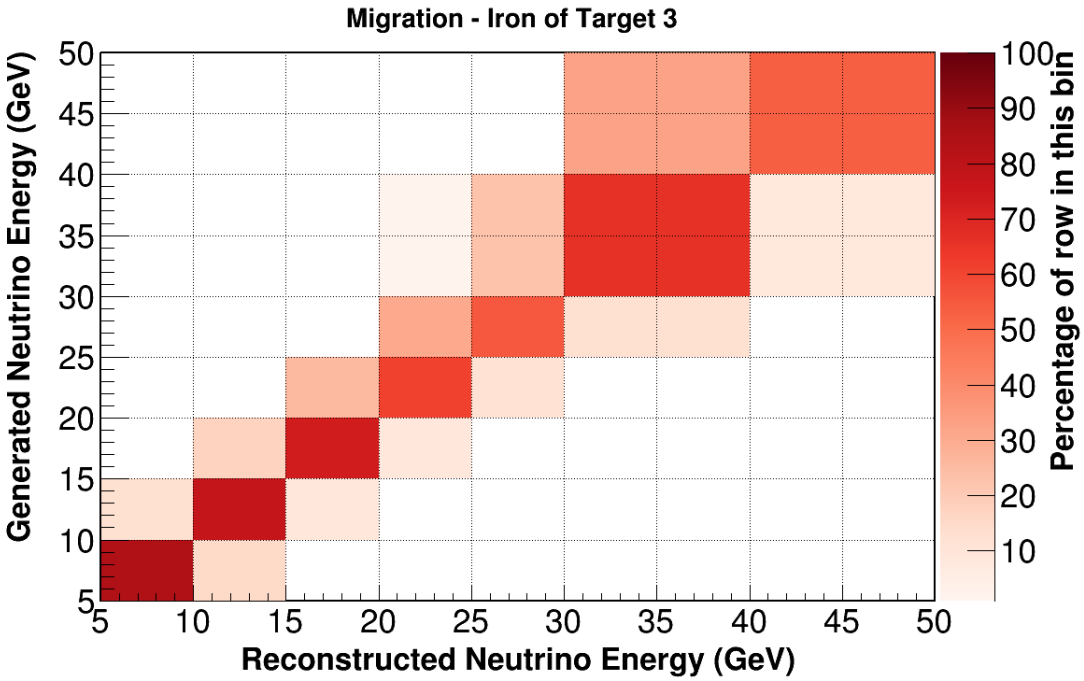

Figure D-6. Migration matrix: target 03 Fe (E_ν)

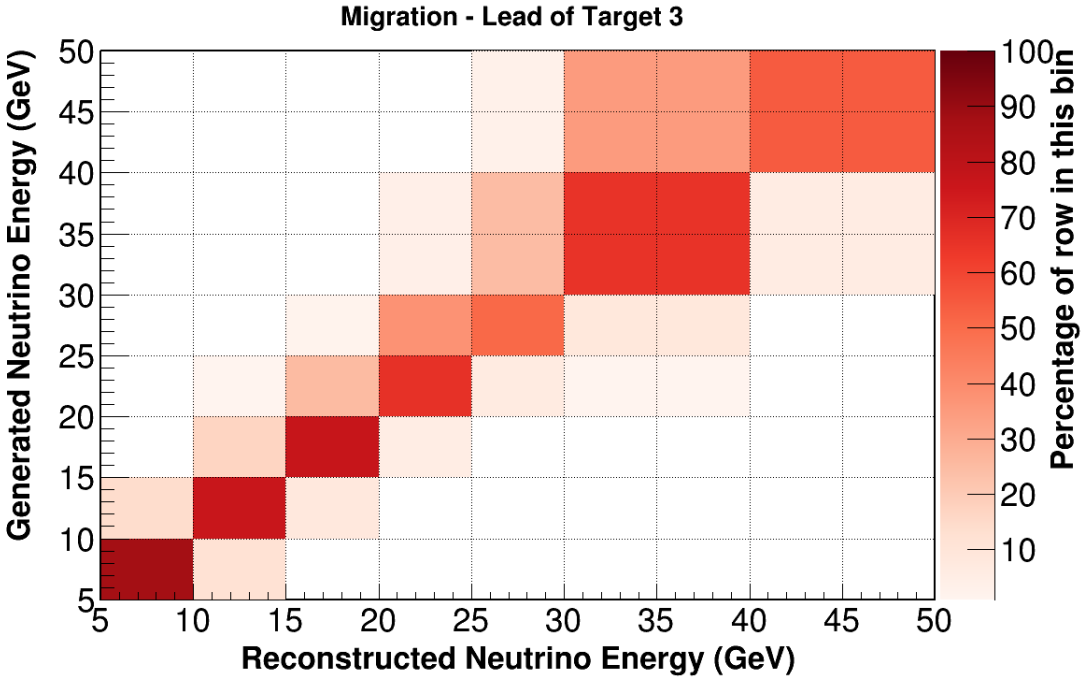

Figure D-7. Migration matrix: target 03 Pb (E_ν)

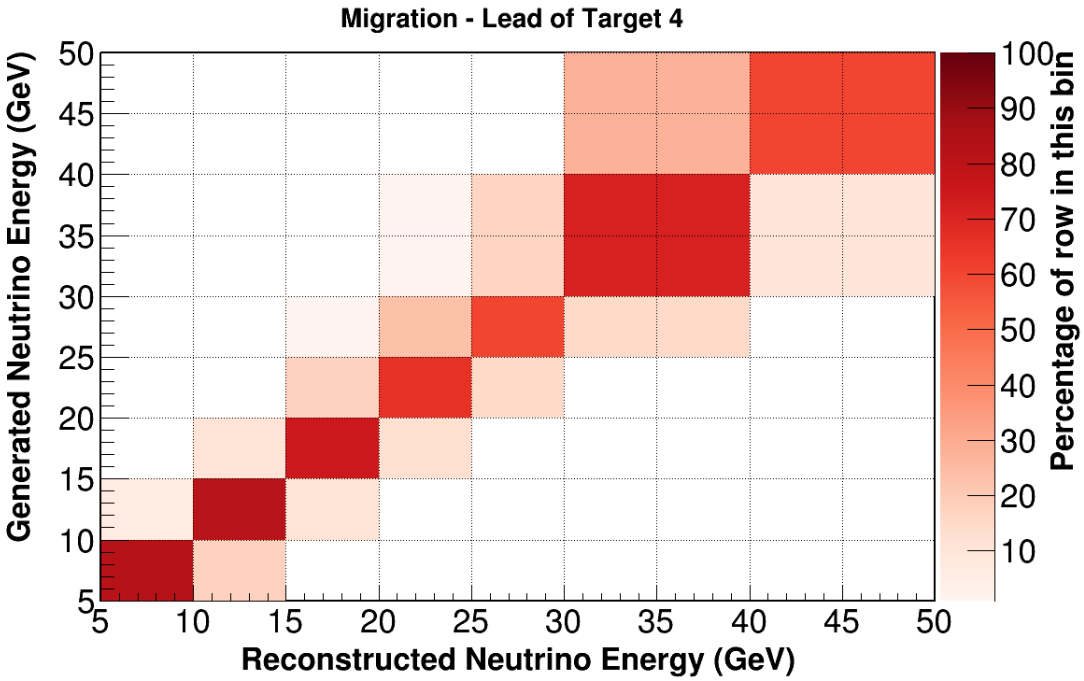

Figure D-8. Migration matrix: target 04 Pb (E_ν)

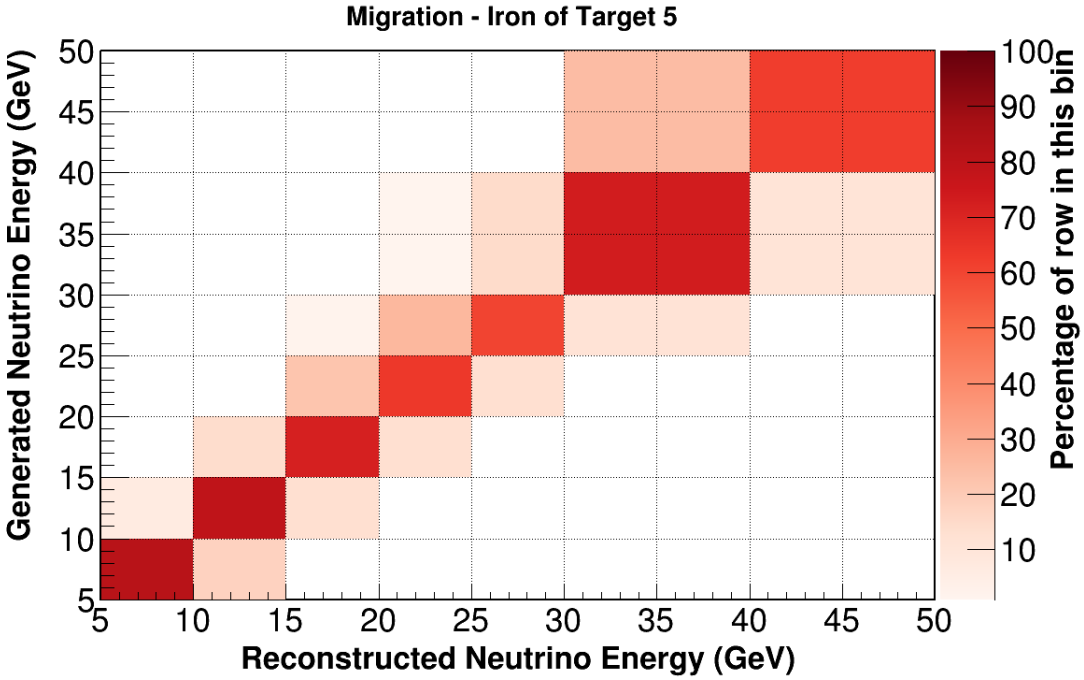

Figure D-9. Migration matrix: target 05 Fe (E_ν)

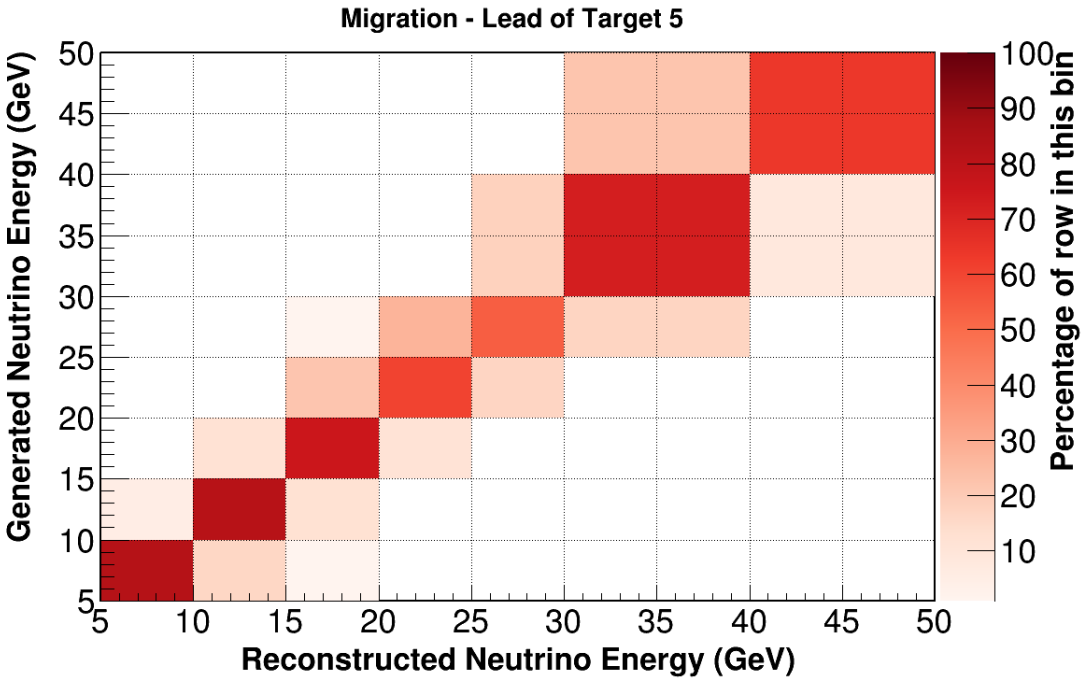

Figure D-10. Migration matrix: target 05 Pb (E_ν)

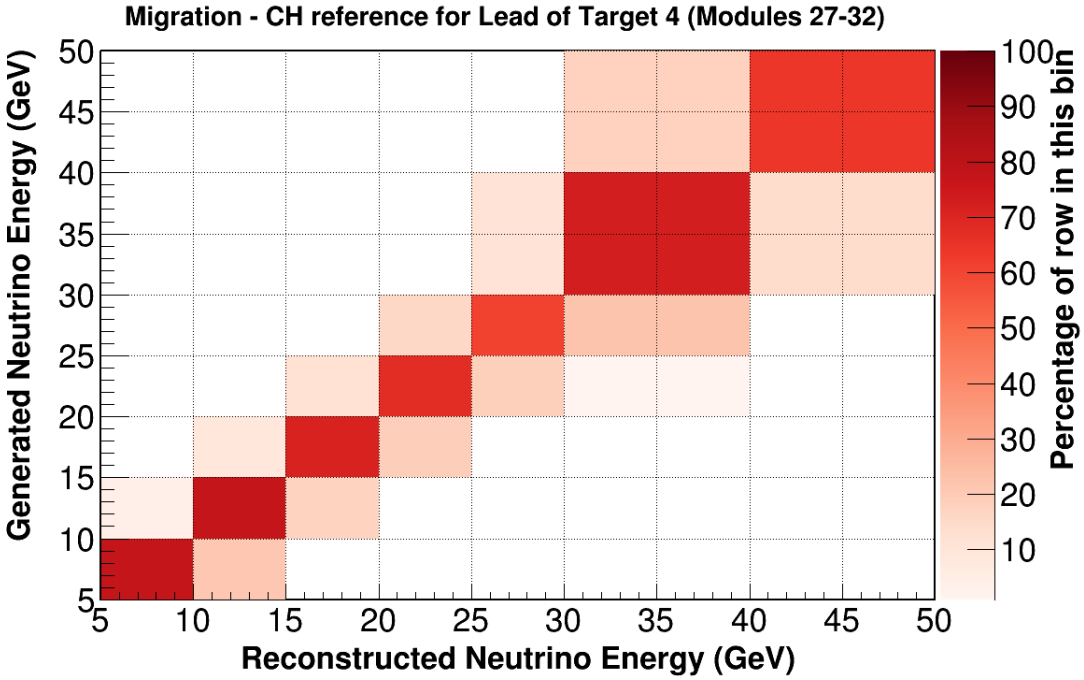

Figure D-11. Migration matrix: tracker mods. 27-32 (E_ν)

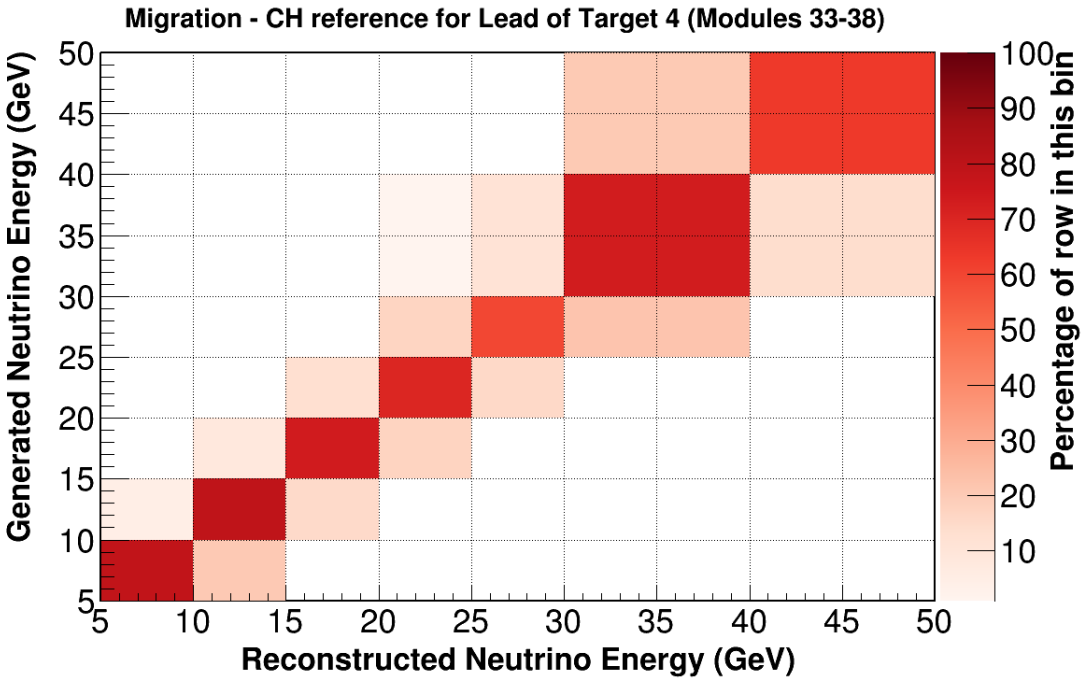

Figure D-12. Migration matrix: tracker mods. 33-38 (E_ν)

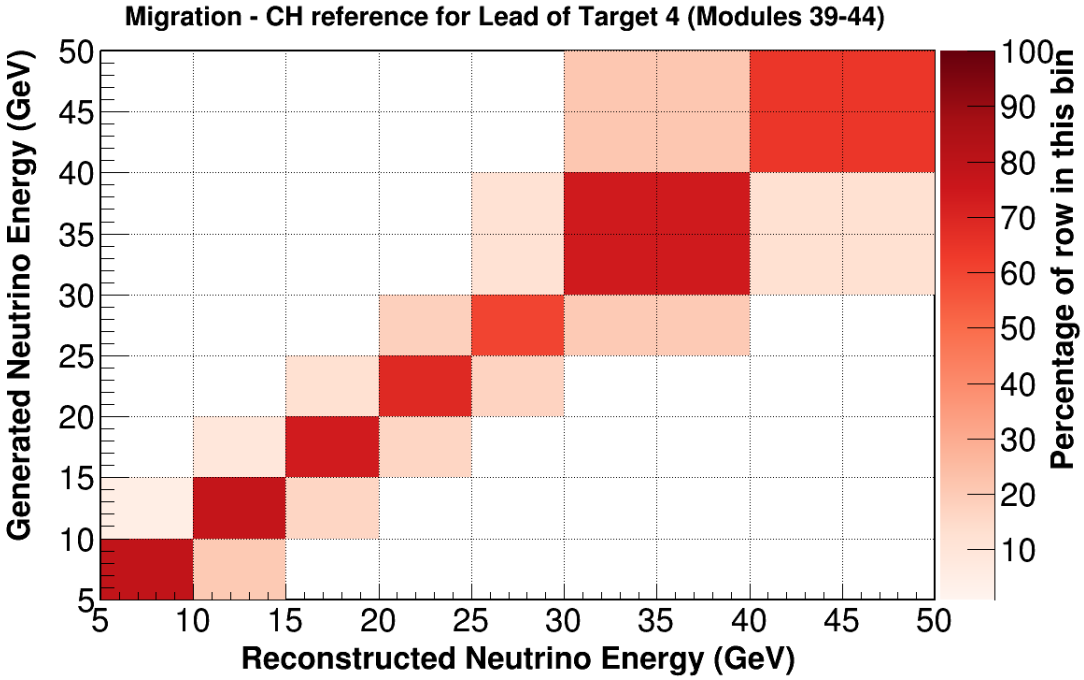

Figure D-13. Migration matrix: tracker mods. 39-44 (E_ν)

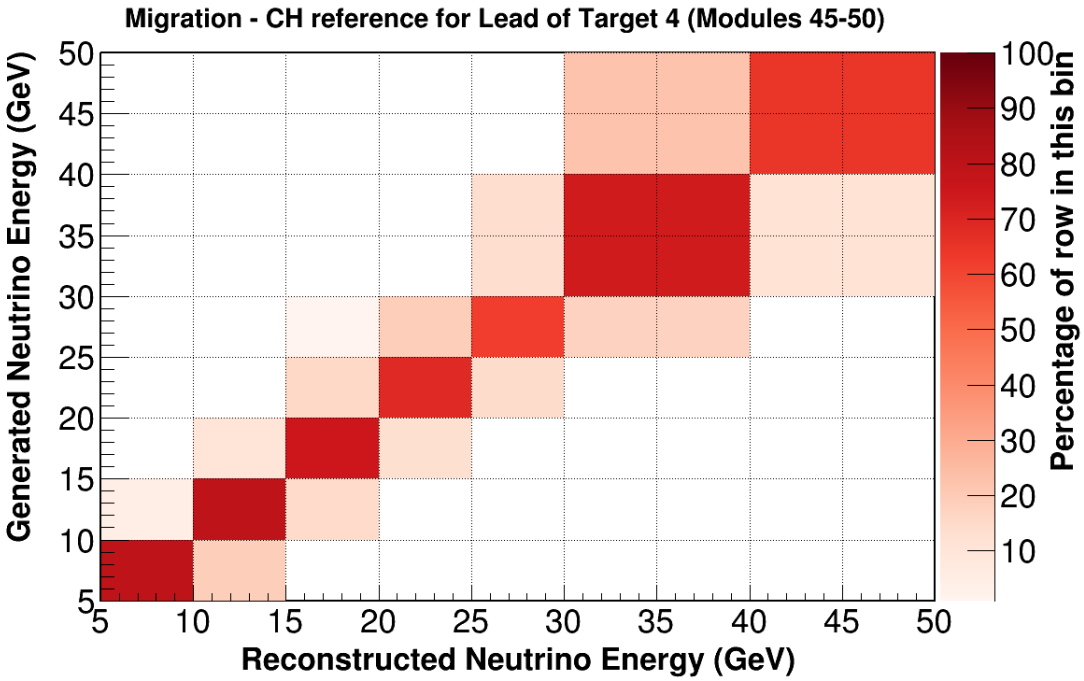

Figure D-14. Migration matrix: tracker mods. 45-50 (E_ν)

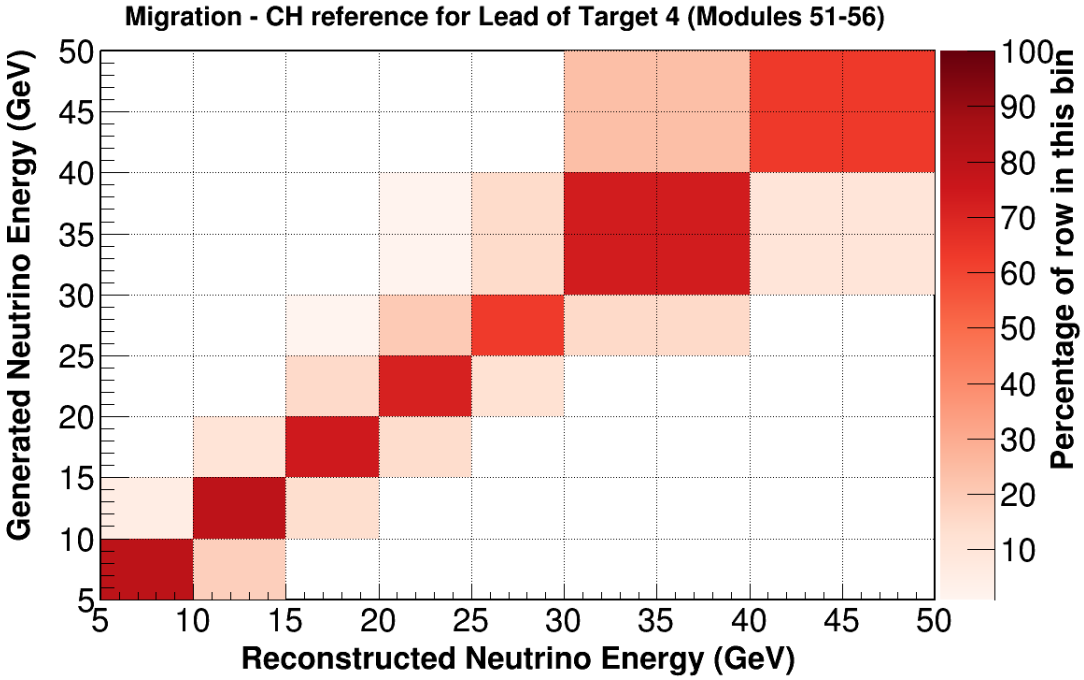

Figure D-15. Migration matrix: tracker mods. 51-56 (E_ν)

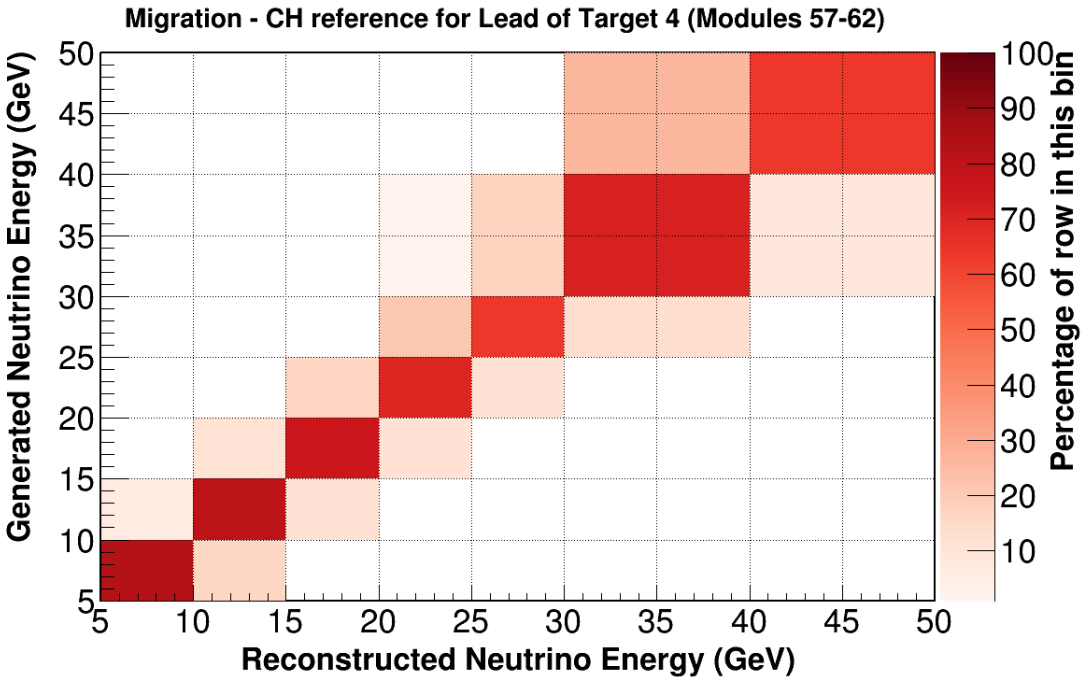

Figure D-16. Migration matrix: tracker mods. 57-62 (E_ν)

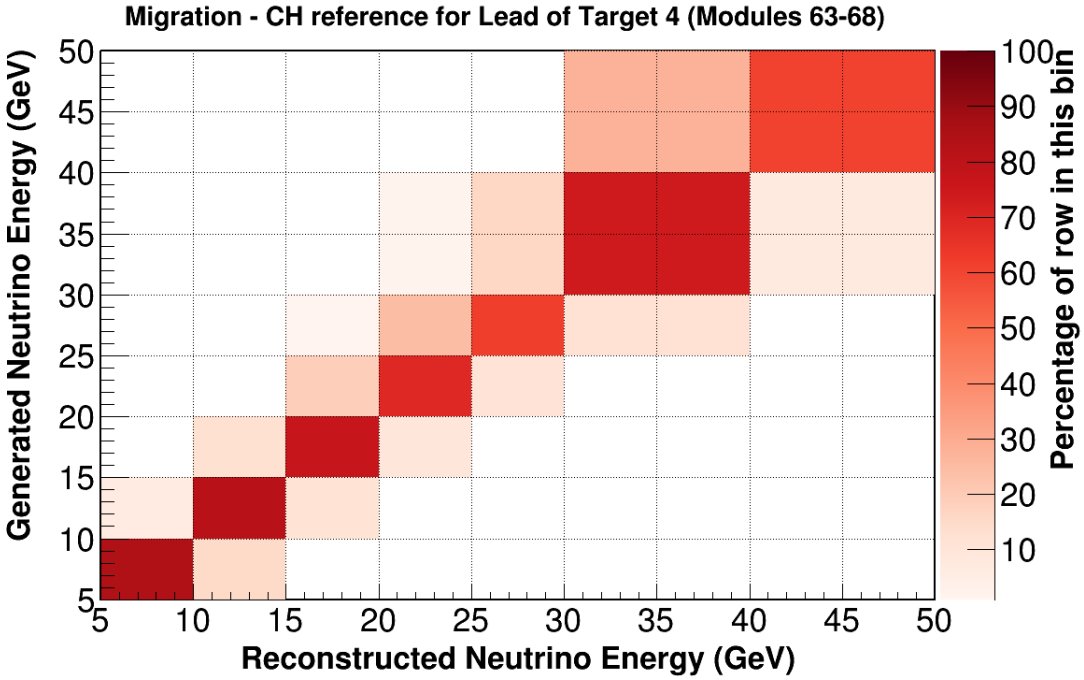

Figure D-17. Migration matrix: tracker mods. 63-68 (E_ν)

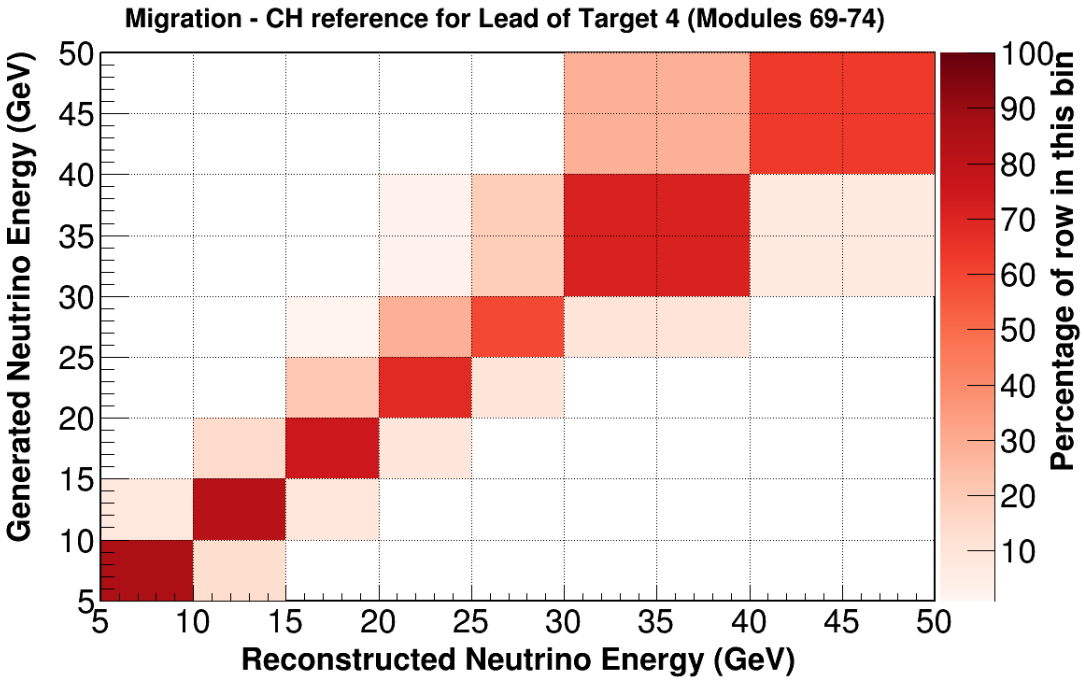

Figure D-18. Migration matrix: tracker mods. 69-74 (E_ν)

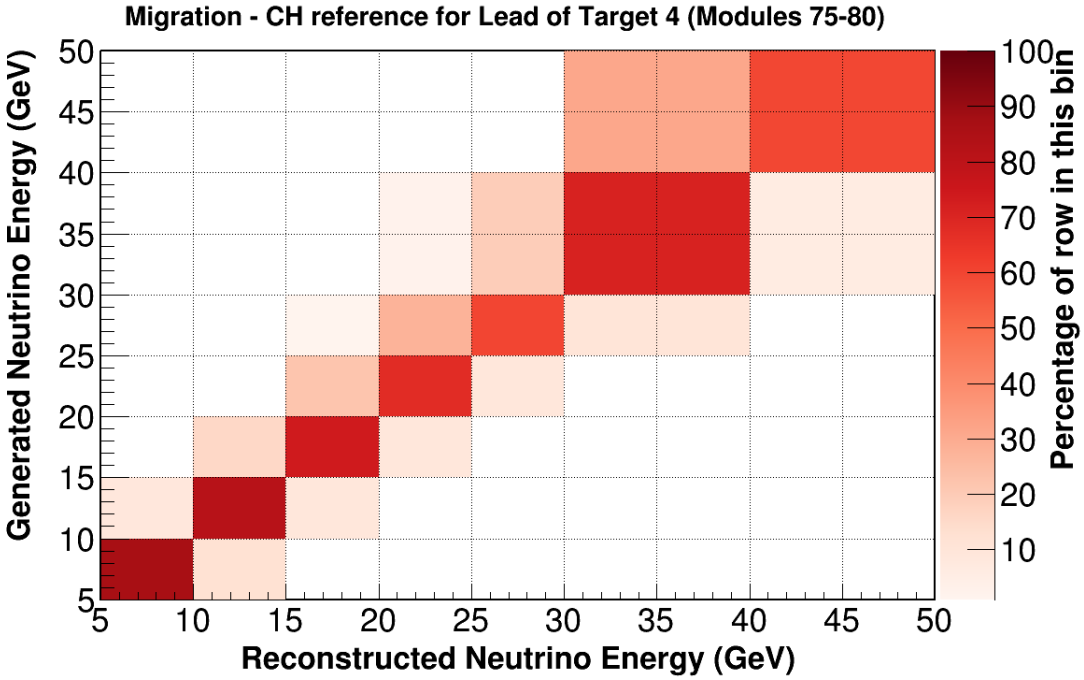

Figure D-19. Migration matrix: tracker mods. 75-80 (E_ν)

Migration matrices are presented for Bjorken-x as 2D histograms of true x_{bj} (y-axis) vs. reconstructed x_{bj} (x-axis):

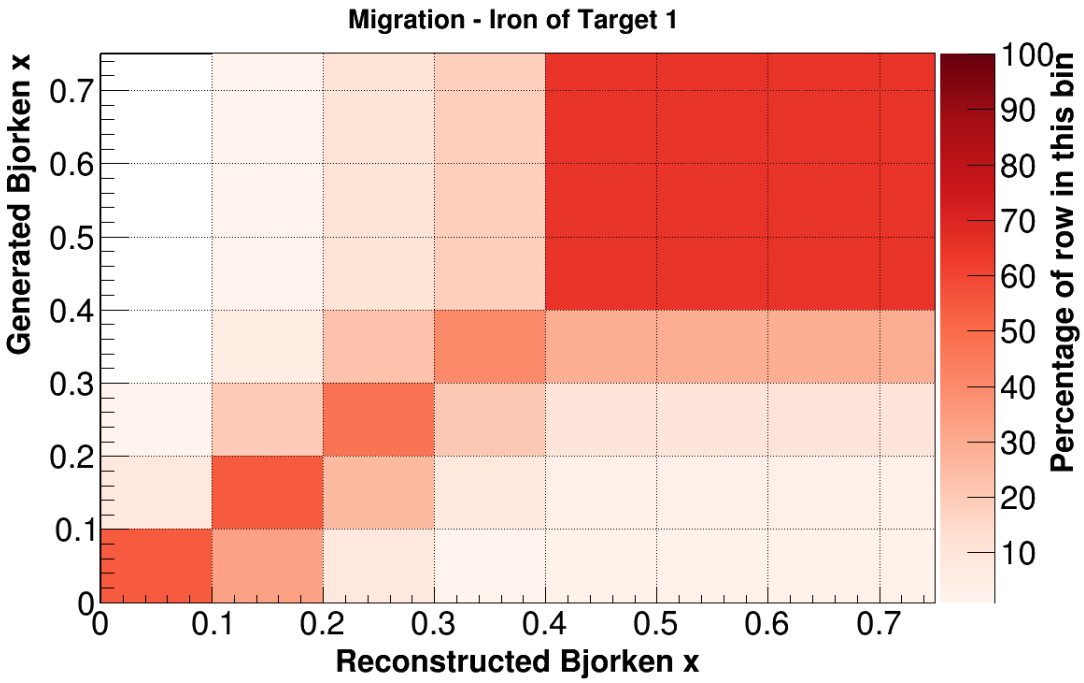

Figure D-20. Migration matrix: target 01 Fe (x_{bj})

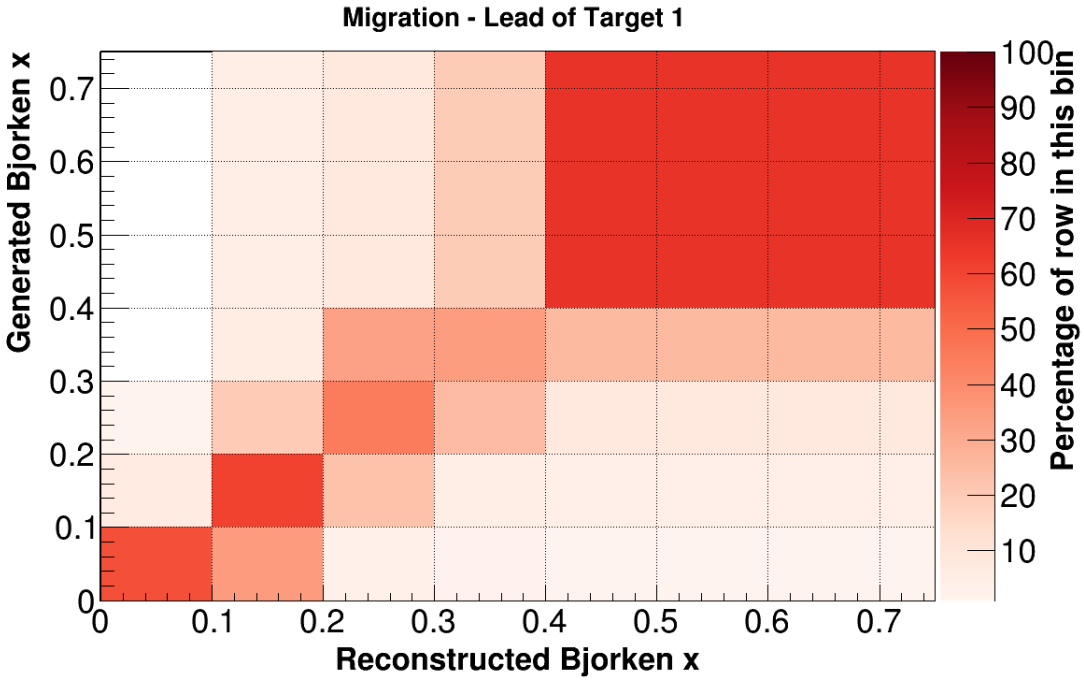

Figure D-21. Migration matrix: target 01 Pb (x_{bj})

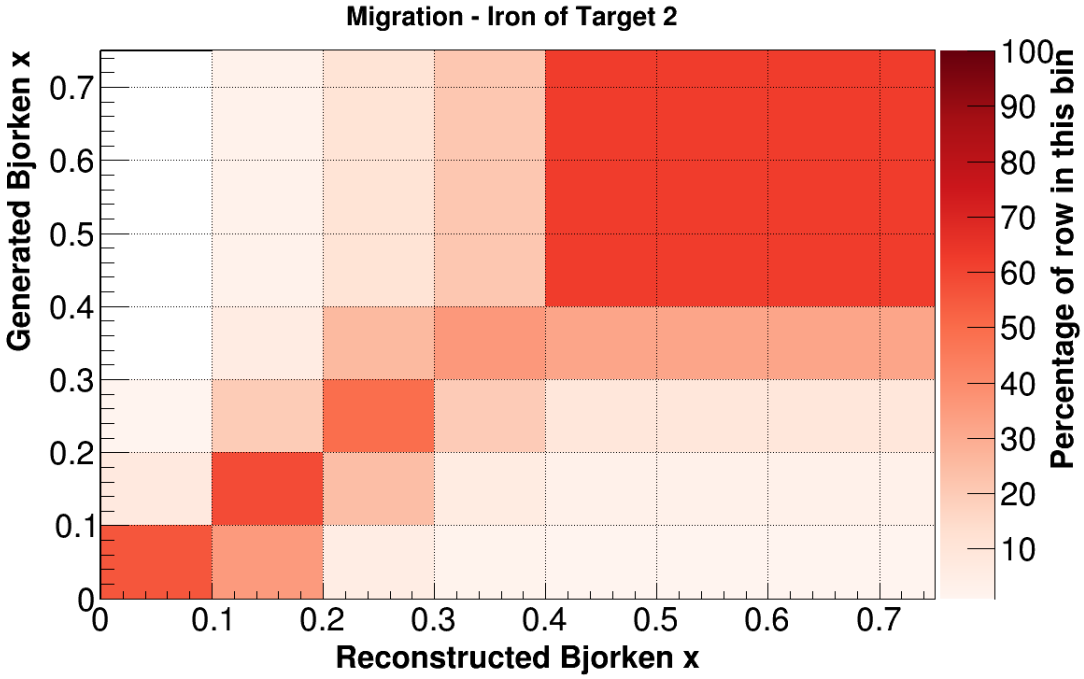

Figure D-22. Migration matrix: target 02 Fe (x_{bj})

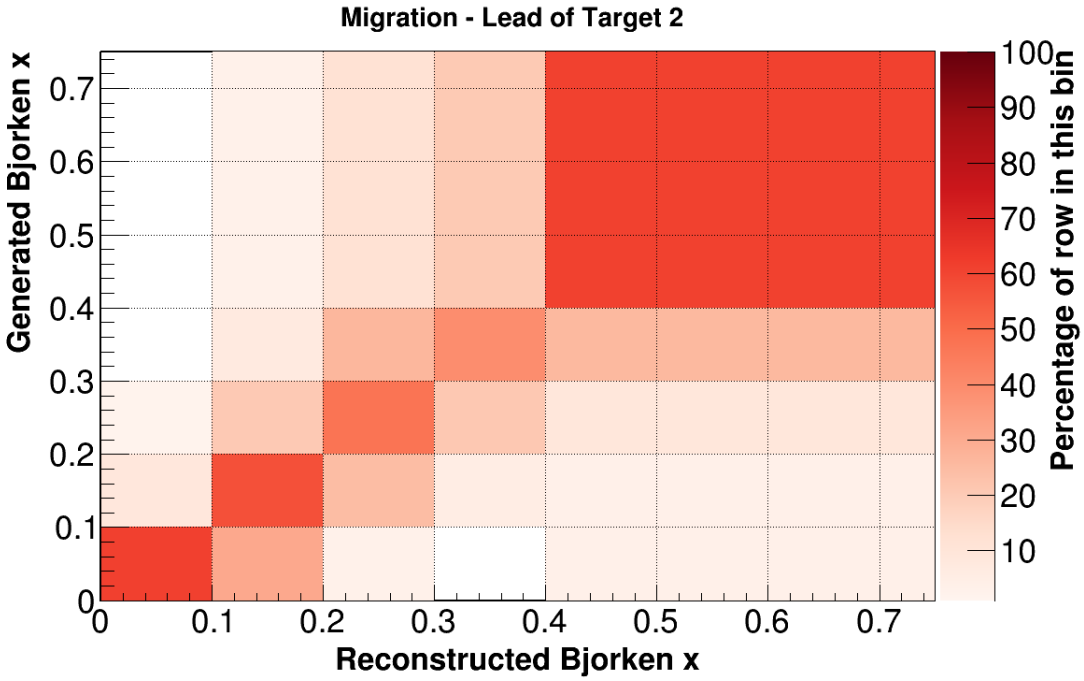

Figure D-23. Migration matrix: target 02 Pb (x_{bj})

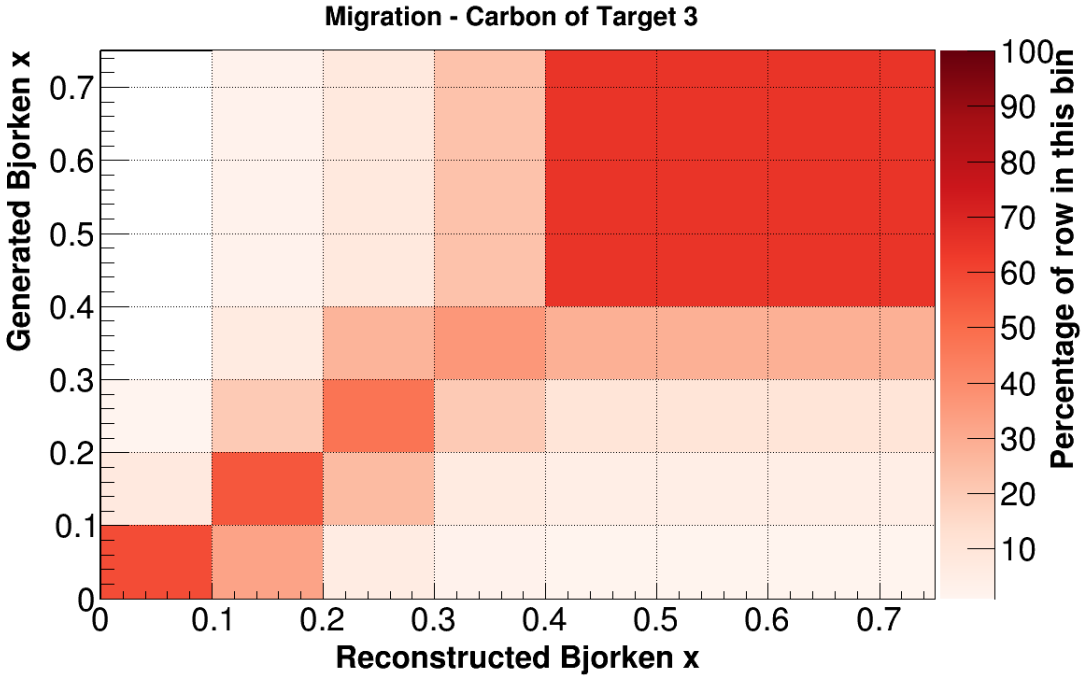

Figure D-24. Migration matrix: target 03 C (x_{bj})

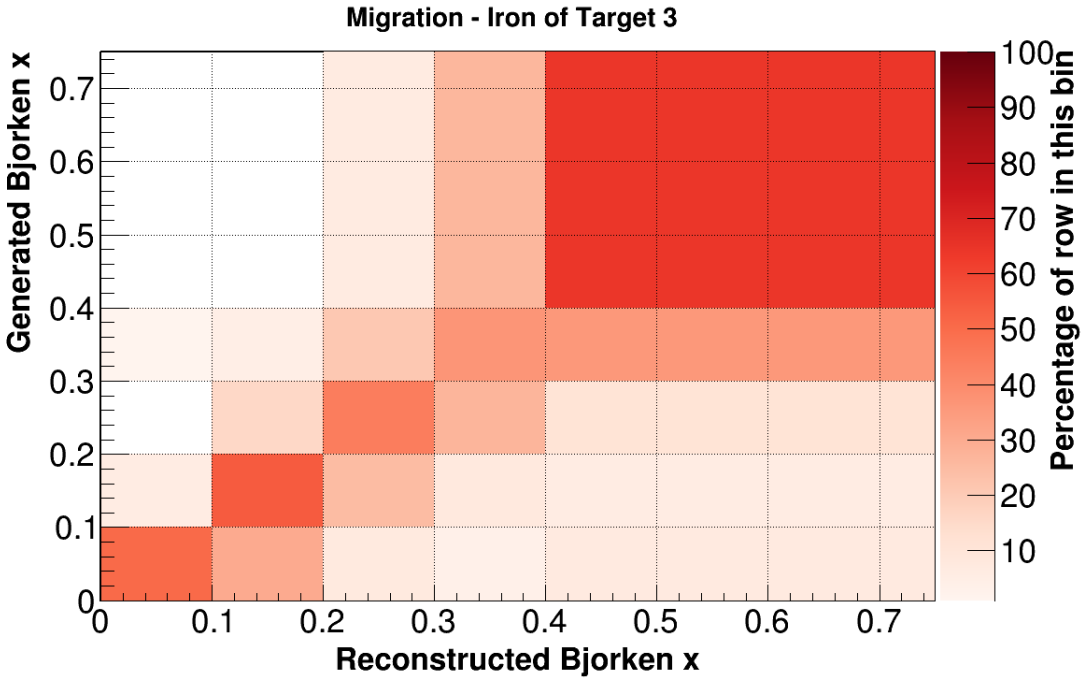

Figure D-25. Migration matrix: target 03 Fe (x_{bj})

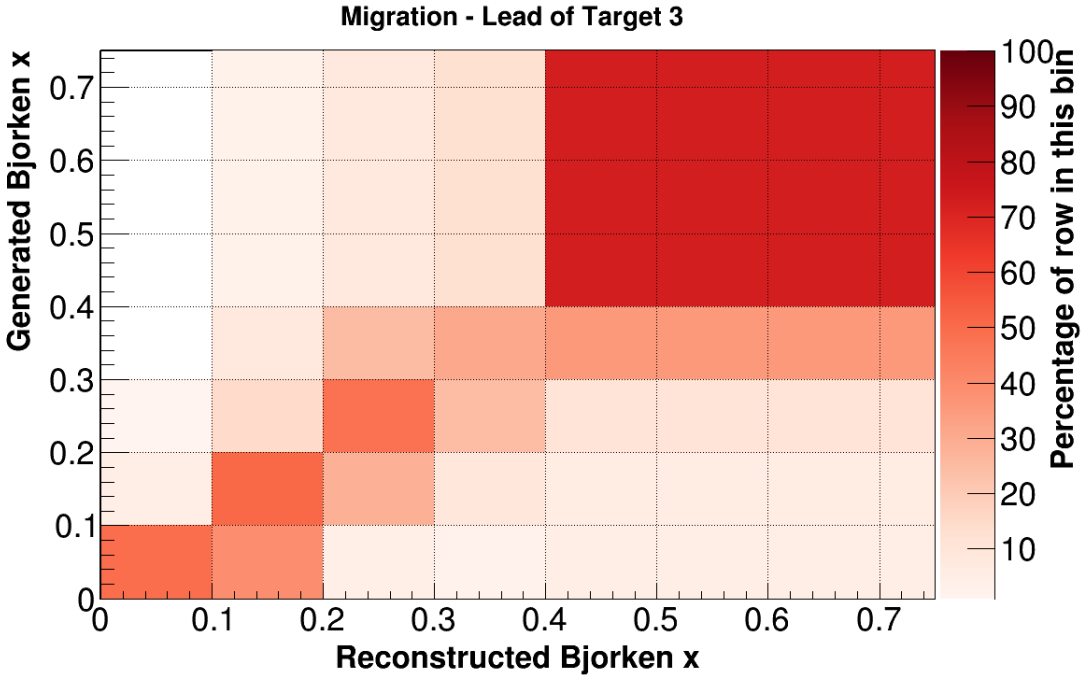

Figure D-26. Migration matrix: target 03 Pb (x_{bj})

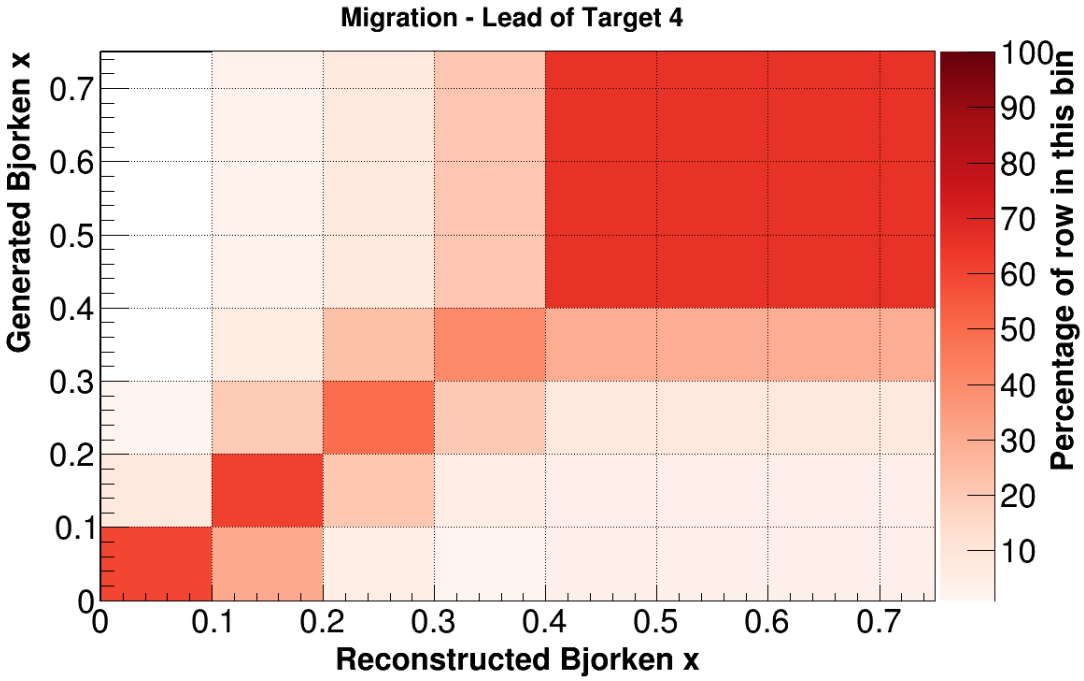

Figure D-27. Migration matrix: target 04 Pb (x_{bj})

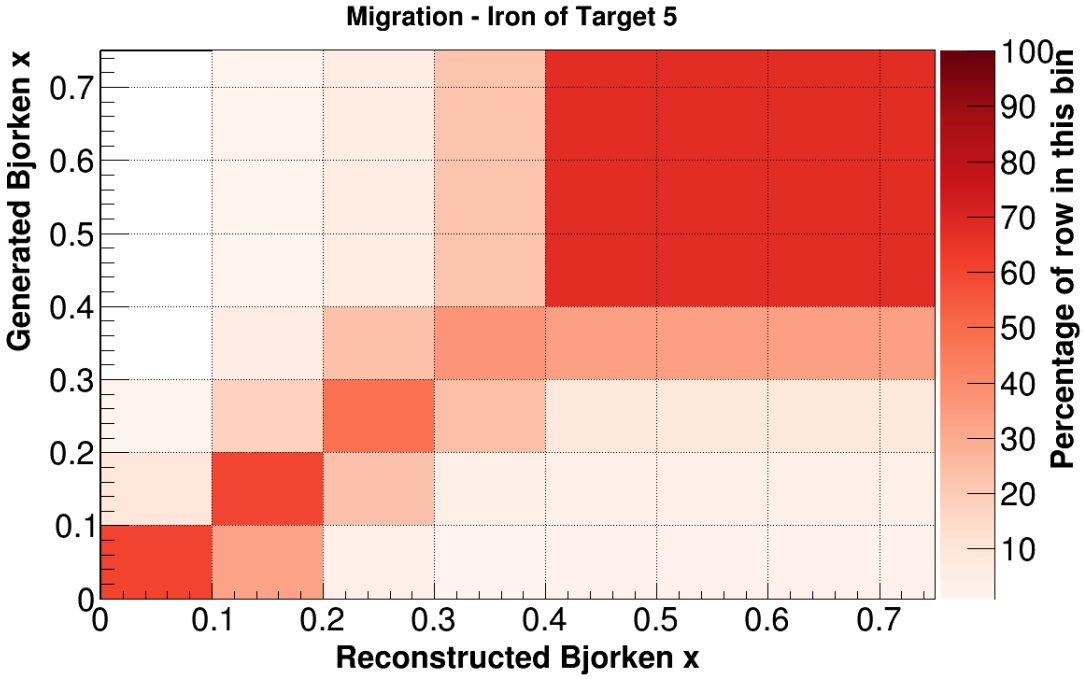

Figure D-28. Migration matrix: target 05 Fe (x_{bj})

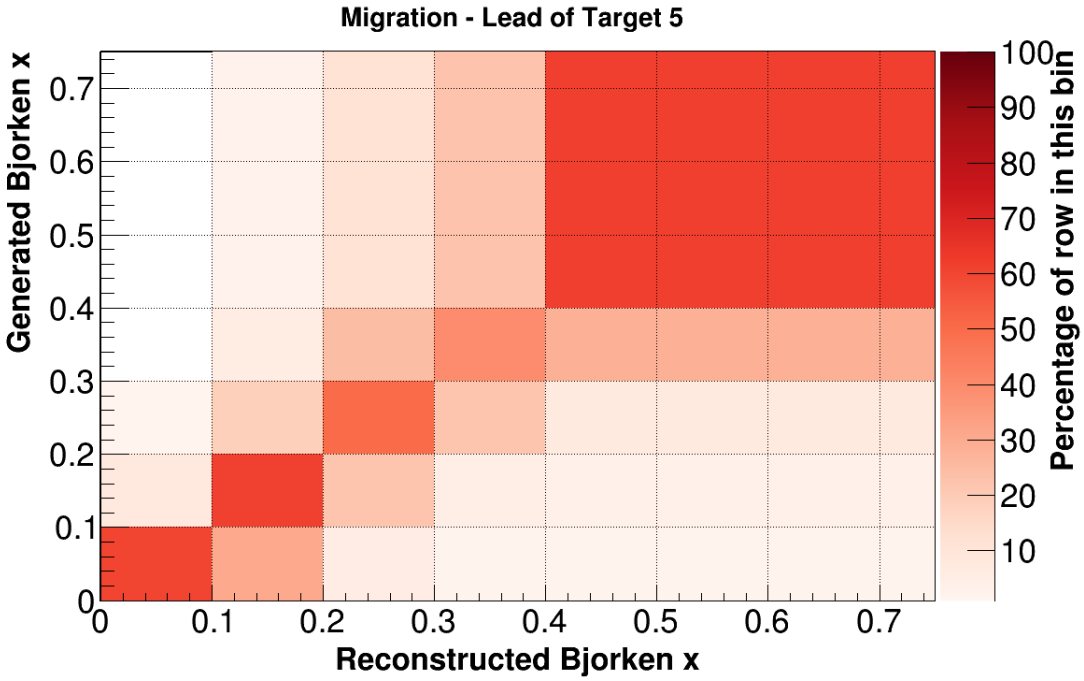

Figure D-29. Migration matrix: target 05 Pb (x_{bj})

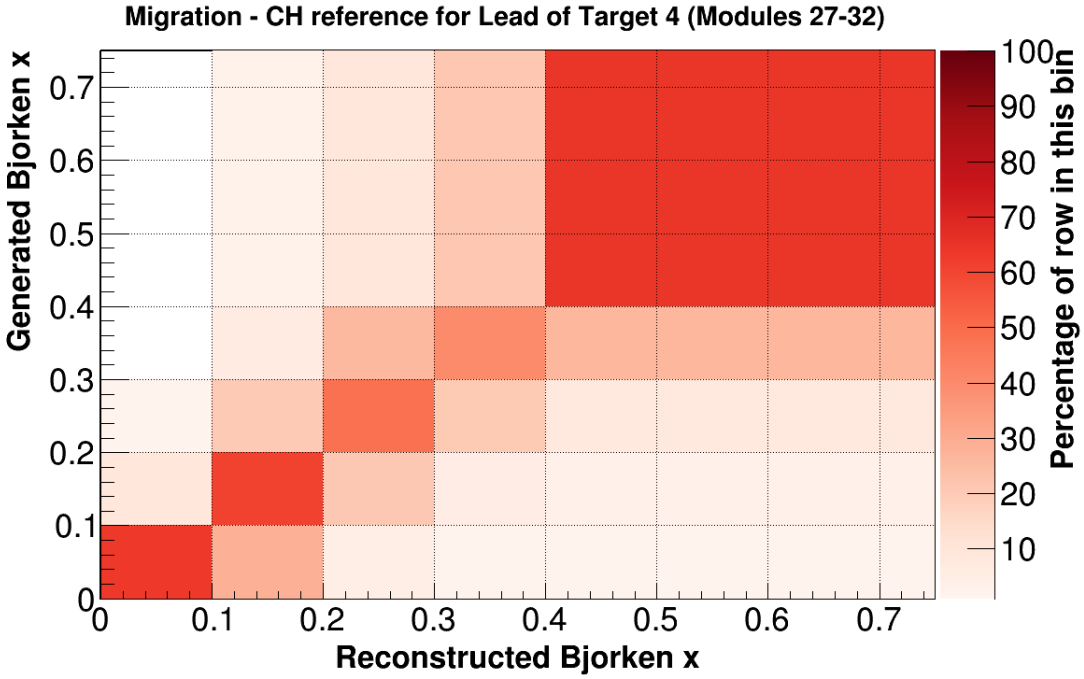

Figure D-30. Migration matrix: tracker mods. 27-32 (x_{bj})

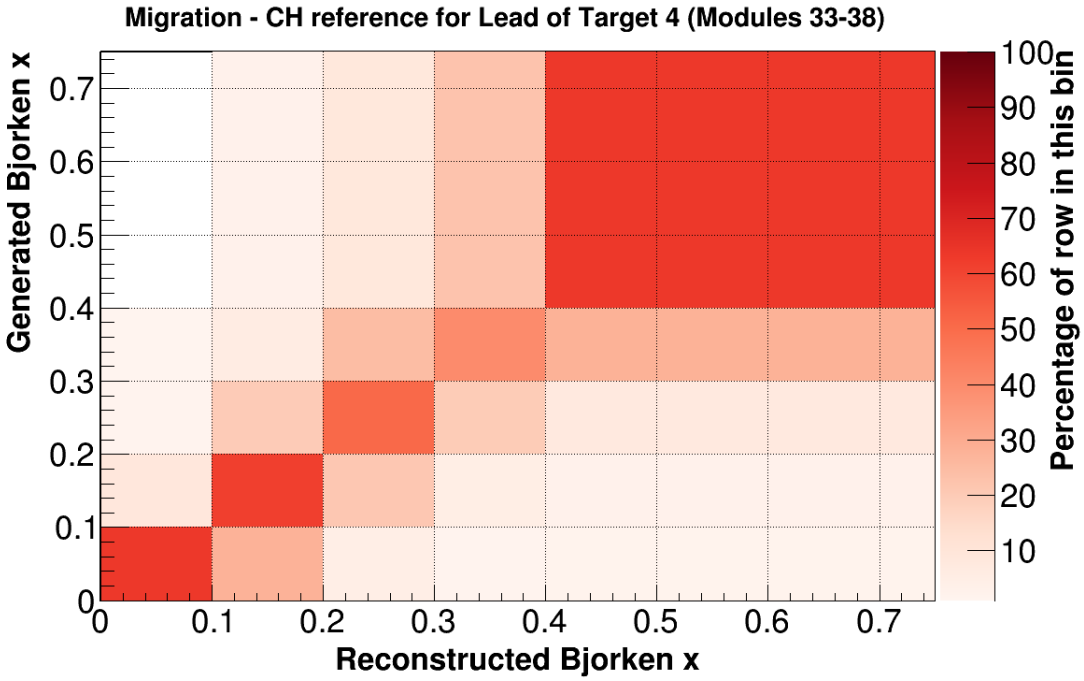

Figure D-31. Migration matrix: tracker mods. 33-38 (x_{bj})

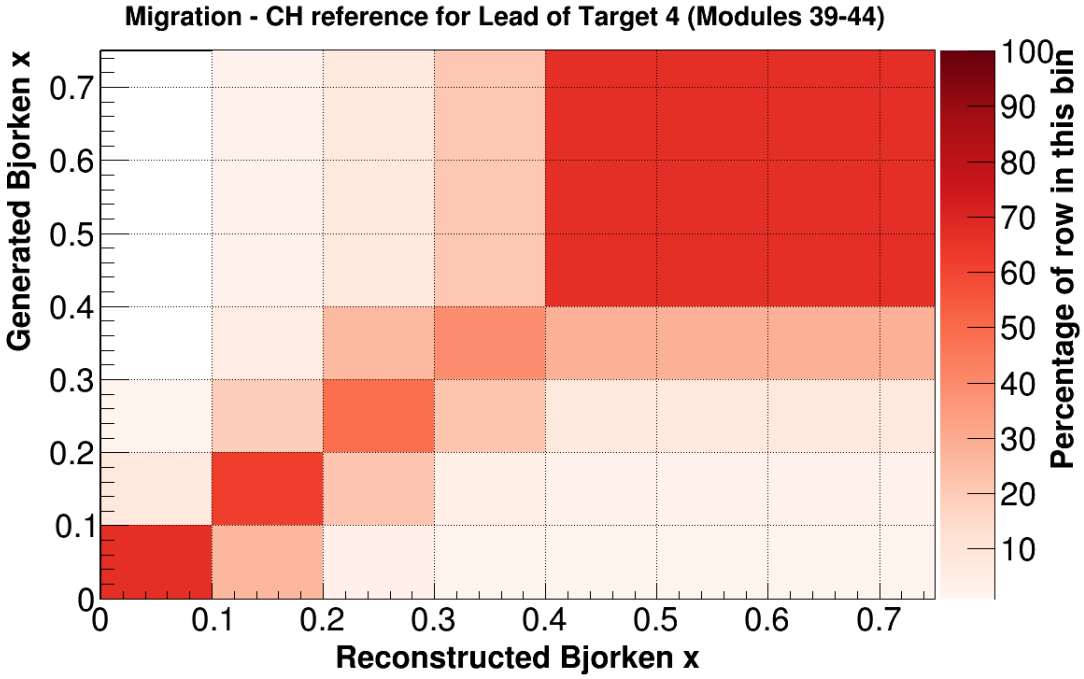

Figure D-32. Migration matrix: tracker mods. 39-44 (x_{bj})

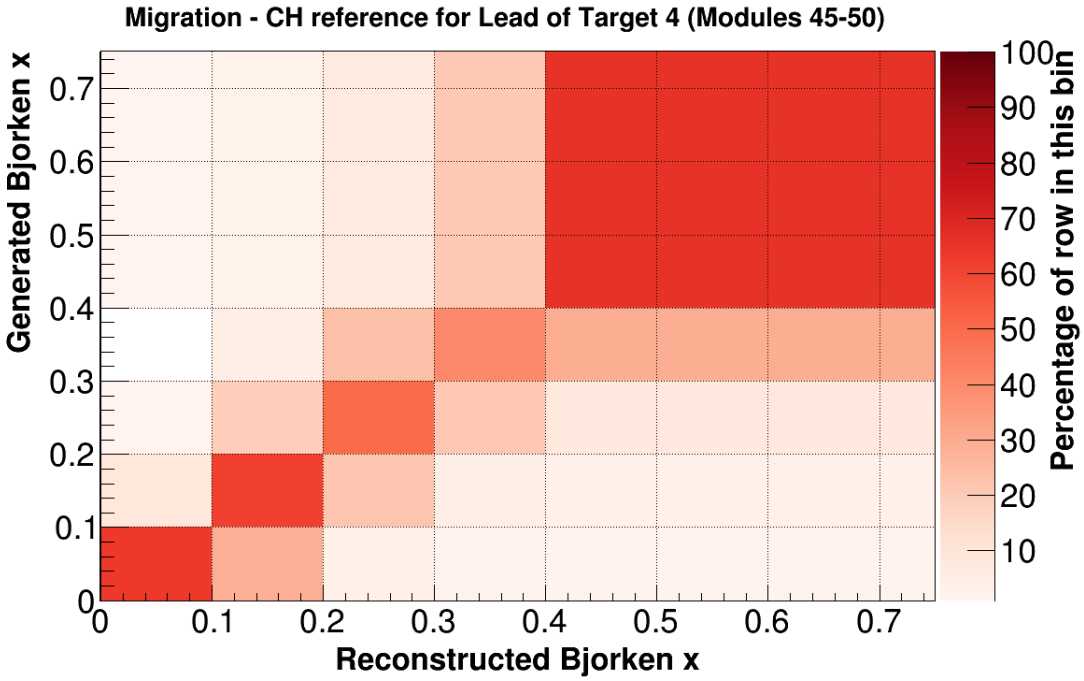

Figure D-33. Migration matrix: tracker mods. 45-50 (x_{bj})

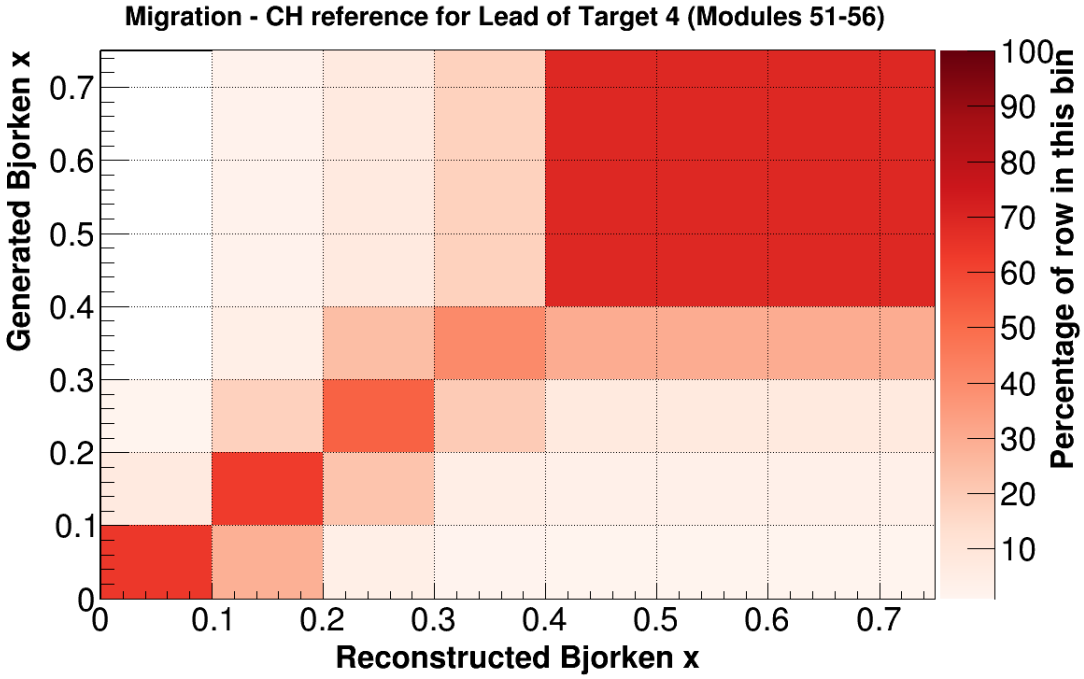

Figure D-34. Migration matrix: tracker mods. 51-56 (x_{bj})

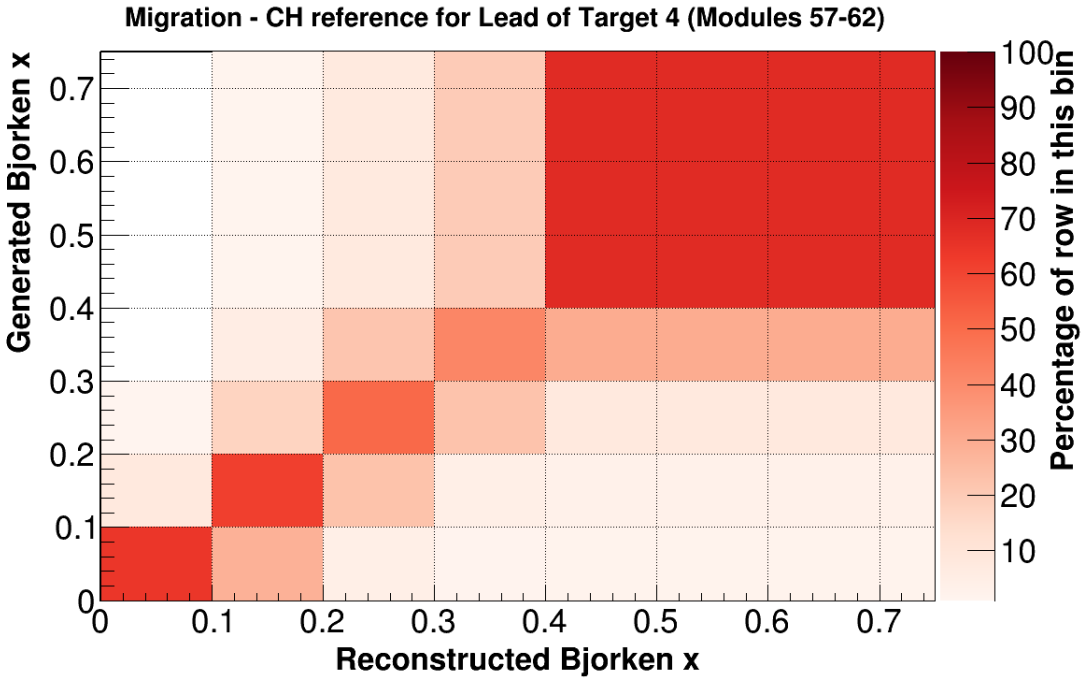

Figure D-35. Migration matrix: tracker mods. 57-62 (x_{bj})

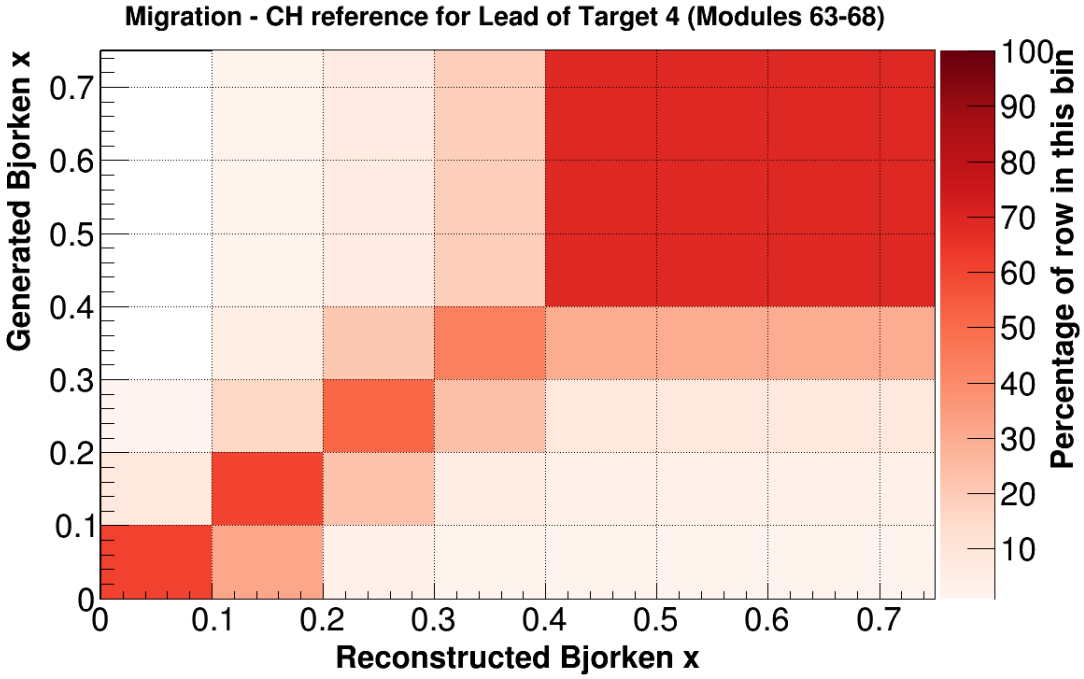

Figure D-36. Migration matrix: tracker mods. 63-68 (x_{bj})

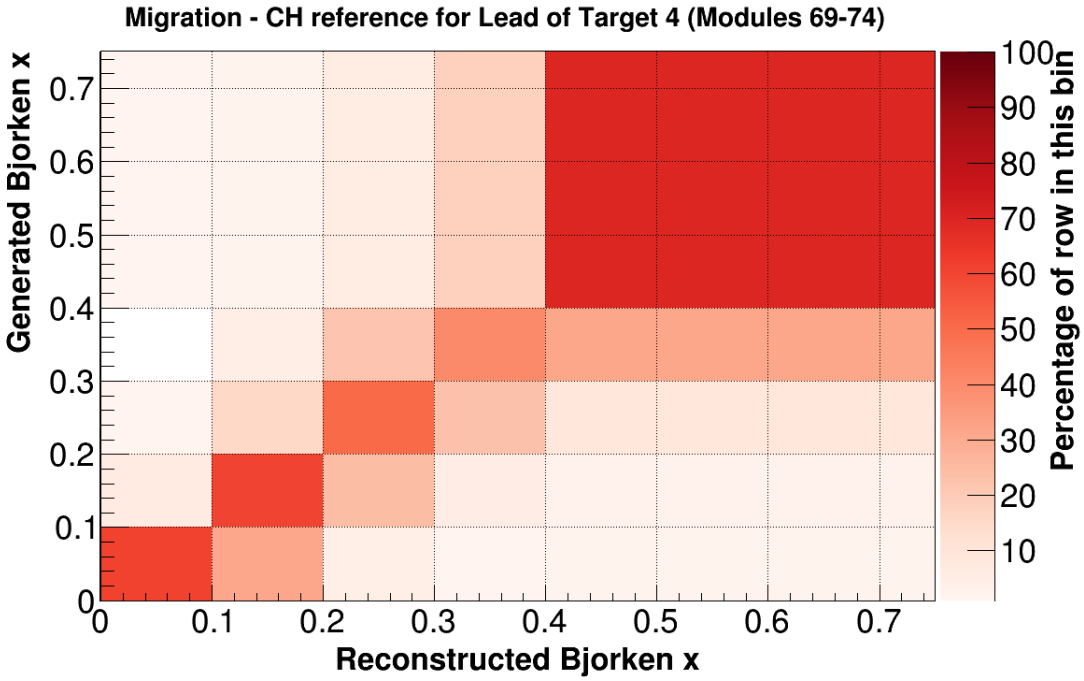

Figure D-37. Migration matrix: tracker mods. 69-74 (x_{bj})

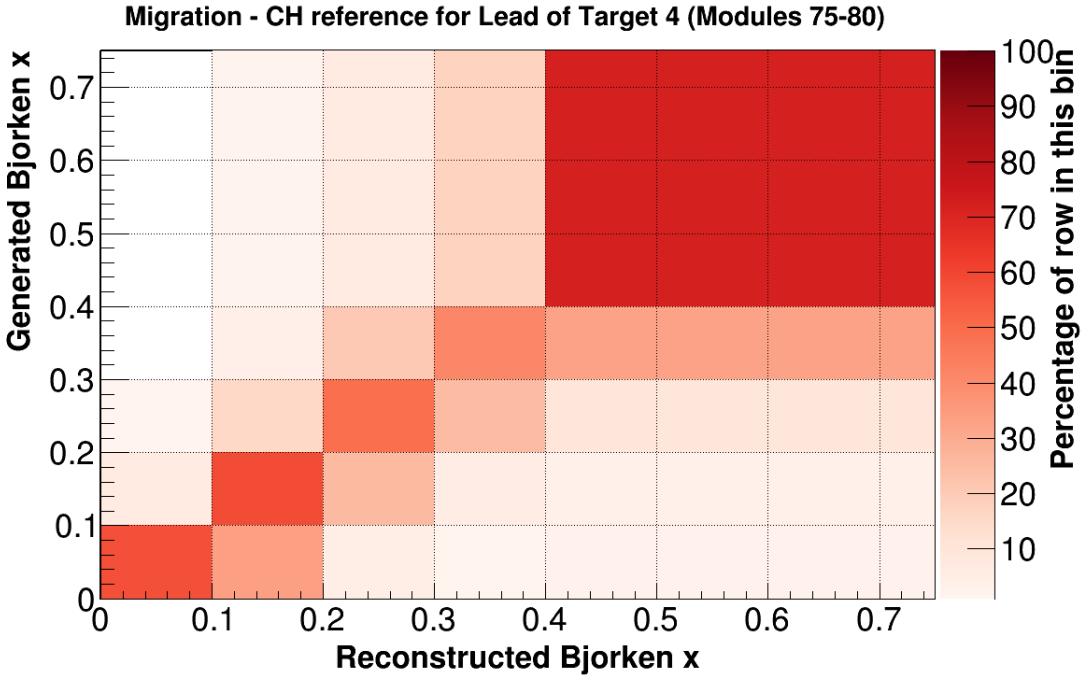

Figure D-38. Migration matrix: tracker mods. 75-80 (x_{bj})

D.2 Migration Plots Bin by Bin

Migration matrices are presented for each gin of neutrino energy as 2D histograms of true E_ν (y-axis) vs. reconstructed E_ν (x-axis).

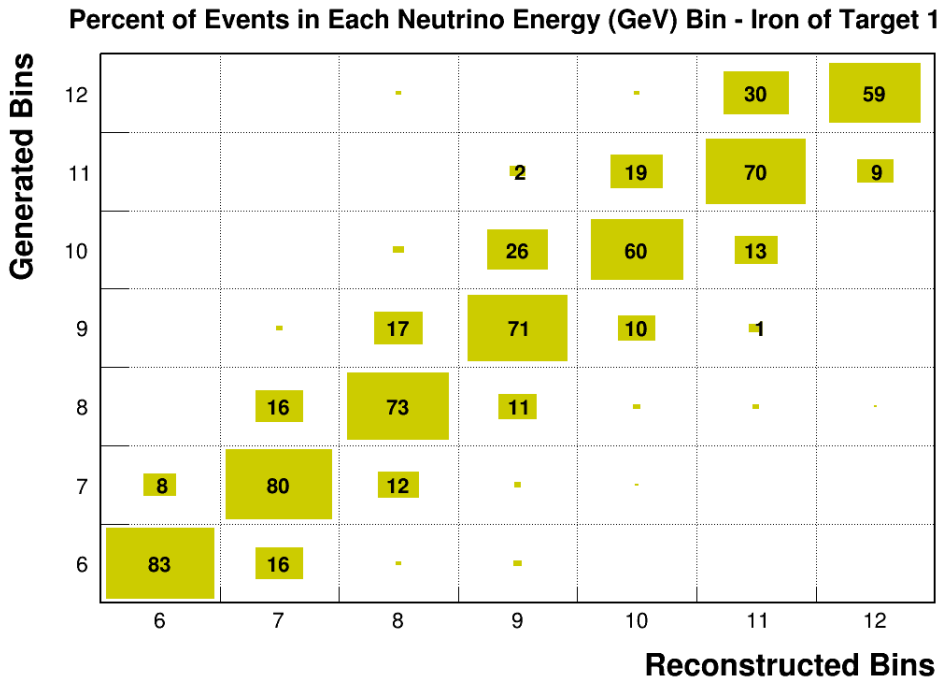

Figure D-39. Bin by bin migtation: target 01 Fe (E_ν)

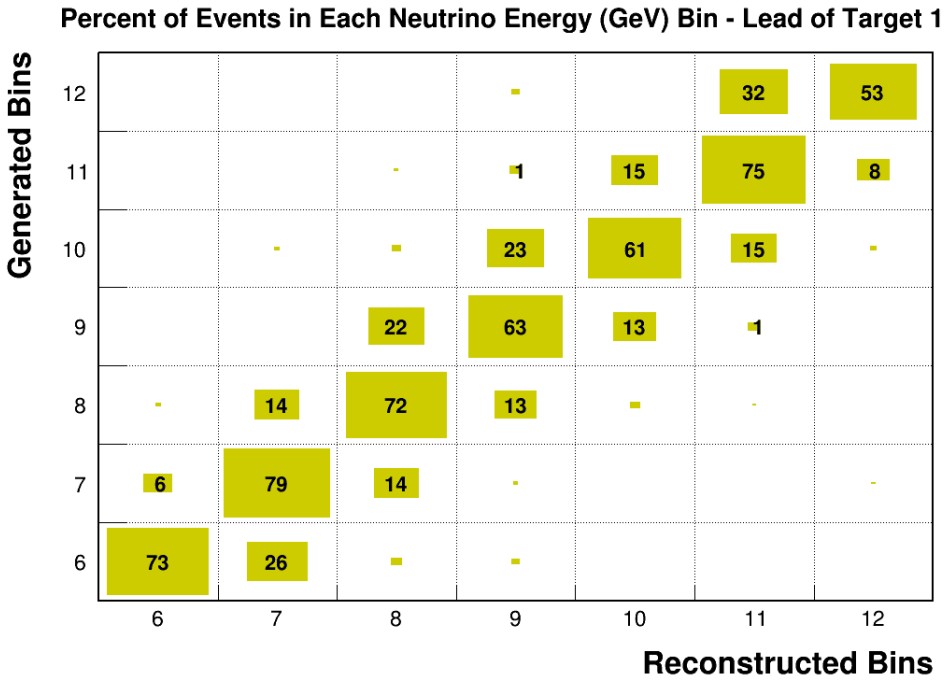

Figure D-40. Bin by bin migtation: target 01 Pb (E_ν)

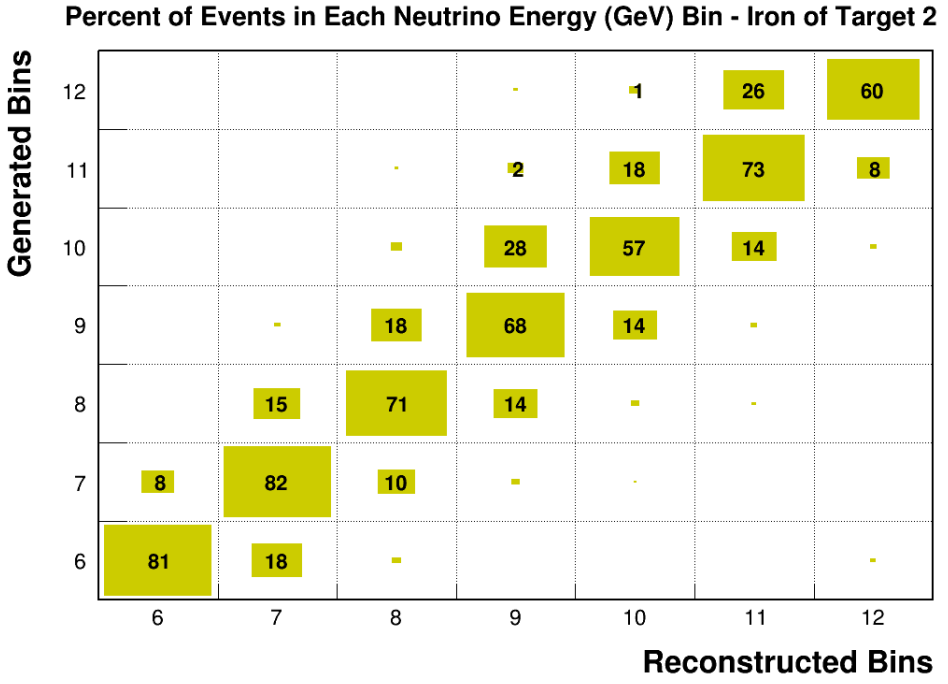

Figure D-41. Bin by bin migtation: target 02 Fe (E_ν)

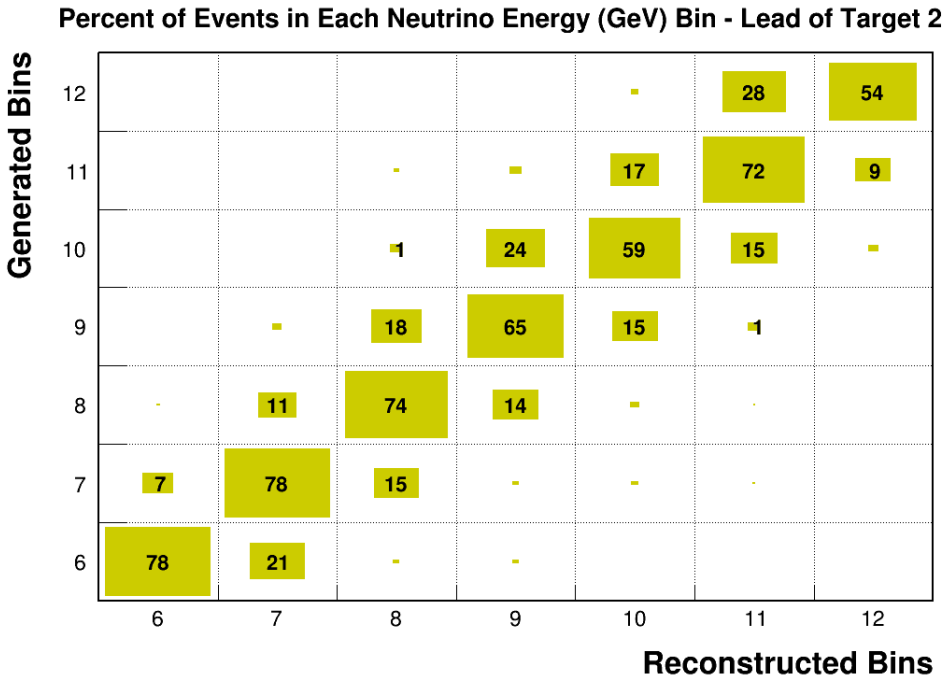

Figure D-42. Bin by bin migtation: target 02 Pb (E_ν)

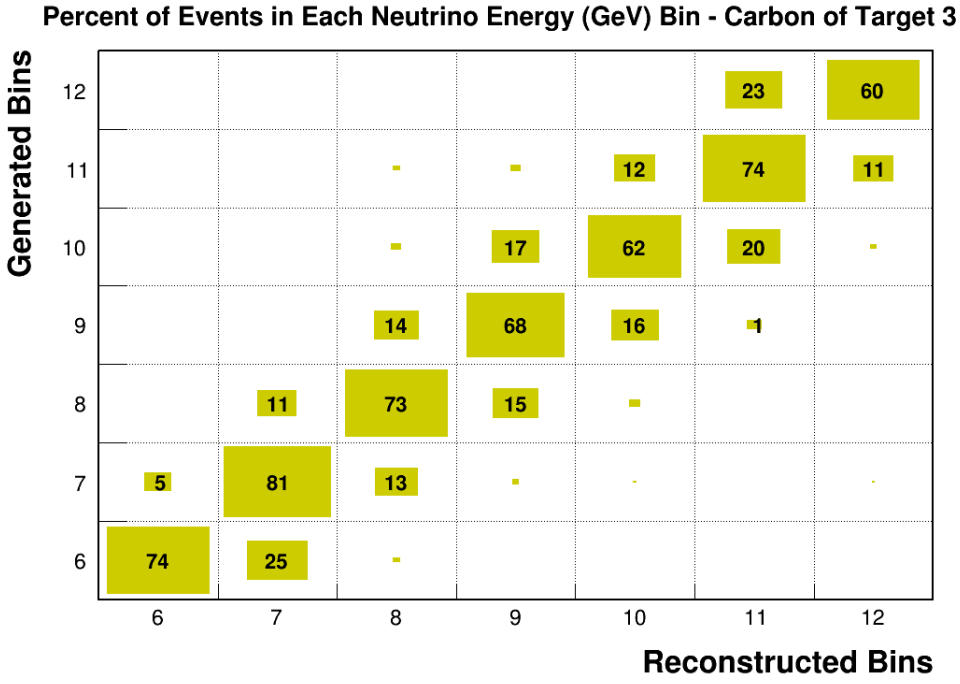

Figure D-43. Bin by bin migtation: target 03 C (E_ν)

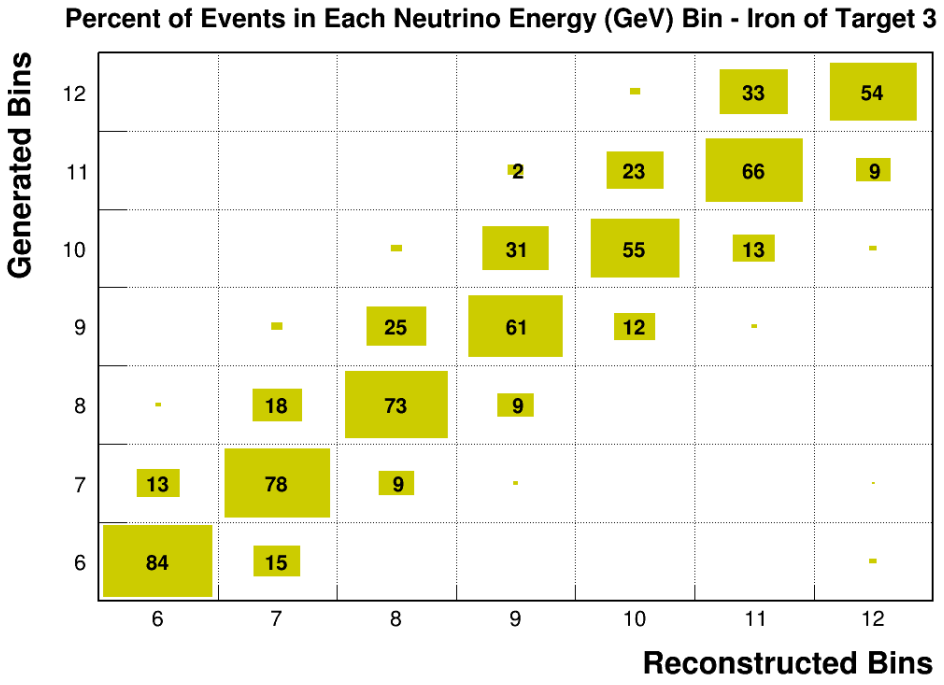

Figure D-44. Bin by bin migtation: target 03 Fe (E_ν)

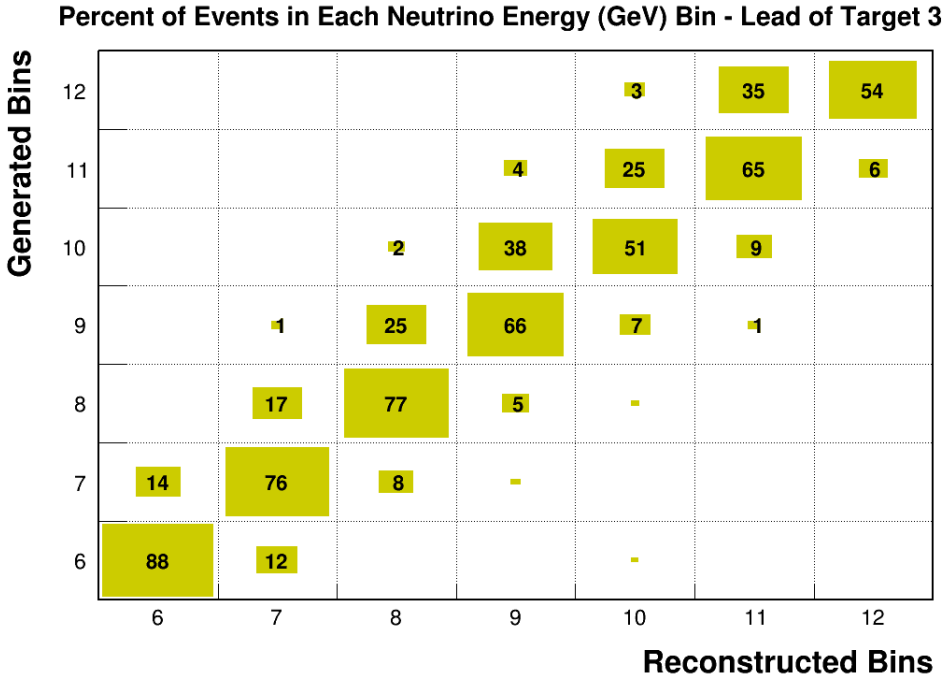

Figure D-45. Bin by bin migtation: target 03 Pb (E_ν)

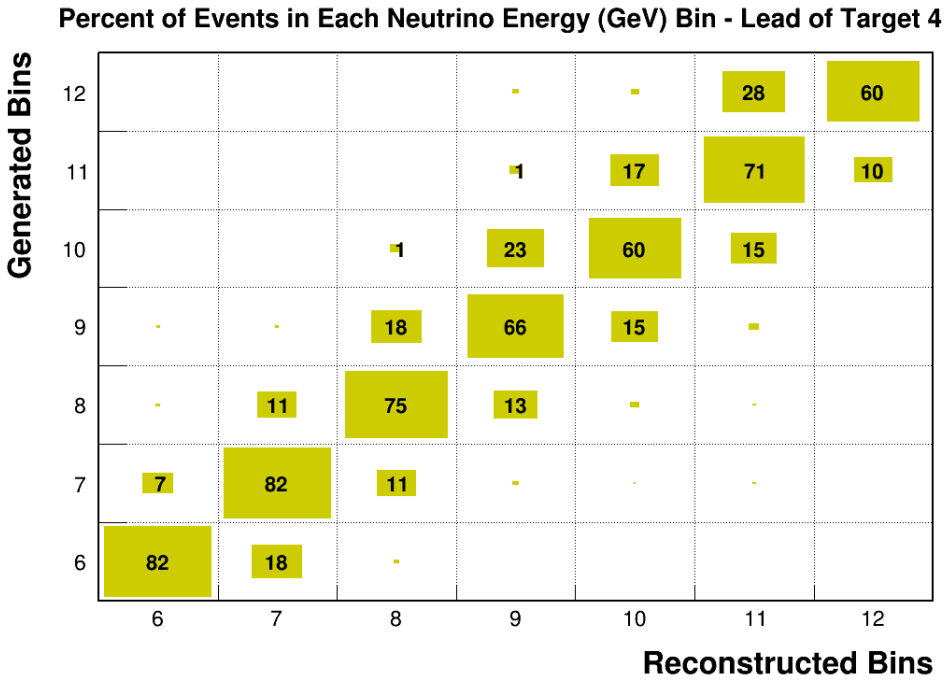

Figure D-46. Bin by bin migtation: target 04 Pb (E_ν)

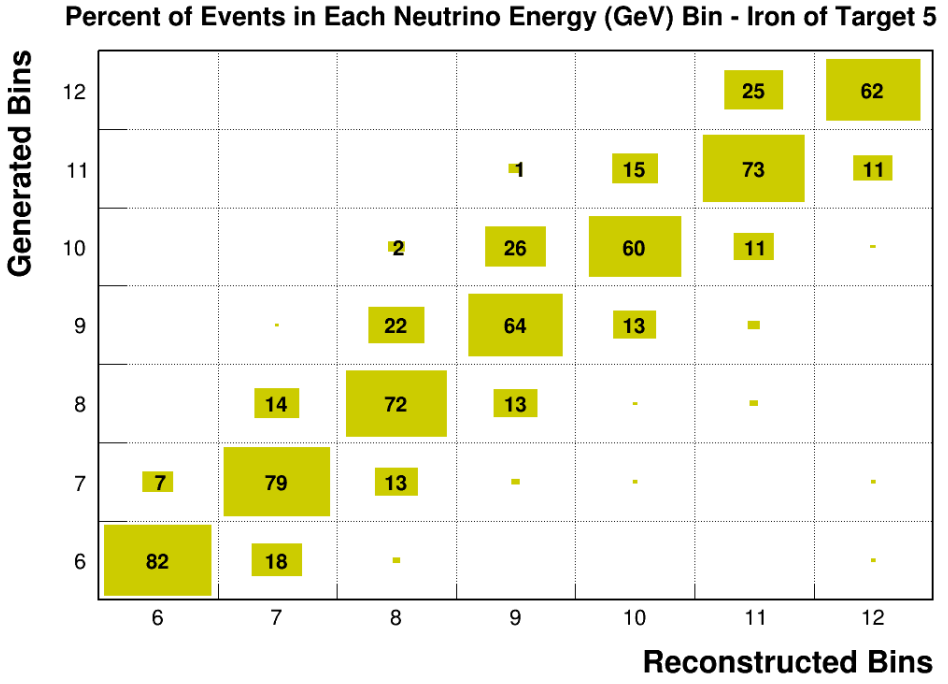

Figure D-47. Bin by bin migtation: target 05 Fe (E_ν)

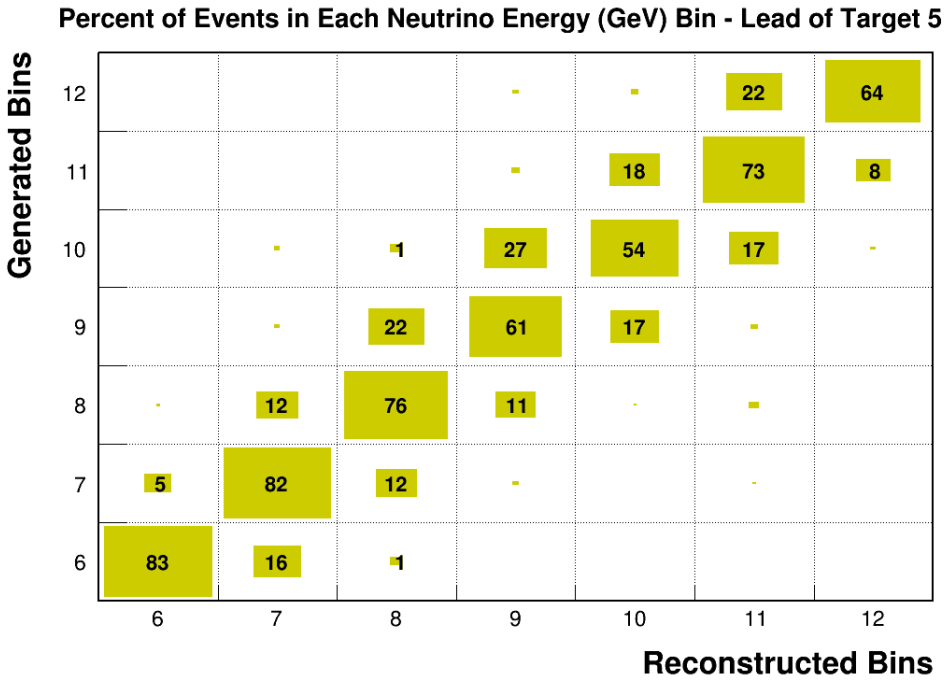

Figure D-48. Bin by bin migtation: target 05 Pb (E_ν)

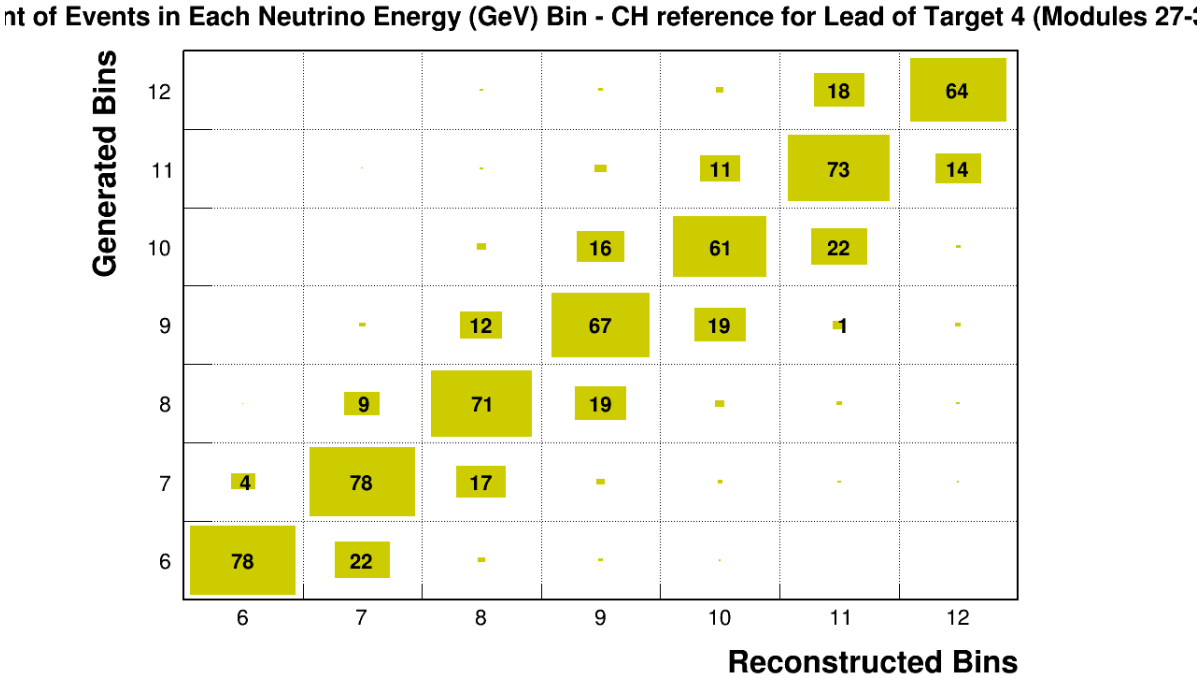

Figure D-49. Bin by bin migtation: tracker mods. 27-32 (E_ν)

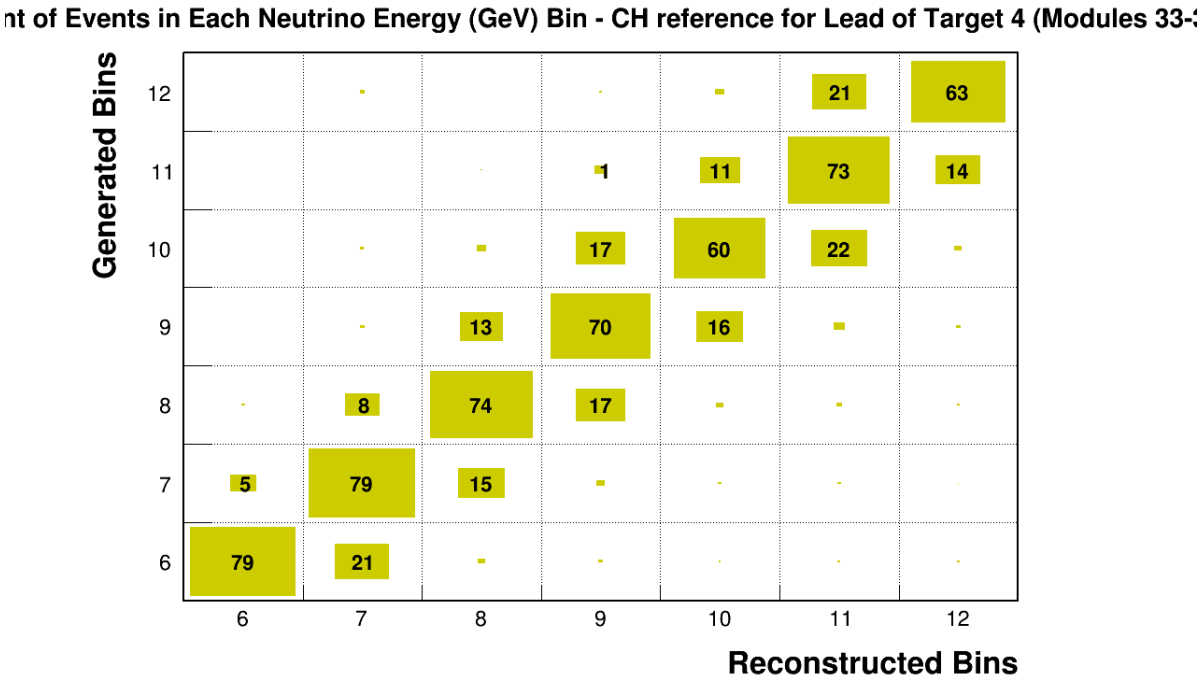

Figure D-50. Bin by bin migtation: tracker mods. 33-38 (E_ν)

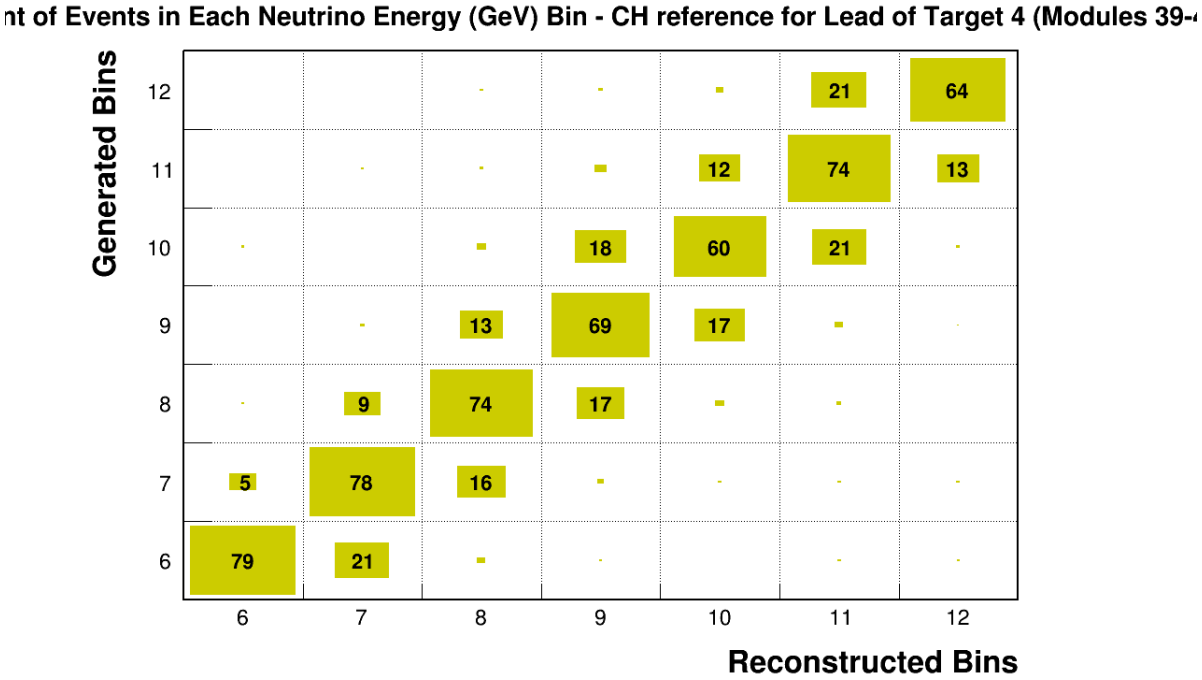

Figure D-51. Bin by bin migtation: tracker mods. 39-44 (E_ν)

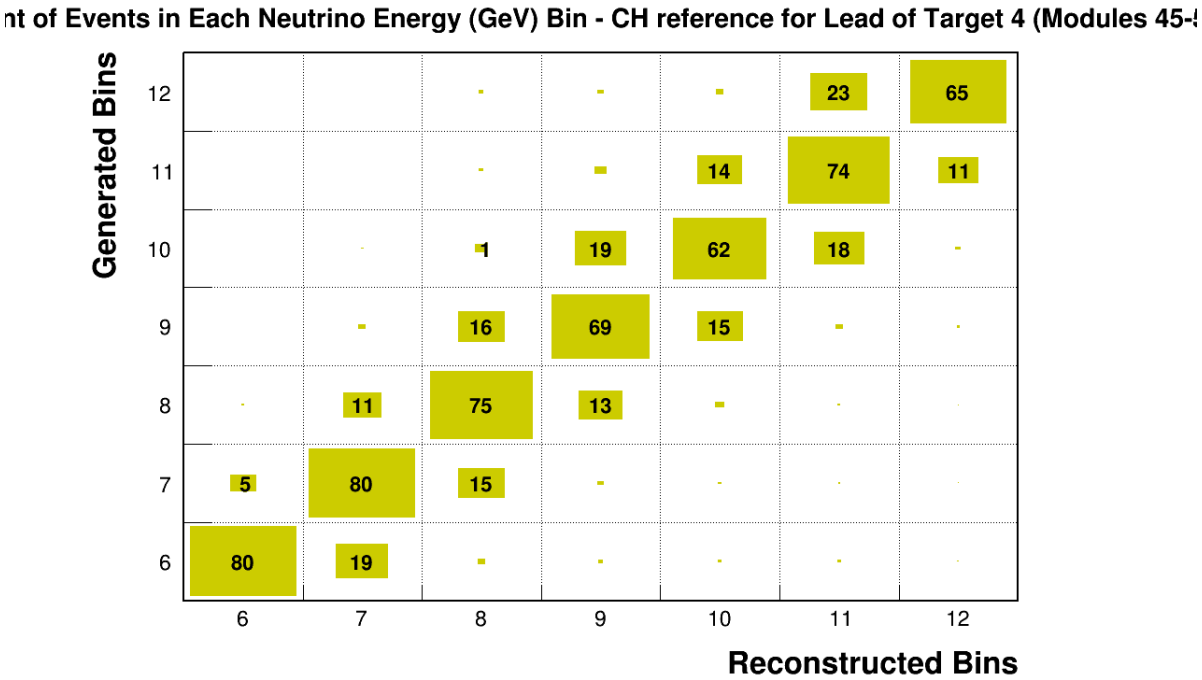

Figure D-52. Bin by bin migtation: tracker mods. 45-50 (E_ν)

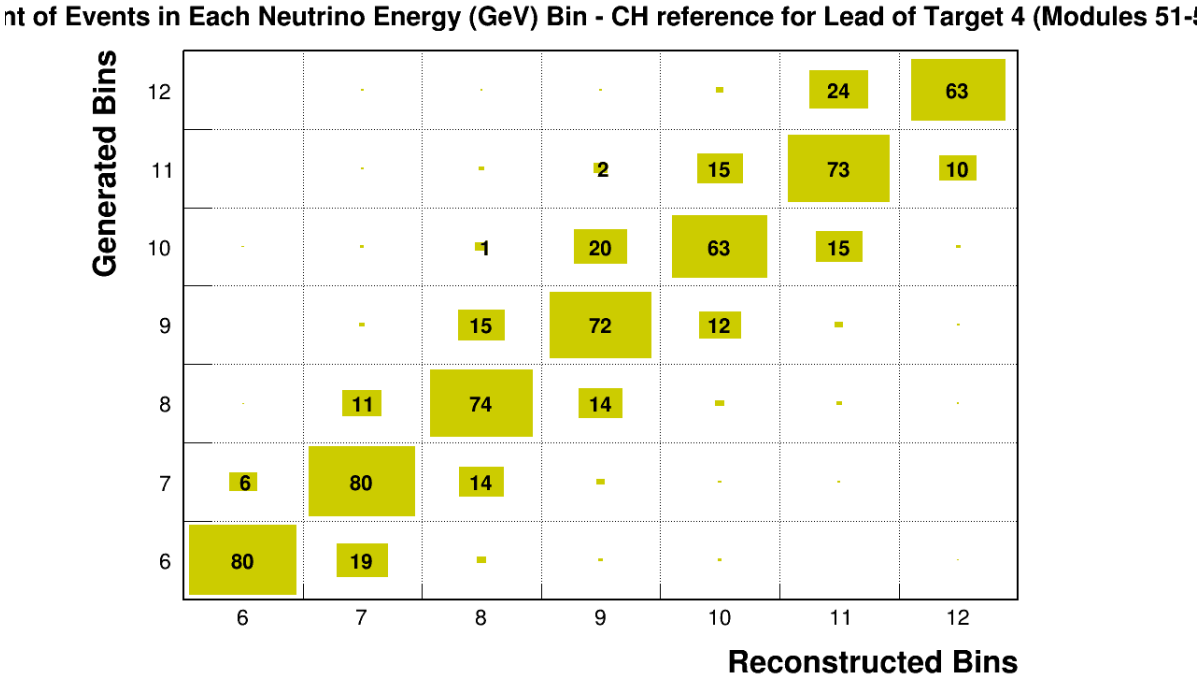

Figure D-53. Bin by bin migtation: tracker mods. 51-56 (E_ν)

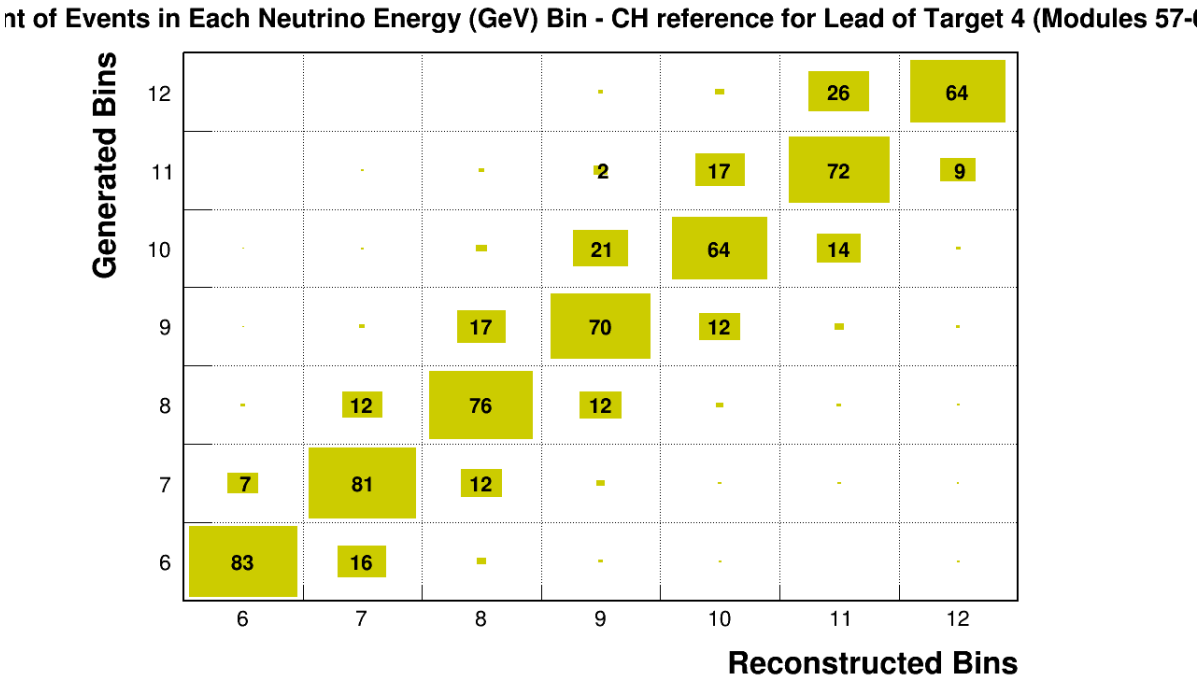

Figure D-54. Bin by bin migtation: tracker mods. 57-62 (E_ν)

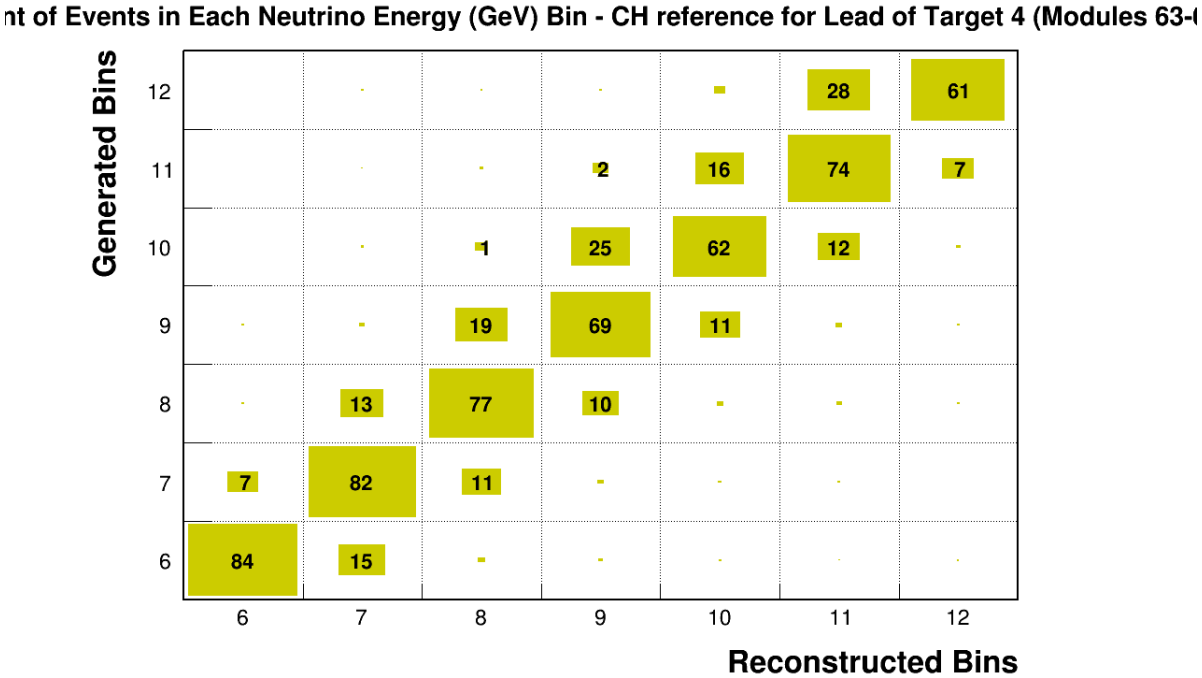

Figure D-55. Bin by bin migtation: tracker mods. 63-68 (E_ν)

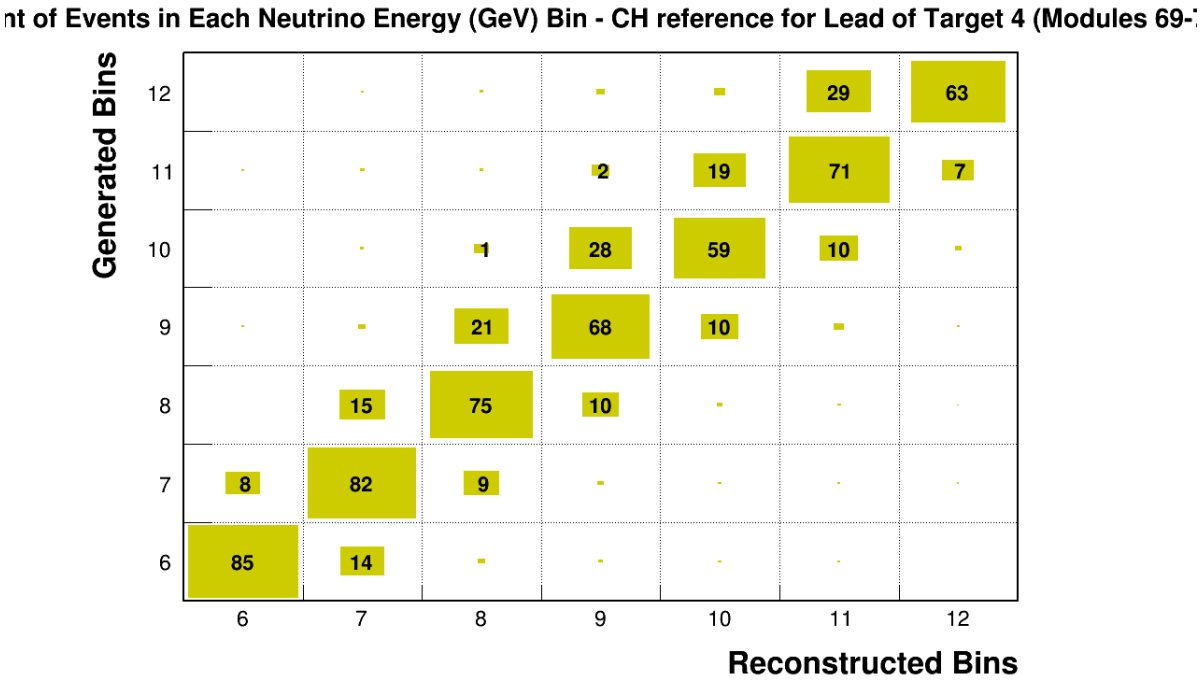

Figure D-56. Bin by bin migtation: tracker mods. 69-74 (E_ν)

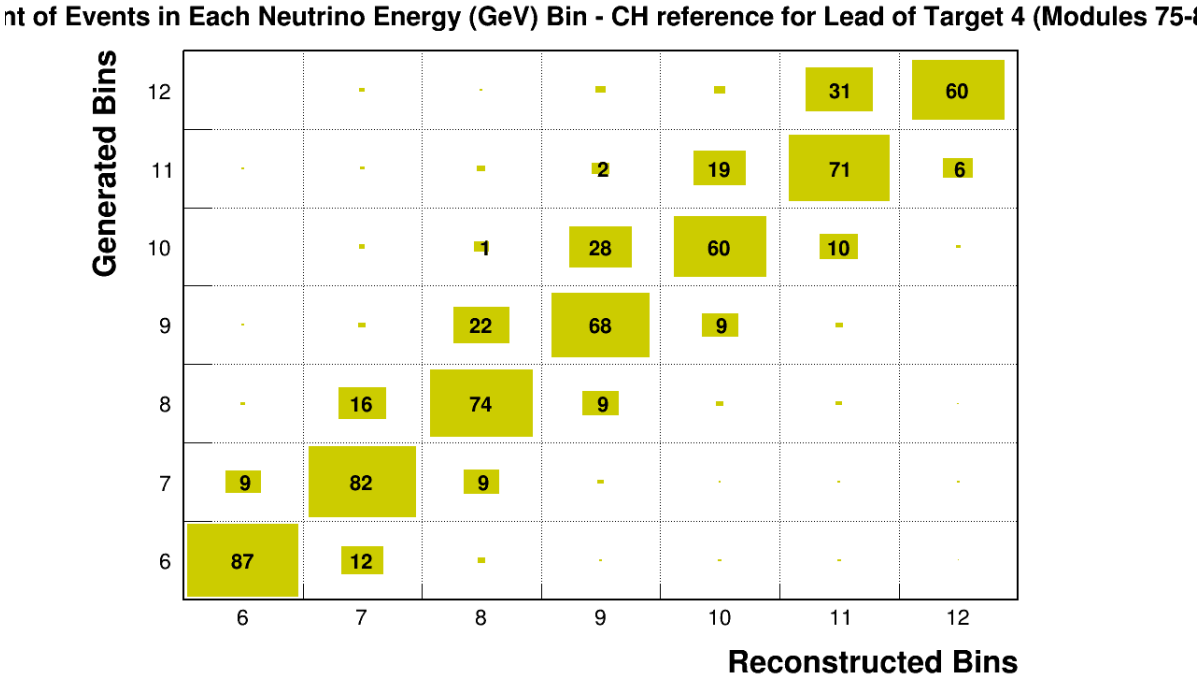

Figure D-57. Bin by bin migtation: tracker mods. 75-80 (E_ν)

Migration matrices are presented for each gin of neutrino energy as 2D histograms of true x_{bj} (y-axis) vs. reconstructed x_{bj} (x-axis). These plots include the reconstructed overflow bin:

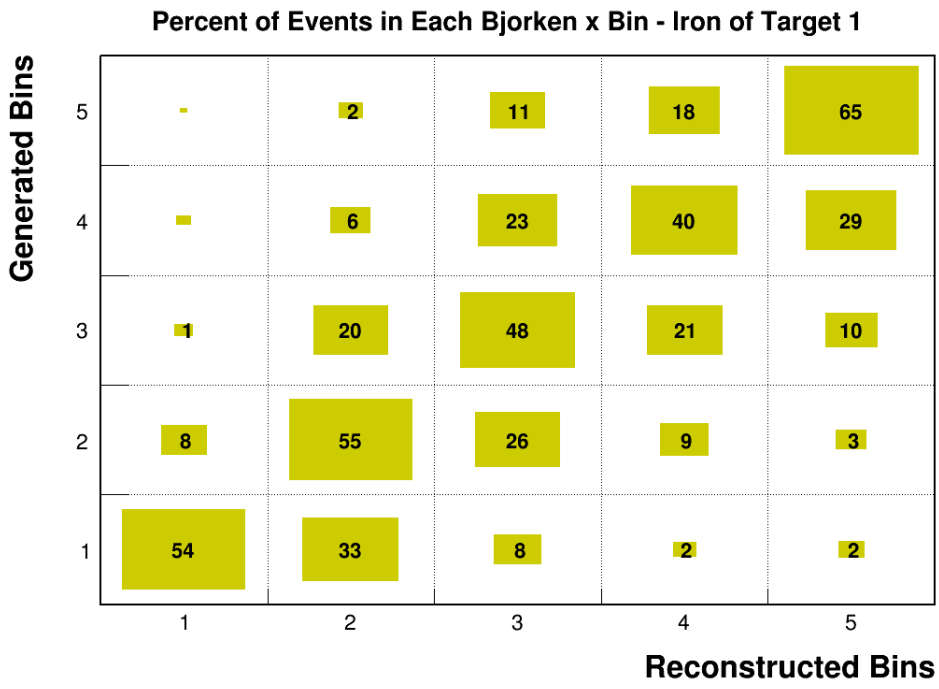

Figure D-58. Bin by bin migtation: target 01 Fe (x_{bj})

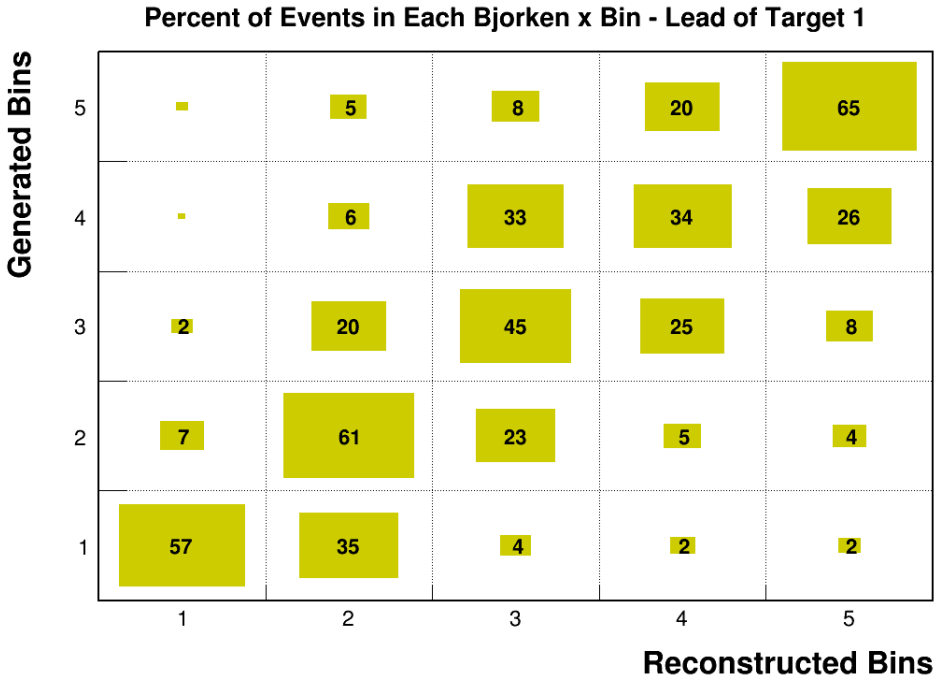

Figure D-59. Bin by bin migtation: target 01 Pb (x_{bj})

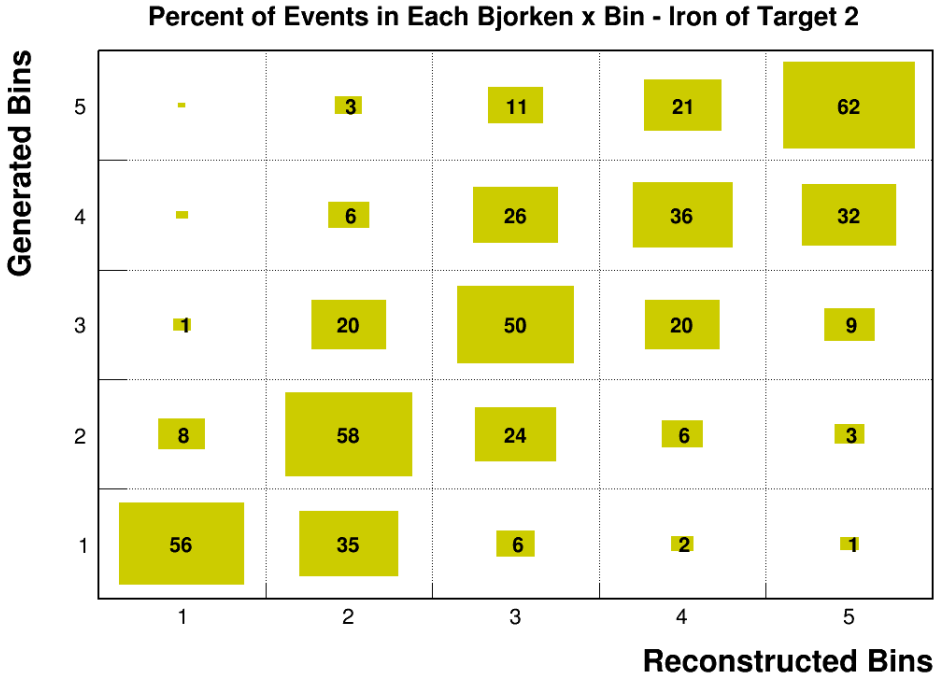

Figure D-60. Bin by bin migtation: target 02 Fe (x_{bj})

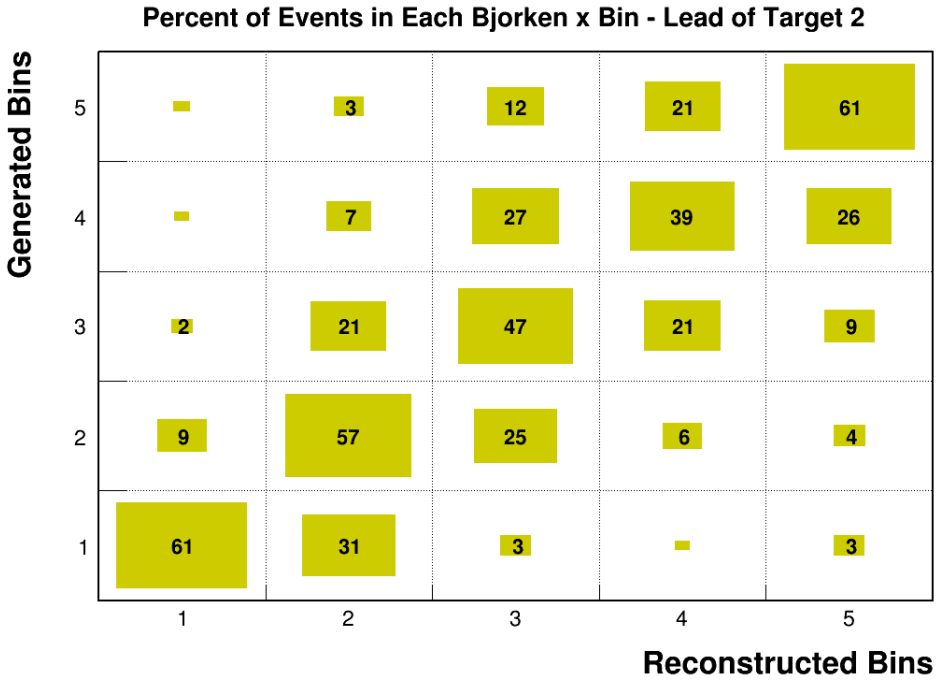

Figure D-61. Bin by bin migtation: target 02 Pb (x_{bj})

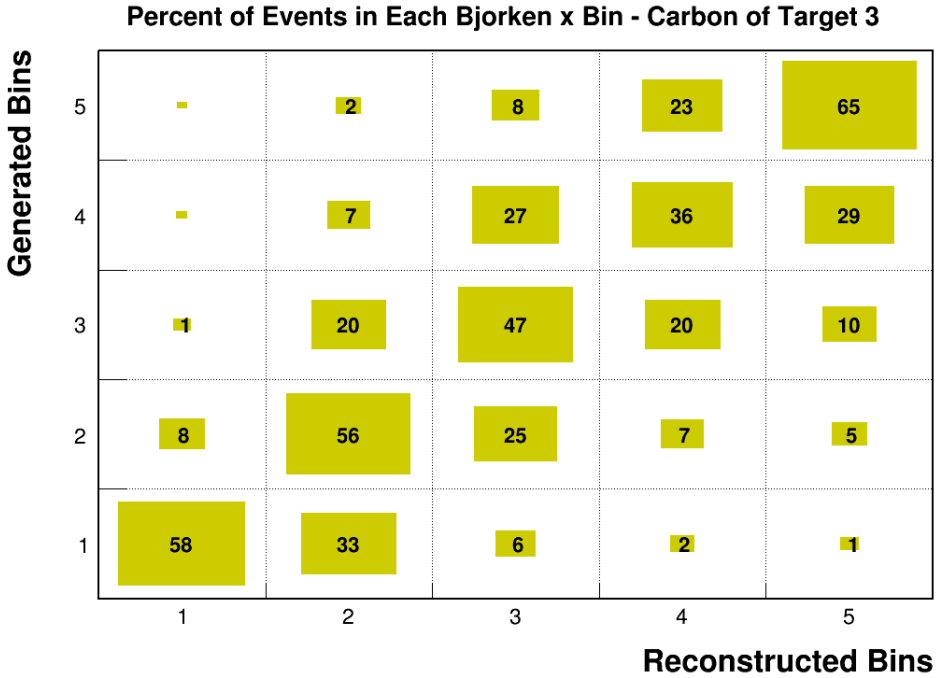

Figure D-62. Bin by bin migtation: target 03 C (x_{bj})

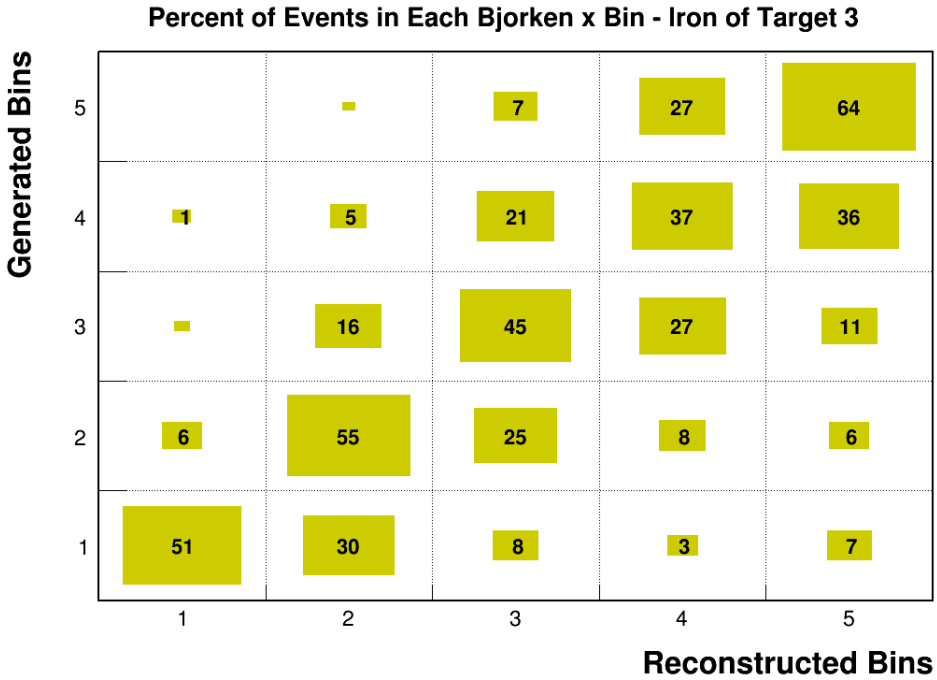

Figure D-63. Bin by bin migtation: target 03 Fe (x_{bj})

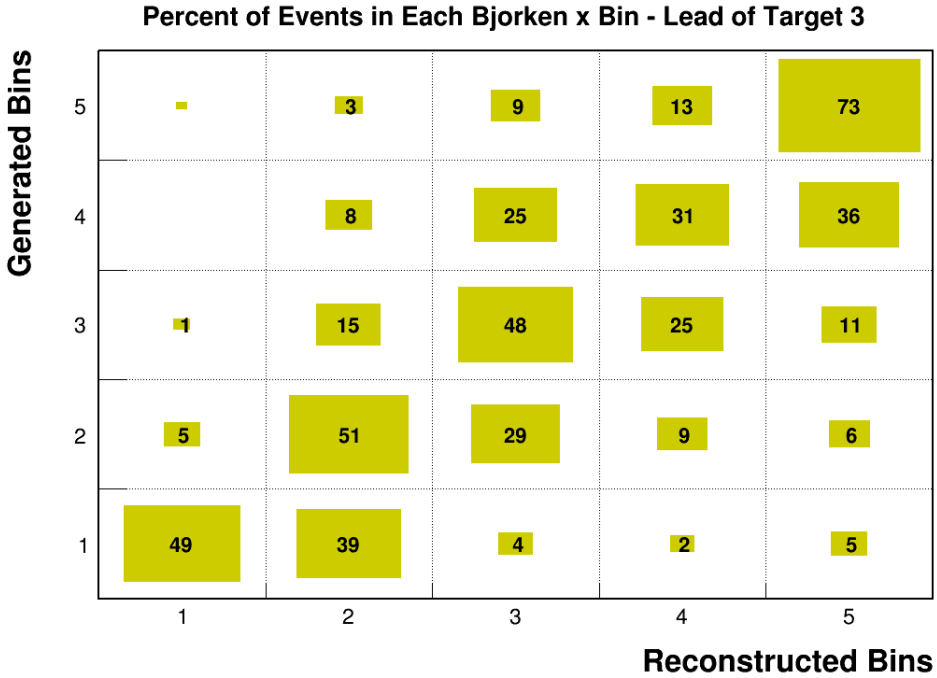

Figure D-64. Bin by bin migtation: target 03 Pb (x_{bj})

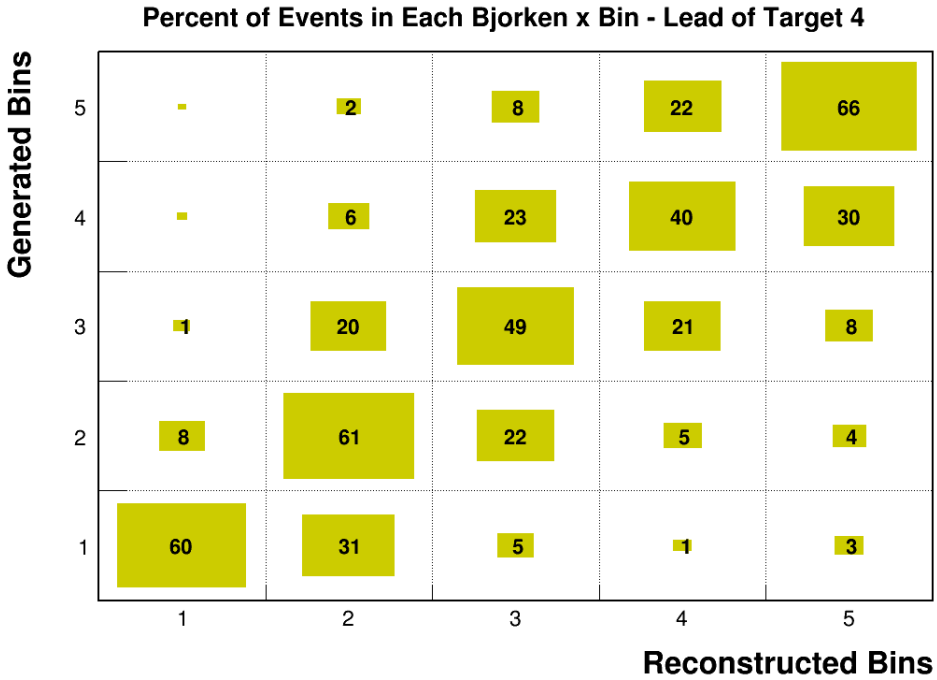

Figure D-65. Bin by bin migtation: target 04 Pb (x_{bj})

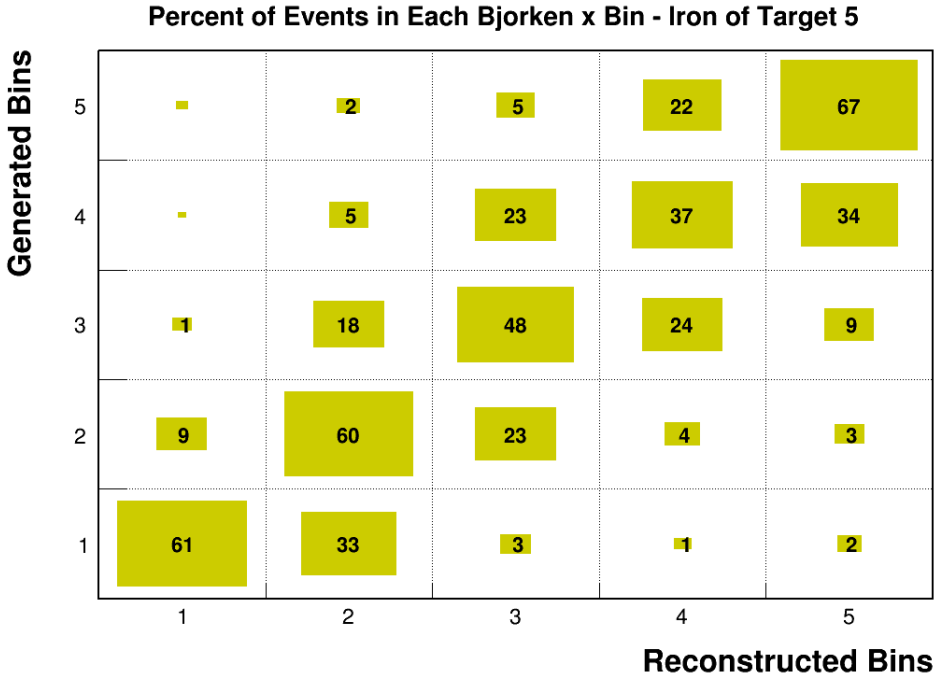

Figure D-66. Bin by bin migtation: target 05 Fe (x_{bj})

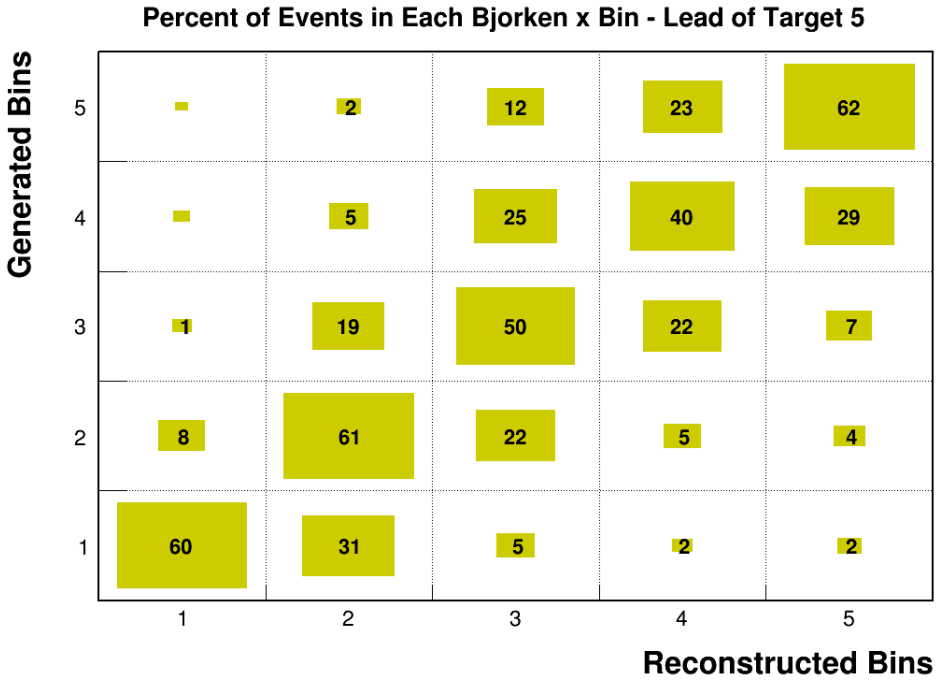

Figure D-67. Bin by bin migtation: target 05 Pb (x_{bj})

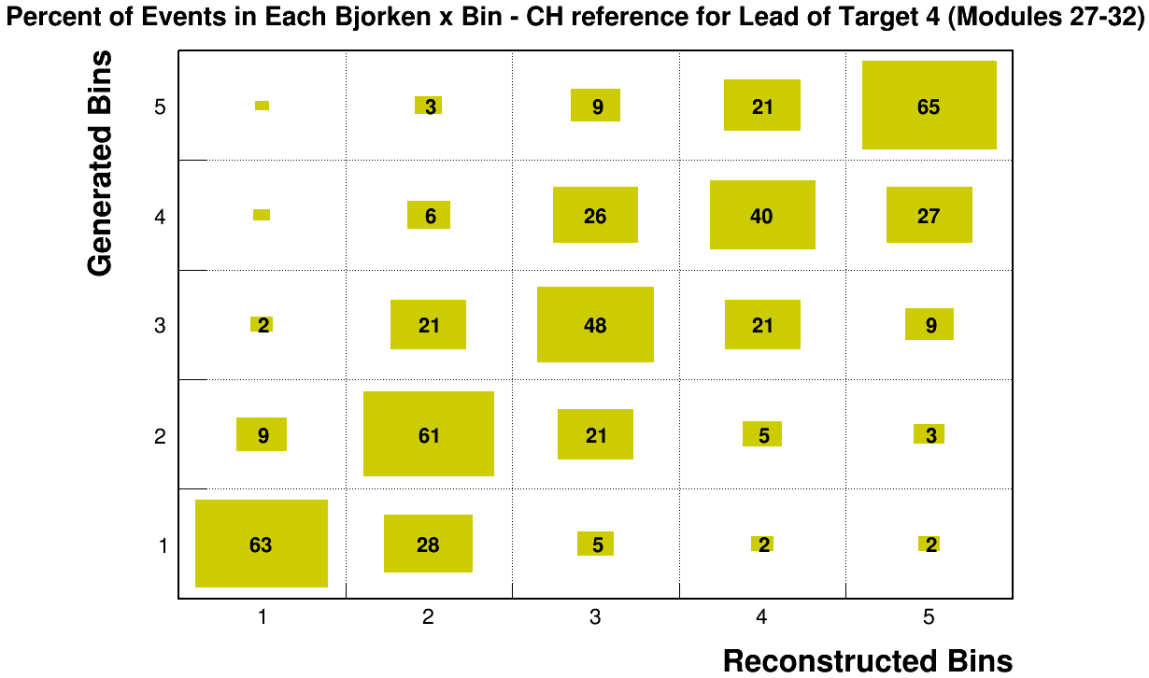

Figure D-68. Bin by bin migtation: tracker mods. 27-32 (x_{bj})

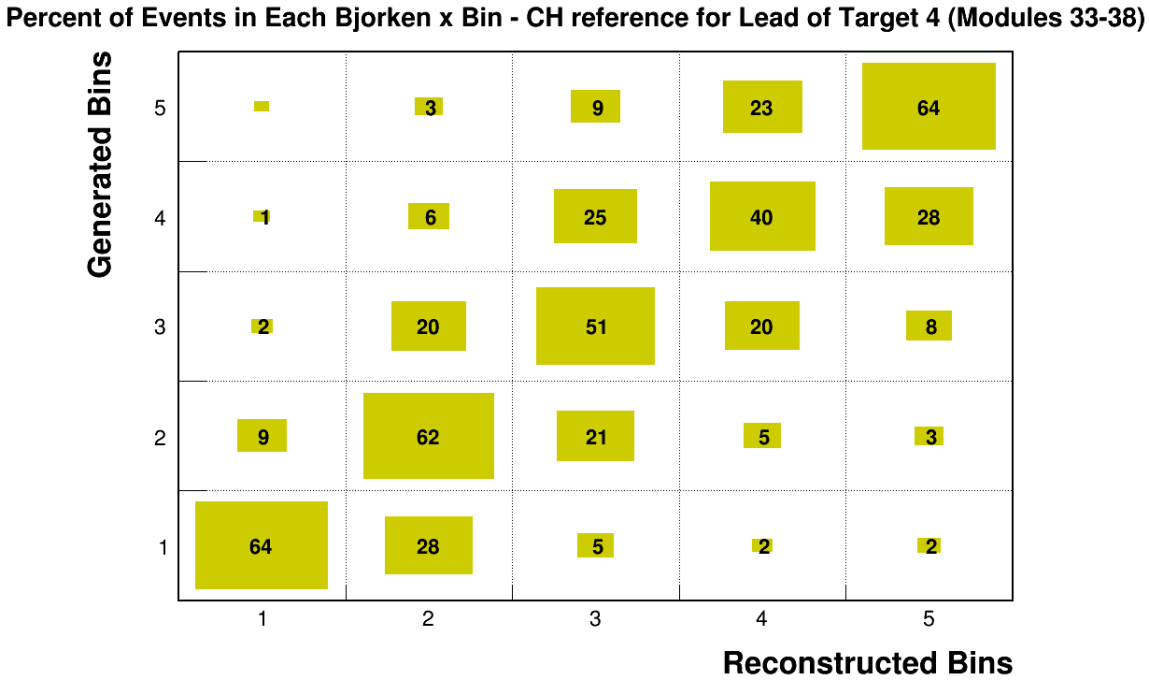

Figure D-69. Bin by bin migtation: tracker mods. 33-38 (x_{bj})

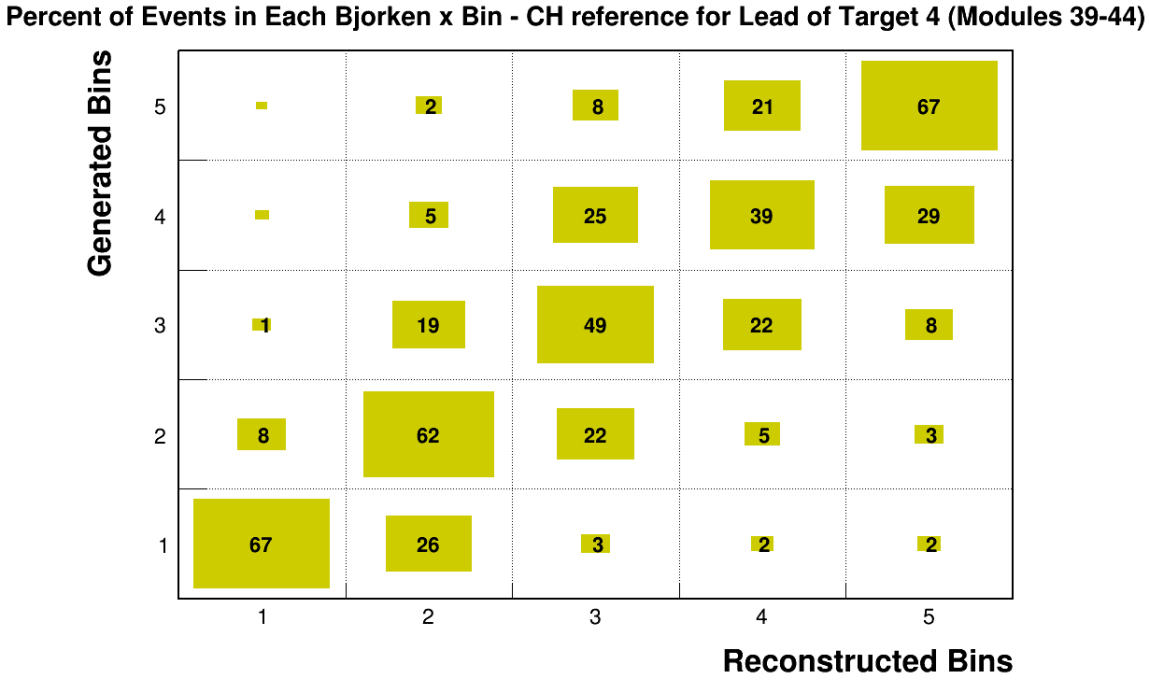

Figure D-70. Bin by bin migtation: tracker mods. 39-44 (x_{bj})

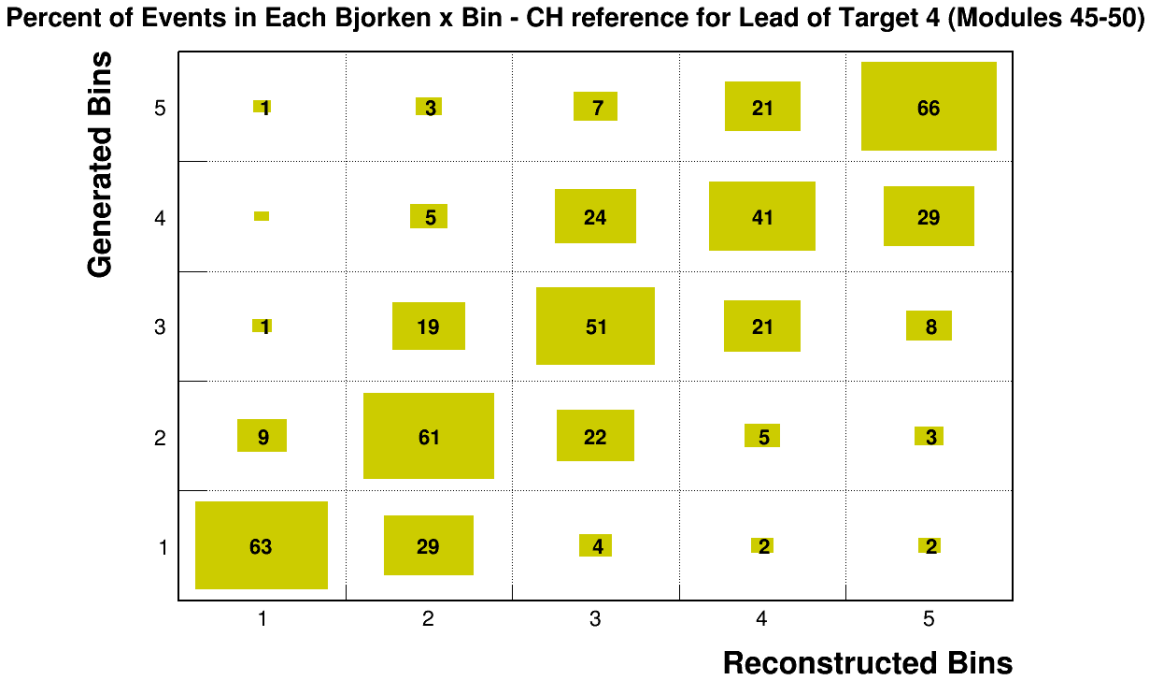

Figure D-71. Bin by bin migtation: tracker mods. 45-50 (x_{bj})

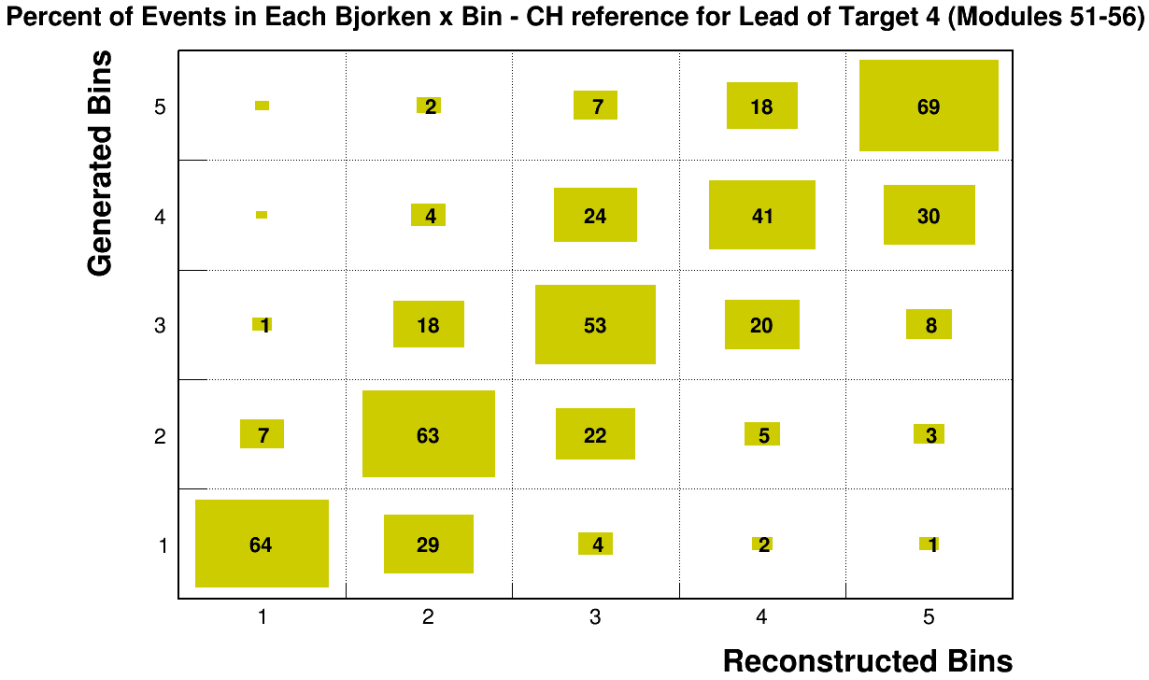

Figure D-72. Bin by bin migtation: tracker mods. 51-56 (x_{bj})

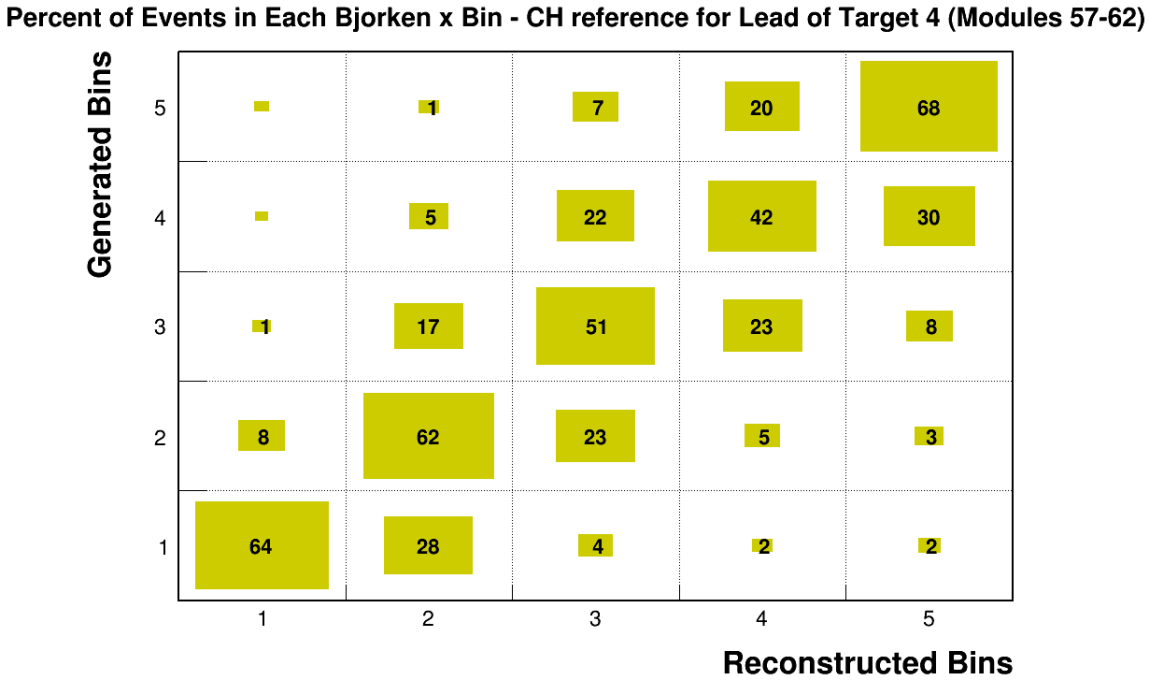

Figure D-73. Bin by bin migtation: tracker mods. 57-62 (x_{bj})

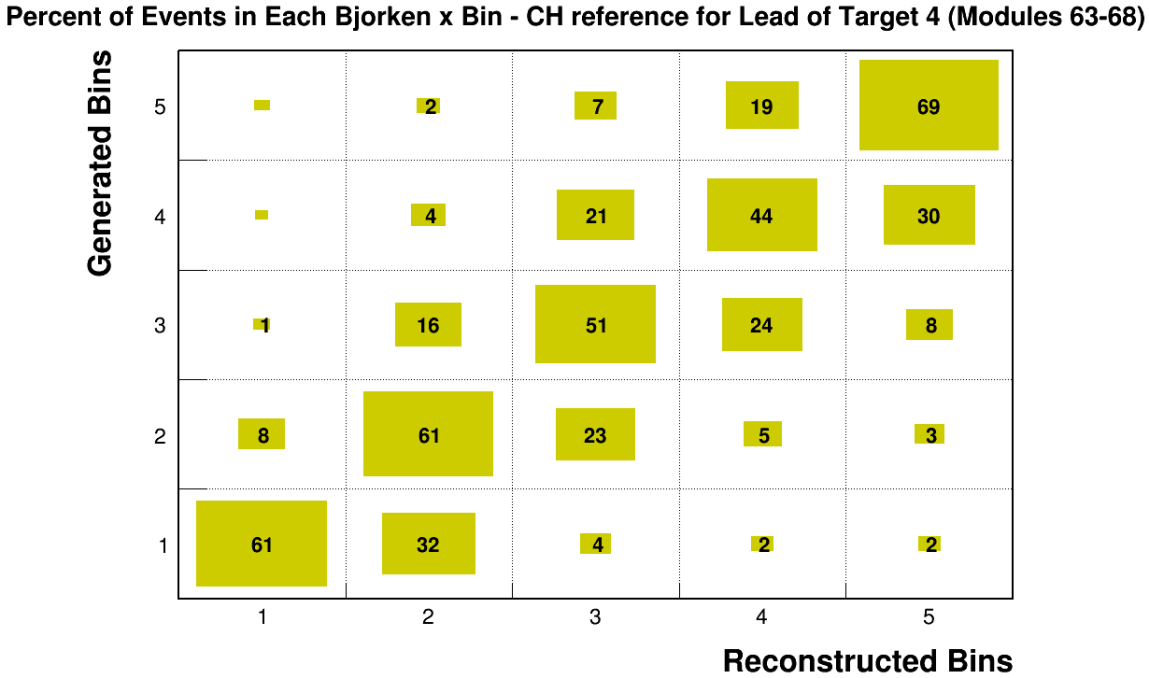

Figure D-74. Bin by bin migtation: tracker mods. 63-68 (x_{bj})

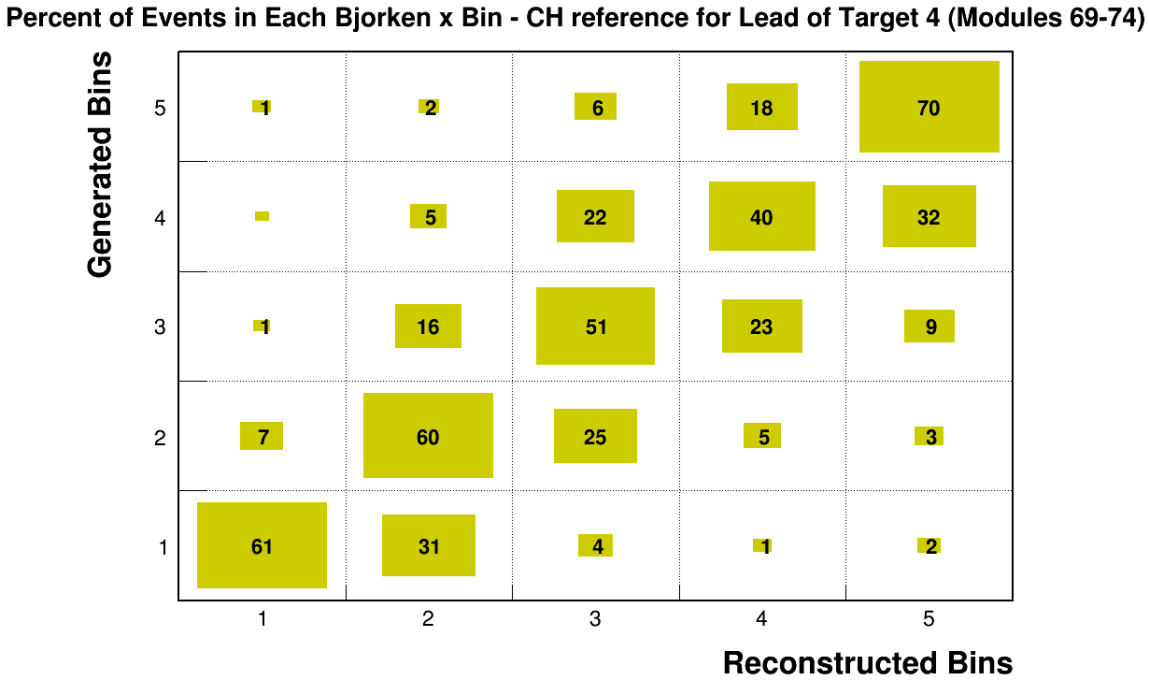

Figure D-75. Bin by bin migtation: tracker mods. 69-74 (x_{bj})

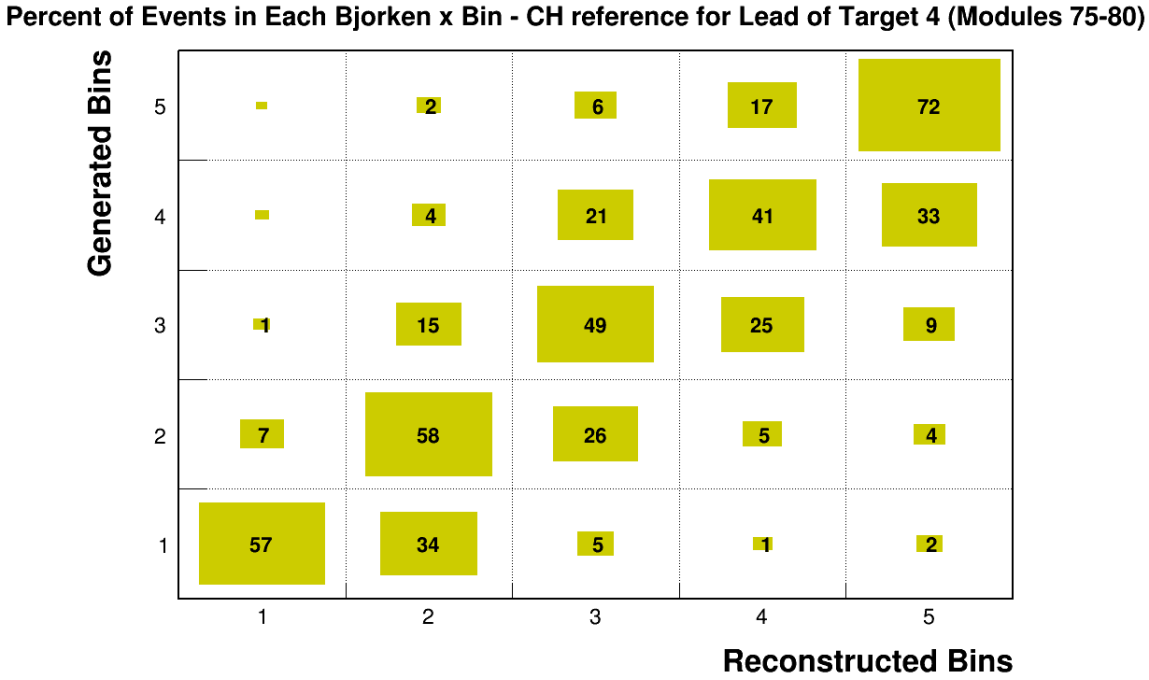

Figure D-76. Bin by bin migtation: tracker mods. 75-80 (x_{bj})

APPENDIX E
EVENT YIELDS (RECONSTRUCTED)

E.1 DIS Event Yields Before CH Subtraction

The following plots show the DIS events in data and MC, after subtracting the non-DIS events. The sample is broken down by target events and events in the predicted events in the surrounding CH. They are plotted as a function of neutrino energy (E_ν):

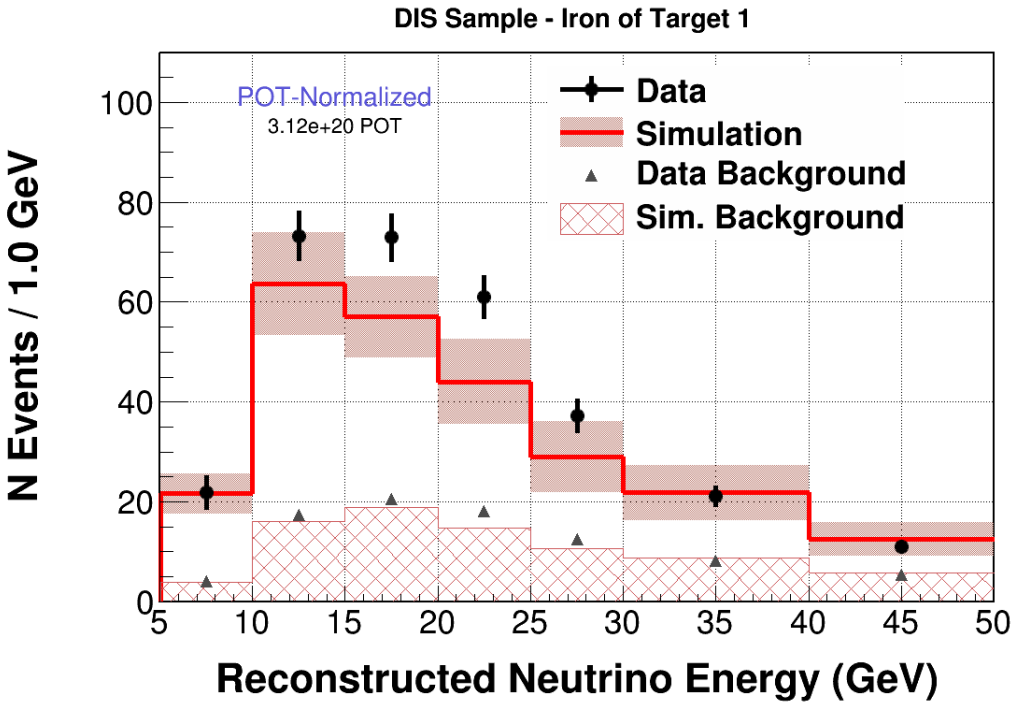

Figure E-1. DIS signal and CH background: target 01 Fe (E_ν)

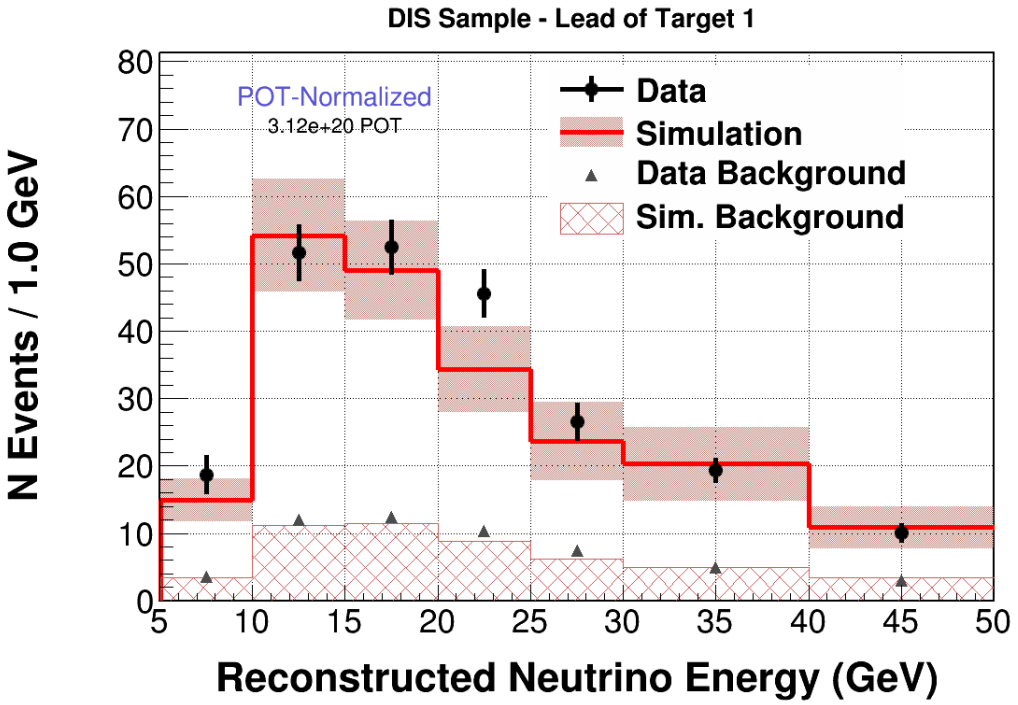

Figure E-2. DIS signal and CH background: target 01 Pb (E_ν)

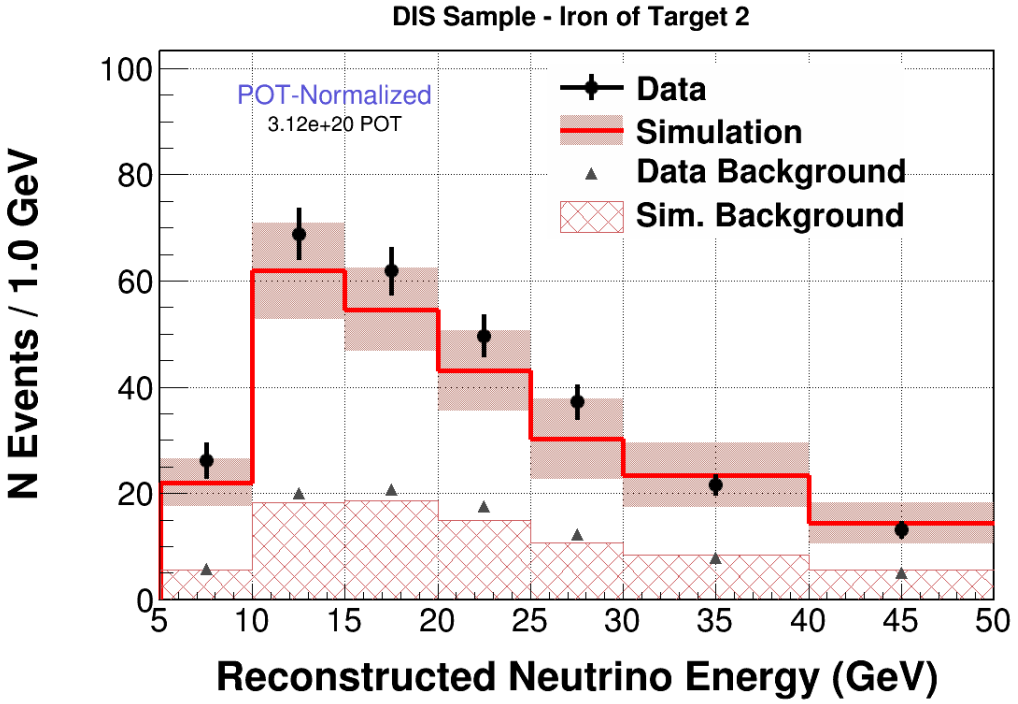

Figure E-3. DIS signal and CH background: target 02 Fe (E_ν)

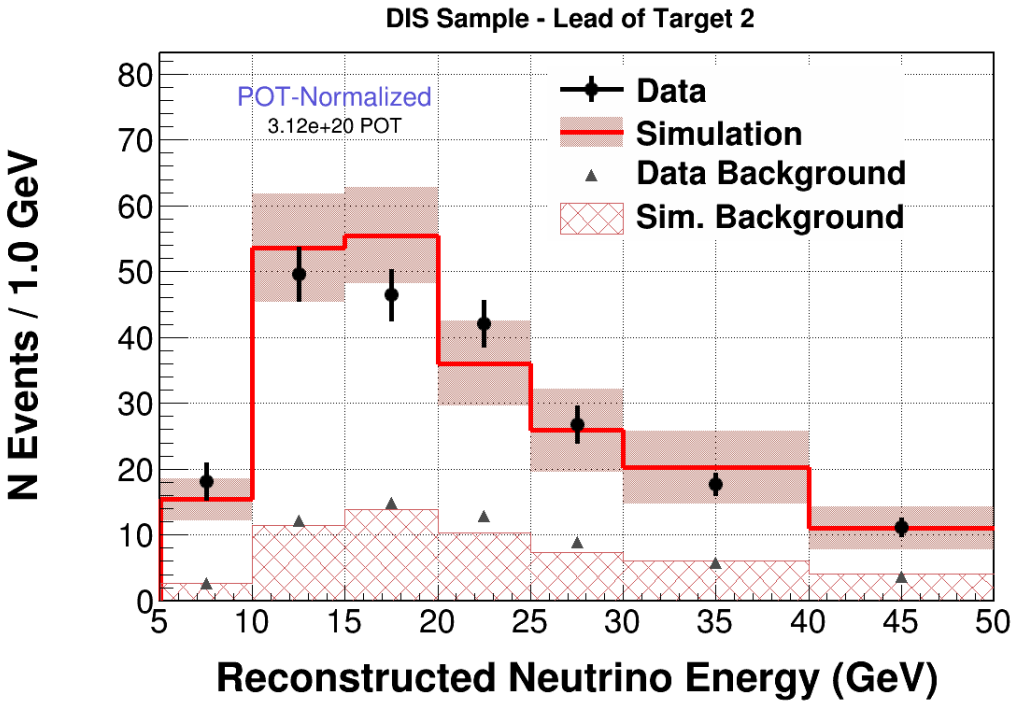

Figure E-4. DIS signal and CH background: target 02 Pb (E_ν)

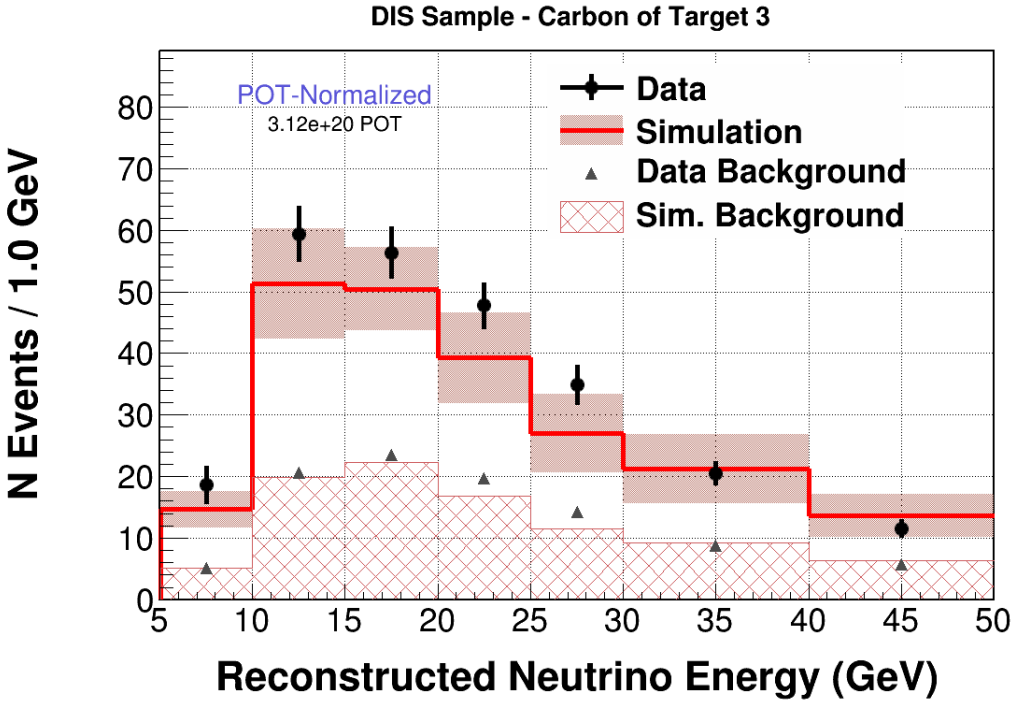

Figure E-5. DIS signal and CH background: target 03 C (E_ν)

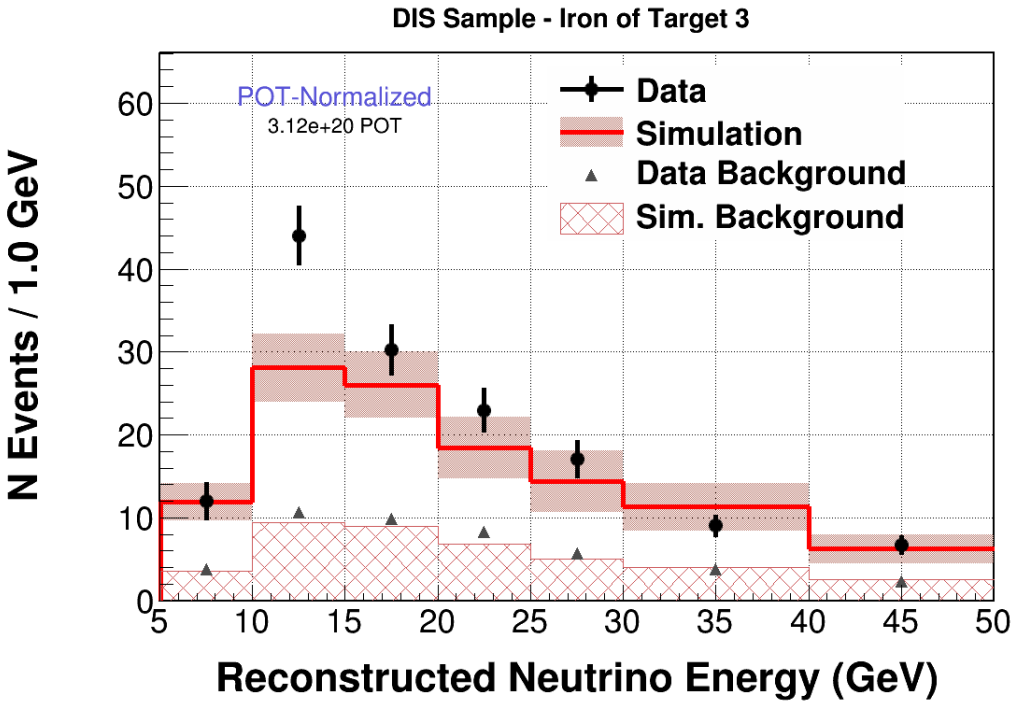

Figure E-6. DIS signal and CH background: target 03 Fe (E_ν)

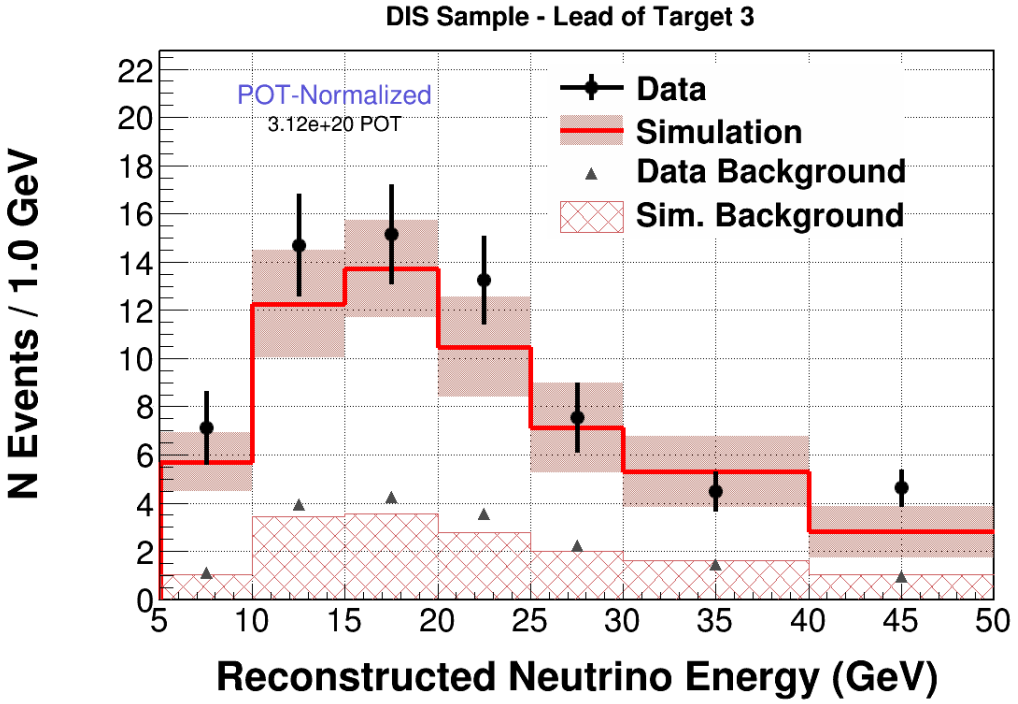

Figure E-7. DIS signal and CH background: target 03 Pb (E_ν)

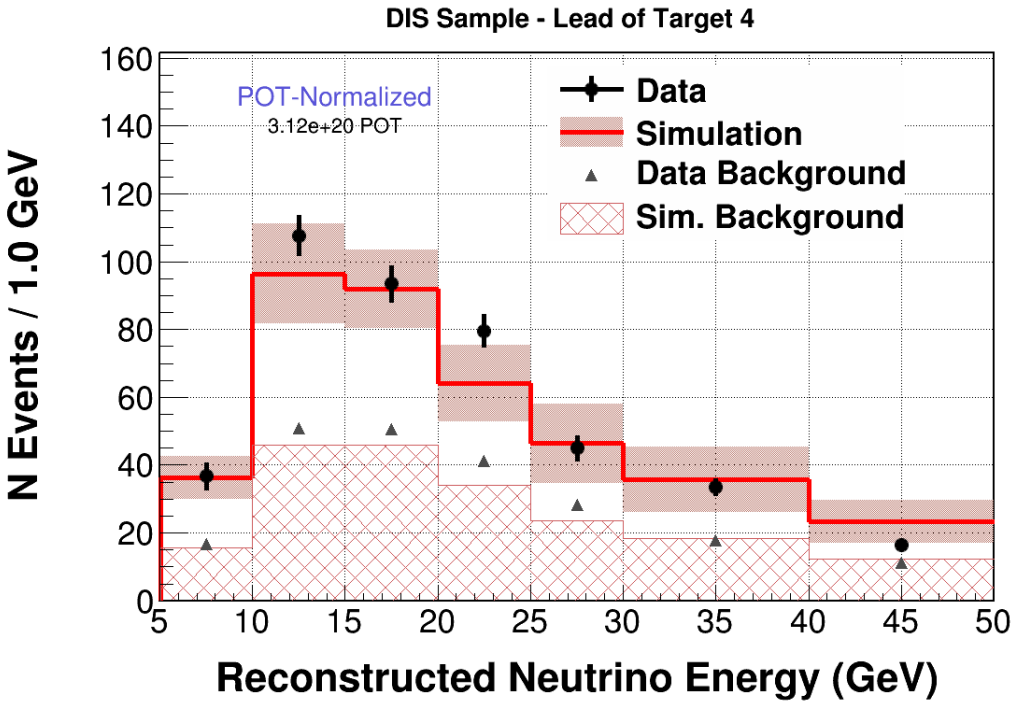

Figure E-8. DIS signal and CH background: target 04 Pb (E_ν)

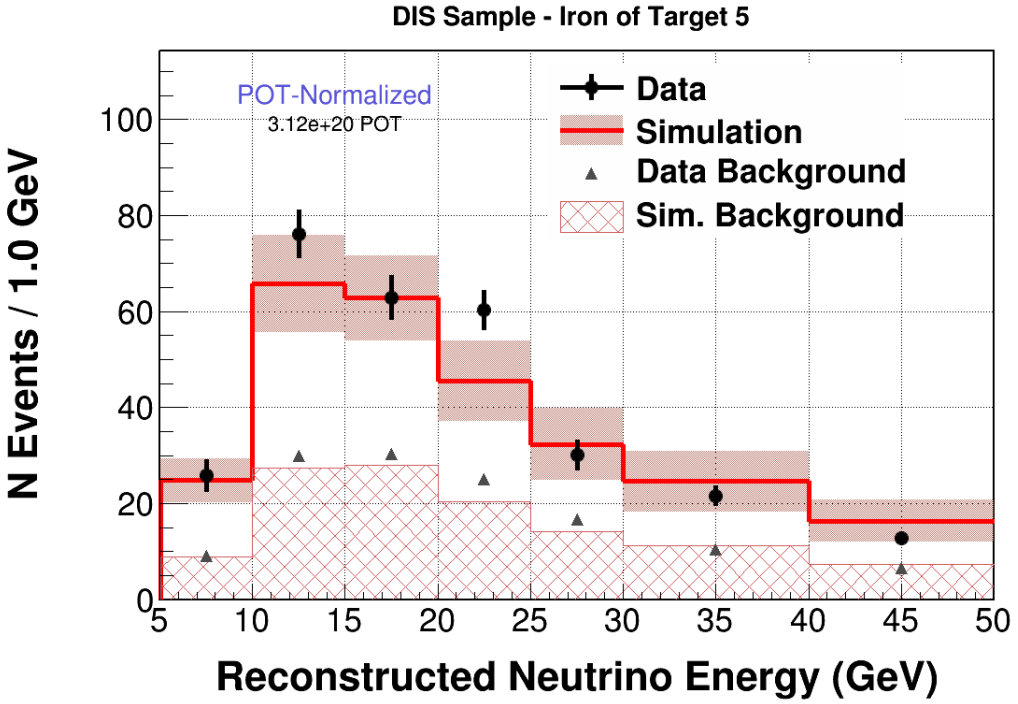

Figure E-9. DIS signal and CH background: target 05 Fe (E_ν)

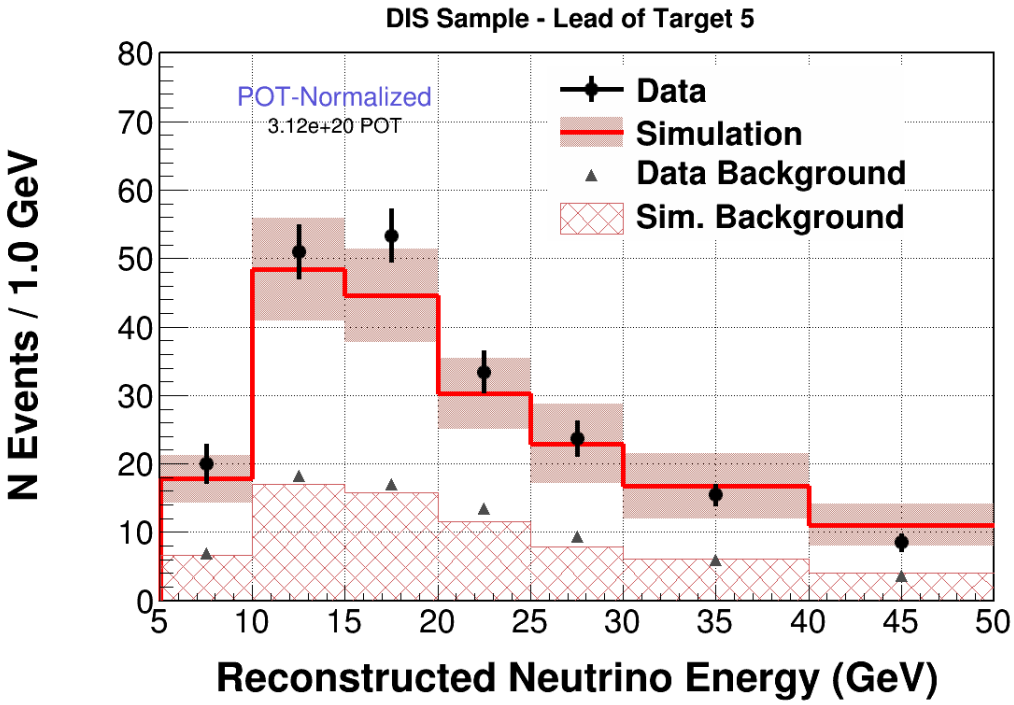

Figure E-10. DIS signal and CH background: target 05 Pb (E_ν)

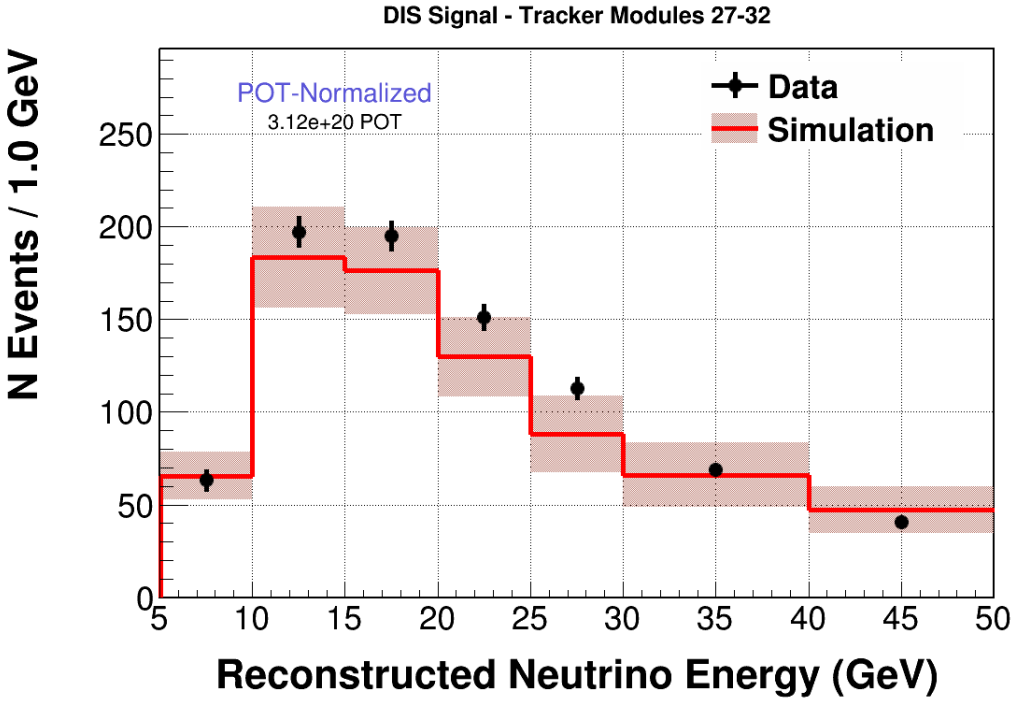

Figure E-11. DIS Signal: tracker mods. 27-32 (E_ν)

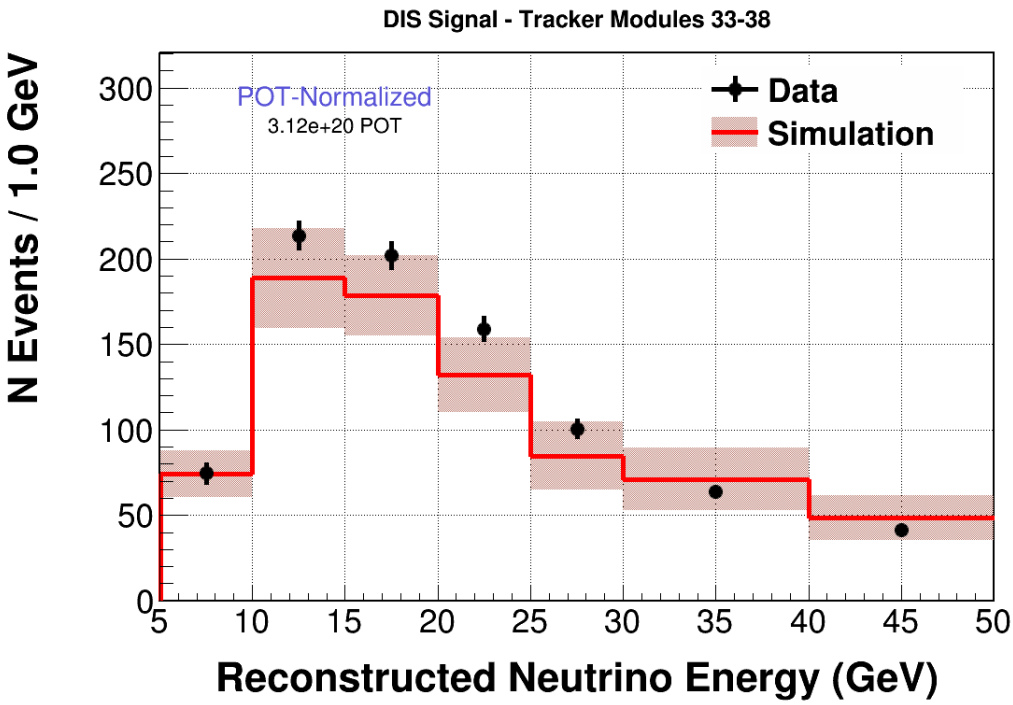

Figure E-12. DIS Signal: tracker mods. 33-38 (E_ν)

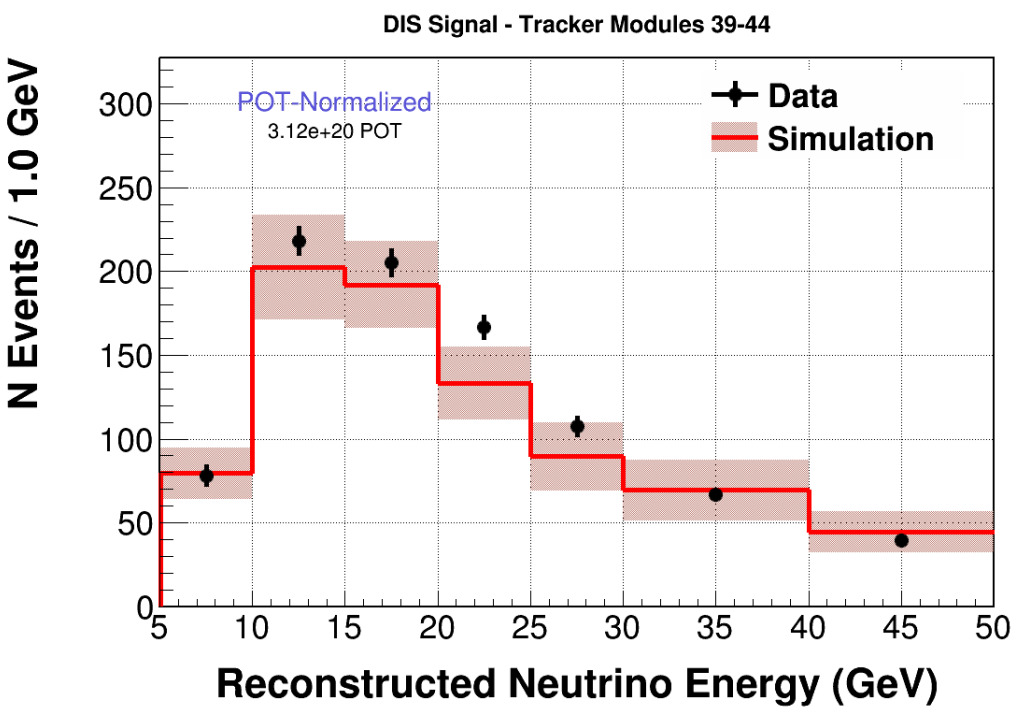

Figure E-13. DIS Signal: tracker mods. 39-44 (E_ν)

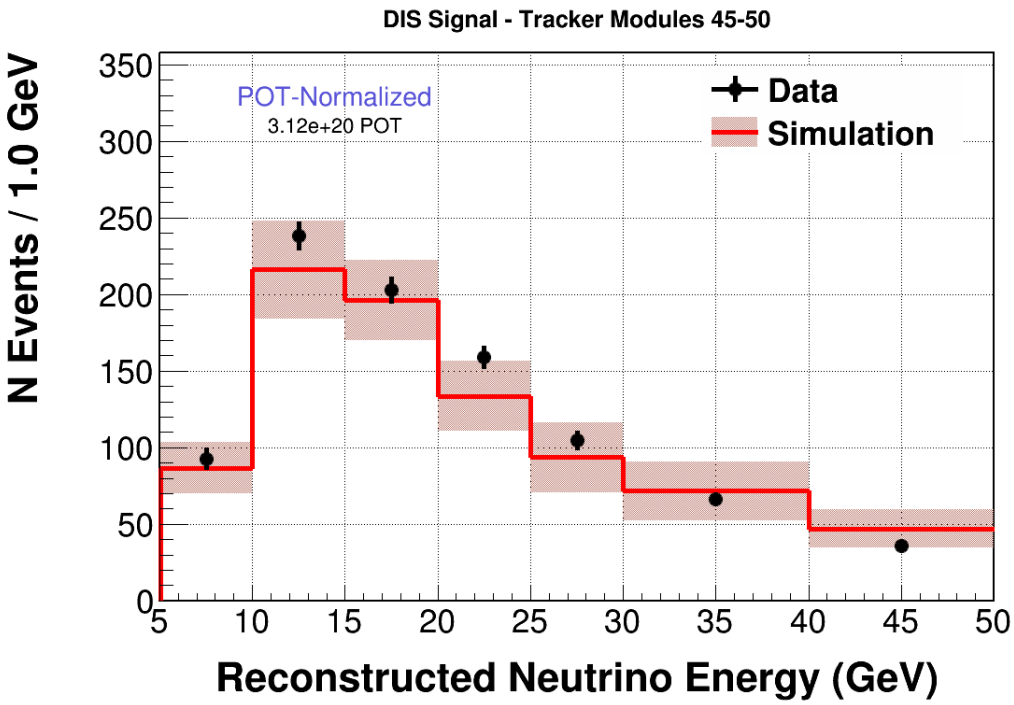

Figure E-14. DIS Signal: tracker mods. 45-50 (E_ν)

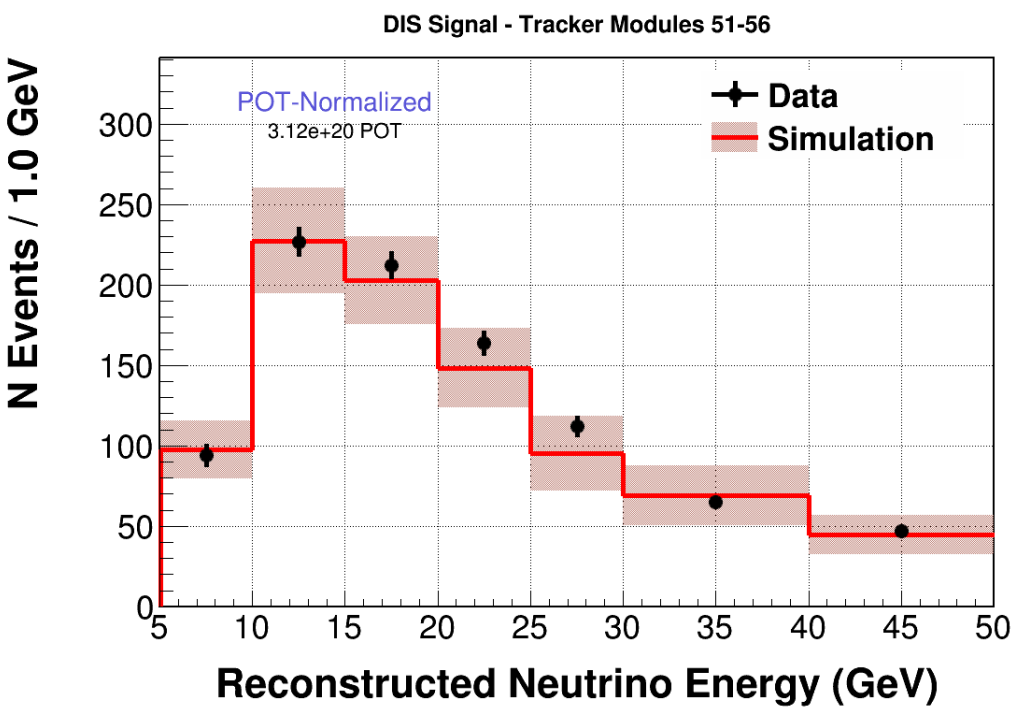

Figure E-15. DIS Signal: tracker mods. 51-56 (E_ν)

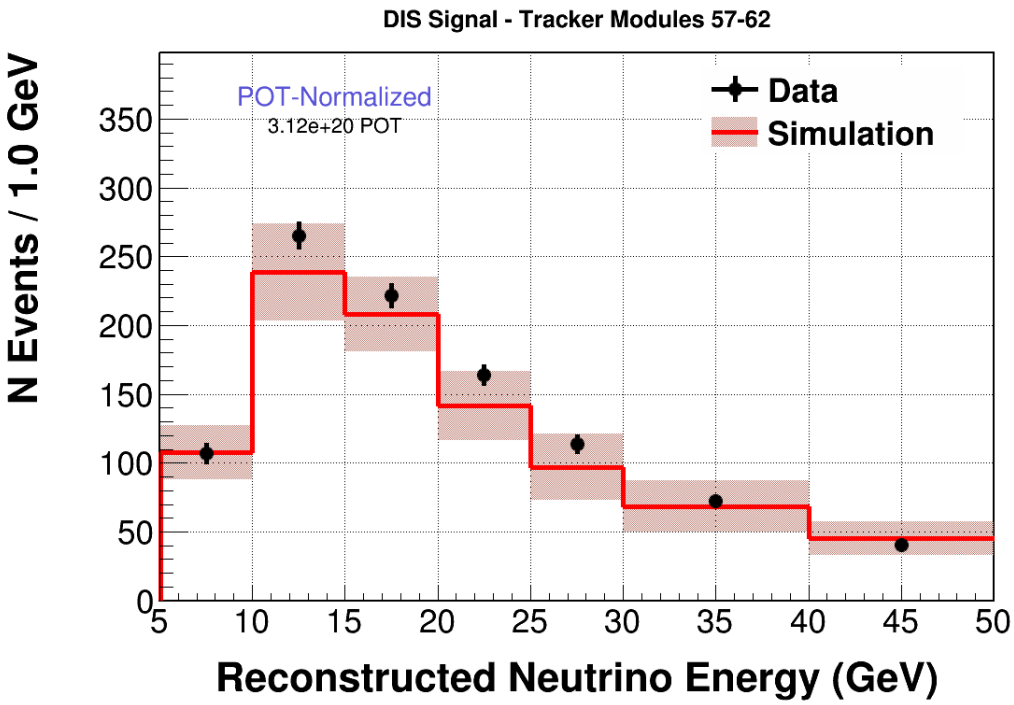

Figure E-16. DIS Signal: tracker mods. 57-62 (E_ν)

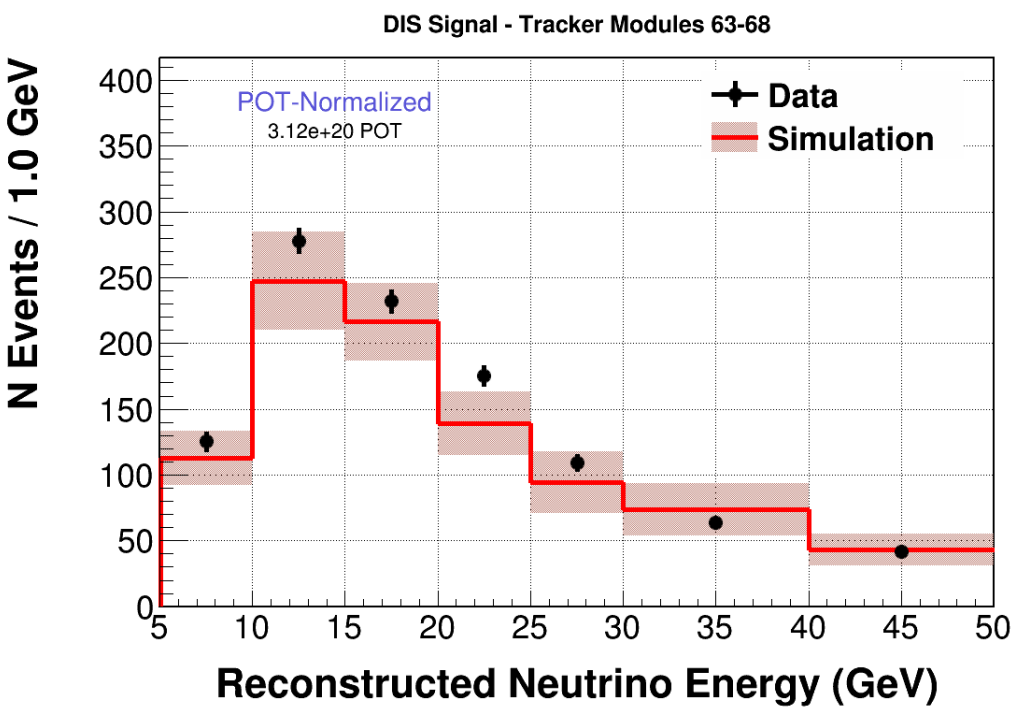

Figure E-17. DIS Signal: tracker mods. 63-68 (E_ν)

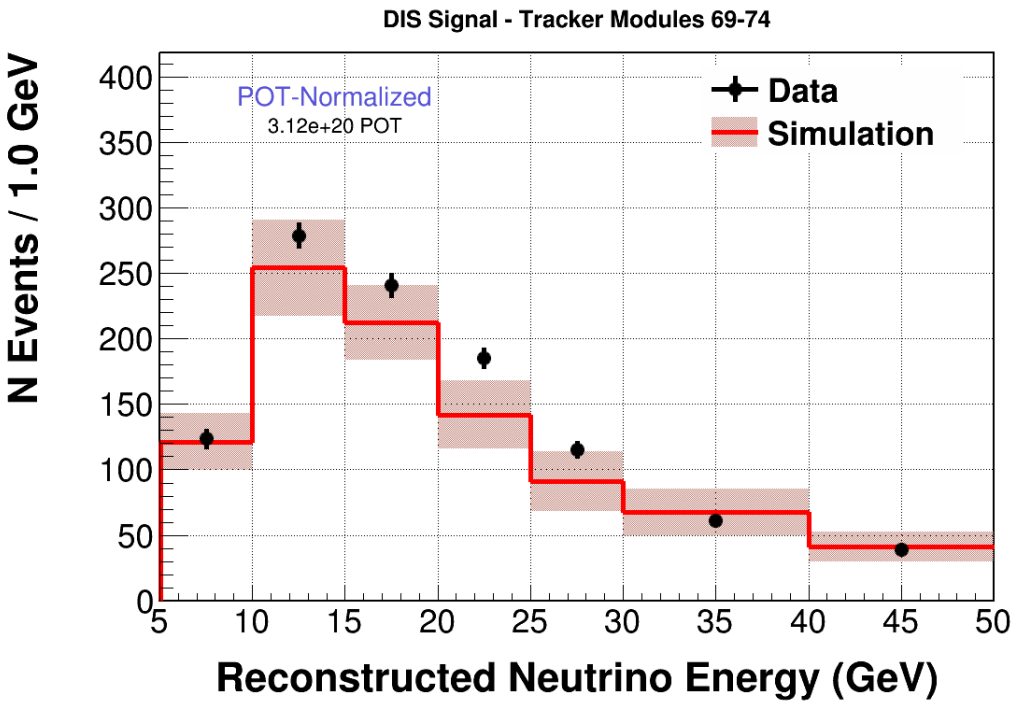

Figure E-18. DIS Signal: tracker mods. 69-74 (E_ν)

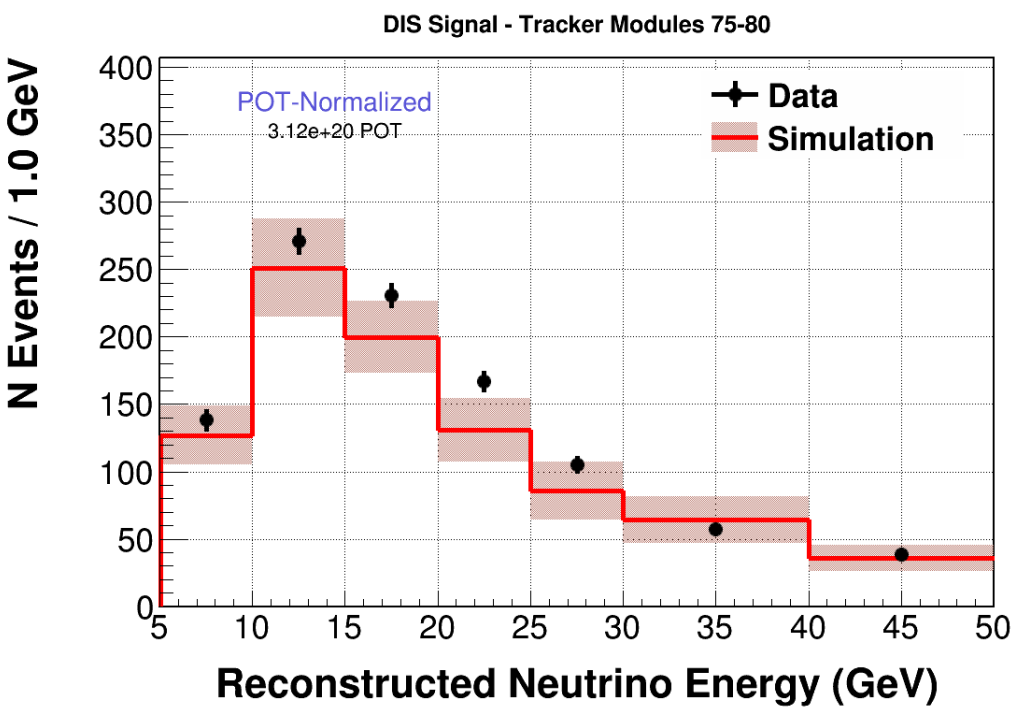

Figure E-19. DIS Signal: tracker mods. 75-80 (E_ν)

The following plots show the DIS events in data and MC, after subtracting the non-DIS events. The sample is broken down by target events and events in the predicted events in the surrounding CH. They are plotted as a function of hadronic energy (E_{had}):

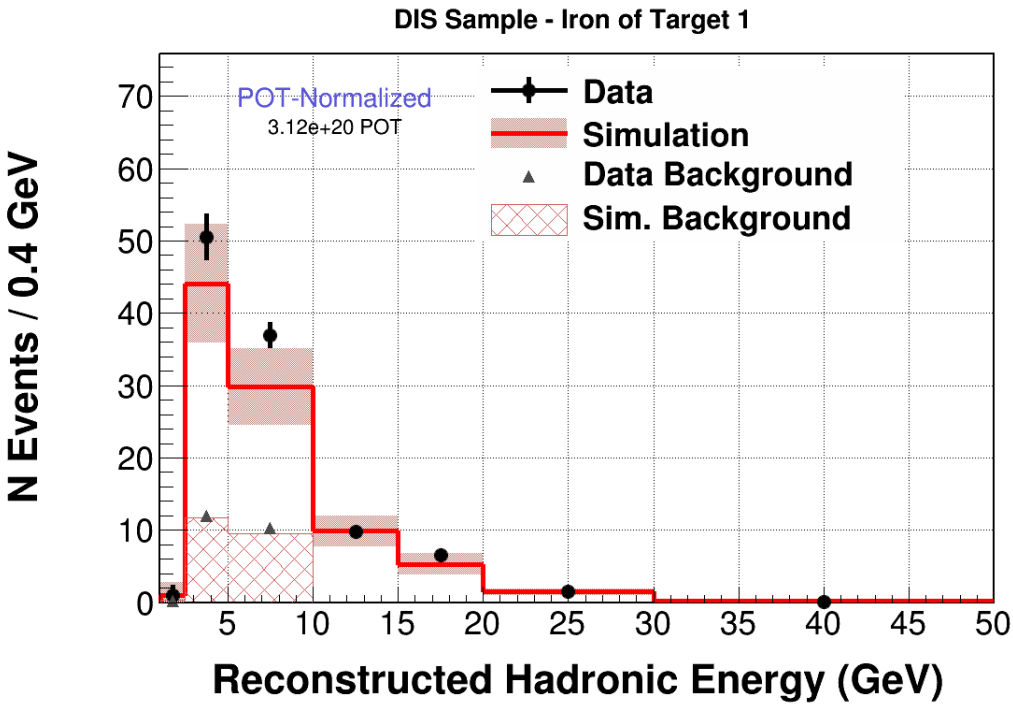

Figure E-20. DIS signal and CH background: target 01 Fe (E_{had})

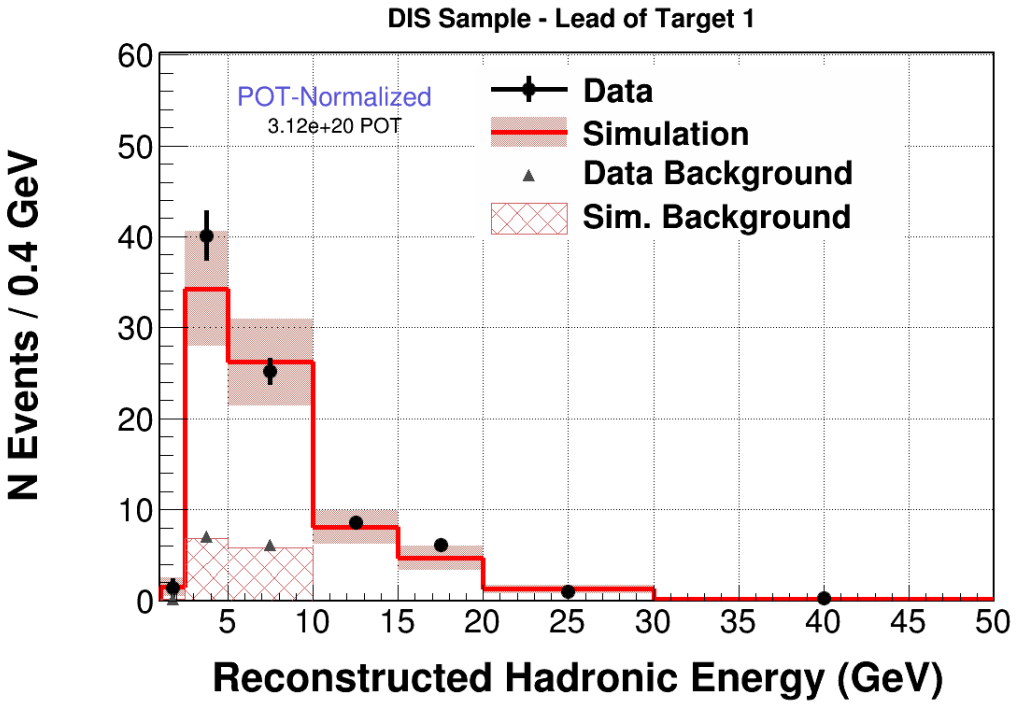

Figure E-21. DIS signal and CH background: target 01 Pb (E_{had})

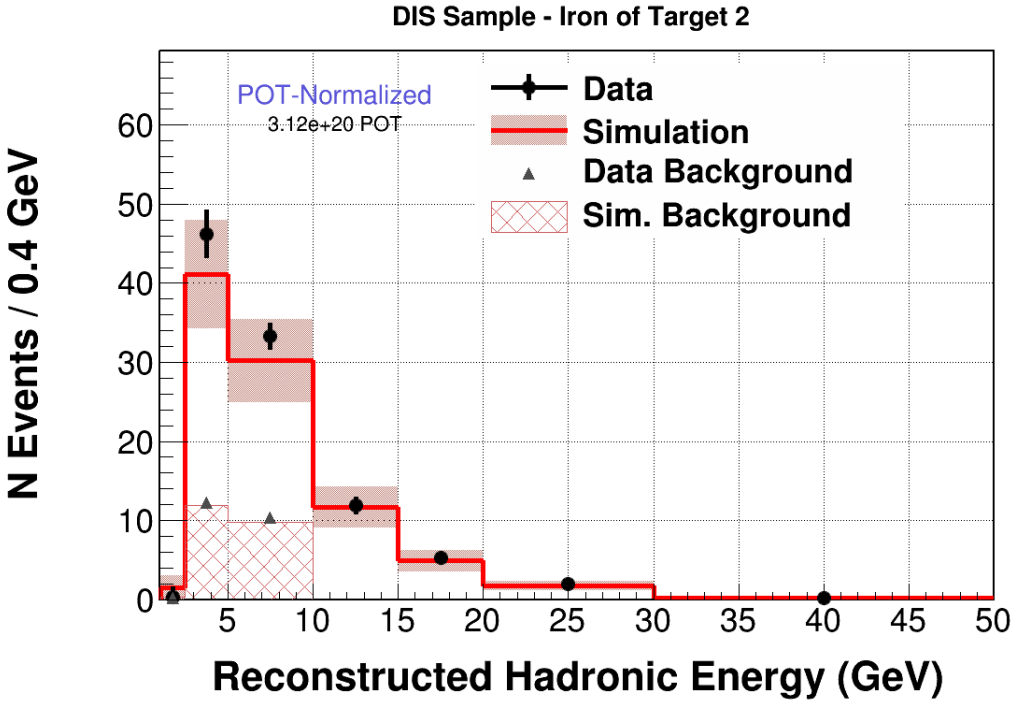

Figure E-22. DIS signal and CH background: target 02 Fe (E_{had})

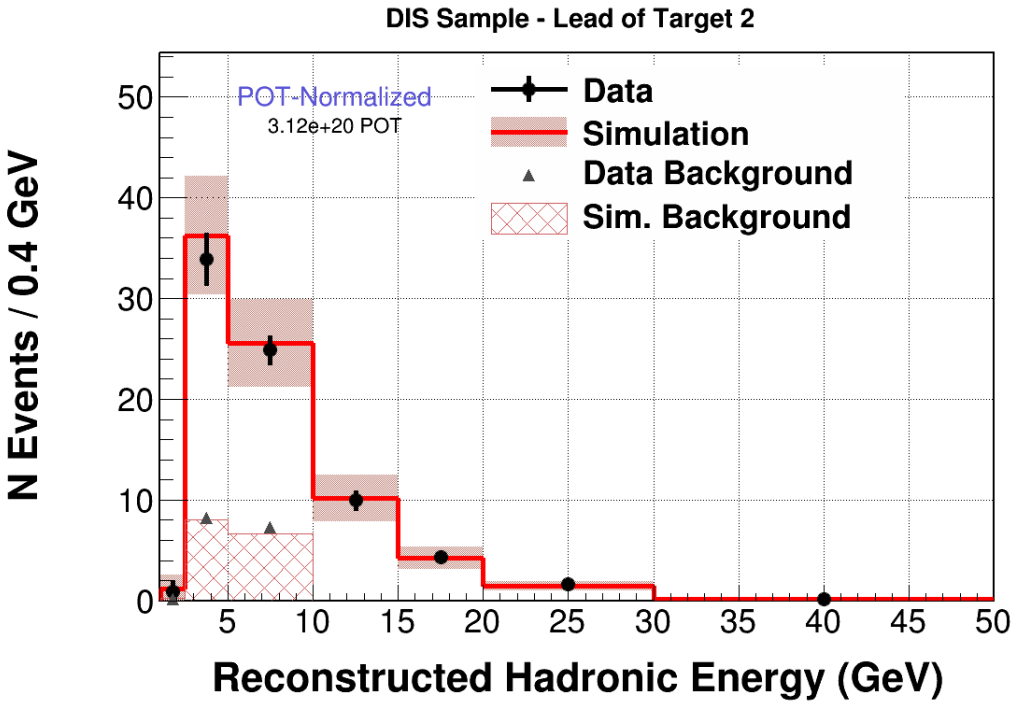

Figure E-23. DIS signal and CH background: target 02 Pb (E_{had})

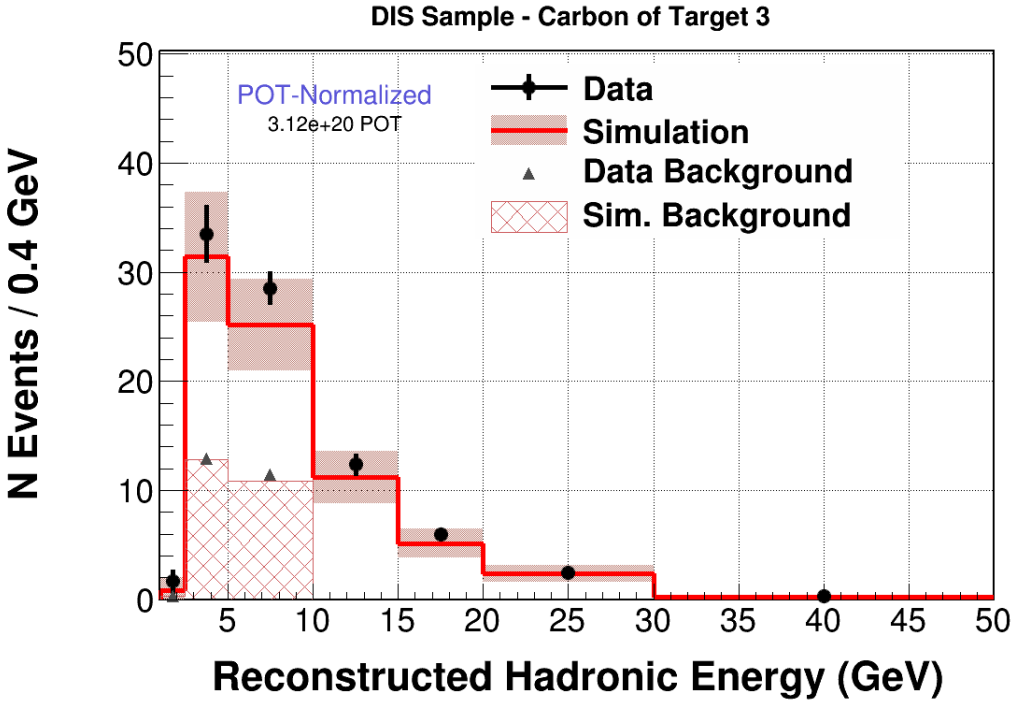

Figure E-24. DIS signal and CH background: target 03 C (E_{had})

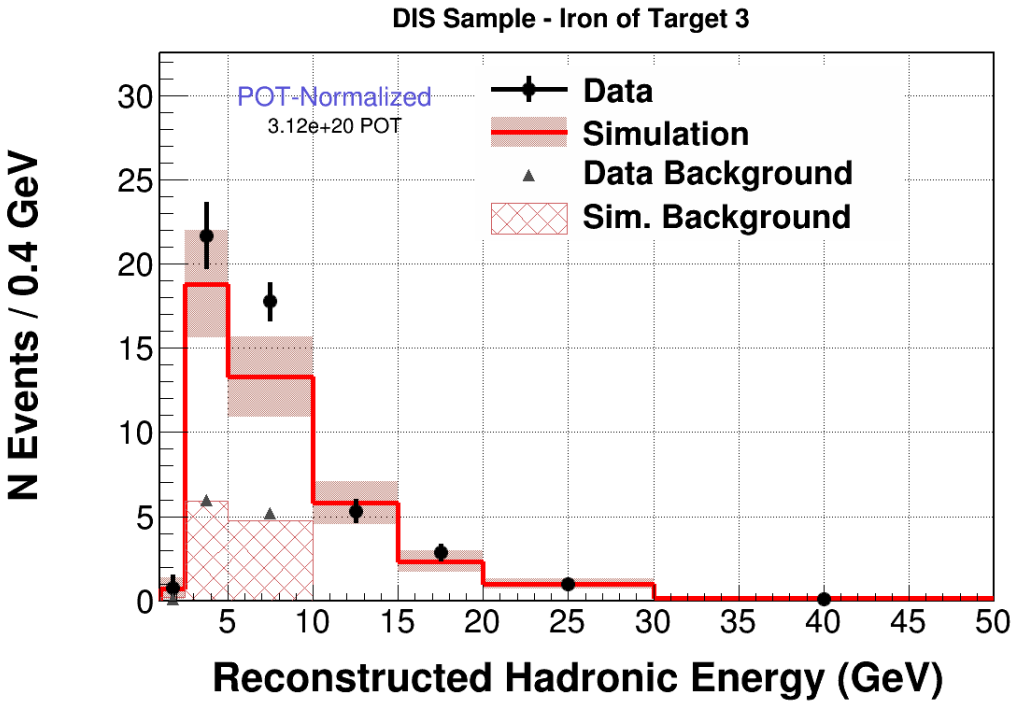

Figure E-25. DIS signal and CH background: target 03 Fe (E_{had})

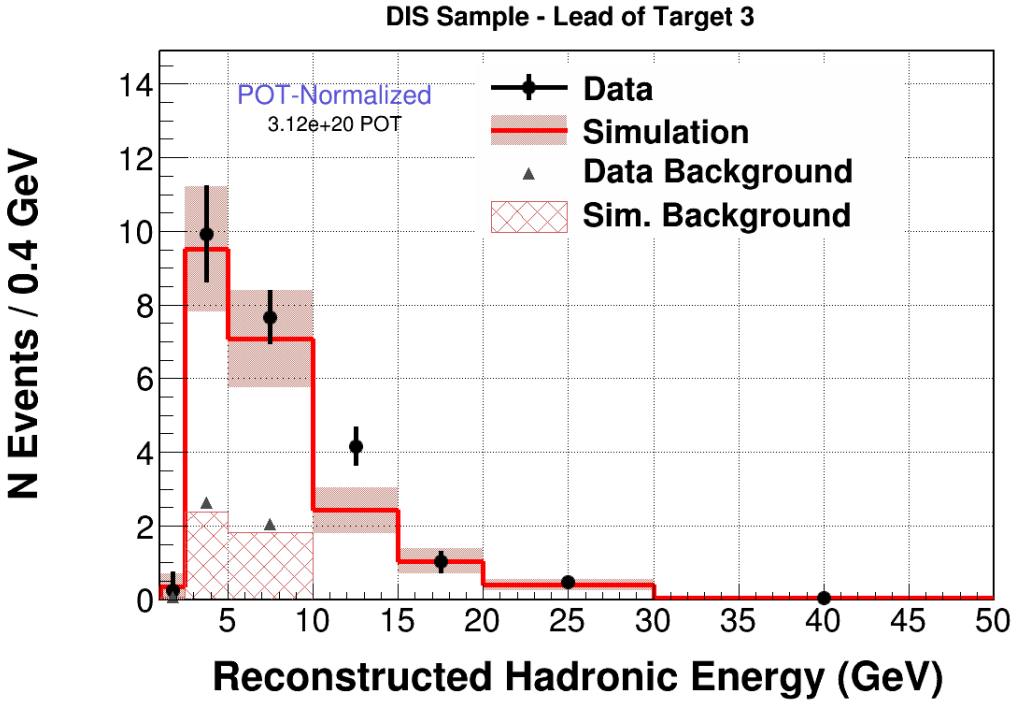

Figure E-26. DIS signal and CH background: target 03 Pb (E_{had})

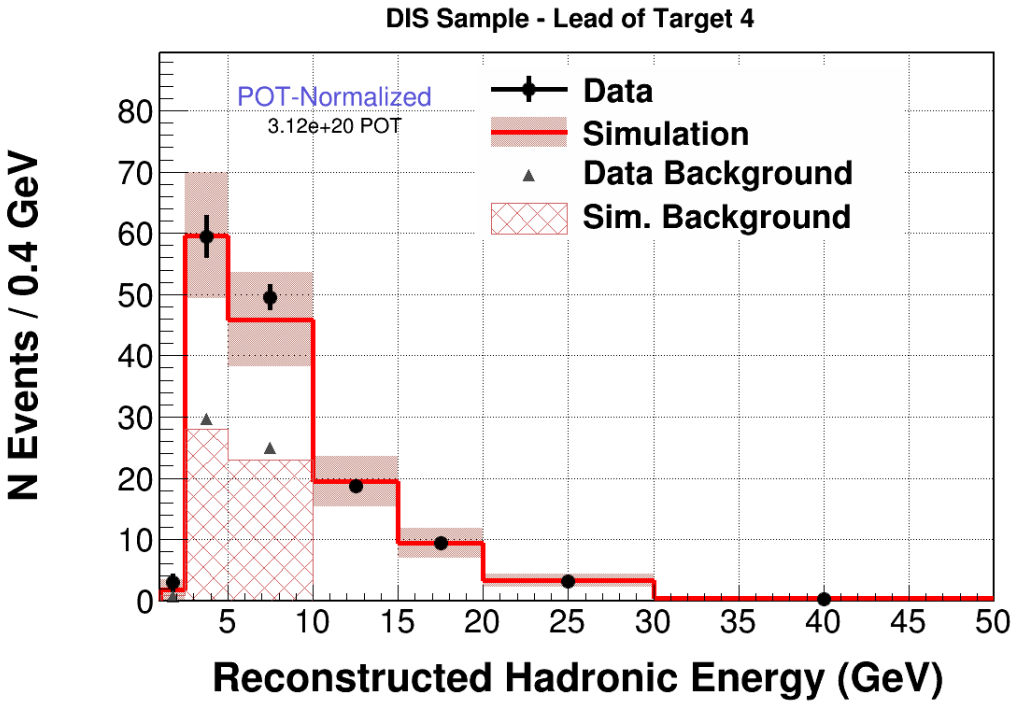

Figure E-27. DIS signal and CH background: target 04 Pb (E_{had})

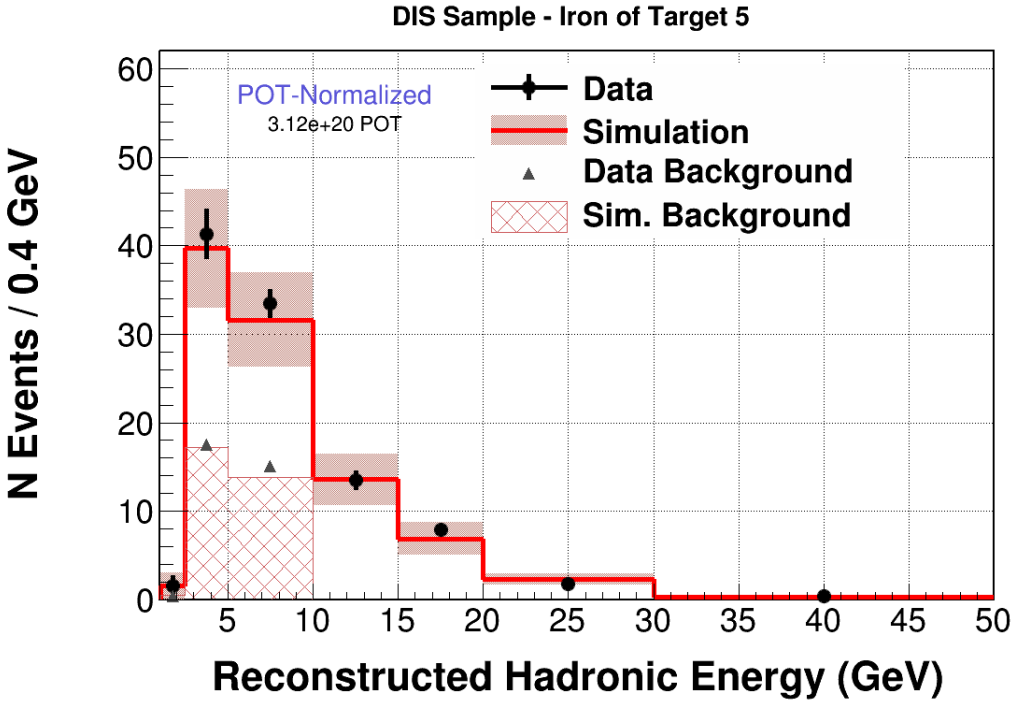

Figure E-28. DIS signal and CH background: target 05 Fe (E_{had})

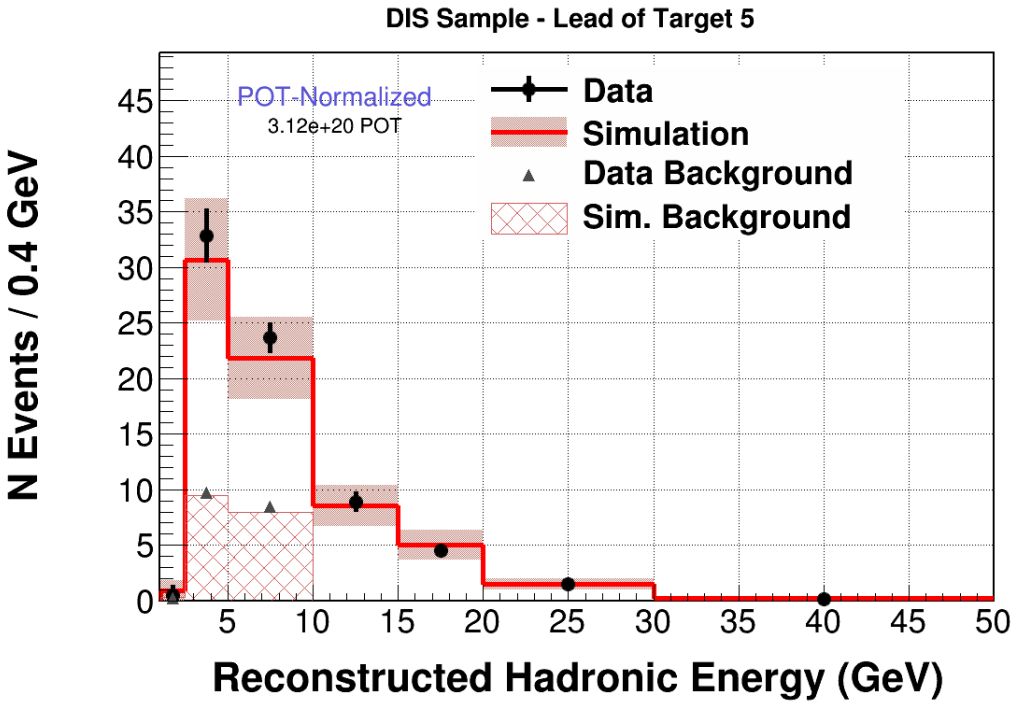

Figure E-29. DIS signal and CH background: target 05 Pb (E_{had})

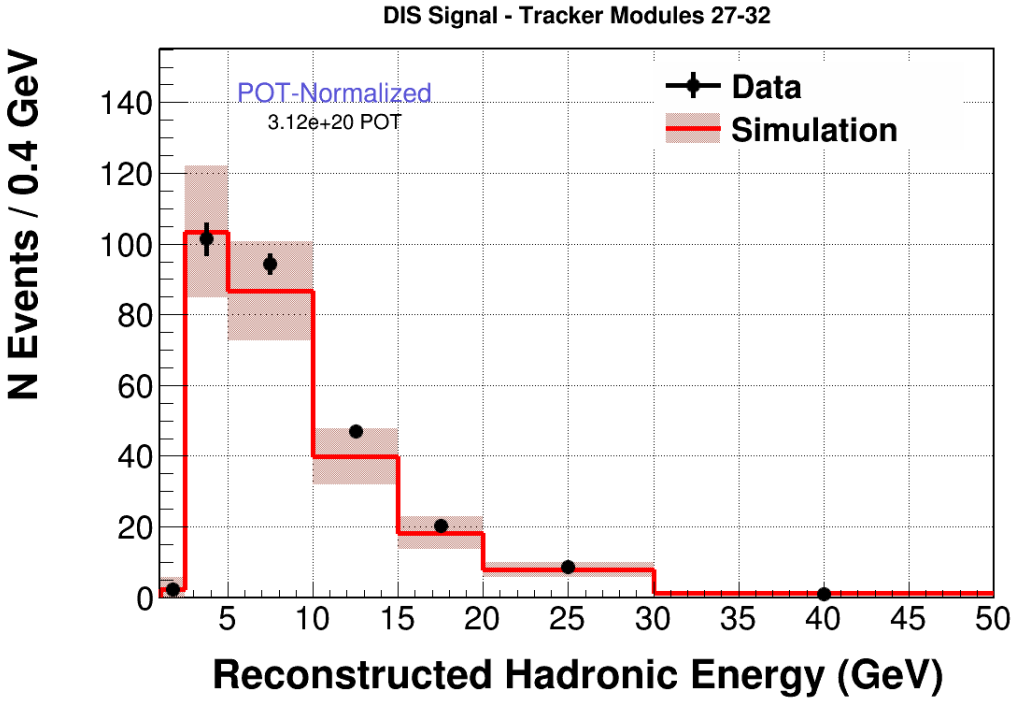

Figure E-30. DIS Signal: tracker mods. 27-32 (E_{had})

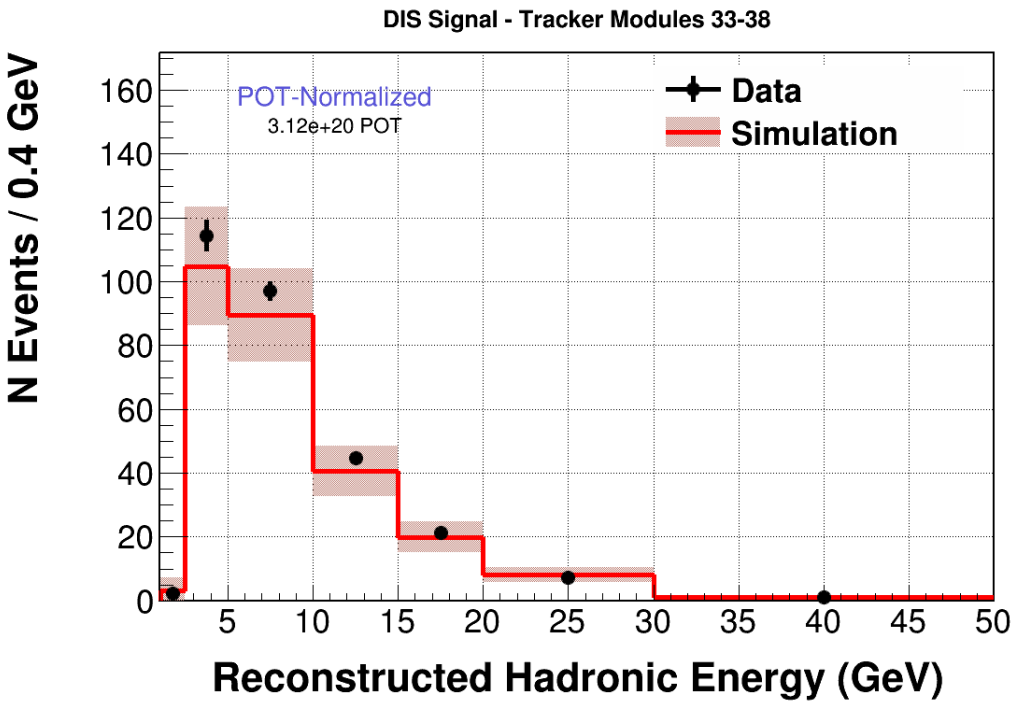

Figure E-31. DIS Signal: tracker mods. 33-38 (E_{had})

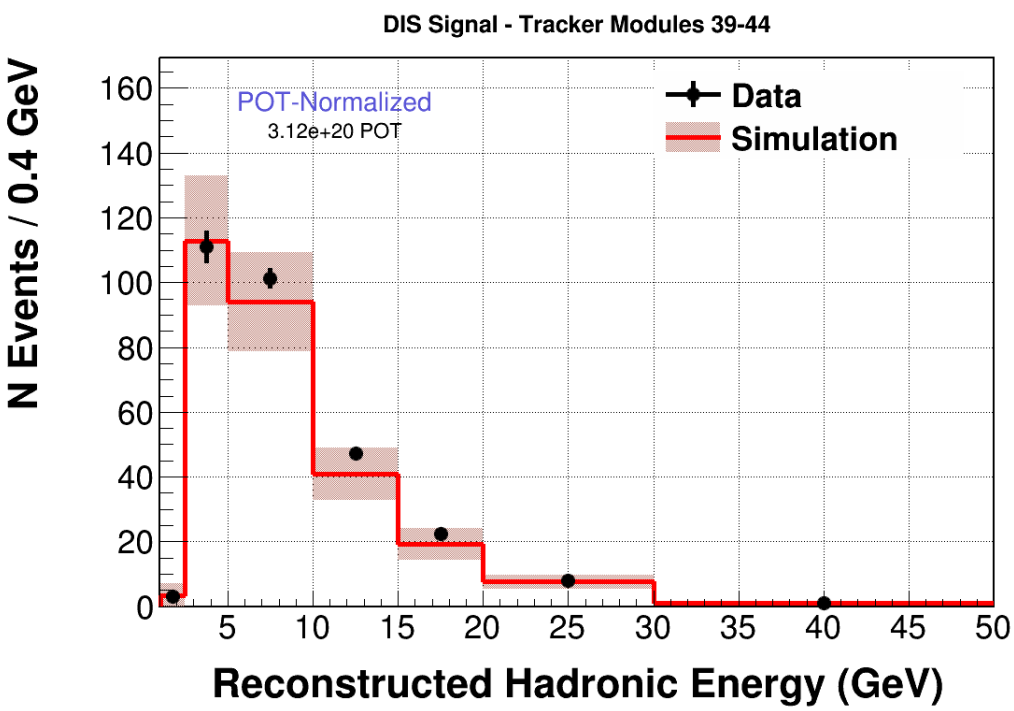

Figure E-32. DIS Signal: tracker mods. 39-44 (E_{had})

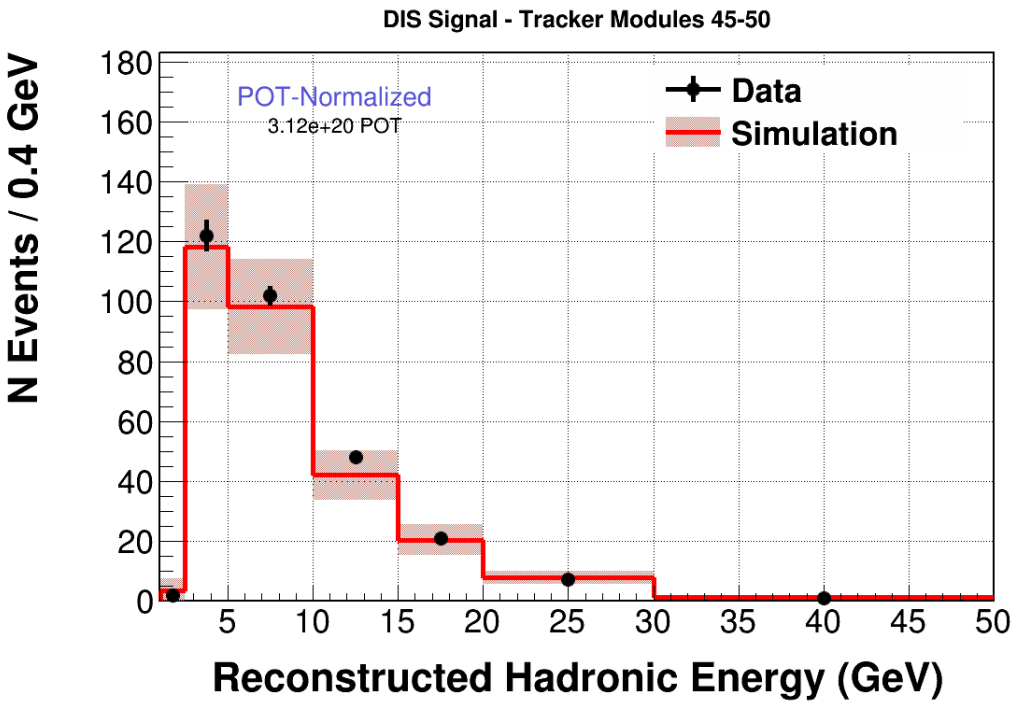

Figure E-33. DIS Signal: tracker mods. 45-50 (E_{had})

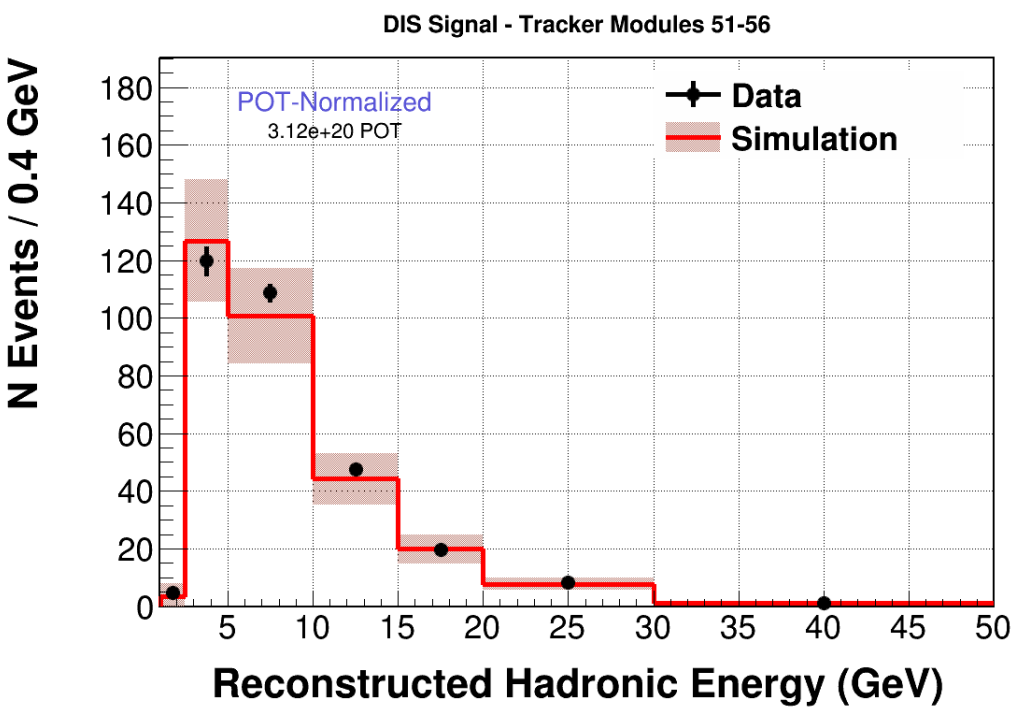

Figure E-34. DIS Signal: tracker mods. 51-56 (E_{had})

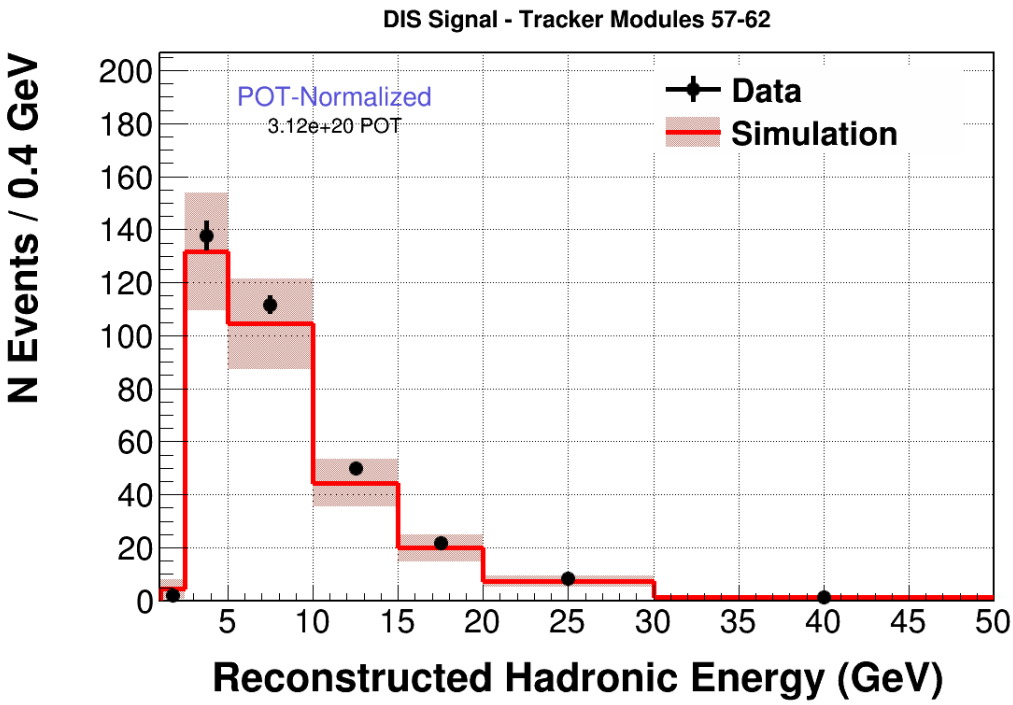

Figure E-35. DIS Signal: tracker mods. 57-62 (E_{had})

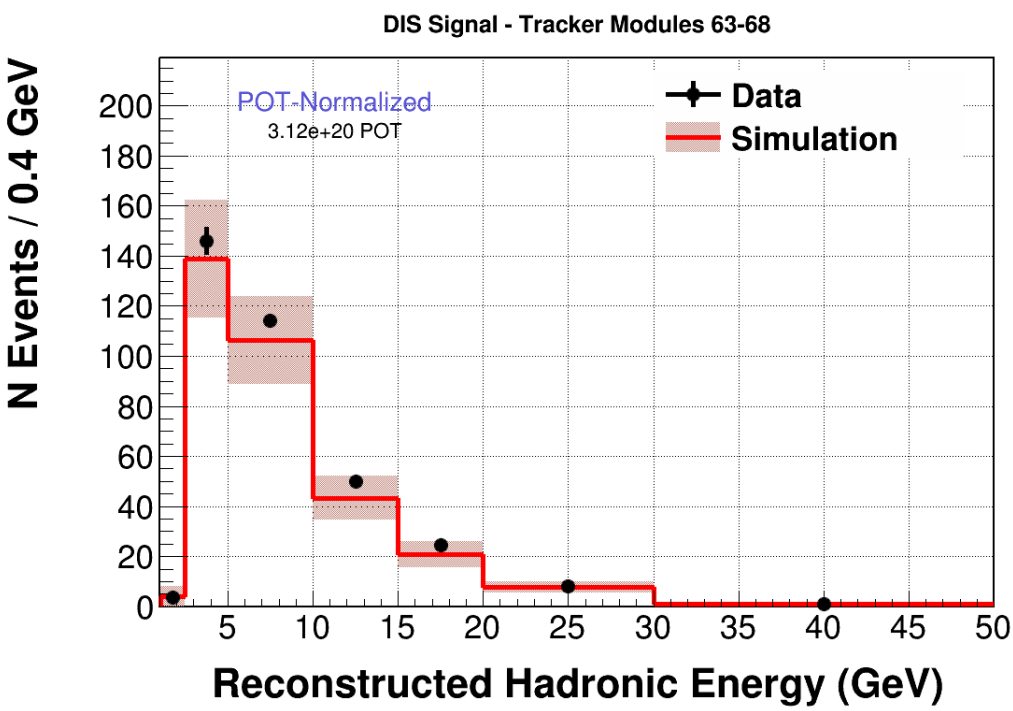

Figure E-36. DIS Signal: tracker mods. 63-68 (E_{had})

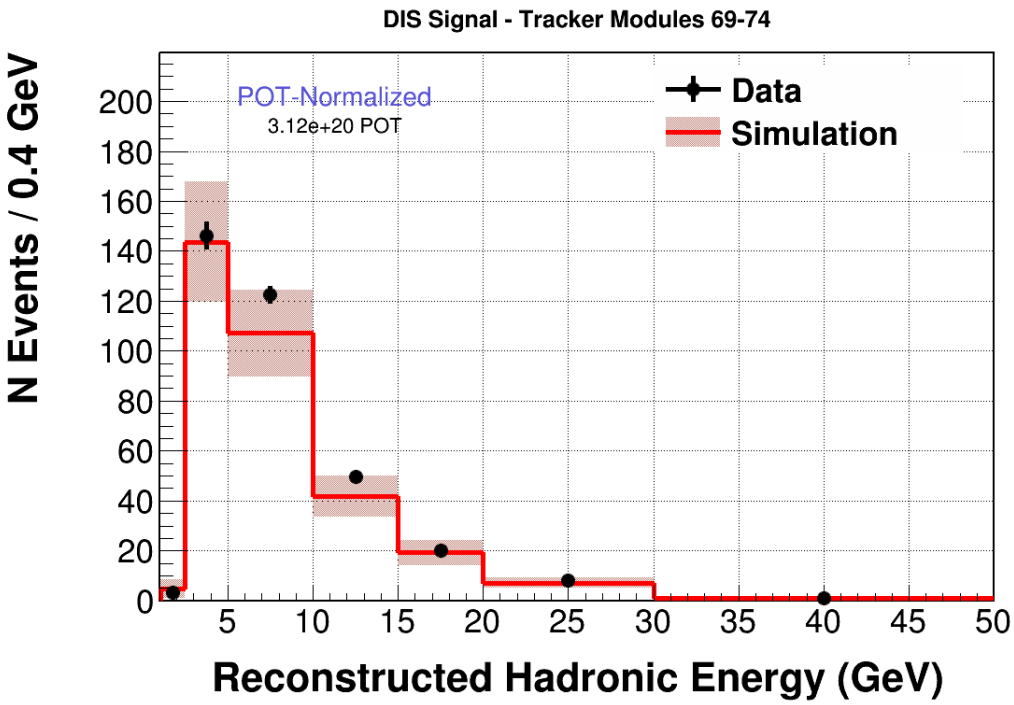

Figure E-37. DIS Signal: tracker mods. 69-74 (E_{had})

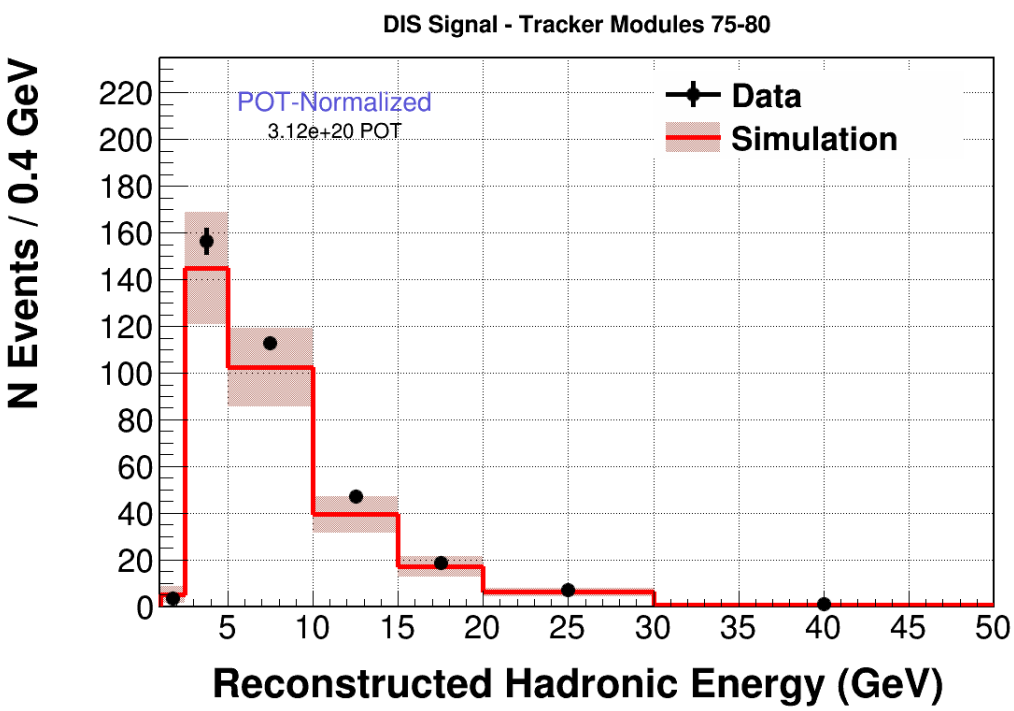

Figure E-38. DIS Signal: tracker mods. 75-80 (E_{had})

The following plots show the DIS events in data and MC, after subtracting the non-DIS events. The sample is broken down by target events and events in the predicted events in the surrounding CH. They are plotted as a function of four momentum transfer squared (Q^2):

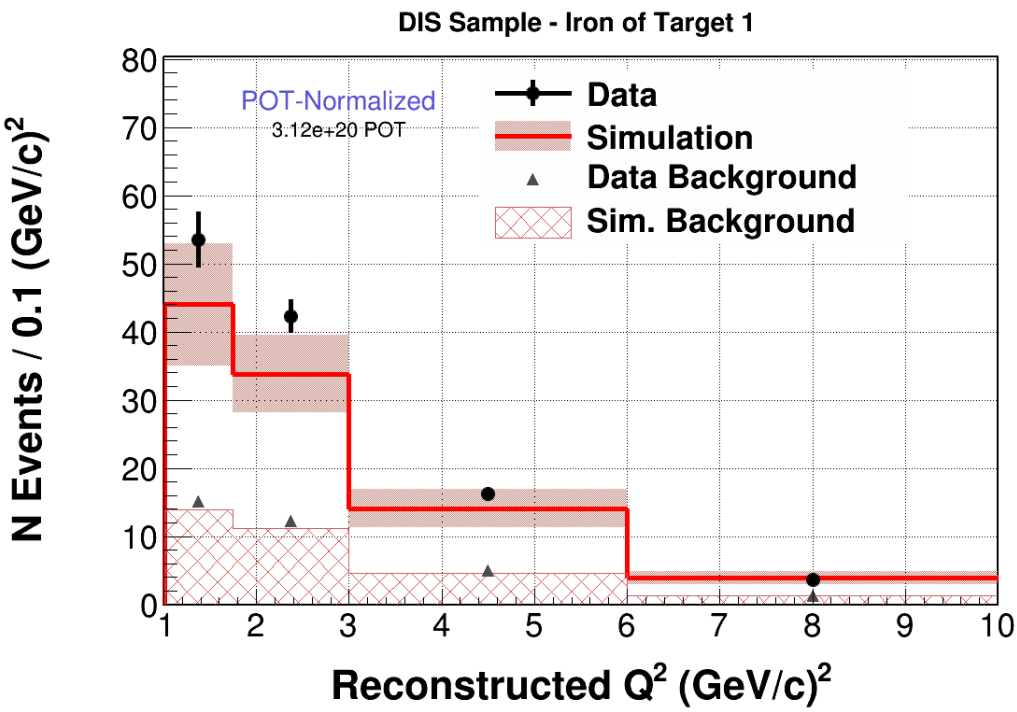

Figure E-39. DIS signal and CH background: target 01 Fe (Q^2)

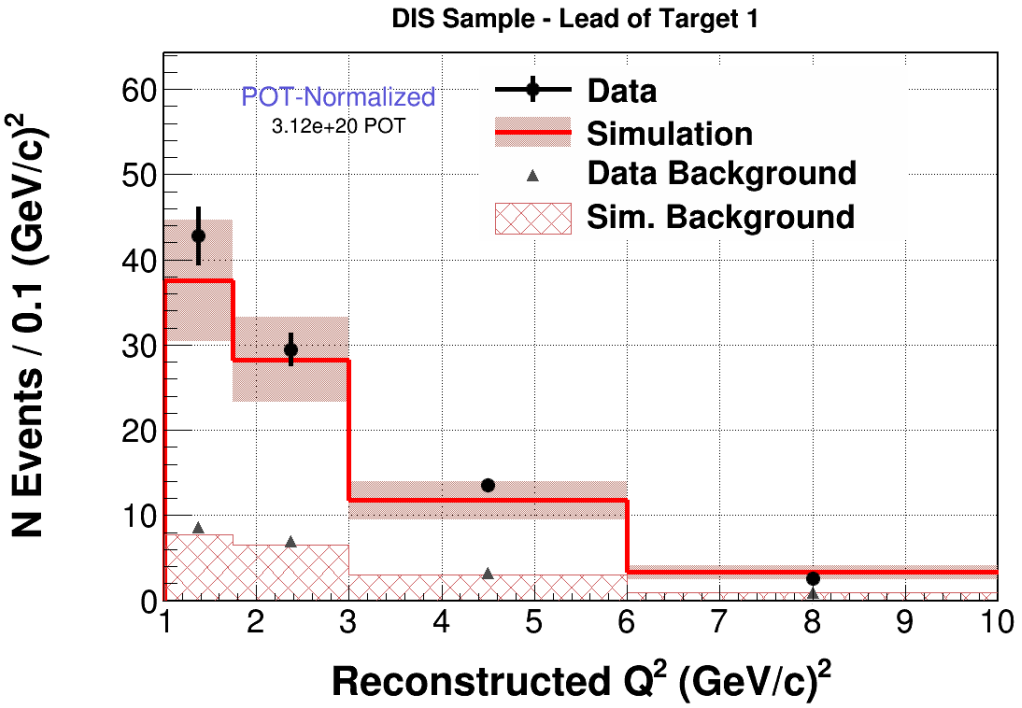

Figure E-40. DIS signal and CH background: target 01 Pb (Q^2)

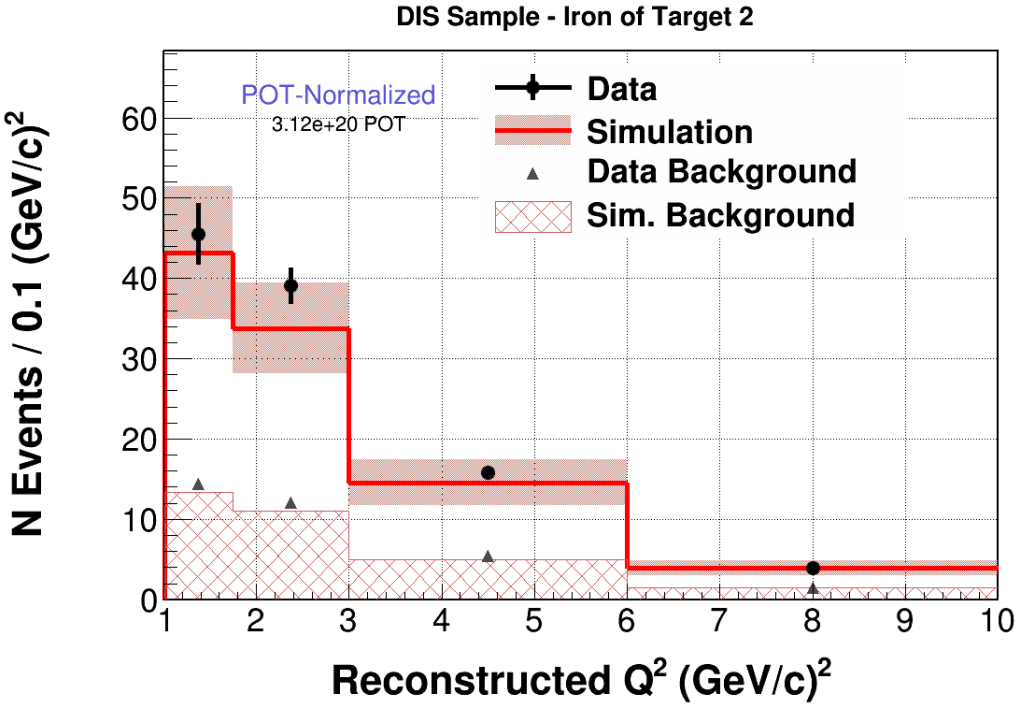

Figure E-41. DIS signal and CH background: target 02 Fe (Q^2)

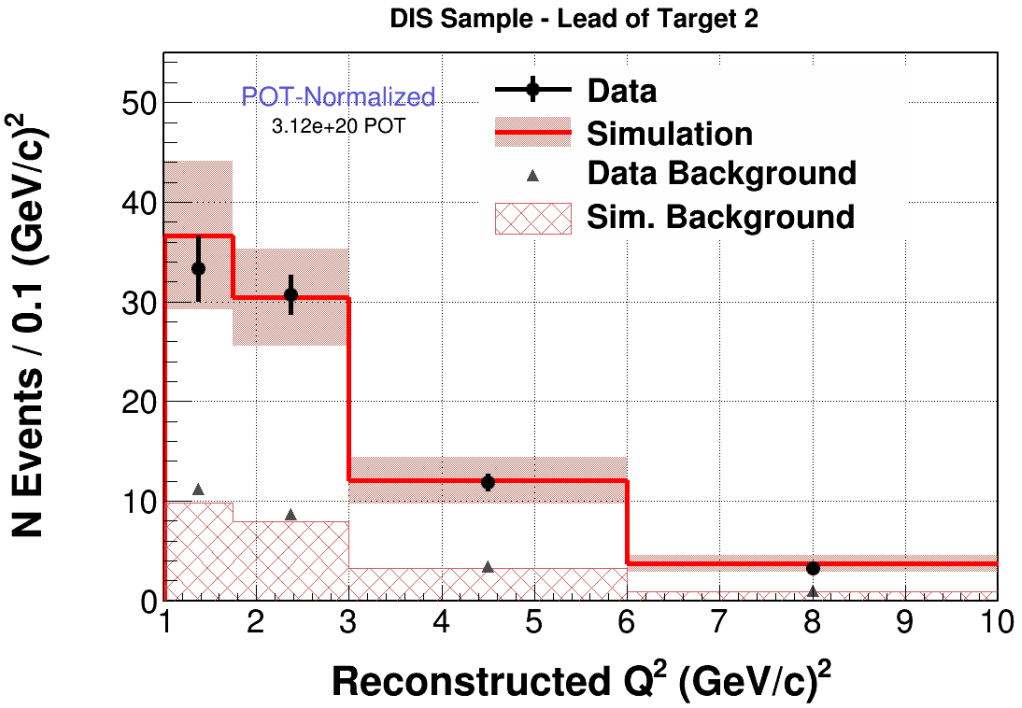

Figure E-42. DIS signal and CH background: target 02 Pb (Q^2)

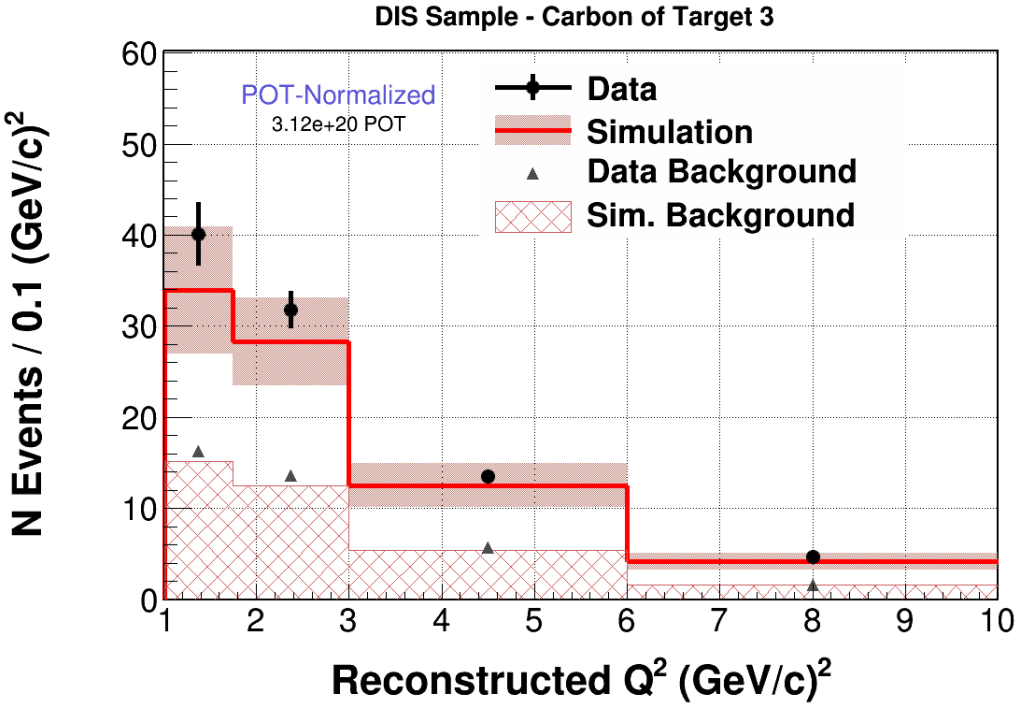

Figure E-43. DIS signal and CH background: target 03 C (Q^2)

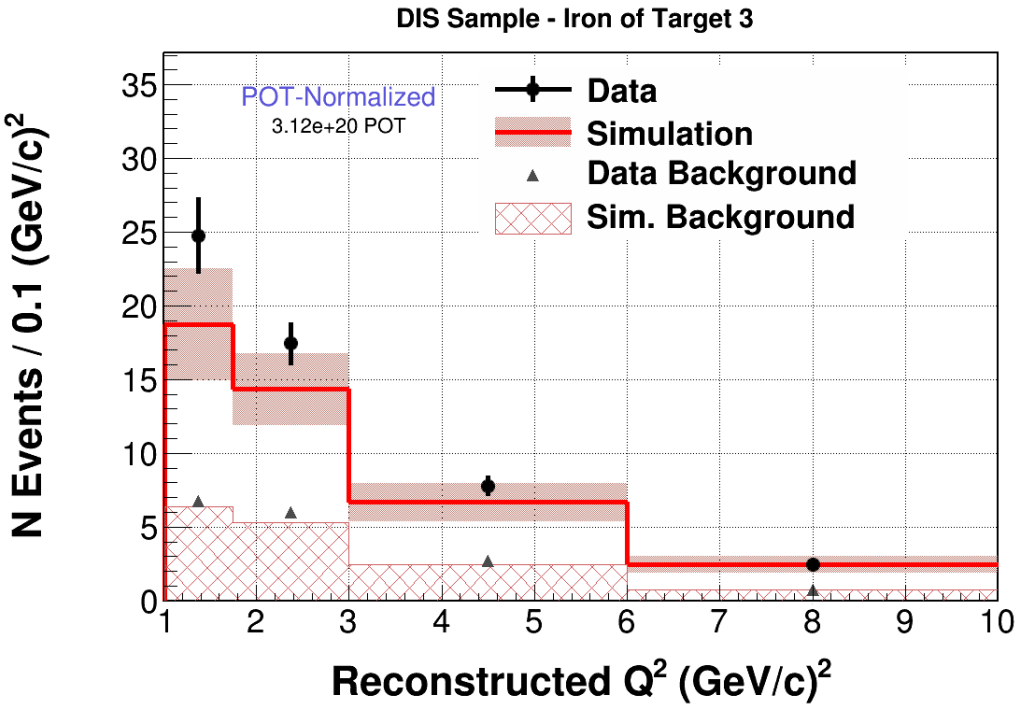

Figure E-44. DIS signal and CH background: target 03 Fe (Q^2)

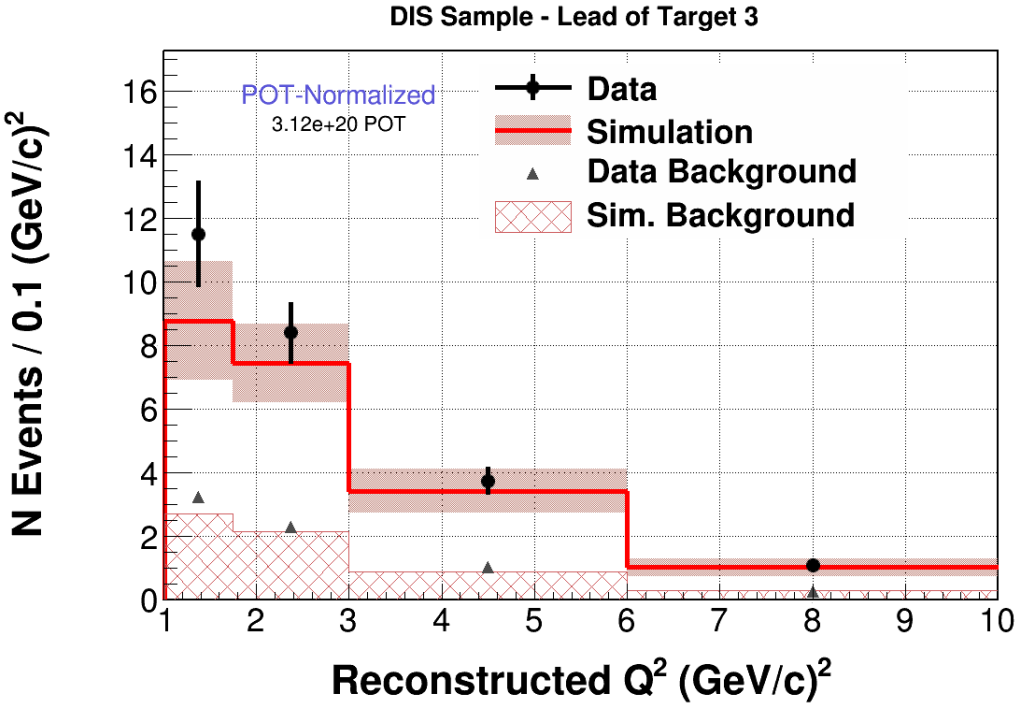

Figure E-45. DIS signal and CH background: target 03 Pb (Q^2)

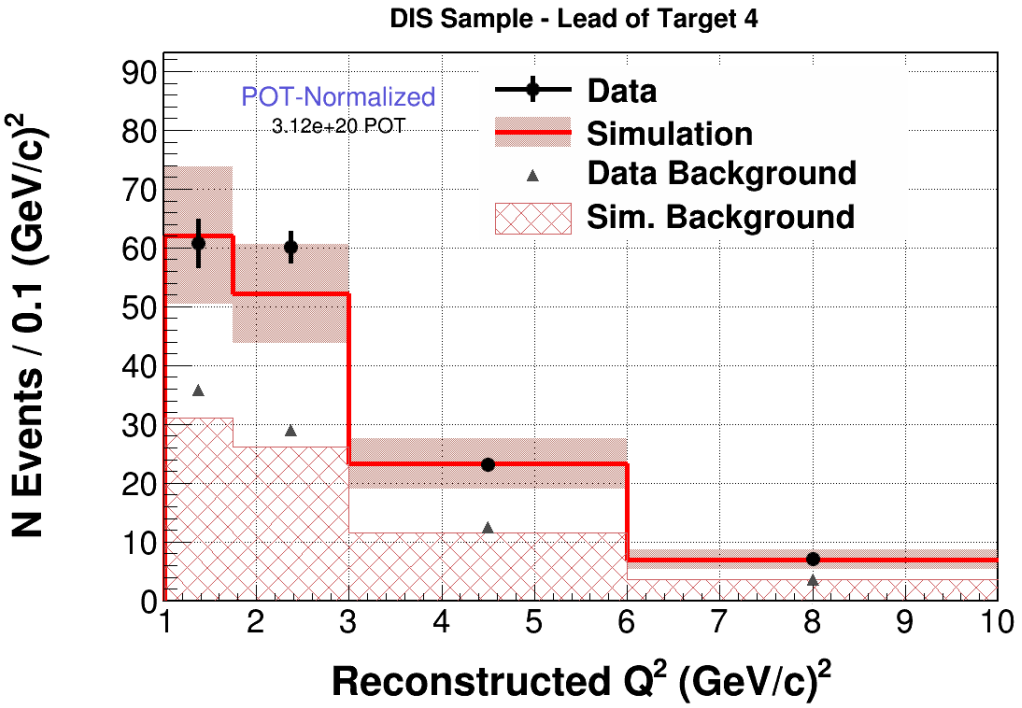

Figure E-46. DIS signal and CH background: target 04 Pb (Q^2)

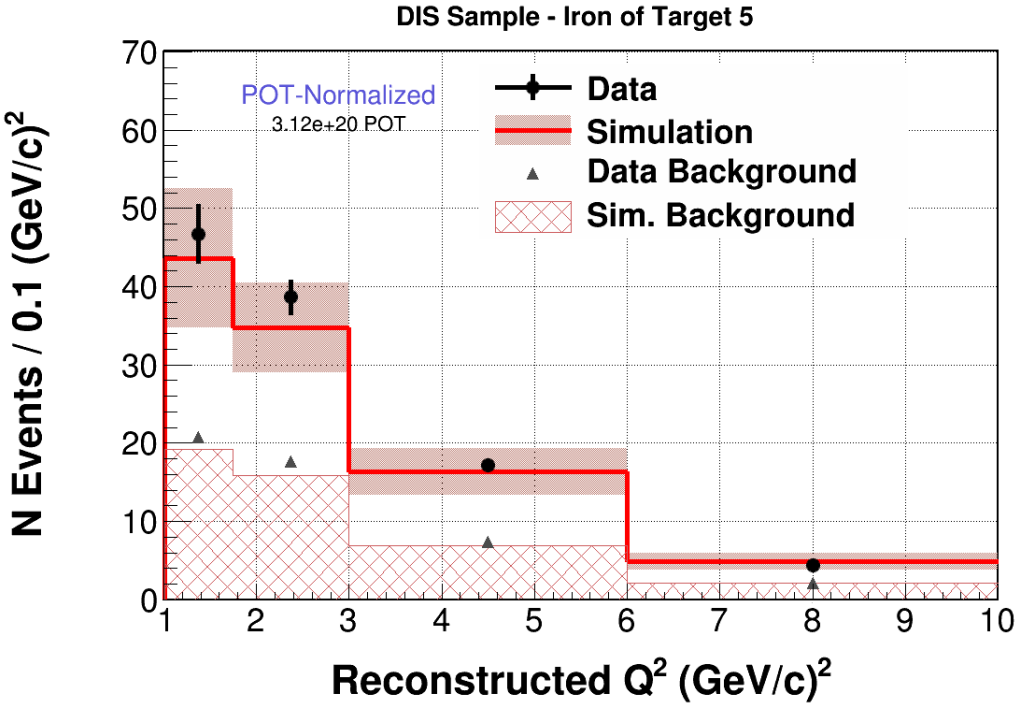

Figure E-47. DIS signal and CH background: target 05 Fe (Q^2)

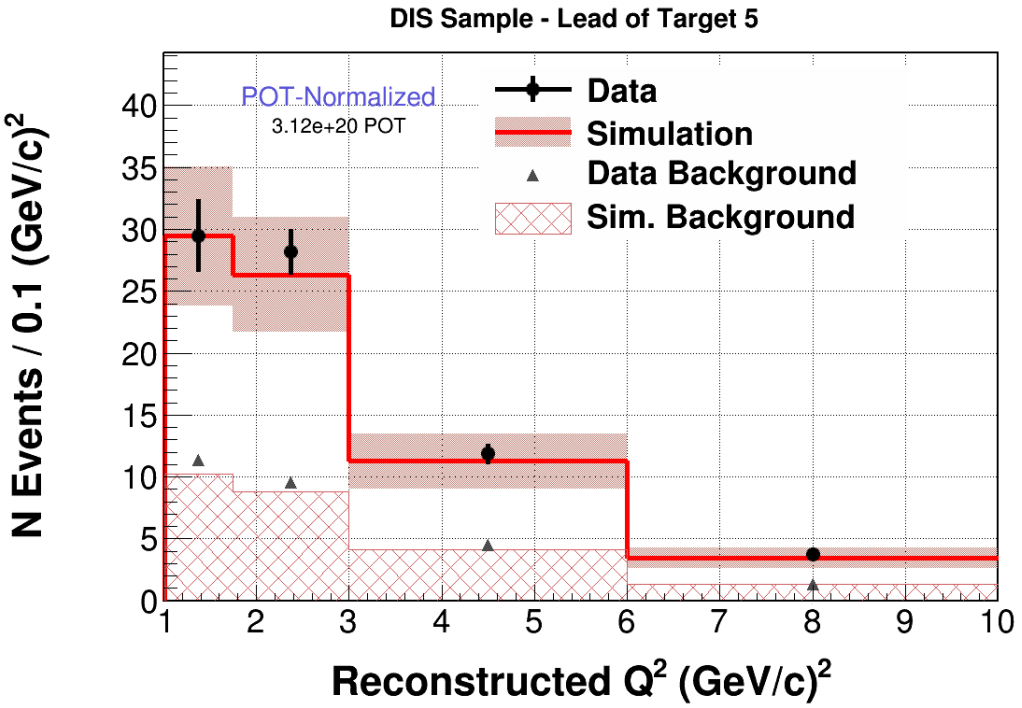

Figure E-48. DIS signal and CH background: target 05 Pb (Q^2)

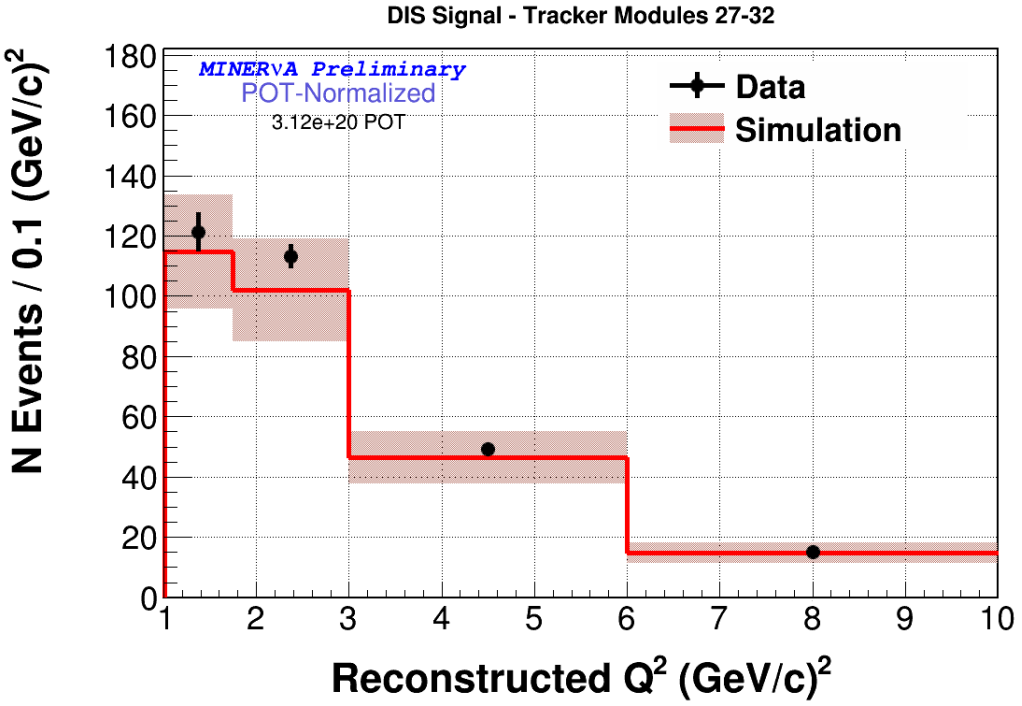

Figure E-49. DIS Signal: tracker mods. 27-32 (Q^2)

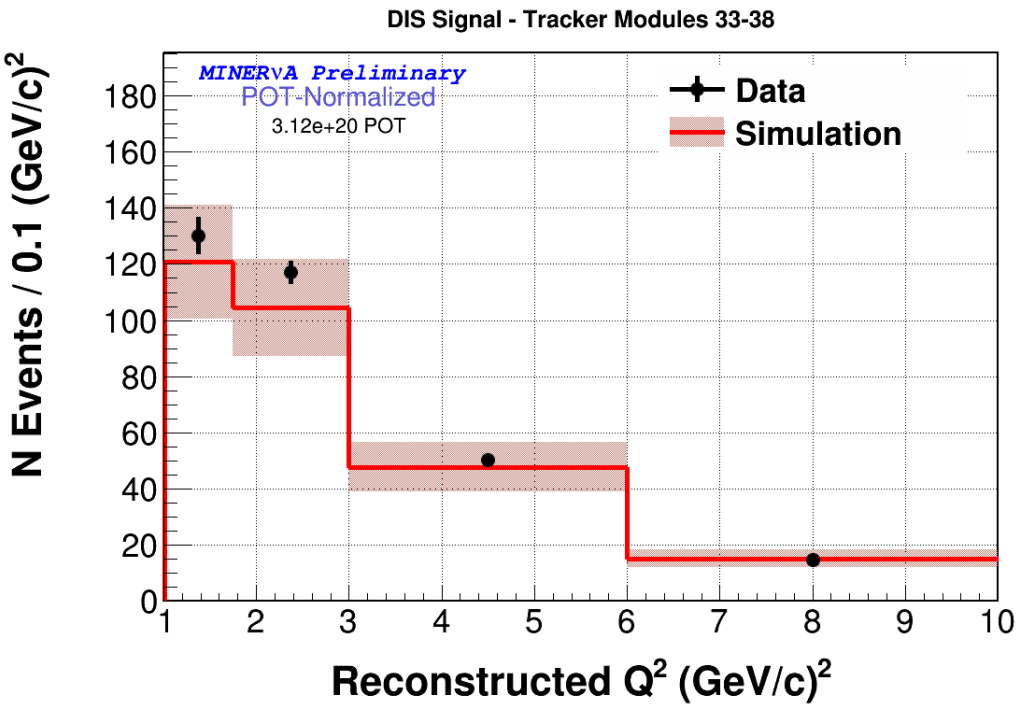

Figure E-50. DIS Signal: tracker mods. 33-38 (Q^2)

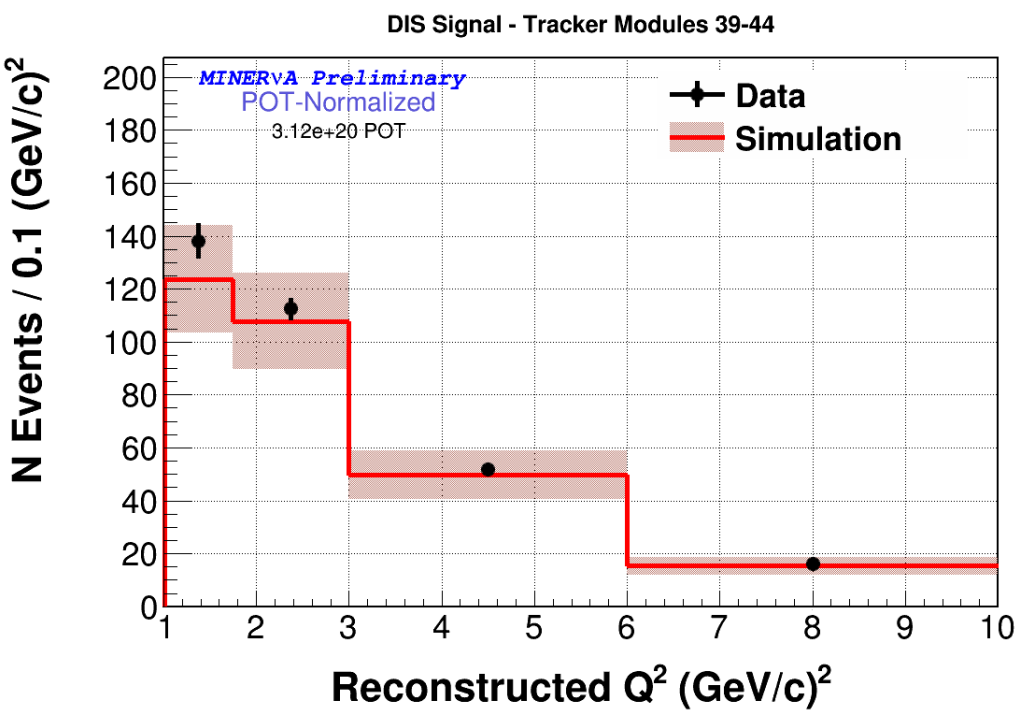

Figure E-51. DIS Signal: tracker mods. 39-44 (Q^2)

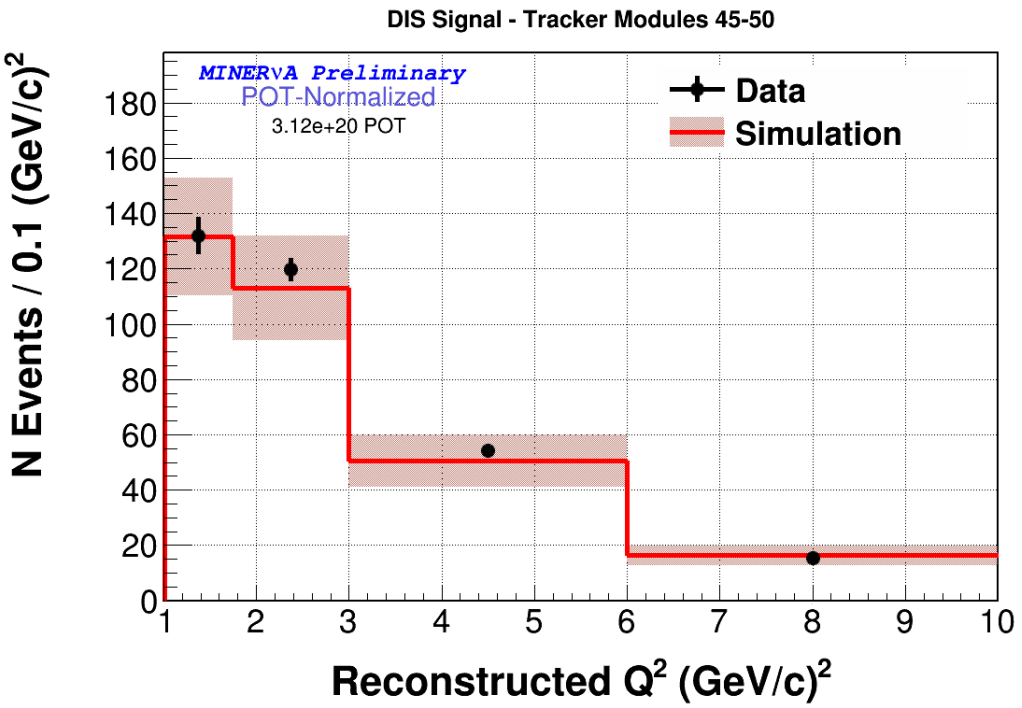

Figure E-52. DIS Signal: tracker mods. 45-50 (Q^2)

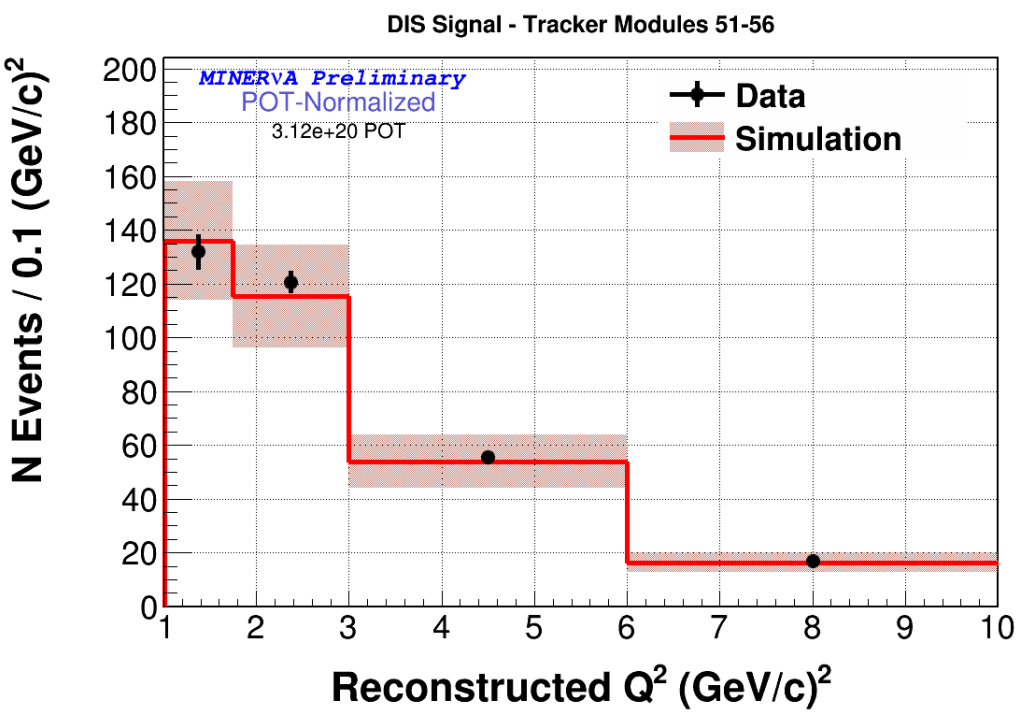

Figure E-53. DIS Signal: tracker mods. 51-56 (Q^2)

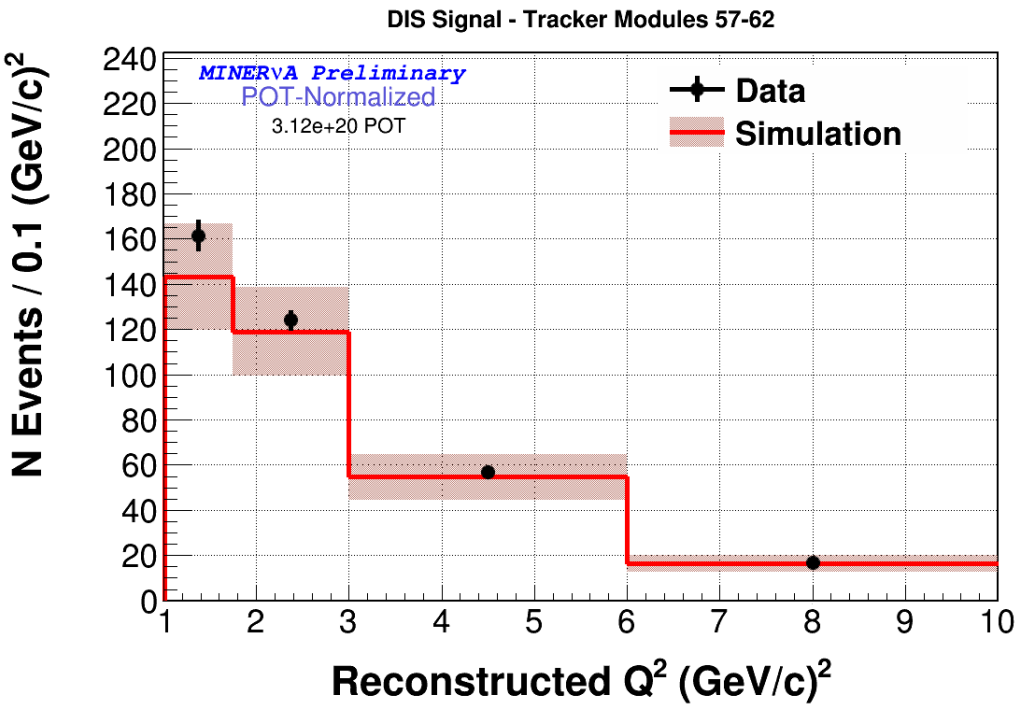

Figure E-54. DIS Signal: tracker mods. 57-62 (Q^2)

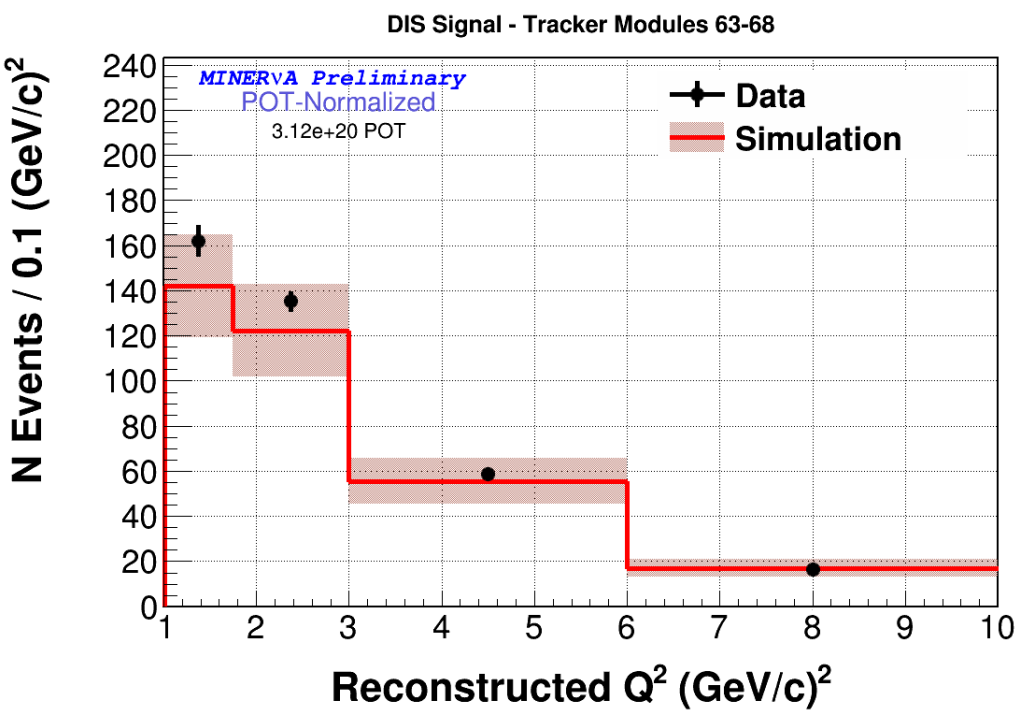

Figure E-55. DIS Signal: tracker mods. 63-68 (Q^2)

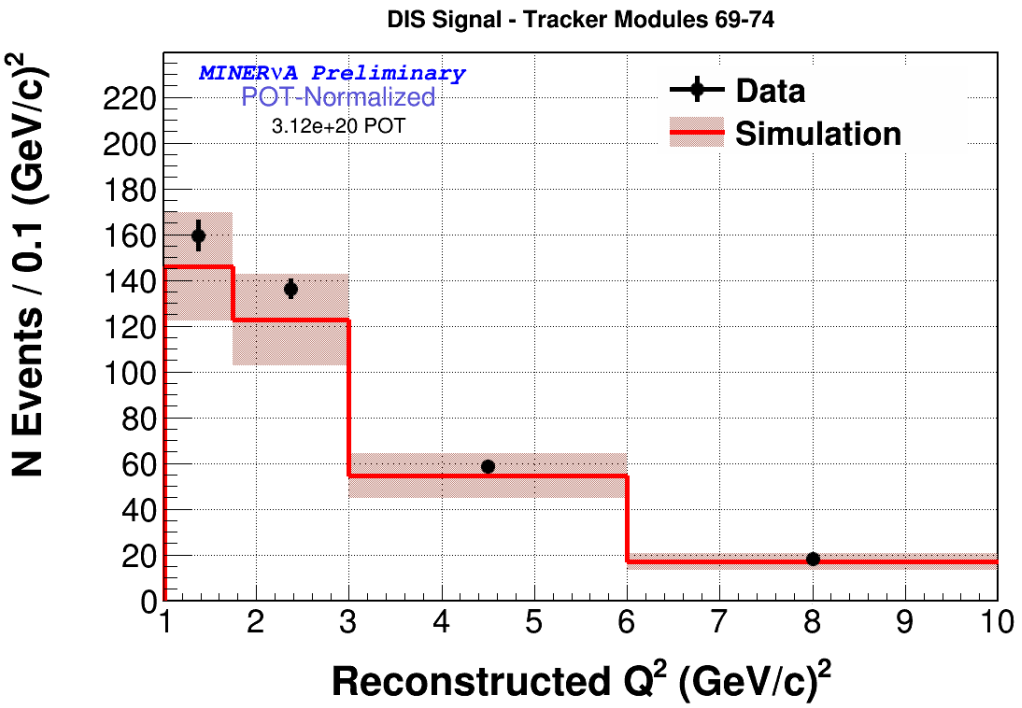

Figure E-56. DIS Signal: tracker mods. 69-74 (Q^2)

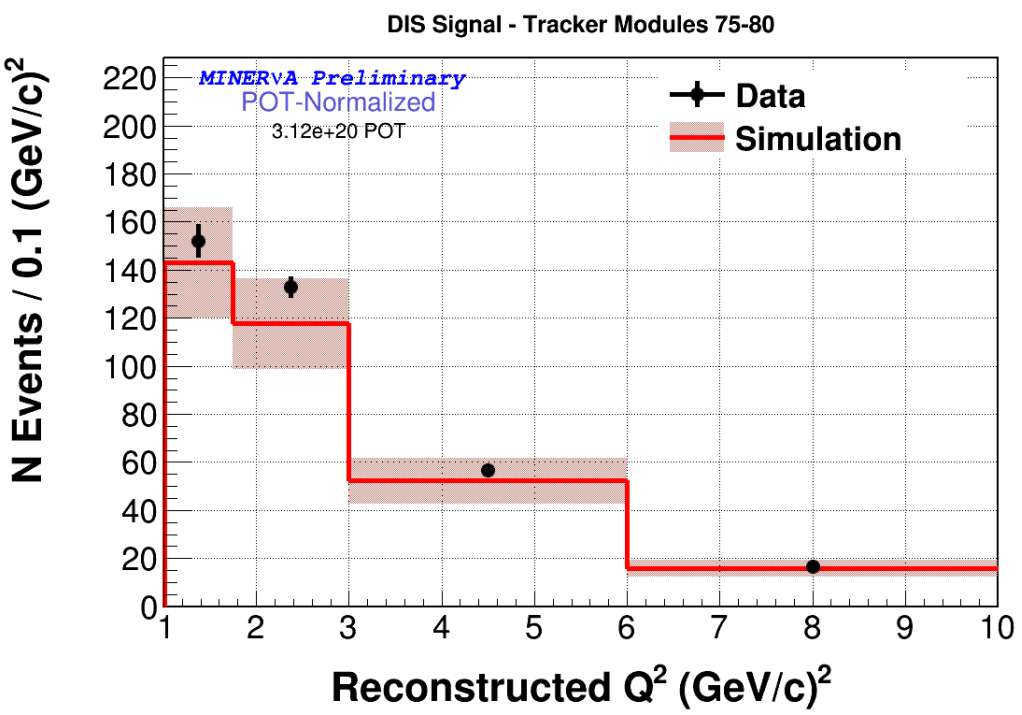

Figure E-57. DIS Signal: tracker mods. 75-80 (Q^2)

The following plots show the DIS events in data and MC, after subtracting the non-DIS events. The sample is broken down by target events and events in the predicted events in the surrounding CH. They are plotted as a function of final state hadronic shower invariant mass (W):

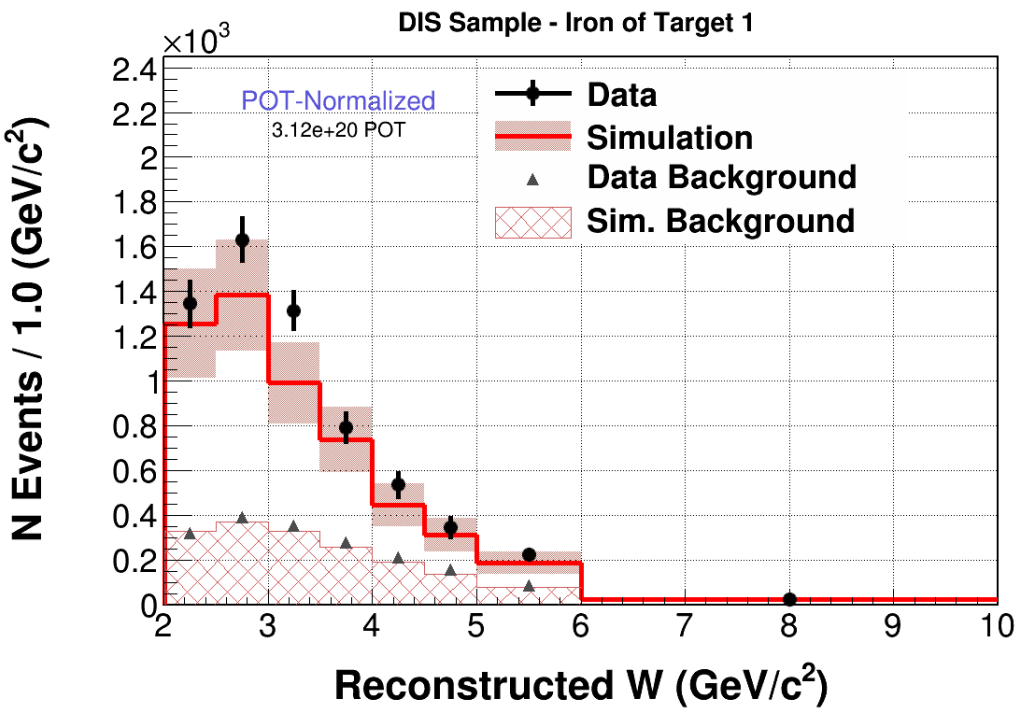

Figure E-58. DIS signal and CH background: target 01 Fe (W)

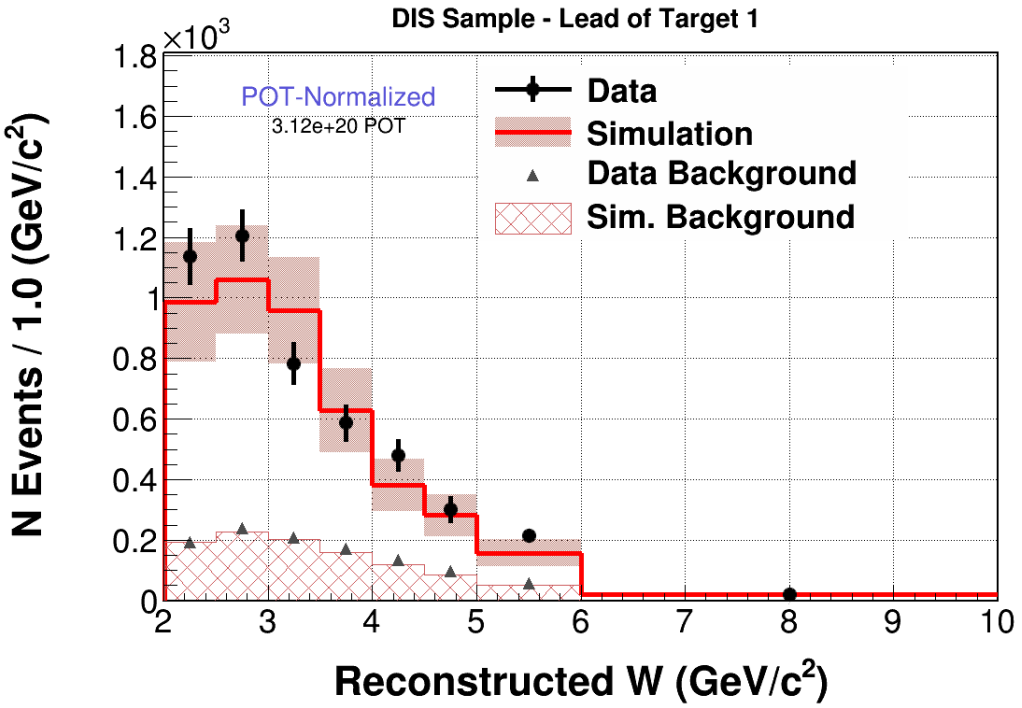

Figure E-59. DIS signal and CH background: target 01 Pb (W)

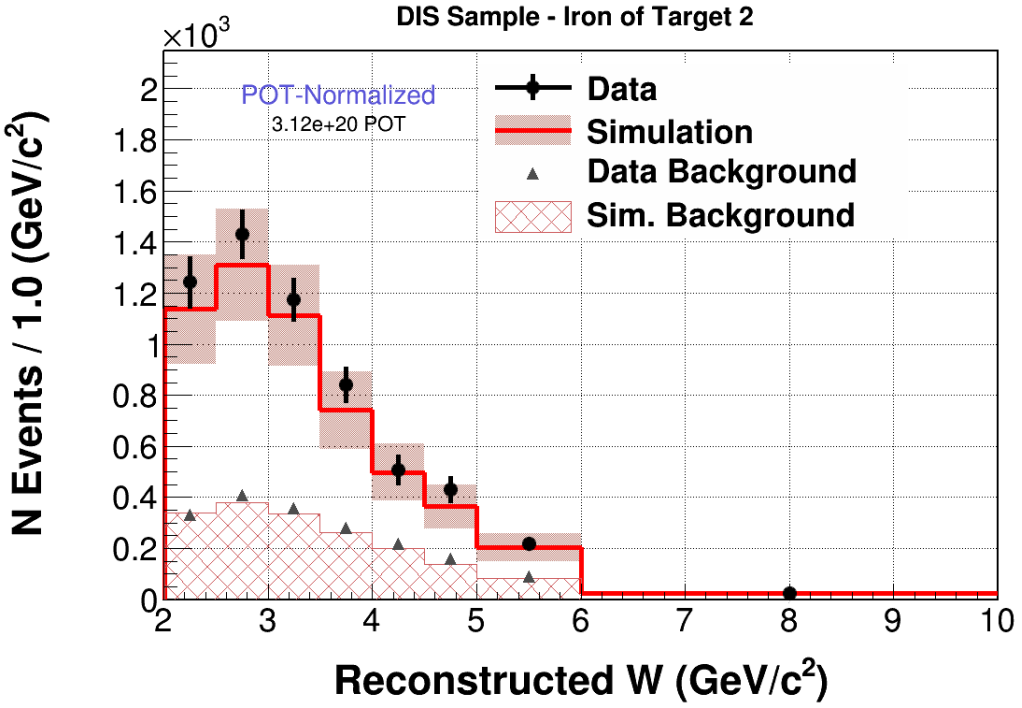

Figure E-60. DIS signal and CH background: target 02 Fe (W)

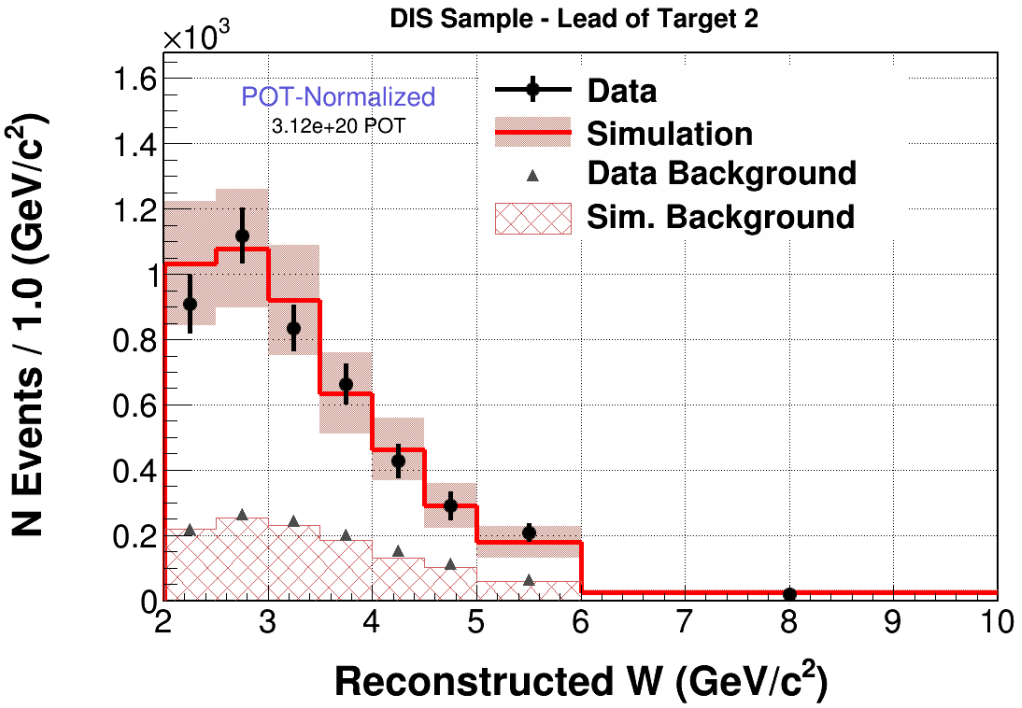

Figure E-61. DIS signal and CH background: target 02 Pb (W)

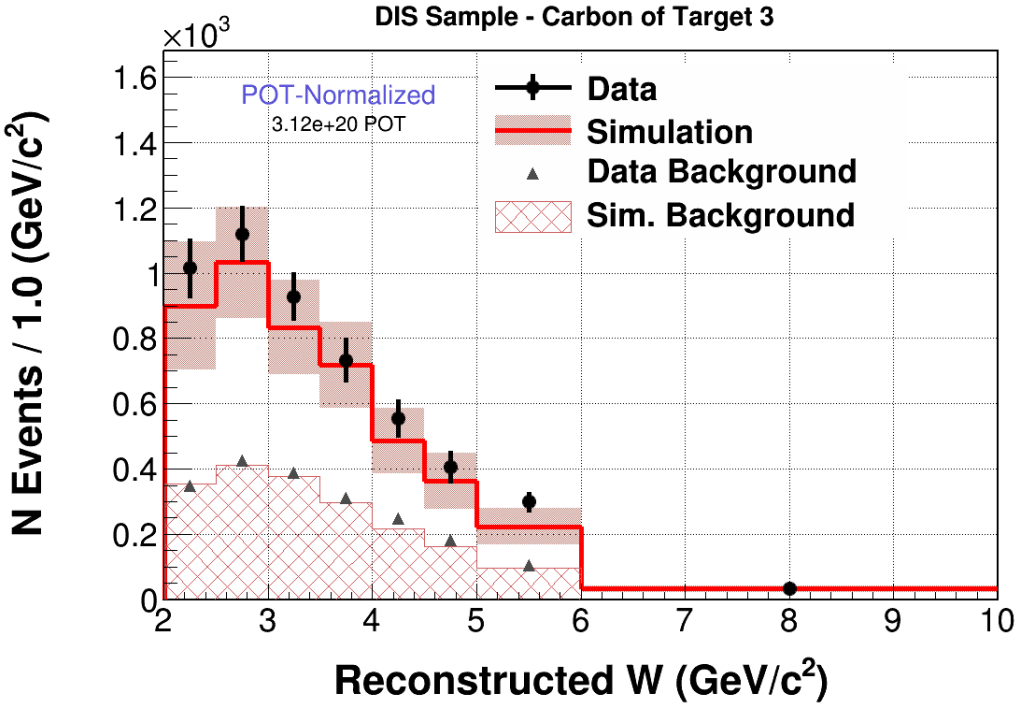

Figure E-62. DIS signal and CH background: target 03 C (W)

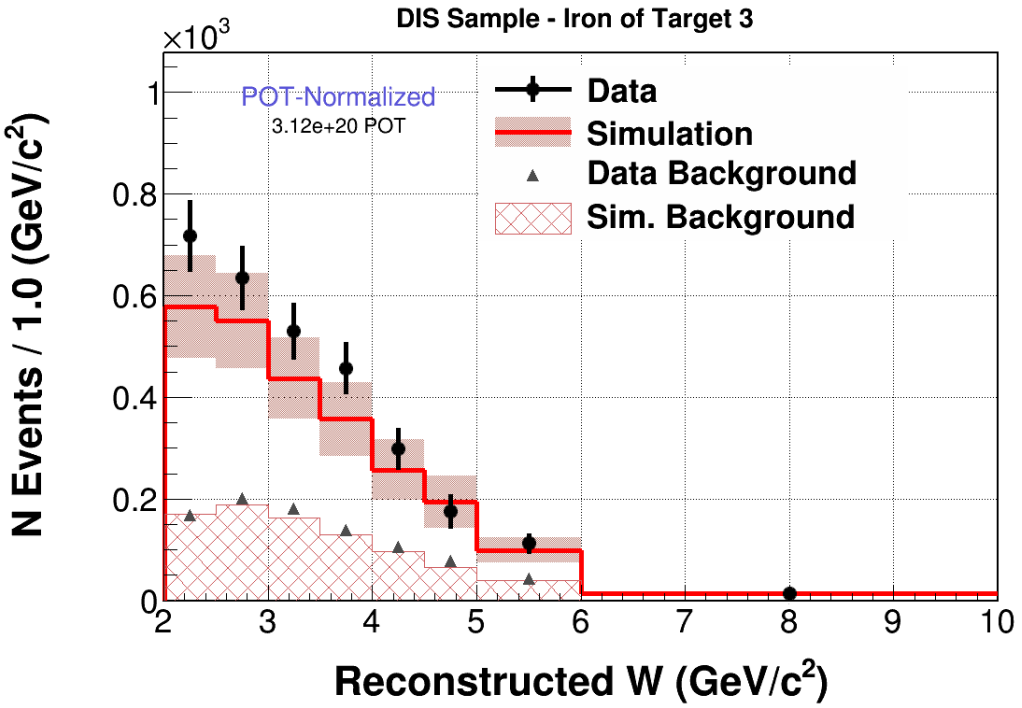

Figure E-63. DIS signal and CH background: target 03 Fe (W)

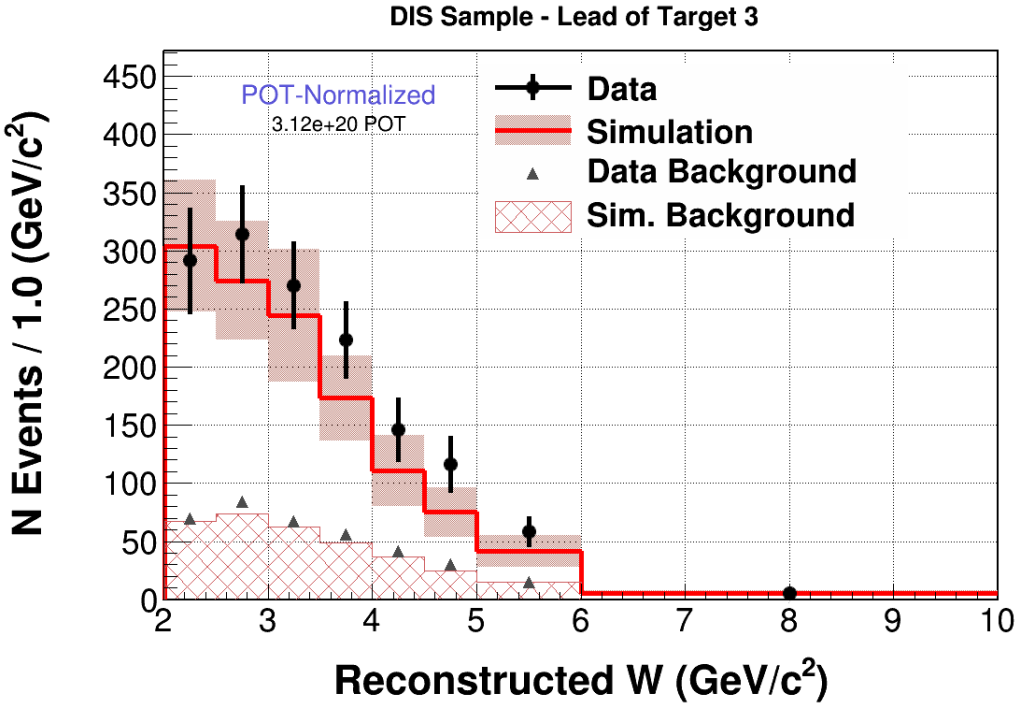

Figure E-64. DIS signal and CH background: target 03 Pb (W)

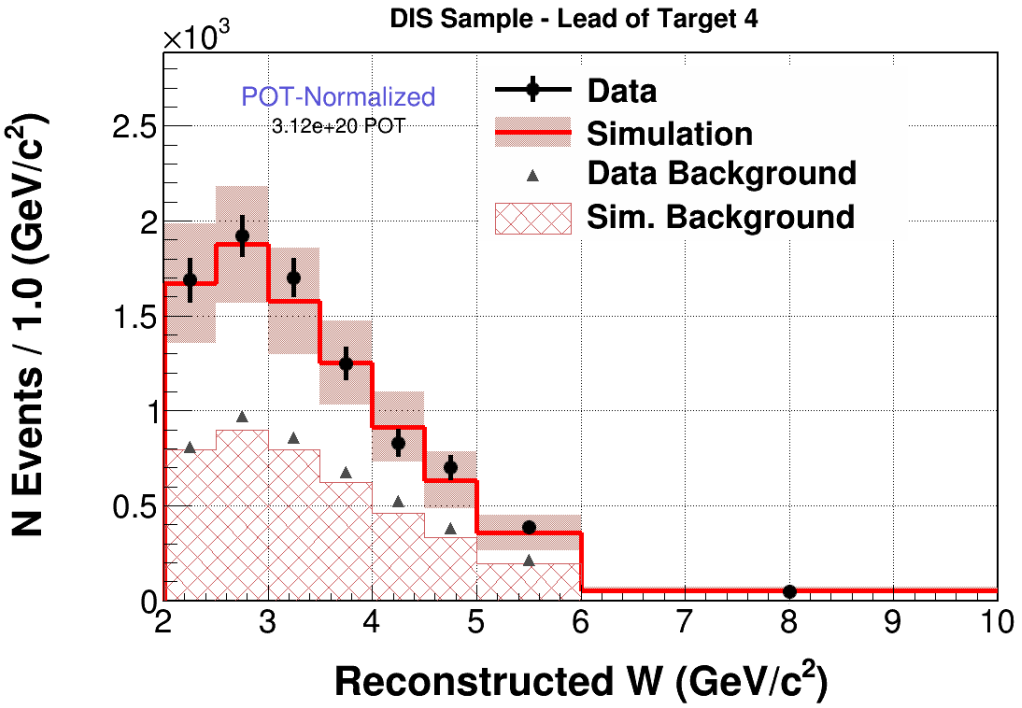

Figure E-65. DIS signal and CH background: target 04 Pb (W)

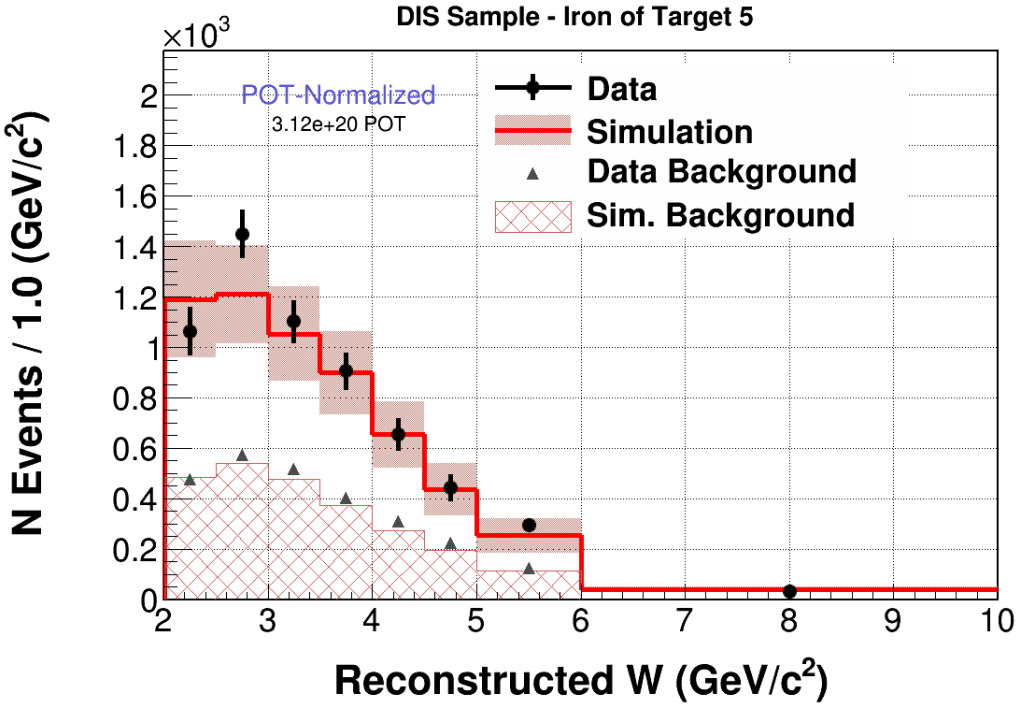

Figure E-66. DIS signal and CH background: target 05 Fe (W)

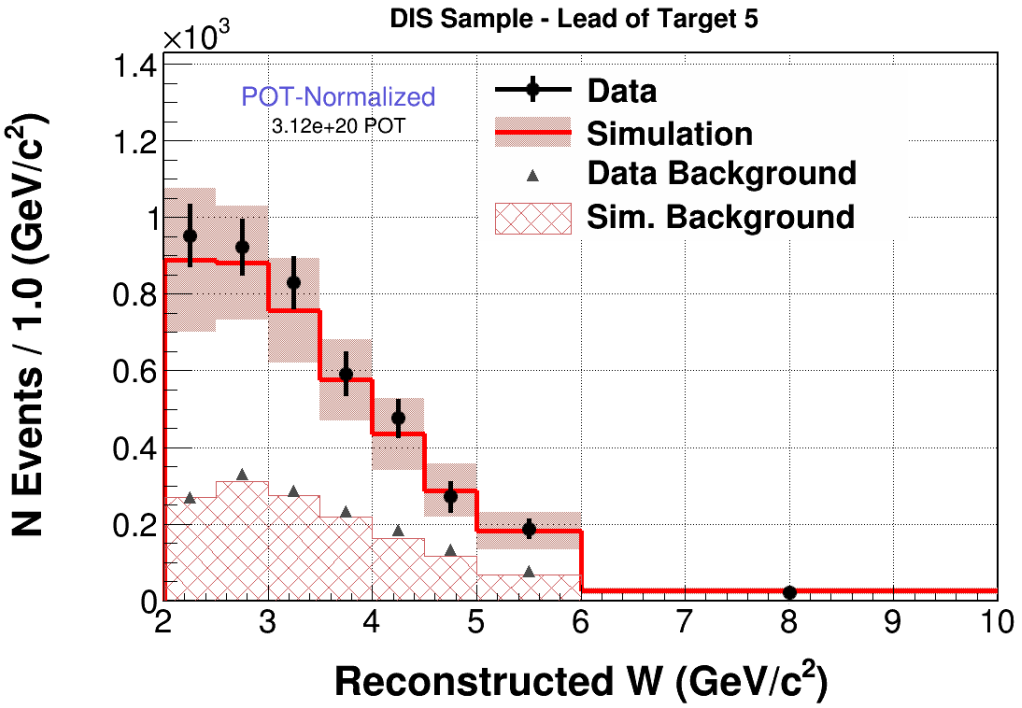

Figure E-67. DIS signal and CH background: target 05 Pb (W)

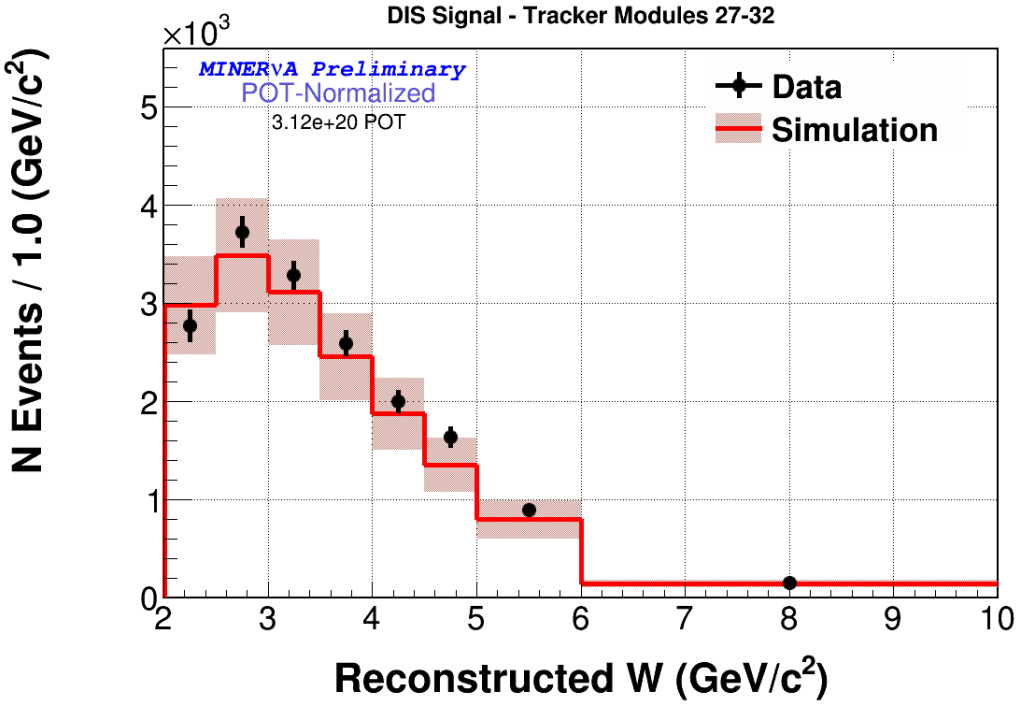

Figure E-68. DIS Signal: tracker mods. 27-32 (W)

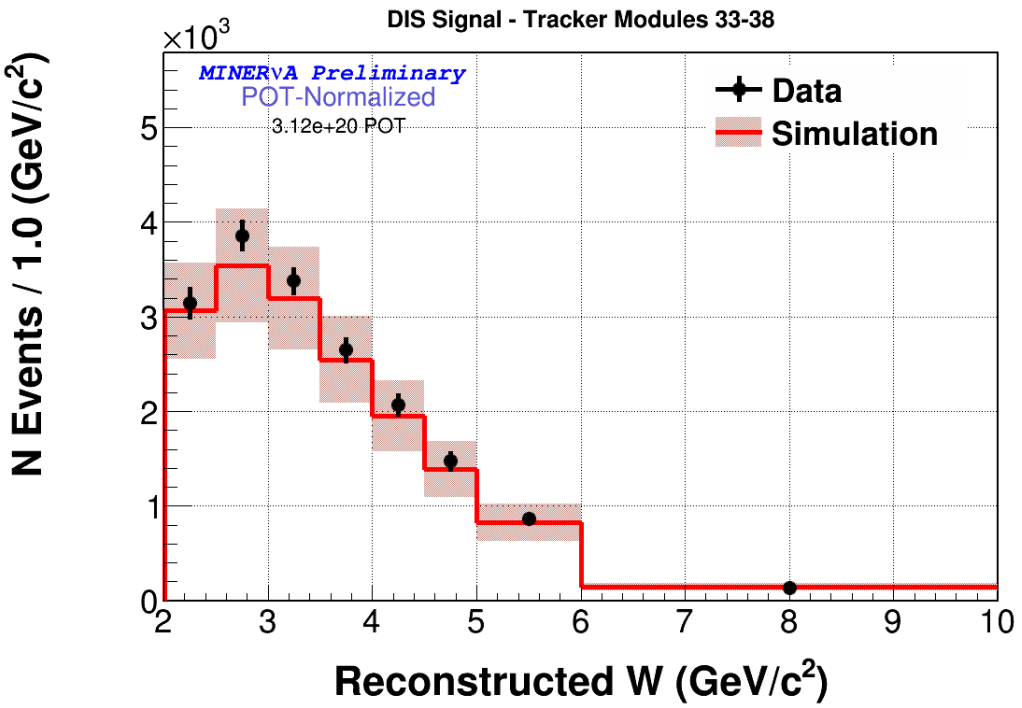

Figure E-69. DIS Signal: tracker mods. 33-38 (W)

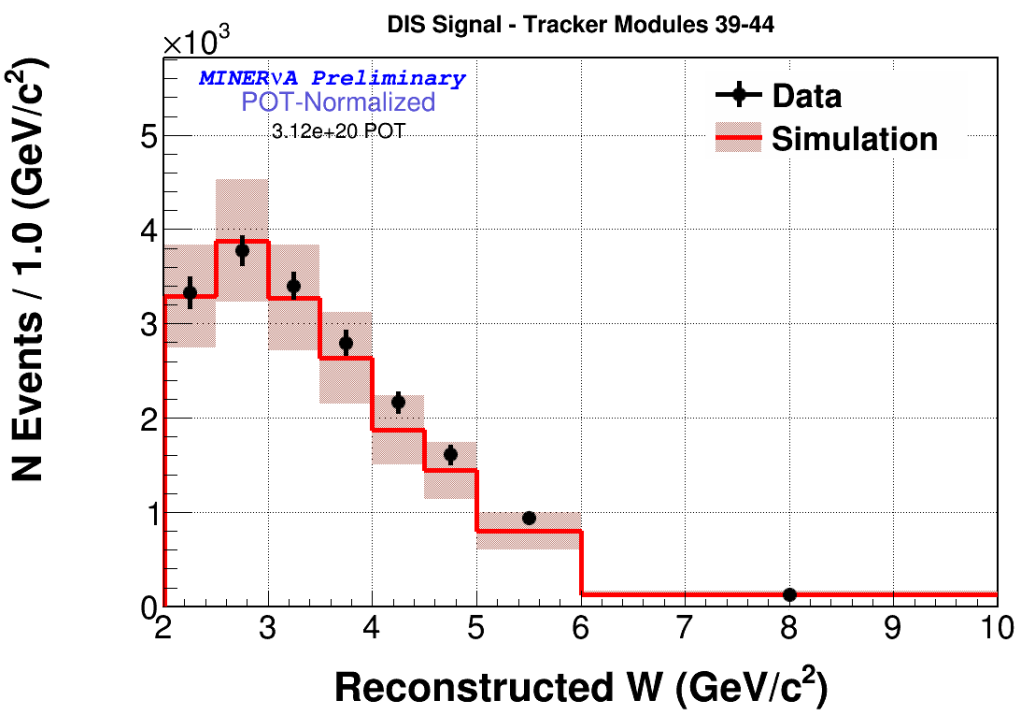

Figure E-70. DIS Signal: tracker mods. 39-44 (W)

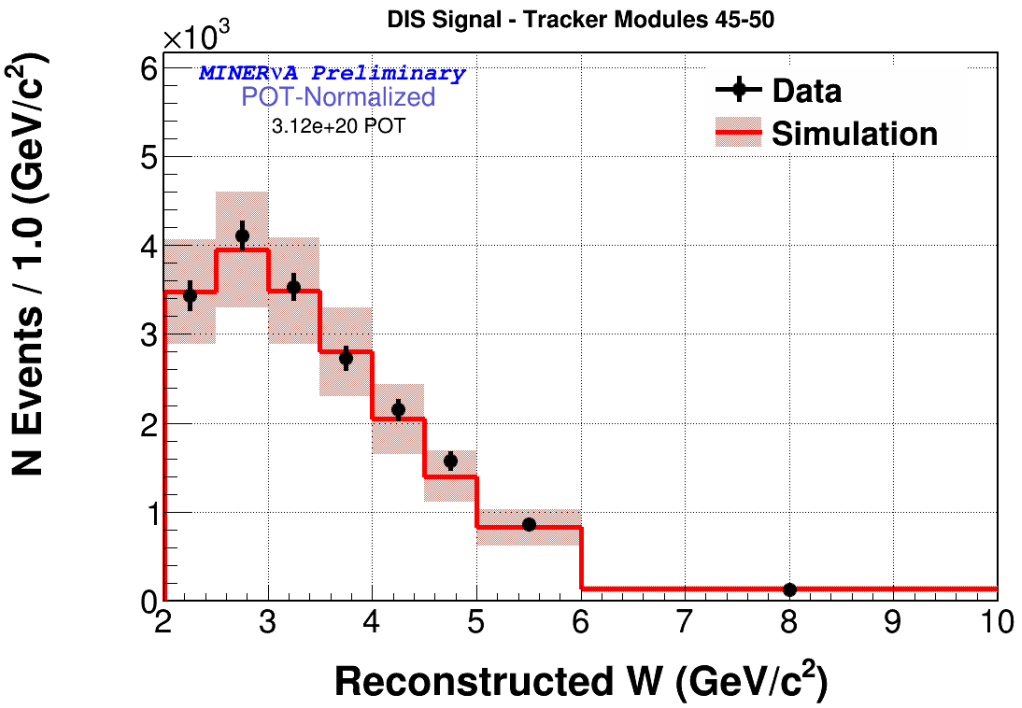

Figure E-71. DIS Signal: tracker mods. 45-50 (W)

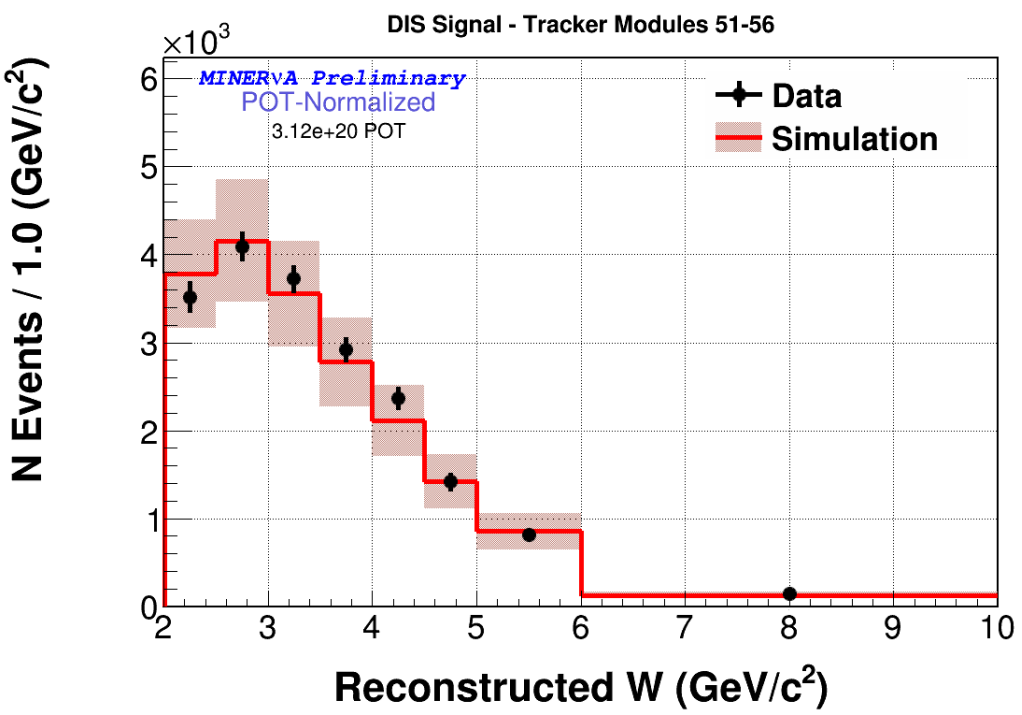

Figure E-72. DIS Signal: tracker mods. 51-56 (W)

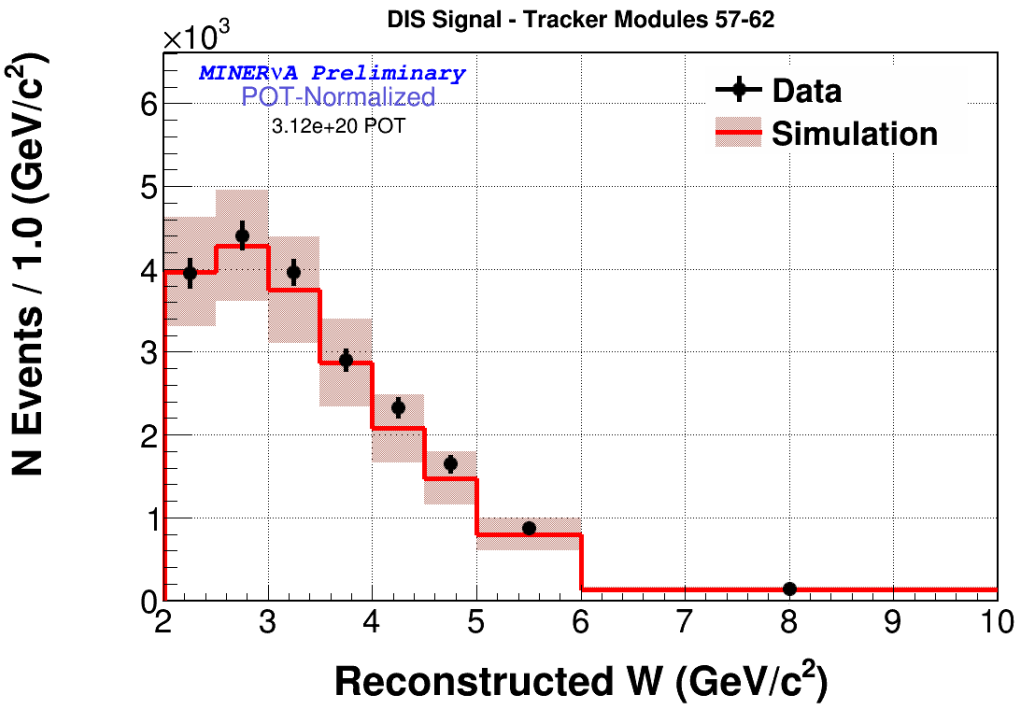

Figure E-73. DIS Signal: tracker mods. 57-62 (W)

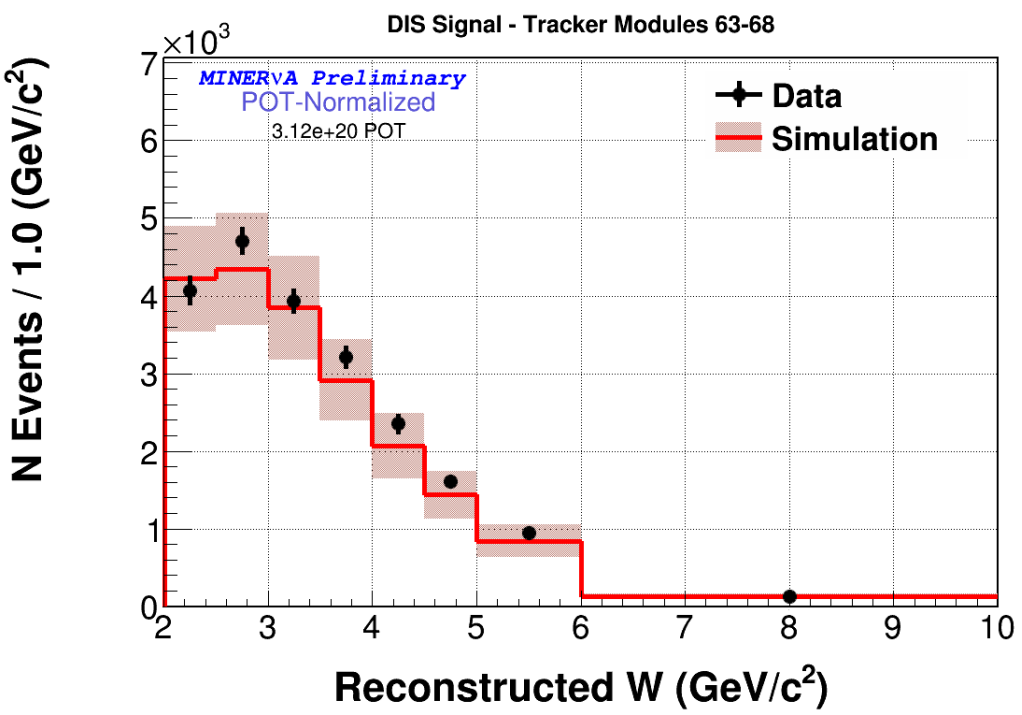

Figure E-74. DIS Signal: tracker mods. 63-68 (W)

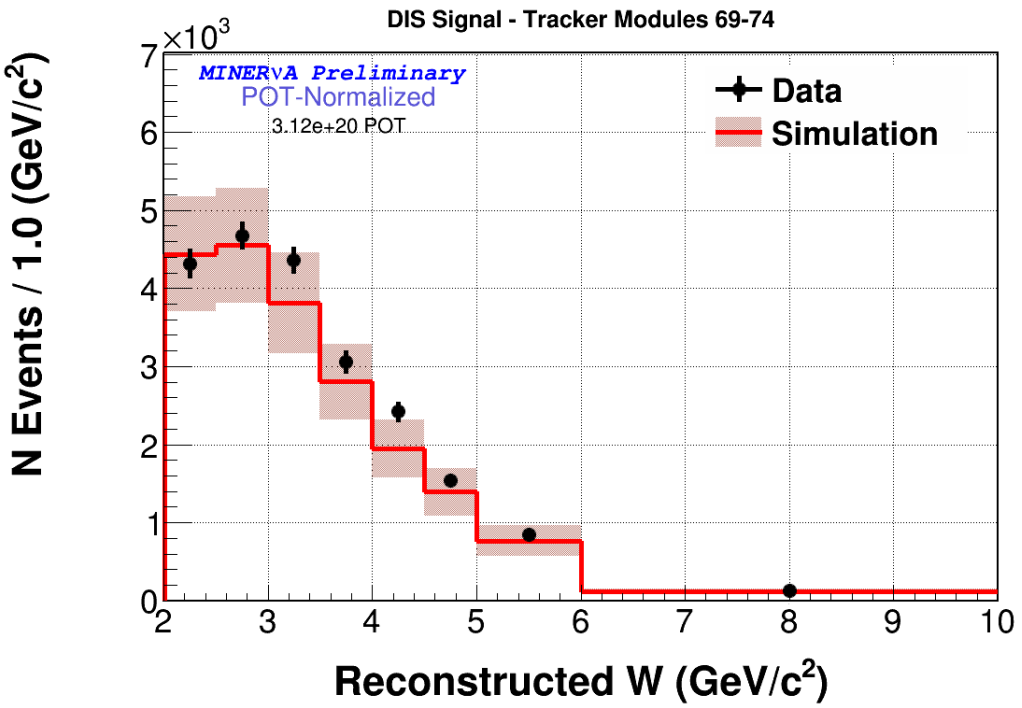

Figure E-75. DIS Signal: tracker mods. 69-74 (W)

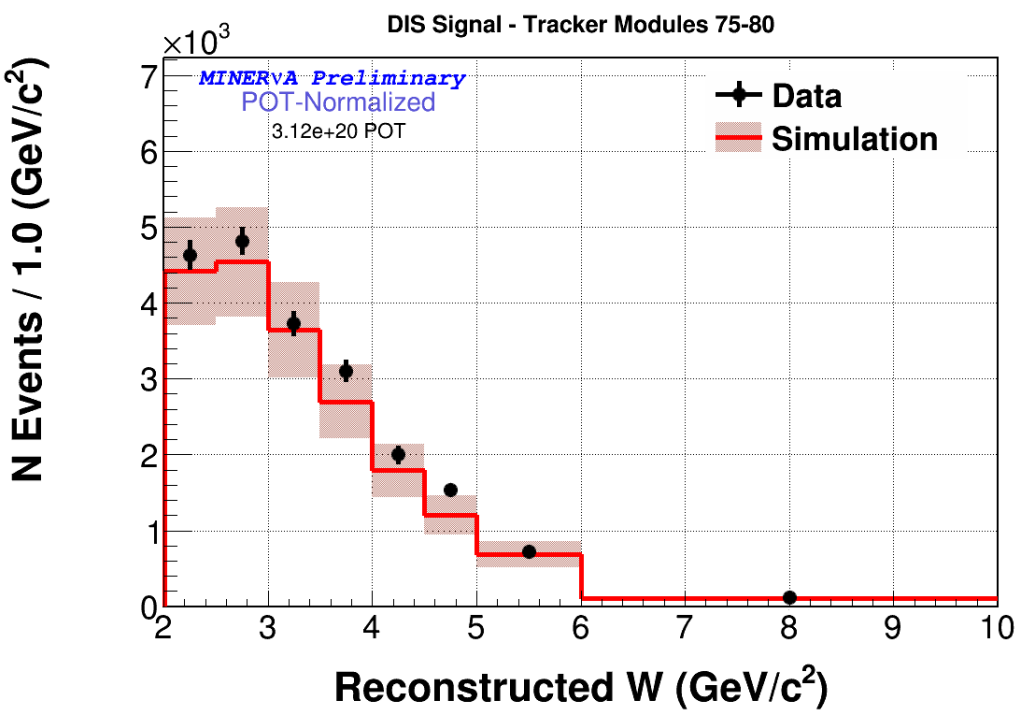

Figure E-76. DIS Signal: tracker mods. 75-80 (W)

The following plots show the DIS events in data and MC, after subtracting the non-DIS events. The sample is broken down by target events and events in the predicted events in the surrounding CH. They are plotted as a function of Bjorken-x (x_{bj}):

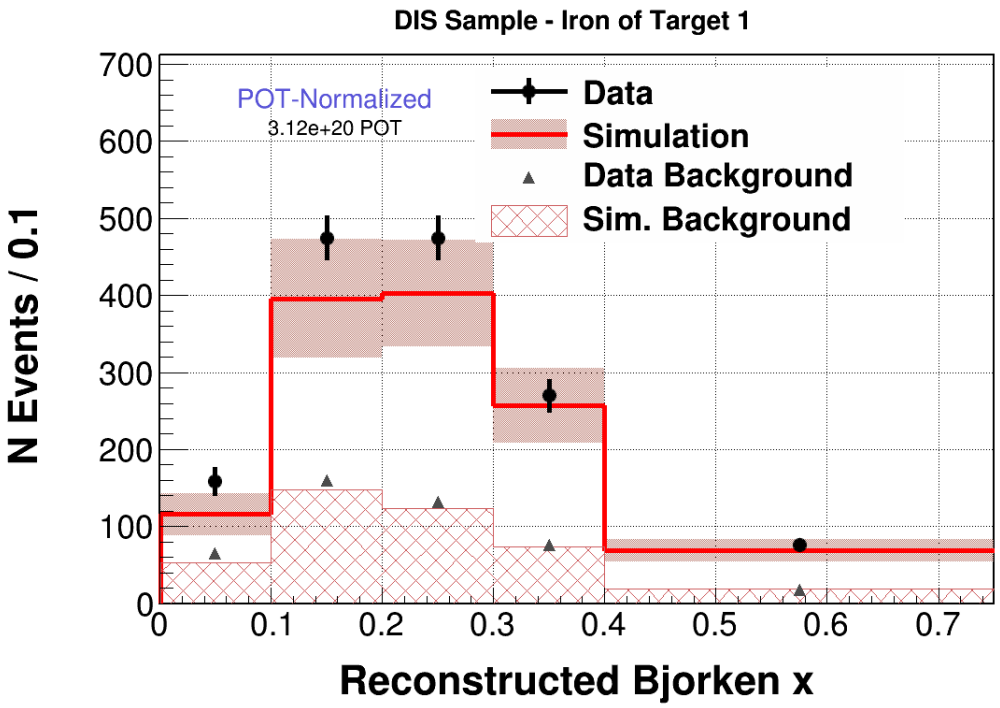

Figure E-77. DIS signal and CH background: target 01 Fe (x_{bj})

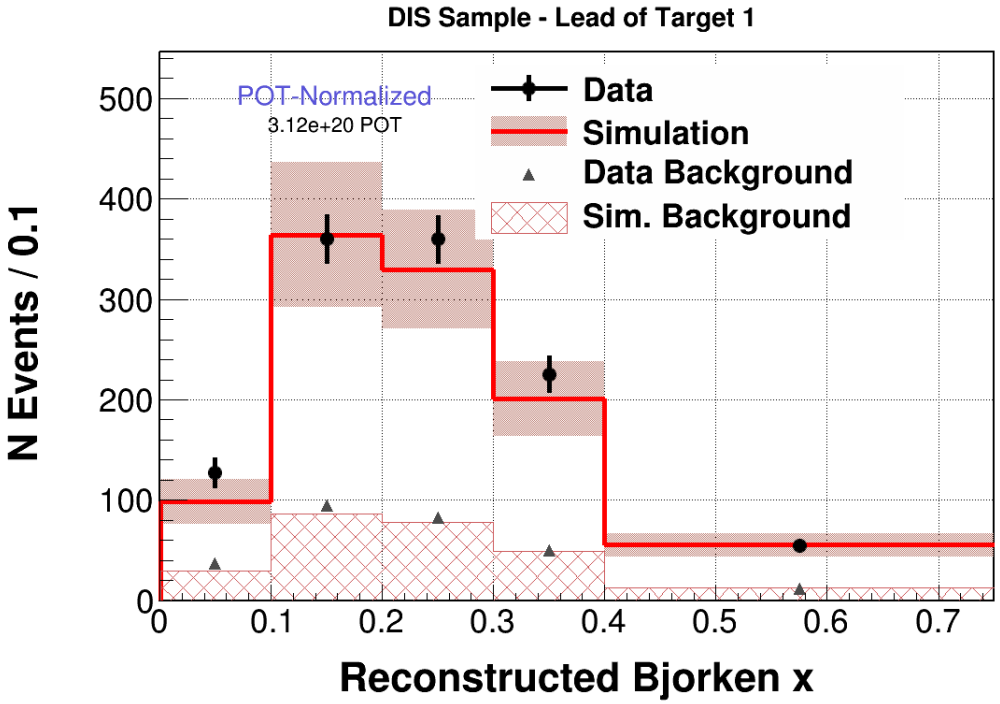

Figure E-78. DIS signal and CH background: target 01 Pb (x_{bj})

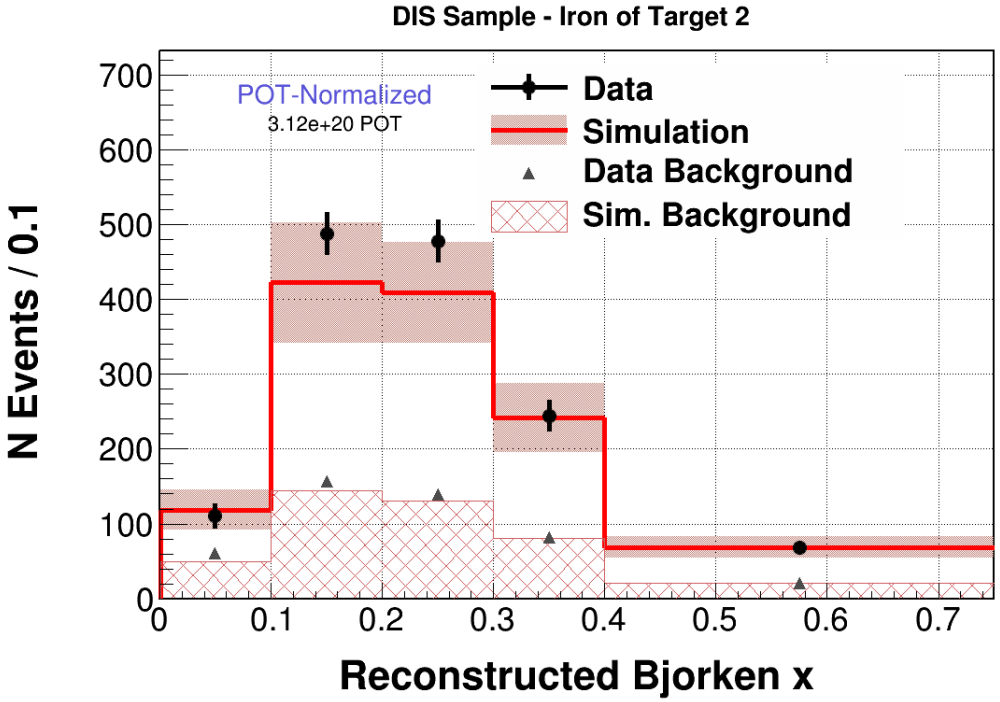

Figure E-79. DIS signal and CH background: target 02 Fe (x_{bj})

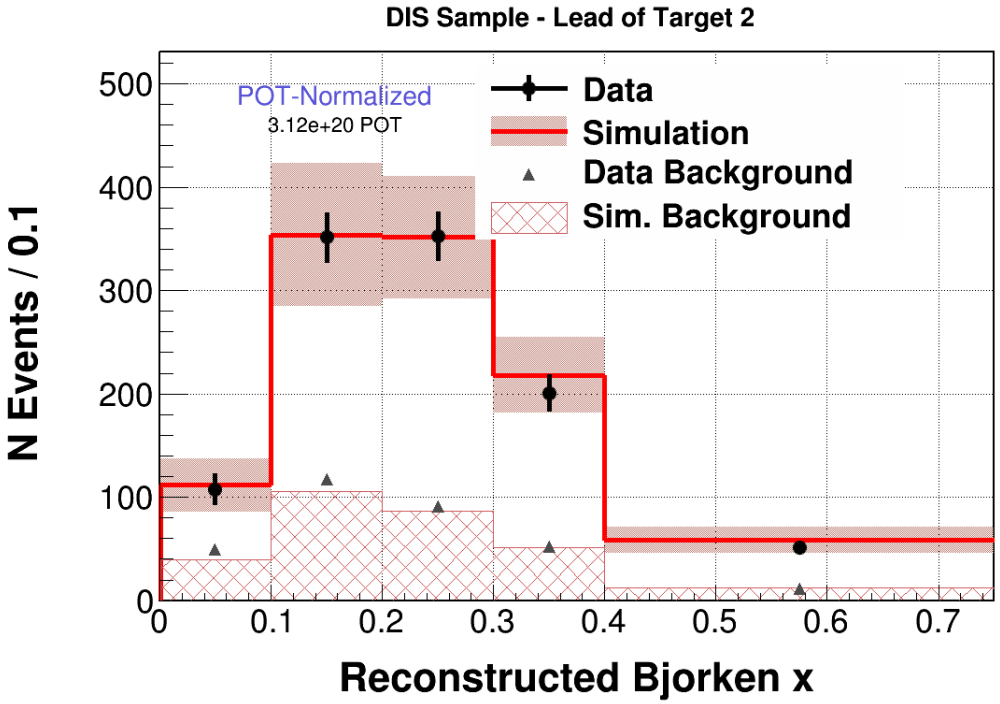

Figure E-80. DIS signal and CH background: target 02 Pb (x_{bj})

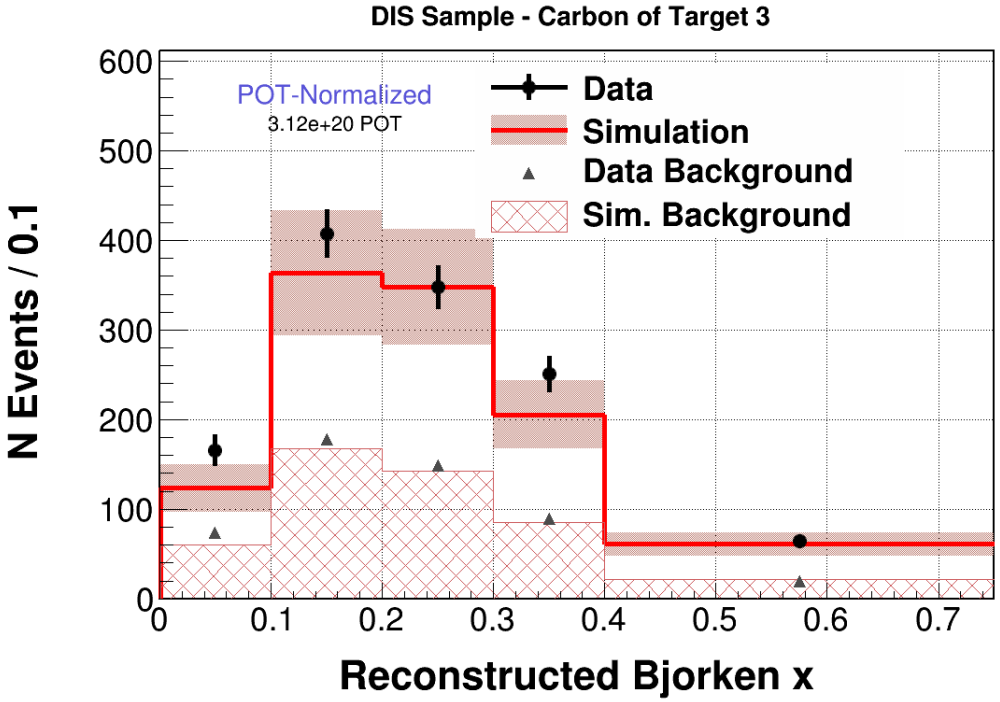

Figure E-81. DIS signal and CH background: target 02 C (x_{bj})

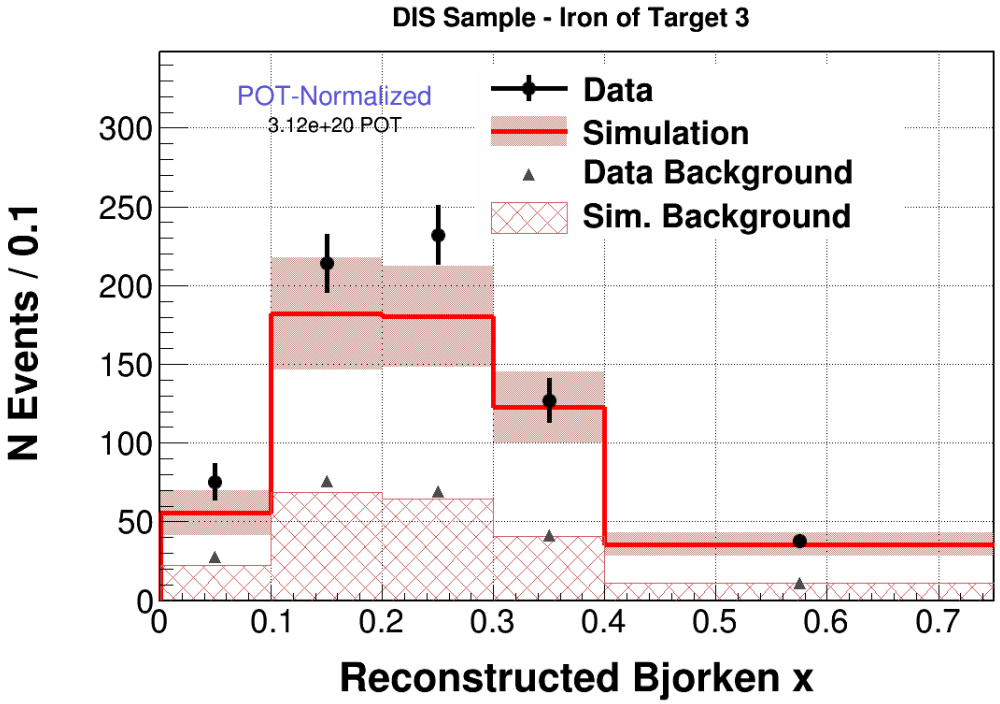

Figure E-82. DIS signal and CH background: target 03 Fe (x_{bj})

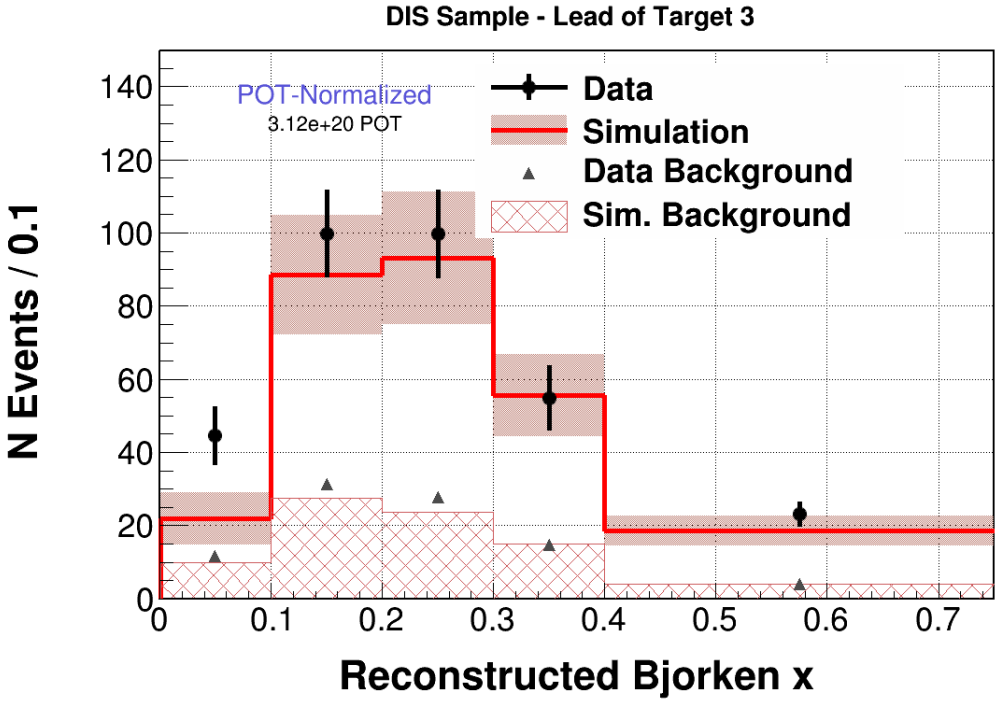

Figure E-83. DIS signal and CH background: target 03 Pb (x_{bj})

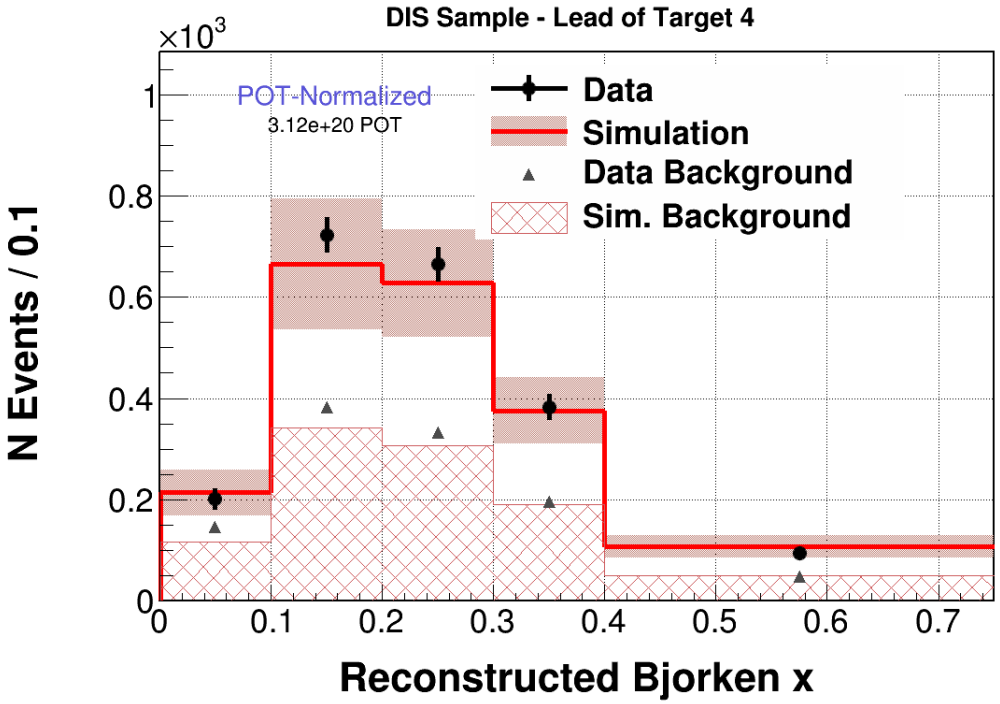

Figure E-84. DIS signal and CH background: target 04 Pb (x_{bj})

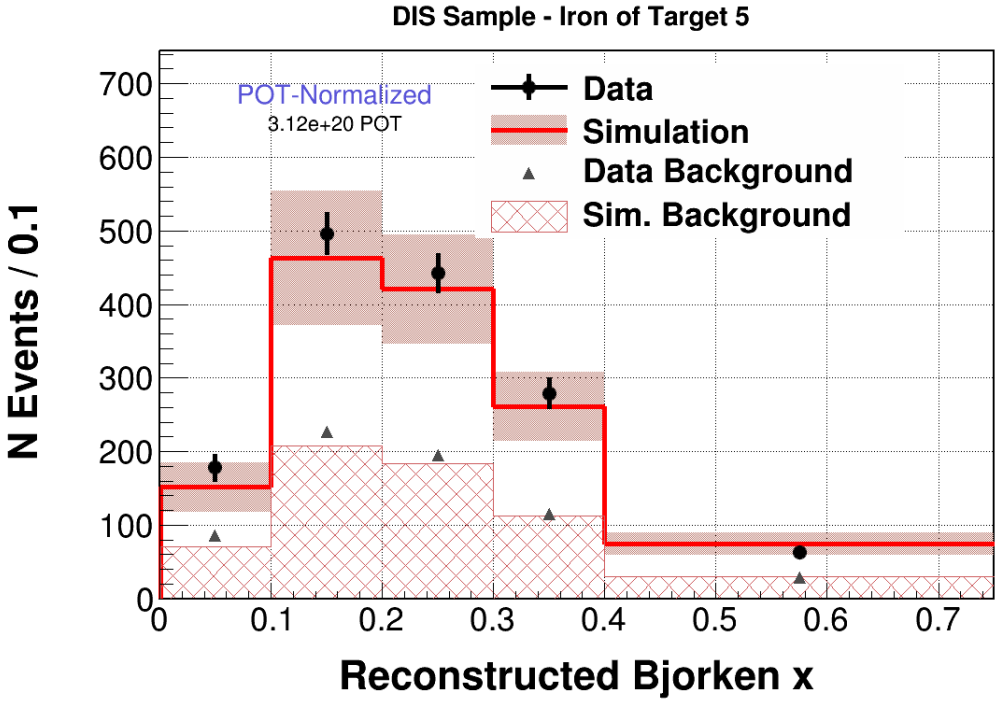

Figure E-85. DIS signal and CH background: target 05 Fe (x_{bj})

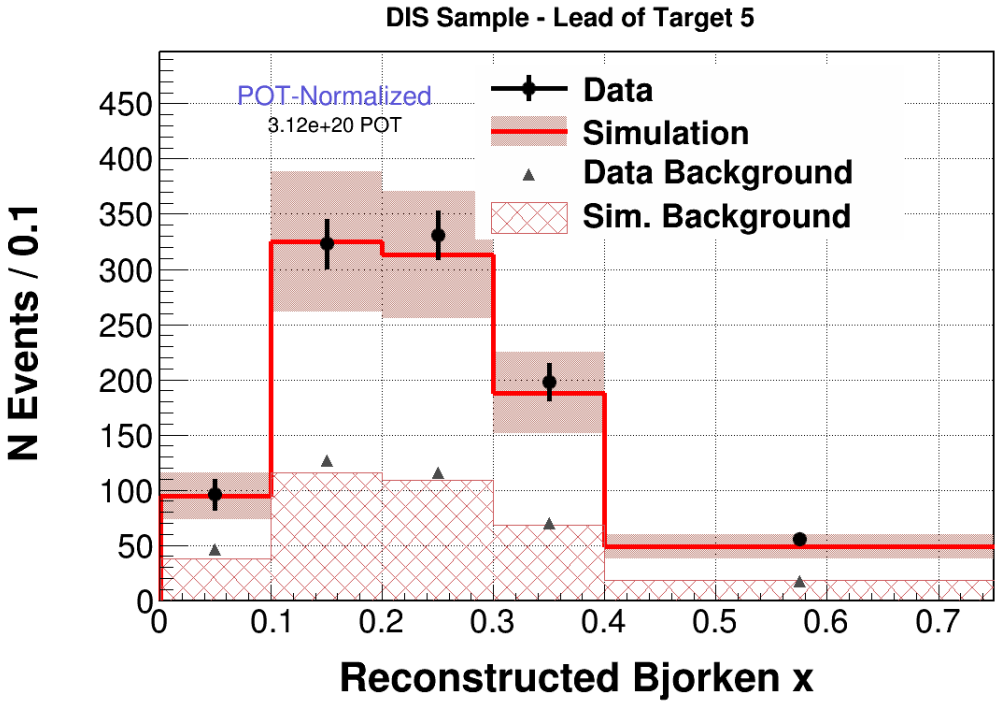

Figure E-86. DIS signal and CH background: target 05 Pb (x_{bj})

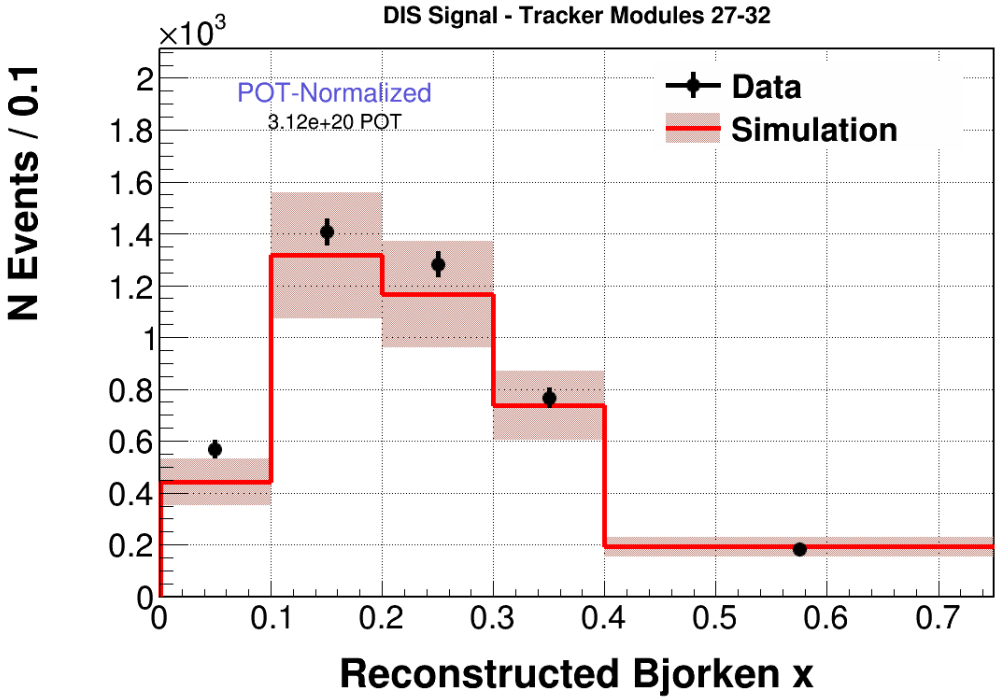

Figure E-87. DIS Signal: tracker mods. 27-32 (x_{bj})

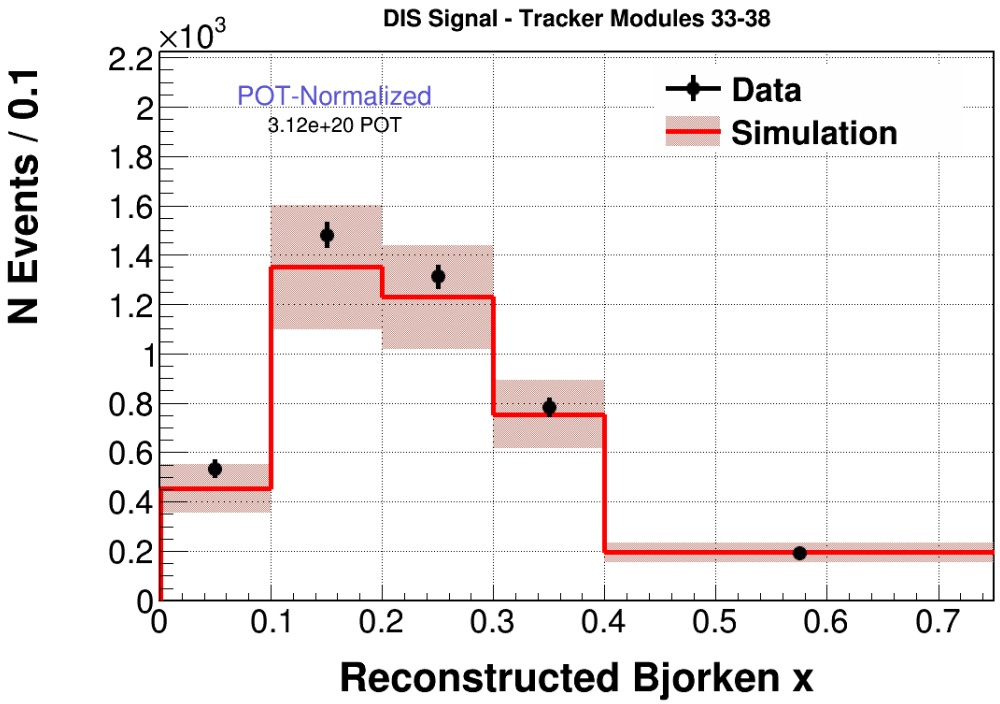

Figure E-88. DIS Signal: tracker mods. 33-38 (x_{bj})

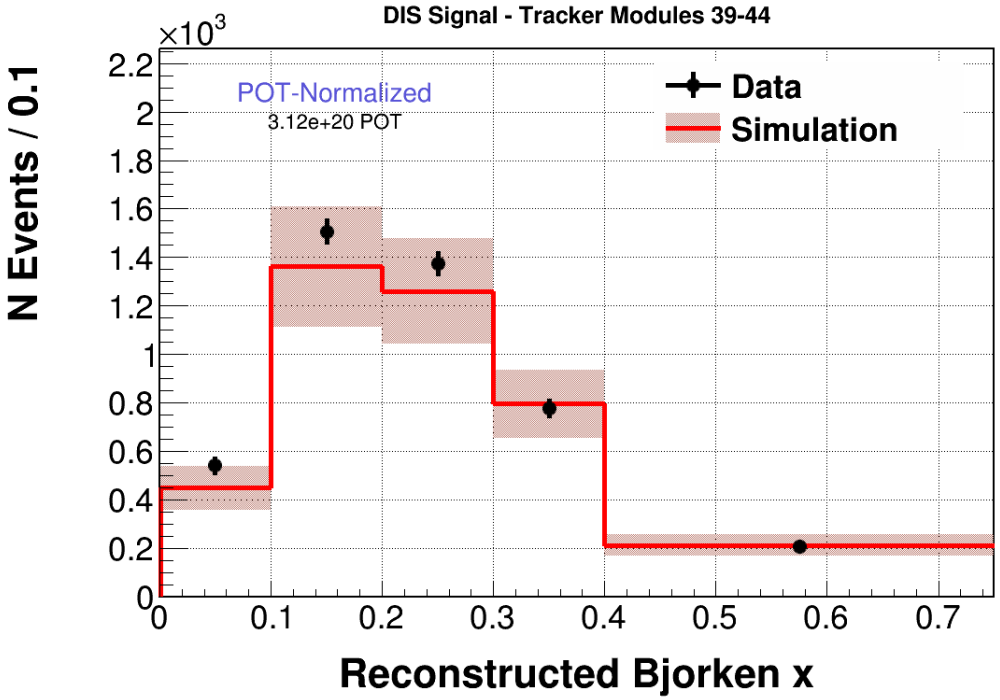

Figure E-89. DIS Signal: tracker mods. 39-44 (x_{bj})

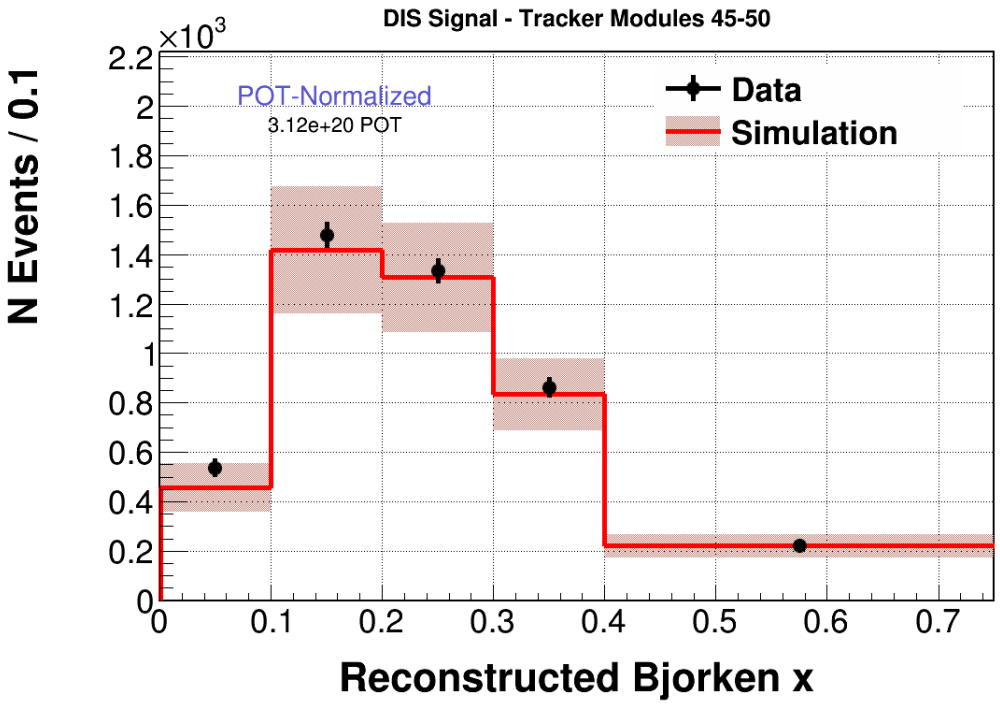

Figure E-90. DIS Signal: tracker mods. 45-50 (x_{bj})

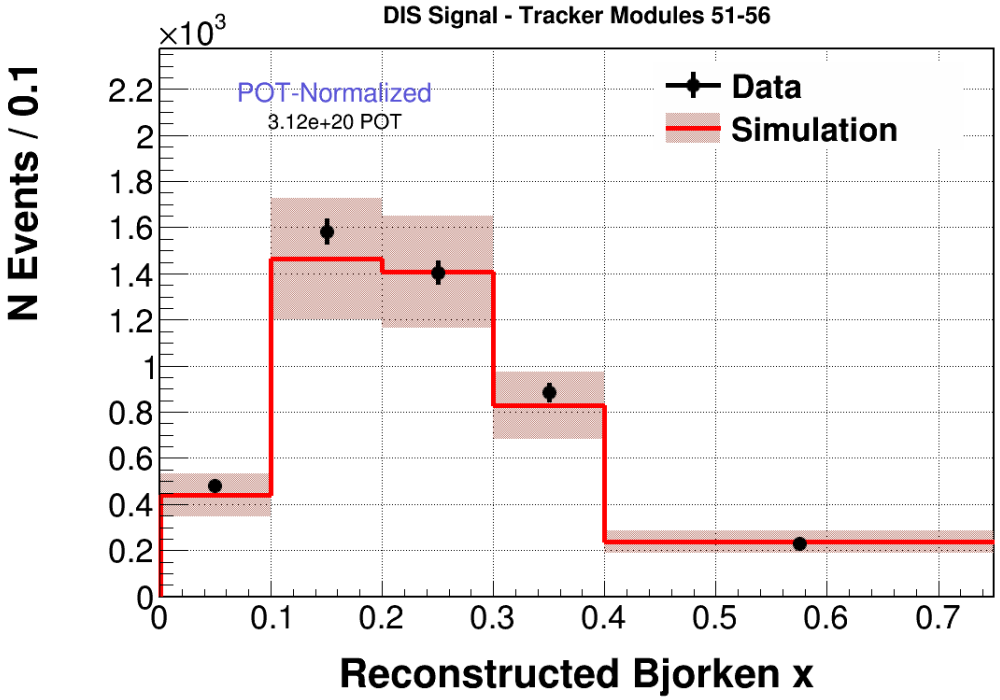

Figure E-91. DIS Signal: tracker mods. 51-56 (x_{bj})

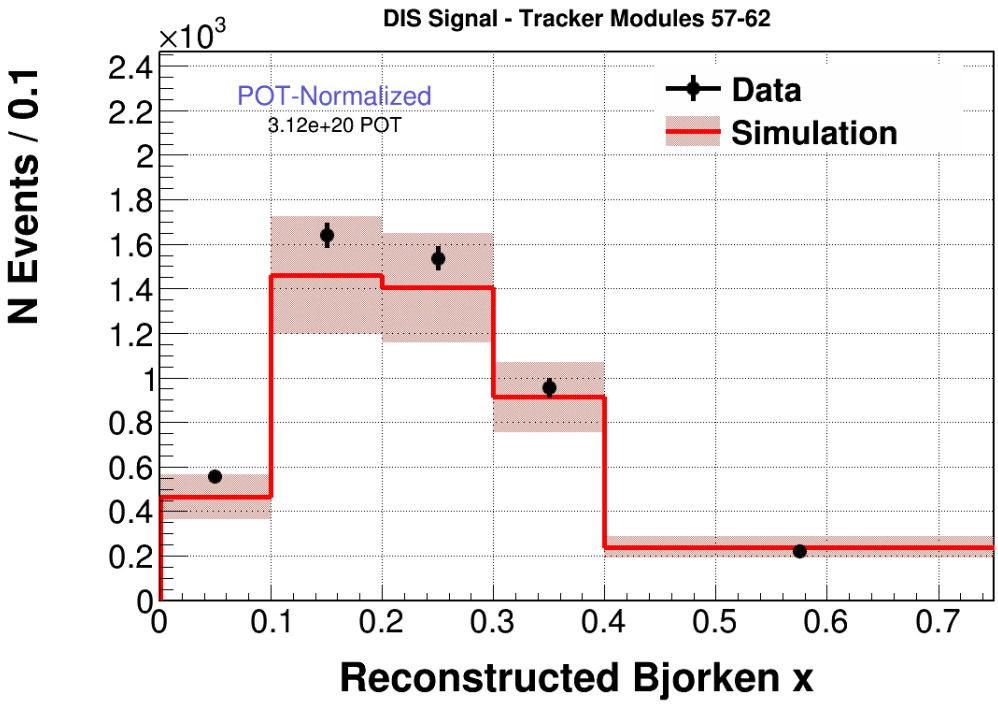

Figure E-92. DIS Signal: tracker mods. 57-62 (x_{bj})

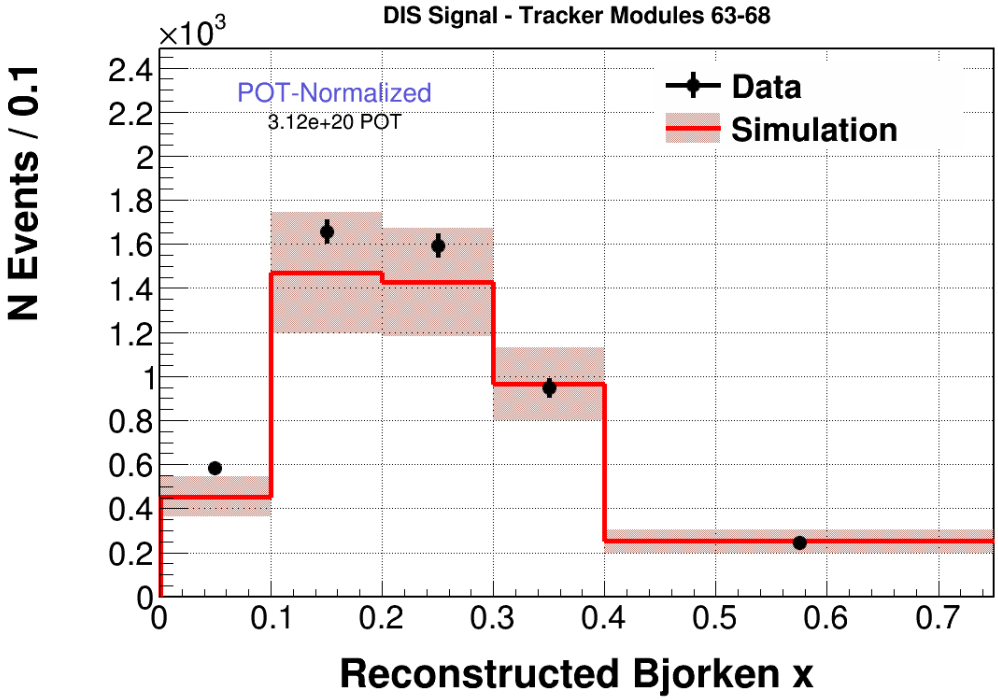

Figure E-93. DIS Signal: tracker mods. 63-68 (x_{bj})

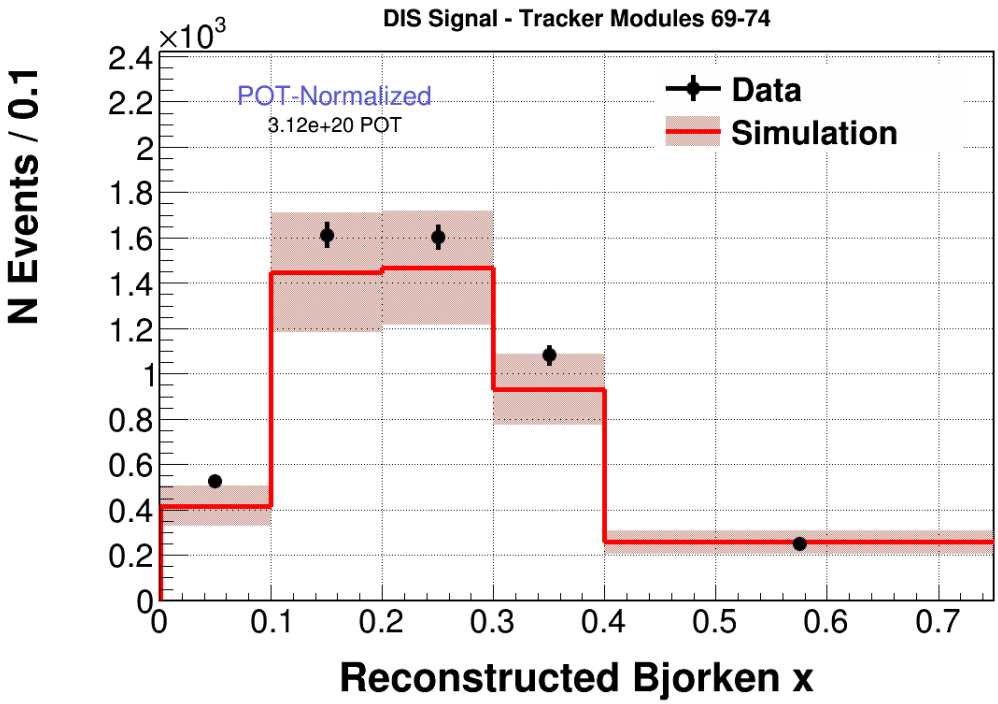

Figure E-94. DIS Signal: tracker mods. 69-74 (x_{bj})

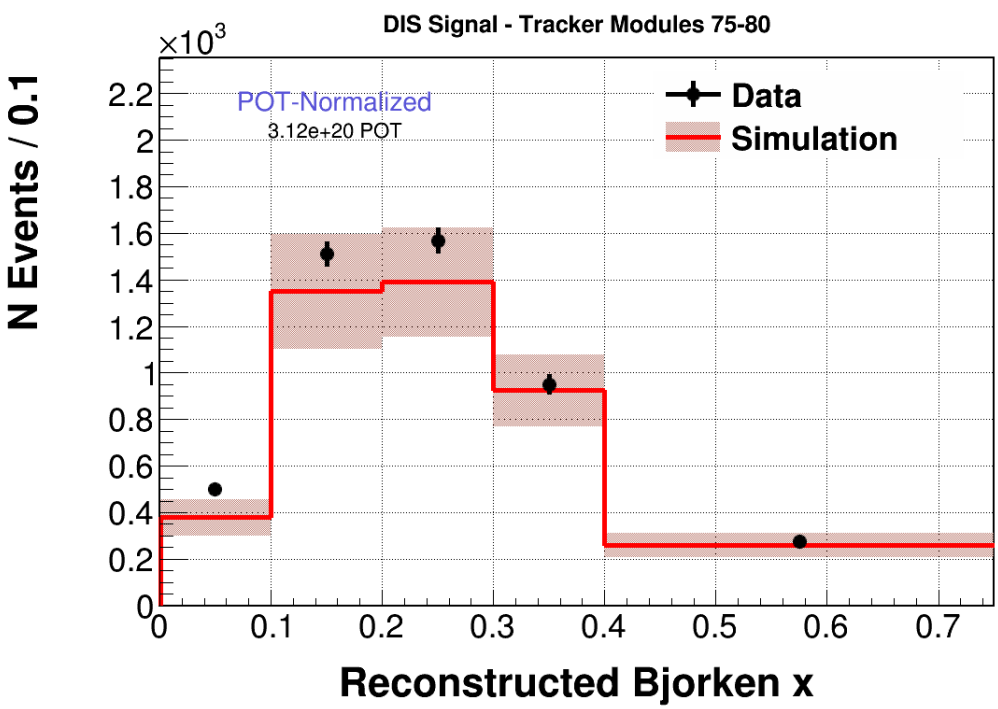

Figure E-95. DIS Signal: tracker mods. 75-80 (x_{bj})

The following plots show the DIS events in data and MC, after subtracting the non-DIS events. The sample is broken down by target events and events in the predicted events in the surrounding CH. They are plotted as a function of muon energy (E_μ):

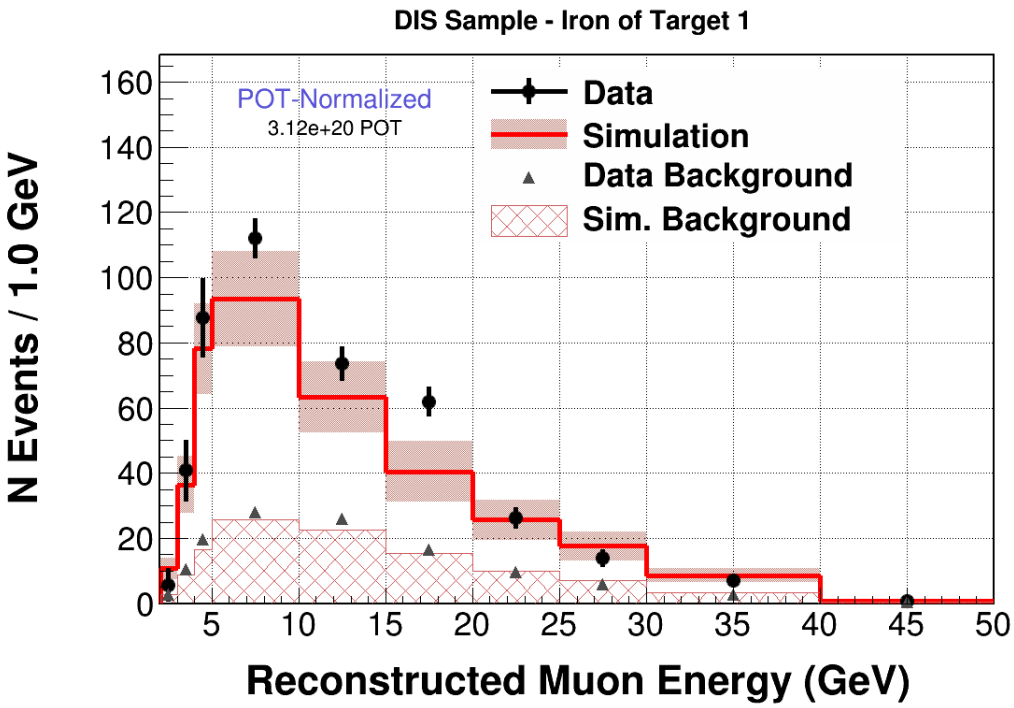

Figure E-96. DIS signal and CH background: target 01 Fe (E_μ)

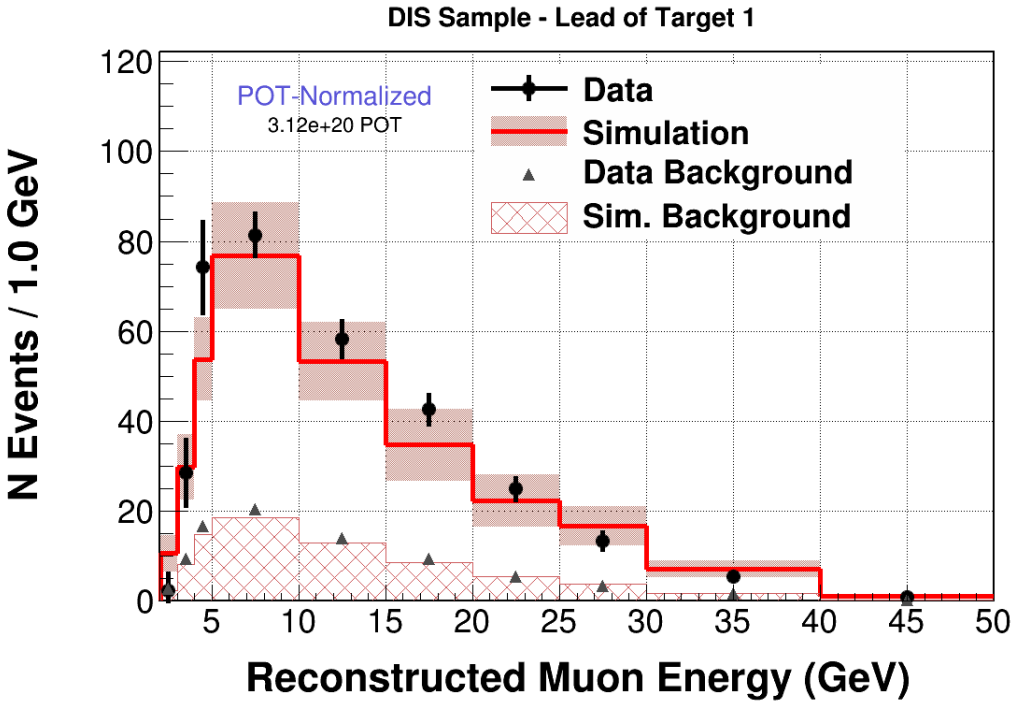

Figure E-97. DIS signal and CH background: target 01 Pb (E_μ)

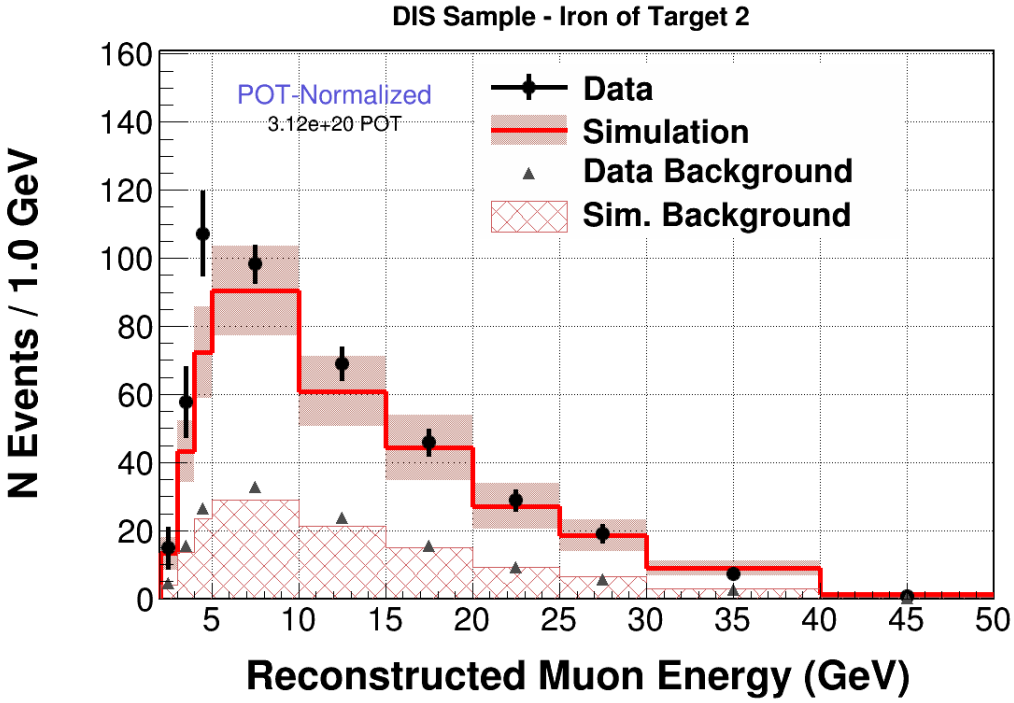

Figure E-98. DIS signal and CH background: target 02 Fe (E_μ)

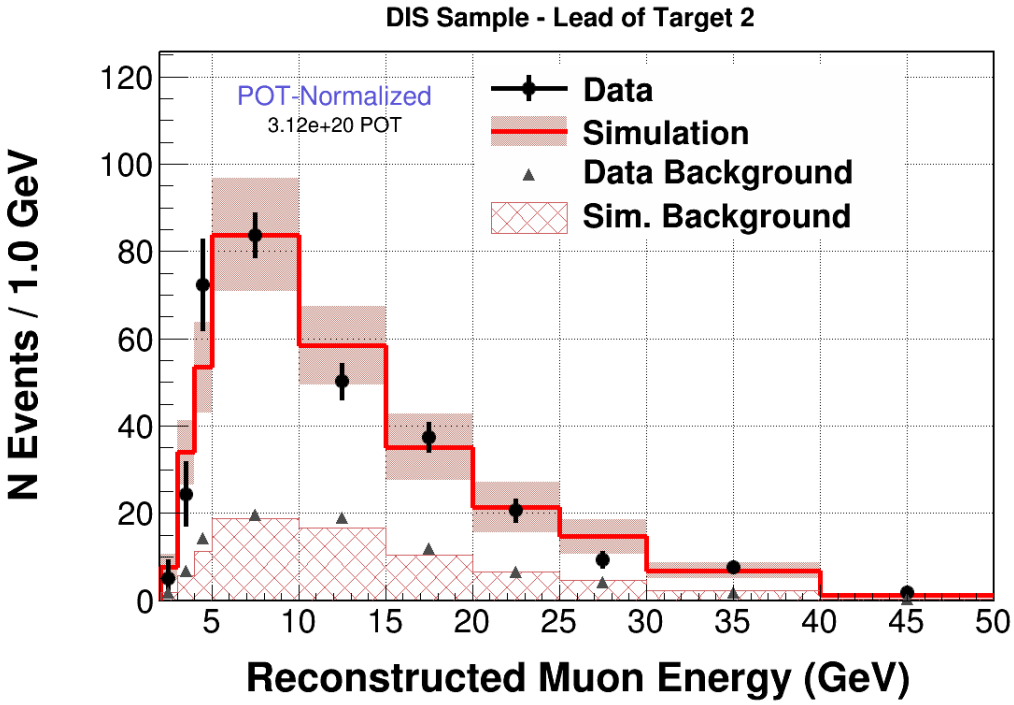

Figure E-99. DIS signal and CH background: target 02 Pb (E_μ)

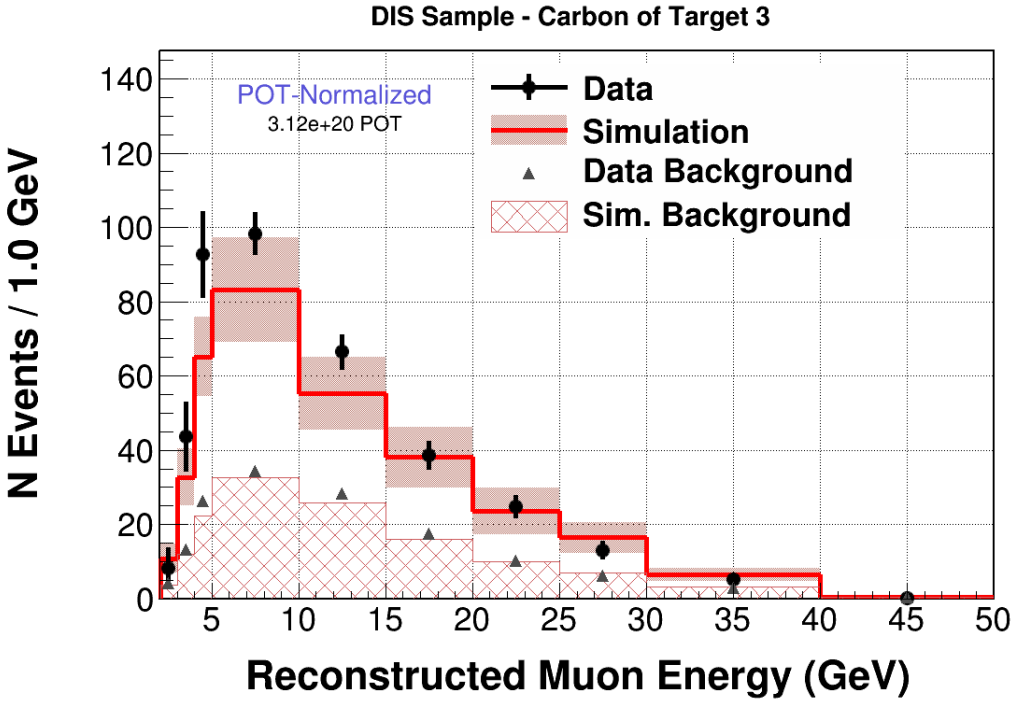

Figure E-100. DIS signal and CH background: target 03 C (E_μ)

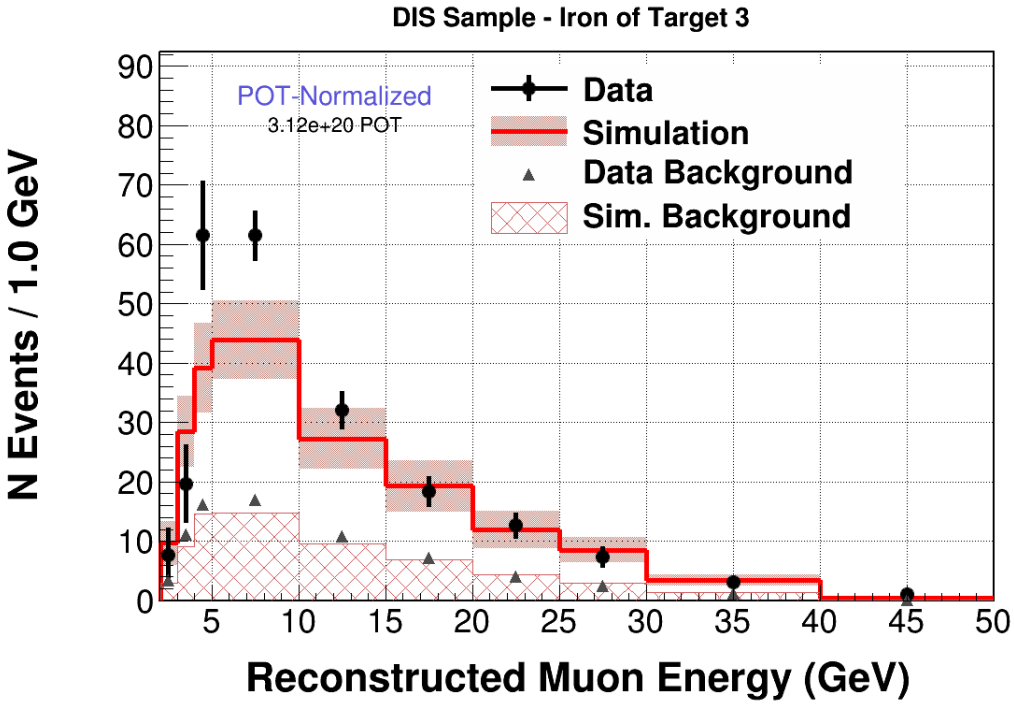

Figure E-101. DIS signal and CH background: target 03 Fe (E_μ)

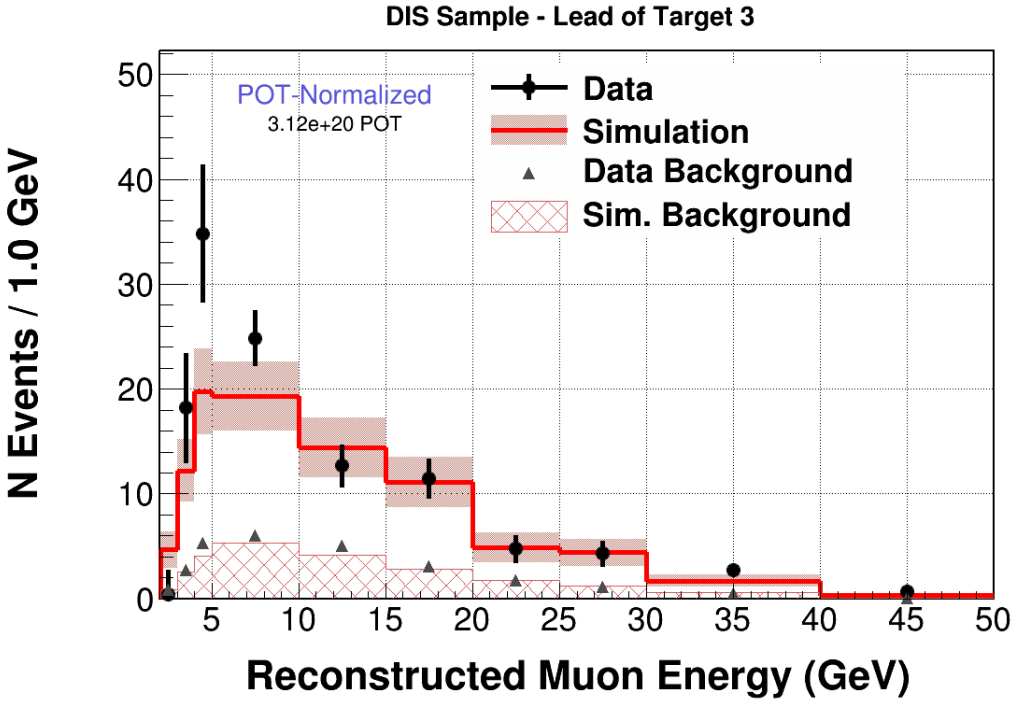

Figure E-102. DIS signal and CH background: target 03 Pb (E_μ)

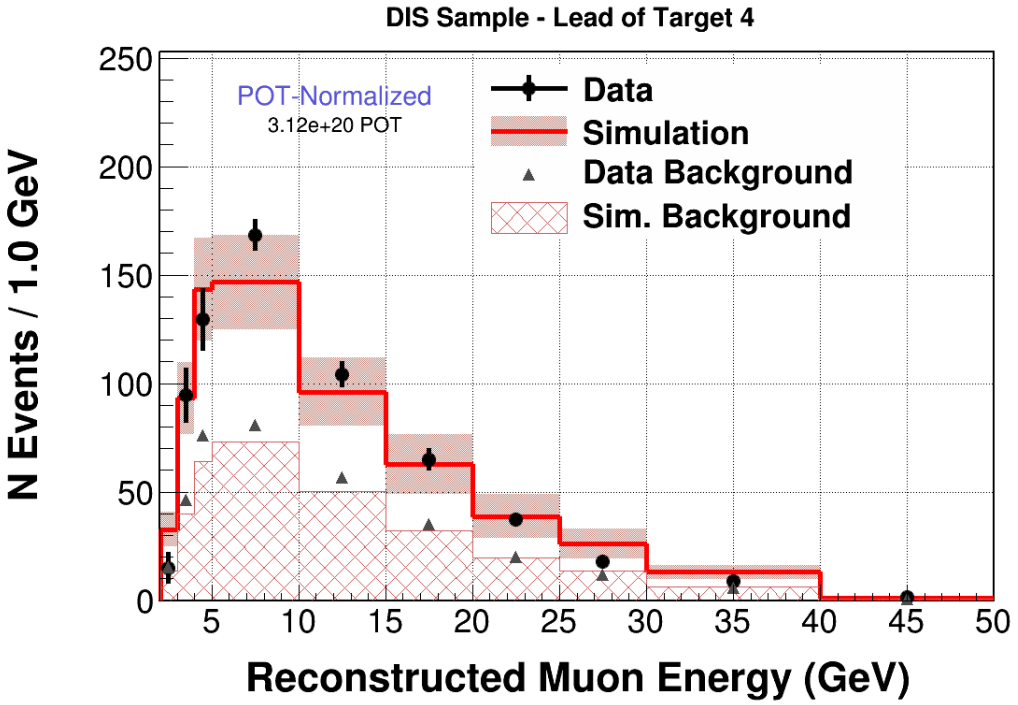

Figure E-103. DIS signal and CH background: target 04 Pb (E_μ)

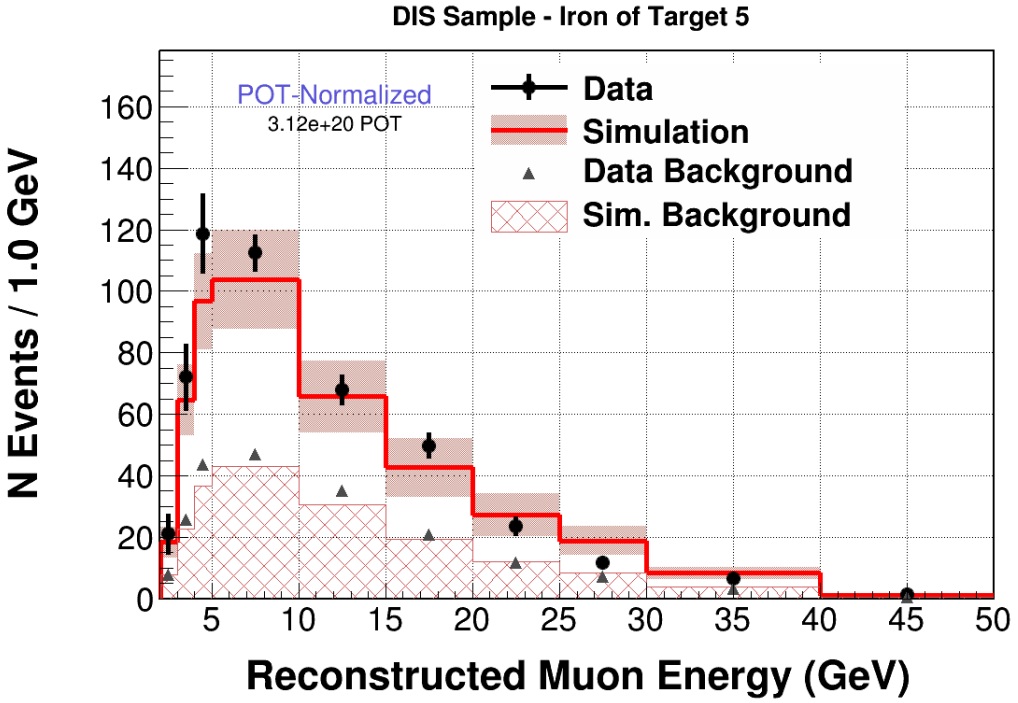

Figure E-104. DIS signal and CH background: target 05 Fe (E_μ)

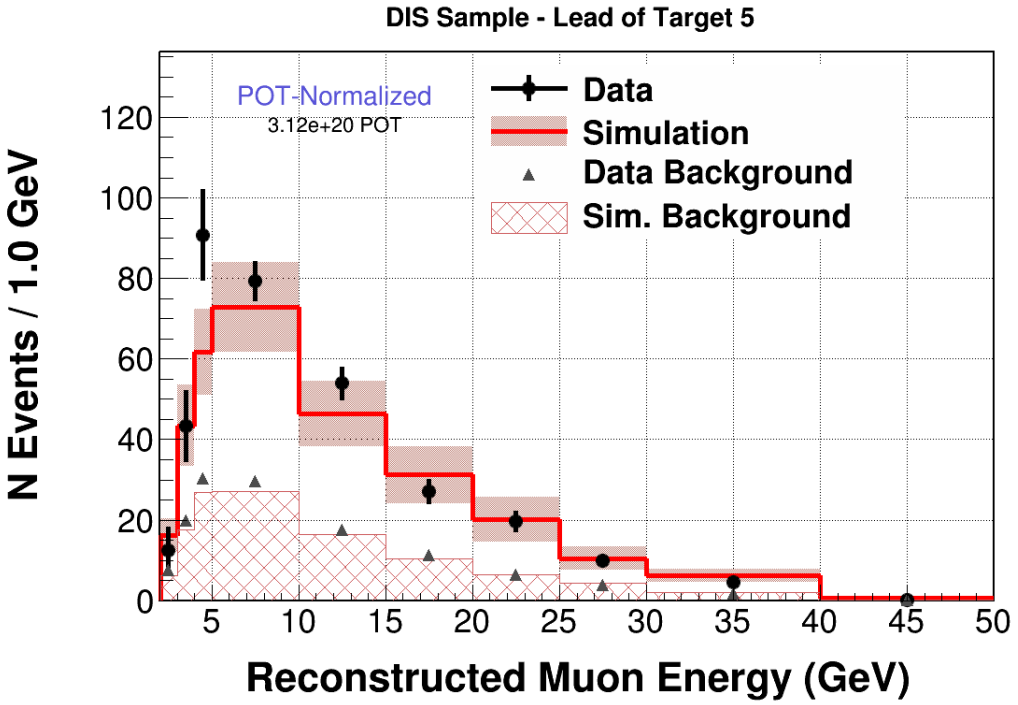

Figure E-105. DIS signal and CH background: target 05 Pb (E_μ)

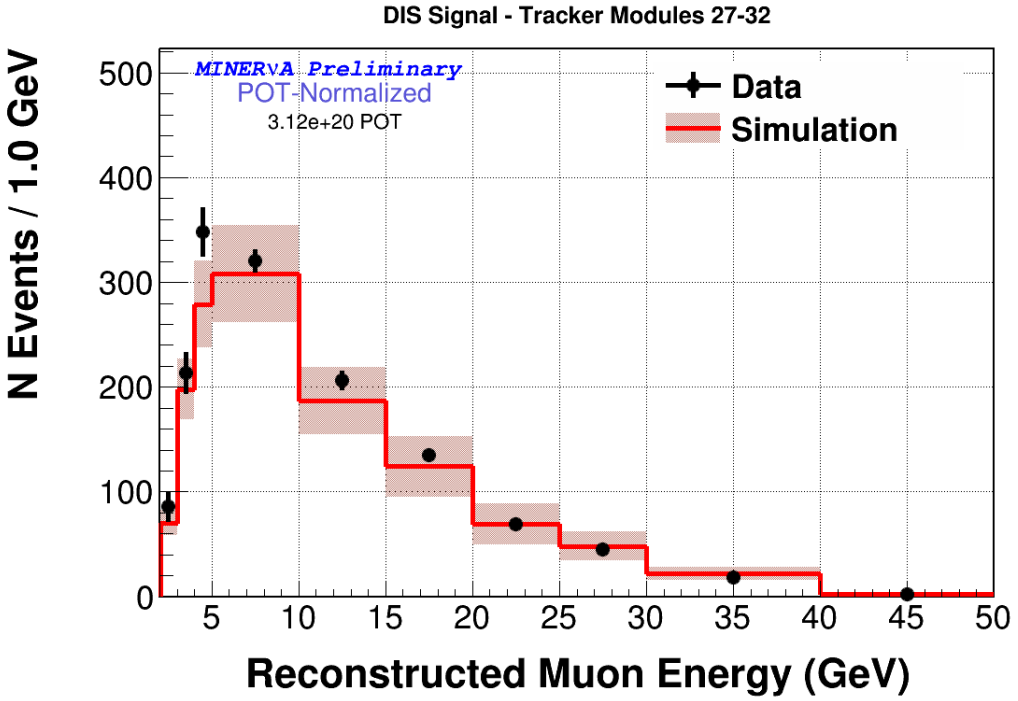

Figure E-106. DIS Signal: tracker mods. 27-32 (E_μ)

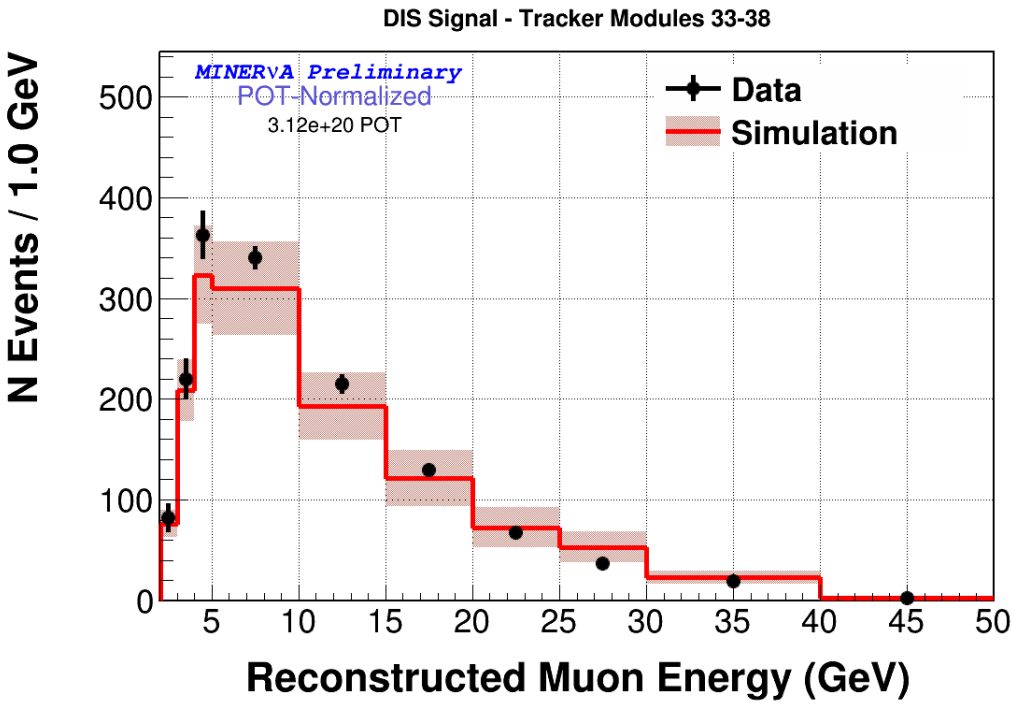

Figure E-107. DIS Signal: tracker mods. 33-38 (E_μ)

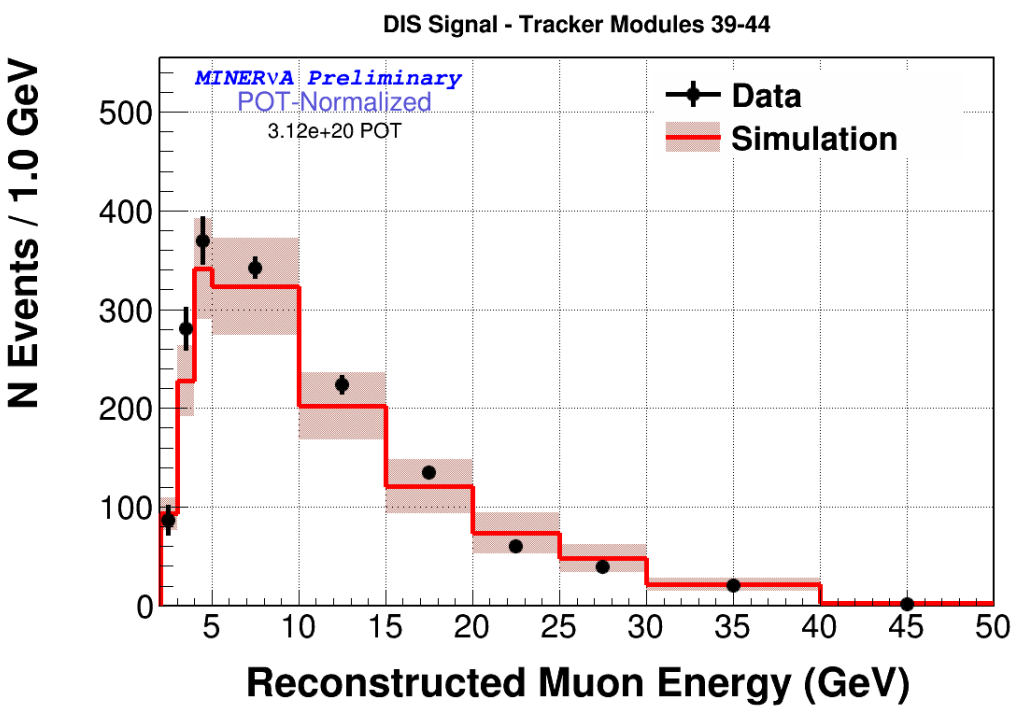

Figure E-108. DIS Signal: tracker mods. 39-44 (E_μ)

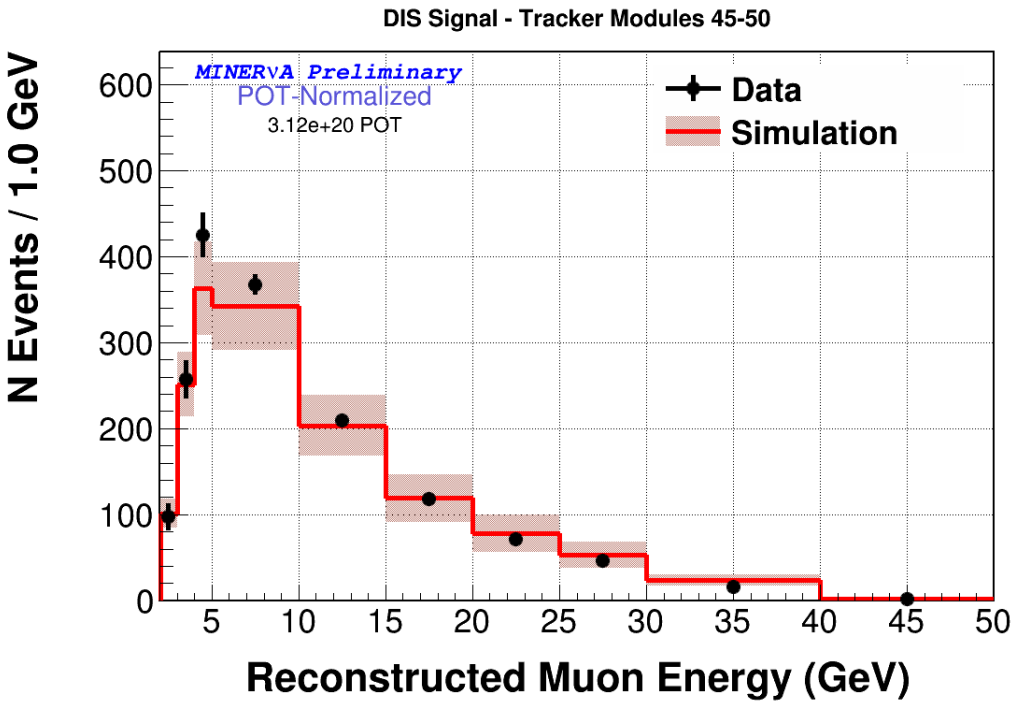

Figure E-109. DIS Signal: tracker mods. 45-50 (E_μ)

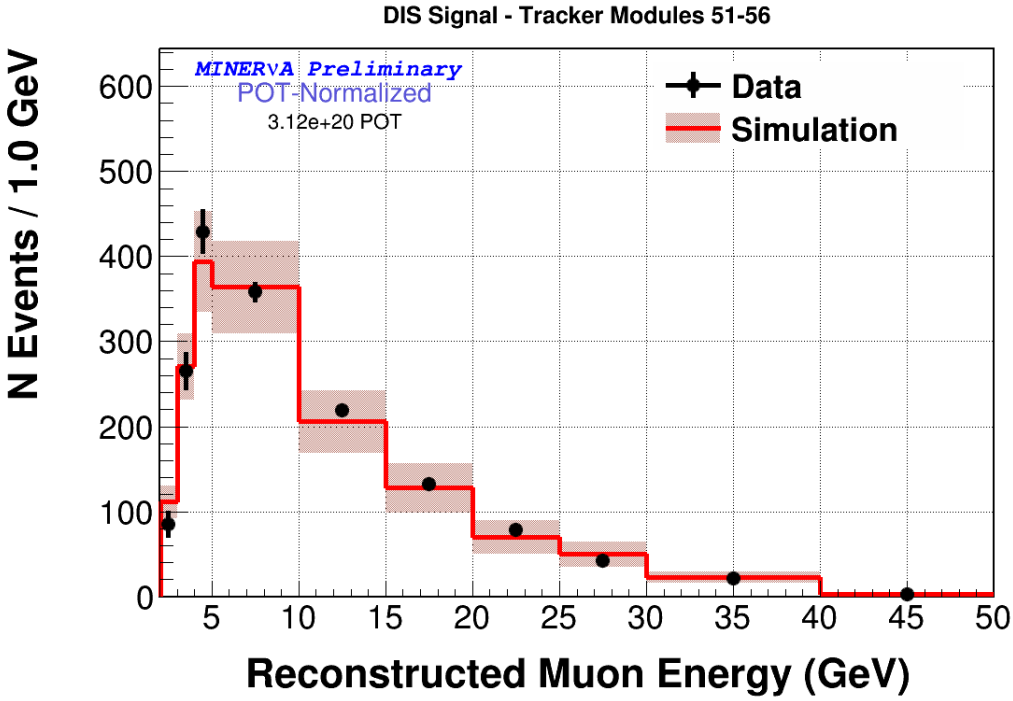

Figure E-110. DIS Signal: tracker mods. 51-56 (E_μ)

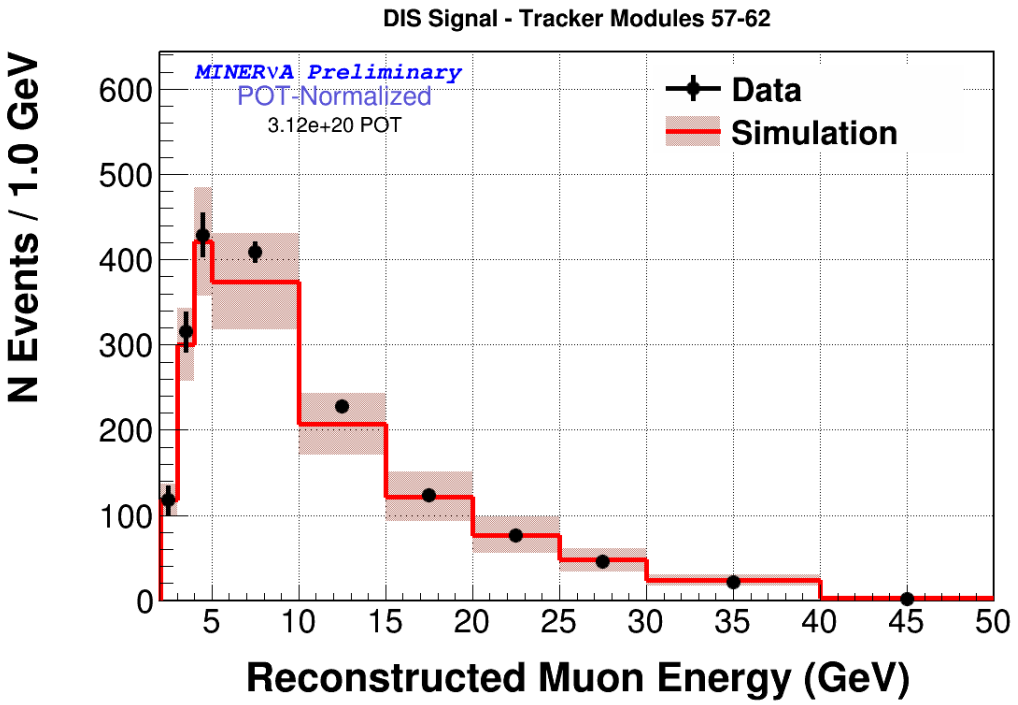

Figure E-111. DIS Signal: tracker mods. 57-62 (E_μ)

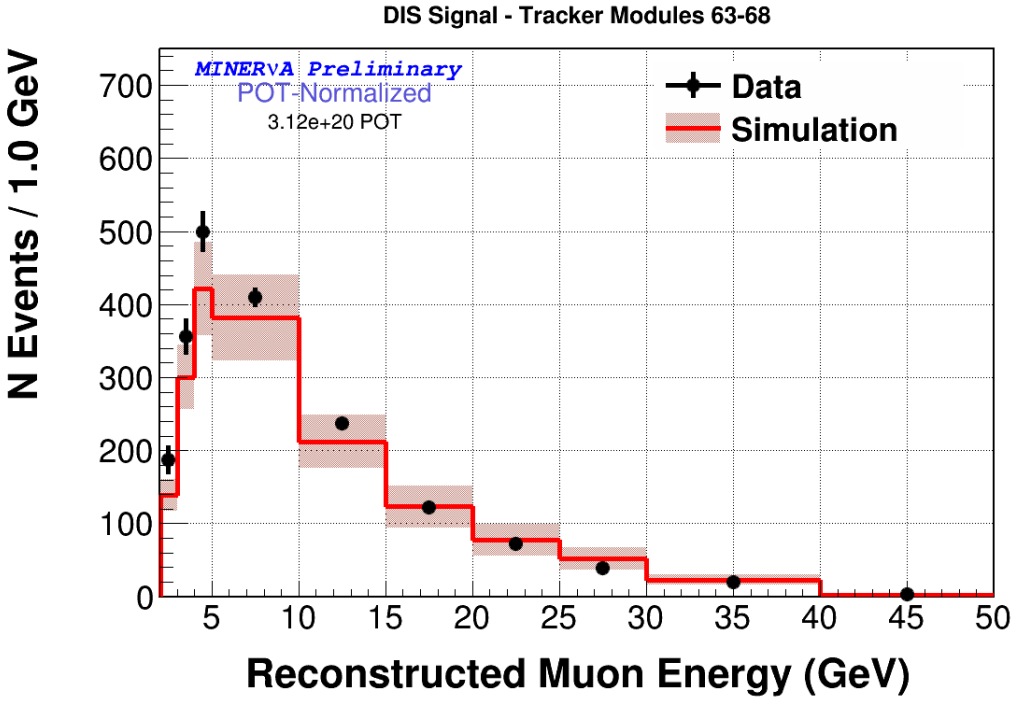

Figure E-112. DIS Signal: tracker mods. 63-68 (E_μ)

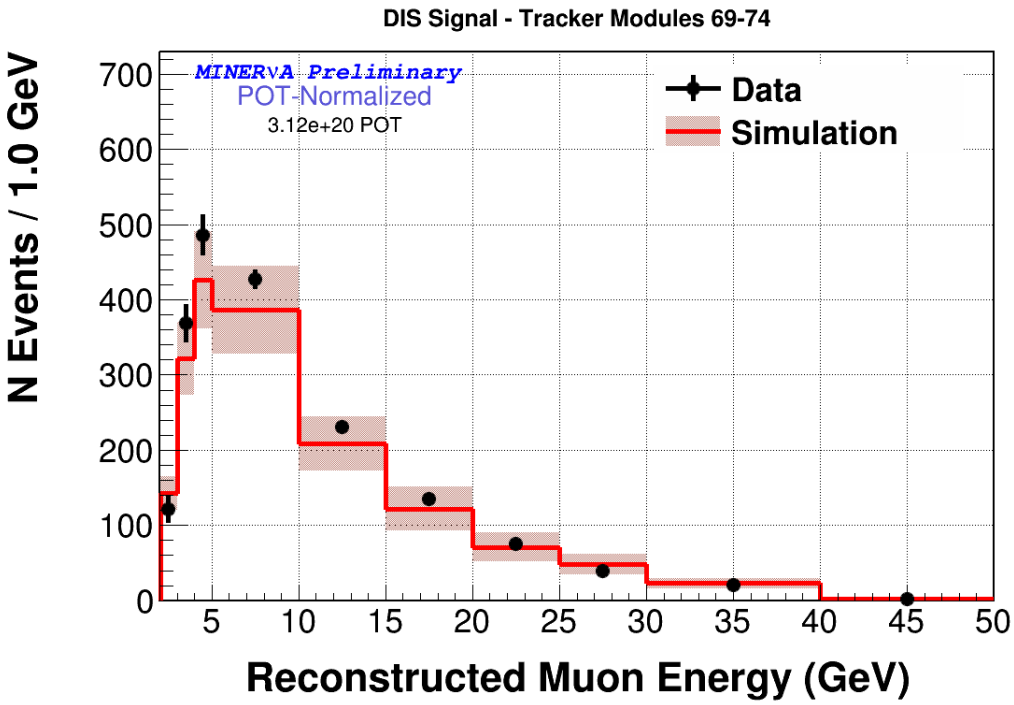

Figure E-113. DIS Signal: tracker mods. 69-74 (E_μ)

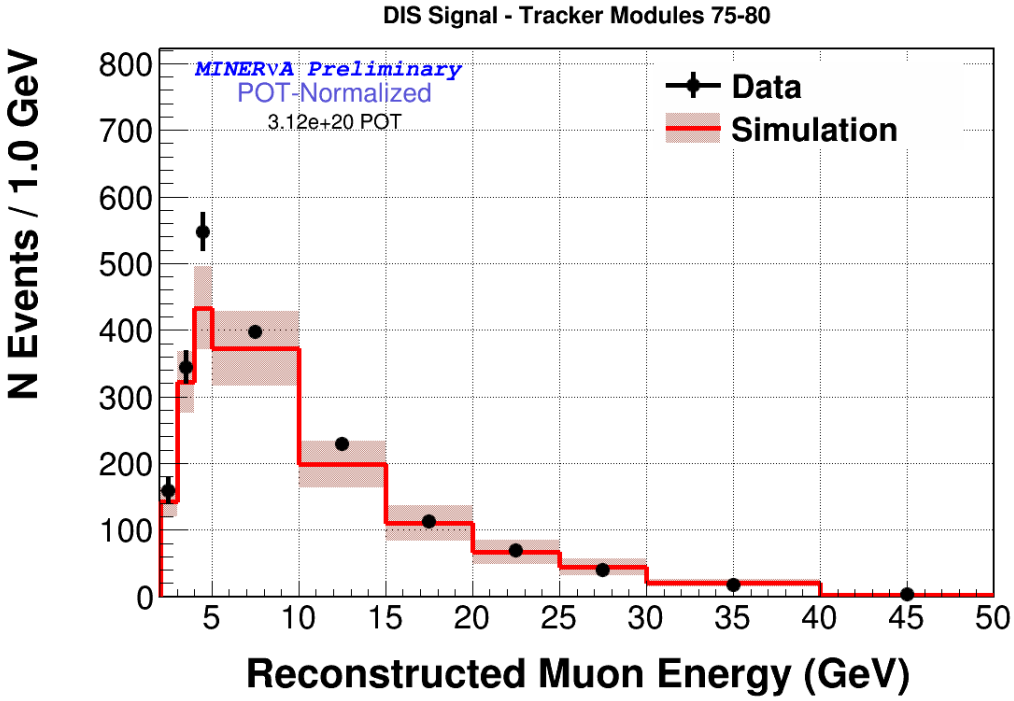

Figure E-114. DIS Signal: tracker mods. 75-80 (E_μ)

E.2 Uncertainties on DIS Event Yield Before CH Subtraction

The following plots show the uncertainty on the number of DIS events, after subtracting the non-DIS events. They are plotted as a function of neutrino energy (E_ν):

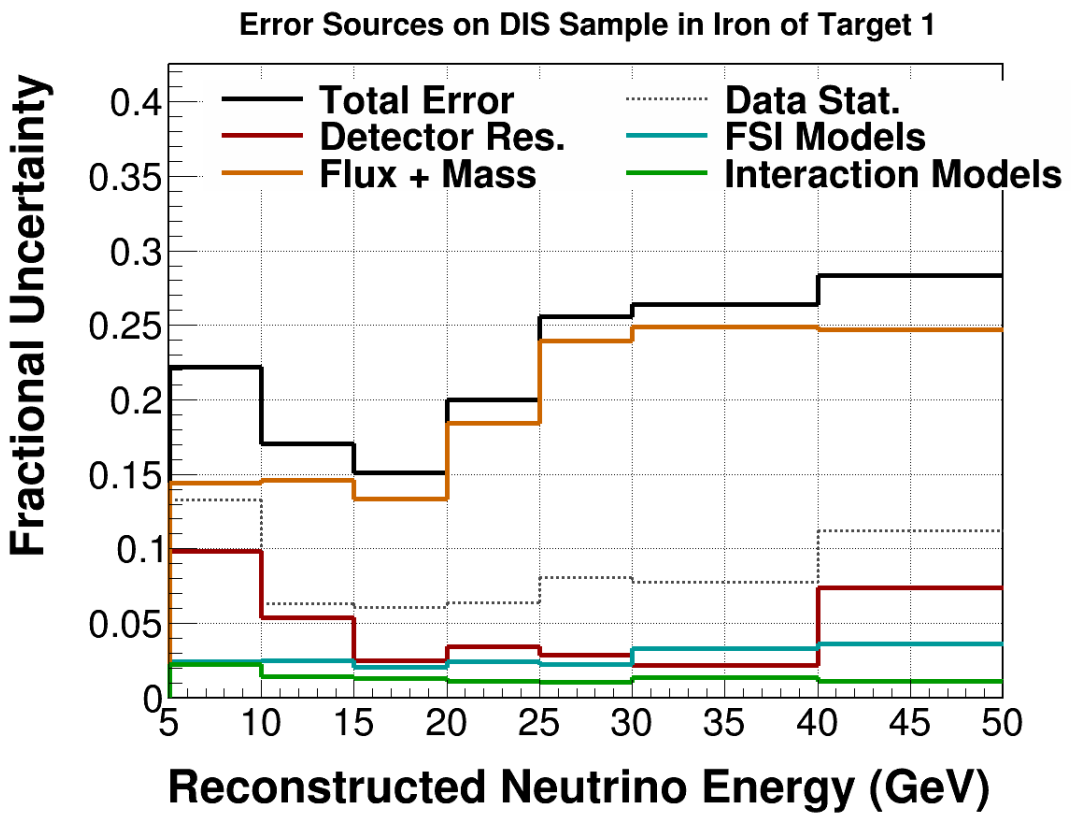

Figure E-115. Event yield uncertainties before CH subtraction: target 01 Fe (E_ν)

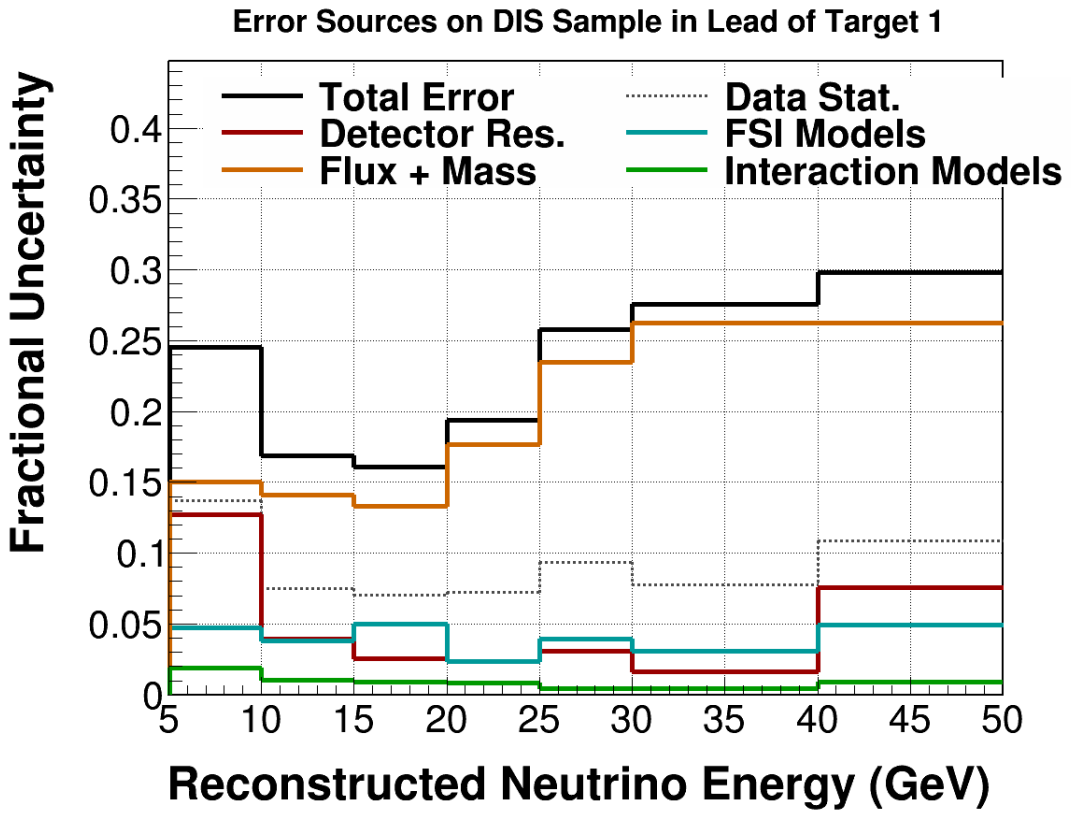

Figure E-116. Event yield uncertainties before CH subtraction: target 01 Pb (E_ν)

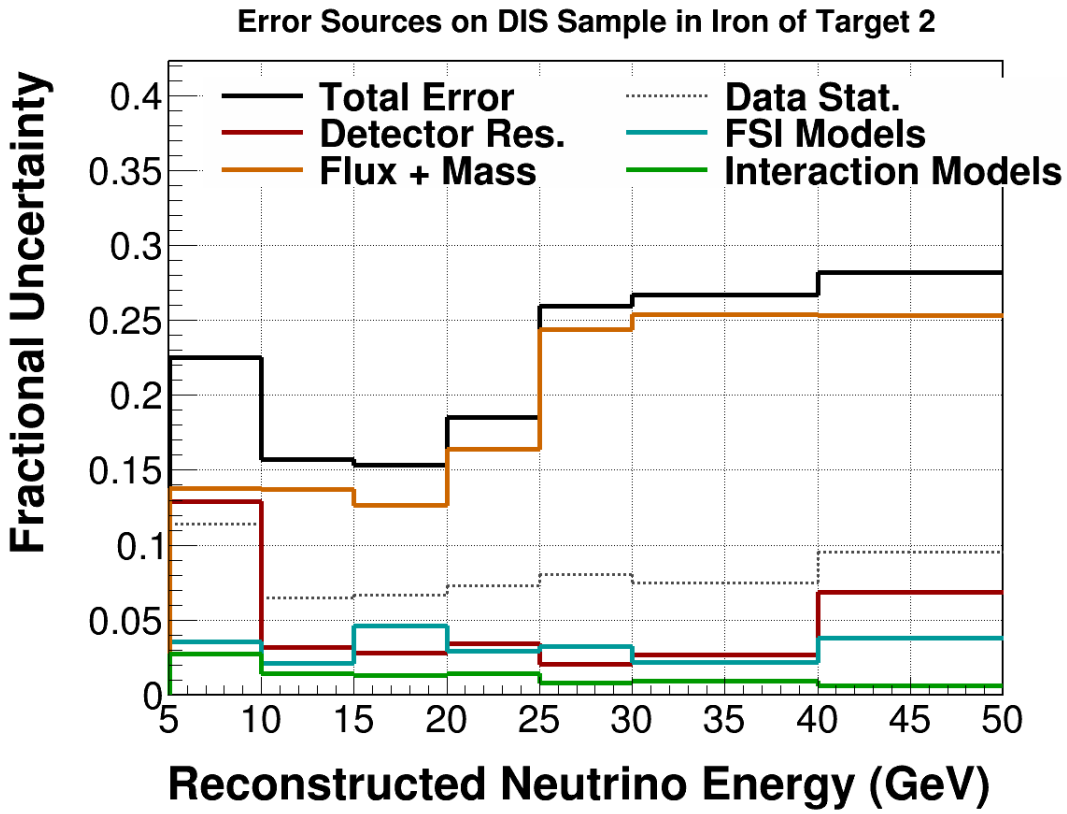

Figure E-117. Event yield uncertainties before CH subtraction: target 02 Fe (E_ν)

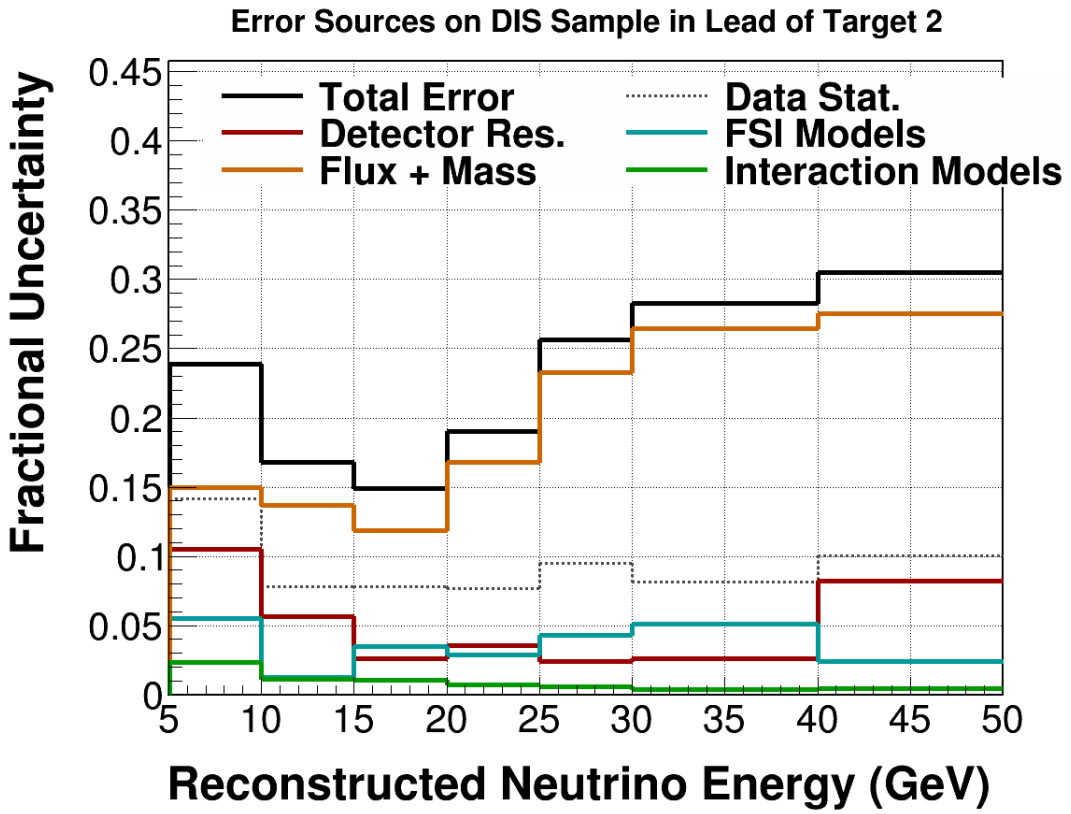

Figure E-118. Event yield uncertainties before CH subtraction: target 02 Pb (E_ν)

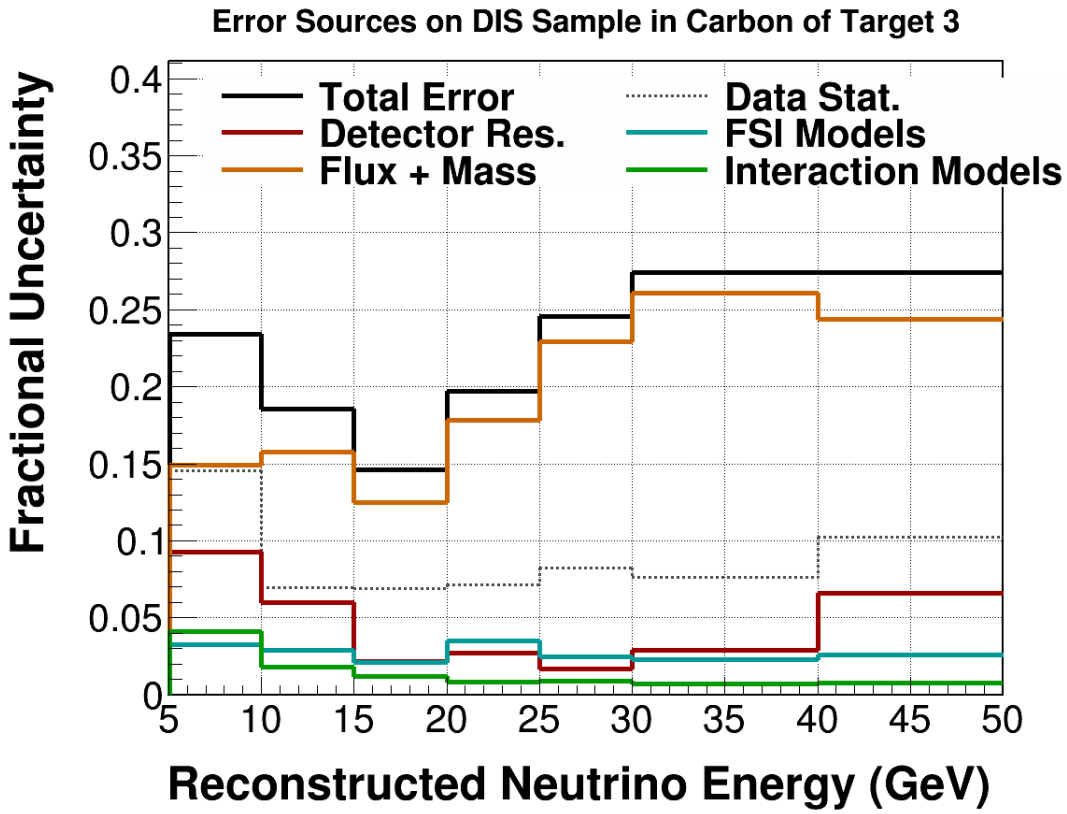

Figure E-119. Event yield uncertainties before CH subtraction: target 03 C (E_ν)

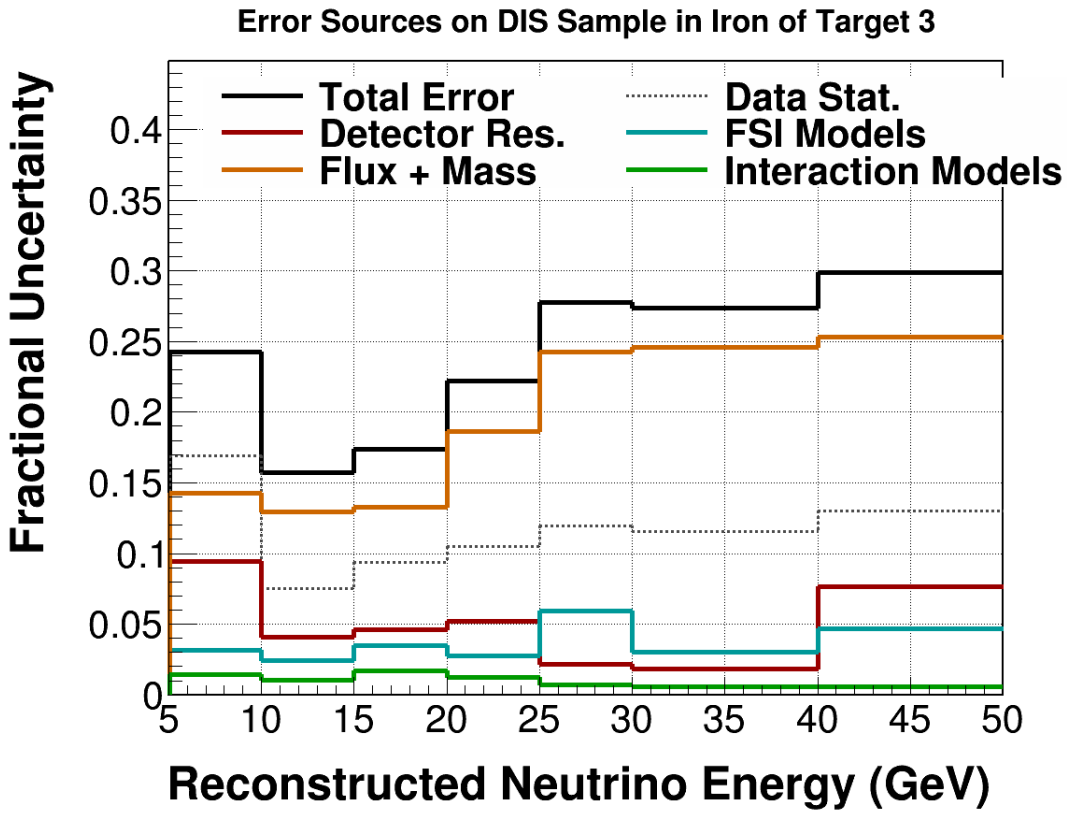

Figure E-120. Event yield uncertainties before CH subtraction: target 03 Fe (E_ν)

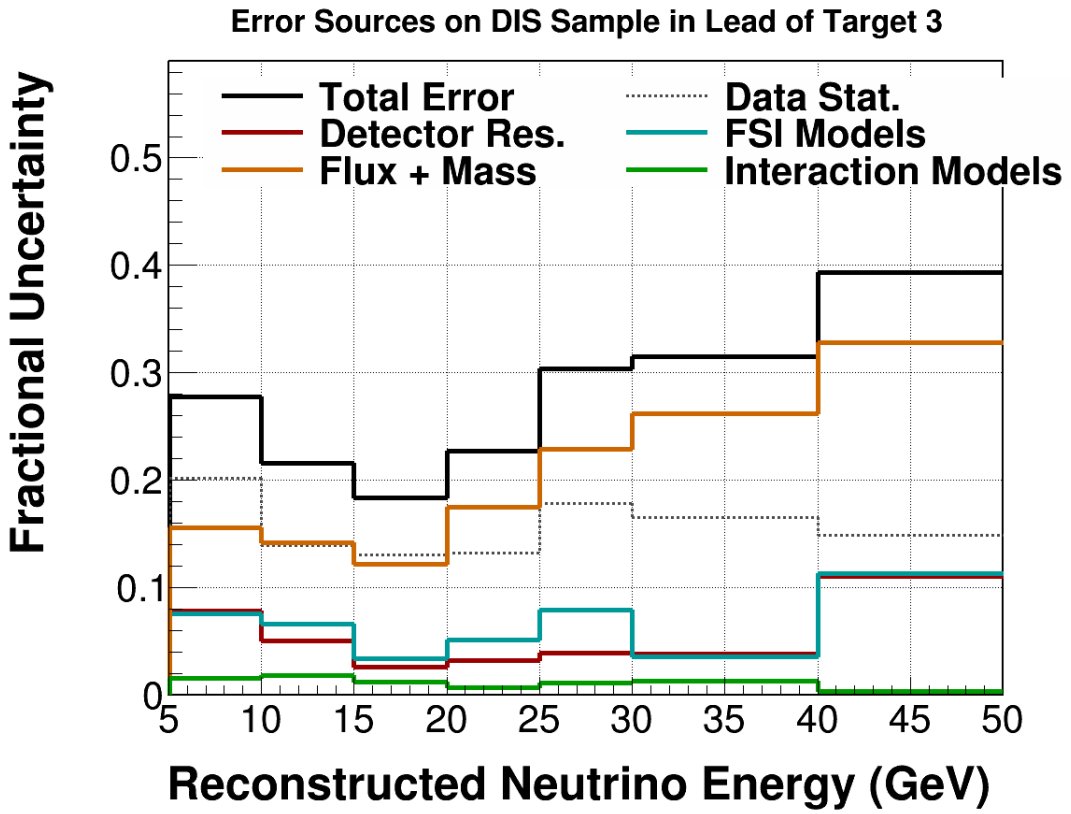

Figure E-121. Event yield uncertainties before CH subtraction: target 03 Pb (E_ν)

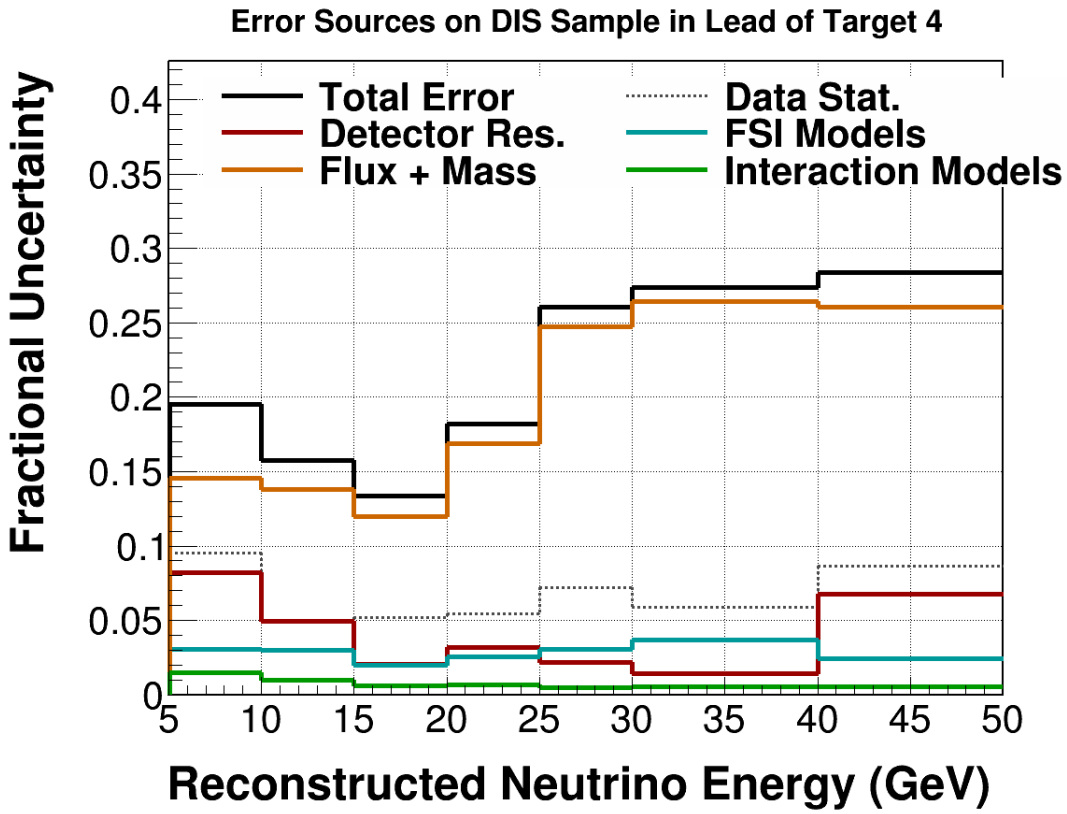

Figure E-122. Event yield uncertainties before CH subtraction: target 04 Pb (E_ν)

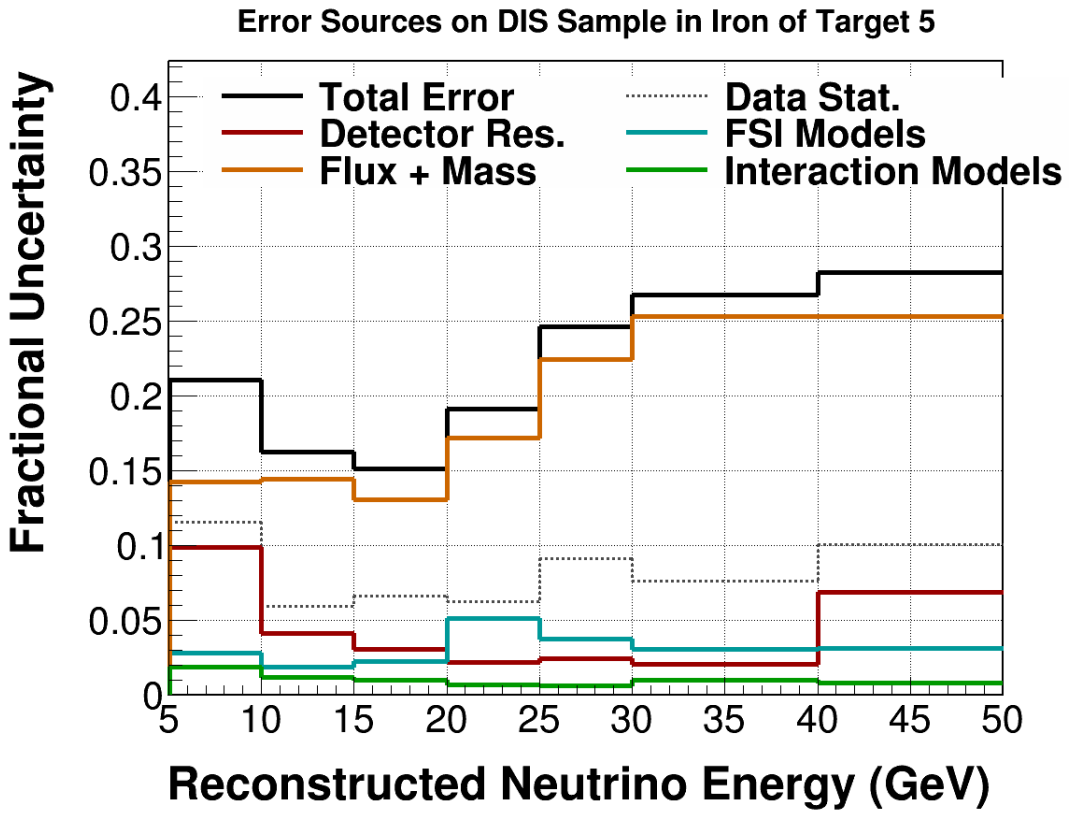

Figure E-123. Event yield uncertainties before CH subtraction: target 05 Fe (E_ν)

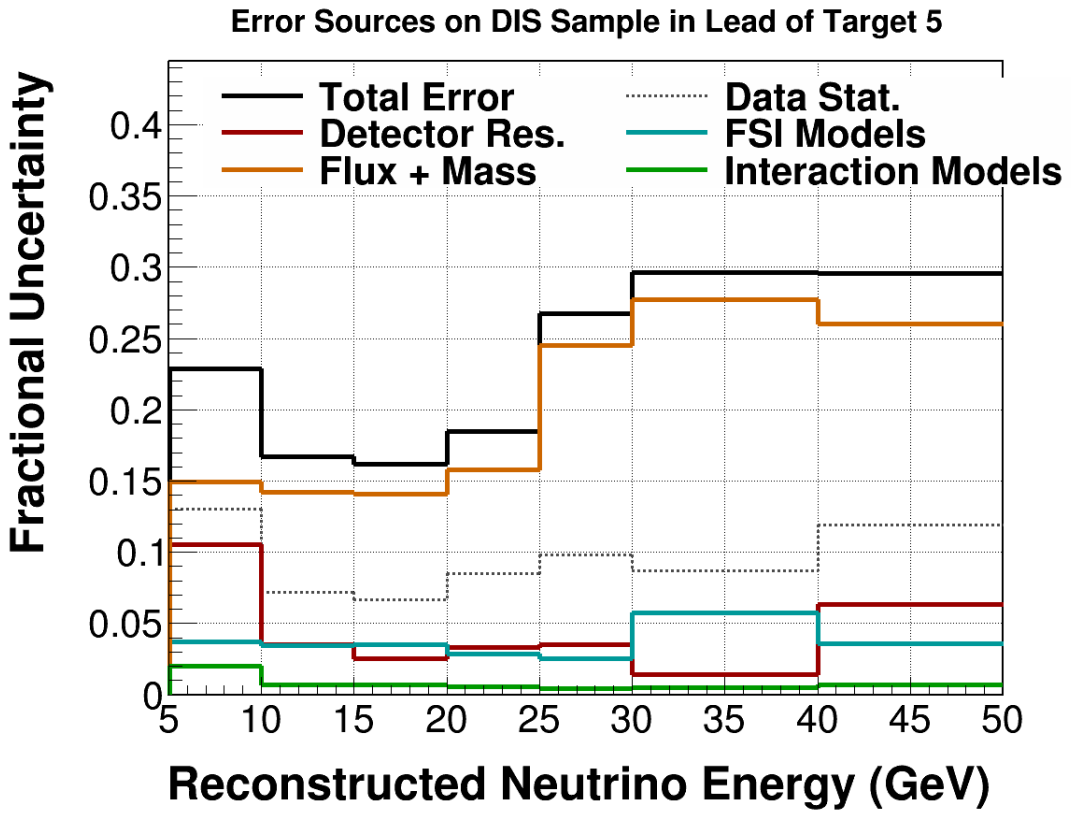

Figure E-124. Event yield uncertainties before CH subtraction: target 05 Pb (E_ν)

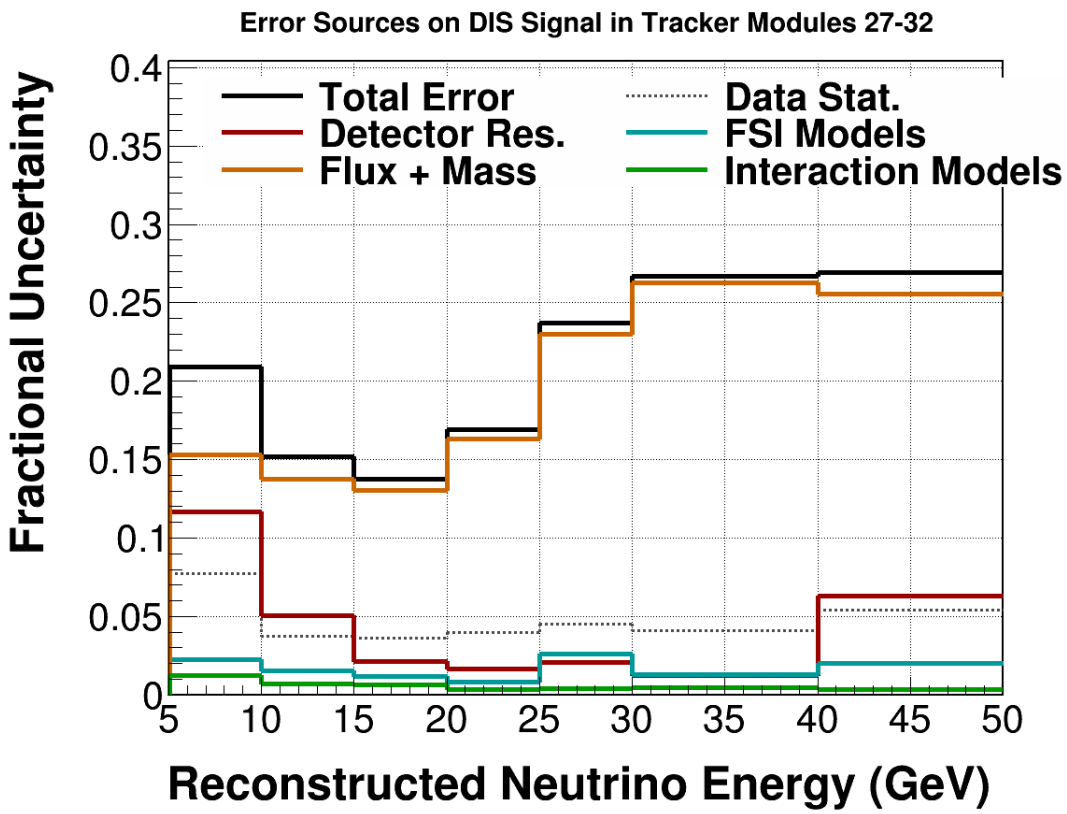

Figure E-125. Event yield uncertainties: tracker mods. 27-32 (E_ν)

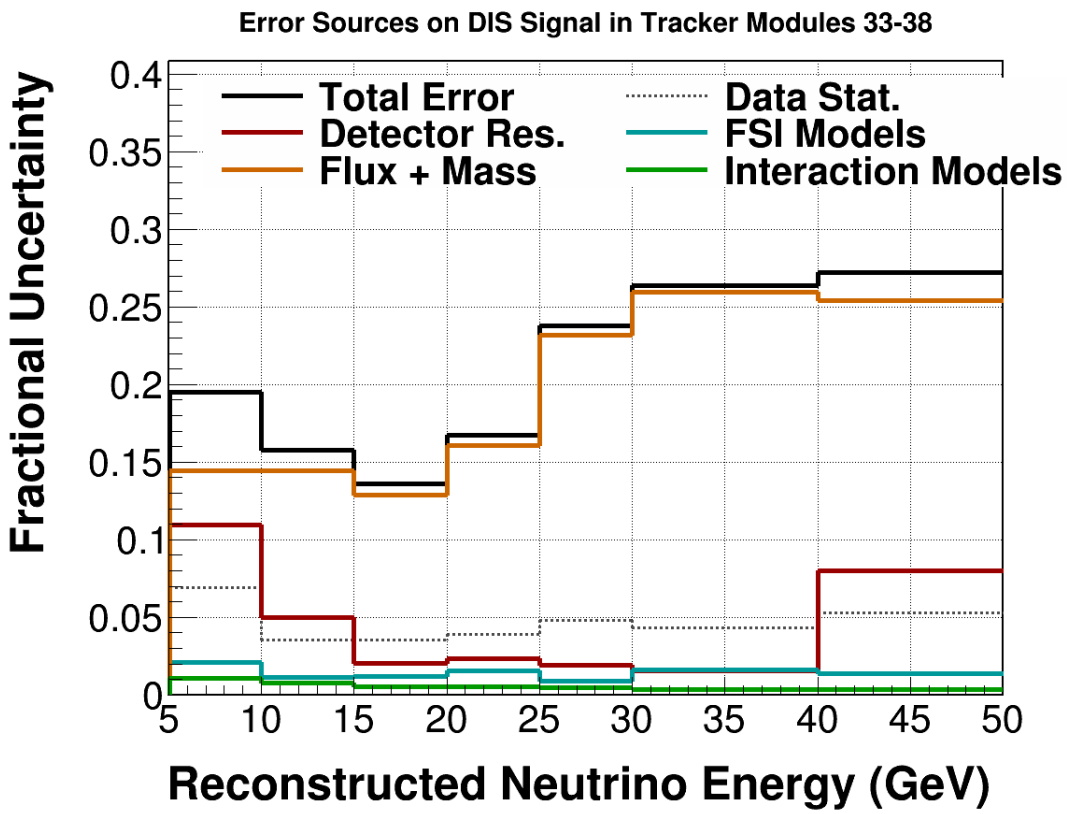

Figure E-126. Event yield uncertainties: tracker mods. 33-38 (E_ν)

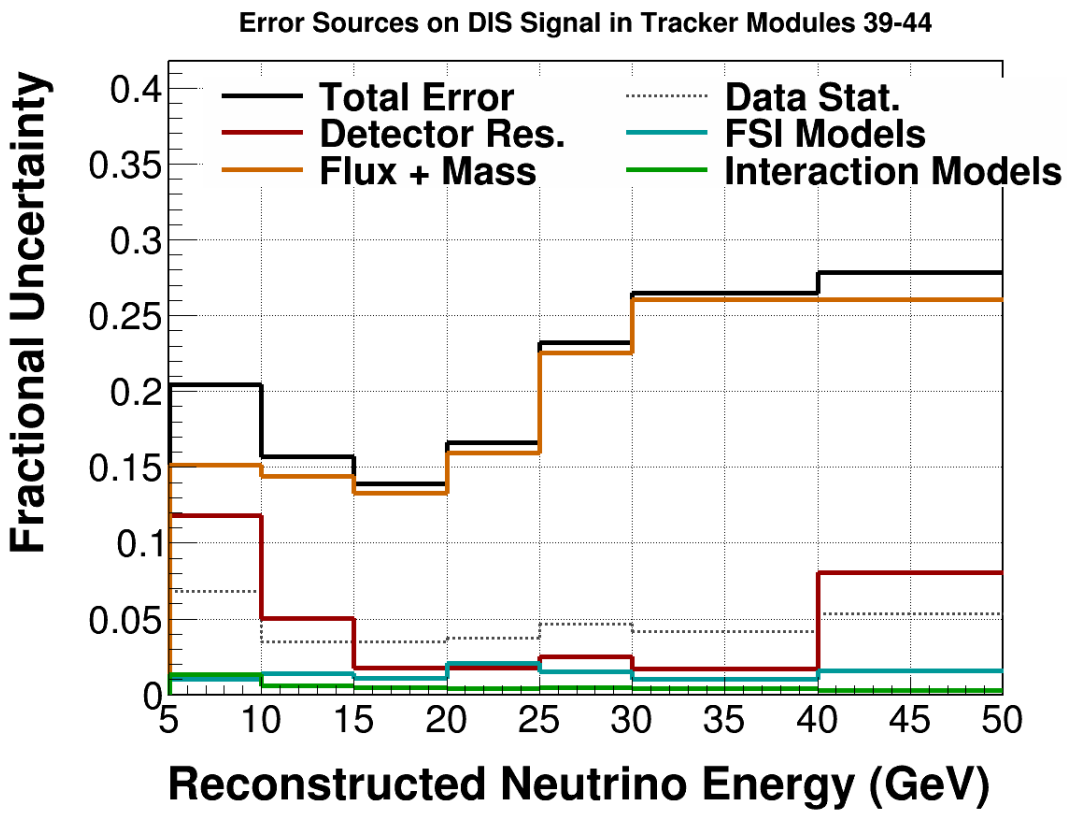

Figure E-127. Event yield uncertainties: tracker mods. 39-44 (E_ν)

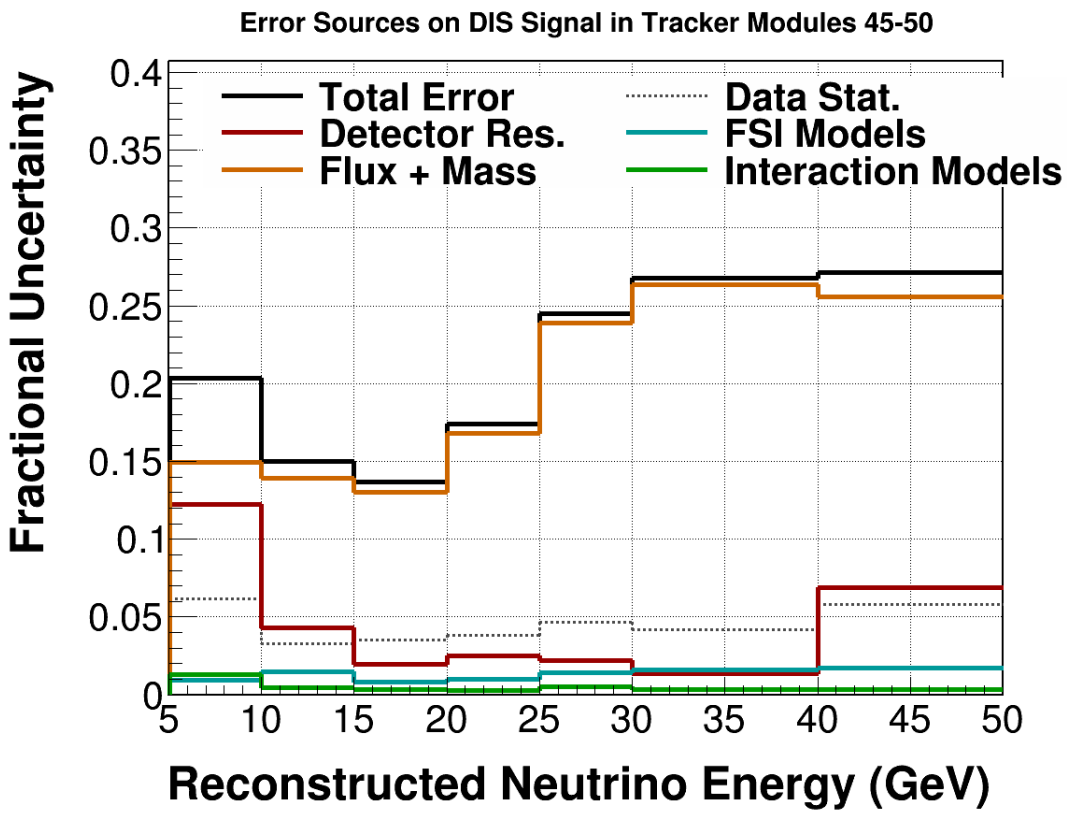

Figure E-128. Event yield uncertainties: tracker mods. 45-50 (E_ν)

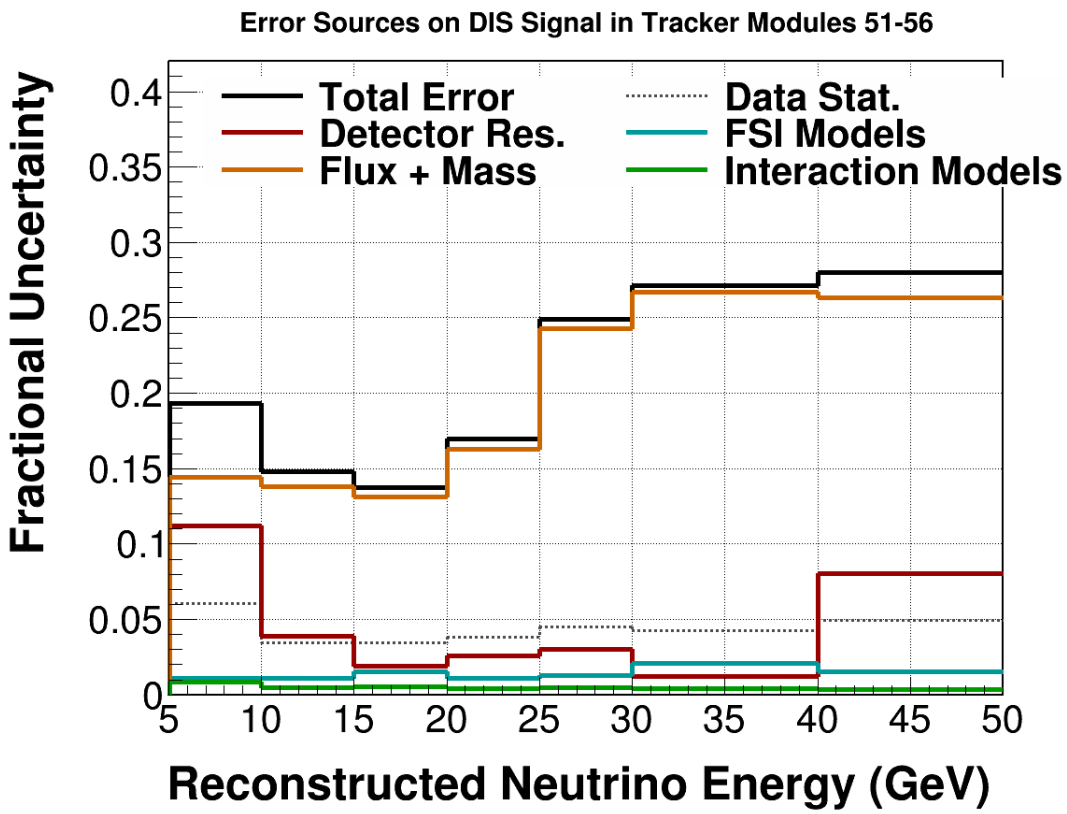

Figure E-129. Event yield uncertainties: tracker mods. 51-56 (E_ν)

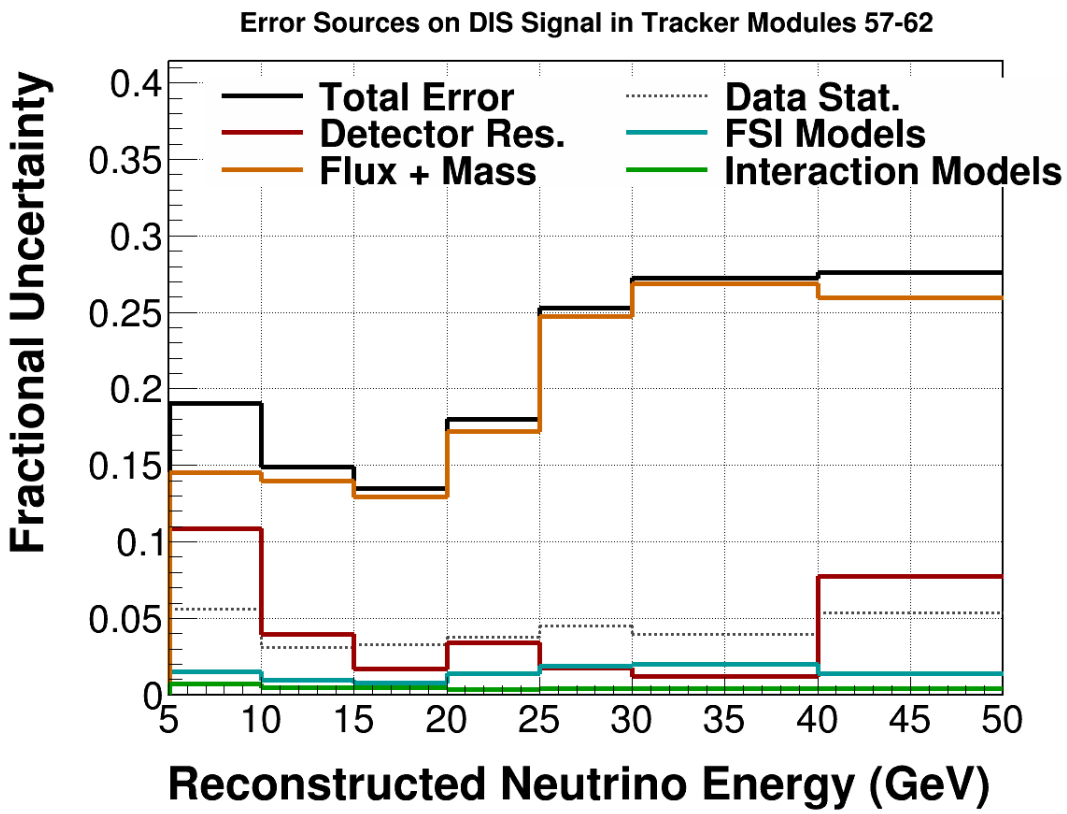

Figure E-130. Event yield uncertainties: tracker mods. 57-62 (E_ν)

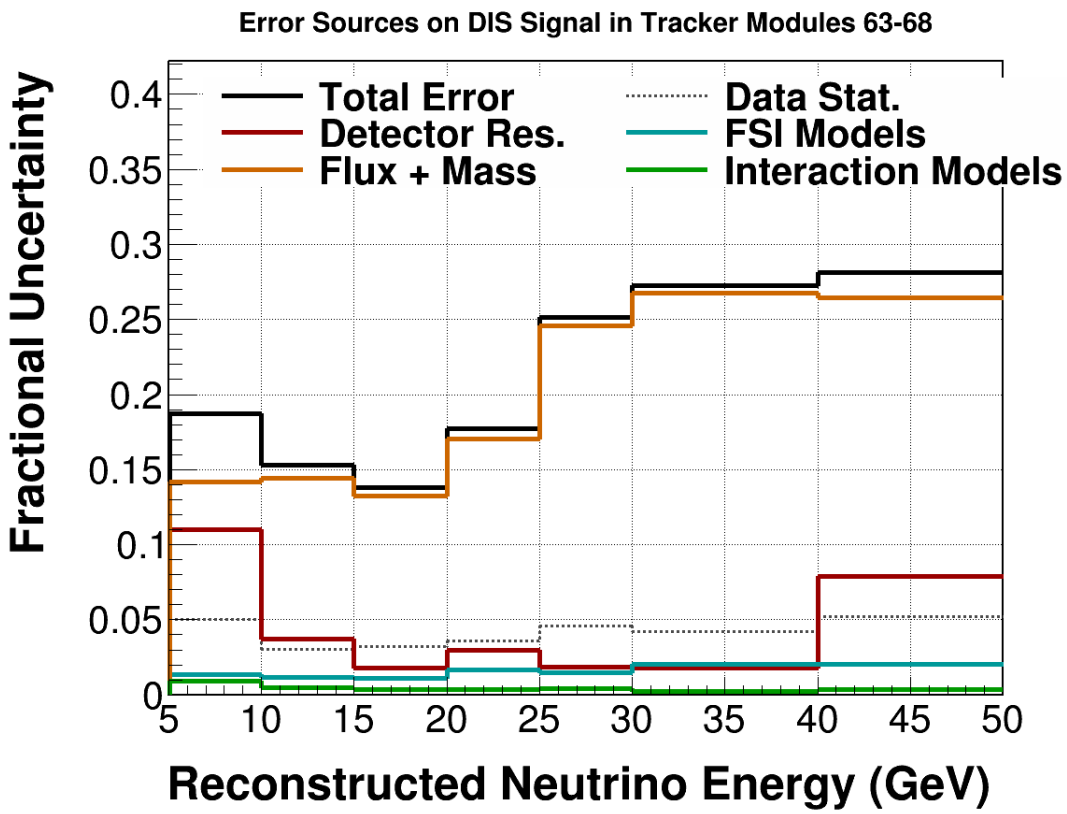

Figure E-131. Event yield uncertainties: tracker mods. 63-68 (E_ν)

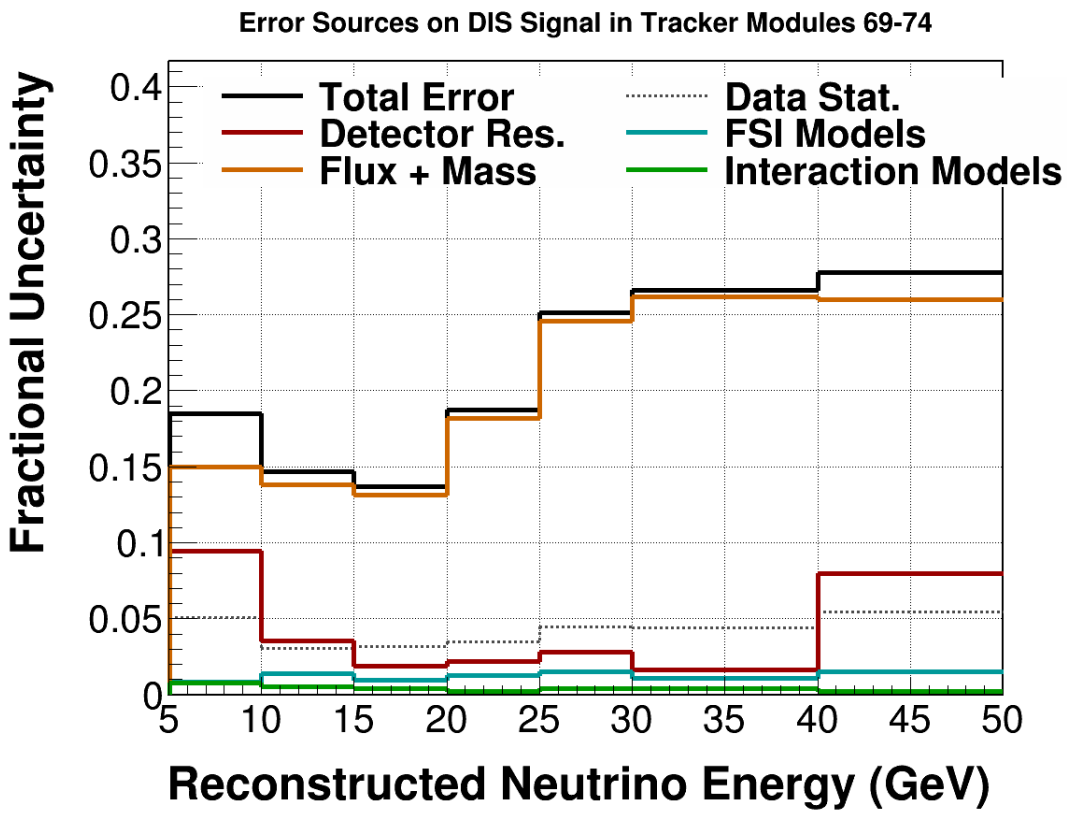

Figure E-132. Event yield uncertainties: tracker mods. 69-74 (E_ν)

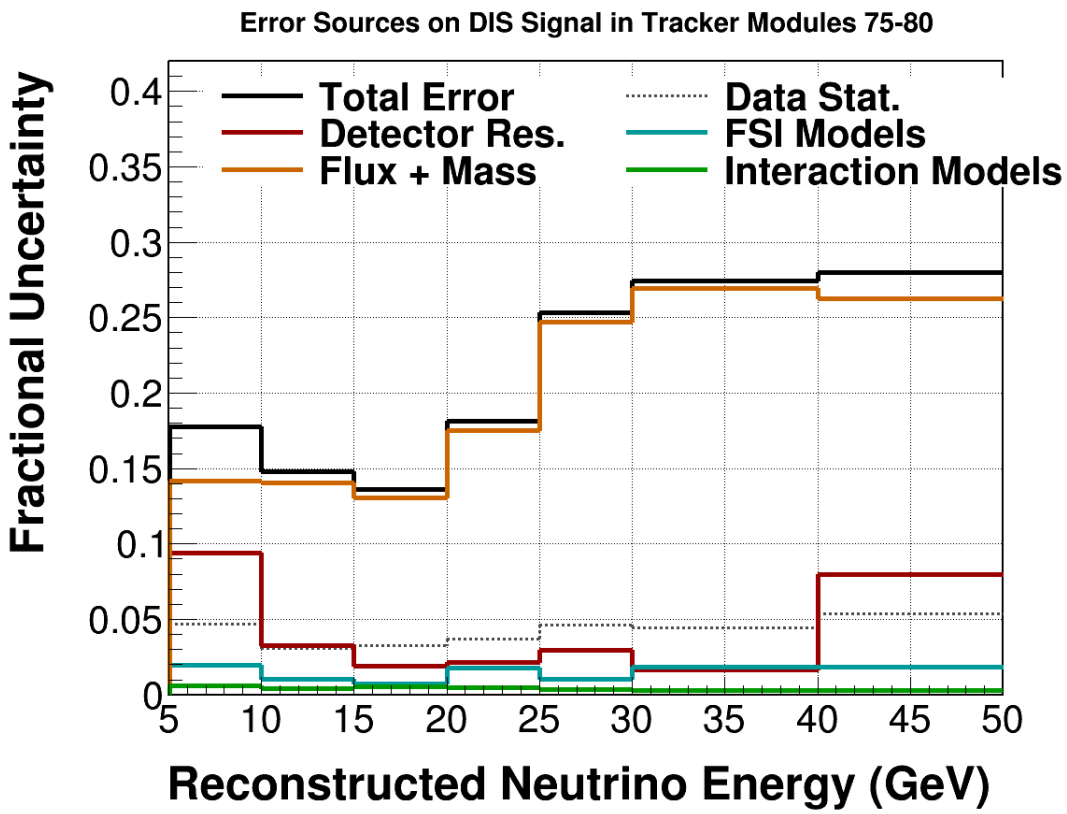

Figure E-133. Event yield uncertainties: tracker mods. 75-80 (E_ν)

The following plots show the uncertainty on the number of DIS events, after subtracting the non-DIS events. They are plotted as a function of hadronic energy (E_{had}):

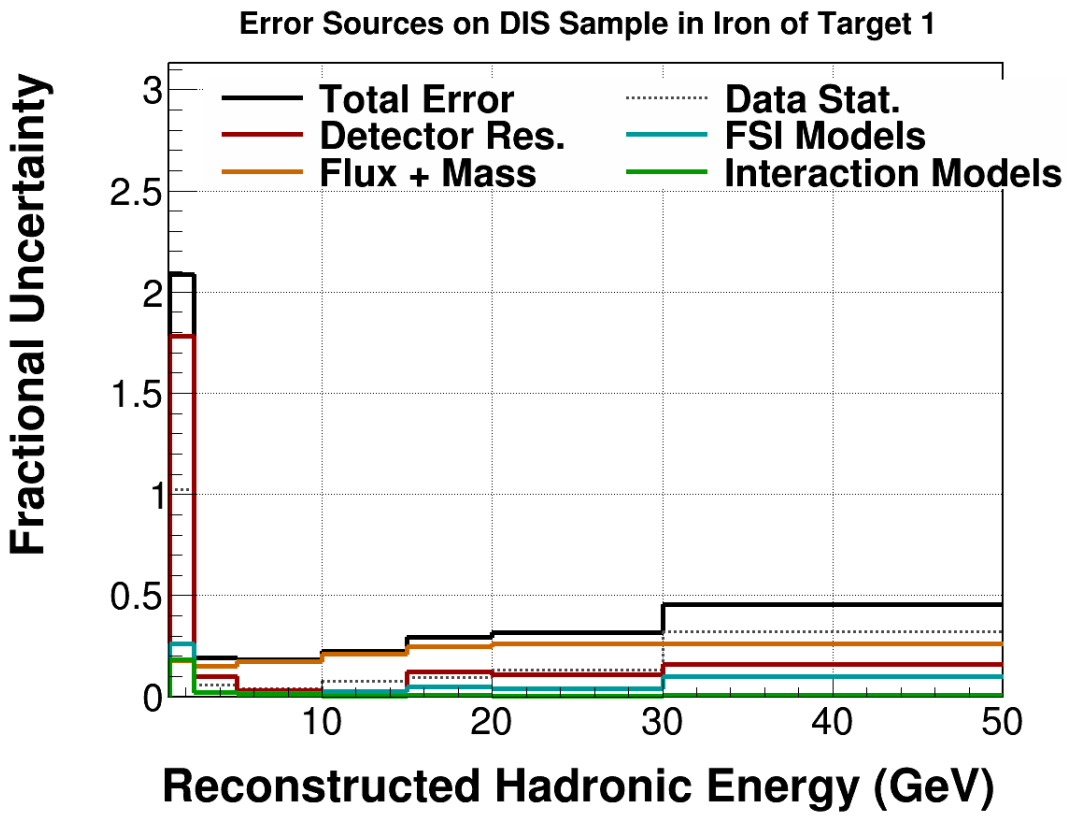

Figure E-134. Event yield uncertainties before CH subtraction: target 01 Fe (E_{had})

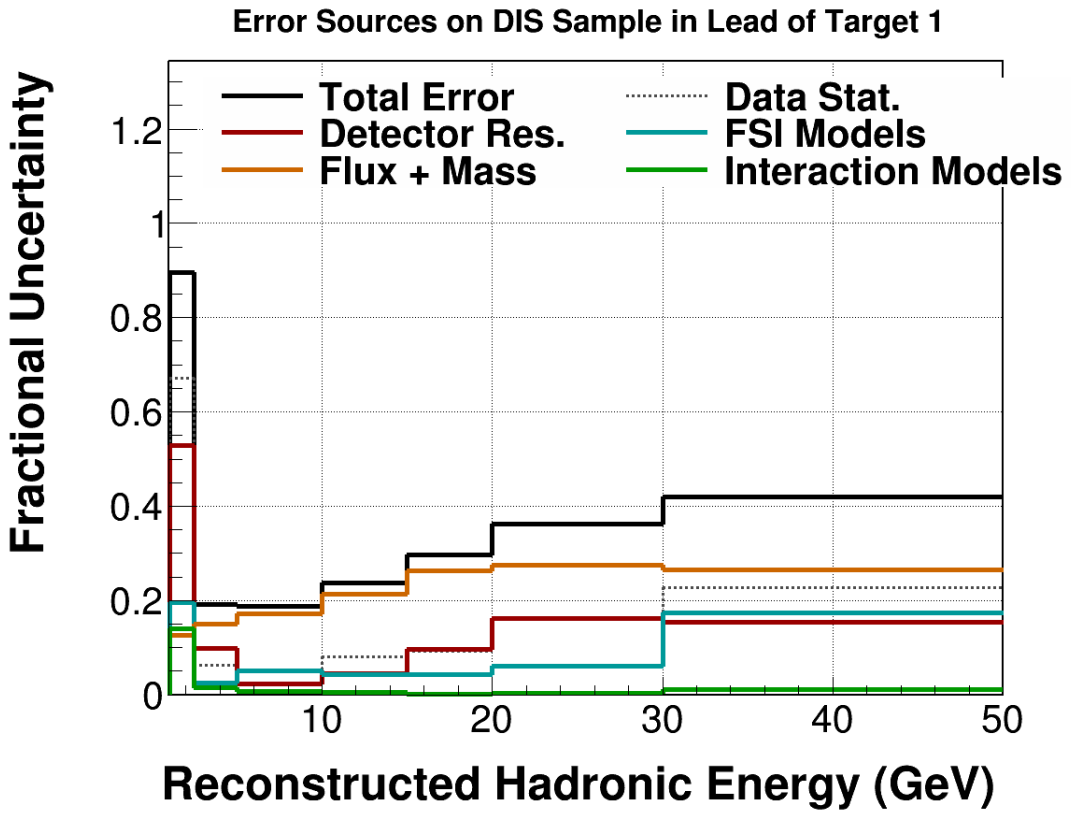

Figure E-135. Event yield uncertainties before CH subtraction: target 01 Pb (E_{had})

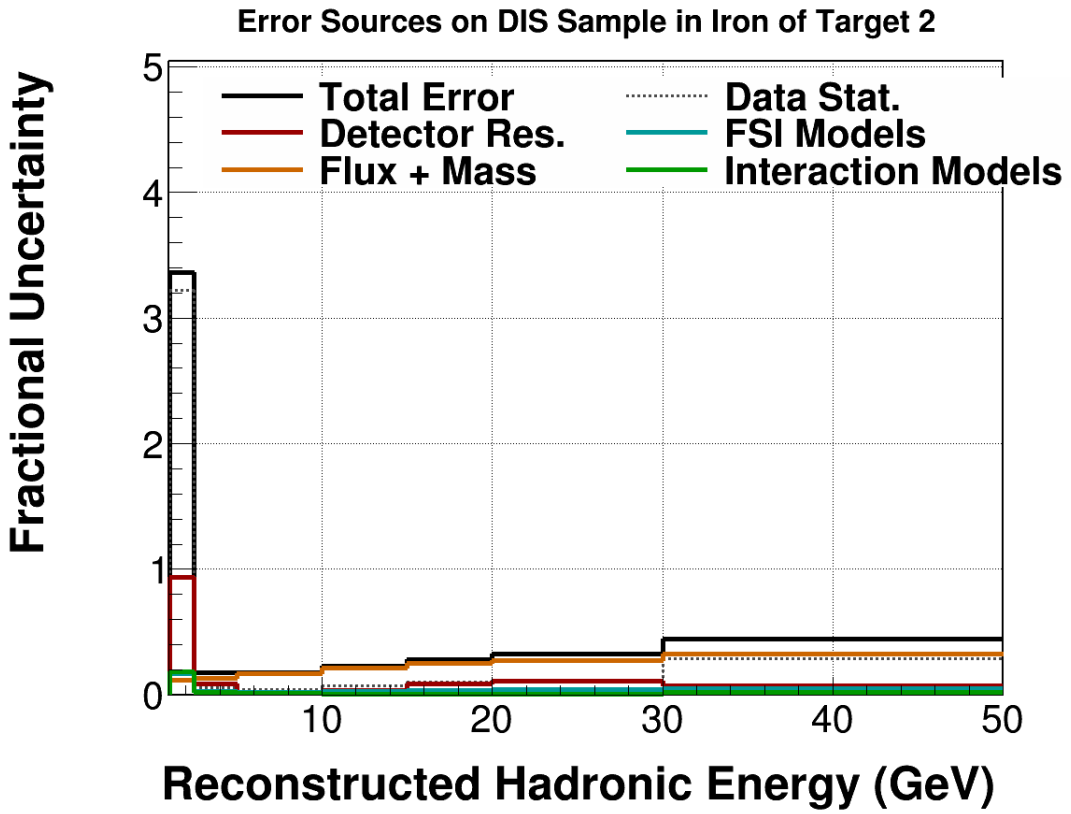

Figure E-136. Event yield uncertainties before CH subtraction: target 02 Fe (E_{had})

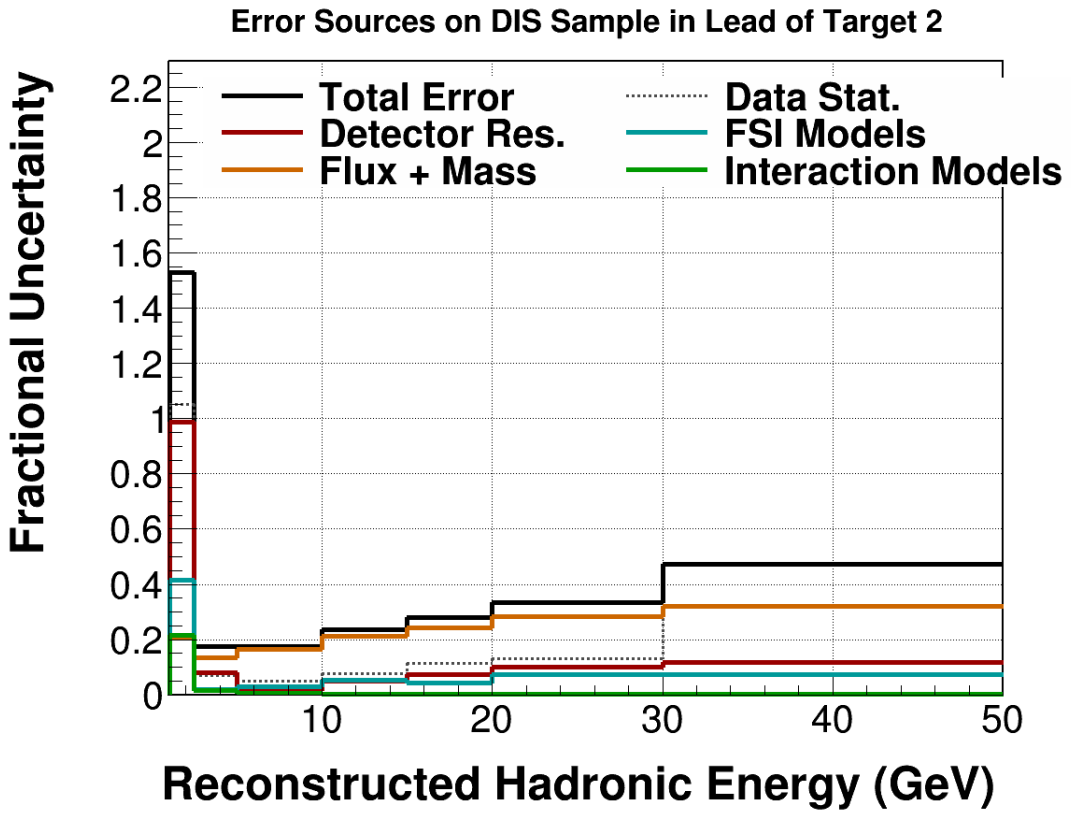

Figure E-137. Event yield uncertainties before CH subtraction: target 02 Pb (E_{had})

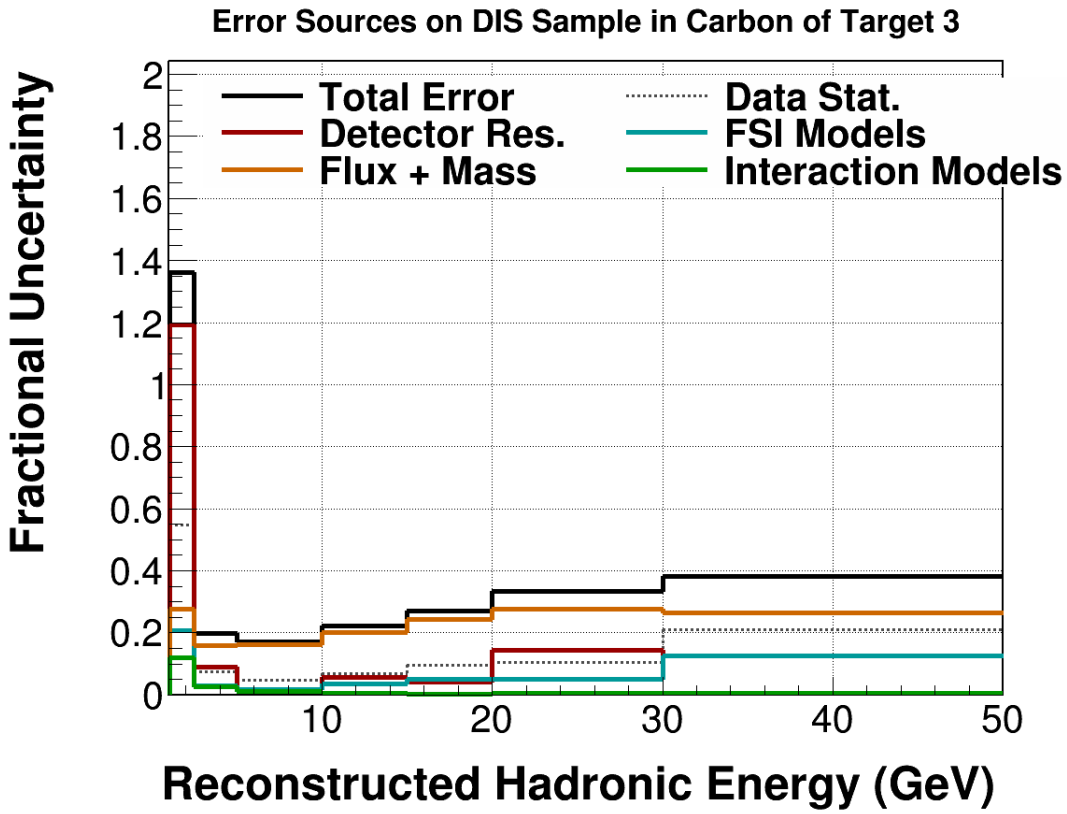

Figure E-138. Event yield uncertainties before CH subtraction: target 03 C (E_{had})

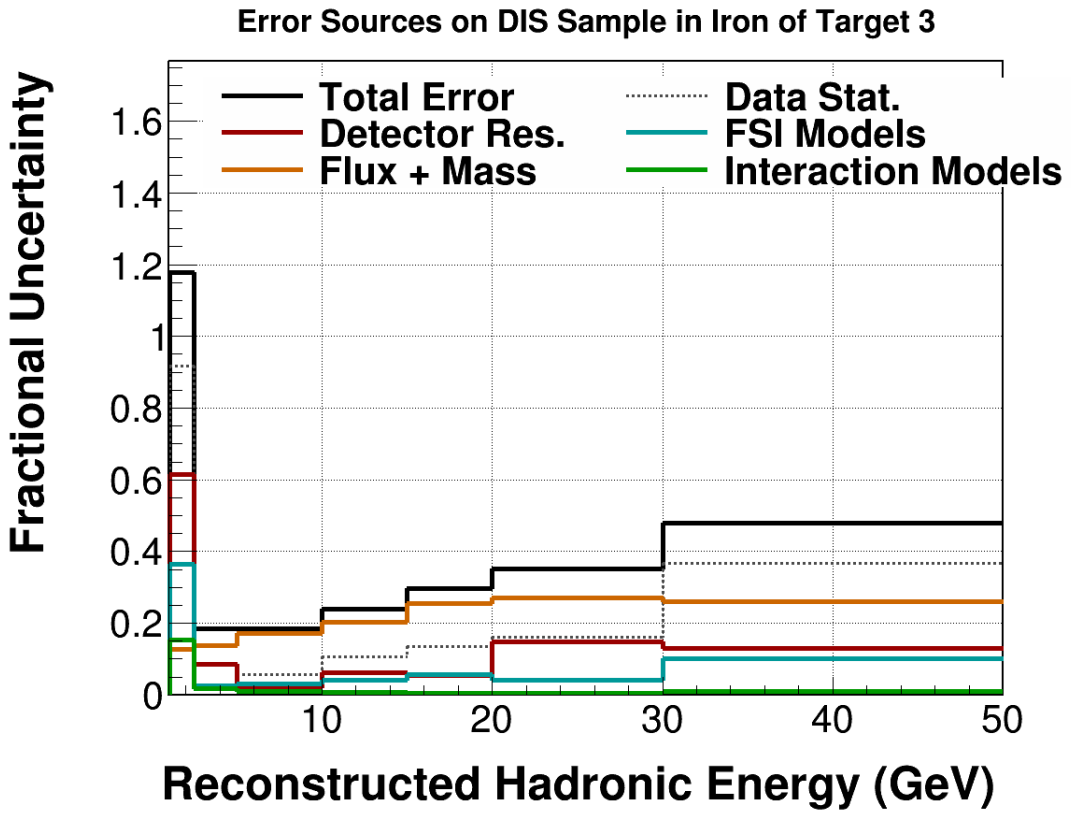

Figure E-139. Event yield uncertainties before CH subtraction: target 03 Fe (E_{had})

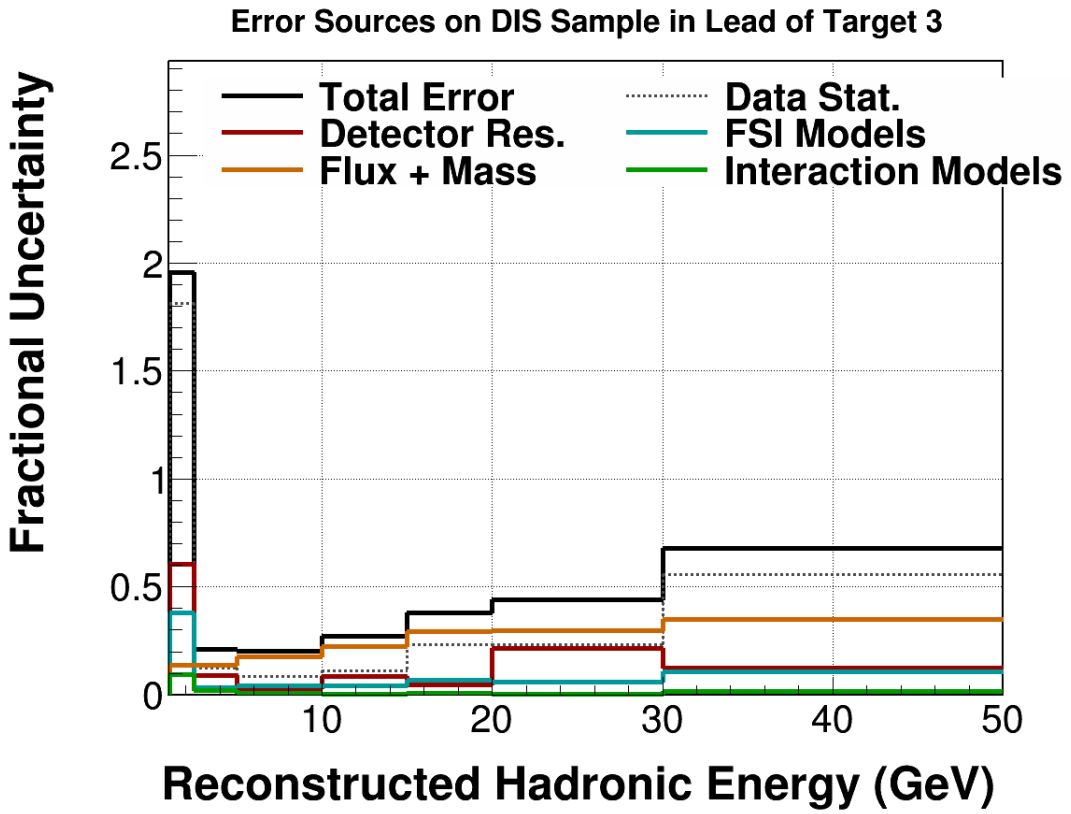

Figure E-140. Event yield uncertainties before CH subtraction: target 03 Pb (E_{had})

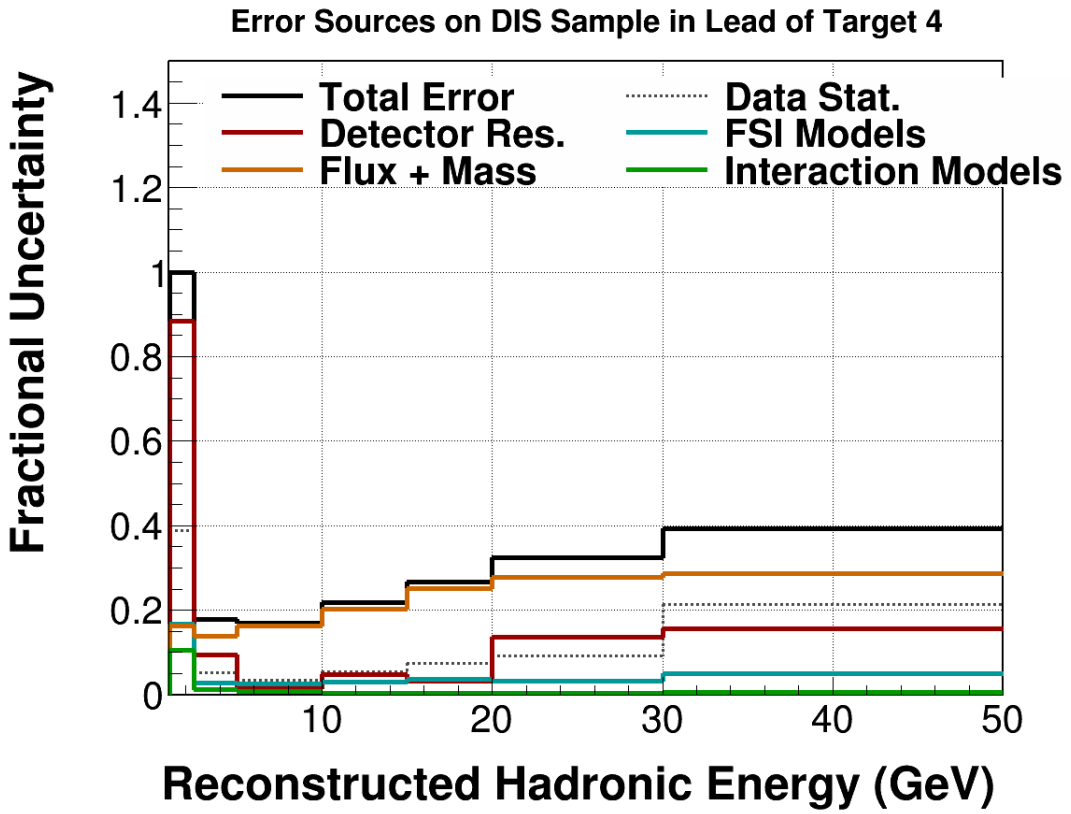

Figure E-141. Event yield uncertainties before CH subtraction: target 04 Pb (E_{had})

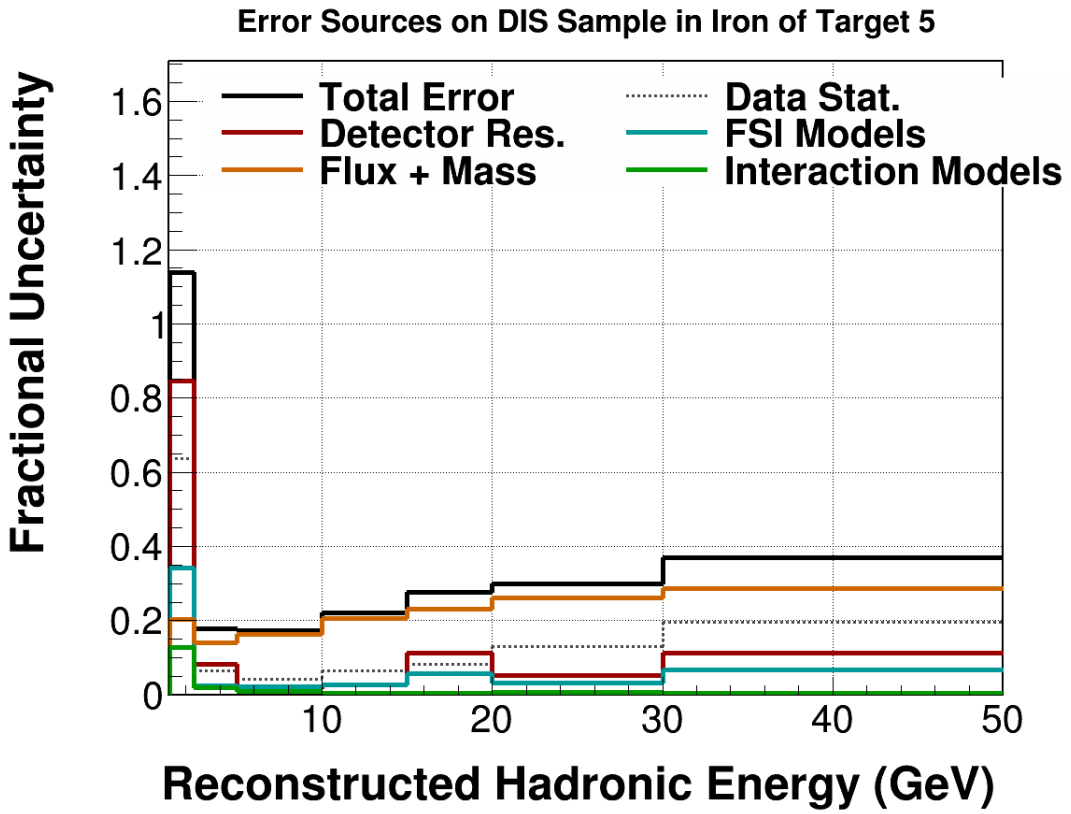

Figure E-142. Event yield uncertainties before CH subtraction: target 05 Fe (E_{had})

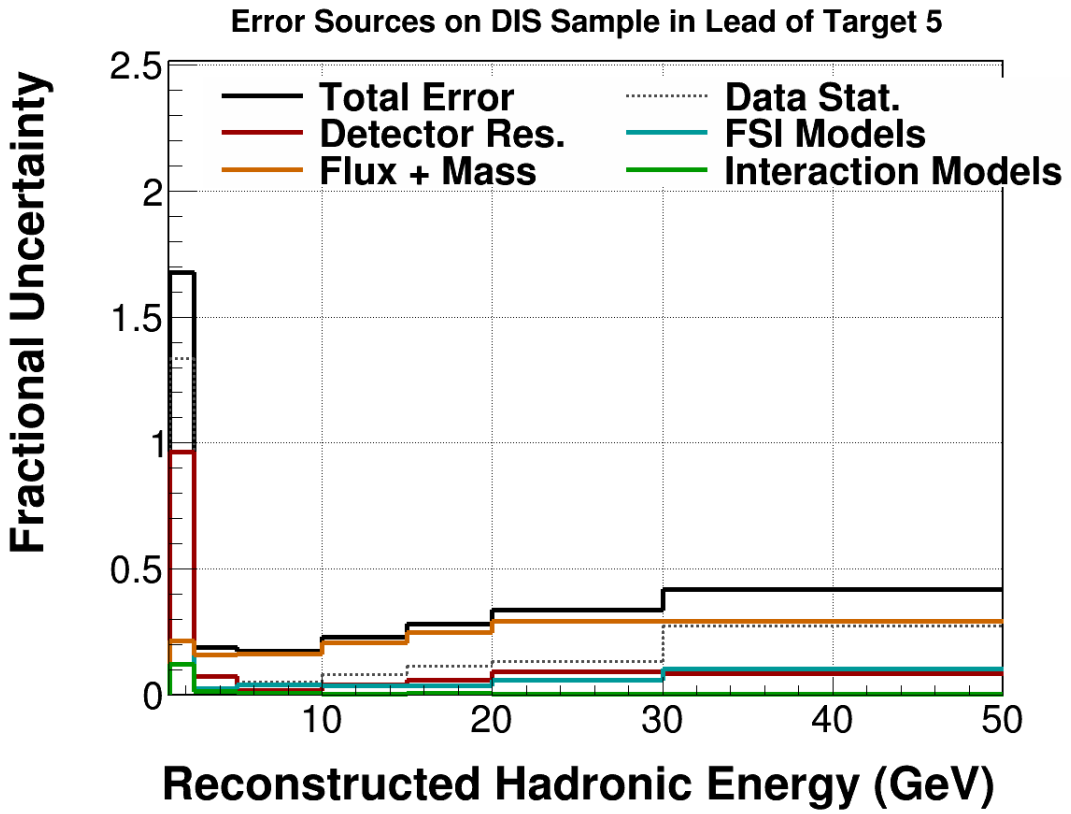

Figure E-143. Event yield uncertainties before CH subtraction: target 05 Pb (E_{had})

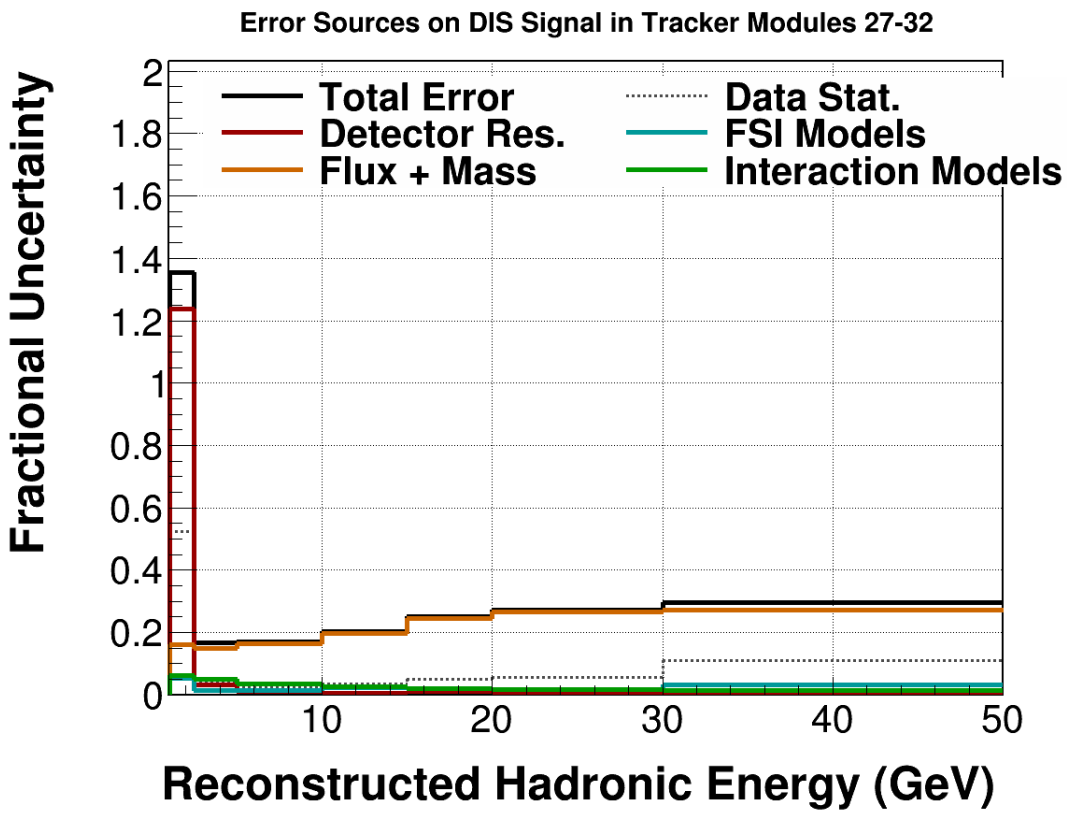

Figure E-144. Event yield uncertainties: tracker mods. 27-32 (E_{had})

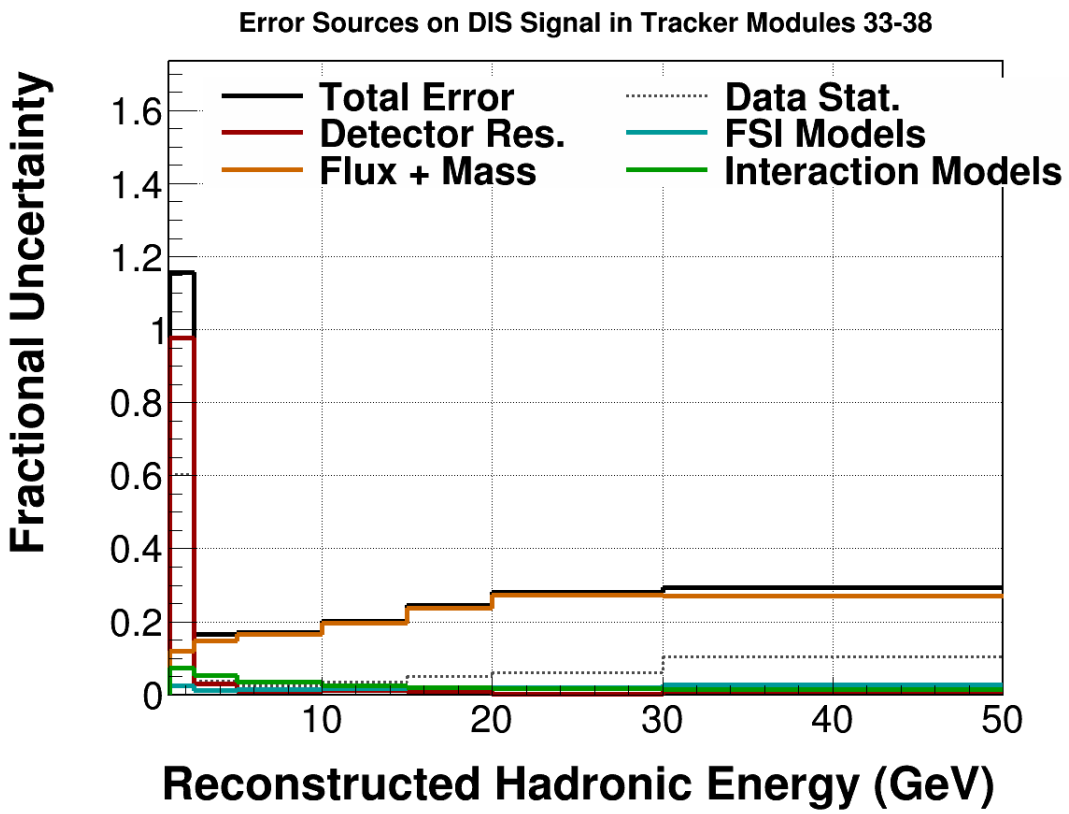

Figure E-145. Event yield uncertainties: tracker mods. 33-38 (E_{had})

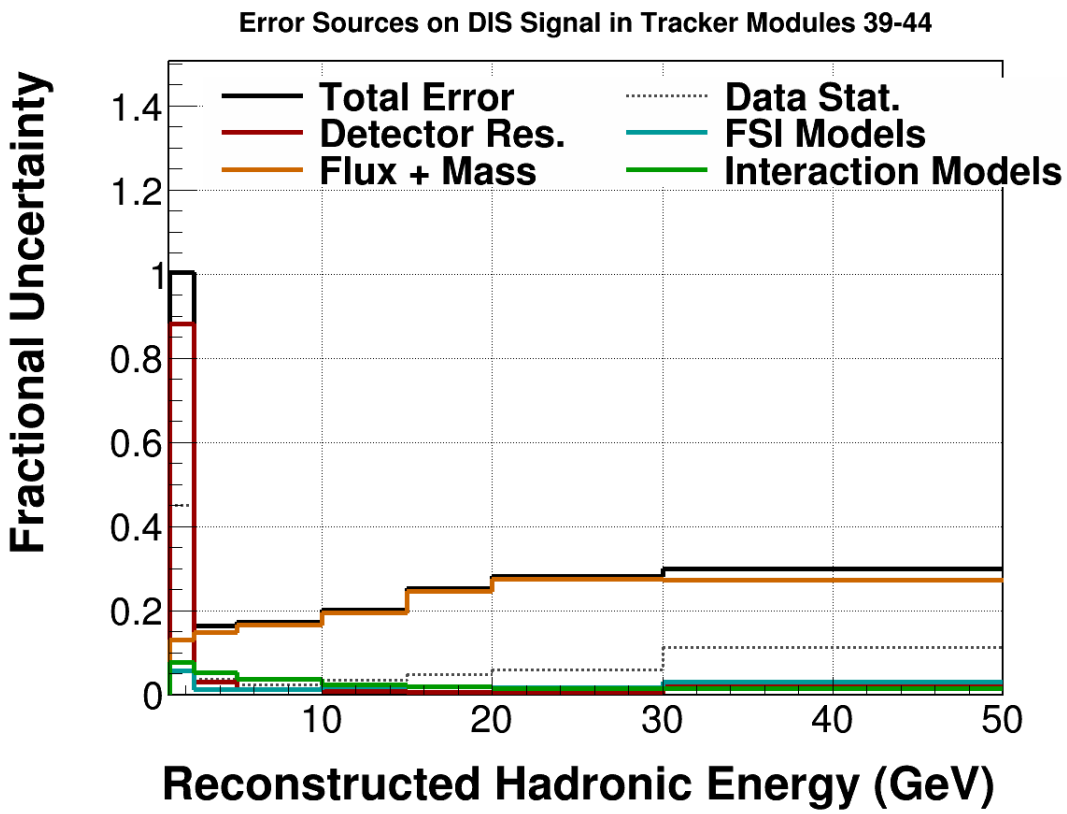

Figure E-146. Event yield uncertainties: tracker mods. 39-44 (E_{had})

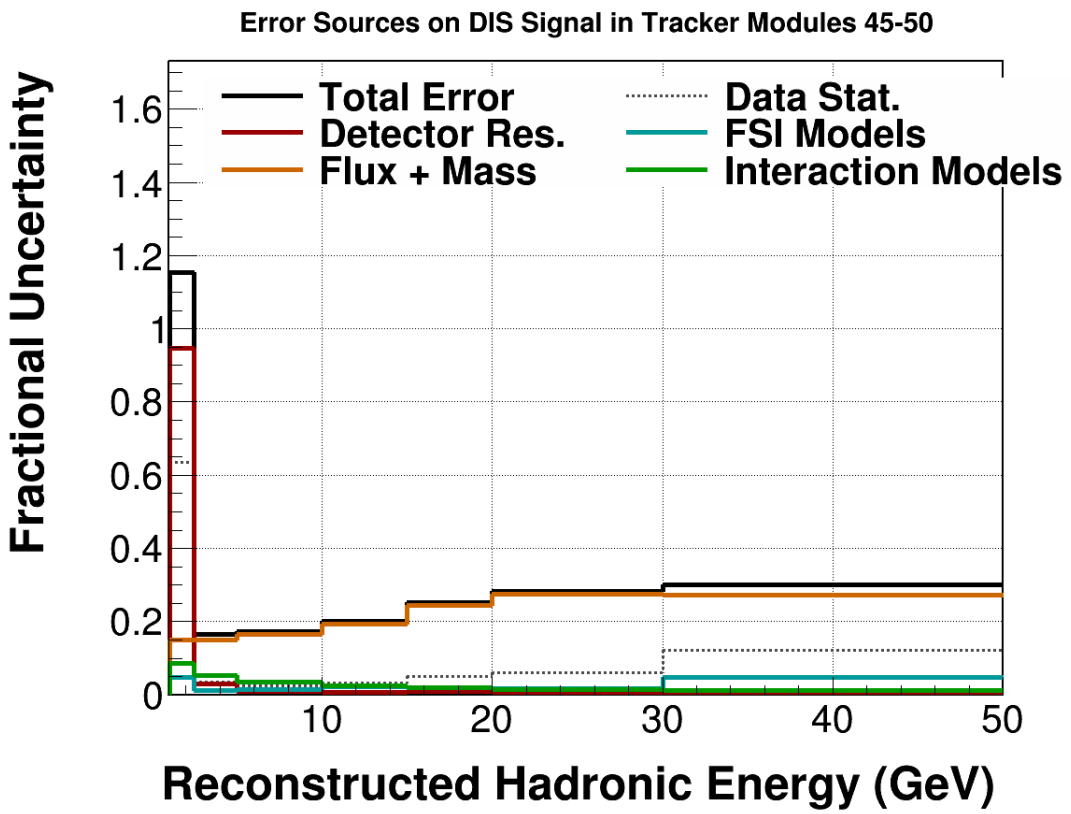

Figure E-147. Event yield uncertainties: tracker mods. 45-50 (E_{had})

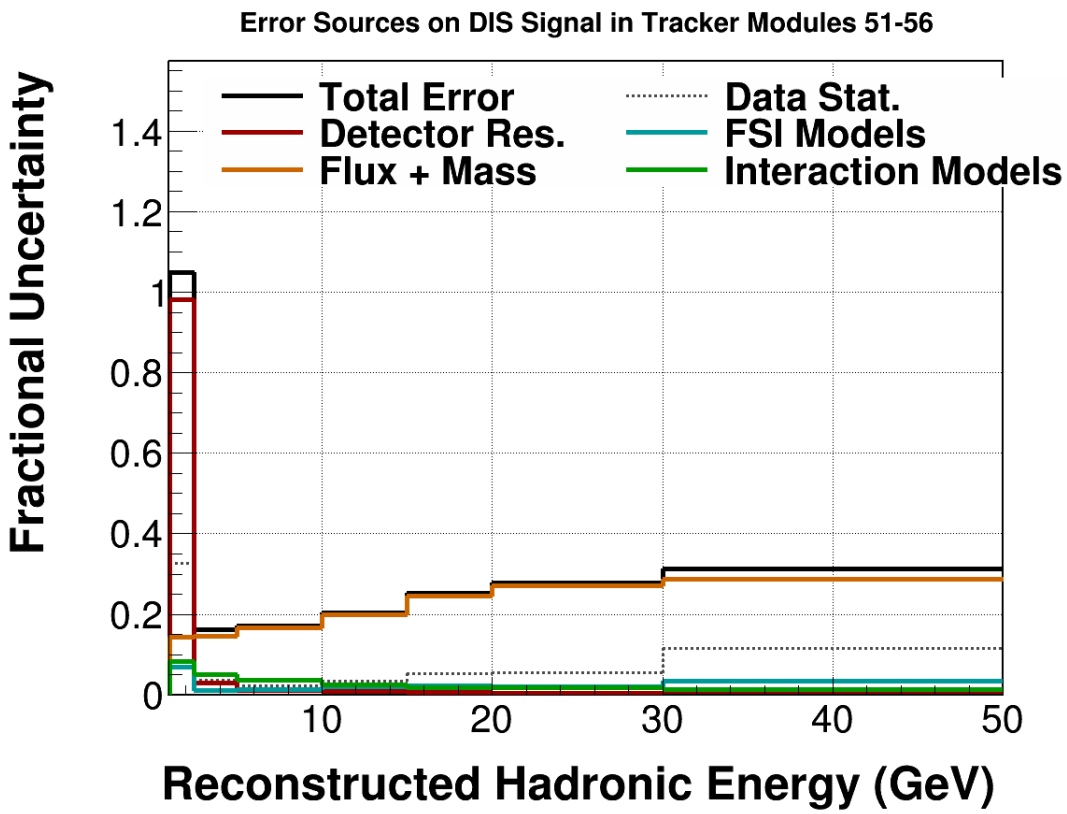

Figure E-148. Event yield uncertainties: tracker mods. 51-56 (E_{had})

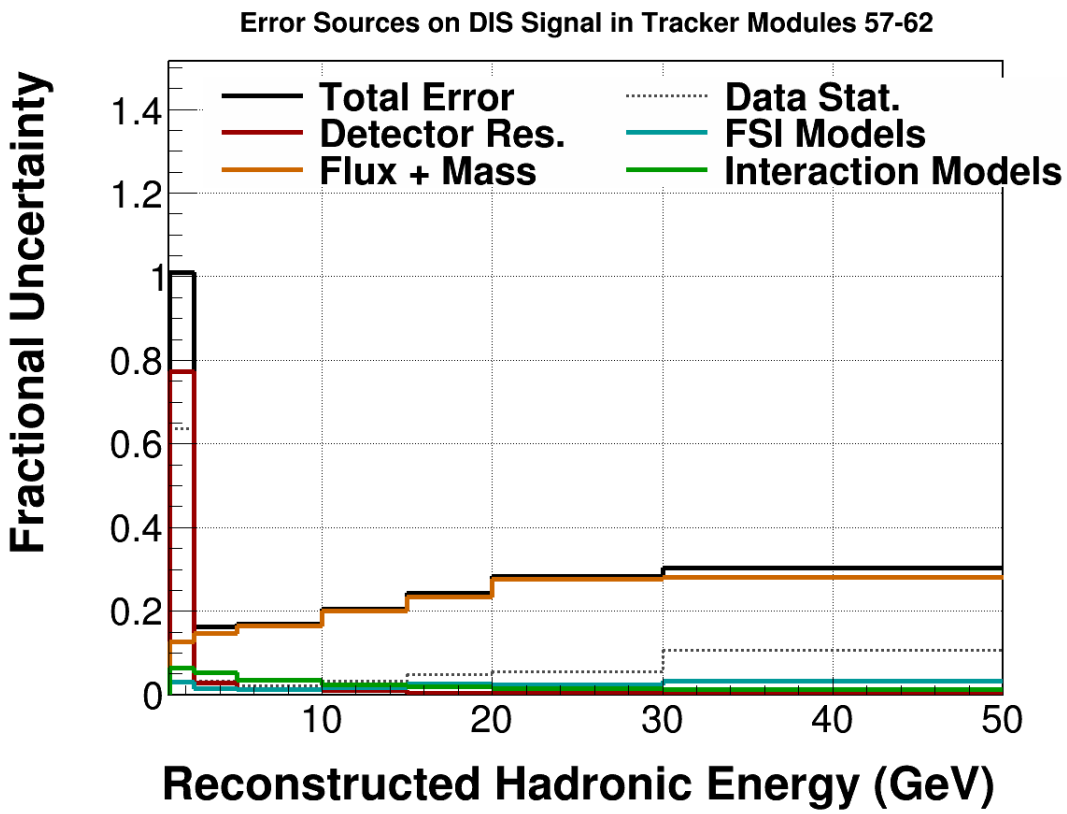

Figure E-149. Event yield uncertainties: tracker mods. 57-62 (E_{had})

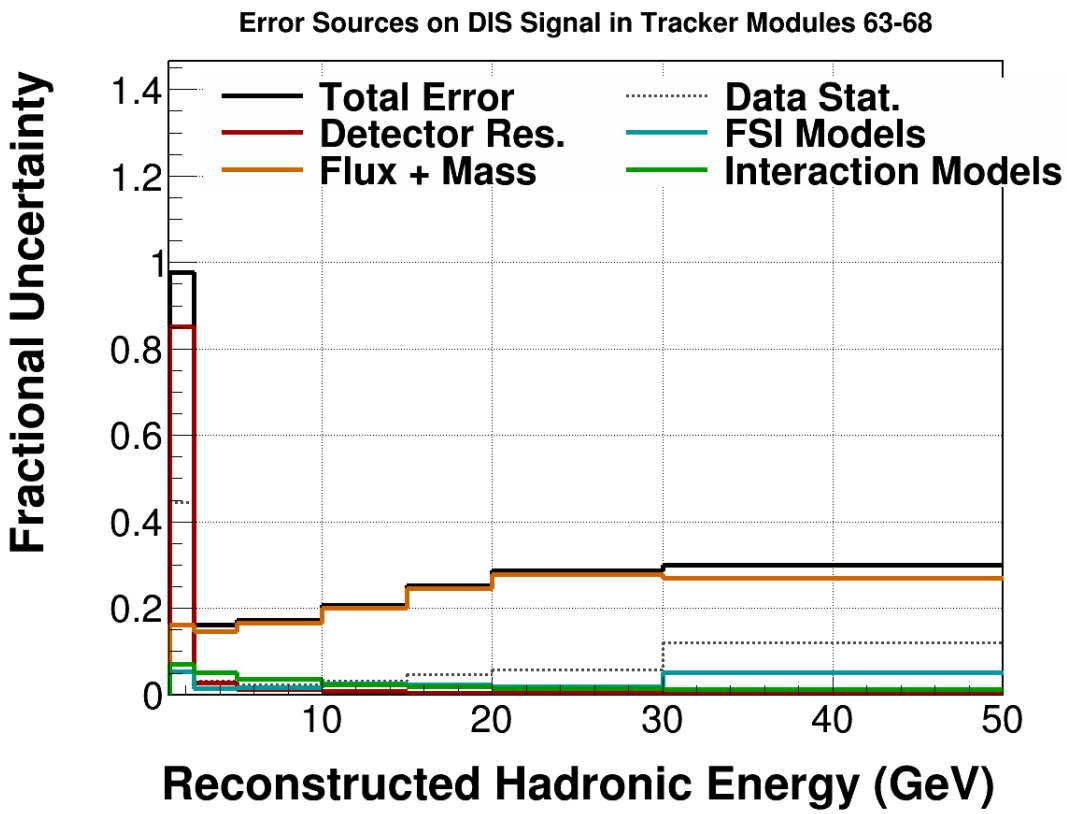

Figure E-150. Event yield uncertainties: tracker mods. 63-68 (E_{had})

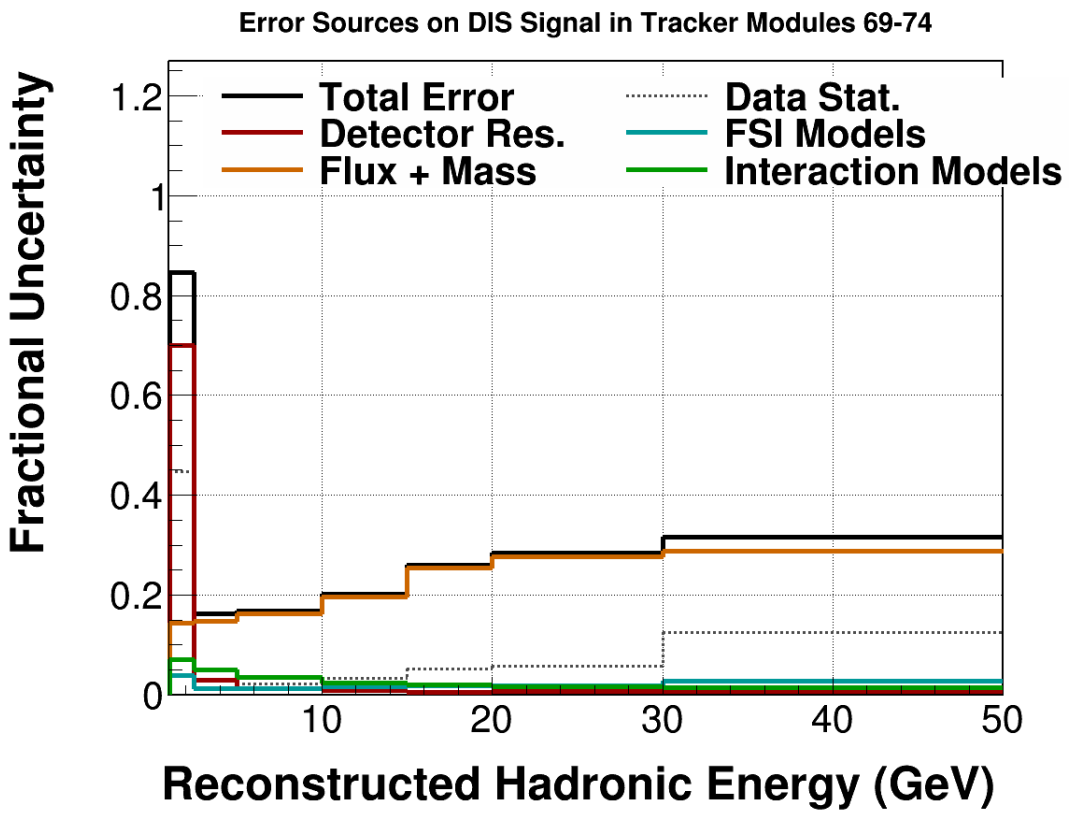

Figure E-151. Event yield uncertainties: tracker mods. 69-74 (E_{had})

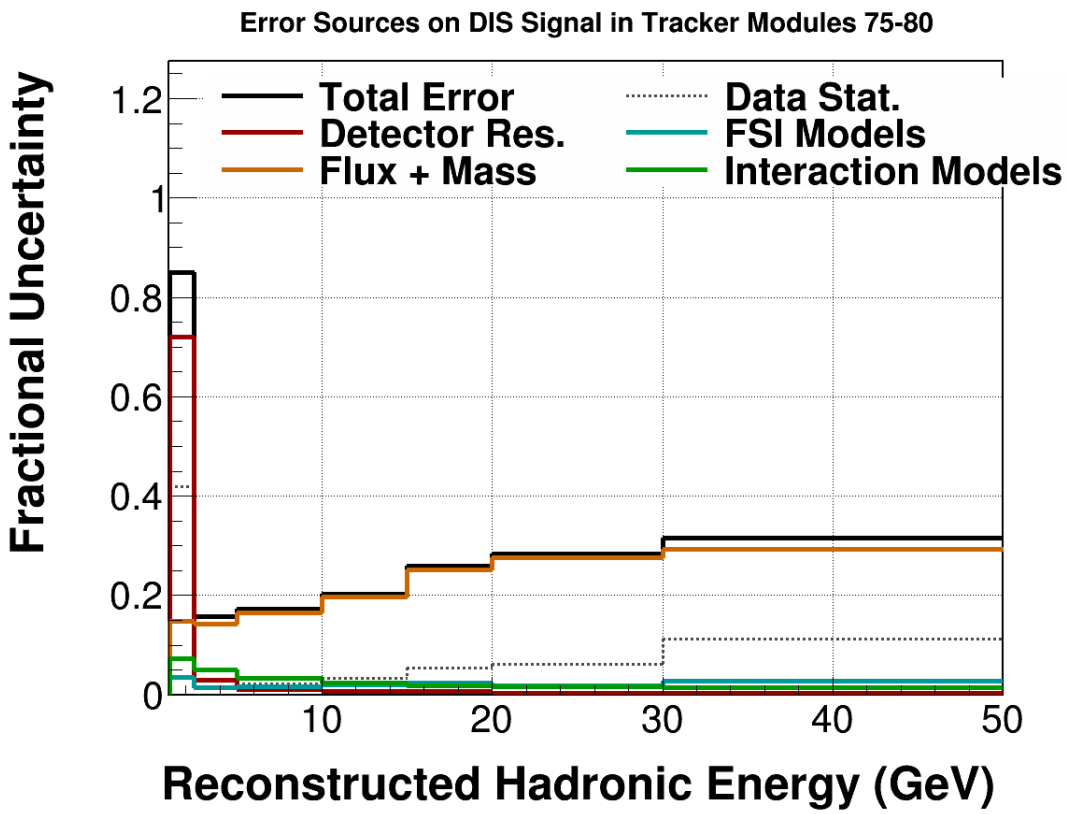

Figure E-152. Event yield uncertainties: tracker mods. 75-80 (E_{had})

The following plots show the uncertainty on the number of DIS events, after subtracting the non-DIS events. They are plotted as a function of four momentum transfer squared (Q^2):

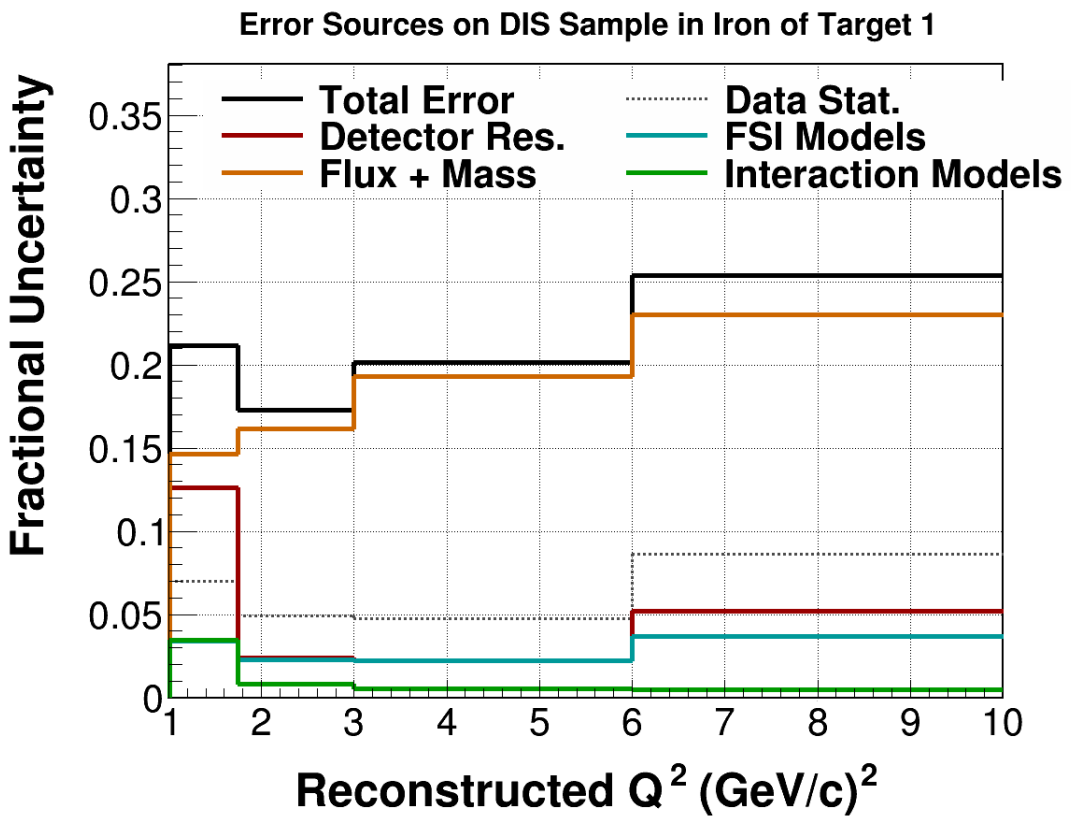

Figure E-153. Event yield uncertainties before CH subtraction: target 01 Fe (Q^2)

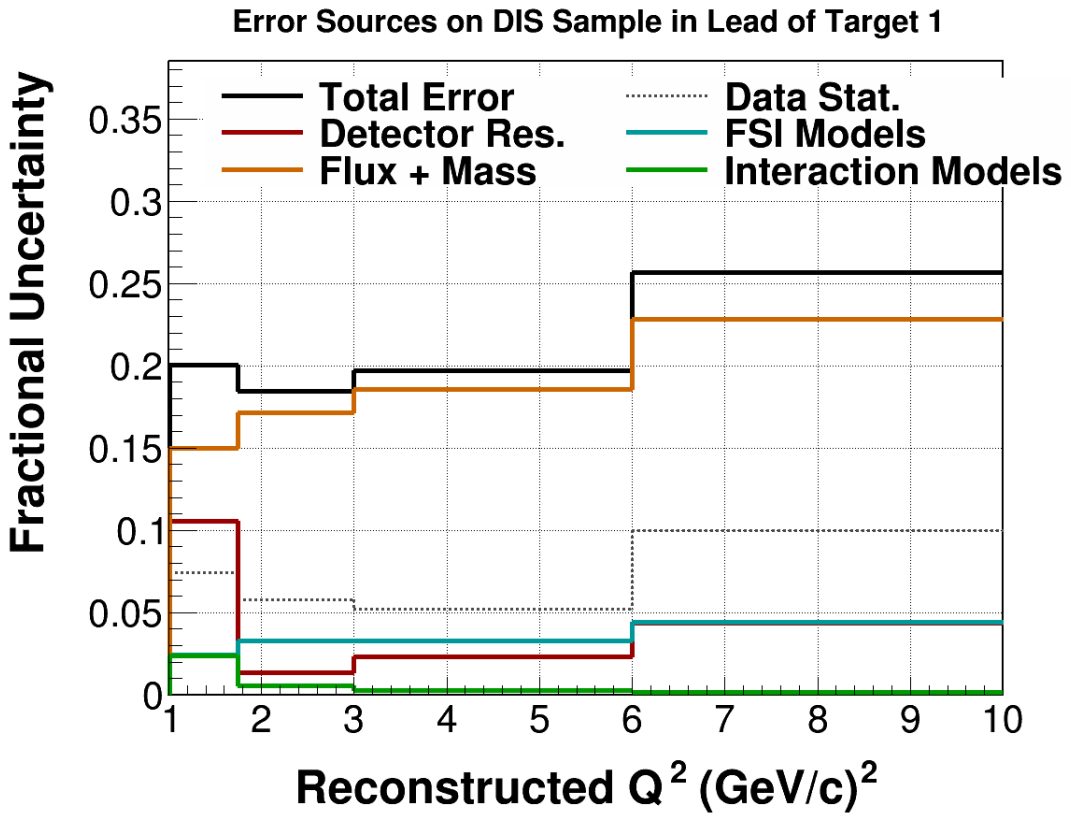

Figure E-154. Event yield uncertainties before CH subtraction: target 01 Pb (Q^2)

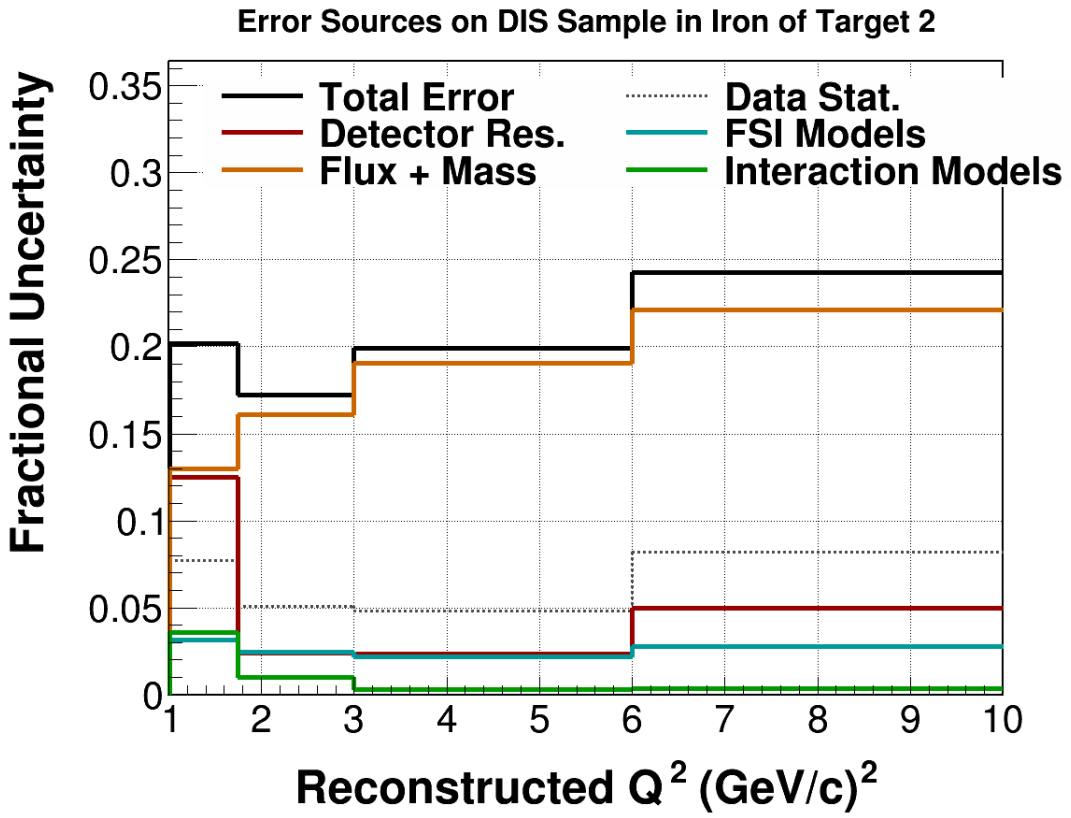

Figure E-155. Event yield uncertainties before CH subtraction: target 02 Fe (Q^2)

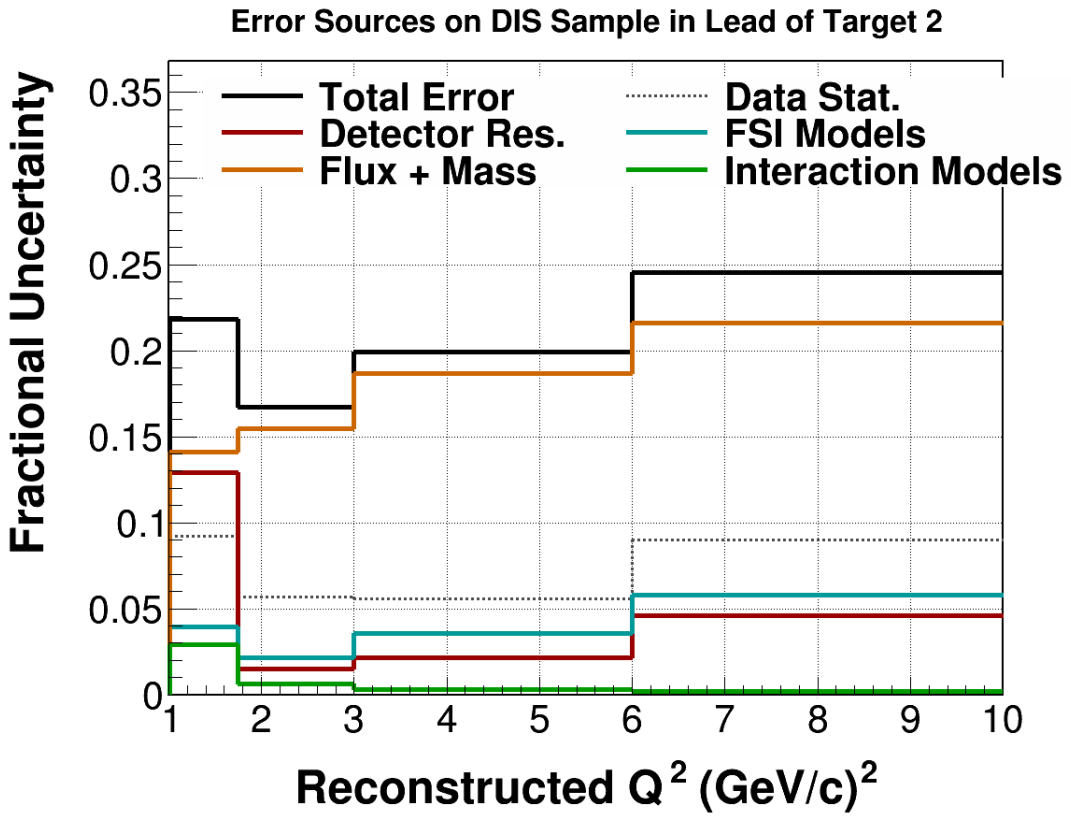

Figure E-156. Event yield uncertainties before CH subtraction: target 02 Pb (Q^2)

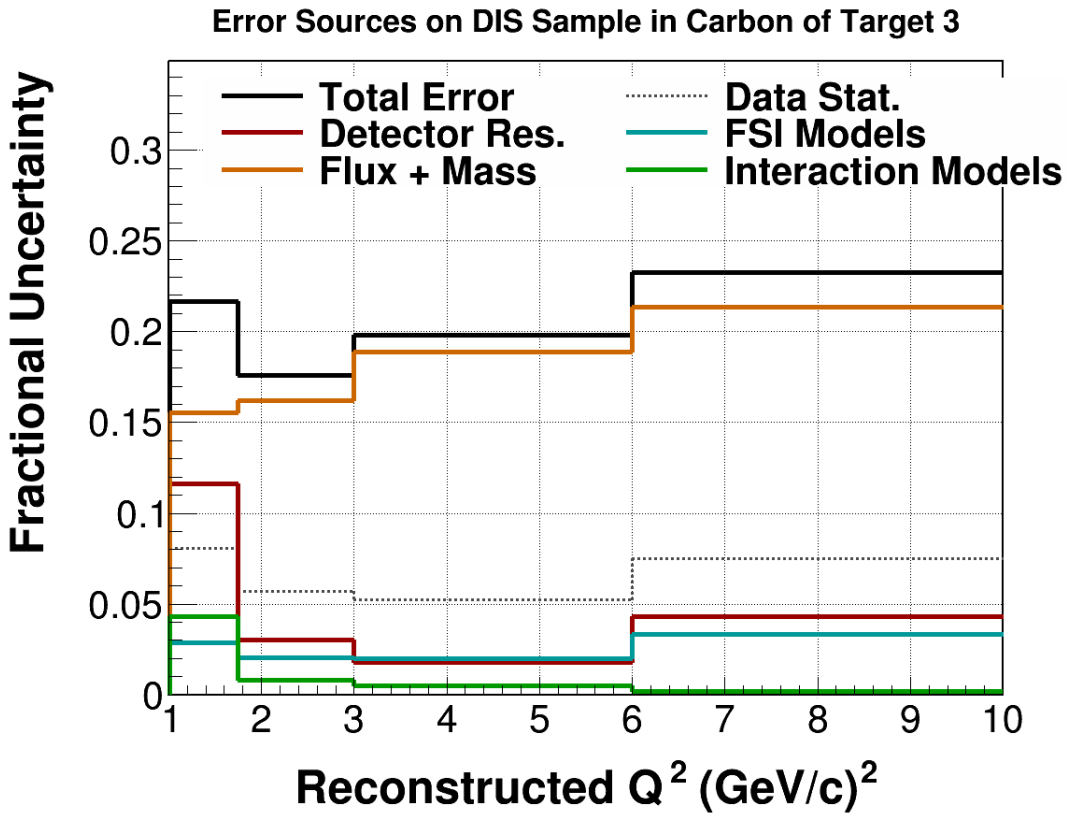

Figure E-157. Event yield uncertainties before CH subtraction: target 03 C (Q^2)

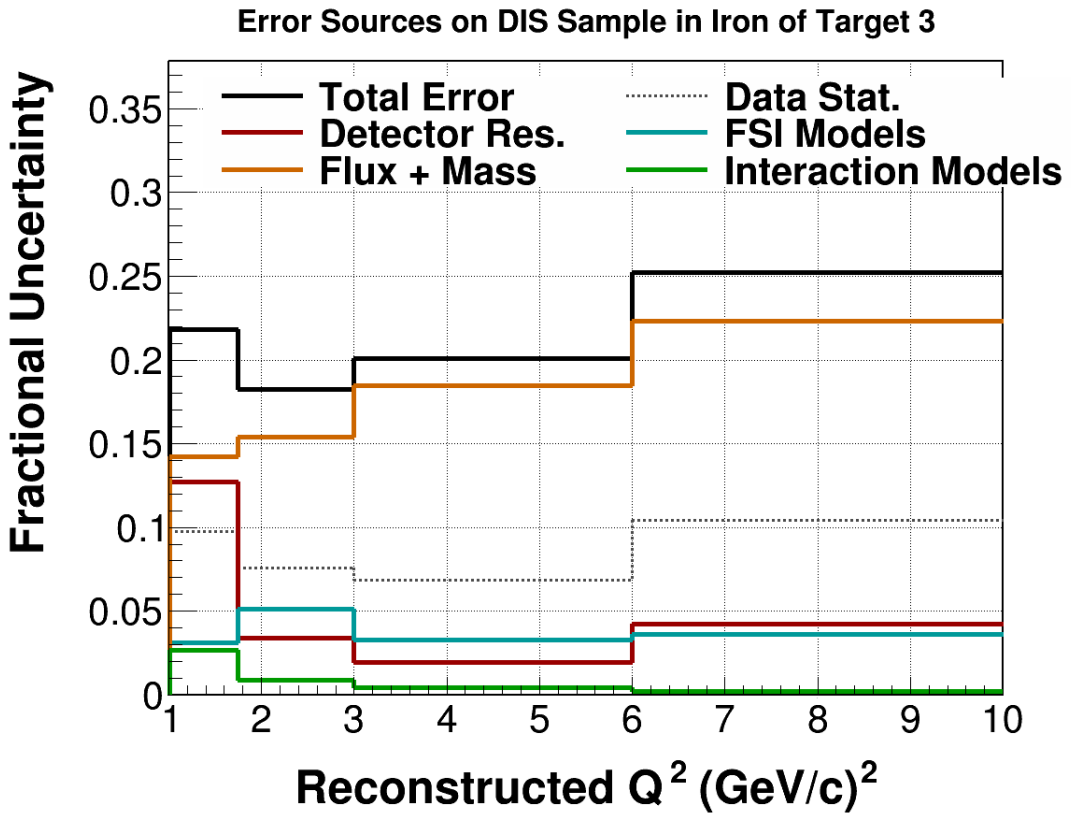

Figure E-158. Event yield uncertainties before CH subtraction: target 03 Fe (Q^2)

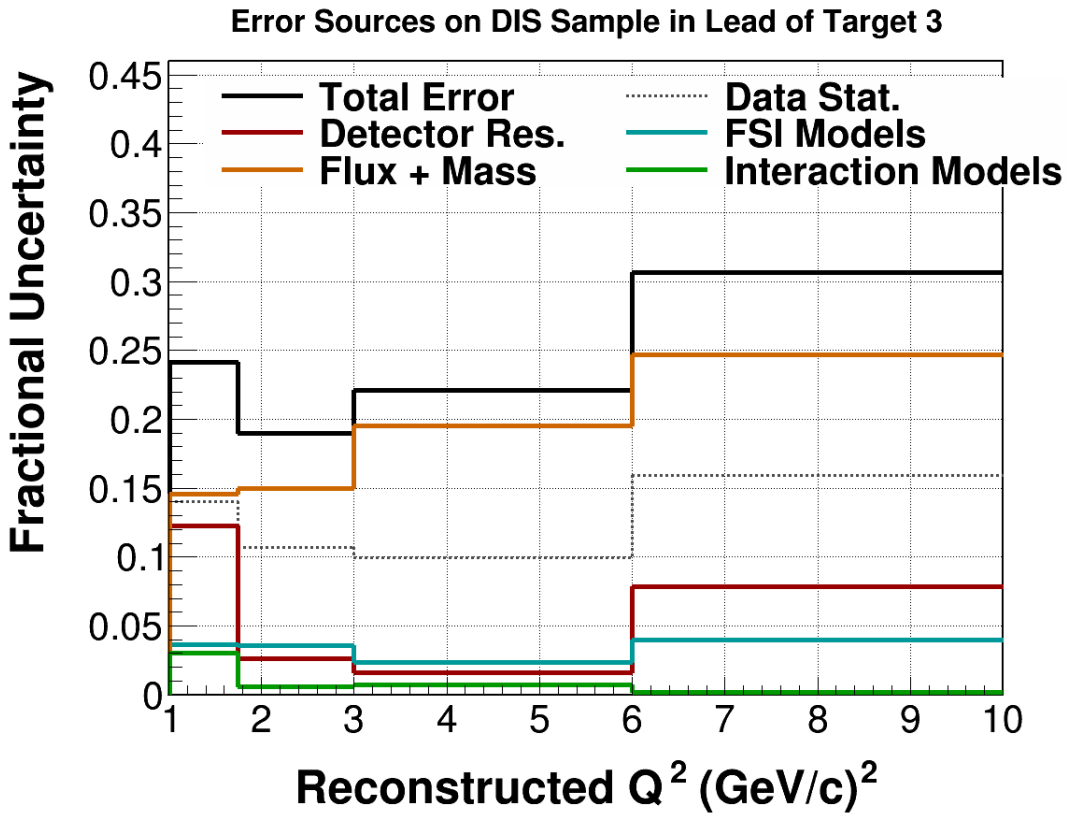

Figure E-159. Event yield uncertainties before CH subtraction: target 03 Pb (Q^2)

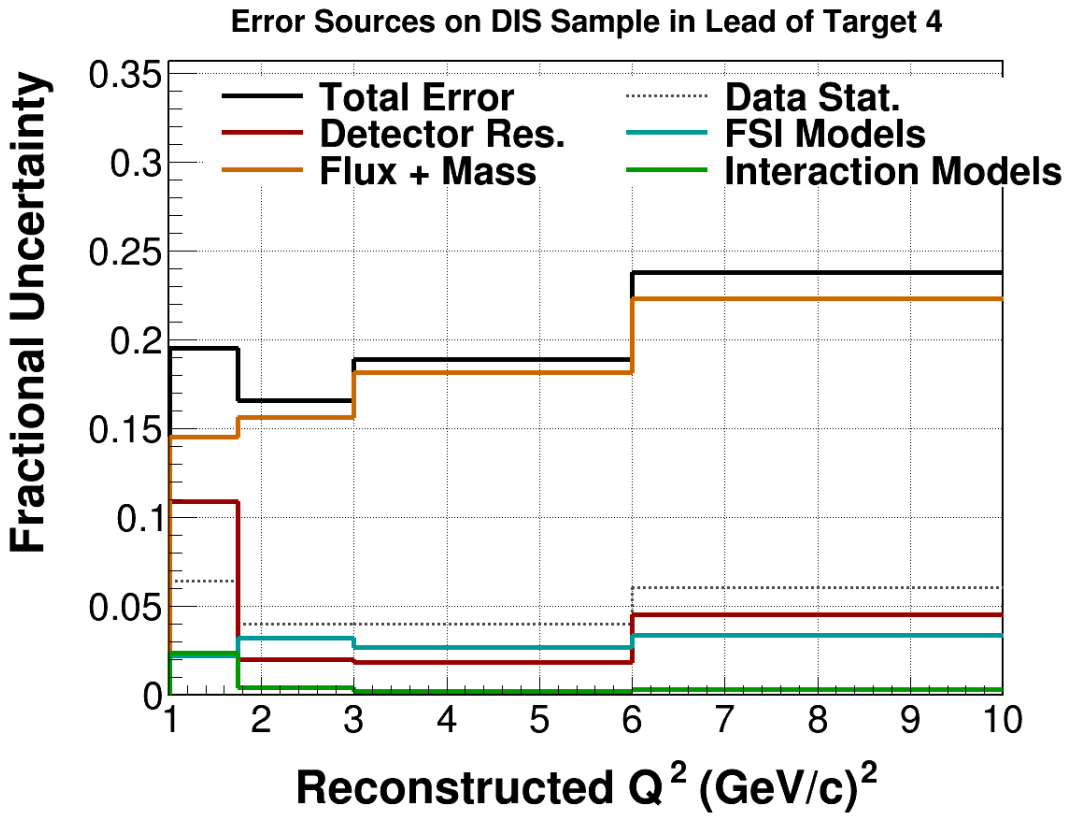

Figure E-160. Event yield uncertainties before CH subtraction: target 04 Pb (Q^2)

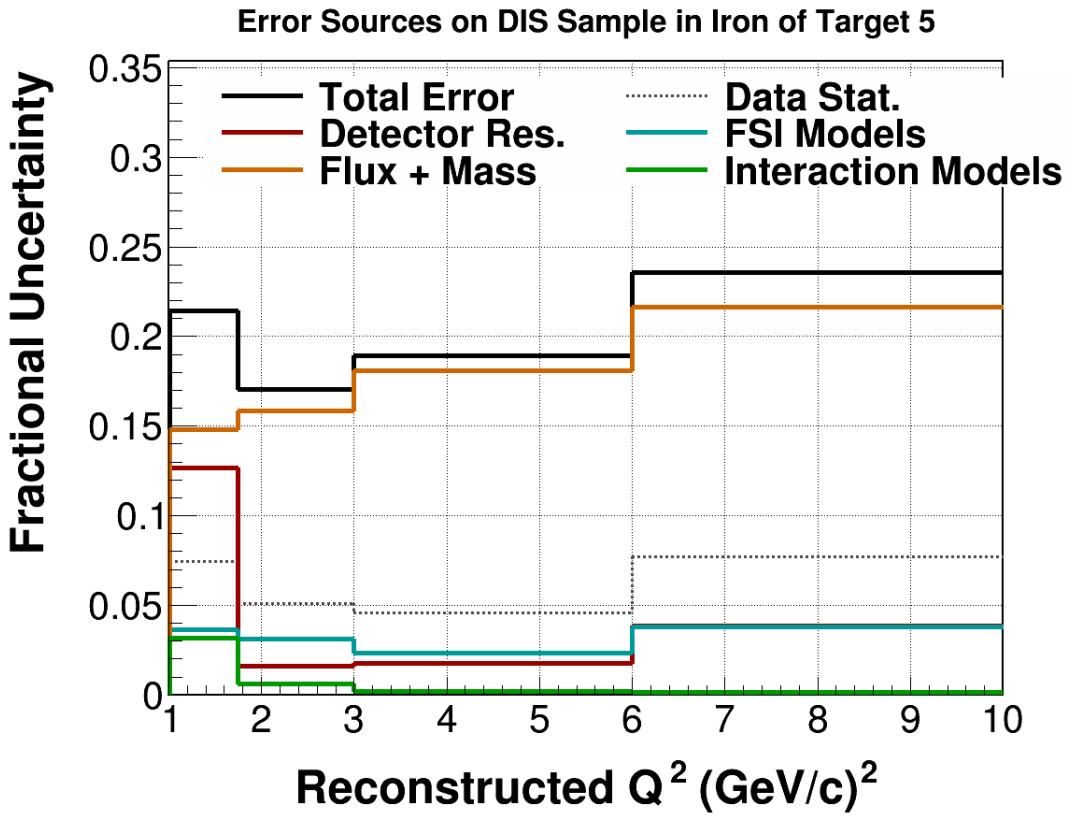

Figure E-161. Event yield uncertainties before CH subtraction: target 05 Fe (Q^2)

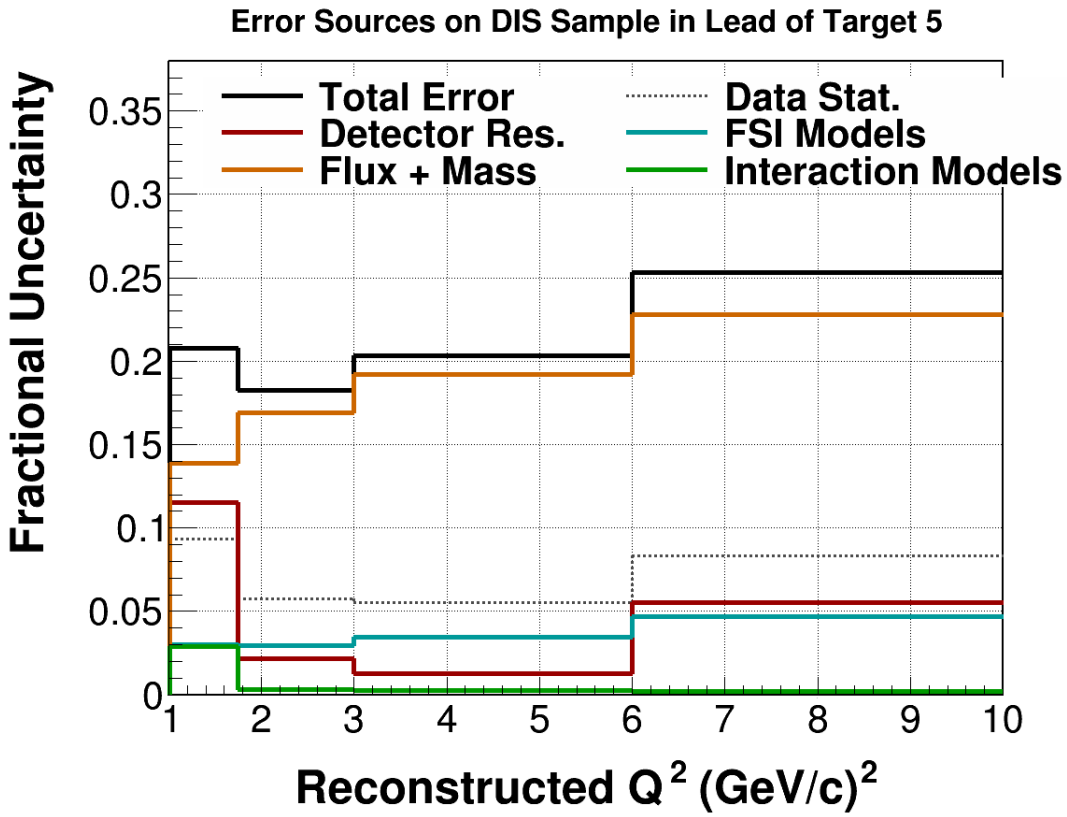

Figure E-162. Event yield uncertainties before CH subtraction: target 05 Pb (Q^2)

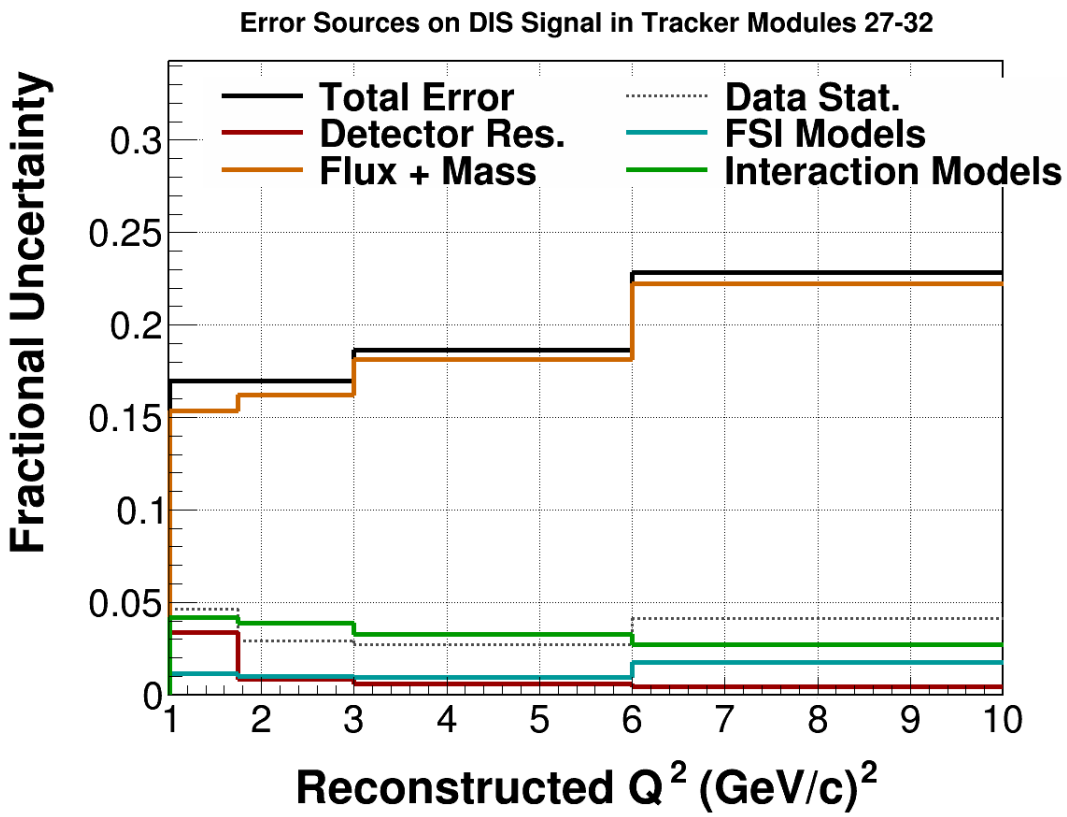

Figure E-163. Event yield uncertainties: tracker mods. 27-32 (Q^2)

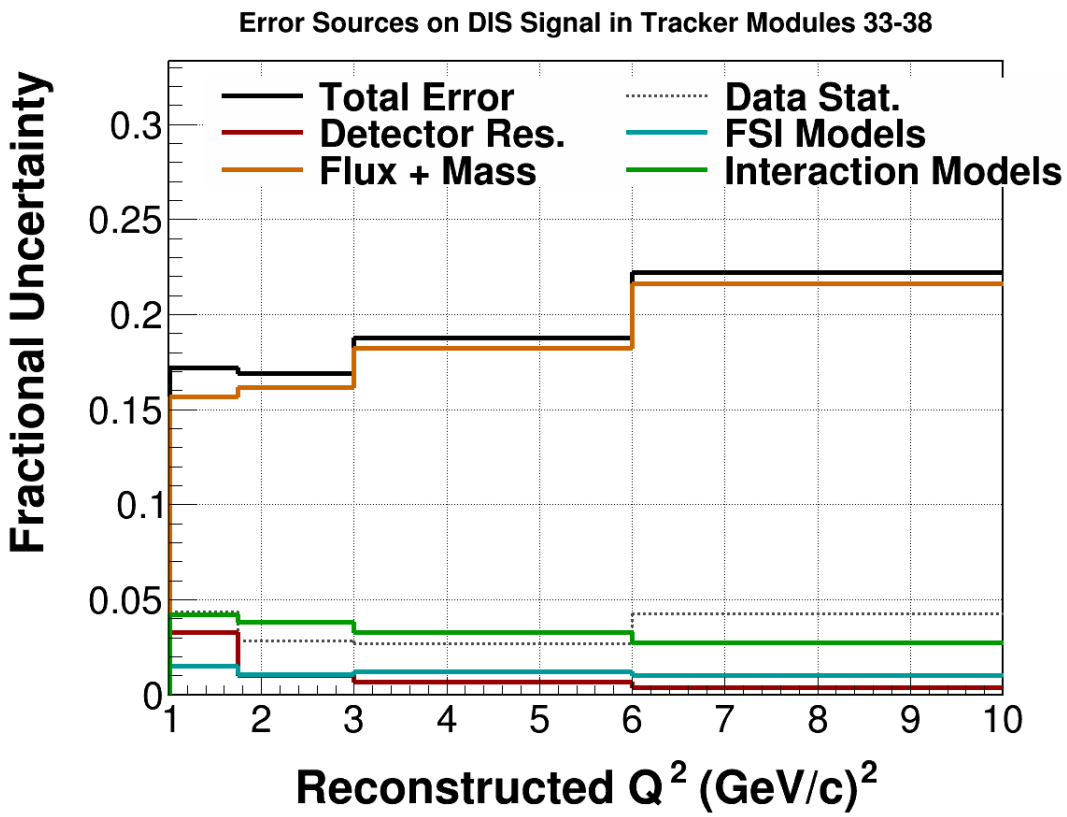

Figure E-164. Event yield uncertainties: tracker mods. 33-38 (Q^2)

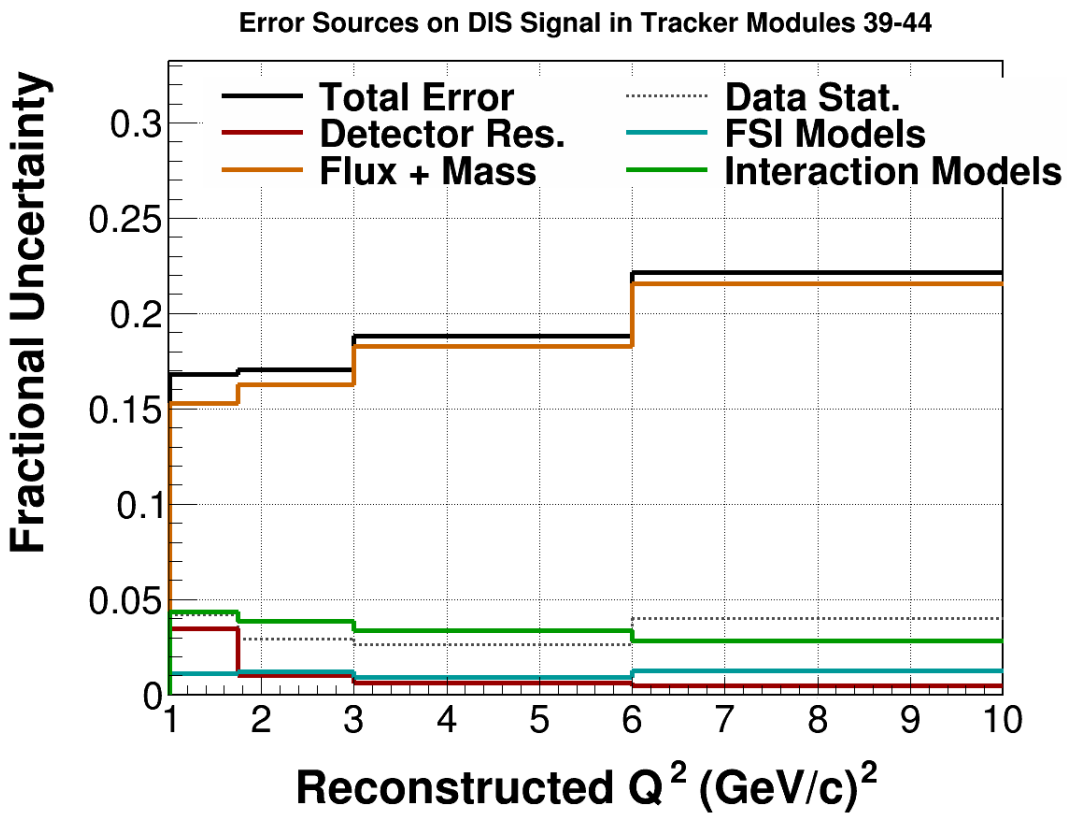

Figure E-165. Event yield uncertainties: tracker mods. 39-44 (Q^2)

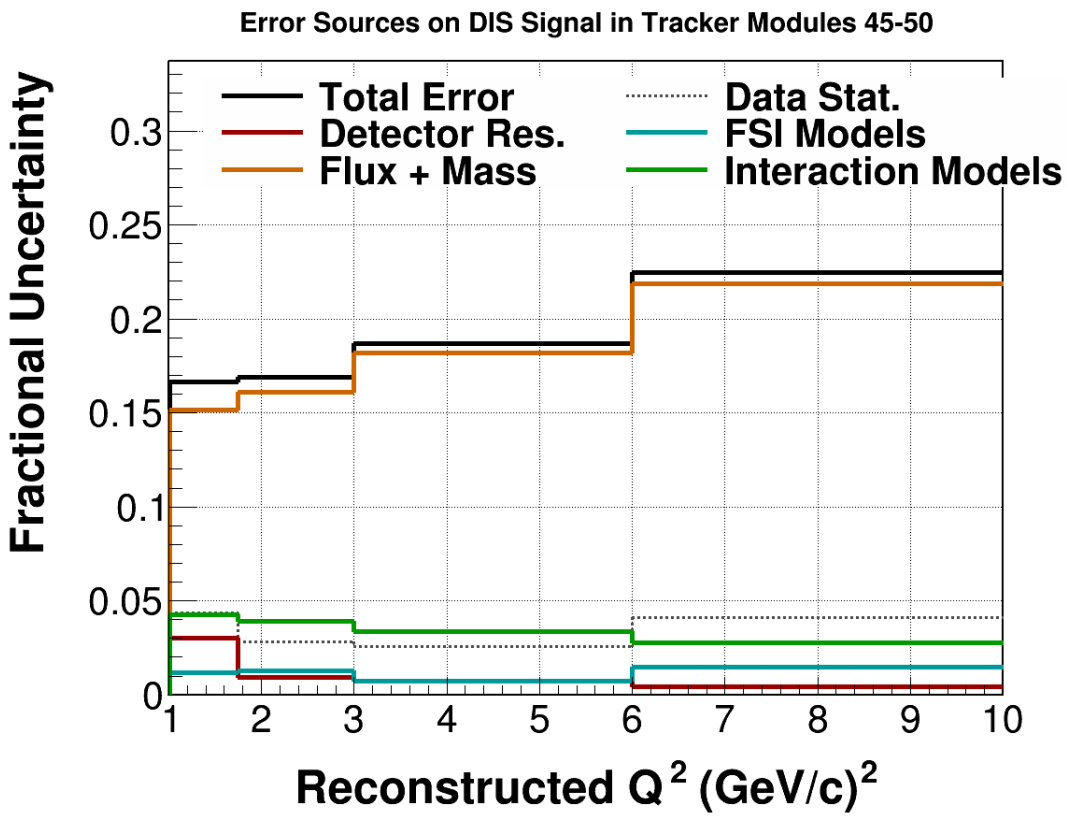

Figure E-166. Event yield uncertainties: tracker mods. 45-50 (Q^2)

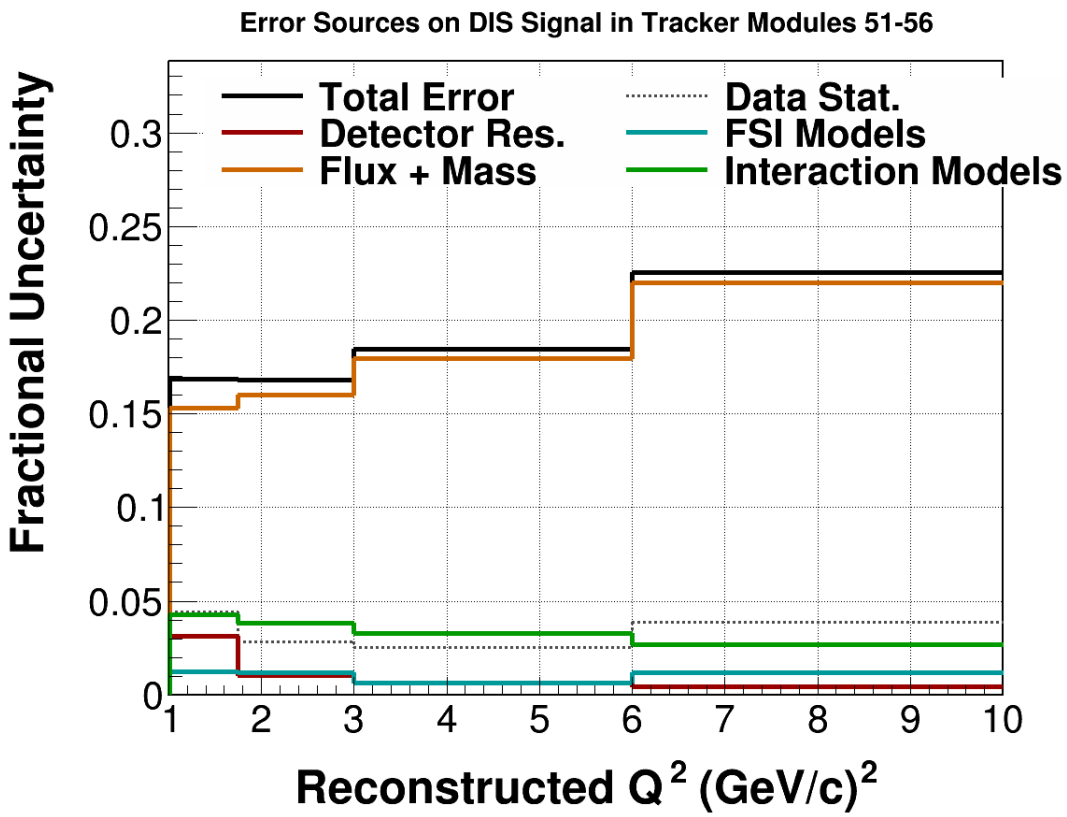

Figure E-167. Event yield uncertainties: tracker mods. 51-56 (Q^2)

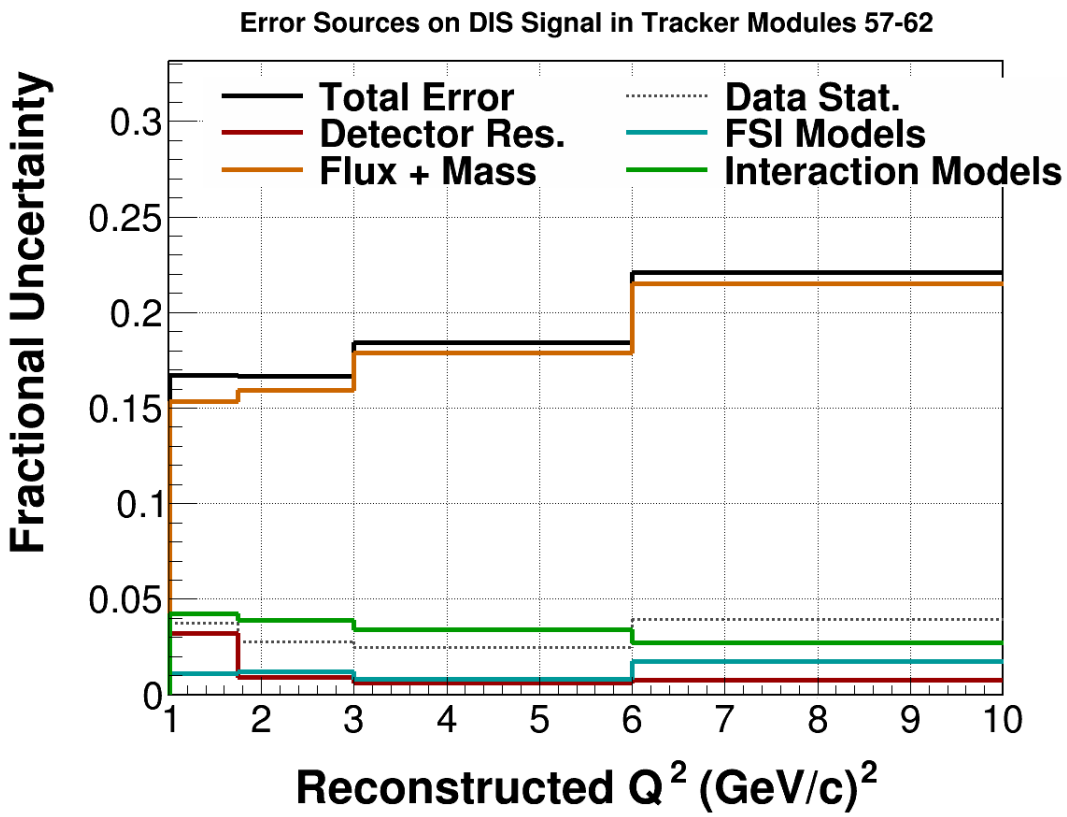

Figure E-168. Event yield uncertainties: tracker mods. 57-62 (Q^2)

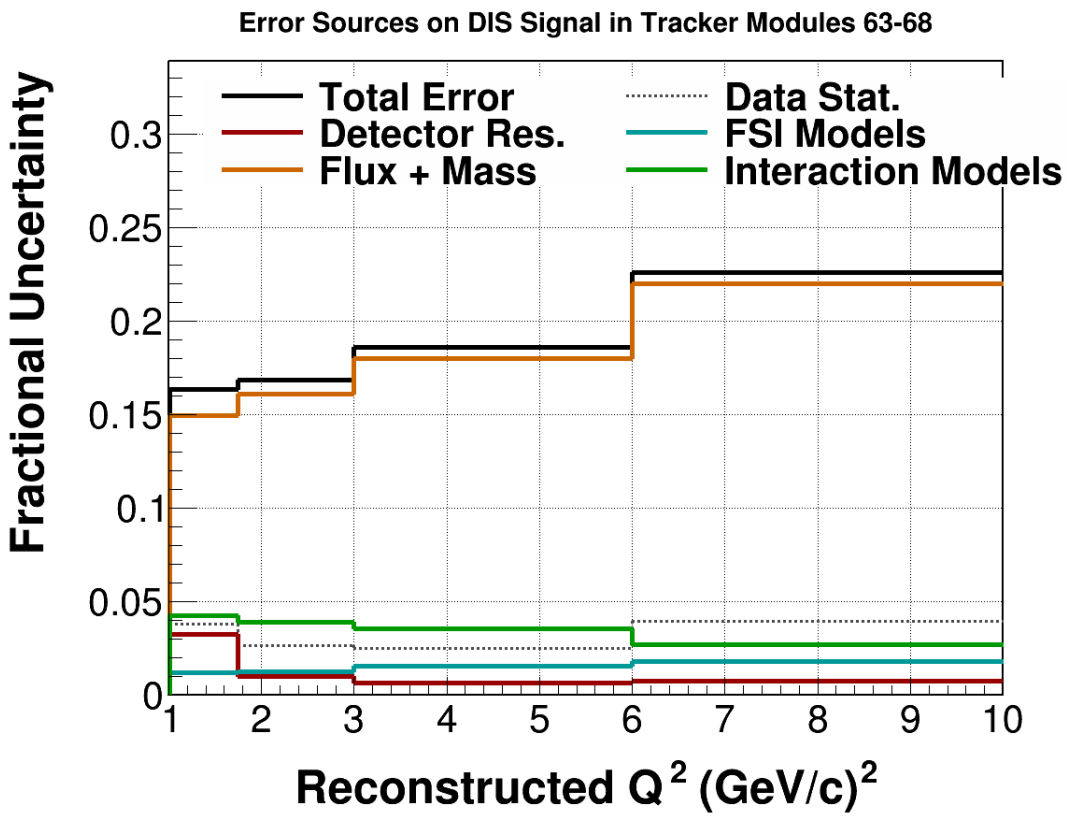

Figure E-169. Event yield uncertainties: tracker mods. 63-68 (Q^2)

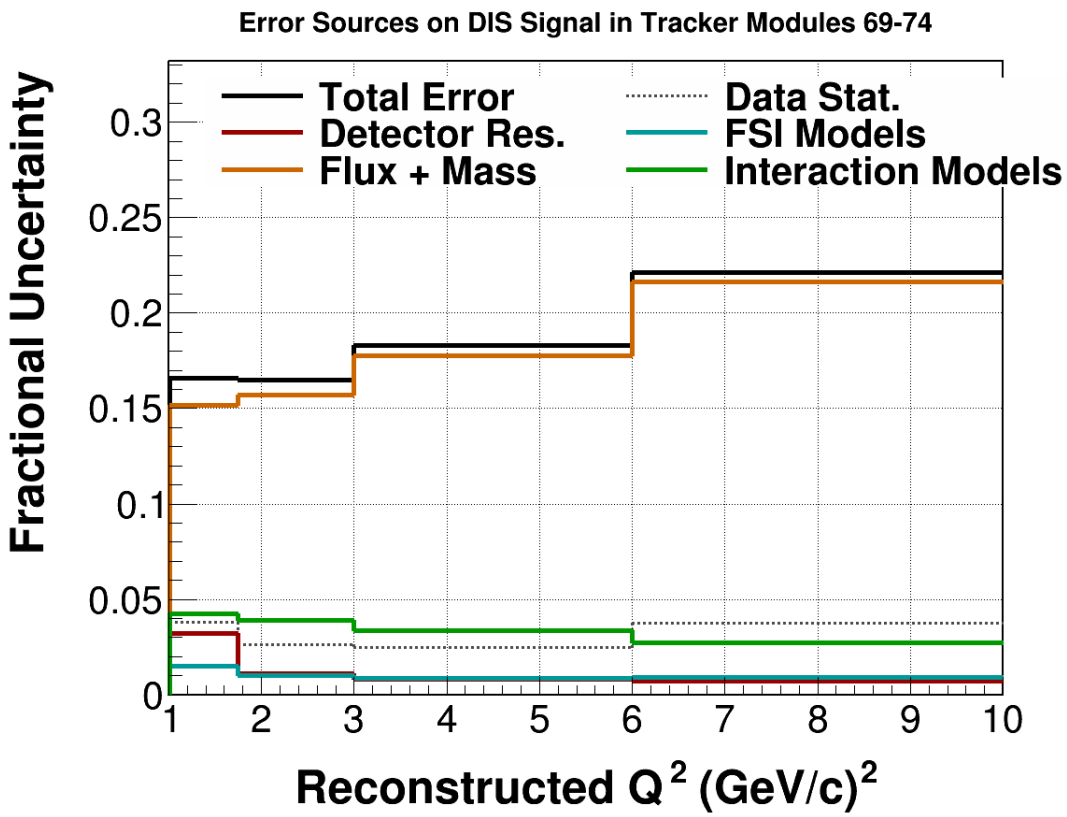

Figure E-170. Event yield uncertainties: tracker mods. 69-74 (Q^2)

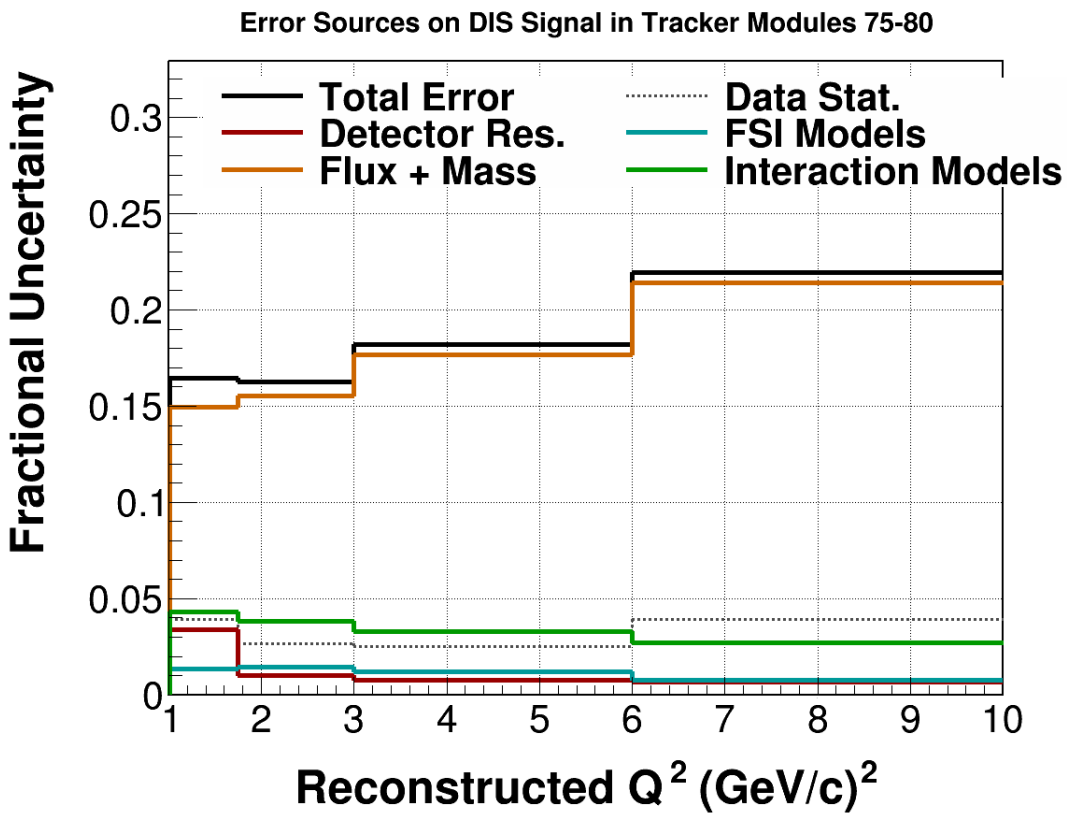

Figure E-171. Event yield uncertainties: tracker mods. 75-80 (Q^2)

The following plots show the uncertainty on the number of DIS events, after subtracting the non-DIS events. They are plotted as a function of final state hadronic shower invariant mass (W):

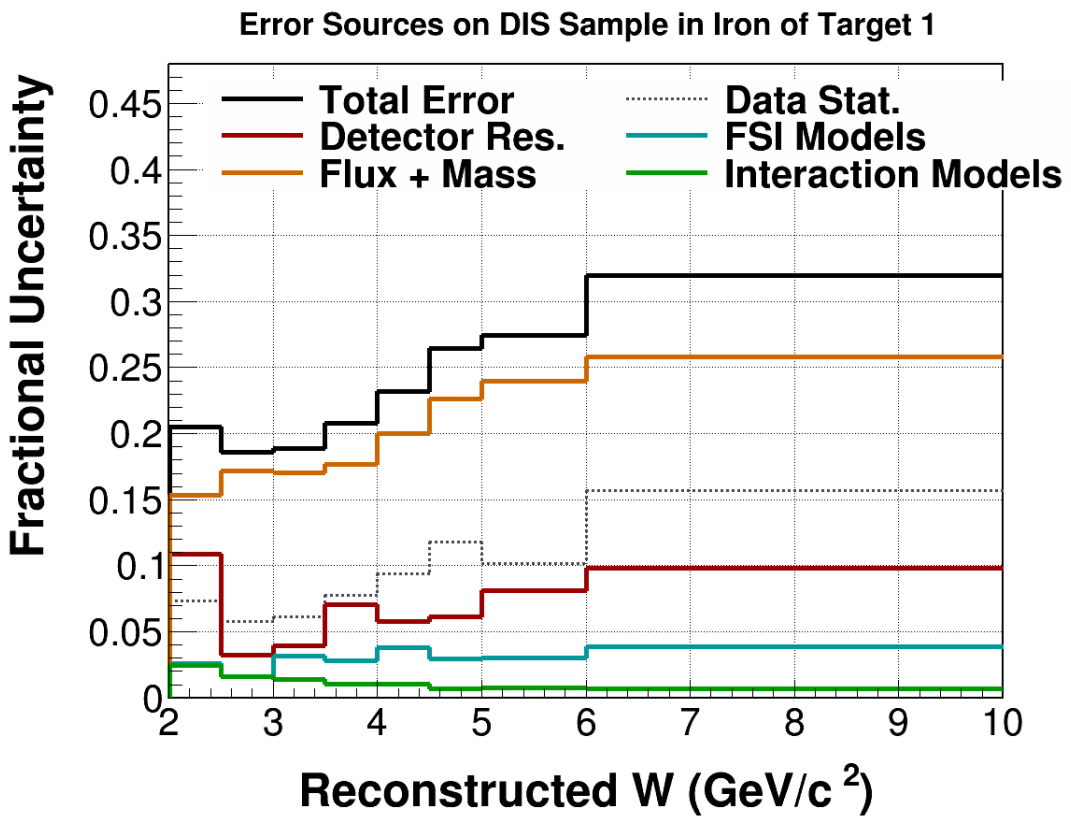

Figure E-172. Event yield uncertainties before CH subtraction: target 01 Fe (W)

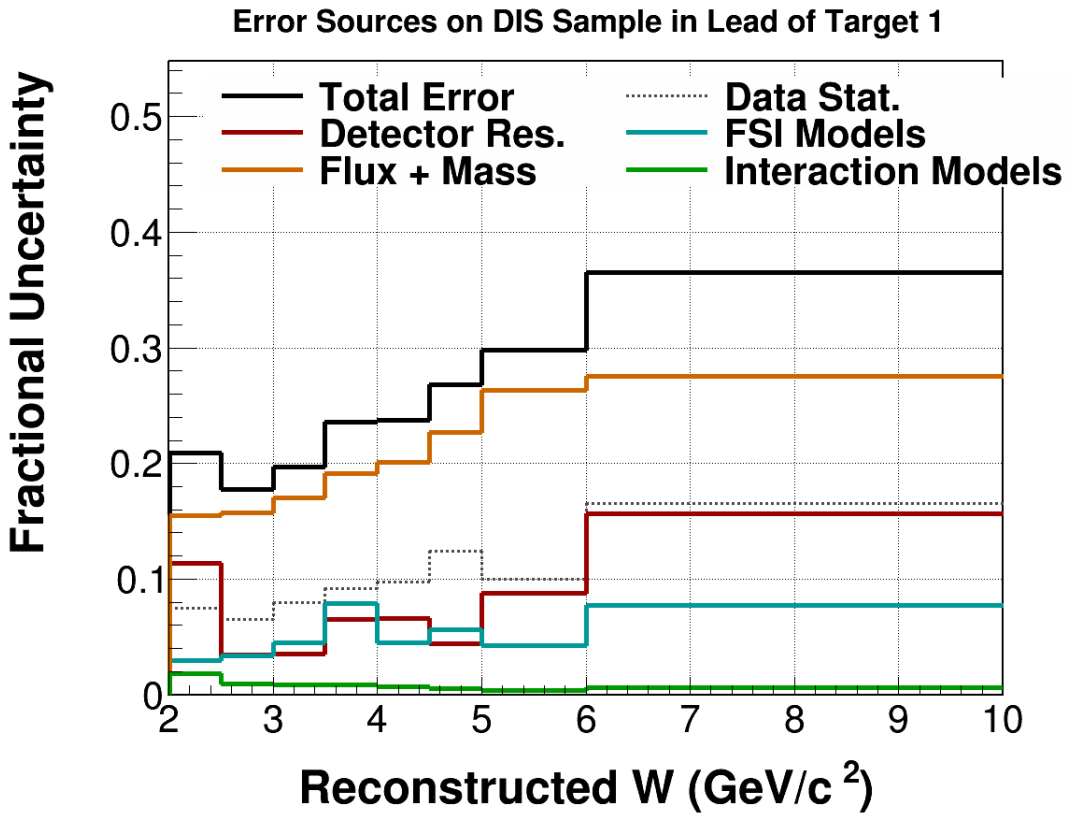

Figure E-173. Event yield uncertainties before CH subtraction: target 01 Pb (W)

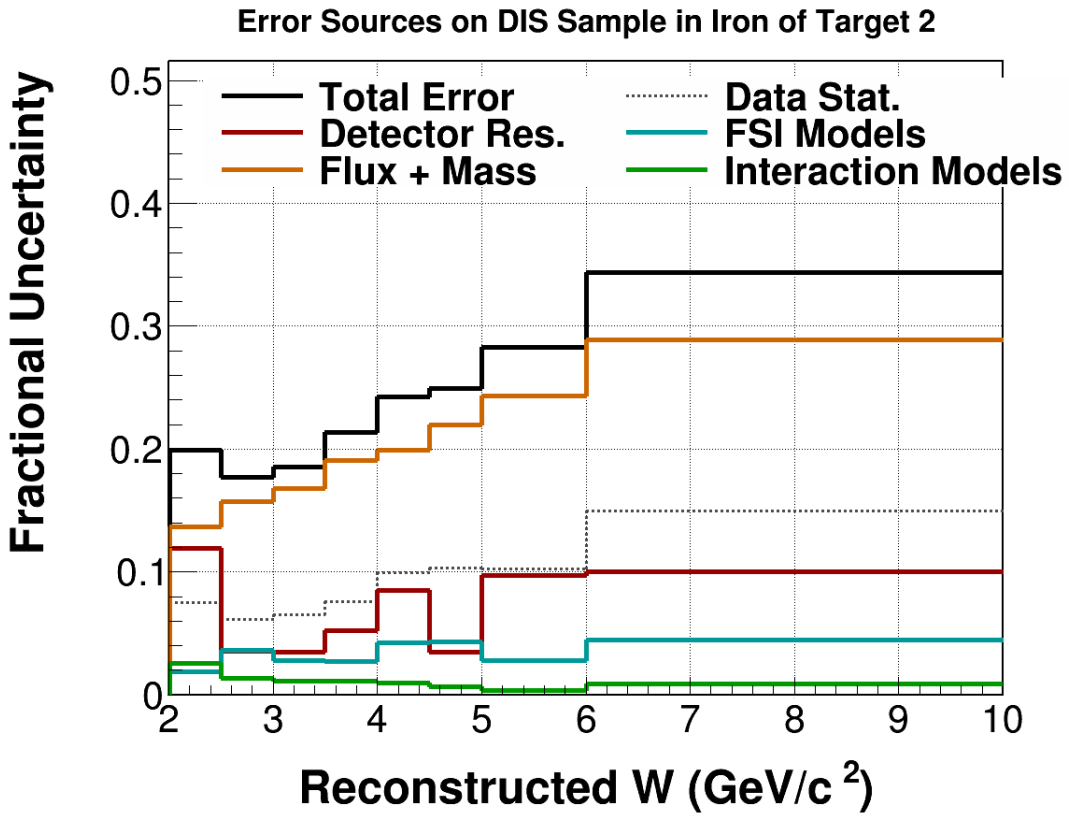

Figure E-174. Event yield uncertainties before CH subtraction: target 02 Fe (W)

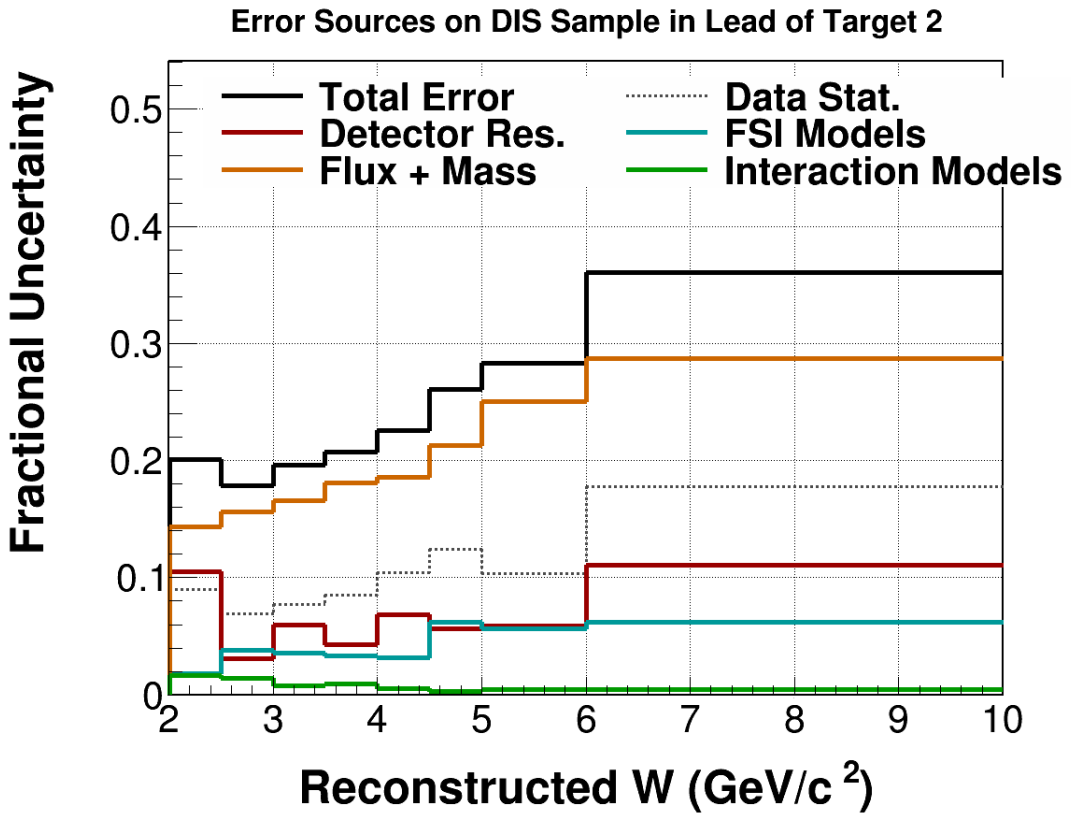

Figure E-175. Event yield uncertainties before CH subtraction: target 02 Pb (W)

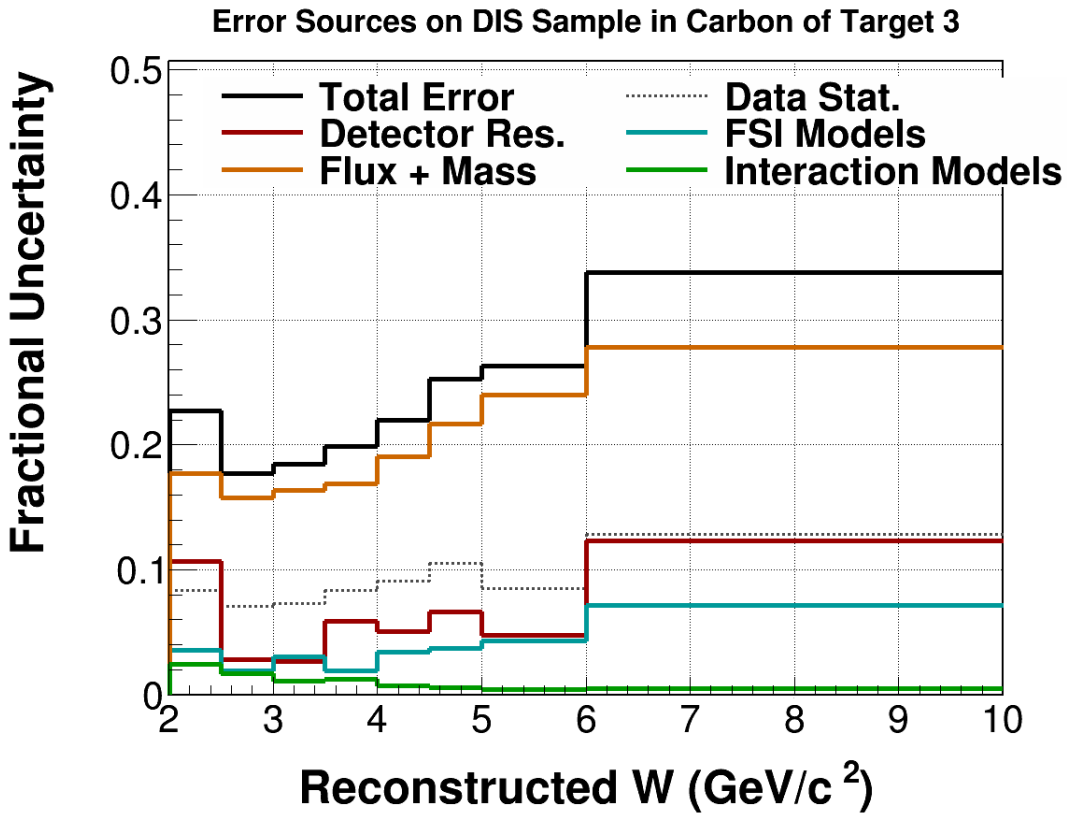

Figure E-176. Event yield uncertainties before CH subtraction: target 03 C (W)

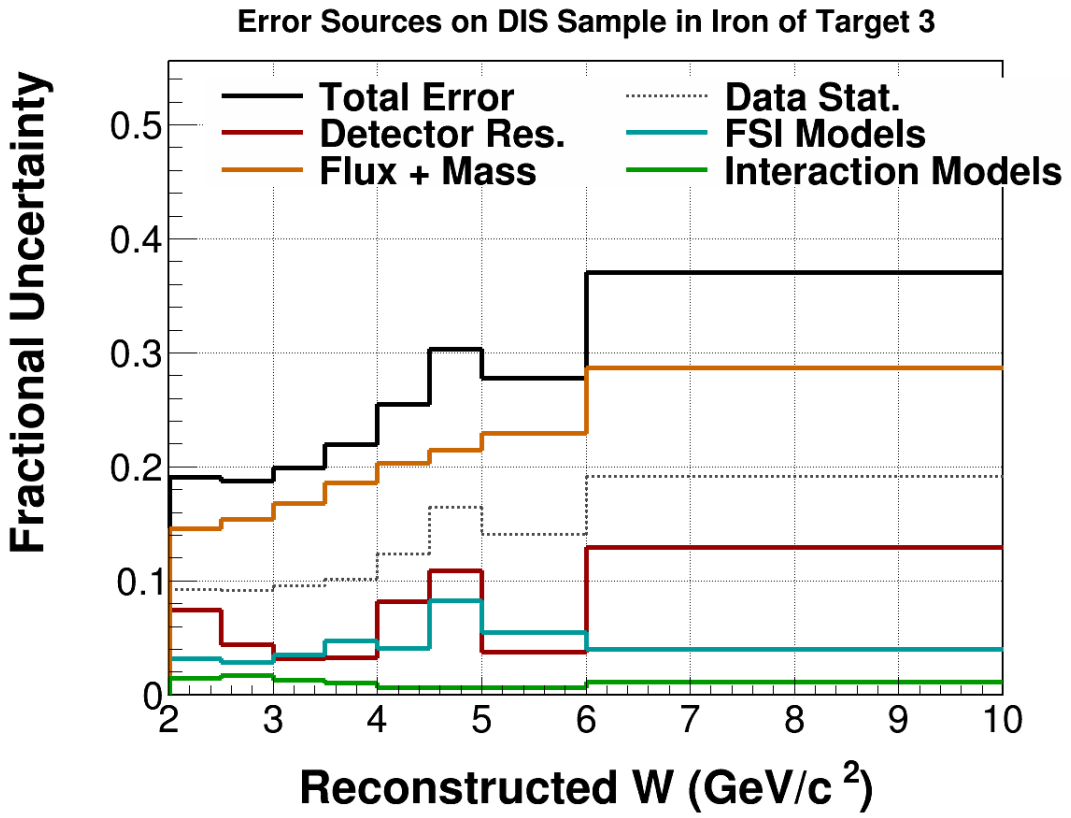

Figure E-177. Event yield uncertainties before CH subtraction: target 03 Fe (W)

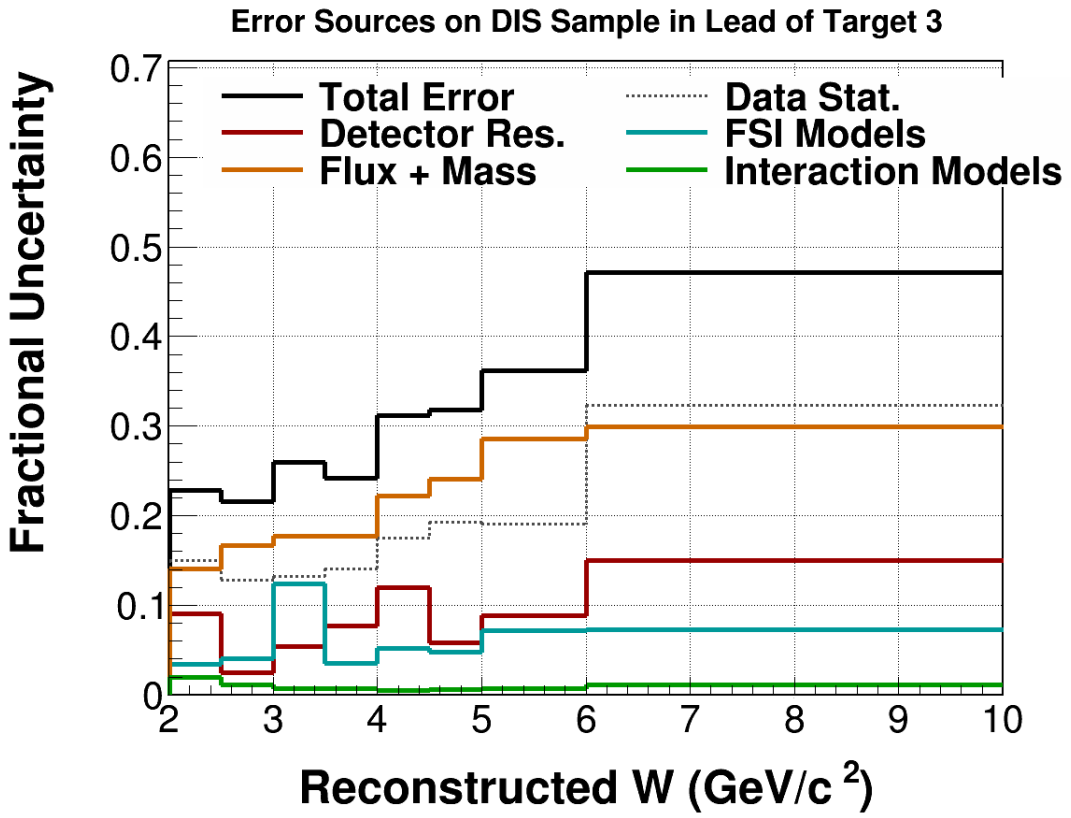

Figure E-178. Event yield uncertainties before CH subtraction: target 03 Pb (W)

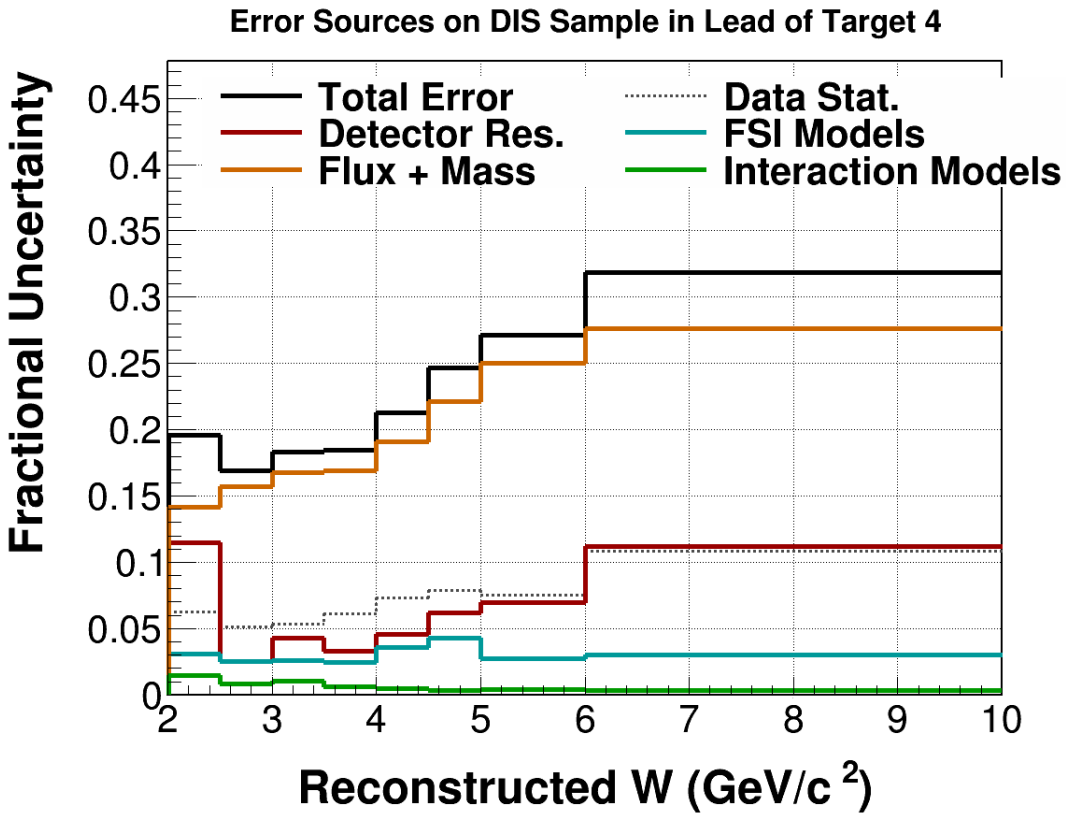

Figure E-179. Event yield uncertainties before CH subtraction: target 04 Pb (W)

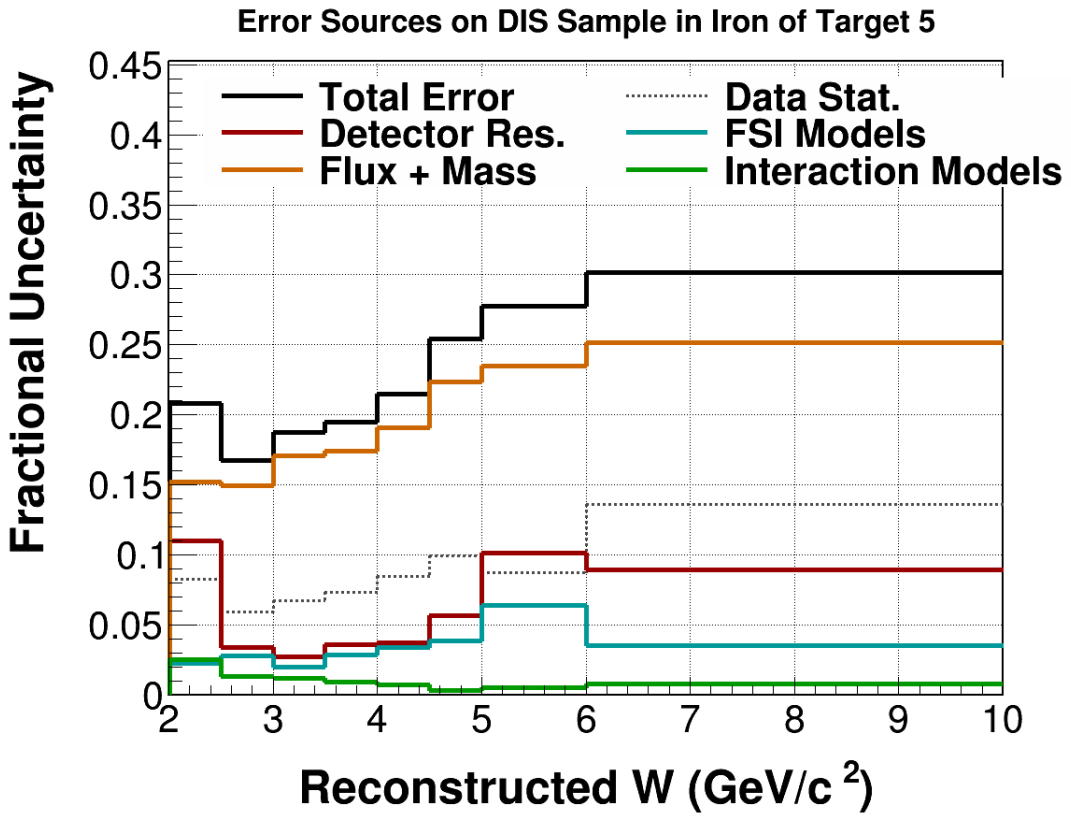

Figure E-180. Event yield uncertainties before CH subtraction: target 05 Fe (W)

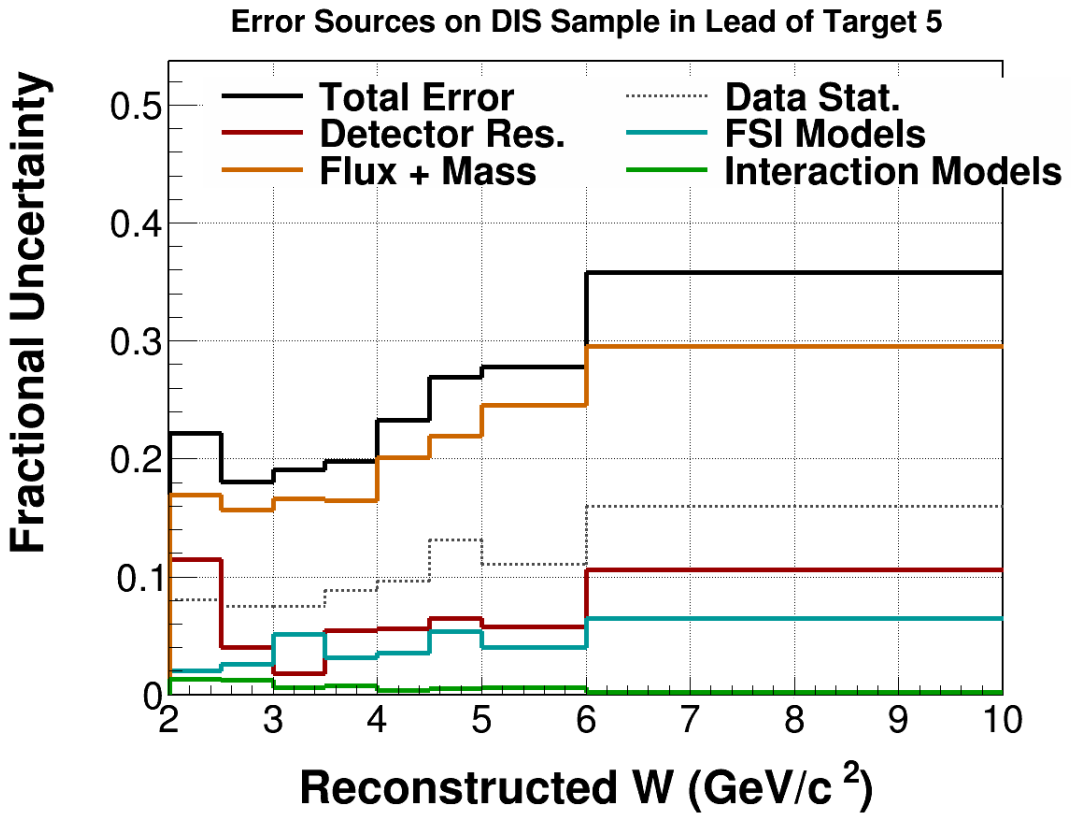

Figure E-181. Event yield uncertainties before CH subtraction: target 05 Pb (W)

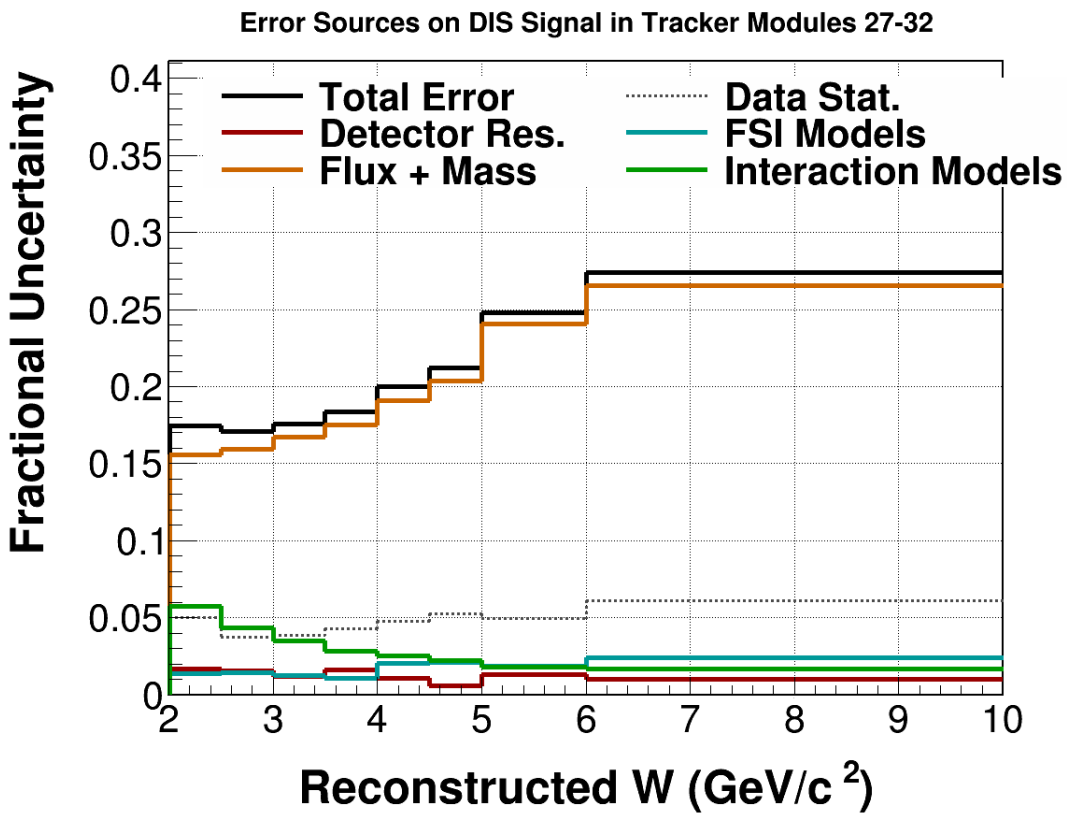

Figure E-182. Event yield uncertainties: tracker mods. 27-32 (W)

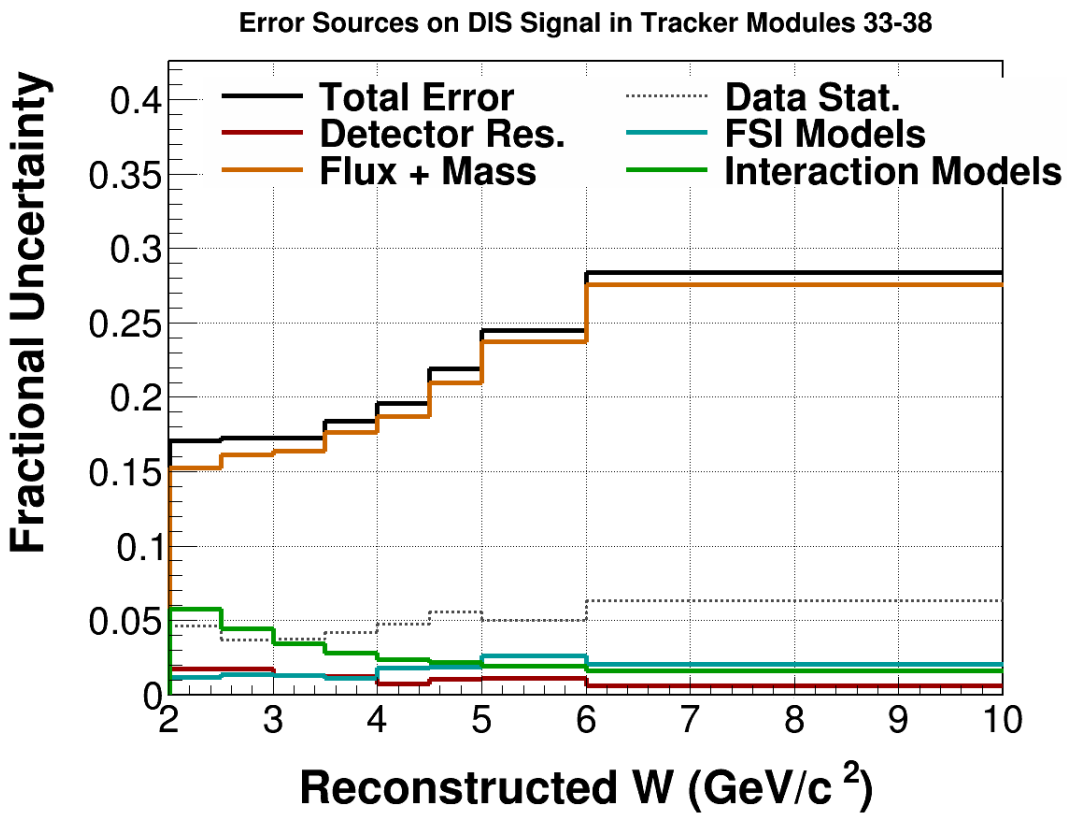

Figure E-183. Event yield uncertainties: tracker mods. 33-38 (W)

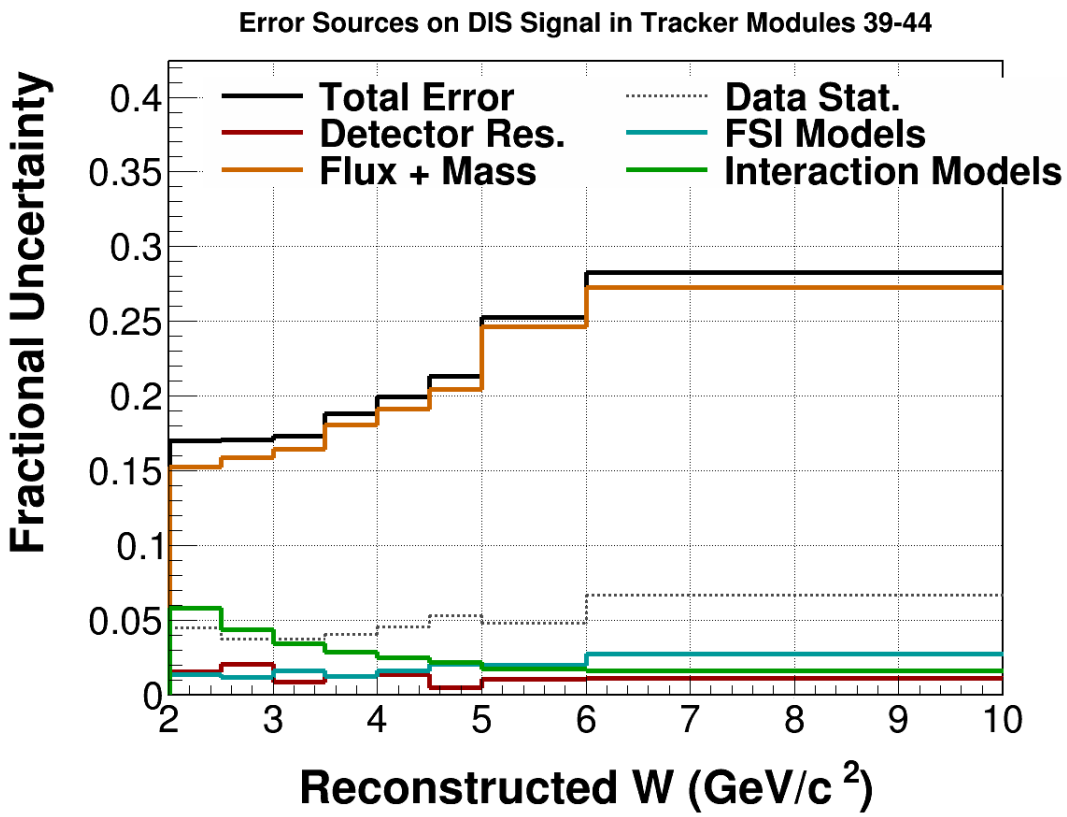

Figure E-184. Event yield uncertainties: tracker mods. 39-44 (W)

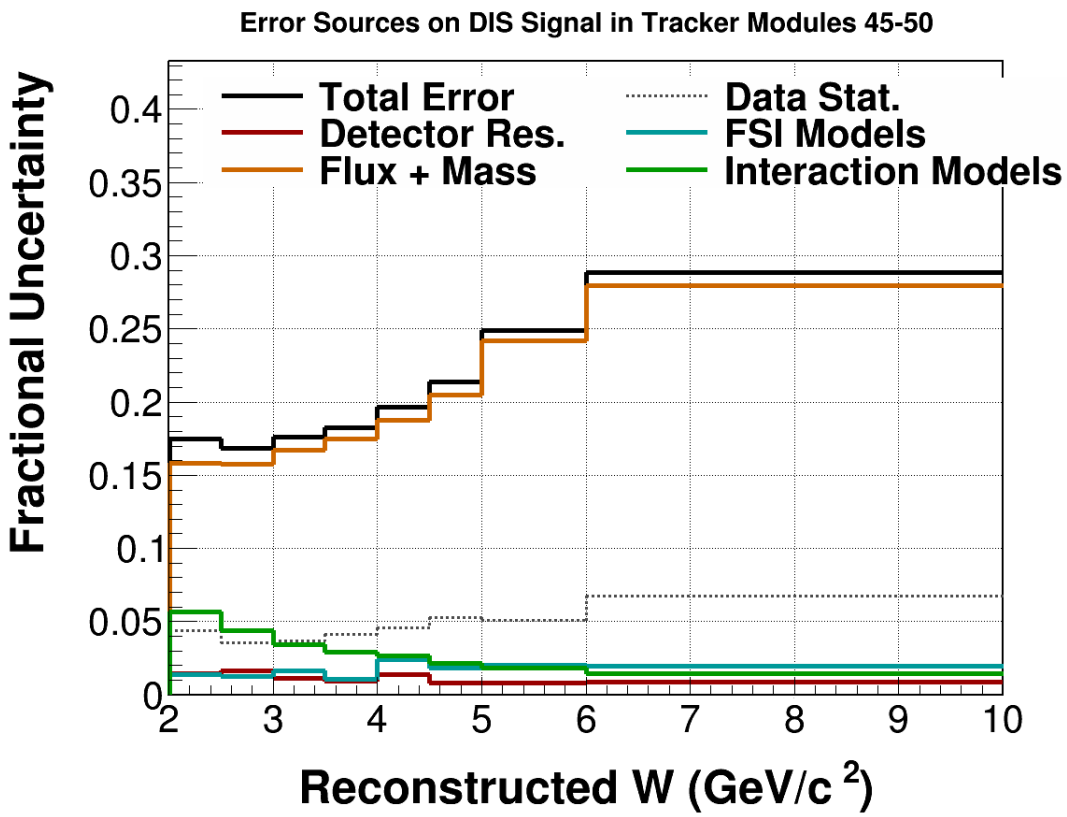

Figure E-185. Event yield uncertainties: tracker mods. 45-50 (W)

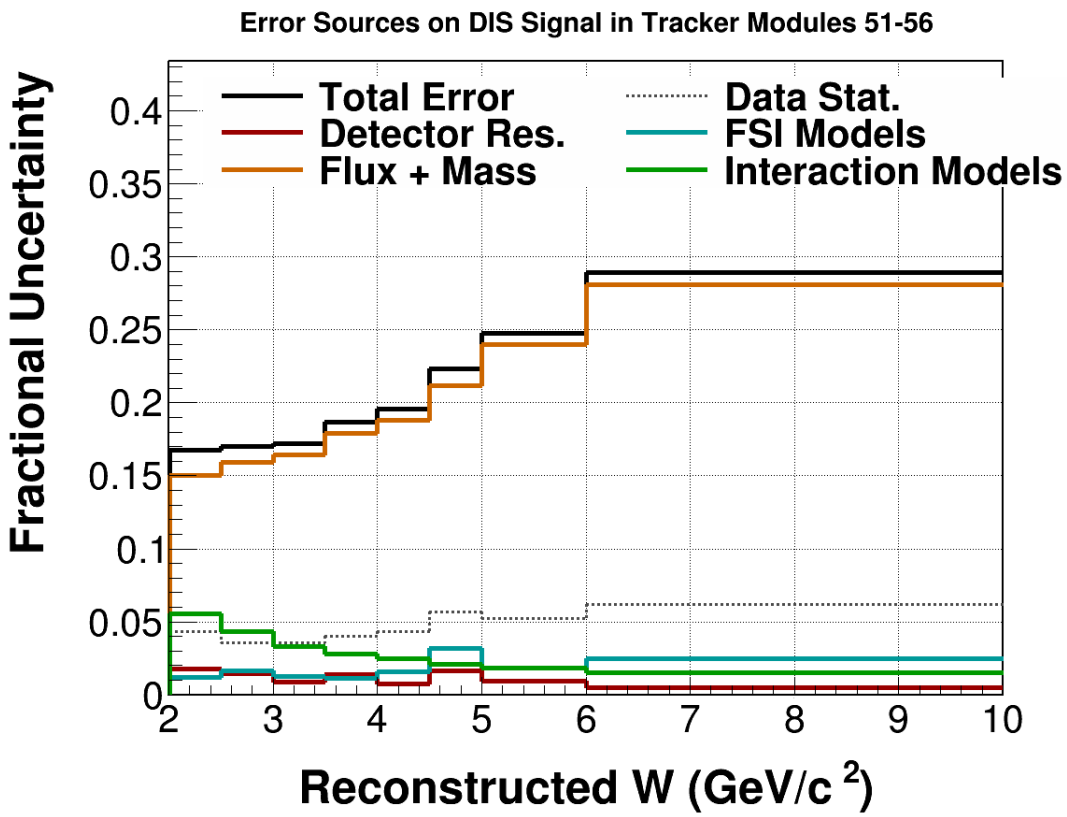

Figure E-186. Event yield uncertainties: tracker mods. 51-56 (W)

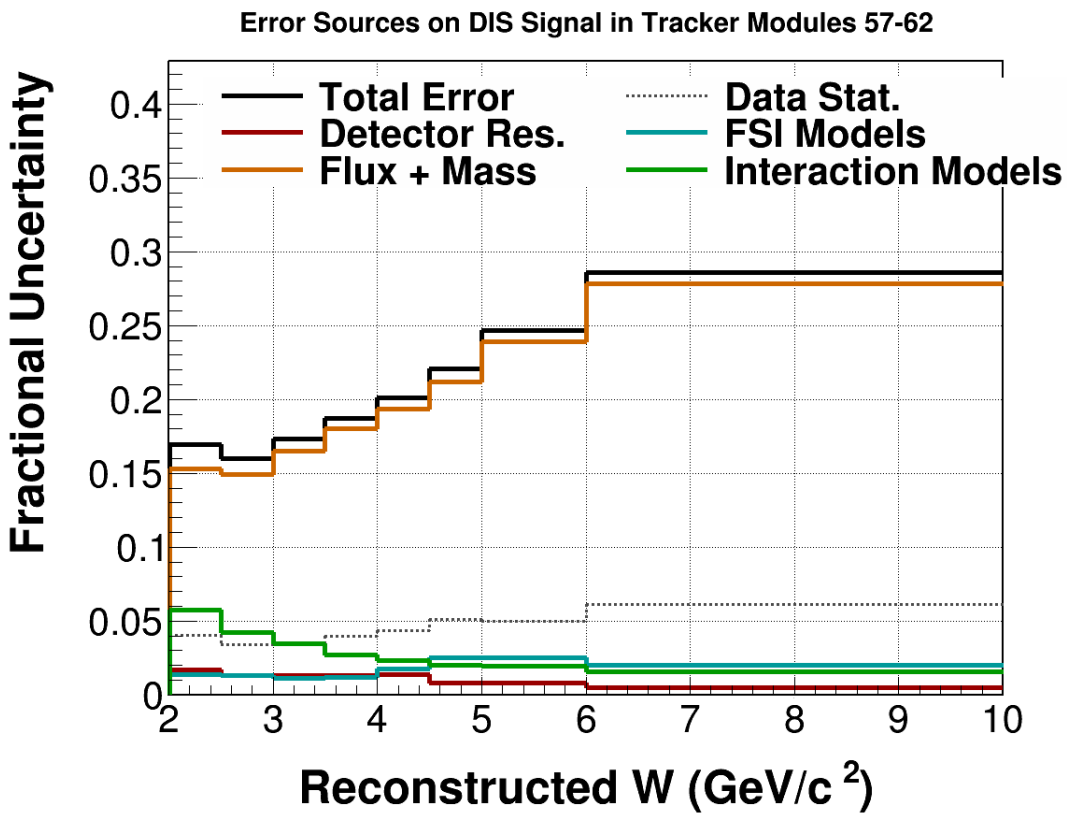

Figure E-187. Event yield uncertainties: tracker mods. 57-62 (W)

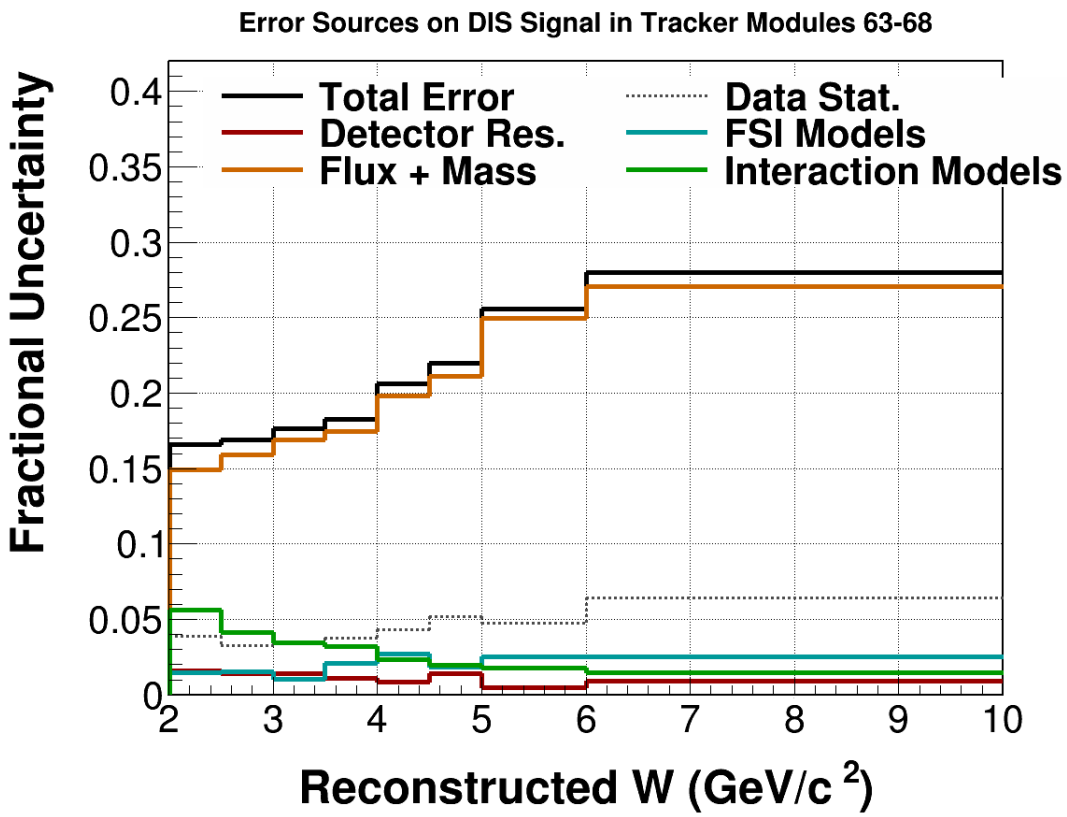

Figure E-188. Event yield uncertainties: tracker mods. 63-68 (W)

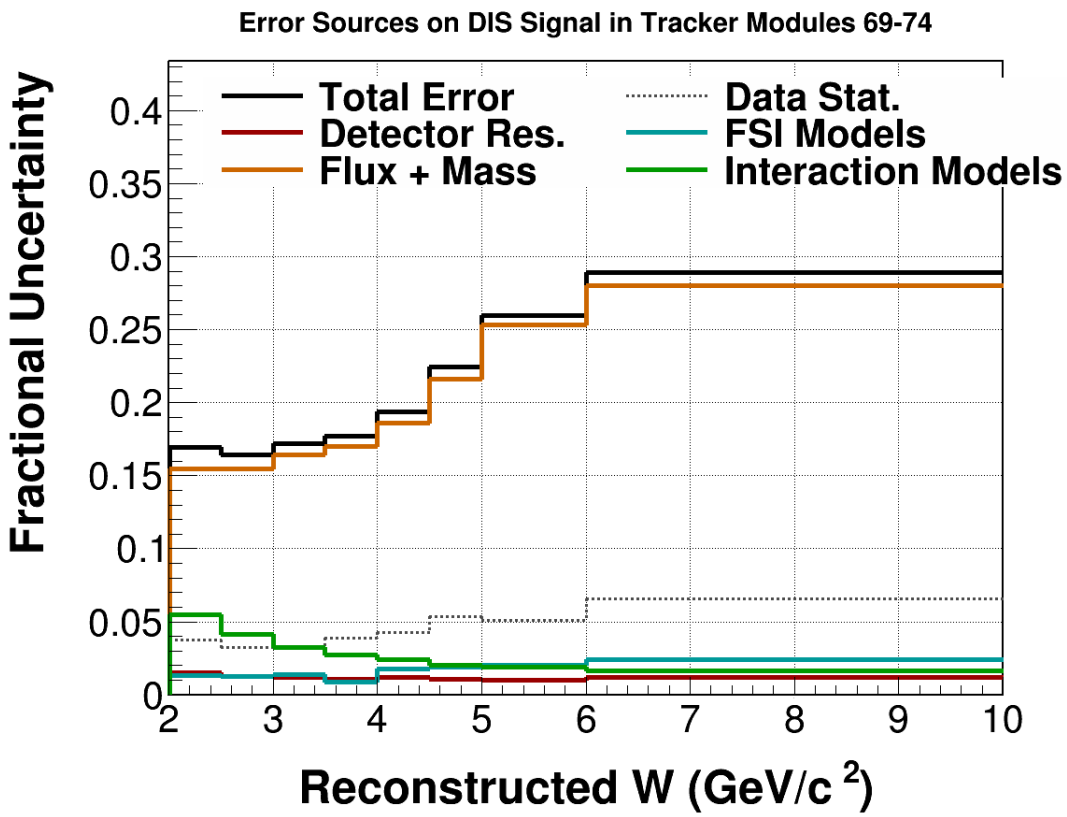

Figure E-189. Event yield uncertainties: tracker mods. 69-74 (W)

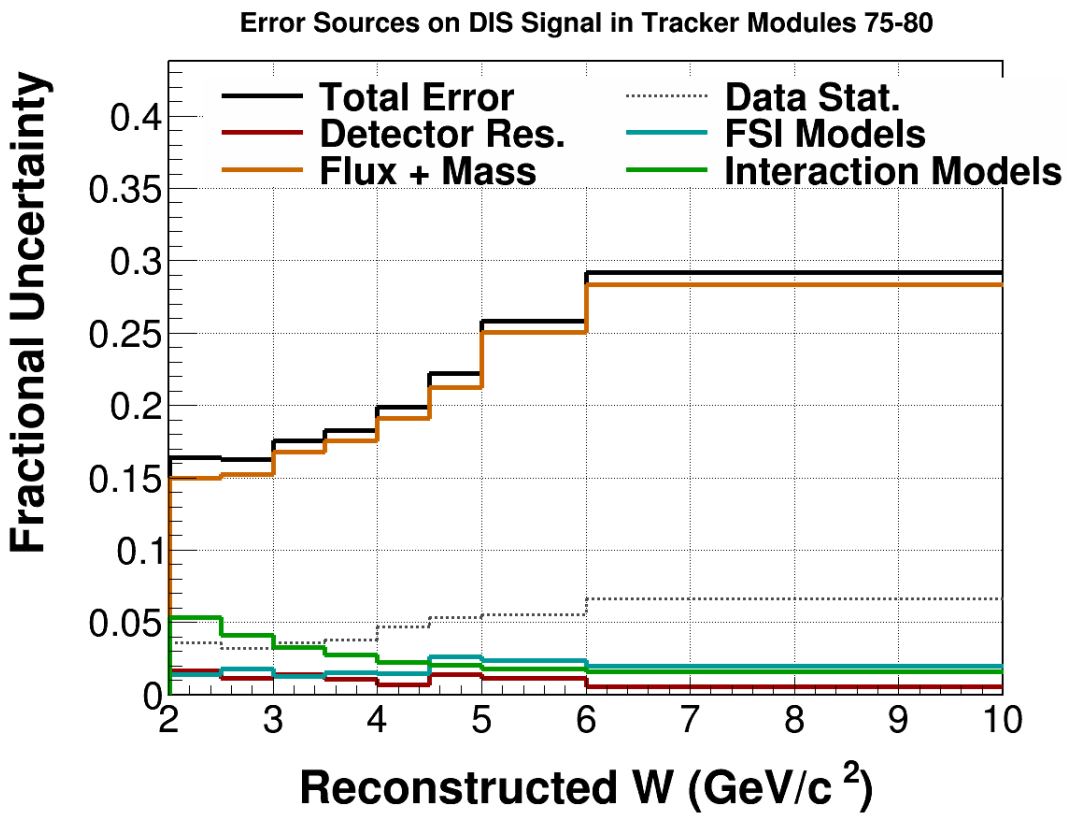

Figure E-190. Event yield uncertainties: tracker mods. 75-80 (W)

The following plots show the uncertainty on the number of DIS events, after subtracting the non-DIS events. They are plotted as a function of Bjorken-x (x_{bj}):

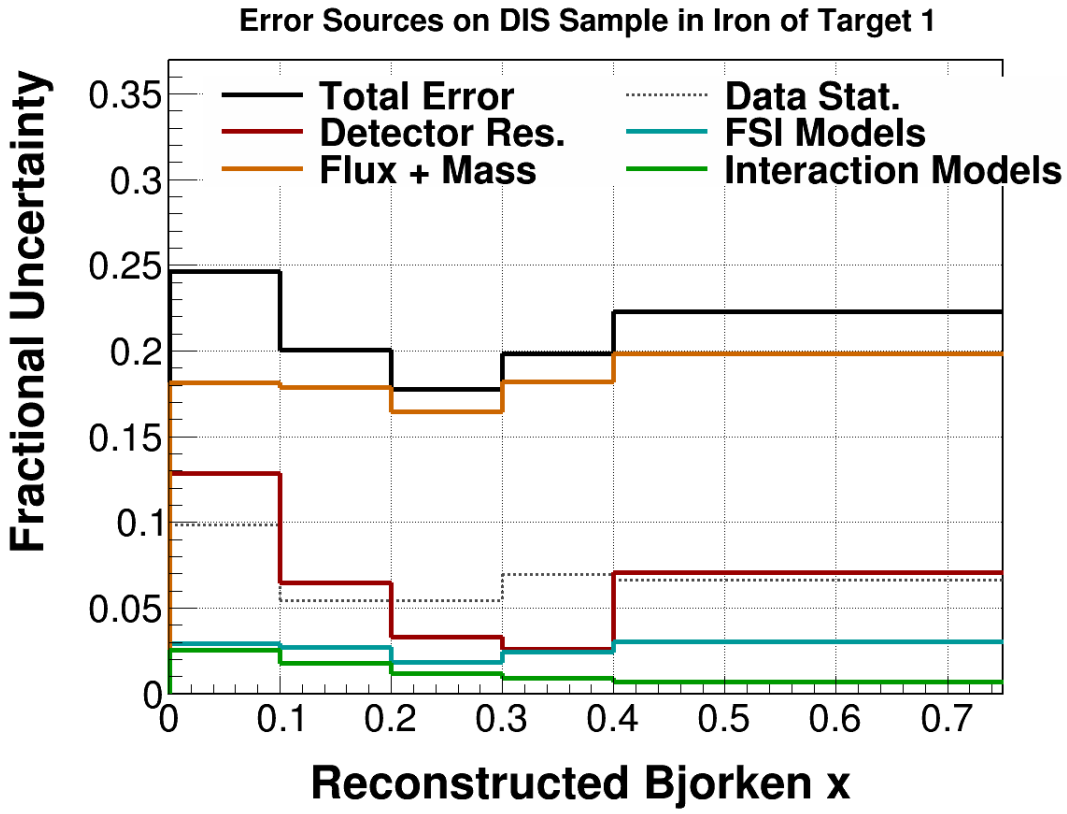

Figure E-191. Event yield uncertainties before CH subtraction: target 01 Fe (x_{bj})

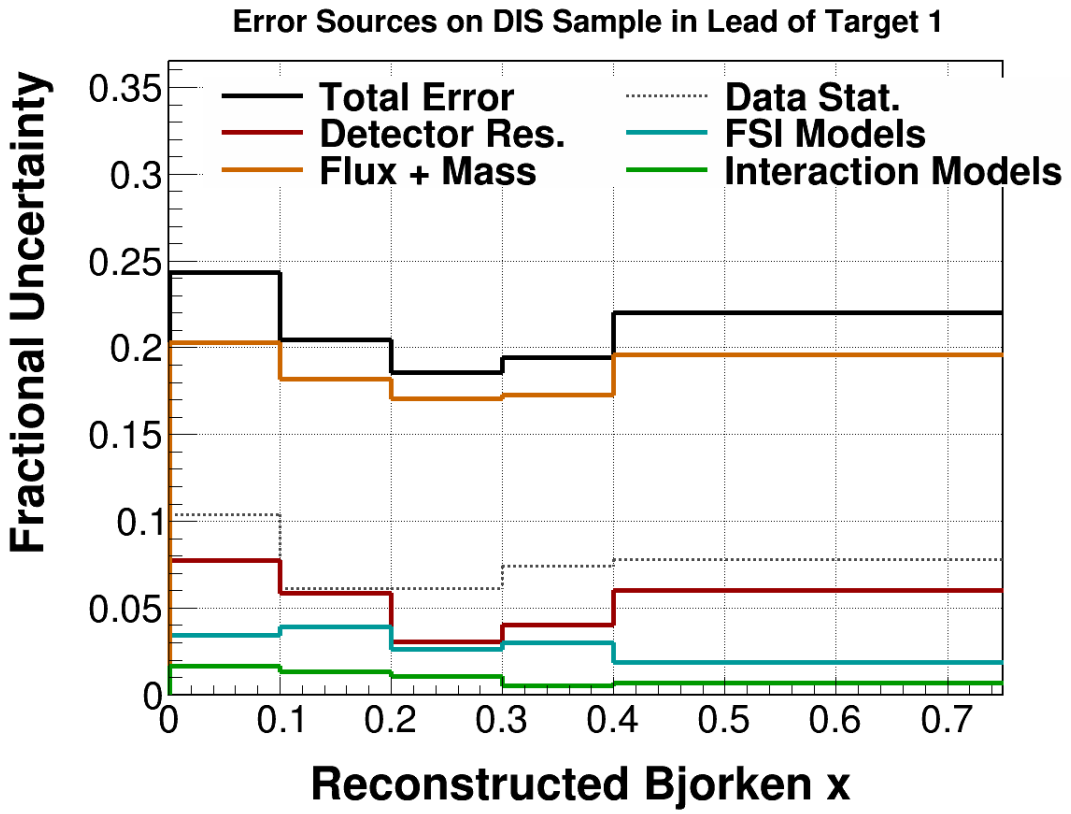

Figure E-192. Event yield uncertainties before CH subtraction: target 01 Pb (x_{bj})

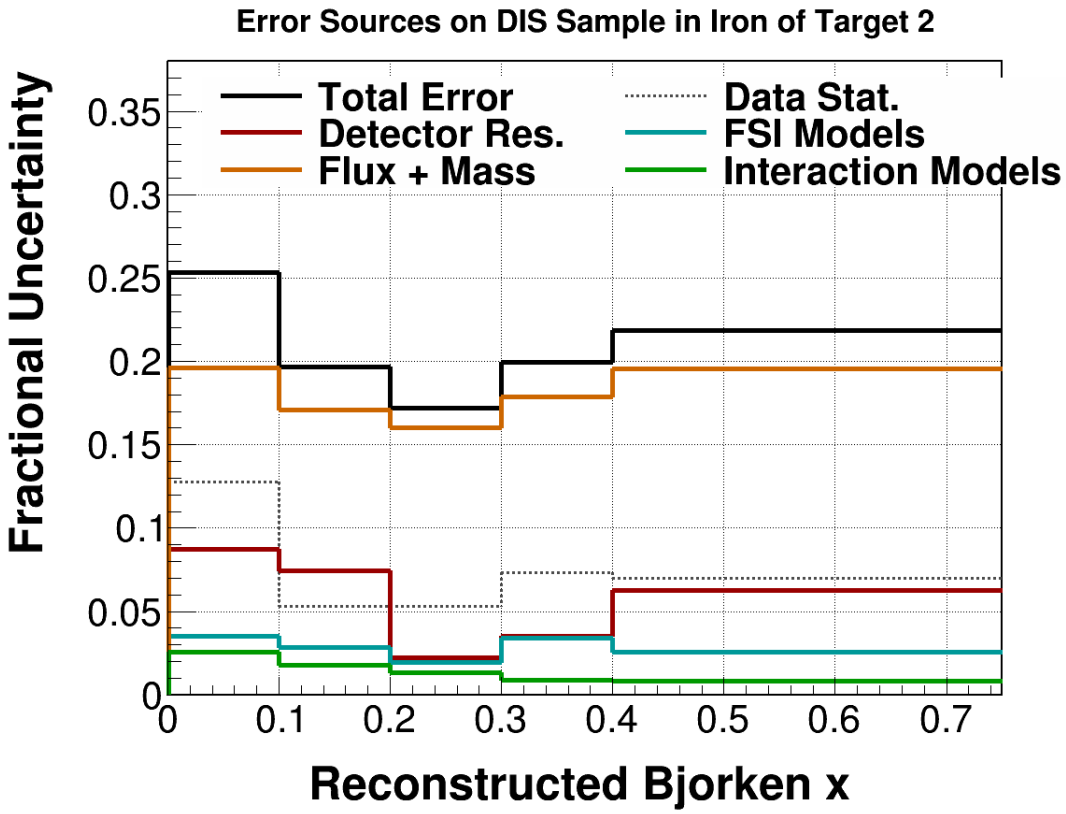

Figure E-193. Event yield uncertainties before CH subtraction: target 02 Fe (x_{bj})

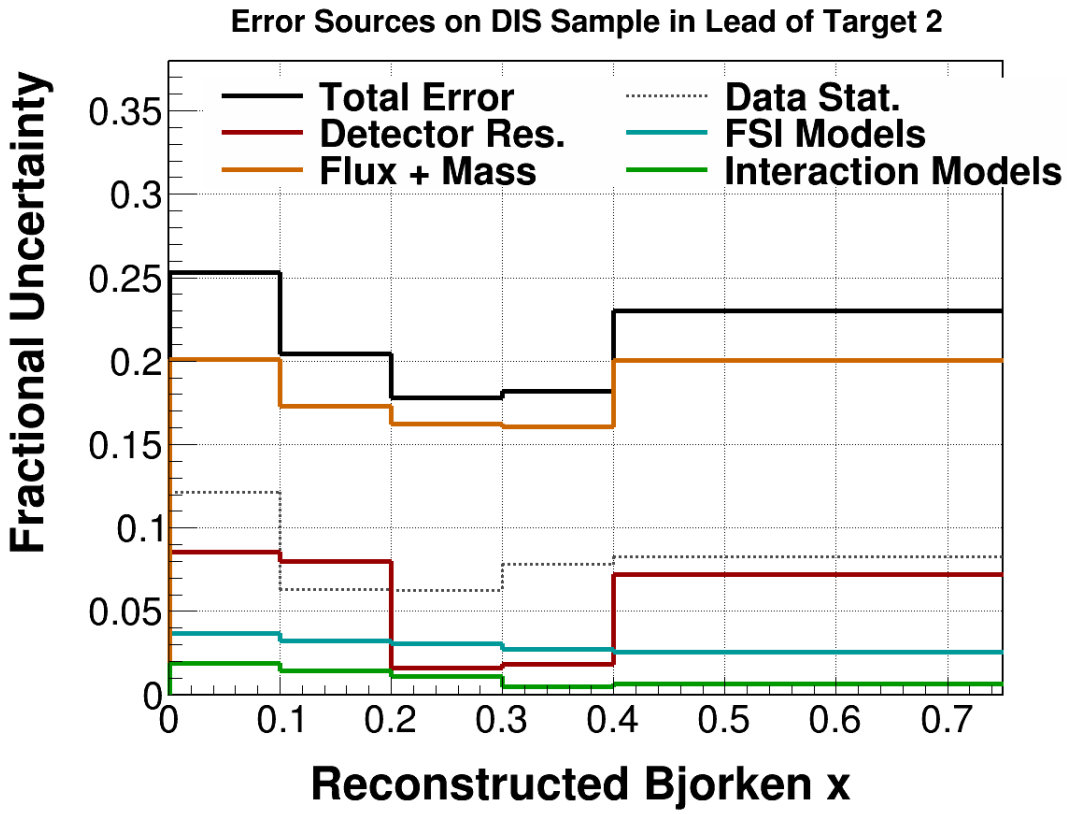

Figure E-194. Event yield uncertainties before CH subtraction: target 02 Pb (x_{bj})

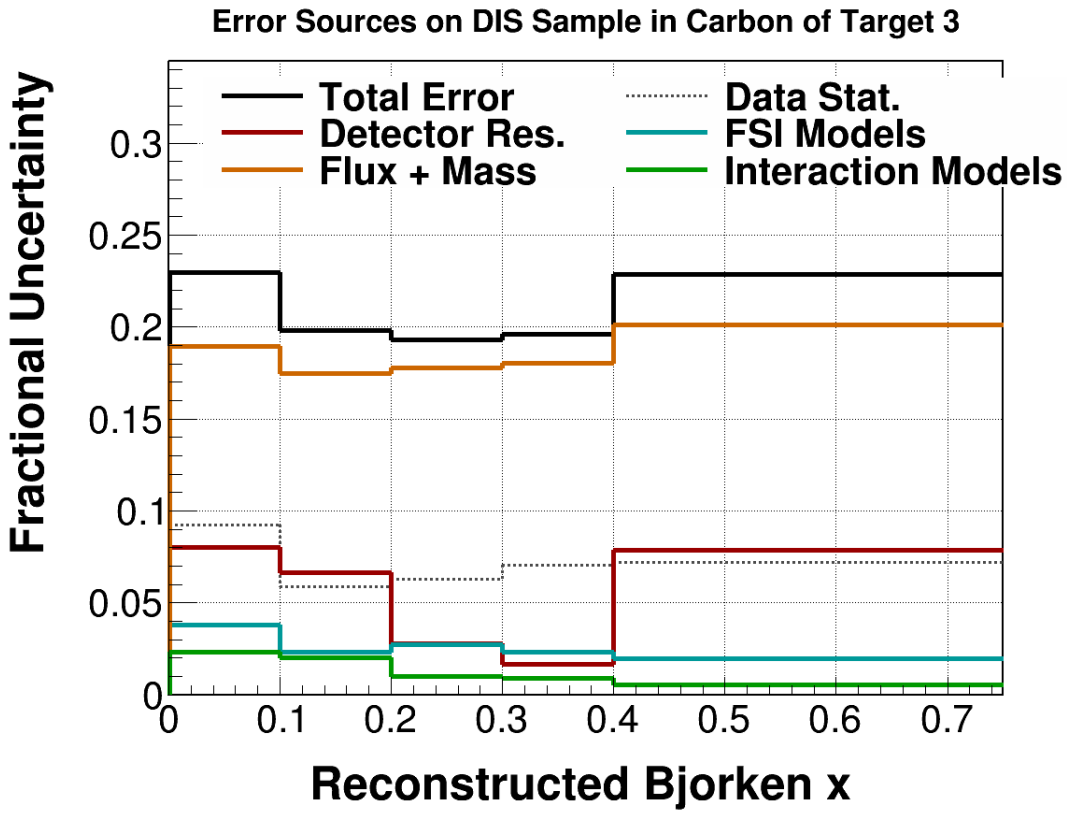

Figure E-195. Event yield uncertainties before CH subtraction: target 03 C (x_{bj})

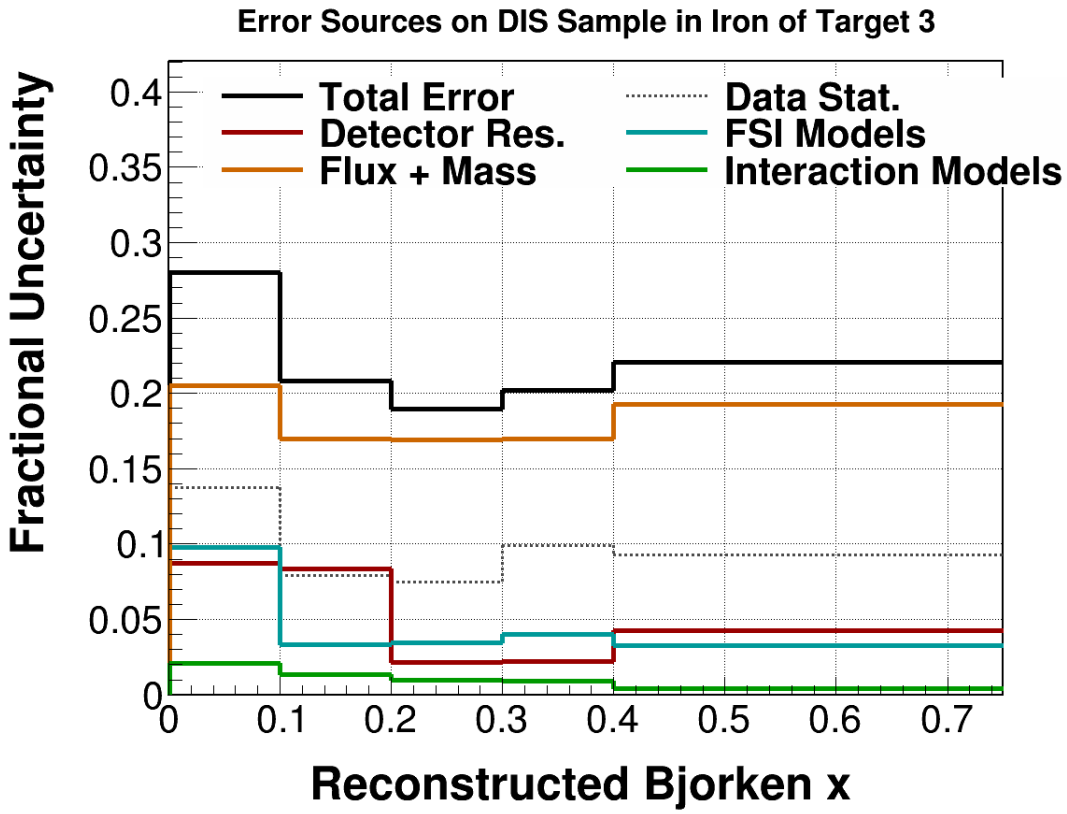

Figure E-196. Event yield uncertainties before CH subtraction: target 03 Fe (x_{bj})

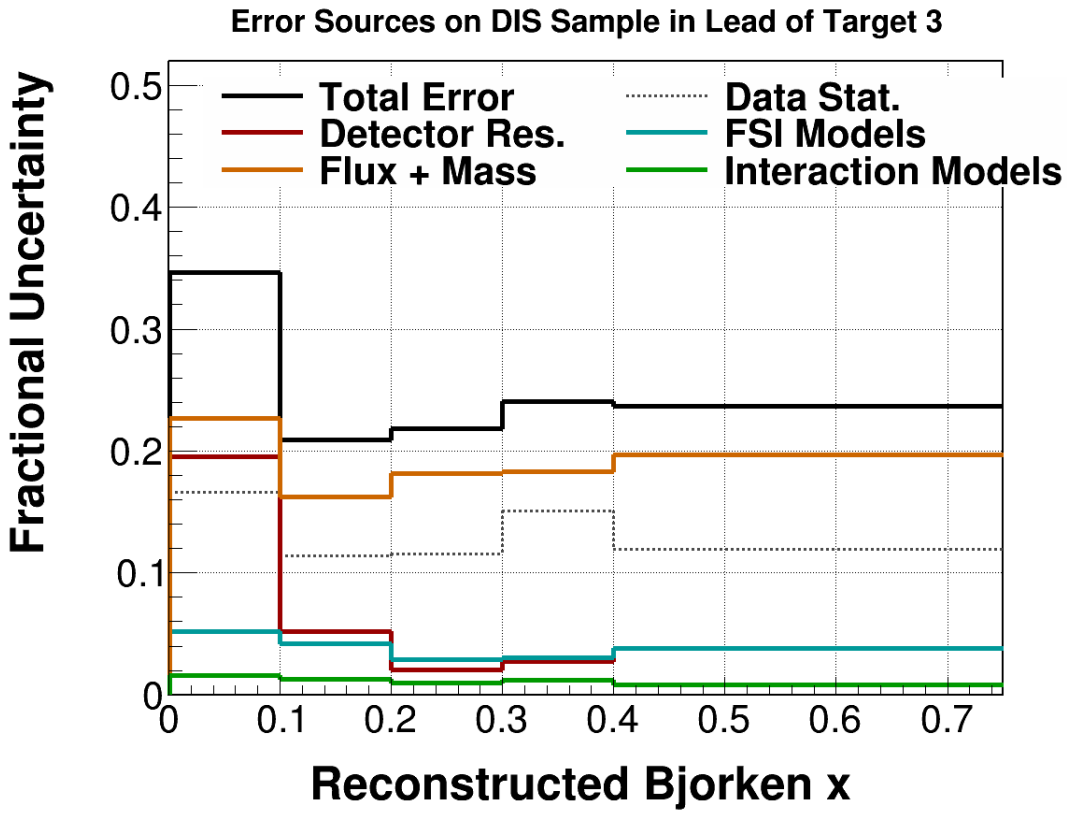

Figure E-197. Event yield uncertainties before CH subtraction: target 03 Pb (x_{bj})

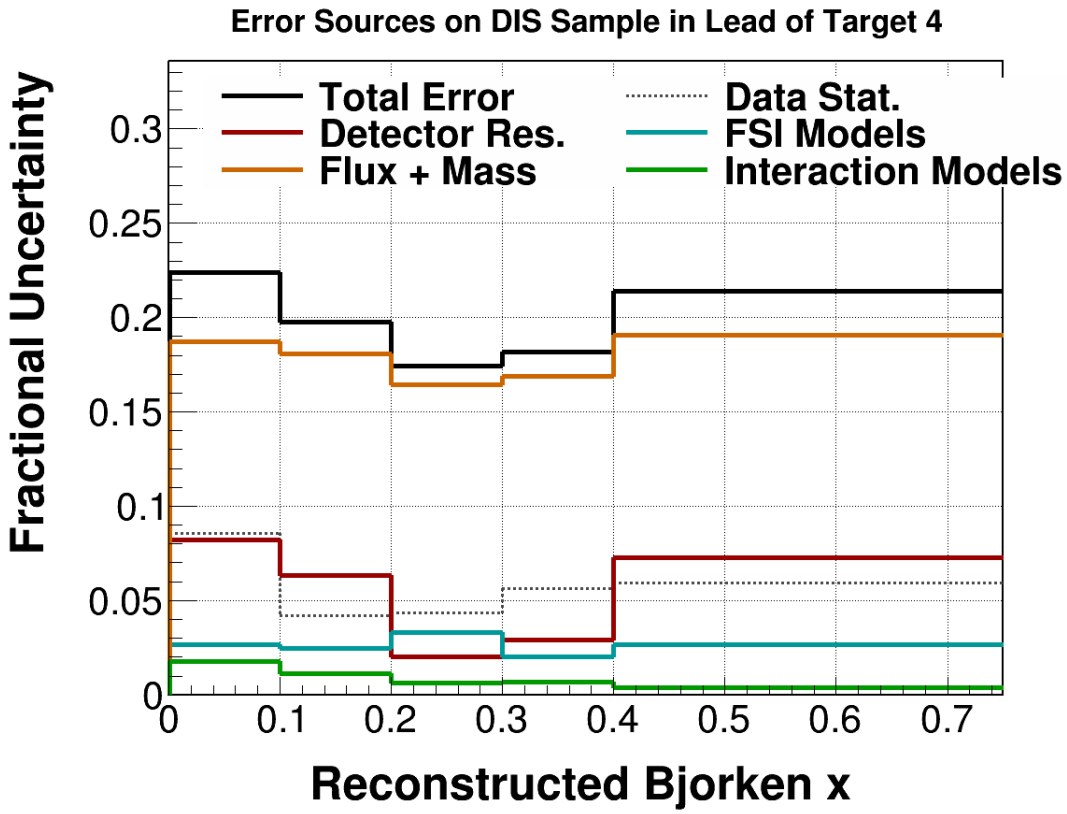

Figure E-198. Event yield uncertainties before CH subtraction: target 04 Pb (x_{bj})

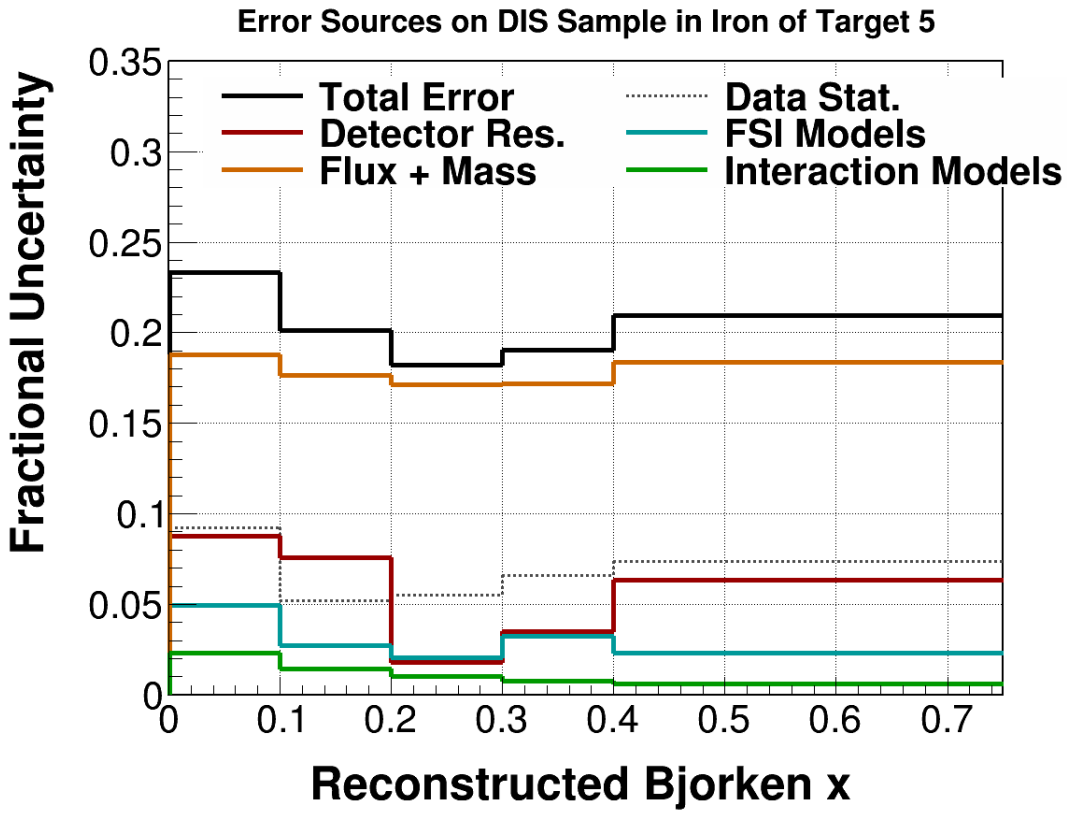

Figure E-199. Event yield uncertainties before CH subtraction: target 05 Fe (x_{bj})

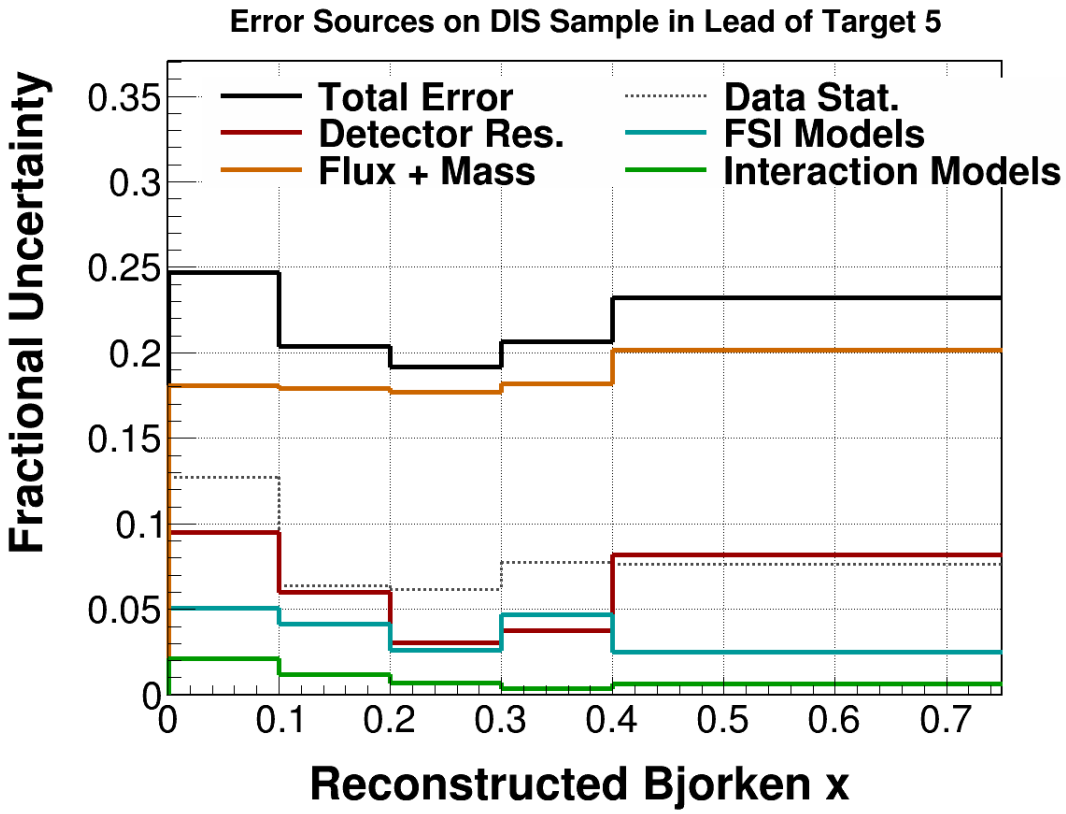

Figure E-200. Event yield uncertainties before CH subtraction: target 05 Pb (x_{bj})

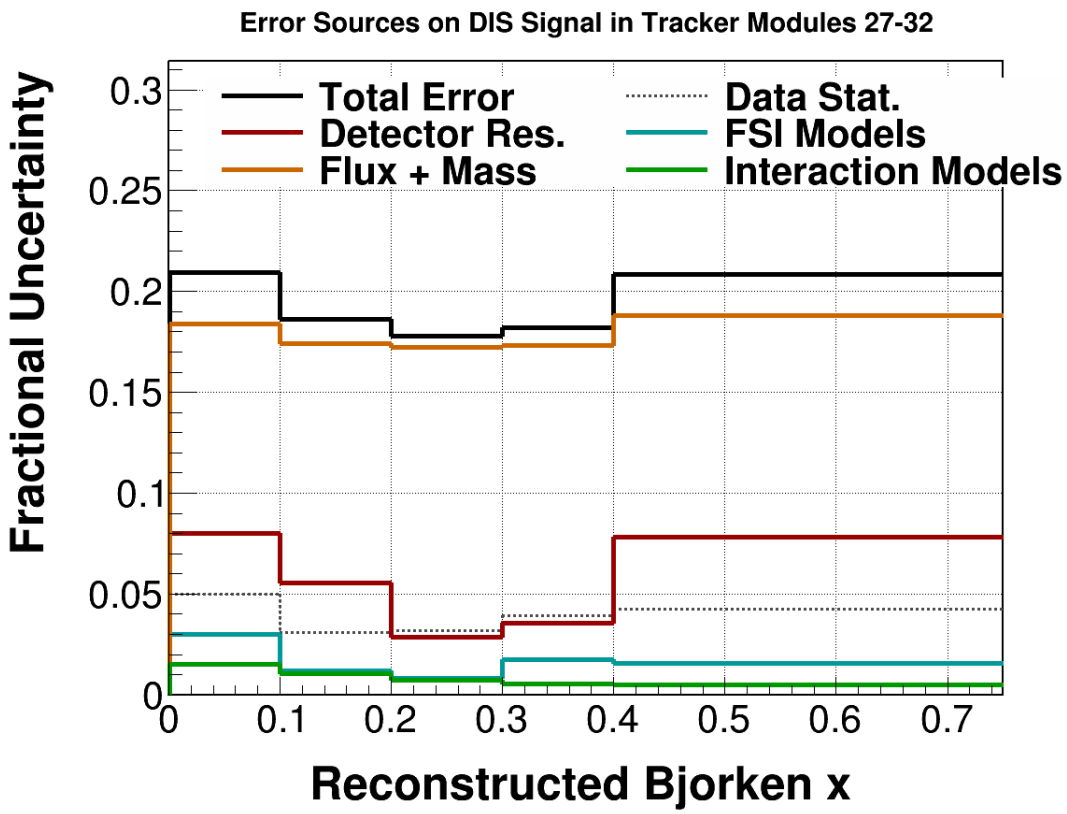

Figure E-201. Event yield uncertainties: tracker mods. 27-32 (x)

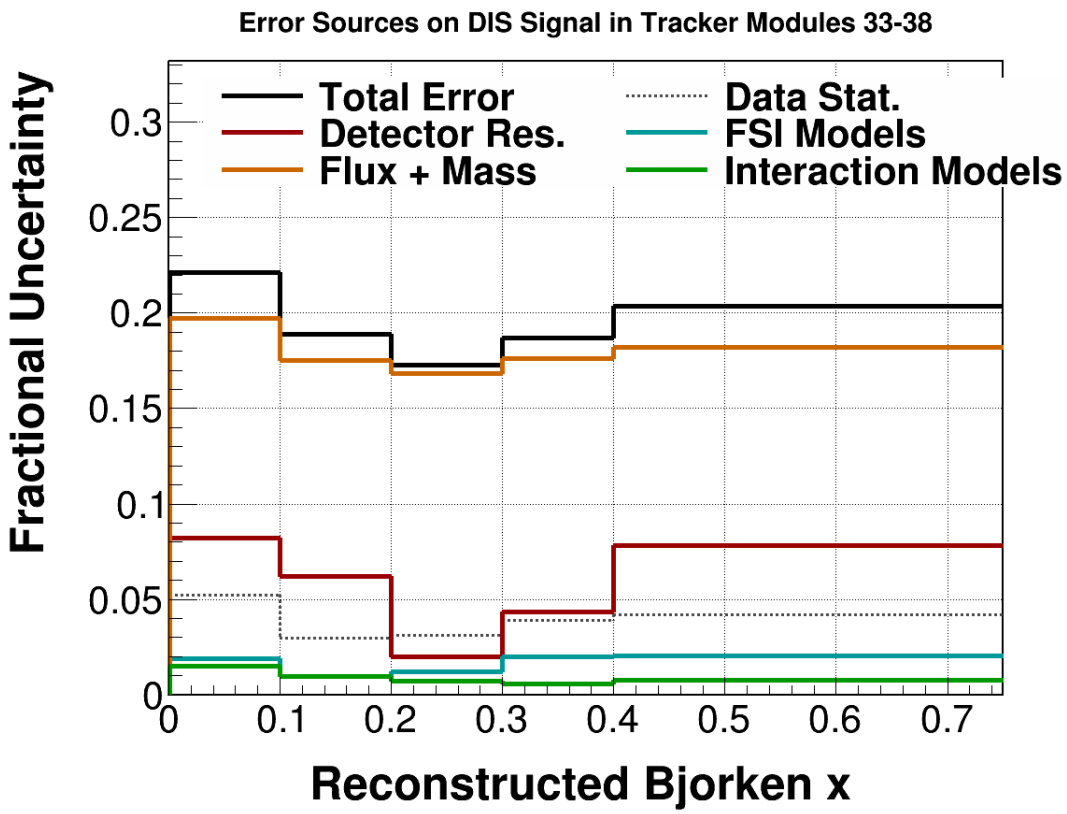

Figure E-202. Event yield uncertainties: tracker mods. 33-38 (x_{bj})

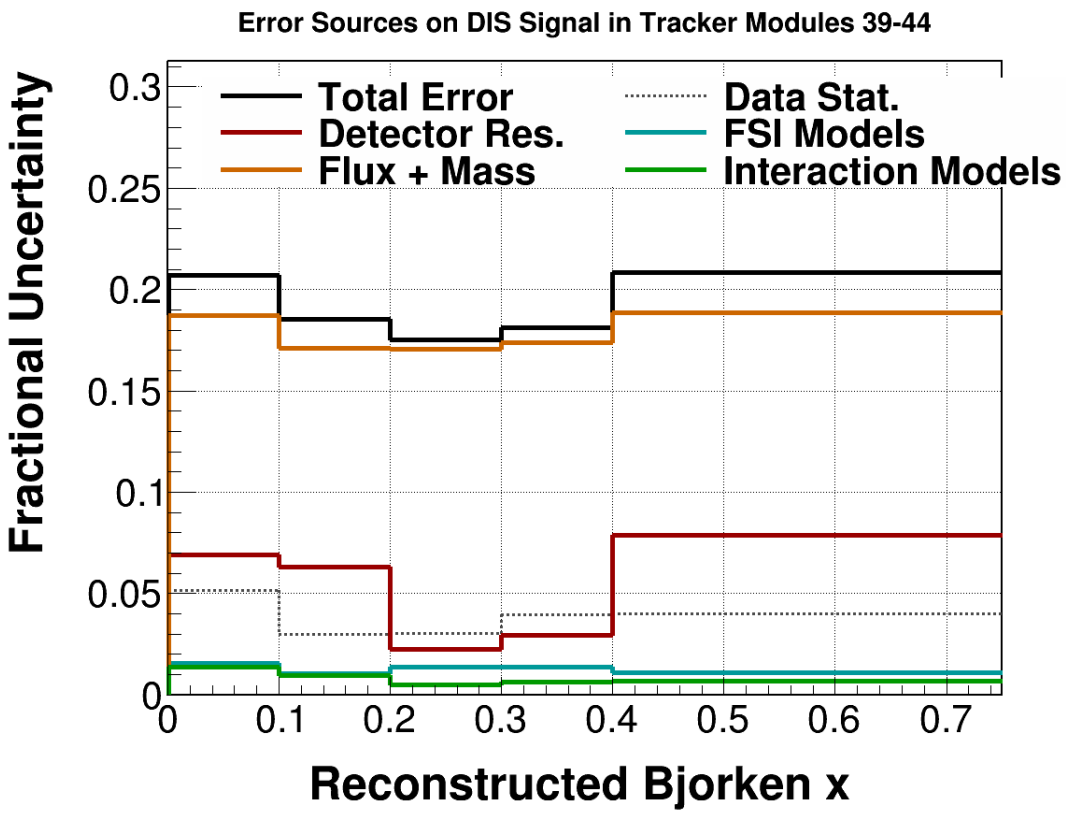

Figure E-203. Event yield uncertainties: tracker mods. 39-44 (x_{bj})

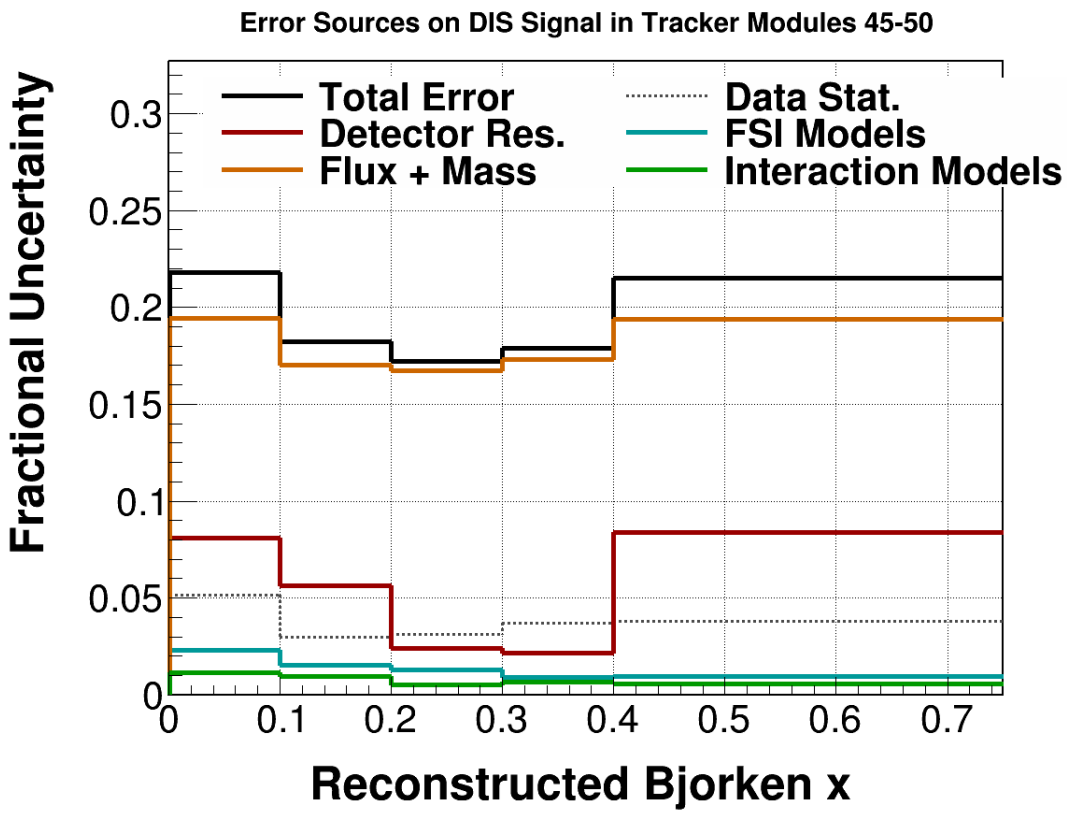

Figure E-204. Event yield uncertainties: tracker mods. 45-50 (x_{bj})

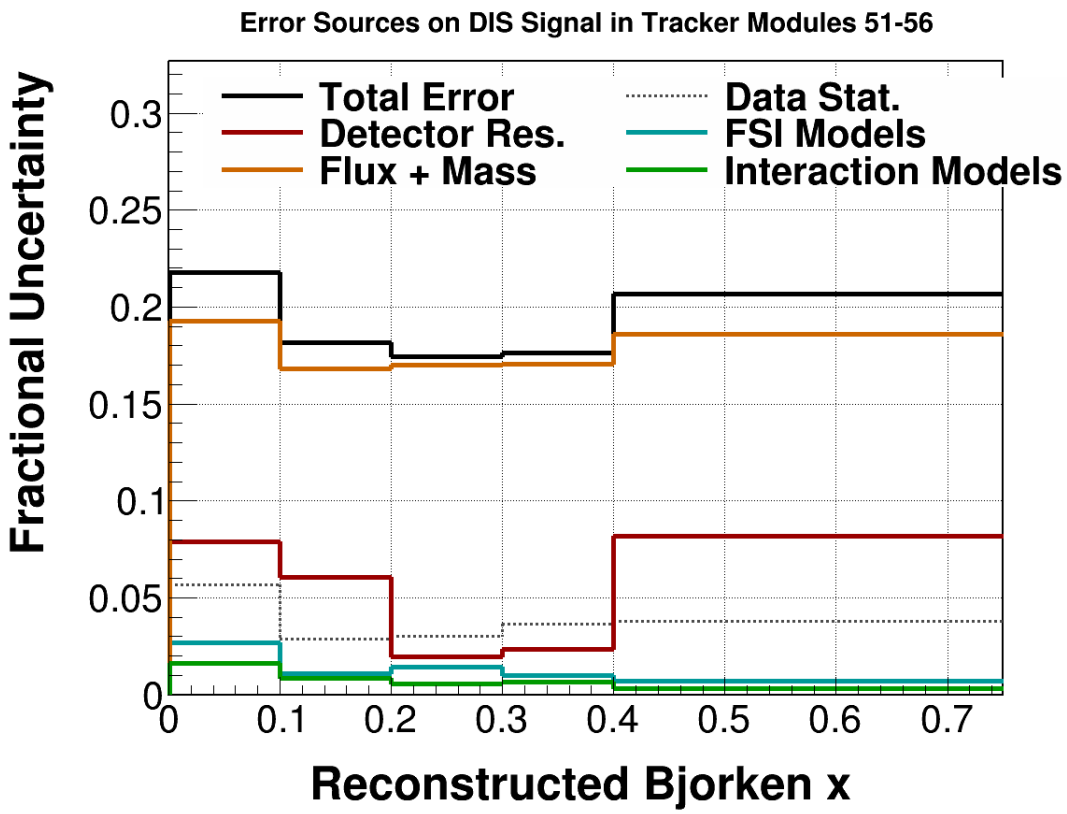

Figure E-205. Event yield uncertainties: tracker mods. 51-56 (x_{bj})

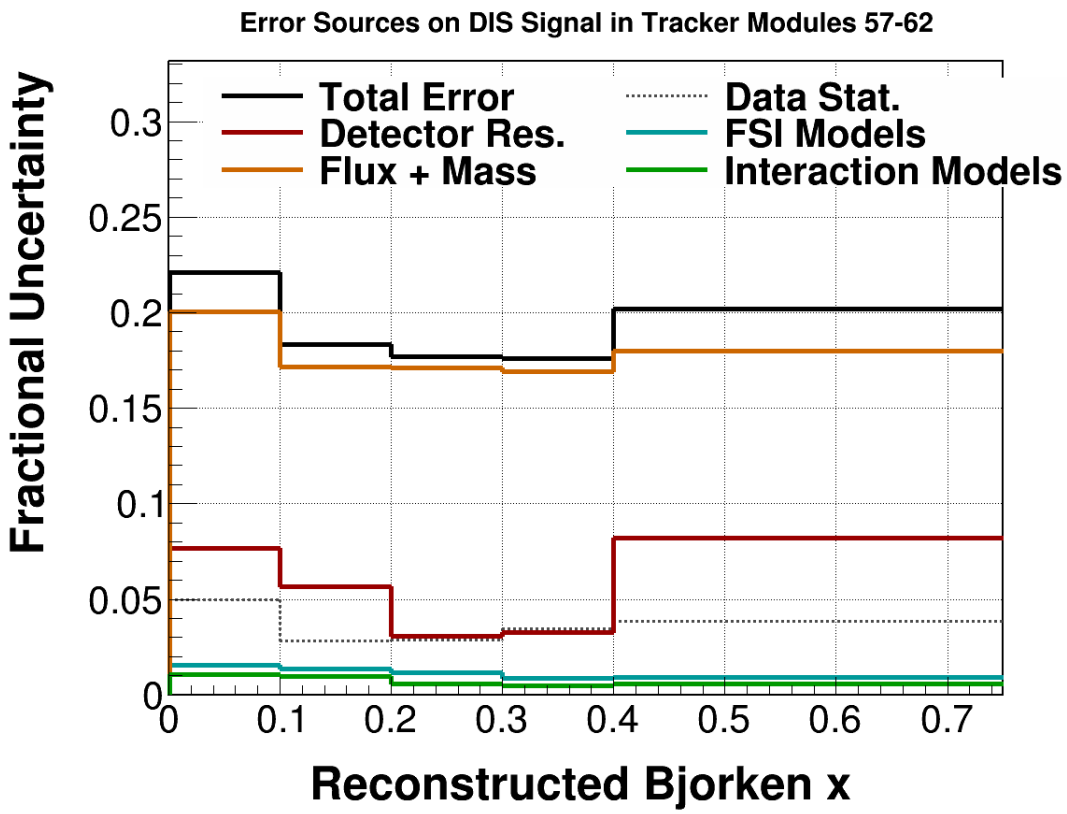

Figure E-206. Event yield uncertainties: tracker mods. 57-62 (x_{bj})

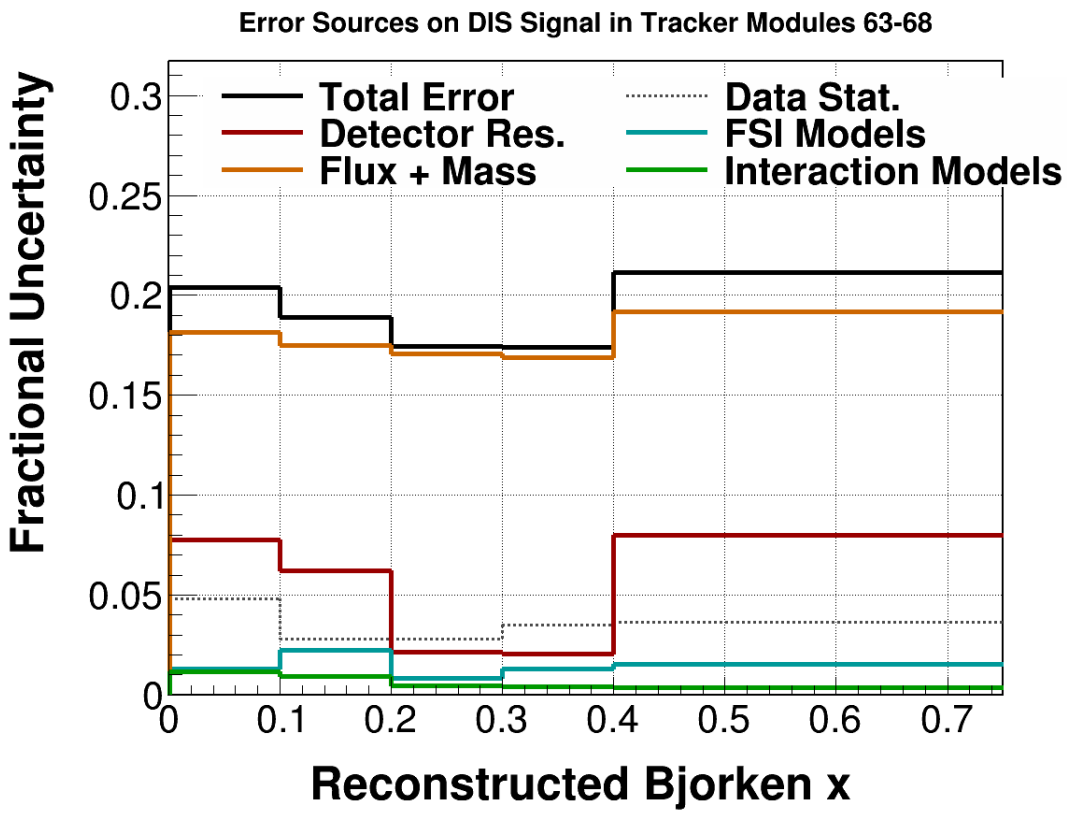

Figure E-207. Event yield uncertainties: tracker mods. 63-68 (x_{bj})

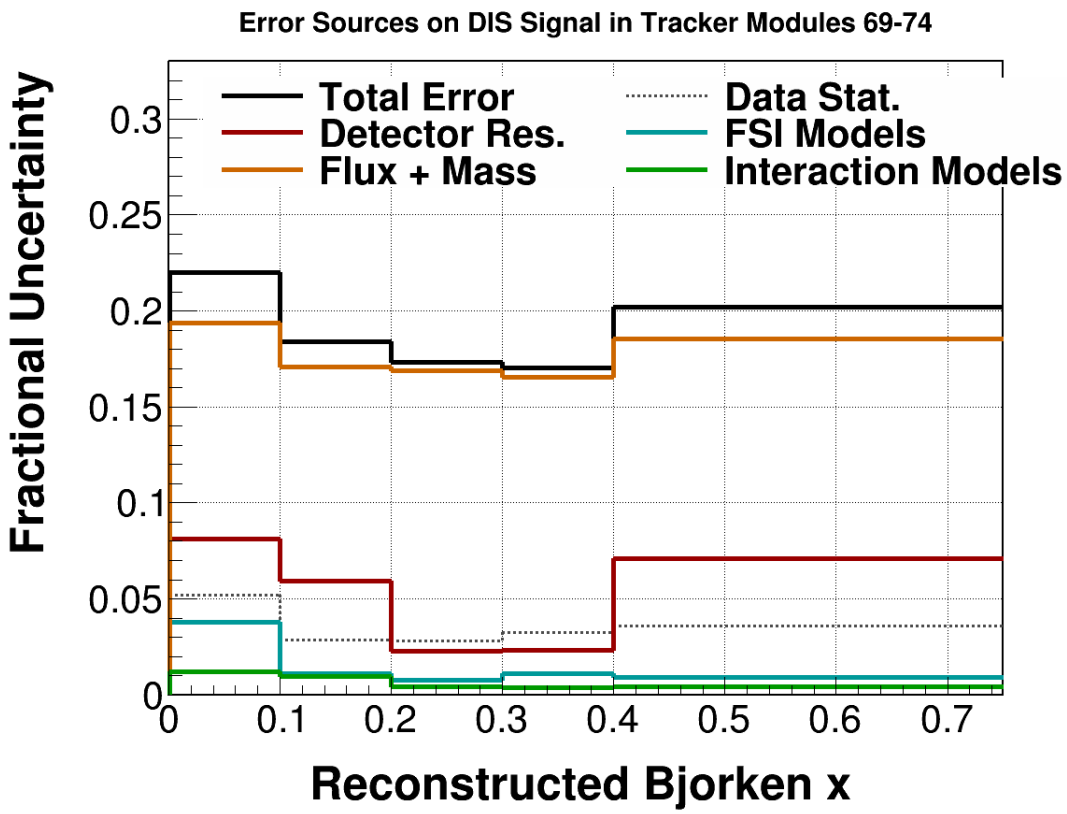

Figure E-208. Event yield uncertainties: tracker mods. 69-74 (x_{bj})

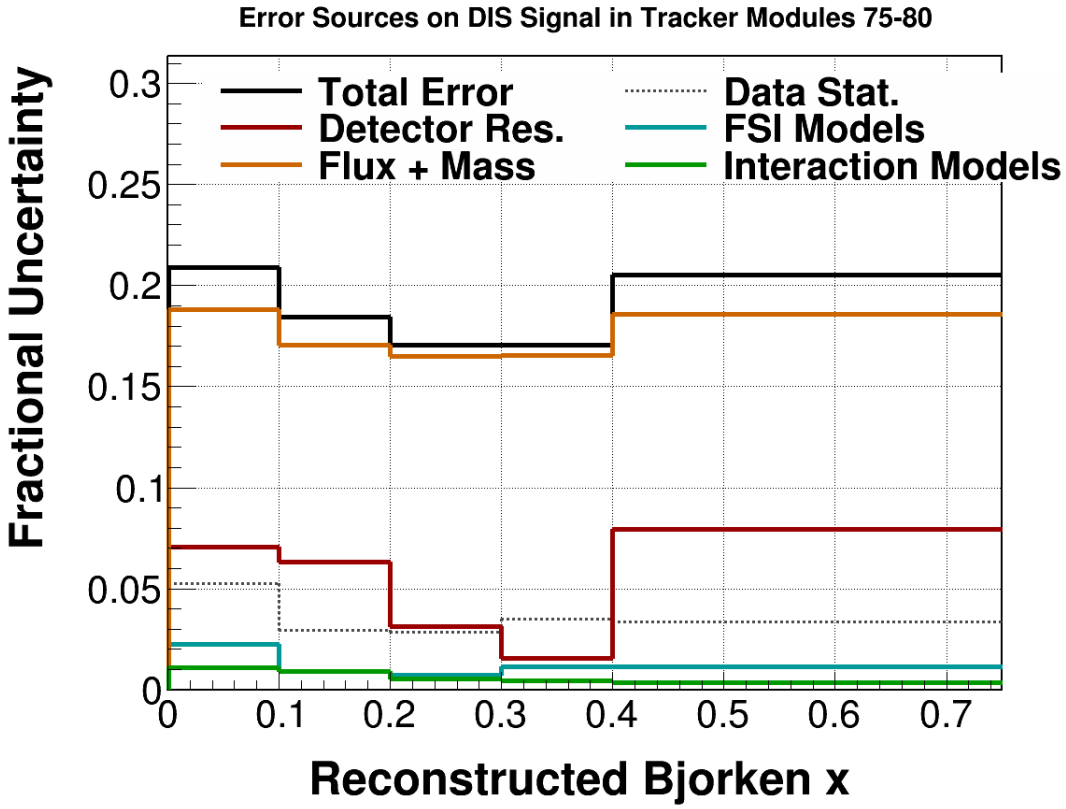

Figure E-209. Event yield uncertainties: tracker mods. 75-80 (x_{bj})

The following plots show the uncertainty on the number of DIS events, after subtracting the non-DIS events. They are plotted as a function of muon energy (E_μ):

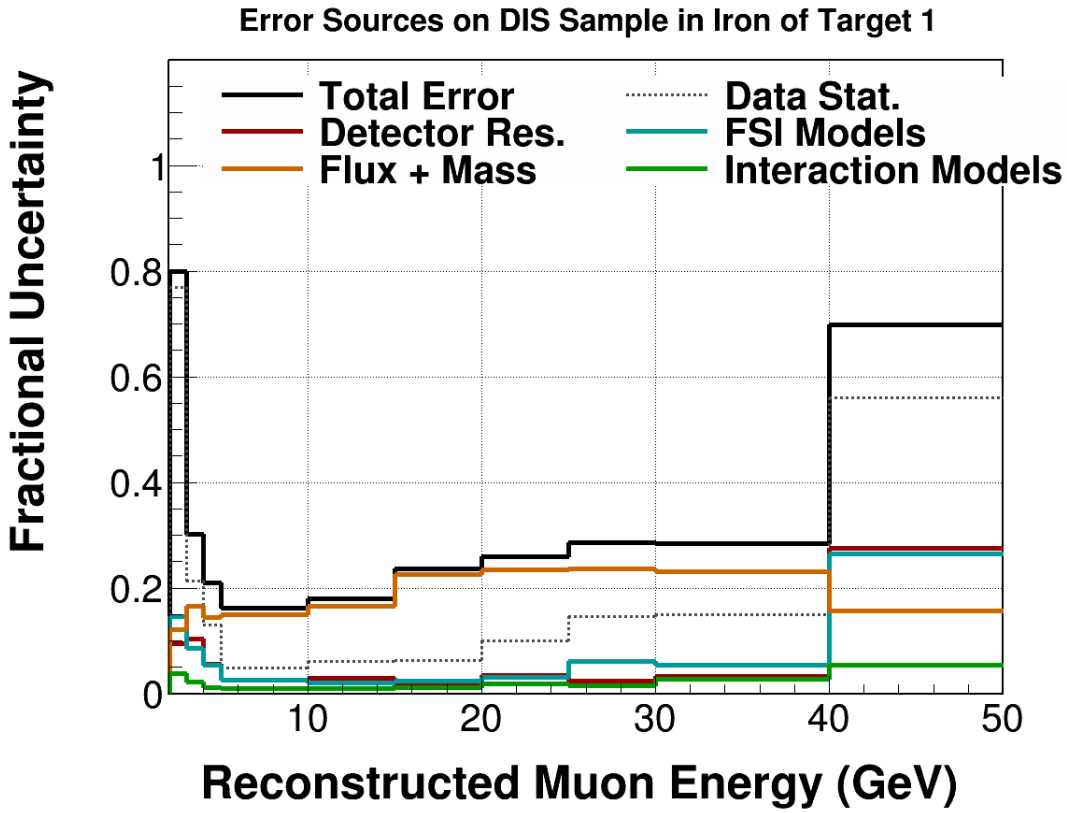

Figure E-210. Event yield uncertainties before CH subtraction: target 01 Fe (E_μ)

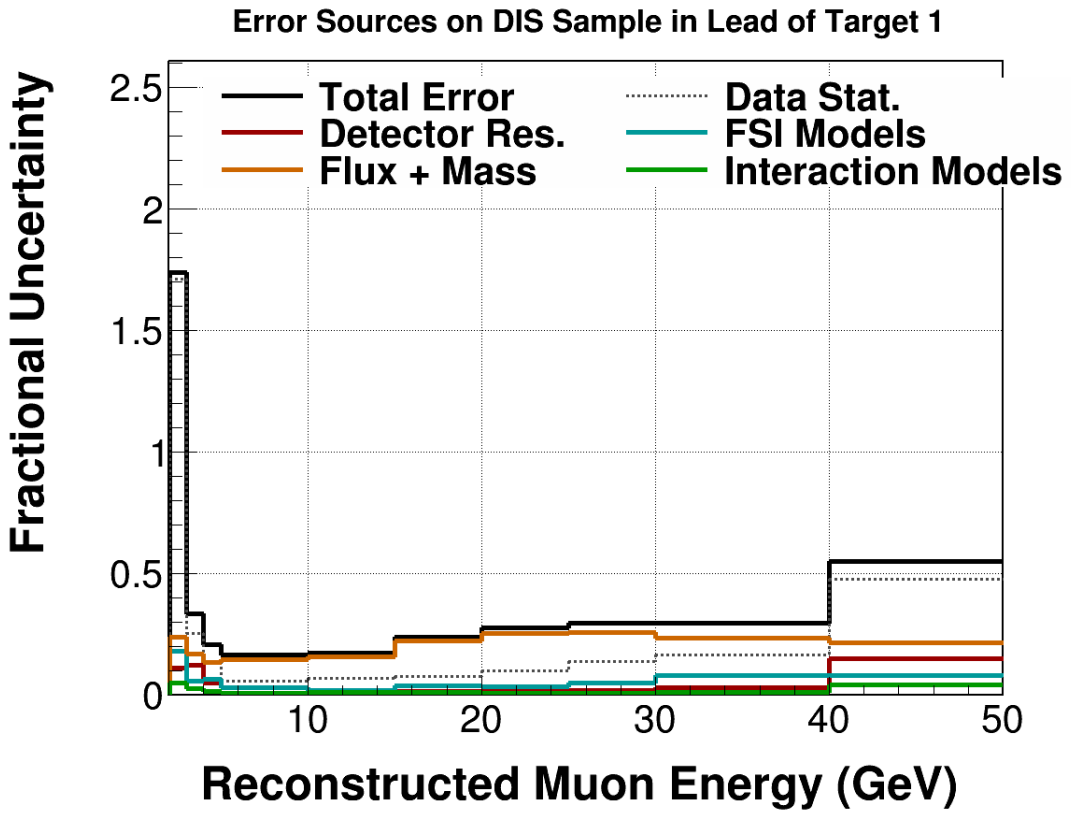

Figure E-211. Event yield uncertainties before CH subtraction: target 01 Pb (E_μ)

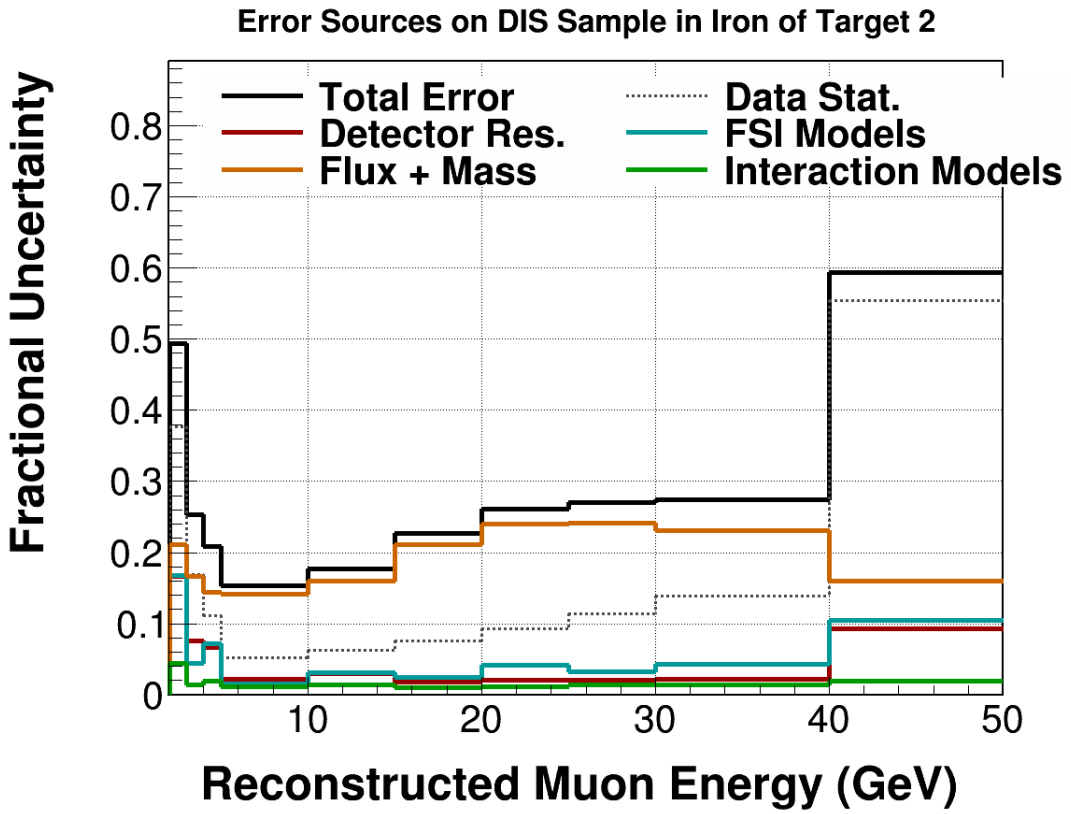

Figure E-212. Event yield uncertainties before CH subtraction: target 02 Fe (E_μ)

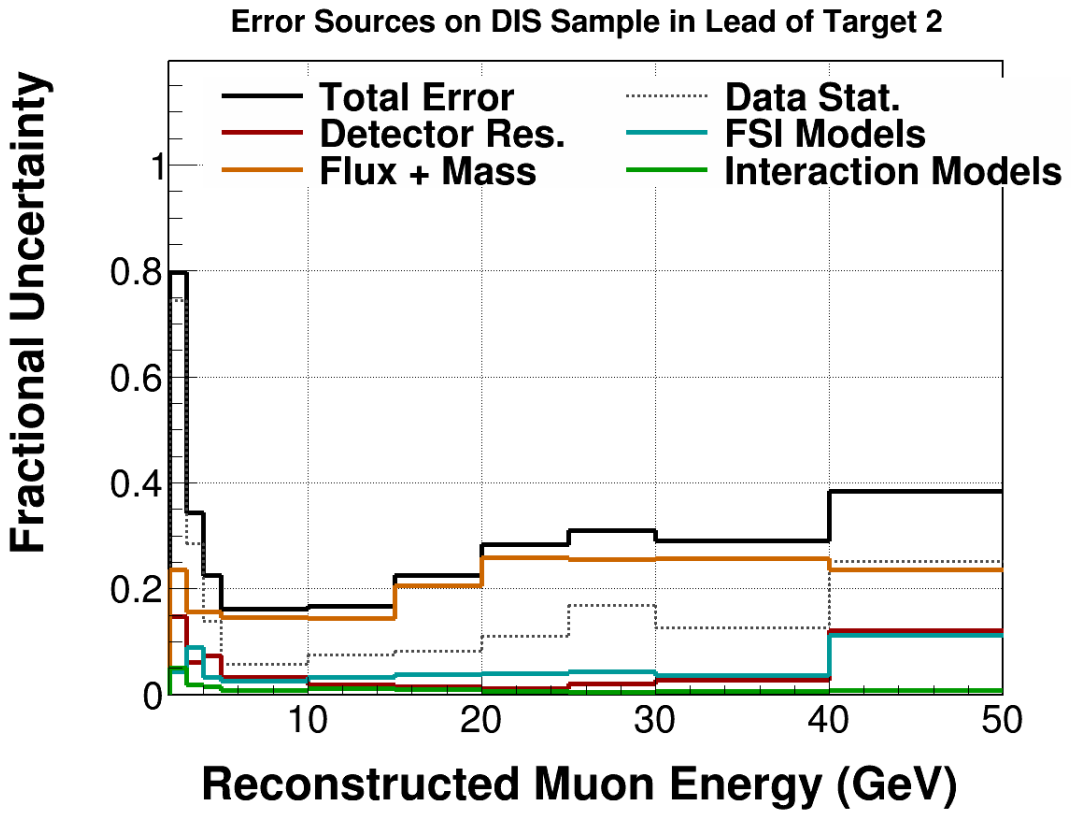

Figure E-213. Event yield uncertainties before CH subtraction: target 02 Pb (E_μ)

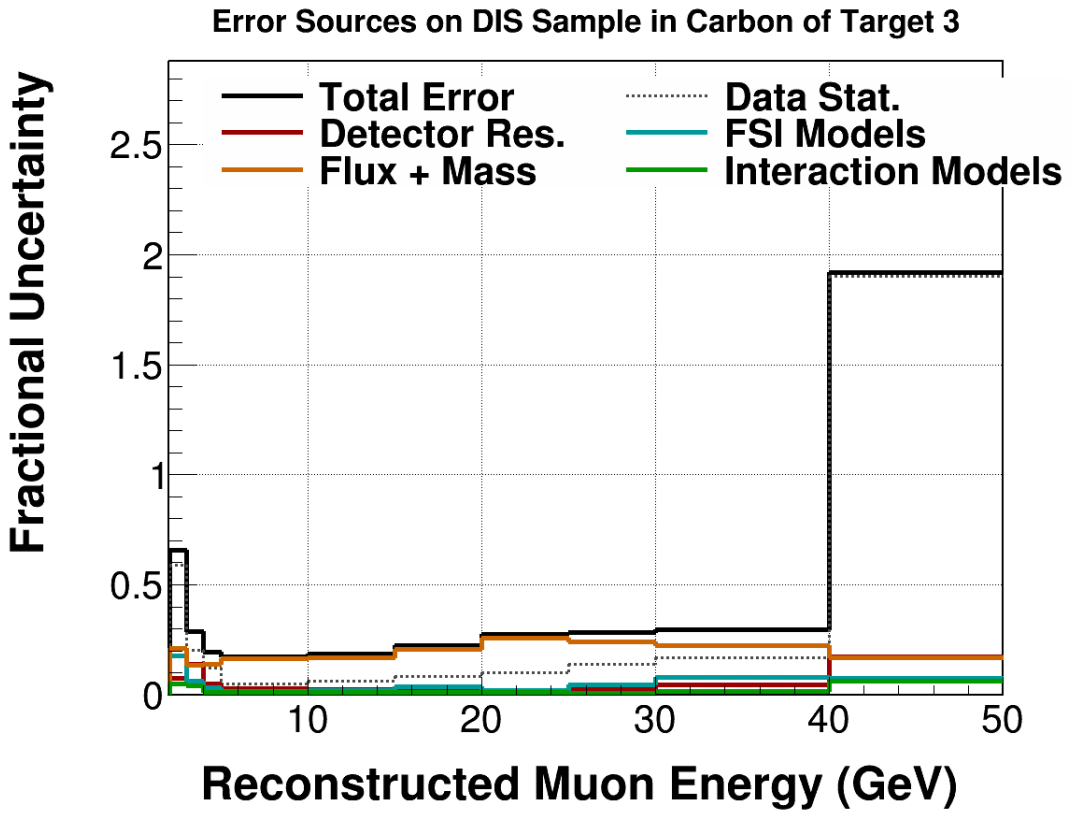

Figure E-214. Event yield uncertainties before CH subtraction: target 03 C (E_μ)

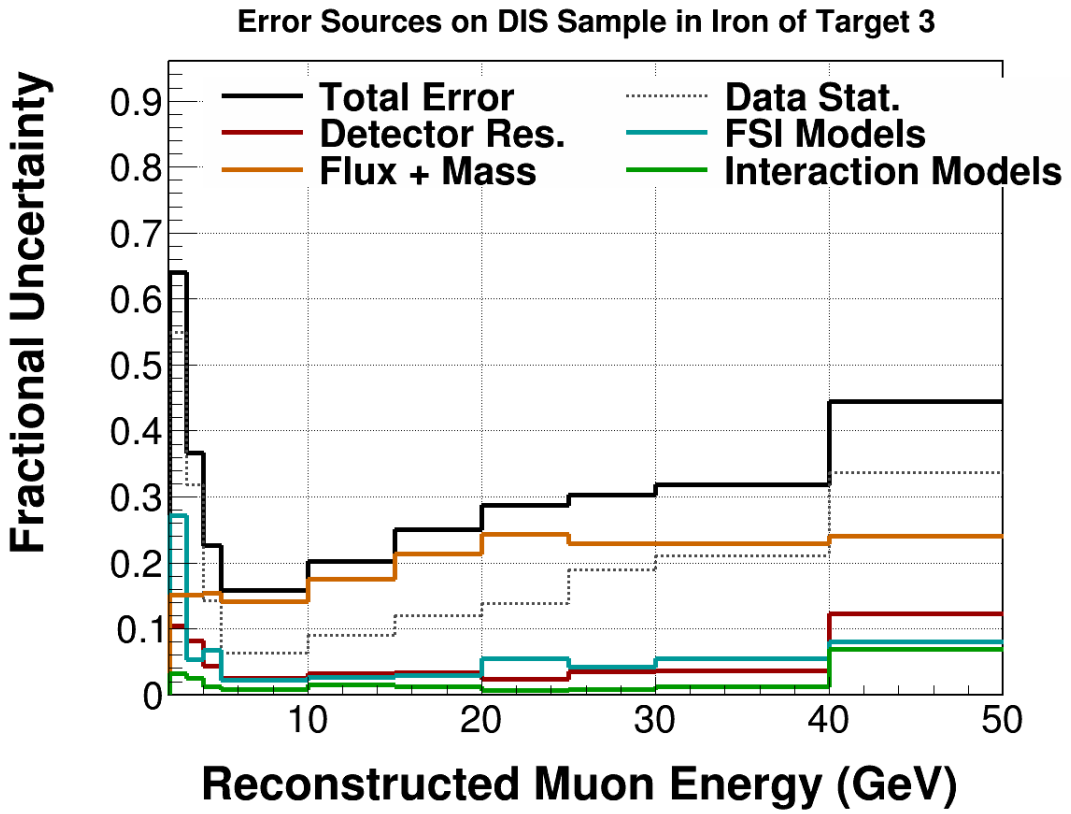

Figure E-215. Event yield uncertainties before CH subtraction: target 03 Fe (E_μ)

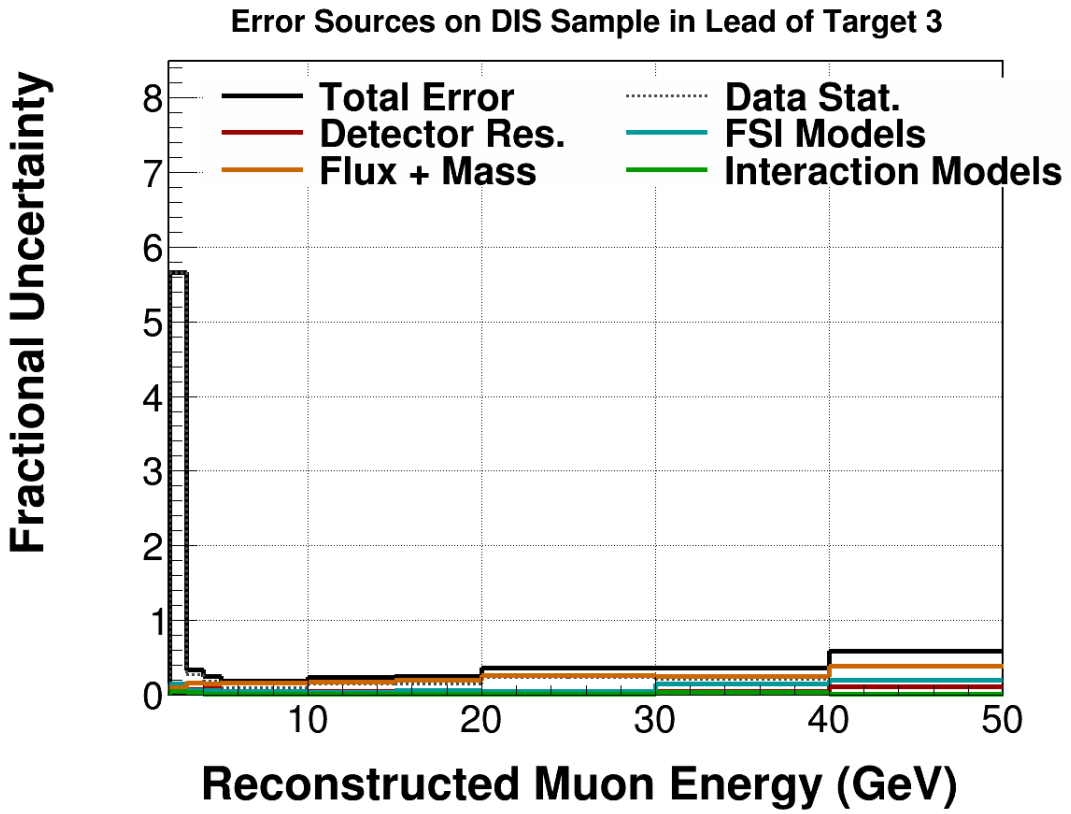

Figure E-216. Event yield uncertainties before CH subtraction: target 03 Pb (E_μ)

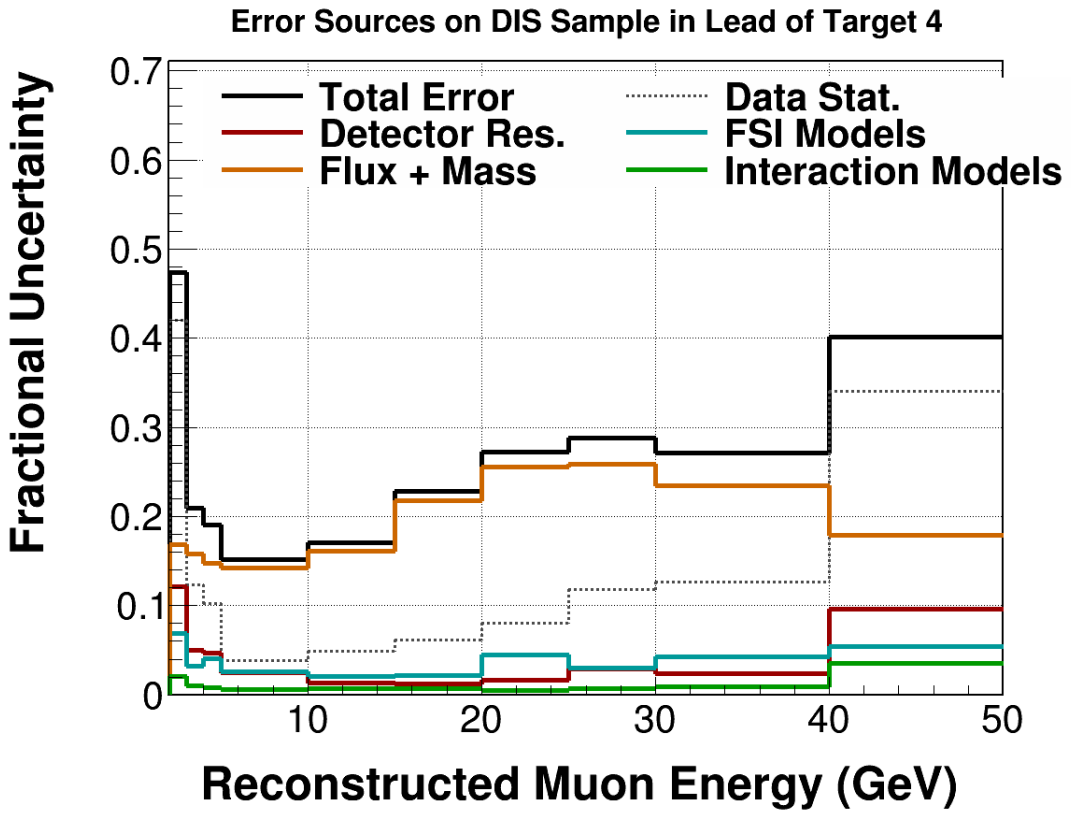

Figure E-217. Event yield uncertainties before CH subtraction: target 04 Pb (E_μ)

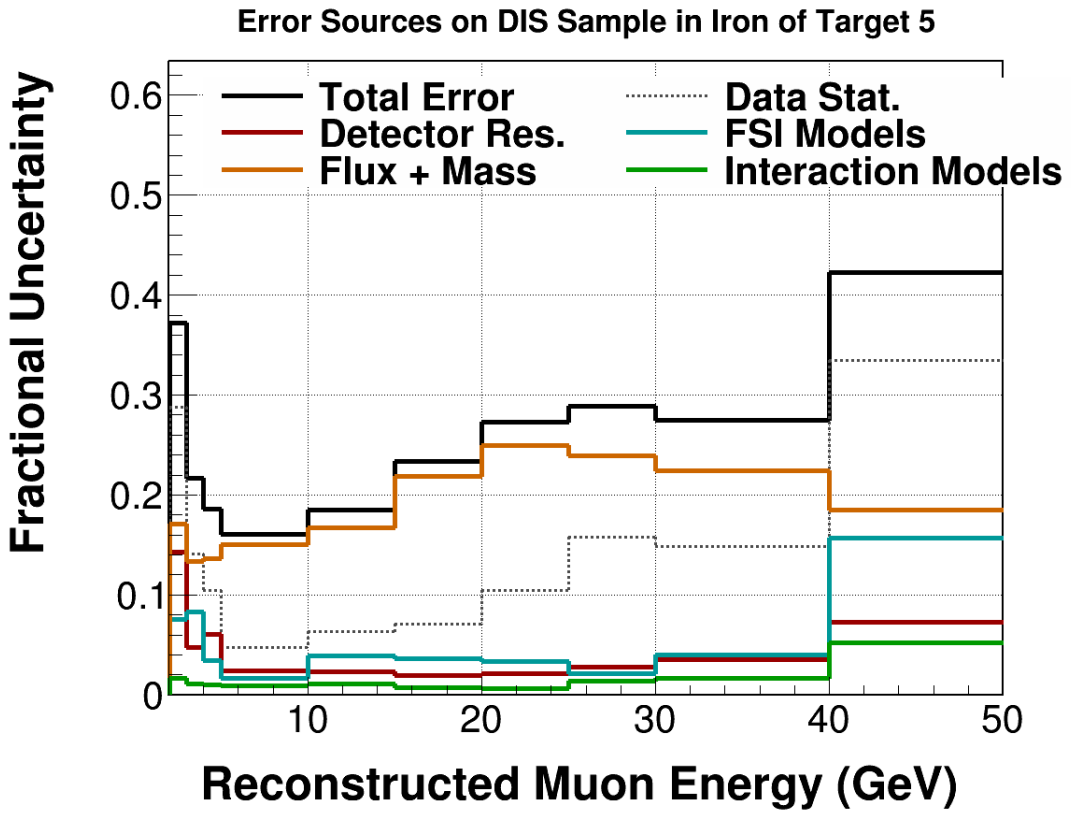

Figure E-218. Event yield uncertainties before CH subtraction: target 05 Fe (E_μ)

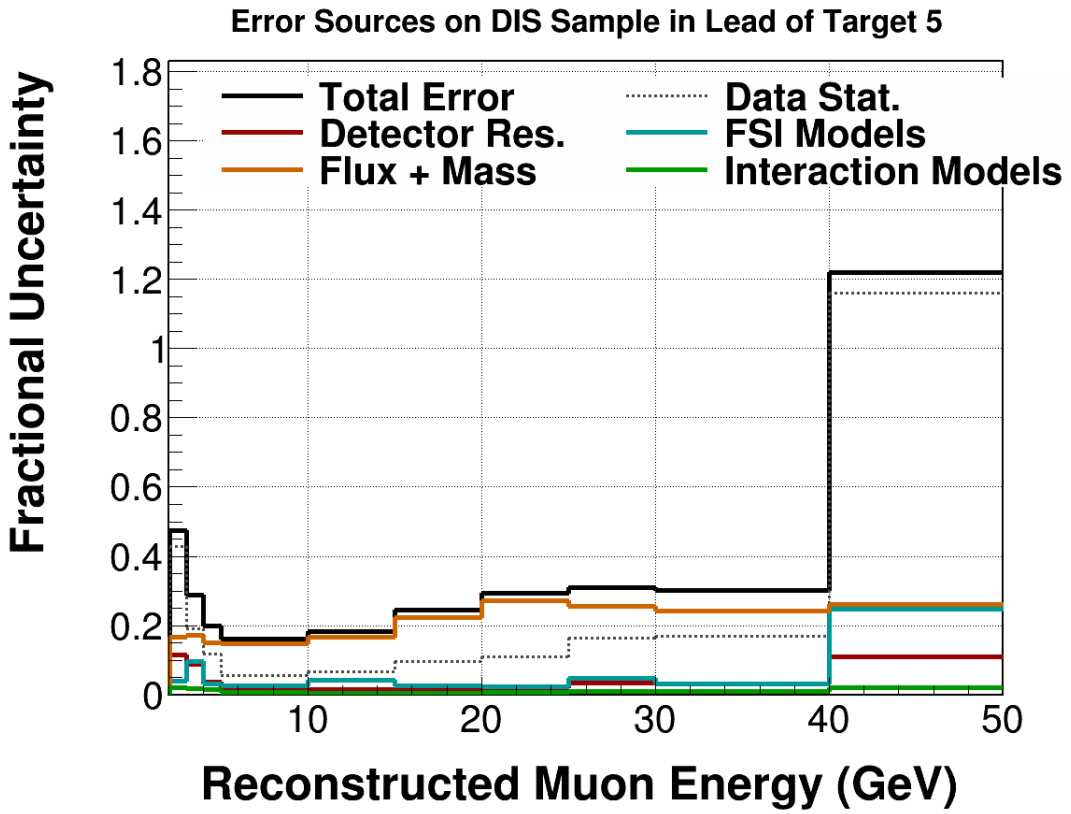

Figure E-219. Event yield uncertainties before CH subtraction: target 05 Pb (E_μ)

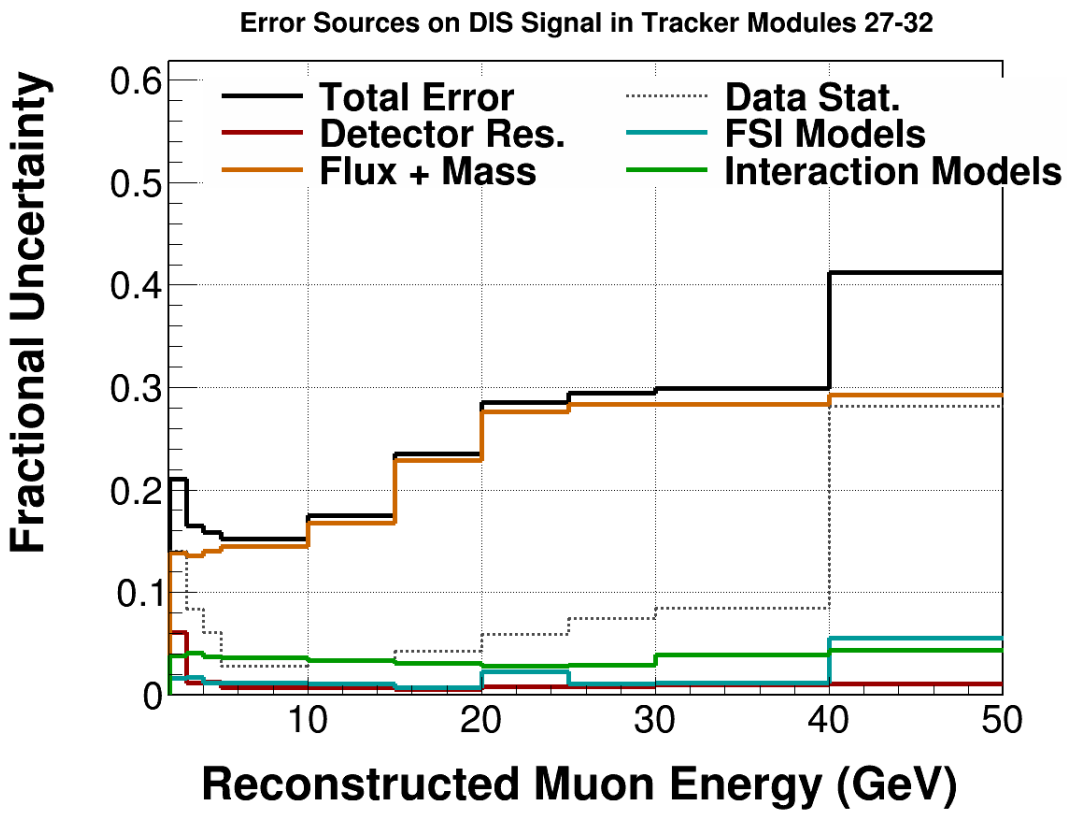

Figure E-220. Event yield uncertainties: tracker mods. 27-32 (E_μ)

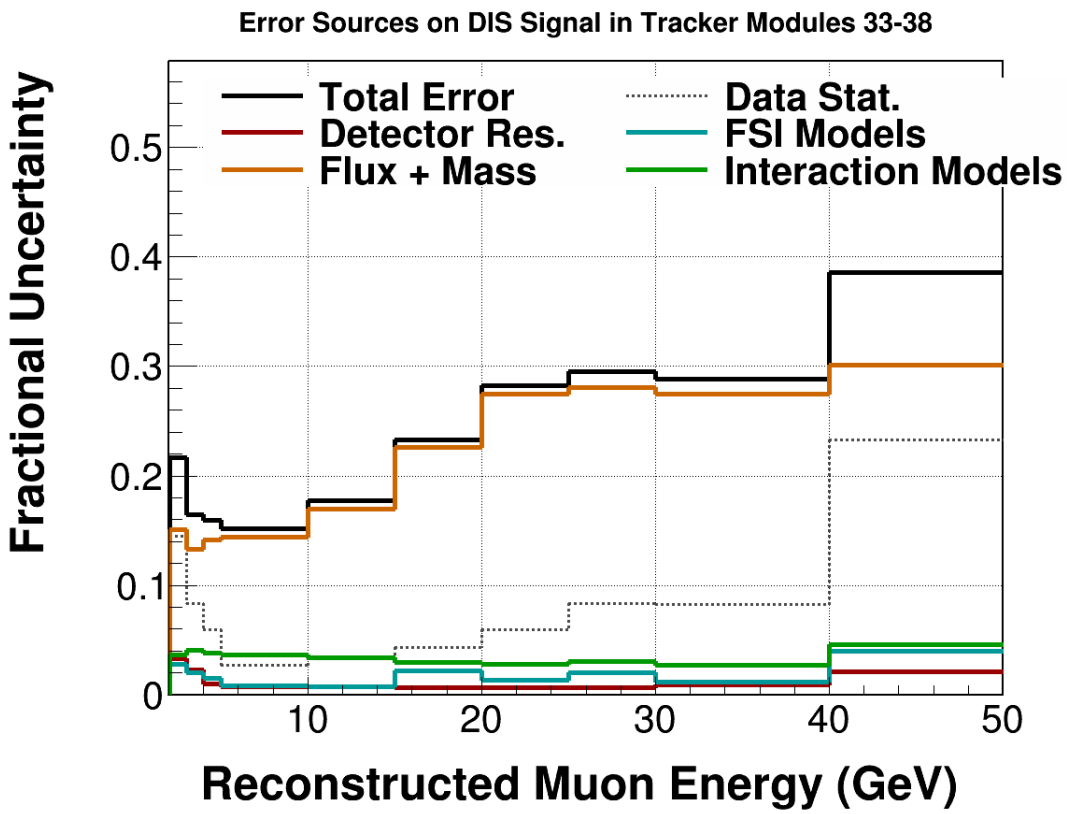

Figure E-221. Event yield uncertainties: tracker mods. 33-38 (E_μ)

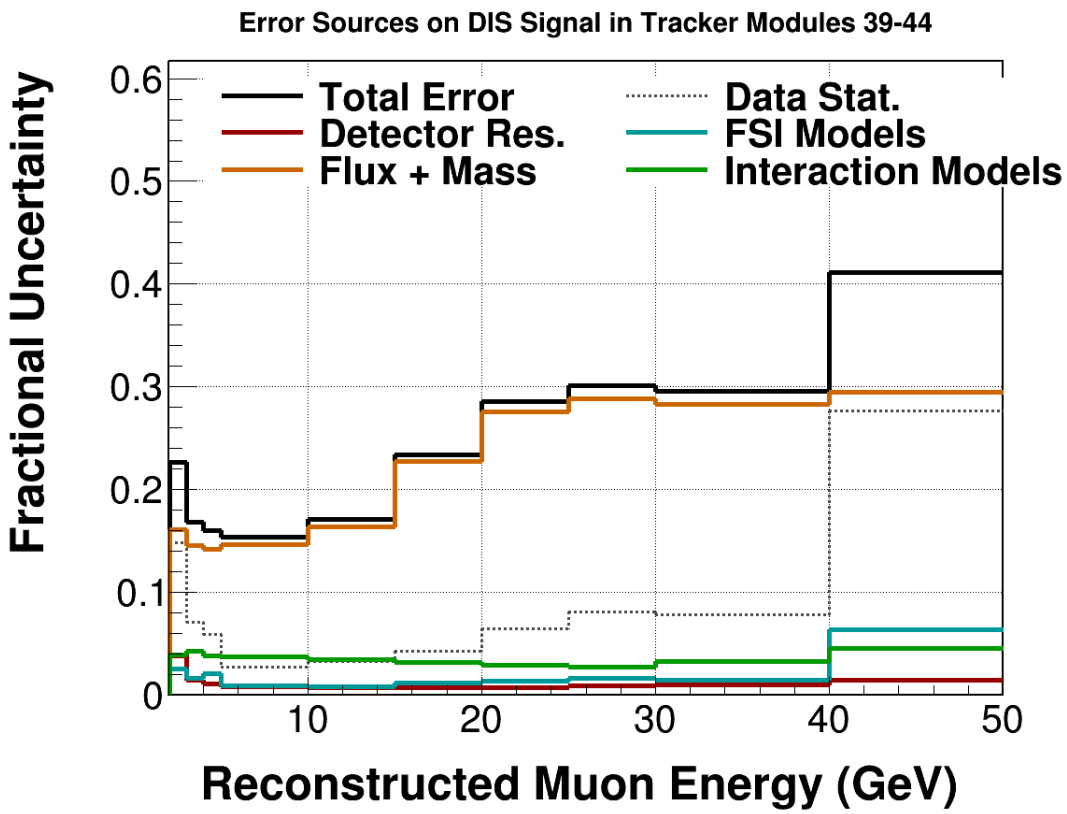

Figure E-222. Event yield uncertainties: tracker mods. 39-44 (E_μ)

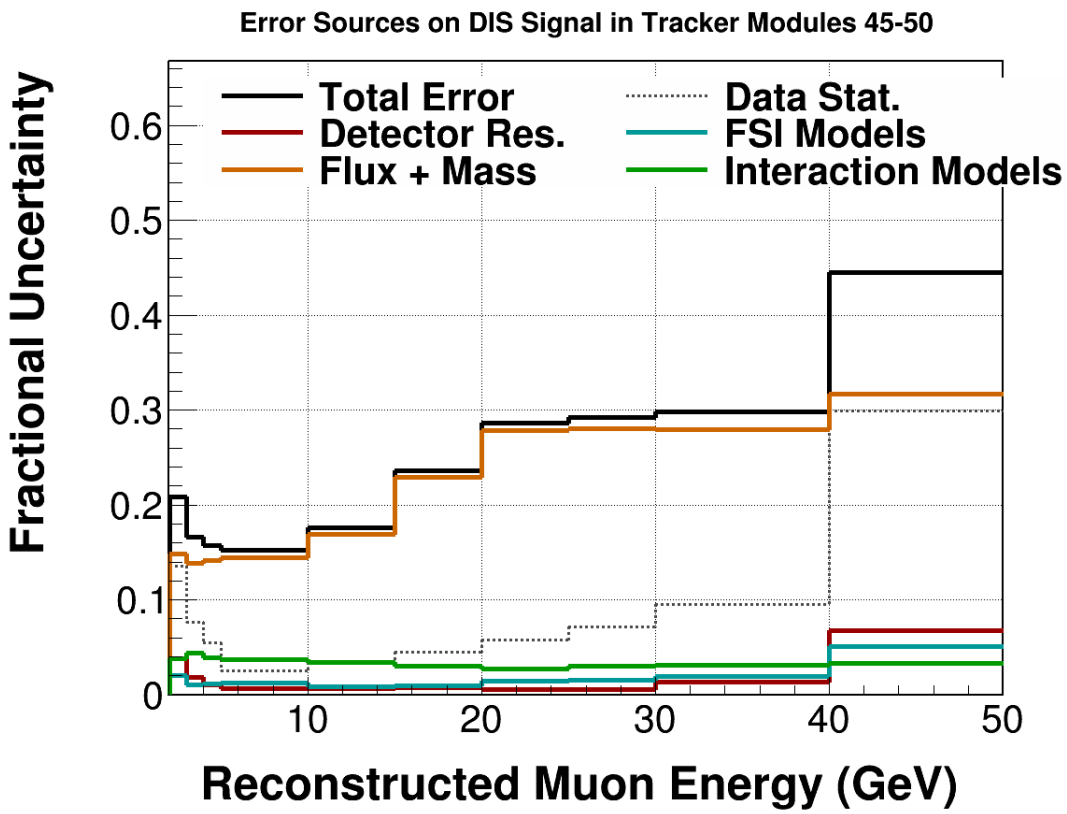

Figure E-223. Event yield uncertainties: tracker mods. 45-50 (E_μ)

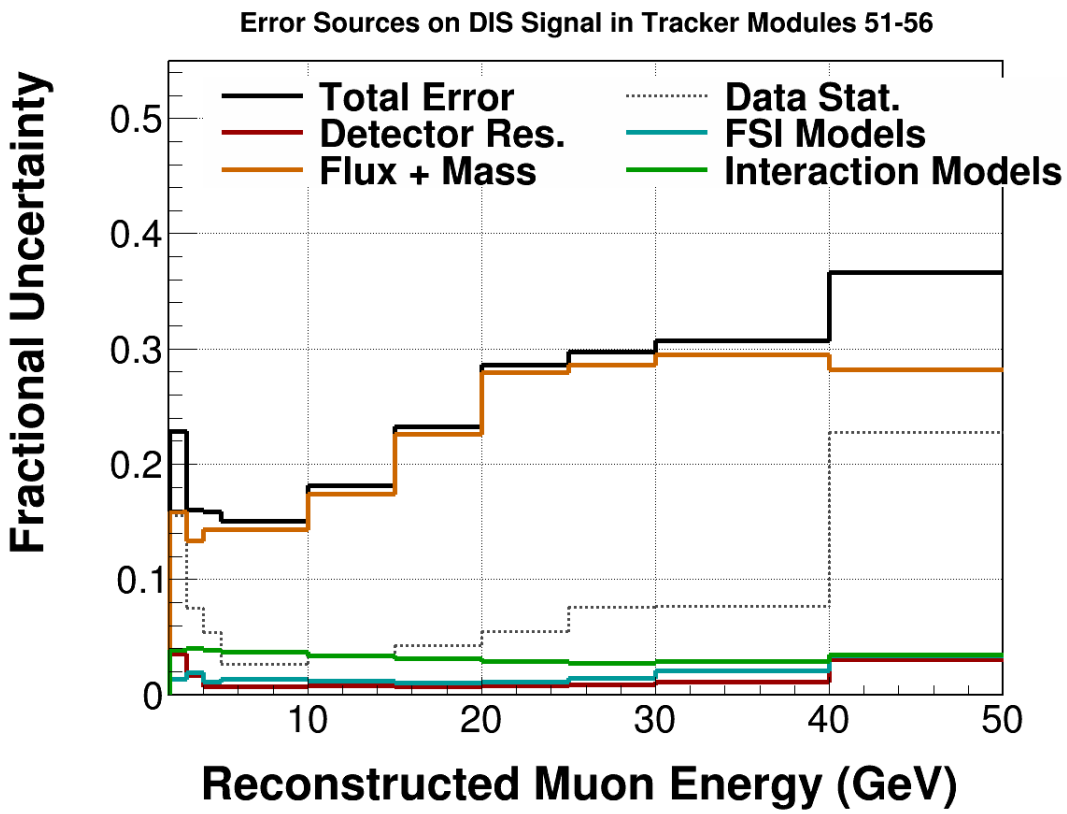

Figure E-224. Event yield uncertainties: tracker mods. 51-56 (E_μ)

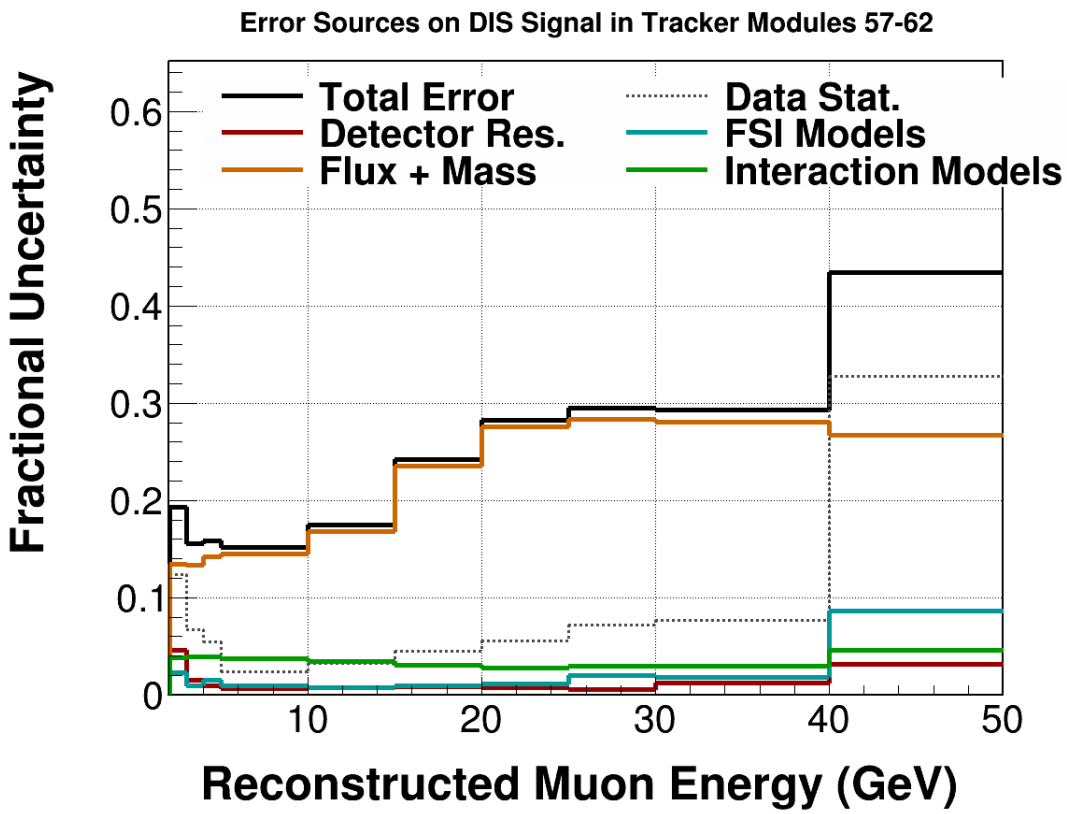

Figure E-225. Event yield uncertainties: tracker mods. 57-62 (E_μ)

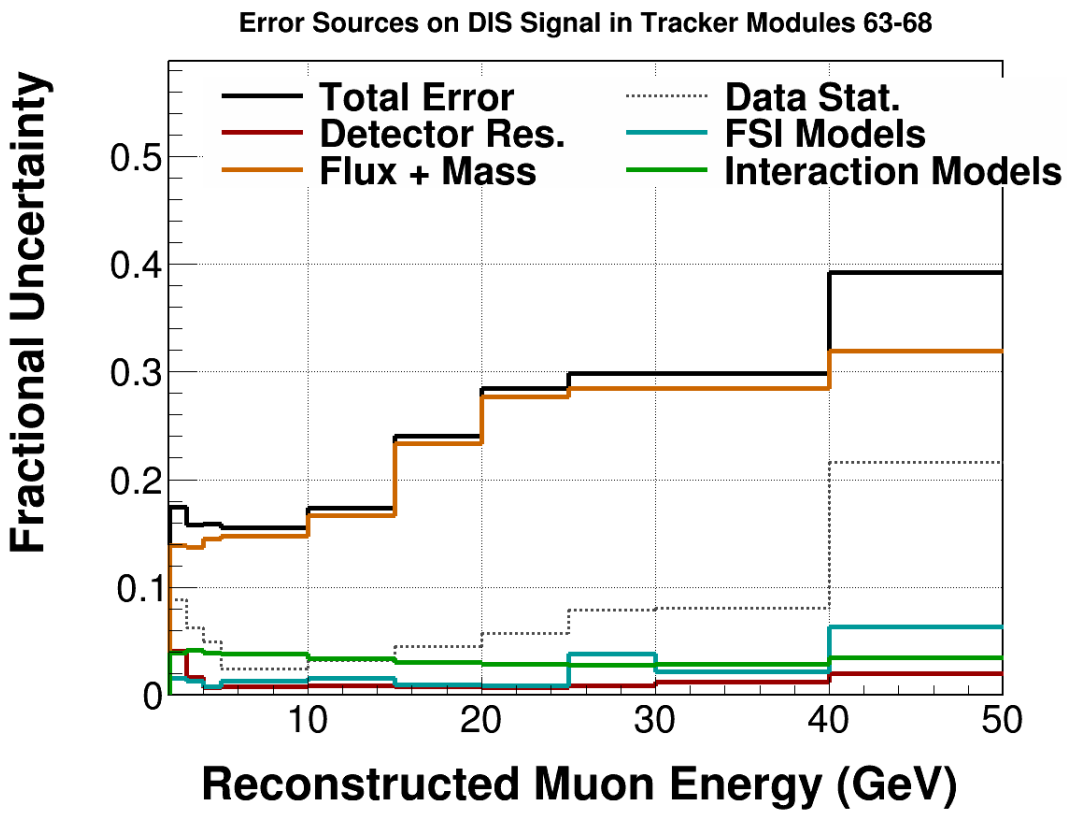

Figure E-226. Event yield uncertainties: tracker mods. 63-68 (E_μ)

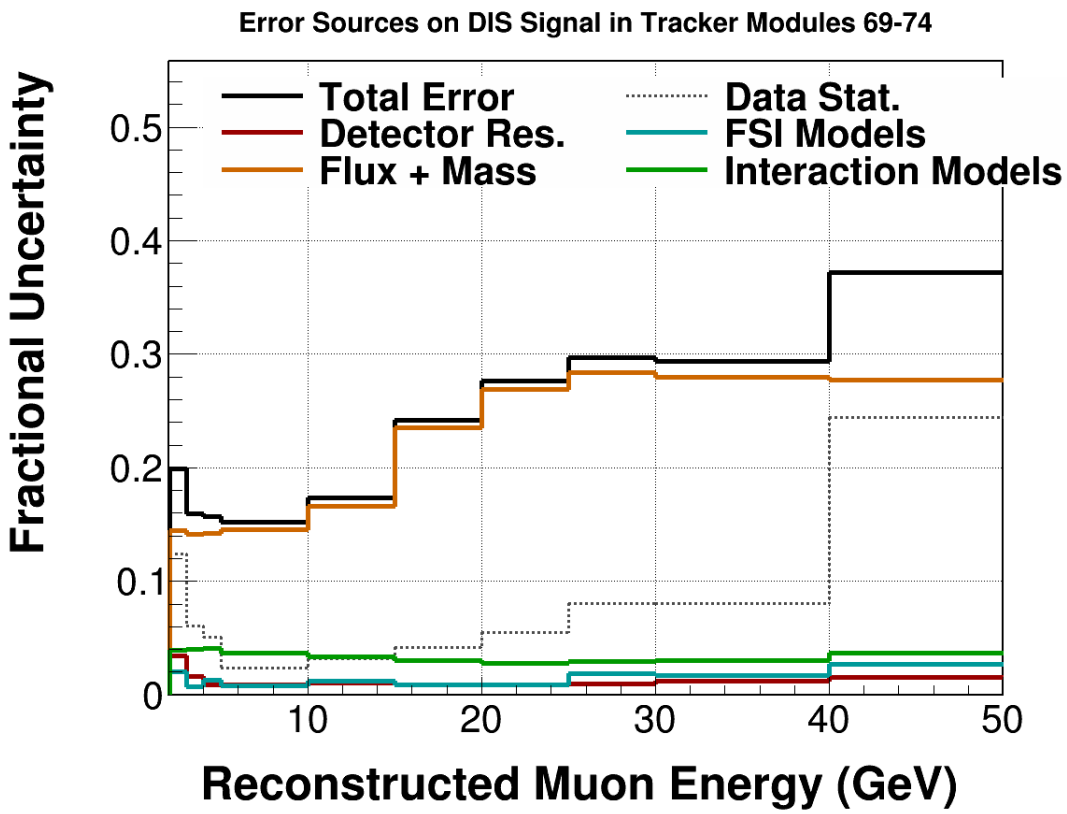

Figure E-227. Event yield uncertainties: tracker mods. 69-74 (E_μ)

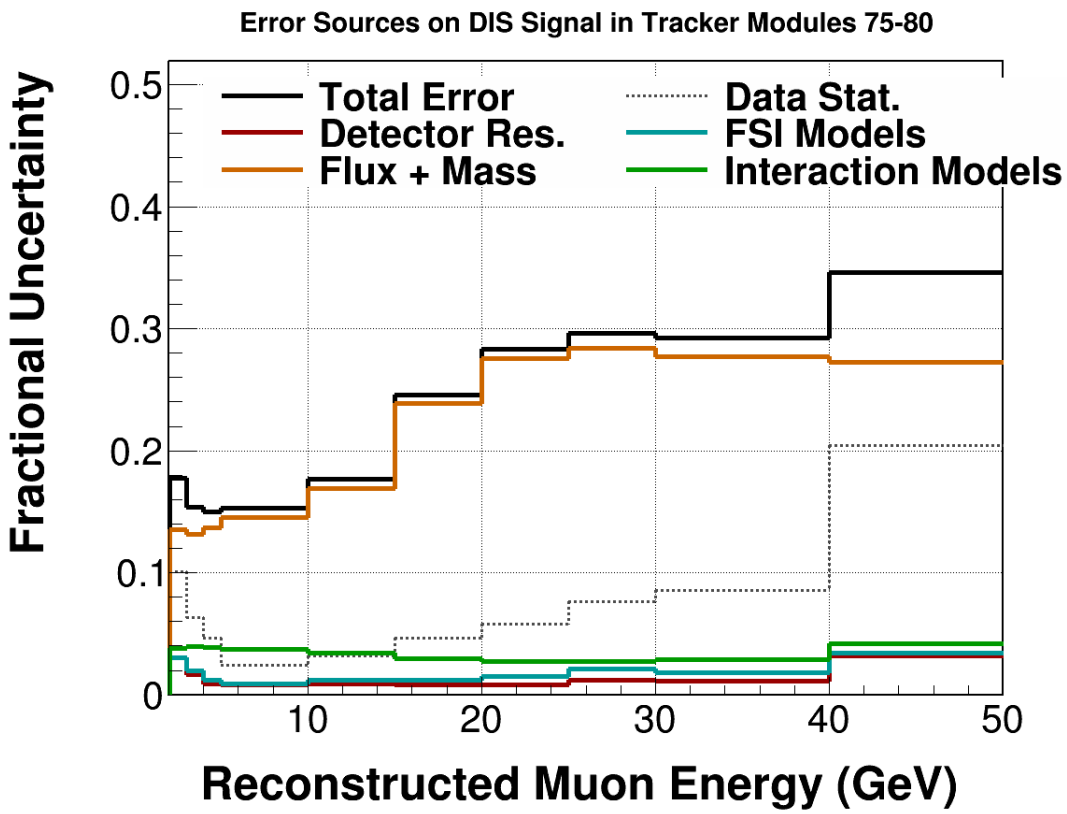

Figure E-228. Event yield uncertainties: tracker mods. 75-80 (E_μ)

E.3 DIS Event Yields After CH Subtraction

The following plots show the DIS events in data and MC, after subtracting the non-DIS AND CH events. They also contain plots of the DIS CH events in different tracker modules. All are plotted as a function of neutrino energy (E_ν):

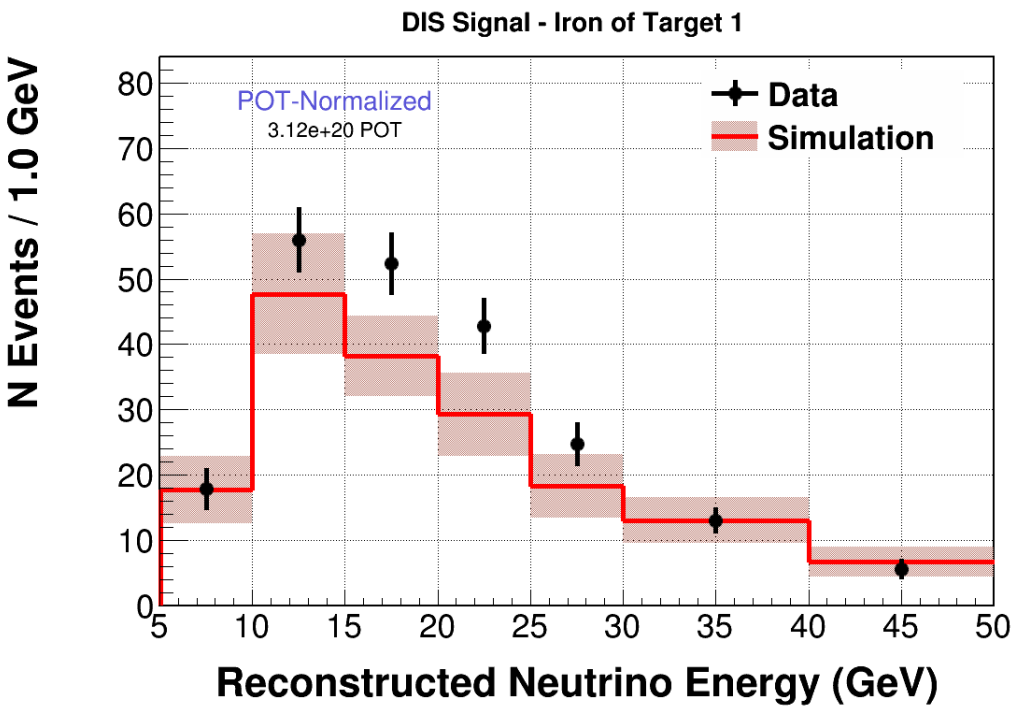

Figure E-229. DIS Signal: target 01 Fe (E_ν)

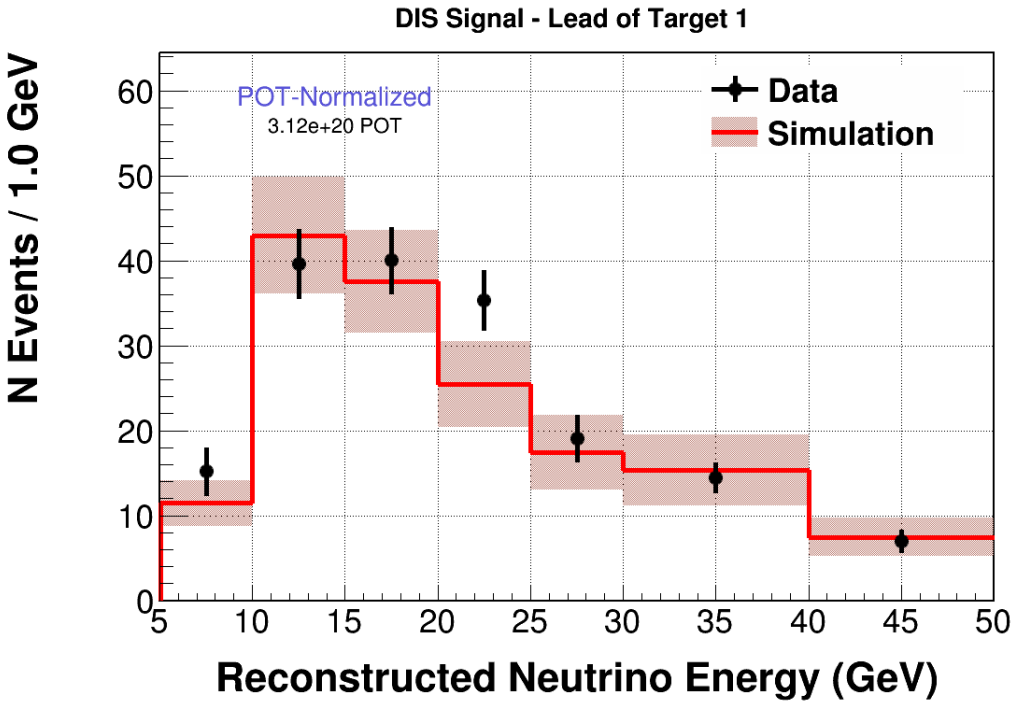

Figure E-230. DIS Signal: target 01 Pb (E_ν)

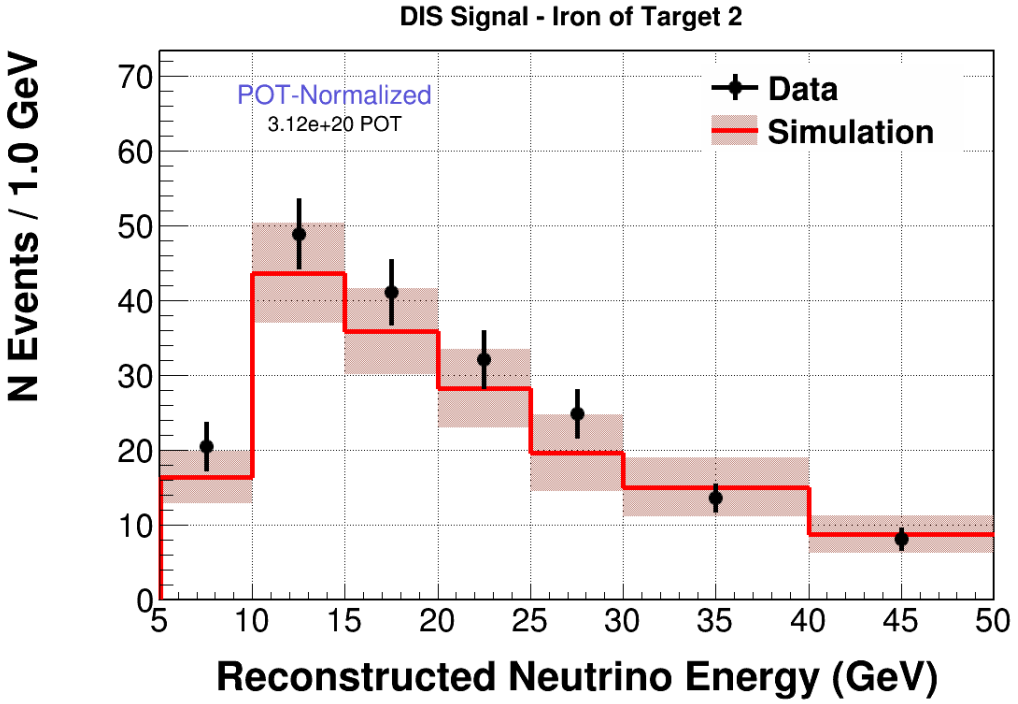

Figure E-231. DIS Signal: target 02 Fe (E_ν)

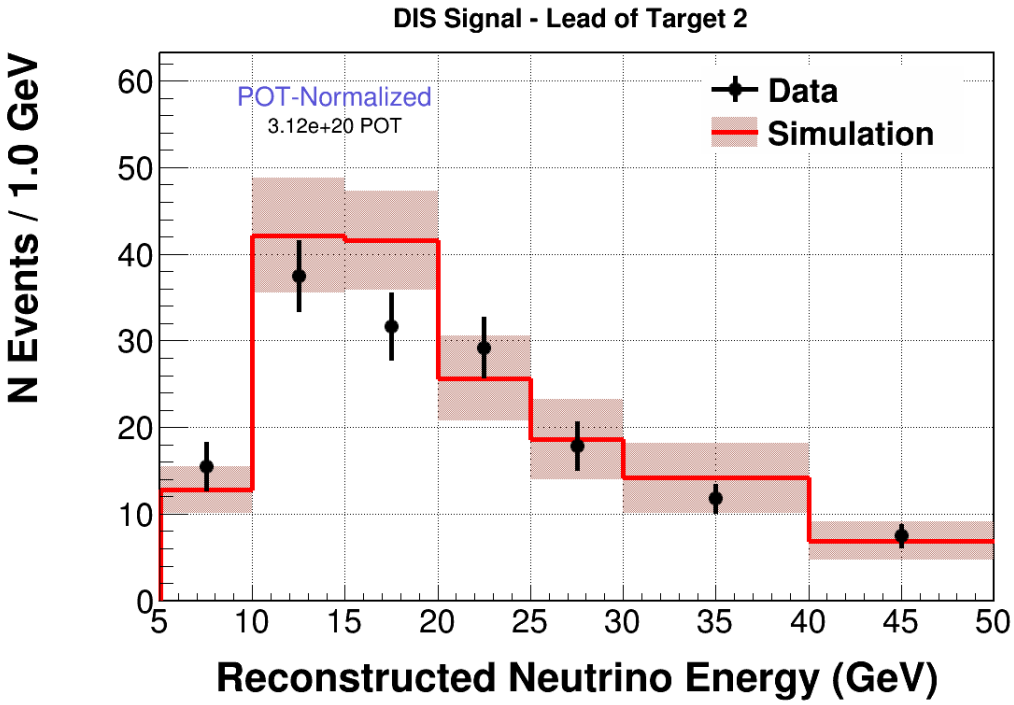

Figure E-232. DIS Signal: target 02 Pb (E_ν)

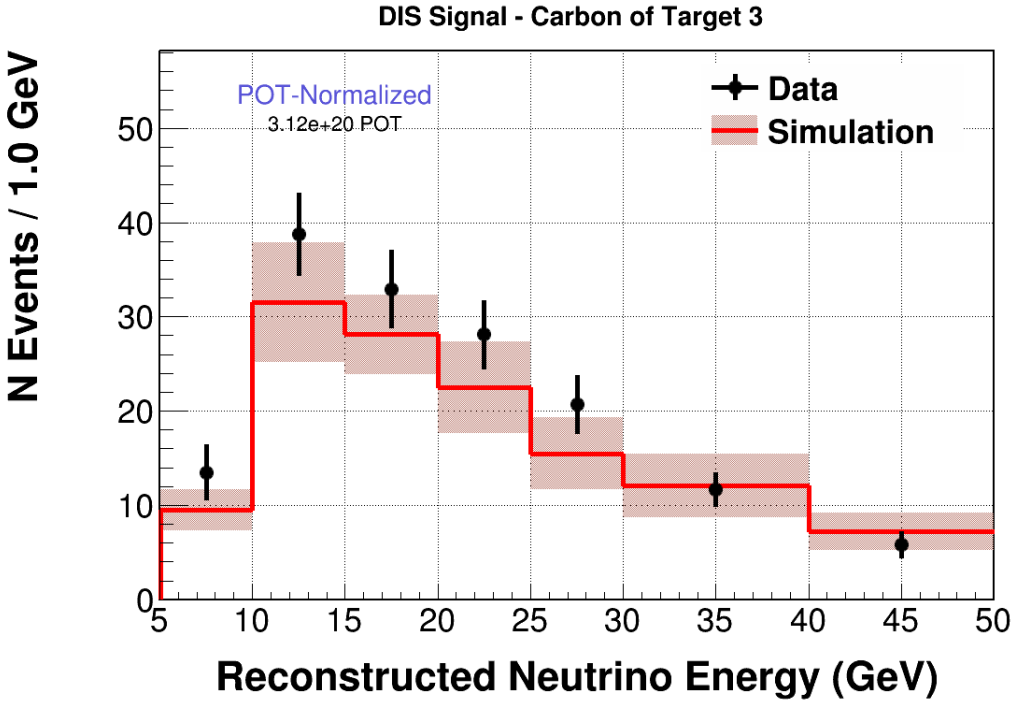

Figure E-233. DIS Signal: target 03 C (E_ν)

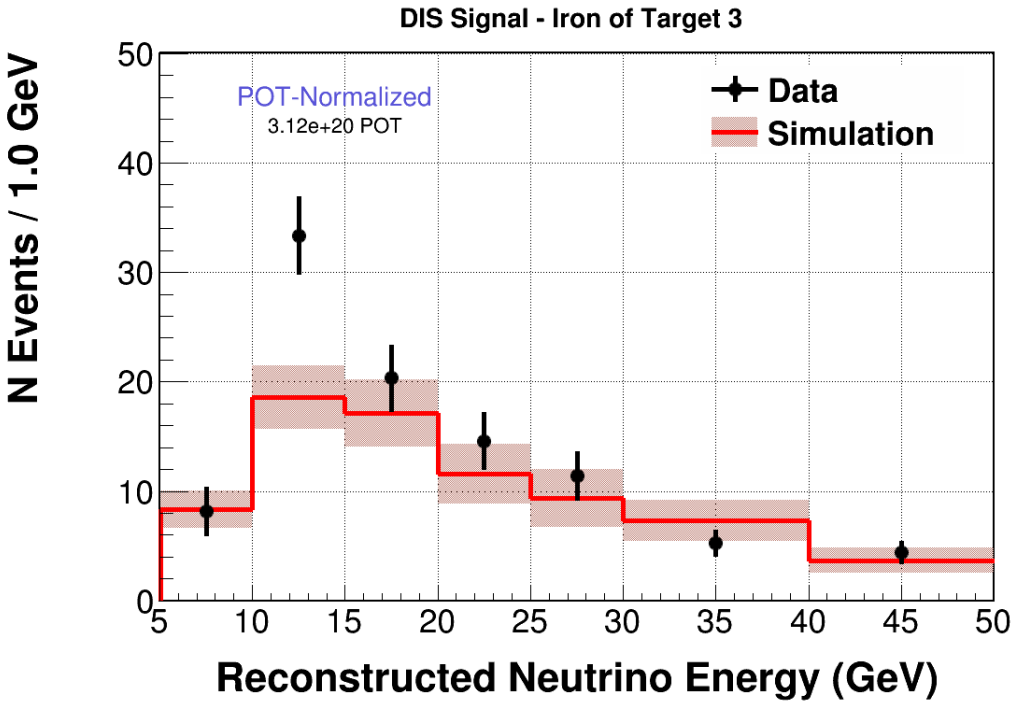

Figure E-234. DIS Signal: target 03 Fe (E_ν)

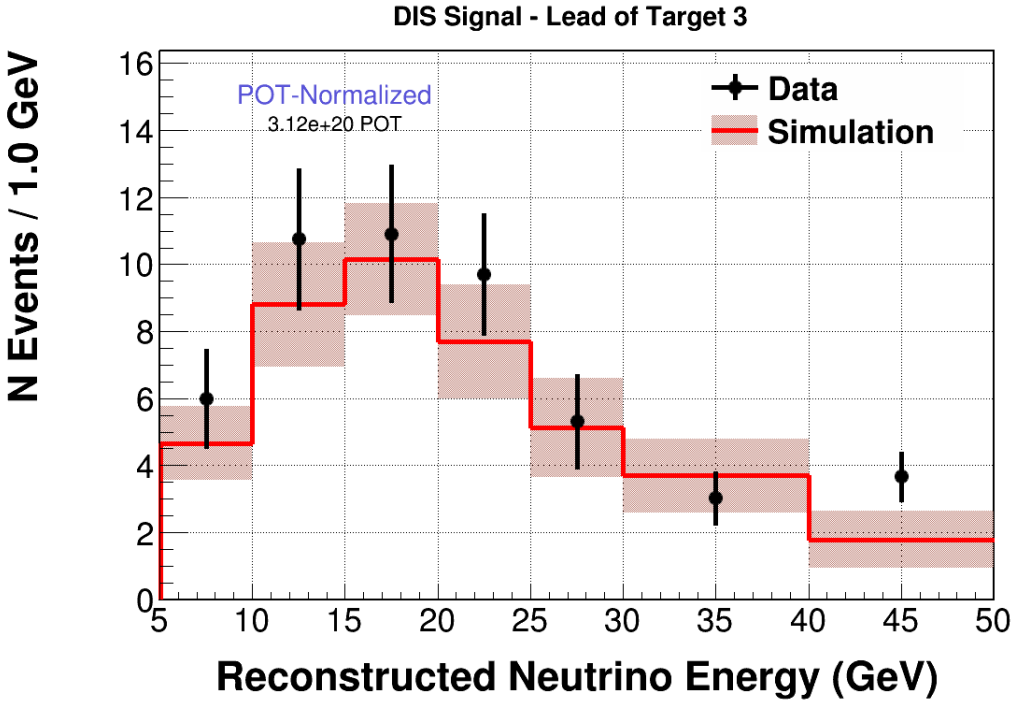

Figure E-235. DIS Signal: target 03 Pb (E_ν)

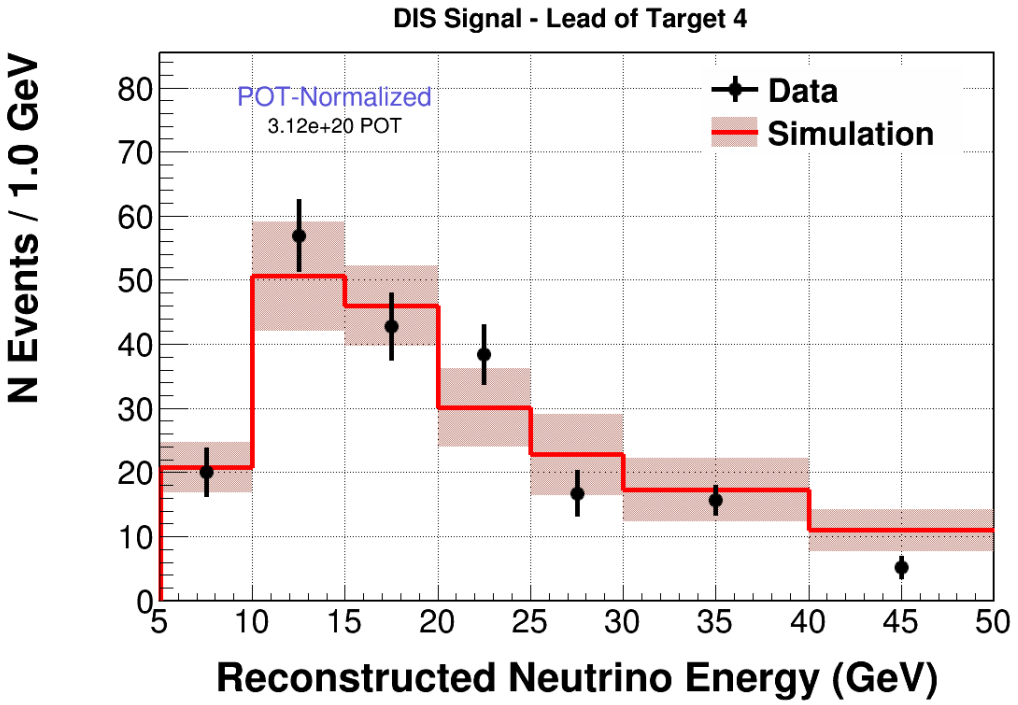

Figure E-236. DIS Signal: target 04 Pb (E_ν)

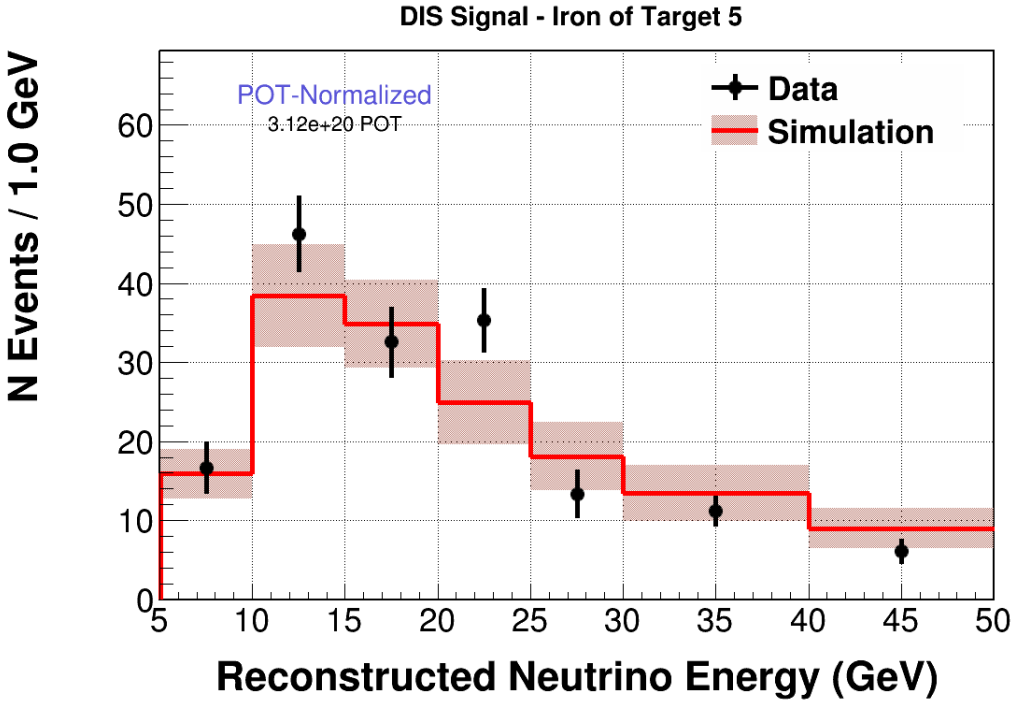

Figure E-237. DIS Signal: target 05 Fe (E_ν)

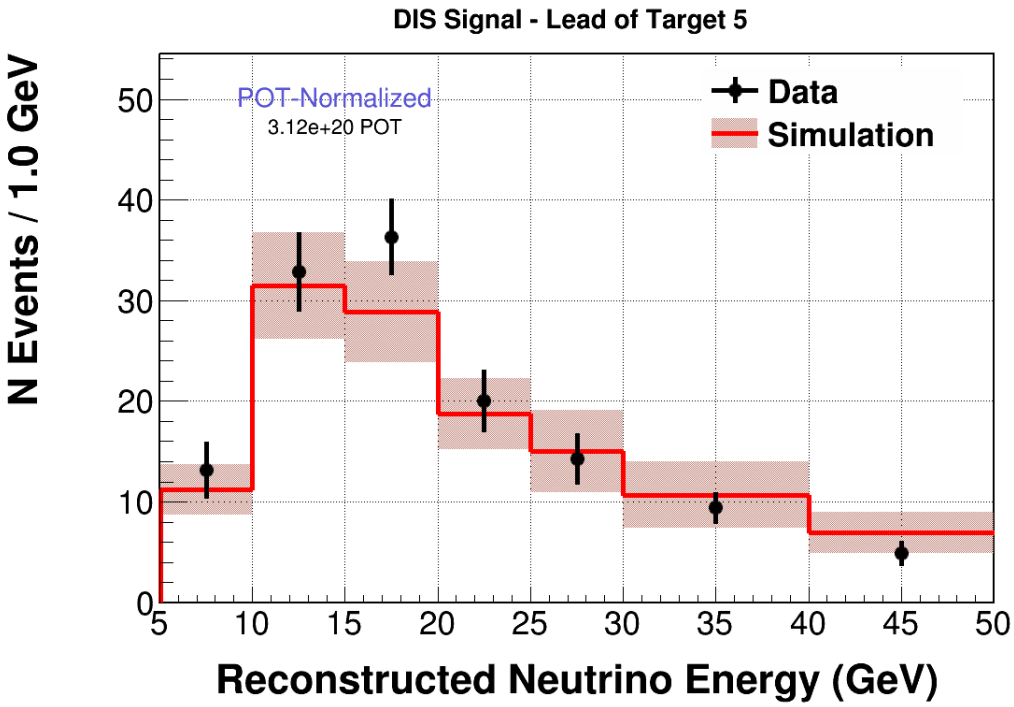

Figure E-238. DIS Signal: target 05 Pb (E_ν)

The following plots show the DIS events in data and MC, after subtracting the non-DIS AND CH events. They also contain plots of the DIS CH events in different tracker modules. All are plotted as a function of Bjorken-x (x_{bj}):

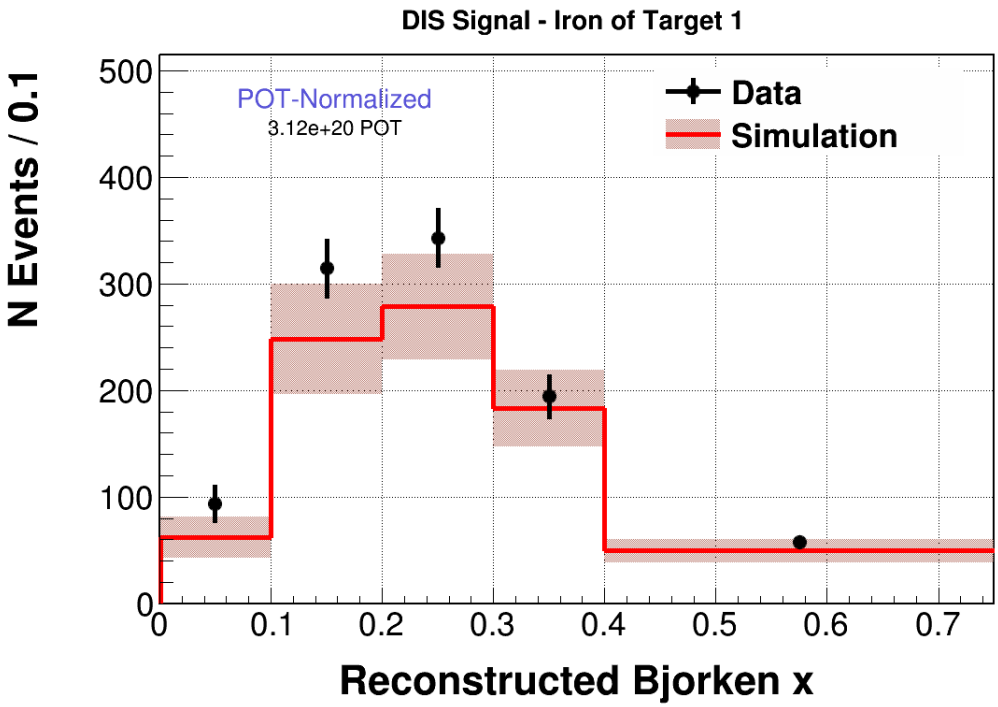

Figure E-239. DIS Signal: target 01 Fe (x_{bj})

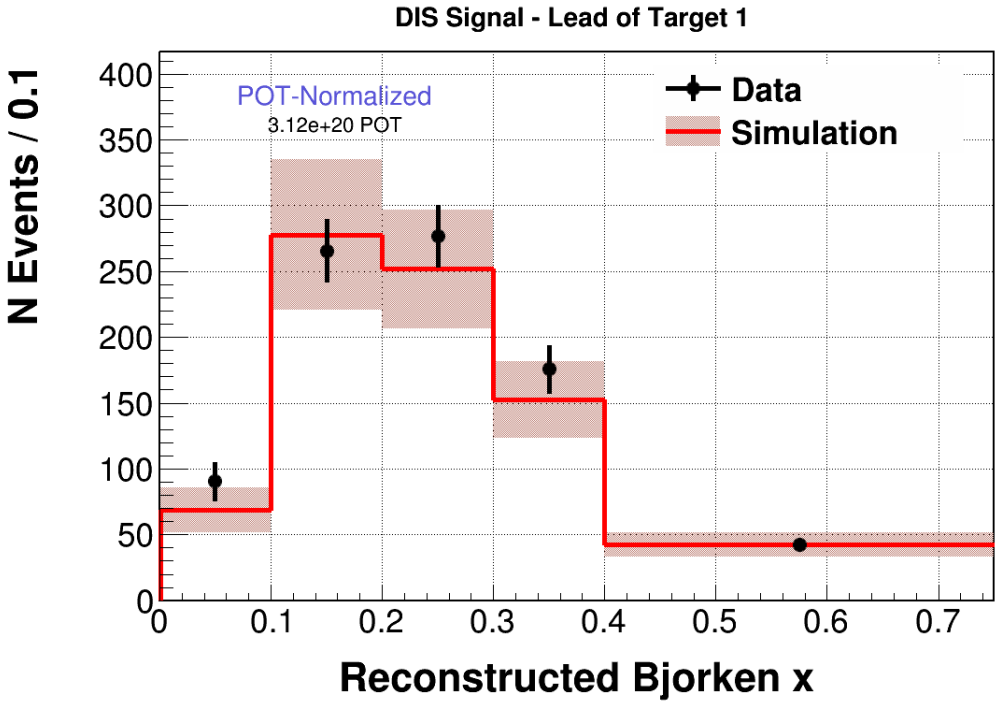

Figure E-240. DIS Signal: target 01 Pb (x_{bj})

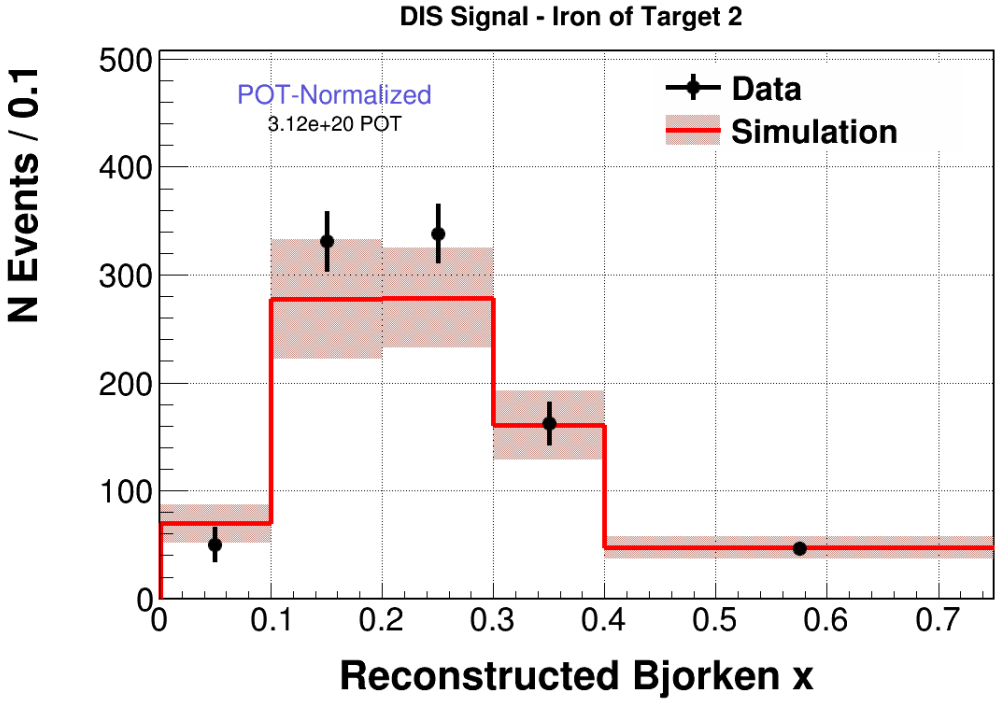

Figure E-241. DIS Signal: target 02 Fe (x_{bj})

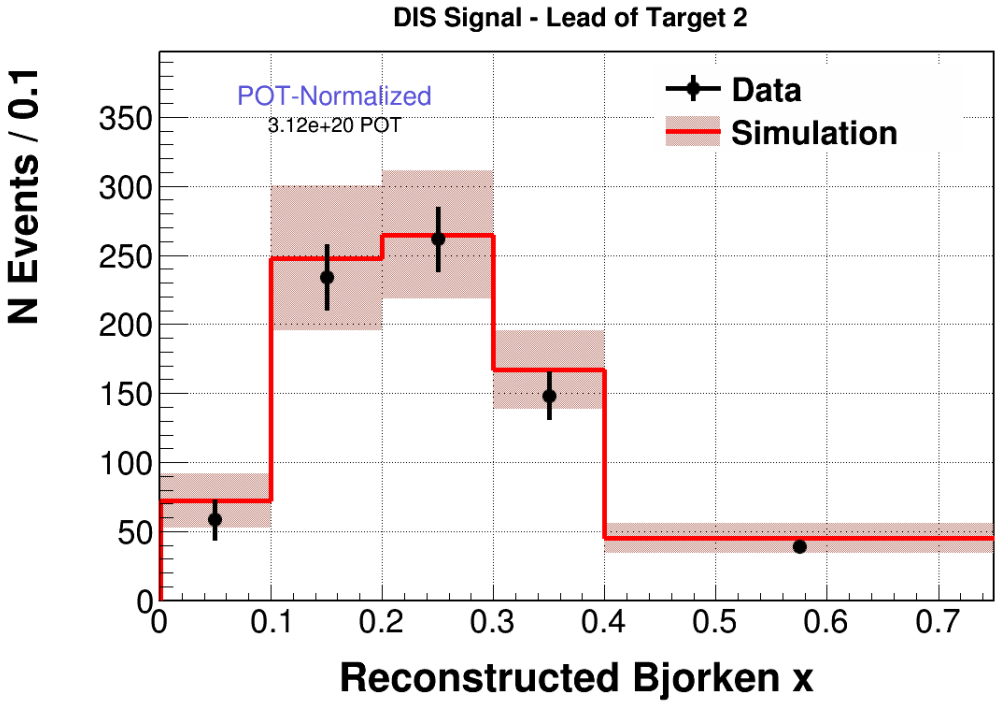

Figure E-242. DIS Signal: target 02 Pb (x_{bj})

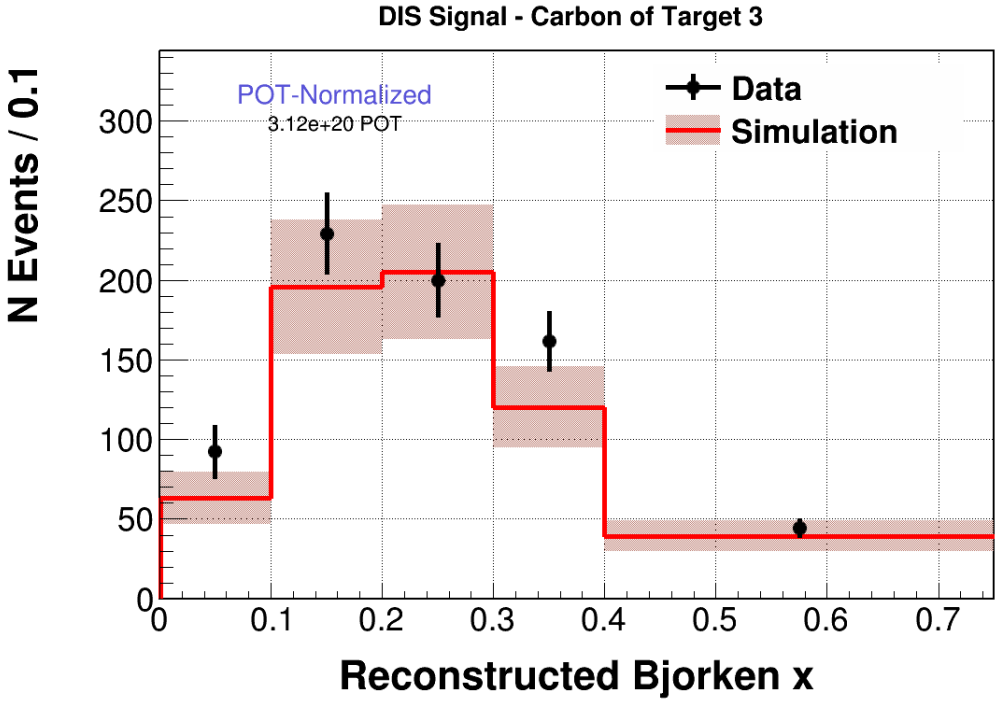

Figure E-243. DIS Signal: target 03 C (x_{bj})

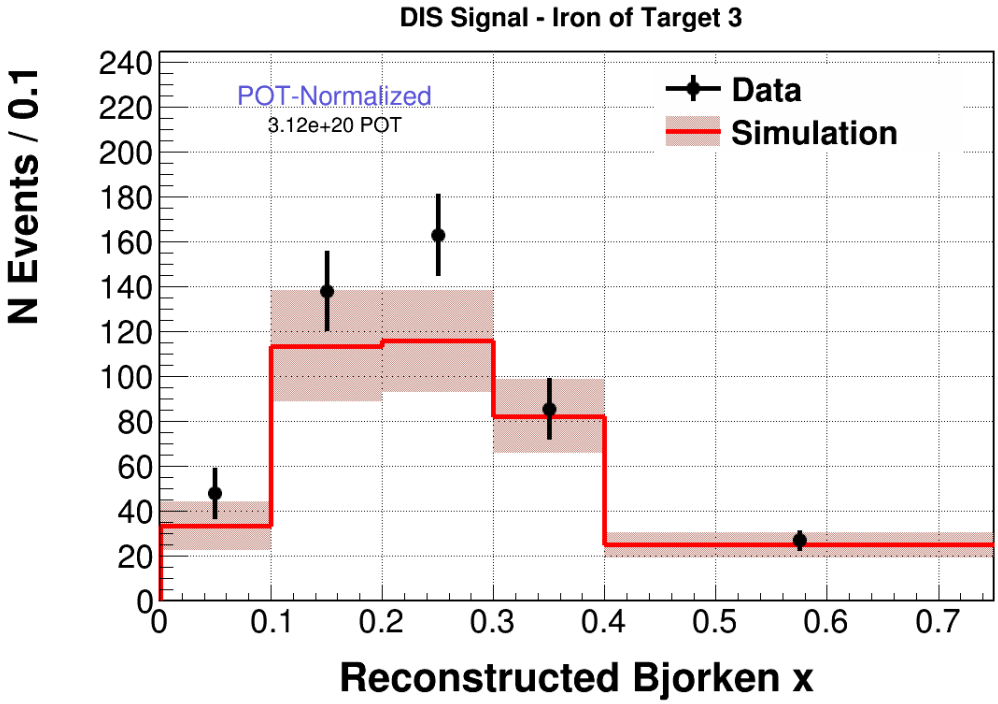

Figure E-244. DIS Signal: target 03 Fe (x_{bj})

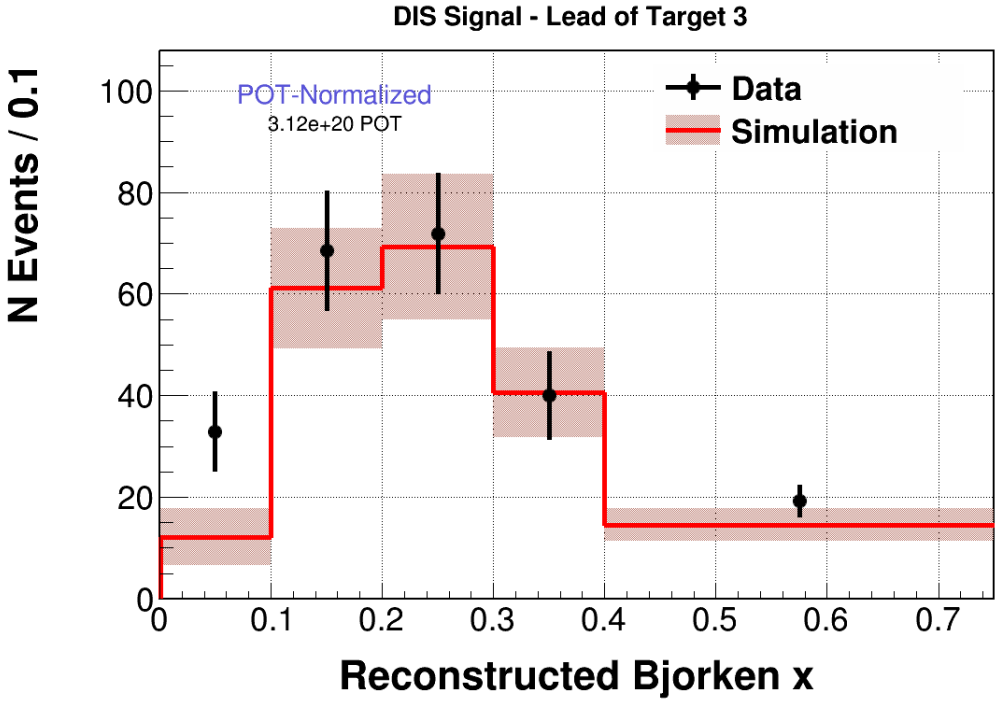

Figure E-245. DIS Signal: target 03 Pb (x_{bj})

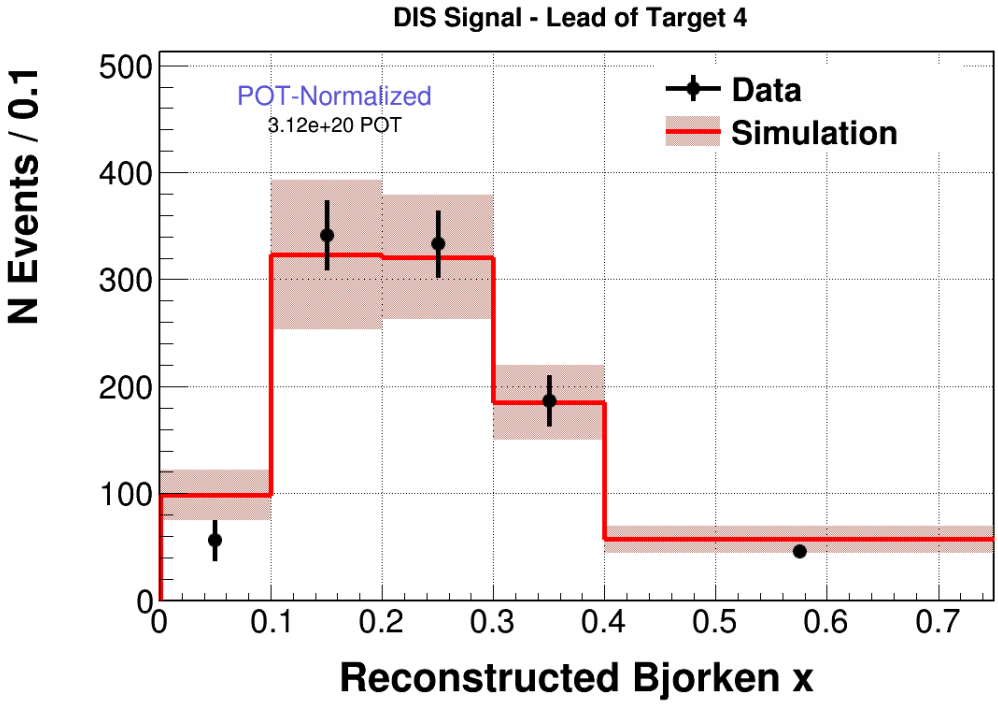

Figure E-246. DIS Signal: target 04 Pb (x_{bj})

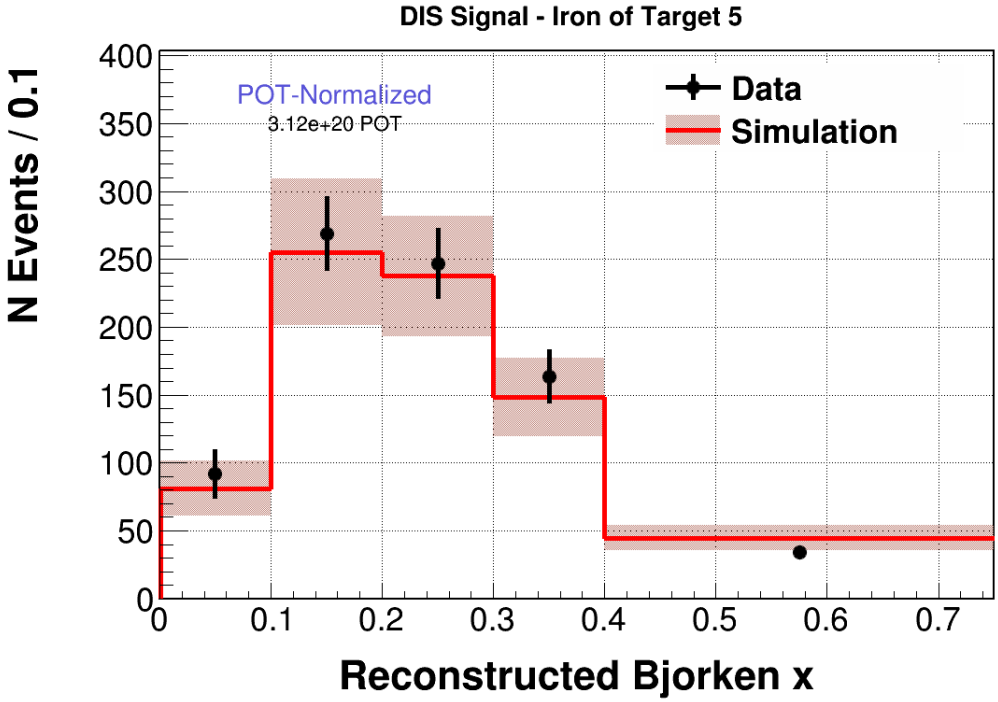

Figure E-247. DIS Signal: target 05 Fe (x_{bj})

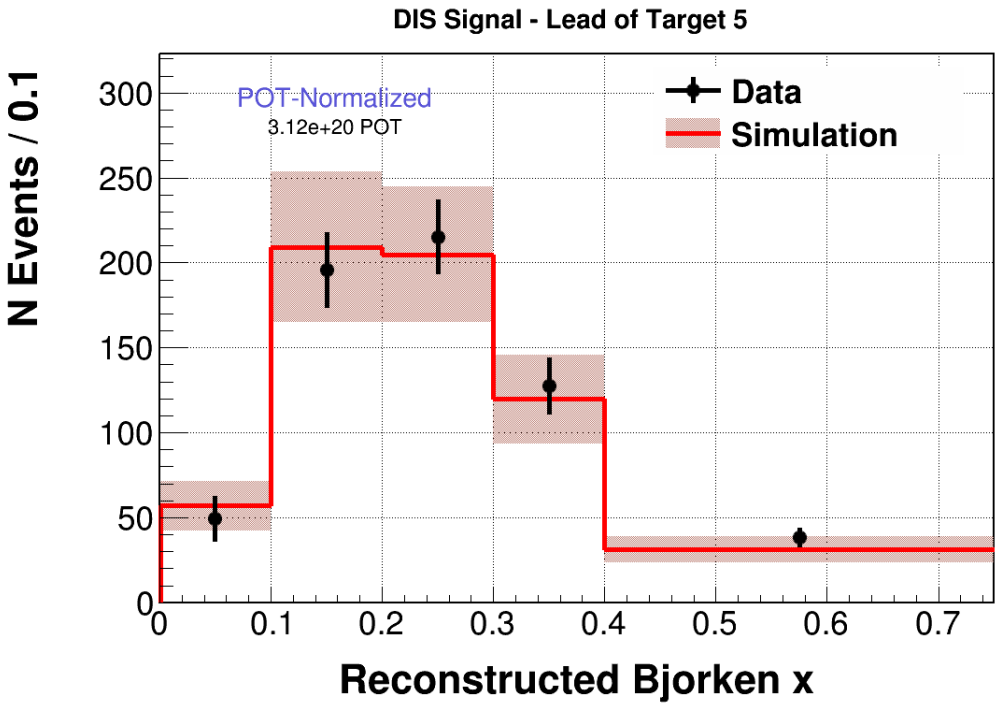

Figure E-248. DIS Signal: target 05 Pb (x_{bj})

E.4 Uncertainties on DIS Event Yield After CH Subtraction

The following plots show the uncertainty on the number of DIS events, after subtracting the non-DIS AND CH events. They are plotted as a function of neutrino energy (E_ν):

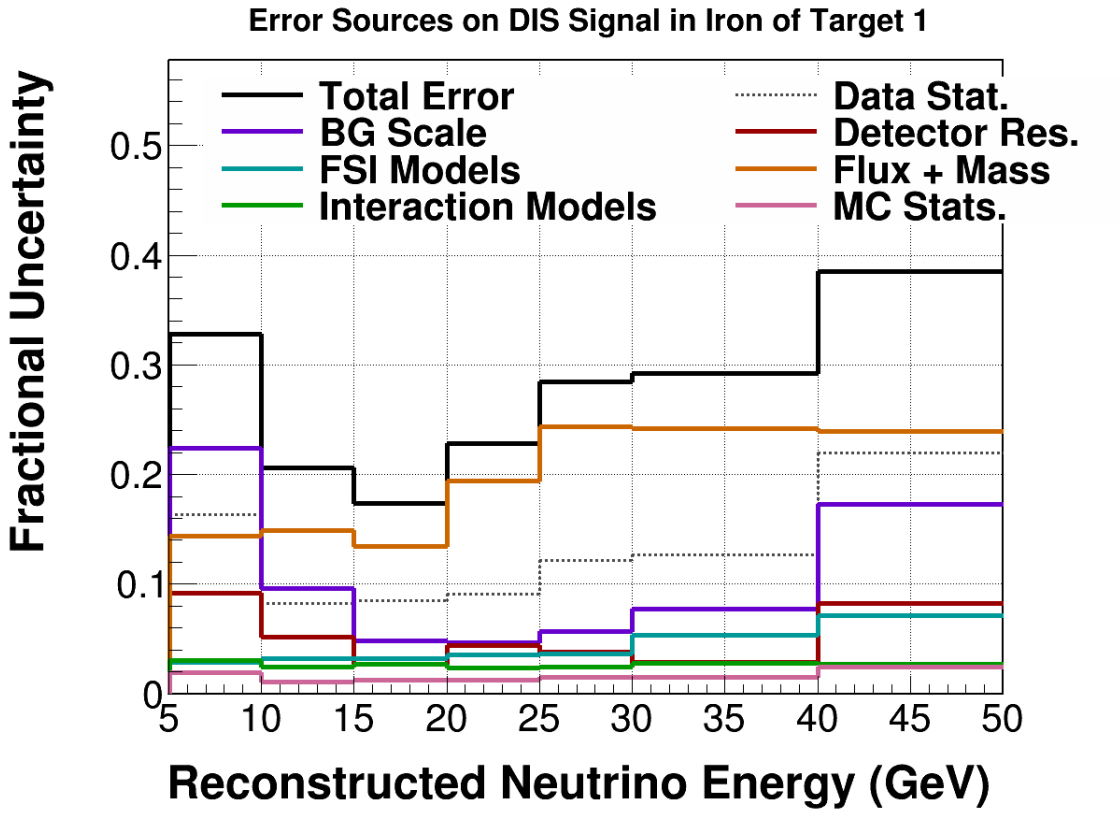

Figure E-249. Event yield uncertainties after CH subtraction: target 01 Fe (E_ν)

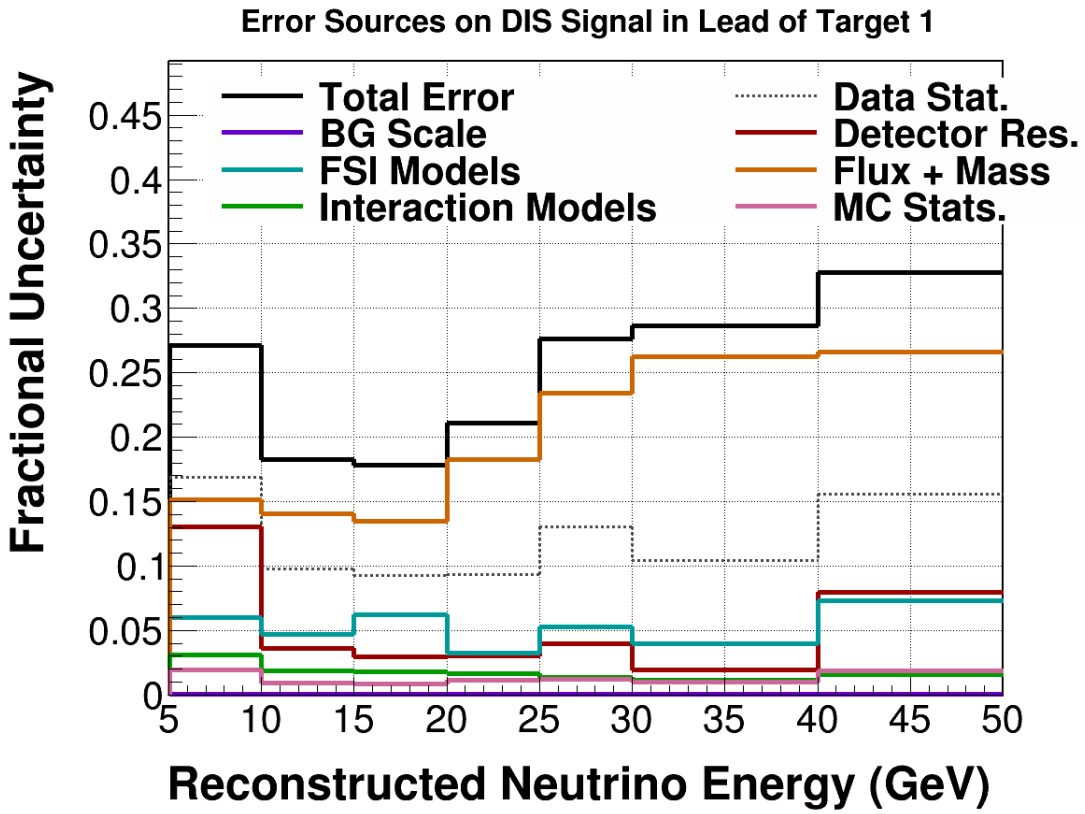

Figure E-250. Event yield uncertainties after CH subtraction: target 01 Pb (E_ν)

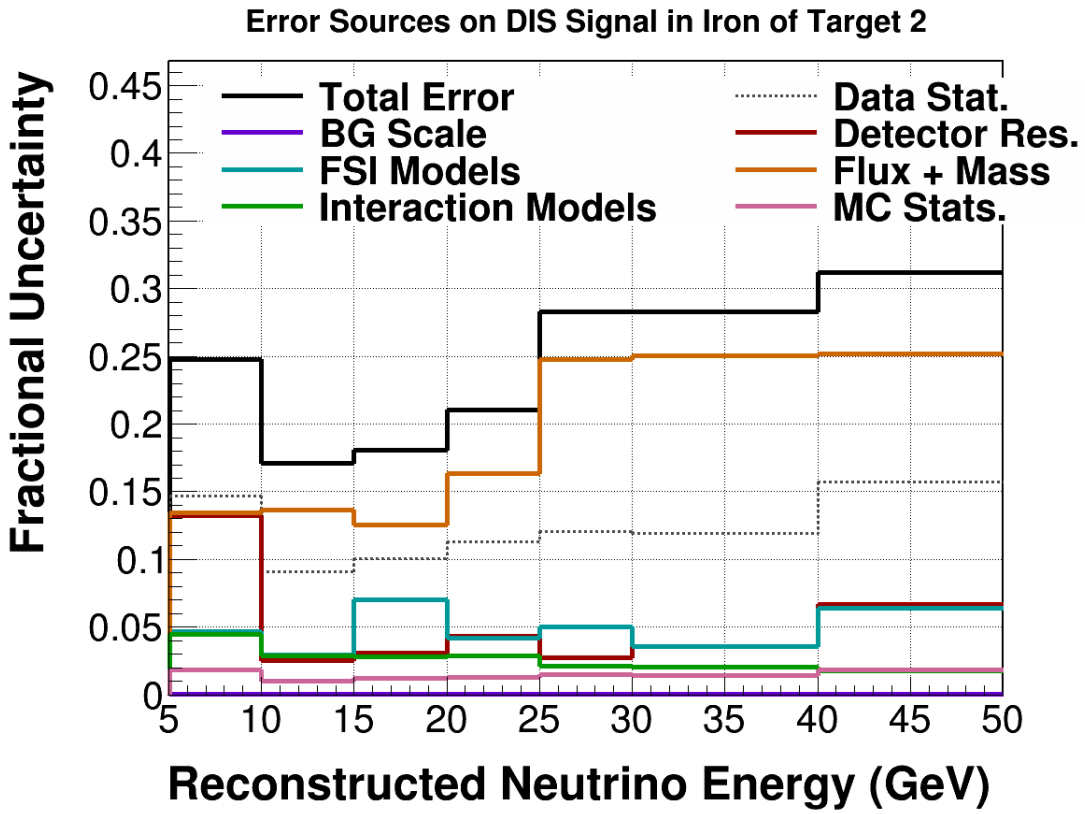

Figure E-251. Event yield uncertainties after CH subtraction: target 02 Fe (E_ν)

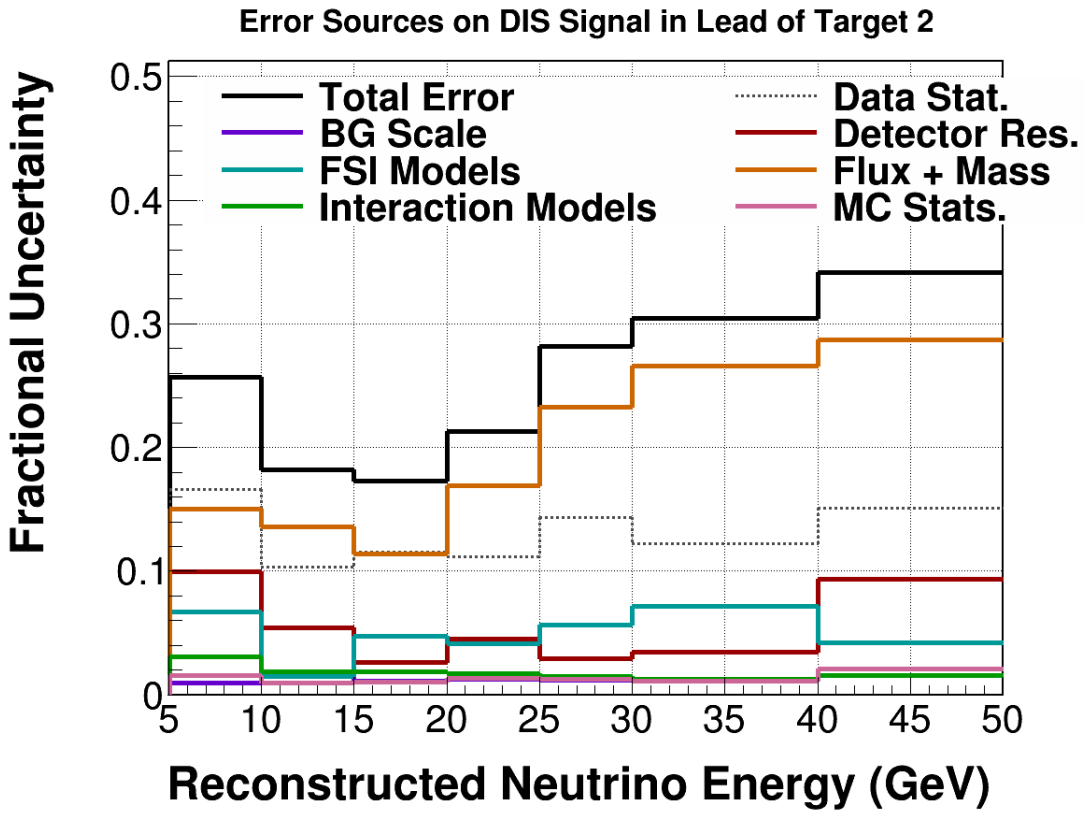

Figure E-252. Event yield uncertainties after CH subtraction: target 02 Pb (E_ν)

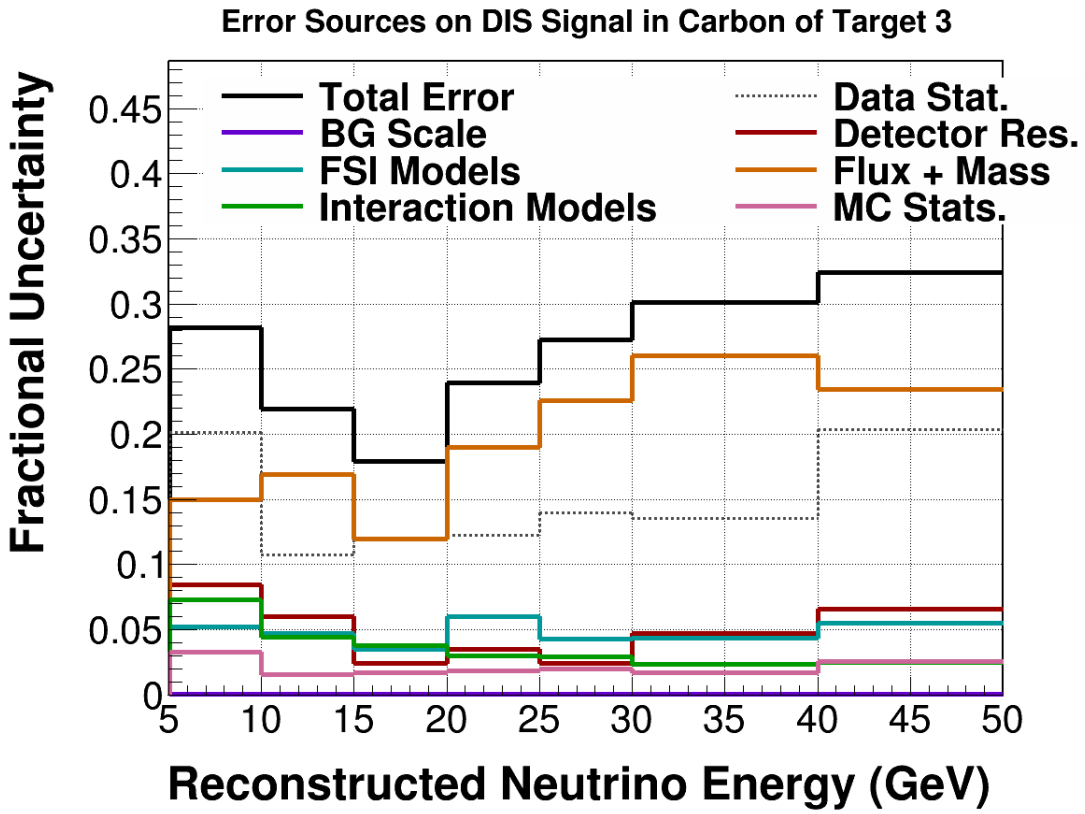

Figure E-253. Event yield uncertainties after CH subtraction: target 03 C (E_ν)

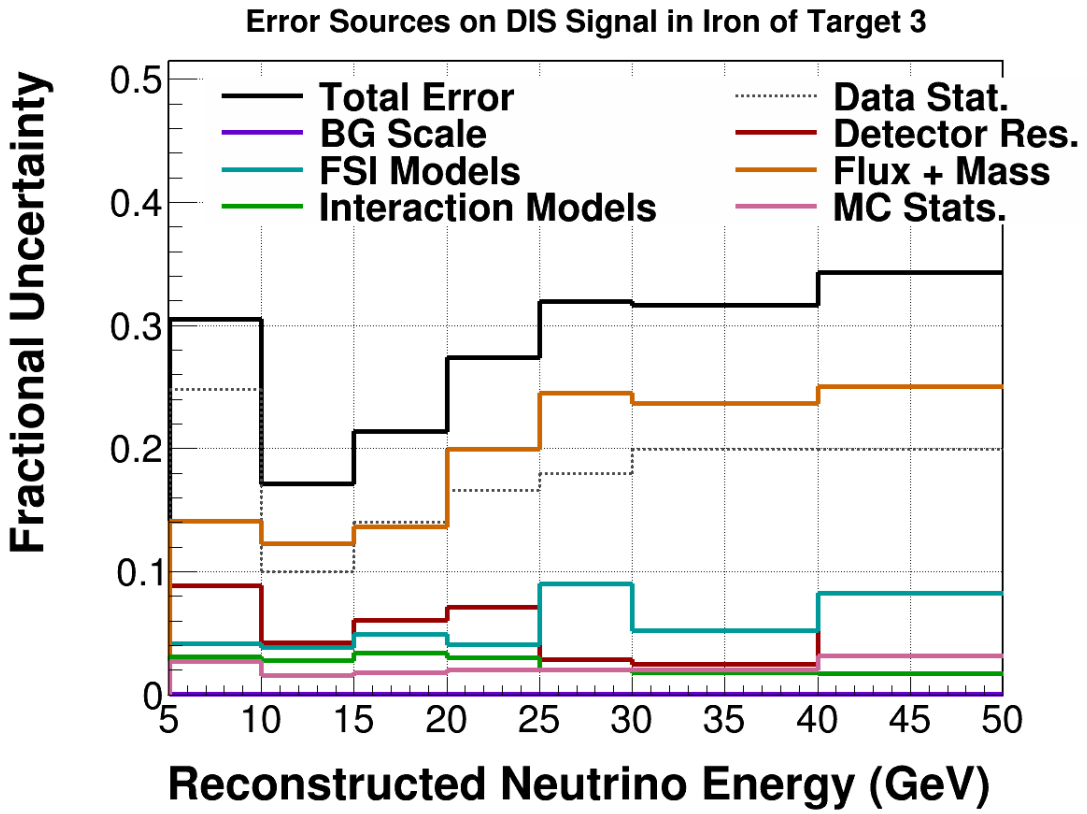

Figure E-254. Event yield uncertainties after CH subtraction: target 03 Fe (E_ν)

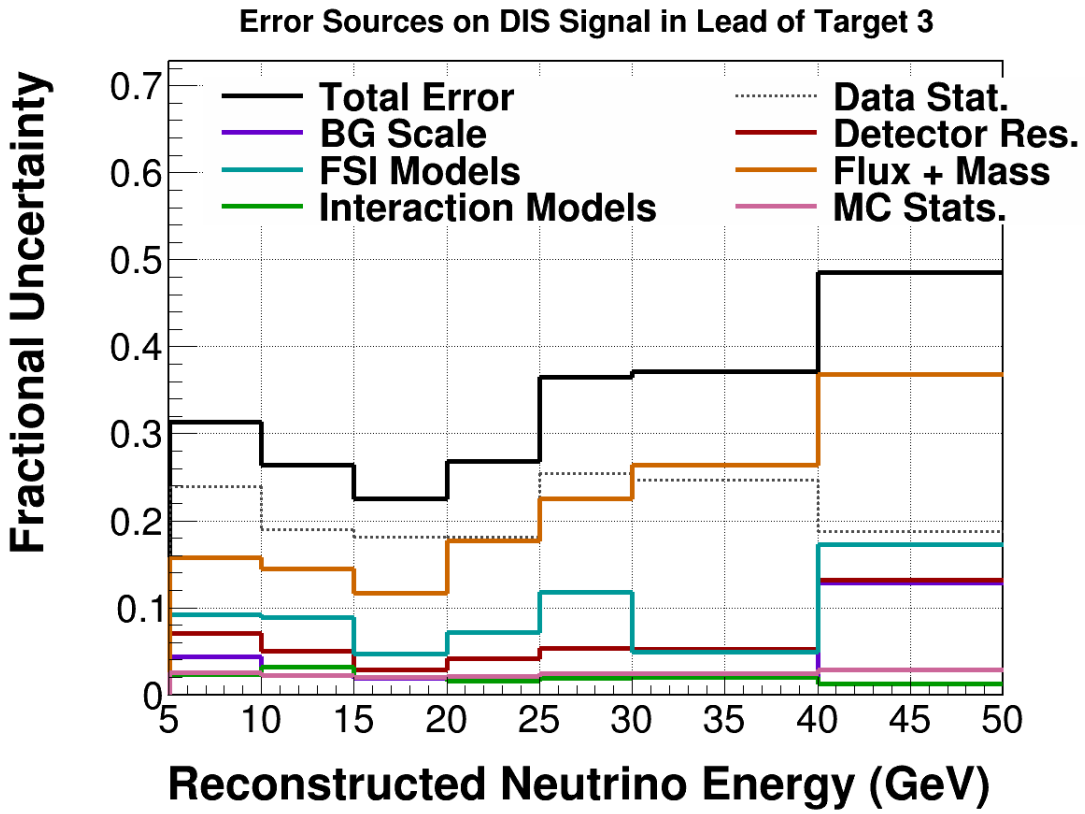

Figure E-255. Event yield uncertainties after CH subtraction: target 03 Pb (E_ν)

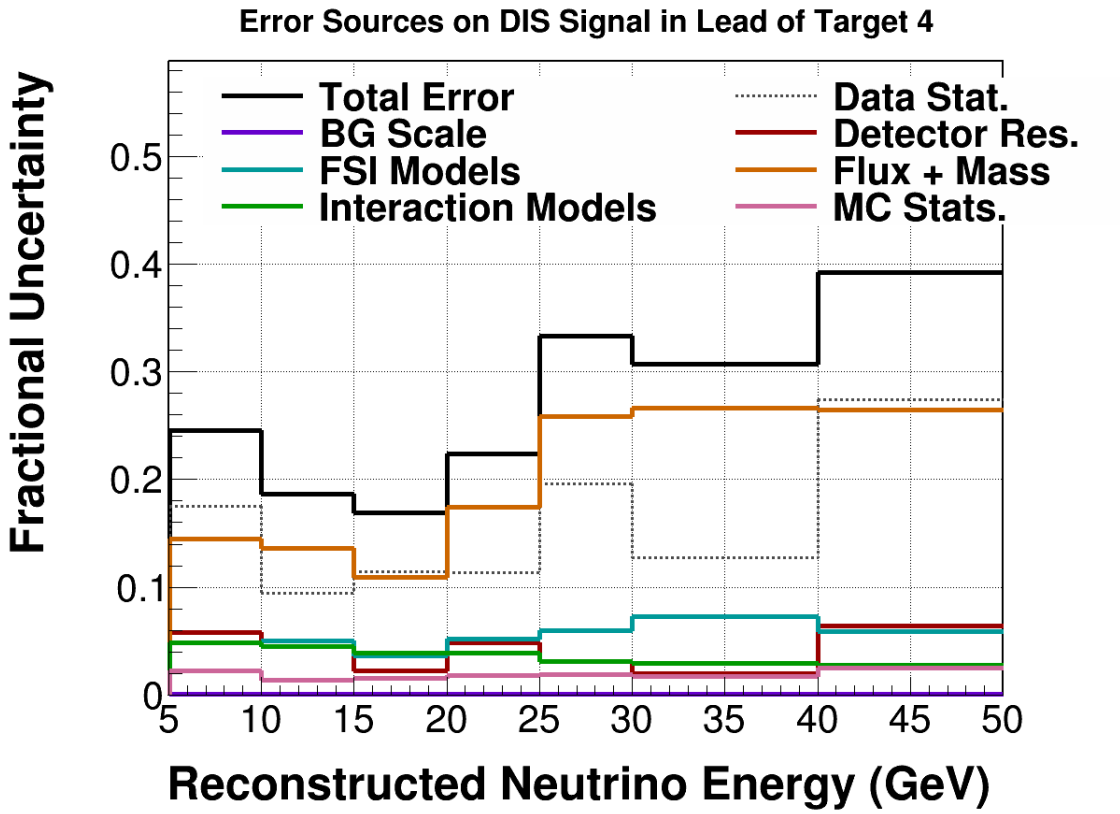

Figure E-256. Event yield uncertainties after CH subtraction: target 04 Pb (E_ν)

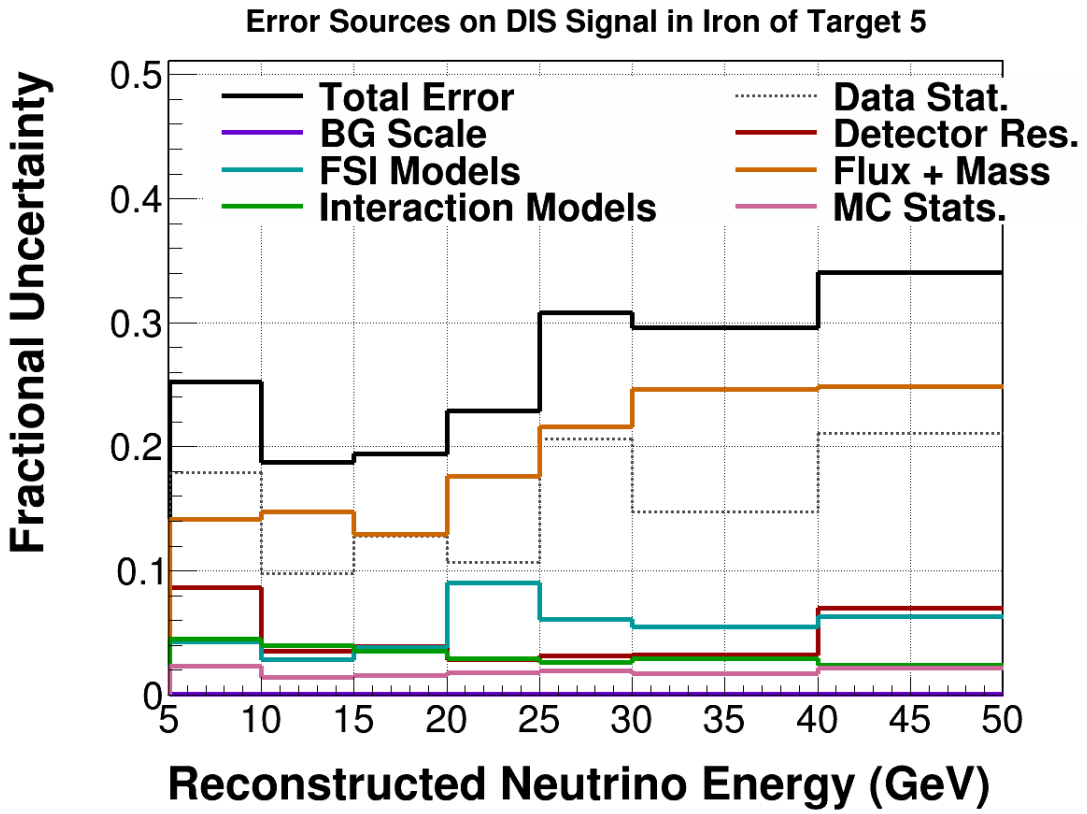

Figure E-257. Event yield uncertainties after CH subtraction: target 05 Fe (E_ν)

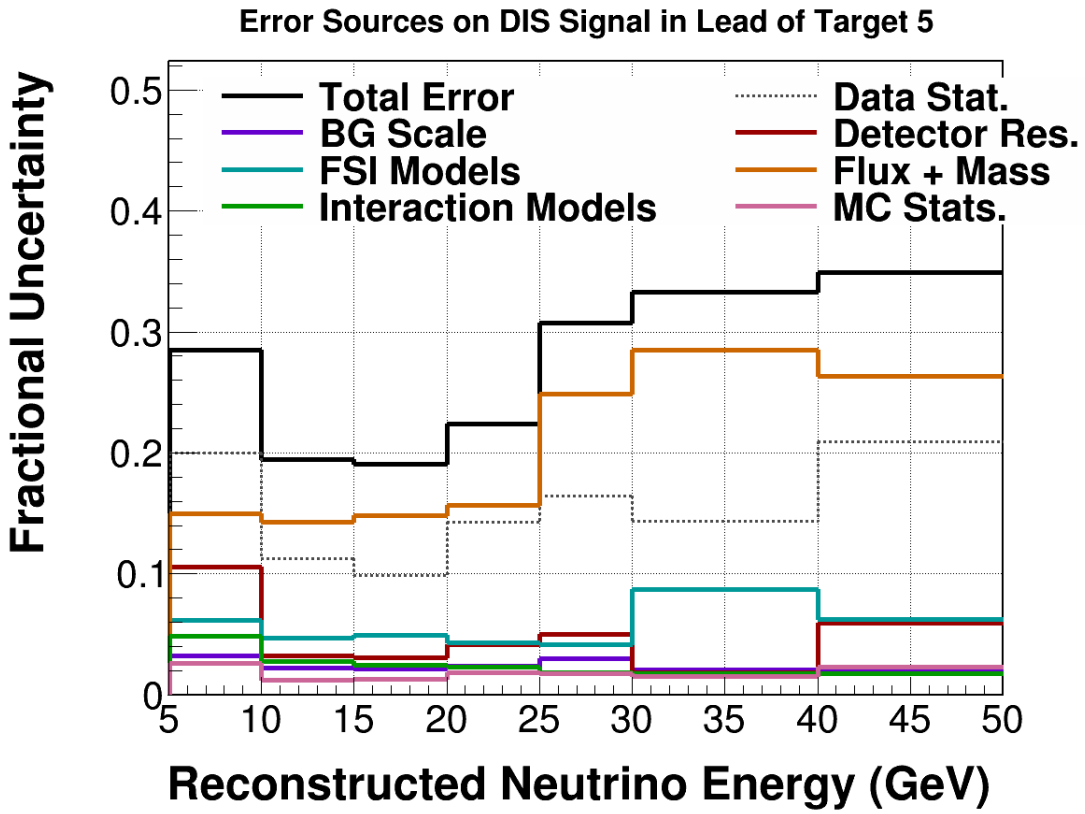

Figure E-258. Event yield uncertainties after CH subtraction: target 05 Pb (E_ν)

The following plots show the uncertainty on the number of DIS events, after subtracting the non-DIS AND CH events. They are plotted as a function of Bjorken-x (x_{bj}):

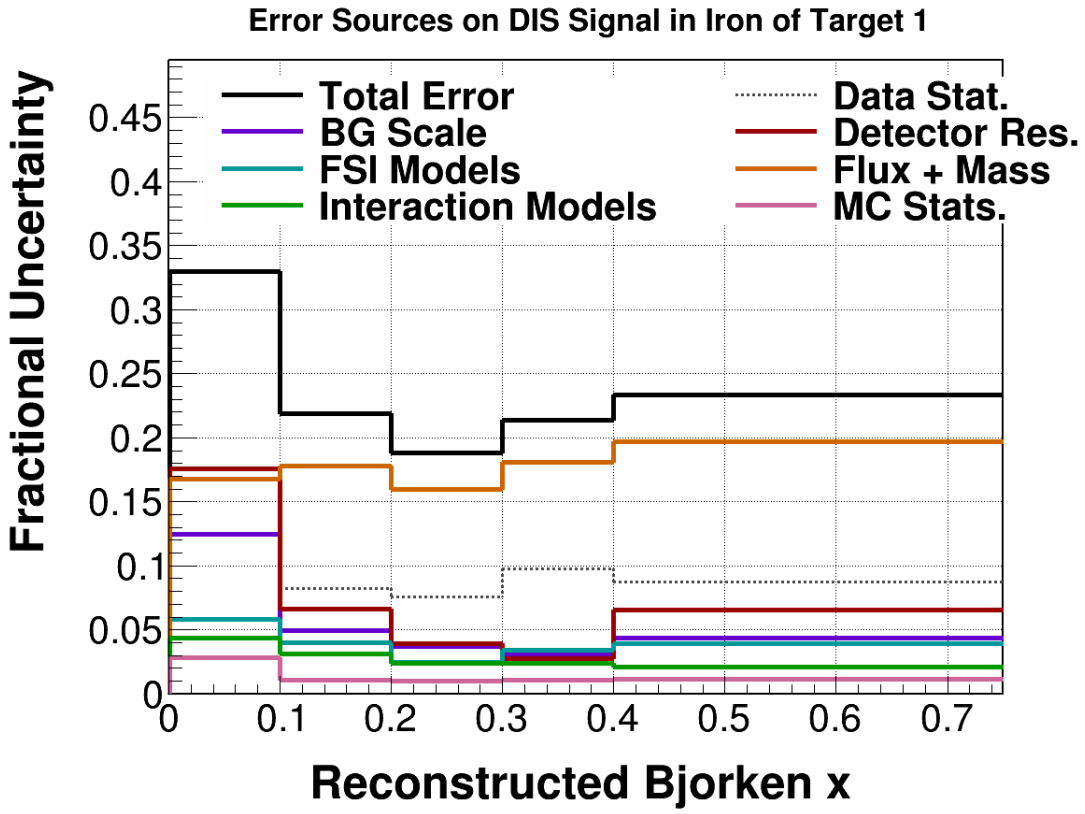

Figure E-259. Event yield uncertainties after CH subtraction: target 01 Fe (x_{bj})

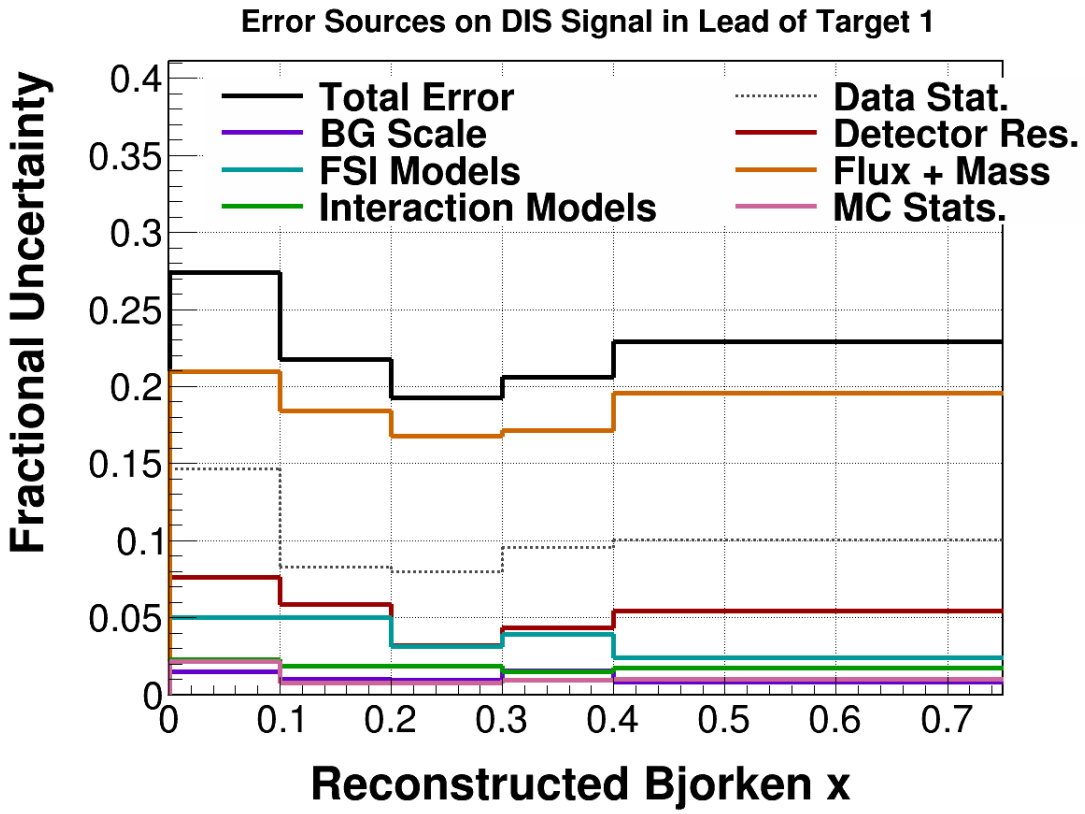

Figure E-260. Event yield uncertainties after CH subtraction: target 01 Pb (x_{bj})

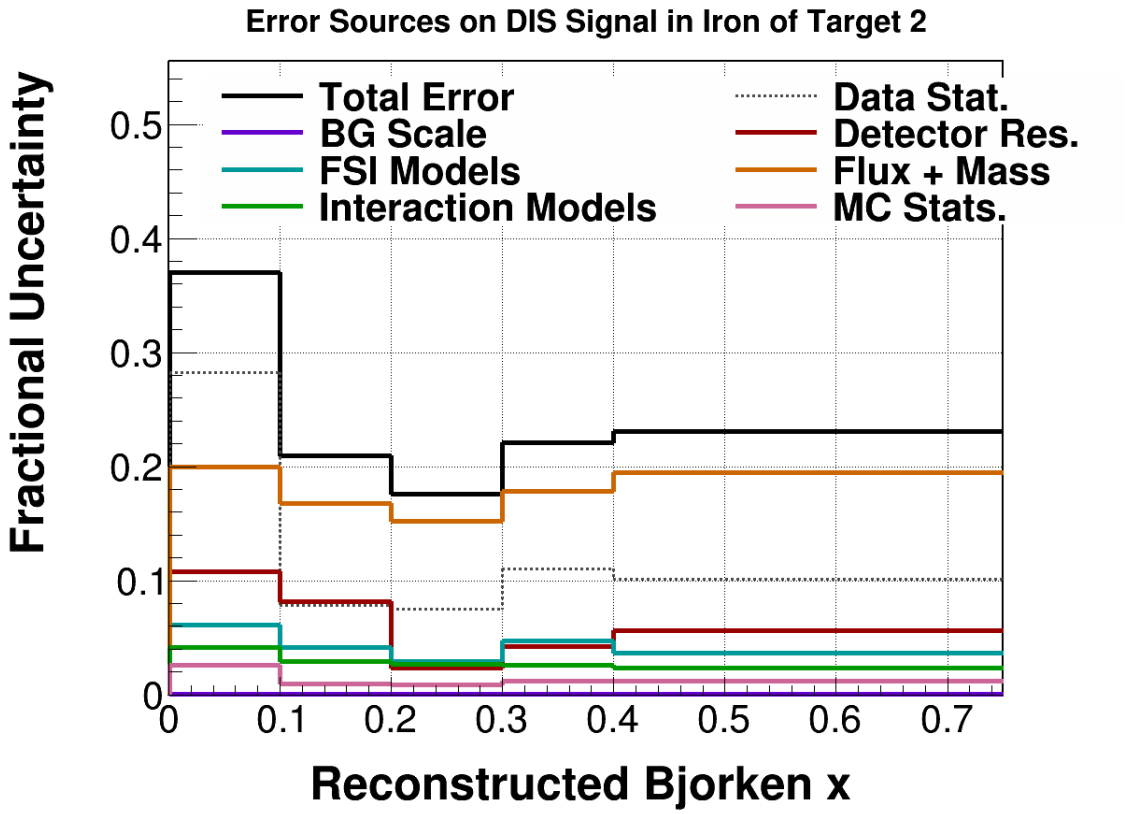

Figure E-261. Event yield uncertainties after CH subtraction: target 02 Fe (x_{bj})

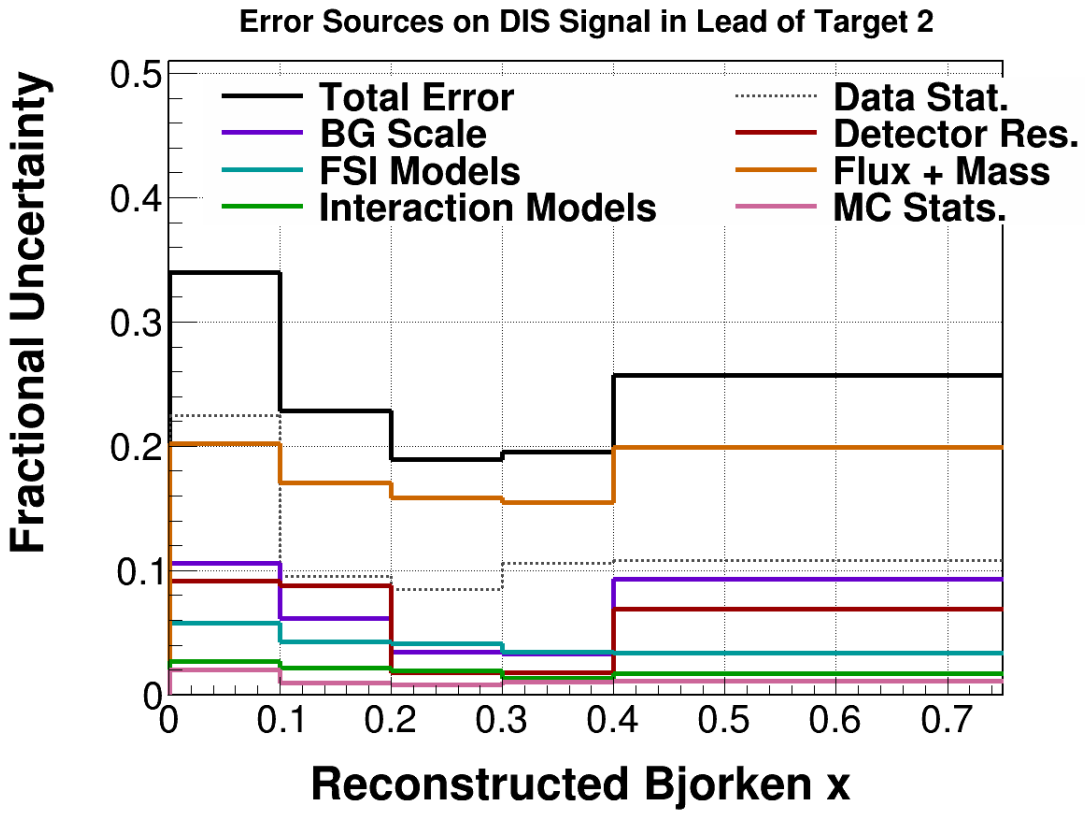

Figure E-262. Event yield uncertainties after CH subtraction: target 02 Pb (x_{bj})

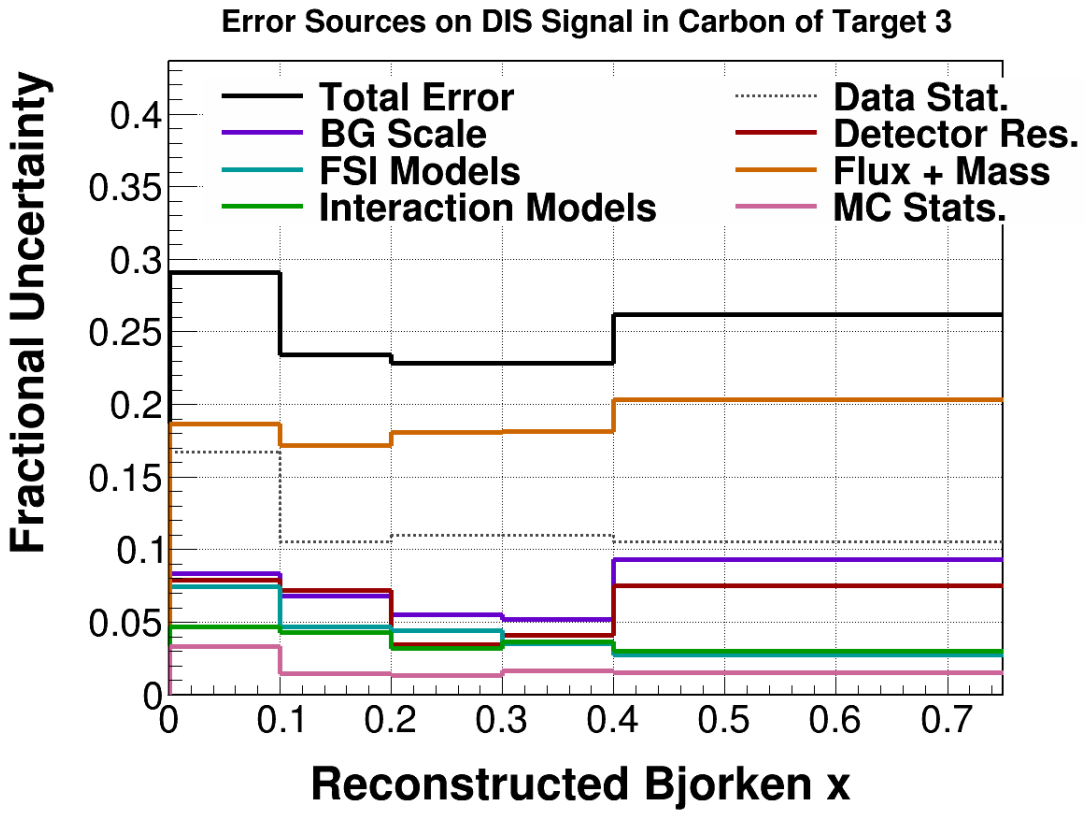

Figure E-263. Event yield uncertainties after CH subtraction: target 03 C (x_{bj})

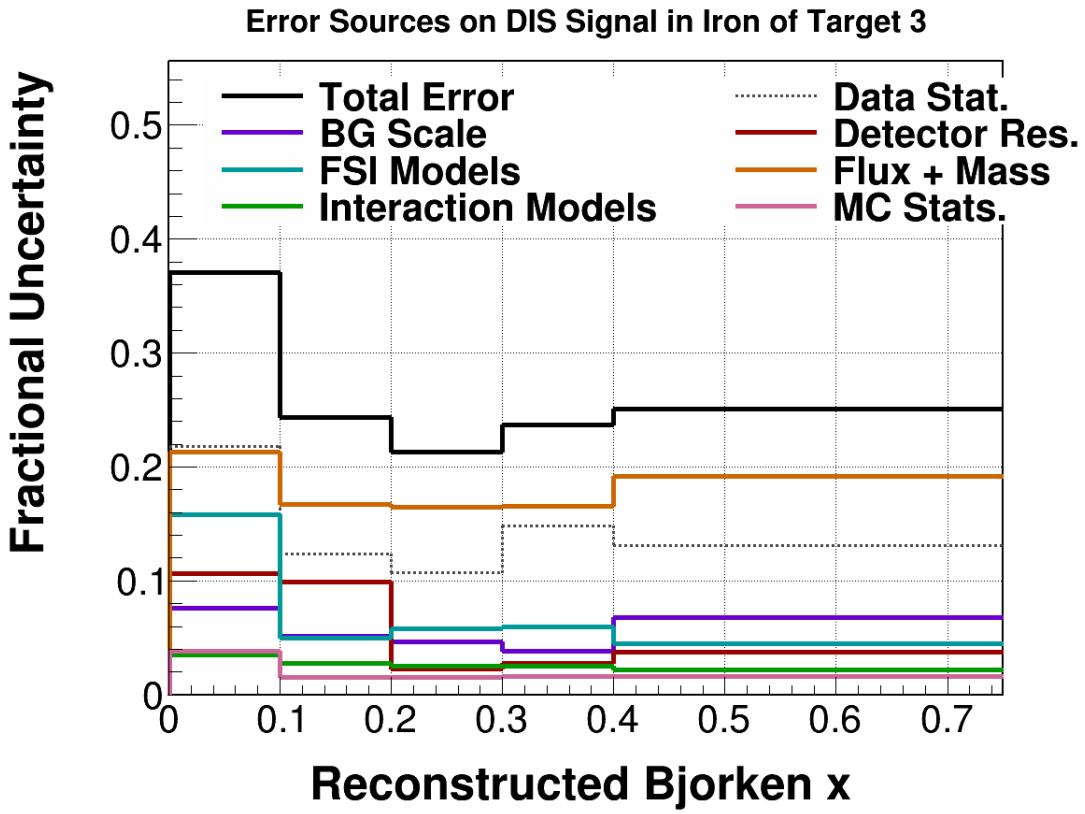

Figure E-264. Event yield uncertainties after CH subtraction: target 03 Fe (x_{bj})

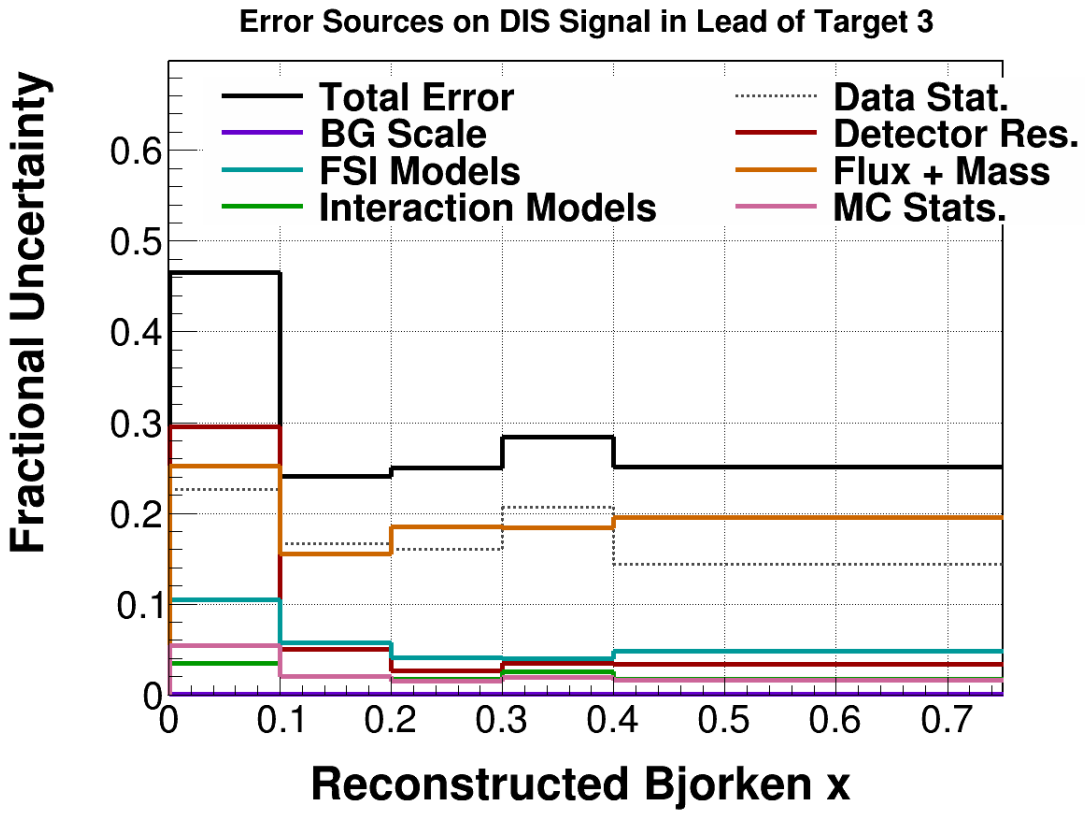

Figure E-265. Event yield uncertainties after CH subtraction: target 03 Pb (x_{bj})

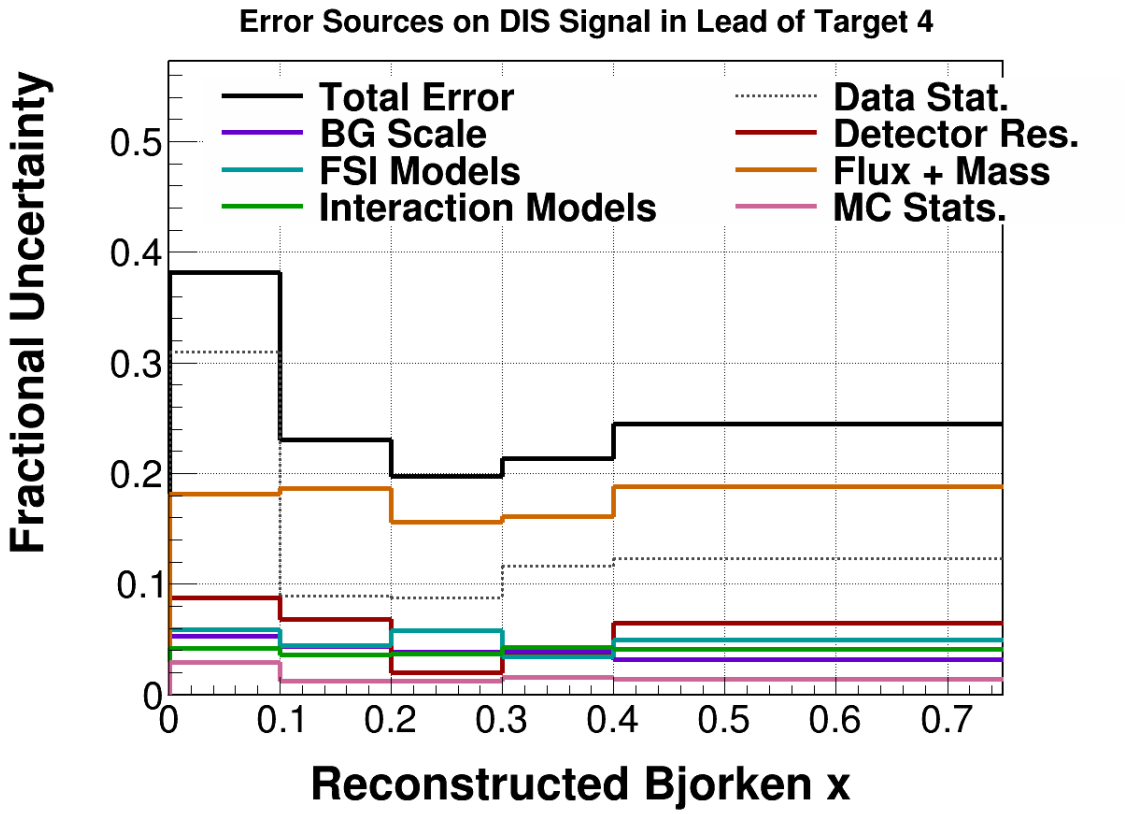

Figure E-266. Event yield uncertainties after CH subtraction: target 04 Pb (x_{bj})

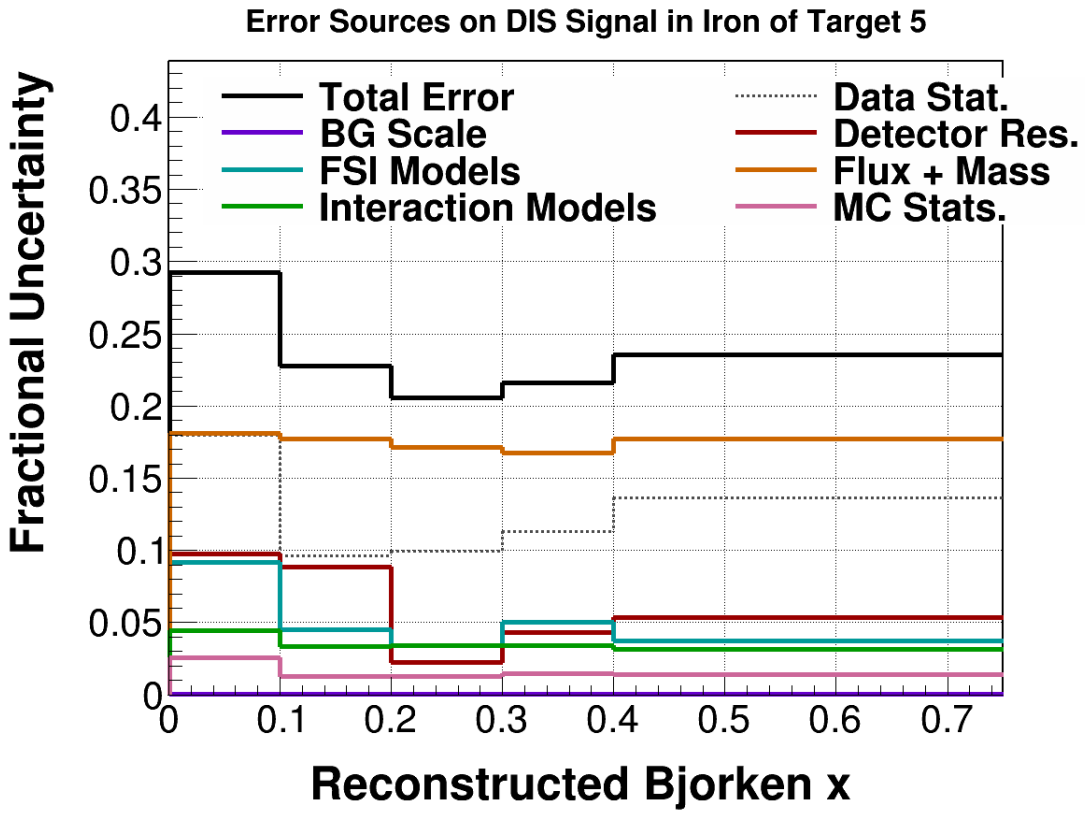

Figure E-267. Event yield uncertainties after CH subtraction: target 05 Fe (x_{bj})

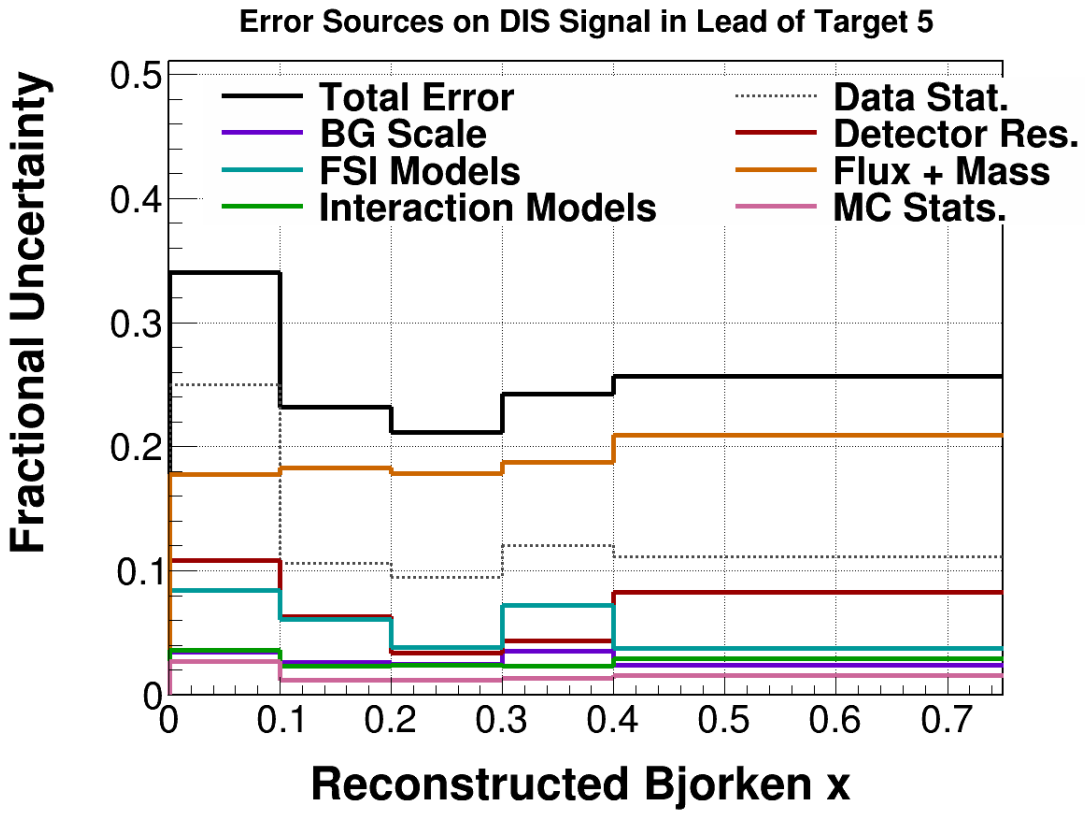

Figure E-268. Event yield uncertainties after CH subtraction: target 05 Pb (x_{bj})

APPENDIX F
DIS EVENT YIELDS (UNFOLDED KINEMATICS)

F.1 DIS Event Yields (Unfolded)

The following plots show the DIS events in data and MC, after subtracting the non-DIS AND CH events. They are plotted as a function of *unfolded* neutrino energy (E_ν):

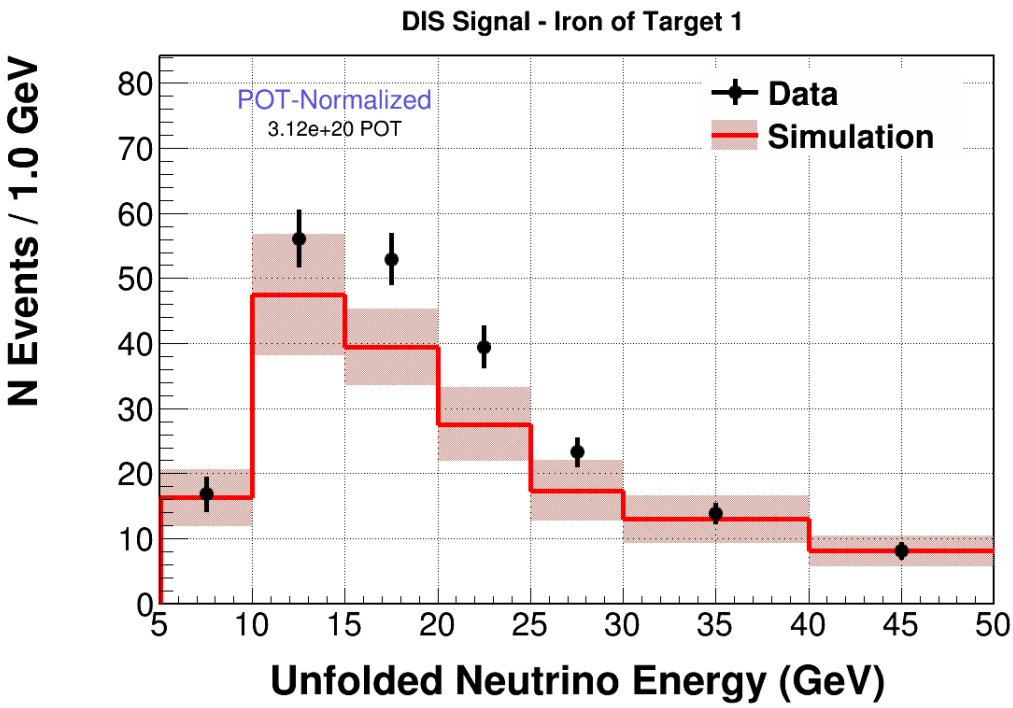

Figure F-1. Unfolded DIS Signal: target 01 Fe (E_ν)

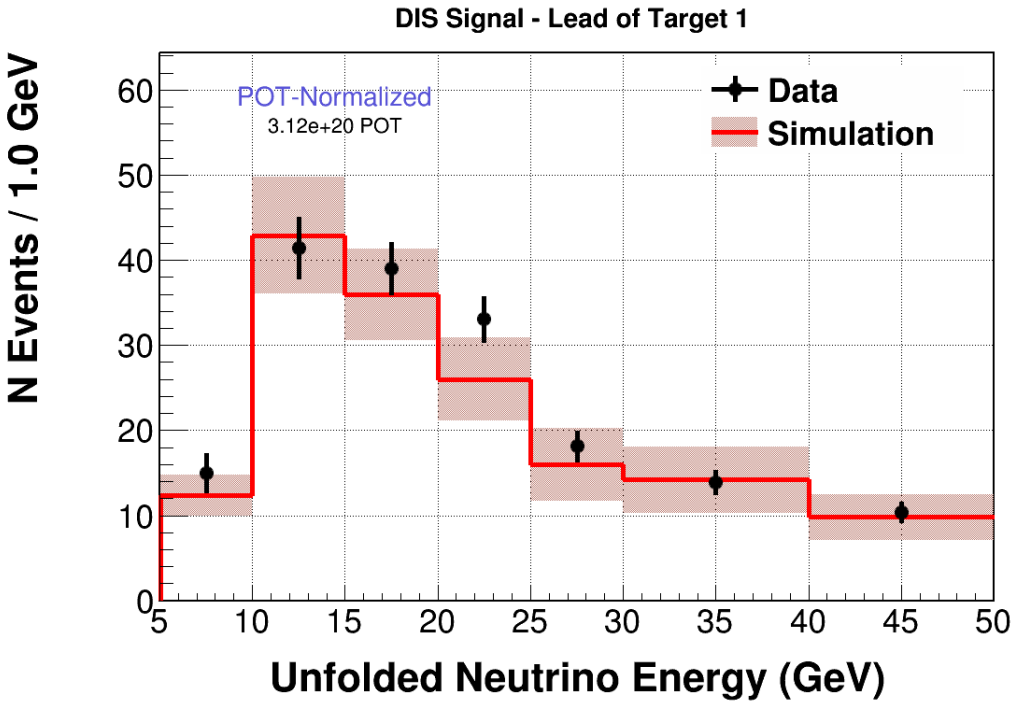

Figure F-2. Unfolded DIS Signal: target 01 Pb (E_ν)

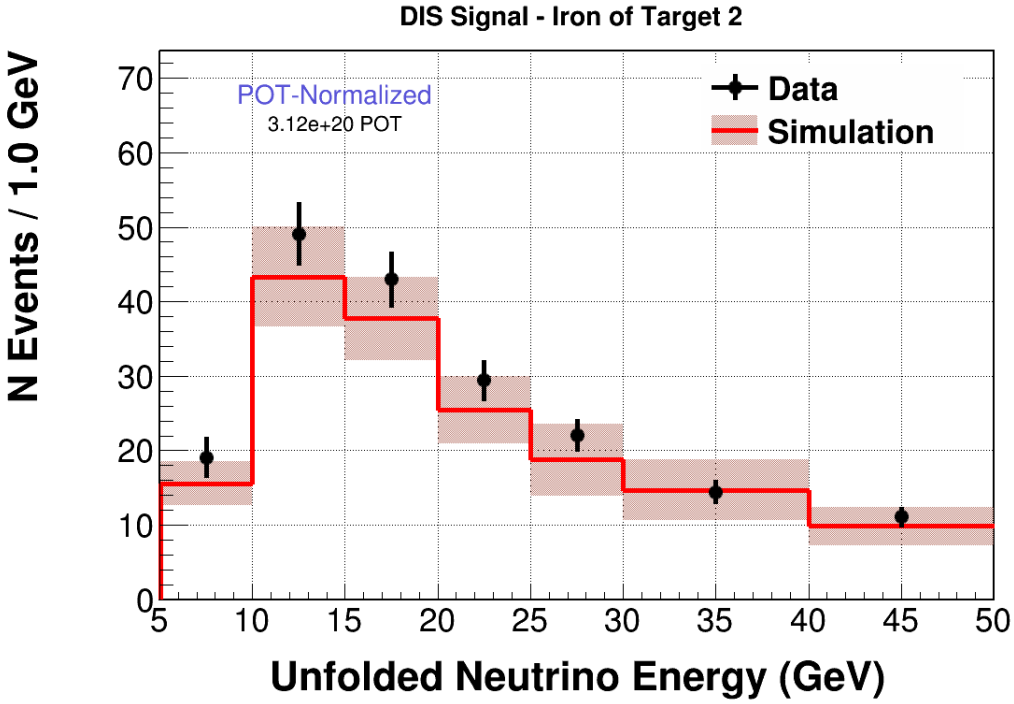

Figure F-3. Unfolded DIS Signal: target 02 Fe (E_ν)

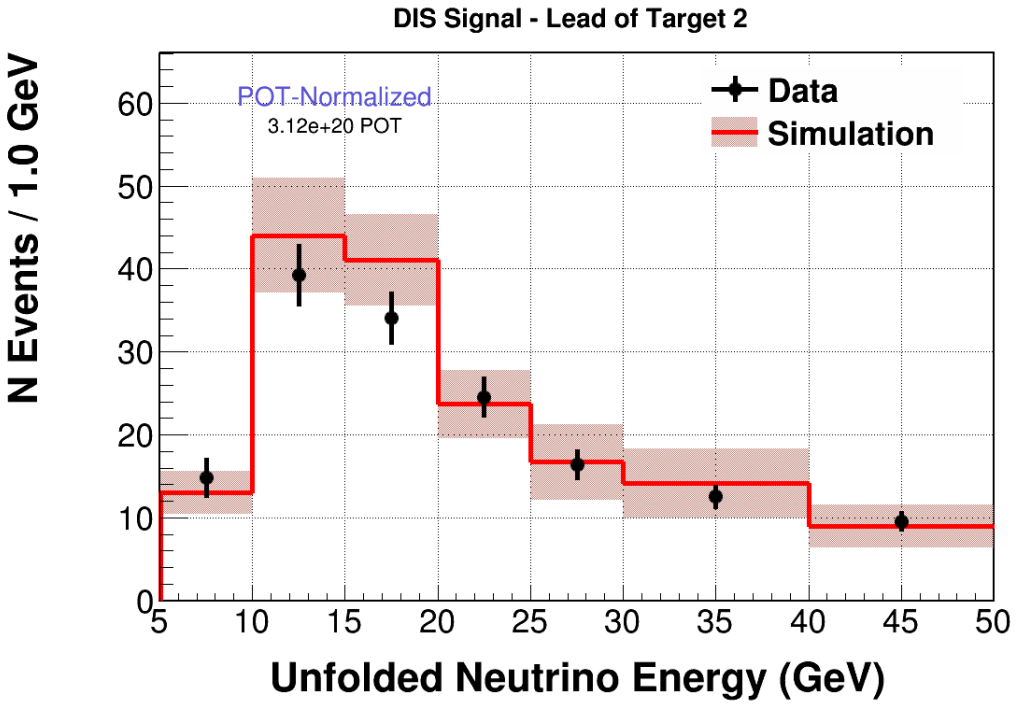

Figure F-4. Unfolded DIS Signal: target 02 Pb (E_ν)

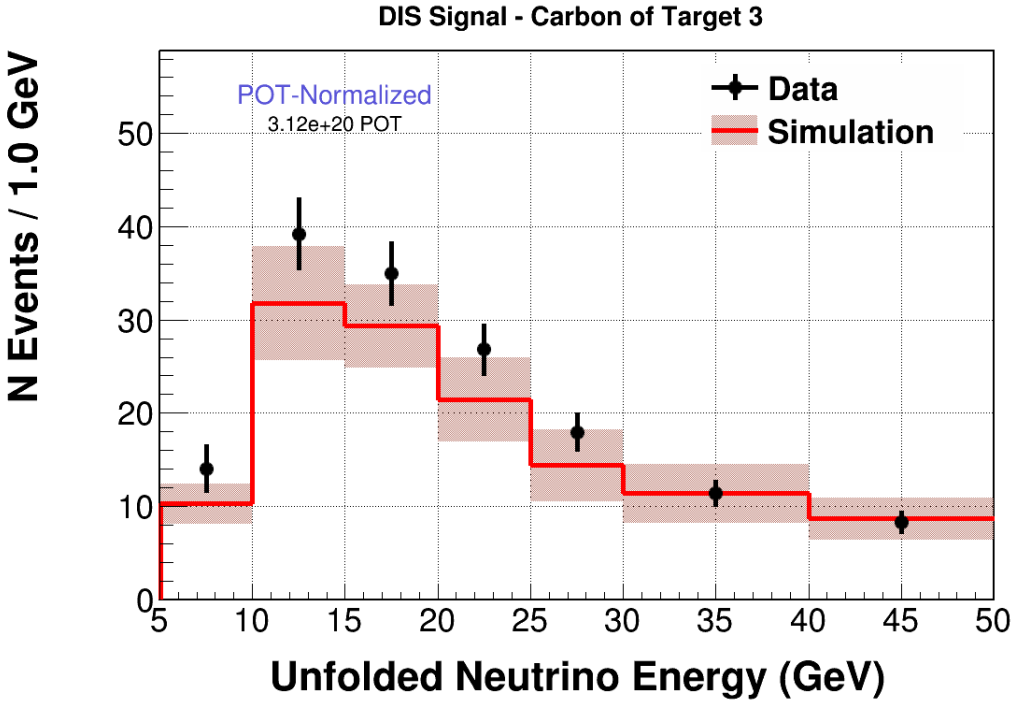

Figure F-5. Unfolded DIS Signal: target 03 C (E_ν)

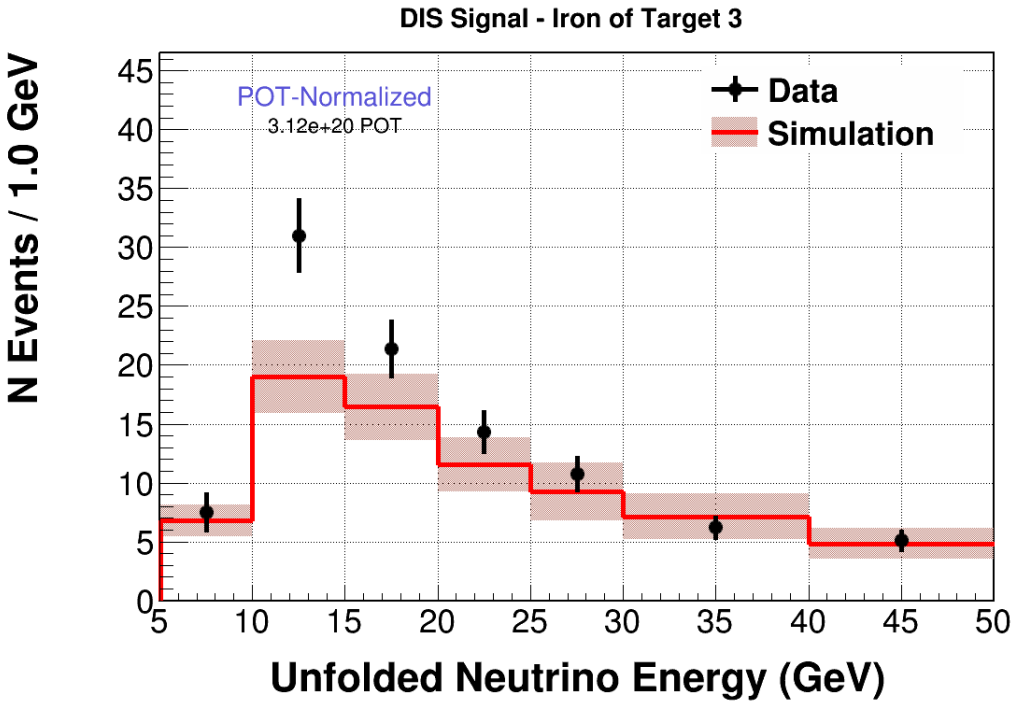

Figure F-6. Unfolded DIS Signal: target 03 Fe (E_ν)

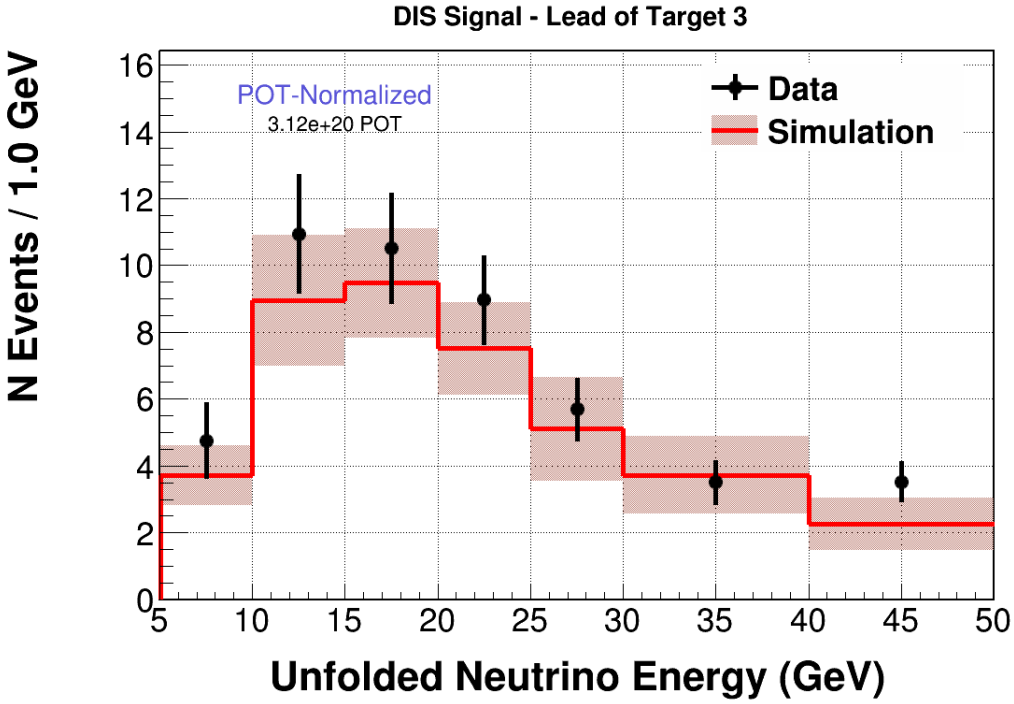

Figure F-7. Unfolded DIS Signal: target 03 Pb (E_ν)

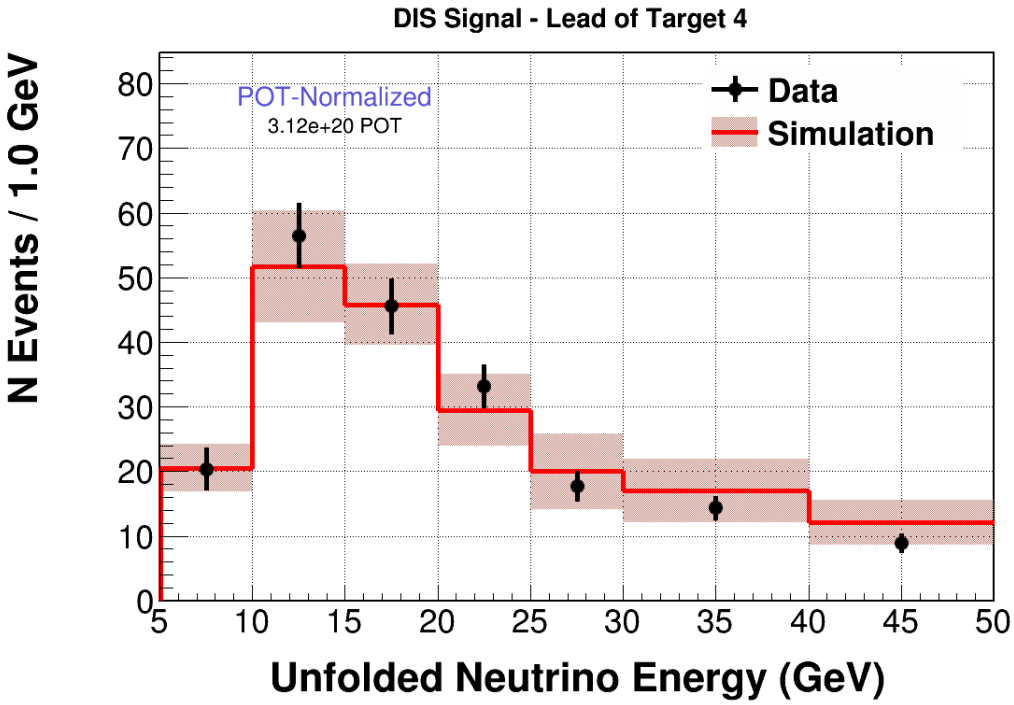

Figure F-8. Unfolded DIS Signal: target 04 Pb (E_ν)

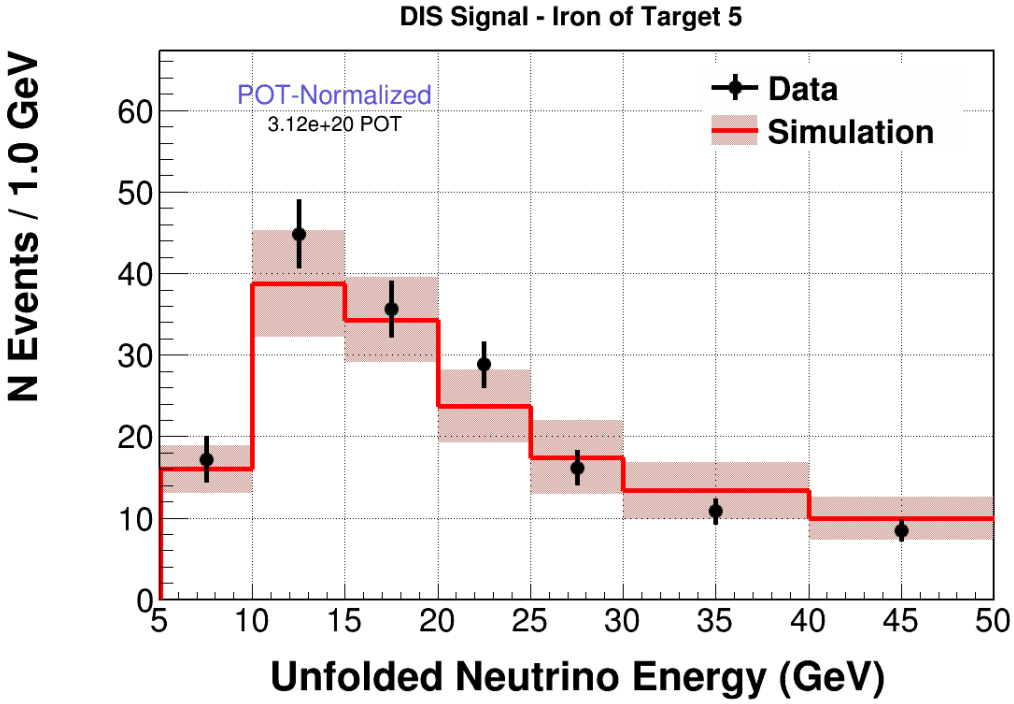

Figure F-9. Unfolded DIS Signal: target 05 Fe (E_ν)

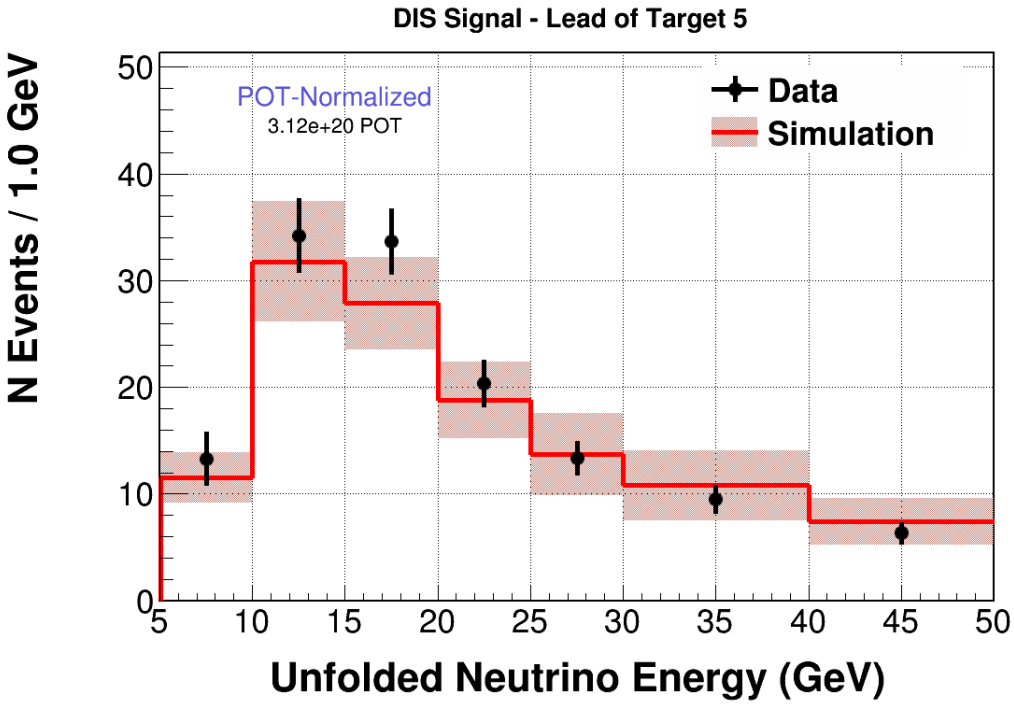

Figure F-10. Unfolded DIS Signal: target 05 Pb (E_ν)

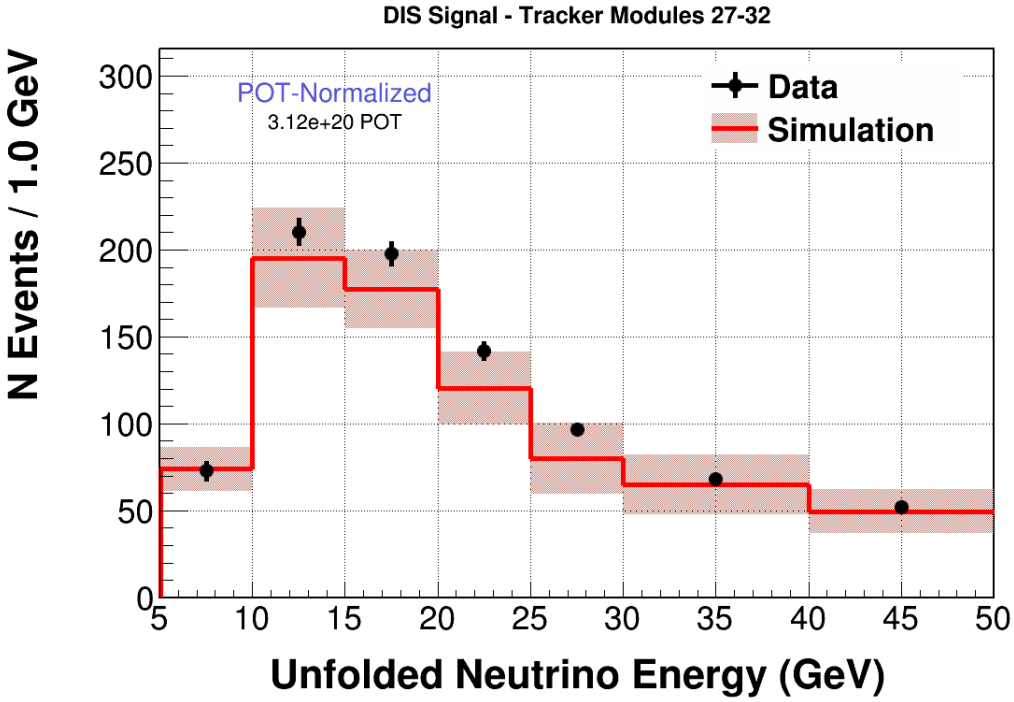

Figure F-11. Unfolded DIS Signal: tracker mods. 27-32 (E_ν)

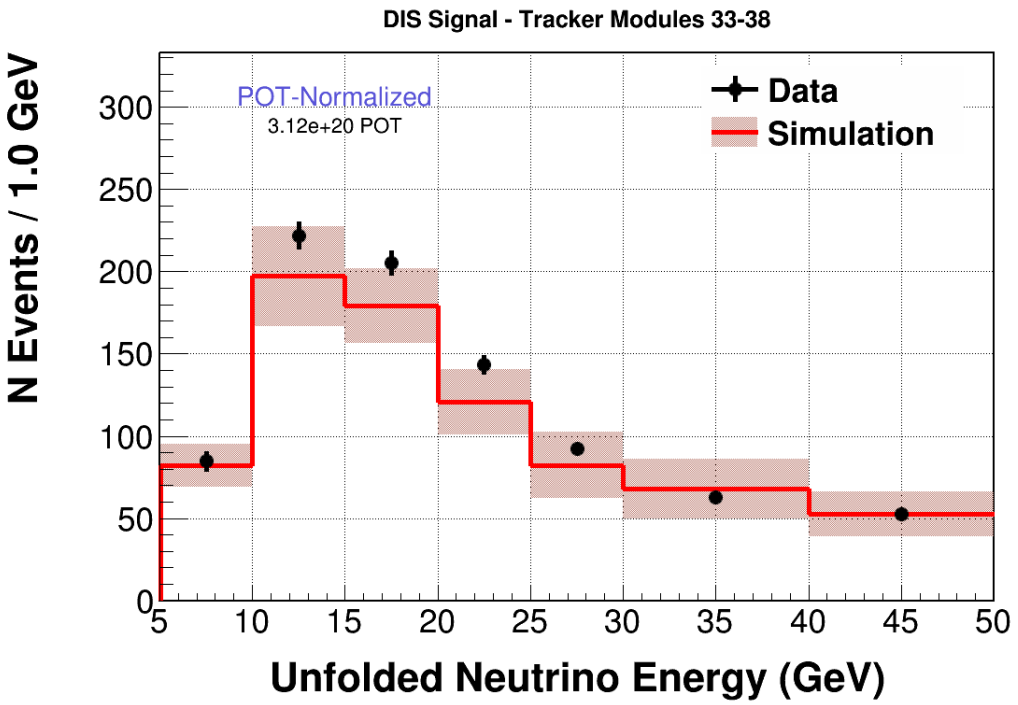

Figure F-12. Unfolded DIS Signal: tracker mods. 33-38 (E_ν)

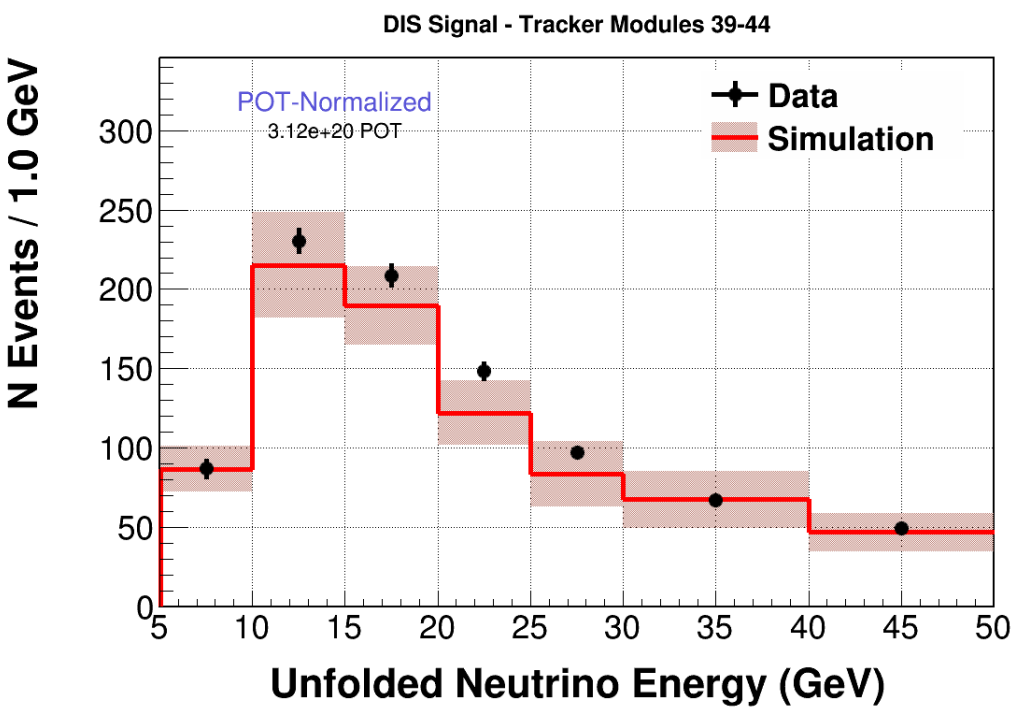

Figure F-13. Unfolded DIS Signal: tracker mods. 39-44 (E_ν)

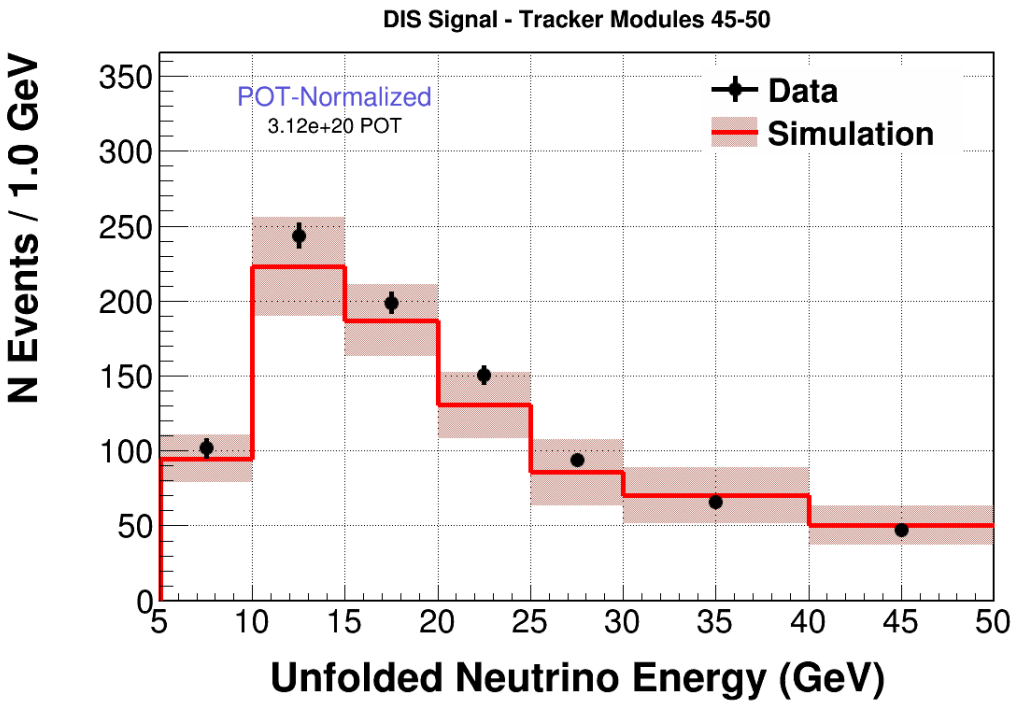

Figure F-14. Unfolded DIS Signal: tracker mods. 45-50 (E_ν)

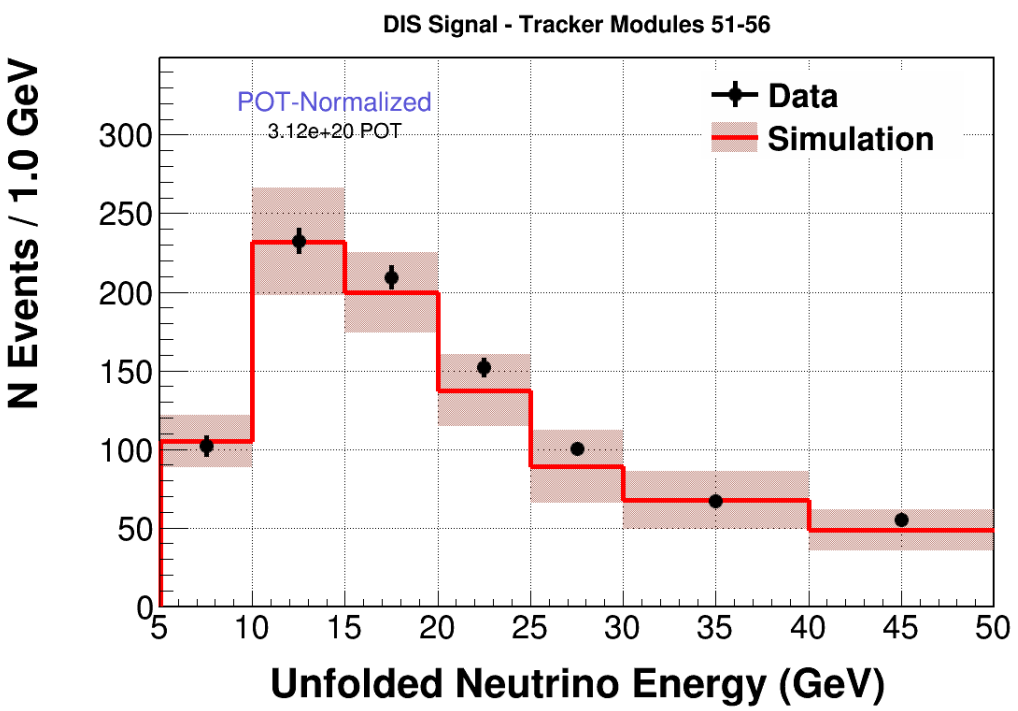

Figure F-15. Unfolded DIS Signal: tracker mods. 51-56 (E_ν)

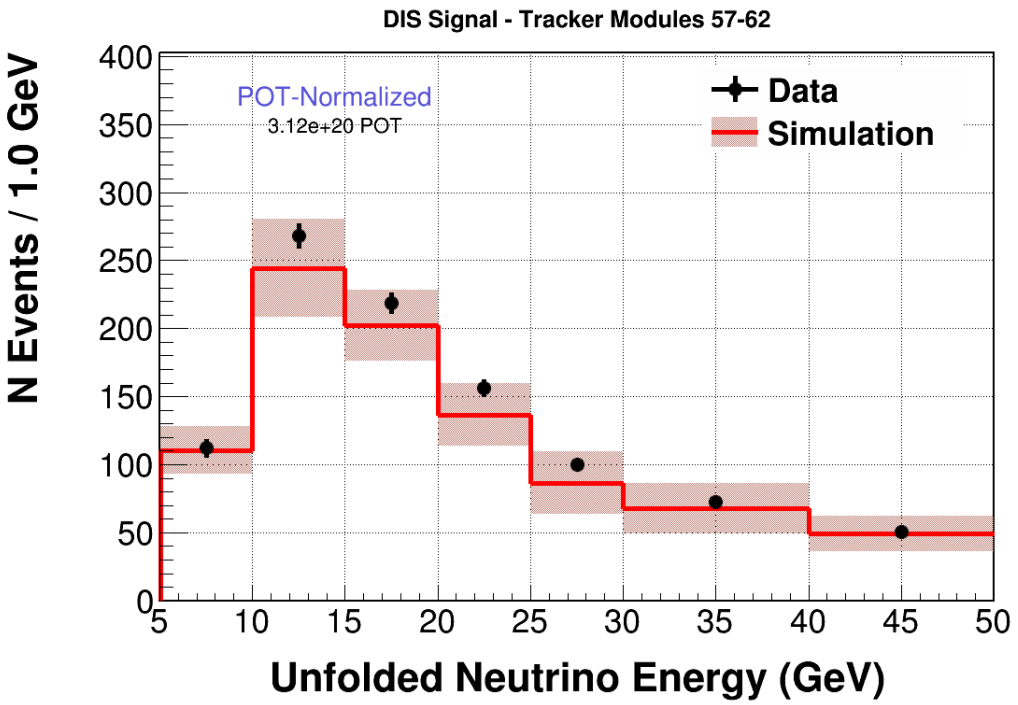

Figure F-16. Unfolded DIS Signal: tracker mods. 57-62 (E_ν)

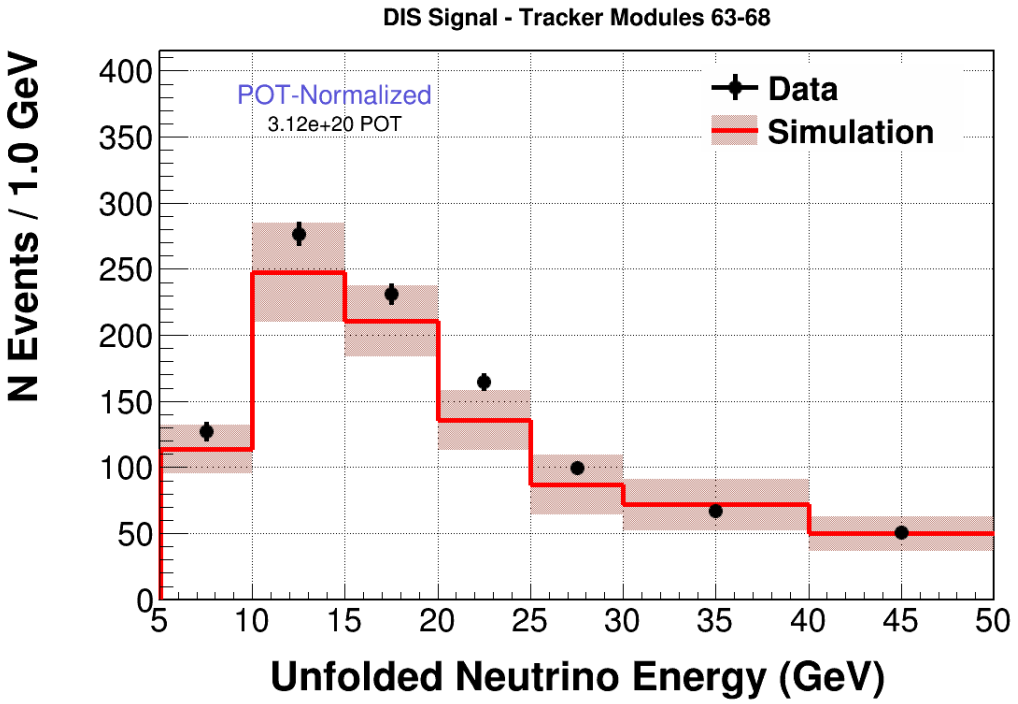

Figure F-17. Unfolded DIS Signal: tracker mods. 63-68 (E_ν)

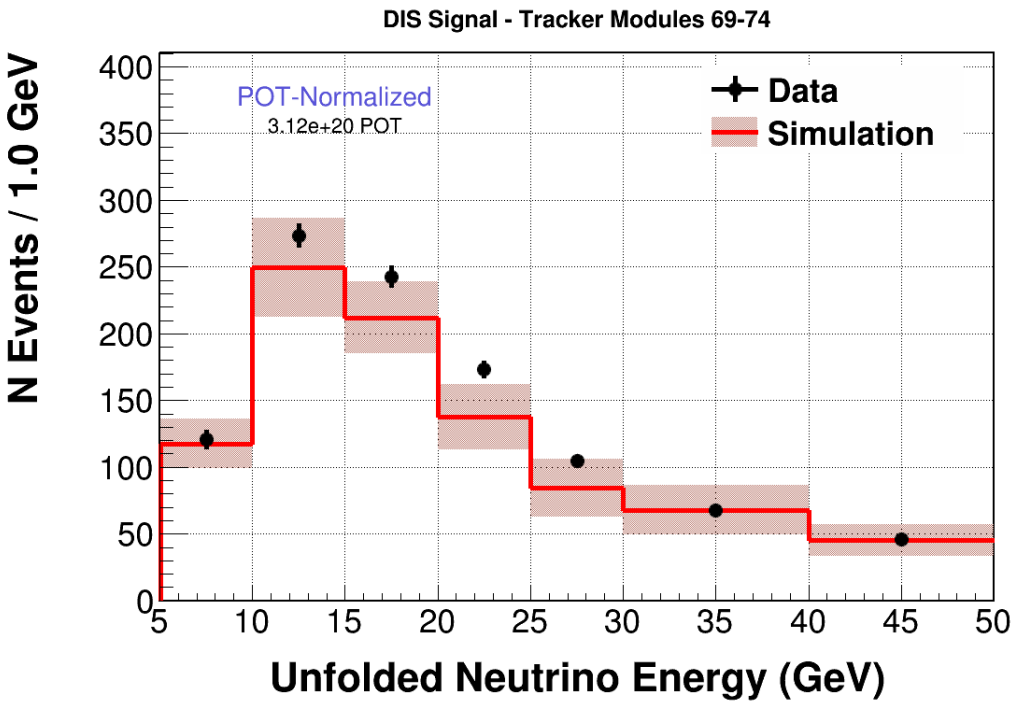

Figure F-18. Unfolded DIS Signal: tracker mods. 69-74 (E_ν)

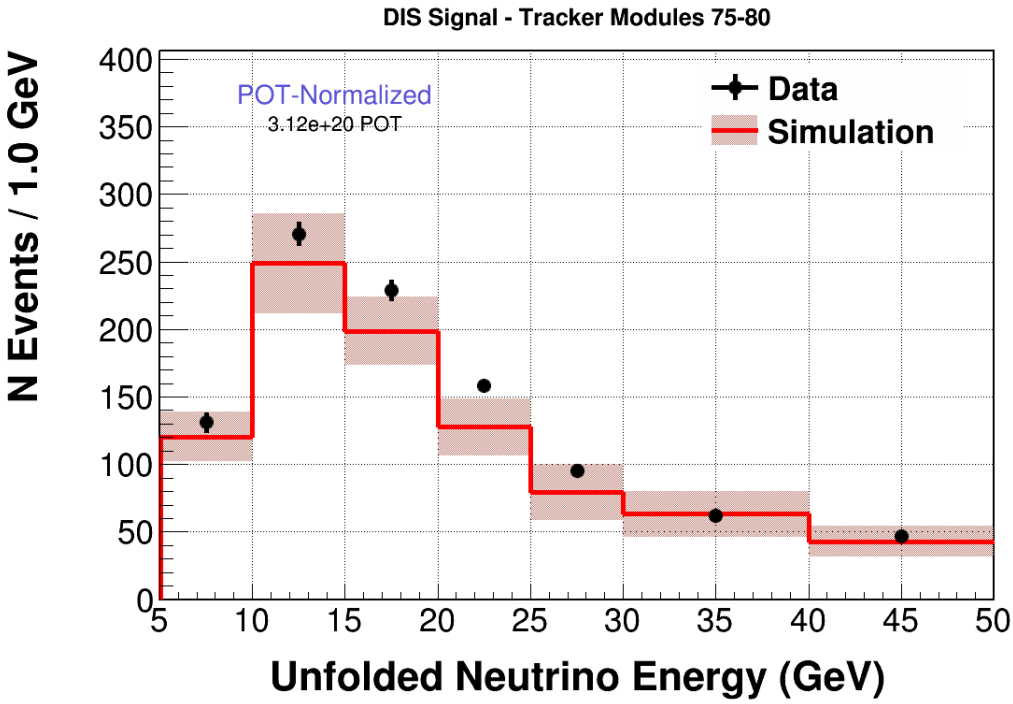

Figure F-19. Unfolded DIS Signal: tracker mods. 75-80 (E_ν)

The following plots show the DIS events in data and MC, after subtracting the non-DIS AND CH events. They are plotted as a function of *unfolded* Bjorken-x (x_{bj}):

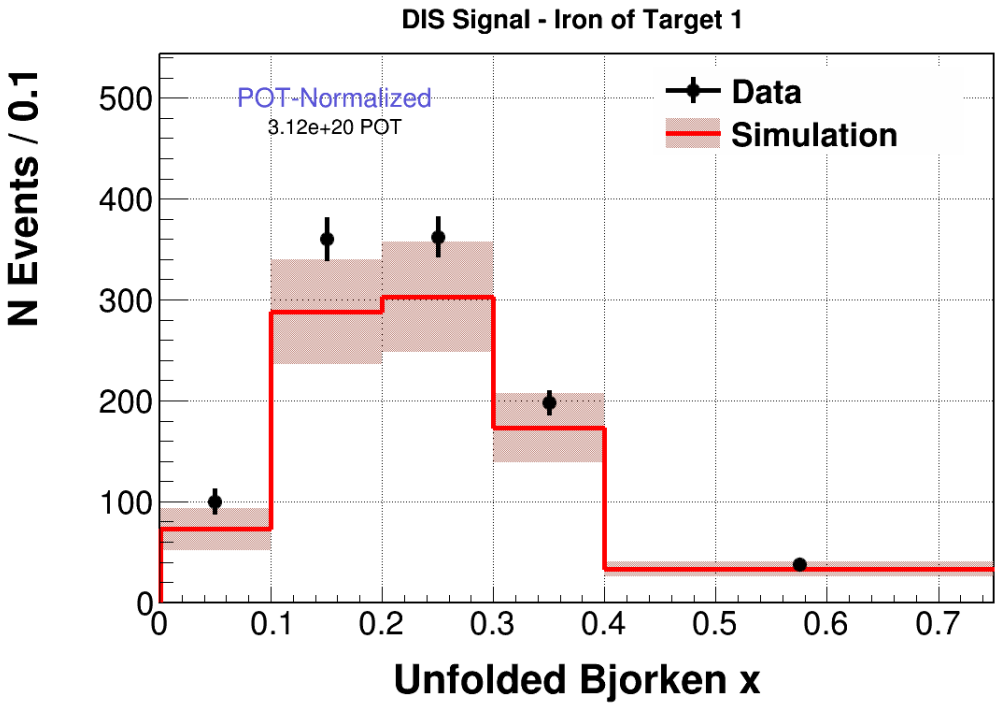

Figure F-20. Unfolded DIS Signal: target 01 Fe (x_{bj})

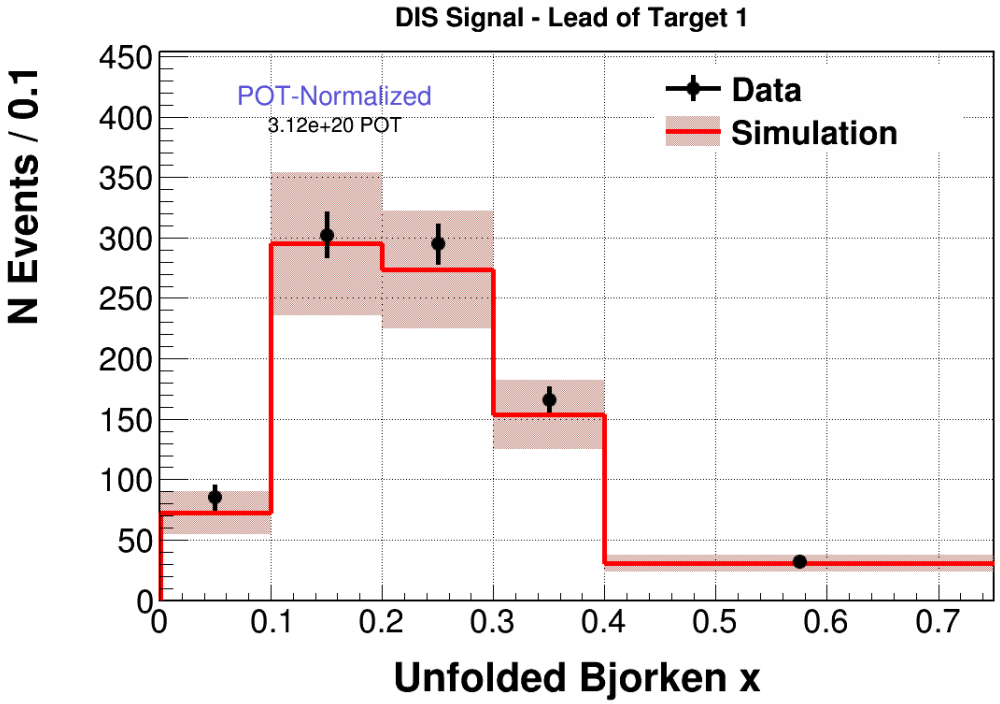

Figure F-21. Unfolded DIS Signal: target 01 Pb (x_{bj})

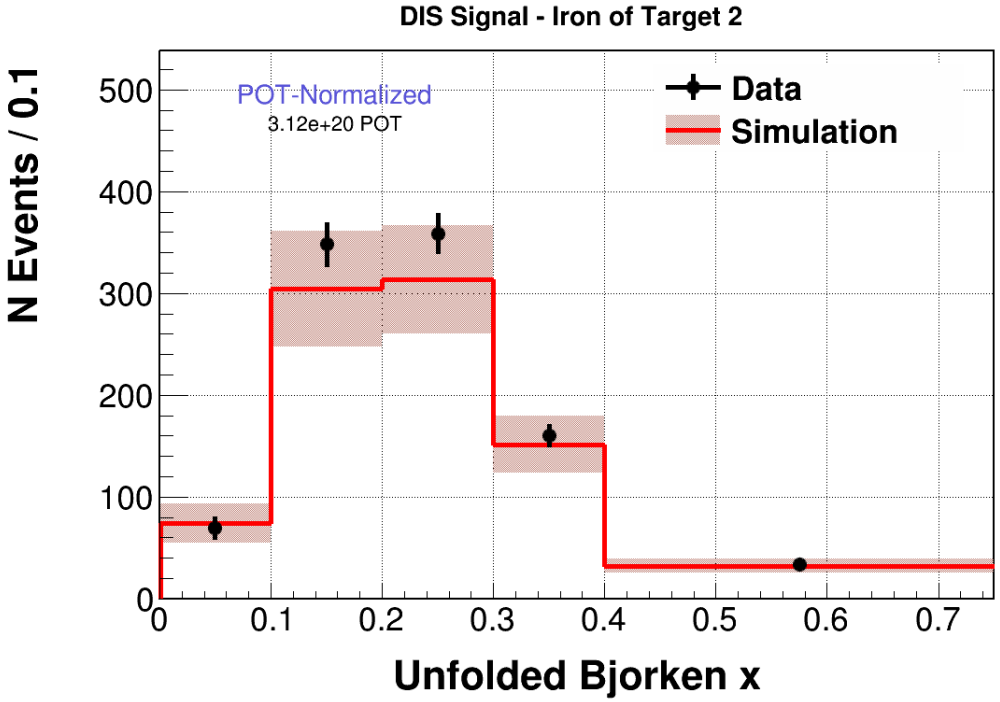

Figure F-22. Unfolded DIS Signal: target 02 Fe (x_{bj})

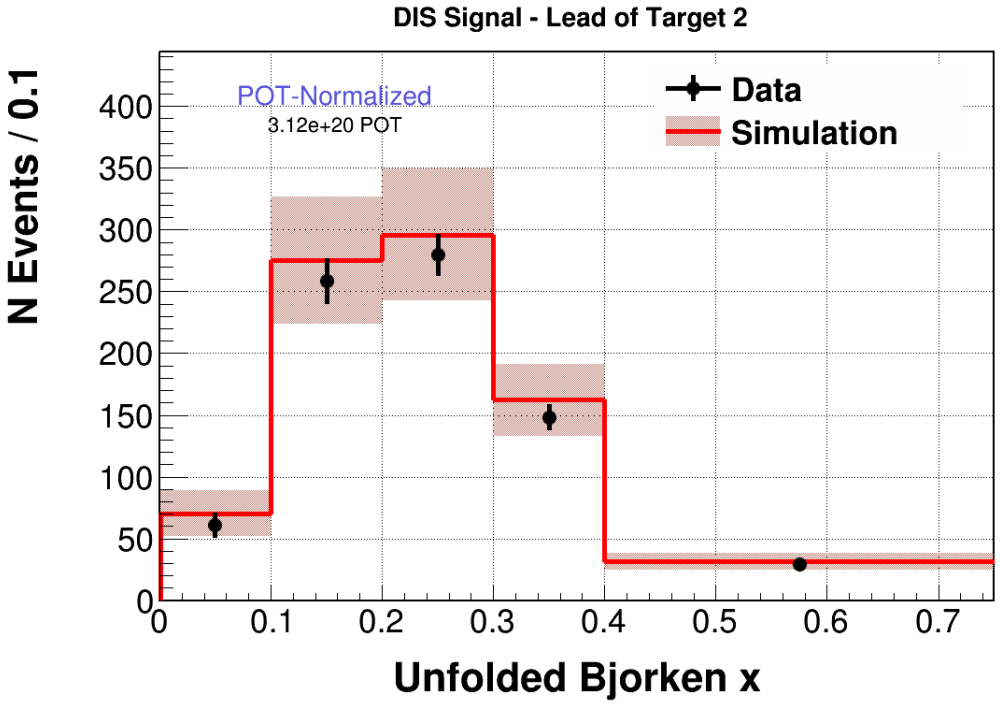

Figure F-23. Unfolded DIS Signal: target 02 Pb (x_{bj})

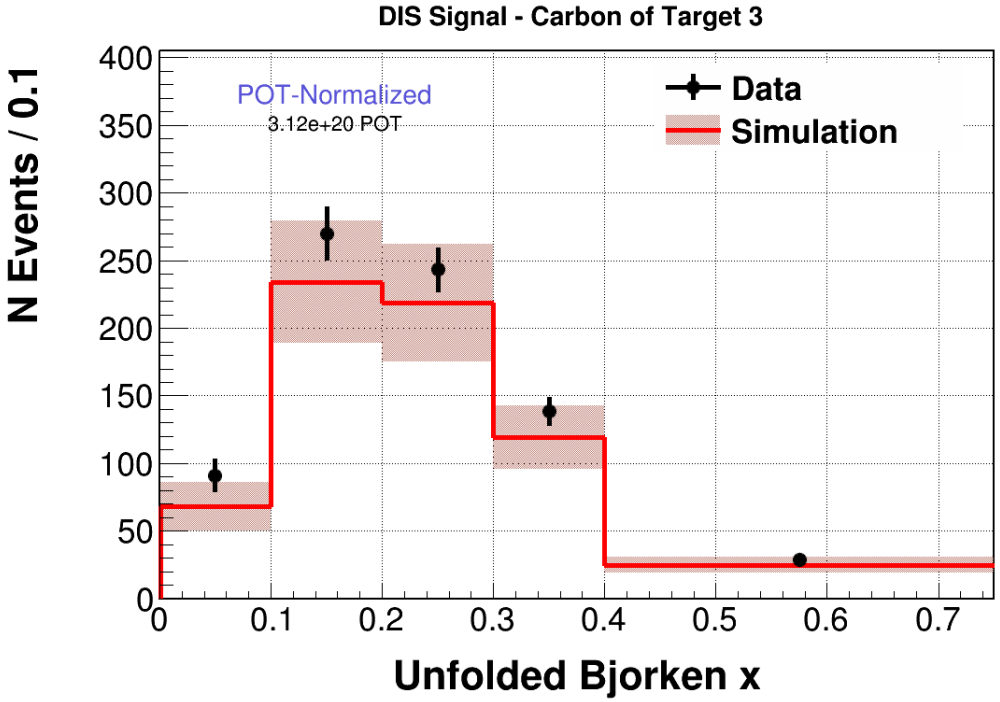

Figure F-24. Unfolded DIS Signal: target 03 C (x_{bj})

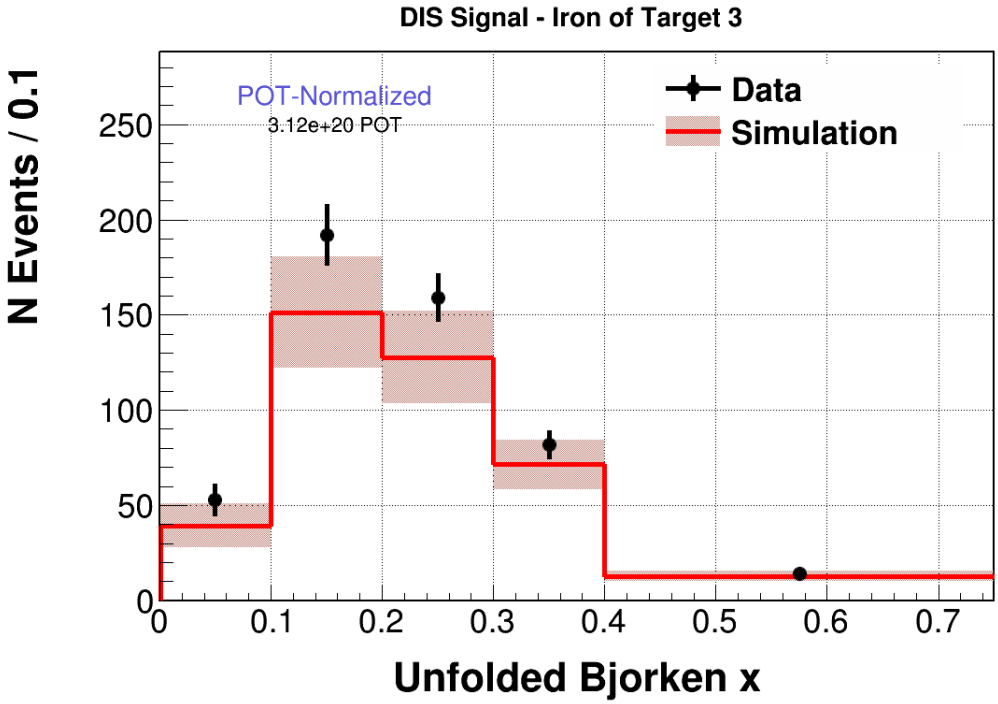

Figure F-25. Unfolded DIS Signal: target 03 Fe (x_{bj})

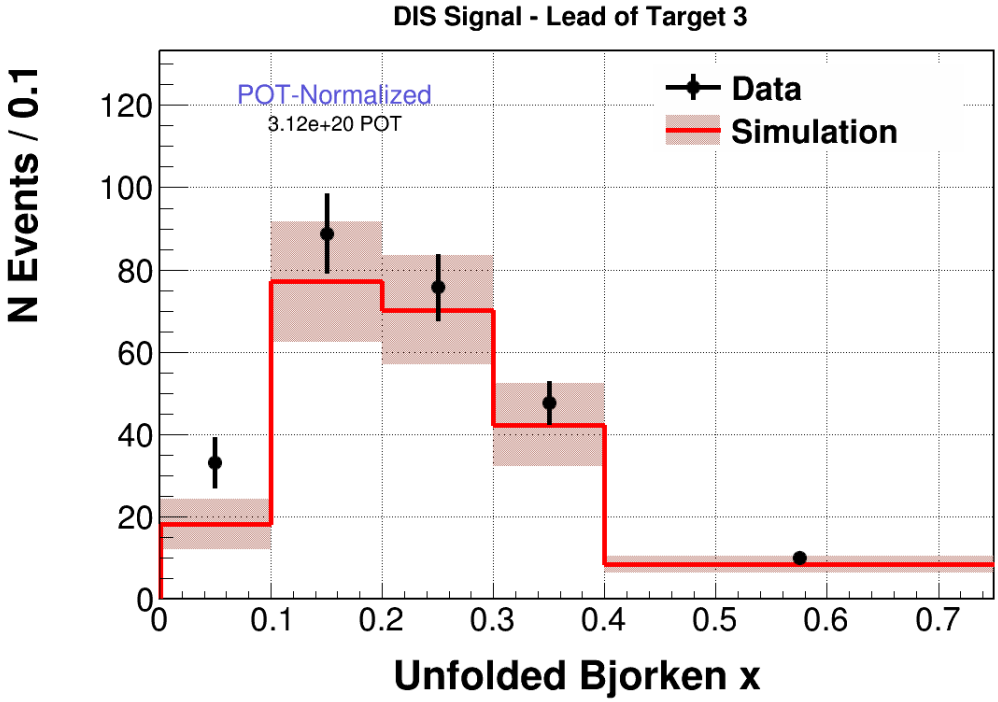

Figure F-26. Unfolded DIS Signal: target 03 Pb (x_{bj})

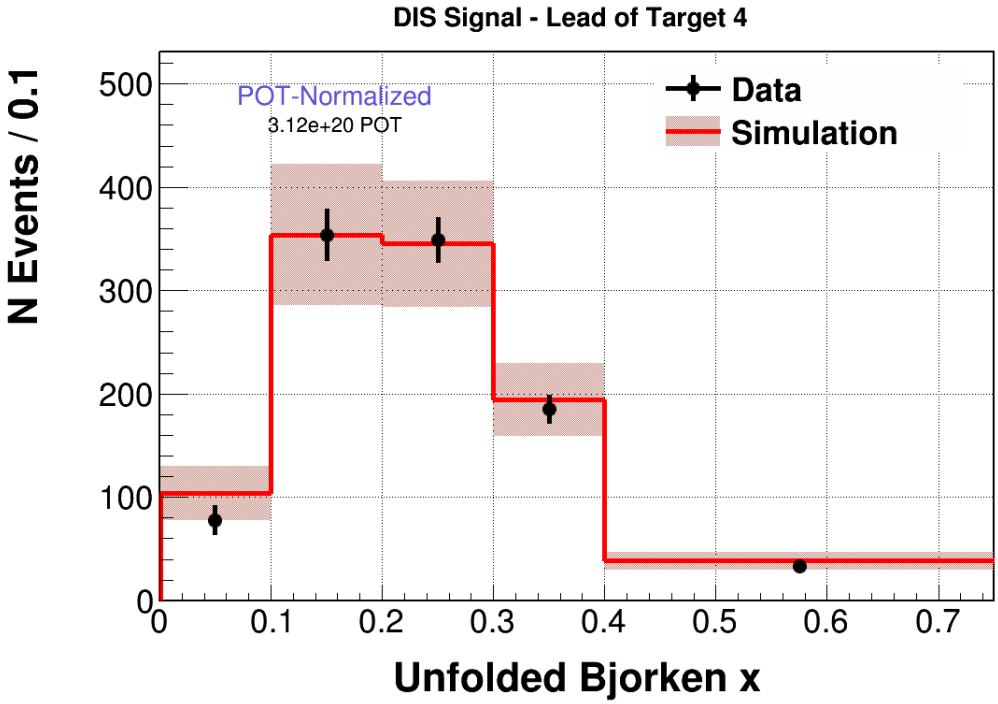

Figure F-27. Unfolded DIS Signal: target 04 Pb (x_{bj})

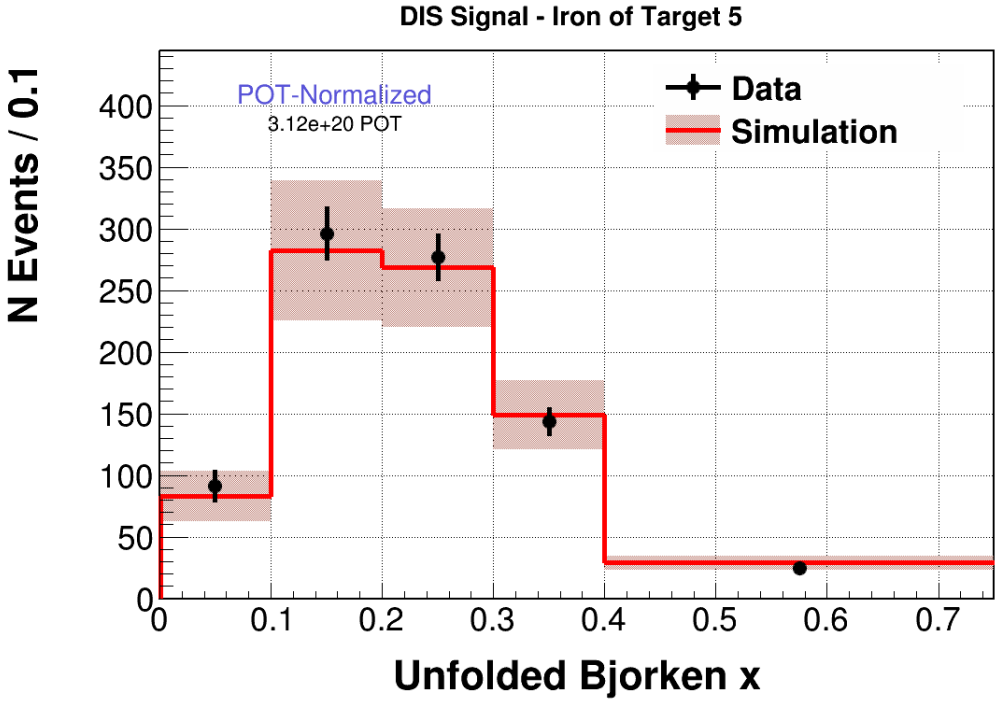

Figure F-28. Unfolded DIS Signal: target 05 Fe (x_{bj})

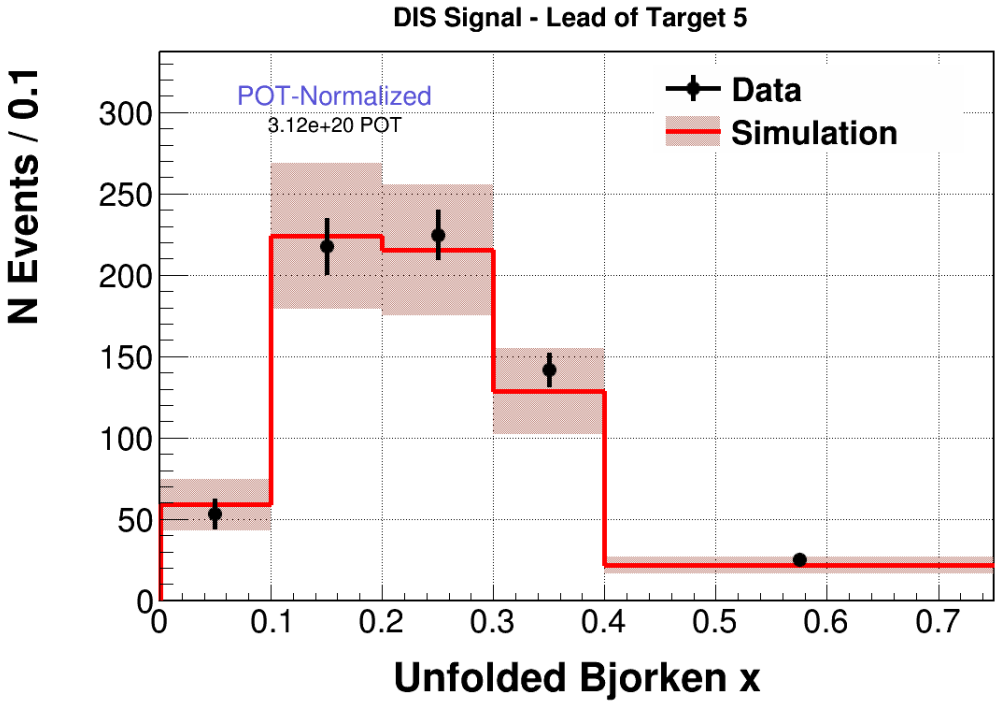

Figure F-29. Unfolded DIS Signal: target 05 Pb (x_{bj})

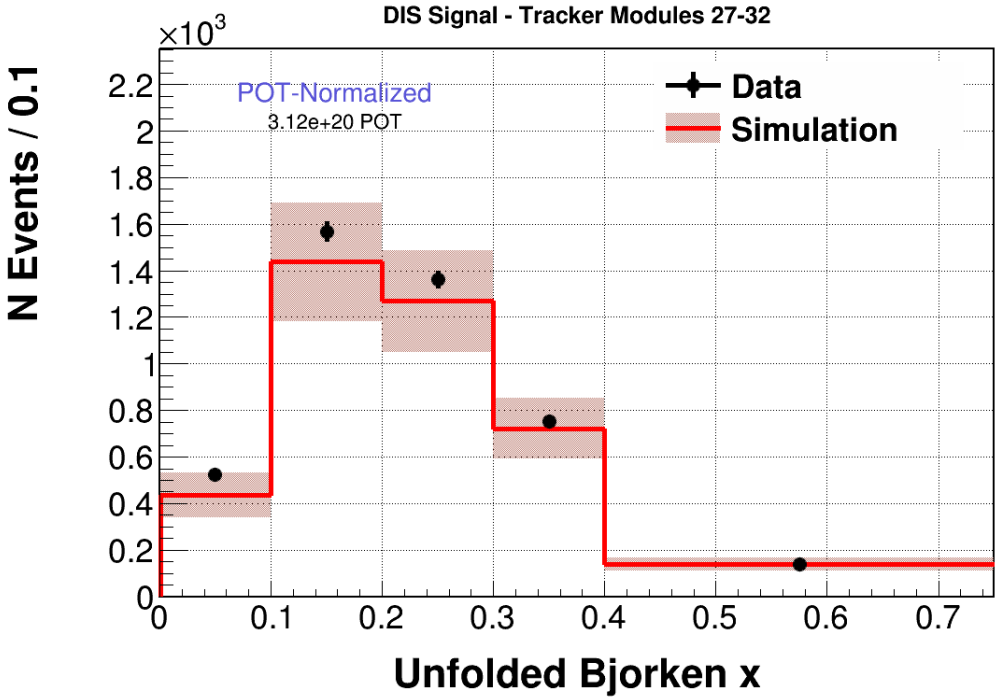

Figure F-30. Unfolded DIS Signal: tracker mods. 27-32 (x_{bj})

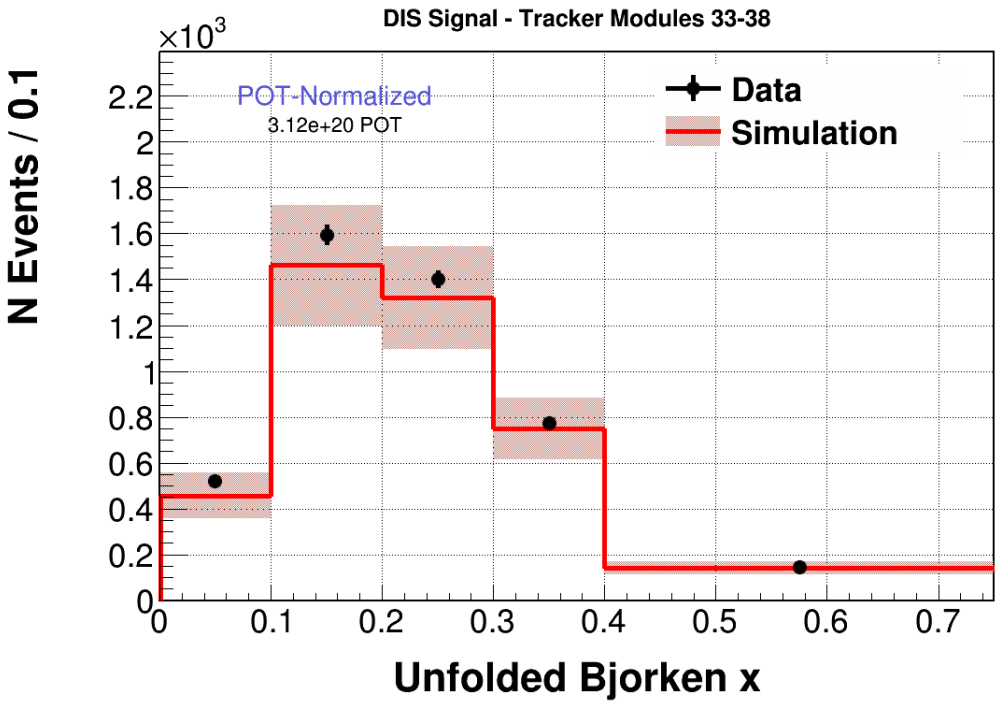

Figure F-31. Unfolded DIS Signal: tracker mods. 33-38 (x_{bj})

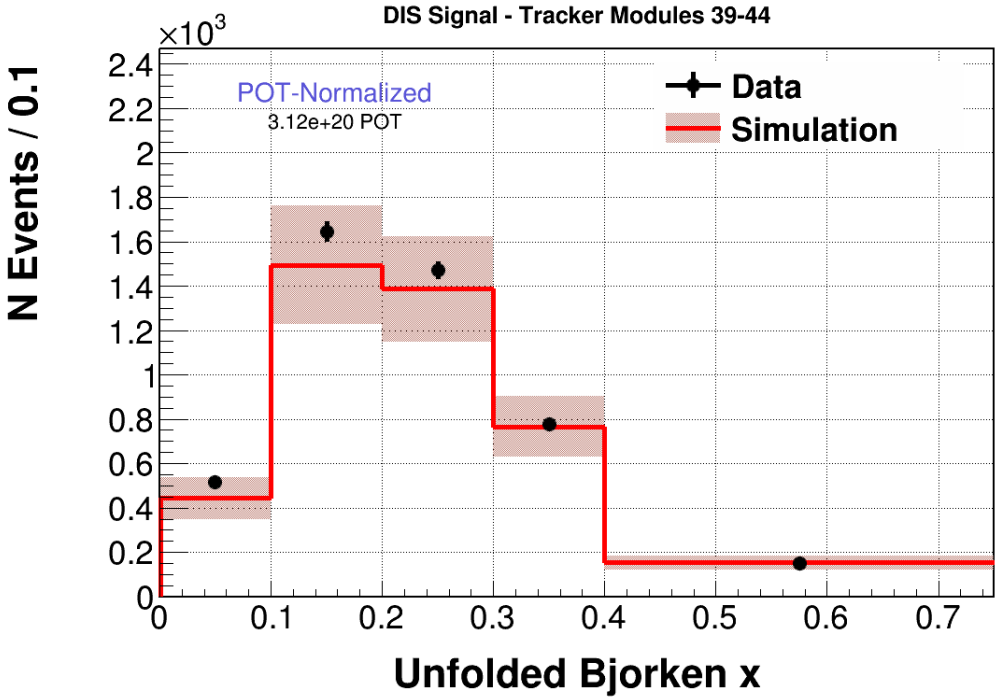

Figure F-32. Unfolded DIS Signal: tracker mods. 39-44 (x_{bj})

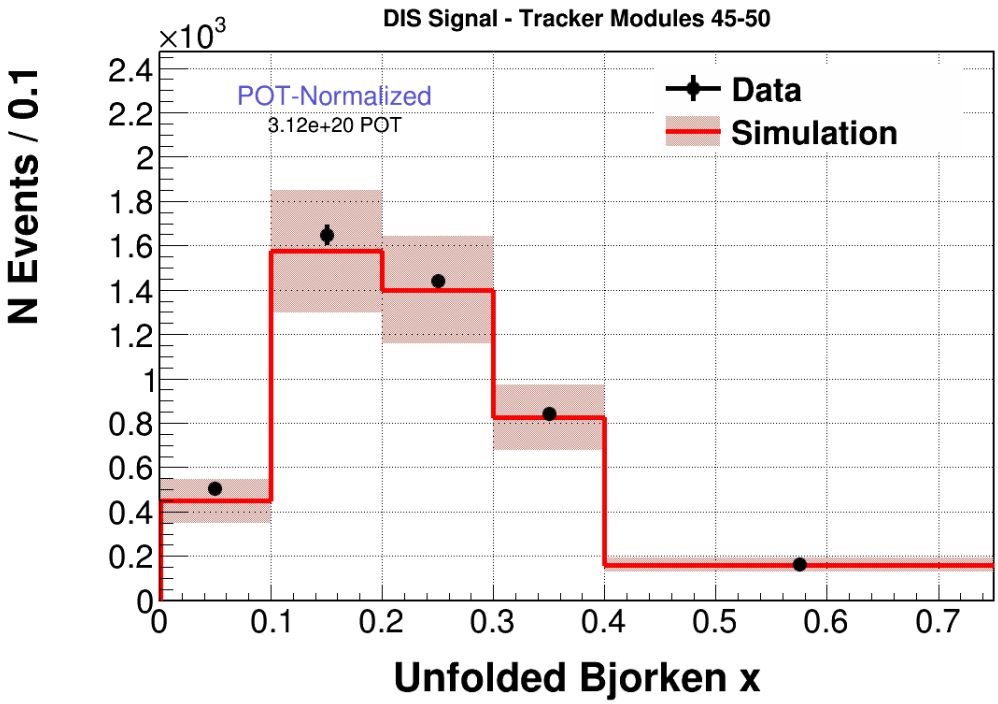

Figure F-33. Unfolded DIS Signal: tracker mods. 45-50 (x_{bj})

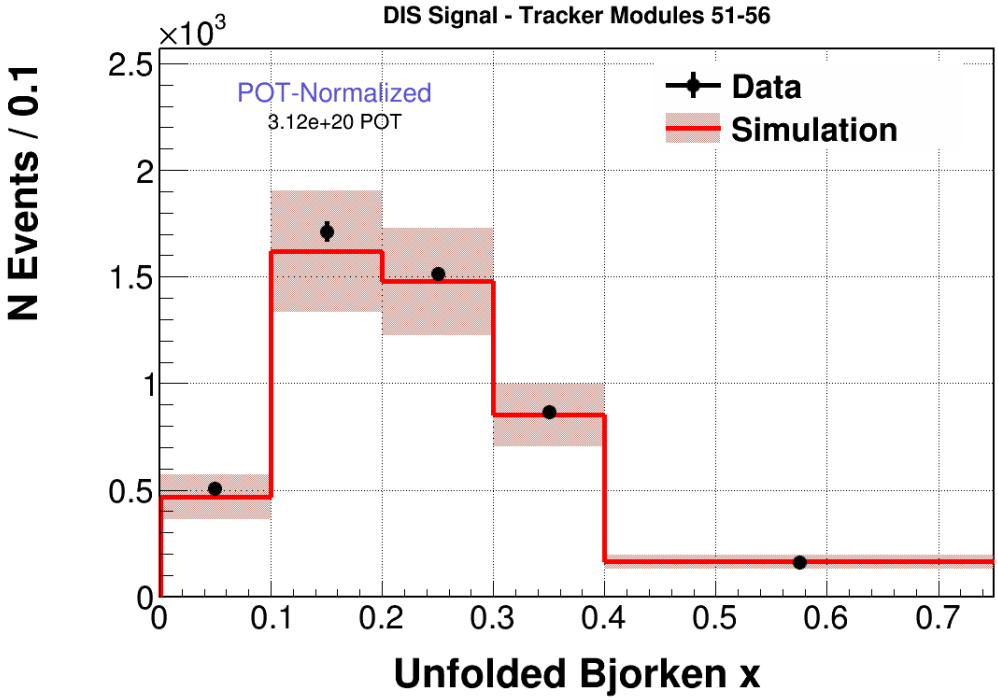

Figure F-34. Unfolded DIS Signal: tracker mods. 51-56 (x_{bj})

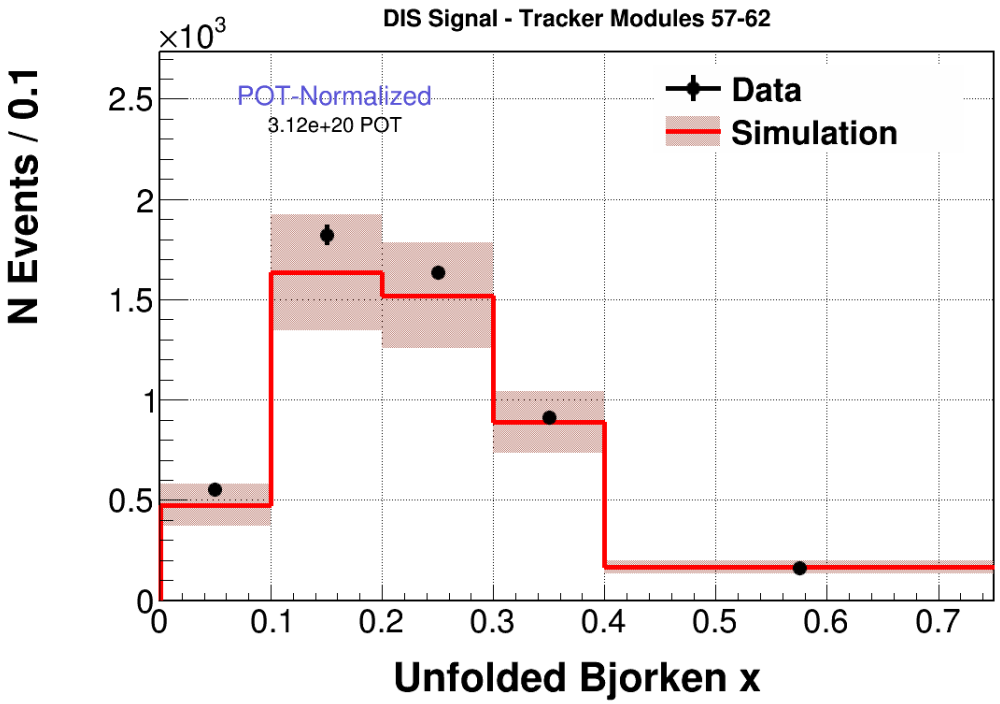

Figure F-35. Unfolded DIS Signal: tracker mods. 57-62 (x_{bj})

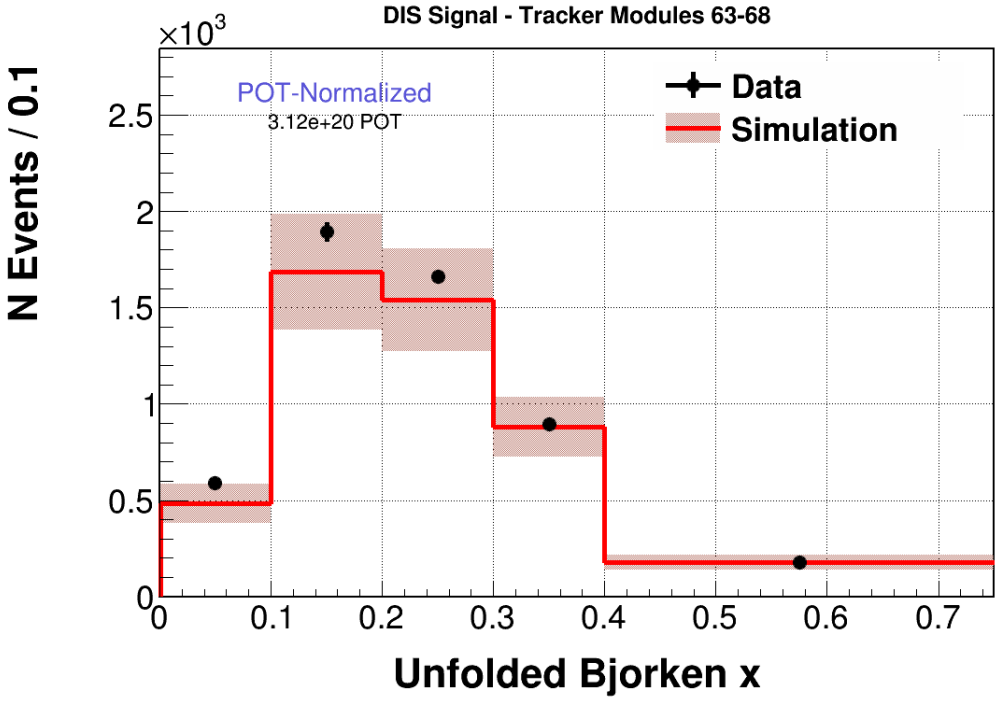

Figure F-36. Unfolded DIS Signal: tracker mods. 63-68 (x_{bj})

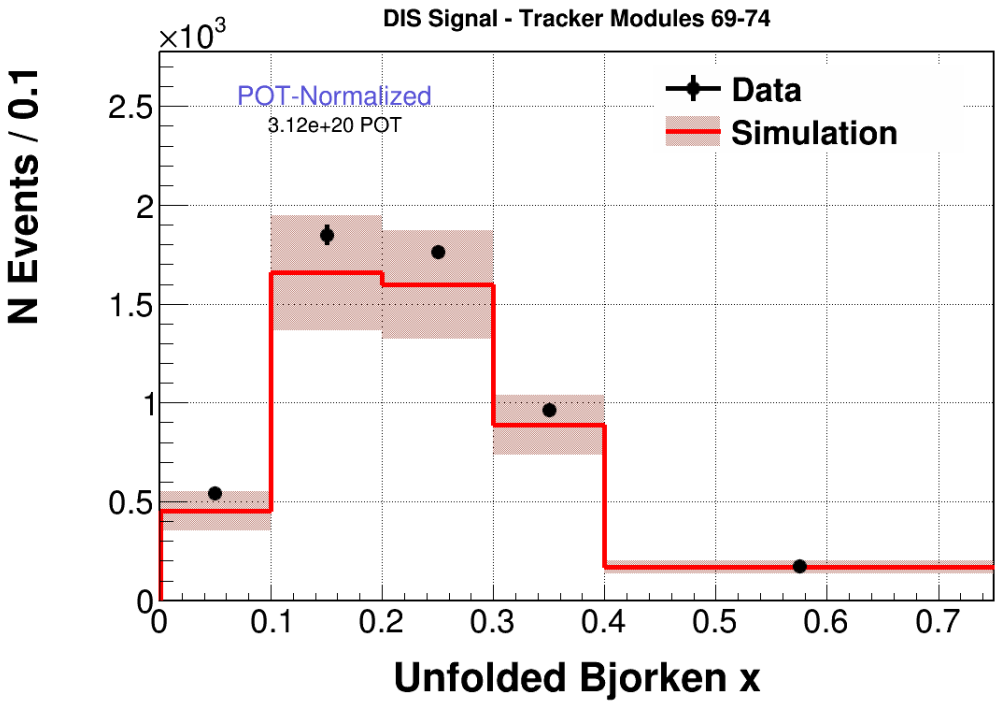

Figure F-37. Unfolded DIS Signal: tracker mods. 69-74 (x_{bj})

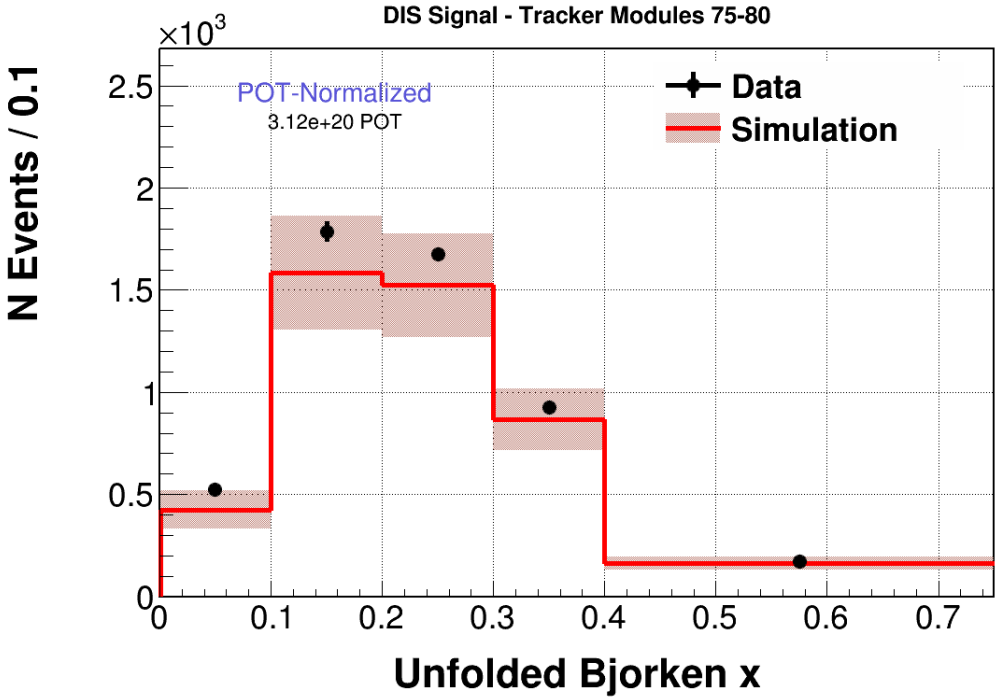

Figure F-38. Unfolded DIS Signal: tracker mods. 75-80 (x_{bj})

F.2 Unfolding Uncertainties

The following plots show the uncertainty on the number of DIS events, after subtracting the non-DIS AND CH events. They are plotted as a function of *unfolded* neutrino energy (E_ν):

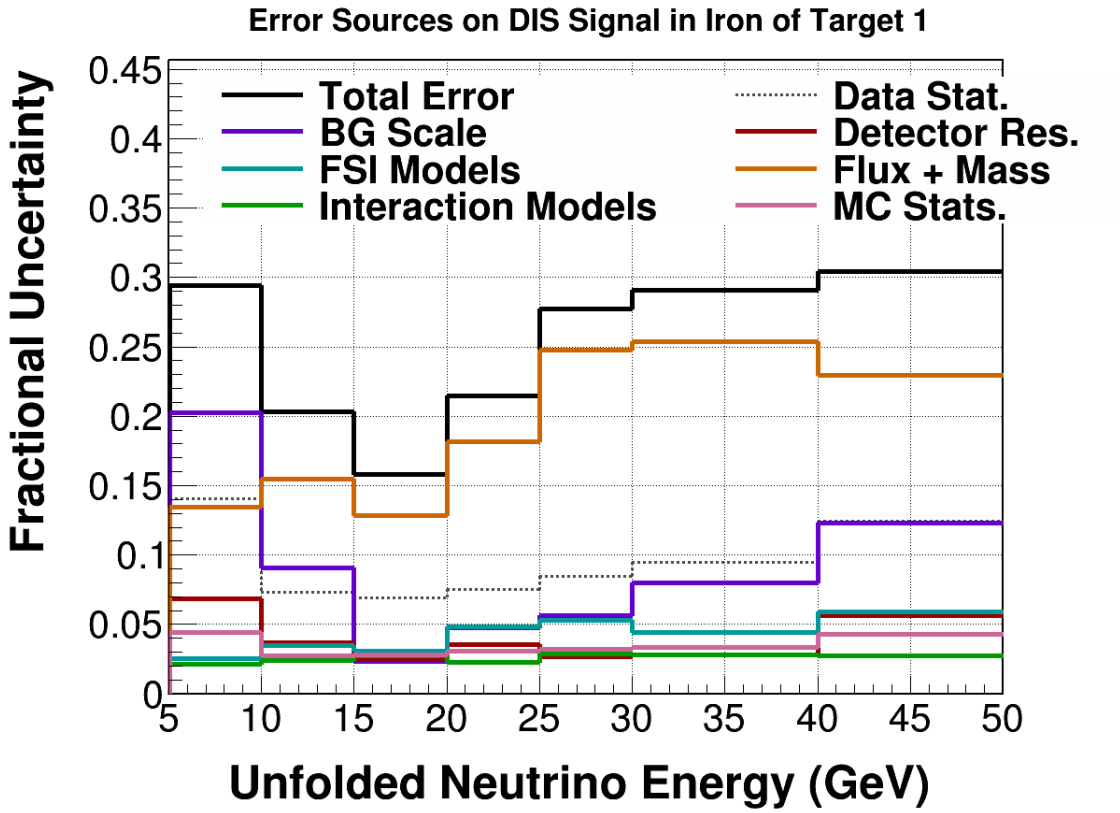

Figure F-39. Unfolded Event yield uncertainties after CH subtraction: target 01 Fe (E_ν)

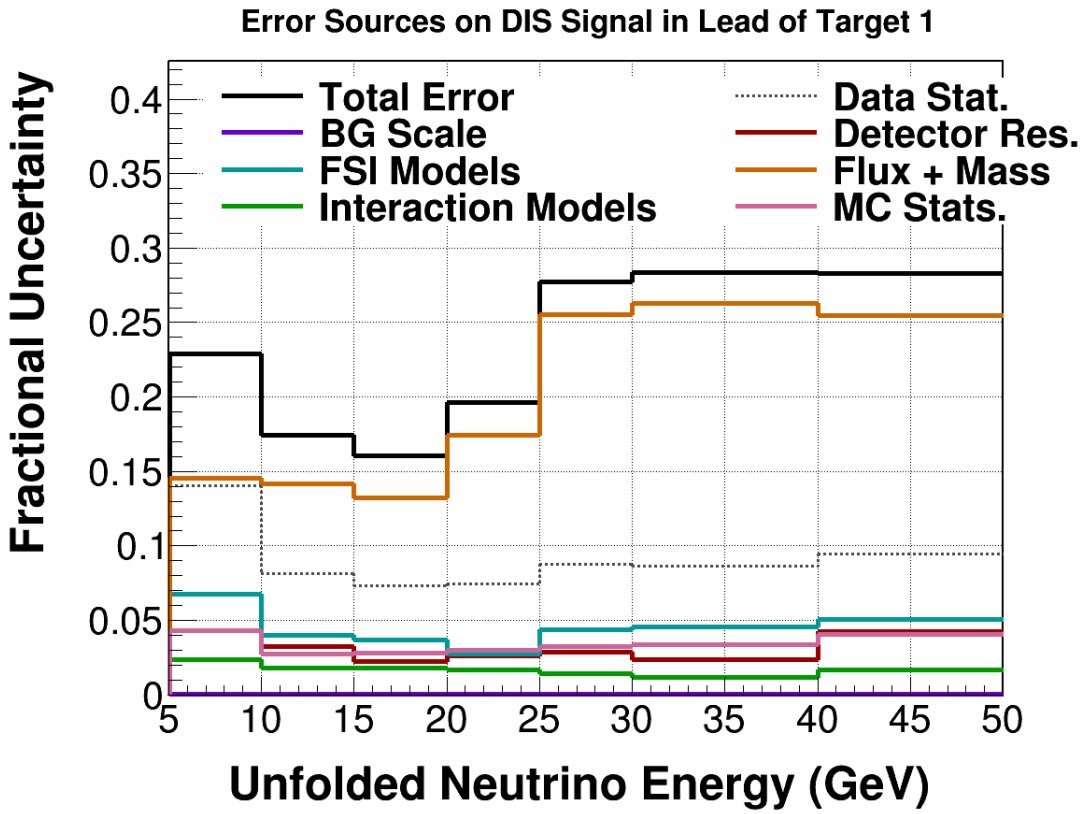

Figure F-40. Unfolded Event yield uncertainties after CH subtraction: target 01 Pb (E_ν)

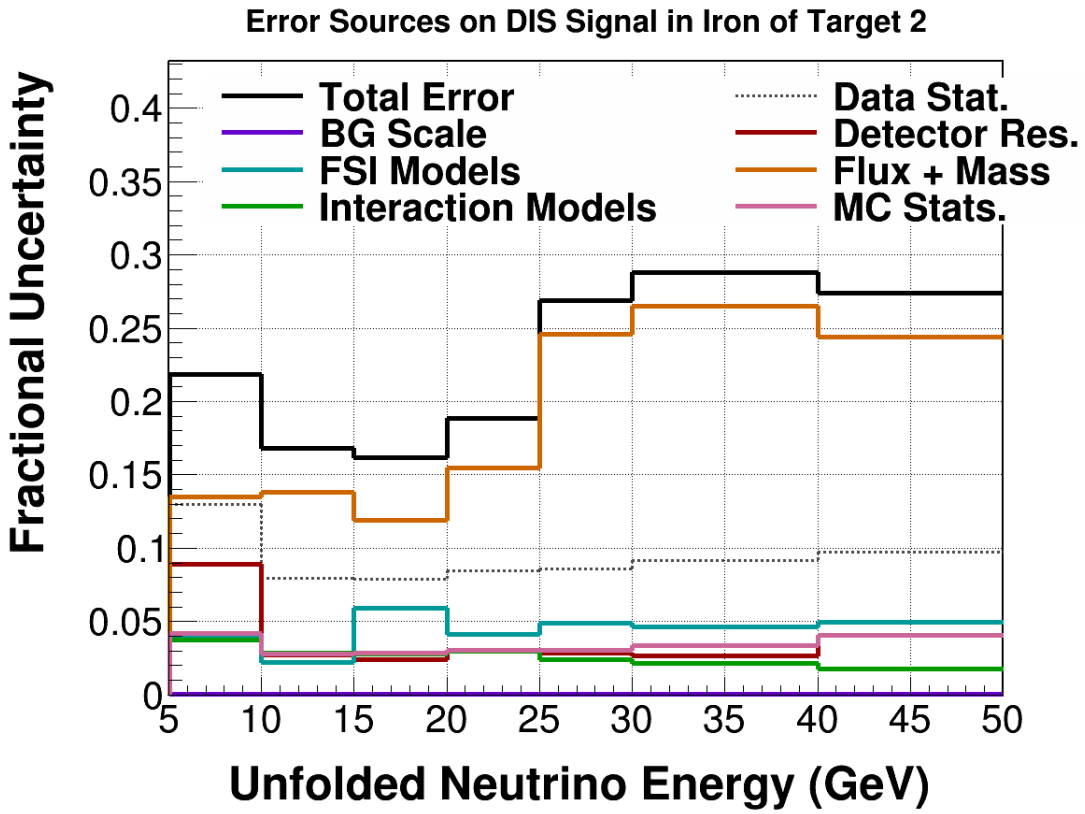

Figure F-41. Unfolded Event yield uncertainties after CH subtraction: target 02 Fe (E_ν)

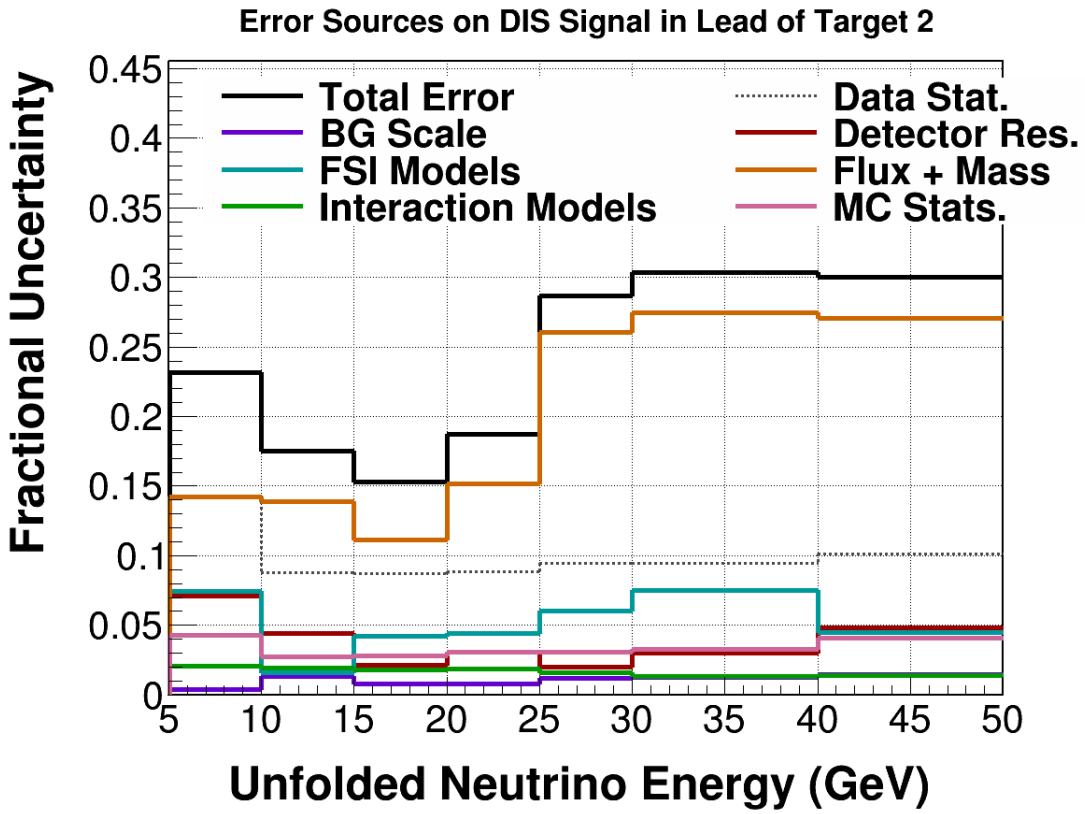

Figure F-42. Unfolded Event yield uncertainties after CH subtraction: target 02 Pb (E_ν)

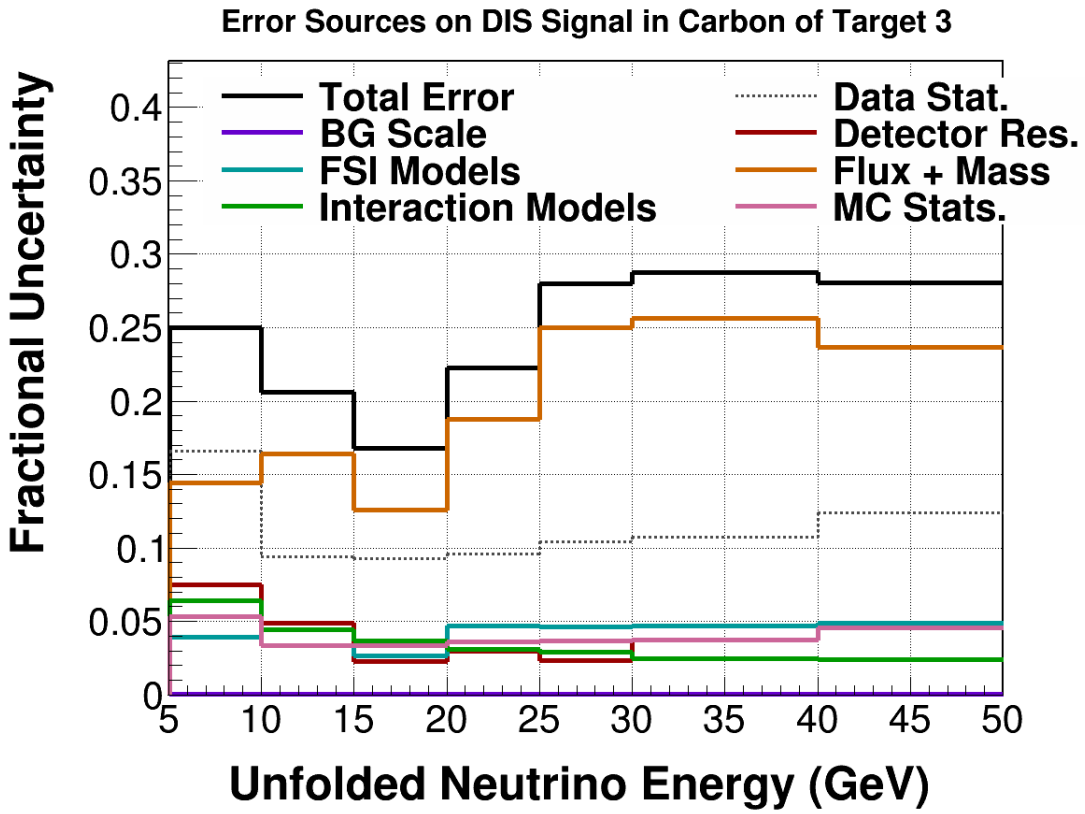

Figure F-43. Unfolded Event yield uncertainties after CH subtraction: target 03 C (E_ν)

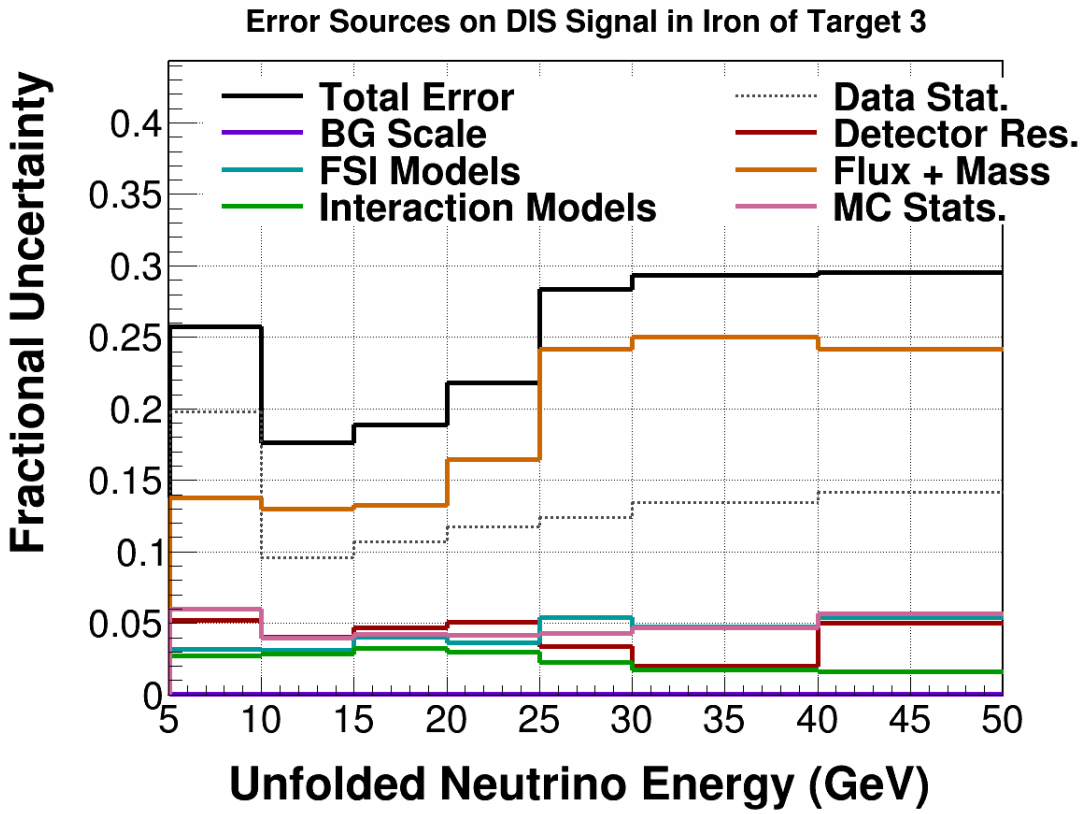

Figure F-44. Unfolded Event yield uncertainties after CH subtraction: target 03 Fe (E_ν)

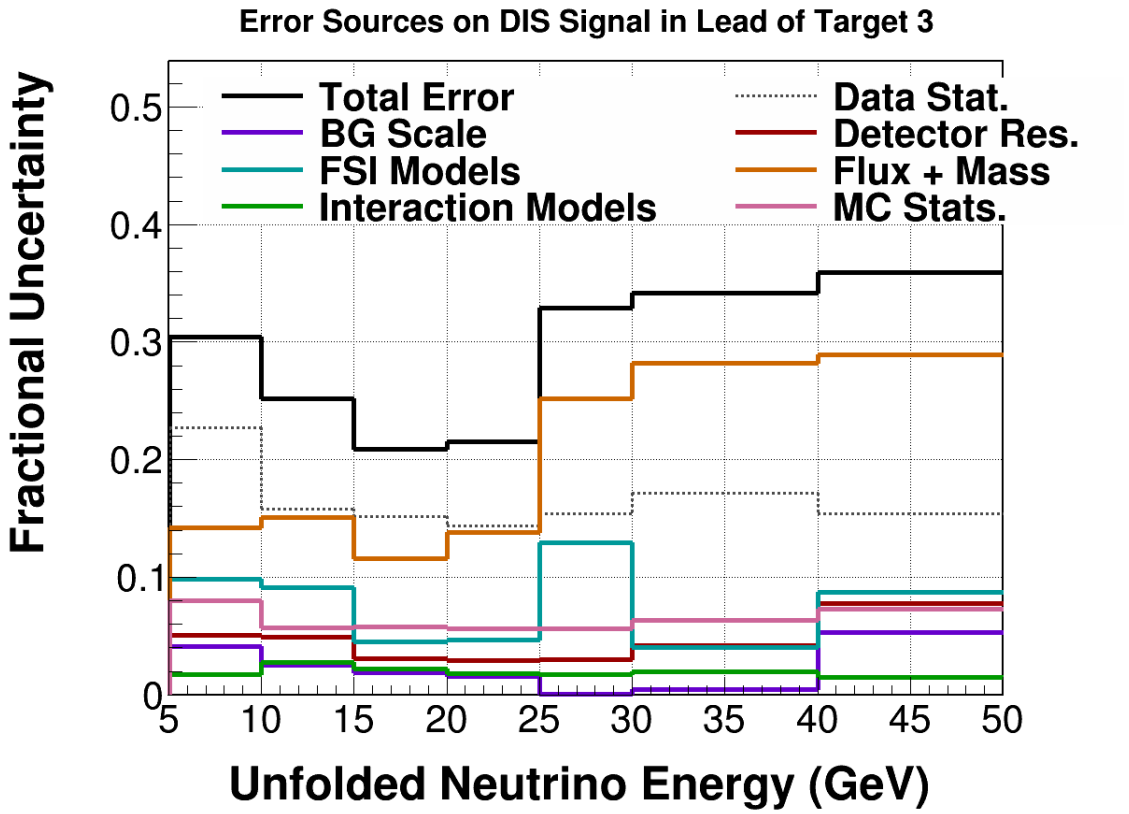

Figure F-45. Unfolded Event yield uncertainties after CH subtraction: target 03 Pb (E_ν)

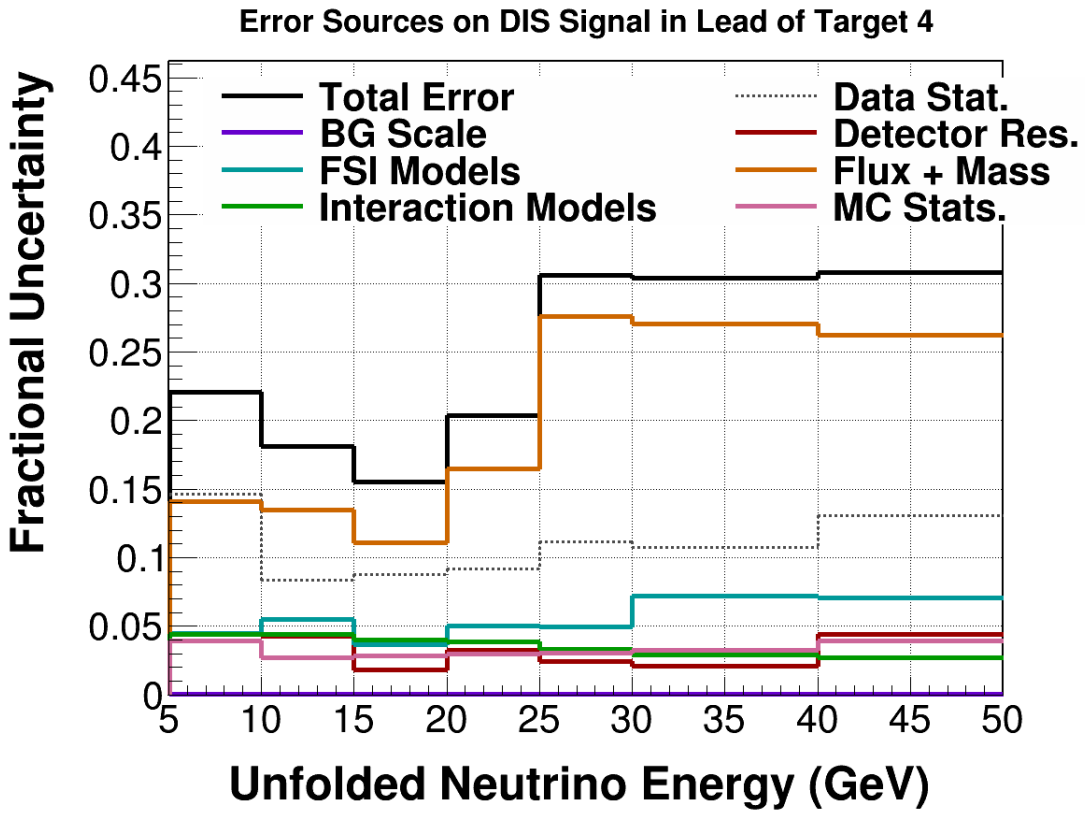

Figure F-46. Unfolded Event yield uncertainties after CH subtraction: target 04 Pb (E_ν)

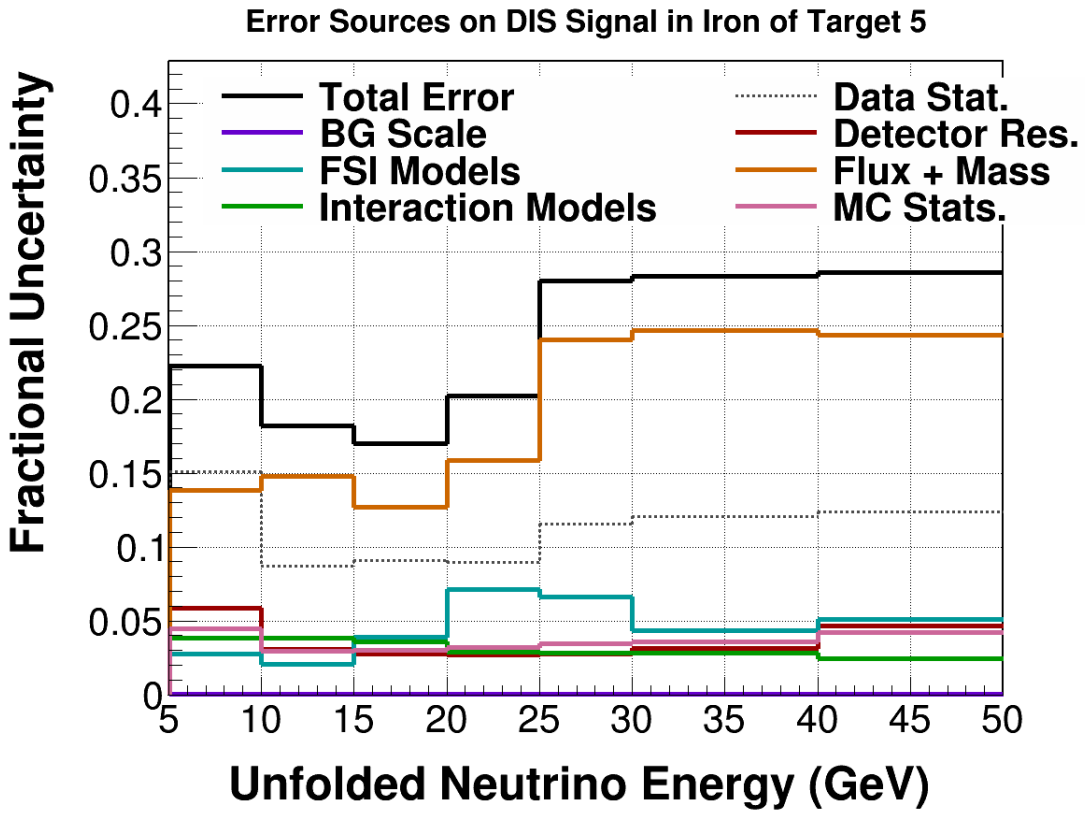

Figure F-47. Unfolded Event yield uncertainties after CH subtraction: target 05 Fe (E_ν)

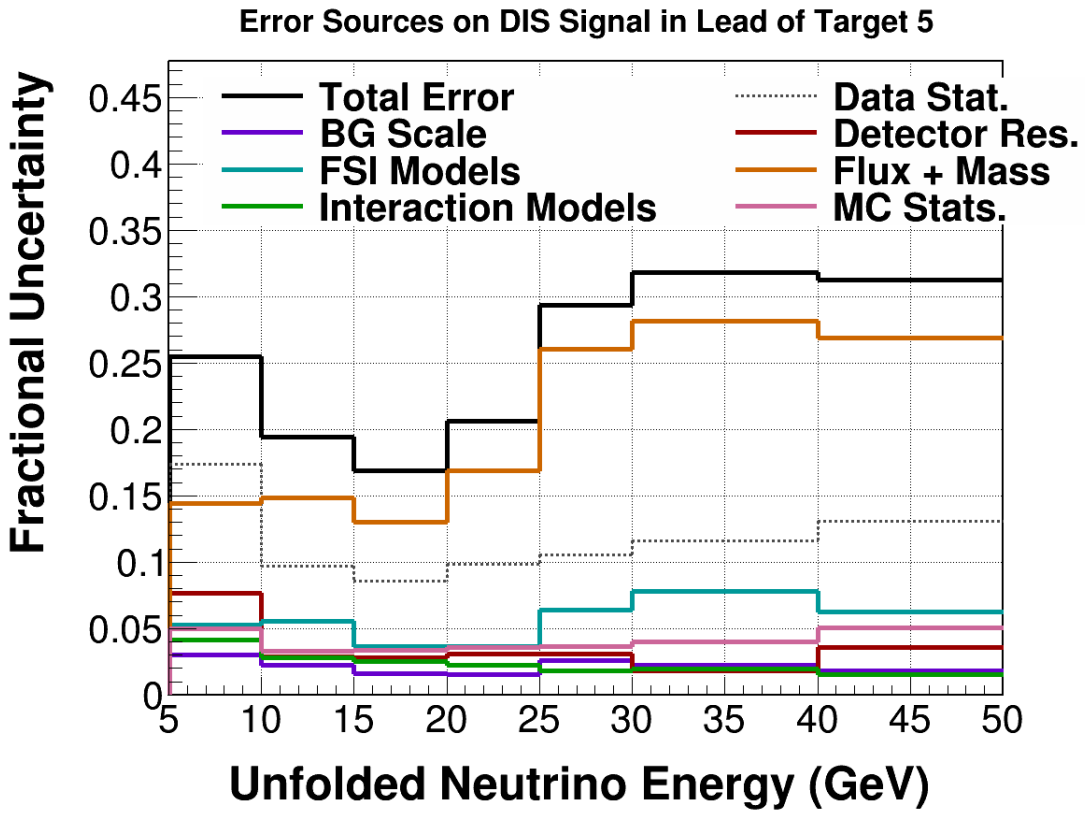

Figure F-48. Unfolded Event yield uncertainties after CH subtraction: target 05 Pb (E_ν)

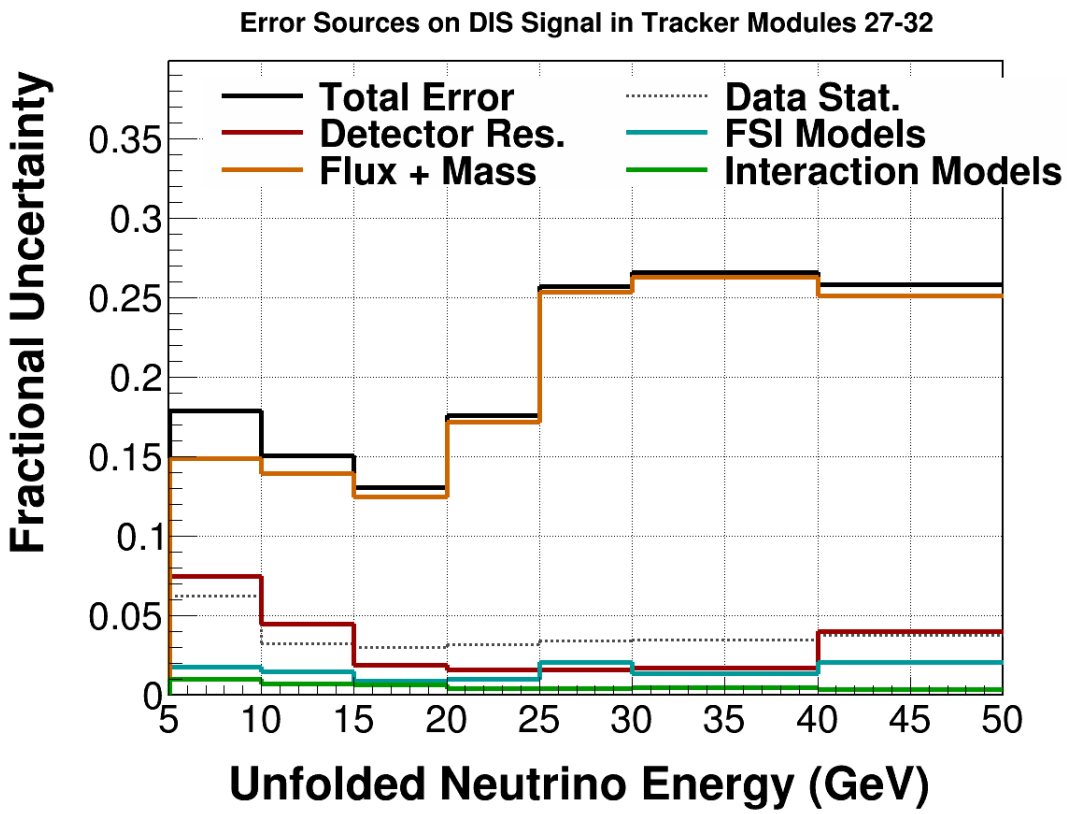

Figure F-49. Unfolded Event yield uncertainties after CH subtraction: tracker mods. 27-32 (E_ν)

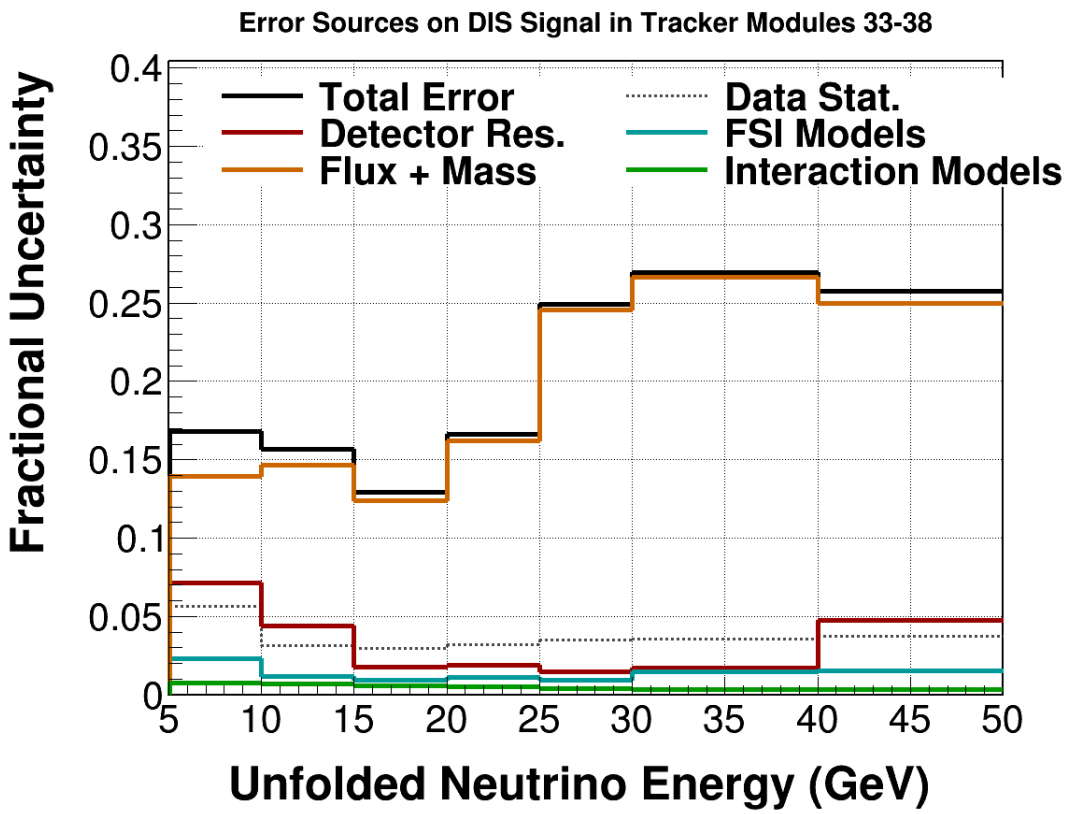

Figure F-50. Unfolded Event yield uncertainties after CH subtraction: tracker mods. 33-38 (E_ν)

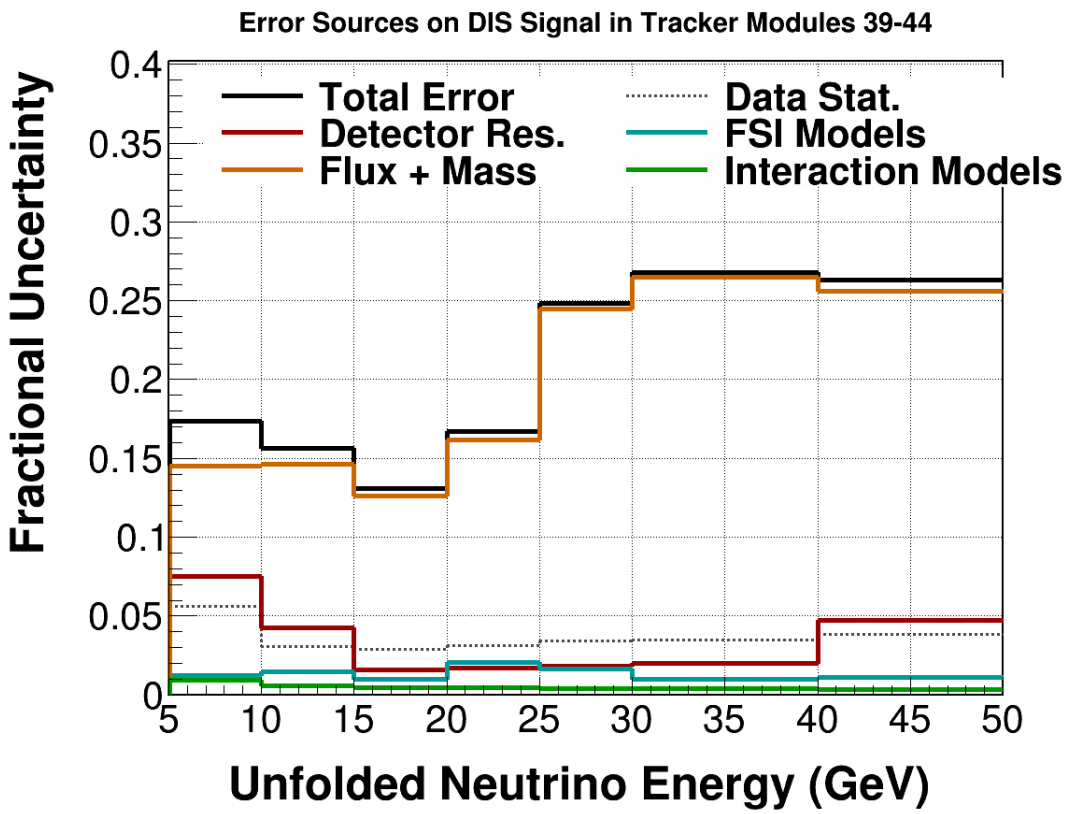

Figure F-51. Unfolded Event yield uncertainties after CH subtraction: tracker mods. 39-44 (E_ν)

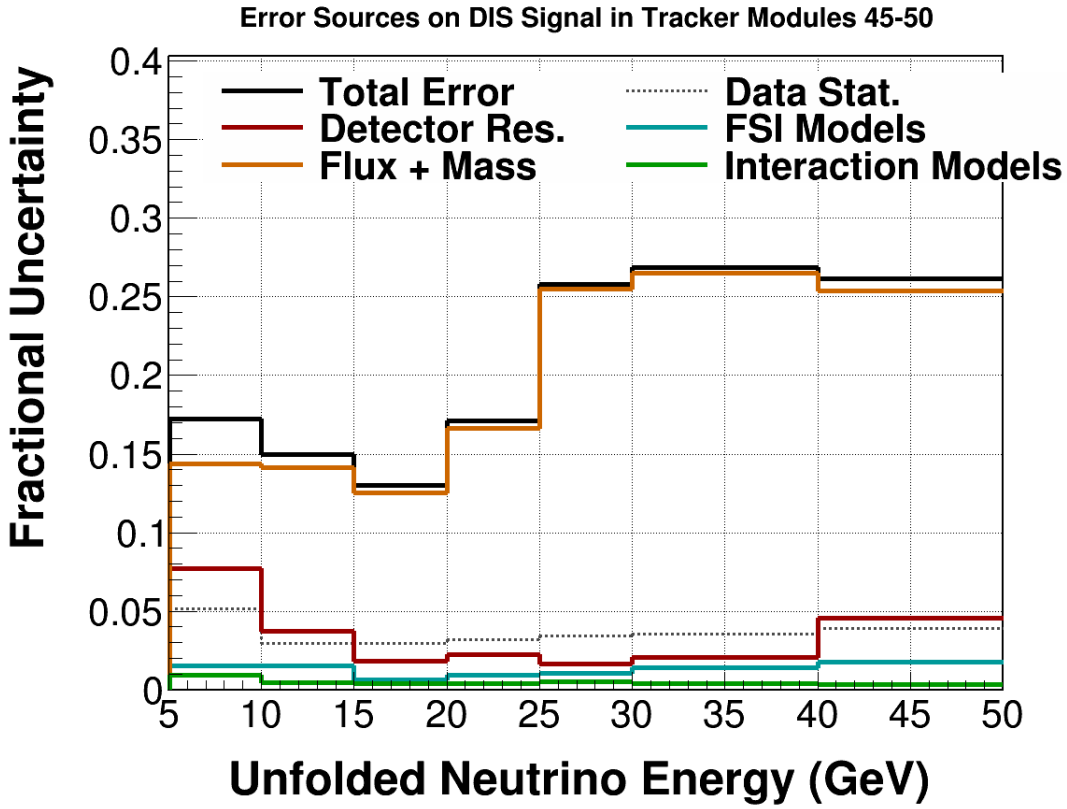

Figure F-52. Unfolded Event yield uncertainties after CH subtraction: tracker mods. 45-50 (E_ν)

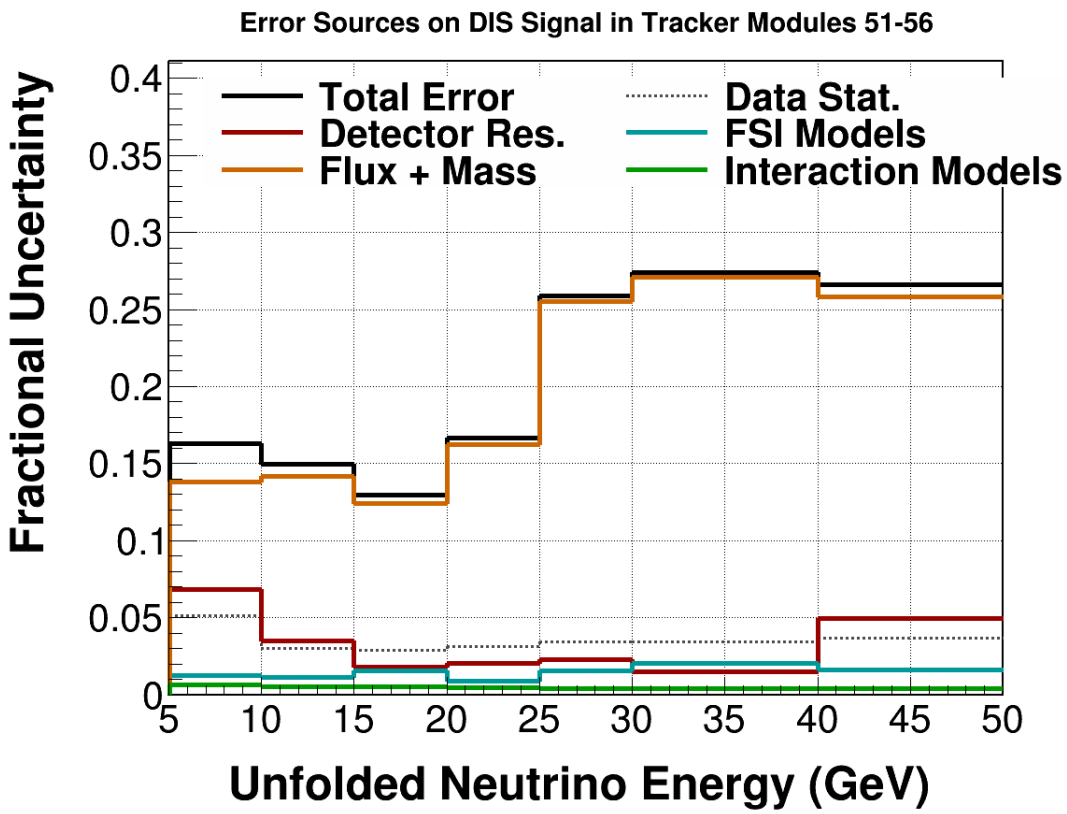

Figure F-53. Unfolded Event yield uncertainties after CH subtraction: tracker mods. 51-56 (E_ν)

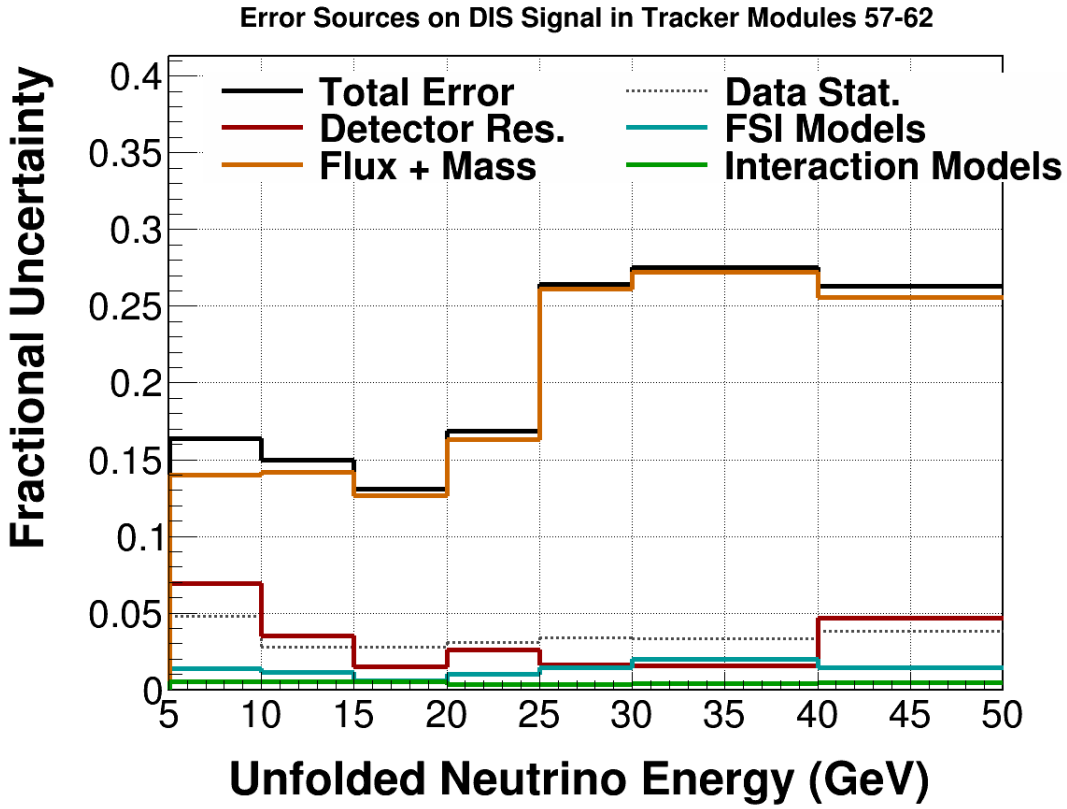

Figure F-54. Unfolded Event yield uncertainties after CH subtraction: tracker mods. 57-62 (E_ν)

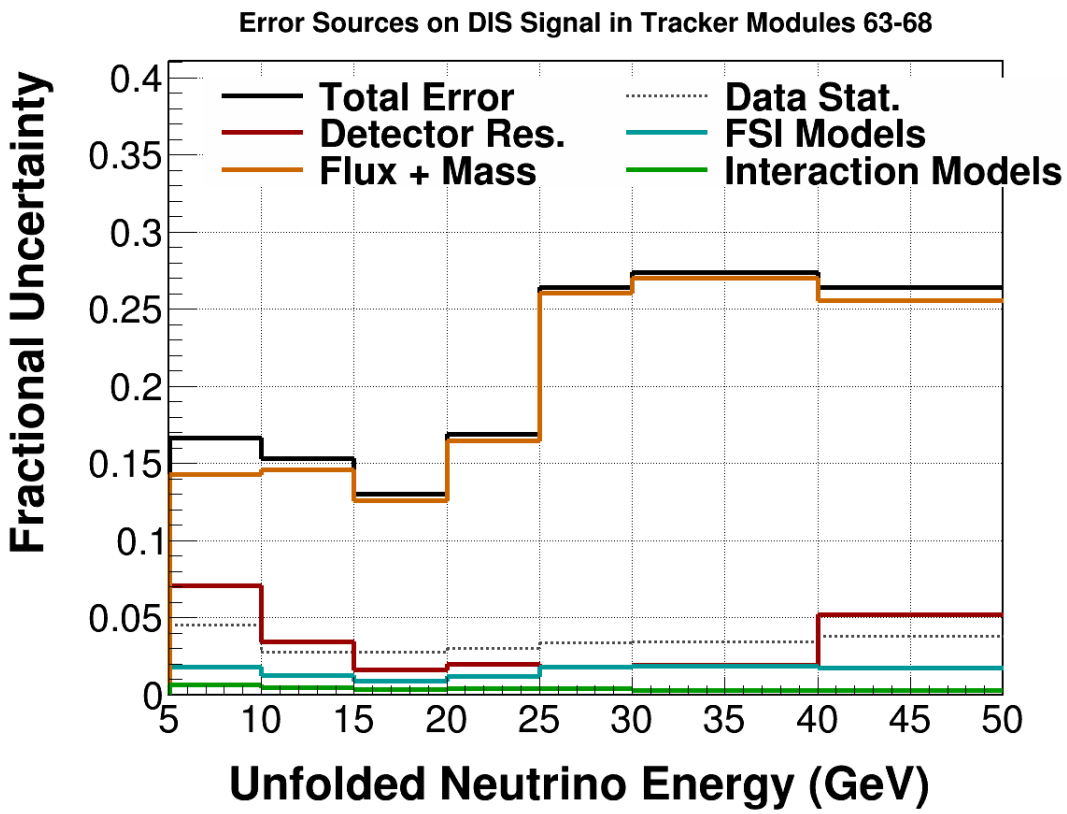

Figure F-55. Unfolded Event yield uncertainties after CH subtraction: tracker mods. 63-68 (E_ν)

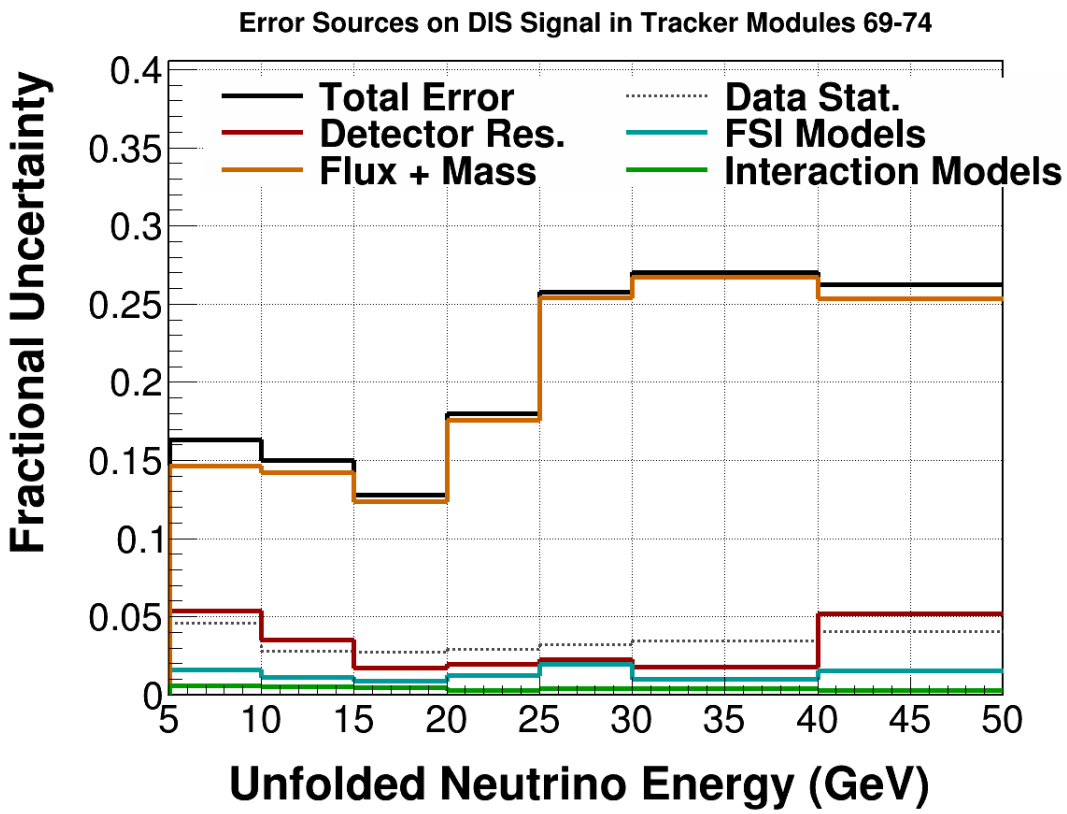

Figure F-56. Unfolded Event yield uncertainties after CH subtraction: tracker mods. 69-74 (E_ν)

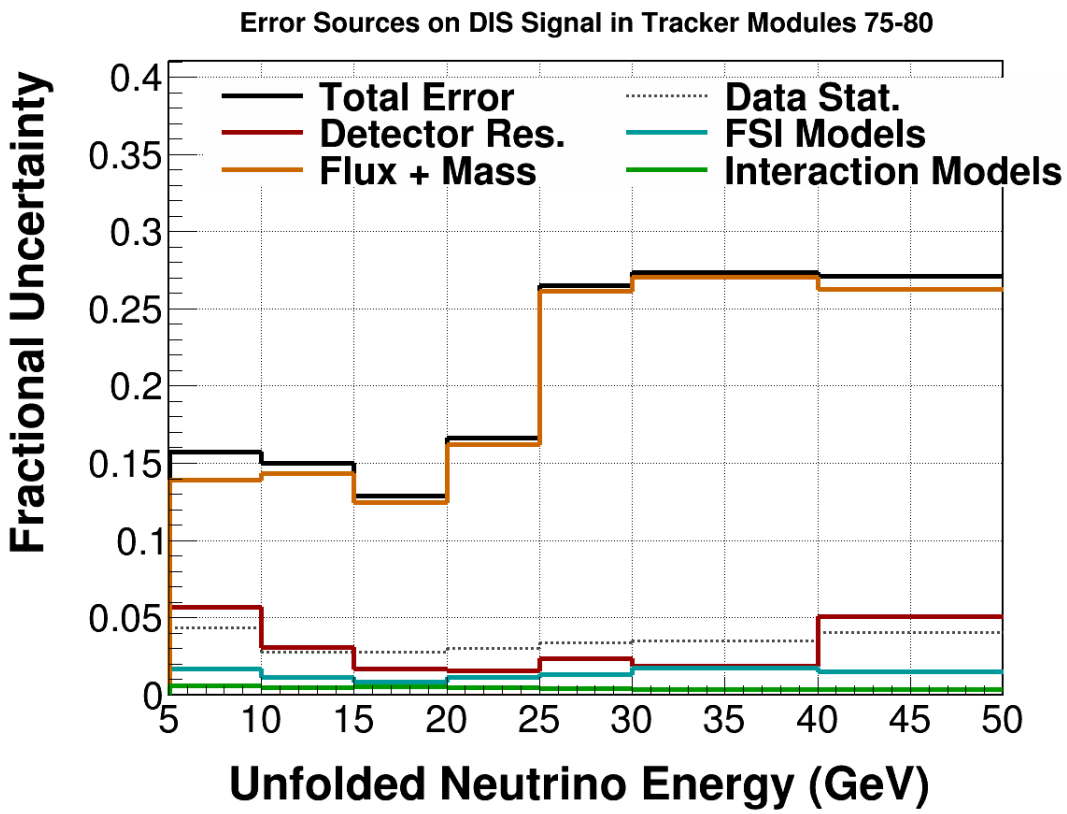

Figure F-57. Unfolded Event yield uncertainties after CH subtraction: tracker mods. 75-80 (E_ν)

The following plots show the uncertainty on the number of DIS events, after subtracting the non-DIS AND CH events. They are plotted as a function of *unfolded* Bjorken-x (x_{bj}):

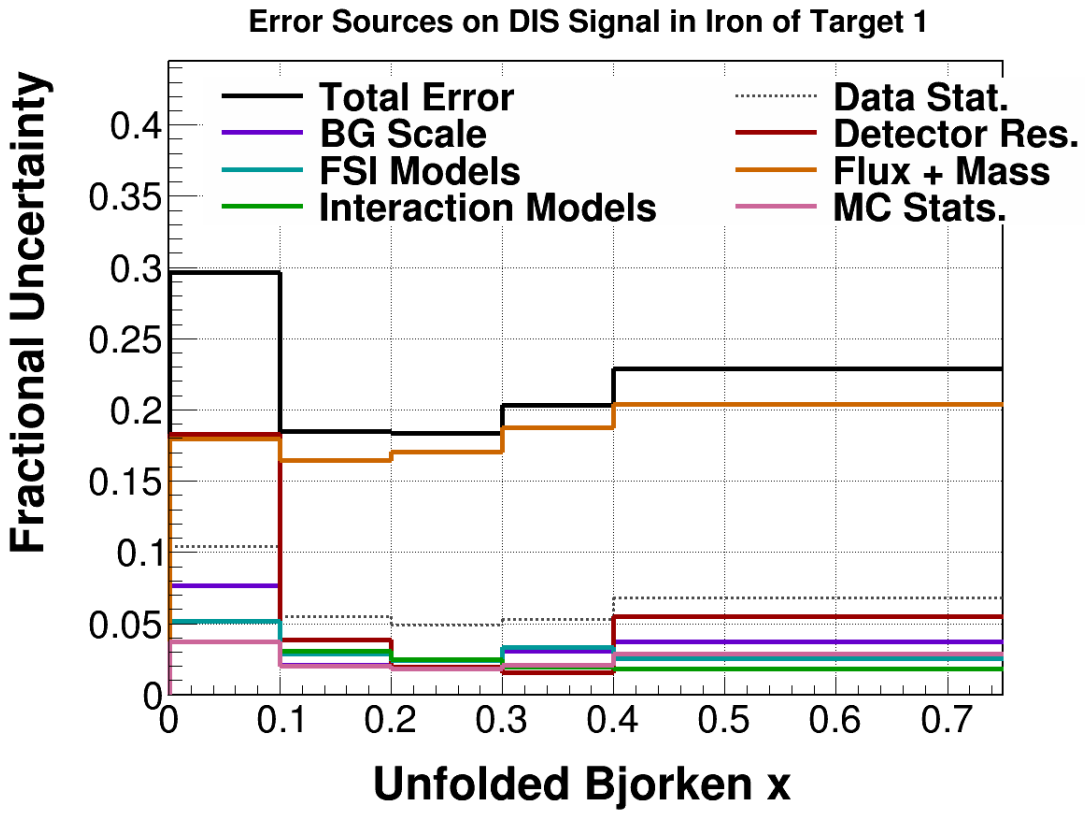

Figure F-58. Unfolded Event yield uncertainties after CH subtraction: target 01 Fe (x_{bj})

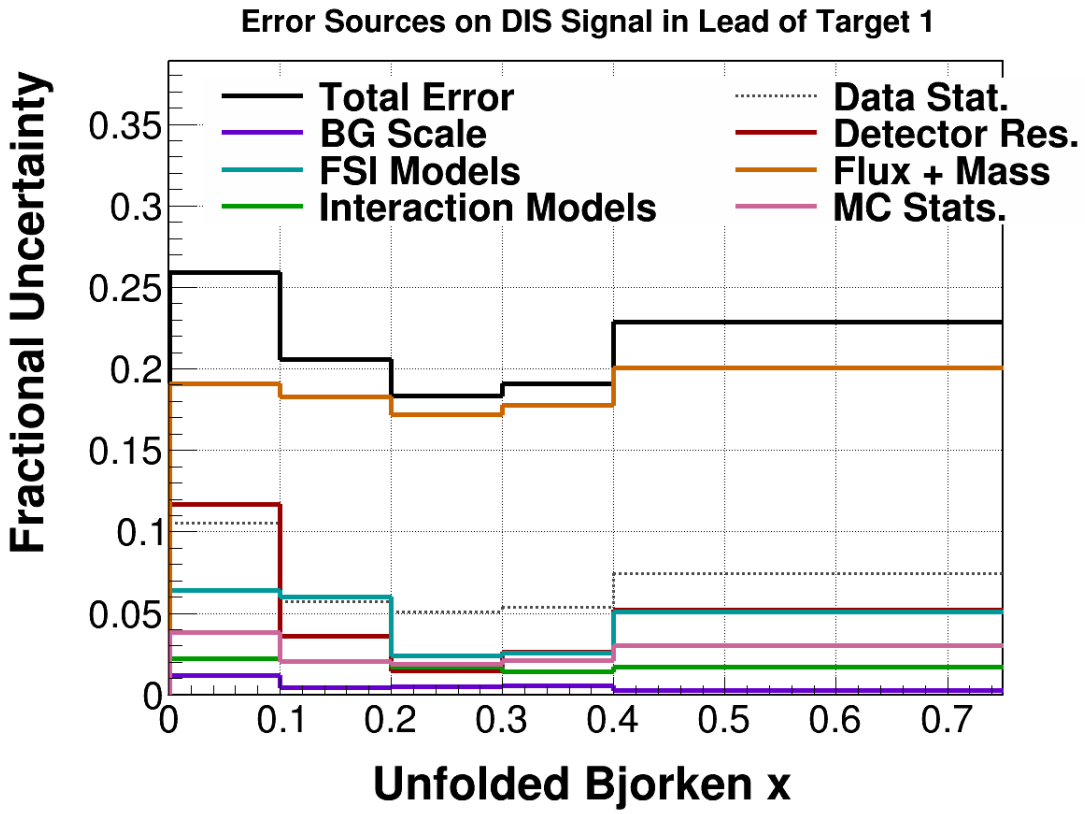

Figure F-59. Unfolded Event yield uncertainties after CH subtraction: target 01 Pb (x_{bj})

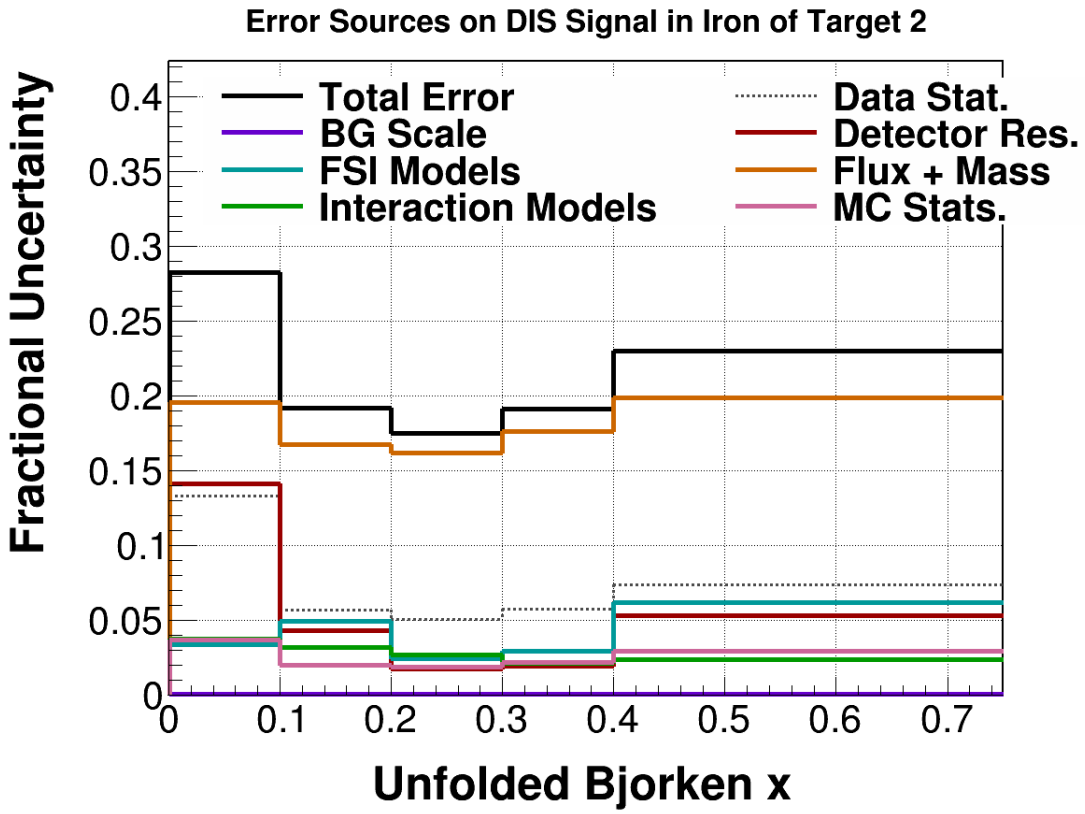

Figure F-60. Unfolded Event yield uncertainties after CH subtraction: target 02 Fe (x_{bj})

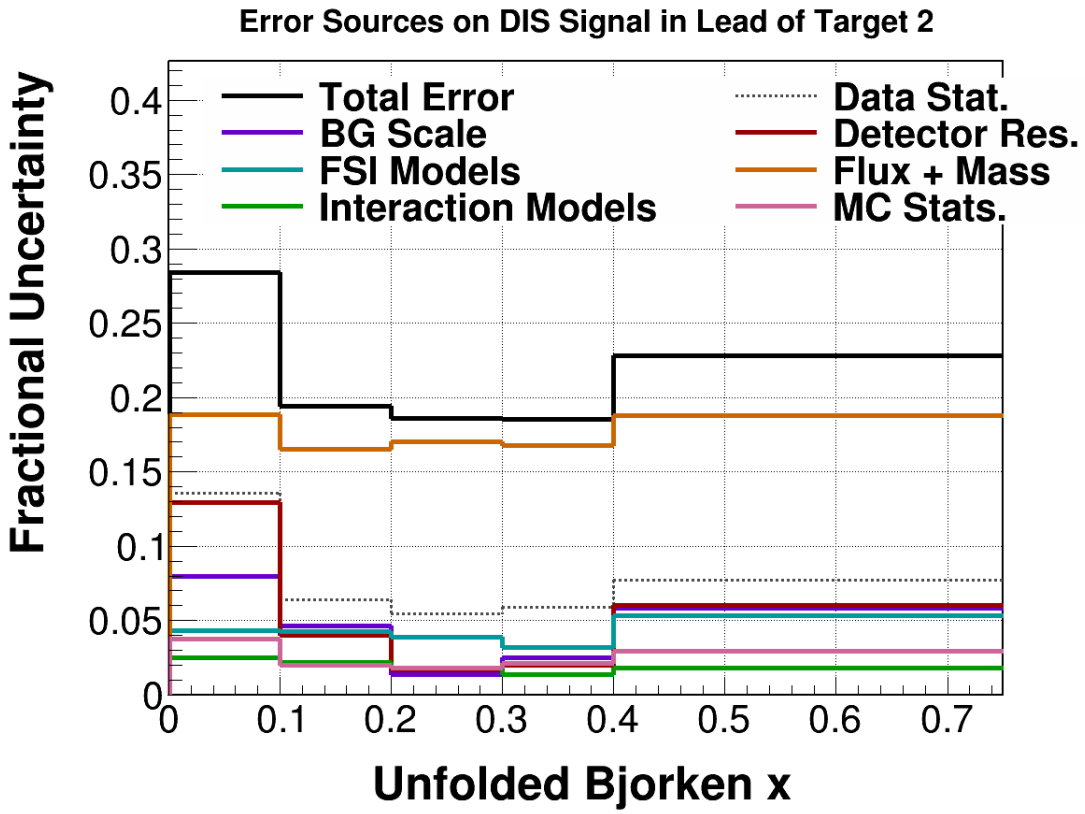

Figure F-61. Unfolded Event yield uncertainties after CH subtraction: target 02 Pb (x_{bj})

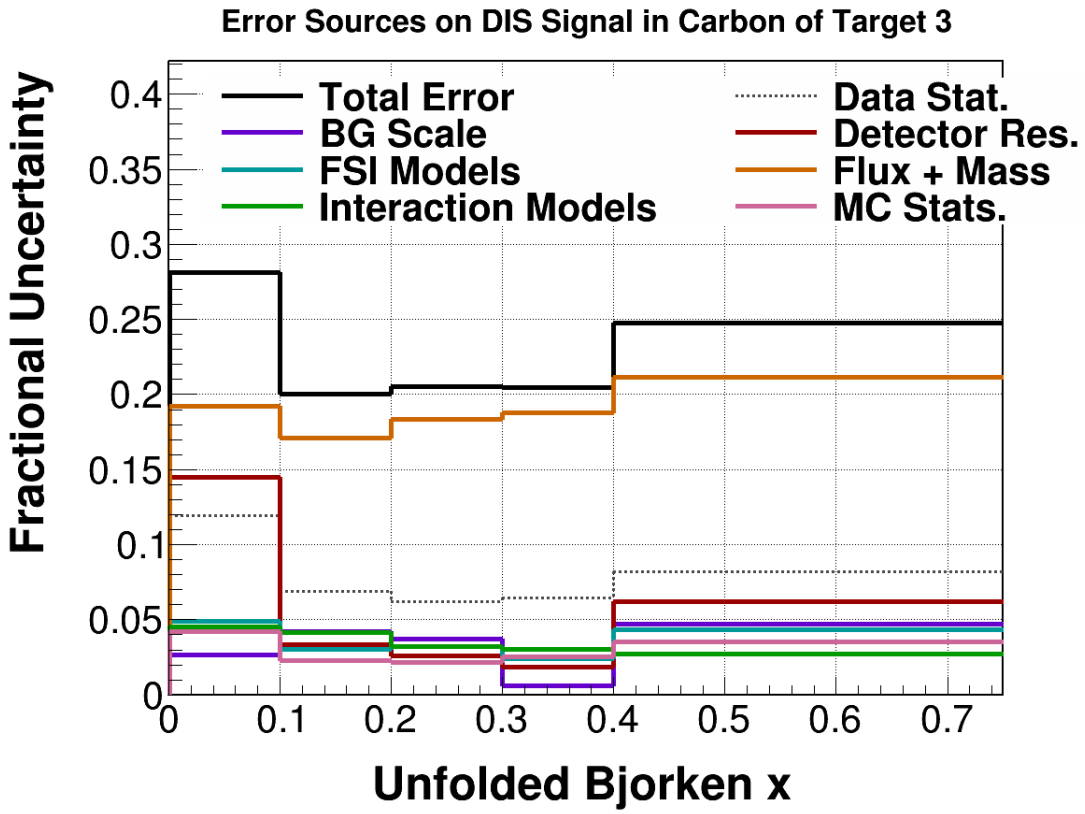

Figure F-62. Unfolded Event yield uncertainties after CH subtraction: target 03 C (x_{bj})

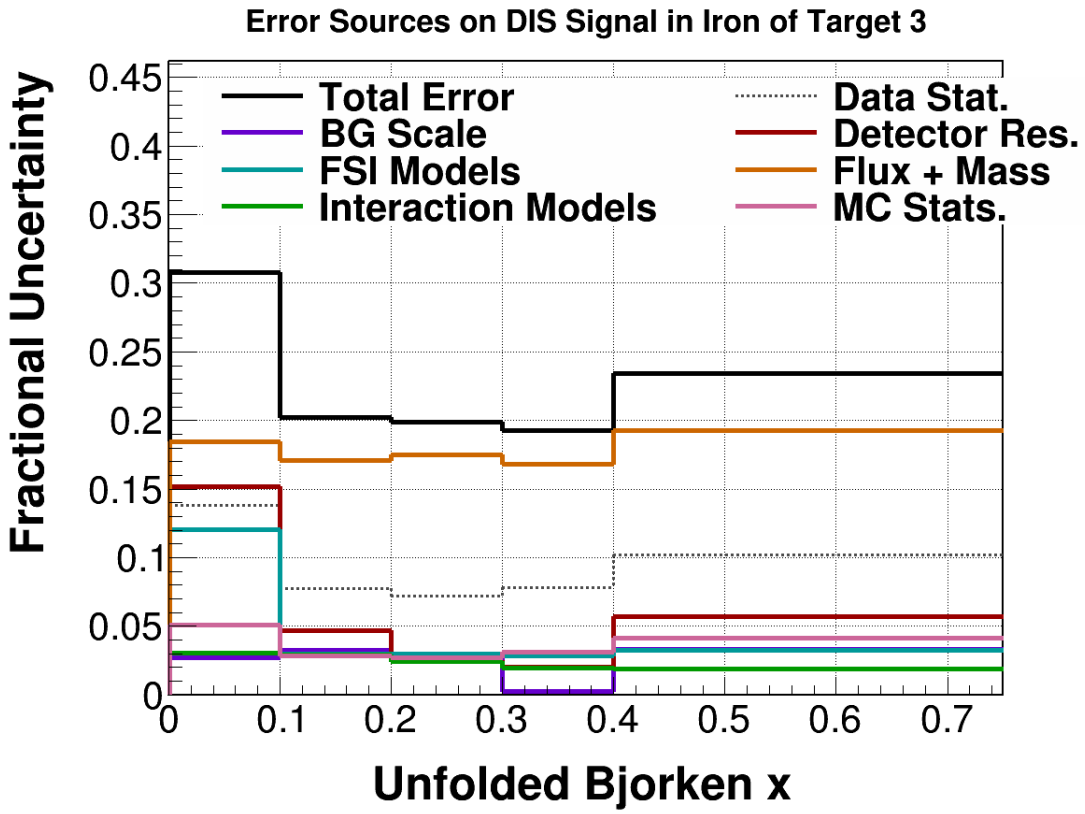

Figure F-63. Unfolded Event yield uncertainties after CH subtraction: target 03 Fe (x_{bj})

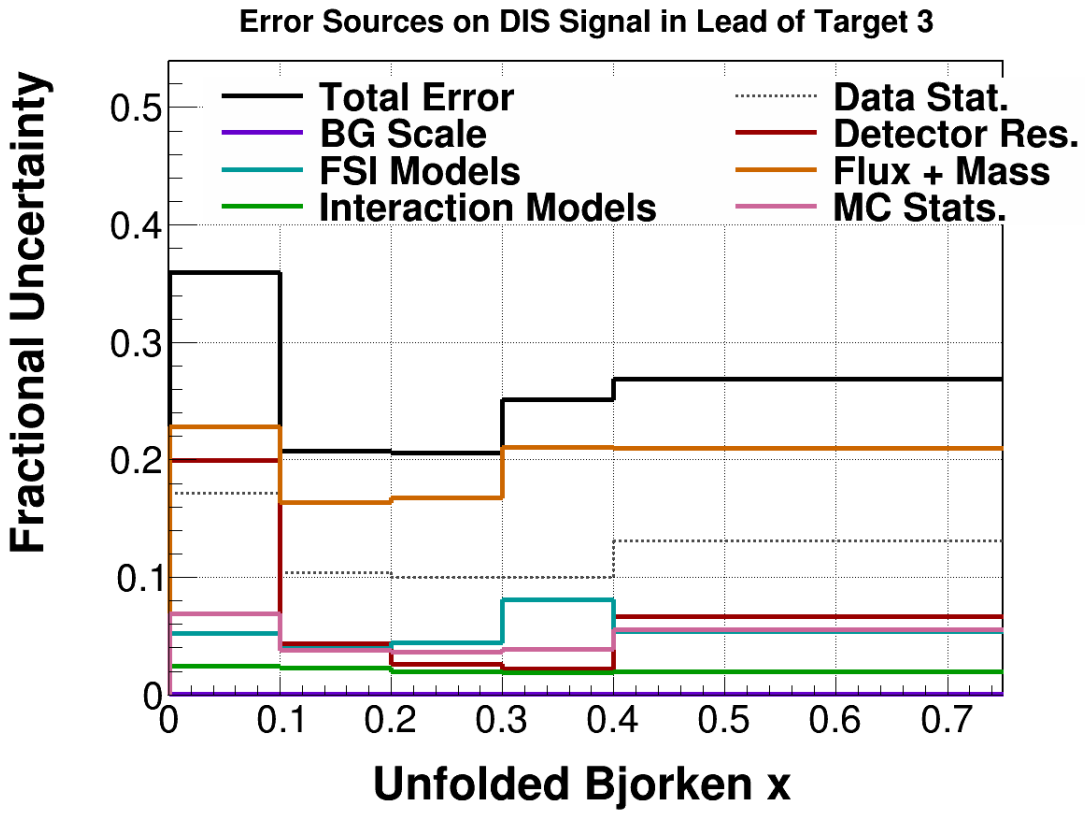

Figure F-64. Unfolded Event yield uncertainties after CH subtraction: target 03 Pb (x_{bj})

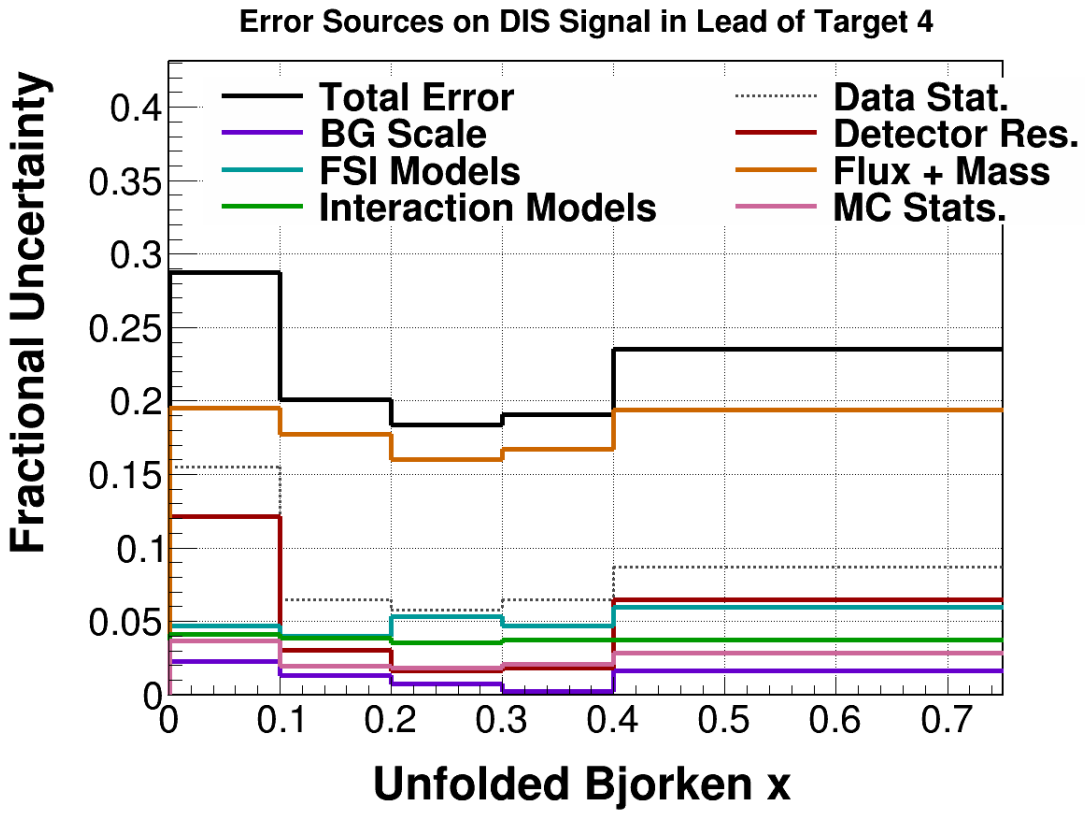

Figure F-65. Unfolded Event yield uncertainties after CH subtraction: target 04 Pb (x_{bj})

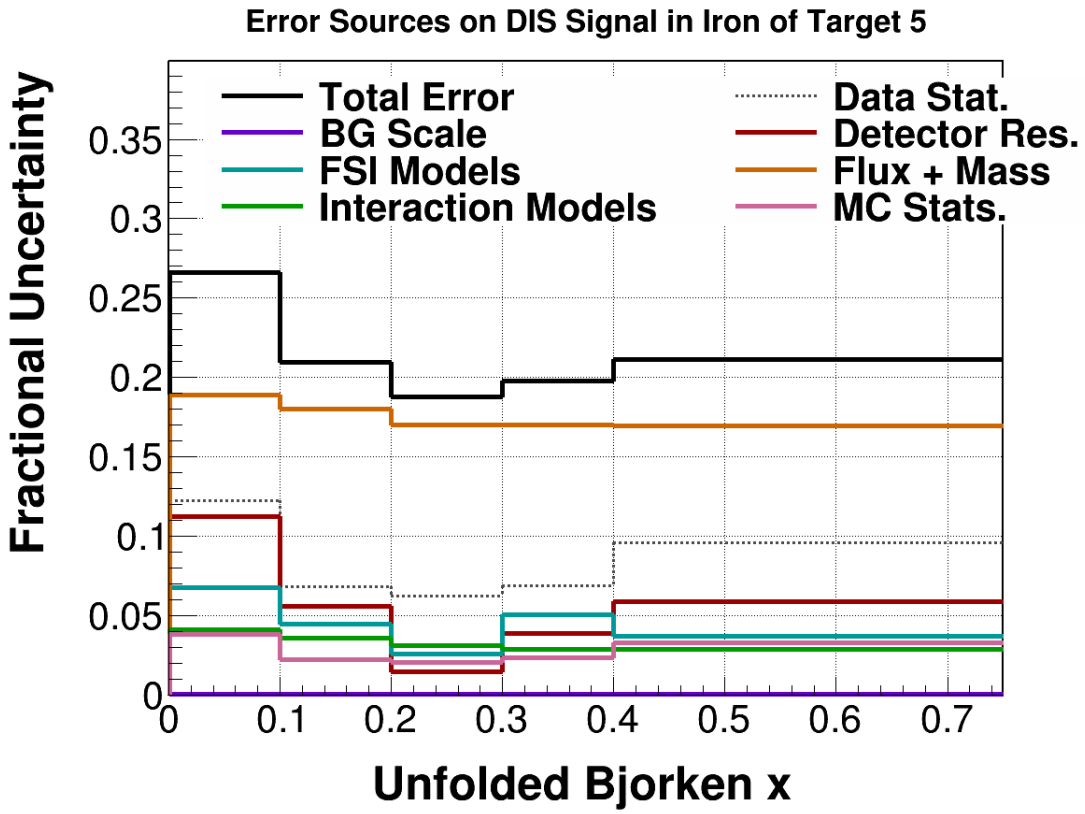

Figure F-66. Unfolded Event yield uncertainties after CH subtraction: target 05 Fe (x_{bj})

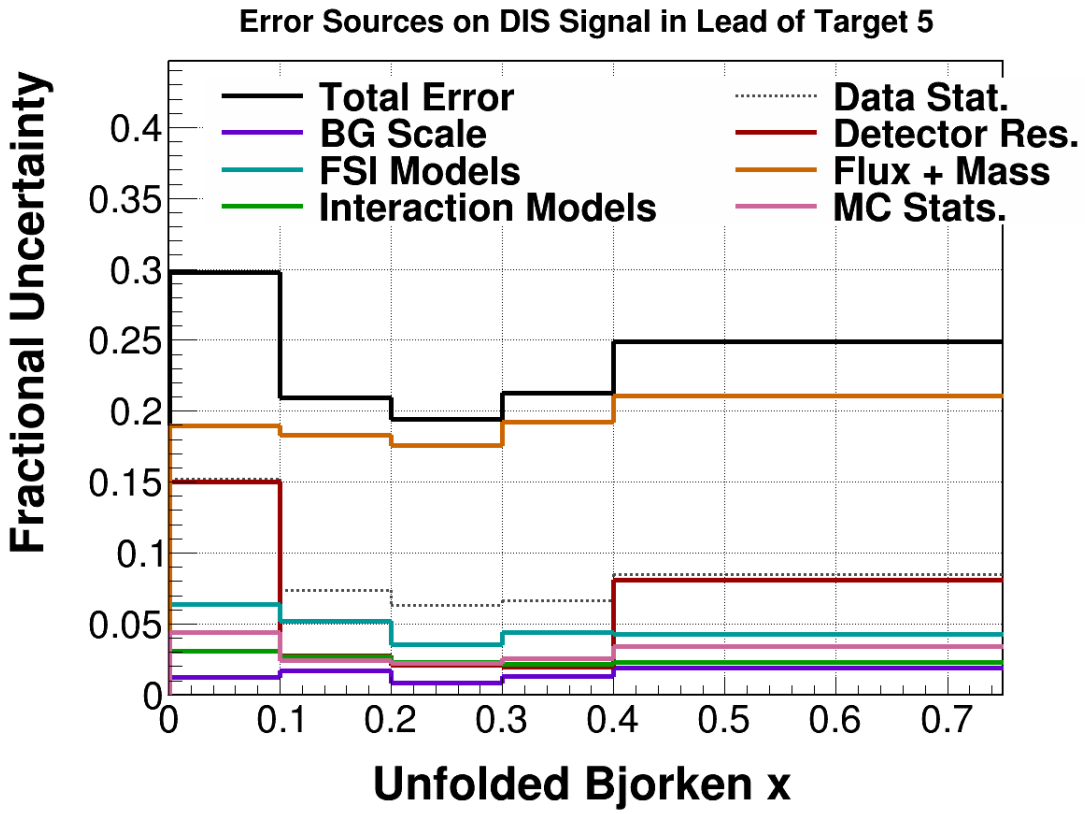

Figure F-67. Unfolded Event yield uncertainties after CH subtraction: target 05 Pb (x_{bj})

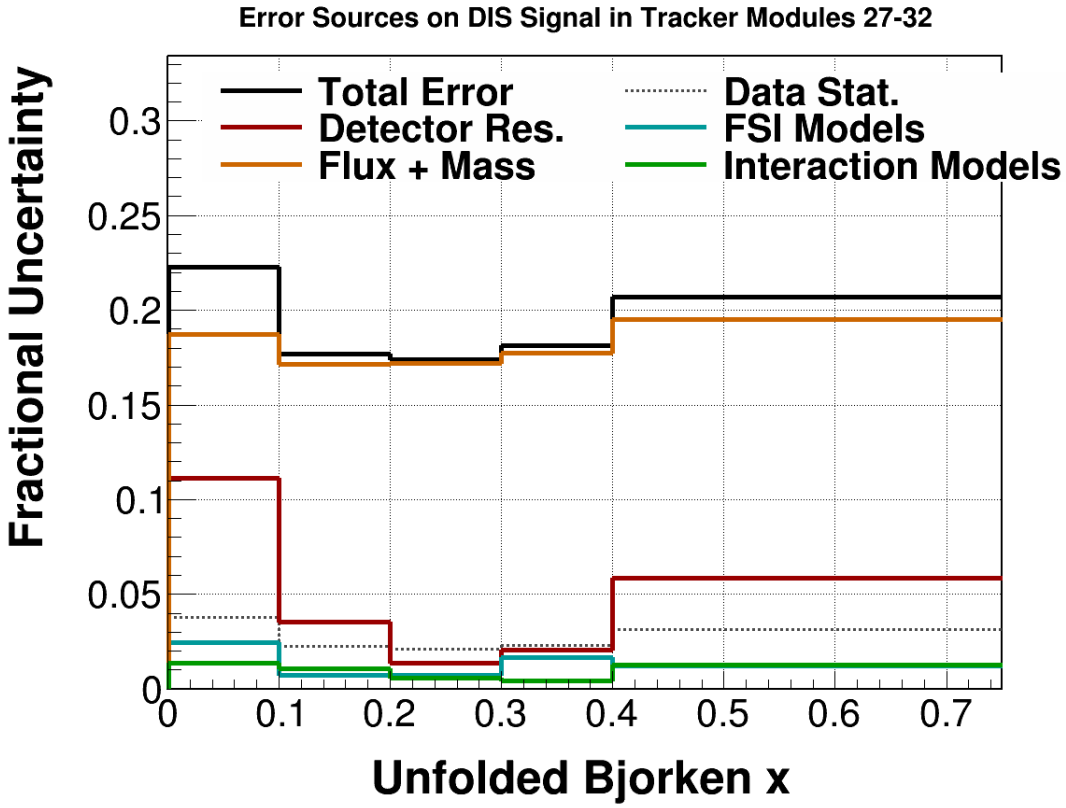

Figure F-68. Unfolded Event yield uncertainties after CH subtraction: tracker mods. 27-32 (x_{bj})

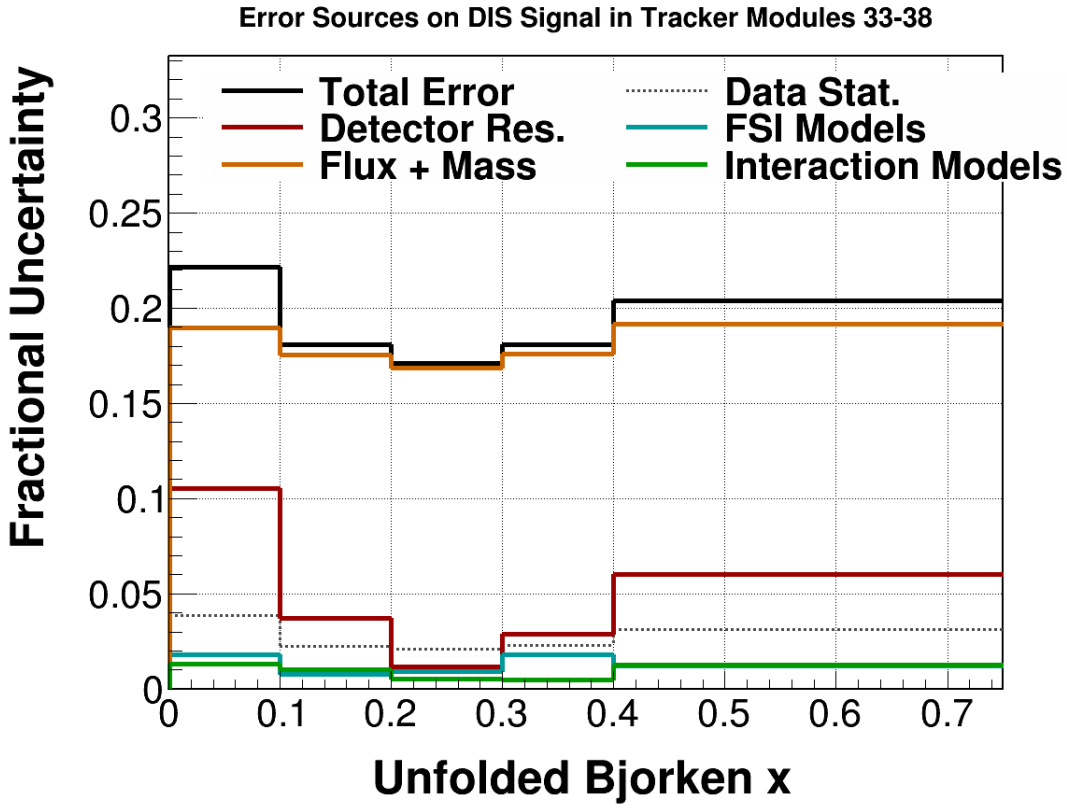

Figure F-69. Unfolded Event yield uncertainties after CH subtraction: tracker mods. 33-38 (x_{bj})

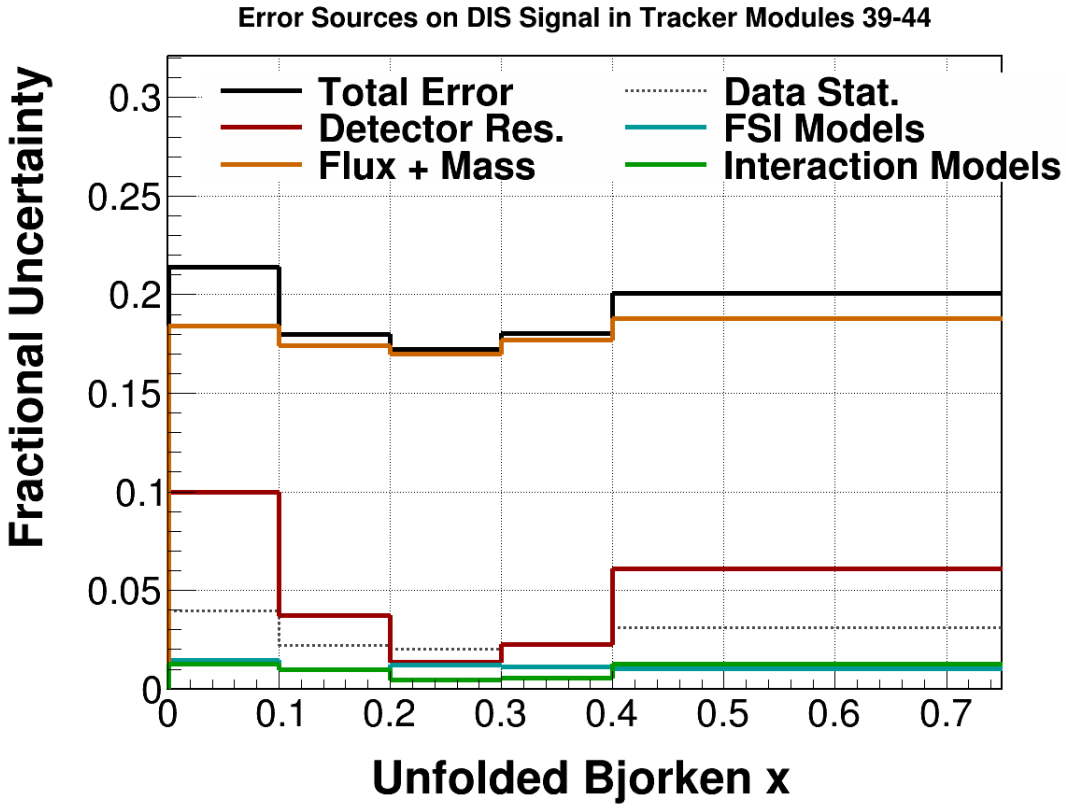

Figure F-70. Unfolded Event yield uncertainties after CH subtraction: tracker mods. 39-44 (x_{bj})

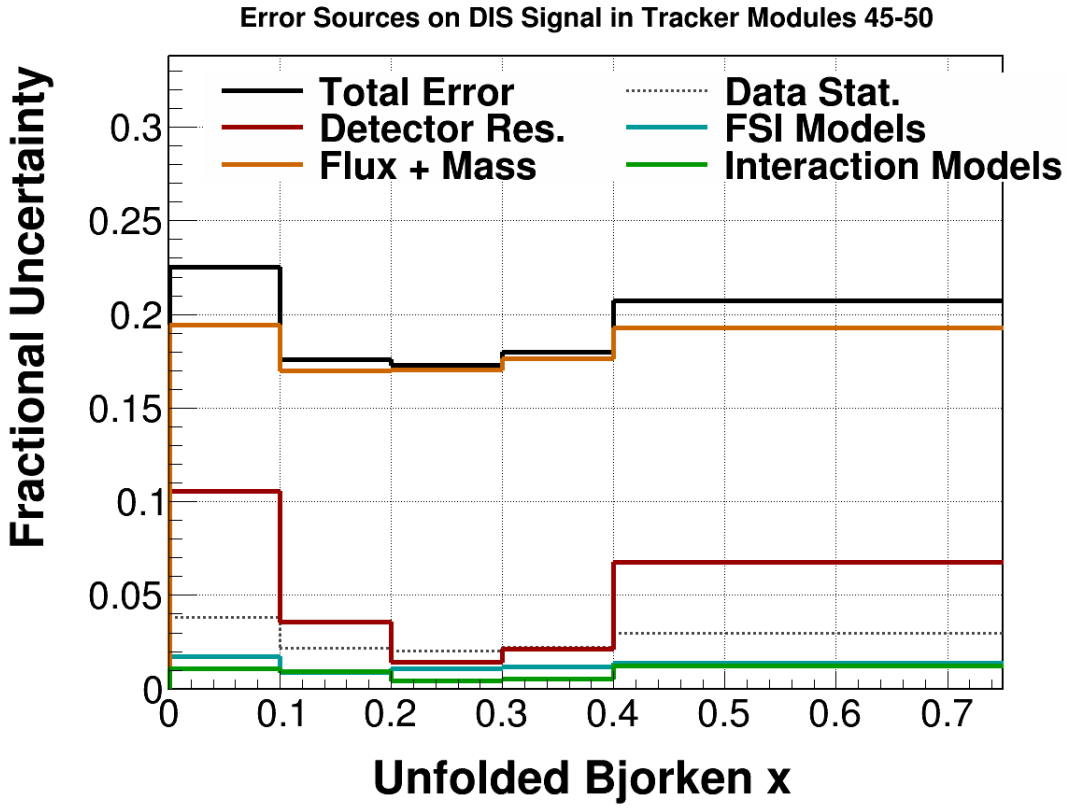

Figure F-71. Unfolded Event yield uncertainties after CH subtraction: tracker mods. 45-50 (x_{bj})

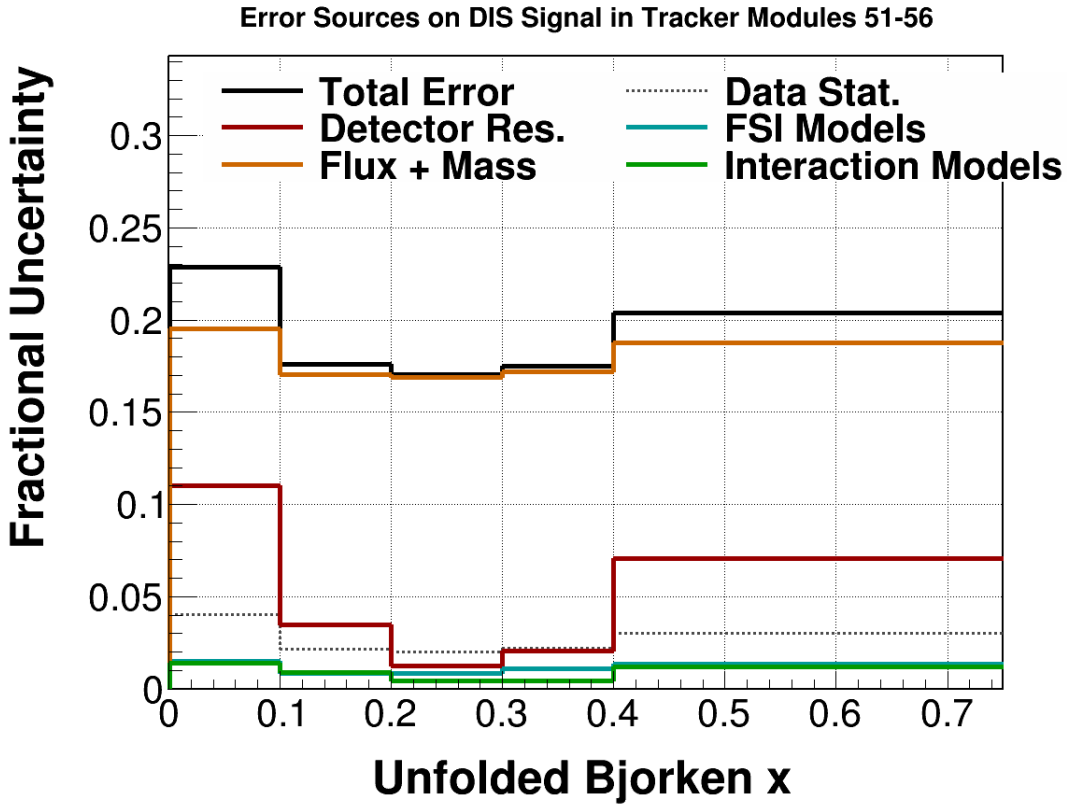

Figure F-72. Unfolded Event yield uncertainties after CH subtraction: tracker mods. 51-56 (x_{bj})

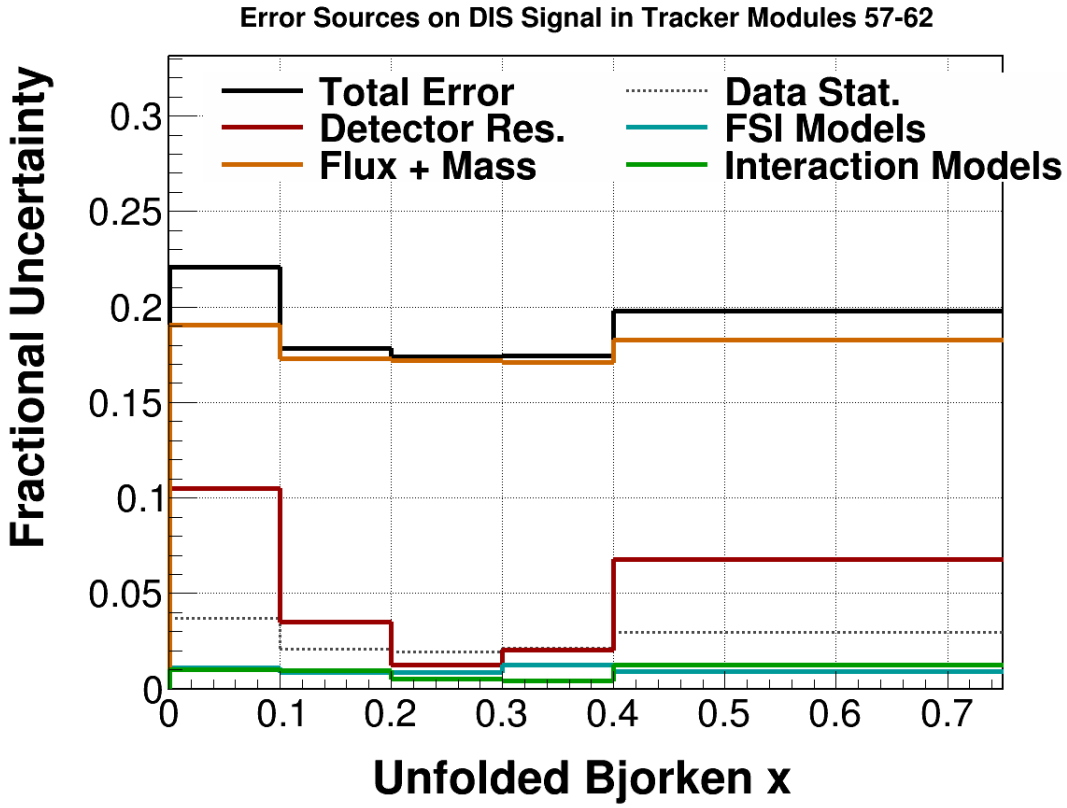

Figure F-73. Unfolded Event yield uncertainties after CH subtraction: tracker mods. 57-62 (x_{bj})

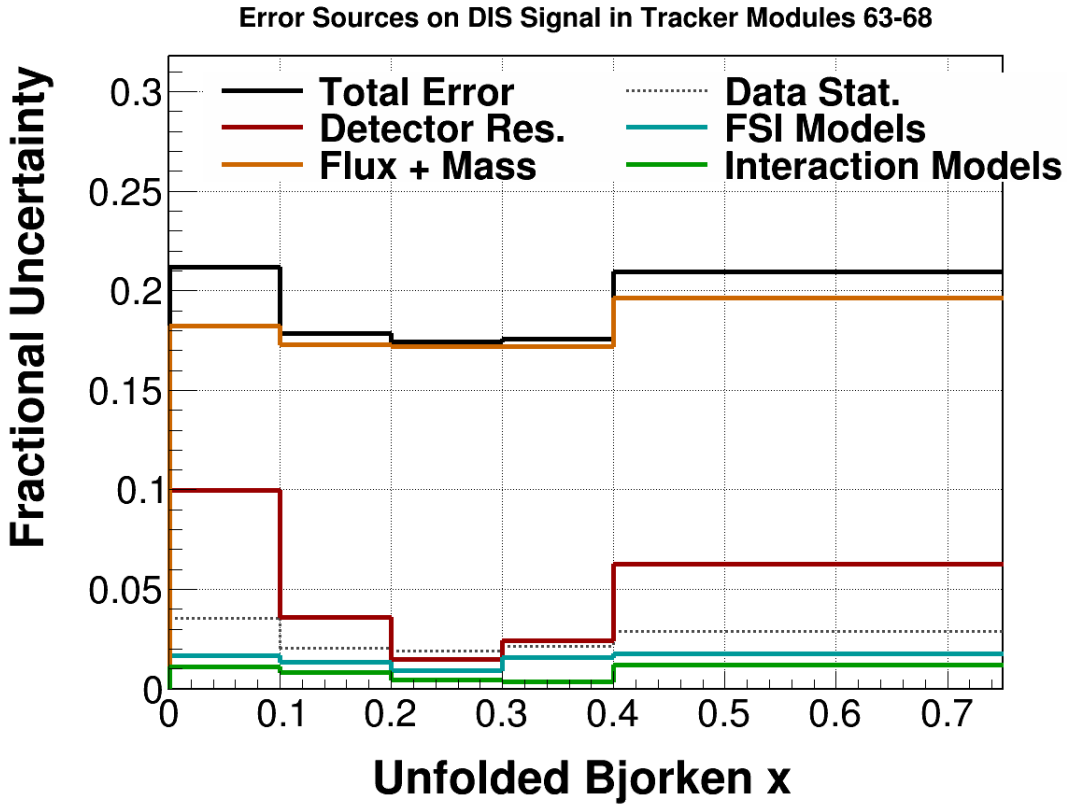

Figure F-74. Unfolded Event yield uncertainties after CH subtraction: tracker mods. 63-68 (x_{bj})

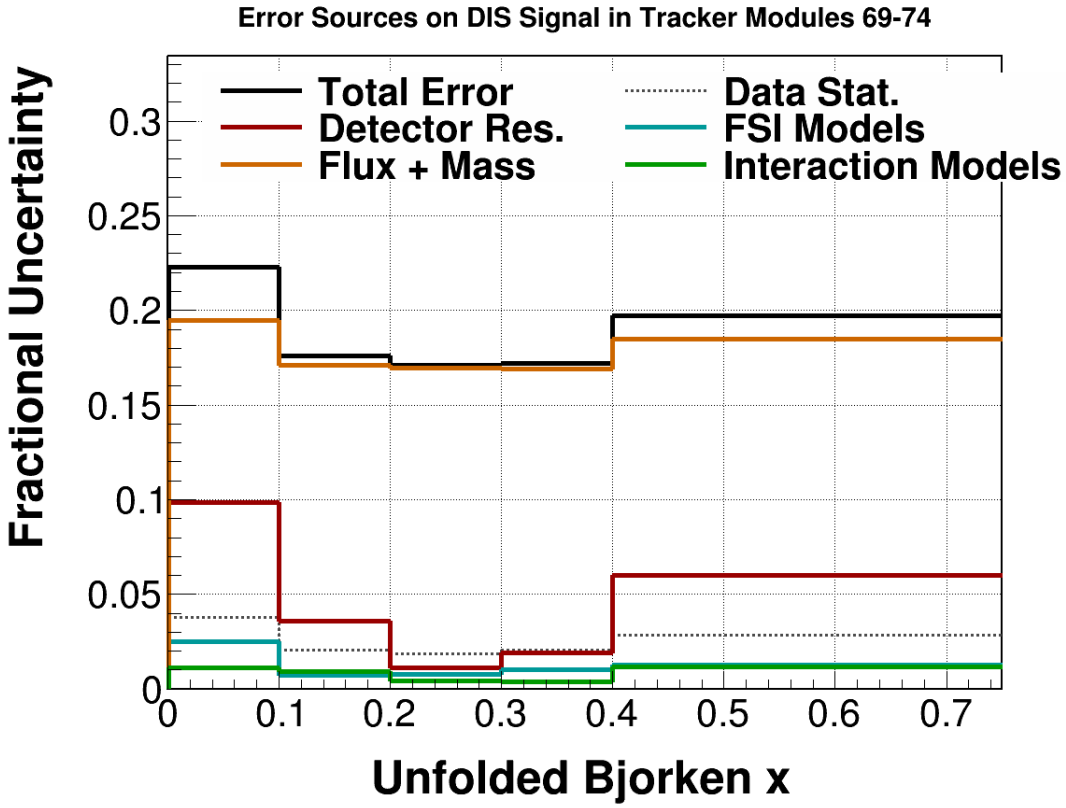

Figure F-75. Unfolded Event yield uncertainties after CH subtraction: tracker mods. 69-74 (x_{bj})

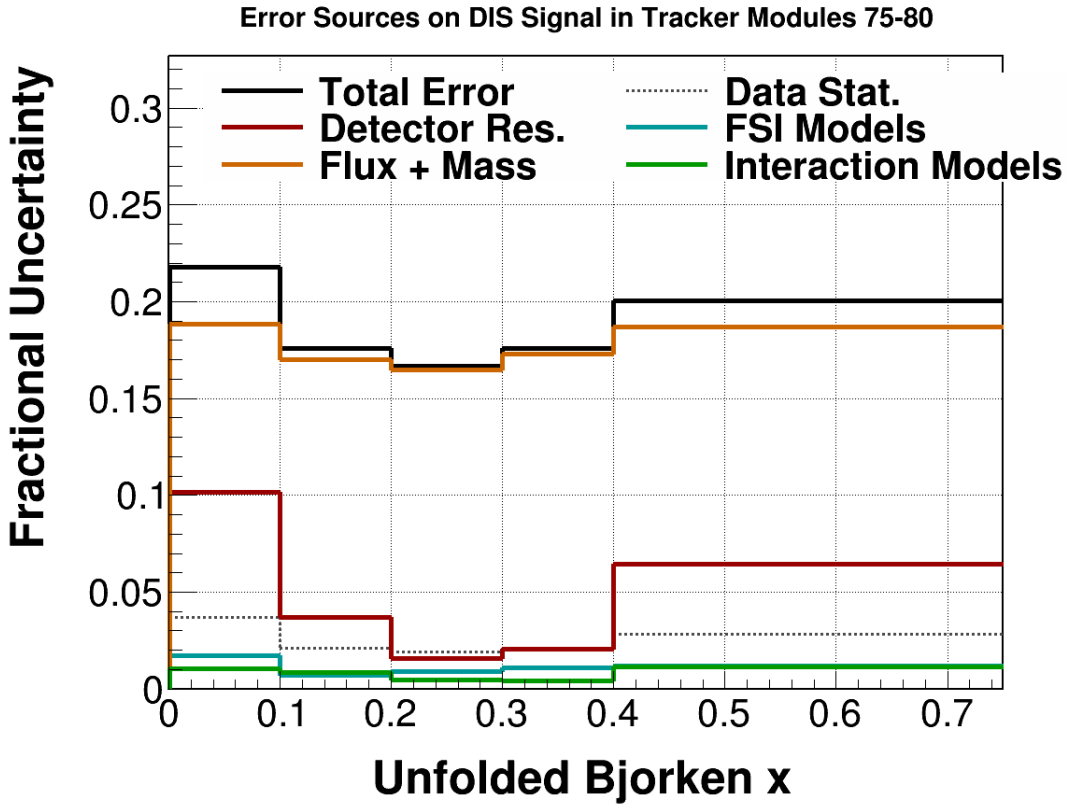

Figure F-76. Unfolded Event yield uncertainties after CH subtraction: tracker mods. 75-80 (x_{bj})

APPENDIX G
EFFICIENCY PLOTS

G.1 Overall Efficiency

The following plots show the overall efficiency of DIS event selection. They are plotted as a function of true neutrino energy (E_ν):

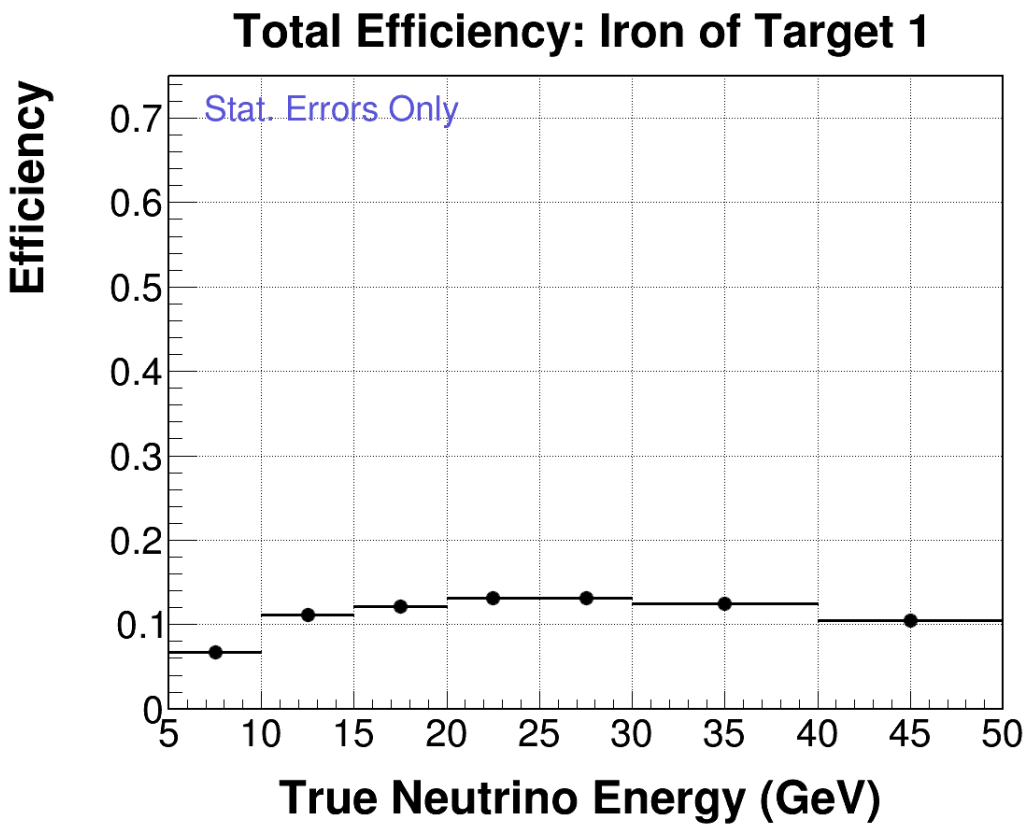

Figure G-1. Overall efficiency: target 01 Fe (E_ν)

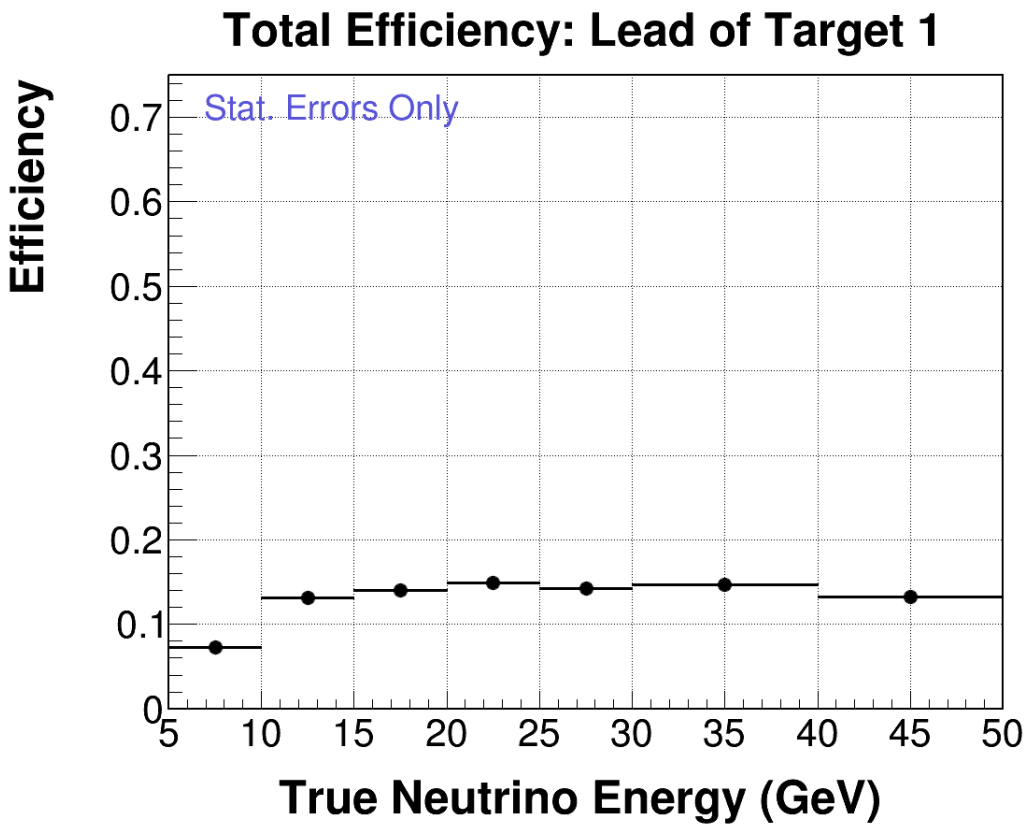

Figure G-2. Overall efficiency: target 01 Pb (E_ν)

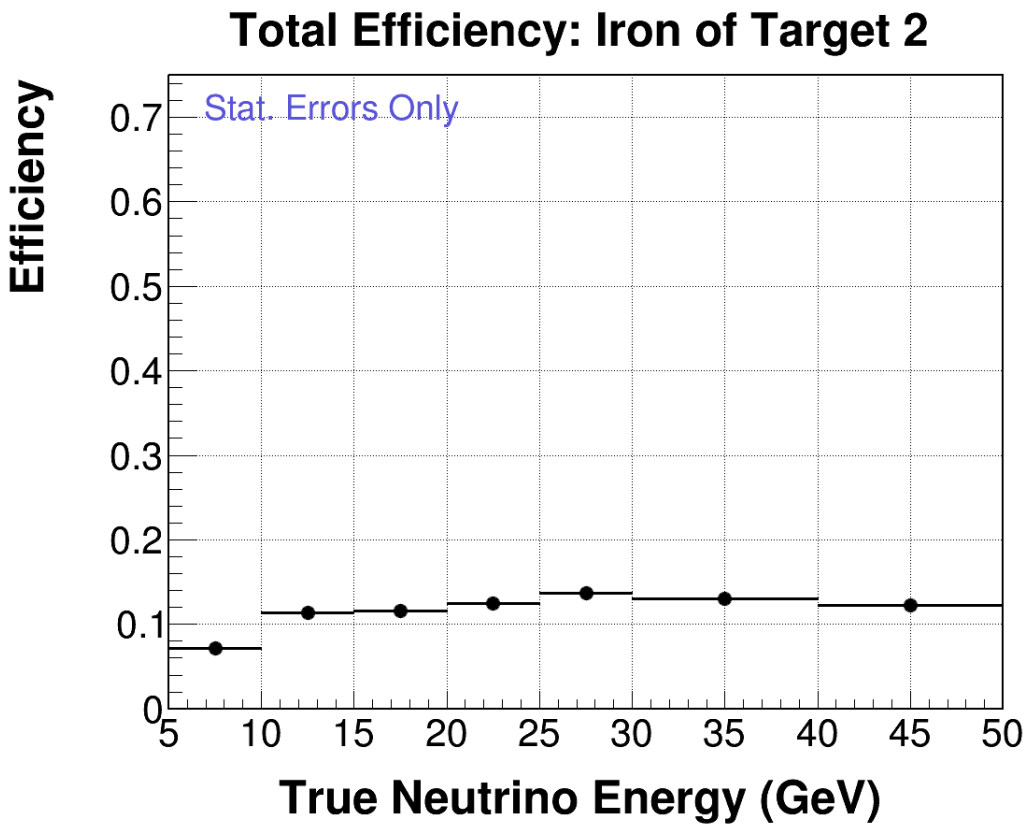

Figure G-3. Overall efficiency: target 02 Fe (E_ν)

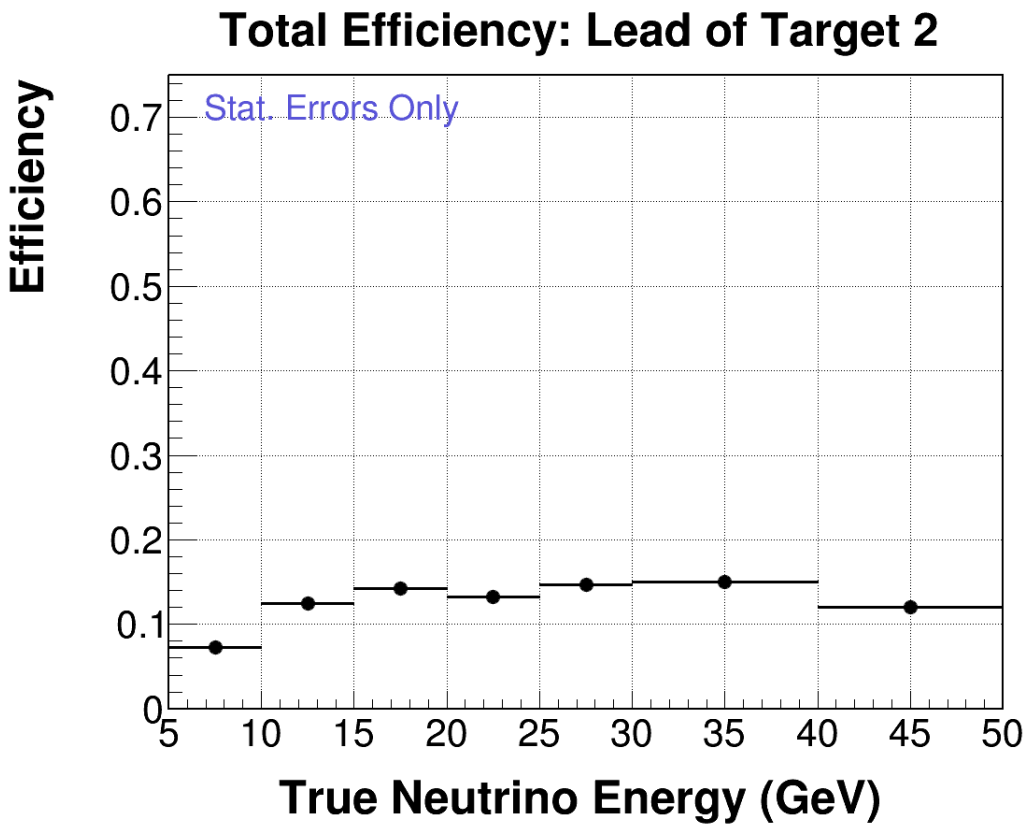

Figure G-4. Overall efficiency: target 02 Pb (E_ν)

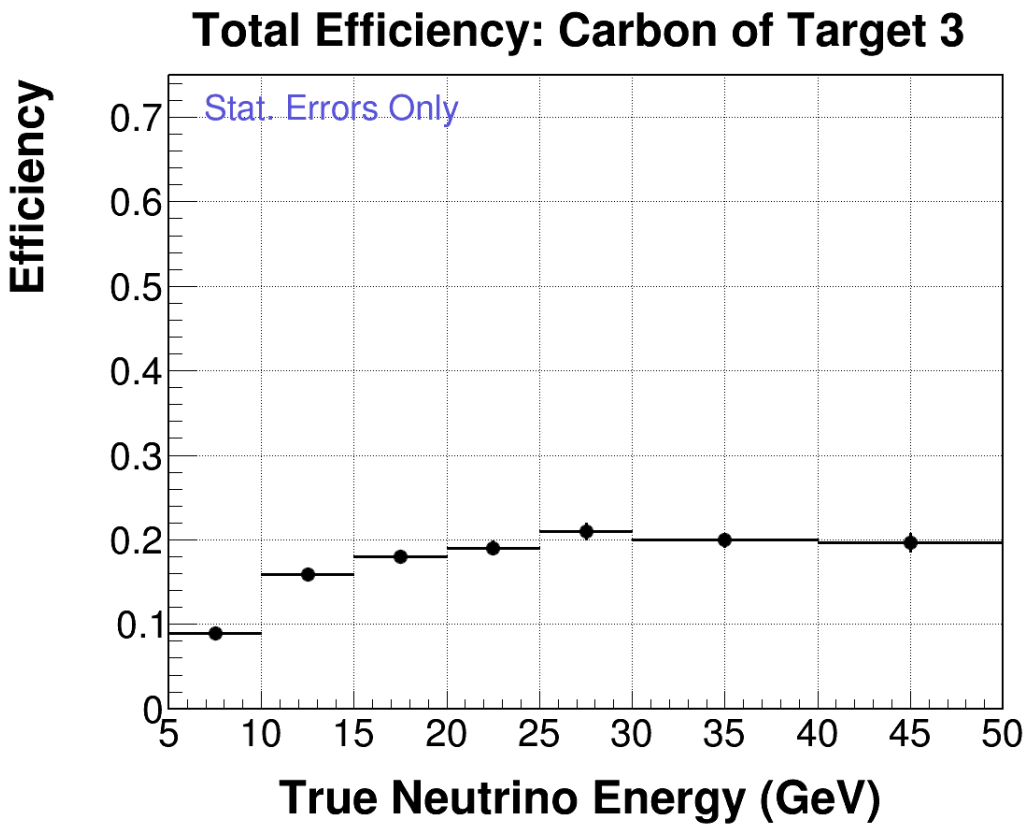

Figure G-5. Overall efficiency: target 03 C (E_ν)

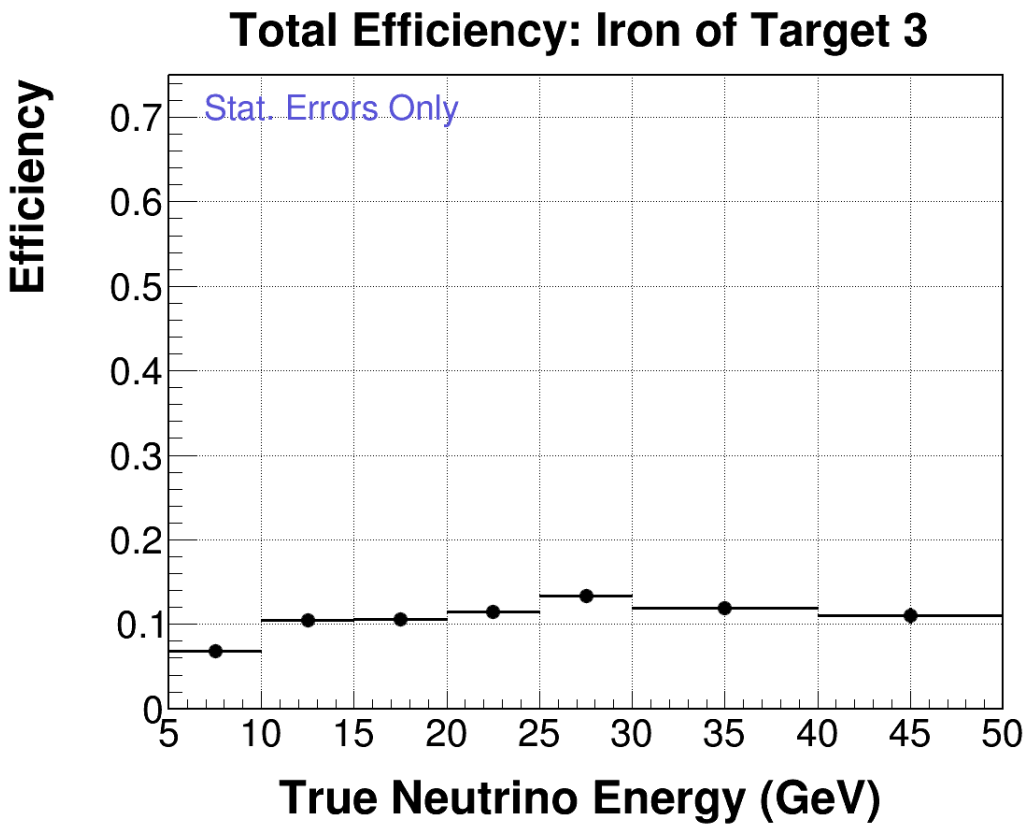

Figure G-6. Overall efficiency: target 03 Fe (E_ν)

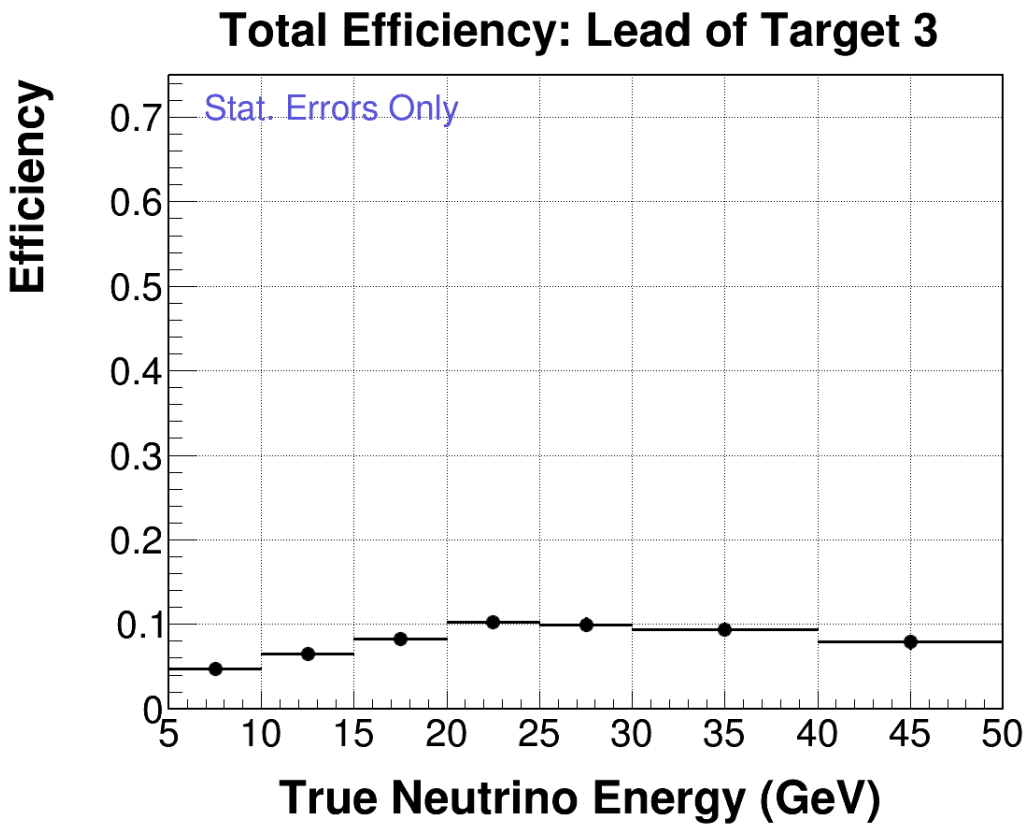

Figure G-7. Overall efficiency: target 03 Pb (E_ν)

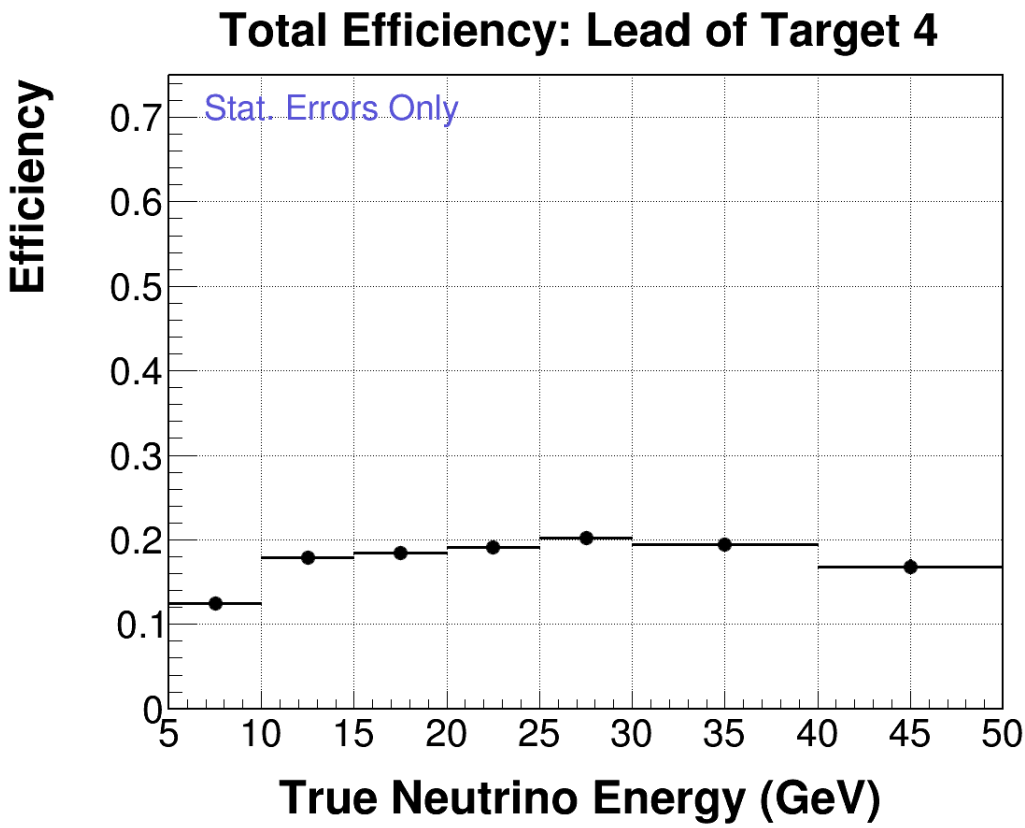

Figure G-8. Overall efficiency: target 04 Pb (E_ν)

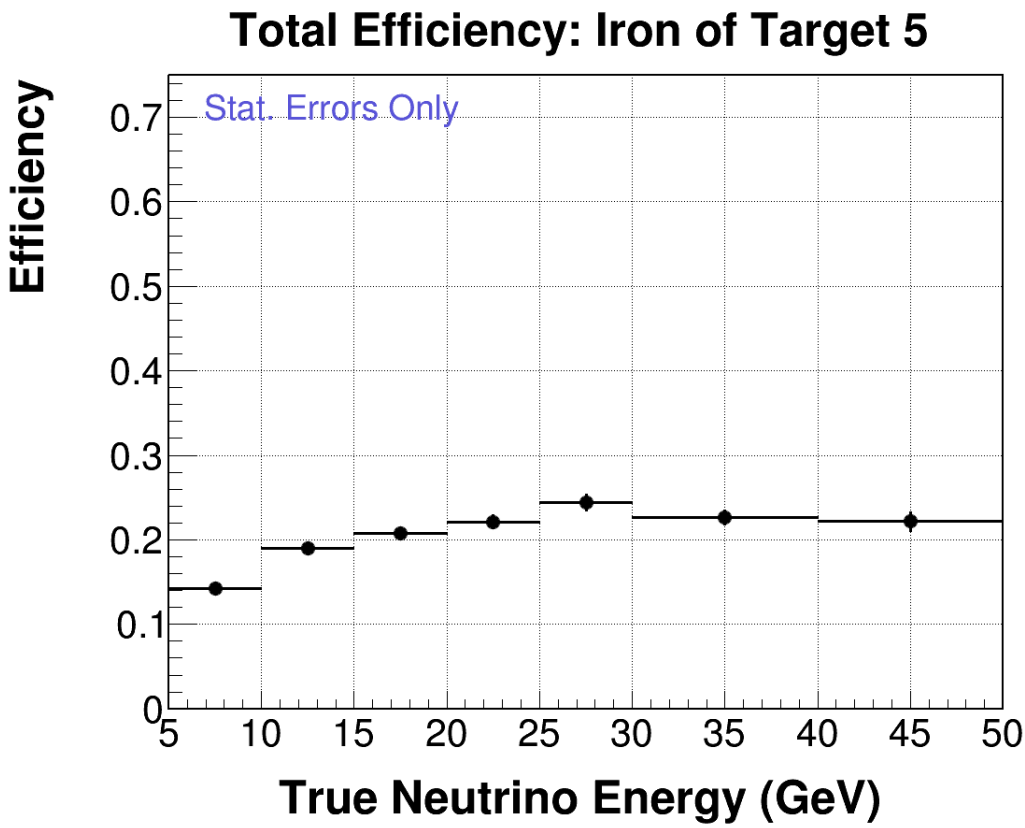

Figure G-9. Overall efficiency: target 05 Fe (E_ν)

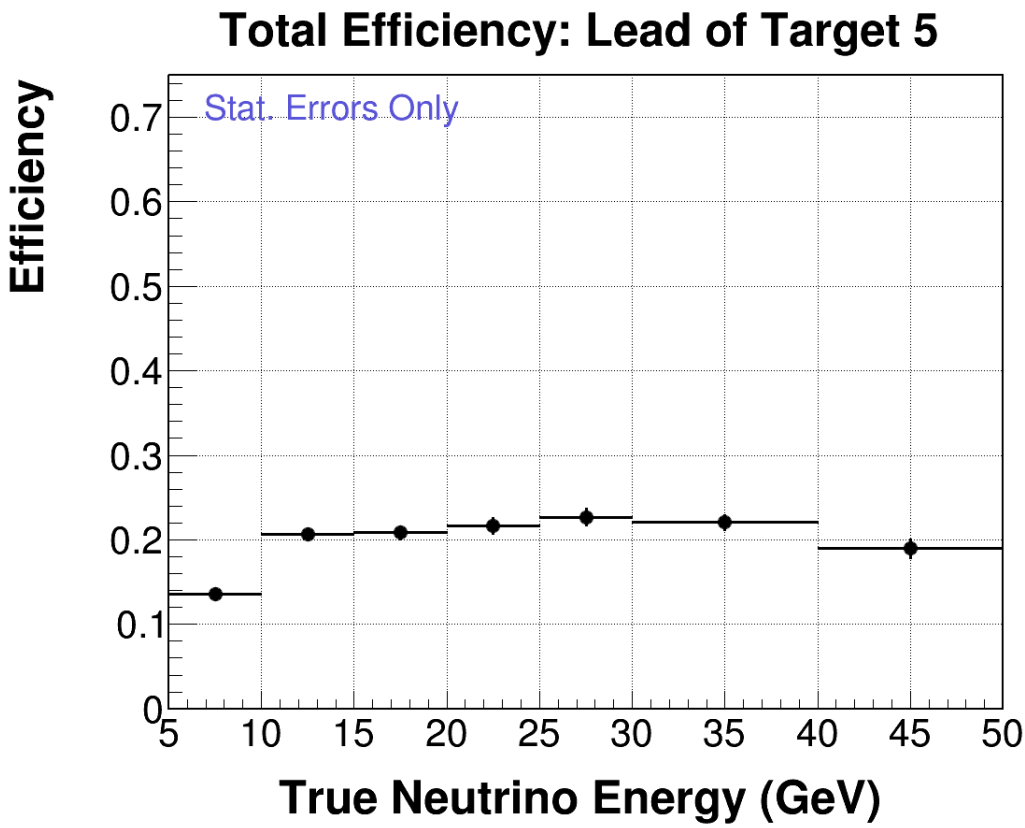

Figure G-10. Overall efficiency: target 05 Pb (E_ν)

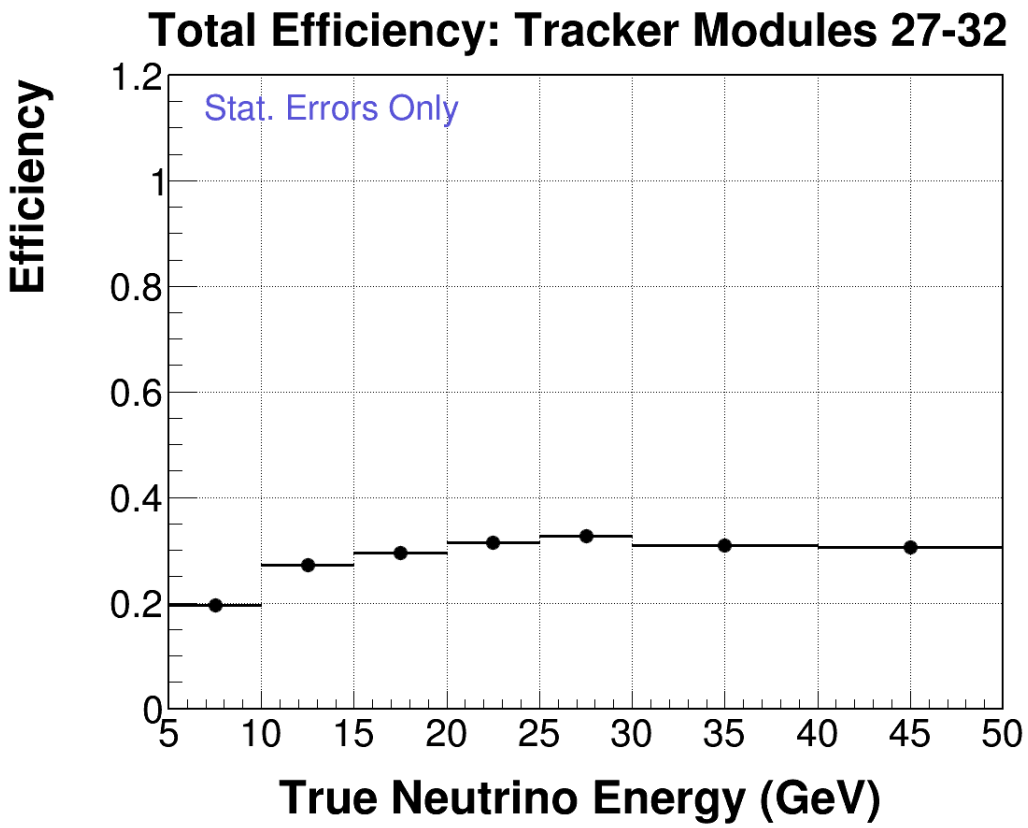

Figure G-11. Overall efficiency: tracker mods. 27-32 (E_ν)

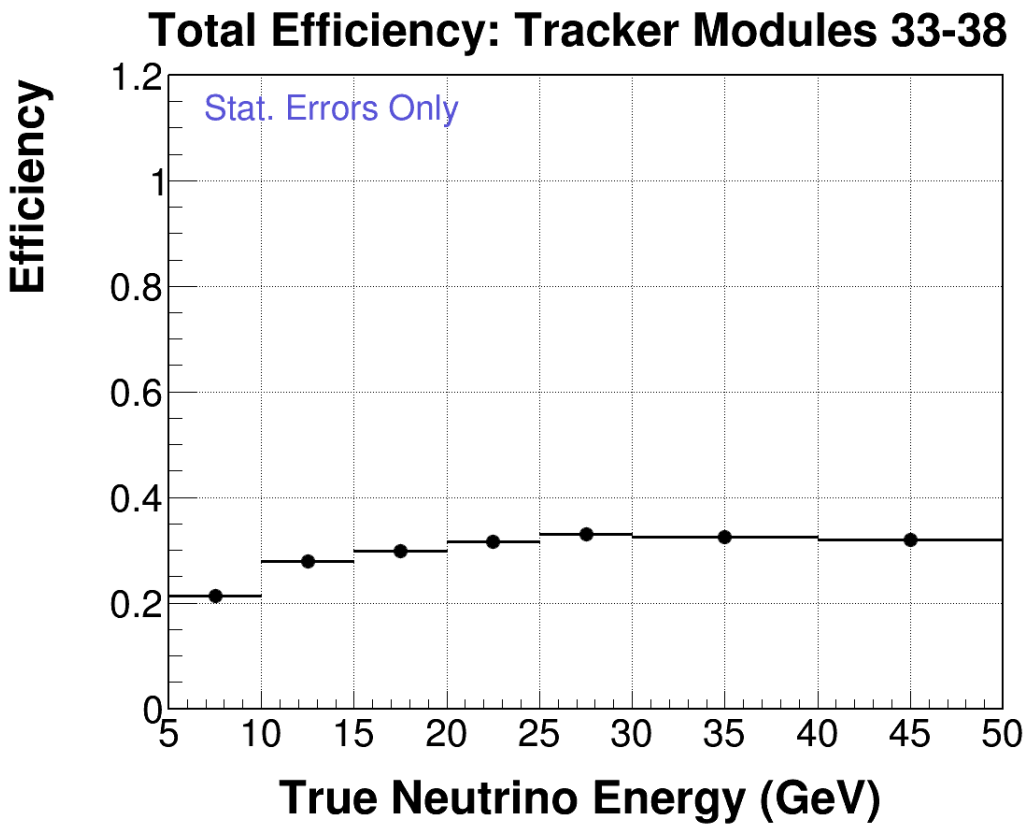

Figure G-12. Overall efficiency: tracker mods. 33-38 (E_ν)

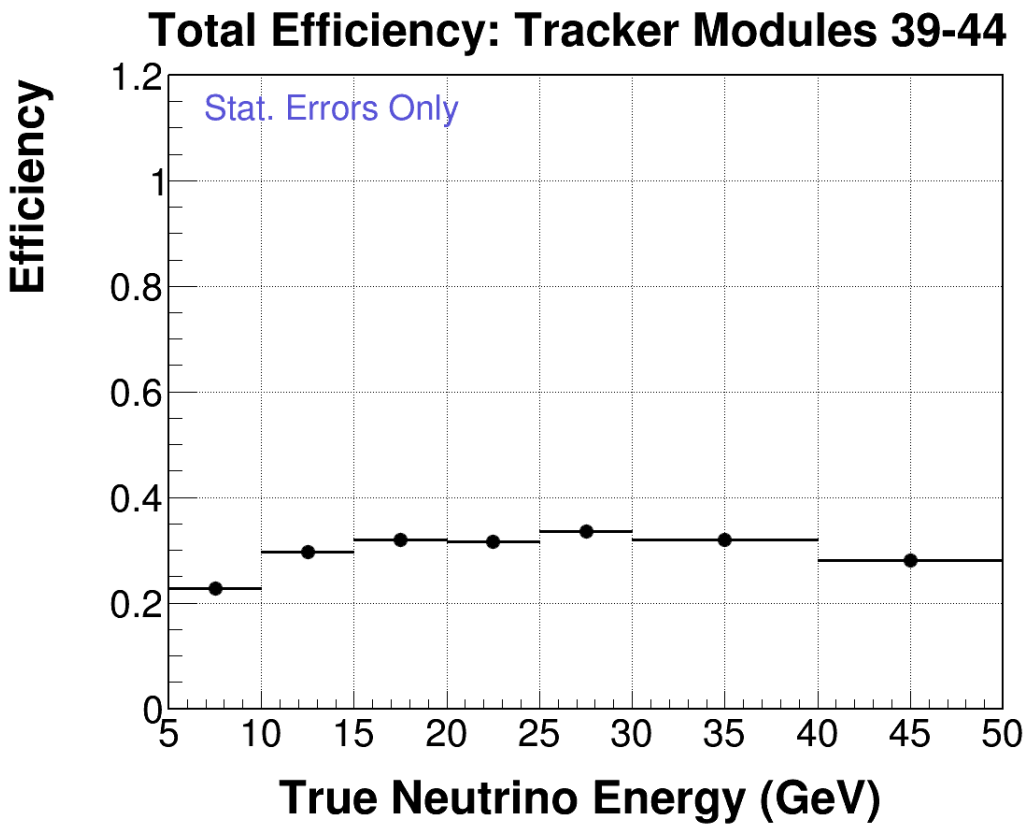

Figure G-13. Overall efficiency: tracker mods. 39-44 (E_ν)

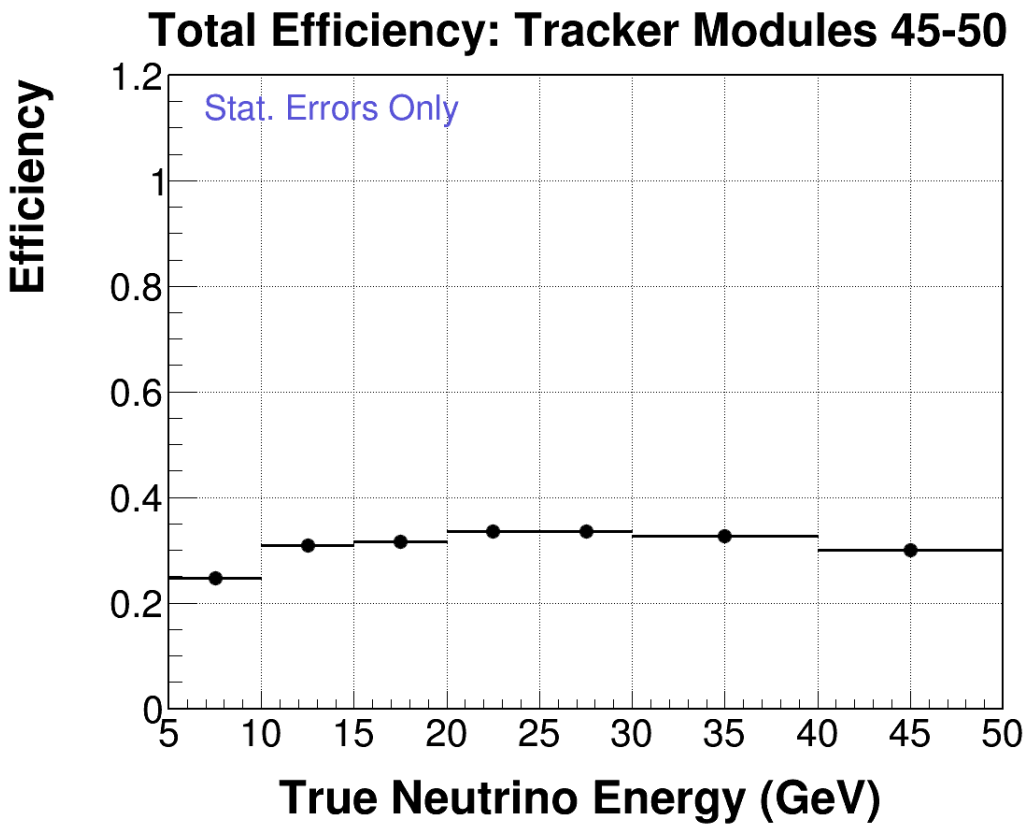

Figure G-14. Overall efficiency: tracker mods. 45-50 (E_ν)

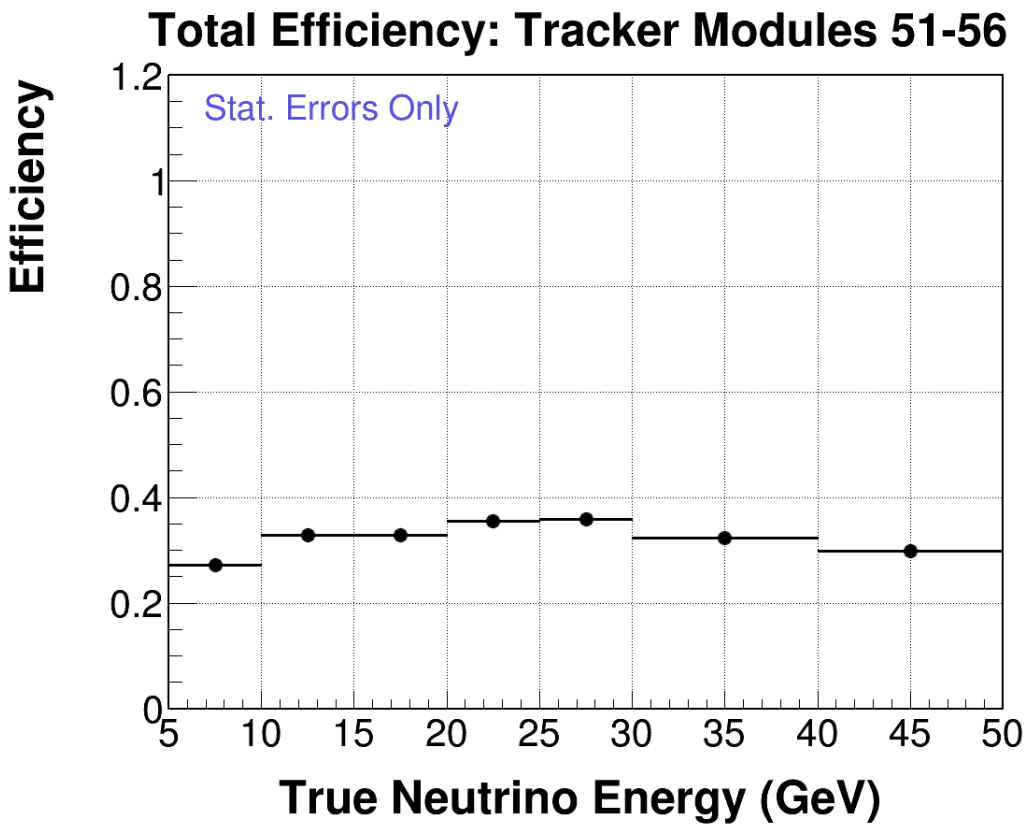

Figure G-15. Overall efficiency: tracker mods. 51-56 (E_ν)

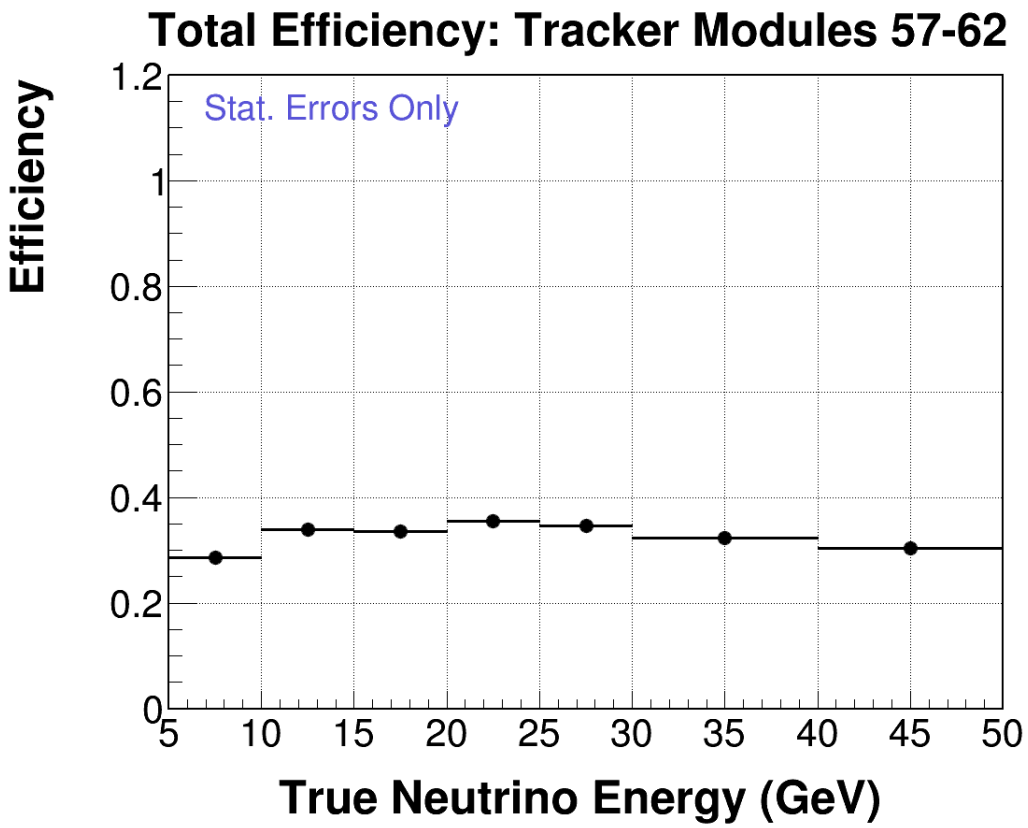

Figure G-16. Overall efficiency: tracker mods. 57-62 (E_ν)

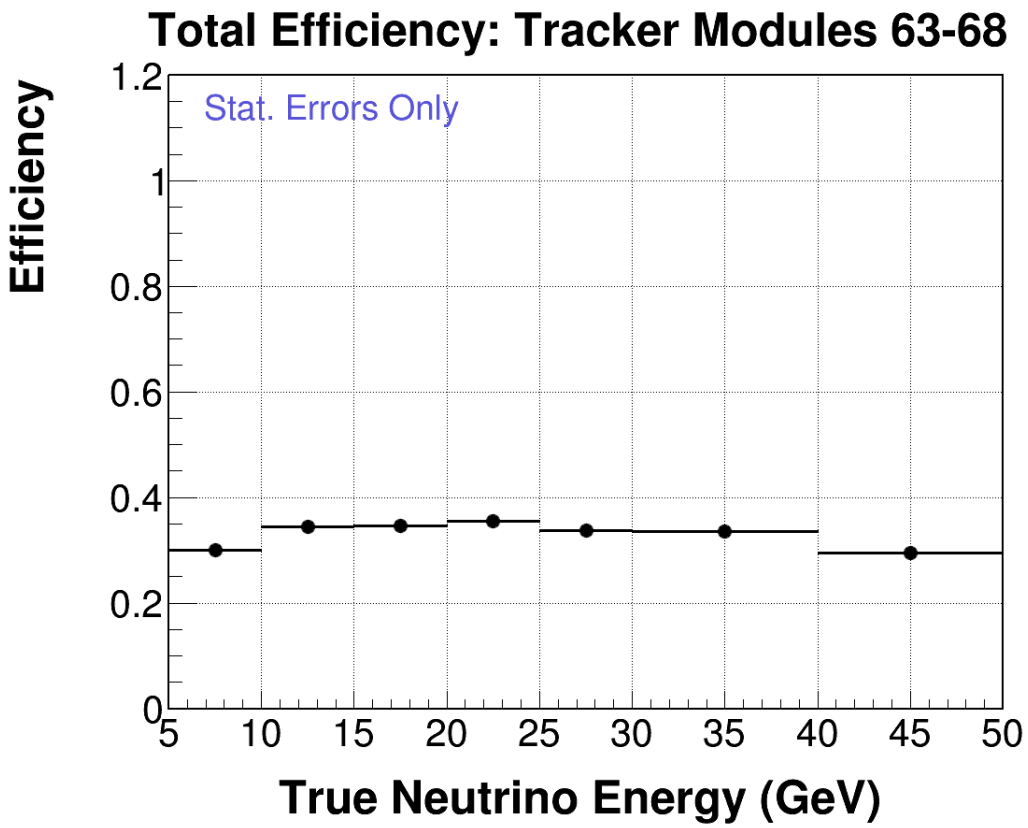

Figure G-17. Overall efficiency: tracker mods. 63-68 (E_ν)

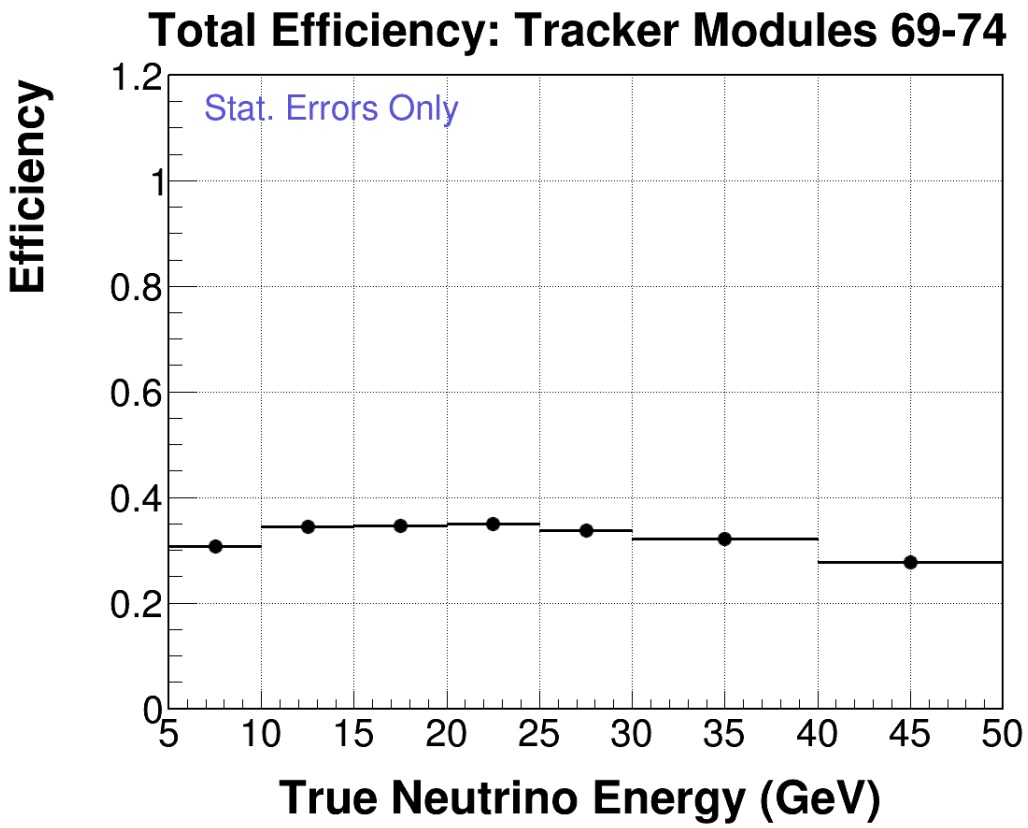

Figure G-18. Overall efficiency: tracker mods. 69-74 (E_ν)

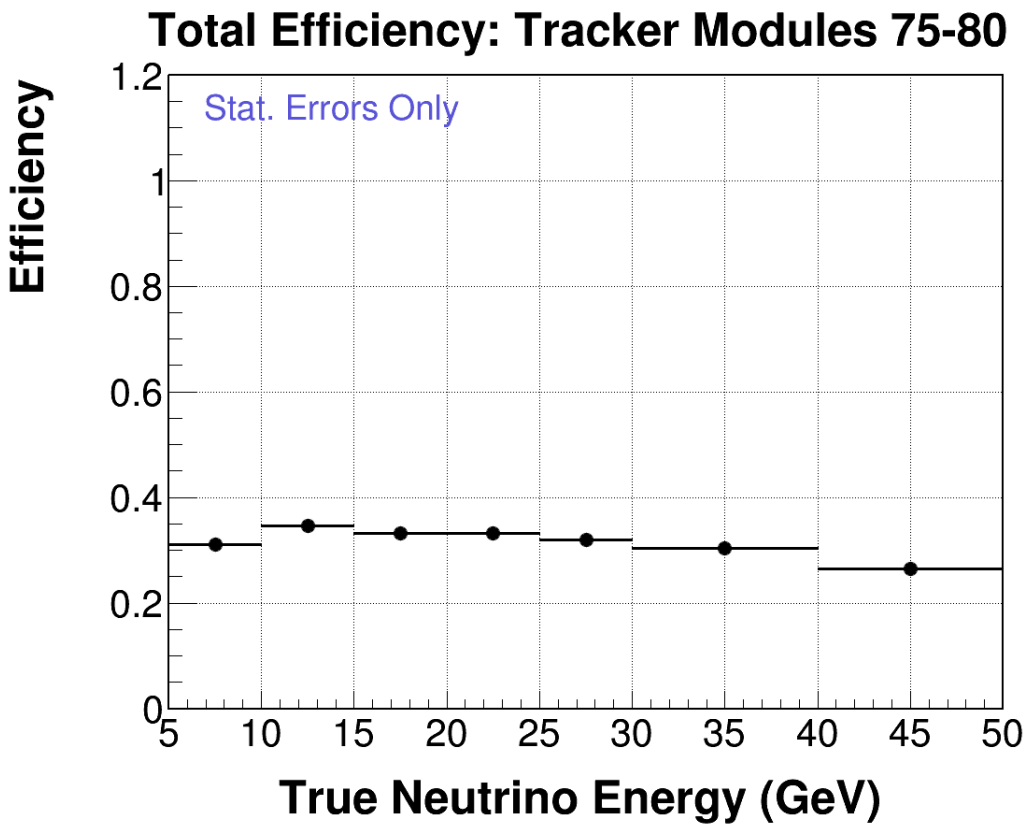

Figure G-19. Overall efficiency: tracker mods. 75-80 (E_ν)

The following plots show the overall efficiency of DIS event selection. They are plotted as a function of true Bjorken-x (x_{bj}):

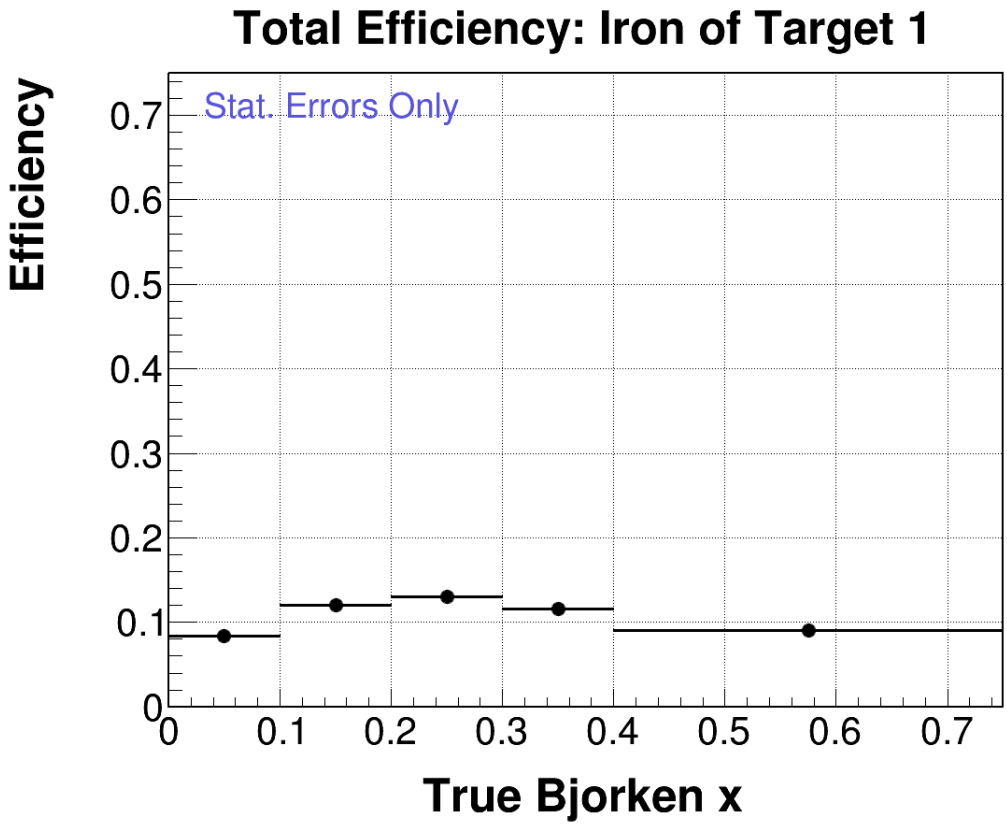

Figure G-20. Overall efficiency: target 01 Fe (x_{bj})

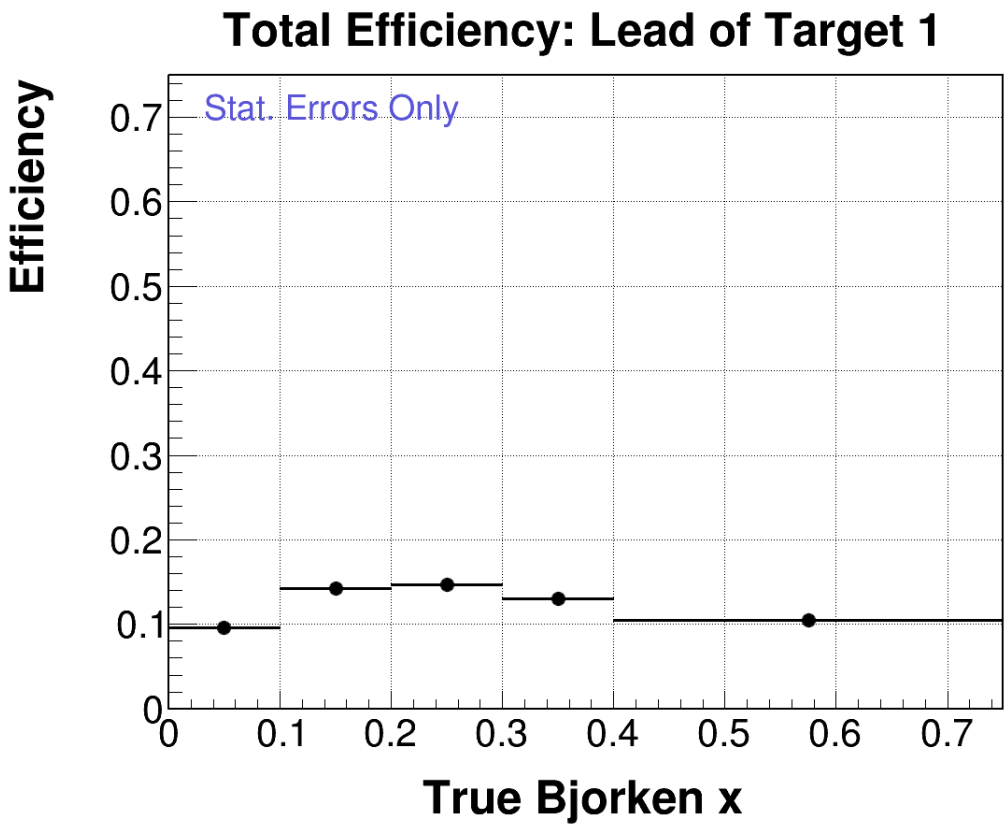

Figure G-21. Overall efficiency: target 01 Pb (x_{bj})

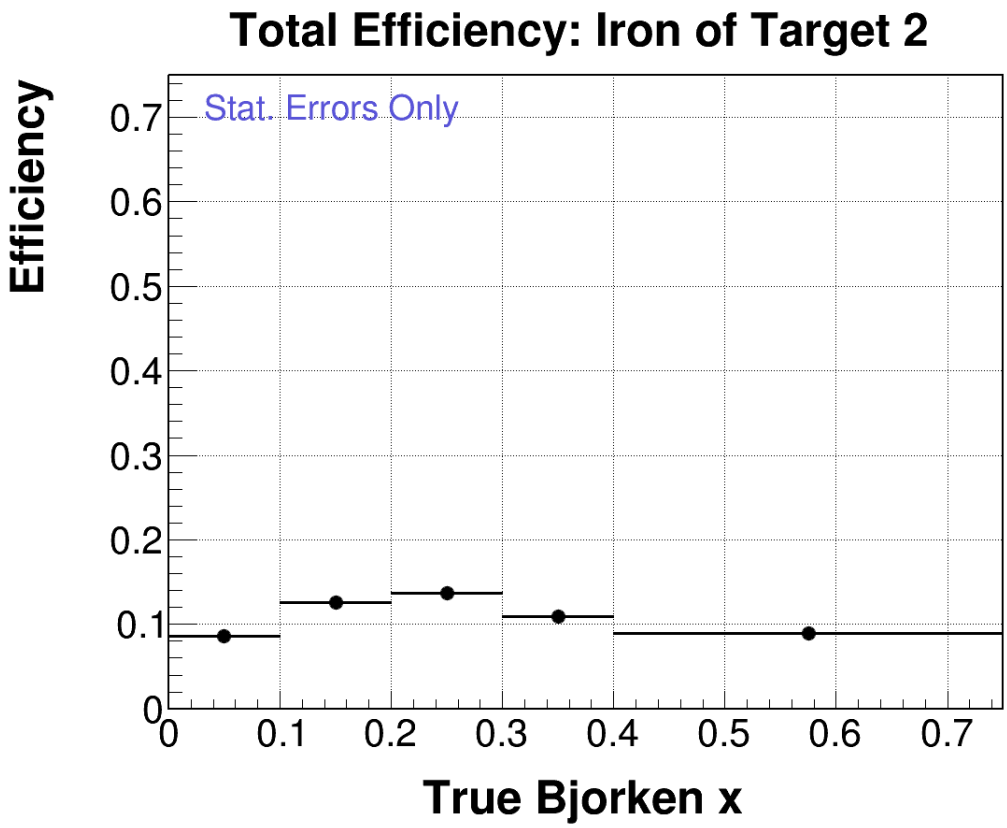

Figure G-22. Overall efficiency: target 02 Fe (x_{bj})

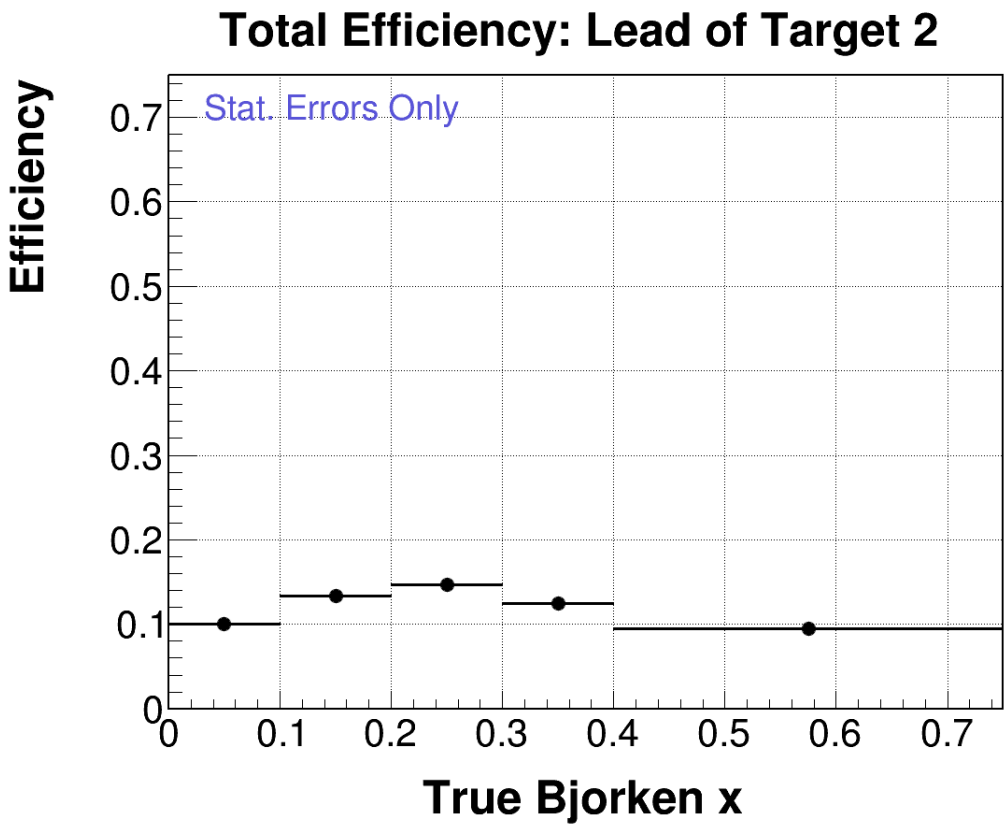

Figure G-23. Overall efficiency: target 02 Pb (x_{bj})

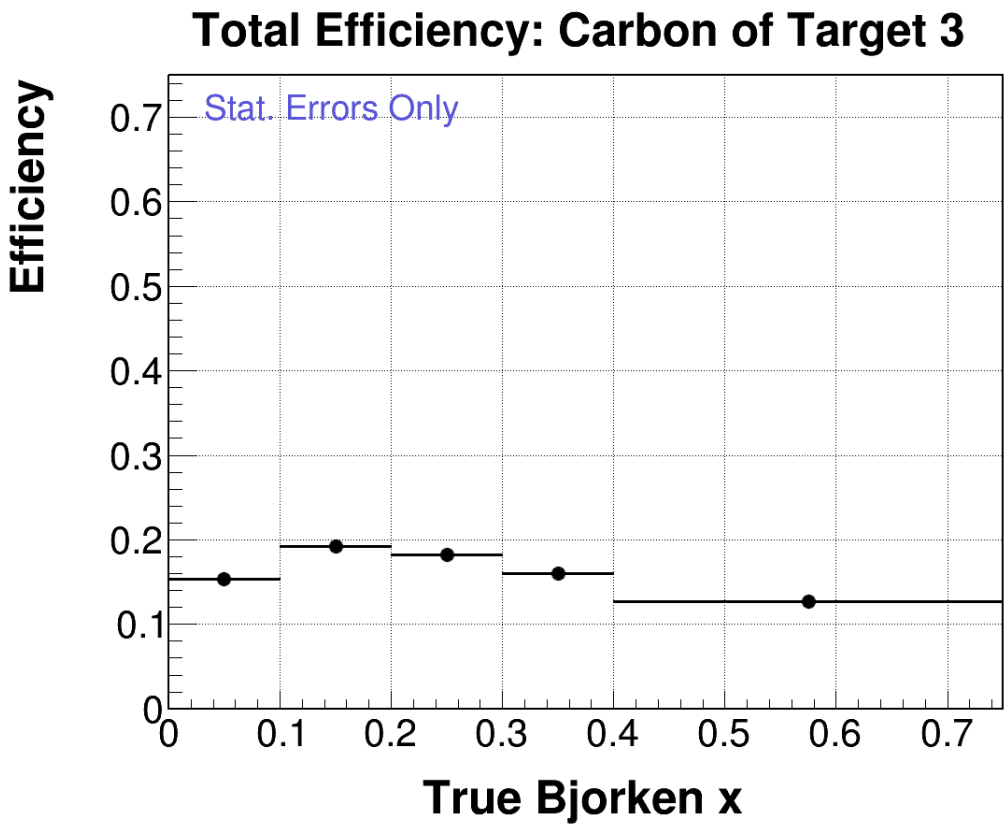

Figure G-24. Overall efficiency: target 03 C (x_{bj})

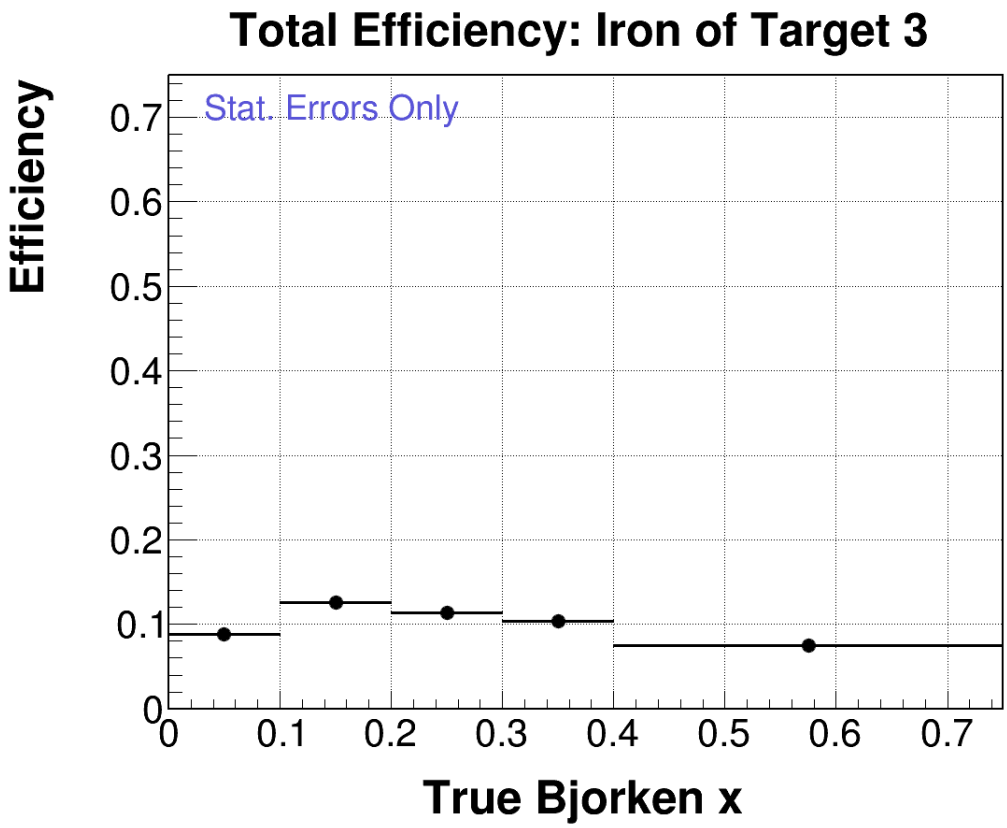

Figure G-25. Overall efficiency: target 03 Fe (x_{bj})

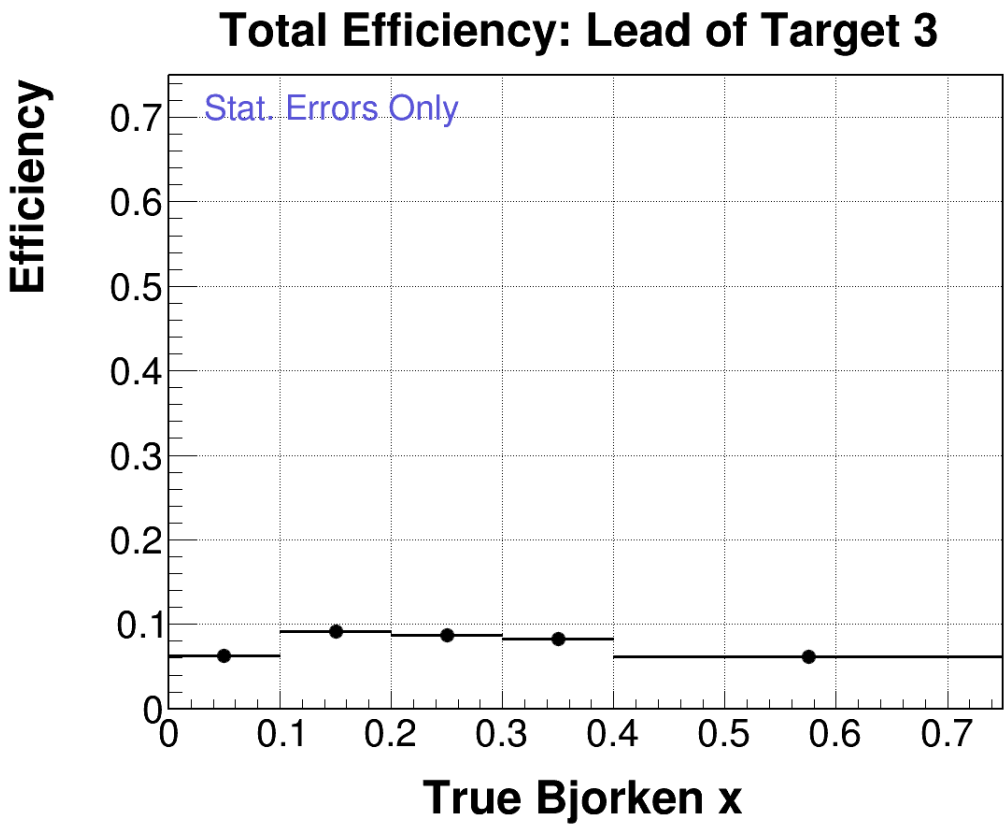

Figure G-26. Overall efficiency: target 02 Pb (x_{bj})

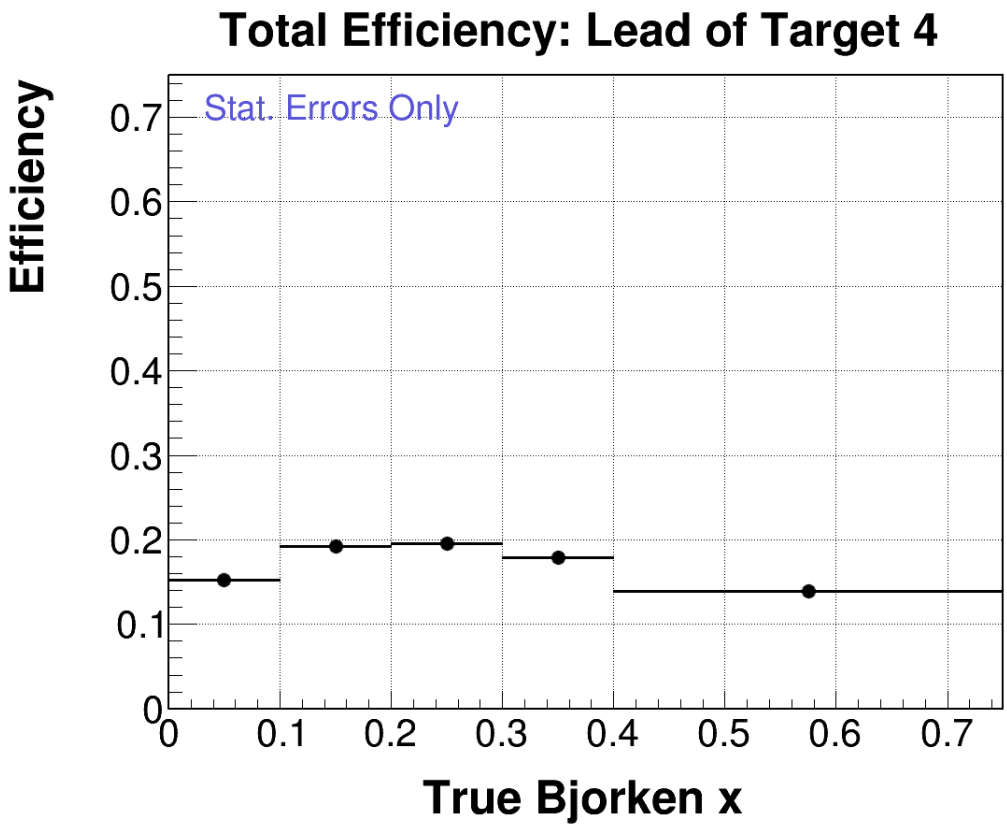

Figure G-27. Overall efficiency: target 04 Pb (x_{bj})

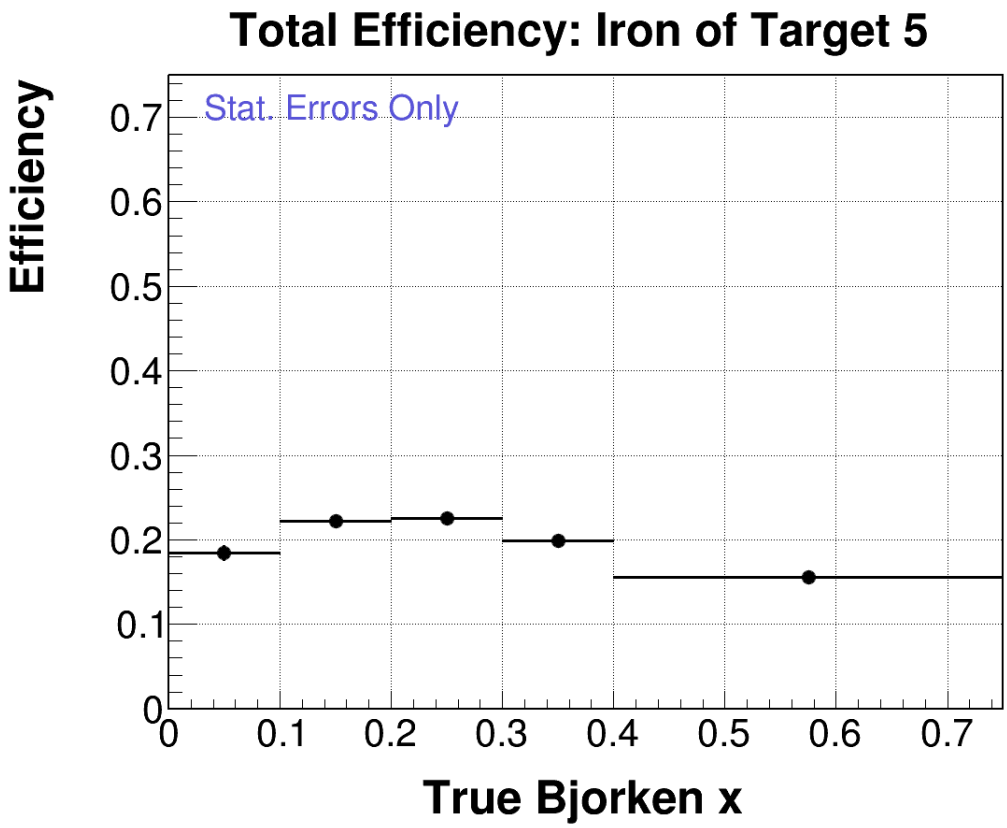

Figure G-28. Overall efficiency: target 05 Fe (x_{bj})

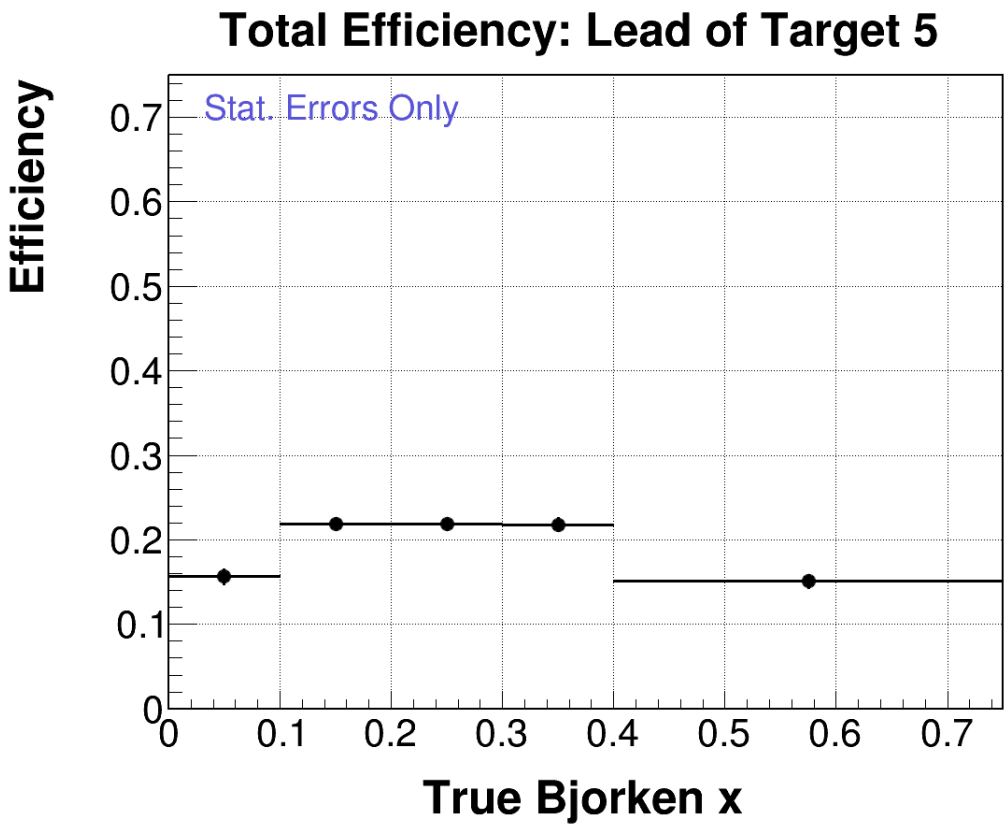

Figure G-29. Overall efficiency: target 05 Pb (x_{bj})

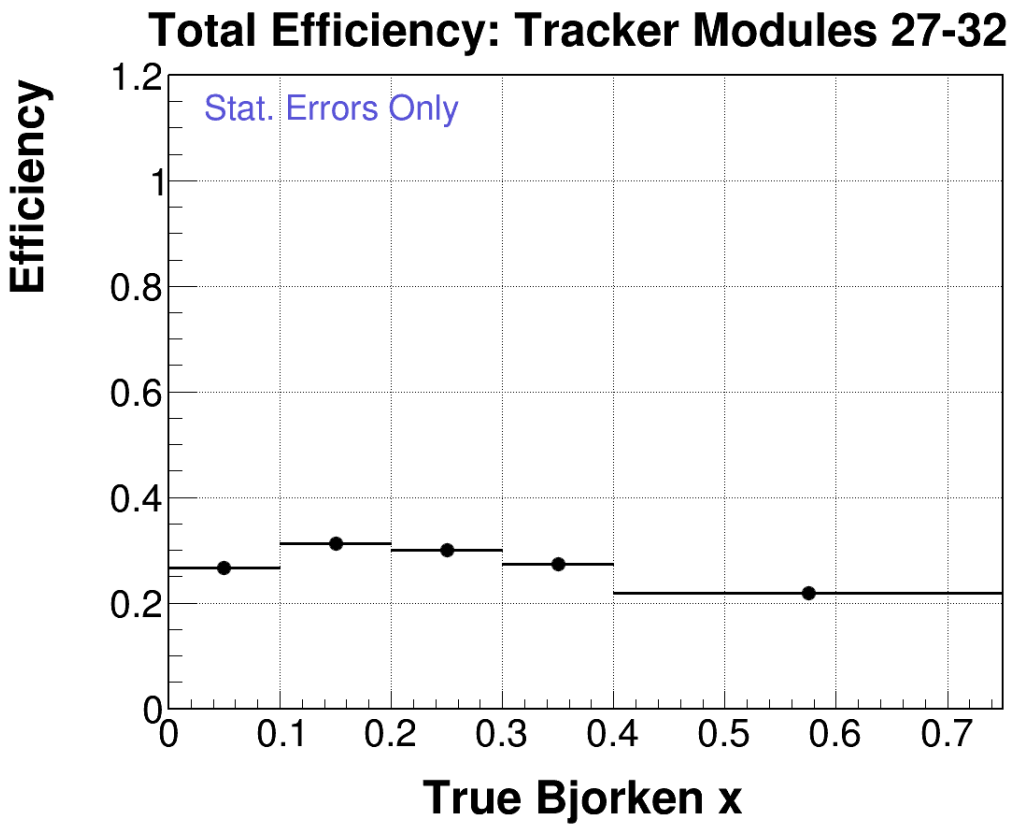

Figure G-30. Overall efficiency: tracker mods. 27-32 (x_{bj})

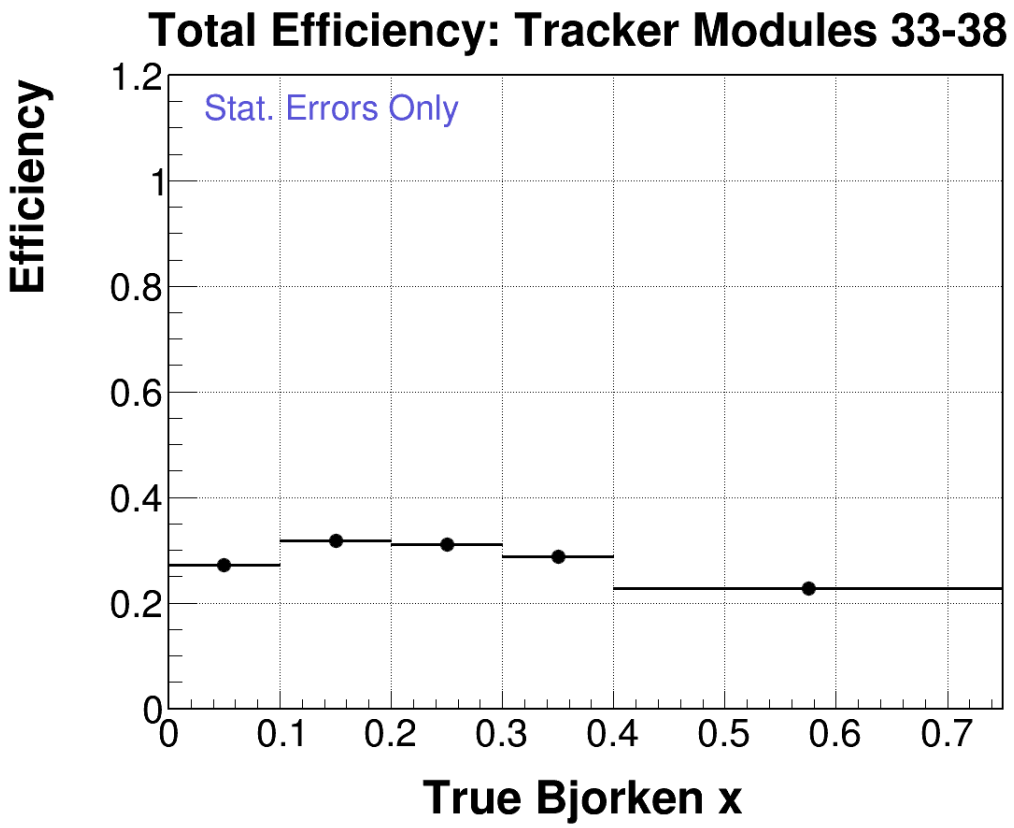

Figure G-31. Overall efficiency: tracker mods. 33-38 (x_{bj})

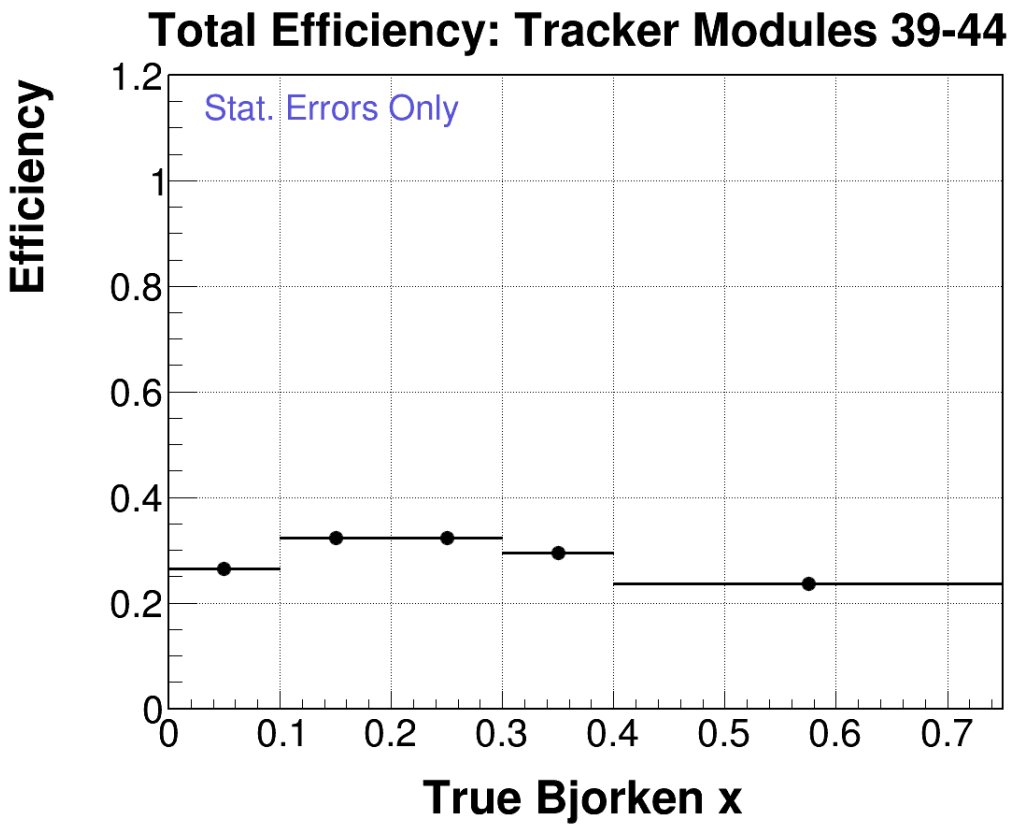

Figure G-32. Overall efficiency: tracker mods. 39-44 (x_{bj})

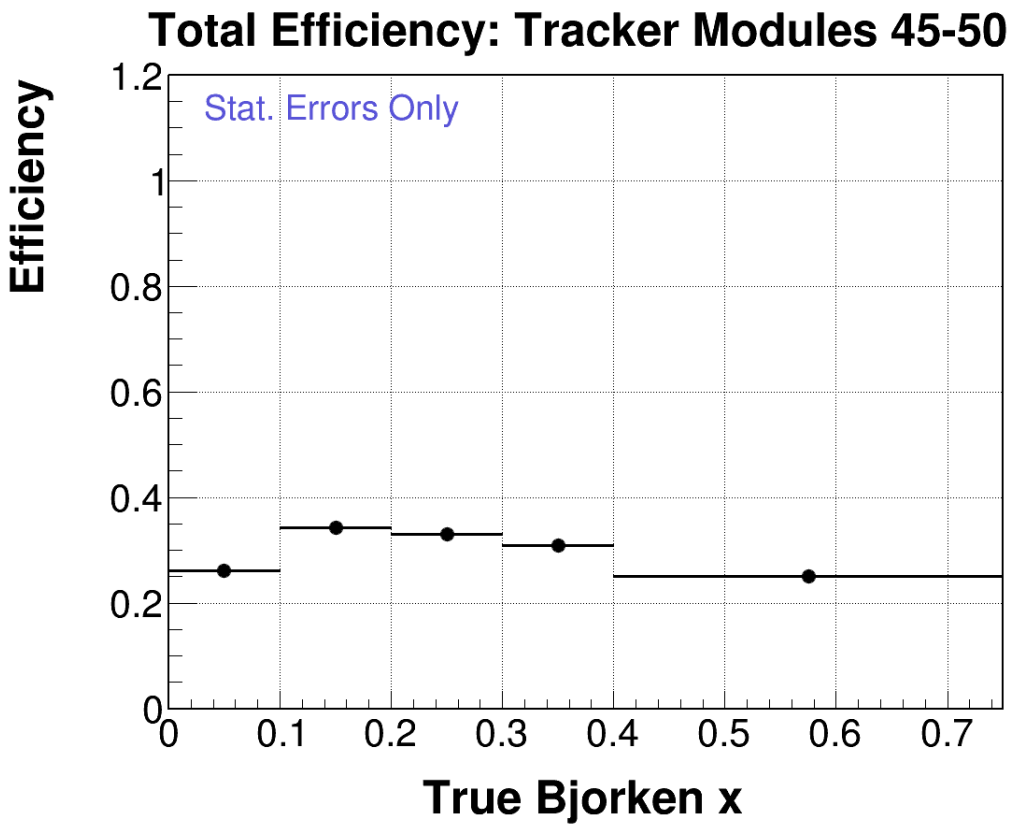

Figure G-33. Overall efficiency: tracker mods. 45-50 (x_{bj})

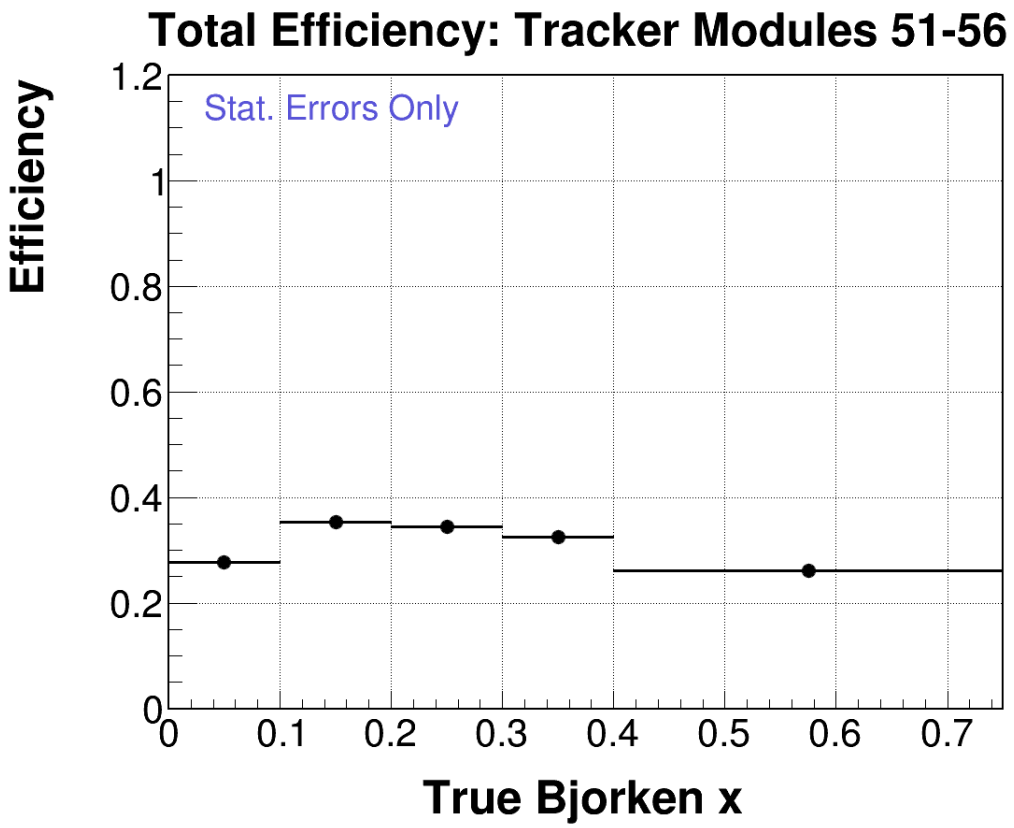

Figure G-34. Overall efficiency: tracker mods. 51-56 (x_{bj})

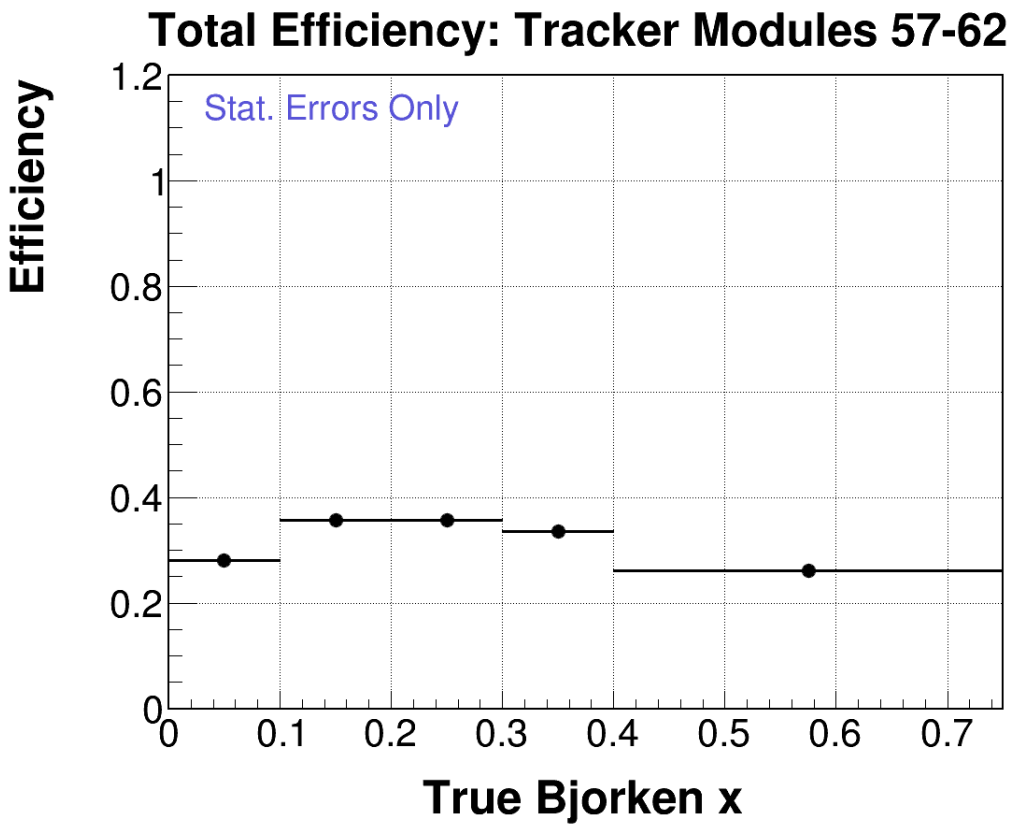

Figure G-35. Overall efficiency: tracker mods. 57-62 (x_{bj})

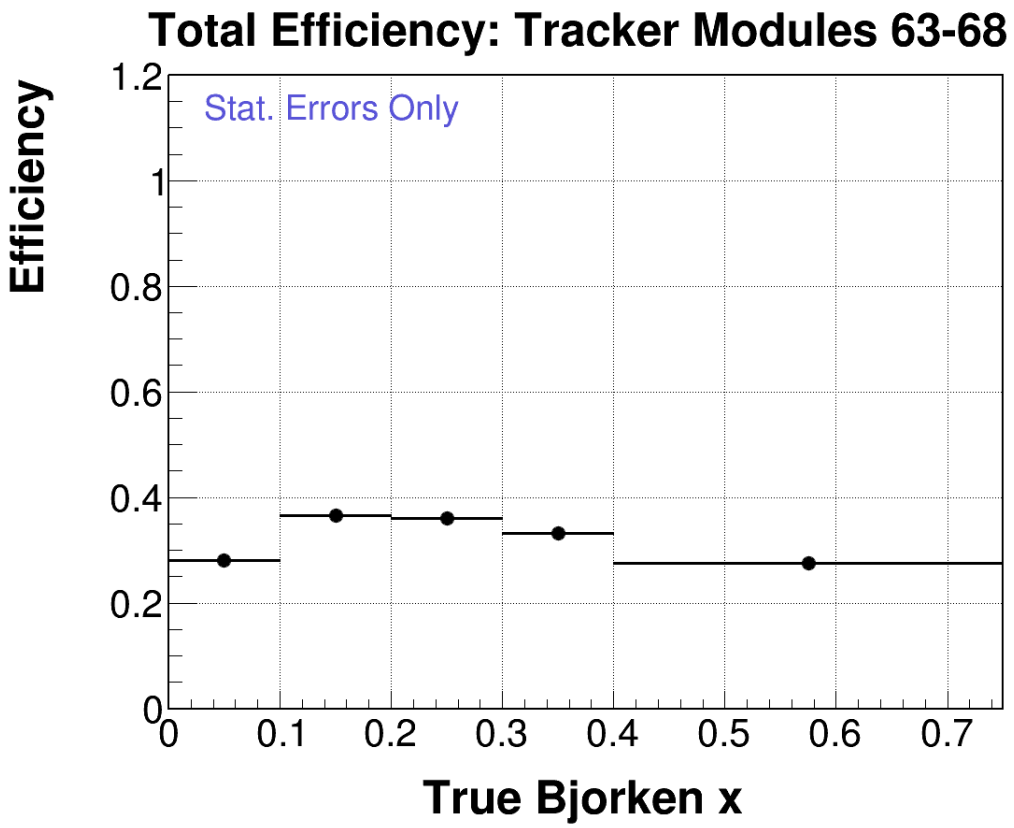

Figure G-36. Overall efficiency: tracker mods. 63-68 (x_{bj})

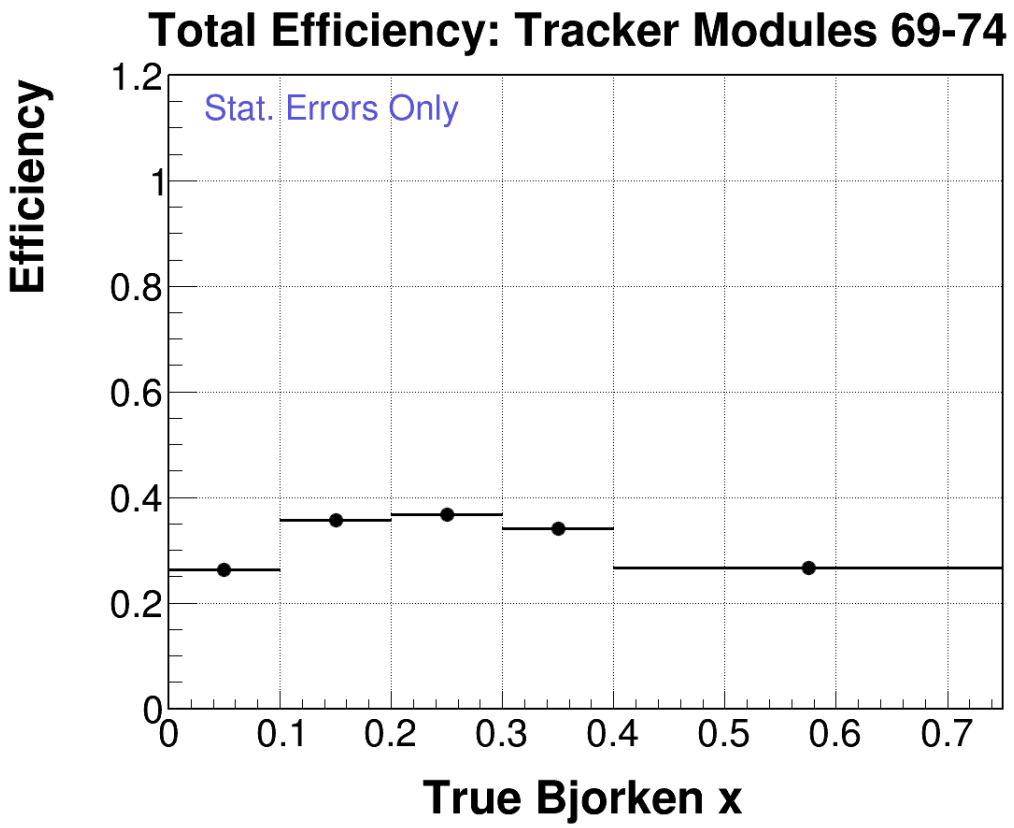

Figure G-37. Overall efficiency: tracker mods. 69-74 (x_{bj})

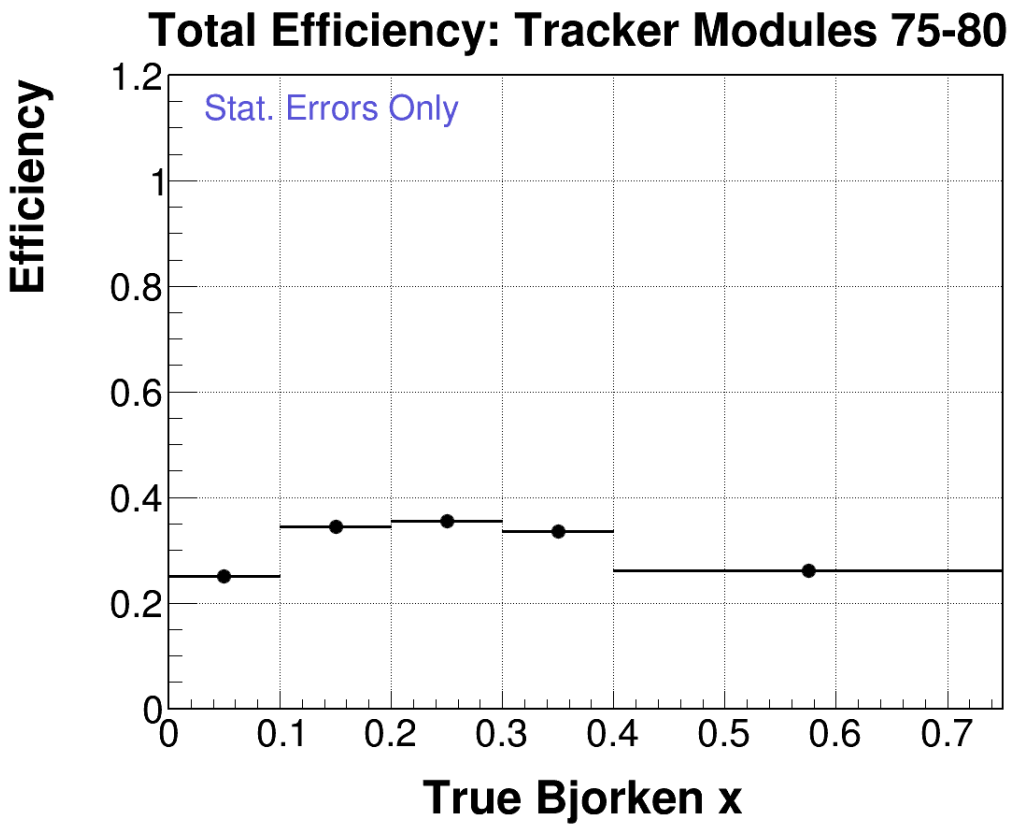

Figure G-38. Overall efficiency: tracker mods. 75-80 (x_{bj})

G.2 Efficiency Uncertainty

The following plots show the uncertainty on overall efficiency of DIS event selection. They are plotted as a function of true neutrino energy (E_ν):

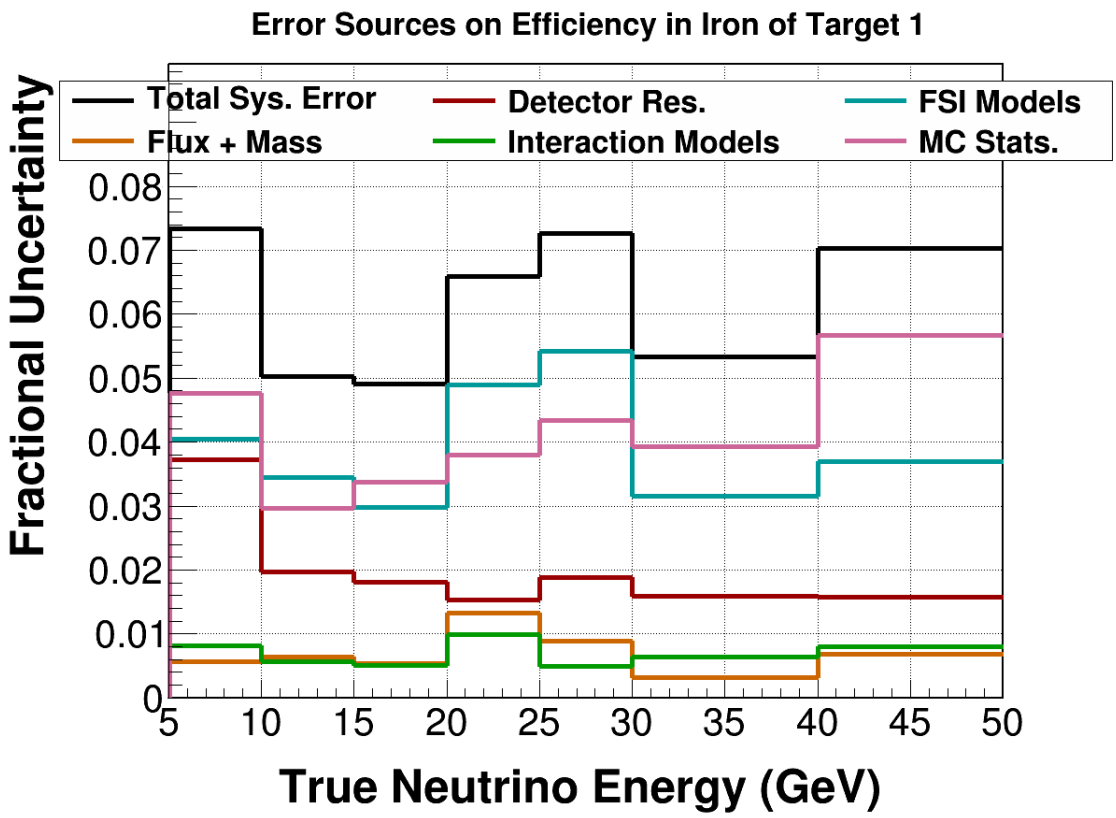

Figure G-39. Uncertainty on overall efficiency: target 01 Fe (E_ν)

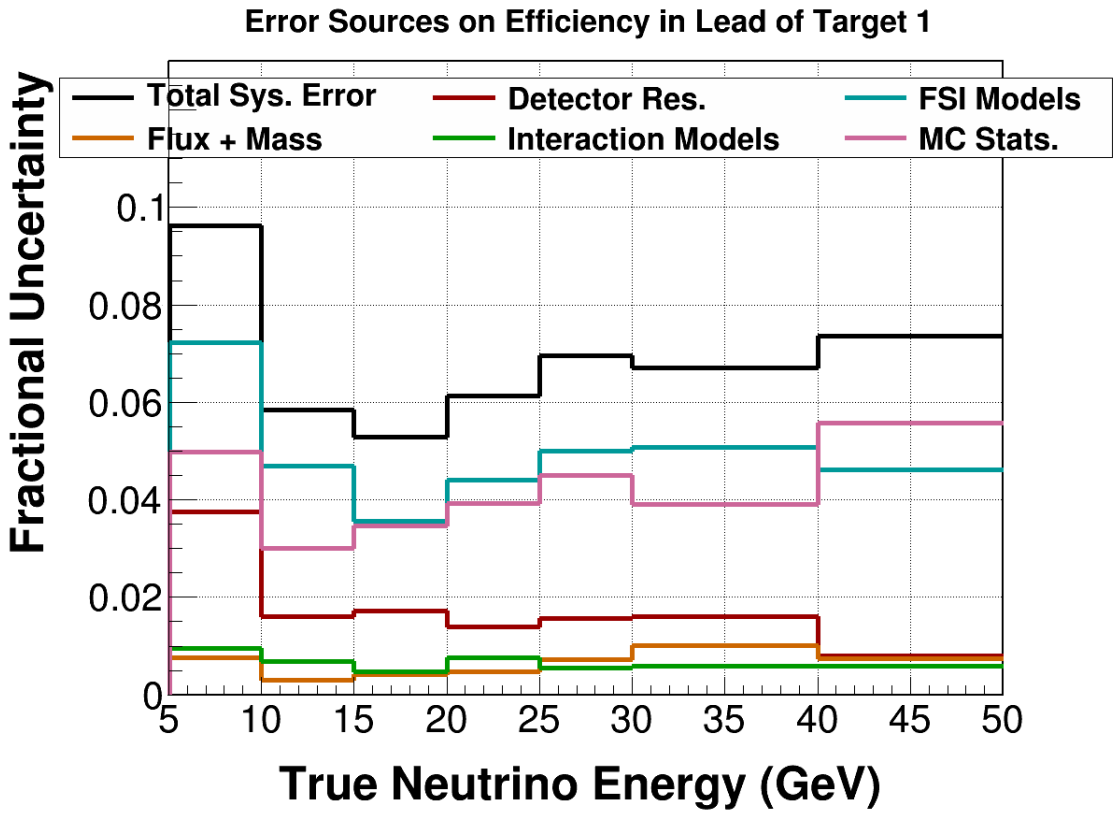

Figure G-40. Uncertainty on overall efficiency: target 01 Pb (E_ν)

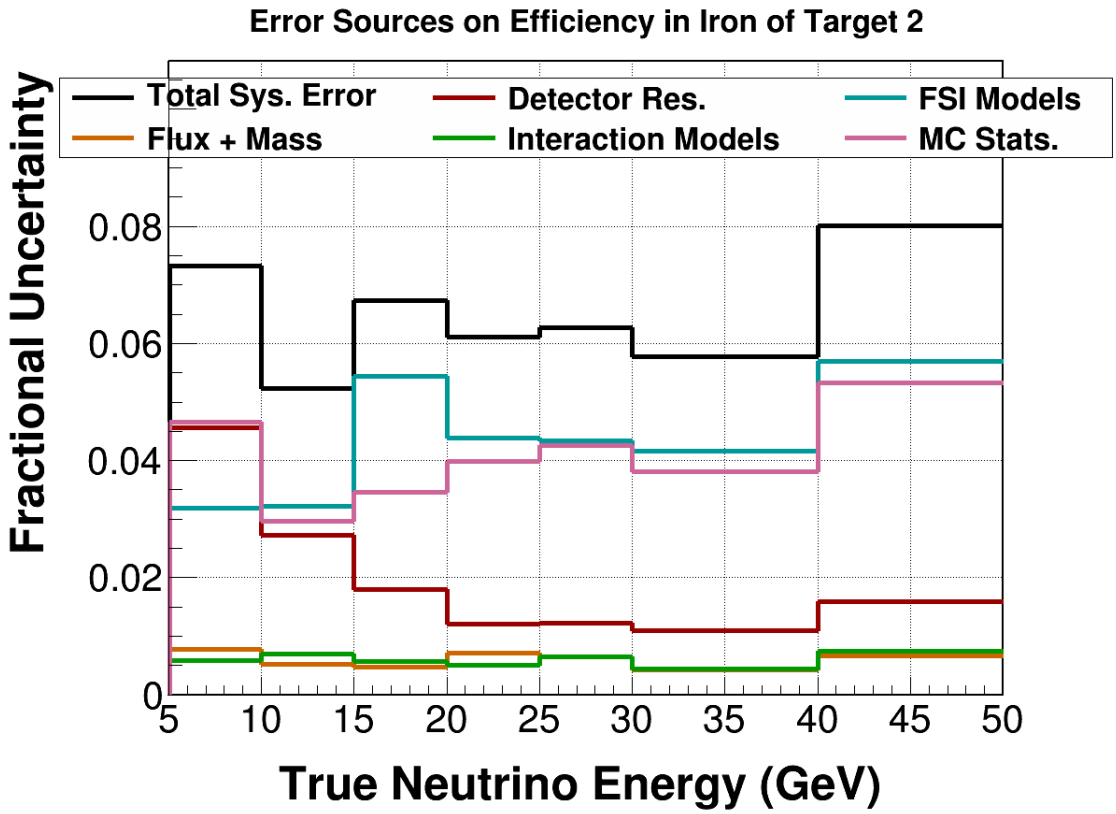

Figure G-41. Uncertainty on overall efficiency: target 02 Fe (E_ν)

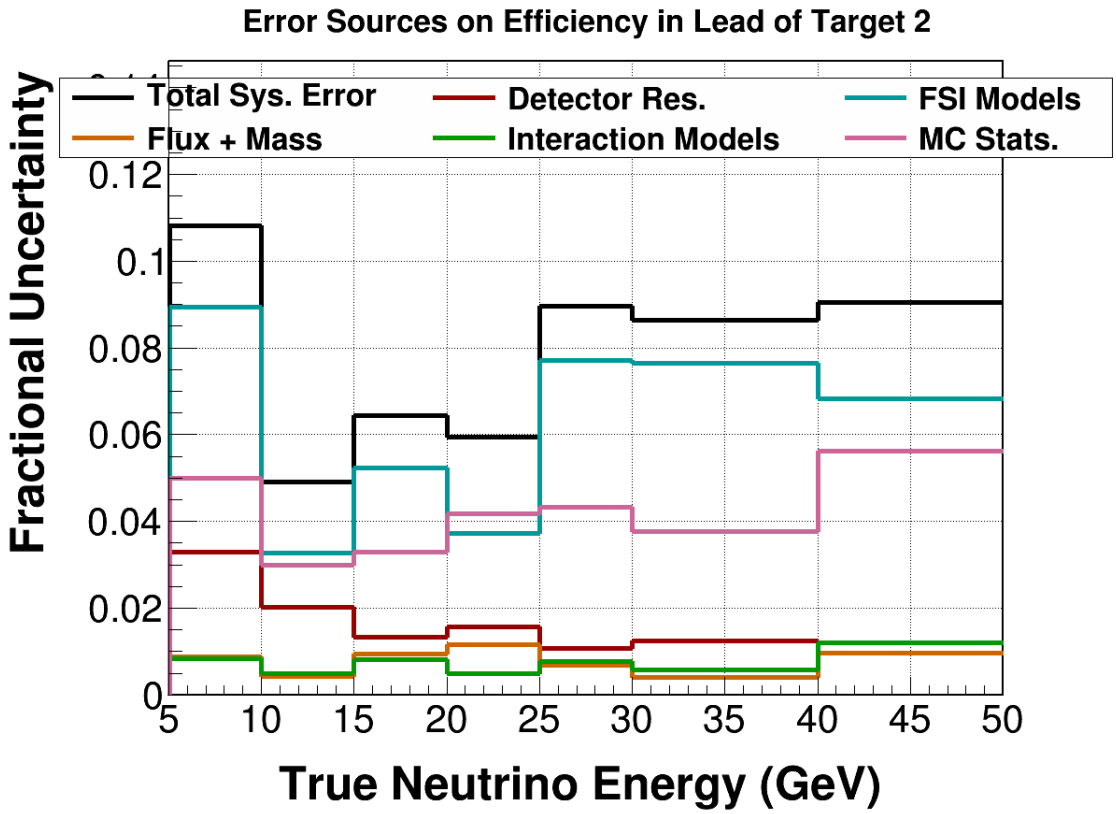

Figure G-42. Uncertainty on overall efficiency: target 02 Pb (E_ν)

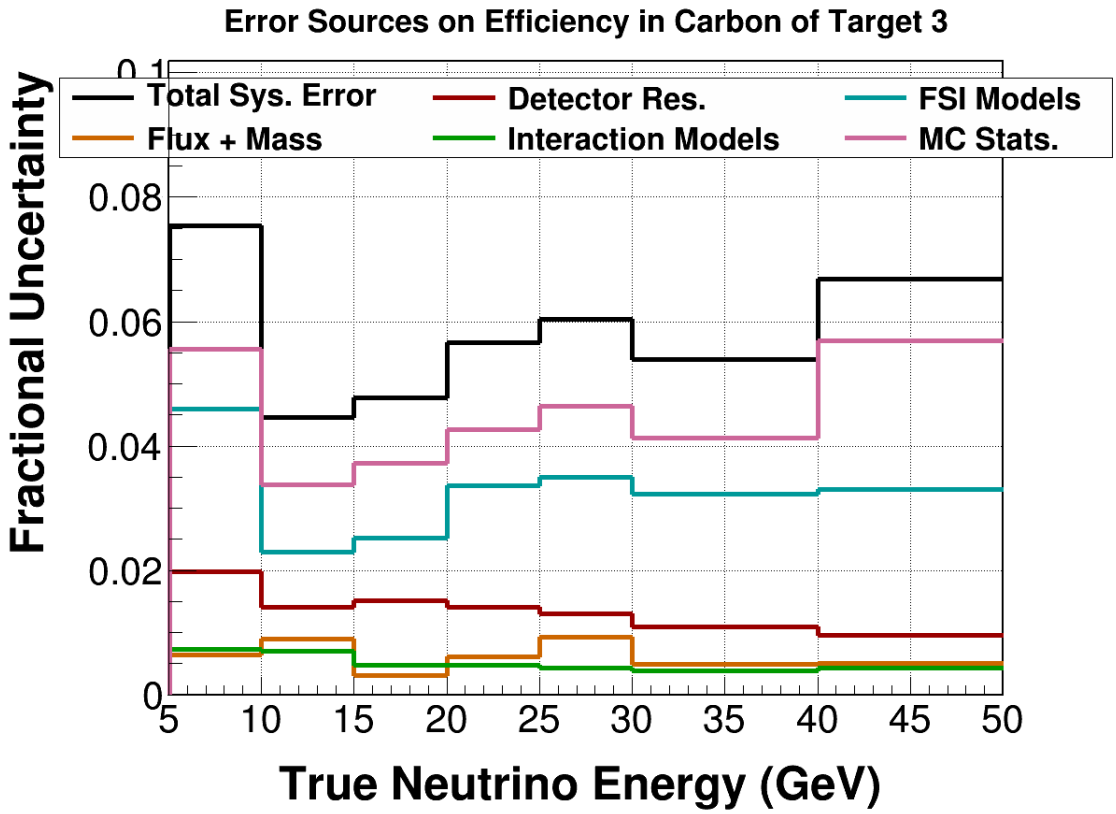

Figure G-43. Uncertainty on overall efficiency: target 03 C (E_ν)

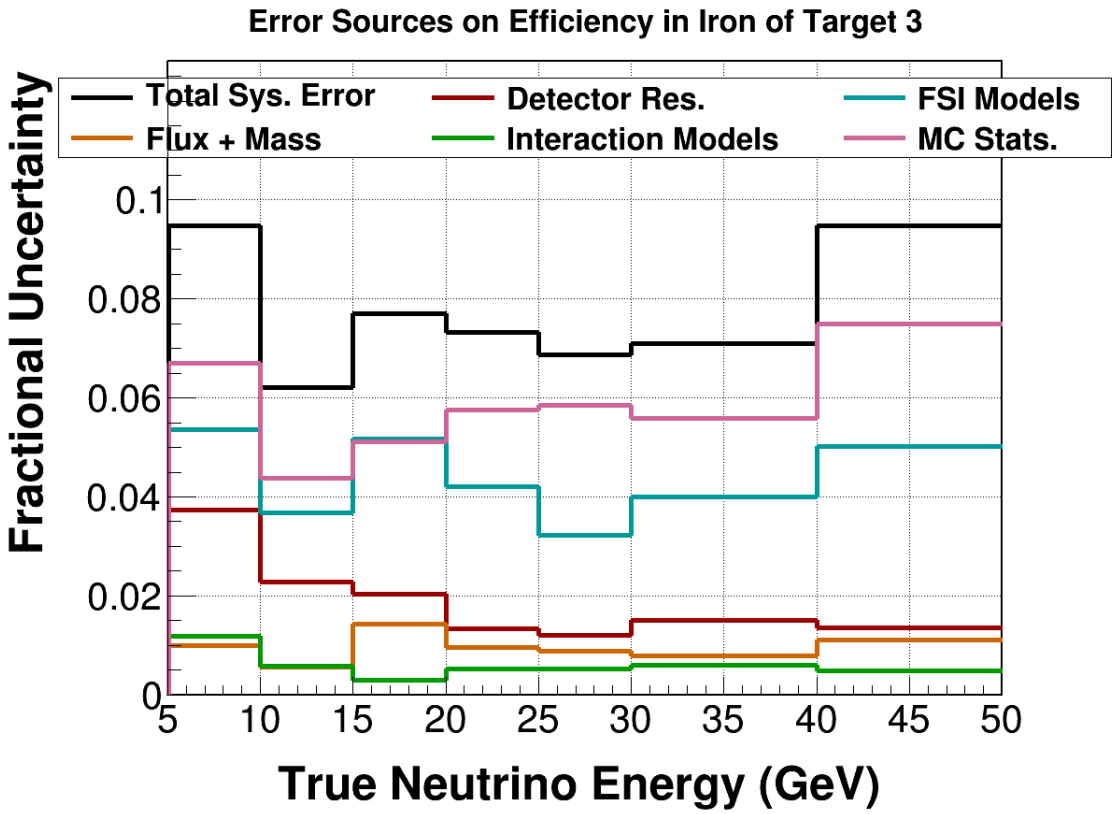

Figure G-44. Uncertainty on overall efficiency: target 03 Fe (E_ν)

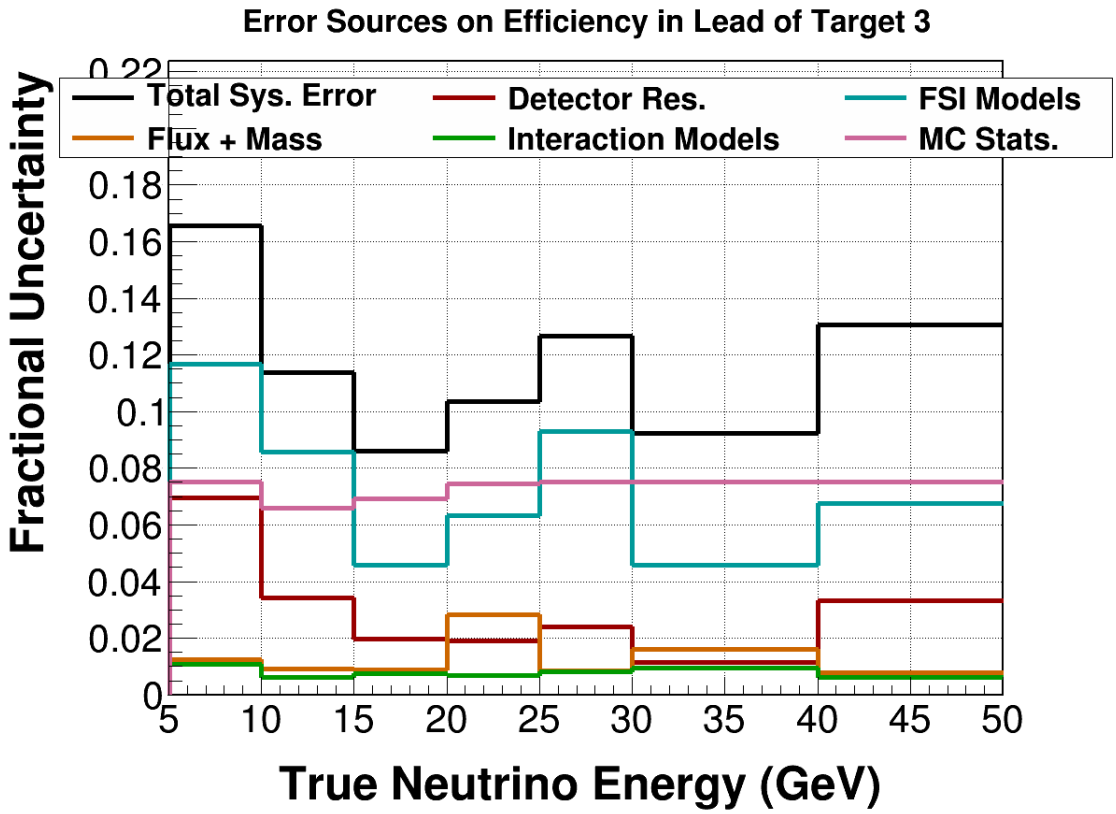

Figure G-45. Uncertainty on overall efficiency: target 03 Pb (E_ν)

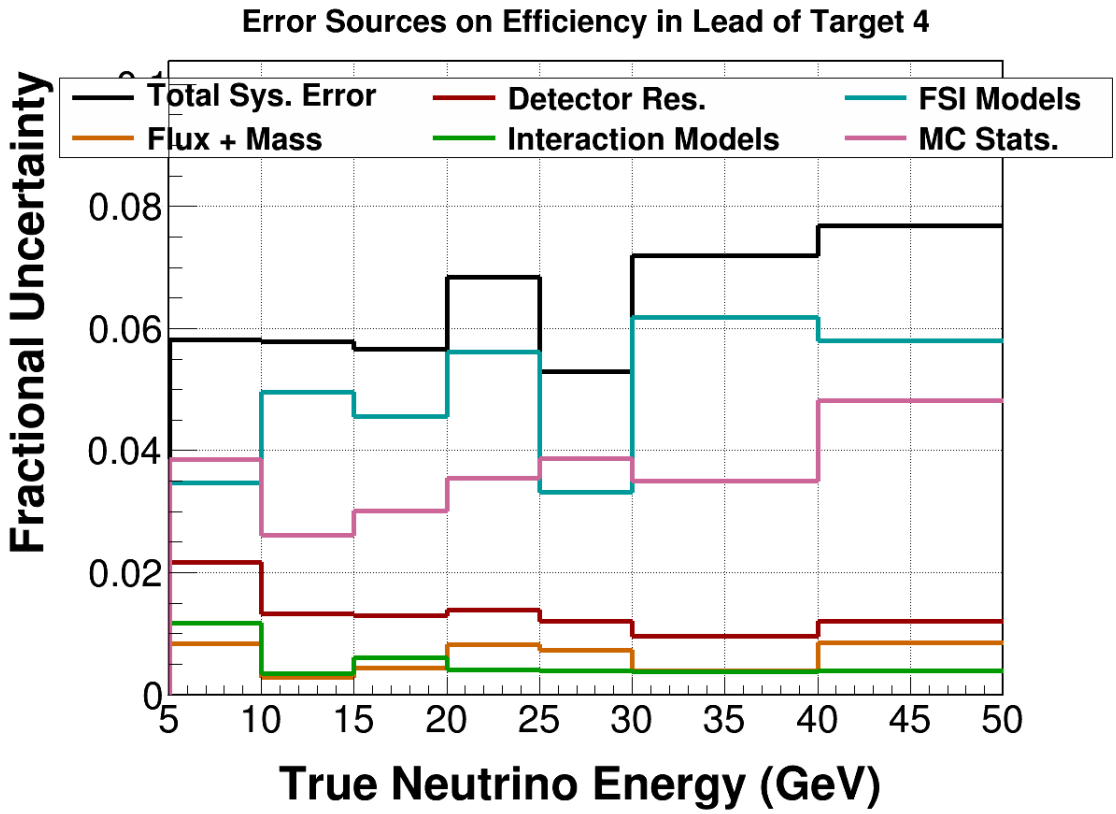

Figure G-46. Uncertainty on overall efficiency: target 04 Pb (E_ν)

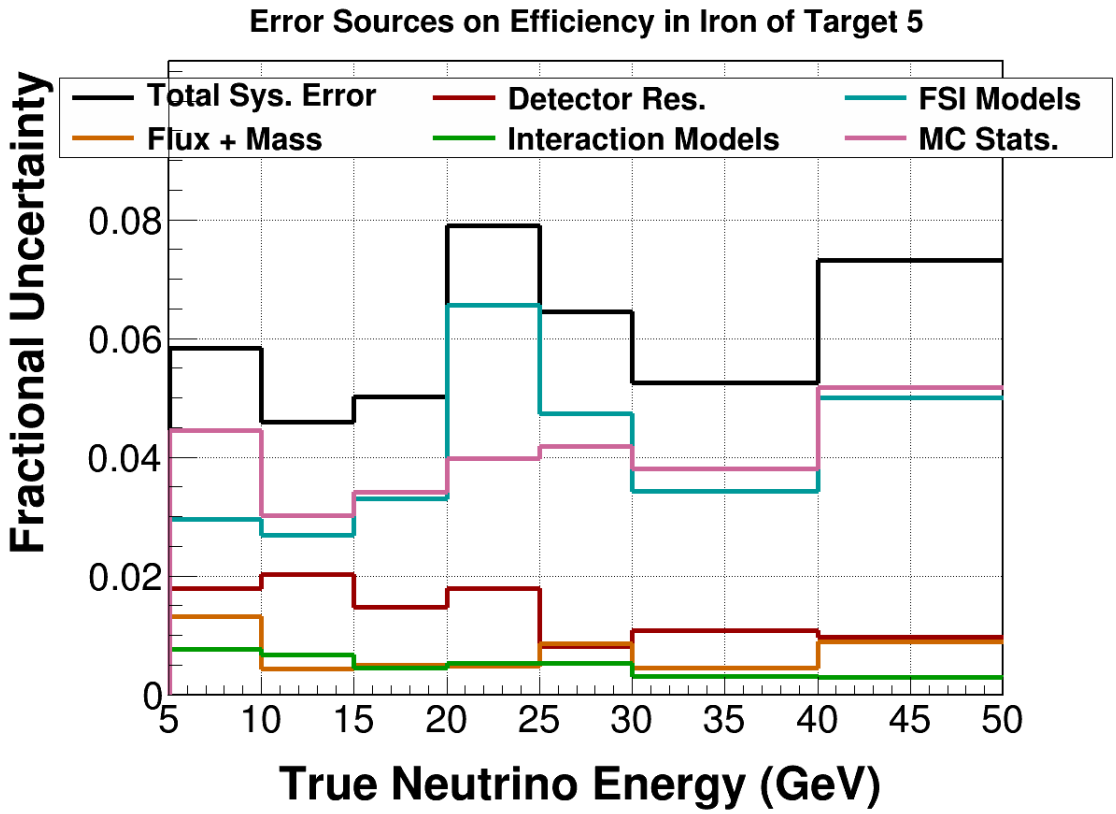

Figure G-47. Uncertainty on overall efficiency: target 05 Fe (E_ν)

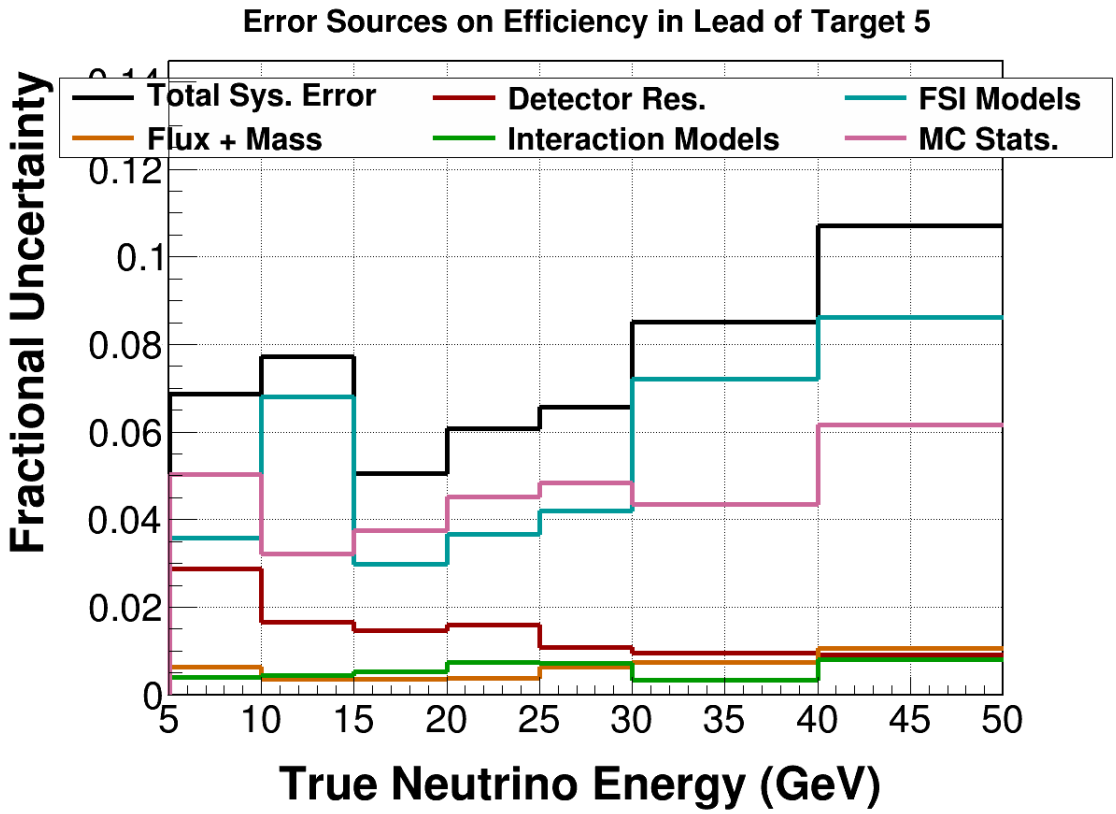

Figure G-48. Uncertainty on overall efficiency: target 05 Pb (E_ν)

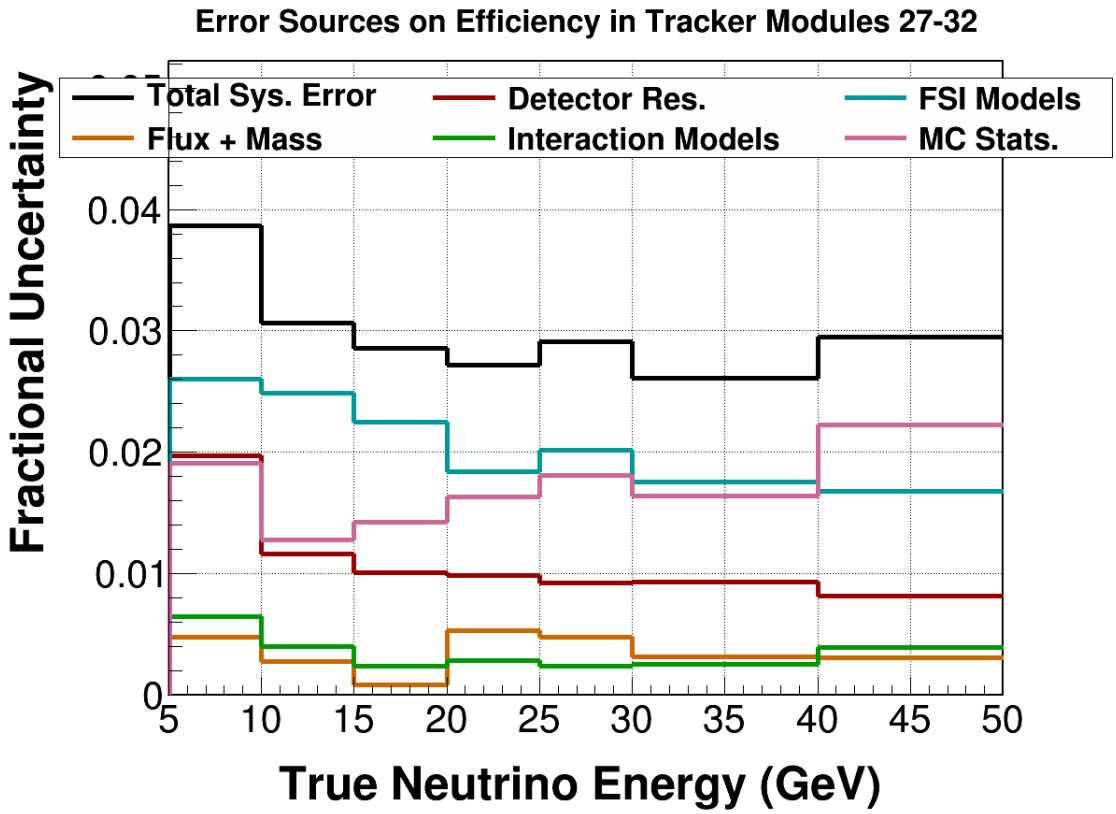

Figure G-49. Uncertainty on overall efficiency: tracker mods. 27-32 (E_ν)

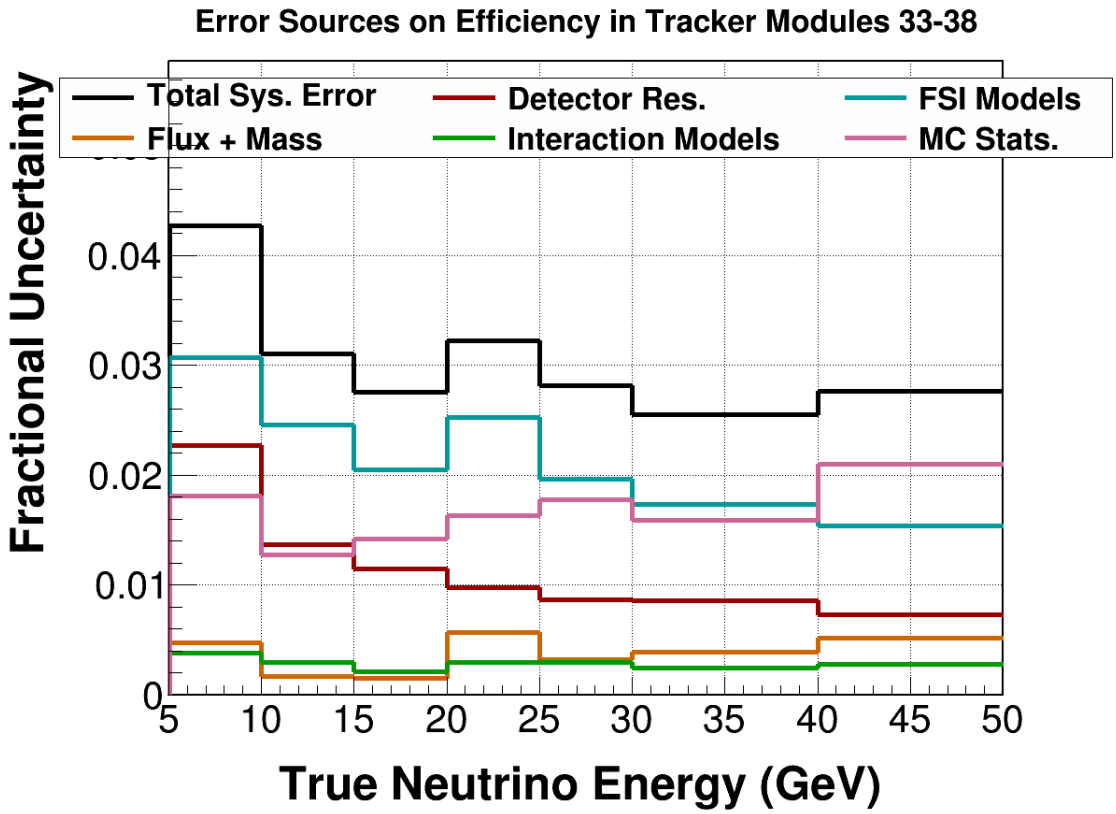

Figure G-50. Uncertainty on overall efficiency: tracker mods. 33-38 (E_ν)

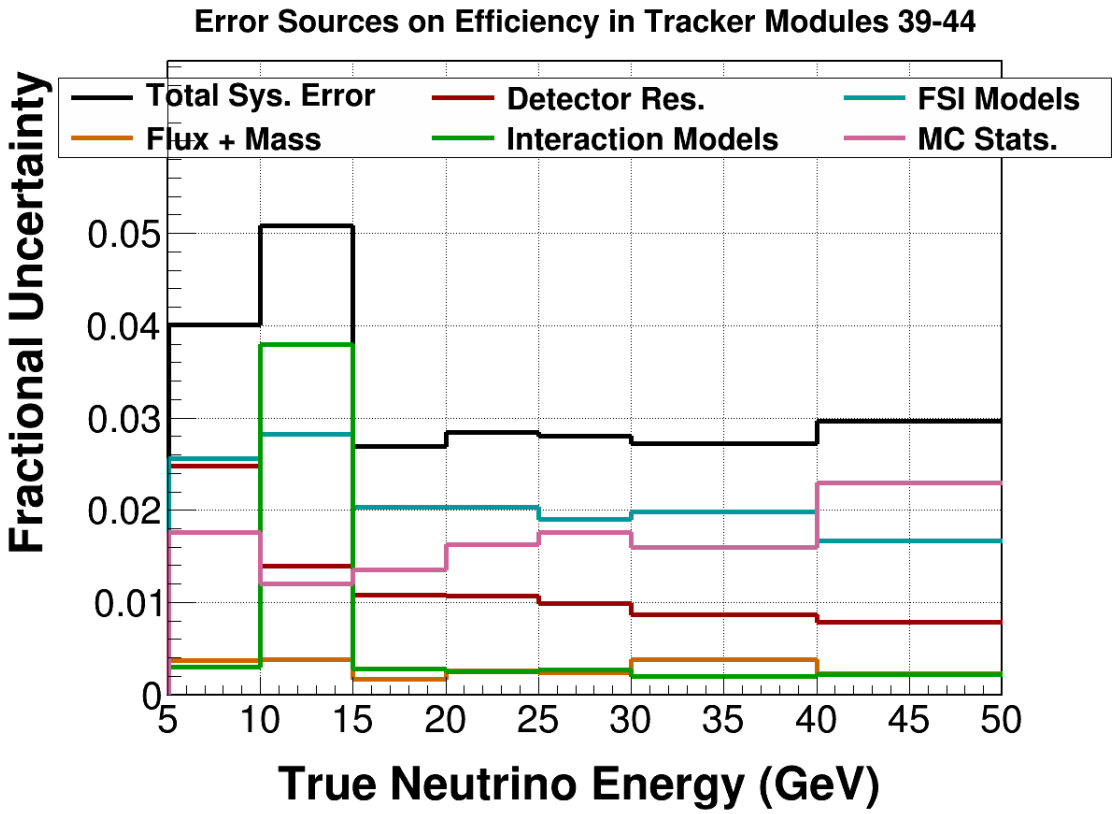

Figure G-51. Uncertainty on overall efficiency: tracker mods. 39-44 (E_ν)

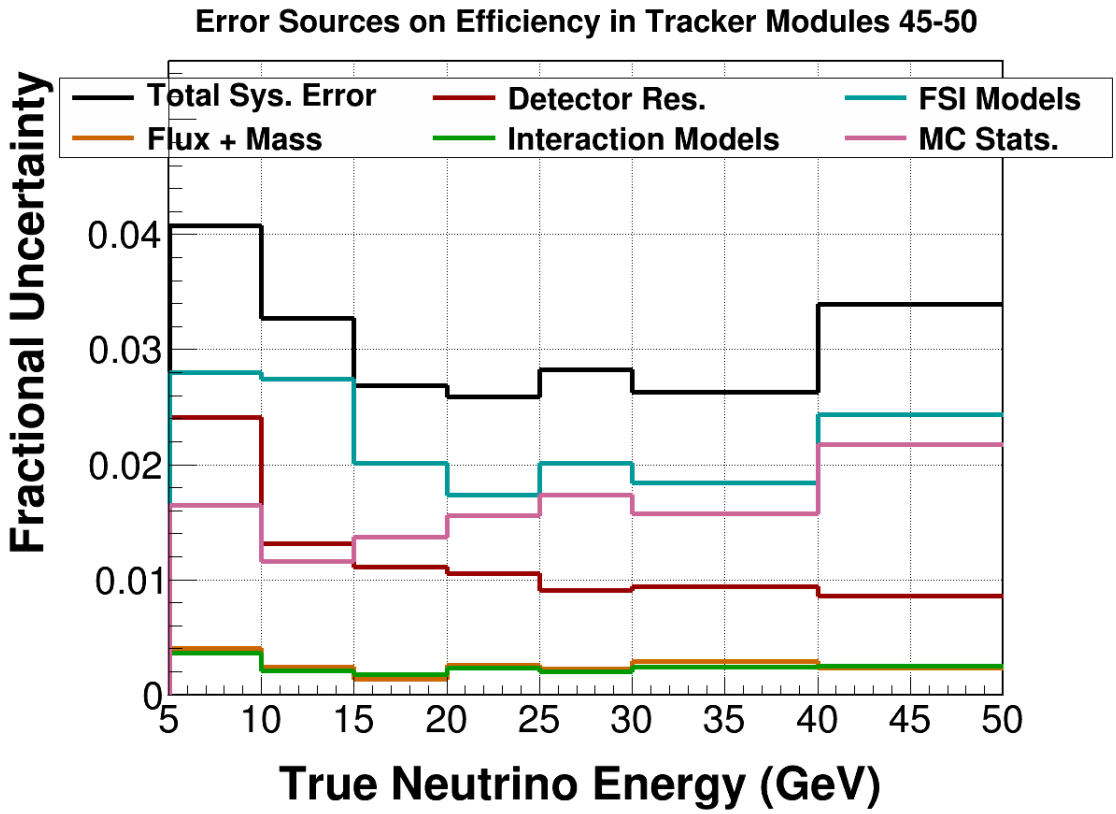

Figure G-52. Uncertainty on overall efficiency: tracker mods. 45-50 (E_ν)

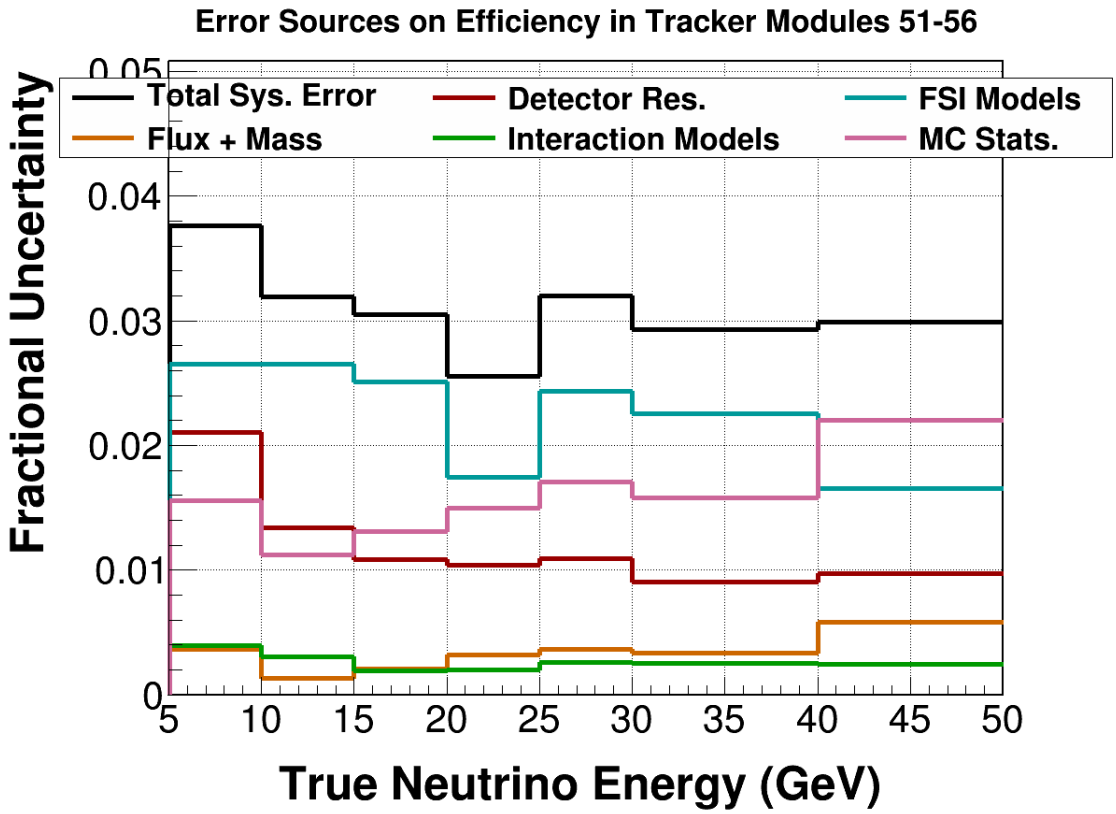

Figure G-53. Uncertainty on overall efficiency: tracker mods. 51-56 (E_ν)

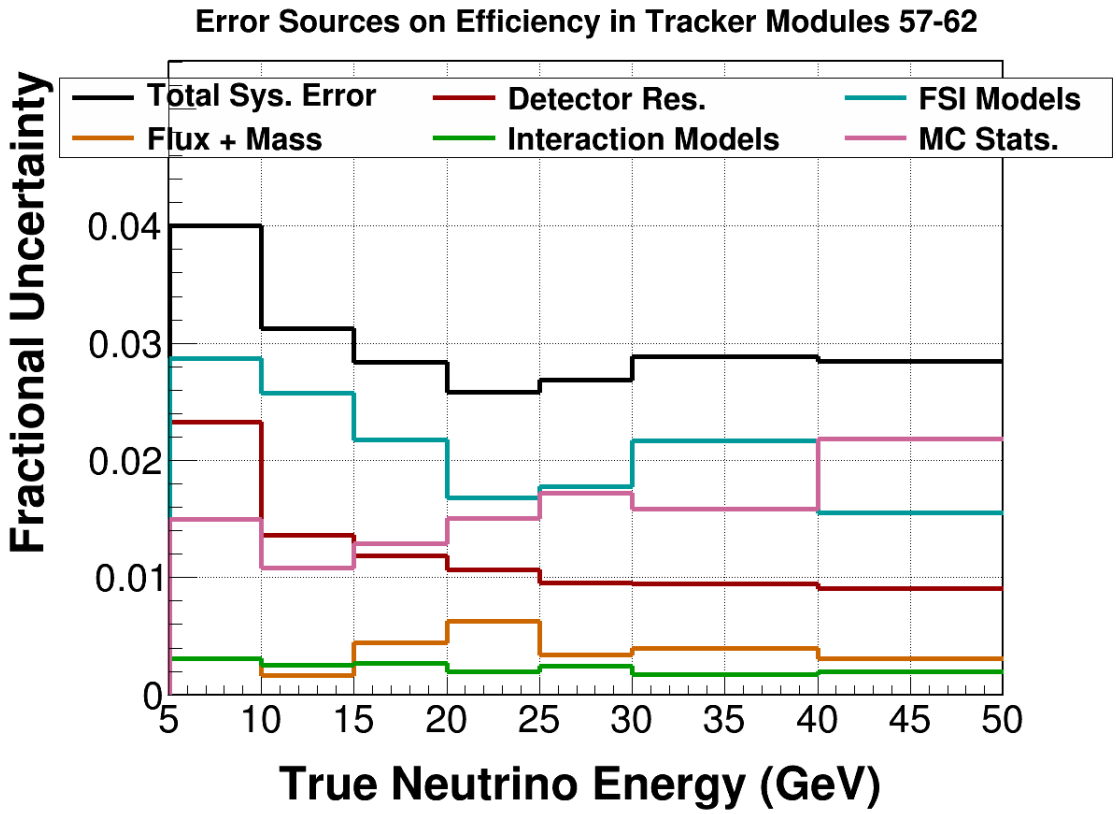

Figure G-54. Uncertainty on overall efficiency: tracker mods. 57-62 (E_ν)

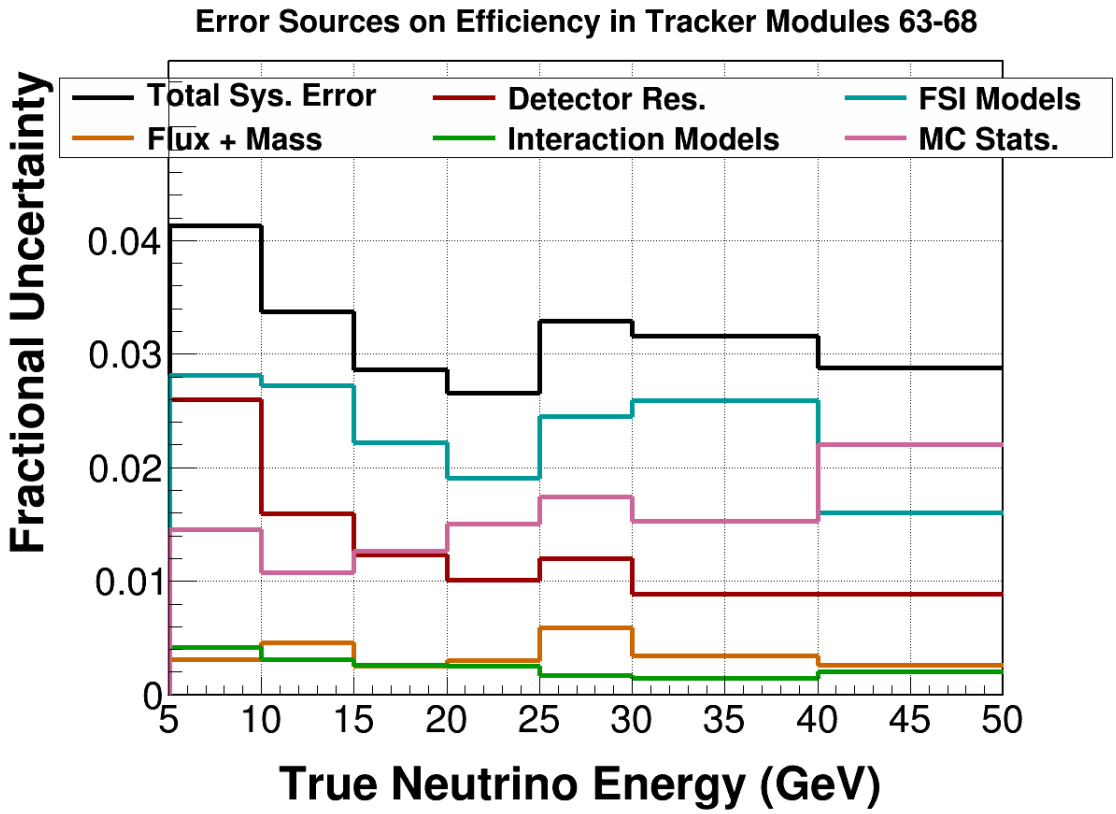

Figure G-55. Uncertainty on overall efficiency: tracker mods. 63-68 (E_ν)

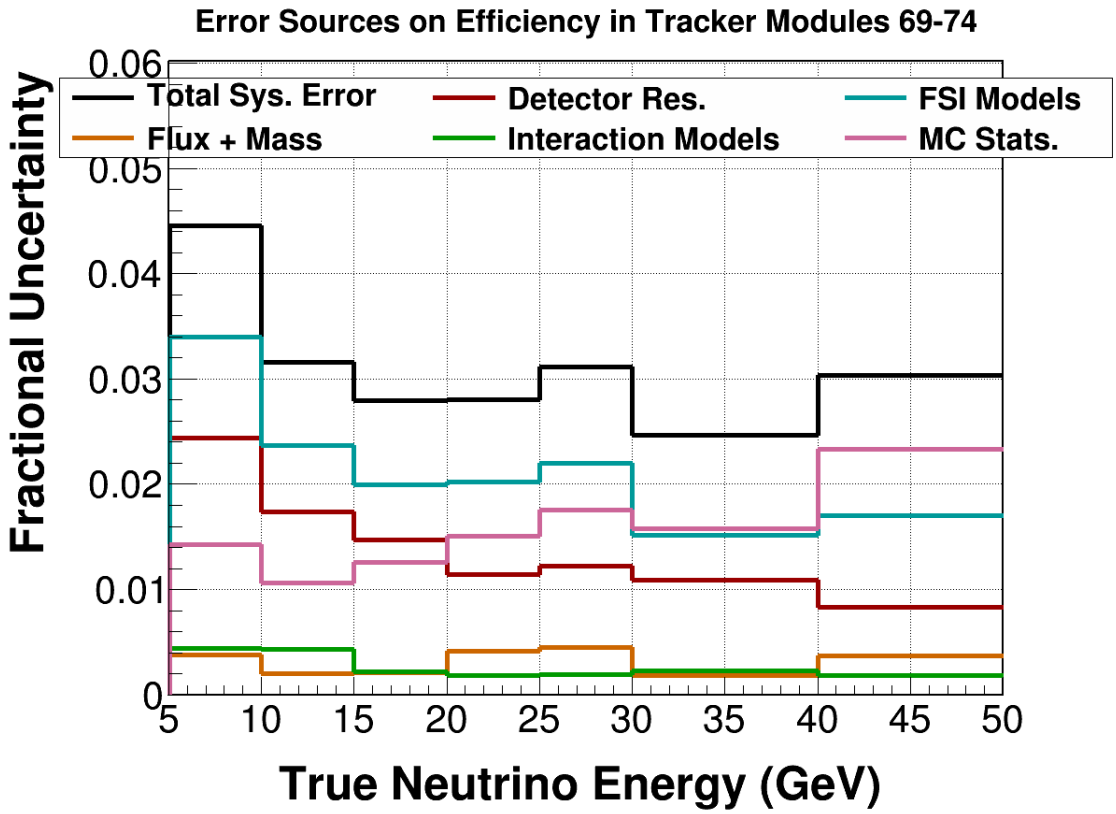

Figure G-56. Uncertainty on overall efficiency: tracker mods. 69-74 (E_ν)

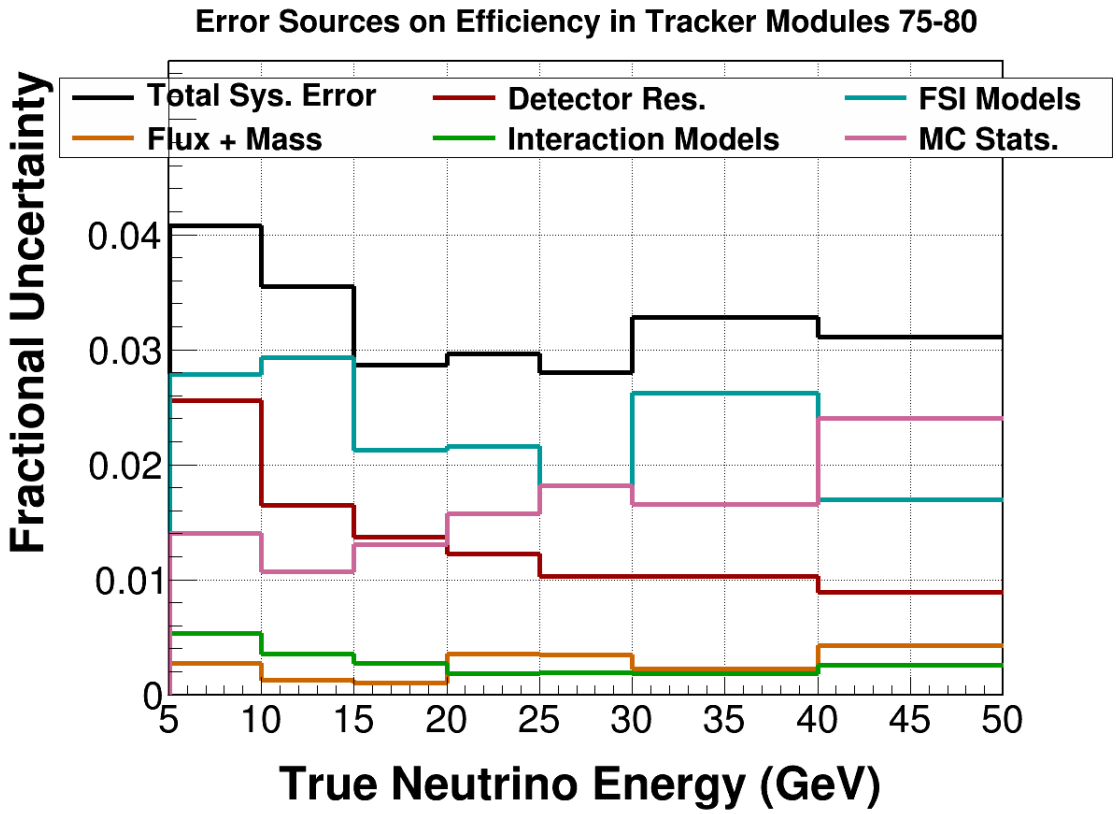

Figure G-57. Uncertainty on overall efficiency: tracker mods. 75-80 (E_ν)

The following plots show the uncertainty on the overall efficiency of DIS event selection. They are plotted as a function of true Bjorken-x (x_{bj}):

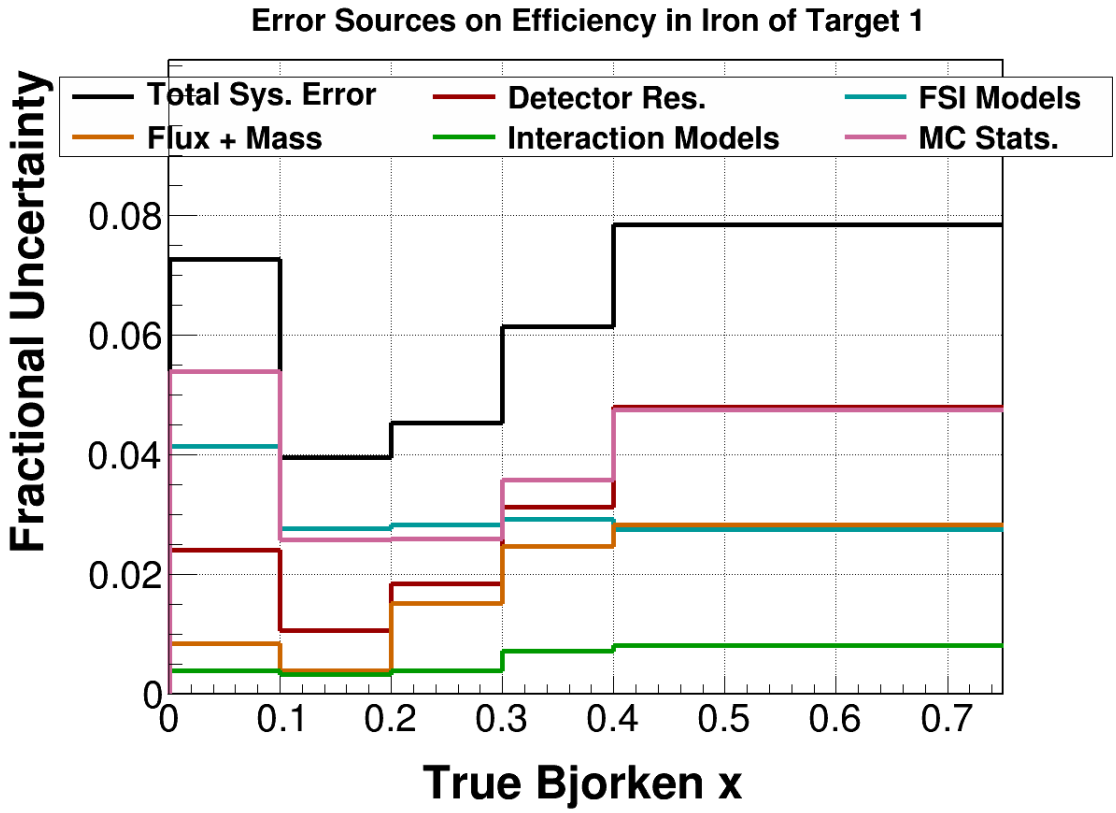

Figure G-58. Uncertainty on overall efficiency: target 01 Fe (x_{bj})

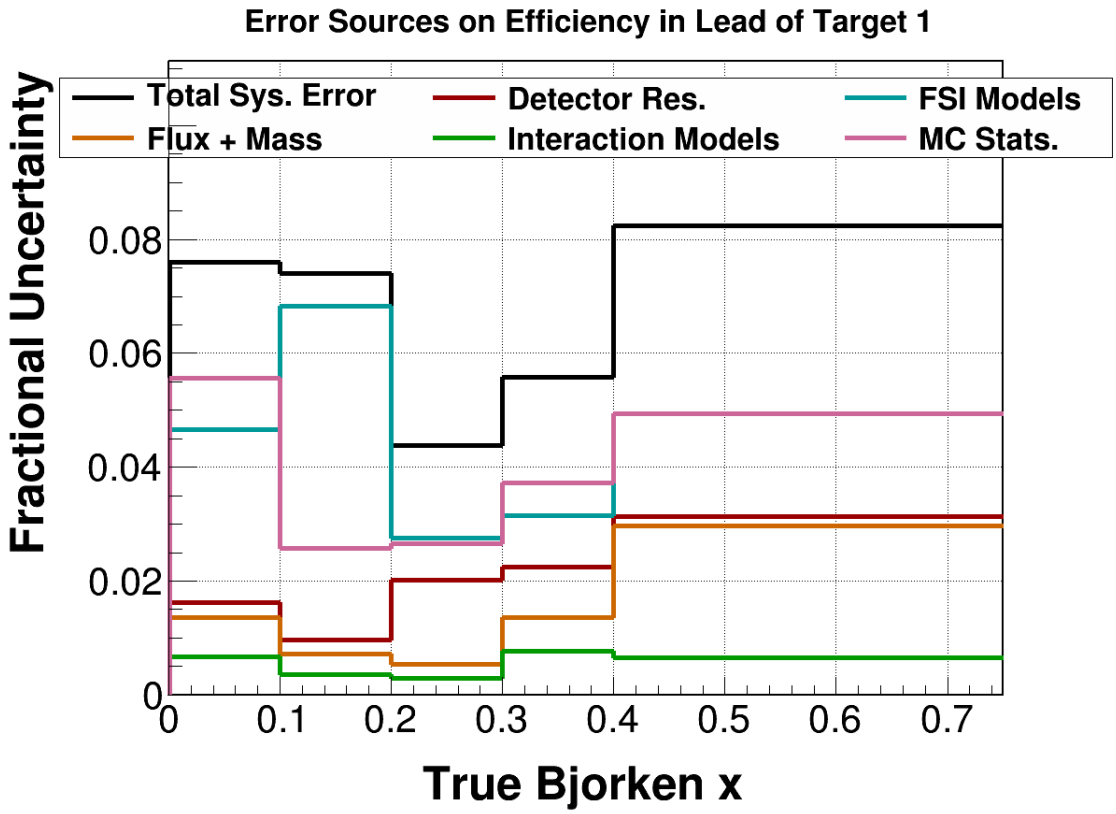

Figure G-59. Uncertainty on overall efficiency: target 01 Pb (x_{bj})

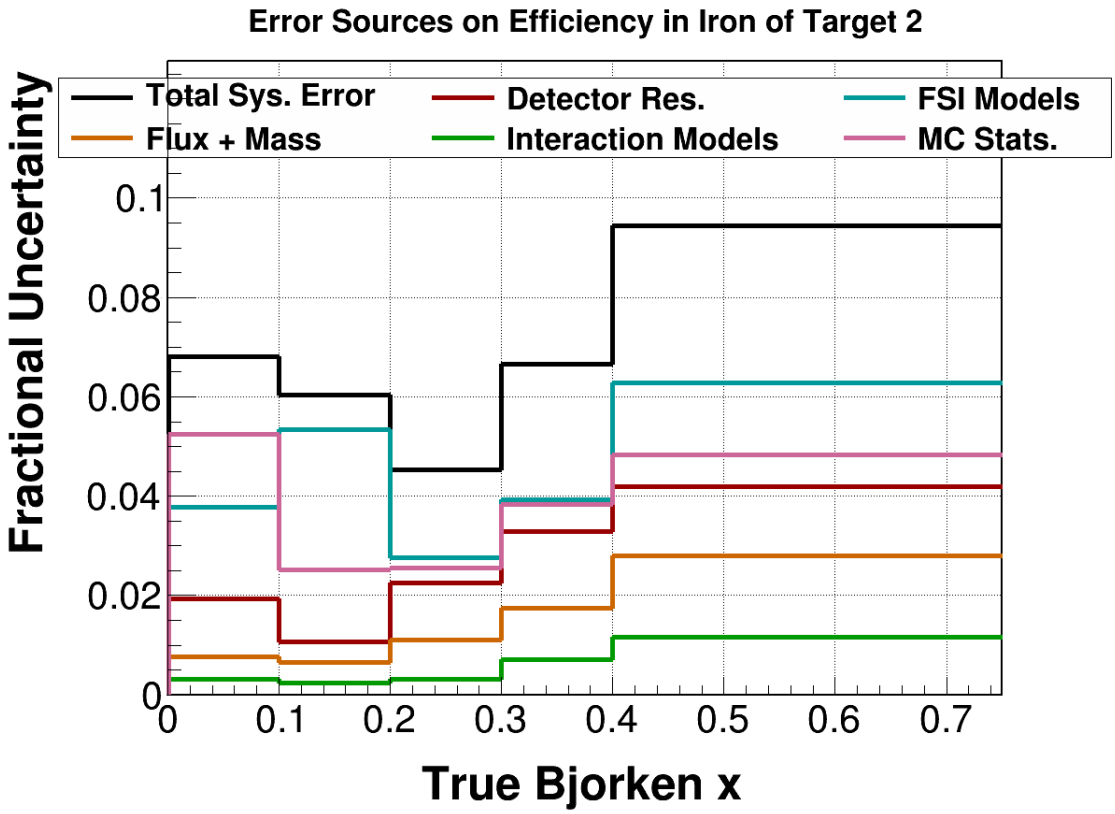

Figure G-60. Uncertainty on overall efficiency: target 02 Fe (x_{bj})

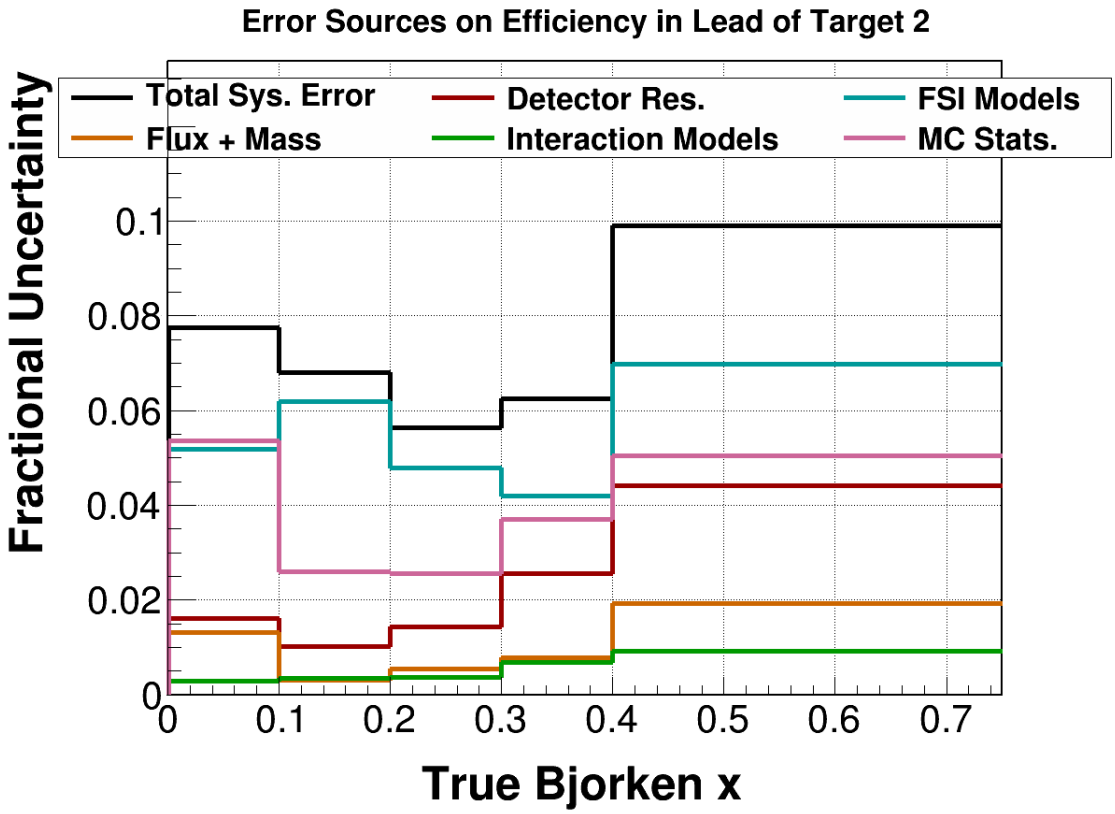

Figure G-61. Uncertainty on overall efficiency: target 02 Pb (x_{bj})

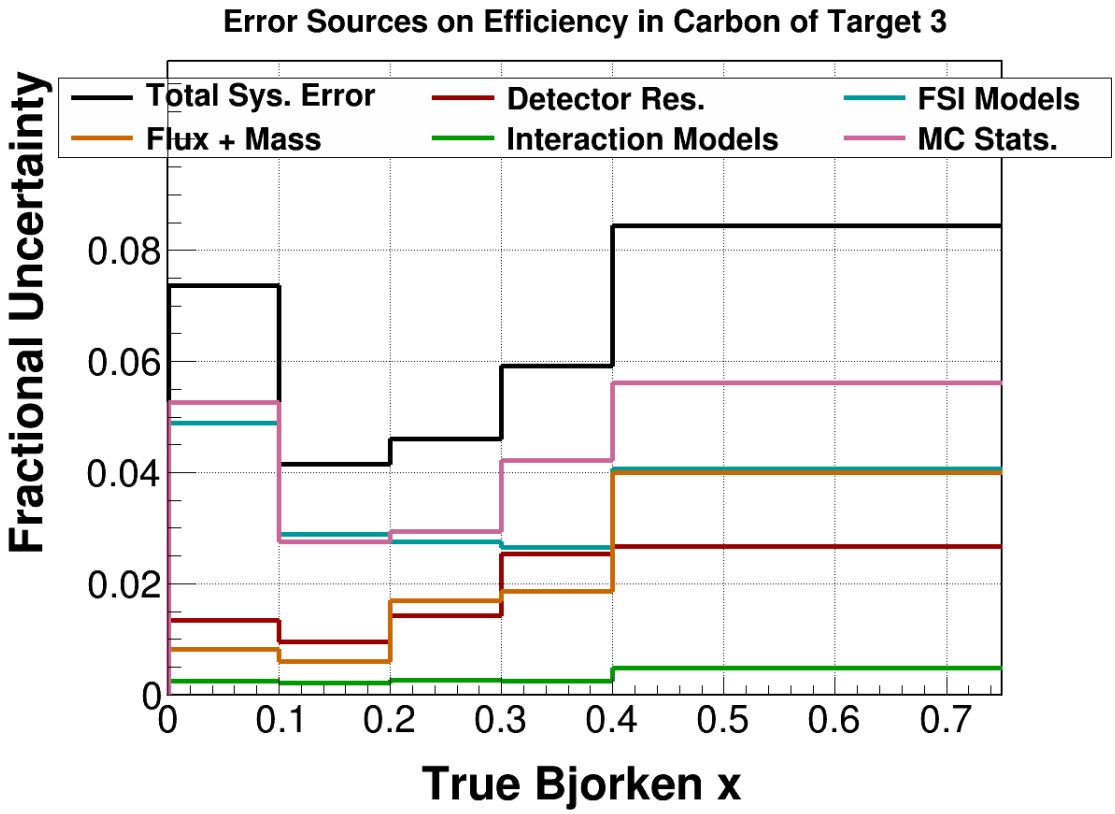

Figure G-62. Uncertainty on overall efficiency: target 03 C (x_{bj})

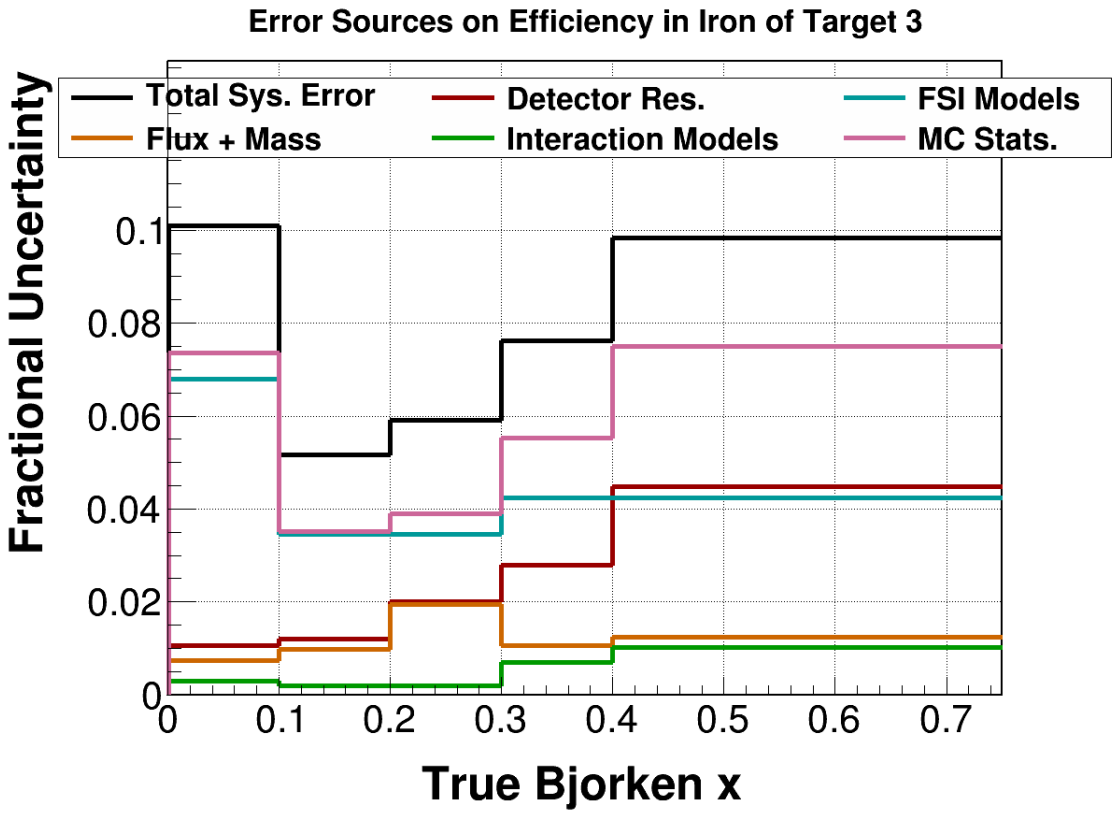

Figure G-63. Uncertainty on overall efficiency: target 03 Fe (x_{bj})

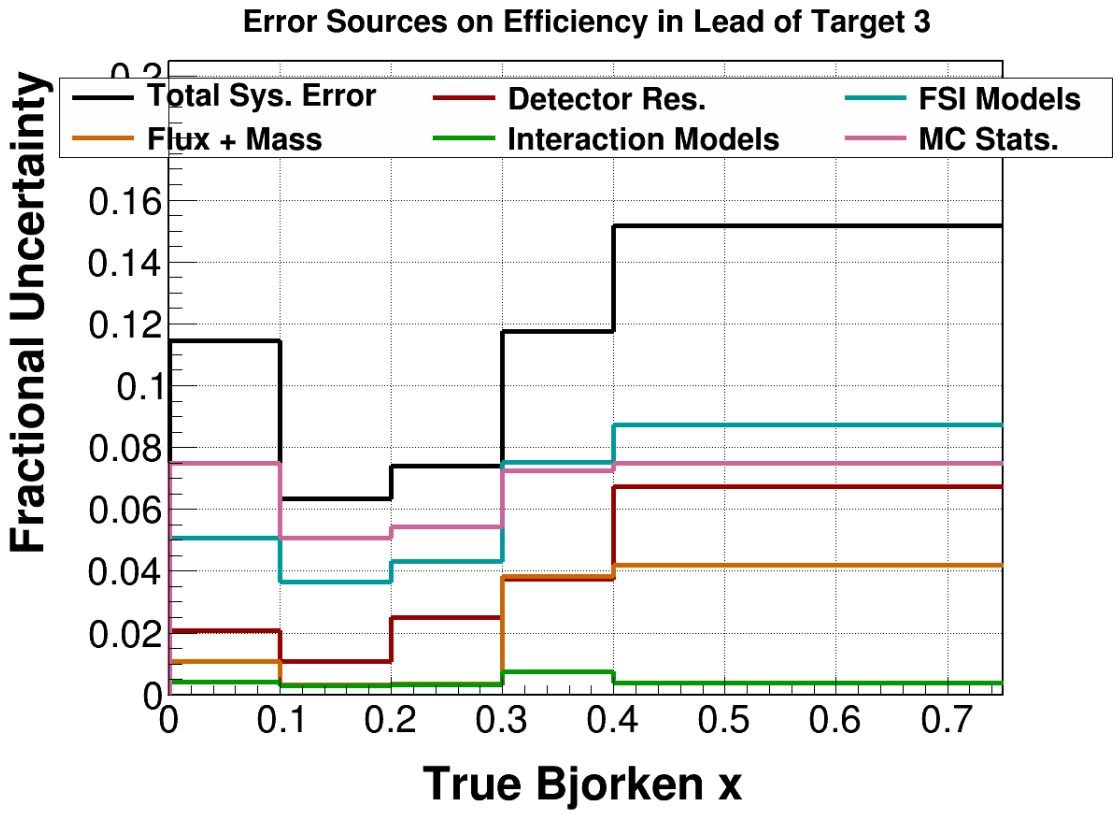

Figure G-64. Uncertainty on overall efficiency: target 03 Pb (x_{bj})

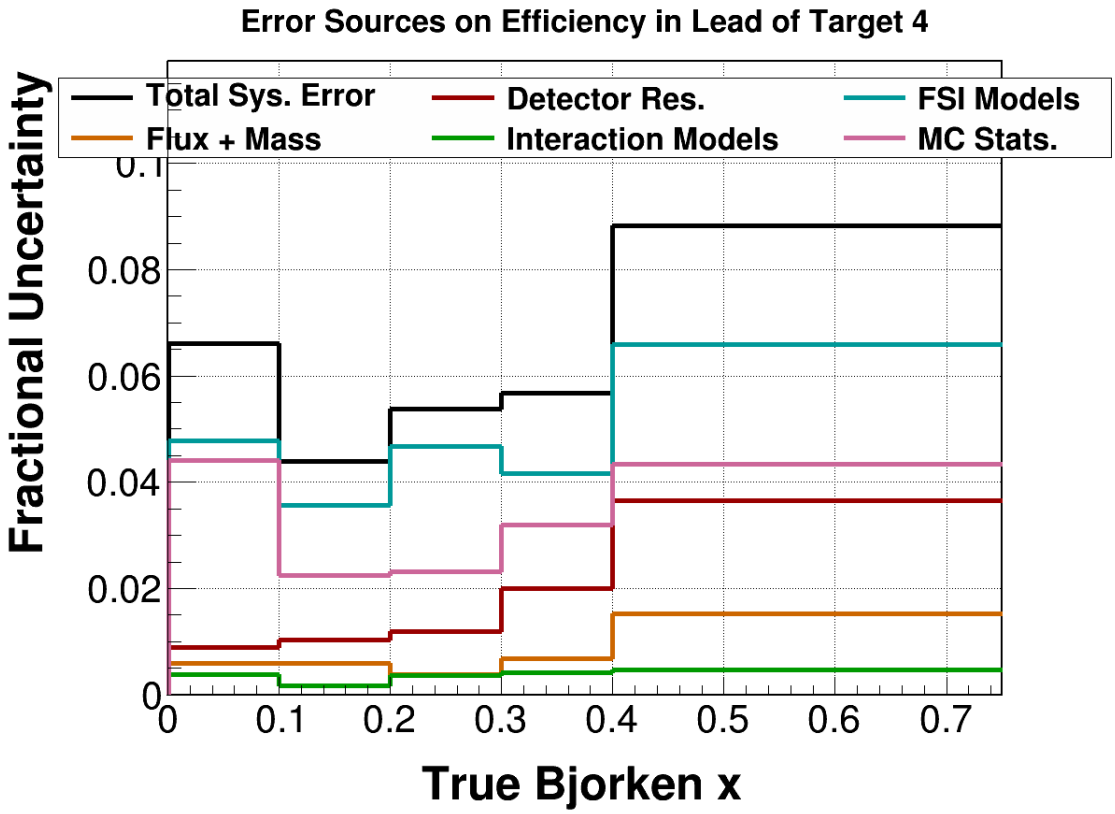

Figure G-65. Uncertainty on overall efficiency: target 04 Pb (x_{bj})

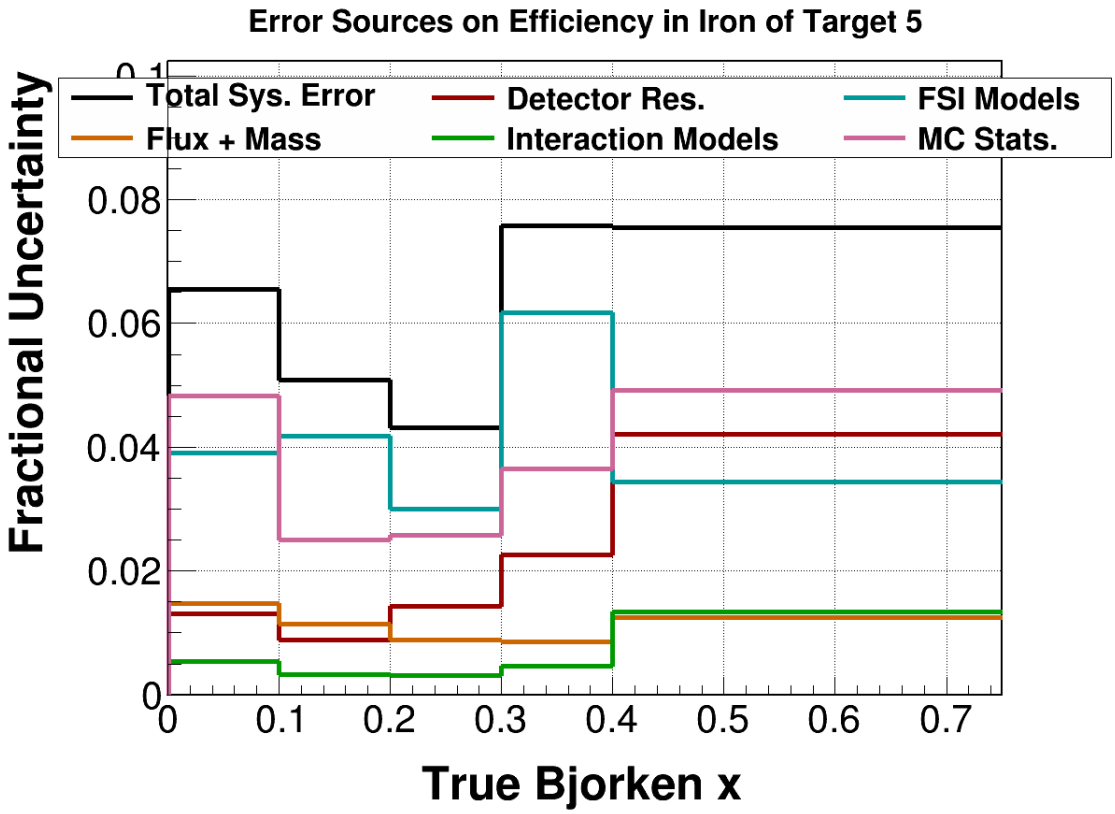

Figure G-66. Uncertainty on overall efficiency: target 05 Fe (x_{bj})

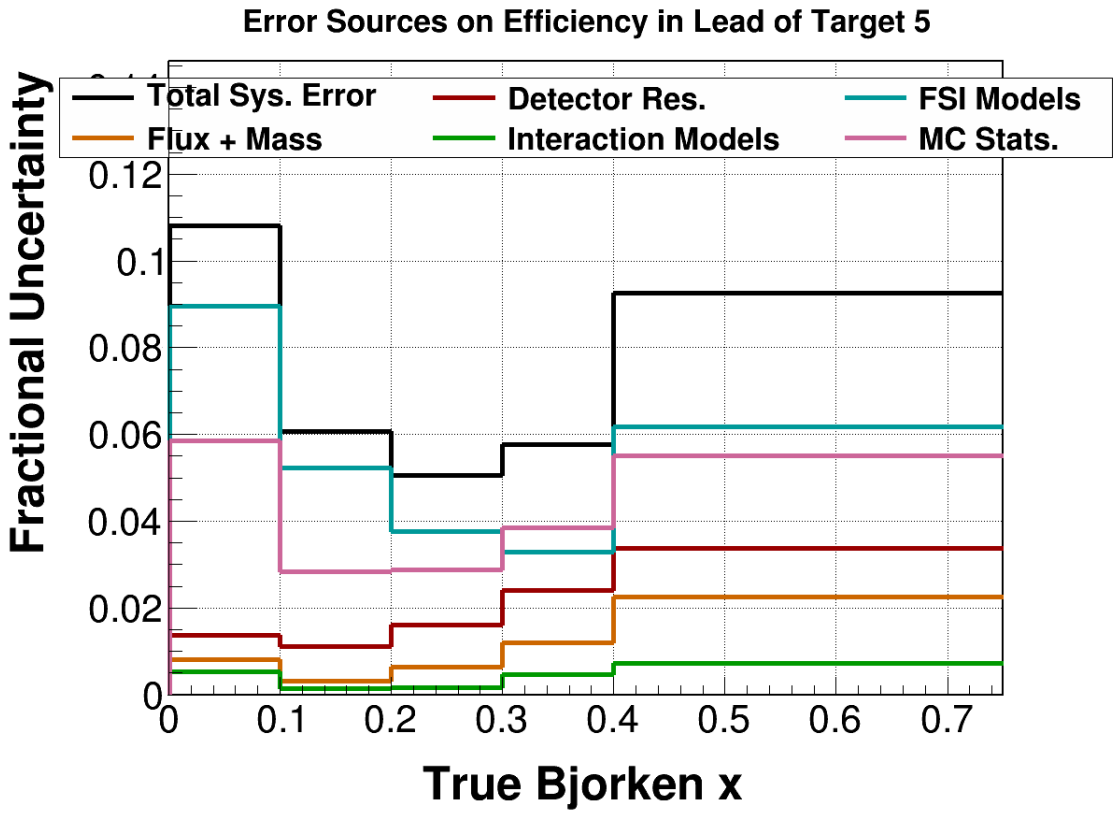

Figure G-67. Uncertainty on overall efficiency: target 05 Pb (x_{bj})

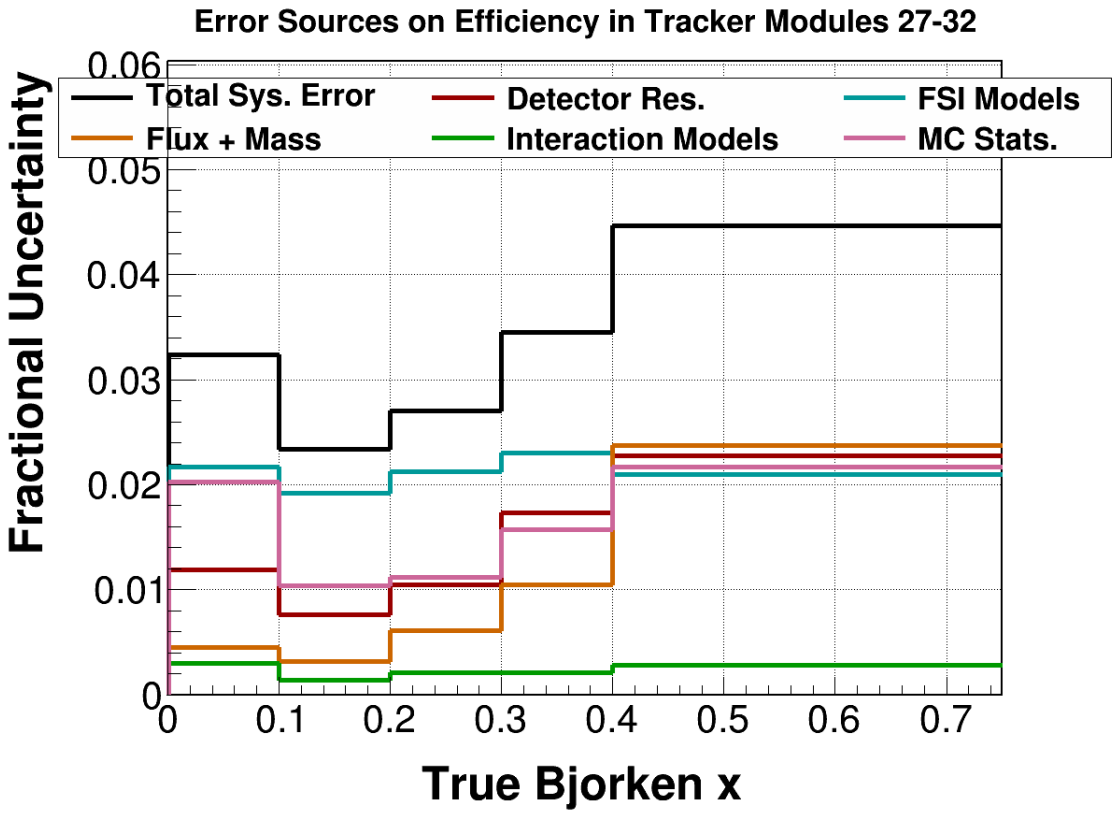

Figure G-68. Uncertainty on overall efficiency: tracker mods. 27-32 (x_{bj})

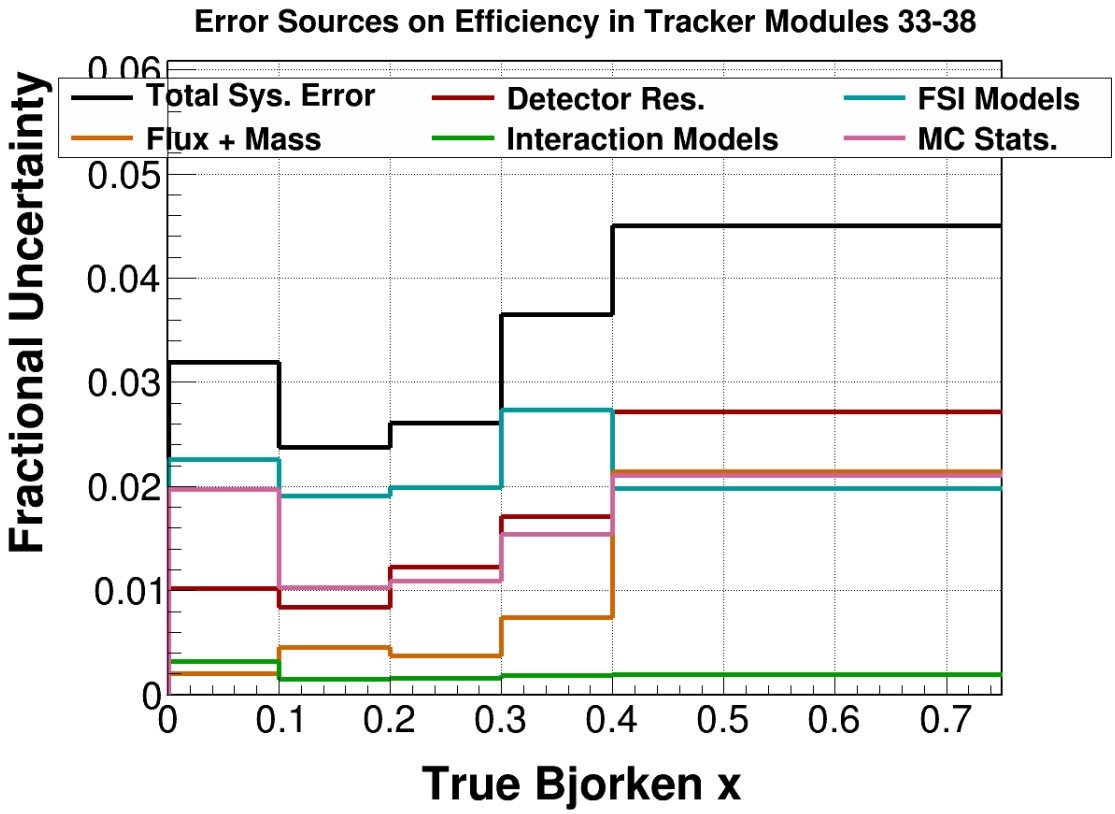

Figure G-69. Uncertainty on overall efficiency: tracker mods. 33-38 (x_{bj})

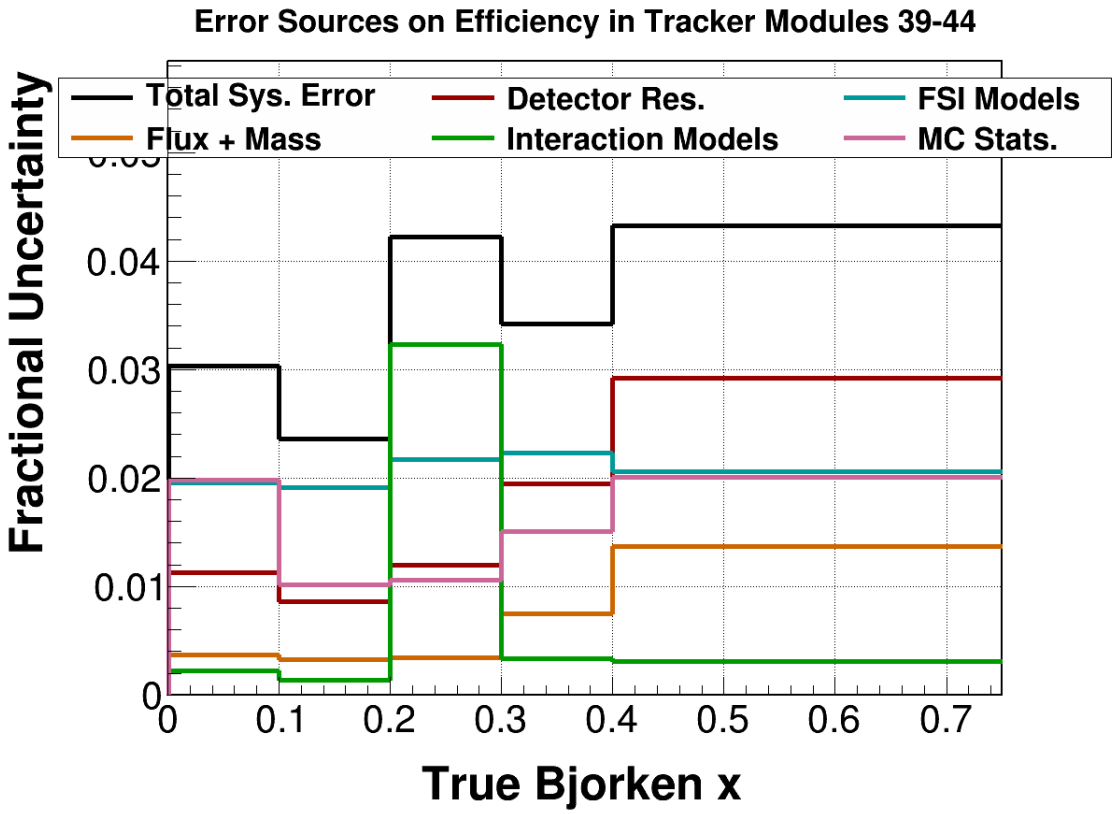

Figure G-70. Uncertainty on overall efficiency: tracker mods. 39-44 (x_{bj})

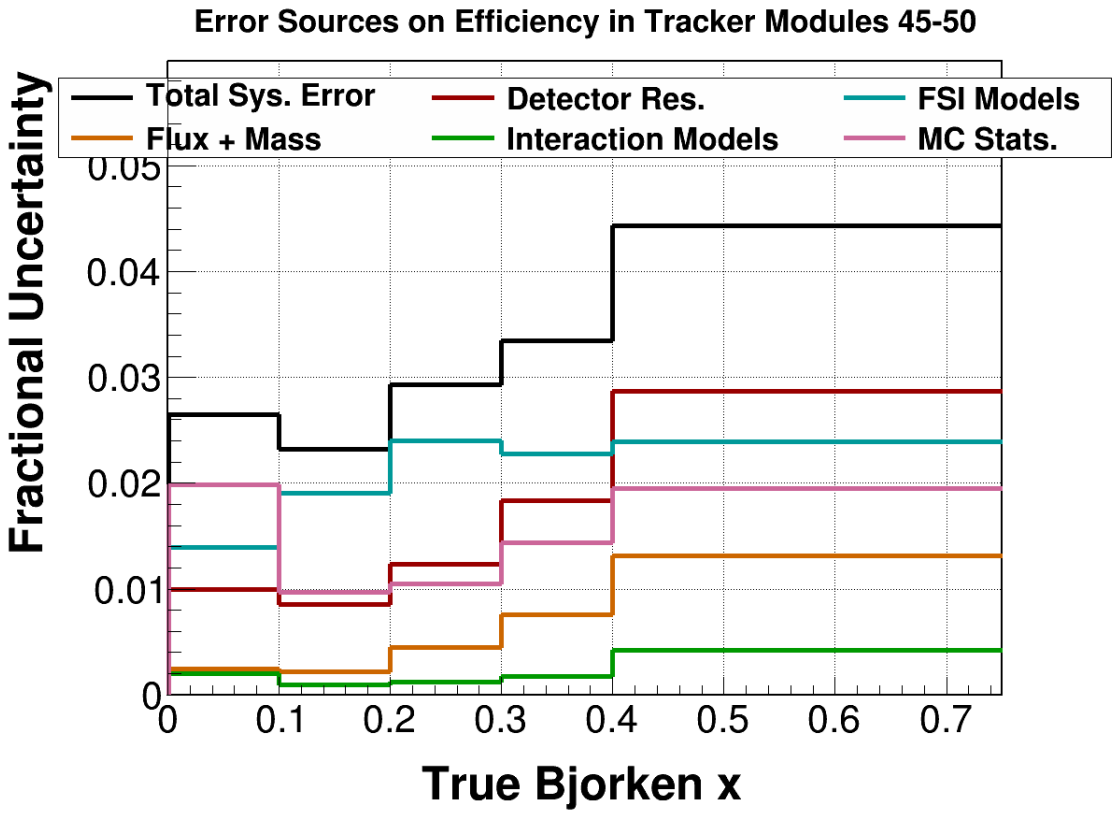

Figure G-71. Uncertainty on overall efficiency: tracker mods. 45-50 (x_{bj})

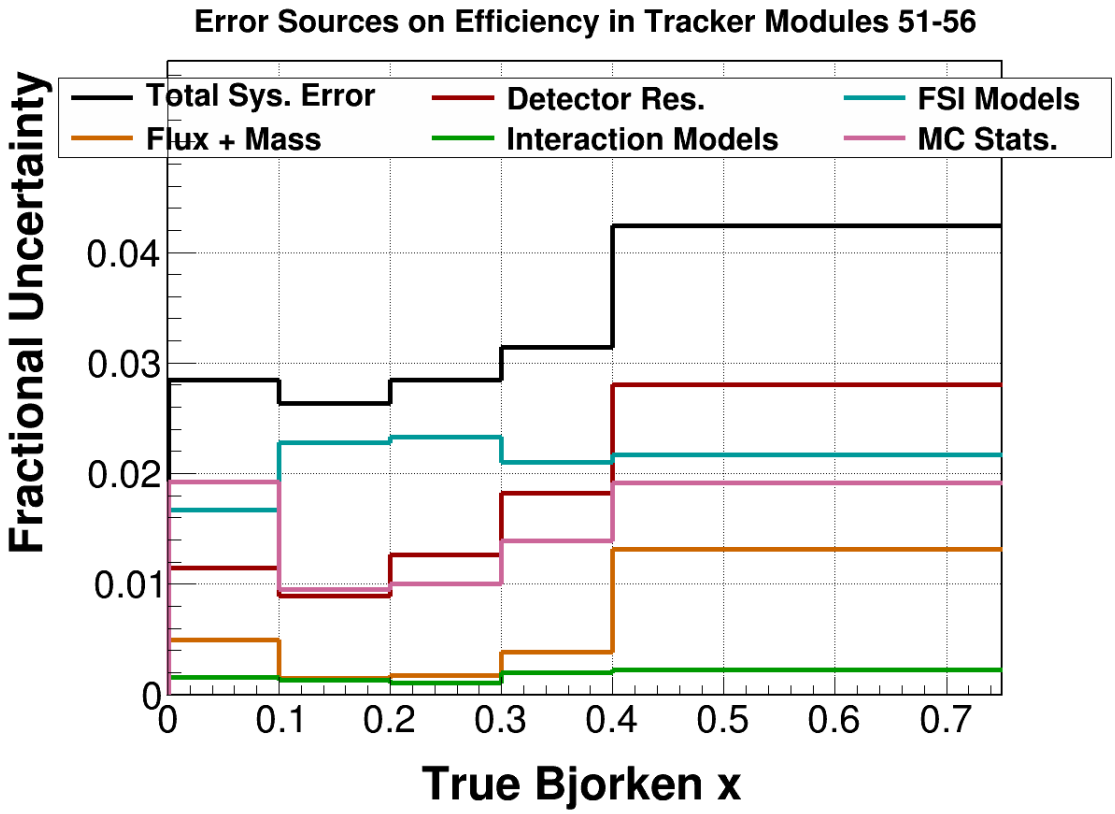

Figure G-72. Uncertainty on overall efficiency: tracker mods. 51-56 (x_{bj})

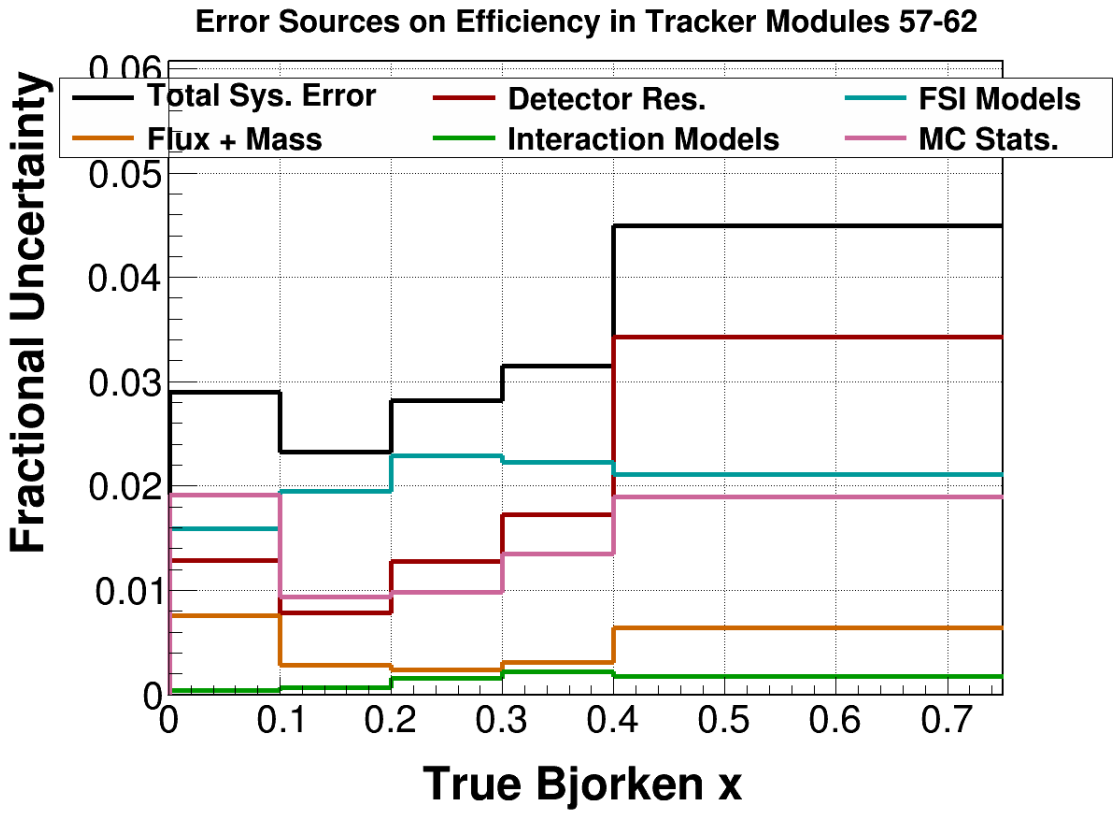

Figure G-73. Uncertainty on overall efficiency: tracker mods. 57-62 (x_{bj})

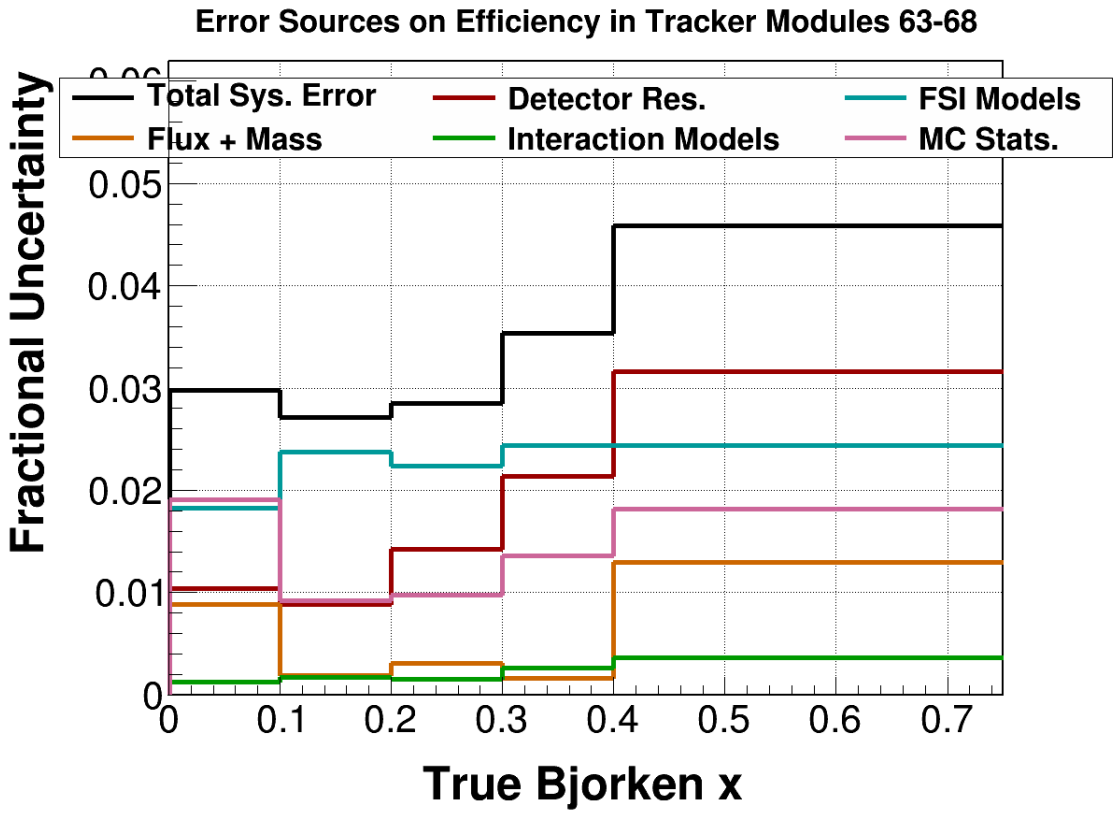

Figure G-74. Uncertainty on overall efficiency: tracker mods. 63-68 (x_{bj})

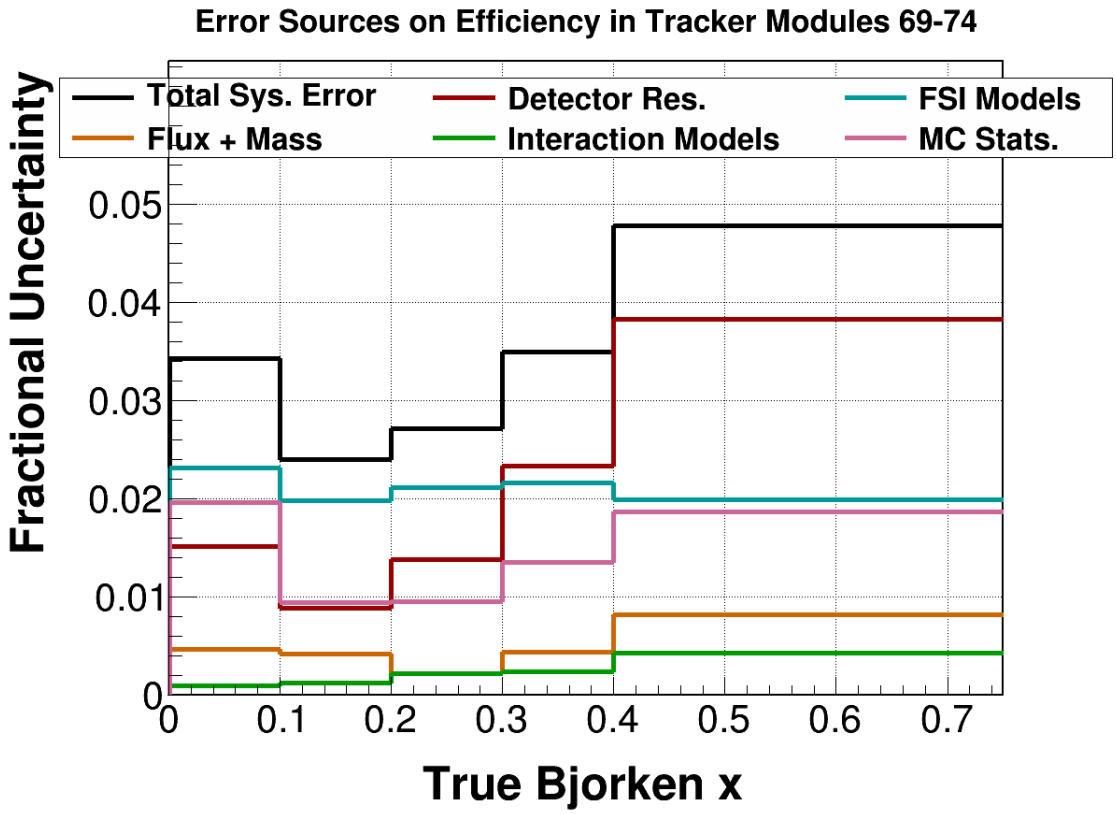

Figure G-75. Uncertainty on overall efficiency: tracker mods. 69-74 (x_{bj})

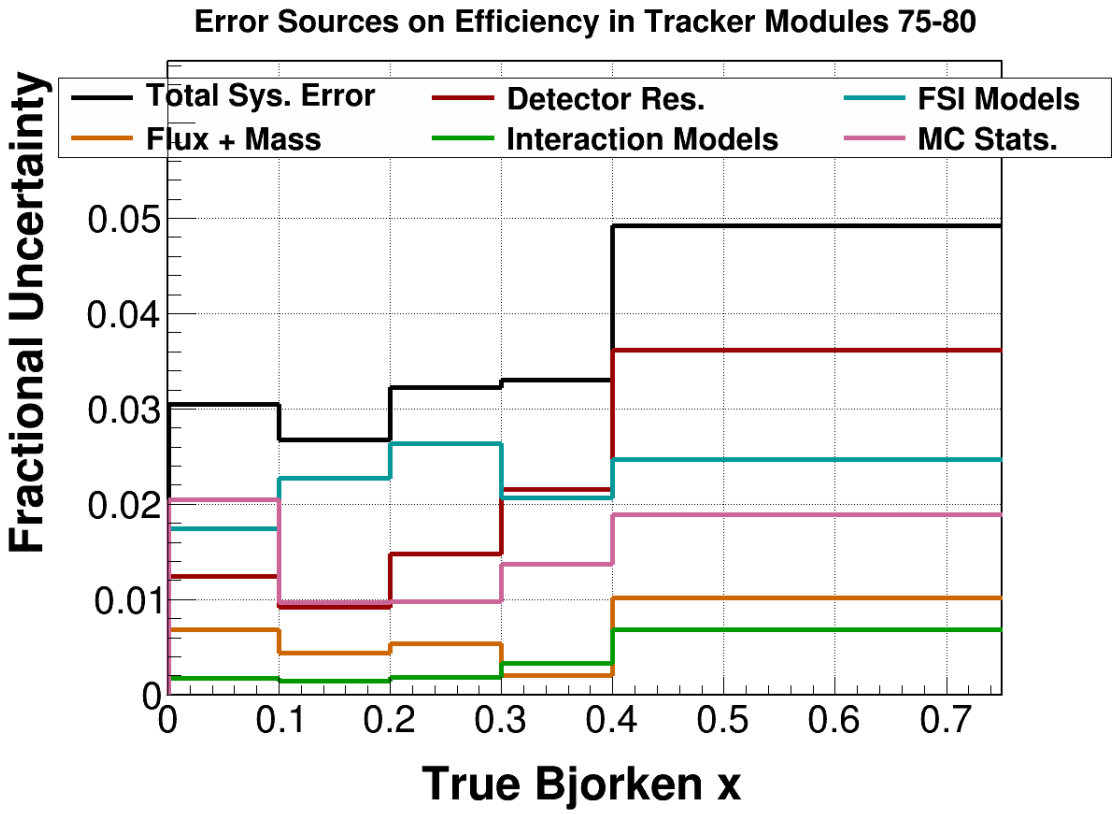

Figure G-76. Uncertainty on overall efficiency: tracker mods. 75-80 (x_{bj})

LIST OF REFERENCES

[1] K.A. Olive *et al.* [Particle Data Group], Chin. Phys. C **38**, 090001 (2014).

[2] As quoted by F. Reines in the Foreward: C. Sutton, *Spaceship Neutrino*, Cambridge University Press, (1992).

[3] Kohan *et al.*, "Self-radiolysis of tritiated water. A comparison of the effects of ^{60}Co γ-rays and tritium β-particles on water and aqueous solutions at room temperature," RCS Adv. **3**, 42 (2013).

[4] C. L Cowan Jr *et al.*, "Detection of the Free Neutrino: a Confirmation," Science **124** (3212) 1034 (1956).

[5] G. Danby *et al.*, "Observation of high-energy neutrino reactions and the existence of two kinds of neutrinos," Phys. Rev. Lett. **9**, 36 (1962).

[6] K. Kodama *et al.* [DONUT Collaboration], "Observation of tau neutrino interactions," Phys. Lett. B **504**, 3 (2001).

[7] Richard Slansky *et al.*, "The Oscillating Neutrino—An Introduction to Neutrino Masses and Mixing," Los Alamos Science **25** (1997).

[8] J.A. Formaggio [for the SNO Collaboration], "Twilight: Results from the 3rd and Final Phase of the SNO Exepriment," Fermilab Joint Experimental Theoretical Physics Seminar, July, 2008.

[9] B. Aharmim *et al.* [SNO Collaboration], "Electron energy spectra, fluxes, and day-night asymmetries of B-8 solar neutrinos from the 391-day salt phase SNO data set," Phys. Rev. C **72**, 055502 (2005). [arXiv:nucl-ex/0502021].

[10] C. Giunti and C. W. Kim *Fundamentals of Neutrino Physics and Astrophysics.* New York, NY: Oxford University Press, 2007.

[11] "Nuclear and Particle Physics - Lecture 16 Neutral kaon decays and oscillations," [Lecture16]

[12] M. Costanzi *et al.*, "Neutrino constraints: what large-scale structure and CMB data are telling us?," JCAP **1410**, (2014).

[13] [Welcome To Katrin] Accessed 5/28/15.

[14] C. S. Wu *et al.*, "Experimental Test of Parity Conservation in Beta Decay," Phys. Rev. **105**, 1413 (1957).

[15] F. T. Avignone *et al.*, "Double Beta Decay, Majorana Neutrinos, and Neutrino Mass," Rev. Mod. Phys. **80**, 481-516 2008.

[16] A. Garfagnini, "Neutrinoless Double Beta Decay Experiments," [arXiv:1408.2455]

[17] G. Pawel, "A Combined Limit for Neutrinoless Double-Beta Decay," [arXiv:1504.08285]

[18] J.L.Hewett *et al.*, "Fundamental Physics at the Intensity Frontier," [arXiv:1205.2671]

[19] D. Perevalov [for the NOvA Collaboration] "First Data from the NOvA Experiment," A presentation at the XXIV Workshop on Weak Interactions and Neutrinos, [http://indico.cern.ch/event/234536/session/1/contribution/11/material/slides/0.pdf].

[20] J. Park [for the MINERvA Collaboration], "Direct Measurement of the NuMI Flux with Neutrino-Electron Scattering in MINERvA," Fermilab Joint Experimental Theoretical Physics Seminar, December, 2013.

[21] A. Higuera *et al.*, [MINERvA Collaboration] "Measurement of Coherent Production of $\pi^{\pm}$ in Neutrino and Anti-Neutrino Beams on Carbon from E_{ν} of 1:5 to 20 GeV," Phys .Rev. Lett. **113**, 261802 (2014).

[22] A. A. Aguilar-Arevalo *et al.* [MiniBooNE Collaboration], "A Search for Electron Antineutrino Appearance at the Delta m**2 1-eV**2 Scale," Phys. Rev. Lett. **103**, (2009).

[23] A. A. Aguilar-Arevalo *et al.* [MiniBooNE Collaboration], "First measurement of the muon antineutrino double-differential charged-current quasielastic cross section," Phys. Rev. D **88**, (2013).

[24] J. D .Bjorken,"Asymptotic Sum Rules at Infinite Momentum," Phys. Rev. **179**, 1547 (1969).

[25] J. I. Friedman and H. W. Kendall, "Deep Inelastic Scattering," Annu. Rev. Nucl. Sci., (1972).

[26] B. Carithers and P. Grannis. "Discovery of the Top Quark," Beam Line (SLAC) 25 **3**, (1995).

[27] Aneesh V. Manohar, "Spin Dependent Deep Inelastic Scattering," [hep-ph/9204208v1].

[28] A. Bodek, *et al.*, "Improved low Q^2 model for neutrino and electron nucleon cross sections in few GeV region," Nucl. Phys. Proc. Suppl. **139**, 113 (2005).

[29] B. Z. Kopeliovich *et al.*, "Nuclear Shadowing in Electro-Weak Interactions," Prog. Part. Nucl. Phys. **68**, 314 (2013).

[30] K. Eva-Maria [New Muon], "Final results from the NMC," AIP Conf.Proc. **407**, 291 (1997).

[31] J.J. Aubert *et al.*, "The ratio of the nucleon structure functions F_2^N for iron and deuterium,". Phys. Lett. B **123**, 275278 (1983).

[32] D. Higinbotham *et al.*, "The EMC effect still puzzles after 30 years," CERN Courier, April 26th 2013.

[33] I. C. Cloet, "EMC and Polarized EMC Effects in Nuclei," Phys. Lett. **B642**, 210-217 (2006).

[34] K. Rith, "Present Status of the EMC effect," [arXiv:1402.5000 [hep-ex]].

[35] R. G. Arnold *et al.* [SLAC-E139], Phys. Rev. Lett. **52**, 727 (1984).

[36] J. Gomez *et al.* [SLAC-E139], Phys. Rev. D **49**, 4348 (1994).

[37] R. Eckhardt, "Stan Ulam, John Von Neumann and the Monte Carlo Method," Los Alamos Science **15**, 3 (1987).

[38] C. Andreopoulos *et al.*, "The GENIE Neutrino Monte Carlo Generator," Nucl. Instrum. Meth. **A614**, 87-104 (2010).

[39] J. Mousseau, "A MINERvANs Guide to GENIE," MINERνA internal technical document, DocDB 9444.

[40] G. D. Harp, "Extension of the isobar model for intranuclear cascades to 1 GeV," Phys. Rev. **10** 6, 2387-2396 (1974).

[41] C. Anderson *et al.* [ArgoNeuT collaboration], 'The ArgoNeuT Detector in the NuMI Low-Energy beam line at Fermilab," JINST 7 P10019 (2012).

[42] D. Ayers *et al.* [NOvA collaboration], "NOvA Proposal to Build a 30 Kiloton Off-Axis Detector to Study Neutrino Oscillations in the Fermilab NuMI Beamline," FERMILAB-PROPOSAL-0929 (2004).

[43] B. Worthel *et al.*, Booster Rookie Book, [http://www-bdnew.fnal.gov/operations/rookie_books/].

[44] Fermi National Accelerator Laboratory, "The Fermilab Main Injector Technical Design Handbook," *FERMILAB-DESIGN-1994-01,* (1994).

[45] Fermi National Accelerator Laboratory, "The NuMI Technical Design Handbook: Chapter 2," [http://www-numi.fnal.gov/numwork/tdh/TDH_V2_2_Overview.pdf].

[46] Fermi National Accelerator Laboratory, "The NuMI Technical Design Handbook: Chapter 4," [http://www-numi.fnal.gov/numwork/tdh/TDH_V2_4.2.3-Target.pdf].

[47] K. Hurtado, "Special Run Plots," MINERνA internal technical document, DocDB 7218.

[48] S. E. Kopp, "The NuMI neutrino beam at Fermilab," [arXiv:physics/0508001].

[49] R. Zwaska, "Accelerator Systems and Instrumentation for the NuMI Neutrino Beam," PhD thesis, University of Texas at Austin, 2005.

[50] D. A. Harris. "Constraining the NuMI Flux," A presentation at 9th International Workshop on Neutrino-Nucleus Interactions in the Few-GeV Region, [http://www.hep.ph.ic.ac.uk/ wascko/nuint14/talks/5.3.1_harris_20140523.pdf].

[51] S. Agostinelli *et al.* [Geant4 collaboration], "G4a Simulation Toolkit," Nucl. Inst. and Meth., Phys. Res. Sect. A **506**, 250303 (2003).

[52] Raja Rajendra. "Proposal to measure particle production in the Meson area using Main Injector primary and secondary beams P-907," Fermilab PAC presentation, [http://www-mipp.fnal.gov/Proposal/P01_PAC_Presentation.pdf].

[53] R. P. Feynman, "Very High-Energy Collisions of Hadrons, Phys. Rev. Lett. **23**, 14151417 (Dec, 1969).

[54] Eur. Phys. **49**, 897-917 (2007).

[55] N. Abgrall *et al.*, "Hadron Production Measurements for Fermilab Neutrino Beams,"CERN-SPSC-2014-032 / SPSC-P-330-ADD-7 14/10/2014

[56] J. M. Paley *et al.* [MIPP Collaboration], "Measurement of Charged Pion Production Yields off the NuMI Target," Phys. Rev. D **90** no. 3, 032001 (2014)

[57] L. Aliaga, "Approved Flux Slides and Plots," MINERνA internal technical document, DocDB 9472.

[58] Ž. Pavlović, "Observation of Disappearance of Muon Neutrinos in the NuMI Beam," PhD Thesis, University of Texas at Austin, 2008.

[59] L. Fields, "Resurrection Flux and Error Plots," MINERνA internal document. DocDB 10294.

[60] L. Aliaga *et al.* "Design, Calibration, and Performance of the MINERvA Detector," Nucl. Instrum. Meth. **743C**. 130-159, (2014).

[61] Minerva Technical Design Report. Chapter 3 and 4. FERMILAB-DESIGN-2006-01.

[62] ChemSpider: [Chemical-Structure.6838] Accessed 6/16/15.

[63] ChemSpider: [Chemical-Structure.14960] Accessed 6/16/15.

[64] J. Mousseau and H. Ray."Veto Wall Efficiency Studies," MINERνA internal technical document, DocDB 8176.

[65] B. Tice *al.* [MINERvA Collaboration], "Measurement of Ratios of ν_μ Charged-Current Cross Sections of C, Fe, and Pb to CH at Neutrino Energies 2–20 GeV," Phys. Rev. Lett. **112**, 231801 (2014).

[66] D. G. Michael *et al.*, [MINOS Collaboration], "The magnetized steel and scintillator calorimeters of the MINOS experiment," Nucl. Instrum. Meth. **A596**, 190-228 (2008).

[67] G. N. Perdue *et al.* [MINERvA Collaboration], "The MINERνA Data Acquisition System and Infrastructure," Nucl. Instrum. Meth. **694**, 179-192 (2012).

[68] J.B. Birks, "Scintillations from organic crystals: Specific fluorescence and relative response to different radiations," Proceedings of the Physical Society, Section A **64(10)**, 874 (1951).

[69] B. Eberly, "PMT Simulation," MINERνA internal technical document, DocDB 4789.

[70] N. Tagg *et al.* [MINERvA Collaboration], "Arachne— A web-based event viewer for MINERvA," Nucl. Instrum. and Meth. **676**, 44-49 (2012).

[71] J. Chovka, "Anti-Neutrino Charged Current Quasi-Elastic Scattering in MINERνA," PhD Thesis, University of Rochester, 2012.

[72] B. Eberly, "Characterization of Final State Interaction Strength in Plastic Scintillator by Muon-Neutrino Charged Current Charged Pion Production," PhD Thesis, University of Pittsburgh, 2014.

[73] B. Tice, "Measurement of Nuclear Dependence in Inclusive Charged Current Neutrino Scattering," PhD Thesis, Rugers, The State University of New Jersey, 2014.

[74] R. Frühwirth, "Application of kalman filtering to track and vertex fitting," Nucl. Inst. and Meth. **262(2-3)**, 444-450 (1987).

[75] E.J. Wolin and L.L. Ho, "Covariance matrices for track fitting with the Kalman filter," Nucl. Inst. and Meth. **392**, 493-500 (1993).

[76] W. Waltenberger, "Adaptive vertex reconstruction," Technical Report CMS-NOTE-2008-033, CERN Geneva (2008).

[77] J. Beringer *et al.* [Particle Data Group], "Review of particle physics," Phys. Rev. D. **86:0100001**, (2012).

[78] J. Mousseau, "E_μ Resolutions part 2: The Return of E_μ," MINERνA internal technical document, DocDB 9920.

[79] J. Mousseau, "Optimizing High Momentum MINOS Muon Selection," MINERνA internal technical document, DocDB 10154.

[80] J. Devan, "Calorimetry Note," MINERνA internal technical document, DocDB 7712.

[81] J. Mousseau [for the MINERvA Collaboration]"Neutrino Nucleon Deep Inelastic Scattering," A presentation at XXIII International Workshop on Deep Inelastic Scattering and Related Subjects, [https://indico.cern.ch/event/341292/session/11/contribution/158/material/slides/0.pdf].

[82] B. Tice, "Analysis of Charged Current Neutrino Interactions on Nuclear Targets," MINERνA internal technical document, DocDB 8854.

[83] B. Tice, "Acceptance Correction Nuclear Targets Update," MINERνA internal technical document, DocDB 8407.

[84] B Tice, "Mass and tracking issues," MINERνA internal technical document, DocDB 8824.

[85] J. Mousseau, "GENIE Cross Section Weight Note," MINERνA internal technical document, DocDB 7565.

[86] G. D'Agostini, "A multidimensional unfolding method based on Bayes' theorem," Nucl. Inst .and Meth., 487-498 (1995).

[87] M. Wospakrik, "Dude, where are my 4500 - 6000 ns target events?," MINERνA internal technical document, DocDB 10849.

[88] B. Tice "ROOT Analysis Tools," presented at MINERνA 101, MINERνA internal technical document, DocDB 10028.

[89] P. Rodriquez and B. Tice, "Extracting Cross Sections from a GENIE Event Sample," MINERνA internal technical document, DocDB 8849.

BIOGRAPHICAL SKETCH

Joel Mousseau earned his Bachelor of Science with an honors concentration in physics and a minor in mathematics from the University of Michigan in 2007. He was awarded a Master of Science from the University of Florida in 2009, and finally his Doctor of Philosophy in physics from the University of Florida in 2015.